TECHNOLOGY • RESEARCH HIGHLIGHTS • VISIONS • SCIENCE

261

Baltica X

International Conference on Life Management and Maintenance for Power Plants

VTT TECHNOLOGY 261

Baltica X

International Conference on Life Management and Maintenance for Power Plants

Helsinki–Stockholm–Helsinki

7–9 June, 2016

Edited by Pertti Auerkari

ISBN 978-951-38-8435-2 (USB)
ISBN 978-951-38-8436-9 (URL: http://www.vttresearch.com/impact/publications)

VTT Technology 261

ISSN-L 2242-1211
ISSN 2242-122X (Online)
http://urn.fi/URN:ISBN:978-951-38-8436-9

JULKAISIJA – UTGIVARE – PUBLISHER

Teknologian tutkimuskeskus VTT Oy
PL 1000 (Tekniikantie 4 A, Espoo)
02044 VTT
Puh. 020 722 111, faksi 020 722 7001

Teknologiska forskningscentralen VTT Ab
PB 1000 (Teknikvägen 4 A, Esbo)
FI-02044 VTT
Tfn +358 20 722 111, telefax +358 20 722 7001

VTT Technical Research Centre of Finland Ltd
P.O. Box 1000 (Tekniikantie 4 A, Espoo)
FI-02044 VTT, Finland
Tel. +358 20 722 111, fax +358 20 722 7001

Cover image: Fortum, photo by Hans Ekestang

Preface

The Baltica Conferences on Plant Life Management and Maintenance have been held triannually since 1988, often with profound changes between the occasions. In 1988 coal and Soviet Union appeared well entrenched, SOx/NOx removal was an issue rather than CO_2, and just two years earlier Chernobyl had changed the agenda for nuclear power. Again today we are living in a transition: in spite of some capacity under construction, there are concerns about the sufficiency of electricity supply, as much of the conventional capacity has lost economic justification to subsidised renewables that could be minimally available at the time of peak demand (Figure 1), and the increasing intermittency of renewable production is threatening the means to supply the balance with the existing fleets. In North America cheap shale gas (about 2 USD/MMBtu) helps to reduce such challenges through a shift from coal to gas, but in Europe the same option is generally not available. Furthermore, the competitive position of conventional combined heat and power (CHP) production is also under pressure like never before. These and many other concerns highlight the need for new solutions to manage not only the regular routines in plant operation and maintenance, but also the productive availability of ageing plants and the risk of unexpected events, developments and their consequences. Numerous related aspects consistent with the Baltica tradition can be seen in the Proceedings, addressing e.g. the condition, life and integrity assessment of plant components, inspections and other characterization, and impact of materials and operating conditions on plant and component performance.

For their effort, the authors and presenters of the papers fully deserve our sincere appreciation. It is the dedication producing the papers, presentations and discussions among professionals that has always created the essential value to the Baltica Conferences. The organizers are grateful to the Baltica X sponsors (in alphabetical order) Fortum, Helen and TVO, as their kind support has helped much to facilitate realising the occasion.

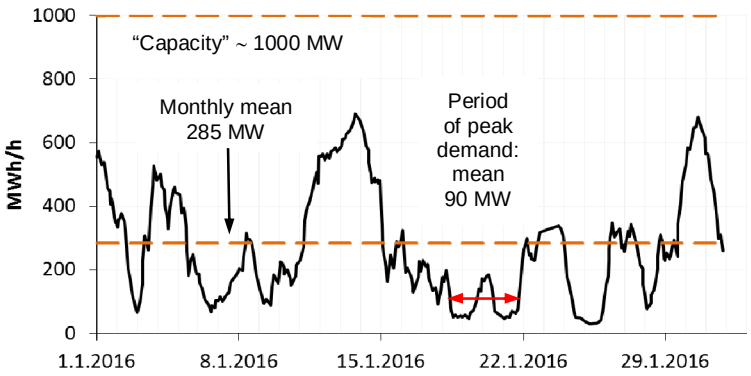

Figure 1. Availability of wind power in Finland (January 2016, data source: Fingrid).

Pertti Auerkari
VTT Technical Research Centre of Finland Ltd

Contents

Power & process: RBI and its implementation

prEN 16991: The new European standard on Risk-Based Inspection (RBI)
Arthur Carlebur, Aleksandar Jovanovic, Flor Angela Quintero & Mehmood Ahmad

Implementing the principles of VGB-S-506 in risk-based inspection and maintenance in a German power plant
Aleksandar Jovanovic, Stefan Husta, Jörg Bareiß, Klaus Metzger & Karl Maile

Full-scale implementation of an integrated RBI-RCM system in a refinery
Svetozar Eremic, Aleksandar Jovanovic, Stefan Husta & Nikola Markovic

RBI in power generation
Alan Bissell, Sophy Dipela, Shanil Narain Singh, Tshifhiwa Nevuwari & Marthinus Bezuidenhout

Large-scale application of RBI and maintenance on the national level: Experiences and lessons learned
Aleksandar Jovanovic, Stefan Husta & Petar Stanojevic

Life time extension project to high pressure polyethylene plant
Marko Api, Ismo Savallampi & Somaina Odiah

RBI application in a CHP plant
Pertti Auerkari, Ulla McNiven & Stefan Husta

Power & process: Steam plant performance

Microstructural features of aged steam piping affected by creep and graphitisation and their detection
Bianca van Niekerk

Monitoring and in-service experiments on plants
Satu Tuurna & Pekka Pohjanne

Improving passivation of carbon steel in steam cycles of power plants with a film forming amine
Essi Jäppinen, Timo Saario & Konsta Sipilä

The structural stability of weld joint of P92 and CB2 steels under creep conditions
Josef Kasl, Dagmar Jandová & Eva Chvostová

Power & process: Turbines & turbine materials

Restoring steam turbine dimensions, tolerances and efficiency
Juha Sipilä, Juha Rintala & Pertti Auerkari

Assessment of metal conditions and ability for further operation of ageing steam turbine rotors
Andrei Dedov, Ivan Klevtsov, Toomas Lausmaa & Aleksandr Hlebnikov

Fatigue performance of steam turbine blading
Juha Viuhko, Jarmo Ivaska, Pertti Auerkari & Jarkko Metsäjoki

Fatigue performance of blade steel T671 for different kinds of loading
Jaromír Janoušek, Stanislav Hřeben, Zbynek Špirit, Josef Strejcius & Josef Kasl

Power & process: (small scale) testing & analysis

Determination of current mechanical properties of components in service using sub-sized specimens
Pavel Konopik, Jan Dzugan, Martin Rund & Radek Prochazka

Tensile and creep property determination of 15-15Ti fuel cladding steel by small punch testing
Stefan Holmström, Igor Simonovski, Stefan Ripplinger, Eberhard Altstadt, Remi Delville, Marta Serrano & Vasile Radu

Development of testing machines and equipment for testing miniaturized samples, proposals for improvement of CWA 15627
Daniel Omacht, Zdenek Kubanek & Roman Dolezal

Impression creep testing for the HAZ of a P22 weld
Juhani Rantala & Jan Storesund

Power & process: Surface & corrosion control

Controlling corrosion with advanced NDT-techniques
Johanna Tuiremo, Kari Latvala, Jan Storesund & Jouni Koivumäki

Comparison of laser clad coatings under simulated 100% biomass firing conditions
Tony Fry & David Gorman

Coatings for high temperature corrosion protection in advanced power plants
Maria Oksa & Jarkko Metsäjoki

Possible solutions to reduce the furnace wall corrosion in used wood power stations
Yousef Alipour & Pamela Henderson

Lifetime assessment: modelling of steamside oxidation
Sanni Yli-Olli, Pertti Auerkari, Satu Tuurna, Rami Pohja & Stefan Holmström

Nuclear plant: Management of life & integrity

Hydrogen-assisted cracking in nuclear power plants?
– The Doel 3 and Tihange 2 case
Walter Bogaerts, Digby D. Macdonald & Aleksandar Jovanovic

Demonstration of fatigue for LTO license of NPP Borssele
Frederic Blom, M.H.C. Hannink, C.G.M. Bont, P.W.B. Quist, A.E. de Jong & W. Besuijen

Study on safety margins assessment practices
Otso Cronvall

Damage relaxation in cyclic strained stainless steel
Jussi Solin

Past, present and future of long term operation in Spanish NPPs
Ignacio Marcelles, Eva Frutos, Pablo Martínez & Xavi Jardi

Collaborative tools for improved maintenance and inspection of power generation plants
Ignacio Marcelles, Pablo Martinez Levy, César Martinez, Juan Azcue & Carlos Casado

Nuclear plant: Spent fuel management & ageing

Relaxation behaviour of copper in disposal canisters
Juhani Rantala, Rami Pohja, Pertti Auerkari, Anssi Laukkanen & Tom Andersson

High temperature mechanical properties of a 17wt%Cr High Performance Ferritic (HiperFer) steel strengthened by intermetallic Laves phase particles
Michal Talík & Bernd Kuhn

Panel discussion on nuclear plant – LTO or oblivion?
Introduction by A. Al Mazouzi & R. Nhili: The Materials Ageing Institute: R&D programme and scientific network to understand and anticipate the ageing phenomena of the main NPP components

Nuclear plant: Microstructure & ageing

Influence of repair welding on microstructure of VVER 1000 pressure vessel
Dagmar Jandová, Miroslava Matějová & Josef Kasl

Short-range ordering of Alloy 690 aged for 10 000 h at 420, 475 and 550°C
Roman Mouginot, Teemu Sarikka, Ulla Ehrnstén, Young Suk Kim, Sung Soo Kim & Hannu Hänninen

Fracture mechanical and microstructural characterization of narrow-gap safe-end dissimilar metal weld
Matias Ahonen, Roman Mouginot, Sebastian Lindqvist, Teemu Sarikka, Pekka Nevasmaa, Ulla Ehrnstén & Hannu Hänninen

Linearization of supports with gaps in dynamic piping analyses
Aapo Ristaniemi

GenIV challenge

Creep-fatigue lifetime assessment for cyclic softening steels
Jarir Aktaa & Mario Walter

Creep-fatigue interaction and cyclic softening of ferritic-martensitic steels
Ulrich Führer & Jarir Aktaa

Creep performance of fuel cladding
Rami Pohja, Ville Tulkki, Timo Ikonen, Pekka Moilanen, Juhani Rantala, Santtu Huotilainen & Ulla Ehrnstén

Overview of SCWR candidate materials stress corrosion tests
Aki Toivonen & Sami Penttilä

Inspection performance

Towards a guideline for a smart in-service inspection concept using the damage tolerance methodology
Detlef Rieck, Axel Schulz & Gerhard Dreier

POD as a function of flaw location in component
Jonne Haapalainen

Artificial flaw detection with ultrasound in austenitic stainless steels
Tuomas Koskinen, Esa Leskelä & Minnamari Vippola

Non-destructive evaluation of the spent nuclear fuel disposal canisters
Ari Koskinen & Tarja Jäppinen

Corrosion and biofouling on stainless steels in Baltic sea water environment: a cooling water pilot study
Maija Raunio, Pauliina Rajala, Outi Priha, Elina Huttunen-Saarivirta & Leena Carpén

Introductory keynotes

Challenges for nuclear and CHP plants

Liisa Heikinheimo

Teollisuuden Voima Oyj
Helsinki, Finland

1. Introduction

For a long time the energy sector was understood as a quite stable and profitable industry. Today this is no more the case - stability has changed for unpredictability and profitable production for close to own cost level?

A huge change has taken place during the last decade, both in regulation and energy market. Still in the beginning of this millennium the trends were given as growth estimates of energy consumption and there was space for new power plants and new technologies. Today, there are elements like politics, public opinion, fluctuation of needs and fluctuation in production, weather changes and daily weather, and as a consequence of these there is in the energy market a fluctuation of offering and prices.

There must be many reasons for these changes, out of which one can mention the strong support for renewable energy production followed by increasing amount of distributed energy production. Also the awareness of the climate change and pollution in general are today strong components in the political decision making. The fact that the distributed energy production is mostly dependent on the weather: sun, wind or rain, makes it difficult to predict the production rates over a long time. Last but not least there are the negative news of nuclear energy production, Fukushima accident after the tsunami, slow progress in developing the nuclear waste disposal solutions and the overall rigidity of NPP projects with delays. All of these are working against the base load energy production, the image and long term planning of base load capacity issues.

However, at the same time we all can list these factors in Europe and most probably also some in USA, the development seems, however, to be different in Asia and in Middle East. This means that the reasons are not caused by laws of natural sciences but are based on human activities and natural events. These are not fully out of control, for example in China there is a vaste programme to build both large units for electricity production but also a large number of renewable energy production units. Although much of it may also be motivated by the rather uniquely strong need to clean air, the solution in China is a strong national programme to match a huge need for energy and top level technology.

2. Energy market in Europe

In Europe and more specifically in northern Europe there is also a high need for energy and electricity because of the cold climate, technology oriented life style and the fact that many industries are based on production demanding energy. Also the human habitation is relatively widely distributed and there is a need for a stable energy grid and distribution for the scattered communities.

How can the energy companies and the base load production survive after the shut down of several coal and oil based power plants with CHP-production? In Germany and Sweden the closure of NPPs is a fact and a large number of base load electricity production will disappear from the Nordic grid. Moreover, the Nordic countries have all different palettes of the energy production (Figure 1). In Sweden hydro and nuclear have the biggest role while in Finland there is much more variation in the production and sourcing. In both countries there has been a constant trend of decreasing electricity prices as a consequence of support and taxing systems, and at the same time the CO_2 trading has not been successful. In the discussions there is a serious struggle between regulation and free energy market.

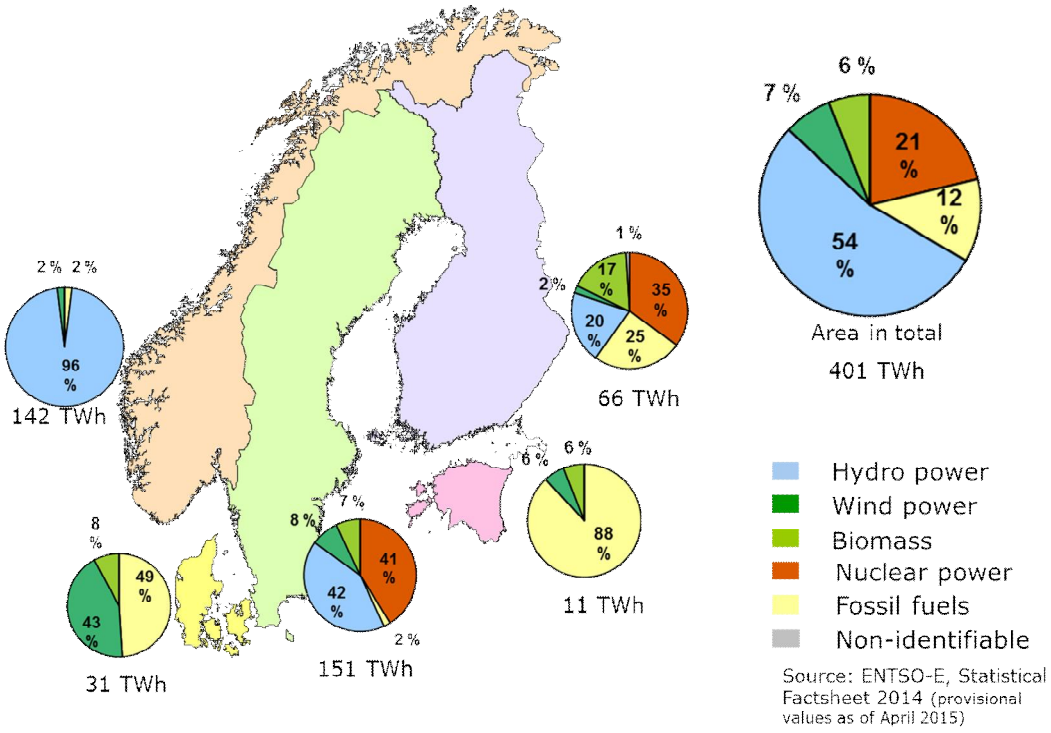

Figure 1. Electricity Generation in Nordic market area 2014, ENTSO-E, Statistical Factsheet 2014.

The closure of nuclear power plants will have a negative effect on the reduction of CO_2-emissions. Sweco in Sweden has estimated that the Swedish nuclear energy programme has saved 2 billion tons of CO_2-emissions till today. This factor should be taken into account when decisions on energy solutions are made. The present fleet has estimated to have capacity for another such a saving in its lifetime if the aging management would be carried out properly and the nuclear power plants would be licensed till the technological life time limits. A summary of the energy production environment is presented in Figure 2 (from a presentation by Sweco /1/). The fuel costs and the CO_2-prices have been the main drivers for decreasing the power prices. In the future, however, increasing amount of RES can change the historical connection between fuel and CO_2-prices with the electricity price.

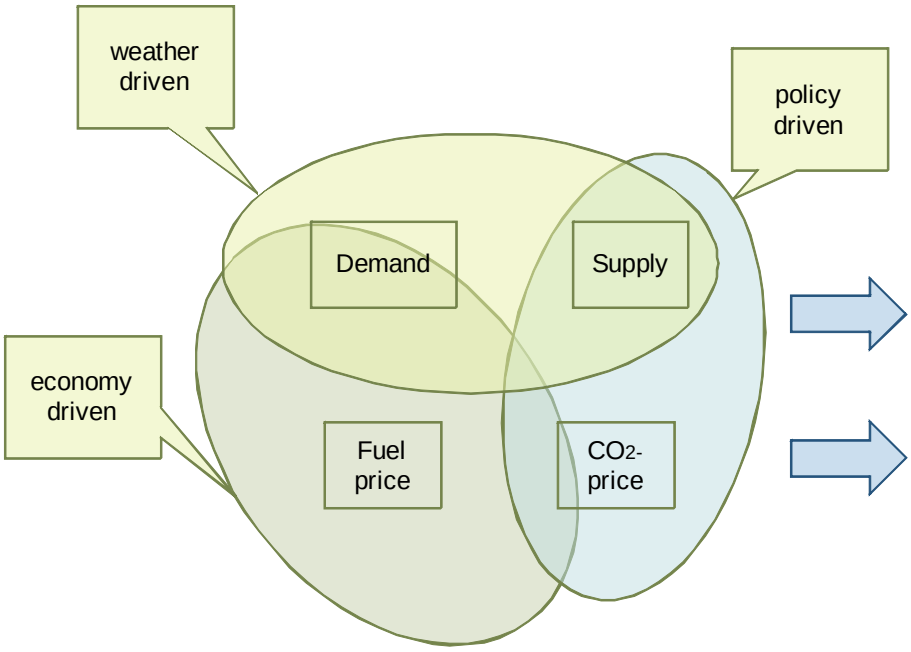

Figure 2. A change in the energy market has taken place after the growth of renewable energy production and various political decisions. The picture is drawn after Johan Bruce, Sweco, 2016 /1/.

3. Role and challenges for R&D

What would be the role of research and development in such a situation - is there any - is a question for this Baltica X Conference to be discussed actively. The main question is can the big energy production units operate in a reliable, safe and profitable manner when the boarder conditions for these arguments are changing. In a modern language this means a demand of resilience for all the levels of organisations and research supply chains.

As an example there is a model for organising R&D function at TVO, a nuclear power company in western Finland with two 880 MW BWR units and a 1600 MW PWR (EPR) nearing the start of operation in a few years /2/. The goal of TVO is to produce electricity with the power units in a climate friendly, safe and efficient way. Figure 3 presents the capacity factor of units OL1 and 2 from the start of operation till 2015. Today, due to the changing operational environment and new requirements for the safety research the research has been organised in three programmes over the TVO organisation:

- Nuclear safety research: covering all aspects of nuclear safety and carried out mostly in a national research programme, SAFIR2018, in Figure 4 /3/. However, international research plays an important role especially in post Fukushima co-operation and there is a constant need for in-house research to support the operational licenses.
- Nuclear power plant technology research: contributing to the needs of TVO nuclear power units in maintenance, modernisations and in new build, especially focus on long term operation and life time management. The development and application of new calculation and modelling methods is included as well. New issues are e.g. fuel development and load follow practices.
- Nuclear waste management research: covers a wide range of research and monitoring activities from the waste handling and storing to the final deposition of LILW at the site in specific repository silos. The support in technical matters and R&D co-operation with Posiva company is important to ensure the final deposition of spent nuclear fuel in the 2020s from all of the TVO power units /4/. Today the decommissioning issues have become topical as well and these could be handled best within the international co-operation to share the expertise and experience.

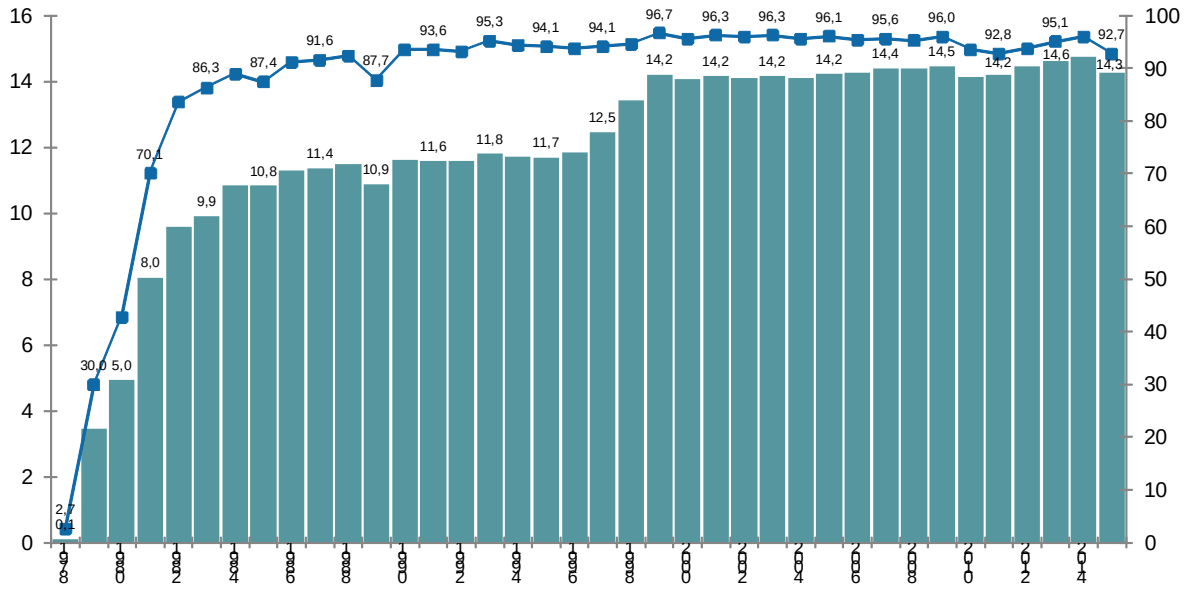

Figure 3. Production (MWh) and load factors of OL1 and OL2 units in 1978 - 2015, Teollisuuden Voima Oyj, 2015.

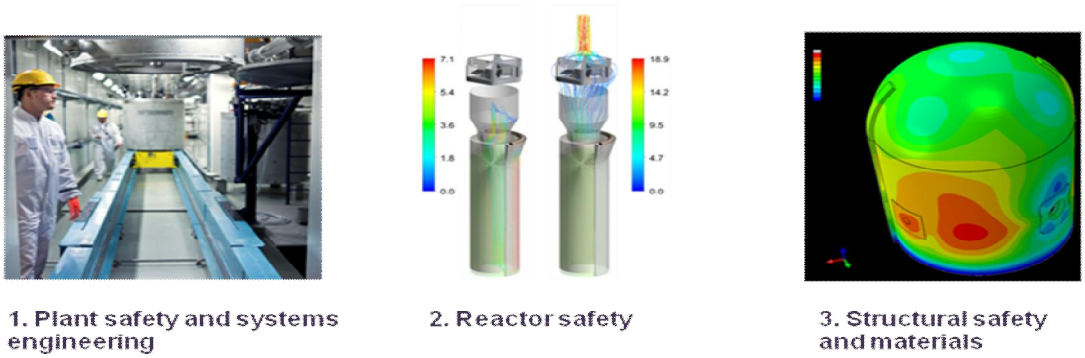

Figure 4. The Finnish Nuclear Power Plant Safety Research Programme 2015-2018, SAFIR2018, has three focus areas /3/.

These programmes are planned for a 5 - 10 years period with goals that are checked yearly with the strategic planning of the company. The programmes consist of projects and further on subprojects that are rather flexible for changes if needed. Programme managers will take care of the project portfolios, the co-operation and experts needed. The project leaders, nominated case by case, will form research groups for each programme. In all of the programmes different types of projects are needed: direct research orders for the research organisations, co-funded projects often parts of international programmes and participation in programmes and projects based on public funding (e.g. national and EU funding).

The goal of R&D work is to serve the nuclear energy production and its full lifecycle. There is a high need for research that can be utilised and benefited at the site. However, this does not mean that the research will be done domestically only, in all of the programmes there is a strong component of international co-operation to reach all the capabilities needed and to learn from the others and to share the common topics and perspectives. As a result any fixed organisation structure inside the company or any fixed long term sub contracting agreement are not needed because the resilience is build in both the

internal and external networks. One may consider this challenging for the experts, but also interesting and offering always room for new needs and new ideas.

References

1. http://www.energiforsk.se/info/nyhetsbrev/

2. http://www.tvo.fi

3. http://safir2018.vtt.fi/

4. http://www.posiva.fi

Risk and resilience: The concept of SmartResilience and its application on energy infrastructure in Finland

A. Jovanovic[1], P. Auerkari[2]

[1] Steinbeis Advanced Risk Technologies & EU-VRi, Stuttgart, Germany

[2] VTT, Espoo, Finland

Abstract

The paper highlights the practical aspects of new EU project SmartResilience and its application in Finland. The basic idea of the project is that modern critical infrastructures are becoming increasingly "smarter" (e.g. cities). Making the infrastructures "smarter" usually means making them smarter in normal operation and use, but it has to be checked if these smart critical infrastructures (SCIs) will behave equally "smartly" and be "smartly resilient" also when exposed to extreme threats, such as extreme weather disasters or, e.g., terrorist attacks. Similarly, the question is, if making existing infrastructure "smarter" is achieved by making it more complex, would it also make it more vulnerable? Would this affect resilience of an SCI as its ability to anticipate, prepare for, adapt and withstand, respond to, and recover? These questions are tackled by the project, which plans answer these questions in several steps: by (#1) identifying existing indicators suitable for assessing resilience of SCIs; (#2) identifying new "smart" resilience indicators (RIs) – including those from Big Data; (#3) developing a new advanced resilience assessment methodology based on smart RIs ("resilience indicators cube", including the resilience matrix); (#4) developing the interactive "SCI Dashboard" tool; and (#5) applying the methodology/tools in eight case studies, integrated under one virtual, smart-city-like, European case study. One of these case studies will take place in Finland, dealing with modern systems of energy supply.

1. Introduction – assessing resilience by means of indicators

In SmartResilience project, resilience of an infrastructure is understood as "the ability to anticipate, prepare for, and adapt to changing conditions and withstand, respond to, and recover rapidly from disruptions [1]. Living organisms are resilient in their ability to persevere through injuries, infections or trauma. Even through severe disease, critical life functions are sustained and the body recovers, often adapting by developing immunity to further attacks of the same type. Modern critical infrastructures (e.g. cyber, energy, water, transportation and communication) generally lack the same degree of natural resilience, typically losing essential functionality following adverse events. The society, therefore, needs a system of resilience governance and resilience management going beyond conventional risk governance/management in order to address the complexities of large integrated systems and the uncertainty of future threats, especially those associated with climate change or adverse human actions. The way to reach this goal is to provide

new holistic approach to the resilience, addressing a broad variety of issues including human factors, security, geo-politics, sociology, economy, etc. and increased vulnerability due to changing threats. This holistic approach has to be based on the new metrics and validated indicators that could be applied to systems in order to assess their level of resilience.

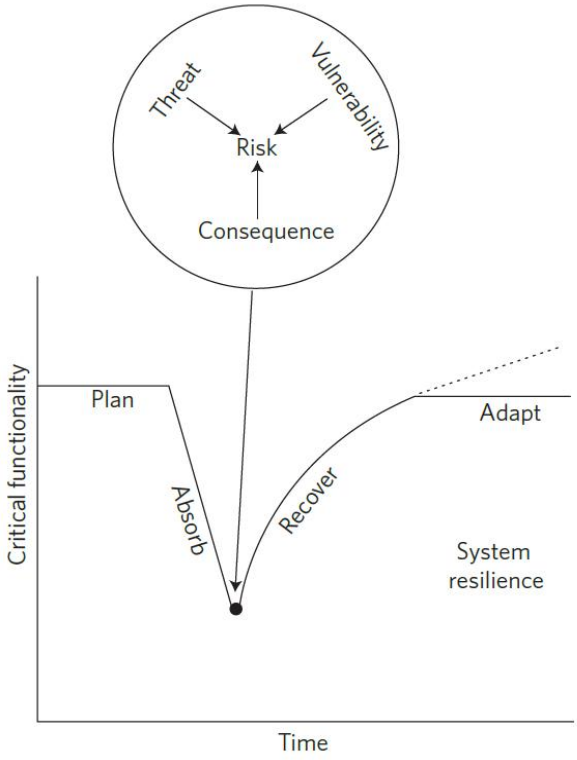

Figure 1: A resilience management framework [1]

A resilience management framework includes risk analysis as a central component. Risk analysis depends on characterization of the threats, vulnerabilities and consequences of adverse events to determine the expected loss of critical functionality. The above definition of resilience places risk in the broader context of a system's ability to plan for, recover from and adapt to adverse events over time. In the system functionality profile, risk in a system is interpreted as the total reduction in critical functionality and the resilience of the system is related to the slope of the absorption curve and the shape of the recovery curve — indicating the temporal effect of the adverse event on the system. The dashed line suggests that highly resilient systems can adapt in such a way that the functionality of the system may improve with respect to the initial performance, enhancing the system's resilience to future adverse events.

In the modern society, the systems decisively determining the overall resilience of the society are the critical infrastructures (energy grids, transportation, government, water, etc.). This is clearly recognized by the EU in its call DRS-14 (*Call: H2020-DRS-2015, DRS-14-2015*) emphasizing the need for *"… a better understanding of critical infrastructure (and)… for defining measures to achieve a better resilience against threats in an integrated manner including natural and human threats/events (e.g. due to human errors or terrorist/criminal attacks)…*". The overall goal of the project is, hence, to improve current approaches by providing an innovative "holistic" methodology for assessing resilience of critical infrastructure. The proposed methodology is based on resilience indicators.

2. Practical problems addressed

The project will address in particular

1. Smart critical infrastructures (SCIs)
2. Emerging risks (primarily those related to New Technologies)
3. Smart indicators (also these from Big Data)
4. Cascading and ripple effects (among multiple SCIs, 8 of them in the project), and
5. Insurance/re-insurance aspects.

In an era that has seen a multitude of high impact disasters ranging from natural events such as earthquakes, floods, tsunami's, volcanic disruptions to man-made acts of terrorism and cyber-attacks, there is a greater need than ever before to assess the resilience of modern societies to withstand and recover from unexpected adverse events. Against this backdrop, concepts of resilience offering all-encompassing, integrated approaches to planning for, responding to and recovering from all manner of man-made and natural disasters have dominated recent discourse on disaster and crisis reduction and management.

In this regard, the removal or suspension of critical infrastructure assets from normal service would significantly affect public safety, security, economic activity or environmental quality. A breakdown in any one of these assets alone can bring about catastrophic consequences, but it is the interdependency of these systems, and by extension, the cascading effects of a breakdown in one system on other interconnected systems, which is of most significant concern [2].

Examples supporting the above statement are numerous. A fault in an electricity transmission network in Northern Germany which resulted in a blackout for more than 15 million people across Western Europe in 2006 exemplifies the type of cascading effects on transport, healthcare systems, financial services and societal security and safety that can quickly arise when there is a failure of critical infrastructure [3]. The London Underground bombings of July 2005 and the commuter train attacks in Madrid in 2004 demonstrated the vulnerability of transport infrastructure to terrorist attack. An attack on transport infrastructure can result in cascading effects on communications and power conduits that are generally located in proximity to transport routes. Damage to water supply infrastructure by natural or man-made disaster could cause major public health and environmental impacts, including possible loss of life.

It is against this context that the concept of resilience as applied critical infrastructures is explored in the project ("SmartResilience"). The project is inspired by the collective experiences of the consortium partners engaged within resilience research, SCI operations, and the recognition of the growing importance of resilience in general. The consortium includes a number of SCI providers (8 cases of SCI are in the scope of the proposed research), owners, operators and also municipal regional authorities with significant levels of experience in the application of resilience. It will deliver enhanced concepts in resilience and risk management that will have the capabilities to address the issues targeted by the call.

3. "Smart(er)" infrastructures

Modern critical infrastructures are becoming increasingly "smarter" (e.g. the "smart cities"). Making the infrastructures "smarter" usually means making them smarter in the normal operation and use: more adaptive, more intelligent… usually by means of enhancing the "IT aspects" of the respective infrastructure. In this sense, the behavior of an infrastructure and its efficiency are generally improved, the infrastructure will behave in a "smarter way", become "smarter". But will these smart critical infrastructures (SCIs) behave "smartly" and be "smartly resilient" also when exposed to extreme threats, such as extreme weather disasters or terrorist attacks? If making existing infrastructure "smarter" is achieved by making it more complex, would it also make more vulnerable? Would this affect resilience of an infrastructure as its ability to anticipate, prepare for, adapt and withstand, respond to, and recover? Proving clear and practicable answers to the above questions, accepted by possibly large group of stakeholders, is the main specific objective of this project.

The project results are supposed to bring-in a breakthrough innovation on both European and the world-level. In particular addressing the Smart critical infrastructures (SCIs – see Table 1) together with Emerging risks (primarily those related to New Technologies), and using Smart indicators, also for analyzing cascading and ripple effects (among multiple SCIs – see Figure 1). The SCIs and related scenarios are the

key element of the project and they cover the SCIs shown in Table 2: , financial hot-spot infrastructure, smart city infrastructure, health care system infrastructure, transportation infrastructure, productions supply infrastructure, water supply infrastructure, urban flood protection infrastructure, energy infrastructure and, last but least, a "virtual (fictitious) European infrastructure". In the "virtual case study", all the single SCIs are exposed to a scenario binding them together and making them interact (Figure 2).

Table 1: Smart infrastructures in comparison with the conventional ("gray") ones

Infrastructure characteristics	gray/conventional CI	smart CI (SCIs)
Stakeholder involvement	stakeholders are often engaged with the aim to create local sup- port for the project, but without active involvement in the project design and operation traditional engineering	extended stakeholders are often required to support the project and may have an active and ongoing role in the project design and operation
Engineering approach	solutions enable standardization and repli- cation which can significantly reduce project costs and delivery times	IC solutions require a custom- made, location- specific design and do not lend themselves to standardization and replication
Environmental footprint	often increased environmental footprint due to material and energy intensive processes (manufacturing, distribution, operation)	often reduced environmental footprint due to the solutions being nature-based and self- regenerating
Susceptibility to external factors	Gray IC is susceptible to power loss, me- chanical failure of industrial equipment and price volatility	the IC solutions are susceptible to extreme weather conditions, seasonal changes in tem- perature or rainfall and disease and similar
Monitoring and control	Conventional	the SCIs are living and complex systems that can be monitored and effectively man- aged by a deep understanding of the key control varia- bles

Table 2: SmartResilience project infrastructures, integrated in a unique exercise EU-wise

Short Name	Name	City/ Country
finances	ALPHA: The City of London - Assessing resilience of a city hosting a critical financial hot-spot of the world	London/ UK
smart city	BRAVO: Heidelberg (Bahnstadt) - Assessing resilience of a future- oriented and sustainable community (smart city, energy)	Heidelberg/ Germany
health care	CHARLIE: Assessing resilience of an Austrian cities' health care system	Austria
transport	DELTA: Budapest - Assessing resilience of large embedded trans- portation infrastructure (airport)	Budapest/ Hungary
supply	ECHO: Assessing resilience of the city in a large industrial zone (production facility / supply chain)	Pancevo/ Serbia
water	FOXTROT: Assessing resilience of drinking water supply in Swedish cities	Sweden
government (flood)	GOLF: City of Cork: Use of indicators and technologies developed and lessons learned to assess resilience of critical infrastructure to tidal and fluvial flooding events	Cork/ Ireland
energy	HOTEL: City of Helsinki - Flooding underground coal storage. Resili- ence of the energy infrastructure (city environment)	Helsinki/ Finland
cascading effects	INDIA: Integrated European virtual Case Study - Framework Scenar- io "Tainted Flood" Cascading and ripple effects on combined scenar- ios on of resilience and its indicators	Europe

The project will answer the above questions in several steps, by addressing the following specific issues:

1. identifying existing indicators suitable for assessing resilience of SCIs
2. identifying new "smart" resilience indicators (RIs) – including those from Big Data
3. developing a new advanced resilience assessment methodology based on smart RIs ("resilience indicators cube", including the resilience matrix)

4. developing the interactive “SCI Dashboard” tool
5. applying the methodology/tools in 8 case studies, integrated under one virtual, smart-city-like, European case study. The SCIs considered (in 8 European countries!) deal with energy, transportation, health, water…

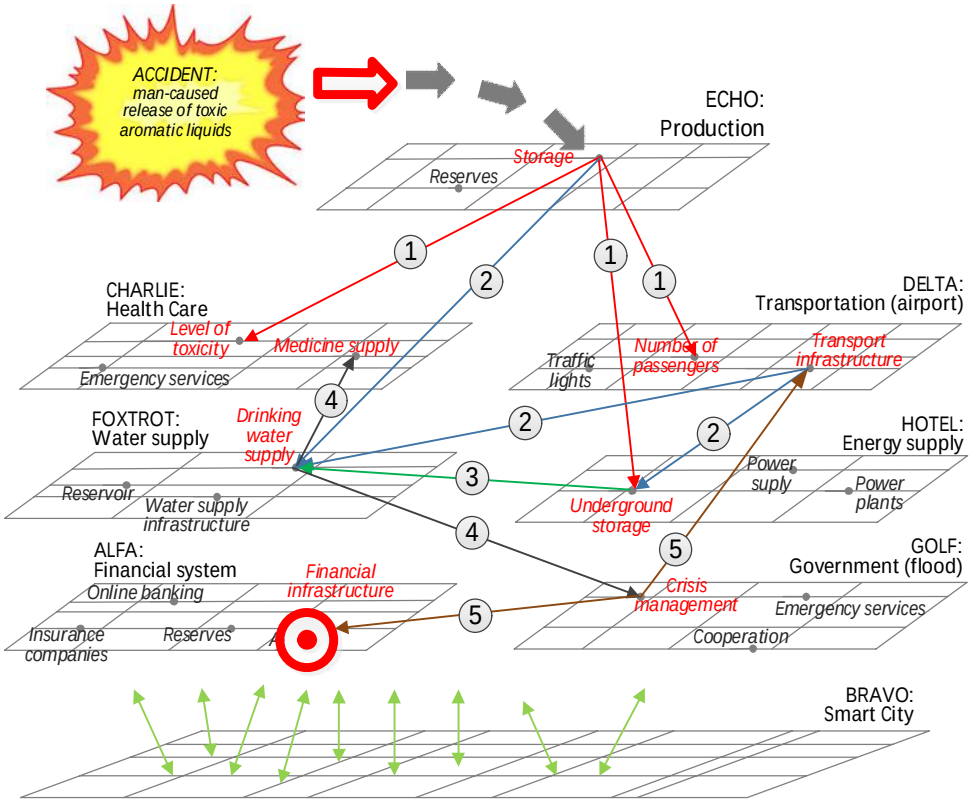

Figure 2: Interaction between the SCIs in the project: Cascading and ripple effects

4. The solution concept

The “infographics” in Figure 3 provides, in a very condensed form, the complete overview of the technical part of the work proposed to be done in this project (dissemination, exploitation and project management activities excluded!). **The solution – the case-study lens:** As shown in Figure 2 the project if focused and “built” around the case studies (Table 2). The case studies are not a mere “verification/validation platform”, the, i.e. the partners involved in them are defining also the requirements for the methodology and indicators development.

The solution – the approach lens: The approach of the project is to look (in the usual way) onto 2 main phases/dimensions of the resilience analysis, including the Pre-event phase / exposure dimension, and the Post-event phase / response dimension, as well as the 3 types of resilience, namely:

- The STRUCTURAL resilience
- The INTEGRATIVE resilience and
- The TRANSFORMATIVE/ADAPTIVE resilience.

The solution – the indicators (RIs) lens: In order to cope with the issue, new methodologies and tools are needed and the project will develop them, taking the “smart resilience indicators” as the basic element of the methodology. The new smart resilience indicators will be built upon:

- Indicators accepted in the related areas, such as risk, safety, business continuity, sustainability, e.g. those proposed by OECD, GRI, API, HSE, IAEA and other organizations;
- New resilience specific indicators proposed by the experts in this project (the “conventional way” of creating and using indicators);
- New resilience indicators derivable out of the Big Data and the Open Data.

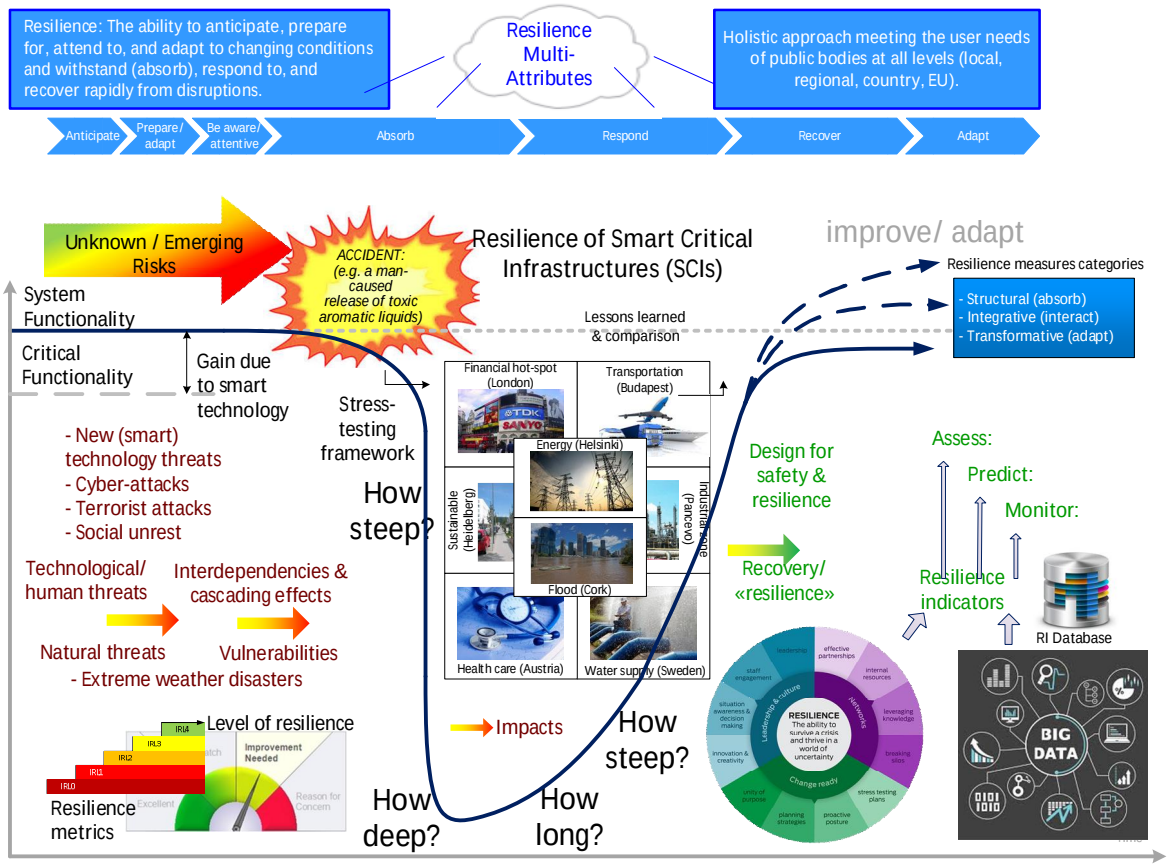

Figure 3: The solution concept: Resilience indicators in different phases of the resilience cycle and their link to the project WPs

The solution – the indicators (RIs) lens: In order to cope with the issue, new methodologies and tools are needed and the project will develop them, taking the “smart resilience indicators” as the basic element of the methodology. The new smart resilience indicators will be built upon:

1. Indicators accepted in the related areas, such as risk, safety, business continuity, sustainability, e.g. those proposed by OECD, GRI, API, HSE, IAEA and other organizations;
2. New resilience specific indicators proposed by the experts in this project (the “conventional way” of creating and using indicators);
3. New resilience indicators derivable out of the Big Data and the Open Data.

Two main categories of resilience indicators should be identified, namely the generic indicators, possibly used across different Cis (SCI-specific indicators).

The solution – the methodology lens: New methodologies, such as web semantics and new tools such as Watson, Cognos and others will be used in order to both identify/define the indicators and determine their values. Special attention will be devoted to the use of these indicators for the quantification of resilience.

5. Overall methodology approach

The principle: The quintessence of the propose methodology is shown in Figure 4. It shows that the indicators characterizing the threats and the SCIs, respectively, are brought up together within the scenario. The indicators, as explained can be, e.g., "supervised" or "unsupervised", lagging or leading, basic (level 1) or more sophisticated (levels 2, 3…), include conventional sources or Big Data, etc.

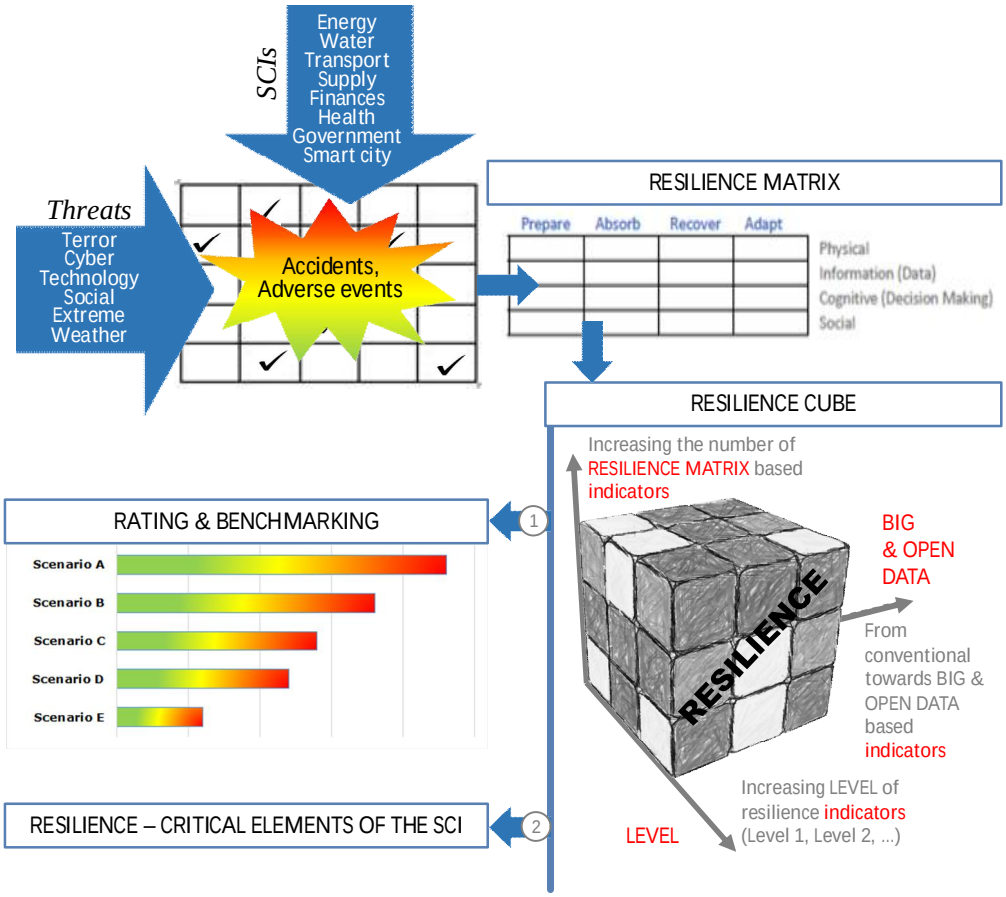

Figure 4: The SmartResilience Methodology: From indicators (SCIs and threats) to benchmarking and identification of the "hot spots" (deficits, issues, problems…)

It is a working assumption of this project that the "unsupervised" can be more dynamic and adaptive than the conventional ones, and, hence, can be considered "smarter" and, as they are, hence, considered as "smart resilience indicators".

The collected set of indicators is then "checked", in order to be sure that the whole resilience assessment process is well covered, the indicators are then ordered within the resilience matrix. The matrix looks at the 4 phases of the resilience cycle (prepare, absorb, recover and adapt) and at the 4 types of indicators (physical, information, cognitive and social) – see Figure 5. The Resilience CUBE is, then, used to "measure" the resilience along the three dimensions of the Cube: resilience matrix, "smartness" and complexity ("the levels"). Once when the set is considered/accepted as representative, the dynamic/"smart" (!) resilience assessment "check-list" can be created and used for the assessment of the respective SCI (e.g. water, energy, smart city,…).

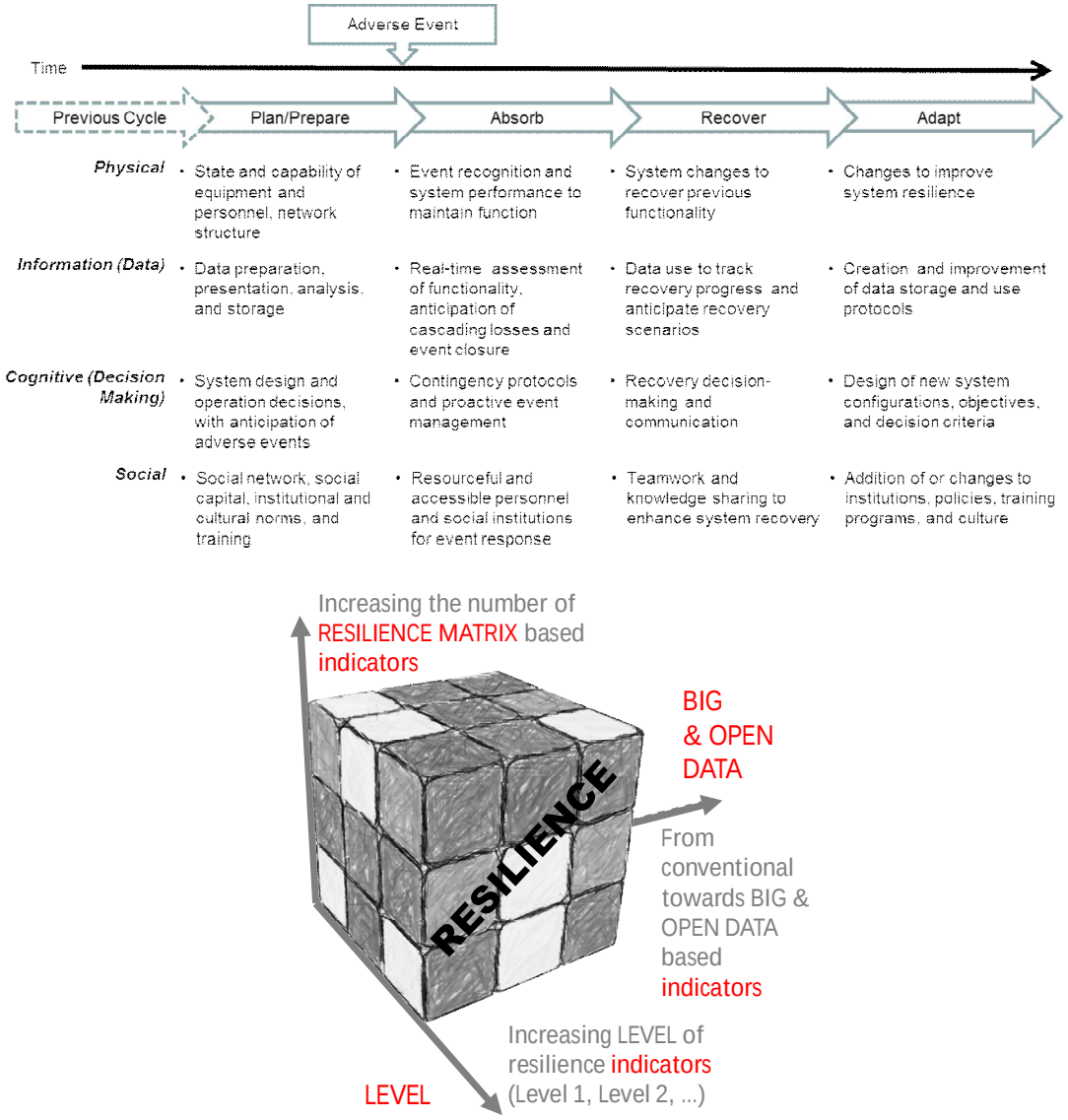

Figure 5: Resilience CUBE – the confidence in the resilience of an SCI increases with the assessment of the more elements of (a) resilience matrix (after Linkov et al. 2014), (b) more resilience indicators (obviously, increasing the number of "unsupervised" indicators possibly derivable from Big Data increases the confidence) and (c) increasing level of details of "supervised" indicators

Deriving resilience indicators from big and open data: It is estimated that currently 2.7 zettabytes of data exist in the digital data universe, that 571 websites are created every minute, 100 terabytes of data are uploaded daily to Facebook. It has also been estimated that in Europe's developed economies, governments could save more than €100 billion in operational efficiency improvements alone by using big data, not including using big data to reduce fraud, tax evasion, and errors (McKinsey, 2011). In this context, the concept of data re-use is rapidly gaining increasing importance, i.e. the use of open data collections for other purposes than those for which the data was originally collected. Following the mantra that "data is too expensive to waste", data re-use is nowadays commonplace in many scientific research areas such as in biomedicine to discover novel drugs and diagnostics, see e.g. (Butte, 2008). Another example stems from the field of election forensics, where statistical tests have been developed to quantify the probability of certain types of electoral fraud based statistical irregularities in the published election results (Klimek, 2012). In this project, we therefore propose to pursue a similar approach and to re-use and leverage existing, open, publicly available data to derive resilience indicators for critical infrastructures.

One of the most pressing challenges in this context is indeed to find trends and patterns in the large and high-dimensional datasets that can be captured in intuitive indicators of high practical use. Many infrastructures lend themselves exceptionally well to be analyzed from a complex network perspective (Albert, 2000), where it was found that many real-world networks (such as communication networks, metabolic networks, or social networks) have a surprising degree of robustness with respect to random errors or perturbation that comes at the high price of extreme vulnerability to targeted attacks. Network science methods have resulted in actionable information on network vulnerabilities in response to disruptive events in the context of transportation (Guimerá, 2005, Barrat, 2004), power (Solé, 2008), and communications (Doyle, 2005). An additional challenge in the design of resilient infrastructures is that multiple interdependencies between mutually dependent networks induce an additional component of fragility (Vespignani, 2010).

6. Application in Finland

A specific task in SmartResilience project is devoted to the case study “HOTEL”, where the energy company Helen of the City of Helsinki is dealing with the impact of defined energy related threats and the assessment and evaluation of resilience, by means of resilience indicators, for the energy infrastructure in the city environment (Figure 6).

Figure 6: Salmisaari CHP plant of Helen: energy infrastructure in the city of Helsinki. Photo: Helen

Energy generation and consumption take ideally place in the same area, i.e. generation within the city or in the vicinity, next to the consumers of households and peri-urban industry. Confined space such as underground siting in a city environment requires resilience and security indicators, particularly mainly leading ones, to help managing the risks at locations of limited access and status information. Cities have limited area available, constraining the options to store energy feedstock, where for example underground storage has special requirements in the inspection of status and security, and it is necessary to recognize the possible consequences of disruption as early as possible. The energy infrastructure will be considered in the test case of risk and resilience in severe disruption. The main aspects and scenarios taken into account are:

- Catastrophic wintertime loss of district heating
- Impact of new technology and developing infrastructure on resilience
- Potential impacts of man-made threats.

The case aims to address all essential aspects of resilience: risk anticipation, preparedness, attention, impact absorbance, response, recovery and adaptation, and where relevant, the rates of the event/response. VTT will lead the task and set up a stress test framework, as well as supervise the relevant aspects and specific expectations of the end-user (Helen in the City of Helsinki), whose data will be needed provide the data considered to be relevant for criticality testing. The unsupervised indicators and their application will be defined and aligned with other case studies.

7. Conclusions

In general, SmartResilience will significantly improve the resilience of critical infrastructure, such as energy & water supply, transportation and information and communication grids etc., by providing a uniform and comprehensive methodology of risk and resilience assessment. SmartResilience will provide the basis for proactive innovations. The project will therefore raise the future viability of critical infrastructure. As SmartResilience will follow a holistic approach to resilience, not only technical issues will be addressed. The project's approach will also cover human factors, societal and economic aspects. SmartResilience will therefore provide solutions that are suitable to enhance the societal resilience in European countries and the organizational resilience among European infrastructure owners, thus allowing the stakeholders to better prepare for the possible "Future Global Shocks" [13].

SmartResilience will develop a new advanced resilience assessment methodology based on a new set of smart Resilience Indicators that enable end-users (authorities, operators and owners of critical infrastructures) to better assess the resilience of the respective infrastructure, especially with respect to future and emerging threats, including those imposed by the enhancement and evolution of critical infrastructures towards "smartness". This improved assessment methodology will be supported by a model to identify interdependencies, between infrastructures as well as between these infrastructures and other sectors. The SmartResilience solutions will be delivered in form of a practical guideline and a supporting tool ("SCI Dashboard") for resilience assessment. SmartResilience is not only focused to technical aspects of resilience. The project covers security needs arising from disaster risks, including threats to life. SmartResilience will therefore also focus indicators of organizational and societal resilience. Devolving these indicators will help to assess the resilience of public authorities, infrastructure providers and the general public. Identifying lacks of resilience will show vulnerability and related with that, needs for improvement. Therefore, the assessment of resilience will help to raise the ability to mitigate the effects of disasters to the society and it will enable public authorities, infrastructure providers and the general public to recover faster from adverse events. The main planned results of SmartResilience are a Resilience Assessment Guideline and a tool ("Smart Critical Infrastructure Dashboard"), both aiming at supporting end-users (authorities, critical infrastructure operators and owners) in improving the disaster resilience of respective critical infrastructures through indicator-based assessment of their resilience capabilities. The solutions provided by SmartResilience are oriented towards practical needs of end-users and will be developed in close collaboration with all relevant stakeholders.

Acknowledgments

The paper is based on the Grant Agreement No. 700621 supporting the work on the SmartResilience project provided by the Research Executive Agency (REA) ('the Agency'), under the power delegated by the European Commission ('the Commission'). This support is gladly acknowledged here, as well as the collaboration of all the partners and their representatives (persons) involved. Special thanks go to Finnish partners VTT and the energy company Helen of the City of Helsinki for their support in the mission critical case study.

References

[1] Linkov, I. et al. (2014). Changing the resilience paradigm. Nature Climate Change, Vol 4, June 2014

[2] O'Rourke, T.D (2007) 'Critical Infrastructure, Interdependencies, and Resilience', The Bridge – Linking Engineering and Society, 37(1), pp. 22-30

[3] Union for the Coordination of the Transmission of Electricity (2006) Final Report System Disturbance on 4 November 2006

[4] McKinsey Global Institute, Big data: the next frontier for innovation, competition, and productivity (McKinsey & Company, 2011)

[5] Butte AJ (2008), Translational bioinformatics: coming of age, JAMIA 15(6), 709-14

[6] Klimek P, Yegorov Y, Hanel R, Thurner S (2012), Statistical detection of systematic election irregularities, Proceedings of the National Academy of Sciences USA 109, 16469-16473

[7] Albert R, Jeong H, Barabási A-L (2000), Error and attack tolerance of complex networks, Nature 406, 378-382

[8] Guimerá R, Mossa S, Turtschi A, Amaral LAN (2005), The worldwide air transportation network: anomalous centrality, community structure, and cities' global roles, Proceedings of the National Academy of Sciences USA 102, 7794-7799

[9] Barrat A, Barthelémy M, Pastor-Satorras R, Vespignani A (2004), The architecture of complex weighted networks, Proceedings of the National Academy of Sciences USA 101, 3747-52

[10] Solé R, Rosas-Casals M, Corominas-Murtra B, Valverde S (2008), Robustness of the European power grids under intentional attack. Phys Rev E 77, 026102

[11] Doyle JC, Alderson DL, Li L, Low S, Roughan M, Shalunov S, et al (2005), The "robust yet fragile" nature of the internet, Proceedings of the National Academy of Sciences USA 102, 14497-14502

[12] Vespignani A (2010) Complex networks: the fragility of interdependency, Nature 464, 984-985.

[13] OECD, Jovanovic, A. (co-author) (2011). OECD Reviews of Risk Management Policies – Future Global Shocks: Improving Risk Governance In: OECD Publishing, Paris, France. ISBN: 978-92-64-09520-55

Practical view on the condition management of some power plant key components

Osmo Koponen, Ville Holmström, Jaakko Mäkelä, Juha Männistö, Jari Tenhunen, Juha Turkia

Fortum Power and Heat Oy, Turbine and Generator Solutions
Kilterinkuja 2, 01600 Vantaa, Finland

Abstract

Condition management is a concept where diagnostic measurements and inspections, analysis methods, expertise and planning are combined to produce high or adequate reliability with reasonable costs.

In practice the level of condition management depends on the importance and value of the equipment, but also on traditions. In this article typical electrical and mechanical condition management and maintenance concepts utilized in Finland for turbine generators, transformers, turbines and process equipment are presented, based on practical experience. Examples of important findings made by measurements, analysis and inspections are also presented.

With on-line methods the condition of the equipment can be monitored, even continuously, during the normal operation of the equipment, without disturbing the production. Regular measurements and trend analysis and/or predetermined alarm limits are utilized for analysing the results. Measurements made in different operational conditions give additional information on the prevailing aging mechanisms. Off-line measurements and inspections are typically utilized during major overhauls or during unplanned production interruptions. Visual inspections can't be fully replaced with measurements.

Even though condition level can be well estimated and actual faults quite reliably detected, accurate prediction of the remaining life time of the equipment is generally not possible.

1. Introduction

The goal of condition management and the resources available for it are various, as well as the utilization of condition monitoring methods (measurements, inspections and analysis). The following coarse division can be used for describing different maintenance philosophies or practices [1].

Breakdown maintenance is the simplest form of maintenance. There is no actual maintenance plan, but actions are taken only after a failure of the equipment. Condition monitoring is not utilized to evaluate the reliability and performance of the equipment. This type of maintenance is only suitable for components with low value and low impact on the operation of the plant.

In *preventive maintenance* service actions are performed regularly, based on a predetermined program. The goal is to schedule the service actions in such way that normal wear and aging of the equipment does not cause outages. The service interval should be short enough to prevent major failures, but long enough to keep the maintenance costs reasonable. The major drawback of this practice is that it does not immediately respond to any unexpected incidents and sudden changes in the condition of the equipment. Condi-

tion monitoring can be utilized to some extent, but the service actions are not primarily scheduled based on the information obtained by condition monitoring.

In *predictive maintenance* the condition of the equipment is regularly or continuously monitored. The service intervals and programs are mainly determined based on the analysis of the condition monitoring results and production schedules, instead of predetermined programs.

Precision maintenance is the highest level of maintenance. It requires thorough analysis of the failure mechanisms and the impact of each component of the systems. It does not cover only the maintenance, but also e.g. investment procedures, commissioning testing, balancing and alignment, lubrication planning etc. The purpose is to predict and prevent coming failures and the need of service by modelling the system as well as possible. The goal is continuous improvement of reliability.

Typical maintenance practice in Finland for key power plant components is a combination of preventive and predictive maintenance. The service intervals are preliminary predetermined, but service actions may be advanced or postponed based on the information obtained by condition monitoring.

There are two main types of condition monitoring measurements. *On-line condition monitoring* measurements are performed during the normal operation of the equipment. They require no or very short production break, but often require permanently installed sensors. *Off-line condition monitoring* measurements are performed for stopped, and in some cases also opened, equipment.

Even though developed condition monitoring methods are available for many purposes, there are fault types and aging mechanisms that can't be reliably detected or can be detected only at a very late stage with measurements. Therefore visual inspections, if applicable, are essential part of condition monitoring.

In many cases the remaining life time of an equipment is dependent on the condition of the weakest point of the system rather than the average condition of the system. It is also typical that the failure is initiated by some abnormal situation causing additional stresses to the system, higher than in normal steady state operation. For example the windings of a generator or a transformer are such systems. The above mentioned factors are generally unknown (e.g. condition of the weakest point of the insulation system of the winding) or unpredictable (e.g. grid fault), therefore accurate prediction of the remaining life time is not possible.

2. Equipment specific maintenance practices

2.1 Turbine generators

2.1.1 Introduction

Here the term turbine generator refers to a generator whose prime mover is a steam or gas turbine. Turbine generators are typically operated at 3000 rpm speed (in 50 Hz system), in some cases 1500 rpm. Some of the practices explained here are also applicable for hydro generators, however hydro generators are quite different from turbine generators, regarding their structure and operation.

The maintenance schedule of turbine generators is mainly dictated by the service interval of the turbine. The actions can be divided in three hierarchical levels: annual inspections - minor overhaul - major overhaul. Factors affecting the scheduling of the inspections and overhauls include: OEM recommendations for overhauls and inspections, design features, duty cycle, costs of down time and importance of reliability, availability of spare parts, environment, on-site maintenance capacity, experiences from operation, experiences from previous overhauls, operational parameters and the age of the equipment.

Special attention in inspections and measurements is paid on the following details:

- Condition of the connections and insulation system of the stator winding (high voltage), e.g. signs of surface discharges.
- Condition of the connections and insulation system of the rotor winding (low voltage but very high mechanical stresses).
- Condition of the mechanical support system of the stator and rotor windings and detection of possible movements, vibrations and deformations in the windings.
- Condition of the retaining rings of the rotor, detection of possible cracks.
- Condition of the magnetic steel core, detection of hot spots caused by inter laminar short circuits.
- Condition of the bearings and lubrication system of the generator.

- Condition of heat exchangers, e.g. leakages or blockages.
- Condition of hydrogen sealing system in hydrogen cooled generators, leak level measurement.
- Correct alignment of the shaft line.
- Settings and performance of the excitation system.
- Settings and performance of the protection and synchronization system.

2.1.2 Annual inspections

Annual inspections are performed during scheduled annual shutdown. In CHP (combined heat and electrical power production) plants the natural window for this is late spring - summer - early autumn, when need for heat production for central district heating is low.

For annual inspection usually only the main connections and the exciter covers are opened. Inspections are made on e.g. to detect possible oil and cooling water leakages, condition of shaft grounding and excitation and rotor earth fault detection system brushes and slip rings, condition of bus bars and connections, exciter (if brushless excitation) and air filters. Also the correct function of voltage and current transformers is checked.

Typical set of measurements includes stator winding insulation resistance and winding resistance measurements, rotor winding impedance (as a function of speed for static excitation machines), insulation resistance and winding resistance measurements and exciter and PMG (if any) insulation resistance measurements.

2.1.3 Minor overhaul

Minor generator overhaul is performed typically every 3 to 5 years, mainly depending on the turbine overhaul needs. In minor overhaul the rotor is not removed from the stator of the generator, which significantly reduces inspection and testing possibilities. The ends of the generator are however opened and exciter stator (if any) removed to make limited visual inspection possible.

The following inspections and measurements are typical for large generators, in addition to the ones listed for annual inspections:

- Visual inspection, as far as possible without removing the rotor.
- Inspection of excitation generator and rotating diode bridge (if brushless excitation) or excitation brushes and slip rings.
- Bearing metal penetrant and/or ultrasonic inspection.
- Testing of bearing insulation.
- Insulation resistance and resistance measurements of stator and rotor windings.
- Impedance measurement of the rotor winding stationary.
- Dissipation factor (tanδ) measurement of high voltage stator winding.
- Partial discharge measurement of high voltage stator winding.
- High voltage test of the stator winding.
- Secondary testing of the protection relay system, where fault situations are safely simulated and the corresponding correct action of the relay is verified. Check of current and voltage transformers and wiring. Check of alarm and trip circuits.
- Testing of excitation system, including check of auxiliary voltages and measurement circuits, inspection of alarm and trip circuits and secondary test of excitation limiters and protection relays.
- Secondary testing of synchronizer, including check of auxiliary voltages and measurement circuits and inspection of control circuits.
- Certain seals and gaskets are replaced.

2.1.4 Major overhaul

In major overhaul, typically every 6 to 10 years depending mainly on the turbine overhaul needs, the coupling between the turbine and generator is opened and the rotor is removed from the stator, which includes also significant risks of damage. However, it enables the following measurements and inspections, in addi-

tion to what is listed above for annual inspections and minor overhaul. Also oil and water piping and coolers are usually removed.
- Full scale visual inspection for stator and rotor.
- Verification of the tightness of stator winding slot wedges.
- Slot specific partial discharge measurement to locate possible problem areas.
- Low flux or full flux stator core test to reveal possible hot spots caused by inter laminar short circuits. Also the tightness of the laminated stator core is checked.
- Verification of tightness/condition of rotor slot wedges.
- NDT (e.g. penetrant test) of the rotor retaining rings and fan blades to detect cracks.
- Evaluation of the need of factory repair of the rotor, which typically includes e.g. removal of retaining rings, complete or partial rewinding and rewedging.

2.1.5 On-line measurements

There are also on-line measurements that are typically performed between or in conjunction to the overhauls for running generator:
- Continuous vibration level monitoring.
- On-line partial discharge measurement is performed typically at least once per year, if there are permanently installed sensors in the machine.
- Shaft voltage and shaft grounding current are measured typically annually to verify the correct action of the shaft grounding system.
- Detailed vibration measurement is especially important after the major overhaul and after all rotor repairs, because the alignment of the shaft line or the balancing of the rotor may have been compromised. Simultaneous, detailed multi-channel measurement of the turbine and the generators gives much more information than simple vibration overall level measurement.
- Air gap flux measurement is typically performed once per year for generators which are equipped with sensors. The main purpose of the measurement is to reveal possible rotor winding turn-to-turn short circuits.

2.2 Power transformers, oil filled

2.2.1 Off-line testing

Electrical off-line condition monitoring measurements are generally performed for power transformers only after or also before a factory / service shop overhaul, which includes opening of the tank and removal of active parts of the transformer. They are also often performed when commissioning a new or transported serviced transformer or if there is any reason to suspect problems (gas generation, serious grid faults etc.). Generally this kind of overhaul where the transformer is opened is performed only once or twice during the lifespan (30+ years) of the transformer. The main actions performed during this are tightening of the support structures of the transformer, drying the insulation materials of the transformer, purifying the oil and servicing the tap changer. It must be noted that most of the moisture, accumulated during the service, is absorbed in the paper insulation of the transformer, and can't be removed by drying the oil alone.

Bushings belong to the most vulnerable components of a high voltage transformer. Failure of a bushing in service is catastrophic and may lead both to loss of the transformer and also collateral damage. Testing of dismounted bushings includes dissipation factor and partial discharge measurements and high voltage test, preferably also at elevated temperature.

Example of an electrical condition monitoring test program:
- High voltage tests with power frequency and surge voltage.
- Winding resistance measurements.
- Turns ratio measurements.
- Insulation resistance measurements.
- No-load current measurements.
- Dissipation factor measurements.
- Partial discharge measurements.

- Bushing condition analysis (HV tests, dissipation factor and partial discharge measurements). Requires dismantling of the bushings.
- FRA (Frequency Response Analysis) measurements to detect internal mechanical deformation e.g. due to short circuit forces.
- Tap changer tests.
- Current transformer and wiring tests.

There are also new methods for estimating the moisture content of transformer insulation by measurements. They are based on low voltage dissipation factor measurement over a large frequency range. The result can be used for scheduling a major overhaul, where the transformer is opened and dried.

2.2.2 On-line condition monitoring

Just like in the case of generators, the power transformers are continuously monitored by protection system (relays, including Buchholz gas relay), whose regular (e.g. annual) secondary testing is important part of the condition management of the plant. However, these systems are made to react on fault situations fast enough to limit the damage, they can't be used for actual condition monitoring.

Most widespread actual condition monitoring method for power transformers is the analysis of dissolved gases in the oil. The purpose of oil analysis is to reveal local overheating and electrical discharges in the winding and insulation structures. Local overheating can be caused by loose or degraded current connections, but also by e.g. induced circular currents in the tank. Overheating and discharges crack the oil molecules creating gases like hydrogen, acetylene and carbon monoxide.

The traditional method for performing dissolved gas analysis has been to take a small oil sample from the transformer and to analyse it in a dedicated oil laboratory. The sample can be taken with caution even while the transformer is on-line. In addition to the analysis of dissolved gases, also some other quantities of the oil like electrical breakdown strength, moisture content and particle content can be analysed. Analysis of the results require expertize and also knowledge on the type and operational and service history of the transformer, but basically an increasing trend in gas contents in oil indicates problems, unless the increase can be explained by operational history. The type of the problem can be roughly estimated by analysing the quotient of different gases, e.g. the chemical fingerprint of local overheating is different from the fingerprint of partial discharges. Typical analysis interval is one to two years, depending on the importance of the transformer. However, fast developing faults can develop to failure faster than that.

There are also systems that are permanently installed on the transformer and perform continuous monitoring of the gas content and the ratio of certain gases in the oil. The range of analyses is limited compared to laboratory analyses, but this kind of system can immediately give an early warning if problems start to develop. This kind of systems are becoming more popular in large power transformers.

Systems for continuous partial discharge monitoring of bushings and also transformer windings are commercially available, but quite rare in Finland.

2.3 Process equipment

For high voltage electrical motors similar condition monitoring measurements as for turbo generators can be applied. However, actual regular overhauls are rarely organized, and the rotor structure of synchronous and asynchronous motors differs significantly from turbine generator rotor structure, and does not require similar attention. Condition of stator and rotor winding is monitored with measurements, and large important machines can be opened for visual inspection as well. Typically the interval is several years.

Vibration measurements can be performed for all rotating equipment: generators, electrical motors, pumps, blowers, conveyors etc. in power plants and factories. The analysis of vibration measurements can be based on trend analysis, predetermined alarm limits and on the recognition of typical frequency distribution and/or waveform shape of specific fault types. Frequency and time domain analysis gives additional information compared to simple vibration overall level of displacement, velocity or acceleration.

The vibration measurement of process equipment is typically organized as a route measurement; the expert measures at the same time a large number of machines defined in a specific route. In this way the cost per machine is low, and even small machines can be included. A modern handheld analyser is a powerful tool and it can obtain much more information, including frequency spectrum, phase angle etc.

analysis, than from permanently installed vibration sensors that generally only give one overall level reading such as velocity (mm/s) or acceleration (g) from a wide frequency range. The route measurement is typically performed several times per year. Bearing faults can be quite fast developing; within months or even weeks.

2.4 Steam turbines

2.4.1 Introduction

A steam turbine is a device that extracts thermal energy from pressurized steam and uses it to do mechanical work on a rotating output shaft. Because the turbine generates rotary motion, it is particularly suited to be used to drive an electrical generator but it can also be used to drive pumps, compressors etc. Steam turbines are made in a variety of sizes ranging from small <100 kW units used as mechanical drives for pumps, compressors and other shaft driven equipment, to 1 500 000 kW (1500 MW; 2 000 000 hp) turbines used to generate electricity. There are several classifications for modern steam turbines. For example there are two blade and stage design, impulse and reaction types.

An impulse turbine has fixed nozzles that orient the steam flow into high speed jets. These jets contain significant kinetic energy, which is converted into shaft rotation by the bucket-like shaped rotor blades, as the steam jet changes direction. A pressure drop occurs across only the stationary blades, with a net increase in steam velocity across the stage. As the steam flows through the nozzle its pressure falls from inlet pressure to the exit pressure (atmospheric pressure, or more usually, the condenser vacuum). Due to this high ratio of expansion of steam, the steam leaves the nozzle with a very high velocity. The steam leaving the moving blades has a large portion of the maximum velocity of the steam when leaving the nozzle. The loss of energy due to this higher exit velocity is commonly called the carry over velocity or leaving loss.

In the reaction turbine the rotor blades themselves are arranged to form convergent nozzles. This type of turbine makes use of the reaction force produced as the steam accelerates through the nozzles formed by the rotor. Steam is directed onto the rotor by the fixed vanes of the stator. It leaves the stator as a jet that fills the entire circumference of the rotor. The steam then changes direction and increases its speed relative to the speed of the blades. A pressure drop occurs across both the stator and the rotor, with steam accelerating through the stator and decelerating through the rotor, with no net change in steam velocity across the stage but with a decrease in both pressure and temperature, reflecting the work performed in the driving of the rotor.

2.4.2 Minor overhaul

Minor turbine overhaul is performed typically every 3 to 5 years. In minor overhaul the turbine is not opened, which significantly reduces inspection and testing possibilities. The following inspections and measurements are typical in minor overhaul:

- Inspection of radial and thrust bearings.
- Inspection of turbine valves (emergency stop valves, control valves, extraction valves, etc.).
- Inspection of actuator cylinders.
- Inspection of control and protection devices.
- Endoscope inspection for turbine blades when it is possible (endoscope holes are available).
- Visual inspections for turbine (thermal insulation etc.).

2.4.3 Major overhaul

In major overhaul, typically every 6 to 10 years, the coupling between the turbine and generator is opened and all the turbine parts are opened, whereby all the parts of the turbine (e.g. casing, rotor, bearings, pipes, valves, etc) and all parts of the turbine accessories are subject to thorough checking, inspection and overhauling.

There are several methods which are suitable and necessary for testing steam turbine:

- Functional test for controls, pumps, etc. normally before and after overhaul.

- Visual inspection usually for all parts when turbine is opened (sealings, division plane, blades, etc.).
- Suitable NDT testing (non-destructive material testing) for bearings, rotor, casing, etc.
- Different kind of measurements are also needed (clearances, natural frequency, etc.).

All this allows findings to be obtained about the condition of all the parts including those of auxiliary aggregates and systems. Defective or worn parts must be replaced by spare parts.

2.5 Gas Turbines

2.5.1 Introduction

Mixture of fuel and compressed air is used in the combustion process by the gas turbine unit to produce the mechanical shaft power and, depending on the application, to drive certain accessories and ultimately the driven equipment. The type of the driven equipment may vary to be a compressor, pump or as typically in power plant applications, the electrical generator. Modern industrial type of heavy duty gas turbines could be simplifying described to be composed of axial-flow compressor, combustion system components and the turbine section. Both compressor and turbine are directly connected with an inline single shaft rotor supported by pressure lubricated bearings. Depending on the design, the generator may be connected directly or via load gear either onto cold or hot end of the shaft line. Typical auxiliary systems consist of air intake system with filtration, possible anti-icing or bleed heating, lubrication and control oil system with heat exchanger, fuel-, exhaust-, acoustical enclosure and ventilation-, fire detection and extinguishing- and control- / permanent monitoring systems.

Operating of the gas turbine, as of any rotating power equipment, must include a planned program of periodic inspections with accompanying repair and replacement of parts as necessary to ensure the required availability and reliability of the unit. Operating factors affecting the maintenance are typically as follows: type of fuel, starting frequency, load cycles and environment. Maintenance philosophy itself may vary owner by owner and may also deviate from OEM recommendations, depending on the gathered information and long term experience from former operation of the unit. OEMs and also third parties have had their own programs to research and develop advanced combustion and turbine parts to extend certain maintenance intervals or eliminate some of the planned maintenance, e.g. combustion inspections, totally.

2.5.2 Borescope inspection

Borescope inspection is rather cost efficient and feasible method for condition based maintenance or for follow up purposes of possible former detected defects. The extent of borescope inspection depends on the amount and locations of inspection ports, which varies depending on the age and manufacturer of the gas turbine. A common and also recommended practice is to perform borescope inspection once a year, even though typically annual operational hours of gas turbines have recently significantly reduced in Europe, due to economic reasons.

2.5.3 Combustion inspection / Minor inspection

The terminology and the actual scope of work varies depending on the manufacturer, but originally when 8000 EOH was still commonly reached in one operational season, this meant in practice an annual inspection. With silo- or annular type of combustion section the minor inspection scope is focused on the inspection of combustion section with relevant replacements of detected required parts, e.g. flame tube tiles or tile holders. Additionally are performed also visual inspections of compressor and turbine sections in applicable parts and time to time also repairs based on findings, like worn areas in the mixing chamber cooling rings or adjacent areas in the inner casing.

With chamber type combustion section the combustion inspection originally meant disassembly, inspection and replacement of combustion parts, at least based on the findings. Visual inspections as applicable to turbine and compressor sections were naturally part of the combustion inspection. This original 8000 EOH interval has been extended first to 12000 EOH and later on to 24000 EOH eliminating the combustion inspections from planned maintenance. This has been made possible by advanced selection of materials with improved creep and wear resistance, thermal sprayed hard face coatings against fretting or thermal

barrier coatings to reduce the surface temperatures of certain parts. In these cases the combustion inspections have been substituted by borescope inspections.

NDT is a necessary supplementary method when any deviations are found in the visual observations. Borescope is also recommended to be utilized during the combustion inspection / minor inspection.

Certain measurements should be taken to evaluate actual condition of parts and to ensure correct installation of replaced parts.

Inspections tailored by experience for control system and auxiliaries are included to the scope of combustion inspection / minor inspection to ensure the reliability for the next planned operational season.

2.5.4 Hot gas path inspection / Hot section inspection

Typical interval of hot gas path inspection or hot section inspection, depending on the terminology of the manufacturer, is 24000 EOH. By using advanced technology turbine parts this interval could be extended case by case. Combustion inspection or minor inspection described above is naturally included to the scope of work. In addition, a detailed inspection or replacement of turbine stationary and rotating parts is performed. To perform this, the top half of the turbine casing needs to lifted off and parts to be inspected or replaced need to be disassembled. In situ inspection methods can be used in certain cases, especially when the history of the parts is well known.

NDT is a necessary method. Borescope device can be used as supplementary method during earlier described in situ inspections as well as for cleanliness inspection prior to closing the casing. Cleanliness inspection is one of the most important actions in reassembly.

A complete set of turbine clearances should be taken during disassembly and reassembly to be checked against their original values, in order to evaluate the actual condition of the parts and to ensure their correct installation.

Inspections tailored by experience for control system and auxiliaries are included to the scope in larger scale than in combustion inspection / minor inspection to ensure again the reliability for the next planned operational season.

2.5.5 Major overhaul / Major inspection

Interval of major overhaul / major inspection, again depending on the terminology of the manufacturer, is typically 32000 EOH to 48000 EOH, but could be extended case by case by using advanced technology parts in turbine and compressor sections. It involves the inspection of the flange-to-flange components of the gas turbine which are subject to wear during normal operation. In addition to the scope of works described above, casings are inspected for cracks, erosion and the condition of stationary part hook fittings. Compressor blades and vanes are cleaned free of fouling, inspected for cracks, rubbing and foreign object damages. IGV hardware should be replaced with new to maintain clearances in the specified values for the coming interval of the major overhaul. Bearings and seals are to be inspected for damages. In certain point of total EOHs recommended by the manufacturer, full rotor inspection including de-stacking, re-stacking and also balancing should be performed.

NDT is a necessary method. Borescope device should be used for cleanliness inspection prior to each casing installation also in the compressor section.

A complete set of clearances related to compressor, turbine, bearings and shaft seals should be taken during disassembly and reassembly to be checked against their original values to evaluate the actual condition of the parts and to ensure their correct installation.

Inspections tailored by experience for control system and auxiliaries are included to the scope in larger scale than in hot gas path inspection / hot section inspection.

3. Case studies

Here some real cases, where further damage and production loss was prevented by detection of a fault by measurements, are introduced. The photographs show the actual damage of the equipment.

3.1 Off-line partial discharge measurements, electrical motor

Visual inspection of the stator winding of a 10.5 kV 9500 kW compressor motor was performed due to high partial discharge level in regular off-line measurement. It was found that a dislocated high voltage cable was leaning on a sharp steel edge, and creating partial discharges.

After the repair the measurement was repeated, and the pulse magnitude was found to be only approximately 10 % of the original.

If the cable insulation had been punctured by abrasion or partial discharges, the result would have been damage or even complete destruction of the important process machine and serious risk of fire or other damages in the production area.

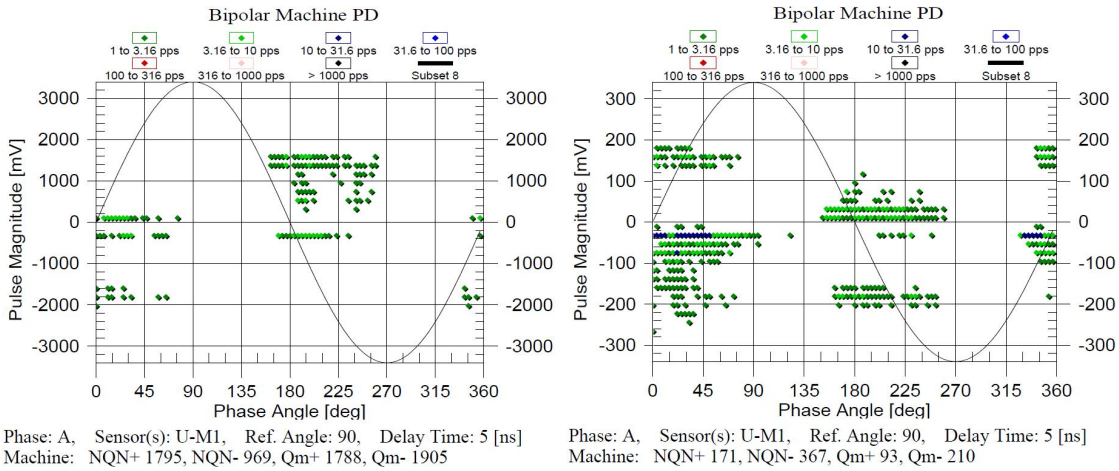

Figure 1. Partial discharge measurement pulse magnitude (in mV) as a function of voltage phase angle, before repair (left) and after repair (right). Note the different magnitude scale (10 x in the left picture).

3.2 Winding resistance measurement, generator

A fault was detected by stator winding resistance measurement during a yearly inspection of a 276 MVA steam turbine generator. The DC resistance was increased by 30% compared to initial values due to a crack in a winding lead. A repair was executed before recommissioning.

Figure 2. Crack in the stator winding lead.

3.3 Winding resistance measurement, transformer

Fault was detected by resistance measurement in a generator transformer. Phase resistance of the faulty phase was appr. 7 % higher than in the other phases. The fault was at first not detected by visual inspection of the opened transformer in scheduled overhaul, because it was hidden under thick insulation layers. In this case there was no clear indication of the problem in the dissolved gas analysis results either.

Figure 3. Overheated connection in a transformer.

3.4 Vibration measurement, electrical motor

In regular vibration measurements of a production critical electrical motor of a power plant a clear increase in vibration level and appearance of new peaks in the spectrum was seen. The bearings were changed, and the old bearings were cut open for inspection. A clear case of bearing current damage, caused by frequency converter drive, was found in both bearings.

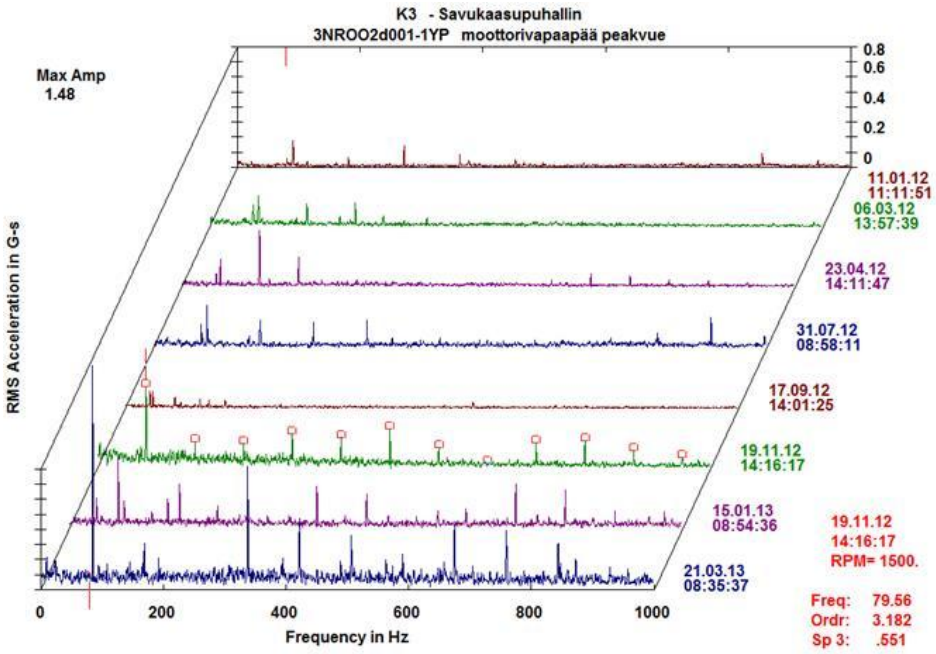

Figure 4. Development of vibration spectrum within 15 months. Note the date on the right side.

Figure 5. Bearing current damage in the outer rings of the bearings.

3.5 Transformer oil analysis

Dissolved gas analysis (DGA) indicated overheating inside an oil filled transformer. The transformer was taken to a service work shop and opened. An overheated connection was found. After repair the DGA results returned back to normal.

Table 1. Dissolved gas analysis of a transformer, before and after repair

Gas type	Concentration (ppm) one year before the appearance of the fault (normal condition)	Concentration (ppm) before the repair (fault condition)
H_2	7	1166
CH_4	4	122
CO	226	423
C_2H_6	0	56
Total concentration of gases	254	1802

Figure 6. Overheated connection in a transformer. Left: wrapped in insulation paper. Right: revealed.

3.6 Thermal condition monitoring of a steam turbine

Isentropic efficiency of high pressure turbine had reduced clearly for a few months. After one turbine shut down and restart the drop of isentropic efficiency of HP-turbine was remarkable. Isentropic efficiency of HP-turbine dropped 0,6 %-units to 89,1%.

HP-turbine was examined by endoscope and during examination it was found out that six blades in Radax-stage were broken. Because blades in Radax-stage are stationary there wasn't any remarkable changes in turbine vibration level.

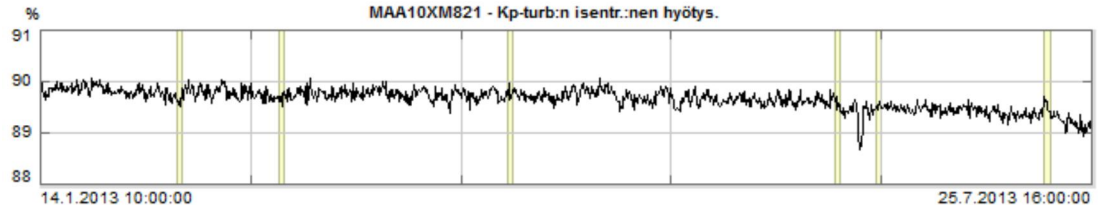

Figure 7. Isentropic efficiency of high pressure turbine.

Figure 8. Six blades in Radax-stage were broken (arrow).

3.7 Gas turbine borescope inspection

During the combustion inspection of a gas turbine quite severe coating failures in some areas of the 2nd stage nozzle in certain vane leading edges were detected. It was recommended to follow up the progress of the failure with borescope inspection in every 2000 EOH. In the first follow up inspection the progress of the coating failure was detected to be rather limited, but much more severe defects were found in several turbine first stage rotating blades. Cracks with length of 2-20 mm located in the first cooling holes counted from the shank. The whole turbine section was earlier visually inspected and none of the 1st stage rotating blade cracks was observed at that time. It is obvious that the progress of the cracking has happened during the 2000 EOH follow up period. Without this observation with borescope, which led to opening of the unit for 1st stage replacement, the downstream consequences could have been fatal due to further progress of 1st stage cracking until liberation of air foil.

Figure 9. Borescope view of 1st stage blade cracking, convex side (left) and cooling hole area (right).

Reference

1. Vibration Training Course Book, Mobius Institute 2013

New interpretations of the Charpy V test

Kim Wallin[1], Päivi Karjalainen-Roikonen[1] & Pasi Suikkanen[2]

[1] VTT Technical Research Centre of Finland
P.O. Box 1000, FI-02044 VTT, Finland

[2]SSAB Europe Oy
Rautaruukintie 155, P.O. Box 93, 92101 Raahe, Finland

Abstract

Presently most structural integrity assessment procedures still allow the use of Charpy-V notch impact tests as a measure of fracture toughness. The use is generally made through some more or less reliable correlations between standard Charpy-V notch energy and fracture toughness or tearing resistance.

Common for the present correlations is that very few studies have been made with respect to their usability to Ultra High Strength Steels (UHSS) with yield strengths in the excess of 900 MPa. This is the topic of this work. Focussing on novel directly quenched high performance steels, the applicability of the Master Curve methodology with special emphasis on the temperature dependence is examined and the validity of the standard T_0-TC_{V28J} transition temperature correlation is checked. Improvements to the criteria are proposed for further considerations. Additionally, a new simple procedure for converting sub-sized Charpy V data to full size specimens, that is in line with BS 7910, is presented.

The new interpretations of the Charpy V test presented here enable an extension of present design rules like the ones in EN 1993-1-12 (2007) to steel strengths well beyond 1000 MPa. Providing a sufficient toughness for the steel is up to the steel manufacturer, but there is no basic reason why UHSS cannot be used based on an identical assessment procedure as for presently accepted steel strengths. Only 2 equations in EN 1993-1-12 (2007) needs to be changed, and the sub-size specimen conversion procedure needs to be adopted.

1. Introduction

Presently most structural integrity assessment procedures still allow the use of Charpy-V notch impact tests as a measure of fracture toughness. The use is generally made through some more or less reliable correlations between standard Charpy-V notch energy and fracture toughness or tearing resistance.

There are two major concepts governing the assessment of fracture toughness of steels in e.g. EN 1993-1-12 (2007). They are: The Master Curve (MC) methodology [1] and the T_0-TC_{V28J} transition temperature correlation [2].

The Master Curve methodology provides a description for the fracture toughness scatter, size effect and temperature dependence both for the transition region as well as the lower shelf. It enables a complete

characterization of a material's brittle fracture toughness based on only a few small size specimens. The method combines a theoretical description of the scatter, a statistical size effect and an empirically found temperature dependence of fracture toughness. The fracture toughness in the brittle fracture regime is thus described with only one parameter, the transition temperature T_0 (Figure 1). At this temperature the mean fracture toughness for a 25.4 mm thick specimen is 100 MPa$\sqrt{m}$.

The Master Curve method is applicable for ferritic structural steels and it has been standardised by the American Society for Testing and Materials, ASTM E1921-97, the present version being ASTM E1921-15 [3]. It is the first fracture toughness testing standard that gives advice on the use of the test result.

The fact that a single parameter (T_0) fully describes the fracture toughness in the brittle fracture regime has enabled the correlation between T_0 and the 28 J Charpy-V transition temperature TC_{V28J}. After subsequent wide validation, the correlation is presently included both in European standardisation like BS 7910 and in the structural integrity methods of SINTAP [4] and FITNET [5].

A problem arises if the structure has such dimensions that standard size Charpy-V notch specimens cannot be used. Application standards contain some guides on how to converse sub-sized specimen data to correspond to full size specimens, but these are often inaccurate and limited in their application range. Procedures like ASTM A370, BS 7910 and API 579 give some advice on the use of sub-sized Charpy-V specimens but none of them cover the whole Charpy-V transition curve.

Common for the basic Master Curve, the standard T_0-TC_{V28J} transition temperature correlation and the sub-size specimen conversion is that very few studies have been made with respect to their usability to Ultra High Strength Steels with yield strengths in the excess of 900 MPa. This is the topic of this work. Focussing on novel directly quenched high performance steels, the applicability of the Master Curve methodology with special emphasis on the temperature dependence is examined and the validity of the standard T_0-TC_{V28J} transition temperature correlation is checked. Improvements to the criteria are proposed for further considerations.

Additionally, a new simple procedure for converting sub-sized Charpy V data to full size specimens, that is in line with BS 7910, is presented. It is shown that it is applicable over the whole transition curve, thus enabling a point-wise conversion of sub-sized Charpy-V data to correspond to full size specimens. The new procedure is applicable for steel strengths ranging from 200 MPa to 1400 MPa.

2. Advanced Master Curve temperature dependence [6]

The fracture toughness Master Curve (MC) method for the description of brittle fracture toughness [1], which forms the test standard ASTM E1921, is included among others in the ASME code and the structural integrity standard BS 7910. The MC has been widely validated for numerous different structural steels. The MC can be divided into a theoretical and an empirical part. The theoretical part, derived from statistical modelling of the cleavage fracture event, gives the scatter of fracture toughness as a function of specimen thickness (crack front length) and median fracture toughness. This part of the standard MC has the form of Eq. (1). B is the specimen thickness (crack front length). B_0 is the normalization thickness taken as 25.4 mm. K_0 corresponds to a cumulative failure probability of 63.2% and is related to the median fracture toughness ($K_{0.5}$) through Eq. (2). The mean fracture toughness is slightly lower than the median, because the fracture toughness distribution is non-symmetrical. The constant in Eq. (2) for the mean fracture toughness becomes 0.906. K_{min} represents a lower limiting stress intensity factor, below which cleavage crack propagation is impossible on a micro-scale [8].

$$P_f = 1 - exp\left\{-\frac{B}{B_0}\cdot\left(\frac{K_I - K_{min}}{K_0 - K_{min}}\right)^4\right\} \quad (1)$$

$$K_{0.5} = 0.912\cdot(K_0 - K_{min}) + K_{min} \quad (2)$$

The size effect and the scatter are interlinked. If the scatter is described correctly, it automatically follows that there will also be a statistical size effect, since both effects relate to the same weakest link nature of cleavage fracture initiation.

The empirical part of the standard MC is related to the temperature dependence of K_0, in accordance with Eq. (3), by which the fracture toughness is expressed in the form of a single reference temperature, T_0. It corresponds to the temperature where a 25.4 mm thick specimen has a mean fracture toughness of 100 MPa√m. The dependence is based on a best fit to a number of large data sets available at the time. The original data is reproduced in Fig. 2 [1]. The T_0 values of the original data cover a temperature range from -109 °C to +51 °C and yield strengths between 280 MPa and 620 MPa. The exponential shape of the temperature dependence comes from the assumption that the events controlling cleavage fracture are thermally activated and as such should follow an exponential trend.

$$K_0 = 31 + 77 \cdot exp(0.019 \cdot [T - T_0]) \qquad MPa\sqrt{m}, °C \tag{3}$$

The standard MC temperature dependence does not contain the assumption that all structural steels would follow Eq. (3). There are too many factors affecting the temperature dependence to assume a universally constant behavior for all structural steels [1]. The ASTM E1921 temperature dependence given by Eq. (3) is only an approximation to fracture toughness data in the temperature region between T_0-50 °C and T_0+50 °C. For applications outside this region, it is advised in the MC methodology [2] to perform tests at the relevant temperature.

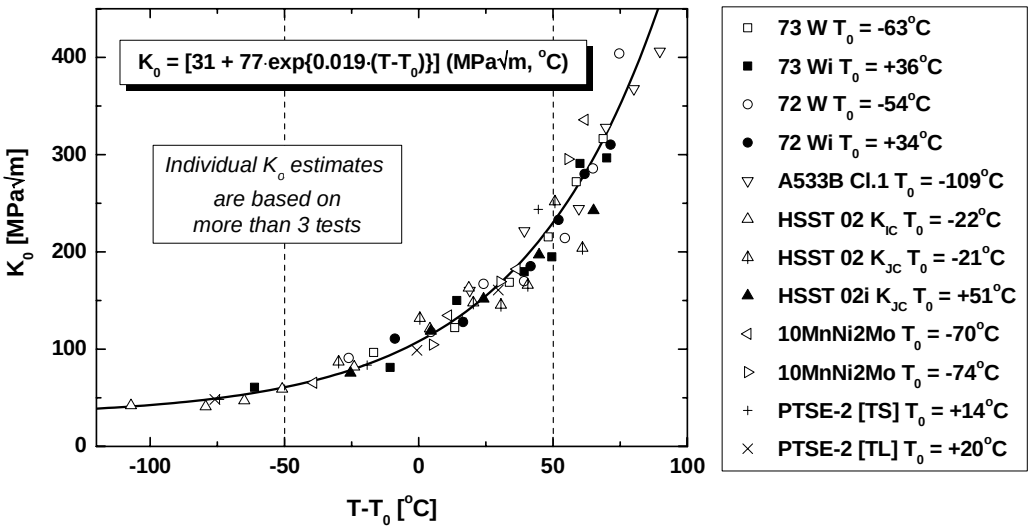

Figure 1. Original data used to define the temperature dependence of the fracture toughness Master Curve [1]. Each point denotes a K_0 estimate based on more than three tests.

Recently, an advanced Master Curve (AMC) for fracture toughness has been developed in the form of Eq. (4) [6]. It gives an approximate estimate of the exponential constant (C) that in the standard expression has the value 0.019 $^oC^{-1}$. The coefficient C for the AMC has the form given by Eqs. (4) and (5).

Eq. (5) is based on the fracture toughness temperature dependence of 86 different structural steels. Data sets each with at least 24 samples fulfilling the MC size requirement were fitted with the MC, with the parameter C as a variable [6]. The materials covered a T_0 range between -172 °C and 179 °C and a yield strength range between 248 MPa and 1082 MPa [6]. The equation should be considered only an approximation, because the temperature dependence is also affected by alloying elements like nickel and probably also to some extent by the microstructure, whereas Eq. (5) accounts only for yield strength and T_0 temperature.

$$K_0 = 31 + 77 \cdot exp(C \cdot [T - T_0]) \qquad MPa\sqrt{m}, °C \tag{4}$$

$$C[°C^{-1}] \approx \left\{0.7 + \left(\frac{161\ MPa}{\sigma_Y}\right)^{0.605} + \left(\frac{155°C}{T_0+273°C}\right)^{1.067}\right\}/100°C \quad (5)$$

For a validation of Eq. (5) a larger number of UHSS data sets, most of which were not included in the fitting of Eq. (5), were analyzed both by the standard MC and the general maximum likelihood method [6]. Only materials with yield strengths in the range between 850 MPa and 1200 MPa were selected for the analysis. The maximum likelihood estimates for the parameter C, together with the normalized log-likelihood values are shown in Fig. 2. For nearly all data sets where the normalized log-likelihood values are in the expected range from -4.6 to -3.6 [6], the values for C follow Eq. (5) within the expected theoretical statistical variability (± 0.005 $^{o}C^{-1}$) [6]. It should be pointed out that a larger experimental variation is expected since the real data sets are not covering the ideal temperature range as used for the estimation of the ideal log-likelihoods. Eq. (5) is thus well validated for UHSS. The apparent outliers to Eq. (5) in Fig. 2 all have either exceptionally low or exceptionally high log-likelihoods. Generally, the outliers are not material-specific, thus indicating that they are related to specific data sets, not to material type per se.

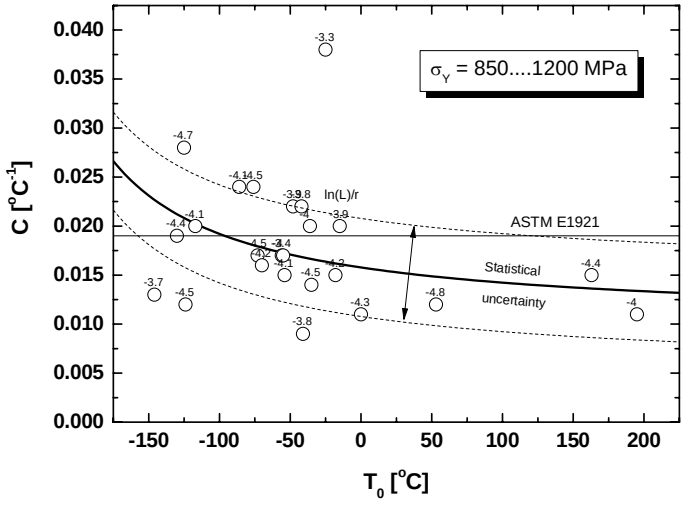

Figure 2. Validation of eq. (5) for ultra high strength steel data [6].

The use of the best estimate instead of the standard MC does not dramatically change the T_0 estimates as seen from Fig. 3. The difference is within 10 °C. It should be emphasized that the best estimate makes use of all test results, whereas the standard estimate is limited to values in the range between T_0-50 °C and T_0+50 °C.

The small difference in standard and best-estimate T_0 values implies that the standard MC can well be applied if the application temperature is within the region between T_0-50 °C and T_0+50 °C. If there are a sufficient number of test results (> 20) over a 100 °C temperature range, a best fit of C can be made. For smaller data sets the modified advanced Master Cuve (AMC_m) can be used so that a first estimate for T_0 is obtained from the standard MC and then Eq. (5) is used to derive a case-specific advanced Master Curve. The same number of specimens and other requirements in ASTM E1921 remains the same for UHSS.

3. Advanced T_0-TC_{V28J} correlation [7]

There are several basic differences between the fracture toughness test and the Charpy-V impact test (CVN). The most important differences are presented in Table 1 [7].

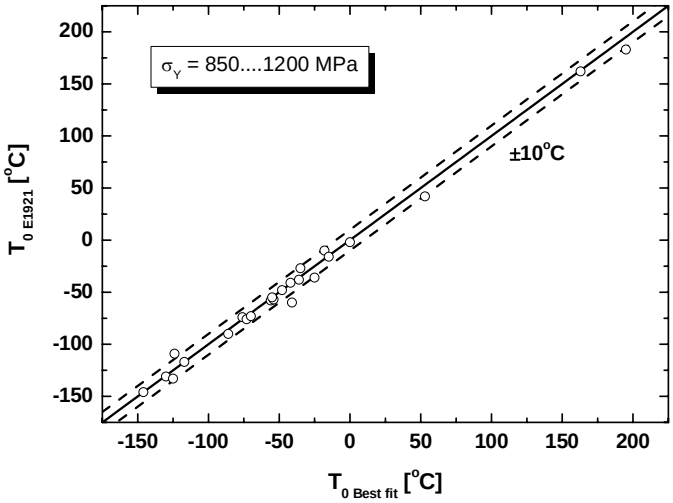

Figure 3. Difference in best estimate T_0 and standard T_{0E1921} for ultra high strength steels.

Table 1. Main differences between fracture toughness and Charpy-V impact test [7].

DIFFERENCE	**CVN**	**K_{IC}, K_{JC}**
Specimen size	*10 x 10 x 55 (standard geometry)*	*Variable*
Loading rate	*Dynamic*	*Quasi-static*
Flaw geometry	*Shallow blunt notch*	*Deep crack*
Event described in test	*Fracture initiation + propagation*	*Fracture initiation*

The effect of the differences is schematically presented in Fig. 4. The basis for a quantitative correlation between CVN and fracture toughness is a minimizing of the effects of the differences, which affect the correlation, by a theoretical treatment

Based on Table 1 and Fig. 4, it is clear that one cannot correlate the impact energy directly with the fracture toughness. One must first clarify which parameters are realistic to correlate. In order to do this, the basic features of each test must be examined separately to see which features are the same.

From the fracture toughness point of view, it is recommendable to choose the temperature corresponding to a particular fracture toughness describing brittle fracture. The chosen temperature must be below the fracture toughness for ductile fracture initiation so that ductile fracture will not affect the result. At the same time it must be clearly higher than the lower shelf in order to be in a region where the effect of temperature upon toughness is large. The T_0 temperature is thus preferable since it removes the effect of specimen thickness.

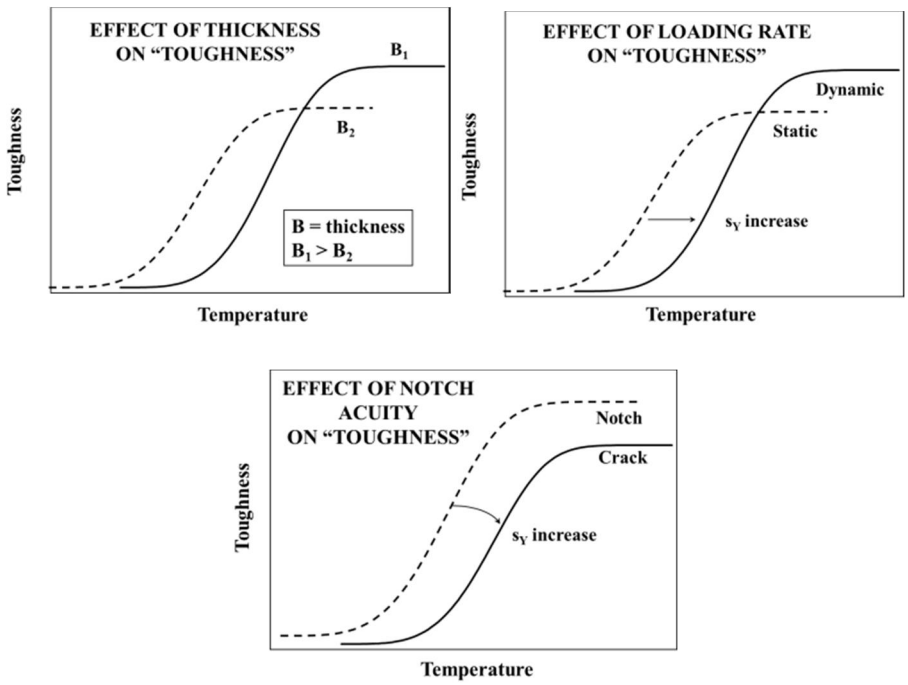

Figure 4. The effect of the basic differences between Charpy-V and fracture toughness tests on schematic presentation of measured "toughness" [7].

If the temperature is chosen as the parameter to correlate in the fracture toughness test, it should also be chosen in the Charpy-V impact test. The chosen temperature must, in addition to fulfilling the same requirements as in the case of fracture toughness, correspond to a low enough energy so that the impact energy value will not depend on the applied testing standard. Also, because ductile crack growth is not allowed, a temperature corresponding close to the lower shelf must be chosen. On the other hand, the chosen temperature should correspond to the increasing part of the transition curve. It is also recommended to choose a commonly recognized energy level. This is why the transition temperature corresponding to Charpy-V impact energy 28 J is a good choice. The energy 28 J comes from the French approximation of the American 20 ft-lb energy. The French philosophy has been to select the closest energy in J units above 20 ft-lb. This differs a little from the German approximation. The German philosophy has been to select the closest energy for 20 ft-lb in J units. The Germans thus use an energy level of 27 J. This value is also used in in e.g. ISO148-1 and EN 1993-1-12. The French value of 28 J is used here, but since the difference between the two interpretations (and the original 20 ft-lb) is of the order of 1 °C, the same correlation can be used to describe all three CVN transition criterions.

The chosen impact energy level is practically independent of testing standards and at this energy level the amount of ductile tearing is small. The remaining, strongly affecting, factors are the effect of the blunt notch and the effect of loading rate difference.

An increasing loading rate shifts the toughness transition to higher temperatures and the magnitude of the effect is partly inversely related to the materials yield strength. A blunter notch on the other hand shifts the toughness transition to lower temperatures. Also, in this case the magnitude of the shift is partly inversely related to the materials yield strength. This is because the "singular" loading experienced by a crack is directly related to the strain hardening exponent and inversely related to the yield strength. A high strength material having a small strain hardening exponent does not "see" such a large difference between a crack and a blunt notch. Even though neither difference can accurately be accounted for, their effects were assumed to be of the same magnitude and opposite to each other. Their combined effect could therefore be expected to be relatively small.

Interestingly enough, an adjustment for either one of the above effects, e.g. trying to correlate CVN with dynamic fracture toughness, will produce strongly material dependent correlations because the combined effect is lost.

The standard correlation has the simple form of Eq. (6).

$$T_0 \approx TC_{V28J} - 18°C \tag{6}$$

The standard T_0-TC_{V28J} correlation with offset of -18 °C, is not capable of describing the UHSS materials correctly as seen by Fig. 5. It is evident that the original correlation has underestimated the effect of the yield strength on the correlation. Therefore, the data in Fig. 5 was combined with the data base in [8] complemented by new data [7] and a new three-dimensional regression-analysis were performed. The new "combined" SE(B) data base consists of 181 different data sets with valid T_0 values. The result of the regression analysis is shown in Fig. 6. The new improved correlation has the form of Eq. (7). There is a clear yield strength effect, but only a small effect of upper shelf energy, indicating that the 28 J energy level is low enough so that ductile tearing only has a minimal effect on the Charpy-V transition temperature. If the correlation would be based on a higher energy level, the upper shelf energy would be expected to have a larger effect. Even if the effect of upper shelf energy is small, it is included for clarity and to be prepared for any future findings.

$$T_{0-Est.-SE(B)} \approx TC_{V28J} - 89°C + \frac{\sigma_Y}{9\ MPa{\cdot}°C^{-1}} - \frac{C_{V-US}}{59\ J{\cdot}°C^{-1}} \tag{7}$$

Fig. 7 shows the new correlation expressed for SE(B) specimens. The 10 °C bias between SE(B) and C(T) specimens that was found in [8] has been accounted for. Even though the new fit was specifically made for SE(B) specimen data, the new correlation provides also an adequate description of the C(T) specimen data. Thus, Eq. (7) can be used as a general T_0-TC_{V28J} correlation regardless of steel strength or quality. This, combined with Eq. (5) and the Master Curve scatter and size effect expressions, enable the estimation of low temperature fracture properties from Charpy-V impact test information, regardless of steel strength.

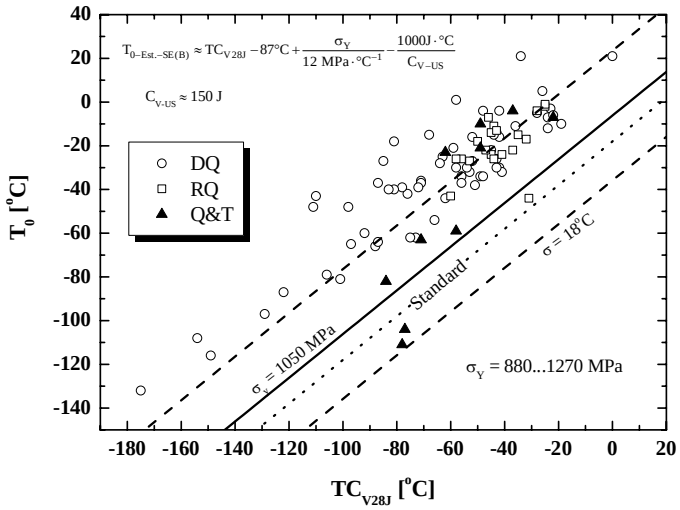

Figure 5. Applicability of standard T_0-TC_{V28J} correlation, Eq. (6), to describe UHSS data [7].

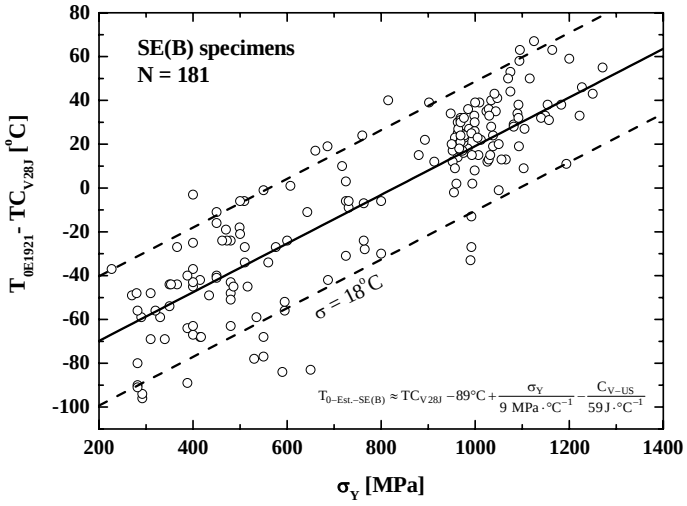

Figure 6. Improved T_0-TC_{V28J} correlation for SE(B) specimens accounting for UHSS materials [7].

4. Sub-sized CVN specimen conversion methodology

A problem arises if the structure has such dimensions that standard size CVN specimens cannot be used. E.g. when the plate thickness is less than 10 mm, testing with standard full-sized CVN notch specimens is impossible. In such cases the testing must be based on sub-sized or miniature specimens. Sub-sized specimens are those where the specimen thickness is reduced, but the other dimensions, including the notch, are kept constant. Miniature specimens are specimens where all dimensions are reduced, including the notch geometry. Both specimen types are recognized by different impact test standards, but no testing standard gives advice about the meaning of test results determined by such specimens.

The difficulty lies in converting the result from the sub-sized or miniature specimen to correspond to the result from a standard sized specimen. Basically two different methodologies can be used. The conversion can be based either directly upon the measured parameter e.g. impact energy (C_V, KV) or on some transition temperature criterion.

The ideal situation would be to be able to extrapolate directly the impact energies from sub-sized or miniature specimens to correspond to standard full-size specimens. In several manufacturing standards, sub-sized specimens are correlated to full-sized specimen by a simple constant multiplier on the energy. Sometimes, the same proportional energy is simply required for sub-sized specimens. This requirement is often but not always also combined with a temperature compensation. Many codes require a higher proportional impact energy for sub-size specimens, but without a temperature compensation. Specifically, for a 5x10 mm^2 specimen, usually the energy is multiplied by 1.5 to make it correspond to a full-size specimen. The problem with the direct extrapolation lies in the fact that the specimen thickness yields different effects in different regions of the transition range. This is highlighted in Fig. 7 where 5 mm sub-sized specimen energy is compared with full-size specimen energy, [8].

On the lower shelf sub-sized specimens yield proportionally higher impact energies as compared to standard size specimens. They may even produce higher absolute energies than a full size specimen. On the upper shelf the behavior is reversed so that sub-sized specimens yield either proportionally equal or even lower impact energies than standard sized specimens. The reason for this controversial behavior is that the different fracture micromechanisms yield different specimens thickness effects. In the transition region there is a competition between ductile and brittle fracture micromechanisms thus yielding a very complex combined thickness effect. This effectively invalidates the method of direct extrapolation which is

commonly used today. In the case of miniature specimens, the correlation is even more difficult, since in this case, also the notch geometry usually changes from case to case.

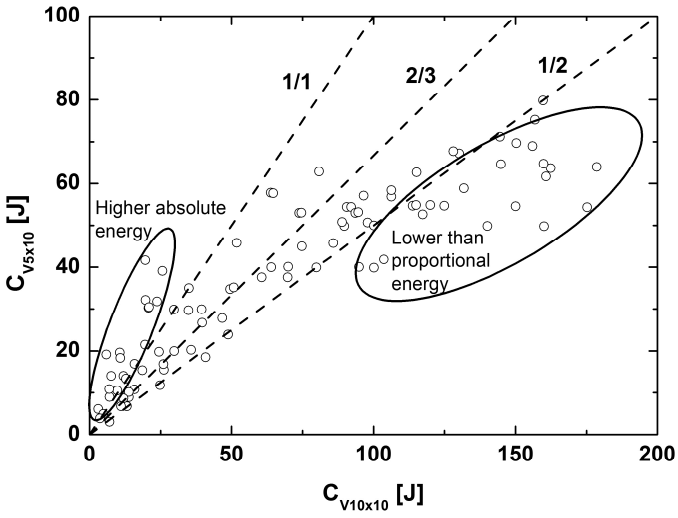

Figure 7. Example of impact energy relations between sub-sized (5x10 mm^2) and full-sized (10x10 mm^2) CVN specimens [8].

The problem is highlighted in Fig. 8 which shows transition curves for different thickness sub-sized specimens [9]. Two things are apparent. First, the ductile-to-brittle transition is moving to lower temperatures with decreasing specimen thickness. Second, the proportional upper shelf energy is reduced with decreasing specimen thickness.

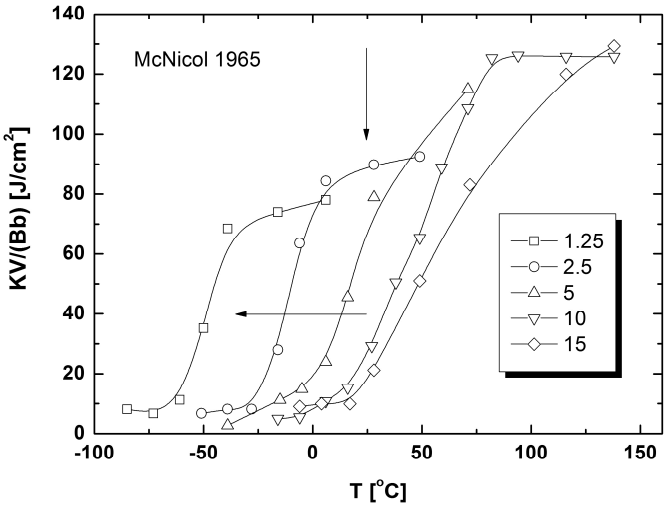

Figure 8. Effect of specimen thickness (mm) on proportional Charpy-V impact energy as a function of temperature [9].

Because of the problem with a direct energy correlation, usually the best correlations between different specimen types are based on some transition temperature criterion.

Application standards contain some guides on how to convert sub-sized specimen data to correspond to full size specimens, but these are often inaccurate and limited in their application range. Procedures like ASTM A370, BS7910 and API 579 give some advice on the use of sub-sized CVN specimens but none of them cover the whole CVN transition curve.

The brittle fracture is affected both by a constraint effect as well as a statistical thickness effect. Both effects act in the same direction so that a sub-size specimen will yield a lower transition temperature than a standard full-size specimen. Thus sub-sized specimens must be "penalized" to fulfil the criterion at a lower temperature than would be required for standard full-size specimens. If the constraint effects are predominant, the thickness effect upon the transition temperature should be dependent on the materials yield strength. On the other hand, if the statistical size effect is predominant, yield strength should not affect the thickness effect.

In order to determine the effect of specimen thickness upon the 35 J/cm^2 transition temperature, T_{35J}/cm^2, data from the literature corresponding to a variety of steels have been assessed by Wallin [10]. The materials corresponded to yield strength levels in the range 200-1000 MPa and specimen thicknesses in the range 1.25-20 mm. The analysis was limited to specimen thicknesses between 3 and 10 mm, because this thickness range is most relevant for brittle fracture assessment. From the data the difference in transition temperature (ΔT), as compared with the standard full-size specimen size, was determined for the different specimen thicknesses. The fitted data is presented in Fig. 9.
The mean thickness dependence has the form of Eq. (8).

$$\Delta T_{35J/cm^2} = 51.4°C \cdot ln\left\{2 \cdot \left(\frac{B}{10\ mm}\right)^{0.25} - 1\right\} \quad (8)$$

The yield strength was shown to have a negligible effect upon the thickness dependence in the thickness range 3-10 mm. This indicates that the main contribution to the thickness effect, at this energy level, comes from the statistical size effect. From Fig. 9 it is seen that Eq. (8), even though not developed for thicknesses below 3 mm, yields a good description of the thickness dependence all the way down to a thickness of 1.25 mm.

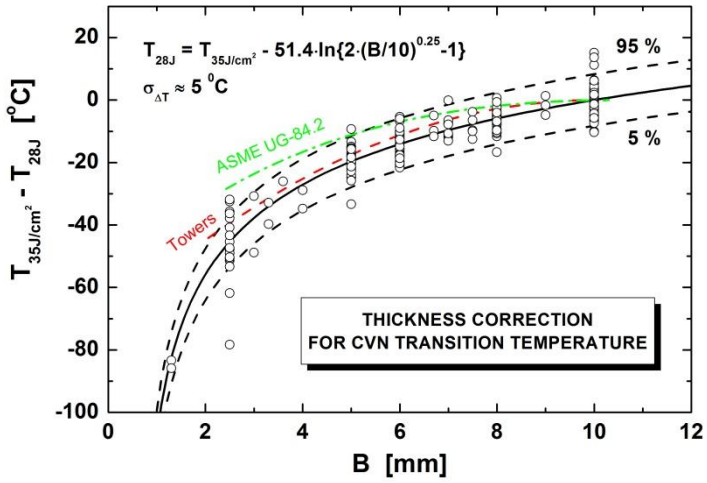

Figure 9. Effect of specimen thickness on the 35 J/cm^2 CVN transition temperature [10].

Fig. 9 includes also two other relations for the effect of specimen thickness on the transition temperature. The relation by Towers [11] is nearly equivalent to Eq. (8) in the thickness range 3…10 mm, which was the focus of the Towers work. The difference between the Towers relation and Eq. (8) is mainly that Eq. (8) is based on a much larger data base. The ASME UG-84.2 relation, that is also included in e.g. ASTM A333 and API 579, is much older and its background is not known. Based on the available data, The UG-84.2 relation is non-conservative and should not be used.

As shown in Fig. 8, sub-size CVN specimens on the upper shelf absorb the same or less amount of energy per area as normal size CVN specimens. The reason for the size effect is related to shear lips. When a Charpy-V specimen fractures by ductile tearing, part of the fracture surface (middle part) will constitute of "flat" fracture and part (sides) of shear fracture regions. When the crack starts to grow, the shear regions (lips) start to develop. Their size increases with crack growth and saturates towards a thickness that is dependent on the tearing resistance of the material. This shear lip development is largely independent of specimen thickness. This means that the proportional amount of shear lips on the fracture surface will increase with decreasing specimen size. Below a certain thickness, the whole fracture surface will show shear fracture. Since the energy absorbed in the fracture process is different for flat fracture and shear fracture, reducing the specimen thickness will lead to a transformation from flat fracture description to shear fracture description.

The fracture energy for 100% shear fracture is only about half of the energy for normal ductile tearing. This is consistent with the differences between tensile and shear flow properties and elastic properties. The description of the data requires thus a sigmoidal equation going from 1 to 0.5. In order to develop a quantitative description of the upper shelf energy relation, all the data corresponding to steels, were normalised by KV10-US/B and simply fitted by a hyperbolic-tangent equation, resulting in the form of Eq. (9) [12].

$$\frac{KV_{B-US}\cdot 10}{KV_{10-US}\cdot B} = 1 - \frac{0.5\cdot\exp\left\{\frac{2\cdot\left(\frac{KV_{10-US}}{B}-44.7\right)}{17.3}\right\}}{1+\exp\left\{\frac{2\cdot\left(\frac{KV_{10-US}}{B}-44.7\right)}{17.3}\right\}} \quad \ldots \quad [J, mm] \tag{9}$$

The equation apparently has one basic flaw. For a specimen thickness of 10 mm, the right hand side of the equation does not become unity. This is, however, not really a flaw, but a result of the physical meaning of the equation. The equation does not directly relate the toughness of one specimen to the other, but relates the toughness affected by shear lips to a case with no effect of shear lips. Thus, the equation can also be used to examine the effect of shear lips on a standard full-sized specimen and it can be used to estimate an upper shelf energy value corresponding to 0% shear lips.

4.1 Conversion methodology

The conversion consists simply of using Eq. (9) for each individual test result, over the whole transition region and to adjust each individual test temperature with Eq. (8). Accounting for shear lip effects also in 10 mm thick specimens mean that Eq. (9) needs to be used twice. First, estimate the 10 mm thick specimen without shear lips ($KV_{10planar}$) iteratively with Eq. (9) and then use this value to estimate the energy for the 10 mm thick specimen with side grooves. As an example of the outcome of the conversion, the data in Fig. 8 were analysed as described above. The result of the conversion is shown in Fig. 10. With the exception of the 1.25 mm thick specimens the conversion works extremely well. The behaviour of the thin specimens is due to that very thin specimens develop 100 % shear lips early and thus reduce the transition region. This, however, generally has a significant effect only on specimen thicknesses below 3 mm.

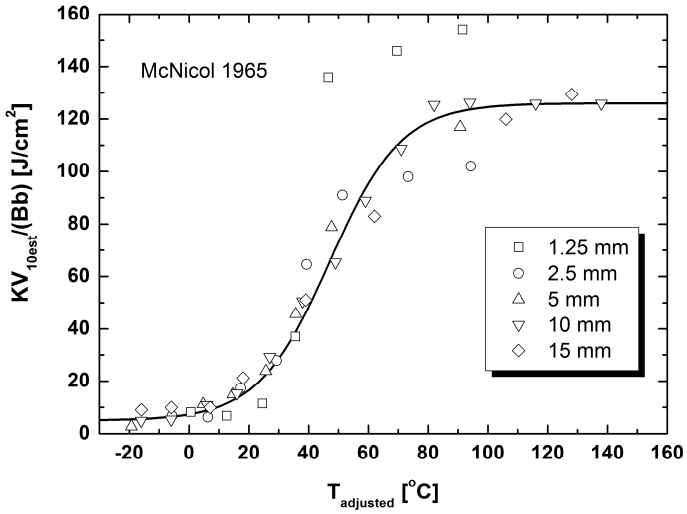

Figure 10. Example of energy conversion for individual specimens. Data taken from McNicol [9].

In order to verify the procedure also for ultra high strength steels, two ultra high strength steels were tested. The steels were 10 mm thick Optim™ 960 QC (σ_y = 1090 MPa) and Weldox™ 960 (σ_y = 1016 MPa) manufactured by SSAB Europe. These steels were tested in the T-S orientation to ensure a uniform microstructure along the crack front. The sub-sized specimens had a thickness of 6 mm. The converted 6 mm data is present together with the full size data in Fig. 11. Considering the natural scatter in Charpy-V test results, the conversion provides an excellent result. It is important to use an orientation where the notch and subsequent crack lies in identical microstructures for both specimen types. Often orientations T-L or L-T are used. In this case the through thickness toughness variations may affect the result and indicate misleading size effects.

The presented methodology provides the first simple reliable conversion of sub-sized to full size specimen CVN energies. The value compared to previous methods is that it is applicable over the whole transition region and provides a single value conversion, unlike a transition temperature adjustment or upper shelf correction. Many of the previous attempts to develop corrections for sub-sized specimens have been clouded by a lack of distinguishing between different fracture micromechanisms. Also, it is of utmost importance that the different specimens correspond to the same microstructure. Often, when specimens are taken in T-L or L-T orientations, the full size and sub-size specimens may correspond to different depths from the plate surface and this may cause apparent different relations between the specimens.

The conversion methodology is not affected by the materials yield strength. It is thus equally applicable to all classes of structural steels showing a ductile to brittle transition. FCC metals that do not fail by cleavage, obviously are not affect by the temperature adjustment.

5. Conclusions

The new interpretations of the Charpy V test presented here enables an extension of present design rules like the ones in EN 1993-1-12 (2007) to steel strengths well beyond 1000 MPa. Providing a sufficient toughness for the steel is up to the steel manufacturer, but there is no basic reason why UHSS cannot be used based on an identical assessment procedure as for presently accepted steel strengths. Only 2 equations in EN 1993-1-12 (2007) needs to be changed, and the sub-size specimen conversion procedure needs to be adopted.

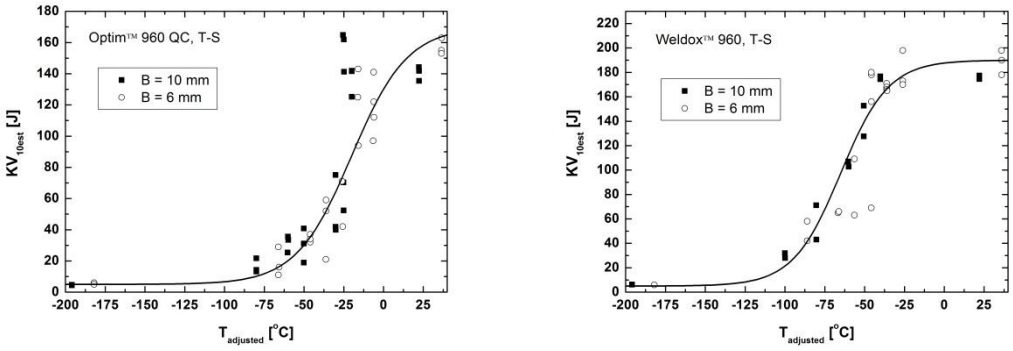

Figure 11. Example of energy conversion for individual specimens for ultra high strength steels.

Acknowledgements

This work is part of the EXTREMEST project that is part of the Finnish Metals and Engineering Competence Cluster (FIMECC Ltd) BSA programme, funded by the Finnish Funding Agency for Technology and Innovation (Tekes), Finnish Industry and VTT.

References

1. Wallin K. The Master Curve Method: A New Concept for Brittle Fracture. Int. J. of Materials and Product Technology 1999;14:342 – 354.

2. Wallin K. A Simple Theoretical Charpy V - K_{IC} - Correlation for Irradiation Embrittlement, PVP-Vol. 170, American Society of Mechanical Engineers, ASME, New York NY USA, (1989) 93 – 100.

3. ASTM E1921 – 15: Standard Test Method for Determination of Reference Temperature, T_0, for Ferritic Steels in the Transition Range. Annual Book of ASTM standards, ASTM International, West Conshohocken PA USA, 2015.

4. SINTAP, Structural Integrity Assessment Procedures for European Industry - Final Procedure, Contract No BRPR-CT95-0024, Project No. BE95-1426. 1999.

5. FITNET, Fitness-for-Service PROCEDURE, Prepared by European Fitness-for-Service Thematic Network – FITNET 2006.

6. Wallin, K., Pallaspuro, S., Karjalainen-Roikonen, P., Suikkanen, P. Applicability of the Master Curve method to ultra high strength steels. Proceedings of the ASME 2015 Pressure Vessels & Piping Division Conference, PVP2015, July 19-23, 2015, Boston, Massachusetts, USA, PVP2015-45554.

7. Wallin, K., Karjalainen-Roikonen, P., Pallaspuro, S. Low Temperature Fracture Toughness Estimates for Very High Strength Steels. Proceedings of the Twenty-fifth (2015) International Ocean and Polar Engineering Conference, Kona, Big Island, Hawaii, USA, June 21-26, 2015, ISBN 978-1-880653-89-0; ISSN 1098-6189.

8. Wallin K. Fracture Toughness of Engineering Materials – Estimation and Application, EMAS Publishing, Warrington UK, 2011.

9. McNicol, R. Correlation of Charpy Test Results for Standard and Nonstandard Size Specimens. Welding Research Supplement, 1965, 385-393.

10. Wallin, K. Methodology for selecting Charpy toughness criteria for thin high strength steels. Part I: Determining the fracture toughness. 1994, Jernkontorets Forskning D 733. Jernkontoret, Stockholm.

11. Towers, O.L. Testing of Sub-size Charpy Specimens. Part 1 - The Influence of Thickness on the Ductile/Brittle Transition. Metal Construction, 1986, 18, 171R-176R.

12. Wallin, K. Upper shelf energy normalisation for sub-sized Charpy-V specimens. Int J of Pressure Vessels and Piping, 2001, 78, 463-470.

Power & process:
Design and performance

Negligible creep temperature curves for EN-13445

Stefan Holmström

European Commission, Joint Research Centre IET, Petten, The Netherlands
Stefan.Holmstrom@ec.europa.eu

Abstract

In this paper a novel but simplified methodology for determining negligible creep temperature (T_{NEC}) curves from standard creep strength tables and tensile properties is presented. The methodology is not material specific and has been applied for 15 non-alloyed and alloyed ferritic/martensitic steels from EN-10028-2 and 9 creep resisting austenitic steels from EN-10028-7. The curves are now assessed for inclusion in the revision of the European standard EN-13445. In this paper the workflow, methodology and key assumptions for the definition of the T_{NEC} curves are described. Verification calculations for time to 0.2% creep strain are given for the steels P22, P91 and 316L/316L(N). The benefits and limitations of the methodology are also discussed.

1. Introduction

The design of a component is simplified considerably if it can be shown that it operates below the Negligible Creep Temperature (T_{NEC}). For instance in the case of nuclear components designed using the RCC-MRx code [1], it is possible to disregard creep as design criterion during normal service operation if the temperature, stress and time limits of negligible creep are respected. Moreover implementation of expensive surveillance programs and/or frequent inspections of (monitoring creep damage) can be avoided. It is quite a challenge to define the limits reliably in the temperature range where creep behaviour (time to strain and/or rupture) can be considered negligible, due to for instance that creep tests are normally performed well above this temperature. The methods and definitions for negligible creep differs between design codes (such as ASME NH and RCC-MRx), and there has not been a consistent way to derive the negligible creep temperature curves from properties found in material standards. In the European FP 7 Project MATTER a methodology [2] based on the Wilshire equations [3] was developed that enables the definition of T_{NEC} curves from creep rupture data [4].

The CEN/TC 54, Work Group 59 (CREEP) is currently revising the European standard EN13445 "Unfired Pressure Vessels" [5] and the above mentioned methodology is used for defining T_{NEC} curves for the non-alloyed and alloyed ferrritic and ferritic/martensitic steels (hereafter F/M steels) in the material standard EN10028-2 [6] and for the austenitic steels from EN10028-7 [7] are defined.

In the revision of the standard the following definition is given for the usage of the T_{NEC} curve: "negligible creep conditions prevail as long the sum of time fractions (time at specified service temperature t_i divided by the maximum time allowed t_{NEC} at that temperature is lower than unity" as given in Eq.1.

$$\sum_{i=1}^{n}\left(\frac{t_i}{t_{NEC}}\right) \leq 1 \qquad (1)$$

The method for determining t_{NEC} is illustrated in Figure 1 together with the different time-temperature regions for creep, no creep and negligible creep.

The time frame at specified service temperatures where creep is still considered to be negligible (t_{NEC}) is defined from the material specific rupture time data (at temperature) calculated for the material type specific reference stress divided by a factor of 1000. For the X10CrMoVNb91 (Grade 91) steel this rupture time correction factor (RTF=1000) corresponds to the time to reach 0.2% strain. The reference stress was chosen to comply with the RCC-MRx time independent design stress of $1/2.7 \cdot R_m$, (where R_m is the ultimate strength), with a safety factor of 1.5 [8]. This reference stress is almost identical to the EN13445 time independent design stress of $2/3 \cdot R_{p02}$ for this steel [9], which simplifies the transfer of the methodology to suit the needs of the standard [5, 11]. For other materials the accumulated creep strain at this RTF will differ but it has been shown that RFT=1000 is conservative in time to stain (≤0.2%) for 10CrMo9-10 (P22) and nearly the same (~0.2%) for X2CrNiMoN17-13-3 (316LN) [10].

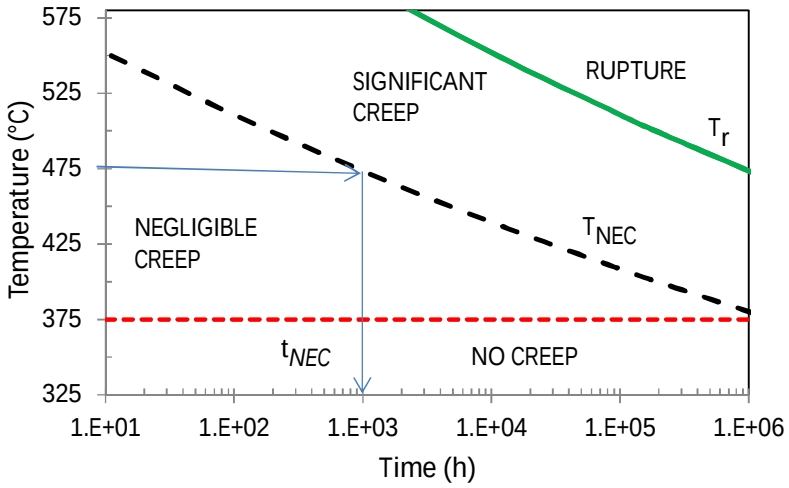

Figure 1. Example of a F/M steel Negligible Creep temperature curve T_{NEC} (black long dash) defined from the creep rupture temperature curve T_r (continuous green line) by dividing rupture time with RTF=1000 at the reference stress ($1/1.5 \cdot R_{p02}$). The T_{NC} (red horizontal long dash) limits the T_{NEC} to a minimum value of 375°C at a material specific time. The maximum allowable time in negligible creep (t_{NEC}) at 475°C is 3000h.

The material specific T_{NEC} curves are influenced by four main variables: the material tensile strength (or yield); the material creep strength; the chosen reference stress; and the chosen rupture time factor. This means that a low-alloy steel can have the same T_{NEC} curve as a creep resistant high-allow steel; the difference lies in the reference stress. Also the chosen tensile properties, i.e. average or minimum values

influence the curve. It is therefore important to anchor the curves to a specific set of tensile properties, i.e. the standard values. For creep it is naturally more conservative to use the higher yield or tensile strength as base for the calculations since a higher stress naturally results in shorter creep life and lower T_{NEC} temperatures. In this work the yield properties acquired from the EN10028-2 and -7 are minimum values.

2. Materials and Methods

The materials of EN10028-2 (F/M steels) and EN10028-7 (austenitic) are presented in Table 1 and 2 respectively.

Table 1. F/M Steels covered in EN10028-2 in the order given in the standard. The maximum temperature for which yield stress R_{p02} values are given ($T_{H\text{-}nc}$), the creep temperature range (T_{min} and T_{max}), stress range (σ_{min} and σ_{max}) and the time minimum and maximum times of the creep rupture data (t_{min}, t_{max}) are given.

Steel name	$T_{H\text{-}nc}$ (°C)	T_{min} (°C)	T_{max} (°C)	σ_{min} (MPa)	σ_{max} (MPa)	t_{min} (kh)	t_{max} (kh)
P235GH	400	380	480	33	229	10	200
P265GH	400	380	480	33	229	10	200
P295GH	400	380	500	30	291	10	200
P355GH	400	380	500	30	291	10	200
16Mo3	500	450	530	45	298	10	200
18MnMo4-5	450	425	525	69	421	10	100
20MnMoNi4-5	400	450	490	194	290	10	100
15NiCuMoNb5-6-4	450	400	500	69	385	10	100
13CrMo4-5	500	450	570	26	285	10	200
13CrMoSi5-5	450	450	570	31	313	100	100
10CrMo9-10	500	450	600	28	306	10	200
12CrMo9-10	500	400	520	107	355	10	100
X12CrMo5	500	475	600	27	147	10	10
13CrMoV9-10	450	400	550	108	430	10	100
12CrMoV12-10	450	400	550	108	414	10	100
X10CrMoVNb9-1	500	500	670	35	289	10	200

Table 2. Creep resistant austenitic steels covered in EN10028-7 in the order given in the standard. The maximum temperature for which R_{p1} values are given ($T_{H\text{-}nc}$), the creep temperature range (T_{min} and T_{max}), stress range (σ_{min} and σ_{max}) and the time minimum and maximum times of the creep rupture data (t_{min}, t_{max}).

Steel name	$T_{H\text{-}nc}$ (°C)	T_{min} (°C)	T_{max} (°C)	σ_{min} (MPa)	σ_{max} (MPa)	t_{min} (kh)	t_{max} (kh)
X3CrNiMoBN17-13-3 (316LNB)	600	550	800	27	164	10	100
X6CrNiTiB18-10 (321H)	600	550	700	29	290	10	200
X6CrNi18-10 (304H)	600	500	700	22	250	10	200
X6CrNi23-13 (309S)	600	550	800	7.5	160	10	100
X6CrNi25-20 (310S)	600	600	910	9	137	10	250
X5NiCrAlTi31-20 (Alloy 800)	600	500	700	38	290	10	200
X5NiCrAlTi31-20 (+RA) (Alloy 800 +RA)	600	500	700	26	315	10	200
X8NiCrAlTi32-21	600	700	1000	2.8	73	10	200
X8CrNiNb16-13	600	580	750	15	182	10	200

The T_{NEC} curves acquired using the RTF time correction can be tested against material creep strain data for time to reach 0.2% creep strain. This strain limit is a good choice since it corresponds to the the smallest strain that can be reliably be acquired from creep testing by classical dead weight machines. Furthermore, the ASME design code [12] and the BS 7910 [13] use the time to 0.2% creep strain as a limit for operating outside the significant creep regime.

In RCC-MRx and ASME the temperature below which the creep is considered negligible for the full design life at any stress below the allowable stress ($T_{NC)}$ is 375 °C for both for non-alloyed steels and the more creep resistant F/M steels. In RCC-MRx the T_{NC} is 425°C for SS 316L and 450°C for 316L(N). These temperatures have been implemented as the lower bound temperatures for the T_{NEC} determination as illustrated in Figure 1 for a F/M steel.

For the EN13445 standard the T_{NEC} curves are constructed at reference stress using four material specific parameters and the maximum time of negligible creep t_{NEC} (see Eq.2-3). The parameters C_1-C_4 are simplifications of the Wilshire parameters (see Eq. 4) optimized from the rupture creep strength values provided in the corresponding material standard. The reference stress σ_{ref} used is 2/3 R_{p02} for F/M steel and 1/1.2 $R_{p1\%}$ for austenitic steel.

In Eq. 4 the parameters *Q*, *k* and *u* are fitting parameters, *R* is the gas constant and *A* is a material specific normalization parameter scaling yield stress R_p (R_{p02} for F/M steels and R_{p1} for austenitic) to mimic the tensile strength, i.e. $A \cdot R_p \approx R_m$. T is the absolute temperature and $\sigma_{u/t/T}$ the creep rupture strength taken from the standard tables for specified rupture times (t_r) at a given temperature. In Eq.1 C_1=Q/R, C_2=-1/k, C_3=1/A/F (normalized reference stress) and C_4=-1/u. The parameter F in C_3 is the design stress factor F=1/1.5 for F/M steels and F=1/1.2 for austenitic steels.

$$T_{NEC} = \frac{C_1}{\ln\left(t_{NEC} \cdot RTF \cdot \left[C_2 \ln(C_3)\right]^{C_4}\right)} \tag{2}$$

$$t_{NEC} = \frac{t_r(\sigma_{ref}, T)}{RTF} \tag{3}$$

$$\frac{\sigma_{u/t/T}}{A \cdot R_p} = \exp\left[-k(t_r \cdot \exp(\frac{-Q}{R \cdot T}))^u\right] \tag{4}$$

The material specific Wilshire models (Eq. 4) for time to rupture are determined by fitting the creep strength data $\sigma_{u/t/T}$, i.e. the stress to cause rupture in 10,000 (10kh), 100,000 (100 kh) and in some cases 200,000h (200 kh) at specified temperatures (see Table 1 and 2). For each steel the activation energy Q is optimized to give a minimal amount of data mismatch between the isotherms with isochronous data, i.e. overlapping isotherms to a smooth curve in the Wilshire plot. For most steels a typical value of Q=300kJ/mol fits the data adequately. For some steels Q had to be altered to avoid large differences between the creep strength isotherms given in the standard. The Wilshire time to rupture plot with NIMS [14] and MATTER low temperature creep rupture and creep strain data [15] on X10CrMoVNb9-1 (Gr. 91) is shown in Figure 2. The RTF=1000 complies with the time to 0.2% creep strain. The location of the arrow indicates the point at which the T_{NEC} curve (Eq.2) was calculated. The methodology has also been shown to be conservative in relation to 0.2% creep strain for both 10CrMo910 (P22) and X2CrMoNiMo17-12-2 (316L) [10]. The predicted T_{NEC} curves are shown in Figure 3A and B.

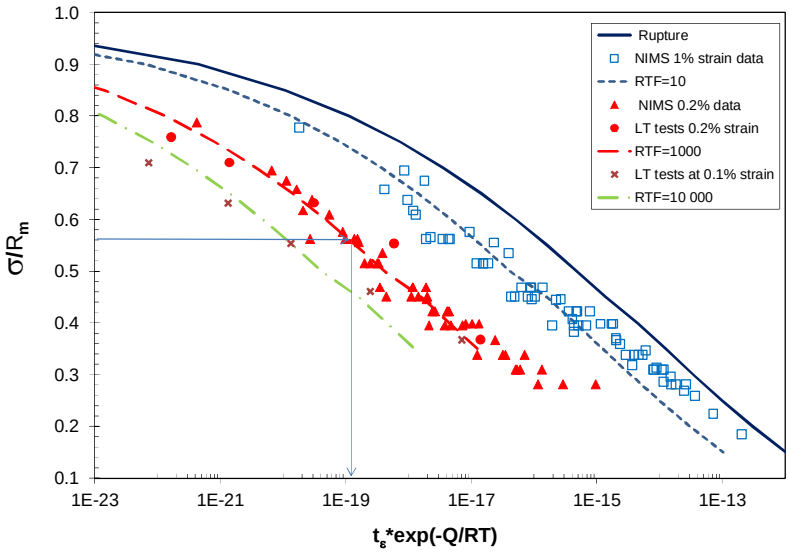

Figure 2. X10CrMoVNb9-1 Wilshire plot for NIMS time to rupture, time to 1% and time to 0.2% creep strain with JRC low temperature tests. The T_{NEC} curve (based on 0.2% strain) is identical to a RTF=1000 corrected rupture time cure.

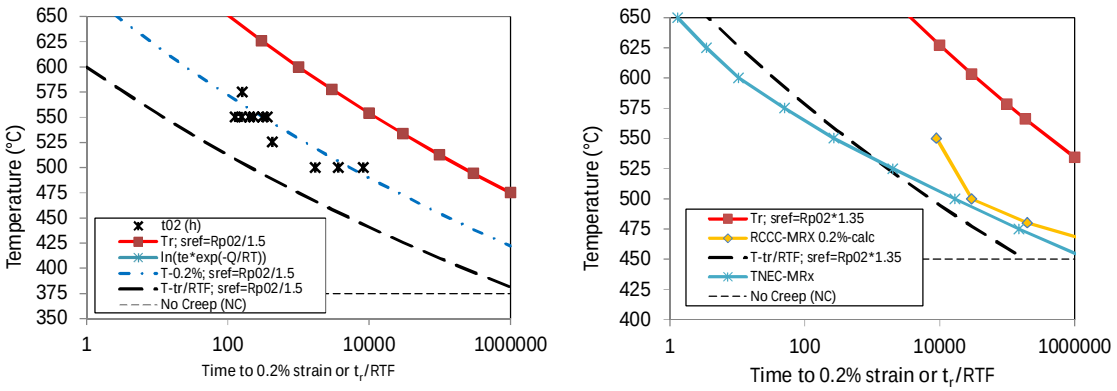

Figure 3. 10CrMo910 (P22) and X2CrMoNiMo17-12-2 (316L) negligible creep temperature plots in comparison to A) time to 0.2% creep strain for 10CrMo910 steel at reference stress ± 10% in stress and B) RCC-MRx T_{NEC} curve and 0.2% strain predictions for X2CrMoNiMo17-12-2 steel. Note that here the reference stress is $R_{p0.2}$·1.35. [10].

3. Results

The material constants C_1-C_4 (Eq.2) for F/M and austenite steels are given in Table 3 and Table 4 correspondingly. The corresponding material specific T_{NEC} curves are depicted in Figure 4 and Figure 5. As can be seen T_{NEC} is for some materials are limited at the high temperature end by $T_{H\text{-}nc}$ +50K, considered to be a reasonable limit for extrapolation in temperature for the tensile properties. At the low temperature end the curves are limited by the T_{NC} temperature.

Table 3. Simplified model parameters C_1-C_4 for defining T_{NEC} temperature (Eq.2) as a function of time (t_{NEC}) for non-alloy and alloy steels (EN10028-2). Note that the temperature calculated with these values is in K.

Steel name	C_1	C_2	C_3	C_4
P235GH	30791	-2.04500E-03	0.23929	-5.5314
P265GH	30791	-5.39100E-03	0.23103	-6.7441
P295GH	36084	-7.14000E-04	0.25769	-5.6923
P355GH	36084	-1.25900E-03	0.29130	-6.2353
16Mo3	36084	-1.80000E-05	0.23929	-3.3794
18MnMo4-5	36084	-1.10000E-05	0.31905	-3.1669
20MnMoNi4-5	36084	-1.05440E-02	0.35263	-9.0754
15NiCuMoNb5-6-4	36084	-4.54800E-03	0.35263	-7.1623
13CrMo4-5	36084	-3.98600E-07	0.27917	-2.4228
13CrMoSi5-5	36084	-3.98600E-07	0.27917	-2.4228
10CrMo9-10	31273	-3.07131E-03	0.26800	-5.2380
12CrMo9-10	36084	-4.66457E-03	0.35263	-6.9899
X12CrMo5	31273	-1.70494E-02	0.29130	-8.5955
13CrMoV9-10	36084	-2.42116E-02	0.35263	-9.8558
12CrMoV12-10	36084	-1.46449E-02	0.35263	-9.3672
X10CrMoVNb9-1	36084	-1.52540E-02	0.39412	-8.1163

*Note that the yield properties of steels 13CrMoV9-10 and 12CrMoV12-10 are the same in standard 10028-2.

Table 4. Simplified parameters for defining T_{NEC} temperature (Eq.2) as a function of time (t_{NEC}) for austenitic steels (EN10028-7). Note that the temperature calculated with these values is in K.

Steel name	C1	C2	C3	C4
X3CrNiMoBN17-13-3	36084	-0.001478151	0.32051	-4.5935
X6CrNiTiB18-10	32475	-0.015067609	0.27778	-6.651
X6CrNi18-10	24056	-0.039135456	0.26042	-5.2336
X6CrNi23-13	24056	-0.044833151	0.27778	-6.2863
X6CrNi25-20	36084	-0.005880624	0.27778	-6.0299
X5NiCrAlTi31-20	32475	-0.003974411	0.2193	-4.8841
X5NiCrAlTi31-20 (+RA)	42098	-0.01424023	0.26882	-9.7858
X8NiCrAlTi32-21	36084	-0.042505277	0.2193	-10.3965
X8CrNiNb16-13	38489	-0.009060362	0.28736	-7.3892

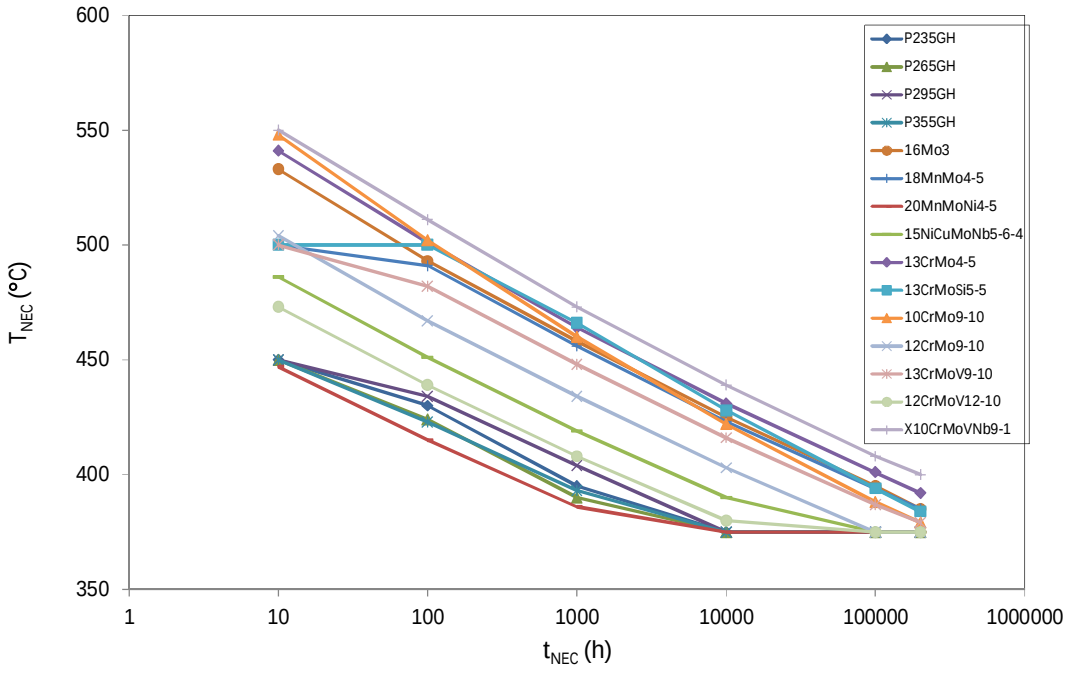

Figure 4. T_{NEC} curves for the F/M steels of EN10028-2 calculated at a reference stress of 2/3 R_{p02}..

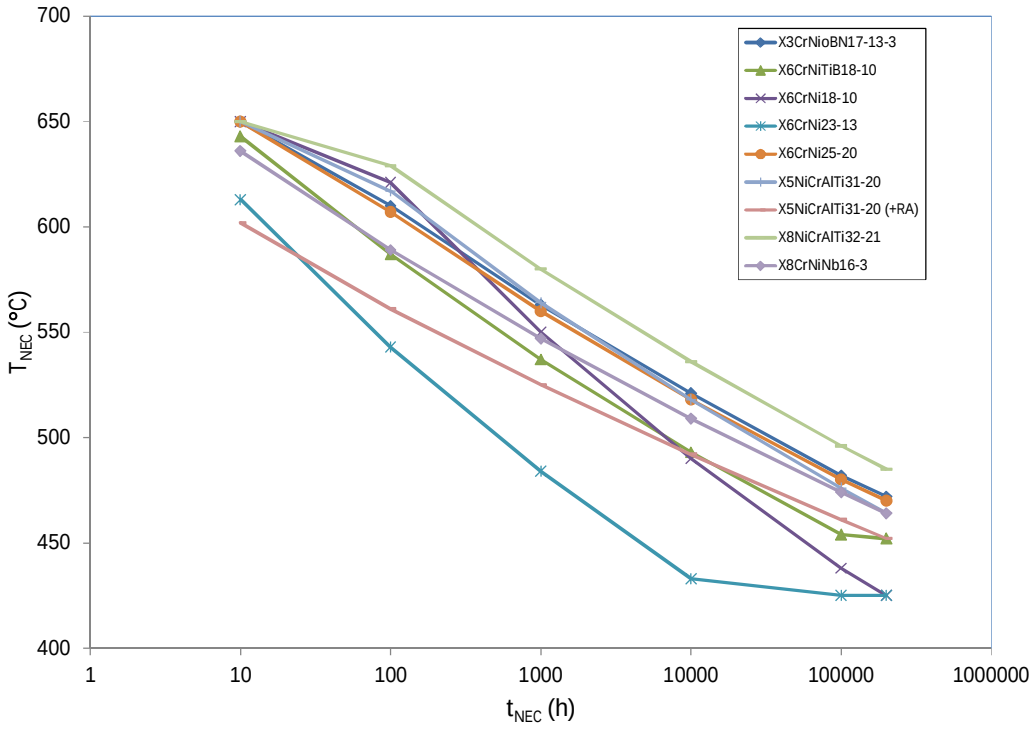

Figure 5. T_{NEC} curves for the austenitic creep resistant steels of EN10028-7 calculated at a reference stress of 1/1.2 R_{p1}.

4. Discussion

The main advantage of the method is its simplicity and the main potential uncertainty is the extent of extrapolation in time imposed by defining the T_r rupture temperature curve at the required low temperatures. To better understand the benefits/capabilities of the different steels for design above the "no-creep" limit the material dependent reference stress (at specified temperature) can be plotted against the Larson-Miller time-temperature parameter LMP=(log(t_{NEC})+20)(T_{NEC}+273), in Figure 6 and Figure 7. The potential design benefit in stress can be estimated from its position in the plot. A material located in high-stress and high LMP region has good strength and creep properties wheras a material in the with low-stress and low PLM region should not be considered for high temperature purposes. It can be seen that there is a trade-off between high tensile strength (or yield stress) and the T_{NEC}. The conservativeness of the proposed T_{NEC} temperatures should be cross checked with any available low temperature low stress tests data to show that the targeted maximum of 0.2% creep strain lies on or to the right of the RTF corrected Wilshire plot. Also the proposed weld strength reduction could potentially be cross checked by simulated HAZ material for the F/M steels and for the austenitic steels by assessing the all-weld material recommended for that steel type.

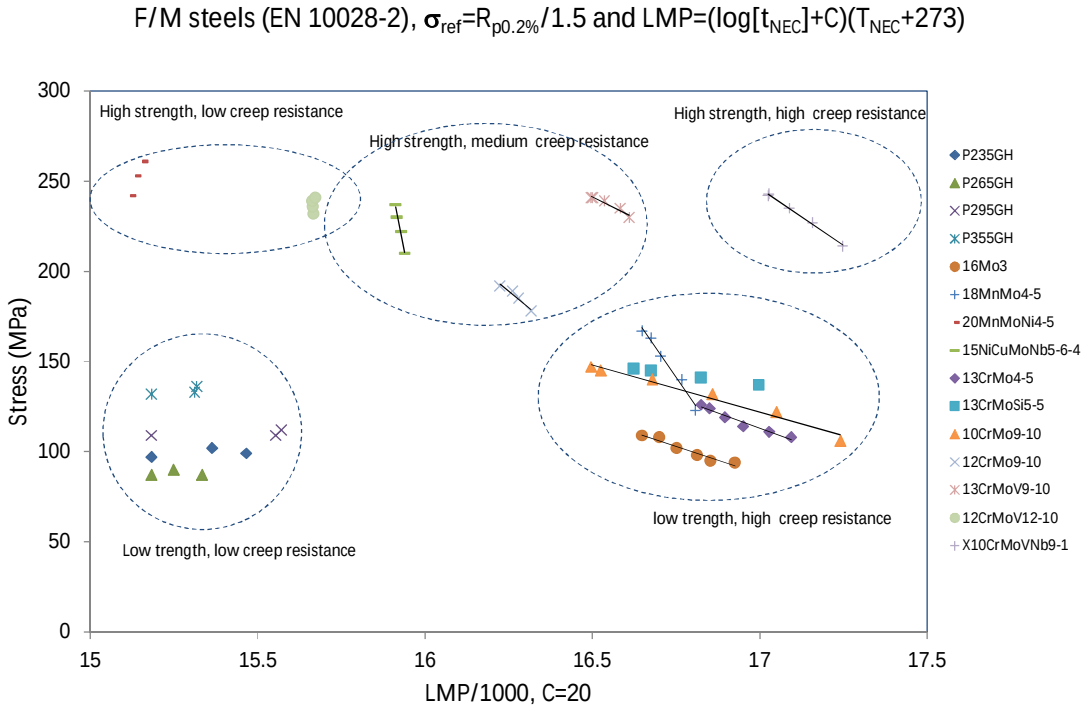

Figure 6. The F/M steels of EN10028-2 plotted as reference stress vs. the time-temperature parameter LMP.

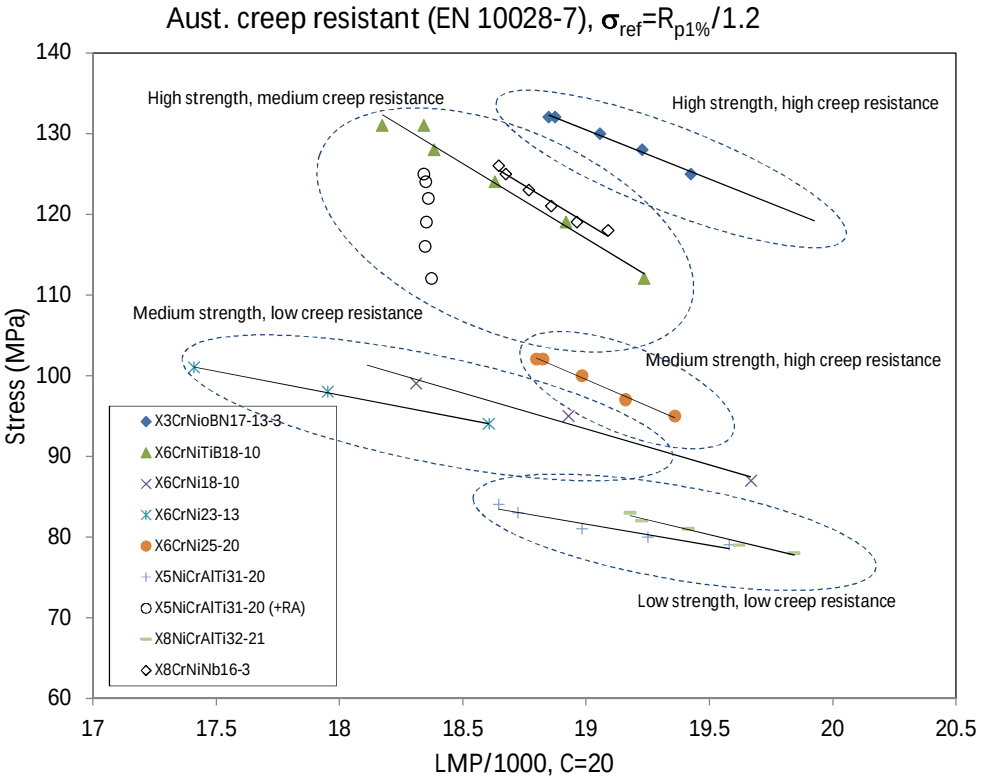

Figure 7. The creep resistant stainless steels of EN10028-7 plotted as reference stress vs. the time-temperature parameter LMP.

5. Conclusions

With the simplified novel methodology for determining negligible creep temperature it is possible to calculate neglibible creep curves based material properties found in standards. The methodology has been verified for for steels like X10CrMoVNb9-1 (P91), 10CrMo9-10 (P22) and X2CrNiMoN17-13-3 (316LN) [11]. The usefulness for standardization purposes has been clearly shown. The presented $_{NEC}$ curves for the non-alloyed and alloyed ferritic/martensitic steels as well as the creep resisting austenitic steels from EN-1002 will be included in the next review of the European EN-13445 standard.

References

1 RCC-MRx. Design and construction rules for mechanical components of Nuclear installations, AFCEN; 2012.

2 Holmström, S. Chen, J. Recommendation for the negligible creep domain for P91, Deliverable report 5.3, 2014, Report EUR 27782, doi: 10.2790/689331,(online 2016)

3 Wilshire, B., Scharming, P.J., Hurst, R., A new approach to creep data assessment, Material Science and Engineering A, Vol.510-511, pp. 3-6, 2009.

4 Holmström S., Luzginova N., Negligible creep of P91 steel, Proc. ECCC conference, Creep & Fracture in High Temperature Components, Design & Life Assessment, May 5-7th 2014.

5 EN 13445-3, Unfired pressure vessels, Part 3 - Design: 2009

6 EN 10028 -2, Flat products made of steels for pressure purposes, Part 2, Non-alloy and alloy steels with specified elevated temperature properties, 2009

7 EN 10028-7, Flat products made of steels for pressure purposes, Part 7, Stainless steels. 2007

8 R5 Assessment Procedure for the High Temperature Response of Structures. British Energy, Gloucester , UK, 2001.

9 Holmström, S. A study of negligible creep criteria based on EN-10028 standard creep strength and yield properties, Report EUR 27783, doi: 10.2790/259684, 2016.

10 Holmström, S. Negligible creep temperature curve verification for steels 10CrMoV9-10 and X2CrMoNiMo17-12-2, Report EUR 27780, doi: 10.2790/208315, 2016.

11 Holmström, S. Negligible creep temperature curves for EN-13445, Report EUR 27926, doi: 10.2790/578396, 2016.

12 ASME. Section III Div. 1 Sub-Section NH, New York USA: ASME; 2007.

13 BS 7910:2005, Guide to methods for assessing the acceptability of flaws in metallic structures.

14 NIMS Atlas of creep deformation property. No. D-1, Creep deformation properties of 9Cr1MoVNb steel for boiler and heat exchangers (2007).

15 S. Holmström and C. Pantry (2014): Uniaxial creep data for tests performed on P91 material in the temperature range 400°C to 600°C, version 1.1, European Commission JRC Institute for Energy and Transport, [Dataset], http://dx.doi.org/10.5290/2500001, http://dx.doi.org/10.5290/2500002, http://dx.doi.org/10.5290/2500076 to http://dx.doi.org/10.5290/2500080 inclusive, http://dx.doi.org/10.5290/2500084 and http://dx.doi.org/10.5290/2500085.

Creep analyses of a steam pipe system

Jan Storesund[1], Kristin Steingrimsdottir[1], Juhani Rantala[2] & Tobias Bolinder[1]

[1]Inspecta Technology
P.O. Box 30100, 10425 Stockholm, Sweden

[2]VTT Materials for Power Engineering
P.O. Box 1000, FI-02044 VTT, Finland

Abstract

Elastic pipe stress analyses are frequently performed to check that the stresses in pipe systems are allowed. For operation in the creep range such analyses may describe the stress distribution in the beginning but not after creep relaxation starts to take place.

In the present work effects of creep are considered. A pipe system of P22 material that had been analysed by software for elastic analysis was also modelled for creep. By use of tabled creep data the following was studied:

- Creep stress relaxation in the pipe system
- The effects of starts and stops on stress and strain distributions
- Creep in T-pieces with super imposed system stresses from the pipe system creep analysis

The creep properties of a virgin weld and a service exposed weld were determined by impression creep testing. The tests were performed in the parent metal, different parts of the HAZ and the weld metal. A weld was included in the model and analysed with these data. Resulting creep strain distributions from analyses with tabled and present creep test data were compared to each other and also to actual creep damage that was observed in components from the system.

1. Introduction

Main steam pipe systems in conventional power plants as well as combined power and heating plants are typically operating at temperatures where the design criterion is creep. The criterion for creep design of steam piping is creep rupture. Creep rupture involves a considerable amount of creep deformation. However, a safety factor of 1.25 and 1.5 on the rupture stress is applied for 200 000 and 100 000 hours design, respectively. The stress dependence on creep life is strong with a power of 3 – 5 at conventional creep design data. This means that the life time for a straight pipe that is fully utilized and built of an average material would be much longer than the design life, typically 400 000 hours or longer. This applies for both 100 000 and 200 000 hours design because of the difference in safety factor.

The safety factor is primarily considered to take account for possible reduction in creep strength in comparison to the average material, which the design stresses are based on. The lower bound in the

creep strength scatter for creep resistant steels is typically 20 % lower rupture stress than the average material. Then, there are other factors in a pipe system that may reduce the life time: system stresses, reduced creep strength in welds, stress concentrations in components with complex geometries that are not caught by the design rules, etc. Hence, it is not possible to know the status with respect to consumed creep life in any detail after long-term operation without inspection and monitor of the system. Established test methods are magnetic particle testing for crack detection and replica testing for monitor of the development of creep cavitation that micro-cracks and finally macro-cracks.

One issue with replica testing is to find out where the critical positions are. Creep damage and creep cracks typically appear locally where the stresses, and thereby the accumulated creep strains, are enhanced [1][2][3]. Up to date, test positions are frequently selected by experience. However, if not all possible critical components can be included in a testing program, it is often impossible to be sure of that the representative ones can be selected by experience only.

Elastic pipe stress analyses are performed on new pipe systems by routine within the design review to check that the stresses due to thermal expansion and dead weight in addition to the internal pressure do not exceed allowed values. After long term operation it is crucial to update the in-data to such analyses since hanger and support adjustments changes. It is also common that reconstructions of the pipe system are performed during its lifetime. Reconstructions will in most cases change the boundary conditions for the remaining part of the system, too. Therefore, updates of the analysis is needed in accordance with results of inspections (walk downs) of the system hangers and supports (which should be performed at least once a year) and any reconstructions.

Elastic stress analyses can be used to pinpoint areas with enhanced stresses at the start of the operation but the effect of creep relaxation is not considered. Stress redistribution due to creep relaxation changes the stress levels and may also change or introduce new positions that are critical with respect to creep damage development [1][4][5]. Thus, it is possible that the elastic analysis cannot fully determine critical positions for replica testing. The elastic analysis will over-estimate the stress levels at some positions and under-estimate them at others and can therefore not be used for estimations of creep life.

By introduction of creep deformation in the analysis it would not only be possible to identify critical position. It would also be possible to calculate the creep strain as a function of time at such positions. This would give at straight forward measure of the consumed life time. The remaining life can be estimated with a high precision and the analysis can be verified by replica testing. Creep analyses of complex pipe systems require powerful hard and soft ware. Therefore, it is not until recently such analyses can be expected to be performed acceptably readily. In addition to develop qualified tools for the analysis it is also crucial to use proper and updated input data from the settings of system hangers and supports [6][7].

The purpose of the present study is to develop *i)* analyses that can pinpoint critical positions for testing correctly and in detail, *ii)* analysis methods that can be used for creep life assessment in live steam pipe system components, *iii)* use creep data of weld constituents from results of miniature creep testing *iv)* make comparisons between analyses by use of tabled data and those where creep test data for the analysed component is used.

2. Pipe system modelling

The main steam pipe system in E.ON Heleneholmsverket was used for the modelling work, see Figure 1. Elastic pipe stress analyses by use of Caepipe have been performed with regular updates since the middle of the 1990´s. In an Energiforsk project in 1996 the system was partially modelled in Abaqus [8] to make it possible to study creep effects in the system. More exactly, the influence of refurbishment of the system on the remaining creep life was studied [5].

Since modelling of pipe systems is very time consuming in Abaqus and very convenient in Caepipe one task in the present project was to produce a script that automatically can translate a Caepipe model to an equal one in Abaqus. During this work the existing model from [5] was used for studies of effects of starts and stops and also in the development of a method for superposition of system stresses from the pipe system to the internal pressure in a T-piece. The system operates at 105 bars and 530°C. For a creep analysis in pipe systems the Norton's creep law is used that includes both elastic and creep response. See equation (1) for the Norton's creep law. The equation only includes secondary creep.

$$\frac{d\varepsilon_{ij}}{dt} = \frac{(1+\nu)}{E}\left[\left(\frac{d\sigma_{ij}}{dt}\right) - \frac{\nu}{\nu+1}\left(\frac{d\sigma_{kk}}{dt}\right)\delta_{ij}\right] + \frac{3}{2}B\bar{\sigma}^{(n-1)}s_{ij} \quad (1)$$

Where ε_{ij}, σ_{ij}, s_{ij} are the respective strain, stress and stress deviator tensor, $\bar{\sigma}$ is the von Mises effectives stress, *E* and *v* is the Young's modulus respective Poisson's number and *B* and *n* are the respective constant and exponent in Norton's creep law. The last term in equation (1) describes the creep response of the material. Creep data for 10CrMo9-10 in EN10028-3:2009 was used for the evaluation of the Norton parameters that were used in the analysis.

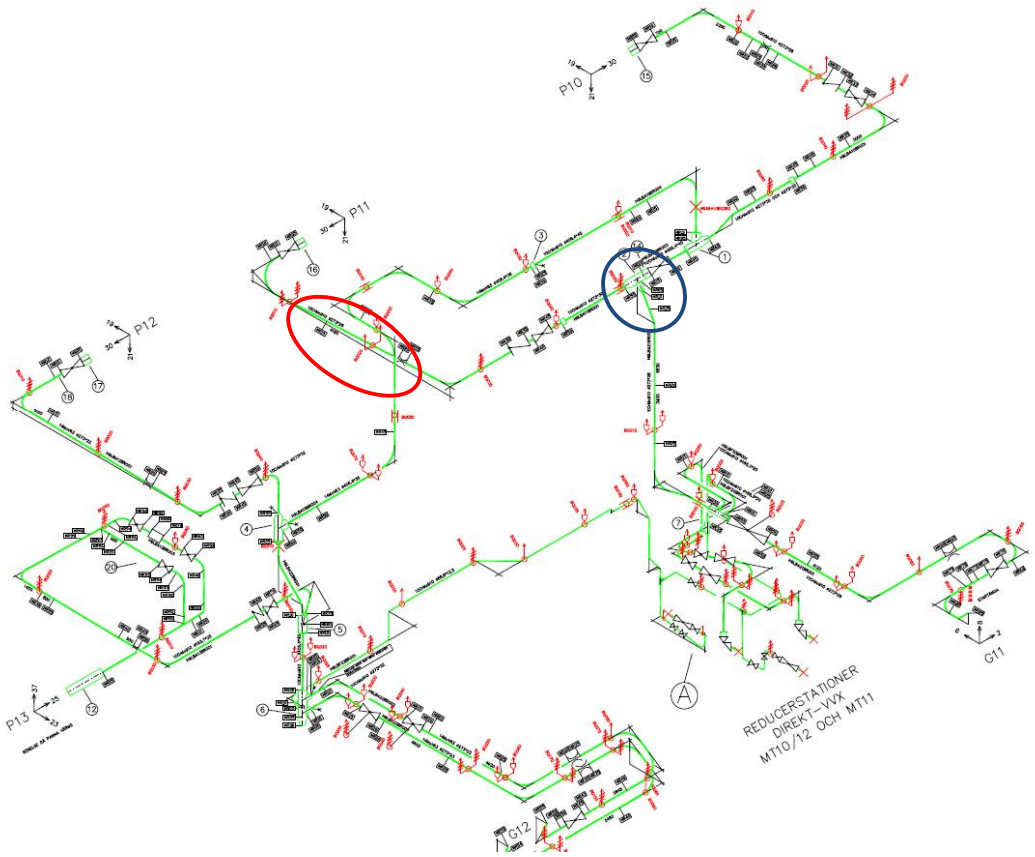

Figure 1. Caepipe model for elastic stress analysis of the steam pipe system in Heleneholmsverket.

To be able to define the parameters *B* and *n* in the creep law for the pipe system material, the creep law is considered in one dimension, see equation (2).

$$\frac{d\varepsilon}{dt} = B\sigma^n \quad (2)$$

The equation is integrated, see equation (3)

$$\int_0^{\varepsilon} d\varepsilon = \int_0^{t} B\sigma^n dt \rightarrow \varepsilon = B\sigma^n t \quad (3)$$

The parameters B and n can then be solved with an equation pair, equation (4) and (5). By use of tabled values [5] of the stresses that result in 1% creep strain at time 10 000 and 100 000 for 10CrMo9-10 at 530°C the equations will read:

$$0.01 = B \cdot 107^n \cdot 10000 \quad (4)$$

$$0.01 = B \cdot 68^{n} \cdot 100000 \tag{5}$$

The resulting values are $B=4.91*10^{-17}$ and $n=5.08$.

3. Influence of creep relaxation and starts and stops

Figure 2 shows the stress distribution in the Abaqus model of the Heleneholmsverket steam pipe system from [5] directly after the first start in service. The result is the same both for elastic and creep analyses since creep relaxation not yet has started. In figure 3 the stress distribution at the end of the first service period, i.e. one year in this case, is seen. A remarkable creep relaxation can be seen. Figure 4 shows the strain distribution after 98 000 hours and one start/stop cycle each 7 000 hours. The highest strains are not in the same positions as the highest stresses in Figure 2 and 3. Thus, the positions with the highest strains in the system after long term base load service could not be fully predicted by the elastic analysis and not by the creep analysis after creep relaxation either.

A recent Caepipe model of the system was then transferred to Abaqus by use of the script that was developed. In this case the actual service time and number of start/stops, 178 000 hours and 130 cold starts, respectively, were used in the analysis. The results are shown in Figures 5 and 6 where it can be seen that the starts and stops give different strain distributions and higher strains compared to a simulated service period without starts and stops.

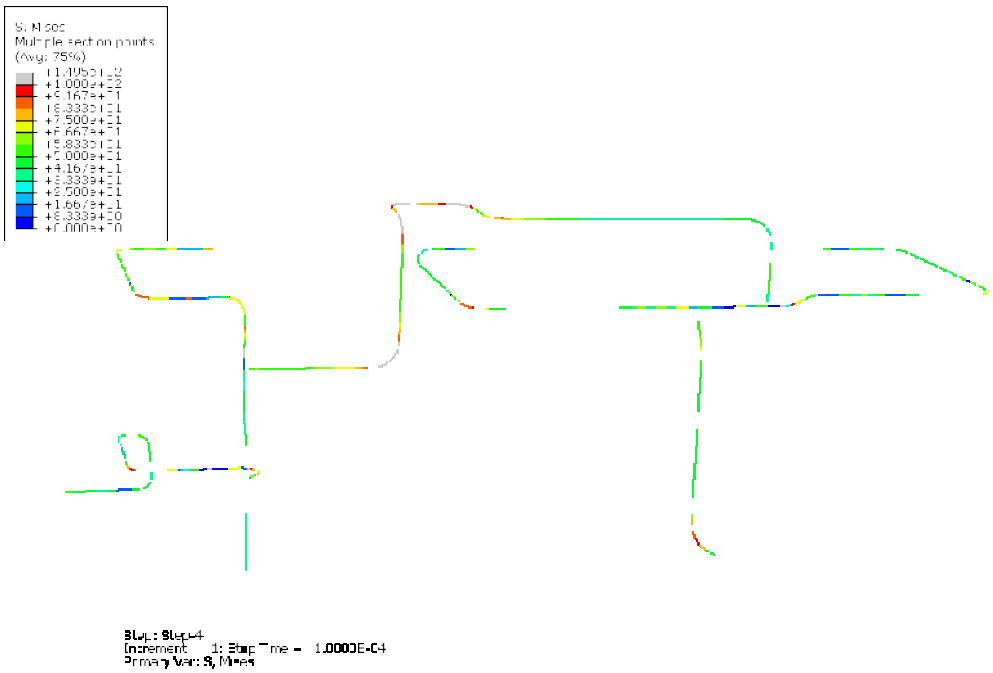

Figure 2. Elastic stress analysis.

Figure 3. Stress distribution after one year in service

Figure 4. Strain distributions after 14 years in service and one stop each year.

Figure 5. Simulated service without stops for 178 000 hours. Maximum equivalent creep strain = 0.5%

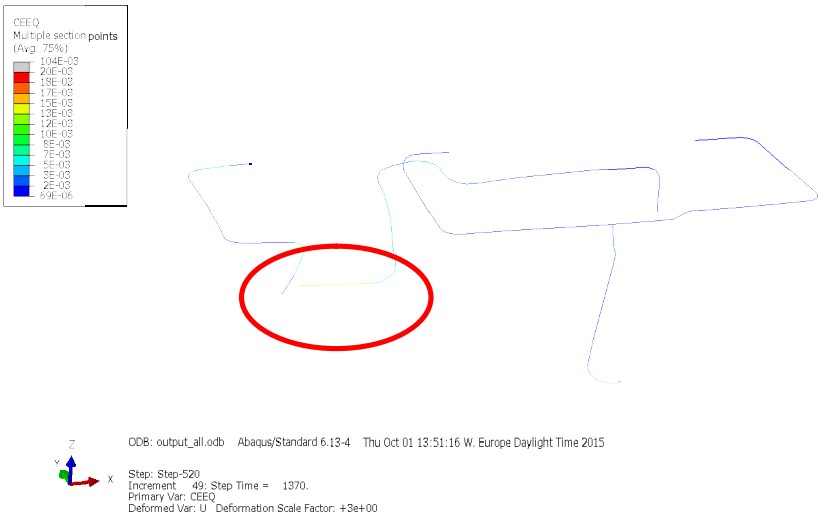

Figure 6. Simulated service with 130 cold starts for 178 000 hours. The maximum equivalent creep strain is higher and in different locations compared to no starts.

4. Superposition of system stresses on component analyses

Analyses with different extensions of a T-piece in a pipe system showed that it is clear that the stiffness of the T-joint in the piping system model is very important for the component analysis. A realistic stiffness in the piping system leads to less sensitivity for the component analysis. But as a thumb rule at least a pipe length of two diameters from each cone of the T-joint should be modelled in the component model. In cases were the stiffness in the piping system is thought to differ much from the actual stiffness a sensitivity analysis is suggested to determine the needed extent of the component model. Figure 7 shows the resulting equivalent strains in a T-piece that was chosen from the system after six years in service. The creep strains are due to internal pressure, dead weight and thermal expansion.

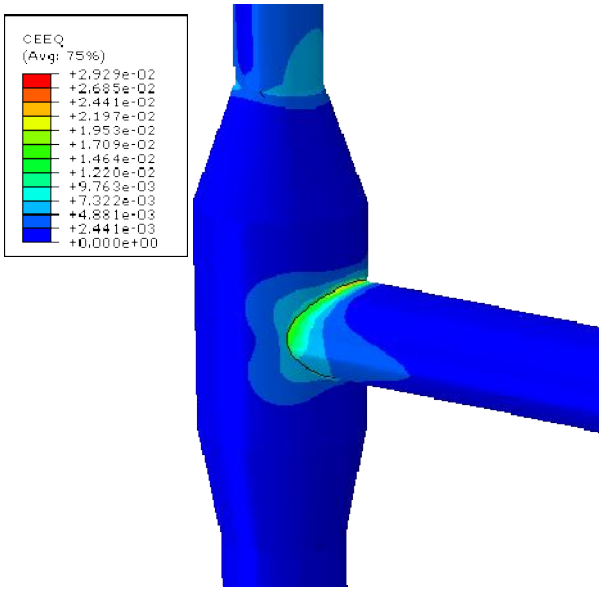

Figure 7. Equivalent creep strains after six years in service.

The highest strain accumulation is in a small area at the right angel position of the T-piece. This indicate that system stresses had a large influence on the strain level and strain distribution since internal pressure only would have given the highest strains at the saddle point position of the T-piece. Any effects of starts and stops were studied also in this analysis but there were no such effects in this position. The highest strain is 2.6 % which is quite a lot after only six years in operation. A significant part, approximately half the life time can be considered to have been consumed.

5. Creep damage in the studied main steam pipe

Three welds were cut from a part of the steam piping that was exchanged in Heleneholmsverket in the summer 2014. Two of them, tagged MR15 and MR20, were butt welds from a straight part of the pipe, circled in red in Figure 1, with a service time of 178 000 hours. The third weld. MR05, was a T-piece branch weld that have had 73 000 hours in operation (it had been exchanged once before). The t-piece is circled I blue in Figure 1. They were exchanged because the calculated life time was expired on bases of elastic analyses and tabled creep data.

The condition of the welds was examined metallographically with respect to creep damage. Creep cavitation was found in all the three welds. In MR15 small amounts of isolated cavities were observed in two thirds of the examined positions of the weld metal and the HAZs as well as the parent metals. One weld metal position revealed a 2.3 mm long creep crack but no creep damage in the remaining positions. In MR20 creep cavitation was observed in all examined positions and in higher amounts than in MR15 in many of them. In MR05 there were even higher amounts of creep damage in the HAZs with oriented cavitation at the saddle point positions. In the weld and parent metals creep damage was found just in quite a few positions. However, the total amount of creep damage in MR05 was higher than might be expected after 73 000 hours in service.

6. Impression creep testing

So far, tabled creep data has been used for the analyses. The influence of the specific creep properties of a component was studied by impression creep testing. This is a miniature creep testing method where an indenter with constant load is pushed into the material at elevated temperatures. The creep deformation during such a test is converted to a corresponding strain for a uniaxial test. Advantages with the impression creep are that only small quantities of material is required for the test, allowing for semi-destructive testing and testing of weld constituents such as HAZs. A restriction is that only primary and secondary

parts of the creep curve are obtained by the testing. However, in creep analyses based on Norton´s creep law, as in the present case, only secondary creep is utilized.

A new butt weld was produced from a pipe that was a spare part in Heleneholmsverket. It was also possible to use a retired T-piece from Heleneholmsverket for the testing. Before the testing the T-piece was investigated with respect to creep damage. Significant creep cavitation was found in the HAZs at both the right angle and the saddle point positions. In the latter position cavities were found also in adjacent parent and weld metals.

A new approach for impression creep testing of a weldment was conducted. A standard specimen is 10x10x2.5 mm but was in this case made thicker and covered parent metal in the top layer, HAZ in the middle and weld metal at the bottom. Testing was performed on the parent metal, and then the specimen was ground to the intercritical part of the HAZ and tested there. This procedure continued with 0.5 mm grinding between each test. The specimen was turned 90° between each test to minimize any effects of deformation from the indenter in the test area. The results are shown in Figure 8, where the creep rate at 500 hours testing and the creep strain after 300 hours testing are shown versus the test position in the weldment. It can be seen that the creep rate is 2.6 times higher at the HAZ/parent metal borderline than in the parent metal. The weld metal strain rate is about half of that in the parent metal. In addition the parent metal was creep tested by use of conventional uniaxial specimens for comparison and verification of the impression creep testing. The uniaxial and the impression creep test results agreed very well [5].

The test results of the retired weld are also shown in Figure 8. This weld was tested in weld metal and in the parent metal adjacent to and remote from the HAZ (BM1 and BM2, respectively). It can be seen that the weld and the parent metal creep rate is 6-8 and 2-5 times higher than in the new weld, respectively.

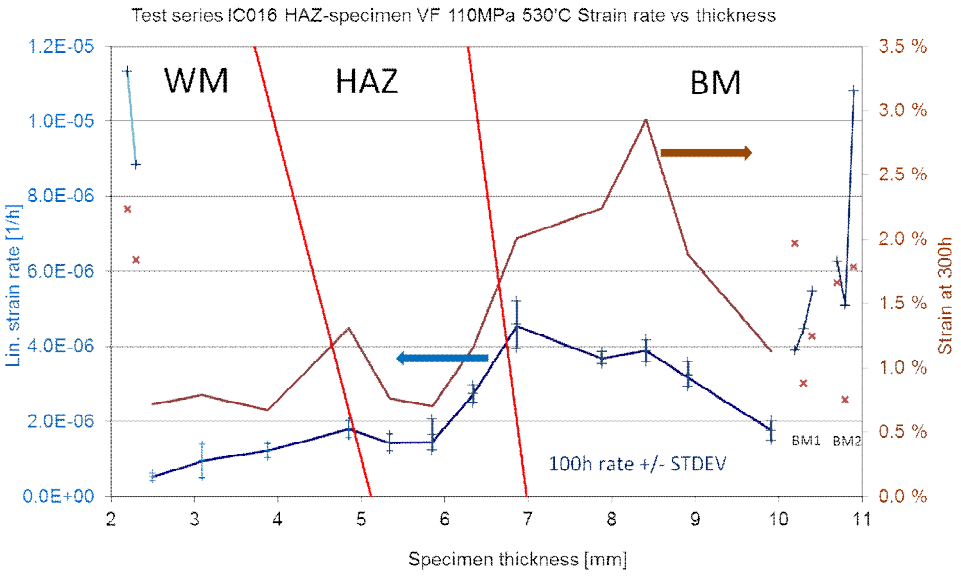

Figure 8. Linear creep rate and strain at 300 h vs. impression creep specimen thickness.

7. Evaluation of remaining lifetime of the main steam pipe system in Heleneholmsverket

7.1 System analysis

The piping system that was translated with the script has been used for analyses with actual operational data from Heleneholmsverket. In addition, the effects of starts and stops according to the service data were studied. Five different parameter combination of the Norton creep material models have been tested for the piping system and will be evaluated against observed creep damages found in welds MR15 and MR20 in a straight part of the piping shown in the red circle in Figure 1. The five models have different material parameters according to Norton's law, presented previously, see Eq. 1 and the representing pa-

rameters *B* and *n* that vary between the models are shown in Table 1. A graphical presentation of the material models is shown in Figure 9, where all material models are shown with minimum linear strain rate vs. stresses amongst with the results of uniaxial creep of new material and data points for base material BM1 and BM2 for the testing of the T-joint base metal.

Table 1. Parameters for Norton's creep material model used for the piping analysis.

Model No.	**Description**	***B***	***n***
1	EN 10028-2	4.92E-17	5.08
2	EN 10028-2 – lower bound, 20 % lower rupture stresses at same creep strain rate.	1.53E-16	5.08
3	LSCP data (logistic creep strain prediction [11].	2.16E-17	5
4	IC testing- new unused material, base material data. Modell is assumed to have the same *n* value as evaluated from EN 10028-2.	7.46E-17	5.08
5	IC testing for a base material that has been in operation in Heleneholmsverket for 73 000 hours of operation.	1.64E-16	5.08

At the end of operation after 178 000 hours the creep strain in element 5 (MR15) and 6/7(MR20) is compared for different material models and is shown in Table 2. In a large part of the welds there were creep damages with index around 2a and 2b, respectively, according to Nordtest TR302 [11]. Locally both higher and lower values were observes, but an average of 2a is estimated for the welds, with MR 20 having slightly higher creep damage on the average than MR15. Creep damage index 2a is estimated to correspond to a creep strain in the range 0.5-1 %.

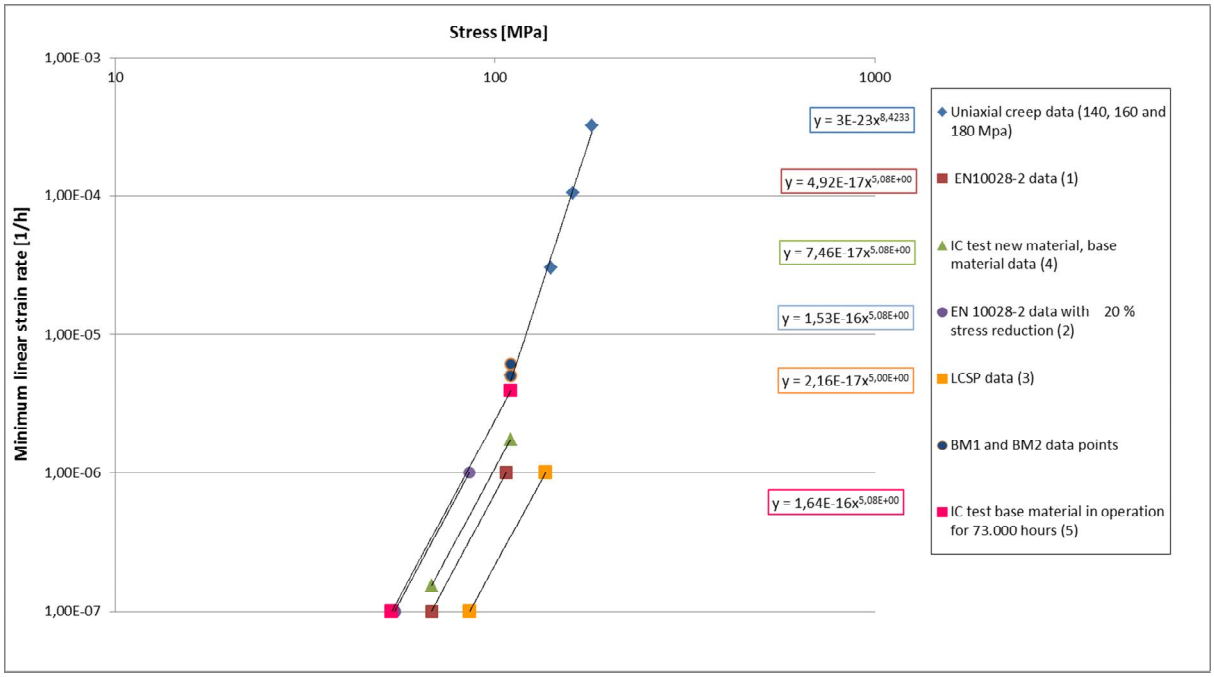

Figure 9. Minimum linear creep rates versus stress of parent metal for several Norton material models (numbered 1-5) as well as for produced data of uniaxial creep on new material and of impression creep on service exposed material (BM1 and BM2).

Table 2. Equivalent creep strain results from the model.

Model No. / **Part in system**	**1**	**2**	**3**	**4**	**5**
Element 5 (MR15)	0.085 %	0.26 %	0.029 %	0.13 %	0.27 %
Element 6/7 (MR20)	0.1 %	0.29 %	0.042 %	0.15 %	0.31 %

Table 3. Correlation between the Norton B factor and the amount of equivalent creep strain.

Norton *B* factor	2,16E-17	4,92E-17	7,46E-17	1,53E-16	1,64E-16
Model	3	1	4	2	5
Equivalent creep strain from table 10 for MR20	0.042 %	0.1 %	0.15 %	0.29 %	0.31 %

8. Component analysis

The T-piece that was cut out for examination and impression creep testing was modelled by FEM. The geometries were taken from the drawing of the T-piece. Also the T-piece branch weld geometry was included in the drawing. The HAZ was measured and modelled to 3.0 mm (Table 4) at the saddle point side of the weld, which is of particular interest since significant creep damage was observed there. Creep rates in weld metal and HAZ with the factors 0.5 and 3 times the parent metal creep rate, respectively, were used in the analysis. These factors are rounded numbers of the relative creep rates of the impression creep results of the new weld.

The analysis was first performed with materials data that correspond to tabled creep data. The creep properties in the weld metal and the heat affected zone were in analogy with the present test results of the new material, where the weld metal and the HAZ had approximately 2 and 3 times higher creep rate than the parent metal, respectively. The same factors were then used in relation to the parent metal properties evaluated from tabled creep data.

Since there was a significant effect of starts and stops on strain distributions in the system analysis, starts and stops were evaluated in the same way also for the T-piece, i.e. each start/stop sequence is 1370 hours.

Figure 10 shows the creep strain distribution at the T-piece weld after the first 1370 hours in operation of the system (the average service period between two start/stop cycles at Heleneholmsverket). Although the T-joint that was received for creep testing and metallographical examination was the third T-joint at the same place it is interesting to study the first period where the effect of creep relaxation is largest.
The highest strains present in the branch weld. The highest strains (red areas) started at the right angle positions at the T-connection and expanded along the HAZs and at 1370 hours the relatively high strains have spread half way to the saddle point, as can be seen in the figure. The maximum strain is 0.14 % already after 1370 hours.

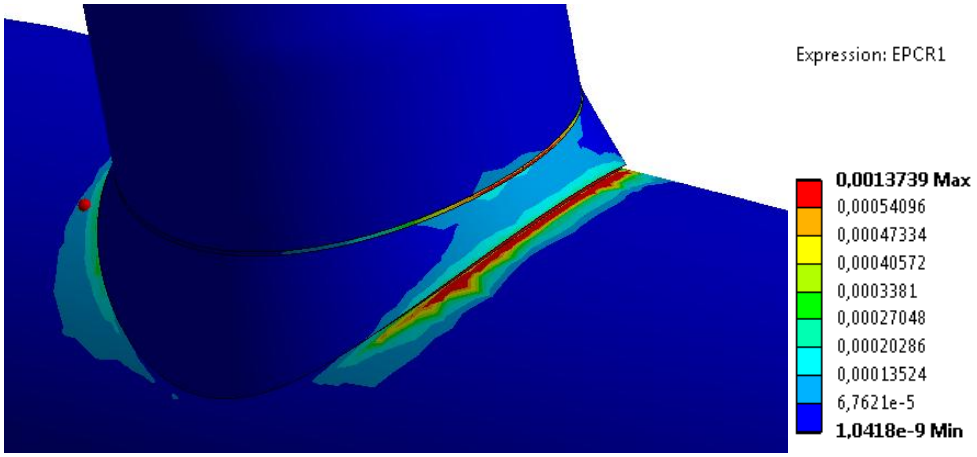

Figure 10. Detail of the T-piece showing the creep strain distribution after 1370 hours.

Finally, simulations that cover the actual life of the studied T-joint were performed. This is in 1990 when the system has an accumulated service time of about 105 000 hours. Thus, the analysis starts with actual system stresses at that time and continues for another 73 000 hours when it is taken out from operation. The resulting strain distribution in the T-piece is shown in Figure 11. Creep data that was produced by impression creep testing of the virgin weld was used in the4 analysis. Creep strains up to 1.5 % appear in the HAZs at one of the right angel positions. Enhanced strains also appear close to the cone at the vertical pipe. Strains in compression appears at the opposite right angel position. The analysis was performed by use of This is consistent with observed creep damage, up to 2000 creep cavities/mm^2, in the real T-joint at the position where the highest strains appear in the analysis. However, significant amounts of creep cavitation also appeared at the saddle point positions which did not have corresponding amounts of creep strain according to the analysis. This can be explained by simplifications of the system model that was needed for the verification of the translation script. The analysis was also performed with impression creep data for

the actual t-piece. Since the HAZ was not tested in this weld the same ratio in creep strength between HAZ and parent metal as for the virgin weld was assumed, The resulting strain distribution was similar to the analysis with data from the virgin weld but the strain levels were higher, up to 3.6 %.

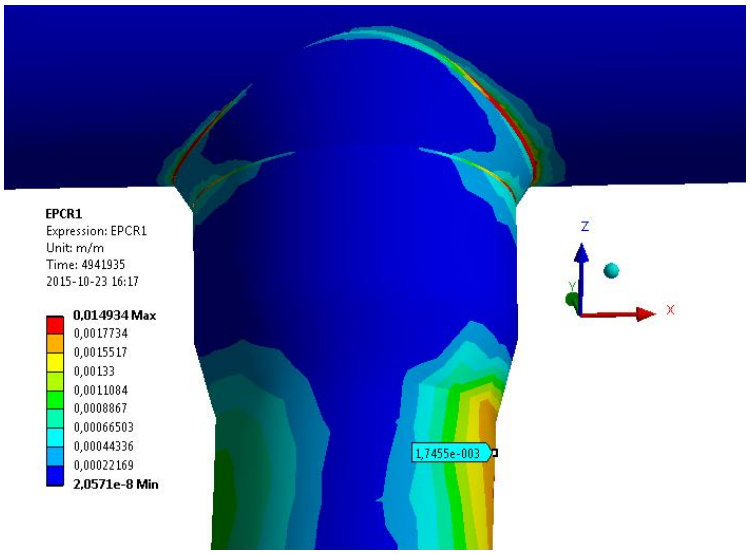

Figure 11. Detail of the T-piece showing the creep strain distribution after 73 000 hours.

9. Result analysis

9.1 Impression creep

The impression creep test results of different parts of the HAZ show relatively small differences in creep rates compared to parent metal. Results with significantly higher HAZ/parent metal creep rate ratio can be found in the literature [13] where HAZ/parent metal creep rates ratios of 10 and higher is reported. These results are based on tests of heat treated material. However, it is impossible to heat treat material in quantities enough for uniaxial creep testing in the same way as the thermal cycle of a HAZ. Although the heat treated materials may have about the same grain sizes and hardnesses as different HAZ microstructures the creep properties necessarily are not similar. The present results show that there is a significant difference between simulated HAZs by heat treatment and the ones.

The impression creep test results are overall consistent except one result of the service exposed parent metal at the test position BM2 where one data point that has about two times higher creep rate than the other five tests of the same material. Unfortunately, it has not been possible to find an explanation to this deviation.

Finite element analysis of impression creep tests by use of the LCSP method gave similar creep curve shapes but much lower creep rates than experimental results. The magnitude of the strain and strain rate reduction is similar to the system analysis when experimental data and Norton data evaluated from the LSCP method are compared, see Table 9-11. Since the LCSP method has been shown to work very well for 10CrMo9-10 material elsewhere [2][11], further analyses are required to sort this out.

9.2 System analysis

Elastic pipe analyses are frequently used for steam piping operating in the creep range to check that the stress levels due to thermal expansion are not higher than allowable. The results are often also used to

indicate critical positions in the system for non-destructive testing such as magnetic particle testing (MT) and replica testing. Present work pinpoints that:

- It is necessary to consider creep relaxations in the system with respect to allowable stresses.
- It is necessary to consider effect of starts and stops on the distribution of accumulated creep strain after long term operation.

Thus, elastic analysis on systems that operate in the creep range may overestimate the actual stresses as soon they have creep relaxed. It is also evident that the results of elastic analysis not always can indicate all critical positions for non-destructive testing.

Although the present analyses have been performed with very well documented background data the system has been reconstructed a few times before the present model of the system. Thus, the effects of thermal expansion for the first 90 000 hours of operation are different to what is shown in the model. However, it is considered that strains in the part of the pipe that include welds MR15 and MR20 should not have been affected by thermal expansions from previously reconstructed parts of the system.

The results of the analyses with different creep data in Table 10 show that lower bound data, i.e. 20 % creep strength reduction, gives about three times higher creep strains than average data (EN 10028-2) at the analysed positions. The analysis with creep data from the new material gives somewhat higher creep strains than average data whereas the corresponding analysis with data from the service exposed material gives slightly lower creep strains than the lower bound data. Thus, it is clear that use of standard average data may overestimate the real creep behaviour and that lower bound data can be considered as conservative enough.

The use of different data in the analyses is also a sensitivity analysis of the model. The 20 % strength reduction and the corresponding 3 times higher creep strain can be compared to creep data in EN13704:2008 which is represented as Larson-Miller parameter (i.e. a commonly used time-temperature parameter for) versus stress. The results are a life time reduction with a factor of 3.2 for the 20 % strength reduction at service data, 105 bar and 530°C. Thus, the agreement with the present results is very good.

The bend at the lower right hand side in figure 59 shows 10 % strain which likely is higher than in reality. This strain appears at the very end of the model. The model was simplified to be able to be verified with [5]. I reality, as can be seen in Figure 8, the system continues and there is less constraint. This shows that it is necessary to model the entire system to ensure that the results are fully accurate.

9.3 Component analysis

Simulations have been performed on T-pieces without and with a weld. Since the HAZ is associated with lower creep strength than the parent metal it is not surprising that creep strains preferably accumulate in these zones. The results show that:

- HAZs are particularly sensitive to creep strain accumulation in case of system stresses. Thus, it is a great advantage to include critical welds in a component model. However, since superimposing system stresses require modelling of the entire component such analyses can be quite time consuming.
- Areas where stress concentrations occur because of the geometrical shape of the T-piece are also sensitive to system stresses. Such areas often coincide with the location of welds, resulting in significant life time reductions.

The simulation of service life of the T-piece in section 8 resulted in strain distributions that did not fully conform with the observed distribution of creep cavitation. A possible explanation for this is that there is an extension of the real system that was not modelled, see above. Instead there is a fix point at the stop of the model which affects the boundary conditions and, unfortunately also seems to affect the displacements at the vertical pipe into the T-piece. Again, modelling of the entire system is crucial also for a component creep life assessment when system stresses are considered.

The critical strain levels are significantly higher in the analysis with the actual t-piece weld creep data compared to the one with virgin creep data. The t-piece weld may also in its virgin condition have had

lower, but not that much lower, creep strength than the creep tested virgin weld. The results indicate that component specific data is desirable for detailed analyses. Creep tests of service exposed material may be used for remaining life assessments. In this case one should bear in mind that another 3.6 % creep strain for the next 73 000 hours may be an underestimation since tertiary creep should be taken into account at such high strains levels.

10. Discussion

Creep data from standards are based on long term testing. Conventional creep testing that is performed on material from power plant components to assess the condition typically involves rather relatively short testing times. It may be possible to compare such results roughly with each other by use of the Larson-Miller Parameter but it is likely that the specific test data is performed at so much higher stresses than those at service that the deformation mechanisms are not exactly the same.

Instead, iso-stress creep testing at a representative stress is frequently used. The testing is performed at a series of temperatures that are higher than the service temperature. The results are then extrapolated the service temperature and a remaining lifetime is obtained. The disadvantage is that constitutive equations, such as the Norton creep law, cannot be used with this method and the results can therefore not be used for creep analysis.

Impression creep testing allows significant lower stresses and the present results indicate that resulting strain rates can be fully comparable with data from uniaxial creep testing. Thus, impression creep data is very useful for creep analyses of pipe systems as well as for components where even welds can be included in the models.

The idea of creep testing of service exposed material can be discussed. First, the results are a measure of the future creep behaviour. Thus, semi-destructive creep testing methods, such as impression creep testing, can be used for determination of remaining life. However, creep testing of service exposed material may result in higher reductions of creep life at higher stresses than at lower. Thus, extrapolations will give the longest creep lives for the service exposed material at service stresses since the stress rupture versus time or stress versus linear creep rate curves will cross each other. In the present project tests on service exposed material was performed at only one stress level. Then, the same slope of the curve as for the new material was anticipated. This seems, paradoxically enough, to be a better approach than linear extrapolation of test results at different enhanced stresses.

It is has been demonstrated that it is possible to model a T-piece in a pipe system including its welds and simulate the development of the creep strain distribution over time. System stresses according to a pipe system analysis are superimposed as well and the creep properties of the weld metal and the HAZ are implemented by use of the results of the impression creep testing. This is a novel and an innovative approach where 3D modelling is required. Only a few studies in this area can be found in the literature. One example is [14], where creep simulations were performed by a 2D model on a straight pipe with a weld under the loading conditions internal pressure with and without an extra axial load which. Simulations with this approach have been performed in previous Energiforsk projects as well, e.g. [15].

11. Conclusions

The following conclusions can be drawn from the present study:

- Significant creep cavitation was observed in two butt welds and in a T-piece from the main steam pipe from a power plant that had been in operation for 170 000 hours and 73 000 hours, respectively. The damage in the T-piece can be considered as pre-mature.
- Impression creep testing with an innovative approach was used by manufacturing a “sandwich” type of specimen of the new weld which allowed the creep rates to be scanned from the base material across the HAZ to the weld metal by steps of 0.5 mm. The maximum creep rate in the HAZ was in the intercritical part and was 2.6 times higher than in the parent metal. The weld metal of the new weld was overmatching by a factor of two.

- Impression creep testing of parent and weld metals with 73 000 hours service exposure showed 3 and 6 times higher creep rates, respectively, than for corresponding materials in a virgin weld.
- The impression creep test results of virgin parent metal were consistent with uniaxial creep testing of the same material.
- Creep analysis of a main steam pipe system showed significant stress relaxation occurs after a relatively short service period. These effects cannot be covered by an elastic analysis, such as a Caepipe analysis.
- Creep analyses of a main steam pipe system including starts and stops resulted in higher levels of creep strain than without the starts and stops. In addition, the positions where the highest strains occurred were not the same. Thus, it is shown that a creep analysis that includes the effects of starts and stops can be needed to show actual creep strains as well as critical positions for non-destructive testing. Identification of critical positions with critical positions by elastic pipe system analysis, which is quite common today, should therefore be carried out with caution.
- Creep analysis of the main steam piping was carried out with creep data from standards and from the impression creep test results. Creep test results of new material and standard data gives similar creep strains in the system, approximately 0.1 % after 178 000 hours. The same analysis but with use of creep tests results of service exposed material and with lower bound standard data resulted in 0.3 % creep strain.
- A component model of a T-piece where system stress can be superimposed to internal pressure was developed successfully.
- A branch weld was then included in the model of the T-piece. The relative differences of creep rates between parent metal, HAZ and weld metal that was obtained by the impression creep testing was used in the model for simulations of service exposure.
- There is a quite good agreement between simulated creep strain distribution after 73 000 hours in service and observed creep damage in the real T-piece after the same time in service.

References

[1] Vilhelmsen T et. al.; ”Utveckling av krypskador hos svetsade komponenter av P91 och X20”, Värmeforskrapport 1197, Stockholm mars 2011.

[2] Holmström S; ”Engineering tools for robust creep modeling”, VTT 728, Espoo, 2010.

[3] Payten W; Large scale multi-zone creep finite element modelling of a main steam line branch intersection. International Journal of Pressure Vessels and Piping 83, 2006.

[4] Yee R K, Cohn M; ”Creep relaxation behavior of high energy Piping”, Journal of Pressure Vessel Technology, Vol. 122, November 2000.

[5] Segle P, Algotsson P, Samuelsson Å; ”Inverkan på ingrepp i ångledningssystem på dess återstående livslängd”, Värmeforskrapport 672, Augusti 1999.

[6] Cohn M, ”Main steam pipe girth weldment stresses and life consumption considering malfunctioning supports. Journal of Pressure Vessel Technology”, Vol. 132, October 2010.

[7] Hahn B et. Al.; ”In-service Condition Monitoring of piping systems in power plant requirements and advanced techniques”, OMMI, Vol. 1, Issue 1, April 2002.

[8] Abaqus, version 6.10 - 6.13, Simulia.

[9] EN10028-2:2009.

[10] Storesund J, Steingrimsdottir K, Rantala, Sollander R, Chen, Z and Bolinder T; Life time assessment of high temperature piping, Energiforsk project M12-218, to be published 2016.

[11] Holmström S, Auerkari P; Robust prediction of full creep curves from minimal data and time to rupture model, Energy materials, Materials Science & Engineering for Energy Systems Vol. 1 (2006), 4, pp 249-255.

[12] Auerkari P, Borggreen K, Salonen J; Guidelines for evaluating in-service creep damage. Nordtest report NT TR 302. VTT Manufacturing Technology, Esbo, Augusti 1995.

[13] Middleton, C. J and Metcalfe, E.; A rewiev of laboratory Type IV cracking data in high chromium ferritic steels. Paper C386/027. Published in IMechE Proceedings, London, 1990.

[14] Vakili-Tahami F, Hayhurst D R, Wong M T; High-temperature creep rupture of low alloy ferritic steel butt-welded pipes subjected to combined internal pressure and end loadings. Phil. Trans. R. Soc. A (2005) 363, 2629–2661.

[15] Storesund J, Borggreen K, Zang W, Nilsson H, Samuelson Å; Krypskador i svetsar av X20CrMoV12-1 stål, Etapp 2 - Studier av långtidspåverkat material och skadedatabas samt beräkning av skadefördelning och skadetålighet. Värmeforskrapport 874, Stockholm, september 2004.

Corrosion in blast furnace gas fired power plants

Arthur Stam[1], Sjef van der Gun[1], Han Raas[2] & Arjan van den Bos[3]

[1]DEKRA Solutions B.V.
Meander 1051 6825 MJ Arnhem, The Netherlands

[2]NUON Vattenfall
Westervoortsedijk 73 6827 AV Arnhem, The Netherlands

[3]NUON Vattenfall
PO Box 41920 1009 DC Amsterdam, The Netherlands

Abstract

NUON Vattenfall operates power plants fired with blast furnace gas in IJmond and Velsen. The IJmond 1 unit experienced heavy corrosion of finned boiler tubes. As a result, the counter pressure of the gas turbine increases, and the plant efficiency drops. Furthermore, the required temperature level of steam delivered to an industrial customer cannot always be maintained. The air preheater (APH) of unit Velsen 24 experienced heavy corrosion and the efficiency of the APH has decreased over the last few years. Samples have been taken from the finned boiler tubes and the APH, and have been analyzed with SEM and XRD. In addition, thermodynamic calculations have been performed. Iron sulphate and iron oxide are formed during operation and standstill. Hygroscopic iron sulphate forms iron sulphate hydrates, and crystal water is released due to load changes, during start-up, or standstill, creating an aqueous environment. Sulphuric acid deposition (i.e. dew point corrosion) does not seem a relevant mechanism in the boiler or APH. The corrosion process during operation cannot be overcome while use of dryers and sealing of the boiler as much as possible during standstill is regarded beneficial. Explosive cleaning of the finned tube boiler pipes was successful while CO_2-ice blasting only showed partly effective due to the boiler design.

1. Introduction

NUON operates plants IJmond 1 and Velsen 24 that are fired with a low caloric gas mix, including Blast Furnace Gas (BFG). IJmond 1 (144 MW_e and 105 MW_{th}) was commissioned in 1997 and was designed by Mitsubishi Heavy Industries. During normal operation, the fuel gas consists of blast furnace gas (BFG; 50% N_2, 25% CO and the remainder is mainly CO_2 and some H_2) and 'oxy gas' (mainly CO), which are both gases resulting from the steel making process of TATA Steel. Natural gas and nitrogen can be added to compensate for the variations in gas composition, so that the Wobbe index and heating value stays within the required bandwidth. A gas with a higher calorific value is needed to start up the gas turbine for which cokes gas is used, or as recently shown to be possible, natural gas (NG).

Heat from gas turbine flue gasses is partly recuperated in a boiler with heat exchangers with finned pipes. A significant pressure drop exists over the heat exchangers, in some cases it has been measured to be 140% higher compared to the design. This high pressure loss is caused by fouling of the pipes. Consequently, the plant efficiency is lower and the temperature of the steam that is delivered to TATA Steel (510°C±5) can not always be maintained.

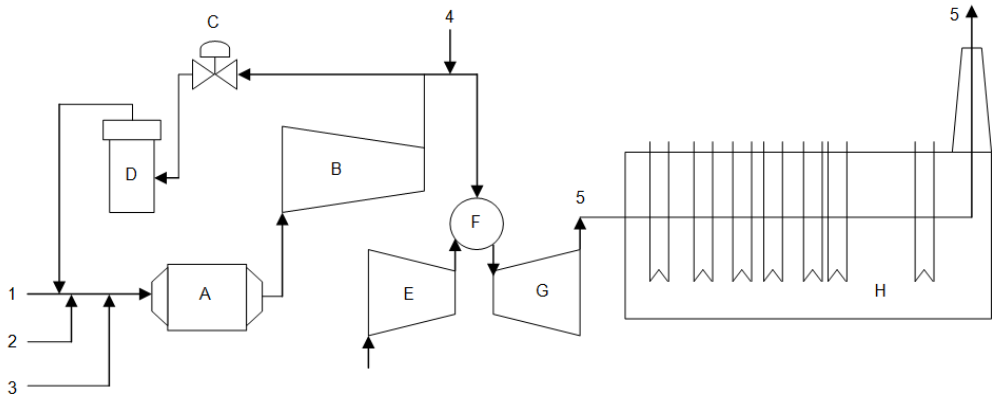

Figure 1. Process flow scheme IJmond 1. Legend: 1) Blast Furnace Gas + Oxy Gas 2) Cokes gas 3) Natural Gas 4) Nitrogen 5) Flue Gas A) Wet ESP B) Gas Compressor C) Bypass D) Gas Cooler E) Compressor F) Combustion Room G) Turbine H) Boiler.

Velsen 24 (470 MW_e) was commissioned in 1974 and was designed by N.V. Kon. Mij. De Schelde. The unit is fired with natural gas and blast furnace gas, and consists of a two-pass boiler and steam turbine. The unit is operated when units Velsen 25 and IJmond 1 are not operational or when market conditions require operation. This results in 7 yearly starts and approximately 1,000 operational hours (2012). The air preheaters (APH's) are heavily corroded. The cleaning system of the APH (water jets) is not in operation since 2006. Damage of the heavily corroded plates of the APH is probably accelerated when the system is used.

Initial investigations showed sulphur-rich corrosion products at the APH's and boiler pipes. Although this might be explained by sulphuric acid dew point corrosion for the cold parts of the boiler and APH, the corrosion mechanism for high temperature parts is unknown. Therefore, corrosion mechanisms are investigated and explained in this paper.

2. Experimental and modelling

2.1 Operational conditions

In IJmond 1, flue gasses from the gas turbine pass a number of heat exchangers before leaving the stack. The design metal temperatures are indicated in Figure 2, and lie between 104 and 518°C. During standstill, steam from TATA Steel is supplied to the tubes for conservation.

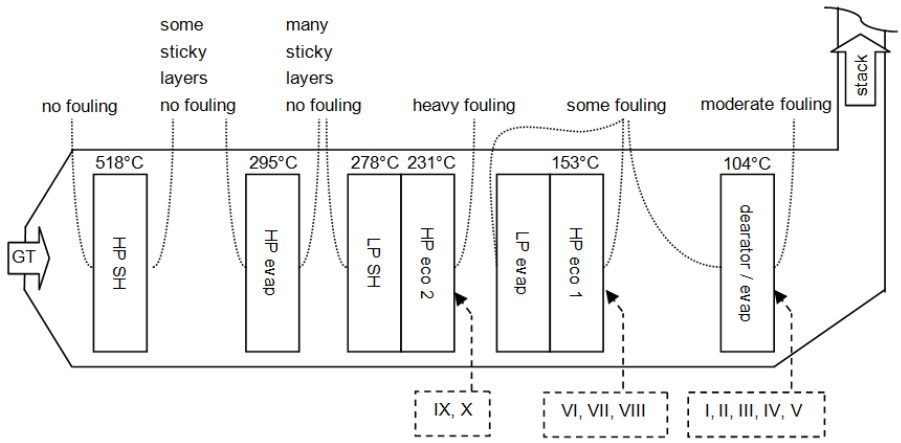

Figure 2. IJmond 1 boiler with indication of design metal temperatures of heat exchangers. The degree of fouling as observed during the inspection is also indicated, as well as the locations of where the samples were taken (I to X).

The composition of the gas mixture fed to IJmond 1 varies as a function of time, due to process conditions at TATA Steel. In five years the concentrations of H_2S and COS (as S) were 2.12 – 3.71 mg/m_0^3 and 31.77 – 45.18 mg/m_0^3, respectively (yearly averaged values). On a weekly basis, the amount of COS (as S) can vary between 25 mg/ m_o^3 and 100 mg/ m_o^3.

Velsen 24 is fired with BFG and NG (35% NG). The air preheaters are regenerative counter flow heat exchangers and are a Rothemühle design. In this design, the baskets are stationary while the air supply revolves (0.8 rev min-1), see Figure 3. The upper baskets are about 1 m in height and the lower baskets are about 0.37 m in height. The baskets are placed in 5 rings. Two air preheaters are installed.

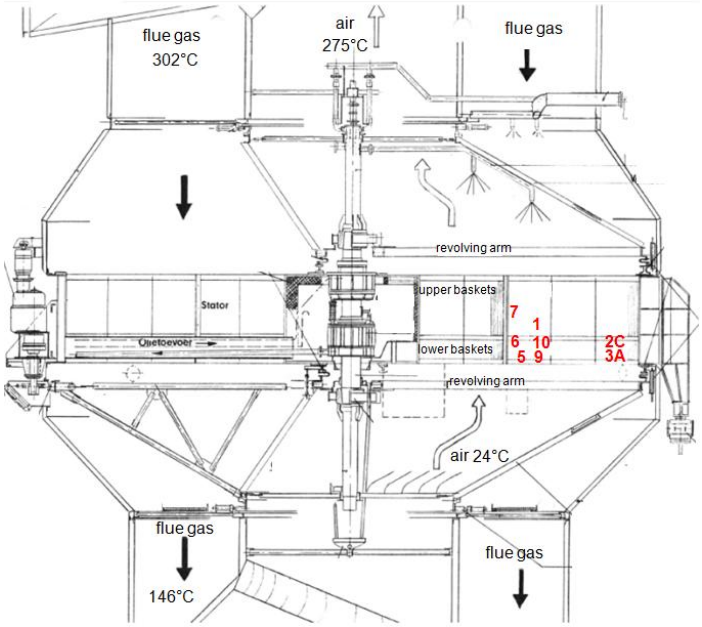

Figure 3. Velsen 24 APH with indication of measured air and flue gas temperatures. Also indicated are sampling locations (samples 1, 2C, 3A, 5, 6, 7, 9, 10).

Velsen 24 is fired with BFG and NG (35% NG). The air preheaters are regenerative counter flow heat exchangers and are a Rothemühle design. In this design, the baskets are stationary while the air supply revolves (0.8 rev min-1), see Figure 3. The upper baskets are about 1 m in height and the lower baskets are about 0.37 m in height. The baskets are placed in 5 rings. Two air preheaters are installed.

Recent measurements show that flue gasses enter and leave the APH at a temperature of 302°C and 146°C, respectively; air enters at 24°C and leaves at 275°C.

2.2 Inspections and sampling

All heat exchangers of the IJmond 1 boiler were visually inspected, and samples were taken at positions indicated in Figure 2. Samples II and III are flakes. Sample II is a flake coloured yellow at one side, and coloured brown at the other side. Sample III is a flake coloured brown at both sides. Sample IV is a collection sample taken from the floor. Sample VII is a fin from the high-pressure economizer 1. Samples VIII and IX are flakes that are collected at the high-pressure economizers 1 and 2, respectively.

Both APH's of Velsen 24 were inspected. The baskets have been inspected to the extent that they were accessible. Complete baskets were removed allowing detailed inspection. Samples have been taken from baskets in rings 3 and 5 (see Figure 3). All samples originate from APH 1. The corrosion products (samples 5, 6 and 7) are very thin flakes. The colour is mostly red-brown while sample 7 also had a yellow stain. The samples 1, 9 and 10 are parts of the remaining plates and have a red-brown colour. Plates were removed from the baskets that were replaced recently (2012). The plates have a dark-brown colour, but the bottom side is stained light-green. Both investigated samples have been obtained from the downside (light-green stained) area of the plates.

2.3 Sample preparation and analyses

The samples were put in slow curing epoxy resin, and cross sections were grinded and polished (water free, to preserve all water-soluble compounds). Light microscopy has been performed to get an overall impression of the sample, and to locate areas fur further investigation. Carbon was deposited on the sample surface to overcome charging during SEM investigations. Backscatter images and secondary electron images were made and the composition was analyzed on micro-scale level with EDS (Energy Dispersive X-ray Spectroscopy). Point analyses were made in combination with back scatter plots. KEMPhase images were made in addition. KEMPhase is an in-house developed tool which enables the results of EDS analysis to be presented as false colour representations of the distribution of predefined phases. X-ray Diffraction (XRD) has been performed on selected samples. After analysis of the samples 'as received', the samples were dried and XRD was repeated (XRD analyses were performed by TCKI in Velp, The Netherlands).

2.4 Modelling

Thermodynamic equilibrium calculations were conducted with FactSage (see [1] for a general description), using the functions ‘Predom’ and 'EpH'. Predom calculates and plots isothermal predominance area diagrams, i.e. it locates domains of stability of each phase as function of gas potential for a given temperature. Pourbaix diagrams were calculated using 'EpH' which maps out possible stable (equilibrium) phases of an aqueous electrochemical system. Predominant ion boundaries are represented by lines. The stability region of water is indicated by dashed lines.

3. Results

3.1 Inspections

The inspection results regarding fouling of IJmond 1 are shown in Figure 2. Little to no fouling was observed at the high temperature end of the boiler while sticky layers were present (see Figure 4), especially at the 2nd and 3rd heat exchanger (numbered in flue gas flow direction). Most fouling was observed halfway at the 4th heat exchanger (HP eco 2), while also the coldest parts were fouled (dearator / evaporator). Typically, flakes are present on the fins, while flakes collect on the flooring as shown in Figure 4.

Figure 4. IJmond 1 boiler inspection results. Left: sticky layers. Middle: flakes on fins. Right: flakes collected on flooring.

Inspection of the Velsen 24 APH showed that seemingly the plates are in good condition when inspected from above. However, when baskets were removed, dismantled and individual plates were inspected, the plates showed to be in very bad condition. The top 5 cm of the plates are in reasonable condition (thickness: ~ 0.5 mm), while the rest has corroded away, see Figure 5. Corrosion products are present between the plates. These results hold for both the upper and lower baskets.

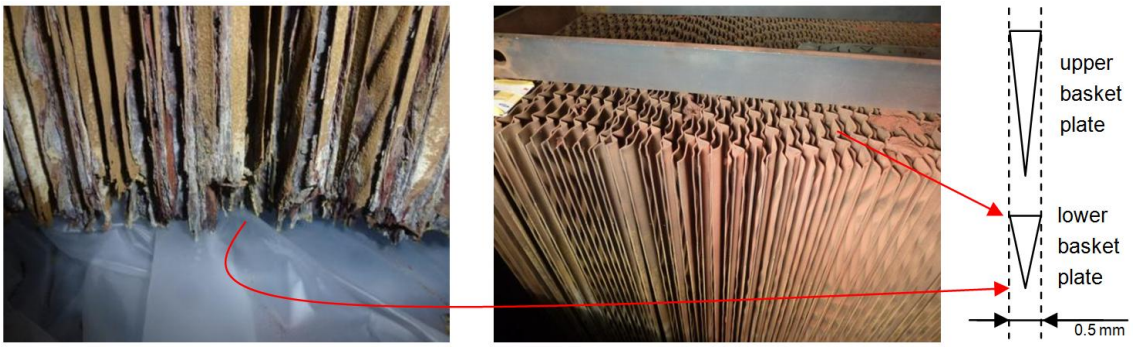

Figure 5. Velsen 24 APH inspection results. Bottom and top of the plates are shown.

3.2 Scanning Electron Microscopy

In regards to IJmond 1: the cross sections of investigated corrosion products are quite alike: 200 – 300 µm thick and up to several mm's in length, while minimum and maximum thicknesses range between 50 and 800 µm. The flakes are solid on the inside with longitudinal cracks. The edge is porous with a 'finger' structure and on top of the edge is a porous phase with, in the backscatter images, a dark grey colour. Examples are shown in Figure 6. The corrosion products from HP eco 2 are the thinnest (50 – 250 µm thick) and differ in structure: the outer S-rich layer is non-porous.

The chemical composition of the corrosion products is quite alike. The lightest grey area in the middle of the through-cut of the sample has the highest Fe content (36 – 38%), and contains < 1% S (in this paper, all element concentrations are given in atom %). Slightly darker areas, adjacent to the lightest areas, contain less Fe (33 - 35%) and more S (~2%). The dark (porous) areas at the outer surface contain least Fe (13 – 16%) and most S (10 -14%). Between the centre and outer edge, different phases co-exist. The areas with highest S-content are not only found at the outer surface, but also directly adjacent to the lightest coloured centre area, and in transversal bands (< 5µm width). K and Na are only detected in areas near the surface, especially with higher S content. In all cases, the sum of K and Na-concentration is < 1%. Chlorine was not detected.

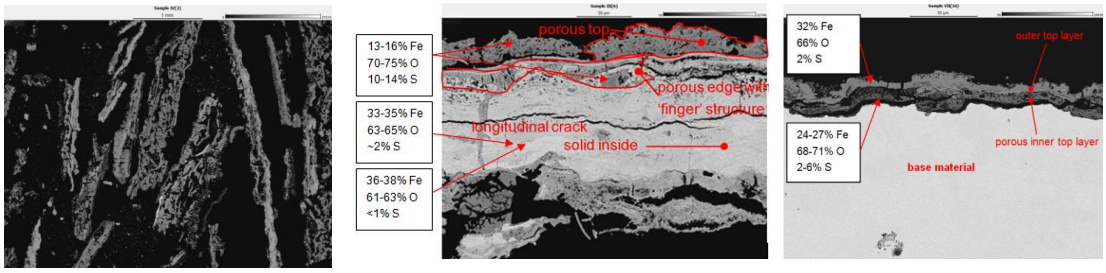

Figure 6. Backscatter images. Left: thin, long and porous flakes of sample IV. Middle: typical build-up of flake, sample III. Right: fin, base material and corrosion layer, sample VII.

A backscatter image of a cross section of a fin with corrosion layer is shown in Figure 6, right. The outer layer contains about 32% Fe, 66% O and 2% S. The layer between base material and outer layer contains 24 – 27% Fe, 68 – 71% O and 2 – 6% S. The outside layer contains hence less sulphur than the intermediate layer. K and Na are sometimes present at areas with higher S concentration in a concentration of Na + K ≤ 1%.

Regarding the Velsen 24 samples: the older plates vary in thickness and 0 – 50 µm to ~1 mm base material is present, depending on the sample was taken from the bottom or top of the plate (also see section 3.1). Newer plates (installed 2012) have ~1 mm base material. Corrosion layers of older and newer plates are 25 – 100 µm thick. The thickness of the corrosion layer varies per location, as can be seen in Figure 7 (left); the corrosion layer thickness does not correlate with the amount of thickness reduction of base material. The S concentration in the corrosion layer is 1 – 2% near the outer surface and highest near the interface of corrosion layer and base material. Highest measured concentrations are 17%, 11%, 5%, 17% and 4% for samples 1, 10, 9, 3A and 2C, respectively. In general, the S concentration can vary widely over the cross section as is shown in Figure 7 (right).

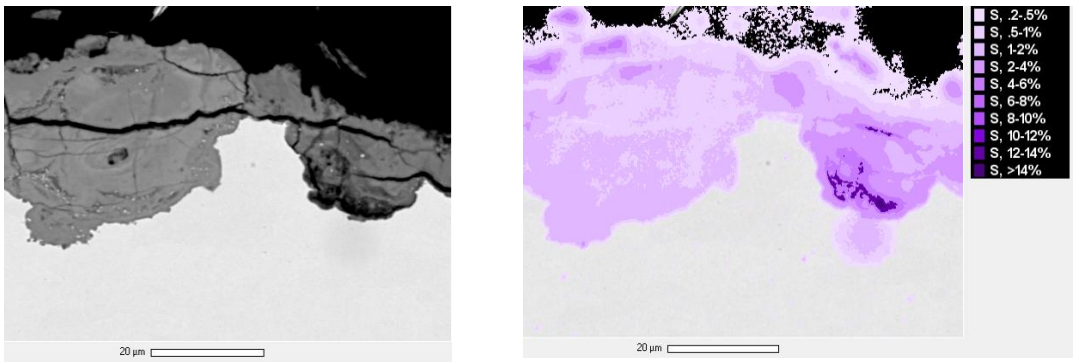

Figure 7. Plate from lower basket, sample 3A. Back scatter image of overview (left) and S concentrations of detail (right).

The corrosion products vary in thickness from ~ 250 µm to ~ 500 µm. All samples are porous and contain cracks. So called 'whiskers' are sometimes present at edges (sample surface or pore edge), see Figure 8. Highest S concentrations, of up to 19%, are present at the surface, and lowest further into the material (0 – 3%). The concentration of S is 7 – 8% at whiskers at the edge of pores directly under the surface (~ 50 µm), see Figure 8.

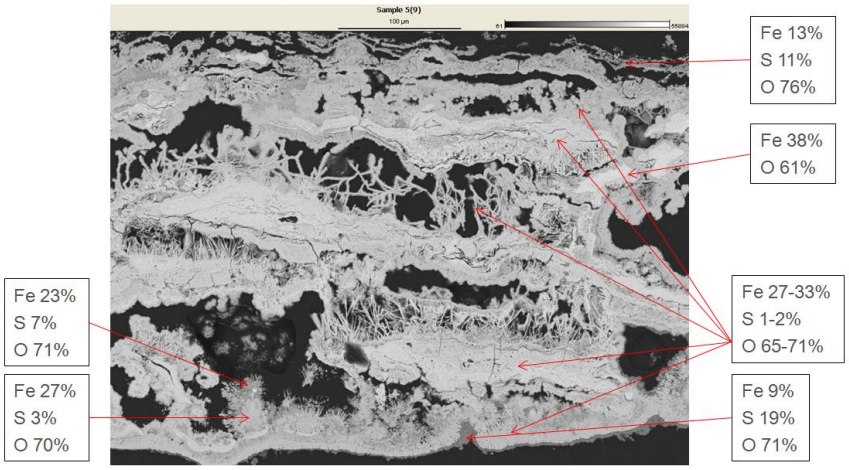

Figure 8. Detail of corrosion products in sample 6, back scatter image. Indicated are concentrations of Fe, S and O.

3.3 X-Ray Diffraction

The compounds found in the samples from the IJmond 1 boiler, as established with XRD, containing iron are hematite (Fe_2O_3), maghemite (Fe_2O_3) and jarosite ($KFe_3(SO_4)_2(OH)_6$). In addition, aluminosilicates were found: plagioclase ($(Ca,Na)(Al,Si)_2Si_2O_8$) and yugawaralite ($CaAl_2Si_6O_{16}$). An overview is presented in Table 1.

The XRD-analysis of the Velsen 24 APH samples showed the presence of the following crystalline compounds: hematite (Fe_2O_3), maghemite (Fe_2O_3) or magnetite (Fe_3O_4), goethite (FeO(OH)), jarosite ($KFe_2(SO_4)_2(OH)_6$) and pyrite, (FeS_2), see Table 1.

Table 1. XRD analysis results of samples from boiler (IJmond 1) and APH (Velsen 24). Results for 'as received' samples and after drying the samples were identical.

plant	component	sample	compound as identified with XRD
IJmond 1 (boiler)	HP eco 2	X	hematite, jarosite
		IX	hematite, maghemite, plagioclase
	HP eco 1	VIII	hematite, maghemite, jarosite
		VI	yugawaralite
	dearator / evaporator	V	no crystalline compounds
		IV	hematite, maghemite, jarosite
		I	hematite, jarosite, yugawaralite
Velsen 24 (APH)	upper basket	1	hematite, maghemite or magnetite
		7	hematite, maghemite or magnetite, goethite, jarosite, pyrite
	lower basket (top)	6	hematite, maghemite or magnetite, pyrite
	lower basket (bottom)	5	hematite, maghemite or magnetite, pyrite

3.4 Thermodynamic modelling

Figure 9 shows the thermodynamic stability diagram of the system Fe-S-O-Cl for different temperatures (25°C – 518°C). The O_2 and SO_2 activities are plotted on the axes. The green point reflects the flue gas composition. At this point, $Fe_2(SO_4)_3$ is stable and can be formed at the surface of the material for temperatures well below 518°C. Fe_2O_3(s) is stable at flue gas conditions at 518°C. Moreover, at temperatures of 302°C and lower, both the O2 and SO2 concentrations in the flue gas can vary with several orders of magnitude while remaining in the area where $Fe_2(SO_4)_3$ is thermodynamically stable.

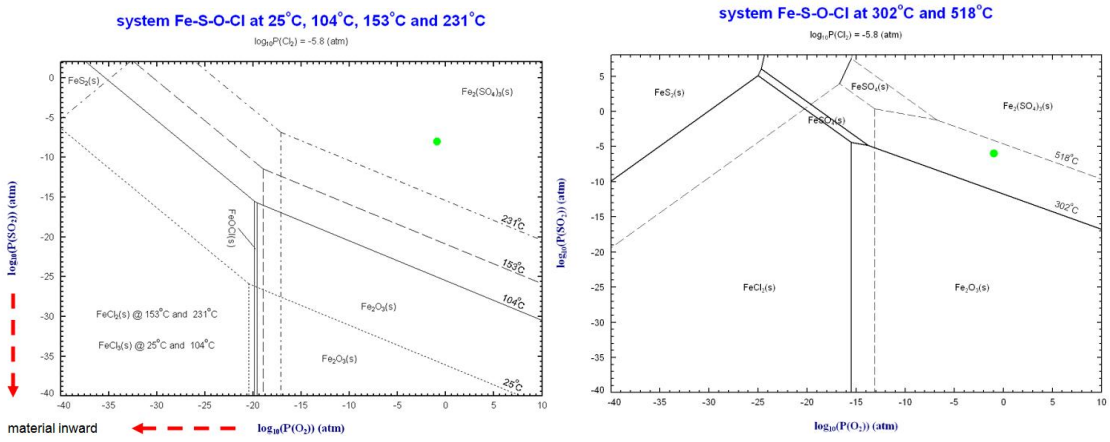

Figure 9. Thermodynamic stability of the system Fe – O – S – Cl with constant Cl concentration of 3 ppm at 25°C, 104°C, 153°C, 231°C, 302°C and 518°C. Green circles indicate flue gas composition (9·10-5% SO_2, 11%O_2).

An aqueous system can be represented by a Pourbaix diagram where pH is plotted against the electrode potential E. Reactions in which oxygen is involved have a relatively high E and a well aerated, or oxidizing environment is associated with higher E and reducing conditions are related to lower values of E. $Fe_2(SO_4)_3$, $FeSO_4$, Fe_2O_3, FeS_2 and $FeSO_4(H_2O)_7$ are stable compounds.

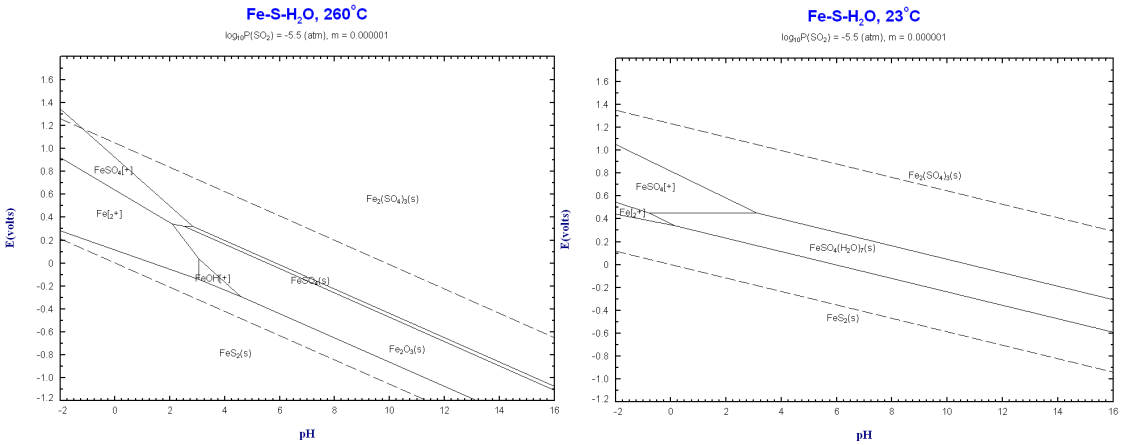

Figure 10. Pourbaix diagrams of the system Fe-S-H_2O for 260°C and 23°C.

4. Discussion

4.1 Interpretation of EDS analyses

Highest concentrations of the detected elements are of Fe, S and O. All the SEM-EDS results have been plotted in a diagram showing Fe and S concentration, see Figure 11. For comparison, (hydrated) iron oxide, (hydrated) iron sulphates and jarosite ($KFe_3(SO_4)_2(OH)_6$) have been plotted. This suggests that based on the relative concentrations, iron oxide, (hydrated) iron sulphates and jarosite are present in a certain ratio in the IJmond 1 boiler and Velsen 24 APH samples. Hydrated iron oxide and pyrite may also be present in the Velsen 24 APH samples.

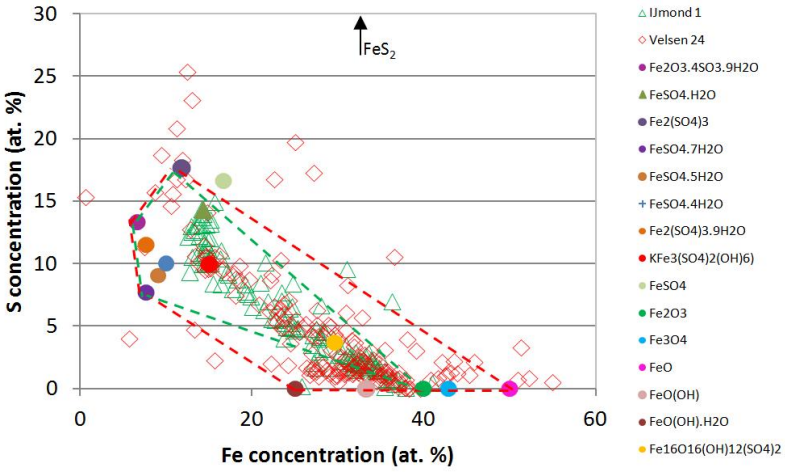

Figure 11. SEM-EDS results plotted in a ([Fe], [S])-diagram (Since the element hydrogen (H) is not detected with EDS, the Fe and S concentration in stoichiometric compounds has been corrected for H). The green and red-dashed area indicates where most results of analyses lie resulting from samples taken from the IJmond 1 boiler and Velsen 24 APH, respectively.

4.2 Formation of (hydrated) iron sulphate

Since S is present in the flue gas and thermodynamically stable as $Fe_2(SO_4)_3$, S will play a role in the corrosion process. During operation, iron sulphate is formed at the interface of metal oxide and flue gas where iron diffuses outward through the oxide scale (unless the temperature is too high, such as the heat exchanger in the IJmond 1 boiler operating at 518°C, see Figure 9). However, also SO_2 will penetrate inwards through micro-fissures and micro-channels in the scale, see [2]. Water in flue gasses are attracted by iron sulphate, e.g. iron sulphate will hydrate as $Fe_2(SO_4)_3$ is very hygroscopic. The temperature region whereby $Fe_2(SO_4)3.5H_2O$ loses its crystal water upon heating is 200°C – 300°C [3]), and for melanterite ($FeSO_4.7H_2O$) this region is room temperature to 200°C [4]). Hence, during load changes, hydrates can be formed and crystal water can be released. This can also occur when the boiler goes out of operation. At room temperature (~300K), different configurations of hydration are stable, dependent on the air humidity, see Figure 12. The change of different amounts of crystal water causes changes in density, and changes of the microstructure. In turn, this will build up internal pressure, resulting in crumbling of the corrosion layers. The corrosion layers fill up the room between the fins, and are the cause of the fouling, resulting in an increased pressure drop and decreased heat transfer.

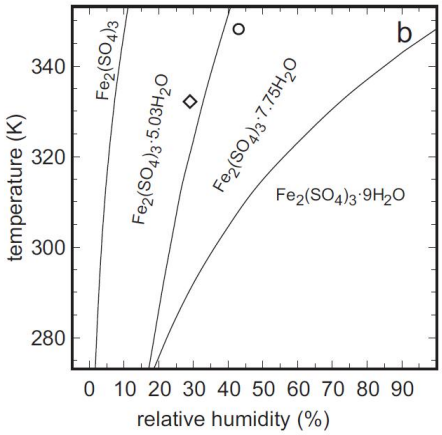

Figure 12. Phase diagram calculated by [5] of iron sulphate and different hydrates.

4.3 Aqueous systems

An aqueous system can exist under different circumstances. Upon heating of hydrated iron sulphates (or during standstill, by changing air humidity), the crystal water is released, creating an aqueous system, and possibly 'rust' (FeOOH) can be formed according to the reaction:

$$Fe_2(SO_4)_3 + 4H_2O \rightarrow 2FeOOH + 3H_2SO_4 \quad (1)$$

This is regarded as the mechanism forming sticky layers as observed during the inspection. The circumstance can exist in both the boiler and in the APH. In addition, if the boiler goes out of operation, water can condense on heat exchanging surfaces. This can also be the case in the APH where relatively cold air is entering.

It is unlikely that the dew point is underrun in the boiler or in the APH. With combustion of BFG or cokes gas with 12% of oxygen in the dry flue gas, this amounts in a water concentration of 0.74% and (assuming full conversion of SO_2 to SO_3 as worst case) a SO_3 concentration of 0.01 ppm (BFG) and 0.17 ppm (cokes gas). The dew point then lies in both cases somewhere between 80 and 90°C. This temperature is not reached in the IJmond 1 boiler or in the Velsen 24 APH when flue gasses are present. In case that incidentally a fuel mix where the both sulphur and water content are approximately a factor of 5 higher, the dew point can be underrun at the coldest part of the boiler (this would be an exception).

In an aqueous system of Fe-H_2O, $2Fe(OH)_2$ is formed. In a further reaction with dissolved oxygen, oxidized ferrous hydroxide oxidizes into ferric hydroxide ($4Fe(OH)_3$). Amorphous iron(III) hydroxide hydrate is thermodynamically unstable and gradually transforms to goethite (α-FeO(OH), alternatively written: $Fe_2O_3.H_2O$) and hematite (α-Fe_2O_3) [6].

In an aqueous system of Fe-S-H_2O, $Fe_2(SO_4)_3$(s) is stable at oxidizing conditions, whereas FeSO4(s) (or $FeSO_4 \cdot 7H_2O$(s), depending on temperature), Fe_2O_3(s) and FeS_2(s) are stable at less oxidizing or reducing conditions. The Pourbaix diagrams also show that at pH < 3, $FeSO_4^+$ and Fe^{2+} ions are formed, and also $FeOH^+$ at higher temperature. In this region, corrosion is a relatively quickly progressing process.

It was found in the studies of mine drainage that in Acid Sulfur Water (ASW) that there is transformation of ferrous sulphate minerals to iron oxyhydroxide minerals. This is explained by [7] as a series of oxidation, dehydration and neutralization (hydrolysis) reactions. The mineralogy that develops at any particular site will be controlled by the relative rates of each of these types of reactions. Jarosite, schwertmannite ($Fe_8O_8(OH)_6SO_4$), goethite, hematite and maghemite (γ-Fe_2O_3) are at the end of the pathway. These minerals will precipitate whereby generally well crystallized minerals are formed that can be detected with XRD, which is the case for jarosite, goethite, hematite and maghemite in our studies. Jarosite precipitates at low pH (pH < 5.9, [8]) according to:

$$K^+ + 3Fe^{3+} + 2SO_4^{2-} + 6H_2O \leftrightarrow KFe_3(SO_4)_2(OH)_6 + 6H^+ \quad (2)$$

The identification of ferrihydrite ($Fe_5HO_8 \cdot 4H_2O$) and schwertmannite is complicated because they occur in small particles close to or below 10 nm in size, so that physical parameters (e.g. X-ray diffraction peaks) become “smeared out”. The identity of these minerals as individual species was consequently long not recognized [9], and misinterpreted as being “amorphous iron oxide“ or “ferric hydroxide”. In general, hydration causes poor crystallization, and as a consequence many of the compounds that are formed, may not be recognized with XRD.

The driving force for the formation of components is thermodynamic stability, and a review of the system Fe-K-S-H_2O indicates what compounds are only stable under certain conditions. However, the database of FactSage is not complete and it doesn’t contain jarosite, schwertmannite and ferrihydrite. [10] calculated a pe-pH diagram for the system Fe-S-K-O-H, see Figure 13. It shows that jarosite and goethite are the phases that ultimately control the solubility of iron. The diagram shows precipitation of jarosite at low pH (pH < 2), schwertmannite at less low pH, and ferrihydrite around neutral pH. Schwertmannite and ferrihydrite are meta-stable phases that hydrolyze slowly, forming goethite.

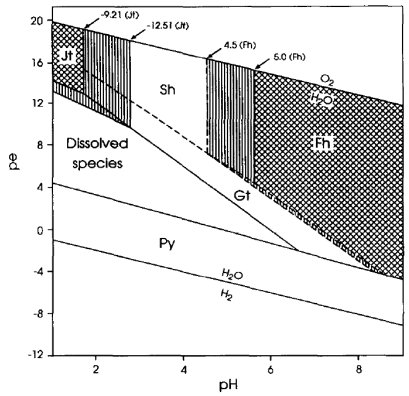

Figure 13. (pe,pH)-diagram (pe = EH/0.0591V) for the system Fe-S-K-O-H at 25°C, calculated by [10]. Jt = K-jarosite, Sh = schwertmannite, Fh = ferrihydrite, Gt = goethite, Py = pyrite. Fields of metastability shown by dashed lines. Source: [10]

4.4 Present phases

The presence of (hydrated) iron oxide, (hydrated) iron sulphate and jarosite are explained by the (equilibrium) systems Fe-H_2O, Fe-O-Cl-S, Fe-S-H_2O and Fe-K-S-H_2O. Iron sulphates and hydrates were not detected with XRD (but present in the XRD database). In general, iron sulphates crystallize poorly, which can be a reason that they have not been detected with XRD. As iron sulphates may have formed hydrates, the XRD-analysis was repeated after drying the samples, the results remained, however, identical.

Ca-containing minerals plagioclase ($(Ca,Na)(Al,Si)_2Si_2O_8$) and yugawaralite ($CaAlSi_2O_{16}$) were detected with XRD analysis in the IJmond 1 boiler samples. These minerals were, however, not indicated by SEM results. Therefore, it is likely that these minerals make up for a small part of the fouling. Yugawaralite is a rare mineral which is a zeolite (that is for instance used in deNOx catalysts). Plagioclase is a group of minerals, many of which are formed at high temperature similar, in a system where also slag is stable. It can therefore occur as blast furnace dust, or coal fly ash (also resulting from the blast furnace). However, mineral wool is produced by heating blast furnace slag with limestone, and plagioclase could be present in the mineral wool. Mineral wool was found at the visual inspection at the heat exchangers and areas of uncovered mineral wool of several square meters were present in the IJmond boiler. Hence, it will be difficult to distinguish between blast furnace dust and mineral wool.

4.5 Indications for cleaning

Off-line cleaning of boiler pipes and APH's with water is not advised. Upon water drying out, an aqueous systems exist at very low pH in which corrosion is an ongoing process. On-line cleaning with water can promote conditions for acid dew point corrosion, and is therefore also not advised. The on-line cleaning system for the APH's has been taken therefore out of operation. Earlier experience with water-free cleaning of boiler pipes, such as with CO_2 ice grit blasting showed to be successful. However, when the pipe configuration is such that pipes are close to each other and in front of each other, not all pipes may be reached and cleaned with this method. Recent experience with explosive cleaning of boiler pipes has shown to be successful for boiler pipes, and will be maintained by NUON Vattenfall. Explosive cleaning is not advised for the APH's as they are in very bad condition, and corrosion products cannot be removed from the narrow-spaced APH plates. Cleaning with soda and sodium hydroxide is currently under investigation. Since crystal water is taken up and released with varying air humidity and temperature (see Figure 12), it is key to keep the conditions as constant as possible. This can be done using dryers and by sealing the boiler as much as possible.

4.6 Natural gas firing

In the Netherlands, no odorant is used in high caloric gas, and almost all sulphur is removed from the gas. Nonetheless, some sulphur is present, and on the long term corrosion products will form on boiler tubes. It is expected that corrosion will progress quicker with natural gas with higher sulphur content, i.e. with added odorant.

5. Conclusion

Iron sulphate is formed on the surface of finned boiler pipes during operation, but not at the highest temperature heat exchangers with a metal temperature of > 500°C where iron sulphate is not stable. Iron sulphates are hygroscopic and will attract water from flue gasses. Crystal water is released upon temperature changes between room temperature and 300°C, and upon changes of air humidity. The change of different amounts of crystal water causes changes in density, and changes of the microstructure. In turn, this will build up internal pressure, resulting in crumbling of the corrosion layers. The corrosion layers fill up the room between the fins, and are the cause of the fouling, resulting in an increased pressure drop and decreased heat transfer.

An aqueous system can exist on boiler tube surfaces and APH plate surfaces. This can be the case when crystal water is released during standstill as a consequence of variations in air humidity or temperature. Also, water from air can condense on pipes. This will cause sticky layers on pipes. At low pH, corrosion is an ongoing process. It is unlikely that the dew point is underrun in the boiler or in the APH.

Explosive cleaning of the finned tube boiler pipes has shown to be successful while CO_2-ice blasting only showed partly effective due to the boiler design. Explosive cleaning for the APH is not an option and suitable cleaning options are currently under investigation.

References

1. Bale CW, Chartrand P, Degterov SA, Eriksson G, Hack K, Ben Mahfoud R, et al. FactSage Thermochemical Software and Databases. CALPHAD 2002, *26*, 189–228.

2. Kofstad (1988) Kofstad P, High temperature corrosion, Elsevier Applied Science Publishers Ltd, Barking (UK), 1988.

3. Majzlan *et al.* (2005) Majzlan J, Botez C, Stephen PW. The crystal structures of synthetics $Fe_2(SO_4)_3 \cdot 5H_2O$ and the type specimen of lausenite. Am Mineral, 2005, *90*, 411-6.

4. Földvári (2011) Földvári M. Handbook of thermogravimetric system of minerals and its use in geological practice. Occasional Papers of the Geological Institute of Hungary, Volume 213, ISBN 978-963-671-288-4, Budapest, 2011.

5. Ackermann *et al*. (2009) Ackerman S, Lazic J, Armbruster T, Doyle S, Grevel K-D, Majzlan J. Thermodynamic and crystallographic properties of kornelite [$Fe_2(SO_4)_3 \cdot \sim 7.75H_2O$] and paracoquimbite [$Fe_2(SO_4)_3 \cdot 9H_2O$]. Am Mineral, 2009, *94*, 1620-8.

6. Cornell *et al*. (2007) Cornell RM, Giovanoli R, Schneider W. Review of hydrolysis of iron(III) and the crystallization of amorphous iron(III) hydroxide hydrate. J Chem Tech Biotechnol, 1989, *46*, 115-134.

7. Jerz and Rimstidt (2003) Jerz JK, Rimstidt JD. Efflorescent iron sulfate minerals: paragenesis, relative stability, and environmental impact. Am Mineral, 2003, *88*, 1919-1932.

8. Baron and Palmer (1996) Baron D, Palmer DC, Solubility of jarosite at 4 – 35°C. Geochim Cosmochim Ac, 1996, *60*, 185-95.

9. Bigham *et al*. (1994) Bigham JM, Carlson L, Murad E. Schwertmannite, a new iron oxyhydroxysulphate from Pyhasalmi, Finland, and other localities. Mineral Mag, 1994, *58*, 641-648.

10. Bigham *et al*. (1996) Bigham JM, Schwertmann U, Traina SJ, Winland RL, Wolf M. Schwertmannite and the chemical modelling of iron in acid sulfate waters. Geochim Cosmochim Ac, 1996, 60, 2111 – 2121.

Power & process:
In-service performance

Waterwall damage by fast internal oxidation of boiler tubes

Anu Lokkiluoto[1], Juha Viuhko[1], Pertti Auerkari[2] & Sanni Yli-Olli[2]

[1]Helen Oy
Helsinki, Finland

[2]VTT Technical Research Centre of Finland Ltd
Espoo, Finland

Abstract

Recurring waterwall leaks have been observed in a coal-fired boiler where subsequent inspections have shown through-wall internal oxidation, mostly at butt welds of 16Mo3 boiler tubes. In several cases the oxide had retained a thick pit plug even after local penetration of the tube wall. The original initiation site is no longer visible as it was removed by oxidation, but away from the most severe damage the internal oxidation appears to have initiated immediately downstream after a protruding weld root. This location, estimated oxidation rate and oxide appearance suggest that the mechanism is related to locally intensive heating in addition to flow turbulence. In the damage history of the same boiler wall, the first comparable leaks were recorded at shop welds with strongly protruding root shape, presumably inducing particularly strongly turbulent flow, and even then only after long term service. The most recent failures, however, occurred at normal repair welds or even within parent material, and after much shorter time in service. The characteristic features and causative factors of the tube failures are discussed in the paper, based on the available evidence and experience from operation and maintenance.

1. Introduction

Waterwalls of conventional coal-fired boilers are mostly made of carbon or low-alloy molybdenum steels, for reasons of low cost and ease of fabrication such as avoiding any heat treatments of large welded membrane wall panels. To some extent this is a compromise in terms of corrosion and oxidation resistance, both for external surfaces on flue gas side and for internal surfaces touched by water. When these steels are not sufficiently resistant to corrosion, for example in some biomass fired or waste incineration boilers, the boiler tubes that need additional protection are normally modified from the flue gas side only, for example by ceramic tiles or metallic high-alloy overlay coating. This is because the environmental attack, when it emerges, is usually more severe on the flue gas side that has much higher temperatures and temperature gradients than the water side, and may include aggressive chemical components in the flue gas and deposits. If water side damage such as corrosion does emerge, it is mostly due to some deviation in the water chemistry.

However, there is an exception: even without any deviation from the normally acceptable water chemistry, the internal surfaces can be attacked if the thermal and flow conditions are sufficiently severe to dissolve the normally protective oxide films on susceptible steels due to the flow-induced increase in the mass transfer at high-flow or highly turbulent locations. With suitable kinetic conditions the oxide front

remains reactive and able to grow even after reaching considerable overall thickness. Sometimes called erosion-corrosion, such fast oxidation is usually recognized by the name flow-accelerated corrosion (FAC). This mechanism typically attacks carbon steel or comparable grades of carbon-manganese and low alloy molybdenum steels in fast flow of high temperature water or mixed water and steam. The phenomenon can be divided into the coupled processes of the initiating electrochemical (corrosion) process and to physical flow dynamics to accelerate metal loss [1-3].

The solubility for the dissolution of magnetite is limited by the thermodynamics of the equilibrium reactions, but a strong adjacent flow will push the system away from equilibrium in two ways shown in Figure 1.

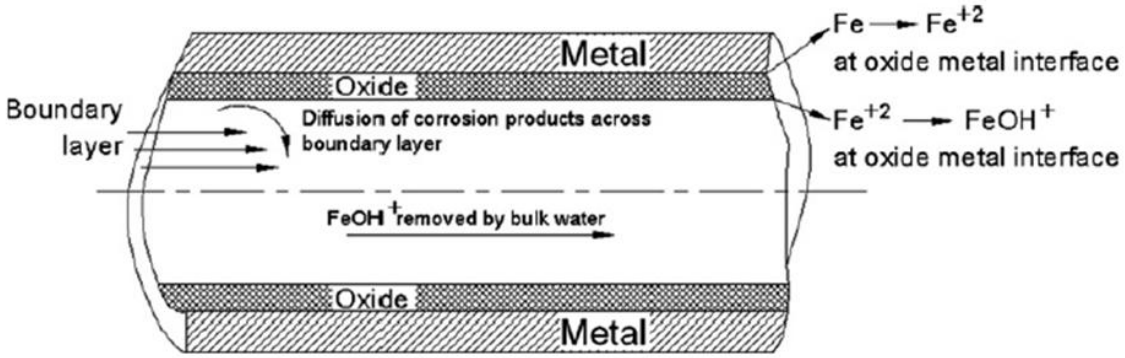

Figure 1. Schematic presentation of flow-accelerated corrosion (oxidation) of steel [4].

The rate of the resulting corrosion is controlled by the rate of diffusion of iron species through the boundary layer into the bulk water. This diffusion depends directly on the concentration of soluble iron species at the oxide surface and inversely on the thickness of the boundary layer. Therefore, a decrease in the boundary layer thickness due to increased water flow rate or local turbulence causes an increase of the corrosion rate. More generally, local hydrodynamics is also affected by surface roughness, geometry of the flow path, fluid shear stresses at the wall, turbulence intensity, and the void fraction of two-phase flow at the wall. Stability of magnetite depends on temperature, pH, dissolved oxygen, oxidizing-reducing potential, iron concentration and impurities in the water [1,5,6].

The cases described below represent somewhat unusual waterwall leaks by internal or water side oxidation. In the boiler concerned, historically such leaks have been occasionally recorded at shop flash welds, even then only after long term service. More recently, tube leaks have become more frequent and appearing also in other welds, and most recently, even in locations outside welds.

The boiler and its similar sister boiler were originally designed for oil firing, but due to the 1970's oil crisis they were retrofitted to burn bituminous coal. Combining heat and power generation, the plant is essential for district heating in the city of Helsinki. More recently, coal has been partly replaced by wood pellets that naturally affect the firing characteristics.

The observed features and causative factors of the tube failures are discussed below, based on the available evidence and experience from operation and maintenance.

2. Cases of leaks from internal oxidation

The earliest waterwall leaks of interest here were similar to one that occurred in January 2013 after about 230 000 service hours, in a membrane wall made of steel 16Mo3, at a location immediately trailing a strongly protruding root of a shop weld (Figure 2). The remaining oxide near the leak position was thick and showed a mixed microstructure behind the metal-oxide interface (Figure 3). Outside the welds the internal oxide showed some growth but the tube microstructure little signs of thermal exposure (Figure 4).

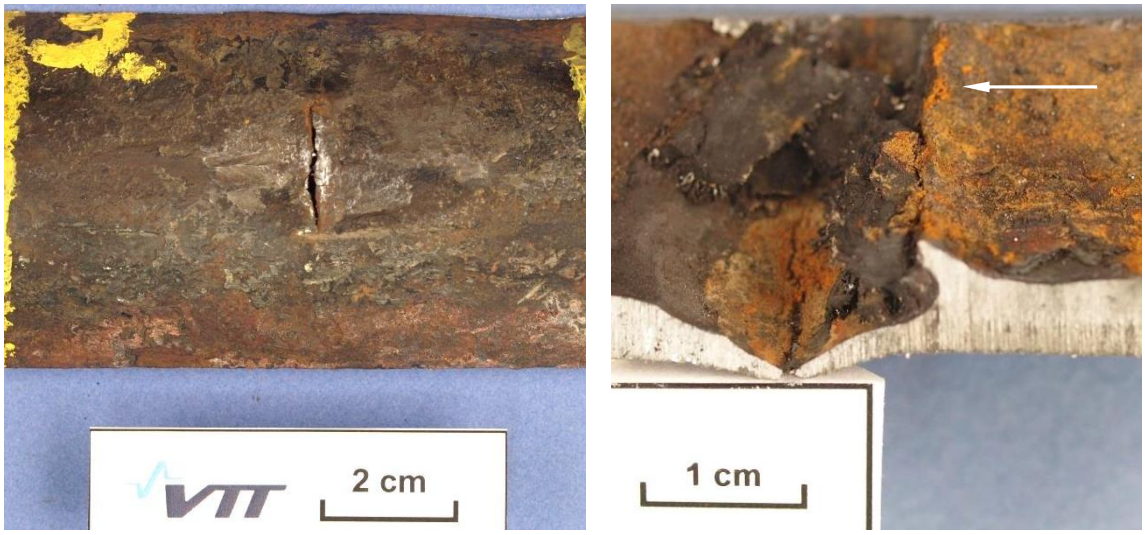

Figure 2. Failure location in 2013 at a protruding root of a shop weld: outside (left) and internal/cross-section appearance (right); white arrow shows flow direction.

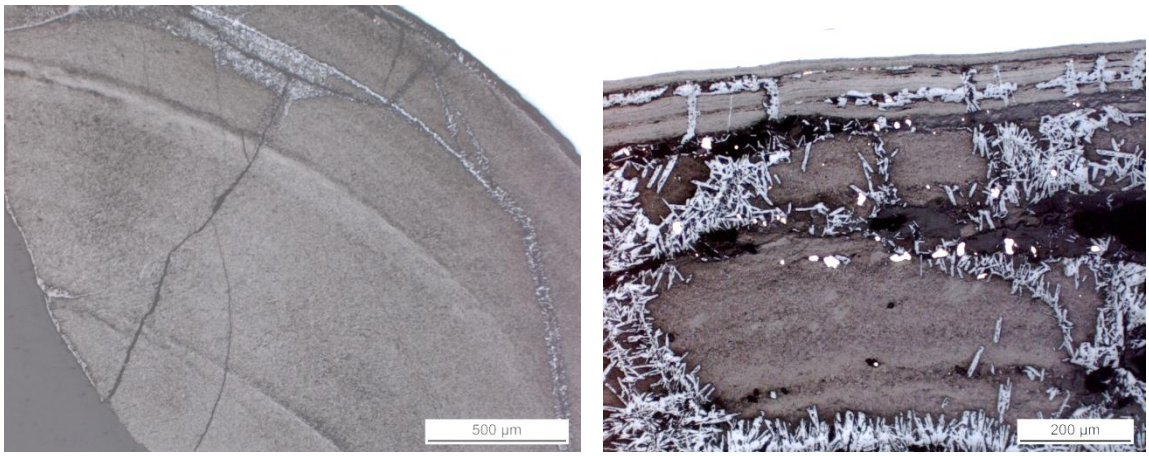

Figure 3. Oxide in the 2013 leak: location close to failure (left) and at an unfailed tube weld (right).

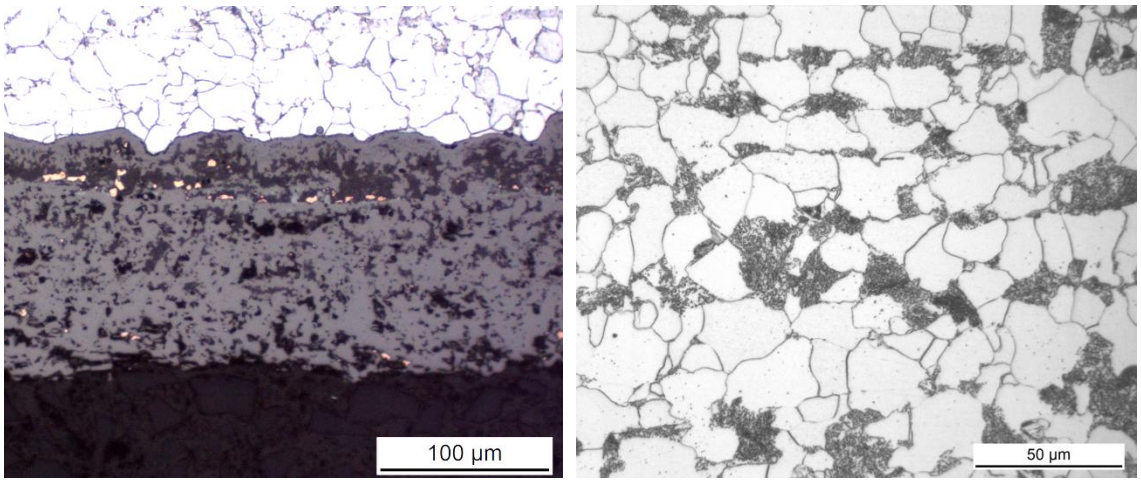

Figure 4. Internal oxide (left) and tube microstructure (right, 16Mo3) outside the failed area in 2013.

After the incident several tubes were replaced in an area where the tubes were showing clear wall thinning. In the fall 2015 a new leak (Figure 5) was observed in a repair weld of a waterwall tube that had been replaced in 2013. Also local thinning at welds was observed in two similar tubes in the vicinity of the failure. The sites of leakage and local wall thinning were located at the trailing sides of the weld roots, and again a thick oxide layer was observed at the failure location (Figure 6). Next to the metal-oxide interface the oxide shows a smooth microstructure with very variable thickness and narrow crack-like paths to the oxidation front, and a coarser more porous oxide structure behind this front (Figure 7). The internal oxide outside the leak region was similar but thicker than that in 2013, and the metal microstructure was similar to that in Figure 4 (right side).

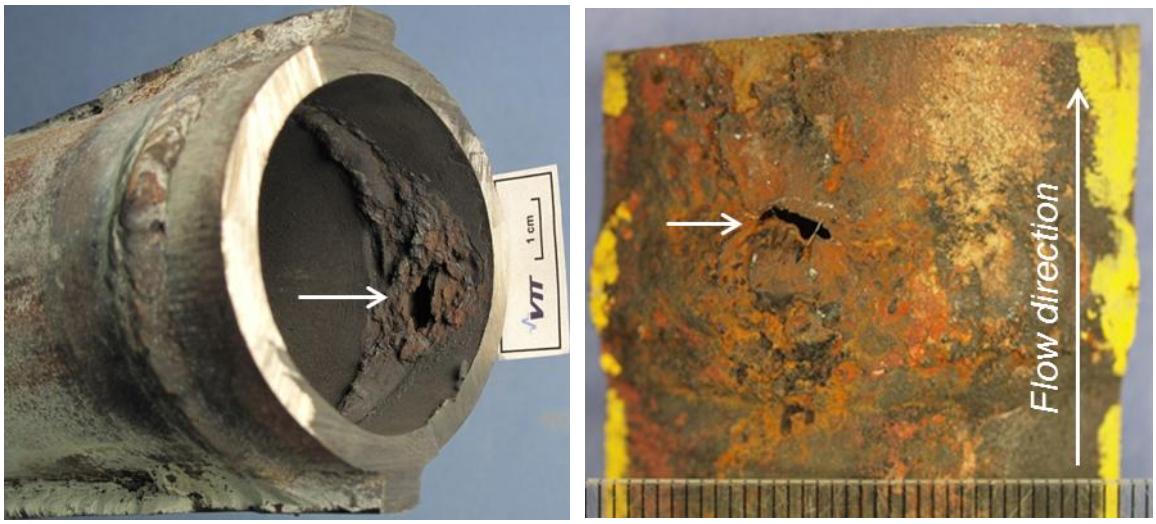

Figure 5. Location of the leak at a repair weld in 2015: internal (left) and external (right) appearance.

In spring 2016 yet again a leak occurred in the same waterwall, similar in structure as previously but this time in parent metal, about half a metre away from the nearest upstream weld (Figures 8 to 10). Note that while also in this case the weld root side suffered deep oxidation, it just did not show the first leak.

In all three cases the cross-sections at the failure locations showed a similar thick oxide at an internal corrosion pit (Figure 11). There was little evidence for any significant deviations in the water chemistry (Figure 12).

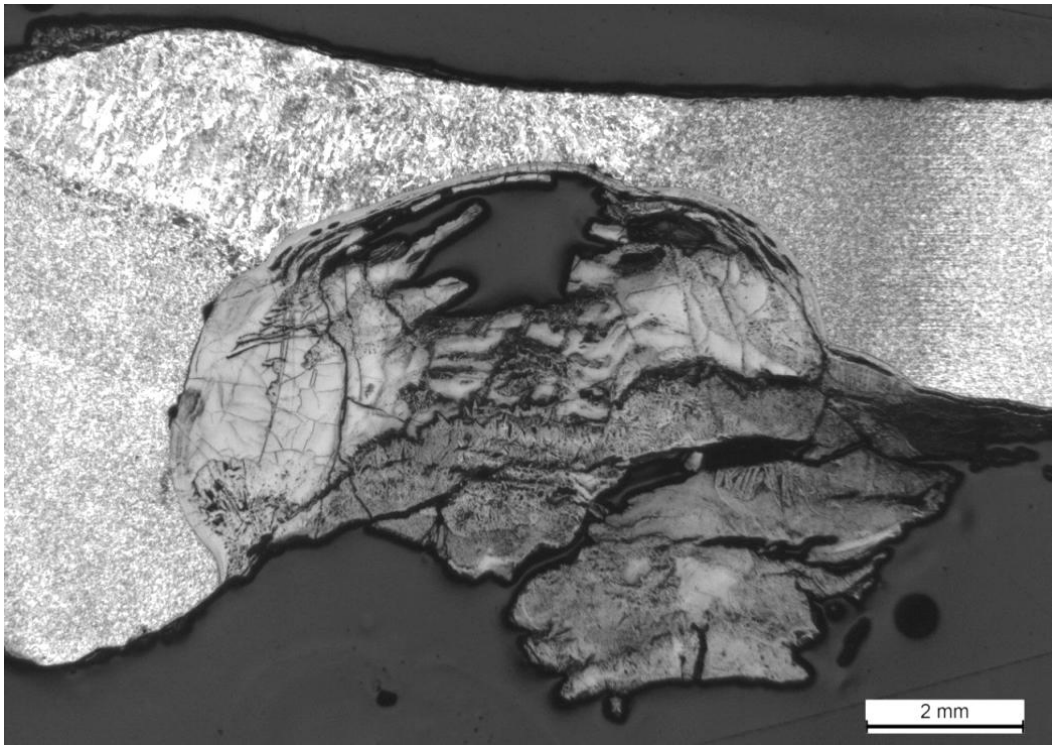

Figure 6. Oxide at a weld root next to the tube leak in 2015 (flow direction to right, etched).

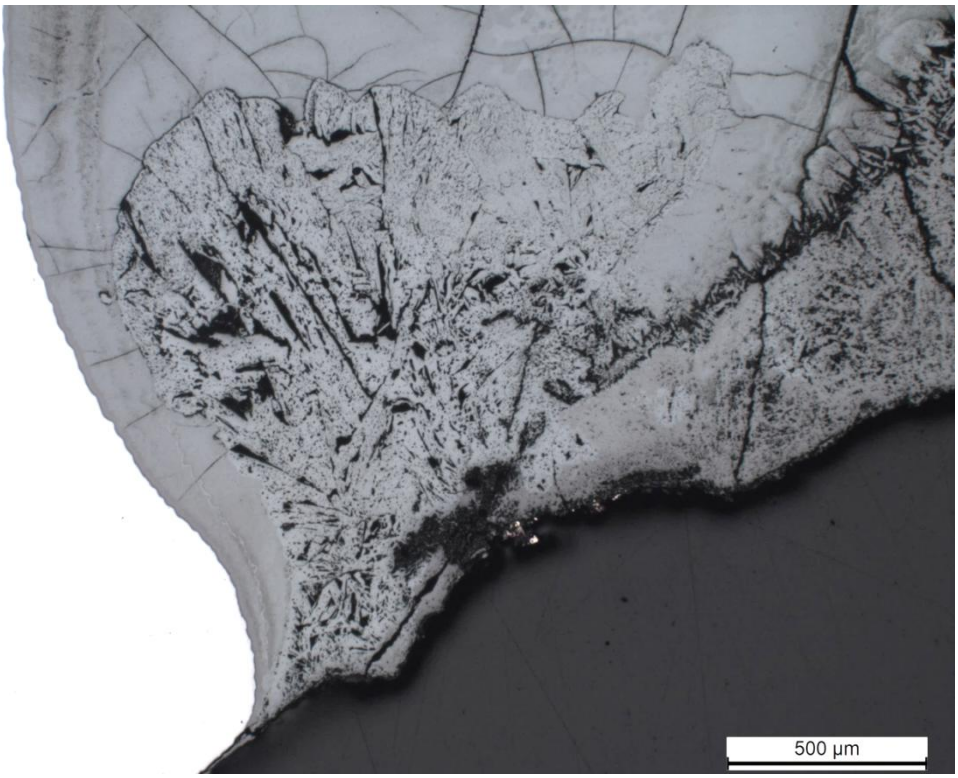

Figure 7. A detail from the bottom left side of Figure 6 (unetched).

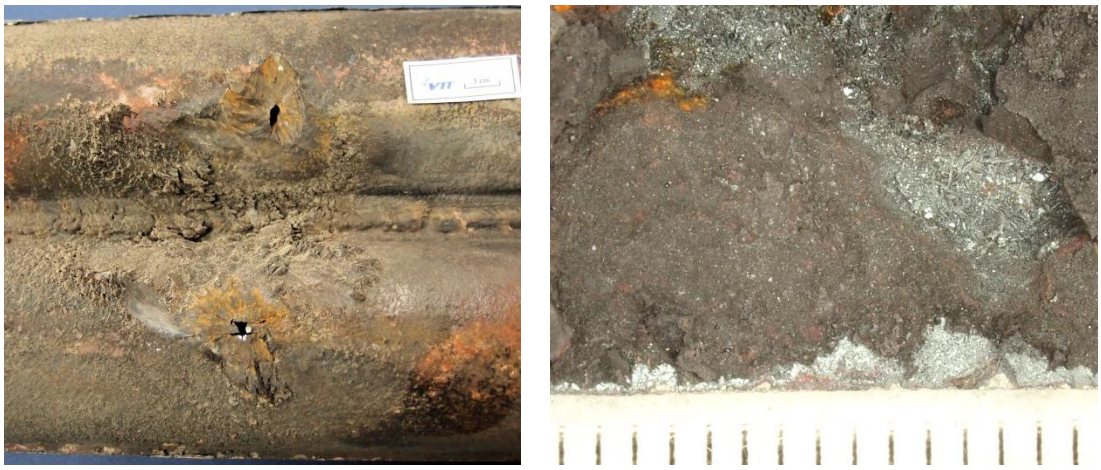

Figure 8. Parent metal leak in 2016 (left, lower tube), with shining black oxide on internal surface (right).

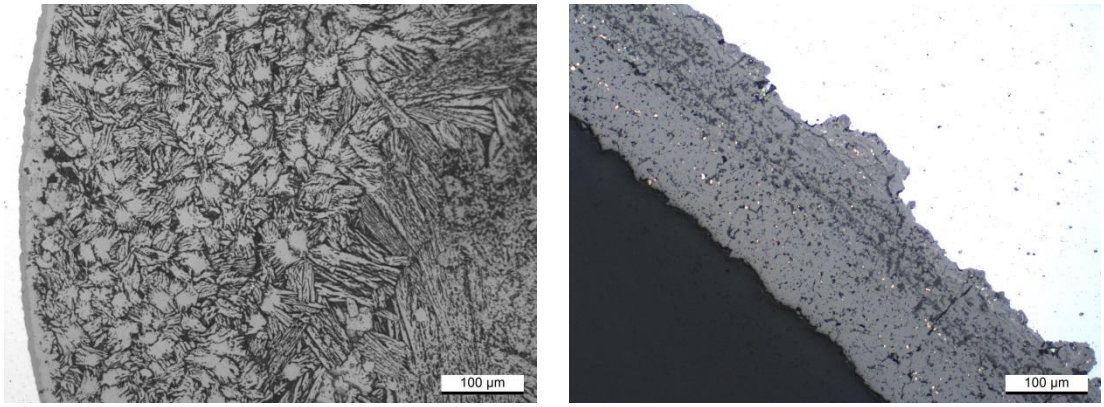

Figure 9. Oxide cross-section close to leak in 2016 (left) and outside the failure area (right).

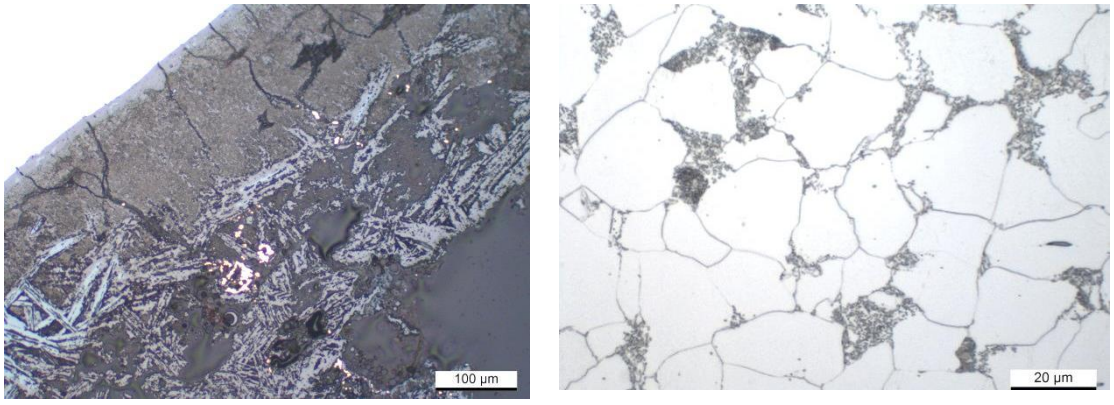

Figure 10. Oxide section close to leak in 2016 (left) and microstructure outside the failure area (right).

a)

b)

c)

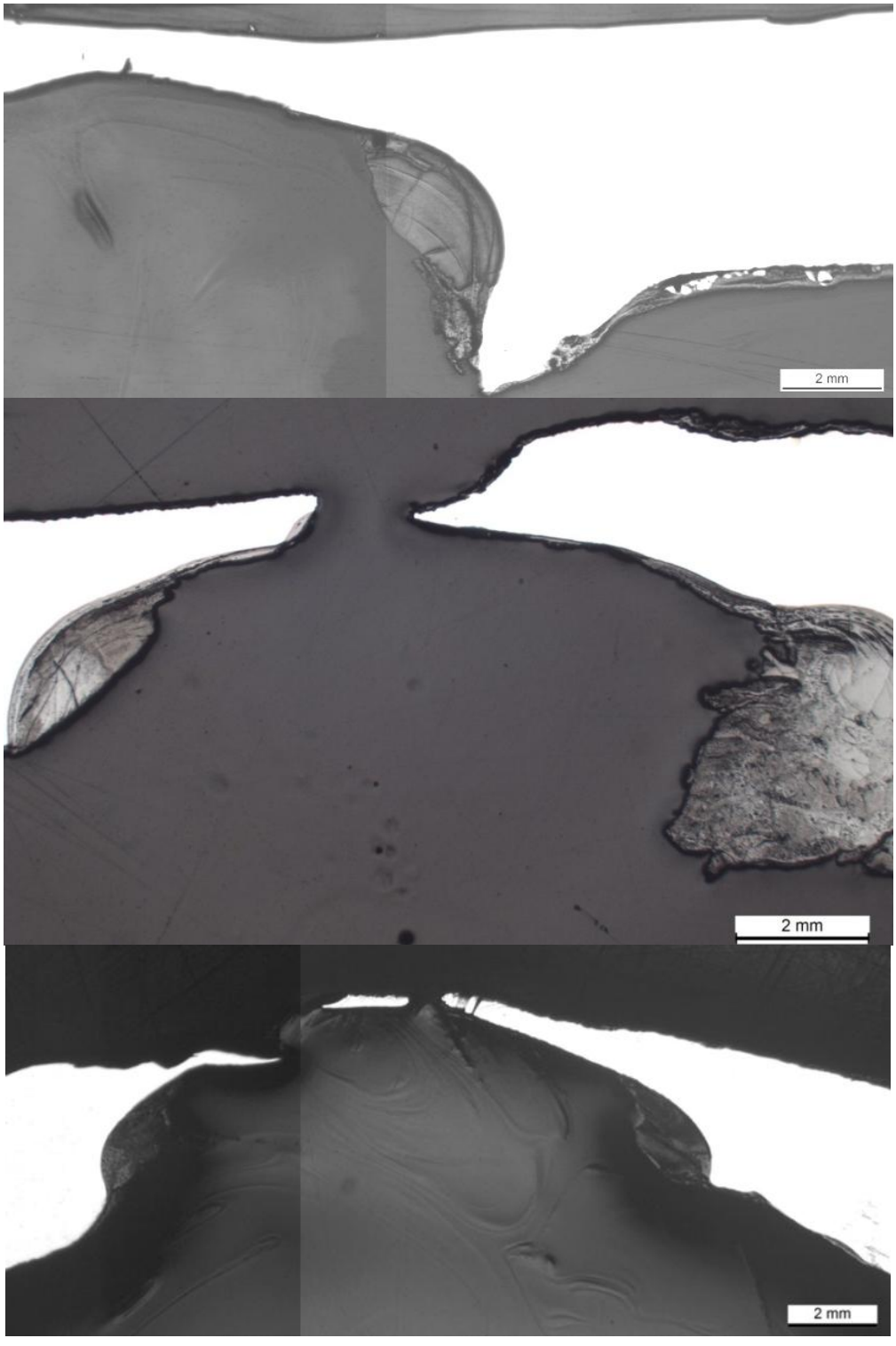

Figure 11. Unetched cross-sections from the leak locations in a) 2013, b) 2015 and c) 2016.

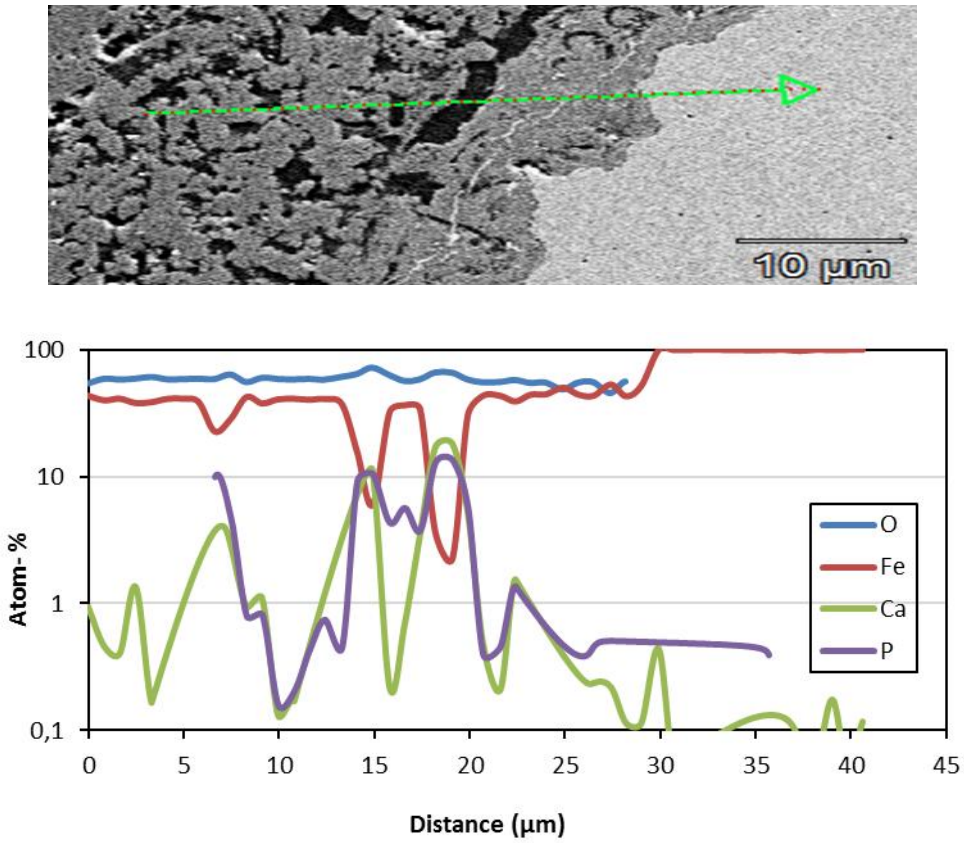

Figure 12. EDX linescan from the internal oxide to the tube (2016 leak).

The boiler is planned to be operated until 2024. Because of required high availability and high total cost of unplanned wintertime shutdowns, even major repairs of the waterwall may be justified.

3. Conclusions

Recurring 16Mo3 tube leaks (Figure 13) have been observed in the same waterwall, initially mostly at the side of protruding roots of circumferential welds, but in the latest case also in parent metal about 500 mm from the nearest weld. By the time of leakage, the oxide has formed a deep pit up to a few centimetres wide, filled by the oxide until local penetration resulted in a blowout at the pit centre. Also outside such pits a relatively thick internal oxide (up to about 100-300 µm) was observed, suggesting higher than usual wall temperatures during service. The metal-oxide interface showed on average a thin smooth layer and next to it a thicker, coarser and more porous layer that appeared partially crystallised.

The thermal and chemical environment on the flue gas side was not challenging enough to cause most significant wall thinning from this side. Instead, sufficiently high surface temperature, turbulent flow conditions at weld root and elsewhere to sustain adverse surface conditions, and tube material of modest oxidation resistance led to rapid internal oxidation on the hot side of the tube. The thickest oxides show both surface appearance and cross-sectional structures similar to flow-accelerated corrosion (FAC), which has been mostly reported from unfired piping at somewhat lower temperatures (closer to 150-250°C).

To avoid or reduce fast oxidation rates, there are at least following options:

- temperature reduction at hot spots by e.g. firing control, thermal shields and/or removal of the existing thick internal oxides,
- change of waterwall material to a more resistant variety such as 13CrMo4-5;
- possible benefit could be obtained through a modified water chemistry.

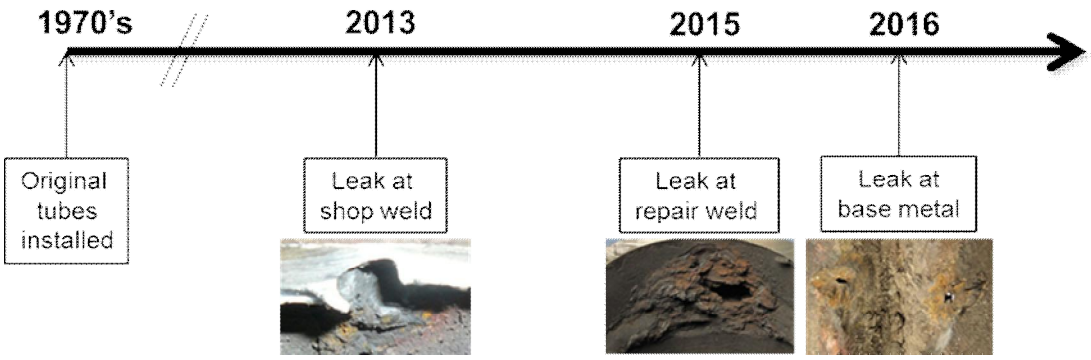

Figure 13. Summary of the history of the observed waterwall leaks.

References

1. H.-P. Seifert, J. Hickling, D. Lister, Corrosion and environmentally-assisted cracking of carbon and low-alloy steels. Comprehensive Nuclear Materials 5, 2012, 105-142.

2. S. Uchida, M. Naitoh, H. Okada, Y. Uehara, S., Koshizuka, Evaluation of flow accelerated corrosion by coupled analysis of corrosion and flow dynamics. Relationship of oxide film thickness, hematite/magnetite ratio, ECP and wall thinning rate. Nuclear Engineering and Design, 241, 2011, 4585-4593.

3. J.H. Moon, H.H. Chung, K.W. Sung, U.W. Sung, U.C. Kim, J.S. Rho, Dependency of single-phase FAC of carbon and low-alloy steels for NPP system piping on pH, orifice distance and material. Nuclear Engineering and Technology 37, 2005, 375-384.

4. V. Kain, S. Roychowdhury, P. Ahmedabadi, D.K. Barua, Flow-accelerated corrosion: experience from examination of components from nuclear power plants. Engineering Failure Analysis 18, 2011, 2028-2041.

5. R.B. Dooley, V.K. Chexal, Flow-accelerated corrosion of pressure vessels in fossil plants. International Journal of Pressure Vessels and Piping 77, 2000, 85-90.

6. K. Fujiwara, M. Domae, K. Yoneda, F. Inada, Model of physic-chemical effect on flow accelerated corrosion in power plant. Corrosion Science 53, 2011, 3526-3533.

Influence of thermal aging on material strength and fracture behaviour in Grade 91 Steel

Hyeong-Yeon Lee[1], Woo-Gon Kim[1]

[1]Korea Atomic Energy Research Institute
Deaduk-Daero 989-111, Yuseong-gu, Republic of Korea

Abstract

The influence of thermal aging on yield strength, tensile strength, ductility and J-Resistance behaviour for Mod.9Cr-1Mo (ASME Grade 91) steel has been investigated. Service exposed Gr.91 steel materials sampled from a reheat steam piping system in an ultra-supercritical (USC) plant under operating condition of 569°C, 46.7 bar at rated power in Korea with accumulated operation time of 73,716 hours were used for the present investigations. The test results of the service exposed material were compared with those of the virgin Gr.91 steel. In addition, those test data were compared with the material properties in the design codes, ASME Section III Subsection NH and RCC-MRx code that are being used for elevated temperature design of generation IV nuclear energy systems.

1. Introduction

Mod.9Cr-1Mo (ASME Grade 91, hereafter 'Gr.91') steel has low thermal expansion, high thermal conductivity and high strength. Due to these characteristics, Gr.91 steel is widely selected as one of the promising candidate materials in generation IV (hereafter 'Gen IV') reactor systems among the heat resistant materials. Gr.91 steel is a material for heat exchangers including steam generator and piping systems in a Generation IV sodium-cooled fast reactor (SFR)[1]. However, Gr.91 steel has been reported to be degraded by thermal aging more steeply than expected in design codes in terms of the material strengths and toughness [2]. It is also known that Gr.91 steel is affected by thermal aging more severely than austenitic stainless steel when it is exposed long time at high temperature in power plants [2].

Current elevated temperature design (ETD) codes such as ASME Section III Subsection NH[3] (hereafter 'ASME-NH') and RCC-MRx[4] do not take thermal aging into account yet as much as they are required [2]. ASME-NH provides some guidelines on thermal aging effect in limited cases and the effect of thermal aging has been taken into account in yield strength (YS) and tensile strength (TS) with the introduction of strength reduction factors but it provides the reduction factors only in TS for Gr.91 steel. In case of RCC-MRx [4,5], influence of thermal aging is taken into account only for austenitic stainless steel. In addition, effect of thermal aging for J-resistance curve is available only for austenitic stainless steel and no property is available yet for Gr.91 steel [6].

The effect of thermal aging on material strength, ductility and J-R behaviour for Gr.91 steel has been investigated in this study based on a series of material tests with virgin and service exposed Gr.91 steel specimens. Service exposed Gr.91 steel specimens were sampled from a piping system of an ultra-supercritical(USC) plant with 73,716 hours service were used for material testing. The test results were

compared with those of the virgin materials and those data were compared with those of the ASME-NH and RCC-MRx.

2. Material strength behaviour of Gr.91 steel with and without thermal aging

Gr.91 steel is a ferritic-martensitic steel and has excellent thermal properties of low thermal expansion and high conductivity while having high material strengths compared to other heat resistant materials listed in elevated temperature design (ETD) code of ASME-NH[3] as shown in Fig. 1. Gr.91 steel is a ferritic-martensitic heat resistant steel and one of the two main materials with austenitic 316SS to be used in an intermediate heat exchanger(IHX), decay heat exchanger(DHX), secondary piping and steam generator(SG) in Korean Gen IV SFR[8].

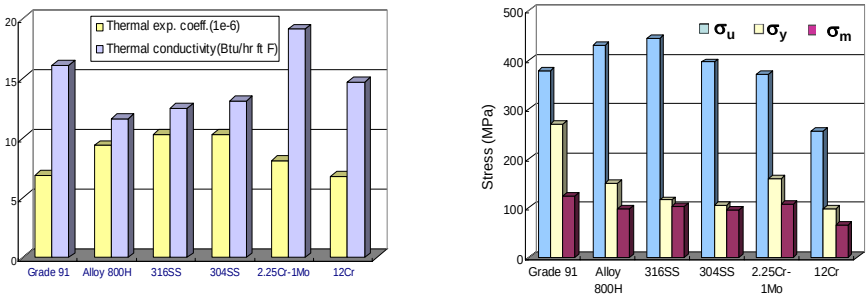

(a) thermal properties (b) mechanical properties

Figure 1. Comparison of material properties for Gr.91 steel in design code [3]

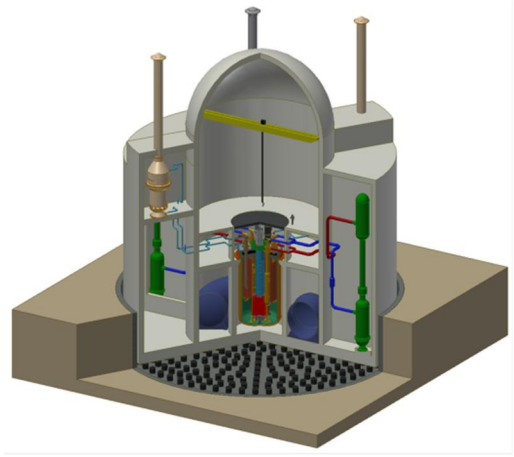

Figure 2. Schematic of Prototype Generation IV Sodium-cooled Fast Reactor (PGSFR).

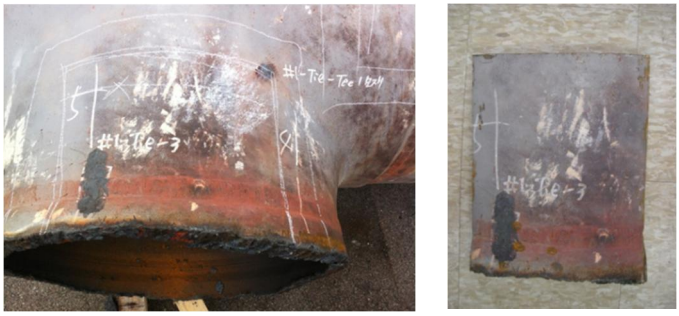

Figure 3. Gr.91 steel Tee part sampled from reheat steam piping after 73,716 h service in a USC plant

The fitting part of Gr.91 steel Tee shown in Fig. 3 has been sampled from reheat steam piping in a Korean USC plant to investigate the effects of thermal aging.

The operating conditions of the reheat steam piping are shown in Table 1. The sampled Tee part with outer diameter of 711.2mm and thickness of 25.4mm was subjected to the high temperature of 569°C and high pressure of 46.7 bar as operating condition for 73,716 hours.

Table 1. Tee fitting specification, operating and design condition of reheat steam piping system.

	Pipe Dimension		Design Condition		Operating Condition	
material	OD (mm)	thickness (mm)	T (°C)	P (bar)	T (°C)	P (bar)
A335-P91	711.2	25.4	574	54	569	46.7

The chemical compositions(wt.%) of the Tee fitting (forged Gr.91 : F91) in ASME Section II Part A, virgin Gr.91 and service exposed Gr.91 steel are shown in Table 2. As a whole, the chemical compositions of virgin Gr.91 steel were within the band or limit of ASME II-A[9]. Chemical compositions of the service exposed Gr.91 steel were analysed with EDS(Energy Dispersive X-Ray Spectroscopy). The analysis results showed that the chemical elements of Mn, Cr, Mo and V of service exposed Gr.91 steel were increased during the service duration of 73,716 hours.

Table 2. Chemical compositions of Gr.91 steel in design code, before and after service at USC plant.

	ID symbol (Type)	C	Mn	P	S	Si	Ni	Cr	Mo	V	Others
ASME II-A (Gr.91)	F91 (Fitting)	0.08 - 0.12	0.3 - 0.6	0.025 max	0.025 max	0.2 - 0.5	0.4 max	8.0 - 9.5	0.85 - 1.05	0.18 - 0.25	Cb 0.03-0.07 Al 0.02 Ti 0.01 Zr 0.01
Virgin Gr.91 (Mill sheet)	F91 (Fitting)	0.08	0.38	0.018	0.003	0.34	0.29	8.75	0.875	0.24	
Aged Gr.91 (73,716h service)	F91 (Fitting)	0.08	*0.52*	0.018	0.003	0.34	0.29	*9.28*	*2.43*	*0.32*	

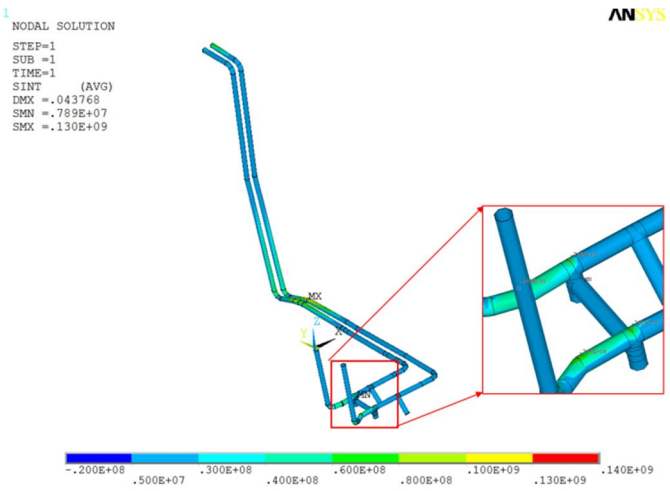

Figure 4. Stress distribution of a reheat steam piping in a USC plant

Yield strengths of Gr.91 steel in ETD codes were compared with those of the KAERI test results with virgin and service exposed (73,716 hours) material specimens as shown in Fig. 3. It should be noted that YS of virgin Gr.91 steel has dropped as much as maximum 35.8% after 73,716h (8.4 years) service at the

operating condition of 569°C and 46.7 bar. It shows that the yield strengths ('KAERI_P91 73,716h service' in Fig. 5) dropped partly below the code properties [3,5,7] at some temperatures as shown in Fig 5. Therefore, it is clear from Fig. 5 that YS of thermally aged material should drop far below the code material properties as the plant operation time is accumulated further, say up-to 60 years which is the target design lifetime of Gen IV reactor systems.

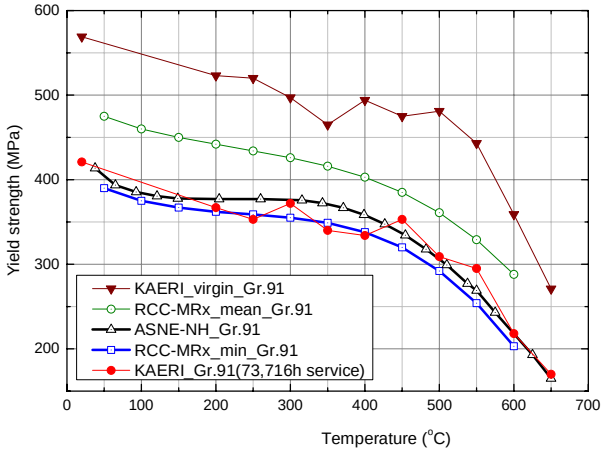

Figure 5. Comparison of yield strength in design codes and test results for virgin and service exposed Gr.91 steel

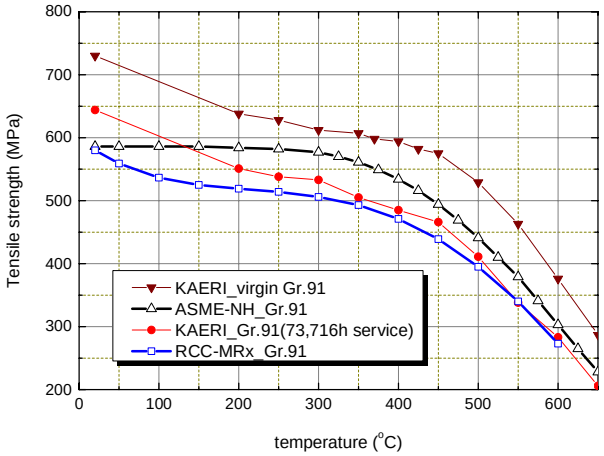

Figure 6. Comparison of tensile strength in design codes and test results for virgin and service exposed Gr.91 steel

Comparisons in yield strengths were made between service exposed Gr.91 specimens and virgin Gr.91 specimens [2]. It was shown that YS dropped maximum 31.1% at room temperature, and 30.4% at 550°C as shown in Fig. 5, which means that strengths of the Gr.91 steel has dropped more rapidly than those of the design codes.

In addition, it is worth noting that serration flow was observed at the temperature range of 350°C to 450°C in the test data for Gr.91 steel in Fig. 5 which is linked to dynamic strain aging (DSA) [10].

In case of tensile strength, degradation trends in terms of material strengths were found to be similar to those of YS as shown in Fig. 6. TS of service exposed Gr.91 steel was shown to drop significantly from that of the virgin Gr.91 steel. TS of service exposed Gr.91 steel dropped below the TS values of ASME code over the temperatures higher than 200°C while they approached to TS of RCC-MRx as the temperature is increased and TS value (338MPa) at 550°C dropped below RCC-MRx value (340MPa). TS has dropped maximum 27% at 550°C. Therefore, similar to the case of YS, it is expected that TS after around 10-year service could drop below the code properties of ASME-NH and RCC-MRx especially over

the operating temperature range at creep regime, which means that the TS properties of the codes might severely overestimate the TS properties.

The above findings of thermal aging effects on YS and TS raise important issues of possibility of overestimation in material strengths under long-time service. ETD codes should address those issues because YS and TS properties in the design codes could overestimate those material properties in non-conservative way. Figs. 5 and 6 show the comparisons for the long-time service of 8.4 years from which the strengths (YS, TS) of Gr.91 steel in actual power plant are expected to drop below code properties even after only 10-year service. This means that although the design lifetimes of the Gr.91 piping systems or components are targeted 60 years, the actual material strengths of Gr.91 material might drop below the design code properties as early as 10-year operation from initial start-up of the power plants.

ASME-NH takes long-time service effects into account through introduction of 'Reduction Factor'. In case of Gr.91 steel, the reduction factor for YS is specified as 1.0 regardless of the temperature which means no reduction in YS needs to be considered while reduction factors for TS are given depending on the temperature and service time as shown in Table 3. In case of wall temperature 575°C, reduction factors become less than 1.0 for the service time longer than 10,000 hours. Fig. 7 shows the location of TS of Gr.91 steel before and after service at 575°C when they are compared with code properties. It was shown that TS value (419.5 MPa) of virgin material was far higher than code properties but TS value (310.5 MPa) of service exposed material was located in-between ASME-NH and RCC-MRx values as shown in Fig. 7. Therefore, ASME TS property is non-conservatively higher than test result. This is the result after 8.4 year service in USC plant, which means that the test result of TS should drop below the RCC-MRx and possibly under ASME-NH values with reduction factors under long-time service because the decreasing rate of TS from test results is steeper than the rate of reduction factors. Consequently the code properties on TS in ETD codes were shown to be non-conservative in case Gr.91 steel is subjected to long-time service.

Table 3. Tensile strength reduction factors of Gr.91 steel due to long-time service [3]

time(h) Temp(°C)	1	3×10^3	10^4	3×10^4	10^5	3×10^5
550°C	1	1	1	0.94	0.92	0.89
575°C	1	1	0.95	0.92	0.88	0.83
600°C	1	0.96	0.92	0.89	0.85	0.84

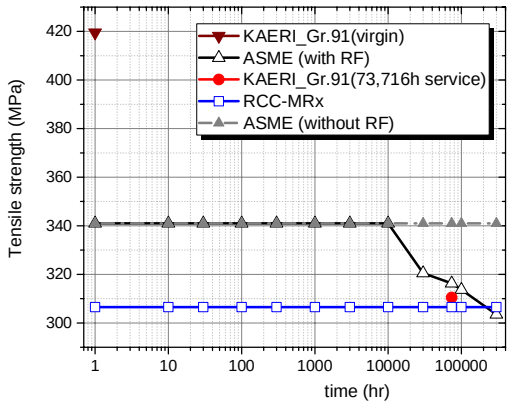

Figure 7. Comparison of tensile strengths with and without strength reduction factors.

The elongation behaviour of the Gr.91 steel before and after thermal aging was also investigated as well because strength, ductility and toughness are important factors in integrity of high-temperature components. As part of investigation of fracture toughness for Gr.91 steel, J-R fracture curves were obtained from material tests and their behaviours were described in next section of this paper.

When comparing the elongations of the Gr.91 steel before and after 73,716 h service, it is shown that the elongation increased as much as maximum 23% while material strength becomes degraded due to long-time service. The other thing of importance is that ductility becomes minimum over the temperature range of 300°C to 450°C as shown in Table 4 that is the range of serration flow in Fig. 5, which means that ductility minimum at the temperature range of serrated flow is one of the typical phenomena of dynamic strain aging(DSA). Elongation properties are provided in RCC-MRx[5] only for austenitic stainless steel of 316L(N) and 316L but not for Gr.91 steel.

Table 4. Elongation of virgin and service exposed Gr.91 steel

Temp(°C) / material	20	200	250	300	350	400	450	500	550	600
Virgin Gr.91	24	18.6	17.8	18.4	18	18	18	22.4	26.4	28.3
Aged Gr.91 (73,716h service)	29.3	24.8	23	22.3	22.7	21.2	22.1	26.8	30.5	34.9

Therefore, it is certain from Fig. 5 that YS of thermally aged material should drop far below the code material properties as the plant operation time is accumulated further. In RCC-MRx thermally aged material coefficients are not available for the material strength data, but thermal aging is explicitly considered in J-R material properties for austenitic stainless steel. Depending on the hold time and wall temperature, thermal aging has been classified as 'moderate thermal aging' or 'advanced aging' as shown in Table 1.

The test results on strength reduction (YS and TS) of thermally aged materials from virgin materials were compared [7]. It was shown that the stress has been dropped maximum 31.1% at room temperature, and 30.4% at 550°C as shown in Fig. 5, which means that strengths of the Gr.91 steel has dropped more rapidly than the those of the design codes.

The elongation behaviour of the Gr.91 steel before and after thermal aging was also investigated as well. It was shown that ductility increased as much as maximum 23% while material strength becomes degraded due to thermal aging. The other thing of importance is that ductility becomes minimum over the temperature range of 300°C to 450°C which is the range of serration flow in Fig. 3. This means that ductility minimum at the temperature range of serrated flow is one of the typical phenomena of dynamic strain aging. Elongation properties are provided in RCC-MRx[5] but currently the properties are available only for austenitic stainless steel of 316L(N) and 316L stainless steel.

3. Fracture behaviour

Fracture properties for austenitic stainless steel are relatively well provided in RCC-MRx [5,6] compared to Gr.91 steel. J-R fracture curves are provided in A9[6] of RCC-MRx for austenitic stainless steel but no material curves are provided yet for Gr.91 steel as of 2012 edition[6]. In addition, the material properties of creep crack growth(CCG) rate and fatigue crack growth (FCG) rate for defect assessment are provided for both Gr.91 steel and austenitic stainless steel in Tome 6 [11] of RCC-MRx but some modifications in the material properties in RCC-MRx for Gr.91 crack growth assessment were shown to be necessary [12].

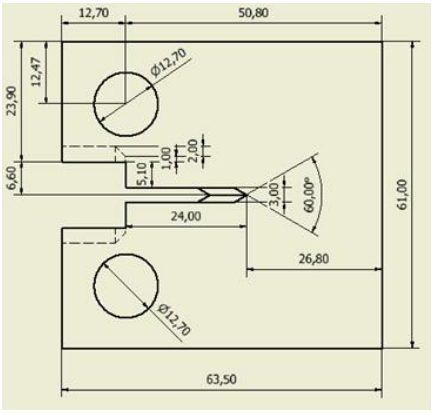

Figure 8. Schematic of Gr.91 steel standard Compact Tension specimen with 1 inch thickness.

Fracture behaviour of Gr.91 steel specimen before and after service has been investigated with the J-R fracture tests in this study. Fig. 9 and Fig. 10 show KAERI's test results on the J-R curve for virgin and service exposed Gr.91 steel, respectively. When comparing the two J-R curves between Fig. 9 of virgin Gr.91 steel and Fig. 10 of 73,716h service, it was shown that J-R curves after service have dropped as much as 47.3% for 425°C curve and 16% for 400°C curve from those of virgin Gr.91 steel which are significant reduction in fracture resistance over the period of 8.4 years.

It is worth noting that the range of temperatures where maximum drop due to thermal aging occurs is closely related to the dynamic strain aging temperature range when the strain rate of tension test and that of J-R test over the gage length is the same. The degree of thermal aging depending on temperature is classified as moderate thermal aging and advanced aging in J-R property and they are quantified as in Table 5 for austenitic stainless steel 316LN[6]. Two J-R curves, one is for moderate thermal aging and the other is advanced aging are provided for 316LN, but no J-R curves are provided for Gr.91 steel in A9.

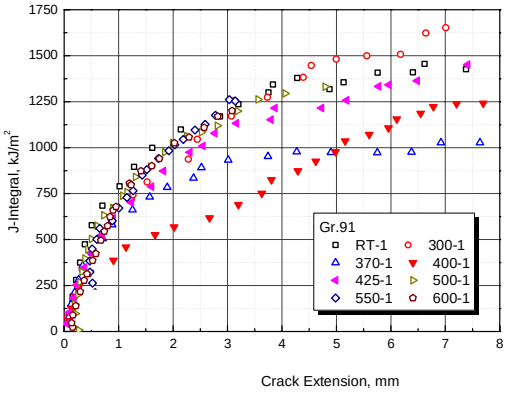

Figure 9. J-R curve of virgin Gr.91 steel.

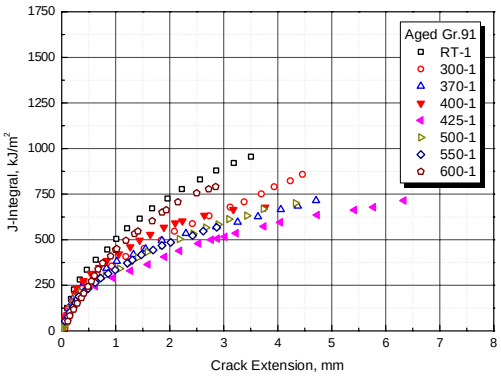

Figure 10. J-R curve of aged Gr.91 steel (73,716 h).

Table 5. Classification of thermal aging for austenitic stainless steel 316LN[6].

	500°C	525°C	550°C	600°C	650°C
Moderate thermal aging	175,000h	64,000h	25,000h	4,000h	950h
Advanced aging	-	280,000h	110,000h	19,000h	4,000h

4. Conclusion

The influence of thermal aging on the strength, ductility and fracture behaviour for Gr.91 steel has been investigated with a series of material tests on material strengths and J-R curves, and comparison with material properties in elevated temperature design codes. The test specimens were sampled not only from virgin Gr.91 steel but also from Gr.91 steel Tee part of reheat steam piping system with 73,716 in service in USC thermal plant under the operating conditions of 569°C and 46.7 bar.

It was shown that yield strength and tensile strength of service exposed Gr.91 steel have dropped maximum 35.8% and 27%, respectively from those of virgin Gr.91 steel due to long-time service for 73,716 h (8.4 yr) while ductility has been enhanced up to 23% when compared with those of the virgin Gr.91 steel specimens. ASME-NH takes thermal aging effect into account with reduction factors, but investigation with test results showed that the reduction factors were not appropriate providing non-conservative values on YS and TS under long-time service. In case of RCC-MRx, coefficients of thermal aging are not provided for Gr.91 steel yet. Considering the findings of the present study on the effect of thermal aging on material strengths, guidelines on taking thermal aging into account in design codes should be provided with concrete data and validation on the guidelines or material properties should be followed.

J-R test results for virgin and service exposed Gr.91 steel showed that J-R curves of service exposed specimens have dropped as much as 47.3% at 425°C and 16% at 400°C from those of virgin specimens. The range of temperatures where serrated flow observed in YS was the same as those where minimum ductility and minimum J-R curves were observed.

Due to long-term service, YS and J-R curve of service exposed Gr.91 steel have dropped significantly with maximum values of 35.8% and 51%, respectively from those of virgin Gr.91 steel while ductility has increased maximum 23%. Since the YS and TS provided in ASME and RCC-MRx were found to be non-conservative under long-time thermal aging environments, revision of those properties is judged to be necessary with a number of related test data.

Acknowledgements

This work was supported by the International Research & Development Program Foundation NRF grant (2013K1A3A7A03078195) funded by the Korea government (MSIP). Technical assistance from Mr. Suk-Woo Hong and Prof. Chang-Sung Seok of Sungkyunkwan University is gratefully acknowledged.

References

1. Status of innovative fast reactor designs and concepts, A Supplement to the IAEA Advanced Reactors Information System (ARIS). IAEA, Oct. 2013.

2. H.Y. Lee, W.G.Kim, S.K. Son, S.W. Hong, C.S. Seok, Effect of Thermal Aging on Material Strength and Fracture Behaviour in Mod.9Cr-1Mo Steel, KSME, 4 (2), 1-7, 2016 (Korean).

3. ASME Boiler and pressure vessel code Section III Subsection NH Rules for construction of nuclear facility component, 2015.

4. RCC-MRx, Section III Tome 1, Subsection NB, Class N1Rx Reactor Components, 2012 Edition Addendum, AFCEN, 2013.

5. RCC-MRx, Section III Tome 1, A3, 2012 Edition, AFCEN, 2013.

6. RCC-MRx, Section III Tome 1, Appendix A9, Property Groups for Welded Joints, 2012 Edition, AFCEN, 2012.

7. ASME Boiler and pressure vessel code Section II Part D, ASME, 2015.

8. Y.I. Kim, J.W. Jang, J.H. Lee, S.J. Kim, S.O. Kim, J.B. Kim, H.Y. Jung, Conceptual design report of SFR Demonstration Reactor of 600MWe capacity, KAERI/TR-4598/2012, 2012.

9. ASME Boiler and pressure vessel code Section II Part A, ASME, 2015.

10. Choudhary,B. K., Samuel, Isaac E., Sainath, G., Christopher, J, Mathew, M.D, Influence of Temperature and Strain Rate on Tensile Deformation and Fracture Behaviour of P92 Ferritic Steel, *Metallurgical and Materials Transactions A*, 44(11), 4979-4992, 2013.

11. RCC-MRx, Section III Tome 6, Probationary phase rules, 2012 Edition, AFCEN, 2012

12. Lee, H.Y., Kim, W.G., Kim, N.H., "Behaviour of Grade 91 material specimens with and without defect at elevated temperature," *Int. J. of Pres. Ves. & Piping*, Vol.125, pp.3-12, 2015.

Failure of a production moulding machine

Iain Le May & Elisabeth Le May

MCS Limited
Calgary, Alberta, Canada

Abstract

The case concerns the failure of a machine used to produce large plastic tanks by moulding, that failed in service. The failure took place after the machine had been re-sited and sold to a new owner. It may have amounted to potential fraud on the part of the former owners.

1. Introduction

When a failure occurs in a piece of equipment, it is usual to postulate the failure mechanisms or series of events, and then to see how the component or structure would perform under the postulated conditions.

At times, and indeed often, there may be a gap in our knowledge of past events, particularly with old equipment, and it may be necessary to postulate an event or series of events and then to see how they would fit into the picture including the consequences. Such a break in the known sequence of events amounts to an information horizon or knowledge horizon. It is commonly found with equipment for which records of inspection are poor or missing.

It is sometimes possible to go back (in time) by means of records or other information obtained from witnesses or reports. All too often, however, there is no (or incomplete) information available.

In some cases where repairs have been made it is possible to deduce the event sequence using a forensic approach. The methodology is similar to that used as would be used in an archaeological study or in the dating of fossils.

The use of the term “horizon” is because visually we are limited in distance vision by the earth’s curvature, which can overcome by raising our vision point or looking for indicators beyond the normal horizon, such as objects and indicators at greater distance rising above the normal horizon, such as a shop’s mast, a distant hill or other feature.

In the particular failure case discussed here, a production line had been established for the manufacture of large moulded plastic tanks, and the facility had been purchased from the former owner, who had used the installation for some time.

The new owner had problems with the moulding machines from an early stage, with failure of many components on them. The writer was contracted by the lawyers for the new owner to investigate the case.

A preliminary visit was made to determine the nature of the problem; subsequently the writer being contracted to determine the source of the problems site, when it had been shut down to investigate operating problems after failure of the main drive shaft at the left side in Fig. 1.

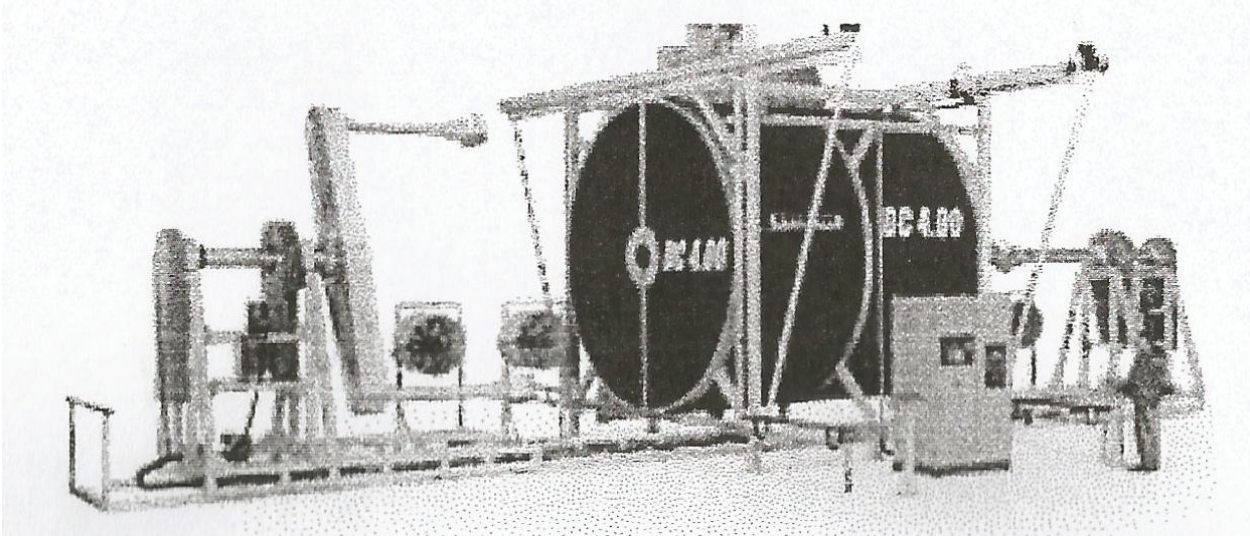

Figure 1. The moulding machine as shown in manufacturer's literature. The main drive shafts are at the extreme left and right ends of the installation. Two molds are employed, alternately being put within the centrally located heating furnace, each mold being carried by the two arms seen at the ends of the unit. Figure 2 shows the unit as installed, but after it had been partially shut down.

Thus, when the writer visited the site only one mold was in use because of operating problems as noted above.

Figure 2. Installation after failure and shut-down.

2. Operation

In operation, plastic in powder form is placed in a mould and the mould and contents are inserted into the heating.

The mould is rotated in two directions to spread the powder evenly while it melts, and is withdrawn from the furnace after the appropriate interval and allowed, to cool before the plastic container product is removed. While it is cooling the other mould has is inserted into the furnace from the other end, allowing an efficient production schedule, at least in theory.

The failure that took was fracture of the left-side drive shaft. Investigation disclosed that this was not the first time that this had failed, the damage having been "repaired" on the first occasion and information not supplied to the purchaser of the production equipment. In this later case the failure was catastrophic with repair not being possible on an economic basis.

The shaft that failed had been "repaired" after the earlier failure, the shaft sections having been welded together with a fillet weld, and the major part of the shaft's cross-section was occupied by the prior fracture surface. The improper "repair" is illustrated in Figures 3 and 4.

Although the prior failure and the "repair" had not been disclosed to the purchaser, he, as the owner in this case, was very well aware of the problem as disclosed by the later non-performance of the equipment after the present investigation was completed.

Action had been contemplated against the original designer and manufacturer of the equipment, but the evidence was that the shaft had been ready to fail because of improper repair, so that action was not taken.

After it was shut-down completely for repair, and to determine the cause of failure of the main drive shaft, it was clear that complete dismantling was required

Now, with the second failure analysed, it is obvious that responsibility falls heavily on the original owner and operator.

It is propriate now to review the history of the machine's operation.

The machine was designed and constructed overseas and had been in use for some time. It had subsequently been moved to a new site, and shortly thereafter it was sold to another company, which encountered problems in operating it successfully. It remained on the site that it had been moved to, nothing having been done to change the operating procedures at that time.

However the new owners found great difficulty in operating the machine successfully: there were vibration problems leading on many fractures on the unit and shortly thereafter the main input shaft on the left side failed.

When equipment fails it is normal practice to postulate some specific failure mechanisms or series of events and then to see how the component or structure would perform under the postulated conditions. If it would not fail under the postulated (severe) conditions it can be concluded as being unlikely to fail in normal service, at least in the near future.

At times, and indeed often, there may be a gap in our knowledge of past events, particularly with old equipment, and it may be necessary to postulate an event or series of events and then to see how they would fit into the picture, including the consequences. Such a break in the known sequence of events amounts to an information horizon or knowledge horizon. It is commonly found with equipment for which records of inspection are poor or missing.

It is sometimes possible to go back (in time) by means of records or other information obtained from witnesses or reports. All too often, however, there is no (or incomplete) information available.

All too often, however, there is no such (or incomplete) information available. However, when repairs have been made, it may be possible to deduce the event sequence using the forensic approach.

In this case failure was of the main drive shaft, without this information being transmitted to the purchaser of the installation. As this was not known to the new owner it was not immediately obvious what the cause was, as the machine was not a simple one.

Thus, much time was wasted by the owner in looking for a cause, including the design of the machine which had been built overseas, and its maintenance record was not disclosed. After all, from the record that the fact that the machine had apparently been used successfully, it was not immediately obvious what

the cause was, as the machine had been reported to have operated successfully for some time before being moved and re-installed.

The handwritten maintenance records kept by Acrylon with respect to the years from 2009 to 2012, indicate that maintenance was conducted frequently. Apart from lubricating, there is (March 12, 2010) a note “inspect offsets for cracks”; another note (June 22, 2010) “Change all main arm bolts and gearbox bolts on Arm #2; another note (Jan 7, 2011) “ inspect all belts, chains, bolts and welds); another note (March 25, 2011); grind and re-weld cracks in; Arm #1; further notes (April 26, 2011); “weld cracks on Arm #1”; (August 12, 2011 “ weld cracks on Arm #1”; (Sept 2, 2011) “weld cracks on Arm #1”; (October 7, 2011) weld crack in weld #1 (Nov. 23, 2011).

When one of the authors first saw the unit, “repairs” had been undertaken and the machine was operating, although production was slow.

However, a second catastrophic failure occurred requiring more detailed investigation, with legal council appointed representing the owner’s insurance company.

It appeared that the unit had been shut down to disguise the repair.

Investigation showed the totally inadequate repair that had been done at some time prior to the installation of the machine on its present site. This is shown in Fig. 3 in which the shaft shows clear visible evidence of fatigue.

Figure 3. Detailed vie e fatigue fracture of shaft showing evidence of fatigue fracture.

This occurred over the centre of the shaft while additional fatigue fracture was present in a fillet weld at the outside of the shaft (Figure 4).

This indicated two separate repairs one to the central drive shaft and another to the outer shaft that had formerly been separate entities driving the mail furnace component and the rotation mechanism for furnace to spread the powder and plastic within the mould.

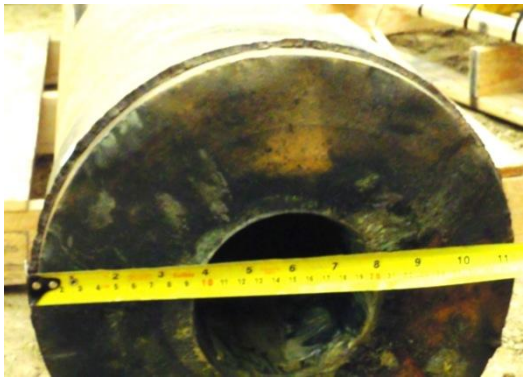

Figure 4. Fatigue fracture of weld connecting repaired and joined inner and outer rotating shafts.

3. Conclusions

Obviously any claim against the manufacturer and or the design company would be pointless, as the machine, as supplied to the new owner, was basically sound and the failure originated in service. To the writer's knowledge the information as to who specified the original repairs has not been determined, but clearly the sale to the company who suffered loss and damage when catastrophic failure occurred was of an actionable nature and constituted fraud. Also, the paper emphasizes the need to look out for disguised repairs that may not be seen at the time of purchase.

Failure analysis of a 2.25Cr-1Mo-0.25V steel heavy wall-thickness multi-pass welded component

Pekka Nevasmaa[1], Sanni Yli-Olli[1], Olli Kortelainen[2], Arto Kiiski[2]

[1]VTT Technical Research Centre of Finland Ltd
Espoo, Finland

[2]Neste Jacobs Oy
Porvoo, Finland

Abstract

Crack-like defects were found in a low-alloy 2.25Cr-1Mo-0.25V steel multipass welded heavy wall-thickness component prior to its usage. After welding, the component had been subjected to local Intermediate Stress Relief (ISR) heat treatment at 600–650°C, with the aim at removing diffusible hydrogen and enhancing partial tempering of the weldment microstructure before the final PWHT. The objective of the present paper was to investigate the actual fracture micromechanism of the discovered damage associated with the manufacturing stage of the component, in order to explain the inherent causes of failure. The metallographic and fractographic studies demonstrated (i) cracks propagating through the weld solidification structure as quasi-cleavage fractures, (ii) the presence of micro-cracks at thereby 'opened' solidification boundaries, as well as (iii) occasional appearance of ductile 'ridges' at the fracture surface; all that were characteristic of hydrogen-induced cold cracking. In line with this, Vickers hardness measurements revealed maximum hardness as great as 381–382 HV and 371–378 HV in cases of the CGHAZ and weld metal microstructures, respectively. Furthermore, hardness traverses in the weld thickness direction revealed higher hardness values in the weld intermediate thickness than closer to the surface or the root, which was ascribed to inadequacy of the thermal effects of the ISR heat treatment. The occurrence of hydrogen cracking was attributed to simultaneous co-existence of several adverse factors: (i) excessively high weldment hardness, (ii) accidentally high initial hydrogen content of the applied SMAW electrode and (iii) inherently high structural rigidity and restraint of the component.

1. Introduction

Low-alloy CrMoV steels are frequently used in petrochemical industry for e.g. hydrocracker reactors processing hydrocarbons in refineries [1], as well as for power plant applications where components need to withstand high service temperatures and therefore exhibit high creep strength and sufficient ductility. Welded joints of CrMoV steels are known to be susceptible to cracking phenomena such as hydrogen cold cracking and reheat (stress-relief) cracking, the risk being accentuated in thick-wall section weldments and joints under severe structural restraint due to complex shapes and/or massive components. Thus, weldability of low-alloy CrMo(V) steels is mainly governed by their cracking tendency, as well as by ductility

of the heat-affected zone (HAZ) and the weld metal. Owing to the relatively high contents of Cr, Mo and V, rapid weld cooling cycles easily lead to hard bainitic-martensitic microstructures. Welding procedures intended for practical service conditions must therefore contain the necessary safeguards against cracking, which calls for appropriate preheating, controlled interpass temperatures and, often, also post-weld heat treatments (PWHT). For power generation applications, the maximum allowable weld hardness is generally limited to below 350 HV, whereas hydrogen containing environments tend to permit hardness of no more than 248 HV [4].

Susceptibility to both hydrogen cold cracking and reheat cracking increases with the structural rigidity of the component. The balance of suppressed cracking sensitivity and sufficient creep strength cannot be considered fully solved particularly for thick-wall components, which curtails practical application of CrMoV materials. Thick section welds generally require the use of also PWHT. For thick-wall applications and multipass welds, welding consumables still require further development to improve creep strength and ductility of weld metal. Welding consumables are mostly of roughly matching composition, with some compensation for arc burn losses, for instance, by adding Ti or replacing Ti with Nb [4, 9-11].

Low-alloy CrMo steels like T22 (10CrMo9-10) are widely used since 1940's at steam temperatures up to 540–565°C. The steel shows fair weldability and ductility, but only modest creep strength. For strength improvement at similar temperature range, modified low-alloy steels have been developed with small additions of elements that improve hardenability and form strengthening precipitates. Early versions of such grades like 0.5CMV (14MoV6-3) steel were successful in considerably improving the uniaxial creep strength at modest operating temperatures, but were also found to suffer from lower creep ductility than CrMo steels, resulting in relatively short mean time to creep cavitation and cracking in the plant inspection statistics [2]. More recently, newer modified grades P/T23 (7CrWVMoNb9-6) and P/T24 (7CrMoVTiB10-10) have been introduced with higher hardenability, small additions of precipitation forming elements such as V, Ti, Nb, W, B and/or N and more complex tempered bainitic to martensitic microstructure [3, 4]. Again, limitations and operational setbacks have been observed when aiming to benefit from the improved creep strength in waterwalls or steam lines. These have been associated with sensitivity to microstructure, weld quality control and/or defects and operating environment, and have resulted in premature failures in service [5]. Any increase in parent material creep strength is hence of little use if it is not reasonably matched by sufficient ductility and properties of welds.

It is a common observation that increasing material strength tends to reduce its ability to deform and yield without damage like cracking or fracture. This certainly applies to low-alloy CrMo steels, and one of the early lessons was with the steel 0.5CMV (14MoV63) that like P/T23 and P/T24 contains vanadium for precipitate (MX) strengthening. In spite of showing better creep strength than P22, this steel has fallen into disuse in new plants partly because of its propensity to creep cavitation and cracking in welded joints. The difference to P22 appears as lower elongation and reduction of area (RA) under nearly any testing conditions including those in standard qualification tests [4]. However, detrimental features can include even partially martensitic weldment microstructure that can be sensitive to hydrogen damage and stress corrosion cracking, simultaneously with the increased likelihood of crack extension from weld defects [3, 5].

Material's low ductility can be indicated by high hardness, but the often quoted limit of 350 HV may not be sufficiently restrictive to guarantee safe, crack-free welds. In practice this will frequently mean requirements to use preheating for welding (150–200°C), possibly followed by PWHT [5-8]. Unfortunately, PWHT will compromise one of the major original advantages of low-alloy CrMo steels, i.e. the option to assemble large-scale structures without mandatory PWHT. The complexity of optimising weld properties was clearly demonstrated in previous work [9, 10] on thick-section P23 tube multipass welds: while the as-welded condition exhibited excessive weld metal hardness (well above 350 HV) and poor impact toughness (less than 10 J at RT), the subsequent PWHT resulted in reheat cracking in the weld metal irrespective of simultaneously improved toughness and decreased weld hardness. It was found that reheat cracking sensitivity of P23 weld metal was reduced by selecting a filler material with its chemical composition more closely matching to T/P24, and that T/P24 is obviously less susceptible to reheat cracking than T/P23 [9, 10].

Overall, low ductility makes material unforgiving against straining under constraint (e.g. in rigid, high-restraint structures), and against any crack-like defects. Low creep ductility may therefore translate into poor performance of welded components that are subjected to more realistic loading conditions than the same material in uniaxial creep testing. Time to failure in cross-weld specimens can correspond closely to the 80% strength level of the mean parent material strength, but may fall slightly lower when compared to

the actual parent material strength. In addition to weld metal, also the coarse-grained heat affected zone (CGHAZ) can show low ductility and significant sensitivity to damage [11].

In the present study, crack-like defects were found in a low-alloy 2.25Cr-1Mo-0.25V steel multipass welded heavy wall-thickness component already prior to its usage. After welding, the component had been subjected to local Intermediate Stress Relief (ISR) heat treatment at 600–650°C. The purpose of the ISR treatment is to remove diffusible hydrogen and enhance partial tempering of the weld and the HAZ microstructures, in order to prevent any damage formation before the final PWHT. According to the available information [1], welding had been carried out according to the appropriate Welding Procedure Specifications (WPS) using a preheat temperature of 250°C, interpass temperature of 250–300°C and post-weld ISR treatment at 650°C (heating rate: 50°C/h). After completion of welding, the component had been transferred without delay into the ISR treatment by simultaneously keeping up a 250°C minimum maintenance temperature during this time interval. The occurrence of cracking was, however, recognised after the ISR treatment of the component. Later, it turned out that of the applied 'Phoenix CHROMO 2V' SMAW electrodes (Ø4mm and Ø5mm), those having a 5mm diameter and used for depositing the weld filling runs exhibited unexpectedly high initial hydrogen content of ≈ 7 ml/100g in Inert Gas Fusion hydrogen test (acc. to ASTM E1447), whereas for 4mm diameter electrodes the corresponding value was 3.5 ml/100g [1].

The objective of the present paper was to investigate the actual fracture micromechanism of the discovered damage associated with the welding fabrication of the component. On the basis of metallographic and fractographic studies, the inherent causes of failure are identified and explained.

2. Materials and Experiments

According to the background information [1], the steel in question was a low-alloy 2.25%Cr–1%Mo–0.25%V grade creep resisting steel frequently used in petrochemical industry for e.g. hydrocracker reactors. The damaged components appeared massive, obviously having high structural rigidity and contained heavy-section weldments with the thickness of 125–135mm.

The received two welded samples (Ø 235mm, thickness: 135mm) were subjected to the following investigations:

(i) Visual inspection of the observed weld imperfections.

(ii) Chemical analysis of the parent material and weld metal using optical emission spectroscopy (OES).

(iii) Metallographic investigation of the polished and polished & etched weld cross-section specimens using optical microscopy (LOM) and, for selected specimens scanning electron microscopy (SEM) with energy dispersive X-ray analysis (EDX): characterisation of weld metal and HAZ microstructures, analysis of elements within and in the vicinity of cracks.

(iv) Fractographic investigation of authentic fracture surfaces of intentionally opened cracks using scanning electron microscopy (SEM) with energy dispersive X-ray analysis (EDX): identification of fracture micromechanism, identification of microcracks, analysis of possible elements on the fractured surface.

(vi) Hardness measurements across the weldment and in the weld thickness direction according to EN ISO 6507-1 using Vickers HV_{10}: weld metal and HAZ maximum hardness, hardness distribution in the weld thickness direction.

3. Results and Discussion

According to the OES analysis, the chemical composition of the studied base material is equivalent to conventional low alloy 2.25Cr-1Mo-0.25V grade steel showing an intermediate carbon content of 0.12%. The weld metal complies with the chemical composition of the parent steel; the C content was somewhat lower than in the base material and the weld metal contained Ti as microalloying element, see Table 1.

Table 1. Chemical composition (w-%) of the investigated base material and weld metal.

Sample	Chemical composition %												
	C	Si	Mn	S	P	Cr	Ni	Mo	Cu	Al	W	V	Ti
Base	0.12	0.05	0.37	.016	.008	2.09	0.09	0.93	0.10	.030	<.01	0.25	.004
Weld	0.072	0.17	0.82	.019	.010	2.22	0.06	0.95	0.03	.002	<.01	0.24	.009

Visual inspection revealed several transversal and longitudinal crack-like defects in the weldment area. Of these, transversal weld metal cracks were bursting open to the surface, often extending across the fusion boundary and into the HAZ side; see Figure 1. The longitudinal cracks, in turn, seem to have been typically initiated from machined steep notches in the weld root side, from where they had grown into the thickness direction up to the weld mid-thickness, often associated with crack branching, and sometimes even burst open to the surface, see Figure 2. A longitudinal crack c.f. Figure 3 had been initiated in approx. 45° angle orientation either from the weld surface or beneath the final weld bead layer, from where it has propagated towards the fusion boundary and further across the HAZ into the base material.

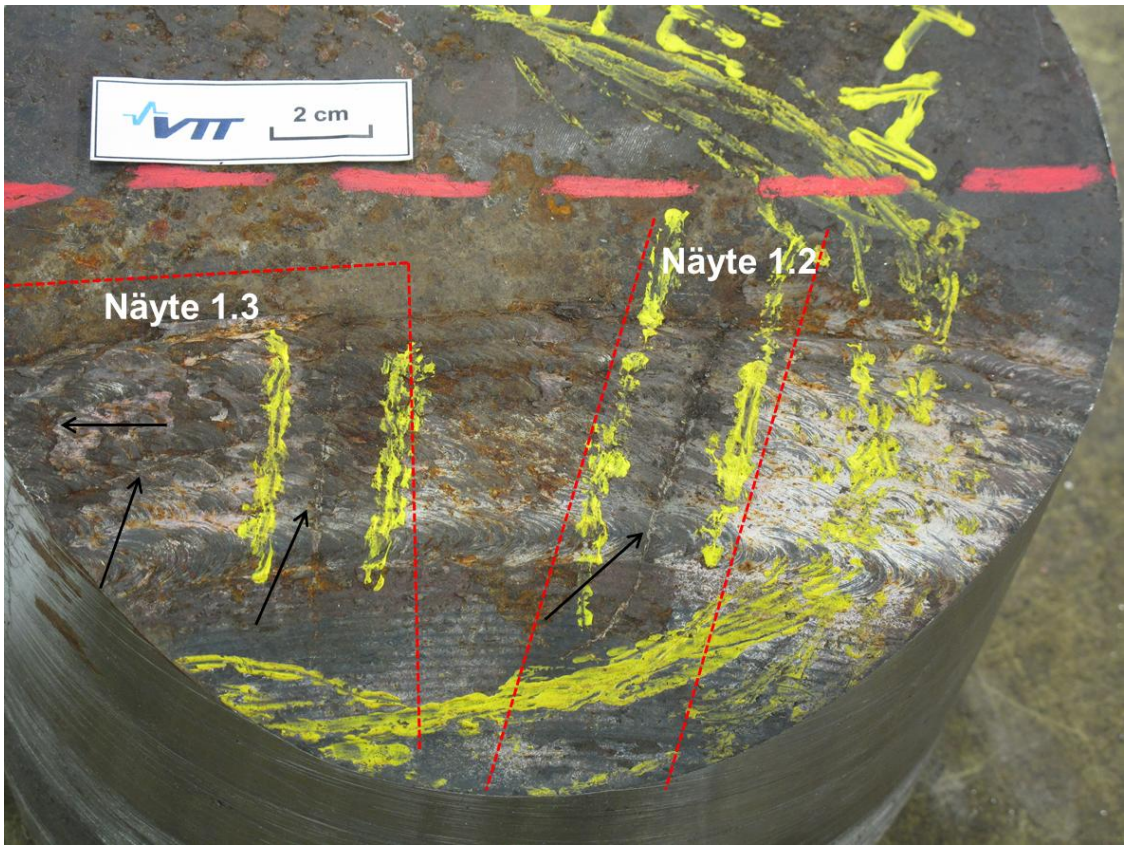

Figure 1. Transversal weld metal cracks at the outer surface of the specimen (denoted with black arrows).

It appeared that crack formation had been very intense. A number of closely-spaced transverse and longitudinal cracks were observed; some of them even crossing each other, which is considered quite uncommon. The discovered cracks showed a meandering 'zig-zag' appearance, which implies that they've been obviously propagating along the grain boundaries; see Figure 3. These features are known characteristic of both (i) hydrogen cold cracking and (ii) reheat (stress-relief) cracking mechanisms.

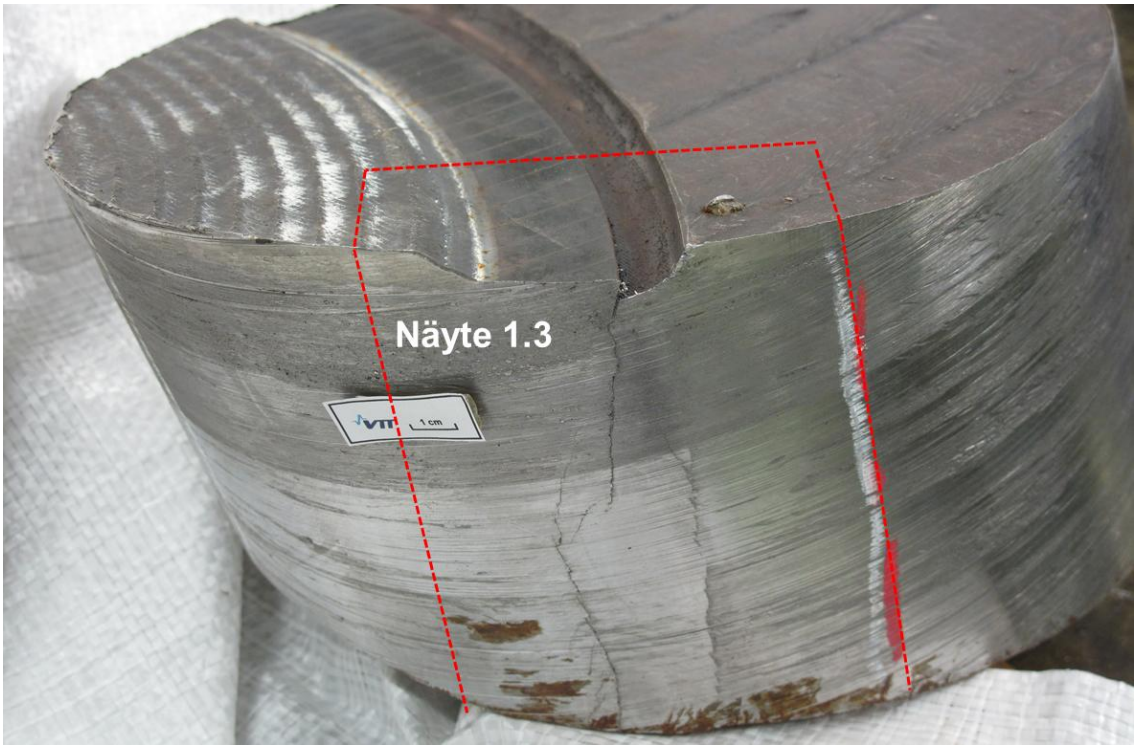

Figure 2. Longitudinal weld metal/HAZ cracks initiated from the corner of a machined notch at the inner surface (see: the top side) and grown into the weld mid-thickness area and finally the outer surface.

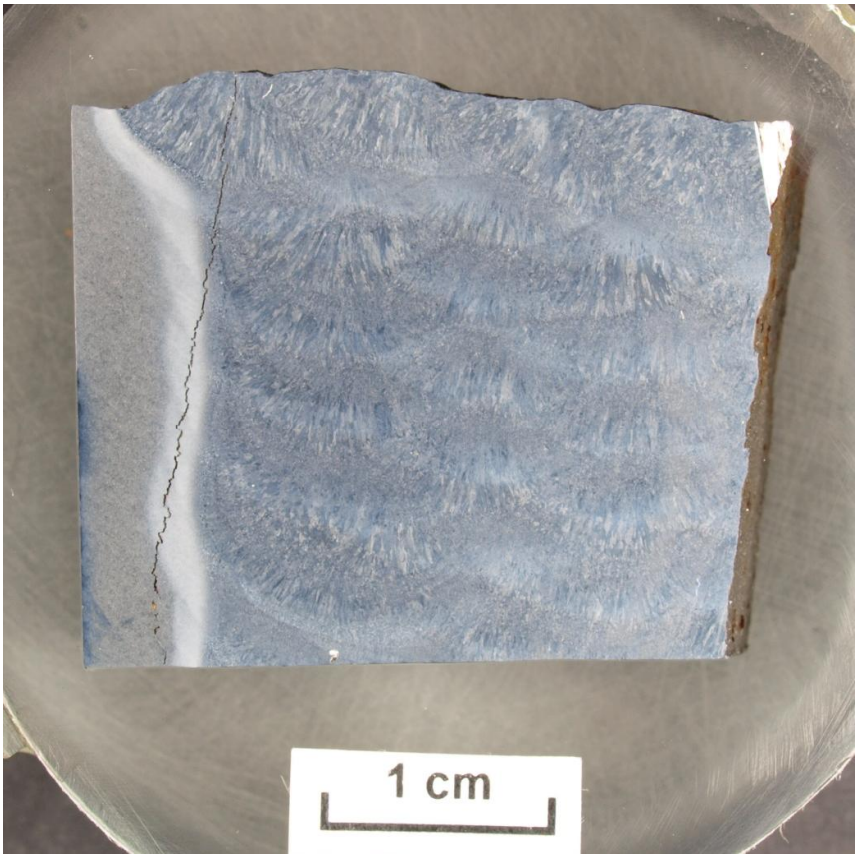

Figure 3. An example of typical appearance of discovered cracks: longitudinal crack in the HAZ region.

Material's risk to reheat (stress-relief) cracking can be evaluated, for instance, using the well-known CS index developed by Nakamura:

$$CS = Cr + 3.3\,Mo + 8.1\,V - 2 \quad (1)$$

If $CS \geq 0 \rightarrow$ risk of reheat cracking exists

For the base material studied here, CS = 5.18. This indicates that the steel itself is susceptible to reheat cracking during PWHT. Thus, one cannot yet exclude the possibility of reheat cracking, until further metallographic and fractographic investigations.

Metallographic investigation using optical microscopy (LOM) revealed a crack starting from the steep corner of a machined notch in the weld root side at the inner surface of the investigated sample; see Figure 4. The crack had been propagating inwards along the weld fusion boundary until it hit a lack-of-fusion weld defect existing in the root area of a subsequent weld bead, c.f. Figure 4. After this, the crack had continued to grow slightly (≈160 µm) within the weld bead. Relatively dense oxide layer was found within the crack (see Figure 5), which indicates that it was presumably formed at a high temperature. The oxide layer continued all the way up to the crack tip, along with a few small Mn-rich slag inclusions that were not found elsewhere within the weld.

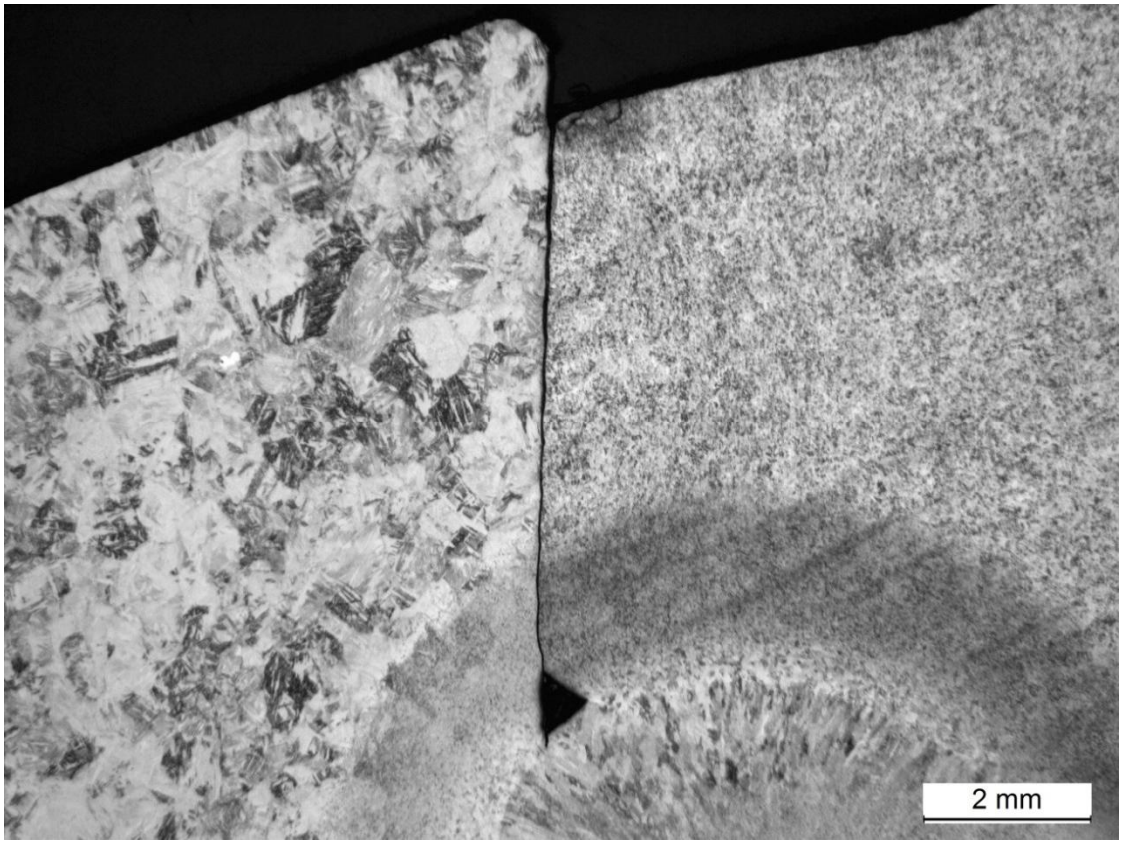

Figure 4. A crack initiated from a machined geometrical notch at the inner surface of the sample. A lack-of-fusion weld defect (triangle shaped) in the weld root area.

Otherwise, there were no detectable oxides associated with the other cracks found within the weld metal or in the HAZ. Small secondary cracks were frequently recognised with the LOM in the immediate vicinity of the discovered primary crack; often these secondary cracks seemed to follow the prior-austenite grain boundaries; see Figure 6. The microstructure of the weld metal and the coarse-grained HAZ consisted mainly of bainite (with both aligned and non-aligned second phase, see Figures 5 and 6).

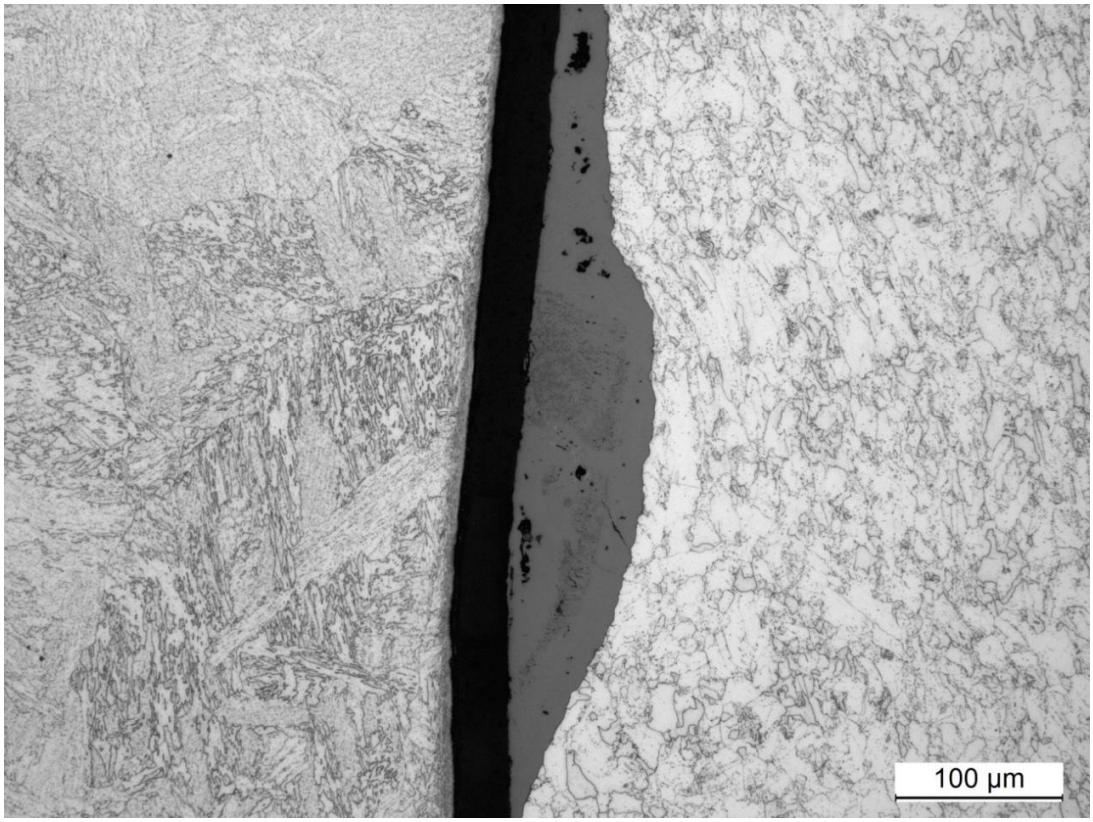

Figure 5. Oxide within a crack depicted in Figure 4. A bainitic HAZ microstructure (in the left side).

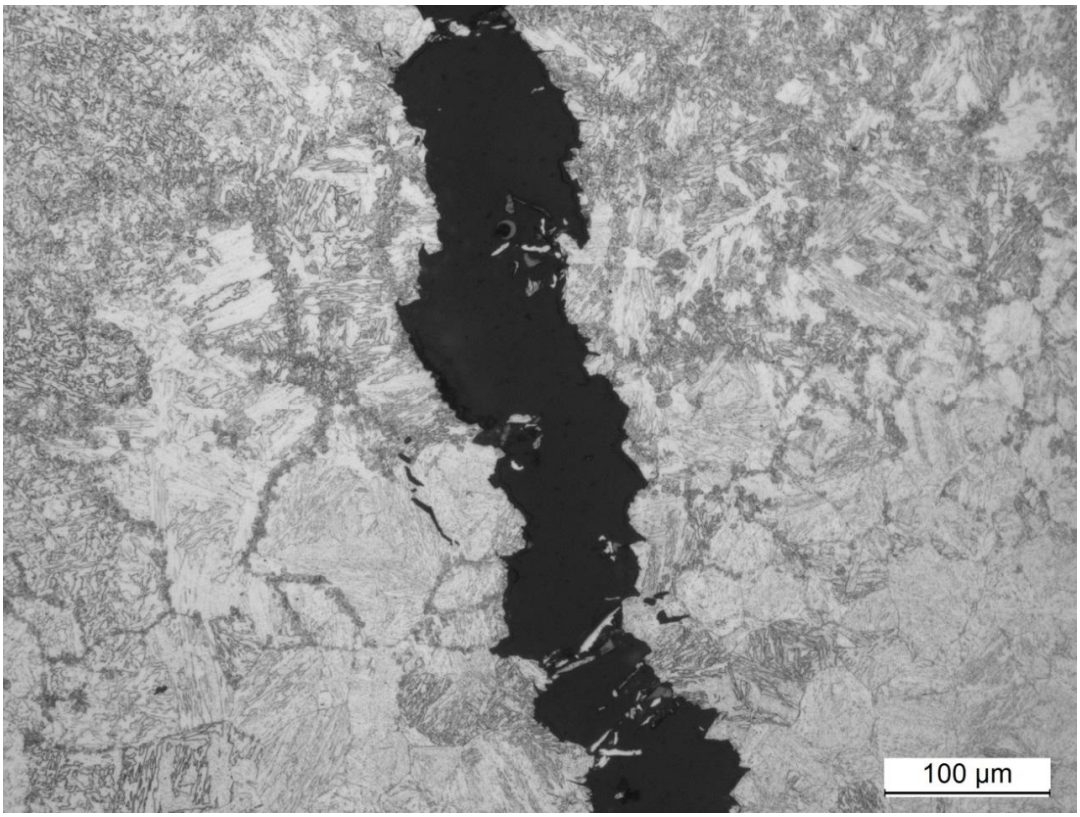

Figure 6. An example of small secondary cracks in the immediate vicinity of the primary crack.

Fractographic investigation of the surfaces of intentionally opened cracks using scanning-electron microscopy (SEM) confirmed that the fracture micromechanism was in all cases identical, irrespective of their location and whether the crack orientation was transverse or longitudinal. As regards the weld metal, (i) areas of transgranular quasi-cleavage fracture, (ii) several solidification boundary microcracks (i.e. locally 'open' grain boundaries), and to a lesser extent, (iii) occasional areas of ductile fracture (i.e. ductile ridges), were discovered; see Figures 7–9. Similar features were found also from the fracture surfaces of those cracks extending across the HAZ into the base material; both (i) transgranular cleavage fracture and (ii) consecutive grain-boundary microcracks resulting in intergranular fracture were recorded from the HAZ.

It is noteworthy that the examined fracture surfaces appeared macroscopically brittle already after opening of the cracks by force in a screw vice at room temperature. No visible plastic deformation was associated with the fracture surfaces and very little force was required to fully open the cracks.

All these aforementioned features can be considered characteristic of hydrogen-induced cold cracking. According to the microplasticity theory [12, 13], diffusible hydrogen in the lattice ahead of the crack tip assists and promotes whatever microscopic deformation and crack growth process the particular microstructure will allow. Thus, hydrogen cracking is not associated with any unified damage micromechanism, but cracking can occur as cleavage, quasi-cleavage, microvoid coalescence (ductile fracture) or intergranular cracking along the grain boundaries.

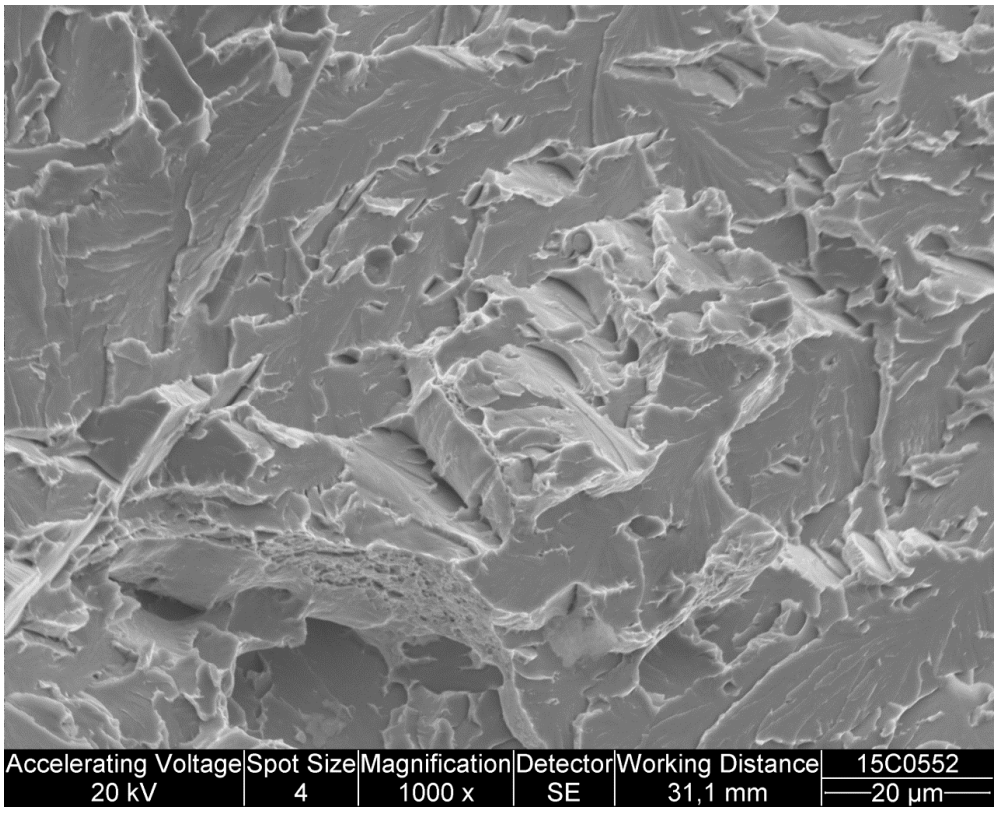

Figure 7. SEM image from the fracture surface of a transverse crack in the weld metal (specimen no 1.2).

No signs of intergranular cracks initiating from grain boundary 'triple-points' connecting several prior-austenite grains were found. The possibility of reheat (stress-relief) cracking as an alternative cause of failure can therefore be excluded. Besides, reheat cracking would obviously have been propagating solely intergranularly, i.e. entirely along the grain boundaries without any transgranular quasi-cleavage or occasional ductile ridges that, in the present study, were recognised from the fractured surfaces.

Neither were any traces of beachmarks or striations discovered on the fracture surfaces, which rules out fatigue fracture. The fact that the component in question had not been in use prior to its damage precludes failure by fatigue or stress-corrosion cracking, anyway.

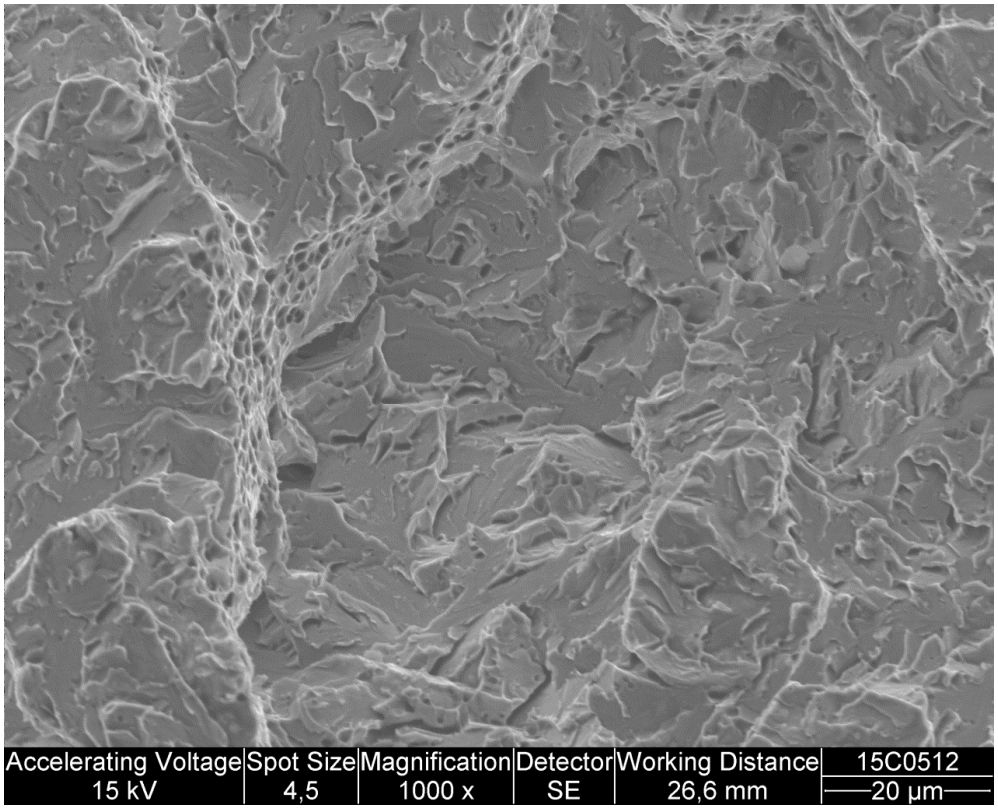

Figure 8. SEM image from the fracture surface of a longitudinal crack in the weld/HAZ (specimen no 1.3).

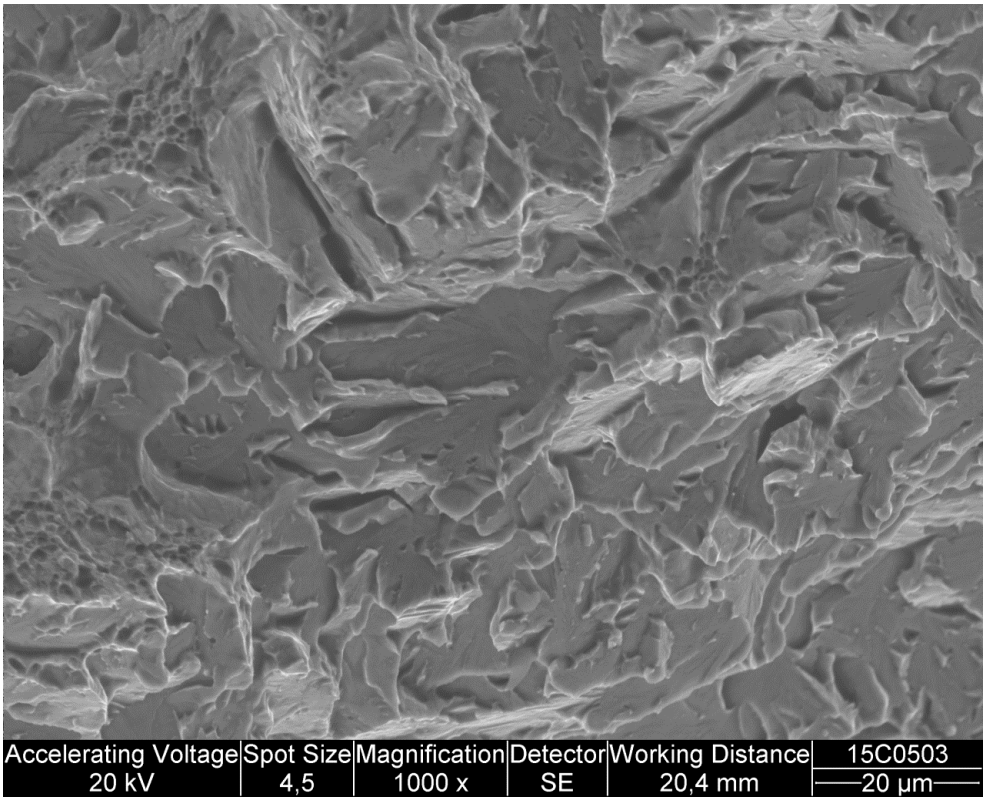

Figure 9. SEM image from the fracture surface of a longitudinal crack initiated from the corner of a machined steep notch on the inner surface of the specimen (specimen no 2.3).

The fact that the examined welds fractured instantly without any notable plastic deformation already when cracks were opened by force using, after all, a very slow deformation rate, implies that the weld metal must have been fully brittle at room temperature. This is certainly uncommon even for low-alloy CrMoV weld metals and hence obviously in contrast with the requirements set in the Pressure Equipment Directive (PED), which specify the minimum required Charpy impact energy as 27 J (average) at room temperature for welds in pressurised components complying with the scope of PED [9]. This brittle behaviour may be explained by the results of the measurements which had shown that exceptionally high initial hydrogen content of ≈ 7 ml/100g (DM) was associated with the SMAW electrodes of Ø 5mm applied for the weld filling layers [1], even though the electrode was classified as H5, i.e. low hydrogen consumable. According to previous numerical analyses [14], excessively high diffusible hydrogen contents in low-alloy steel weld metal can accentuate its embrittlement via reduction of cohesion strength of grain boundaries with increasing hydrogen accumulation and local hydrogen concentration.

The results of the weld hardness measurements made horizontally on three different weld cross-section specimens using Vickers HV_{10} showed that the maximum individual hardness values for the weld metal and the CGHAZ were 356, 371, 378 HV, and 358, 381, 382 HV, respectively. The results of additional hardness measurements made into the weldment thickness direction on (i) filling beads close to the surface, (ii) weld mid-thickness and (iii) weld root area are given in Table 2.

Table 2. Results of additional hardness measurements (HV_{10}) made into the weld thickness direction.

Vickers hardness (HV) / Weldment location	Weld metal		Coarse-grained HAZ	
	HV(max)	HV(ave)	HV(max)	HV(ave)
Weld surface area, filling runs	360	335	332	295
Weld mid-thickness	364	335	361	339
Weld root area	370	355	343	327
All measurements	**378**	-	**382**	-

For low-alloy steels the weld/HAZ maximum hardness levels around 370–380 HV clearly indicate a pronounced risk of a microstructure to hydrogen cold cracking. It is noteworthy that the highest individual hardness value of 382 HV in the CGHAZ was immediately accompanied by a long neighbouring crack starting from the weld root and extending into the weld mid-thickness area, as shown in Figure 2. Moreover, certain discovered features on this crack surface and at the crack tip, such as oxides (see Figure 5) indicate that the crack must have existed already at the time when the ISR treatment was performed. All these findings demonstrate that the high hardness measured for the investigated weldments is directly linked to the occurrence of intense cracking in the present case. In fact, hardness level this high is generally considered typical of low-alloy CrMoV steel weldments in the as-welded condition rather than after PWHT which usually results in around 250–300 HV hardness range. Taking account of the 250°C preheat /interpass temperature according to the available WPSs for the present case [1], which should be adequate for low-alloy CrMoV steels, inevitably points to the performance of the ISR heat treatment. Although the purpose of the ISR was not to relieve welding residual stresses, but to enhance partial tempering of the weldment microstructure (before the final PWHT), it is no doubt that an ISR treatment at the 650°C temperature for several hours should in any case yield some reduction in weldment hardness and, if done immediately after welding without letting the weldment to cool down to room temperature, also remove any weld diffusible hydrogen, hence practically eliminating the possibilities of hydrogen-induced cold cracking.

Additional hardness measurements made into the weld thickness direction revealed that the highest hardness values for the HAZ were recorded from the weldment mid-thickness areas, while lower values were encountered for the surface and root areas, see Table 2. In cases of the weld metal, the root area exhibited the highest hardness – obviously because of dilution; however, overall, the difference in the hardness between the surface, mid-thickness and root areas was much less for the weld metal than the HAZ. The observed variations in the through-thickness hardness distribution hence strongly suggest that the thermal effects of the ISR treatment in the present case have not been consistent throughout the component thickness and had remained weakest in the weldment mid-thickness, in particular.

Consequently, all the aforementioned findings demonstrate that some accidental, aberrant features must have been affiliated to the practical performance of the ISR treatment in the present case.

According to the results of the metallographic and fractographic studies, in can be concluded that an unambiguous failure mechanism was responsible for the discovered damage, despite various orientations and locations of an uncommonly great number of crack-like defects. The occurrence of (i) cracks propagating through the weld solidification structure as quasi-cleavage fracture, (ii) the presence of several microcracks at thereby 'opened' solidification boundaries, as well as of (iii) occasionally appearing ductile 'ridges' at the fracture surfaces are all characteristic of hydrogen-induced cold cracking. Similar features were associated with cracks propagating from the weld metal across the HAZ towards the base material; namely, both transgranular quasi-cleavage fracture and discontinuous intergranular microcracking at the prior-austenite grain boundaries. In line with this, the Vickers hardness measurements revealed maximum hardness as great as 381–382 HV and 371–378 HV in cases of the CGHAZ and the weld metal microstructures, respectively, thereby indicating an elevated risk to hydrogen cold cracking. Furthermore, hardness traverses in the weld thickness direction revealed higher hardness values in the weld intermediate thickness, while the weld filling beads and root passes both were associated with somewhat lower hardness. After welding, the component had been subjected to local Intermediate Stress Relief (ISR) heat treatment at 600–650°C, with the aim at removing diffusible hydrogen and enhancing partial tempering of the weldment microstructure before the final PWHT. The hardness results, however, imply that the thermal effects of the ISR heat treatment had been inconsistent and hence weaker in the weld mid-thickness than elsewhere; consequently, the entire ISR treatment obviously was inadequate for the purpose in the present case, as it comes to sufficient reduction of the weldment hardness and removal of weld diffusible hydrogen, which were the aims of conducting the ISR treatment for the investigated CrMoV steel component.

Additionally, (i) the unfortunate use of Ø5mm SMAW electrodes with unusually high initial hydrogen content (≈7 ml/100g DM) to deposit the weld filling runs, in conjunction with (ii) the existence of deliberately machined, yet obviously impermanent, steep notches in the weld root side of the studied component, have certainly contributed to the present failure. There is no doubt that properly re-dried basic electrodes should be able to more or less meet the H5 condition (≈ 5 ml/100g (DM) weld hydrogen). Thus, the high recognised weld hydrogen content associated with these electrodes in the present case is most likely a result of somehow inappropriate handling of the consumable in question. Since cracking occurred also in the weld root area and not only in filling runs, hydrogen in the Ø5mm SMAW electrode, however, cannot be the only critical conclusive factor in this case. It is obvious that the presence of steep machined notches adjacent to the weld root side in the inner surface of the component had contributed to damage formation by acting as local geometrical discontinuities that created an elevated tri-axial stress state accelerating the solid-state diffusion and accumulation of hydrogen in the vicinity of the root side fusion boundary, i.e. at the site where the most severe cracks had initiated. The reason for these intentionally machined notches remained unclear. Nevertheless, the combination of (i) steep geometrical discontinuity, (ii) hardened microstructure and (iii) incidentally high weld hydrogen content prevailing in the investigated component under high structural restraint are, in fact, consider to a large extent represent critical conditions resembling many cold cracking experiments, such as oblique-*y* groove Tekken test or Implant test. This is thought to largely explain the occurrence of intense weld hydrogen cold cracking in the present case.

4. Conclusions

This paper deals with failure analysis of a low-alloy 2.25Cr-1Mo-0.25V steel heavy wall-thickness multipass welded component, from which several crack-like weld defects were found already prior to its usage. The objective of the present study was to investigate the actual fracture micromechanism and primary causes of the discovered damage associated with the welding fabrication. On the basis of the results, the following conclusions were drawn:

The fracture micromechanism was identified as hydrogen cold cracking. The occurrence of cracking was attributed to a simultaneous co-existence of several adverse critical factors, namely: (i) excessively high weldment hardness (max. 382 HV) as a result of an inadequate ISR treatment, in the combination with (ii) an accidentally high initial hydrogen content (≈7 ml/100g DM) of the SMAW electrode (Ø 5mm) used to deposit the weld filling beads and (iii) inherently high structural rigidity and restraint state of the welded component. Additionally, (iv) the existence of deliberately machined, yet obviously impermanent, steep notches in the weld root side have undoubtedly contributed to damage formation by acting as local geometrical discontinuities that created elevated tri-axial stress state accelerating the solid-state diffusion

and accumulation of hydrogen in the vicinity of the root side fusion boundary where the most severe cracks had initiated.

References

1. 'Confidential information from the manufacturer, Espoo, March–May 2015.

2. Auerkari P. *et al.* "Evaluation of creep damage from replica inspection results". Nordtest project 1306-96. VTT, Espoo 1996. Research Report VTT VAL B 211. 33 p.

3. Vaillant J.C. *et al.* "T/P23, 24, 911 and 92: New grades for advanced coal-fired power plants - Properties and experience". *International Journal of Pressure Vessels and Piping*, Vol. 85 (2008), pp. 38-46.

4. Auerkari P. *et al*. "2%CrMo(W)V steels for welded high temperature applications", VTT, Espoo, 2005. Research Report TUO74-055258. 40 p.

5. Nowack R., Götte C., Heckmann S. "Quality management at RWE using T24 boiler material as an example", *VGB Powertech* (2011). 5 p.

6. Nevasmaa P. *et al*. "Evaluation of weld metal hydrogen cracking risk in a 2.25-1Mo-0.25V-TiB (T24) boiler steel". In: *Proc. Baltica VI, Vol. 2*, Helsinki-Stockholm-Helsinki, June 2004. VTT Symposium 234, pp. 393-407.

7. Dhooge A. & Vekeman J. "New generation 21/4 Cr steels T/P23 and T/P24 weldability and high temperature properties". *Welding in the World*, Vol. 49 (2005), pp. 75-93.

8. Benedick W. *et al*. "New low alloy heat resistant ferritic steels T/P23 and T/P24 for power plant application". *International Journal of Pressure Vessels and Piping*, Vol. 84 (2007), pp. 13-20.

9. Nevasmaa P. & Salonen J. "Reheat cracking susceptibility and toughness of 2%CrMoWVNb (P23) steel welds". *Welding in the World*, Vol. 52 (2008), pp. 68-78.

10. Nevasmaa P. *et al*. "Reheat cracking susceptibility of P23 (7CrWVMoNb9-6) steel welds made using matching and mis-matching filler metals". In: *Proc. 9th Liege Conference on Materials for Advanced Power Engineering*, Liege, September 2010. 10 p.

11. Auerkari P. *et al*. "Performance of welded joints in low alloy steels T/P23 and T/P24 for challenging high-temperature applications". In: *Proc. 10th Liege Conference on Materials for Advanced Power Engineering*, Liege, September 2014. Vol. 234, pp. 89-90.

12. Gedeon S.A. & Eagar T.W. "Assessing hydrogen-assisted cracking fracture modes in high-strength steel weldments". *Welding Journal,* Vol. 69 (1990), pp. 213-s–219-s.

13. Beachem C.D. "A new model for hydrogen-assisted cracking (hydrogen embrittlement)". *Metallurgical Transactions*, Vol. 3 (1972) 2, pp. 437-451.

14. Laukkanen A. *et al.* "Numerical Evaluation of Hydrogen Cracking using Transient Finite Element Analysis and Concentration Dependent Damage Mechanics Constitutive Model'. In: Proc. *7th International Seminar: Numerical Analysis of Weldability (NAW-7) / Mathematical Modelling of Weld Phenomena 7*", Graz-Seggau, September–October 2003. 16 p.

Power & process:
RBI and its implementation

prEN 16991: The new European standard on Risk-Based Inspection (RBI)

A. Carlebur[1], A. Jovanovic[2], F. A. Quintero[2] & M. Ahmad[2]

[1] NEN, The Netherlands
arthur.carlebur@nen.nl

[2] Steinbeis Advanced Risk Technologies, Stuttgart, Germany
jovanovic@risk-technologies.com

Abstract

This paper highlights some of the aspects of the new European standards on the risk based inspection (RBI). This new standard is based on further developing the CWA 15740:2008 document and encompasses the risk based inspection framework (RBIF) and the basic guidelines for risk-based inspection and maintenance (RBIM) in process, power, steel and other industries. The new European standard helps to achieve the harmonization of the in-service maintenance activities that are still not harmonized throughout the European Union (EU). Furthermore, the paper highlights some of the basic aspects of the risk based inspection as set up in the CWA 15740:2008 document and the updated aspects in the new European standard. The inclusion of factors for qualitative analysis, key performance indicators (KPIs) and the ageing model to the new European standards will be explained in this paper. The inclusion of these parameters enhances the optimization process of the RBI inspection and maintenance. This new European standard will not only provide harmonization to the risk based inspection and practices but also improve the overall process's productivity by minimizing the un-planned shutdowns and by optimizing the inspection and maintenance process.

1. Introduction

Since the late 1990's, the inspection and maintenance approaches in industry have been globally moving from prescriptive, time-based towards the risk-based. This trend has been clearly driven by the wish to increase the on-stream production time, to reduce unscheduled downtime due to breakdown maintenance and/or to reduce equipment condition which could ultimately cause a shut down or have an undesirable impact on the process safety. The CWA 15740:2008 [[1]] to [[4]], provides the essential elements of risk based assessment of industrial assets according to the RIMAP approach which has been developed and demonstrated in and by the European R&D project RIMAP (GIRD-CT-2001-03008 and the corresponding RIMAP Network: "Risk-Based Inspection and Maintenance Procedures for European Industry"). One of the main goals of the project, as well as of this CWA, has been to contribute to the harmonization of the EU national regulatory requirements related to the inspection and maintenance programs in the industrial plants and make them more cost-efficient while, at the same time, safety, health, and environmental performance is maintained or improved.

In order to record the current maintenance practices/regulations in various countries especially the European Member States, the RBI-Atlas had been developed. The RBI-Atlas has demonstrated the requirements for further actions in order to obtain the harmonization of maintenance practices/regulations. The periodically maintained RBI-Atlas by dedicated editors from respective countries ensure that current practices/regulations are considered in this tool.

The new European standard provides the criteria for risk-based assessment according to the approach which has been developed and demonstrated in and by the European pre-standardization document CEN CWA 15740:2008 (validity prolonged in 2011) and the corresponding RIMAP Network: “Risk- Based Inspection and Maintenance Procedures for European Industry. Various elements of this new European standard have been improved in order to effectively implement it across the European Member States compared to the initial CWA 15740:2008 document.

2. The CWA Document of 2008/2011

The objective of the CEN workshop agreement (CWA) is to present a set of clearly defined and accepted levels of risk related to safety, health, environment and business/production/operation. These objectives are achieved using resource-efficient methods of inspection and maintenance. The methodology for RBIM described here is based on that developed in the European project RIMAP (Risk-based Inspection and Maintenance Procedures for European Industry) [[2]]. Within the RIMAP project, the RBIM methodology has been developed and validated for chemical, petrochemical, power and steel industries in Application Workbooks [[5]], [[6]], but the methodology as such is intended to be industry independent. The methodology addresses the following aspects:

- Inspection and maintenance;
- All types of equipment, e.g. pressure containing, rotating, electrical, instruments and safety devices;
- Technical and managerial aspects of maintenance and inspection planning;
- Asset management related to inspection, maintenance and life assessment for plants, systems and components;
- Production and operation.

2.1 The Principles

The key principle behind the risk-based approach is to improve the productivity by minimizing the unnecessary shut downs and downtimes in plants. In general terms, if a company wants to apply a simple prospective maintenance/inspection approach then it is necessary to apply strictly conservative criteria for the decision making process. A risk-based approach on the contrary needs a detailed multi-disciplined engineering analysis to ensure that safety issues are not compromised by implementing a maintenance/inspection planning process. An appropriate risk-based methodology covers the following principles:

- Plan the primary work products of RBIM assessments and management approach in a prescribed way;
- Define the RBIM methodology in a framework according to the good engineering practices or industrial reference standards;
- Address a generic work flow and competencies needed to handle projects in an appropriate manner.

Define minimum requirements for performing and documenting RBIM assessments in order to comply with legal or normative regulations and guidelines.

2.2 General requirements

The general requirements of RIMAP as applied to RBIM are as followed:

a) The objectives and risk criteria should be clearly defined for the assessment;

b) The assessment and the applied detailed procedure should comply with the locally applicable legal and regulatory framework;

c) The required level of input information should be available for the assessment;

d) The assessment should be performed in a multidisciplinary team by personnel with the required competence, and using procedures and tools that can provide the required results on the selected level of assessment;

e) The assessment and the applied procedures should be able to provide results, which are:

- Safe;
- Conservative;
- Representable in a risk matrix, auditable and consistent with both the objectives and applied risk criteria;
- Supporting RBIM planning and decision making on the target system or component.

f) RBIM should be based on a team approach.

g) RBIM should reflect the prevailing conditions in the plant, i.e. RBIM needs to reach the "evergreen" status.

2.3 Requirements related to risk assessment

All requirements specified for personnel, PoF assessment and CoF assessment are also applicable to risk assessment requirements [[11]]. In addition, the following requirements shall also be satisfied for conducting risk assessment:

a) Development of a scenario for each failure mode is a critical step. Even though various techniques are available such as fault tree analysis, event tree cause-effect methods, etc. The bow-tie modelling is recommended due to the simplicity of charting different scenarios and the ease with which the result can be understood. When the help of bow tie approach (the fault and event tree can be establish) different scenarios for the failure modes can be developed by following different paths from root cause/damage mechanism to potential final consequences.

b) It is not allowed to combine PoF's and CoF's related to different scenarios (e.g. different failure modes) even if they refer to the same equipment.

c) Efficiency of the risk mitigating activities shall be connected to identified failure modes and the projected risk reduction shall be quantified.

3. New developments in the new European Standard (EN) – *prEN 16991: Risk-Based Inspection Framework*

The new prEN 16991: Risk-Based Inspection Framework tackles a number of particular issues, among which the three most important one are the following ones (in annexes of the new prEN):

- The qualitative probability factor (probability of failure related)
- The key performance indicators (KPIs)
- The ageing model

The qualitative probability factors refer to factors that can influence the probability and consequences of potential failures. However, in order to consider these factors into the qualitative risk assessment, it is required to assign them a comparative level. These qualitative levels are different for screening and detailed assessment steps. Table 1 demonstrates the probability and consequences factors used in the new standard for qualitative analysis and their respective levels.

Table 1: Probability and consequence factors for qualitative analysis

Risk analysis – Screening level		Risk analysis – Detailed level	
Probability Factors	**Assessment Criteria**	**Probability Factors**	**Assessment Criteria**
Age (since installed)	High: Less than 50k hours or more than 150k hours of operations Low: Between 50k and 150k hours of operation	Age (since installed)	Very low: 30k to 99k hours Low: 100k to 149k hours Medium: 150k to 199k hours High: 200k to 250k hours Very high: <30k or >250k hours
Material issues	High: Known Low: Not known	Total starts per year	Very low:<10 Low: 10 to 49 Medium: 50 to 99 High: 100 to 200 Very high: >200
Last inspection	High: >6 years Low:<6 years	Material issues	Very low: No Medium: Possible High: Yes
Damage / Degradation present	High: Yes Low: No	Repairs / Damage	Very low: No repairs Medium: Possible repairs High: Known repairs
Failure type	High: Burst Low: Leak	Failure type	Very low: Pin hole leak Low: Minor leak Medium: Medium leak High: Major leak Very high: Burst
Safety	High: Likely fatalities Low: Unlikely fatalities	Estimated area affected by failure	Very low: 5m diameter Low: 6-10m diameter Medium: 11-20m diameter High: 21-40m diameter Very high: Over 40m diameter
Health	High: Major implications Low: Minor or No implications	No. of people in area	Very low: 1 Low: 2-3 Medium: 4-5 High: 6-7 Very high: >8
Environment	High: Major impact Low: Minor or No impact	Time in area	Very low: up to 1 hour Low: 1-2 hours Medium: 3-4 hours High: 5-6 hours Very high: >6 hours

The key performance indicators (KPIs) are the management tool to measure and to react on a specific development within a plant. In general events, one can count events that have been occurred in the past called “lagging indicators” (e.g. Loss of Primary Containment (LoPC) events). The indicators that are more predictive are considered leading indicators.

The leading indicators are usually related to the organizational attributes that potentially have an impact on the safety and safe operations of the plant. Therefore, the leading indicators can provide a strong judgment to optimize the safety and risk based maintenance /inspection. In API 754 [[12]], a hierarchy of lagging indicators downwards to leading indicators is shown using the process safety metric pyramid as illustrated in Figure 1.

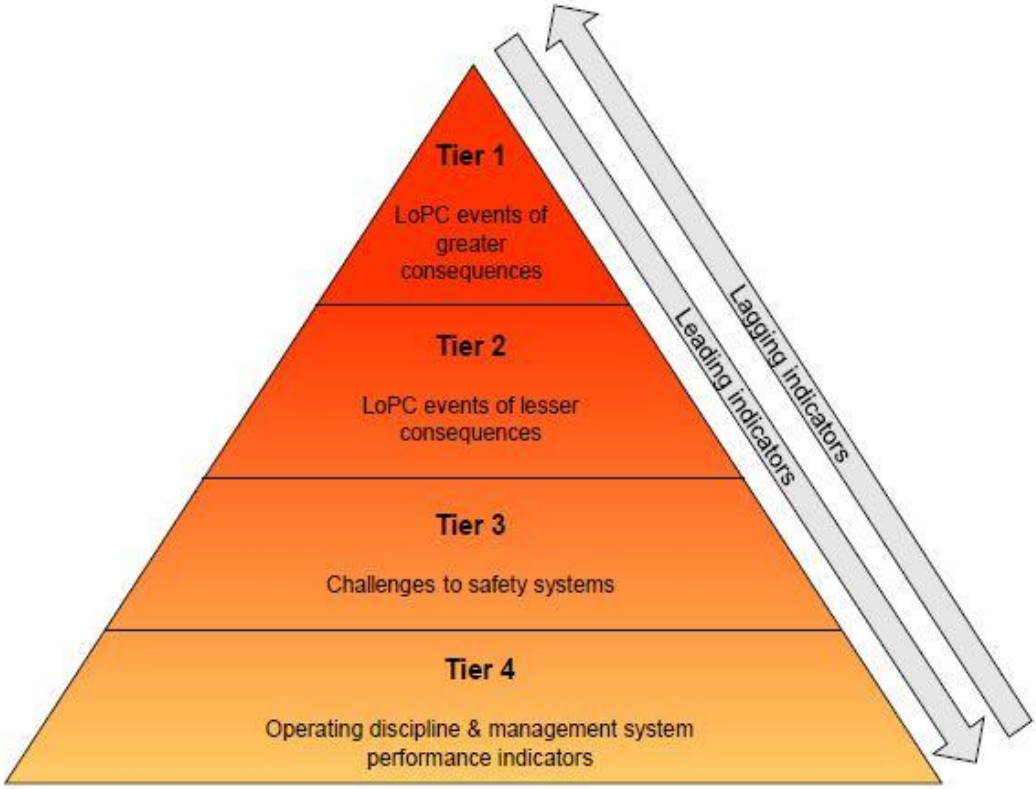

Figure 1. KPI pyramid, adapted from API 754 [[12]]

Furthermore, examples of the KPIs and relevant template for developments are shown in the Figure 2 and **Figure 3**, respectively. Figure 2 highlights some of the examples about KPIs. Further KPIs can be developed according to the plant/ operational situation. These KPIs and their relevant values should be coherent across the assessment section of a plant or the entire plant, since the follow up actions are generated based on the KPI score. Additionally, most relevant/critical KPIs can be selected with preference for further assessment in order to optimize the evaluation procedure. Therefore, with the help of KPIs, most critical sections/units can be traced out, that required an immediate attention to maintain their operational integrity. The **Figure 3** highlights the most relevant specifications of a single already selected KPI. The KPIs can be gathered from different well known and acceptable sources. The prescribed template of the form illustrated in the **Figure 3** can assist to remain coherent across the assessment section and to keep record of the follow-up actions generated during this step.

Objective	KPI
Improve safety and environmental conditions. It is recommended to distinguish between severe leakages and those with a minor severity; (see for instance Tier 1 and Tier 2 events in [24])	Number of overall safety and environmental incidents with focus on LoPC events.
Indicator of integrity management system efficiency	Leaks and Near Leaks with a pressure equipment impact that result from a breach of the pressure-retaining boundary # leaks / near leaks by internal corrosion # leaks / near leaks by external corrosion # leaks / near leaks by mechanical damage # leaks / near leaks from gasket/packing # leaks / near leaks by other cause ## near leaks/
Legal or internal compliance (License to operate threatened)	Number of overdue Inspection Schedules on Static Equipment, Piping and RV's
Integrity / compliance management	Number of overdue Notifications for once off inspection jobs (Non-recurring jobs)
Legal or internal compliance (License to operate threatened)	Number of recurring inspection schedules on static equipment, piping and RV's that do not have a Maintenance Plan
Track progress against RBI plan (Loss of control of RBI plan and unquantified level of risk)	% static equipment + piping covered by RBIF
Follow through on exceedances	Number of IOW corrective actions (Completed and outstanding)
Performance measure of operational control of key RBI assumptions	Number of critical IOW exceedance (12 months rolling average)
Integrity Control: Ensure compliance to RBI assumptions	Actual % implemented of monitoring points of agreed IOW
Increase asset/plant utilization	Unplanned downtime % Unplanned down time per equipment type %Plant/Unit utilization %
Assessment of the RBI inspection plan	# inspection findings according plan

Figure 2. KPI examples and objectives of selection

KPI #	Process Team: Process Definition:	Description:
What is the purpose of this KPI?		
What is the consequence of not having this KPI?		
What are the parameters required to measure this KPI?		
What is the formula for this KPI?		
Who is the owner of KPI's?		
Who make use of this KPI's?		
What corrective action(s) can be taken in case of significant deviation between measured and target?		
Where does the data come from? e.g. applications		
What is the reporting frequency of KPI? Monthly, quarterly etc.		

Figure 3: Example of KPI template

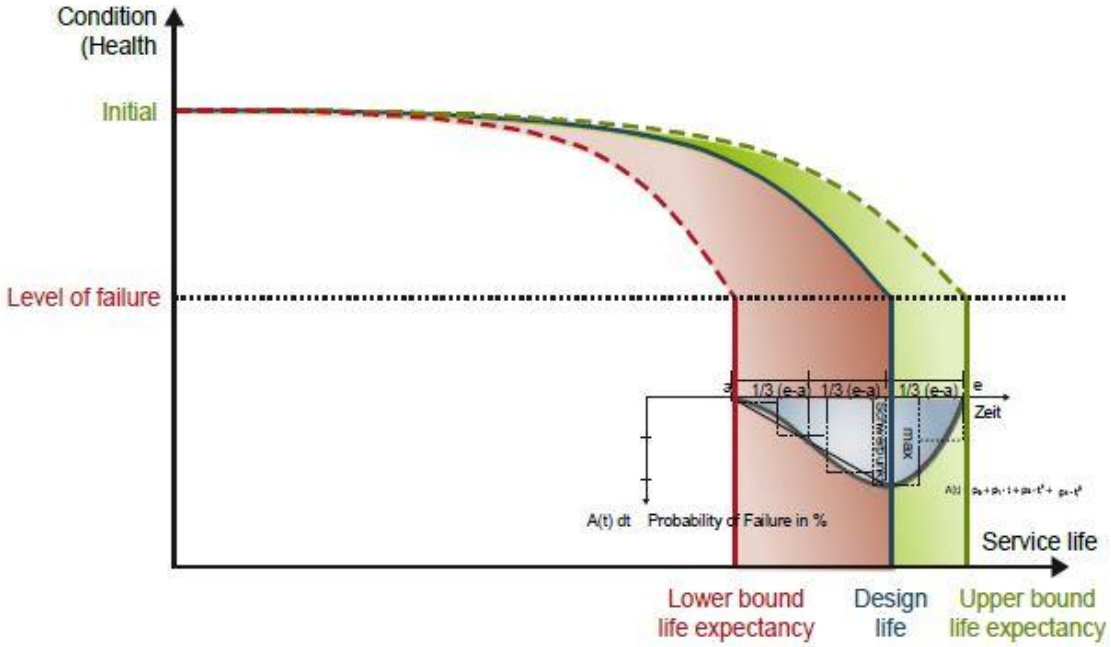

Figure 4. General concept of structural ageing

The ageing model: The risk based inspections are usually carried out in discrete time steps within the life cycle of an equipment. In order to describe the changes within a component, structures or industrial systems, it required a mathematical formulation of degradation (i.e. ageing) of the asset. Within CWA 63:2012 "*Ageing behavior of Structural Components with regards to integrated Lifetime Assessment and subsequent Asset Management of constructed Facilities*" an exemplary mathematical formulation has been proposed and accepted. It directly fits into asset management activities where the changes to a system within the period between two specific inspections are required to be determined.

The normal ageing prediction model involved certain uncertainties. Therefore, it is required to minimize the uncertainties in the prediction process in order to optimize the maintenance interventions. The used model inside the European standard is rather generic in order to enhance its application across various industrial domains. However, this adapted model allows incorporating the new knowledge about the system into the prediction process. The Figure 4 shows the generic ageing model for structures. This model can define the range of service life for structures by incorporating the various uncertainties and system's behavior into consideration.

The ageing process in general depends on following major sources of impact:

- Year of construction;
- Static system;
- Material;
- Cross section.

To describe the individual deterioration process properly, the following additional aspects are of relevance with regard to structural performance over time:

- Direct loading frequency (e.g. freight traffic volume);
- Direct loading intensity (e.g. level of freight traffic impact);
- Quality in manufacturing;
- Environment influences;
- Chemical exposure.

The following equations describe the lifeline-progression within a stated service life expectancy. The so-called deterioration capacity "$C_i\,(t)$" for a structure is determined by the expression as shown in the Eq. 1.

$$C_i\,(t) \;= C_l + \; a_n \times \; (S_i - S_l)^c \qquad \text{Eq. 1}$$

with

$$a_n \;= \; (C_F - C_l)/(S_F - S_l)^c \qquad \text{Eq. 2}$$

where

C_i	initial condition
a_n	slope of deterioration
S_i	current year of service life
S_l	initial year of service life
c	deterioration power exponent; empirical, constant value derived from sensitivity analysis for bridge components c = 3 is established
C_F	final condition (early-warning level)
S_F	final (assumed) year of service life.

4. Mapping the RBI practices: The RBI-Atlas

As mentioned earlier that one of the purpose of the new European RBI standard would be to harmonize the RBI practices/ regulations along with proving the RBIF and basic guidelines for the risk based inspections and practices. In order to collate the information about the RBI practices /regulations in various countries, the RBI-Atlas tool was developed. The RBI-Atlas is a web-based geographic information system (GIS) tool, that helps to collect the information about the RBI practices/regulations and constantly update them. The Figure 5 shows the initial screenshot of the RBI-Atlas highlighting the status of information related to RBI for a particular country. Further analyses have been carried out from the information gathered in the RBI-Atlas about the status of RBI in a region or in a country.

The RBI-Atlas has helped to identify the RBI status in a particular country or in a region and allowing future steps for their normalization. The three main equipment types are considered for each of the countries in the RBI-Atlas: pressure vessels, steam boilers and piping. The considered equipment classes helped to identify the differences in approach with respect to the inspection / maintenance activities. Moreover, three main inspection types are usually considered (external, internal and the hydraulic pressure test).

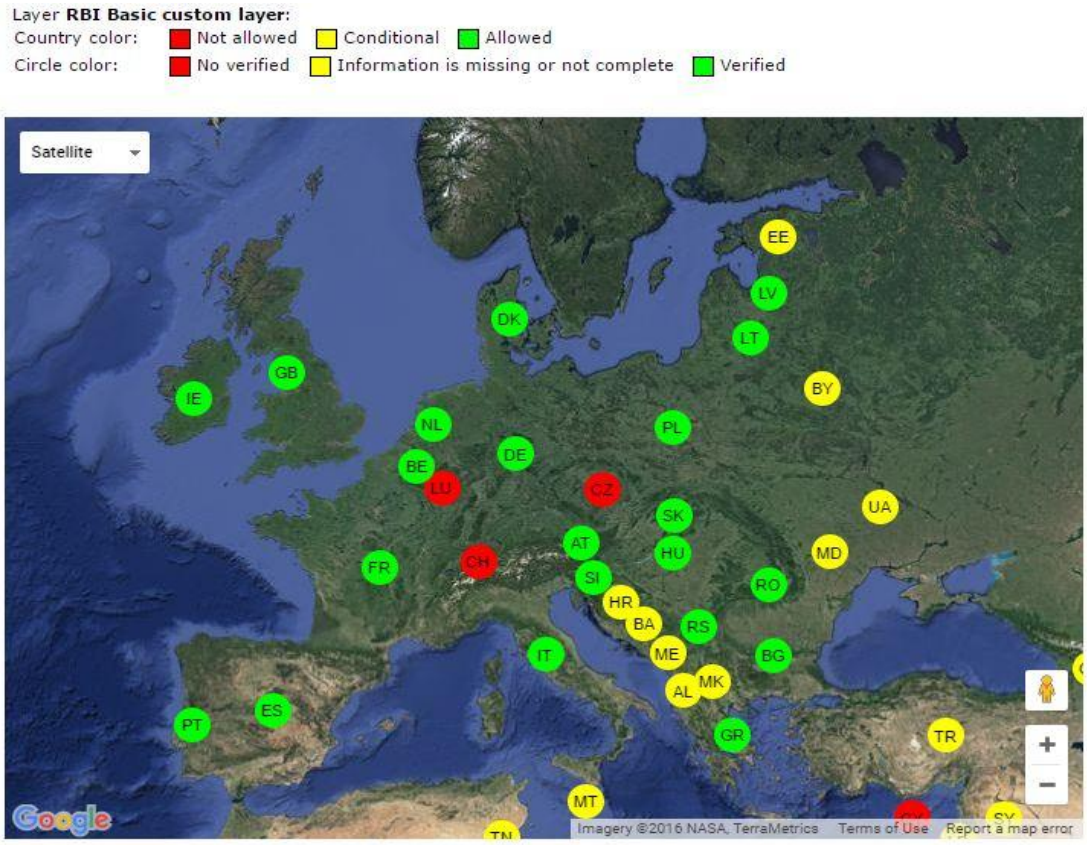

Figure 5. RBI-Atlas tool (http://www.rbi.risk-technologies.com/)

5. Conclusions

The new European standard can fulfill the requirements for the RBI normalization by defining the steps and procedures to carry out the RBI. The scope of this new standard is mainly the process, power and steel industry. However, other relevant industries can also be considered. But, it is limited to the non-nuclear application. The RBIM framework defined in the new Europeans standard is only applied to systems/equipment during the in-service phase of the operations. For the design or fabrication phase, the relevant legislations and engineering standards should be followed. If RBIM principles or procedures are used, it shall be ensured that all measures are in compliance with local and national legislation. The new European standard prEN 16991 helps to achieve the harmonization of the in-service maintenance activities that are still not harmonized throughout the European Union (EU). The inclusion of factors for qualitative analysis, key performance indicators (KPIs) and the ageing model to the new European standards is an important innovative element of the standard. The inclusion of these parameters enhances the optimization process of the RBI inspection and maintenance. Thus, the new European standard will not only provide harmonization to the risk based inspection and practices but also improve the overall process's productivity by minimizing the un-planned shutdowns and by optimizing the inspection and maintenance process. The approaches used in the standard are compatible with those of API [[13]], VGB [[14]], [[15]] or ASME and intended broadly for similar purposes. The RBI-Atlas can provide a user-friendly tool to provide the in-detailed and updated information about the RBI practices / regulation in various countries.

Acknowledgements

The support of organizations, which in the Working Group 12 of the CEN Technical Committee 319 at both the EU and the respective national level have supported the development of this standard is gladly acknowledged here.

References

[1] Jovanovic, A. (2008). EU RBI Guide document CEN CWA 15740:2008, API RBI European Workshop, Milan, Italy (The Equity Engineering Group, Inc., USA), October 27-31, 2008

[2] CEN CWA 15740:2008 Risk-Based Inspection and Maintenance Procedures for European Industry, CEN EU 2008 (Chair A. Jovanovic)

[3] Jovanovic, A. (2010) Role of Risk-Based Inspection when dealing with risks related to new technologies in industry. In: Proceedings for the 2nd International Conference on Reliability, Safety and Hazard - Risk based technologies and physics of failure methods. Mumbai, India. 14-16 Dec. 2010

[4] Jovanovic, A. (2010) Globalization aspects of Risk-Based Inspection and Reliability-Centered Maintenance practices world-wide. In: Proceedings for the RBE-5 5th International Workshop on Risk-Based Engineering. Convention Center University of Science & Technology, Beijing, China. Nov 16-18

[5] RIMAP WP4/D4.3 - “RIMAP Application Work book for the Chemical Industry”, by Rino van Voren, GROWTH project GIRD-CT-2001-03008 “RIMAP”, RIMAP RTD Consortium, Version: Rev. 0, (2003)

[6] RIMAP WP4 - “RIMAP Petrochemical workbook”, by Stefan Winnik, Andrew Herring, Rick Gregory, GROWTH project GIRD-CT-2001-03008 “RIMAP”, RIMAP RTD Consortium, Version: Rev. 1.1, (2003)

[7] EN ISO/IEC 17020 (ISO/IEC 17020) – “General criteria for the operation of various types of bodies performing inspection”, European Committee for Standardization (CEN)

[8] EN ISO/IEC 17025 (ISO/IEC 17025) – “General requirements for the competence of testing and calibration laboratories”, European Committee for Standardization (CEN)

[9] EN ISO/IEC 17025 (ISO/IEC 17025) – “General requirements for the competence of testing and calibration laboratories”, European Committee for Standardization (CEN)

[10] RIMAP WP3/I3.3 – “Assessment of Probability/ likelihood of failure”, by A.S. Jovanovic, P. Auerkari, R. Giribone, GROWTH project GIRD-CT-2001-03008 “RIMAP”, RIMAP RTD Consortium, Version: Rev. 10, (2004)

[11] RIMAP I3.2 - “Assessment of the Consequence of Failure”, by J. Heerings, A. den Herder, M. Johanson, J. Reinders,, GROWTH project GIRD-CT-2001-03008 “RIMAP”, RIMAP RTD Consortium, Version: Rev. 1, (2003)

[12] API 754:2010. Process Safety Performance Indicators for the Refining and Petrochemical Industries.

[13] ANSI/API RP 580 – “Risk-Based Inspection”, American Petroleum Institute (API), (2002); www.api.org/publications/

[14] Empfehlung zur Einführung Risikobasierter Instandhaltung VGB – KRAFTWERKSTECHNIK GmbH, 2004, ArtNr.:M130, existing English version: Recommendation for the introduction of Risk based maintenance ArtNr.:M130e

[15] VGB-Standard Condition Monitoring and Inspection of Components of Steam Boiler Plants, Pressure Vessel Installations and High-Pressure Water and Steam Pipes VGB-Standard- S-506-R-00;2012-03.EN Second edition (published 2012) (Formerly VGB-R 506e), VGB PowerTech e.V.

Implementing the principles of VGB-S-506 in risk-based inspection and maintenance in a German power plant

A. Jovanovic[1], S. Husta[1], J. Bareiß[1], K. Metzger[2], K. Maile[1]

[1] Steinbeis Advanced Risk Technologies, Stuttgart, Germany
jovanovic@risk-technologies.com

[2] Grosskraftwerk Mannheim AG, Mannheim, Germany
klaus.metzger@gkm.de

Abstract

The paper presents results of the RBI study (risk-based inspection) concept on components and welds of the main steam line of GKM (Grosskraftwerk Mannheim AG, Mannheim, Germany) Unit 8. The application was taking into account the principles of the Standard "Condition Monitoring and Inspection of Components of Steam Boiler Plants, Pressure Vessel Installations and High-Pressure Water and Steam Pipes" of VGB (VGB-S-506). The standard aims to provide guidance for implementing a concept to improve the inspection planning process with respect to the new (national) regulations and technical rules. One of the concepts (RBI/RBM-concept) based on the development in the European research project RIMAP – Risk-based Inspection and Maintenance Procedures for European Industry. On this basis, GKM started to study possible advantages/benefits of a combination of methods already used at GKM with RBI. The paper highlights the scope and practical aspects of the preliminary RBI assessment, the technical RBI process performed in the single phases of the process (the "multilevel" risk analysis), as well as decision-making procedure. It also shows possible contents of the Risk/RBI Report. One of the major outcomes of the study is the conclusion, independently of all the "usual" advantages of RBI related to safety and economy, that the RBI analysis significantly improves transparency of the component life assessment and management.

1. Introduction

Grosskraftwerk Mannheim Aktiengesellschaft (GKM) with a current installed gross capacity of 2,146 MWe has been operating one of Europe's most efficient coal-fired power stations in the South of Germany for over 90 years (Figure 1). GKM generates electricity for over 2,5 million people, trade and industry, as well as district heating for around 120,000 households via the environmentally sound and cost-effective principle of combined power and heat (CPH). GKM is also an important supplier of single-phase railway power for the DB Energie GmbH.

In 2015, Unit 9 with a capacity of 911 MWe was commissioned. Beside this new highly efficient ultra-supercritical unit, also rather old units are in operation. For these units - some of them already have reached end of designed lifetime – the inspection and maintenance of GKM is based on the long-term experience of own experts, but also on TÜV and/or other third party experts. Inspection is done using

adequate inspection methods according to the state of art and relevant German standards and guidelines, thus fixed inspection intervals are used [5].

Another cornerstone of the GKM strategy is the supervision of the quality of design/material/manufacturing during erection of power plant and - if needed - during repair and replacement of damaged/failed components.

Figure 1: GKM Mannheim site, at the beginning in the 1920s and today with an installed gross capacity of 2,146 MWe

Aim of the RBI study presented here [6] is the investigation of possible advantages/benefits of a combination of methods already used at GKM with the RBI approach, as concerning:

- the documentation of risk with increasing operation time, changing of operation modus and damage mechanisms,
- ranking of critical components,
- establishing of adequate inspection intervals and inspection tools,
- maintaining and managing expert knowledge.

It is in line with relevant German standards and guidelines (e. g. the VGB[1] guideline [1], and other related documents [7]) as well as new PED guideline 2014/68/EU [8] and the German Operational Safety regulation [9].

2. Scope of the RBI assessment

For carrying out this RBI study, the main steam line from Unit 8 / Boiler 19 was used, Figure 2. Unit 8 was put into operation in October 1992. It has approx. 150,000 operating hours. Inspections for the monitored components were carried out in accordance with the applicable rules and regulations and with the

[1] VGB PowerTech e.V. as a technical association for power and heat generation is a non-profit organisation and a voluntary association of companies of power plant operators and manufacturers

notified body (TÜV SÜD). Consequently, the detailed documentation was made available for the inspections carried out, and it was fully integrated into the RBI-based approach.

GKM Block 8 Kessel 19	Main Steam Line (A-System)
Commissioning date	Oktober 02, 1992
Operating hours	146409 (Juni 2015)
Design temperature	545°C
Design operating temperature	535°C
Design pressure	211 bar
Design operating pressure	190 bar
Material	X20 CrMoV 12 1 (1.4922)

Figure 2: Design and operating data of GKM unit 8 (boiler 19) and the main steam line (A-System)

For the implementation of this RBI study following 110 components and welds of the main steam pipe (A-system) were assessed, Figure 3:

- 80LBA01 BR010 (16 welds, 7 bends)
- 80LBA02 BR010 (16 welds, 7 bends)
- 80LBA03 BR010 (6 welds, 3 fittings)
- 80LBA04 BR010 (15 welds, 6 bends)
- 80LBA05 BR010 (14 welds, 7 bends)
- 80LBA11 BR010 (6 welds, 7 bends)

Data collected for the chosen components and welds for this RBI study:

- Material properties (e.g. average creep rupture strength for the component material and fatigue strength at given temperature)
- Previous inspection records (NDT), [10-15]
    - Ultrasonic wall thickness measurements on bends and straight sections at 12, 3, 6 and 9 o' clock positions (UWT).
    - Ovality checks acc. to VGB-R 508 L (Dim).
    - Hardness tests of base material on either side of the weld, and consumable weld material (HT).
    - Magnetic particle inspection (MP).
    - Replication on weld, and heat affected zone and base material upstream and downstream (Rep).
- Data from the on-line monitoring system (e.g. pressure, temperature)
- Performed calculations data (e.g. TRD codes 300/301/508) derived from
    - component geometry (e.g. inside diameter, wall thickness, design wall thickness, …)
    - design temperature and pressure
    - operating temperature and pressure
    - service time of the component (operational hours)

As a part of the Level 2 risk assessment, one of the factors considered is the calculated exhaustion of the individual elements or components, according to TRD 508 [16]. During the project, MPA Stuttgart has performed calculations on components belonging to Unit 8.

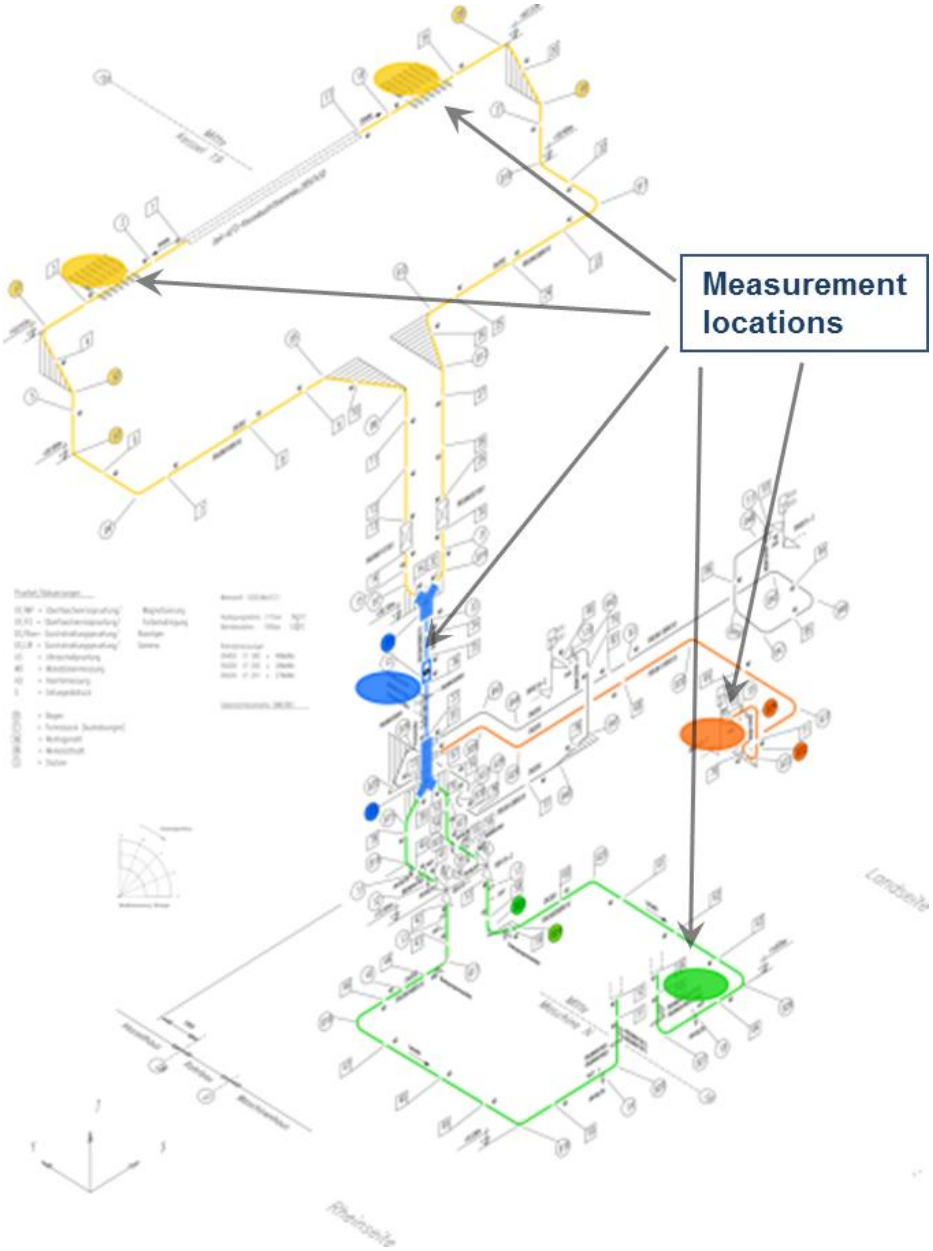

Figure 3: Main Steam Line (A-System)

3. The VGB-S-506 and RBI principles

The Standard “Condition Monitoring and Inspection of Components of Steam Boiler Plants, Pressure Vessel Installations and High-Pressure Water and Steam Pipes” from VGB PowerTech e.V. (VGB-S-506) aims to provide guidance for implementing a concept to improve the inspection planning process with respect to the new (national) regulations and technical rules. One of the concepts (RBI/RBM-concept) based on the development in the European research project RIMAP – Risk-based Inspection and Maintenance Procedures for European Industry. The RIMAP procedure [1] is applicable to many industries and to different types of equipment (for example static equipment, rotating equipment, safety systems, and elec-

trical/instrument equipment). The steps in the procedure are the same for all cases, even if the models and tools for assessing probability or consequence of failure may vary from one application to another [4]

The main results contained principles of the following sources:

- German regulation „Betriebssicherheitsverordnung“ [9]
- VGB-S-506 Condition Monitoring and inspection of components of steam boiler plants, pressure vessel installations and high-pressure water and steam pipes [1]
- CEN CWA 15740 Risk-Based Inspection and Maintenance Procedures for European Industry (RIMAP) [3], [17]
- RIMAP-based new EN, Risk-Based Inspection Framework [2]
- Good practice applied by GKM in this area [5]

4. Multilevel RBI assessment and results

The technical RBI process is performed in distinct phases as follows:

Data gathering

Level 1 – screening assessment

Level 2 – intermediate risk assessment

Level 3 – detailed risk assessment

This RBI study at GKM was limited to Level 1 and Level 2 of RBI. The level of risk is determined by means of a scorecard process with various risk influencing criteria, which are used to establish the relative risk of the components, Figure 4. Level 0 risk ranking of components represents an initial assumption of the risk, based on selecting a Generic Failure Frequency (GCC) and a Generic Consequence Class (GCC), from literature (statistics) and experience in the industry, Figure 5.

After the initial Level 0 assumptions, the assessment moves to Level 1 (screening) analysis. At this level, each component (or sub-component) is assessed (score assigned) according to a set of probability modifying and consequence defining factors, adapted from VGB S-506, see Chapter 3. The probability-affecting factors modify the initial GFF assumed on Level 0, to obtain a more accurate Probability of Failure (PoF). The initially assumed GCC is superseded by a Consequence of Failure (CoF) score obtained by answering the consequence factor questions. The combination of this PoF and CoF gives the relative risk of the component on Level 1, Figure 6.

Based on the assessed risk of the components an action is selected, in accordance with the screening matrix and procedure adapted from DNV RP-G-101 [18], shown in Figure 8 below. The action for Level 1 is typically to subject the high risk components to more detailed Level 2 assessment, in order to better ascertain the risk and determine the appropriate actions. Medium risk components fall into two groups:

1. Level 1 components which have a medium risk resulting from a combination of very low or negligible consequences, and a higher probability generally fall into the category of nuisance events. Inspection can be applied to these components to reduce the risk, but it is unlikely to be cost effective, and the cheapest solution is often to carry out corrective maintenance when they fail. They may be assessed on Level 2, in order to obtain a more accurate risk score, but it is not absolutely necessary.
2. Level 1 components which have a medium risk resulting from a combination of non-negligible to severe consequences, and a low probability of failure should be considered for inspection and preventive maintenance, to ensure continued low probability. The consequence of failure for these components is high, and changes in conditions can increase the PoF and result in high risk. These components have to be subjected to Level 2 assessment, in order to determine the correct course of action.

The typical results of this analysis include:

- Risk matrix, as shown in Figure 10.
- Risk maps of the assessed system, showing the risk of individual components and component parts on an operator-provided drawing, as shown in Figure 11.

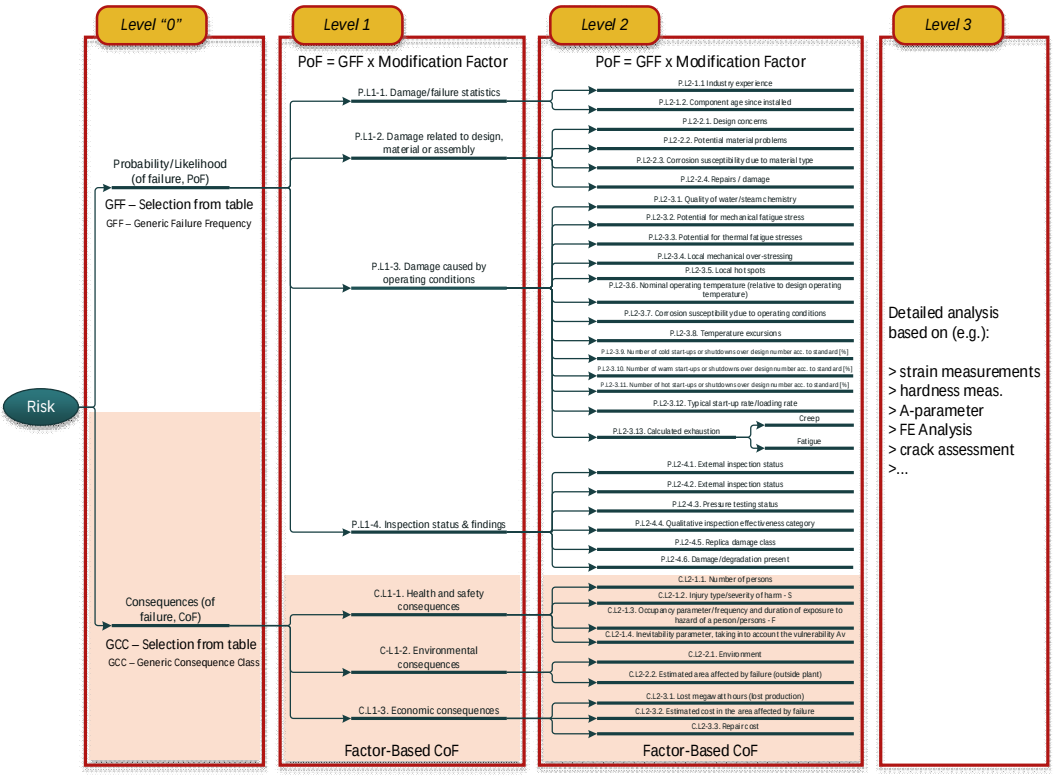

Figure 4: Multilevel risk analyses of GKM RBI procedure (overview)

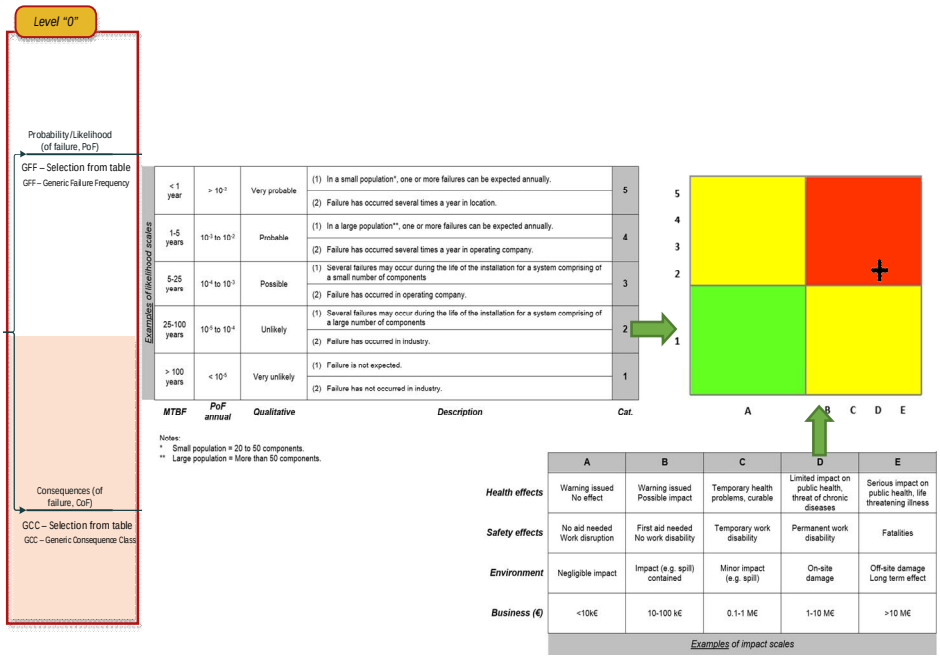

Figure 5: Level 0 with initial expert-based assumption of Generic Failure Frequency (GFF) and Generic Consequence Class (GCC) for component or location (e.g. weld)

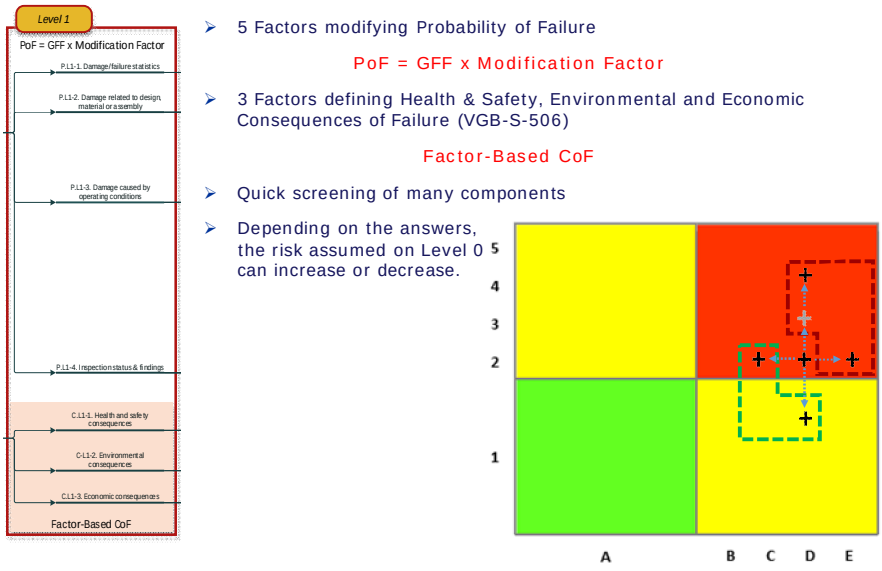

Figure 6: Level 1 (screening) based on Level 0 risk assumption by modifying PoF and CoF

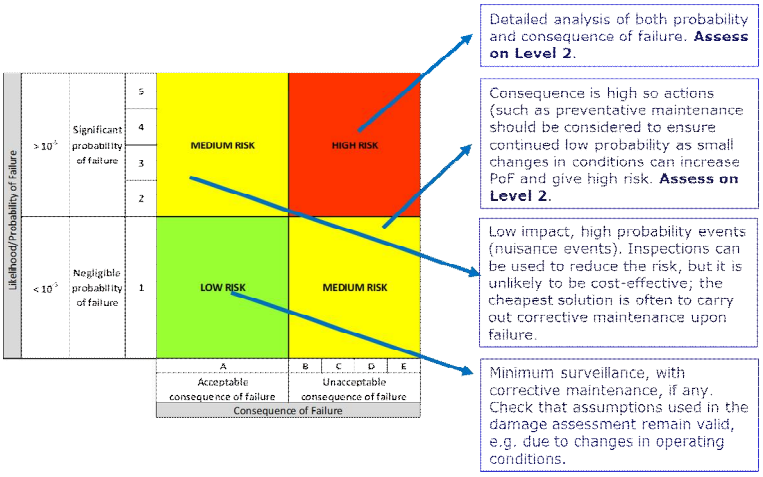

Figure 7: Examples of action resulting from Level 1 (screening) assessment

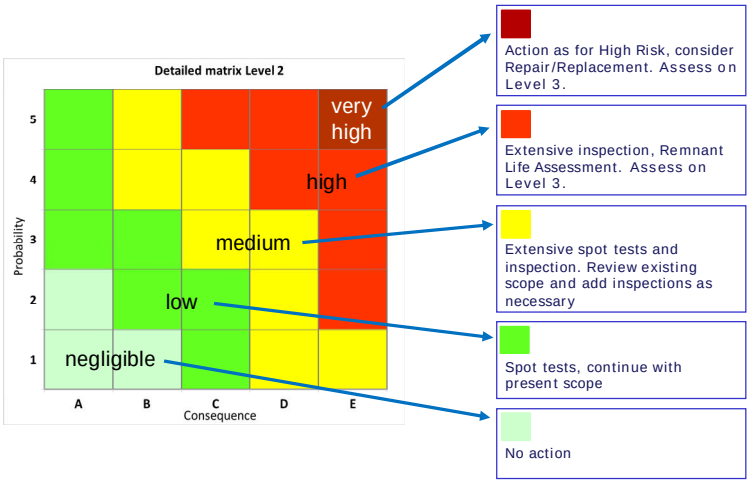

Figure 8: Decision making procedure Level 1, 2 and action planning Level 2

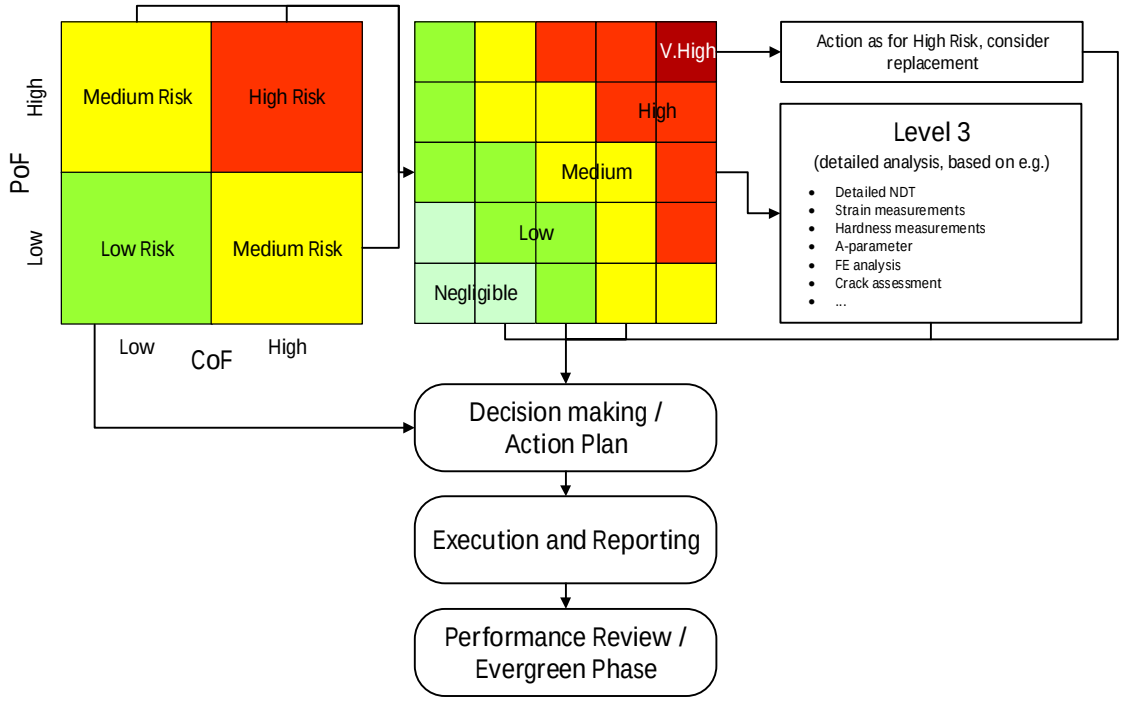

Figure 9: Decision making procedure Level 1, 2 and action planning Level 2 and Level 3

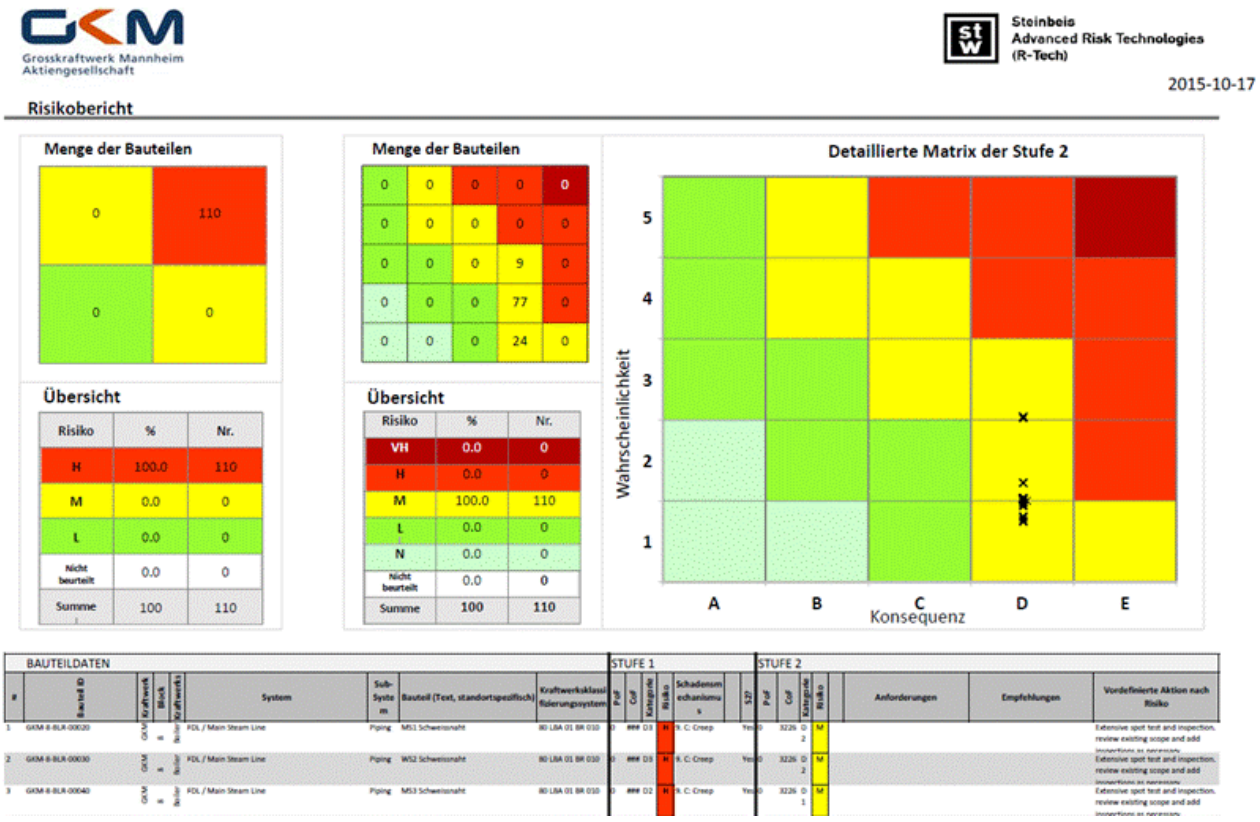

Figure 10: Example contents of a Risk Report (overview of all components)

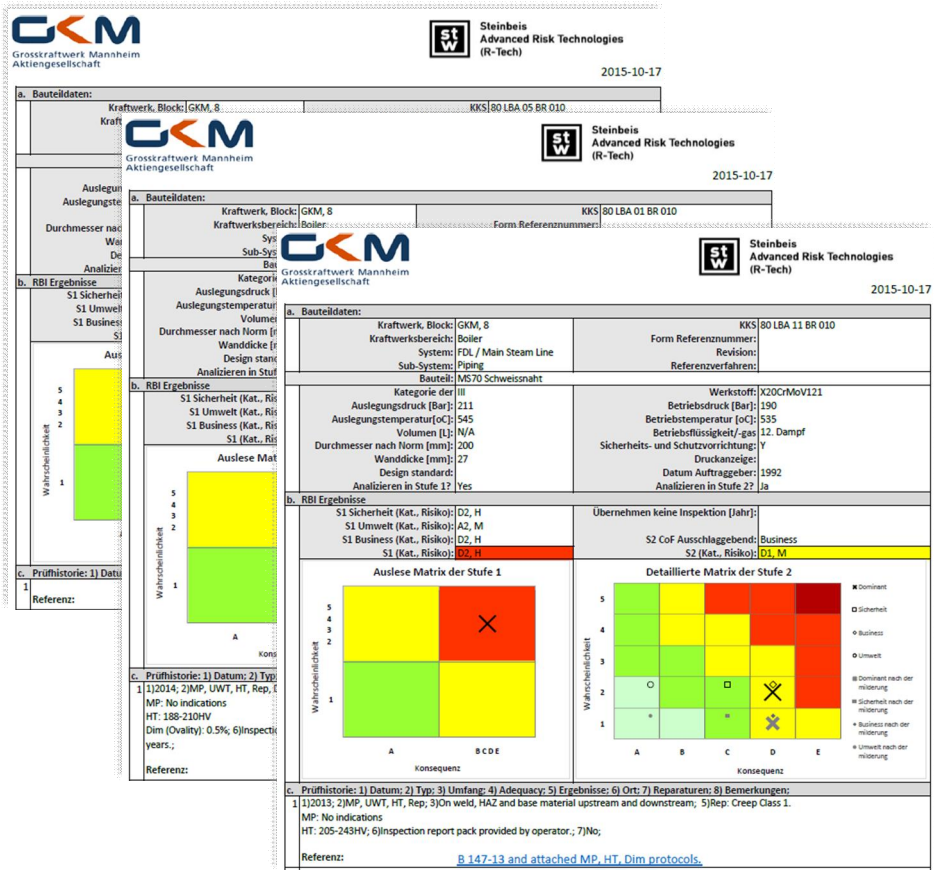

Figure 11: Example contents of a Risk Report (individual component summary)

5. Conclusions

The RBI study presented in the paper shows that RBI is a useful tool to structure data and knowledge needed to complete the already existent and proven inspection strategy and methods at GKM in a meaningful way. Combining the RBI approach with the standard practice at GKM and conventional life management and inspection methods, it was possible to identify, rank and analyze the critical components in a more transparent and structured way. The “good practice wisdom” and in-house expertise applied so far have been extended in a meaningful and useful way. RBI, as a quantitative and systematic approach bridges the gap between the qualitative principles of good asset management, on one side, and the structured, quantitative and IT-oriented data management. Most importantly, this RBI study has shown that the results of the RBI analysis are compatible with the approach applied so far in GKM and the position of the notified body. Another major outcome of the study is the conclusion, independently of all the “usual” advantages of RBI related to safety and economy, that the RBI analysis significantly improves transparency of the component life assessment and management.

Possible future application of RBI should include the analysis of the GFFs (Generic Failure Frequencies), for the plant components that could be possibly improved based on the data available in the KISSY database of VGB[2].

Acknowledgements

The authors wish to acknowledge the support provided for this work by the utility company GKM Mannheim, Germany and the TÜV SÜD Mannheim, Germany.

[2] https://www.vgb.org/en/kissye.html

References

[1] VGB-Standard Condition Monitoring and Inspection of Components of Steam Boiler Plants, Pressure Vessel Installations and High-Pressure Water and Steam Pipes VGB-Standard- S-506-R-00;2012-03.EN Second edition (published 2012) (Formerly VGB-R 506e), VGB PowerTech e.V.

[2] CEN TC 319 WI 0031902x:2015 Risk Based Inspection Framework (Work item for the new EN Standard)

[3] CEN CWA 15740:2011 Risk Based Inspection and Maintenance Procedures for European Industry (RIMAP)

[4] RIMAP Application Workbook for Power Industry PART II: System / Component related considerations, item by item

[5] Schröder, H.C., (1998). Prinzipielle Überlegungen zur Bewertung und Überprüfung von älteren Kraftwerksanlagen (Basic Considerations for Assessment and Inspection of Older Power Plants), VGB KraftwerksTechnik 78. Jahrgang, Heft 9/98, Seite 38-47

[6] Steinbeis Advanced Risk Technologies GmbH. (2015). Pilot Implementation of Risk-Based Inspection (RBI) at Grosskraftwerk Mannheim, Stuttgart

[7] VGB-TW 507:1992 Guideline for the Assessment of Microstructure and Damage Development of Creep Exposed Materials for Pipelines and Boiler Components

[8] Directive 2014/68/EU of the European Parliament and of the Council of 15 May 2014 on the harmonization of the laws of the Member States relating to the making available on the market of pressure equipment (former directive 97/23/EC)

[9] Verordnung über Sicherheit und Gesundheitsschutz bei der Verwendung von Arbeitsmitteln (Betriebssicherheitsverordnung - BetrSichV), 3. Februar 2015 (BGBl. I S. 49), Ersetzt V 805-3-9 v. 27.9.2002 I 3777 (BetrSichV)

[10] replica Ingenieurbüro für zerstörungsfreie Werkstoffprüfung GmbH. (2014). Inspektionsbericht B 126 / 14 Block 8, Engelskirchen

[11] replica Ingenieurbüro für zerstörungsfreie Werkstoffprüfung GmbH. (2013). Untersuchungsbericht B 147 / 13 Block 8 / Kessel 19 A- und F- Leitung Ü4 Austrittsammler Zue2 Austrittsammler, Engelskirchen

[12] replica Ingenieurbüro für zerstörungsfreie Werkstoffprüfung GmbH. (2011). Untersuchungsbericht B 192 / 11 Block 8 / Kessel 19 A- und F- Leitung, Engelskirchen

[13] Grosskraftwerk Mannheim. (2008). Aktennotiz 10 / 08 IK / QS – Revisionsarbeiten Block 8 / 2008, Mannheim

[14] replica Ingenieurbüro für zerstörungsfreie Werkstoffprüfung GmbH. (2004). Bericht B 173 / 04 über metallographische Untersuchungen an diversen Bögen, Sammlern und einem Fornstück von Block 8, Engelskirchen

[15] Grosskraftwerk Mannheim. (2004). Aktennotiz 34 / 04 IK / QS – Revisionsarbein Block 8 / 2004, Mannheim

[16] TRD 508 Inspection and Testing - Additional tests on components, calculated with time dependent design strength values

[17] A. Jovanovic, J. M. Bareiss, P. Stanojevic & Liu Yan. Risk-Based Inspection (RBI) in fossil-fuel fired power plants: Developing further the EU approach and applying it in the large-scale projects. Baltica IX “International Conference on Life Management and Maintenance for Power Plants”. 11–13 June, 2013, Helsinki–Stockholm–Helsinki

[18] DNV-RP-G101:2010 Risk Based Inspection of Offshore Topsides Static Mechanical Equipment

[19] VGB TW 104 VGB Research Project 361, Reliability Indicators with KISSY (VGB Power Plant Information System), VGB PowerTech Service GmbH Verlag technisch-wissenschaftlichen Schriften, Essen, ISBN 978-3-86875-751-4

Full-scale implementation of an integrated RBI-RCM system in a refinery

Svetozar Eremic[1], Aleksandar Jovanovic[2], Stefan Husta[2] & Nikola Markovic[2]

[1] NIS Gazprom Neft, Serbia
svetozar.eremic@nis.eu

[2] Steinbeis Advanced Risk Technologies, Germany
jovanovic@risk-technologies.com

Abstract

The paper presents results of the implementation of an integrated RBI/RCM (Risk-Based Inspection / Reliability-Centered Maintenance) system on a large scale, covering one entire refinery (Pančevo, Serbia). An integrated RBI-RCM software system was custom-developed, to accommodate the requirements of the user, based on the principles of API Recommended Practices for Risk-Based Inspection (API 580, API 581) and the European document RIMAP - Risk Based Inspection and Maintenance Procedures for European Industry (CEN CWA:15740:2008/2011). The paper highlights the elements of the full-scale application of the integrated RBI-RCM tool to analyze large amounts of data (about 15,000 components) and enable risk-based and risk-informed decision making related to inspection and maintenance optimization and prioritization. The system was applied in the conjunction with a computerized maintenance management system (CMMS) and, apart from providing the direct benefits of RBI/RCM, brought additional benefits related to better structuring and organizing large amounts of asset data from different sources centrally.

1. Introduction

The Petroleum Refinery in Pančevo (RNP – Rafinerija Nafte Pančevo) is the largest producer of crude oil products and the largest refinery in Serbia, with a crude oil processing capacity of 4.8 MTY. The main construction work on the refinery was carried out in the period between 1968 and 1975 in two phases: Crude Distillation Unit I was commissioned in 1968, and Crude Distillation Unit II was commissioned in 1975. Since then, several extensions have been carried out, with the aim to increase capacity and process complexity and the main are FCC complex – 1984 and MHC/DHT – 2012. The refinery contains an integrated truck-loading terminal, a railway station with facilities for crude oil delivery and dispatch of products and jetties.

The refinery has been mainly supplied by crude oil through a pipeline connection from the island of Krk (Croatia) to Pančevo, with a capacity of 6 MTY, and by ship on the Danube River. The majority of processed crude oil is imported, and the refinery units are predominantly designed for Russian (Ural) and Iraq (Kirkuk) crude oil. The main products groups of the refinery include Liquefied Petroleum Gases, Gasoline, Paraffin Solvents, Aromatics, Kerosene, Diesel Fuel, Fuel Oils, Bitumen and Other products (liquid sulfur, solvents, diluents). In 2015, the total refinery staff numbered approximately 800 people.

During the 1999 bombing of Yugoslavia, the refinery was damaged, causing a stop of production until the second half of 2001, when processing was rebuild and restarted with a production of approximately 3-4 MTY of products.

Figure 1: NIS Gazprom Neft Petroleum Refinery Pančevo

As part of the contract with the refinery, the consultant (Steinbeis R-Tech) developed and implemented the iRiS system (integrated Risk Management System,, applied for Petrochemical Plants ("iRiS-Petro") and for power plants ("iRiS-Power"), [1], [2], [3]), comprising of 3 main elements/modules:

- The RBI module, which allows the user to perform qualitative, semi-quantitative and fully quantitative risk assessment of static equipment and pressure vessels, in accordance with API580 [4], RIMAP [5] and API 581 [6], [7]
- The RCM module, which allows for reliability-centred assessment and maintenance of rotating equipment, in accordance with the guidelines and procedures specified by NIS Gazprom Neft
- The NDT module, which allows for the assessment, monitoring and prediction of corrosion rates and remaining life of piping and process equipment, in accordance with NIS Gazprom Neft internal guidelines [8]

2. Scope of the implementation

The scope of the implementation encompassed the entire refinery, including approximately 15,000 components. In addition to the further development and customization of the tool, the project foresaw the data collection, input and Level 1 (screening) RBI analysis actions. The data collection and import action of pressure equipment and piping for the RBI, RCM and NDT modules resulted in the following numbers of components, tied to the respective modules, in the system database:

- approx. 9,600 components, as well as all process, steam/water and auxiliary piping tied to the NDT module
- approx. 1,500 components, including pumps, compressors and turbines tied to the RCM module
- approx. 15,000 components, including equipment also covered in RCM/NDT, tied to the RBI module

The RBI (screening), RCM and NDT (remaining life based on wall thickness) analysis of these components was automatically performed in the respective modules where possible, depending on the amount of data provided/collected, following import into the database. An overview of the component types covered (at the moment) in relation to the total sum is given below in Figure 2.

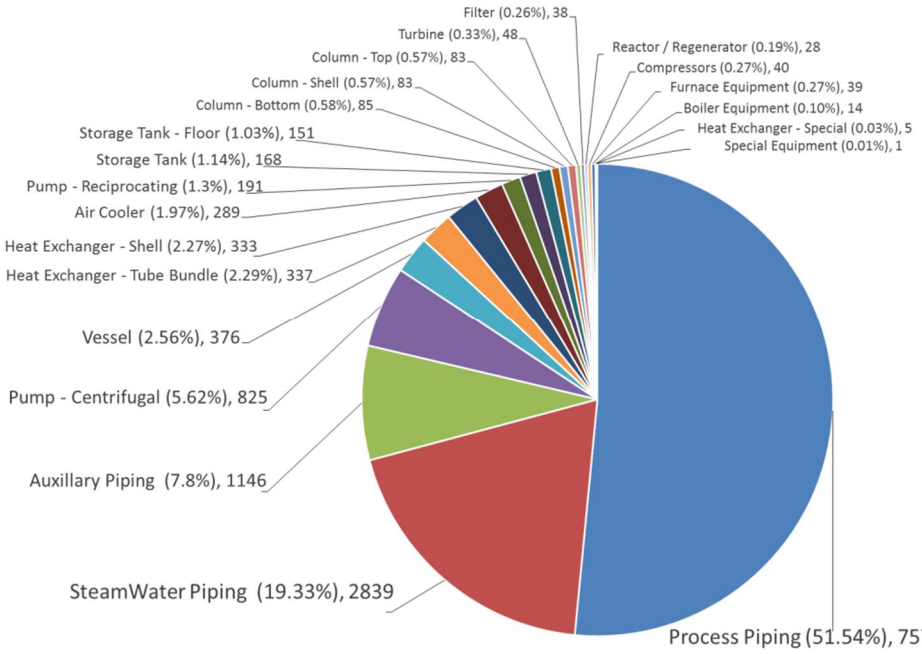

Figure 2: Breakdown of component types uploaded into the system database, by number and percentage

The integrated system provides:

- A hierarchical “tree” overview/organization of the refinery, areas, individual process units and components (and their respective analyses)
- A search and compare function which allows the identification of components by design, operating and analysis-related criteria, and the comparison of any number of components

The hierarchical “tree” view might be the most obvious and practical solution for navigation and locating individual components and their associated analyses. Starting from the whole refinery (RNP, Figure 3), it is possible to focus onto the area of interest (e.g. GP2, Figure 3), and then select the respective process unit with its components (e.g. S2300, Figure 3). Once when the target component is found, the analyses performed for that component, and the attached documents are visible (e.g. DC-2301, Figure 3).

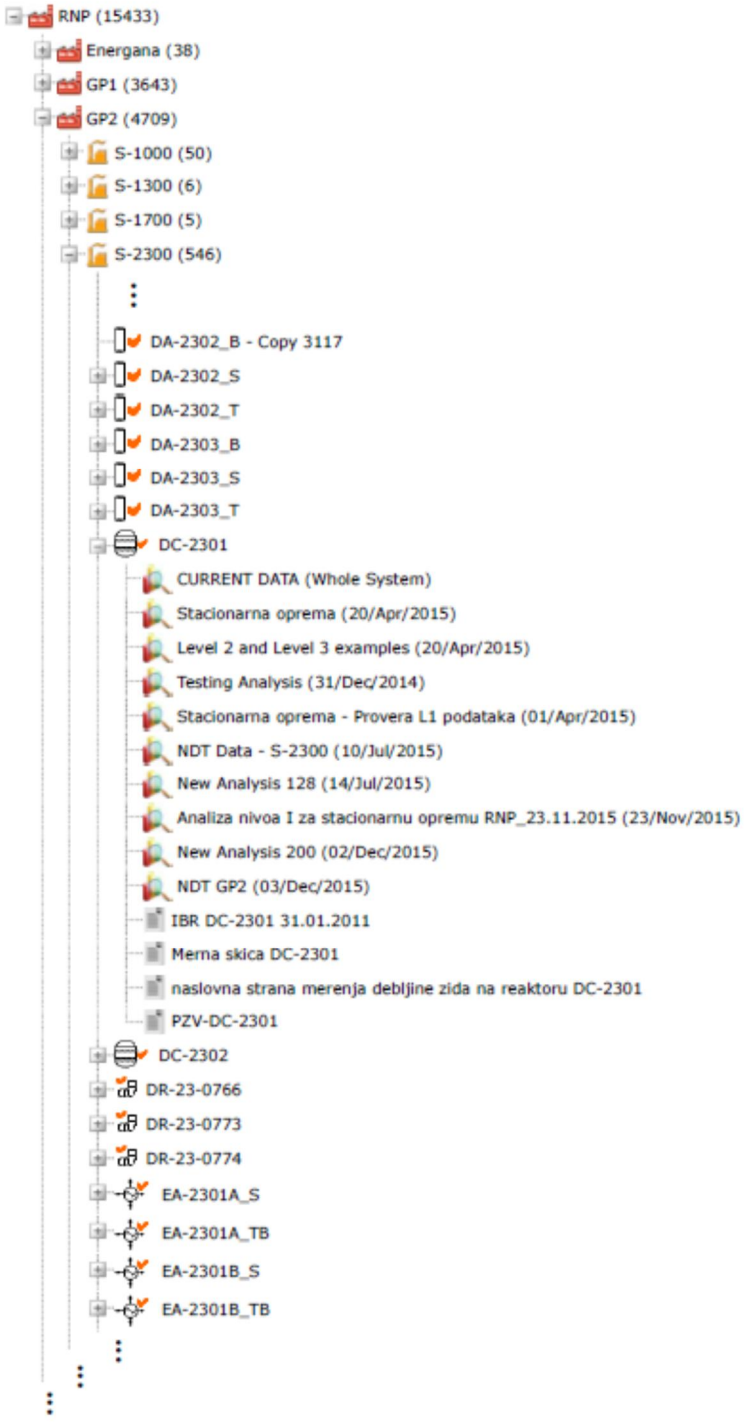

Figure 3: Organization of the refinery, areas, process units and components in the tree structure.

The Search and comparison function could be the most practical solution, if a component is searched for according to any design, operating or analysis-related criteria (or any combination thereof), including the items such as name, type, commissioning date, temperatures and/or pressures (design/operating), risk (e.g. only “high risk”), etc.

If more components corresponding to the input criteria are found, they can be compared. This can be beneficial for the analysis of any new components, when similar (by type, service) already assessed components can be used as a starting point.

SEARCH COMPONENTS PREVIEW

Risk Matrix	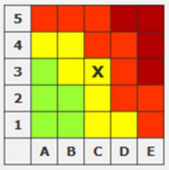	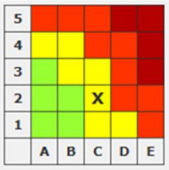	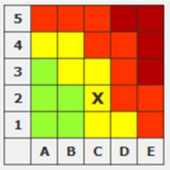
Analysis Name	Testing Analysis	Stacionarna oprema - Provera L1 podataka	Stacionarna oprema - Provera L1 podataka
RBI Level	Level III - Quantitative	Level I - Qualitative	Level I - Qualitative
Equipment Name	**DA-2302_T**	**DA-2303_B**	**DA-2303_S**
Equipment Type	Column - Top	Column - Bottom	Column - Shell
ProcessUnitPID	S-2300	S-2300	S-2300
Description	LCGO Stripper	STRIPER KOLONA	STRIPER KOLONA
Service Start Date	1984	1985	1985
Consequence Category	C	C	C
Likelihood Category	3	2	2
Risk	Medium	Medium	Medium
Consequence of Failure [m2]	274.00		
Likelihood of Failure [events/year]	0.0140		
Risk Area [m2/year]	3.84		
Financial Risk [€/year]	27,428.44		
Material	Carbon Steel - Carbon Steel	Carbon Steel - Carbon Steel	Carbon Steel - Carbon Steel
Outer Diameter [mm]	1370	1418	1418
Length [m]	7.9	8.3	8.3
Wall Thickness [mm]	12	12	12
Corrosion Allowance [mm]	2.5	6.4	6.4
Post-Weld Heat Treated	✔		
Insulated	✔		
Design Temperature [°C]	277	302	302
Design Pressure [bar]	3.6	3.5	3.5
Operating Temperature [°C]	200	270	270
Operating Pressure [bar]	1.1	1	1

Figure 4: Comparing searched components.

3. Assessments and results

The main goal of the risk-based methodologies such as RBI is to classify the components in classes according to their risk level and define the inspection and maintenance activities according to this level. Practically it means to map the components in the risk matrix according to the predefined risk levels (in the case of NIS into 4 categories: “low risk”, “medium risk”, “high risk” and “very high risk”, Figure 5). For Level 1, a basic qualitative inspection plan was automatically generated for the assessed components, providing suggestions for inspection intervals based on the risk level, in accordance with API 581 (Figure 6). Following more detailed analysis of screened “high risk” components, it is possible to semi-automatically generate a more detailed suggested inspection plan, following the principles of API 581 ([6], [7])

		9179 (62%)	1234 (8%)	4061 (28%)	184 (1%)	31 (0%)	14689
LIKELIHOOD	5	2	2	18	3	2	27 (0%)
	4	369	369	169	12	2	921 (6%)
	3	3819	11	2313	39	1	6183 (42%)
	2	3558	848	682	127	25	5240 (36%)
	1	1431	4	879	3	1	2318 (16%)
		A	B	C	D	E	
		CONSEQUENCES					

Low - 9660 (66%) | Medium - 4626 (31%) | High - 395 (3%) | Very High - 8 (0%)

Figure 5: Example of the distribution of all components in the risk matrix (here: example Level 1)

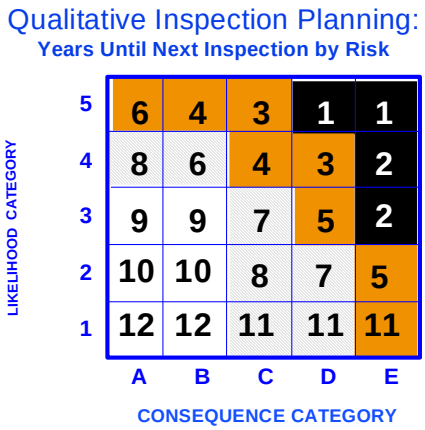

Figure 6: Qualitative inspection planning according to API 581 (numbers represent suggested inspection intervals in years).

Levels II and III

No.	Name	Type	Insp. Type	Insp. Effect.	Insp. Subtype	Inspection Description	Insp. Year	Risk
1	23-0102	Piping > 16"	SCC	B	Unknown	Dye penetrant testing.	2015	Very High
2	23-0102	Piping > 16"	Piping_Fatigue	A		Piping hanger survey. Check for vibrations and movement. Piping fatigue inspection in the form of ultrasoni8c crack detection is not effective and does not contribute to a reduction of the TMSF. The user should concentrate on mitigating the conditions which can cause Fatigue.	2015	Very High
3	DA-2301_B	Column - Bottom	Lining	A		Automatically suggested inspection. Internal visual inspection of lining.	2015	High
4	DA-2301_B	Column - Bottom	Thinning	B		Internal visual examination of 20% of surface, if possible during accompanying liner inspection, and spot external ultrasonic thickness measurements.	2015	High
5	DA-2302_B	Column - Bottom	Thinning	A		Automatically suggested inspection Internal visual examination of 50% of surface, and ultrasonic thickness measurements.	2015	High

Figure 7: Example inspection plan based on Level 2 and Level 3 (quantitative) assessment in the system.

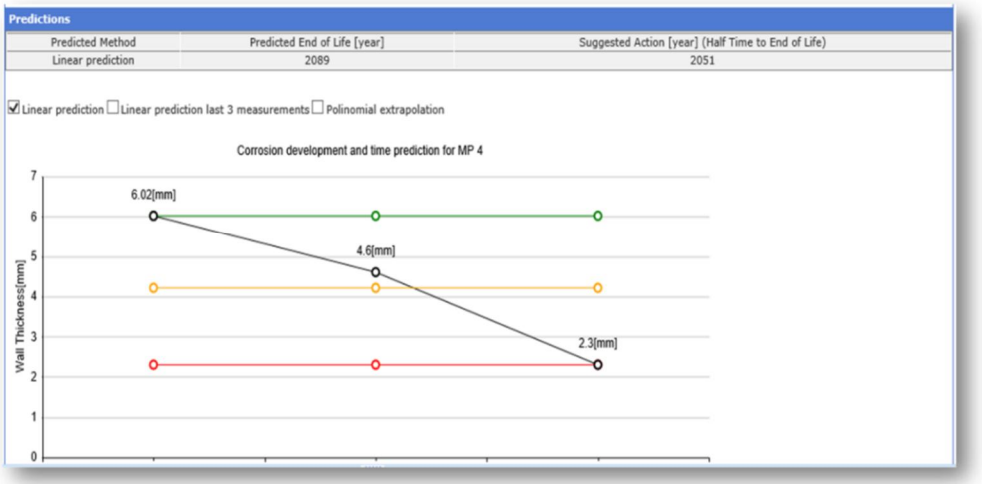

Figure 8: Corrosion rate and remaining life prediction in the NDT module.

The main goal of the assessments in the NDT module is the prediction of equipment remaining life based on corrosion rates derived from consecutive wall thickness measurements, as per NIS guidelines [8]. The corrosion rate results obtained from measurements and prediction can be the basis for more accurate inputs for the calculation of time-dependant corrosion-type damage mechanisms (Figure 8) in RBI.

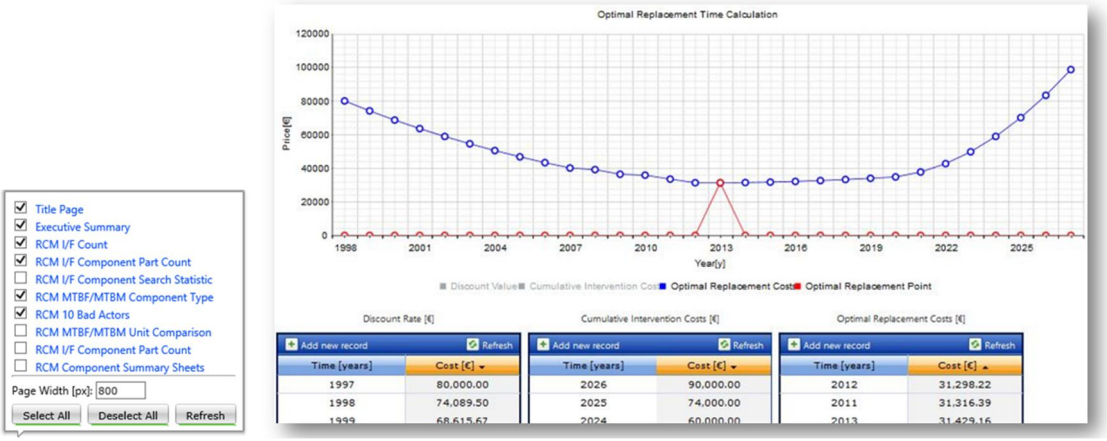

Figure 9: Determination of optimal replacement time in the RCM module

The goal of the RCM analyses is to determine Mean Time Between Failure/Maintenance (MTBF/MTBM) from collected intervention and replacement records, according to standing NIS guidelines, as well as to suggest an optimal replacement time, based on planned and unplanned repair/replacement costs associated with the equipment, derived from Glasser's optimal replacement equation [9].

4. Risk-Based Decision Making

RBI and RCM represent optimal maintenance concepts. The various functionalities of the Financial Risk Module in the integrated system can be used to aid the operator in the decision making process, related to the planning and prioritization of inspections and maintenance at the plant.

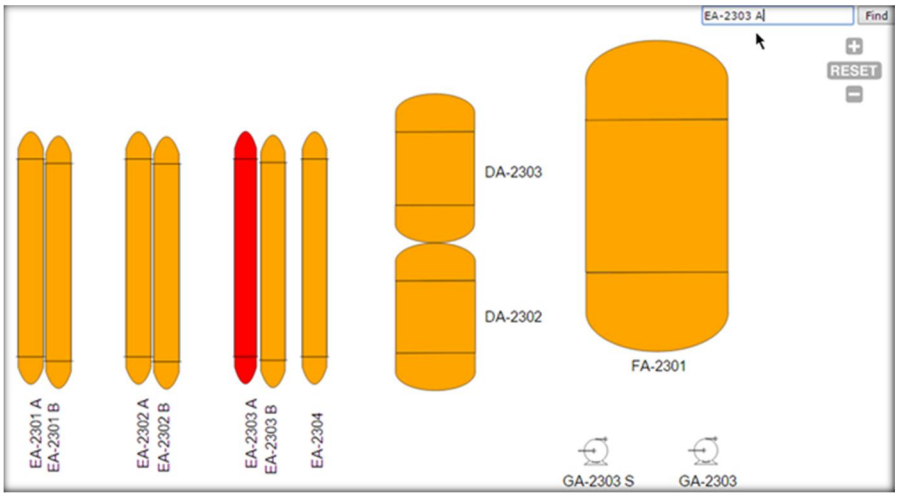

Figure 10: Overview of risk in the risk map (red component – the most critical one)

A high-level overview of the risk or damage progression is possible through the application of appropriate maps tied to the results obtained in the modules. In the case of RBI, it is possible to plot the risk associat-

ed with individual pieces of equipment (or entire process units/areas) in overlays on refinery arrangement drawings (Figure 10). Similarly, in the case of wall thickness results in the NDT module, the criticality of individual measurement locations can be indicated on attached equipment/piping isometric drawings (Figure 11).

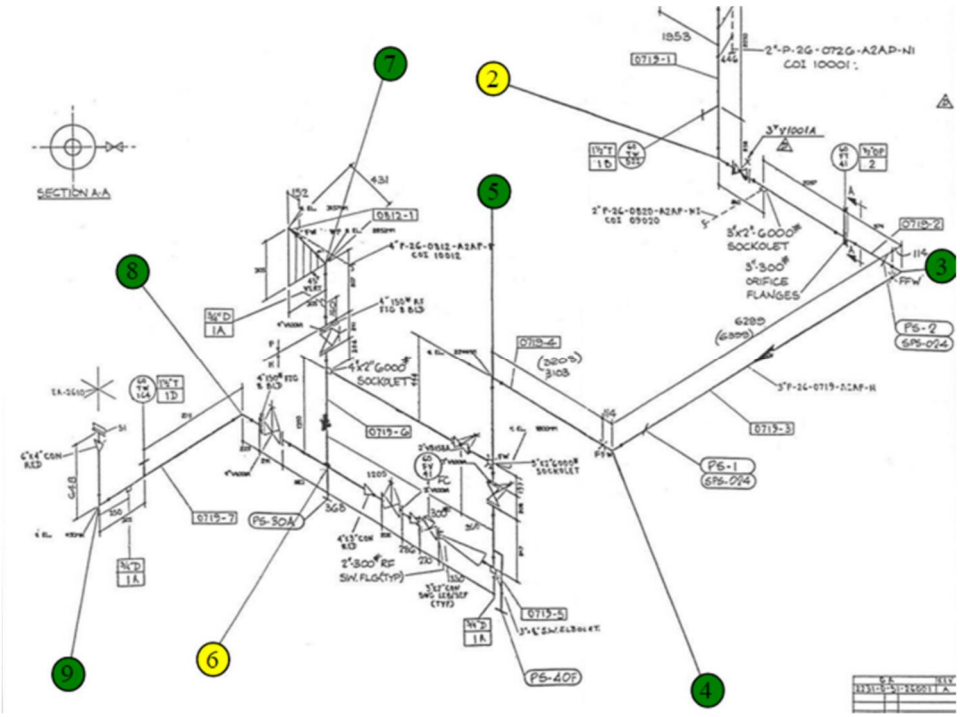

Figure 11: Overview of measurement location criticality in the NDT module

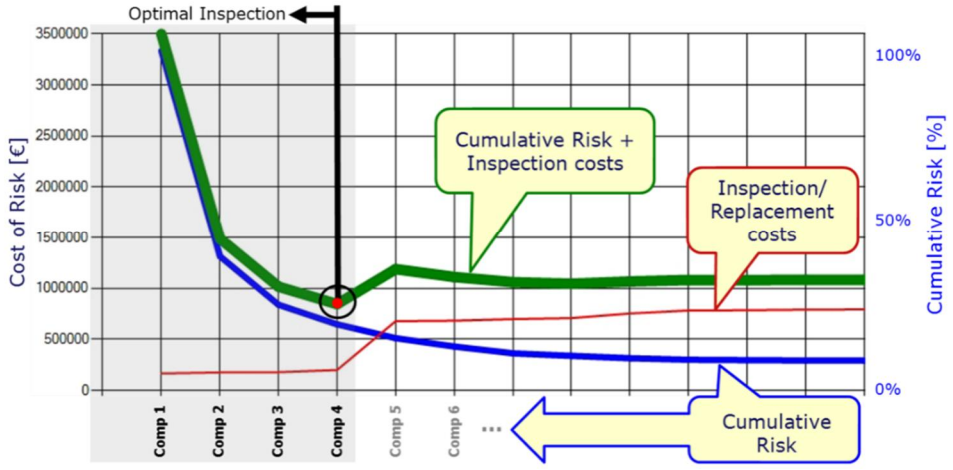

Figure 12: Optimizing inspections through the Financial Risk Module

The Financial Risk Module of API 581, as implemented in the system, allows the operator to view the financial impact of the risk of all of the components covered by an analysis, as well as the financial impact (gain) which can be obtained through the reduction of risk by taking the appropriate action on individual components (Figure 13). The Financial Risk chart, as implemented in the system (Figure 12), allows for the optimization of actions/inspections. This diagram considers that cumulatively, the cost of actions always increases, as more components are added to the scope of work. On the other hand, the cumulative risk decreases through actions taken to reduce the risk in individual components. The sum of the cumula-

tive risk line and the cumulative inspection/action cost line gives a function which can have a minimum (Figure 12), in the vicinity of the point where the cumulative inspection cost line intersects with the cumulative risk line. The minimum of this function represents the optimal inspection limit.

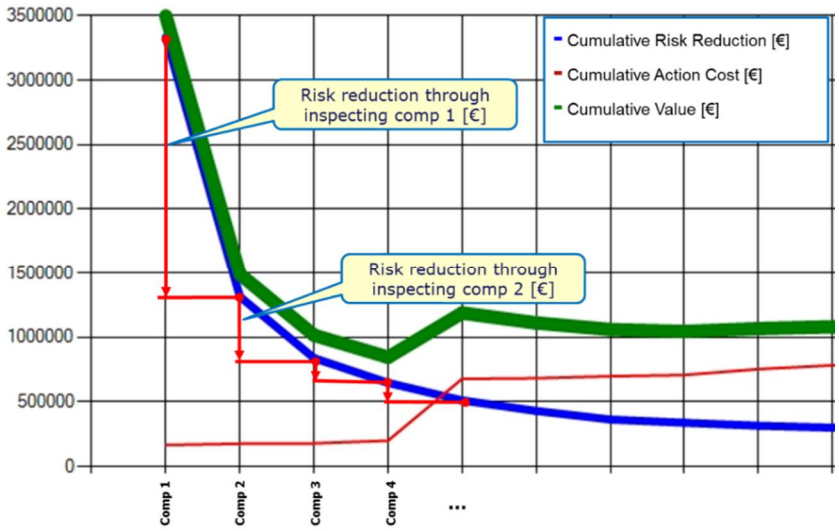

Figure 13: Diminishing risk reduction through inspection of additional components

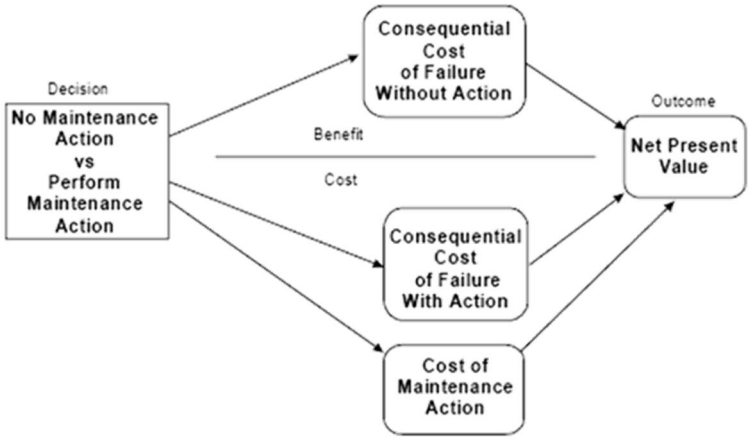

Figure 14: Basic concept of Gain-Loss and Net Present Value

The most common representations of risk in API 581 are Area-Based Risk [m^2/year], and Financial-Based Risk [€/year].The Financial-Based Risk representation provides the possibility to express a component's Net Present Value (NPV) in the function of risk (Figure 14). This Gain-Loss diagram (Figure 16), serves as another tool to aid in the decision making process, when prioritizing and planning inspections/actions. The Gain-Loss diagram works on the basis of the calculation of risk from the current RBI Date to the Plan End Date, and shows the potential benefits obtained through risk reduction by inspection, and the potential losses incurred through increase in risk, with no action taken, for each component. The difference between the gain and loss represents the component Net Present Value. As shown in the Gain-Loss diagram (Figure 15), several cases can be distinguished:

1. Components with high gains though inspections performed until Plan End Date, and high losses, if no inspection are performed

2. Components with losses at Plan End Date, no matter whether inspected or not. These are components with increasing risk, regardless of inspections, e.g. components approaching the end of their useful life
3. Components with very little gain through inspection, and small losses, if no inspections are performed. These are components with a stable risk level, and additional inspections before Plan End Date may not be worthwhile, when a prioritized plan is required.

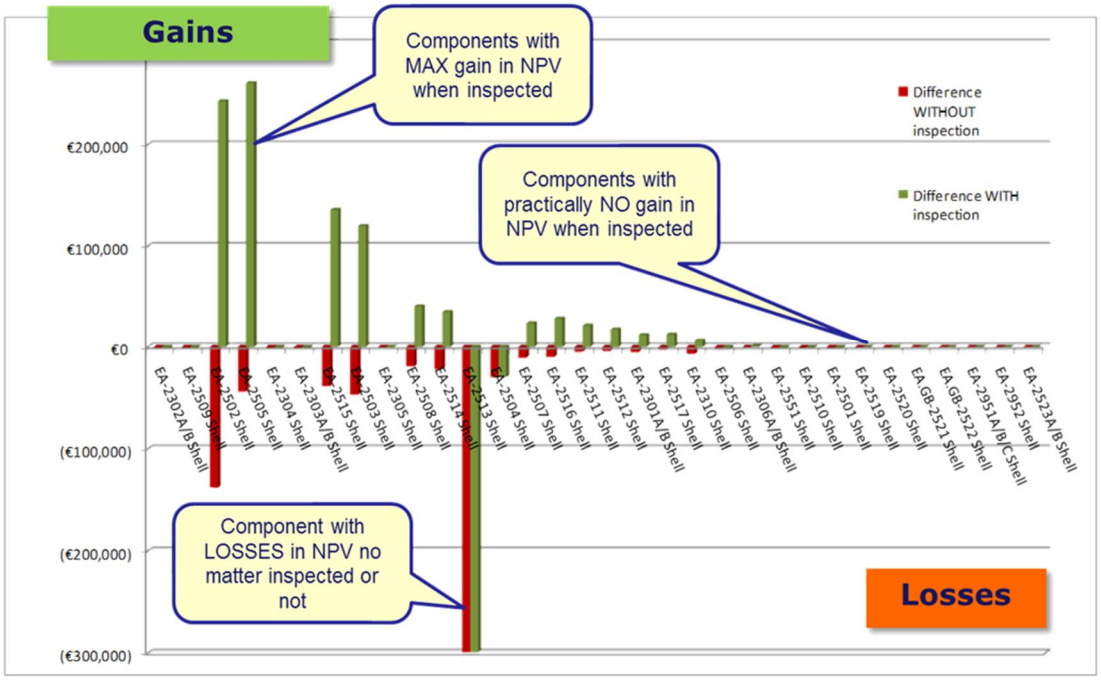

Figure 15: Gain-loss diagram

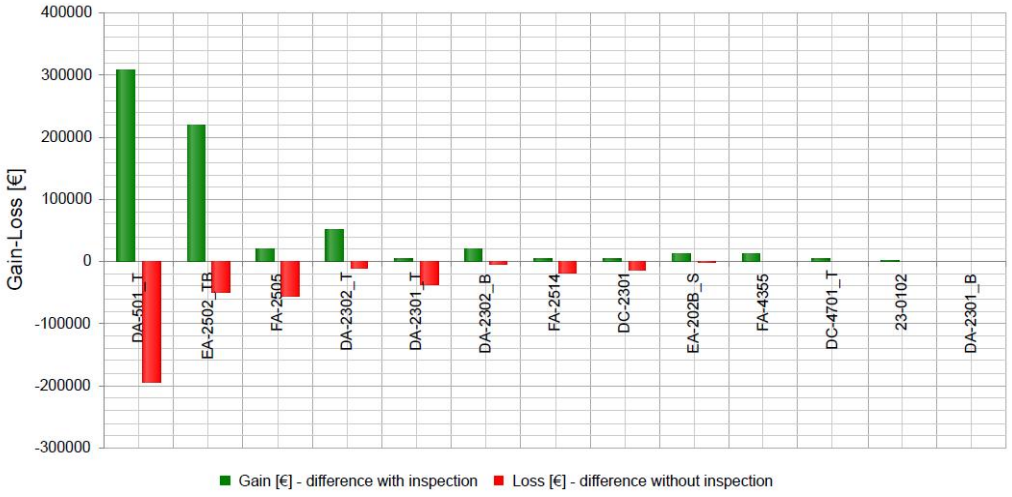

Figure 16: Implementation of Gain-Loss in the integrated system

The S-Factor (Figure 18) gives the return on the investment (cost) of the inspection/action of equipment by taking into account the calculation of the future risk for the component (at the defined Plan End Date) without any additional inspections/actions, the future risk of the component with actions/inspections, and the cost of the planned actions/inspections.

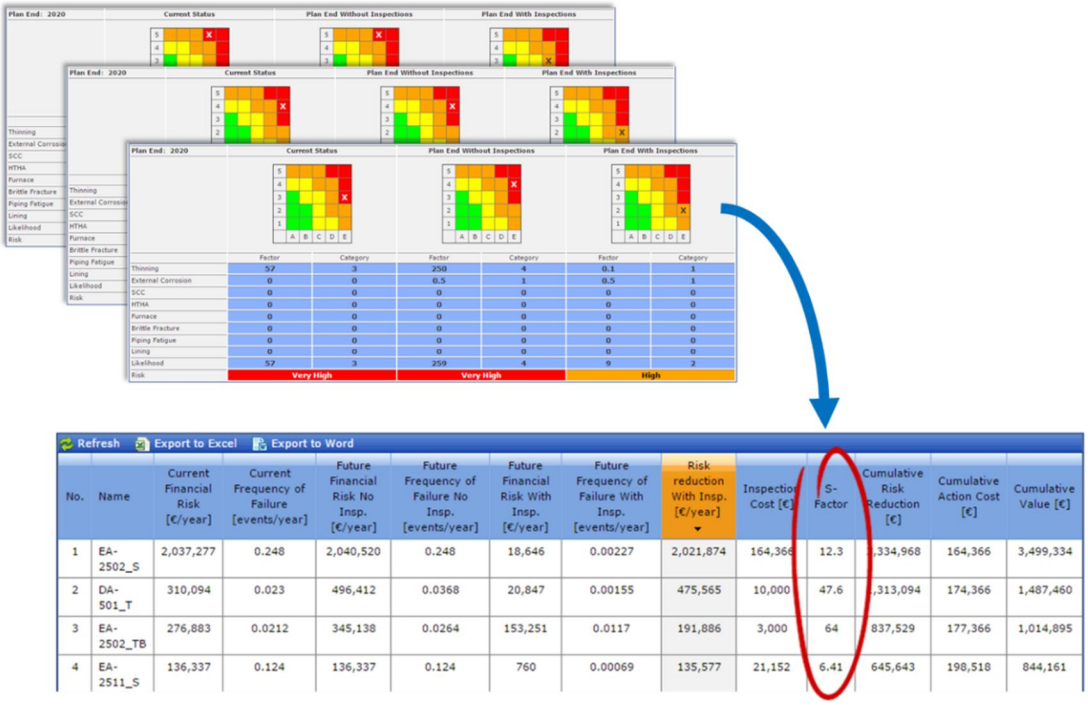

No.	Name	Current Financial Risk [€/year]	Current Frequency of Failure [events/year]	Future Financial Risk No Insp. [€/year]	Future Frequency of Failure No Insp. [events/year]	Future Financial Risk With Insp. [€/year]	Future Frequency of Failure With Insp. [events/year]	Risk reduction With Insp. [€/year]	Inspection Cost [€]	S-Factor	Cumulative Risk Reduction [€]	Cumulative Action Cost [€]	Cumulative Value [€]
1	EA-2502_S	2,037,277	0.248	2,040,520	0.248	18,646	0.00227	2,021,874	164,366	12.3	1,334,968	164,366	3,499,334
2	DA-501_T	310,094	0.023	496,412	0.0368	20,847	0.00155	475,565	10,000	47.6	313,094	174,366	1,487,460
3	EA-2502_TB	276,883	0.0212	345,138	0.0264	153,251	0.0117	191,886	3,000	64	837,529	177,366	1,014,895
4	EA-2511_S	136,337	0.124	136,337	0.124	760	0.00069	135,577	21,152	6.41	645,643	198,518	844,161

Figure 17: S-Factor – application in the integrated system

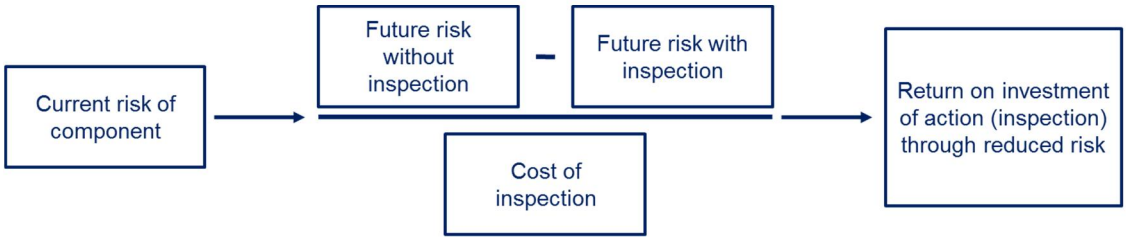

Figure 18: S-Factor – return on investment of action through reduction of risk

5. Conclusions

The RBI study presented in the paper shows benefits which can be obtained from implementing an integrated computerized RBI-RCM system, especially when dealing with large amounts of data. The advantages include the possibility of structuring and centralizing data and knowledge in one location, the possibility to complement the existing in-place inspection strategies and methods with recommendations from industry accepted recommended practices ([6], [7]). Another advantage of the implementation of these systems is the flexibility and possibility they provide as concerning visualizing large sets of data from a decision making standpoint, allowing for the creation of risk-informed and risk-optimized action prioritization.

The benefits of the implementation and integration of a computerized RBI and RCM solution at the refinery have included:

- The centralization of relevant component-specific input data (design, operating, inspection) into one database/source for the whole plant
- The ability to rank areas and equipment by risk, identify and rank critical components and present these results in a clear, easily understandable manner

- The ability to establish optimum inspection intervals, scopes and techniques, using recognized industry guidelines as a basis [7]
- The ability to make risk-informed decisions with regards to inspection and maintenance prioritization

The system has been applied in the conjunction with a computerized maintenance management system (CMMS) and, apart from providing the direct benefits of RBI/RCM, brought additional benefits related to better structuring and organizing large amounts of asset data from different sources centrally.

The possible future development of the integrated system should focus on tighter integration with the existing Computerized Maintenance Management System (CMMS) in order to further automate the process from the monitoring, analysis and decision-making steps to the automated issuing of work orders. These will take into the consideration also the further developments taking place in the area, e.g. those referenced in [10] and [11].

Acknowledgements

The authors wish to acknowledge the support provided for this work by NIS Gazprom Neft, Serbia.

References

[1] Jovanovic, A. et al. (2010). Harmonizing Risk-based Inspection and Maintenance Practice in Europe, In: VGB PowerTech, Vol. 90, No. 6, pp. 44-52.

[2] Jovanovic, A. et al. (2006). Risk-based Maintenance Concept – European Development and Experience in Implementation on High-temperature Steam Tubes and Pipe. In: VGB PowerTech, Vol. 86, No. 1-2, pp. 77-82.

[3] Jovanovic, A. (2010). Globalization aspects of Risk-Based Inspection and Reliability-Centered Maintenance practices world-wide. In: Proceedings for the RBE-5 5th International Workshop on Risk-Based Engineering. Convention Center University of Science & Technology, Nov. 16, 2010. Beijing, China.

[4] API RP 580:2009 Risk-Based Inspection, Second Edition, November 2009.

[5] CEN CWA 15740:2011 Risk Based Inspection and Maintenance Procedures for European Industry (RIMAP).

[6] API RP 581:2000 Risk-Based Inspection Base Resource Document, First Edition, May 2000.

[7] API RP 581:2008 Risk-Based Inspection Technology, Second Edition, September 2008.

[8] UP-03.05.04-040 Guideline for the definition and application of strategies for measuring and control of wall thicknesses on process equipment and piping installations in the ‘Processing’ block (in Serbian)

[9] G.J. Glasser, The Age Replacement Problem". Technometrics, 1967, 9.

[10] Jovanovic, A., Carlebur, A., Quintero, F.A. (2015). European Standardization of Risk Based Inspection Framework (RBIF), MPA Seminar, Stuttgart, Germany, Oct. 5-6, 2015.

[11] Jovanovic, A., et al. (2015). Extending the RBI (Risk-Based Inspection) concept: Use of data mining and extended benefit analysis, MPA Seminar, Stuttgart, Germany, Oct. 5-6, 2015.

RBI in Power Generation

Alan Bissell[1], Sophy Dipela[1], Shanil Narain Singh[2], Tshifhiwa Nevuwari[2] & Marthinus Bezuidenhout[2]

[1]Sebenzana Engineering, 70, 7th Ave., Parktown North, Johannesburg, South Africa

[2]Eskom, Megawatt Park, Maxwell Drive, Sunninghill, Sandton, Johannesburg, South Africa

Abstract

Risk assessment and Risk Based Inspection (RBI) are well established within the refining and petrochemical industries. The fossil fuel power generation industry, however, has not generally used a formalised RBI process for managing the integrity of its pressure equipment. Due to legislative changes in South Africa (SA) the national electricity producer (Eskom) has embarked on what is perhaps the largest roll-out of an RBI process in power generation in the world (more than 80 units totalling more than 40,000MW). The Eskom RBI process RBI was based on the European RIMAP process. This paper will describe some of the challenges faced in the development and implementation of the process.

1. Introduction

In 2009 the South African Department of Labour revised the pressure equipment regulations [1]. The revision requires that all pressurised equipment must be subject to hydraulic testing every 3 years unless an RBI process is used to demonstrate that the level of risk associated with continued service of the vessel is at an acceptable level. Historically Eskom had an exemption from the 3 year pressure vessel hydraulic test rule and only needed to test every 6 years i.e. in alignment with the Eskom's major outage frequency. Eskom consequently decided to initiate the development and implementation of an RBI process not only to meet regulatory requirements but to also to also focus on, and improve, plant safety. This process will eventually become the basis of all future inspection planning. This paper describes some of the main aspects of the development and implementation of at Eskom.

2. Background

During the life cycle of a plant, inspection, testing and maintenance programs are established to detect and evaluate deterioration and damage arising from operation. Regular inspection is generally implemented to provide a periodic assurance of integrity, and thus safety and reliability and is particularly important for plant that are subject to time dependent degradation. Historically the high frequency and consequences of failing pressure vessels resulted in the development of design rules [2] and eventually statutory inspection requirements for many countries. Over and above these requirements many strategies were developed within the various industries utilizing pressure equipment for these activities and traditionally they have been based on general and specific experience, reinforced by statute, requirements, consensus view within the industrial sector and perceived company need, according to the criticality of the

item. Naturally, concepts such as failure likelihood and failure consequence are implicit in the thinking behind common practice, but it is only recently that they have been treated as a defined process

The value of inspection as a means of detecting incipient plant failure is well known. There are numerous examples where inspection has identified cracking which, if not detected, would have led to failure with potential for loss of life and commercial penalties through lost production and the costs of covering/repairing consequent damage. However, the costs of inspection and maintenance related activities are increasing being examined, particularly in competitive markets, in order to find areas in which savings can be made.

The risk based approach to defining plant inspection programs possibly has its origins in the nuclear industry in the late 1970's [3], and the off-shore industry's work on structural integrity. These were developing hazard based inspection methods which became reasonably well established in these industries. This approach has found ready acceptance in the refinery and chemical industries, as a means of optimizing the cost of inspection whilst ensuring safety, health and environment. The approach developed for these industries is detailed in API 580 and 581 [8]. Many of the larger companies have also developed their own in-house based procedures.

The potential benefit of application of risk based methods within the fossil power industry has attracted much interest but, even though a fossil fuel related process was developed [4], to date, application has been limited as statutory requirements with defined inspection intervals, have been slow to change. The recent change in the South African (SA) pressurised equipment legislation [1] has led to an increased interest in RBI within SA as a means of ensuring safe operation of such equipment without the need to conduct hydraulic pressure testing.

Risk based inspection (RBI) is a process that uses an assessment of a component's risk to determine if the component needs to be inspected and if so to what extent. Risk is the product of the likelihood or probability of a component to fail and what consequences will result if the failure occurs i.e.

Risk = Probability of Failure (PoF) X Consequence of Failure (CoF)

Consequences are typically defined in terms of safety, commercial, environmental etc.

A risk based approach is generally applied in a progressive manner such that all equipment is identified and addressed by qualitative methods and only the most critical items are analyzed quantitatively. At all levels, both the probability and consequences of failure are determined to calculate the risk exposure. At the quantitative levels, the variation of risk with service time is also determined where relevant.

The main objective of this approach is to focus inspection activities where risk is high. This obviously has the potential to reduce inspection related costs without increasing the overall level of risk. A number of risk assessments have indicated that risk follows the Pareto principle or 80:20 rule in that typically about 80% of risk is associated with about 20% of the components on a site [6] which indicates that correct focussing of inspections can be cost effective.

1. Process Development at Eskom

2. Technical Requirements

The principle requirements for the Eskom process were as follows:

- Alignment with RIMAP process
- Needed to be simple and robust
- Focus on safety
- Repeatability and consistency of results
- 6 year look ahead for PoF

- Alignment with existing Eskom plant life and integrity management processes
- Certified by designated RBI auditors
- Sustainable

3. Project requirements

In addition to the technical requirements Eskom required to control the implementation of the process via detailed project management involving several key areas including:

- Steering committees
- Training of staff
- Weekly and monthly feedback reporting
- Change management
- Internal audit checks
- Communications between various departments within Eskom
- Project risk management

Eskom ensured a dedicated team of resources with the necessary skills were made available to the project. Project risks where assessed, reviewed and mitigated on a regular basis by a dedicated team using the Eskom integrated risk management process.

4. Eskom RBI process

The Eskom RBI process is based on a European multi-industry based process (RIMAP) [14] which allows flexibility in the methodology used to determine risk provided specific aspects of the process are included.

The Eskom process covers all of the essential aspects required by the RIMAP process as shown in Table 1 below.

Table 1. Comparison of RIMAP process requirements with Eskom RBI Process.

RIMAP	Eskom RBI Process
Policy statement and commitment of Senior management	Integrated into existing SHEQ policy and signed-off
Initial analysis and planning	Detailed in Process manual
Data Collection	Detailed process documented within process procedures
Data Validation	Validation and sign-off process developed
Risk Analysis	
Critical equipment List	All equipment listed and screen based on SANS categorisation
Damage Mechanisms	Developed within project based on ASME PCC-3 [12]
Develop risk matrix and criteria	Eskom RBI risk matrix (5x5) and risk level action criteria developed
Screening	
Identify Hazard	Component specific defaults developed for the type of failure and the Generic Failure Frequencies for each degradation mechanisms.
Procedure for determining Consequences	Simplified calculation developed for Safety, Commercial and Environmental
Procedure for determining Likelihood	Simplified assessment procedure developed
Screening process (level 1: Qualitative) – conservative	Checks on the screening process indicated it is conservative in the vast majority of cases.
Escalation criteria (to detailed assessment (level 2: Semi-Quantitative)	Conservative risk level basis for escalation to Level 2 documented.
Detailed Assessment	
Bowtie Assessment of Risk	Not used* except for consequence mitigation
Mitigation procedures	Some available
Procedure for determining Consequences -(level 2: Semi-Quantitative)	Level 2 CoF mainly qualitative – moves to quantitative at Level 3
Procedure for determining Likelihood – (level 2: Semi-Quantitative)	Some detailed procedures available for some components e.g. HP piping
Escalation criteria	Defined in terms of risk levels
Integrity Risk register	Available under existing Eskom procedures (IRM) [13]
Decision making **Action Plan**	Procedures developed for short term high Risk items and for assessment of as – found degradation during an outage
Execution	The inspection plan is passed to the outage Team for implementation in accordance with Eskom procedures
Reporting	Detailed component specific Risk assessment summary sheets prepared as part of the overall report
Performance review	The process is Certified at each station via an independent audit, with follow-up audits each year
Evergreen Status/Sustainability	Ongoing

**During the pilot study it was found that aggregating the PoF of different potentially active damage mechanisms with the highest CoF resulted in unrealistically high risk scores.*

Initially the scope of the Eskom RBI was all pressure equipment operating at 50kPa or over, as well as turbine centreline components, but was later reduced to primarily focus on the pressure equipment operating at 50kPa and 100^{o}C and above. As such, up to 4000+ components per unit are required to be screened. With this in mind the Eskom RBI was developed using a novel scorecard based process which allows relatively rapid assessment. In keeping with most risk assessment methodologies the process is team based i.e. representatives from operations, system engineers, maintenance, metallurgist, plant specialists etc. are required to be present at the risk assessment meetings.

The Eskom RBI process involves several main stages as follows:

- Definition of scope
- Component data gathering (design, operating etc.)
- Categorisation of components according to SANS 347 [7]
- Pre-outage Risk Assessment
    - Level 1: high level screening (qualitative) assessment for SANS Cat 2, 3 and 4 components) – medium and high risk components go forward to next stage
    - Level 2: semi – quantitative assessment – identifies components required to be inspected at next outage.
    - Development of RBI plan
- Level 3.1: If required conduct a refined assessment of components that are high risk before the outage occurs. This is largely expert opinion based and aligns the Eskom expert view of risk level with the process determined risk level. If required critical high risk components are escalated via Corporate Integrated Risk Management system to force critical inspection outages.
- Perform RBI plan at outage
- Post-outage risk assessment
    - Repeat Level 2 assessment with new inspection data
    - Evaluate risk at different timescales as required
    - Identify re-inspection intervals as required
    - Perform Levels 3.1 and/or 3.2 for high risk components as required
    - Update corporate Integrated Risk Management system

The basic assessment process flow diagram is shown in Fig 1.

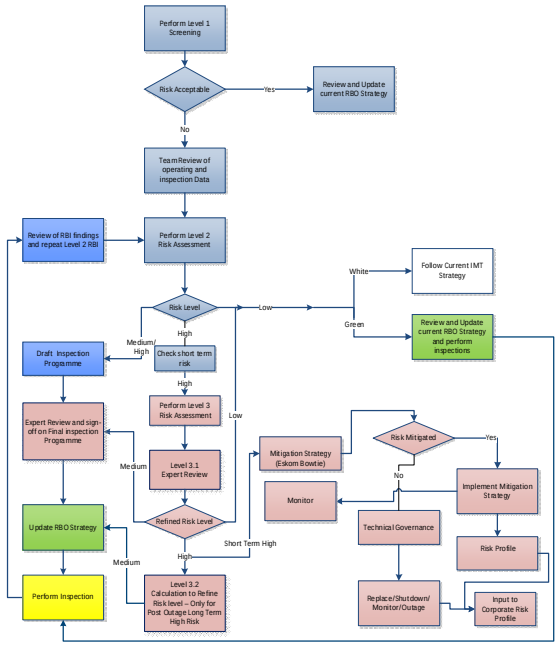

Figure 1. Eskom Risk assessment flow diagram.

The level 1 assessment uses 10 criteria to determine the PoF and 3 criteria for safety CoF. At Level 2, which requires a more detailed assessment, 19 criteria are used to determine the PoF and 5 criteria for the safety CoF. The results of the RBI assessment are plotted on a risk matrix as shown in Figure 2. The process currently focusses on **safety** related risk with commercial risk a secondary factor.

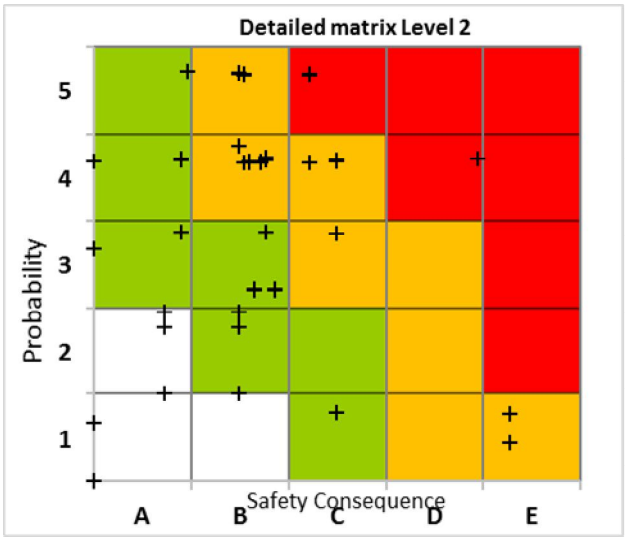

Figure 2. Example output of Level 2 Boiler Component Risk levels.

Once the RBI plan has been implemented at the outage the Level 2 assessment is repeated (i.e. a post–outage risk assessment with the new inspection findings) to establish the risk profile over the next 6 years and identify any components requiring inspection before the next major outage.

The Eskom RBI process was initially trialled on a pilot unit and after some modifications has been implemented on one unit at almost all 14 coal fired power stations. In addition, the process was implemented at the nuclear power station's secondary cooling system and other non-primary cooling related compo-

nents. Due to outage deferrals many of the post-outage assessments have yet to be undertaken. The first post outage assessment was completed early in 2016 with others now ongoing.

As mentioned above a key objective of the EskomRBI is to establish the risk associated with pressure equipment. Once established it can be used to justify **not** pressure testing pressure vessels. This has potentially significant time and cost savings for Eskom and avoids the statutory requirement to pressure test every 3 years, and maintaining (and potentially extending) the historical 6 year hydraulic test interval.

5. Challenges

Developing a new RBI process and implementing it is not without its challenges. A few of the challenges faced, and how they were overcome, are discussed below.

5.1 Generic Failure Frequency (GFF)

In a similar fashion to the API process the Eskom process uses a GFF to determine the PoF. Indeed, in Level 2 a GFF is required for each potentially active degradation mechanism. In API there are some data on the frequency of occurrence of damage relating to hole size [8]. These data predominantly relate to corrosion degradation mechanisms many of which are rarely found in power generation plant equipment and as such the use of such data was considered questionable. Unfortunately, within power generation, there is no similar database of failure frequencies for most components types (Eskom, along with other large utilities, have detailed information on the failure frequency and associated degradation mechanisms associated with boiler tubing but not on other component types). Whilst some information is available from NERC generation availability reports [9] there is often insufficient detail on specific components. A detailed review of the literature was also carried out but the majority of information came from small sample sizes and did not relate to specific degradation mechanisms. These data were therefore considered not to be appropriate. It was therefore decided to use an indicative GFF and apply a concept of “relative” PoF rather than “absolute” PoF.

Due to the size of the Eskom fleet (more than 80 units) it is envisaged that, over time, Eskom specific component failure frequencies will become available and will eventually be used in place of GFF. This should ultimately improve the estimate of the probability of failure.

5.2 Consistency of assessments

The determination of the relevant GFF was initially left to the various RBI teams but review of the results indicated significant variations in risk levels for the same component. This could obviously arise merely from different responses to the assessment criteria but on closer examination much of the variability stemmed from different inputs for some key CoF criteria and GFF. It is not uncommon for risk assessments carried out by different teams to yield significantly different results. A result of one such comparison [10] is shown in Table 2. These results are based on assessments carried out by different companies (A, F, E, G) using their RBI process on the same vessel with same operating information. Similar comparisons with other vessels types in this study yielded similarly variable results.

Table 2. UK Health and Safety Executive RBI comparison (taken from Ref).

Damage Mechanism	A	F	E	G
Internal corrosion	VT + some UT	√	UT	UT ?*
External corrosion	VT,UT	√		UT?*
Under lagging corrosion	UT		VT, creep UT	**some VT**
Brittle fracture			TOFD*	**TOFD*?**
Deformation/buckling	VT			**?**
Fatigue	MPI/EC + some UT		**TOFD/MPI***	**UT?/MPI?some TOFD**
SCC	MPI/EC + /some UT*	√	UT	**UT?/MPI?***
HIC	MPI/EC + some UT*	**MPI (UT) or UT***	UT(MPI,TOFD)	**UT?/MPI?**
Erosion			UT	**UT/MPI?**
Creep	√			√
Cavitation				√

* Mechanisms considered by participants to be active or having a possible or higher likelihood of occurrence.
√ means mechanism considered but no specific NDT method referenced
NDT1 (NDT2) means NDT method 1 recommended as primary method and NDT method 2 recommended if degradation detected.
Some NDT means recommended at specific locations
UT? means not explicitly stated but most likely method

As can be seen there is a large difference in degradation mechanisms considered by the various practitioners and in the proposed inspection that is required.

It is important for Eskom to be able to compare component risk levels between units and between different Stations. To improve the comparability of results a set of “default” component specific degradation mechanisms, expected failure type and GFF’s was developed. It is considered that if the same starting point is used for a potentially active degradation mechanism of a specific component, then the various assessment criteria will change the PoF making comparison between the same components in different units directly comparable. In the main the results have been consistent with industry expert expectations and tend to confirm and justify the existing Eskom integrity management programmes currently in place. For example, the current high temperature piping programme [11] is comprehensive in application of inspection techniques to monitor creep related degradation and the existing programme has been seen to integrate well with the RBI process.

5.3 Certification of process

A critical element of the project was to ensure that the process would be certified by independent auditors. This required the preparation of a suite of RBI related documents detailing all technical and procedural aspects of the RBI process. In total 13 documents have been produced covering a variety of topics ranging from qualifications of RBI engineers, meeting attendance requirements, system definitions as well as the technical assessment procedure etc. In order to prepare for the independent audits a team of internal auditors reviewed all aspects of the risk assessments in advance and highlighted any areas for improvement both at head office and at the individual stations. This proved to be extremely successful with all Stations assessed to date being certified.

5.4 Process development

As with any new process there will always be some areas for improvement. As more results become available areas for improvement have been highlighted and after detailed consideration by the technical steering committee have been introduced into the process manual. In some instances, changes were made to weighting factors of specific criteria e.g. the weighting associated with one of the PoF criteria which deals

with design aspects of components was increased to ensure that both operational and mechanical design aspects were more accurately accounted for. Elsewhere definitions have been improved and aspects of procedures clarified. In keeping with Eskom's own philosophy and the "evergreen" requirement of RIMAP, the process will continue to be modified and enhanced over the coming years.

5.5 Transition

It is always difficult for seasoned staff to accept changes in the way that things are done. Moving from a long established expert based integrity management culture to an RBI based process, has, as expected, not been without some challenges. A comprehensive programme was developed to manage this challenge. This consisted of an extensive communication programme, training (>100 staff trained to date), workshops and involvement of both plant experts, metallurgists and station engineers in the development of the process and creation of its supporting documents. The RBI related training has improved staff understanding of the various degradation processes that can affect their plant. This approach has allowed a gradual move towards ownership of the new process. Indeed, some of the staff that were initially reticent to the change have now become staunch advocates of it.

Looking to the future, Eskom has already focused on the sustainability of the process by continued development of training programmes including "training of trainers" for the future. Whilst there is still much work to be done to fully embed the process throughout all of the stations and the supporting technical departments the current evidence is that Eskom will become the first power utility to fully adapt RBI as the primary tool for ensuring plant integrity and safety.

6. Concluding remarks

The Eskom RBI process has been successful in fulfilling all of the original requirements of the process. The process has been independently Certified according to the SA statutory requirements of the Occupational Health and Safety act. In several instances the process has highlighted some areas which had been overlooked by the current programmes and has identified some areas where inspection programmes can be reduced. Such factors, together with the increased staff awareness of degradation related risks, the increased focus on safety, and the ability to continue with or even extend the 6 year inspection interval for pressure vessels are clear benefits to Eskom.

7. Acknowledgements

The authors would like to thank all those involved in development and roll out of the RBI process with particular thanks to the Eskom RBI steering committee for providing the enabling environment. This paper has been prepared by the kind permission of Eskom Holdings Ltd.

8. References

1. Occupational Health and Safety Act (85/1993): Incorporation of Health and Safety Standards into the Pressure Equipment Regulations, July 2009.

2. www.asme.org: The History of ASME's Boiler and Pressure Vessel Code.

3. A tentative approach to a more rational preparation of in-service inspection programmes: Buchalet, C.B.; Martin, G. Courbevoie, Vauterin, M. Vienna; Symposium on application of reliability technology to nuclear power plants; Vienna, Austria; 10 - 13 Oct 1977.

4. ASME: Fossil Fuel-Fired Electric Power Generating Station Applied Risk-Based Inspection, Volume 3, 1994.

5. ASME: Risk-Based Inspection-Development of Guidelines: General Document: Volume 1, 1991.

6. Risk Based Maintenance Application Study: Risk Evaluation and Prioritization at a Fossil Power Plant, EPRI, Paulo Alto, CA: 2003, 1004898.

7. SANS 347:2012 – “Categorization and conformity assessment criteria for all pressure equipment”, South African Bureau of Standards (SABS).

8. Risk Based Inspection Methodology, API Recommended Practice 581, First Edition, 2000, Second Edition, 2008 and Third Edition, 2016.

9. North American Electric Reliability Corporation: Generating Availability Report, 2007-2011.

10. Risk Based Inspection - A Case Study Evaluation of Onshore Process Plant, UK HSE Report HSL/2002/20.

11. Integrity and lifing of defect free components in ESKOM power plant: M E J Bezuidenhout, P Doubell, A Downes, F C Havinga, M Mkhize, M Newby, W Smit, HIDA-5 Conference, 23-25 June 2010, Guildford, Surrey, UK.

12. ASME PCC-3: Inspection Planning Using Risk-Based Methods, 2007.

13. Integrated Risk Management Standard, 32-2, 2008, Eskom.

14. Risk-Based Inspection and Maintenance Procedures for European Industry (RIMAP): CEN Workshop Agreement: CWA 15740 April 2008.

Large-scale application of RBI and maintenance on the national level: Experiences and lessons learned

Aleksandar Jovanovic, Stefan Husta & Petar Stanojevic

Steinbeis Advanced Risk Technologies
Stuttgart, Germany

Abstract

Risk-Based Inspection (RBI) approaches, anchored in a number of national and international standards and regulations, are becoming an unavoidable part of modern asset management in power and process industry. However, especially in large projects, the end-users face the problem of quick assessing of huge amounts of data, ensuring the consistency of assessment and ensuring that the effort invested in the RBI is bringing in the benefits announced and expected at the initialization of the projects. Current approaches (e.g. API, ASME, VGB, CEN/EN, etc.) generally rely on the multi-level qualitative and quantitative approaches that suggest to “drill-down” with the analysis on the spots indicating higher risks. However, practically few of these approaches proposes how to benefit from the analyses already made and none proposes the way how to do it practically. In principle, the more one knows about the plants/components already analyzed by RBI, the more efficient the analysis of the new, not yet analyzed components should be.

This paper proposes to solve this issue by means of the continuous and dynamic data mining over the data already acquired and results already achieved. Practically it means that the components are dynamically clustered (e.g. “all superheater outlet headers”) according their characteristics and associated risks. Based on their characteristics, the new, yet to be analyzed components (e.g. a new superheater), can be than pre-assigned to the corresponding clusters and a preliminary, “automatic” risk assessment made (e.g. “medium risk”). The approach can provide the following main benefits: (a) speeding-up the assessment process, (b) ensuring more consistency in the RBI process and (c) allowing assessing the technical benefits of the RBI process better. The assessment of benefits is partly covered by the existing approaches, but it is mainly based on economic considerations. The above extension of the basic RBI concept has been test-applied onto the sample data from large RBI projects in Finland, Germany and South Africa, targeting over 40,000 MWe of installed capacity and these results indicate the great potential for the practical use of the proposed extension of the basic concept.

1. Introduction

The acceptance of risk and risk-based approaches in inspection, maintenance and management in power and process plants has increased nowadays. Technical risk has become economic, public relation and political issue. Who invests both risk management and in risk mitigation or reduction, expects an economically and otherwise measurable benefit. This paradigm means in the practice that it is important to know and manage the risk, to not only re-duce or eliminate it “by all means”. In the particular area of the existing often very aged plant (power/process) the risk-based approaches play a special role.

The approaches to risk propose solutions requiring to:

- assess risk/cost (statically, i.e. for one given set of conditions)
- establish the “distance” between the current level of risk/cost and the limit one, and
- propose/introduce measures for risk/cost reduction.

In the case that the measures have been successful, the plant can be kept in operation for longer time. Much of the consideration in this classical approach is devoted actually only to the internal plant costs, e.g. those of maintenance. Therefore, the main issue appears to be finding of the right balance between gain/profit obtained by risk-reduction measures (e.g. life extension, higher availability and similar), and cost of the risk reduction measures. In the conditions of the liberalized market, the above approach is not sufficient, because it does not take into account the fluctuation of market prices. Therefore, the new market-oriented approaches advocate on-line dynamic analysis of the price cost ratio.

Including risk considerations into the daily practice of maintenance was not a straightforward and easy process. In order to come to its current state, the practice has passed through a number of phases, which can be described as

- corrective (“repair upon failure”) maintenance
- scheduled (“time-based”) maintenance and
- risk-informed inspection and condition-based maintenance, leading nowadays to concepts known as reliability-centered maintenance (RCM), risk-based inspection (RBI) and similar concepts.

These risk-aware solutions mean that it is necessary to move away from the traditional (officially prescribed) and time based practices, and to adopt strategies based on the condition state of the component and related risk. Thus, the overall safety, reliability and economy of the plant can be improved and the resources optimally used by ensuring that inspection is focused onto the critical components. Two elements of risk have to be assessed separately: probability (likelihood) of occurrence and nature of consequences. To derive the probability, a detailed knowledge of the continuing degradation mechanisms, which can affect each item of equipment, is required. This must be based on a thorough evaluation of the component itself (“condition assessment”), its operating conditions and the process in the plant. Similarly, assessment of the consequence requires a full understanding of the mode of failure and its con-sequent effect.

The interest for assessing risks in aged plants can be different. For instance, it is often the lack of other options available – e.g., lack of free space and/or time for building completely new ones. The need to use the existing infrastructures, networks and plants as reserve or fallback position during the introduction of new technologies – e.g., in the case of renewable technologies requiring “reserve” supply in the stand-by, is a common reason, too. Aged infrastructure and plants often need to operate beyond their design lifetime or in combination with other heterogeneous systems. An example of the latter could be the use of aged plants in energy systems as a “smart” reserve for the renewables. The effective agreed strategies to address aging issues are yet to be developed and consistently applied.

2. Identifying and using the patterns in data

In the case of independent search, user wants to filter all criteria independently. Figure 1 depicts an example to get the sub set of component where they are in the two stations belonged to main steam piping system (LBA). The advantages of this search are All list items are seen, User is free to select , Works faster because it reads the list items only once at start whereas the disadvantage of independent search is that it might bring empty results or too many results.

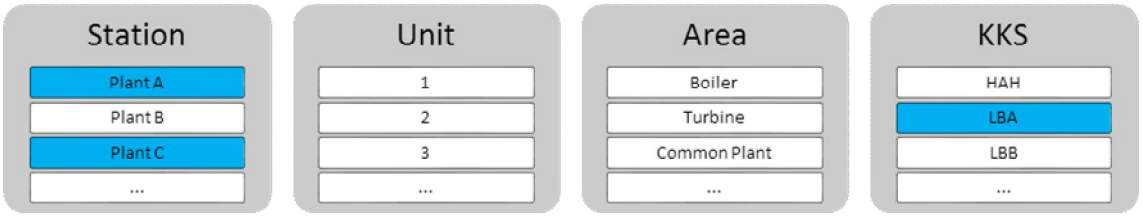

Figure 1: Selection of criteria independently to narrow down to a component or to a set of components.

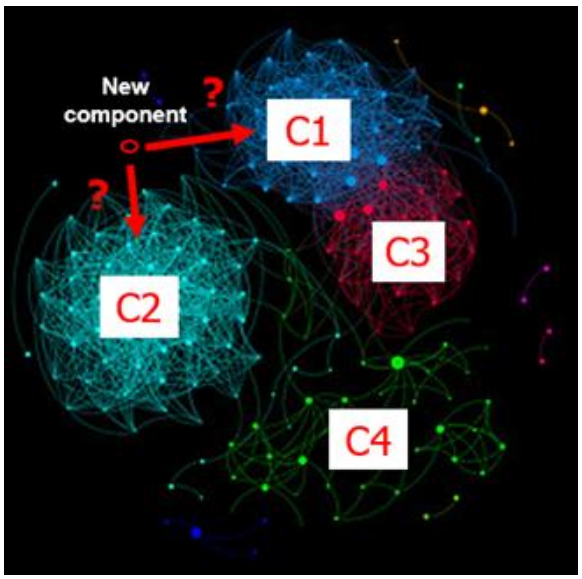

Figure 2: Selection of criteria independently to narrow down to a component or to a set of components.

Furthermore, other important problem in databases is, showing different risk status despite similarity of components. In order to understand the reason of this difference, clustering methods are proposed to be used. After creating clusters, there is another problem which should be solved: placing new components into the right clusters. Because components contain different types of characteristics (such as design pressure, operational temperature, diameter, etc.), they can take part in different clusters at the same time. An example representation of clusters and new component positioning can be seen in Figure 2. In order to figure out the reason of different results from similar components in a database, first of all, the problematic data should be eliminated. In order to do that, a comprehensive “search” should be realized. After selecting the problematic data from the pool, some data analysis methods (such as FCM (Fuzzy C Mean)) can be used for clustering and grouping the data. With this approach, influential factors can be detected. After figuring out the factors, prediction methods (like neural network multilayer perceptron) can be implemented in order to emplace new components into the current clusters truly. Between clustering and prediction steps, life cycle cost analysis methods can also be used in order to help prediction process (Figure 3). Analytics is generally used to find meaningful patterns in data. In valuable areas like rich with recorded information, analytics use application of statistics, computer programming and operational research in order to quantify performance [4]. Data analytics methods can be separated in three section: classical data analysis, fuzzy logic and neural networks.

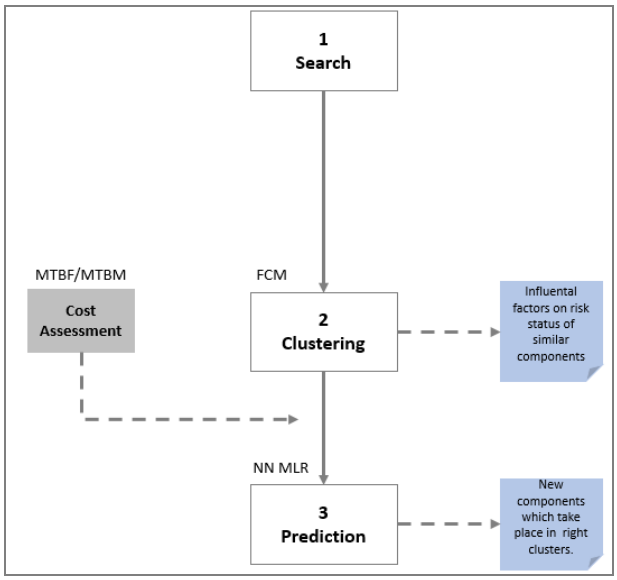

Figure 3: Selection of criteria independently to narrow down to a component or to a set of components.

3. Application example (power plants)

3.1 RBI analysis

Risk based inspection and maintenance management requires experienced personnel at all levels as well as appropriate routines for the execution of the work. Current relevant standards do not set fully comprehensive formal requirements for the qualifications of people that perform inspection and maintenance planning, even if the execution of inspection and maintenance activities is partly regulated through qualification schemes, such as e.g., ISO standards such as 17020 [1], 17025 [2], and European standard EN 473 (International Standard ISO 9712, since 12-2012) requirements [3]. RBIM planning requires a multidisciplinary team with engineering competency within:

- Inspection and maintenance
- Specific equipment disciplines (e.g. materials, corrosion, electrical, fixed and rotating equipment)
- Safety and health issues
- Plant operation and process
- Reliability and risk assessment

The failure probability (likelihood) is calculated based on modelling of influencing factors, e.g. corrosion, fatigue, fracture toughness, extreme loads, etc., and including reliability of input data, especially data coming from inspections. The approach as such is often reaching the limits of its applicability when confronted with large number of components for which the data are not available and the time available for analysis limited. For instance, in a large utility company, with say 40,000 MWe of installed power, the number of components needing the RBI analysis can go in hundreds of thousands. In a practical example taken here, the amount of installed power is distributed over 14 large power stations with approx. 80 units and over 4,000 components in each unit, ending up to be over 300,000 components (internal pressure over 50kPa). Performing detailed quantitative analysis for such a large number of components can be a challenge. Possible solution can be recurring to the more qualitative approach, and in such a case, e.g. for power plants, it is important to structure the quantitative analysis as much as possible. New EN standard being developed within the CEN TC 319 Maintenance has provided an extension exactly in that sense (Table 1).

Table 1: Example of assessment of damage susceptibility

	Questionnaire	H&S factors influence consequence PoF / CoF				
		Very Low	Low	Medium	High	Very High
	Damage statistics, failure statistics					
Q1.1	Shows no evidence of failure	*	**			
Q1.2	Isolated cases only (internal or external statistics)					
Q1.3	Damage after occurring in similar components (internally or externally)					
Q1.4	Damage regularly occurs on similar components					
Q1.5	Statistics not available					
	Damage related to design, material, or assembly					
Q2.1	Not expected	*	**			
Q2.2	Not expected under known operating conditions and design					
Q2.3	Could rise under known operating conditions and design					
Q2.4	Increased damage could rise due to known operating conditions and design					
	Damage caused by operating conditions, including process fluids					
Q3.1	Not expected	*	**			
Q3.2	Not expected under known operating conditions and design					
Q3.3	Could rise under known operating conditions and design					
Q3.4	Increased damage could rise due to known operating conditions and design					
	Health & Safety					
Q4.1	None possible					
Q4.2	None expected					
Q4.3	Minor or negligible effects					
Q4.4	Minor injuries with non-productive time losses					
Q4.5	Major injury, fatality possible					

3.2 Advanced analytical methods

In this example, a case study is generated. For realizing clustering and predicting approaches, a commercial program called Data Engine was used. Totally, 1134 valve data are selected from similar components, which has different risk status, in the project database and 261 of them are used in order to generate clustering process. In this phase, 7 characteristics of valves are used as inputs, namely

- Design pressure
- Design temperature

- Nominal diameter
- Cr%
- Operating pressure
- Operating temperature
- Risk

Clustering process realized by Data Engine Program's Fuzzy C-Means model. Regarding valve characteristics and data, cluster centers were identified as Table 2. After that, the distribution of characteristics for each cluster are found and given. After finding distributions of characteristics and naming the clusters, a positioning for possible new cases are created. According to 7 characteristics of components, positions of 4 clusters are given with a 3-D diagram in Figure 4. In order to create the figure, design pressure, design temperature and nominal diameter are selected as XYZ chart inputs. The cluster centers and new data points are shown in Figure 5. In the diagram, red color refers to "cluster centers" and blue color refer to "new cases". The new case 1 is quite related to Cluster Center 1. From this point of view, it can be mentioned that, New Case 1 is a small but critical valve according to its high design temperature and pressure data as given above.

Table 2: Cluster centers for given characteristics data

Cluster Centers						
Design Pressure	Design Temp.	Nominal Diameter	Cr%	Operating Pressure	Operating Temp.	Risk
25850,401	312,616	89,979	0,749	18819,224	274,327	0,076
11377,388	516,103	101,974	1,477	9563,869	498,621	0,125
13862,614	267,932	96,588	0,878	10368,124	235,766	0,055
5732,171	349,437	85,160	0,415	3058,279	296,933	0,038

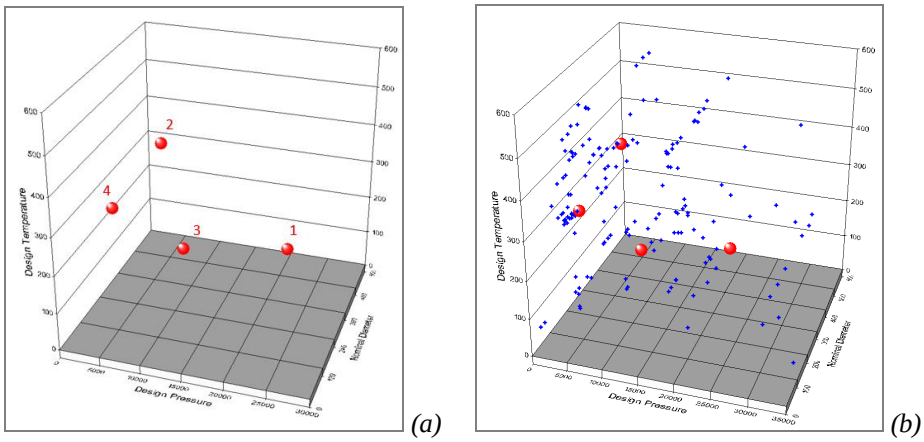

(a) *(b)*

Figure 4: Cluster centres in 3-D diagram (a) and the single valves (b).

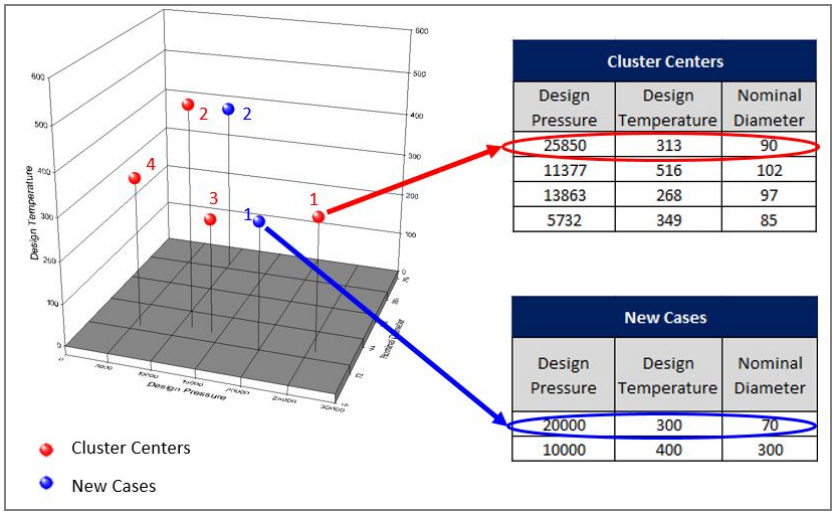

Cluster Centers		
Design Pressure	Design Temperature	Nominal Diameter
25850	313	90
11377	516	102
13863	268	97
5732	349	85

New Cases		
Design Pressure	Design Temperature	Nominal Diameter
20000	300	70
10000	400	300

Figure 5: Comparison between current clusters and new cases (blue).

3.3 RCM analysis

During the component lifetime, components loses their value. All the costs (planed repairs, unplanned repairs, regular check-outs…) are cumulated during the time and due to this situation the main question arrives: “When is the best time for component replacement? When can we expect the best results (outputs) for the minimum investments (inputs)?”

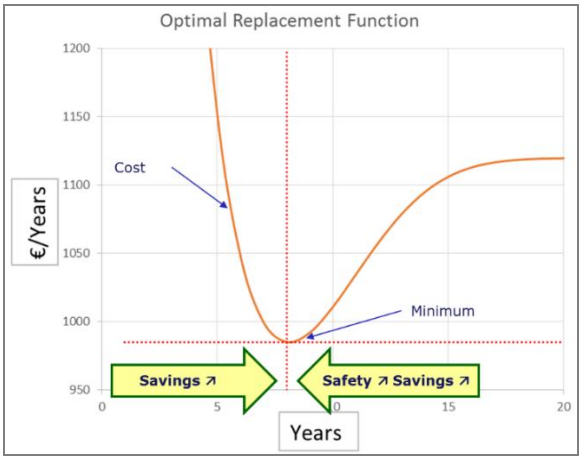

Figure 6: Optimal replacement time - solution of U-Curve Calculation.

The LCC (Life Cycle Cost) analysis is considered more as a guideline of the costs of the as-sets (land, building, computers, industrial components …). It takes into considerations all the costs through the complete lifetime of the asset. Due to the repetition of the curve through time, usually for the first lowest value is considered as an optimal replacement value in time. As one of the examples for the usage of this methodology dictates from the 1990 and the purpose was for the Federal Energy Management so it is shown that methodology is not only usable for the assets with the physical dimensions. For industrial components the life-cycle cost, is calculated based on the predefined component parameters. In this sense the starting point for the methodology has to be a predicted component life and also the component starting date (year). During this lifetime, there are phase in the components “growth”. Until the component reaches the “adolescence” phase in the “bathtub curve” the interventions are certain. During the steady life-time, number of the interventions are common during time, and in the latest period of the component life, this number grow. The number of interventions is used for calculating MTBF/MBTM (Mean Time Between Failures /

Mean Time Between Maintenance). Based on this parameter, parameter β (shape factor) which shows where is the component on her "adolescence" life. If β<1 and β=1 will not have an effect in optimum replacement time, the period what is relevant is when β>1 when component gets into her "failure mode". One of the examples for the predictions is that the optimal replacement time is a summary of the decreasing value of the component over time and the cumulative costs (planned / un-planned interventions / repairs / inspections) over time. Early replacement and also late replacement can cost you a lot. No matter what methodology is selected, savings are savings and every company policy depends on it (Figure 7).

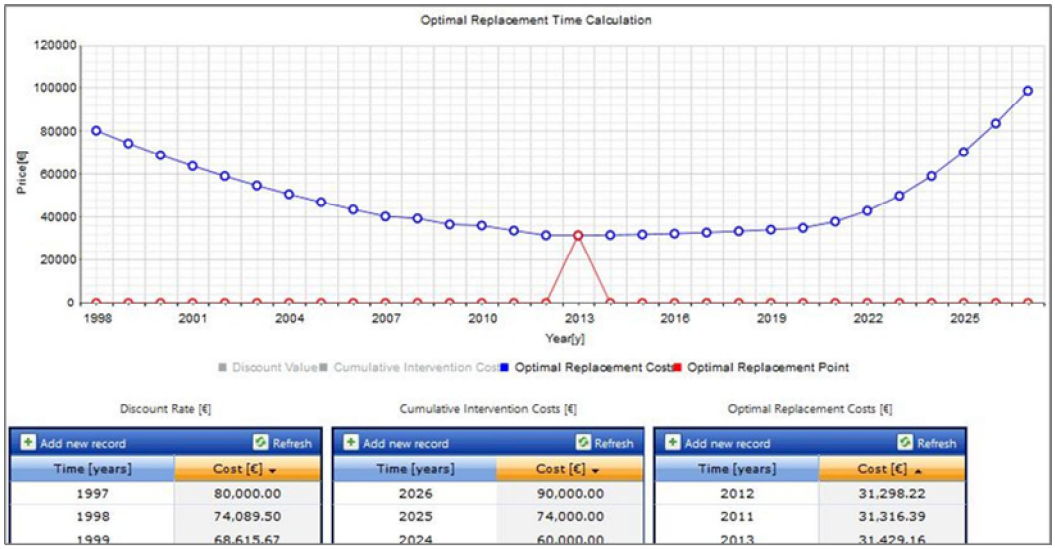

Figure 7: U curve with the minimum costs – a practical example from a power plant.

4. Conclusions

The approaches presented here can provide the following main benefits:

- speeding-up the assessment process,
- ensuring more consistency in the RBI process and
- allowing assessing the technical benefits of the RBI process better.

The assessment of benefits is partly covered by the existing approaches, but it is mainly based on economic considerations. We, therefore, suggest improving the assessment of the technical benefits by the use of the "U-curves" over the single clusters of components, indicating the optimal time of replacement/intervention for each of the clusters. The test-application onto the sample data from large RBI projects targeting over 40,000 MWe of installed capacity indicate the great potential. The experience and the practical examples confirm that importance of aligning and agreeing qualitative approaches, such as those anchored in the new EN standard should be emphasized.

Acknowledgments

The authors express their gratitude to the partners of the EskomRBI projects of Steinbeis Advanced Risk Technologies GmbH, as well as to the WG12 (RBIF) of the CEN TC319 Committee for their constant and precious support of the RBI-related activities presented in this paper.

References

[1] N ISO/IEC 17020 (ISO/IEC 17020) – “General criteria for the operation of various types of bodies performing inspection”, European Committee for Standardization (CEN).

[2] EN ISO/IEC 17025 (ISO/IEC 17025) – “General requirements for the competence of testing and calibration laboratories”, European Committee for Standardization (CEN).

[3] EN473 – “Non destructive testing - Qualification and Certification of NDT personnel – General principles”, European Committee for Standardization (CEN), since 12-2012: DIN EN ISO 9712 – “Non-destructive testing – Qualification and certification of NDT personnel”, International Organization for Standardization (ISO).

[4] Code of Practice for The Determination of Uncertainties in Mechanical Tests on Metallic Materials, Contract SMT4-CT97-2165, Technical Report: Task 3.1: Applicability of Advanced Statistical Methods, 1999.

Life time extension project to high pressure polyethylene plant

Marko Api, Ismo Savallampi & Somaina Odiah

Borealis Polymers Oy
P.O. Box 330, Porvoo, Finland

Abstract

This paper describes the Lifetime extension project phases, which will be executed in several steps to guarantee safe and reliable lifetime to Borealis two high pressure autoclave unit Porvoo, Finland.

1. Introduction

The LDPE -process with autoclave reactor was estimated to fade out over the years. Process with tubular reactor was seen to be the future at the beginning of 21st century. This led to reduce investments to autoclave processes. Last decade has shown that there still is a need for polyethylene produced by autoclave reactor because of special properties of product portfolio.

Two high pressure ethylene plants were built 1972 in Porvoo, Finland. The third LDPE -plant was built in 1978 next to two existing plants. The first plant (called line A) was closed and dismantled 1997. Nowadays Borealis operates two LDPE –plants in Finland. Since the plants were taken into operation no major repairs or equipment upgrades are executed, except main compressor foundation renewals 2005-2006.

In 2012 it was decided to start up Porvoo LDPE life time extension project, where several risk based selections were evaluated from three different categories. This paper will highlight some of the key phases of selection process and criteria for selection.

Photograph 1. Borealis Porvoo Polyolefin production plants [1].

Process:	High pressure autoclave
Start-up:	Units A&B 1972 (unit A was closed 1997)
	Unit C 1976
Licence:	National Distillers and Chemical Corporation
Combined:	150 000 t/a
Applications:	LDPE film & extrusion coating
Reactors:	Two high pressure autoclave, pressure area 1200-2000 bar

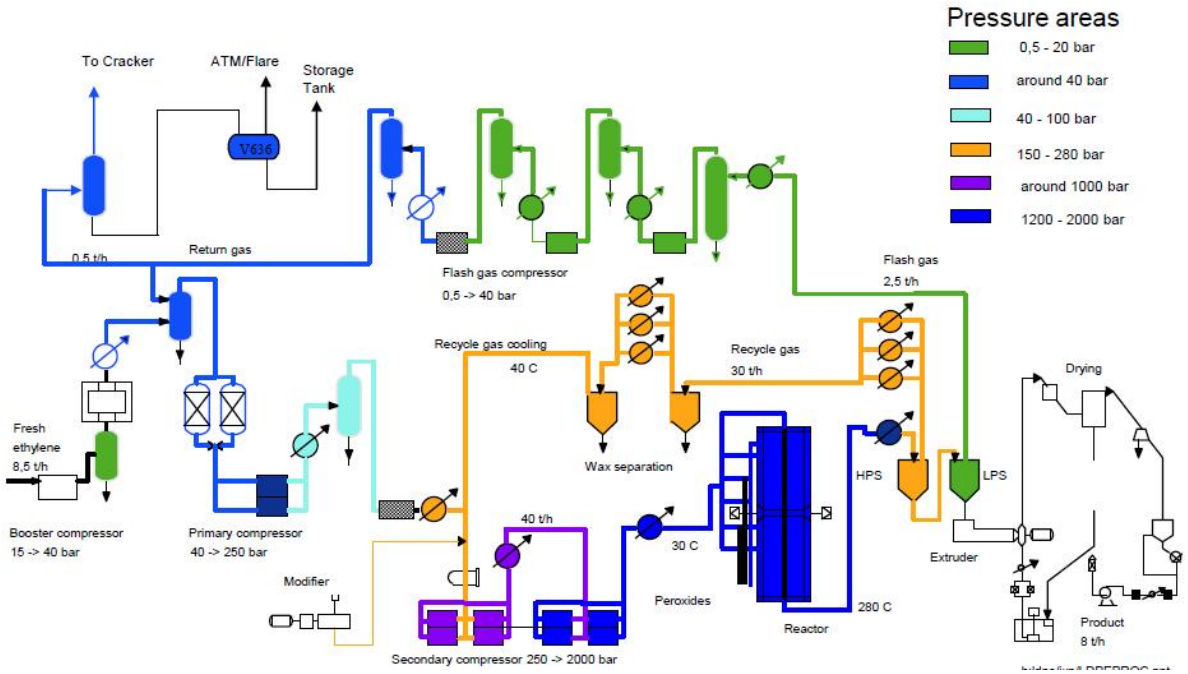

Figure 1. Simplified High pressure polyethylene process [2].

2. Methods used

The Risk Based Maintenance (RBM) methodology was performed into both units between 2006 - 2009. Risk Centred Maintenance (RCM) was executed to all major rotating equipment. Risk Based Inspection (RBI) methodology was used for main static equipment. Safety Critical Instrumentation Systems (SCIS) evaluation was also executed. One of the key elements for evaluating the plant risk was Layer of Protection Analysis (LOPA), which is semi-quantitative risk analysis technique. LOPA is a common analysis for process industry. Every Borealis process units will execute Retrospective hazard review timely. This is a team based risk assessment technique that enables continuous improvement in process industry. The units were built at beginning of 1970's and some of the systems are not according to today's engineering standards, e.g. ATEX, instrument and electrical systems. These weaknesses were identified during retrospective hazard reviews.

On top of all risk ranking analysing methods, expert values and benchmarking to similar high pressure production units failure history were used as a reference.

Borealis is using risk scenario mapping, called Risk Register, where all possible risk scenarios are stored and evaluated. Each and every risk scenario is evaluated and categorized into OPEX (related to operability), HSE and End of Life (EOL). Additionally, if risk scenario would be materialized the possible media attention was evaluated. It is vital for all hazardous chemicals using company to evaluate risks and media attention if a hazard will occur. Negative media attention may lead to lose key customer and remarkable economical losses.

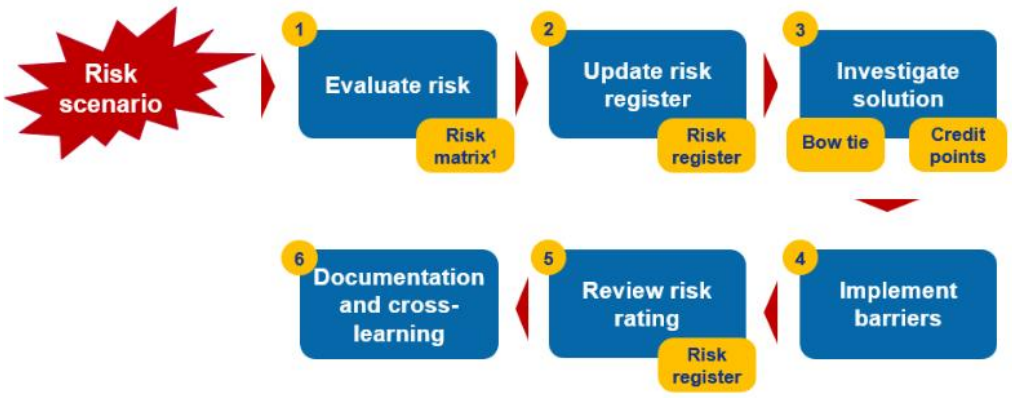

Figure 2. Risk evaluation steps [3].

All different risk ranking systems were collected and after several expert sessions it was concluded to have totally 37 risk scenarios, which were taken into Porvoo Lifetime Extension –program. The identified risk was rated and each case was separately approved by management.

The risks were categorized to instrumental and automation, static equipment and piping, rotating equipment, high pressure valves, electrical and civil. By doing this the 'owner' of the case was easy to define. Every case owner was responsible to create necessary study and apply the approval from management.

2.1 Risk evaluating organization

The risk evaluation process stared with a small group of people. Project Manager had a long background from Porvoo process units and project management. Other group members were from Plant Availability, LDPE -process unit, Technical development & Engineering and Project execution organization. Each group member had a special competence and responsibility. It is essential to have competent knowledge in a team when risk scenarios are evaluated.

It is up to company's risk tolerance, which risk matrix is used and what is company's accepted residual risk. These values are the key decisions which are required to be accepted in all organization levels.

Table 1. Common risk matrix without and with mitigation actions [4].

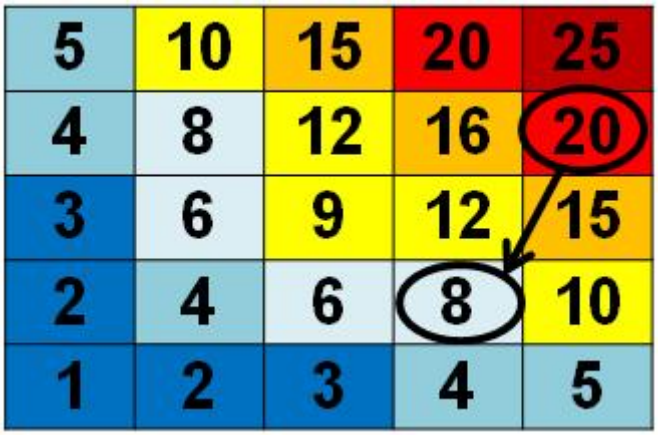

Parallel with Risk evaluation the Borealis Business Unit (BU) was evaluating the possible plant production scheme and customers' needs. Close contact with BU and evaluation team is vital to fix dates for plant shut down.

The main risk driver was selected to categorize the risk. There could be several different risk categories for one risk scenarios, but it was selected to categorize the main contributor to the risk score to increase visibility and transparency.

When the equipment falls into category EOL, certain criteria has to be fulfilled. Bath tub curve [4] is widely known and accepted to be a basis for evaluation. Every equipment or system which was evaluated as EOL needed in depth study for justification. The study included a basic justification and additionally strategic justification. Without transparent and proper justification EOL- case would be rejected or post-poned.

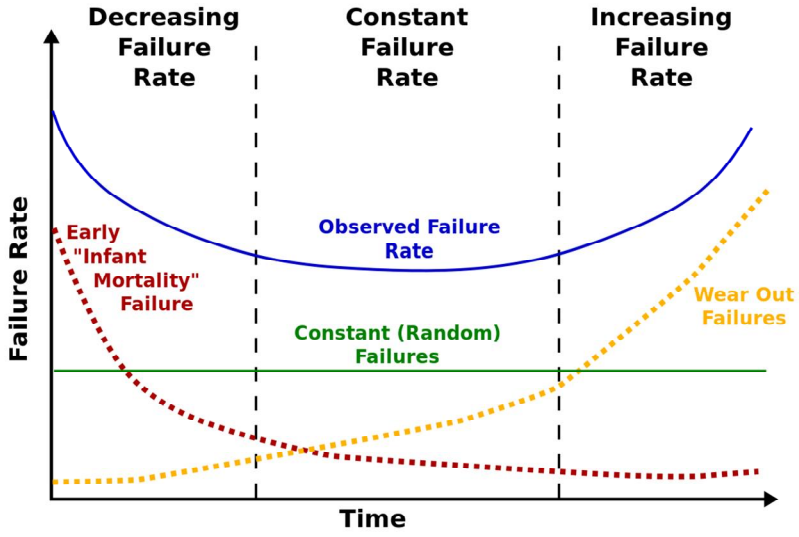

Figure 3. Bath tub curve [5].

3. Execution

After detail studies and approval levels the risk reduction implementation phase was divided into three steps. BU and LTE -project management estimated necessary time needed for major equipment repairs or renewals. High pressure equipment is engineered for special purpose and most of them are tailor made. Those equipment delivery times are normally 12 to 24 months. This had to be taken into account when evaluating earliest implementation window. Long lead time items were prioritized and commercial and technical negotiations started immediately.

3.1 Implementation Step 1

The first implementation phase was planned to execute to B-line. At line B there was no such high risk scenarios identified, which would require long lead time equipment repairs or renewals. After official management approval the detail engineering started. The first step of LTE project was executed on April 2015. During this step 1 several plant improvements were implemented. These were e.g. emergency isolation valve renewal, rotating equipment condition monitoring upgrade, centrifugal pellet drier and main steam and condensate system piping. These were selected due to highest score of risk matrix and earliest possible implementation time.

3.2 Implementation Step 2

The step 2 was originally planned to execute in October 2015, but due production challenges in other units, it was decided to postpone the Step 2 implementation phase to April 2016. Borealis Porvoo production units are fully integrated, so challenges in one unit may influence rapidly to whole production chain.

Step 2 was executed to Line C. During this implementation phase several major equipment were renewed. Most complex renewals were Hyper compressor electrical motor and three Hyper compressor intercoolers. The 6,8MW synchronous motor was needed to renew due to old motor stator deterioration. Todays' ATEX-requirements were taken into consideration when new motor was ordered. To fulfil European legislation only few manufacturers could be considered. Lifting almost 77 tons electric motor from far distance required in depth safety planning.

Photograph 2. Installation of new Hyper compressor E-motor [6].

The old intercoolers suffered high vibration level. Due to inadequate cooling water chemistry control during early 80's, jacketed high pressure tube supports suffered intergranular stress corrosion cracking. Constant failures in high pressure pipe supports led to fatigue failures in high pressure pipe. Ethylene leakage from approximately 1000 bar gaseous ethylene to 4 bar cooling water circulation is not acceptable, even if implemented mitigation actions indicated ppm level ethylene in coiling water circulation.

Photograph 3. Old intercooler removal [7].

Photograph 4. One of the new intercooler installations [8].

3.3 Implementation Step 3

Execution Step 3 is planned to execute during Porvoo Site turnaround 2017. The majority of the projects are already executed but still a number of sub-projects will be implemented. Renewal of electric distribution substations and common instrumental systems like DCS and plant ESD system will require both units shutdown. These activities are only possible during Site turnaround. Recently finalized LOPA will also bring some requirements to 3rd Step.

4. Discussion

High pressure plants maintenance costs are higher compared to low pressure polyethylene plant regardless of licenced technology. This is mainly due to requirements of high operating pressure and temperature, and their requirements from equipment.

The executed investments in Porvoo LDPE units have shown their benefits. Operability at line B increased clearly. Maintenance cost comparison is not reliable yet, but the future will show if executed investments were effective. It is clearly seen in all process industry that improving reliability will reduce maintenance costs. The total investment cost in Porvoo LDPE-plants will be over 15M€. This investment will enable safe and reliable production years far to the future.

5. Conclusions

To implement a proper investment plan to aged process unit will require several in-depth analyses. There is no single tool or analysing method, which would give clear image of plant risks and investment requirements. Continuous postponing investments will eventually hinder the plant reliability, operability and safety. If the decision of the plant closure will be made only based on maintenance cost and plant age will several opportunities be unused. Continuous plant maintenance and well planned investments would be the optimum strategy to keep plant in sustainable condition. If a clear step change has to be done, only proper evaluation to all plant risk scenarios will bring the best result.

It is usually forgotten the importance of investment to human. Company investments to an old production plant will motivate plant operators, supervisors, plant availability and plant management.

References

1. Borealis image library, Porvoo PO-plants.
2. LDPE -Process training material.
3. Borealis Risk register –training material.
4. Borealis Risk ranking tool- training material.
5. *https://en.wikipedia.org/wiki/Bathtub_curve*
6. Porvoo LTE-project; project documents, installation of E-motor.
7. Porvoo LTE-project; project documents, removal of intercooler E-207C1.
8. Porvoo LTE-project; project documents, installation of new intercooler.

RBI application in a CHP plant

Pertti Auerkari[1], Ulla McNiven[2] & Stefan Husta[3]

[1]VTT Technical Research Centre of Finland Ltd
Espoo, Finland

[2] Fortum Power and Heat Oy
Jyväskylä, Finland

[3]Steinbeis R-Tech
Stuttgart, Germany

Abstract

Risk-based inspection (RBI) has become common approach to support asset management in e.g. refineries, chemical industry in general and a few other industrial sectors. Although there are regionally established traditions to use RBI also in power plants, recently the interest has been spreading to include a widening base of common power plants. This is partly due to increasingly established standard practices, tools and availability of the techniques also for smaller scale users, and partly due to the generally established benefits and needs for safety and optimization of resources. In this paper we show how RBI was applied in a small scale for the main steam line of a CHP (combined heat and power) plant in Finland. The experience showed some typical features of initiating RBI, for example how important and beneficial (although at first somewhat tedious) it is to systematically gather and handle the required background information of design, fabrication, inspections, maintenance and operational history for RBI of an ageing plant. In the case of the example plant, the steam system had been significantly modified because of process changes, and the level of documentation was not equally thorough everywhere. Existing conventional guidelines and experience were found to be useful to support relatively lean RBI by suggesting typical areas of elevated probability of failure and therefore recommended areas to be inspected, for example at welds of large branches, locations of high strains in thermal system displacement or deviations in the function of the piping supports. Observed indications in the inspections were largely consistent with expectations and only resulted in repairs within the planned outage period. The resulting risk-based (or -informed) inspection and action plans are the main outcomes of the RBI exercise, aiming to produce the best justification and return on the maintenance investment, and to support safe operation and long-term lifecycle performance of the plant.

1. Introduction

The Joensuu (Iiksenvaara) power plant (Figure 1) of Fortum is a combined heat and power (CHP) plant from 1980's that in addition started to produce pyrolysis oil from biomass in 2013. This plant, and specifically its main steam line, has been subjected in 2015 to a small pilot scale risk-based inspection (RBI) exercise, conducted in cooperation between Fortum, VTT and Steinbeis R-Tech. The exercise is a part of the project where the life of the main components will be assessed for the investment planning purposes. All this is aiming to assure safety and optimize maintenance and investment actions during the life of the plant.

Figure 1. The Joensuu (Iiksenvaara) CHP plant with the integrated pyrolysis plant (picture Fortum).

2. Risk based inspections (RBI) – principles

A common definition of risk of an unwanted event (failure) is simply the probability of failure (PoF) times the consequence of failure (CoF). Even when one can estimate the consequences with reasonable justification, for example as foreseen monetary losses in euros, it can be harder to estimate PoF. This is partly because PoF can vary within a wide range, and partly it may be challenging to obtain sufficient clues on reasonable direct values of PoF. Fortunately there are ways to help and support the human expertise by interpreting the numbers as what they really are, or combinations if influencing factors. It is often possible to obtain some idea of a general industry experience on the failure rates or “generic failure frequence” or GFF for a given type of component and service conditions from certain public or proprietary databases [1-5]. Even when this is the case, it is generally not enough for proper risk assessment of a particular component in a given plant for two reasons: first, the component in question does not need to represent the average industrial experience in terms of type, design or material. Secondly, its operational and maintenance history also does not need to reflect this average, and in the general case the condition is also a moving target, in other words PoF (and risk, and RBI related inspection plans) are necessarily time-dependent.

To manage this complexity and fully benefit from the expertise of the people responsible for the plant, operation, maintenance and inspections, the modern guidelines and tools for supporting RBI activities often recommend using an approach where the estimated GFF is modified by additional factors related to for example the details and experience on design, operation, maintenance and inspections to either reduce or increase the likely value of GFF at present, and its development in future operation [3-5]. When doing this it is important to consider different essential aspects of risk, such as safety, environmental and financial (business) aspects, and consider the potential consequences of failure (CoF) for each of these.

In practice, RBI exercises happen in phases where much of the decisive work is conducted by teams of people with the relevant expertise, somewhat similarly as in RCM (reliability centred maintenance) that concentrates on functionality while integrity is the focus of RBI. The important initial phases of RBI work include system definitions, initial data gathering, and a screening phase to find the essential focus points where the effort of inspections and maintenance is likely to give best return on investment. Example risk matrices for screening and later phases of assessment are shown in Figure 2.

There is an emerging European RBI framework standard prEN 16991, based on concepts from the former European RIMAP project that aimed to develop industry-independent principles for RBI, with application workbooks including one for power plants [5,6]. The framework standard is being introduced in more detail elsewhere in this conference. The procedure and application tool used in the present exercise aimed to follow the same standard approach, first for screening (level 1) and then for a somewhat more detailed (level 2) risk assessment. Finally, in a few particular cases where damage required it, more attention was paid to evaluate the detailed condition, residual life or needs for further action like repair. The results are to be implemented in inspection and maintenance planning and subsequent schedules of maintenance actions.

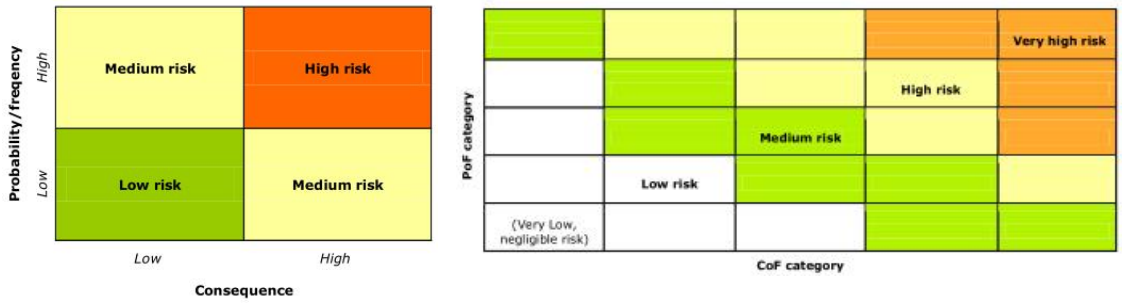

a) b)

Figure 2. RIMAP type risk matrices for a) screening level and b) more detailed risk assessment [6].

3. Inspections: main steam line and locations of interest

The main steam piping had accumulated about 220 000 service hours for the old parts of the system, except for the newer section that after modification had clocked about 100 000 hours. Some of the details on main dimensions, design and service temperatures and materials are summarized in Table 1. An example piping section is shown in Figure 3.

In the steps of RBI, the first assessment is the screening level, and this is to be conducted with sufficient conservatism to avoid missing items associated with significant risk, and in the same time avoiding so much conservatism that endanger the purpose of screening, i.e. censoring of less important items away from further assessment. An example is shown for a spherical Y-piece made of 10CrMo9-10, where the screening assessment has taken it to red, suggesting need for further assessment (Figure 4a). The subsequent more detailed assessment was successful to reduce the risk back to tolerable levels for all risk items considered (Figure 4b). Less prominent risk reduction was shown for the branch to reduction valve (X20, red arrow in Figure 3) as can be seen from Figure 5.

Even more detailed assessments may be needed at some stage when aiming to ensure safe and economically justified performance of ageing structures. In case of high temperature equipment, such an as-

sessment is already done in design, and also later life assessment can use similar principles, or “inverse design”. To satisfy a design code, the uncertainties in the information on materials properties, structural geometry, impact of fabrication and future operation are dealt with a combination of minimum requirements and standard safety factors based on general experience.

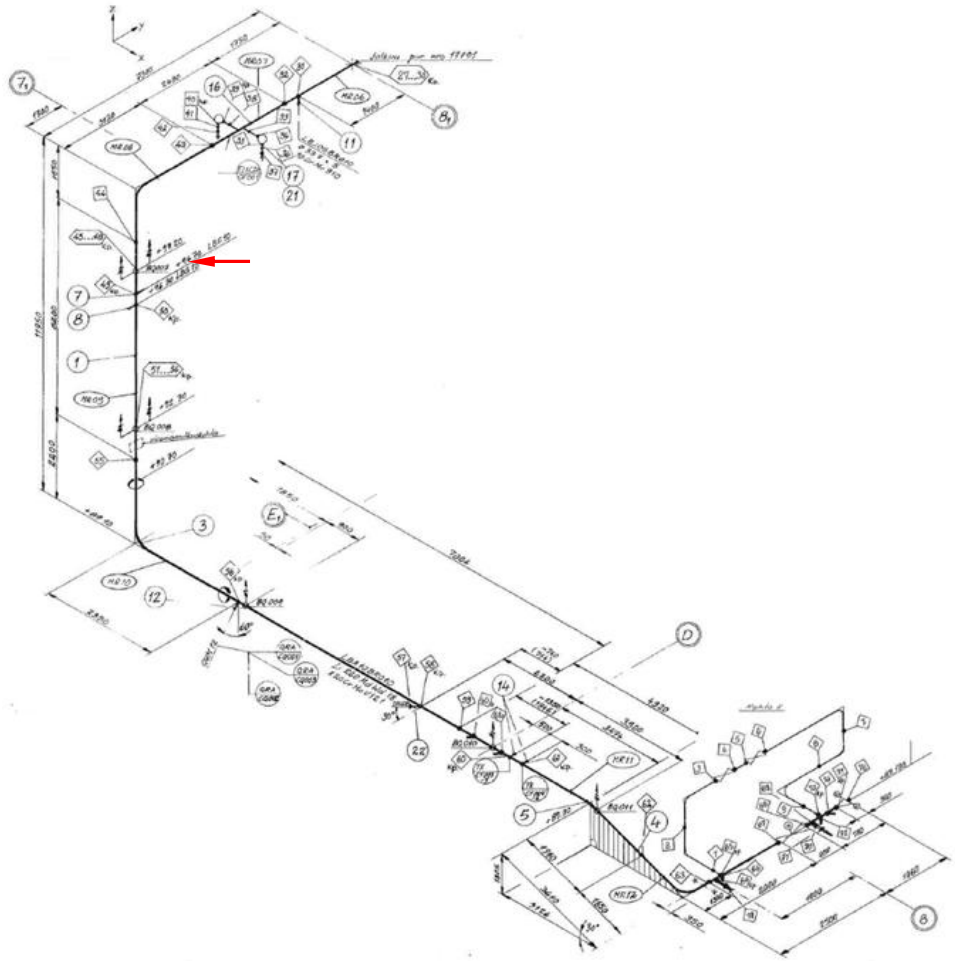

Figure 3. Lower section of the piping; red arrow shows the branch for the line to the reduction valve.

Table 1. Brief summary of design, service and maintenance information of the piping

Item/issue	Information	Notes
Dimensions	273 x 36 mm (initial part) 323,9 x 42 mm (initial part) 260 x 18 mm (the rest)	Partly old, from SH header to spherical piece From sphere to cone, 10CrMo9-10 X20CrMoV11-1 after cone
Branch (max)	245 x 29/16 mm	To reduction valve (and one blind branch)
Supports	Constant load hangers	No slides, one fixed point
Time in service	220/100 kh (old/new part)	New part includes partly old sections
Steam temp/pressure	540/535^{0}C // 130/110 bar	Design / service
Startups	Cold starts 3-4 / year	

Latest piping inspections were conducted in 2014 and 2015. In 2014 there was a crack indication in the saddle point position of the reduction line branch (in X20 material), and the indication had been removed by grinding. A similar indication reappeared in the 2015 inspection, and this time a boat sample was ex-

tracted at the defective region (Figures 6 to 8). The crack was found to be growing by creep in the type IV position in the heat affected zone of the branch weld, on the main pipe side, rather similarly to some earlier experience on X20 saddle point weld damage [8]. The results of the analysis led to a decision that the recurring damage justified a weld repair but no component replacement was necessary. The repair was conducted during the planned outage (Figure 9).

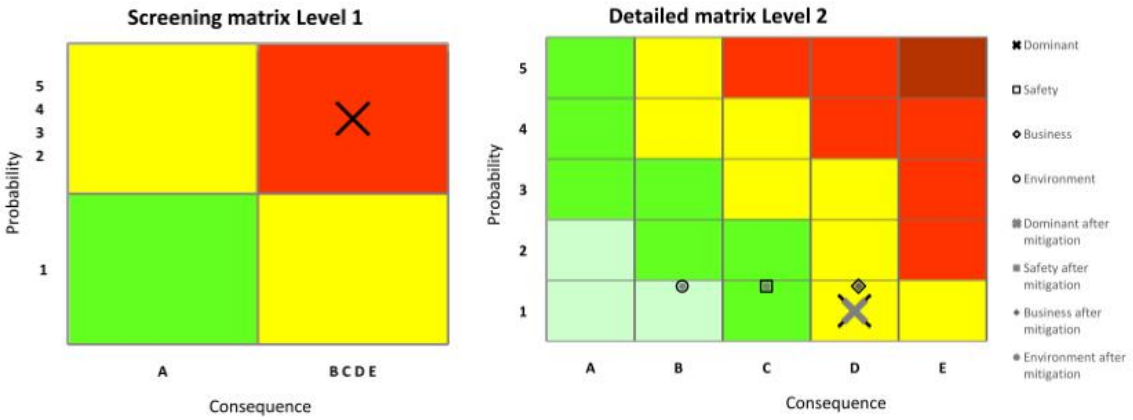

Figure 4. Assessment results of a spherical Y-piece: on left screening, suggesting further assessment, and on right side more detailed assessment, suggesting tolerable risk (here financial risk dominates).

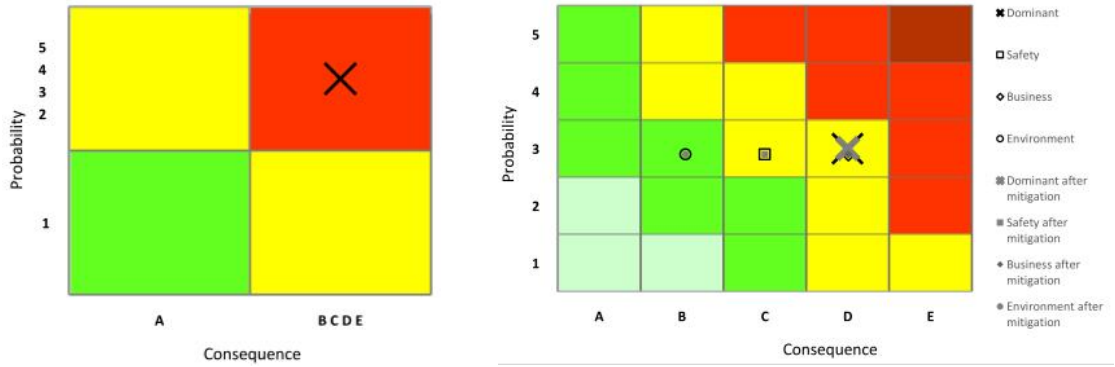

Figure 5. Assessment results of the branch to reduction valve: on left screening, suggesting further assessment, and on right side more detailed assessment, suggesting reduced risk (financial risk dominates).

Figure 6. Outline of the branch to reduction valve, showing the saddle point position (left); and the extracted boat sample with a surface crack in the marked area (right).

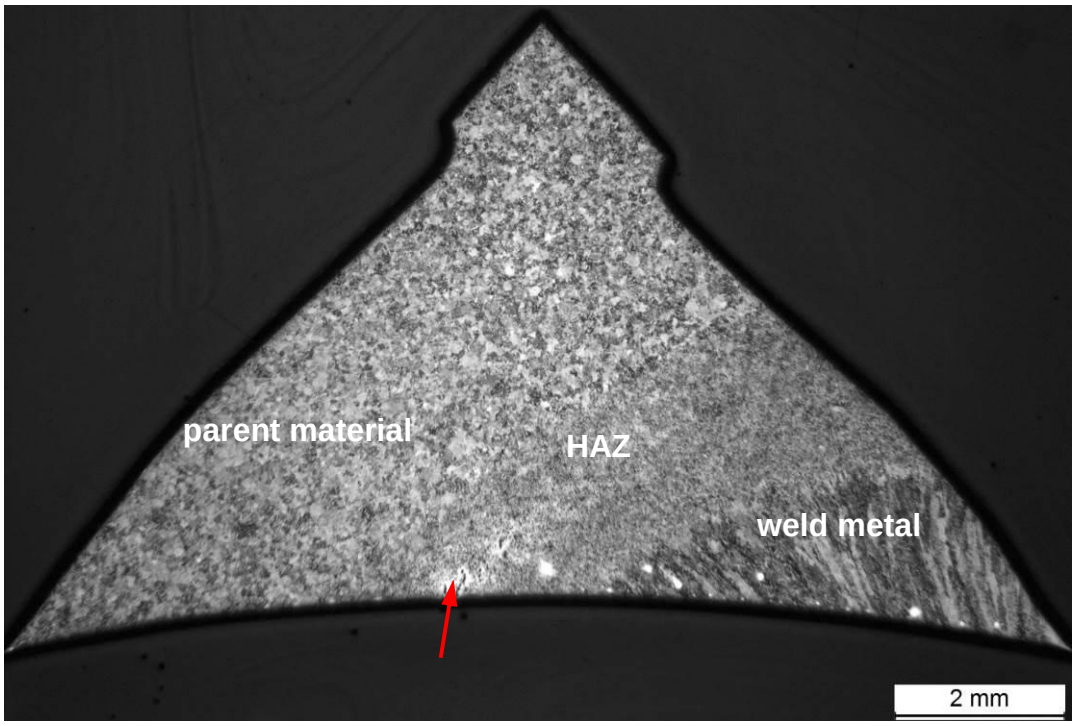

Figure 7. Cross-section of the boat sample, showing the position the creep crack (arrow).

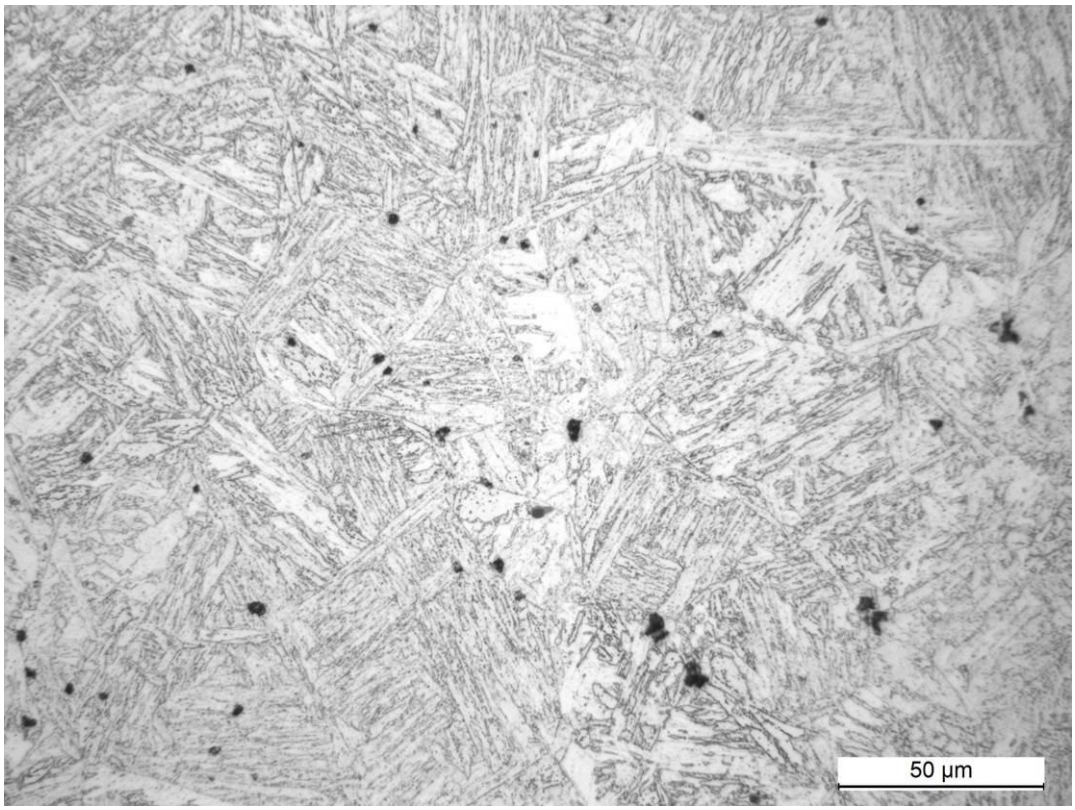

Figure 8. Cross-section surface of the boat sample in the type IV HAZ region, with creep cavities.

Figure 9. Repair welded branch to reduction valve (photo: Ville-Veikko Kylliäinen, Fortum).

In addition, a few crack indications were observed in smaller tube attachment welds close to the main stop valve, towards the right hand end of the piping section of Figure 5. Based on the findings it was suggested that more of such attachments are included in the future inspections. Apart from the observed local damage at the attachment welds as noted above, the steam piping appeared to be in fair condition for extended future service. This is also supported by the CHP operation, meaning essentially base load service.

4. Discussion

In the present case the selected RBI procedure was applied on a relatively small pilot scale but in parallel with conventional inspection, assessment/analysis and maintenance routines. From the current experience it can be concluded that the applied methodology and support tool are in no way contradictory to the approaches otherwise used, but appear helpful in keeping track and then using the necessary information that otherwise exists, was stored or is being created at disparate sources or supporting systems/expertise. Although RBI may show much of its strength only from repeated inspection cycles, the limited first experience from the small scale pilot study also suggests that the approach can promote the transparency of life assessment and related activities. In the present case the few cases of observed significant damage were dealt with during the planned outage, and with some recommended additional locations included in the inspection plans, the assessment results suggest that the overall piping is in fair condition for extended further service. The participation of the plant personnel and the experience from the plant was useful and well utilized in the level 1 session where experts and the best practical plant experts work together. The lessons learnt from the project include the need to highlight the importance of the good data management at the plant.

5. Conclusions and summary

RBI is well established in certain industrial branches nearly worldwide but in some industries the penetration remains partial, regional or is only applied by very large operators. Very partial it is for European smaller power plants, where lack of resources could be a reason to avoid non-mandatory activities. However, with progress in European standardisation, increasing availability of guidelines, tools and external help, RBI could become much more widespread. The advantages and benefits should be clear from the systematic means to justify the best return to the inspection and maintenance investments.

A small scale pilot study was conducted on RBI application for the main steam line of a CHP plant in Finland. The experience showed typical features of initiating RBI, such as the importance of available background information of design, fabrication, inspections, maintenance and operational history. In the example plant the steam system had been modified and the level of documentation was variable. The conventional guidelines can apparently support relatively lean RBI, to suggest typical areas of elevated probability of failure and recommended areas to be inspected, but the applied supporting tool can provide further help. The observed indications in the inspections were consistent with the general expectations and only resulted in repair within the planned outage. The resulting risk-based (or -informed) inspection and action plans are the main outcomes of the RBI exercise, aiming to produce the best justification and return on the inspection and maintenance investment for safe operation and long-term lifecycle performance of the plant.

Acknowledgements

Fruitful discussions within the partnership of the EU project SafeLife-X are gratefully acknowledged. The project is grateful to the plant management in Joensuu for the interest and participation in the pilot project. The inspection work was carried out as a joint effort of Replico Oy and Fortum.

References

1. Auerkari, P., Pohja, R., Yli-Olli, S., Tuurna, S., Pohjanne, P. & McNiven, U. RBI and probabilistic life assessment for components of coal and co-fired power plants. 41st MPA-Seminar, 5 - 6 October, 2015, Stuttgart, Germany. 11 p. http://seminar.mpa.uni-stuttgart.de/s-2015/Download/AllItems.aspx

2. Auerkari, P. & Jovanovic, A. New trends and perspectives of the global RBI: Standards, applications, challenges. International Symposium on Science, Engineering, and Strategy for Risk Based Maintenance (RBM 2015) Nov 30-Dec 1, 2015, Waseda University, Tokyo, Japan.

3. API RP 580. Risk-Based Inspection. API Recommended Practice 580, 2nd Edition, November 2009.

4. API RP 581. Risk-Based Inspection Technology. API Recommended Practice 581, 2nd Edition, September 2008.

5. Jovanovic, A., Bareiss, J. M., Stanojevic, P. & Liu, Yan. Risk-based inspection (RBI) in fossil-fuel fired power plants: Developing further the EU approach and applying it in the large-scale projects. Baltica IX, International Conference on Life Management and Maintenance for Power Plants, Helsinki-Stockholm-Helsinki, 11 - 13 June, 2013. Espoo, VTT Technology 106, pp. 19-49.

6. CWA 15740, 2008. CEN – Workshop Agreement on Risk-Based Inspection and Maintenance Procedures for European Industry (RIMAP).

7. Holmström, S., Auerkari, P., Salonen, J., Nikkarila, R. & Junttanen, J. Creep damage and long term life of steam line components: case X20. Baltica VIII, Life Management and Maintenance for Power Plants 2010. Espoo, VTT Symposium 265, Vol. 2, pp. 154-166.

Power & process:
Steam plant performance

Microstructural features of aged steam piping affected by creep and graphitisation and their detection

Bianca van Niekerk

Metallurgical Services, Sebenzana Consulting (Pty) Ltd.
Johannesburg, South Africa

Abstract

Carbon and Carbon-Molybdenum steels have been utilized in high temperature applications throughout the world. These steels have been in-service at elevated temperatures for a significant amount of time, sometimes well past their original design life. A substantial lack of information has been identified with regards to long term overheating (creep) and graphitisation both as separate and combined mechanisms with regards to carbon steels. A tentative interaction has been witnessed on large bore high temperature and pressure pipework recently. Of particular interest to this paper is the microstructural features and detection thereof.

1. Introduction and Background

1.1 Graphitisation Nucleation and Growth

During the solidification process free carbon precipitates in the form of cementite (Fe_3C) which is metastable. However, the decomposition of cementite does not occur easily [2]. Given enough time and a suitable temperature, cementite will either spheroidise or graphitise.

Graphitisation is defined as the formation of free carbon in iron or steel [3]. Primary graphite forms during the solidification process and can mainly be found in cast irons. Secondary graphite occurs when cementite decomposes to iron and graphite at elevated temperatures and is the primary concern of this paper [3]. Spheroidisation is the process where carbides precipitate and coarsen over time at elevated temperatures. The steel composition and microstructure as well as the exposure temperature determines whether carbide spheroidisation or graphitisation will occur [3]. Spheroidised cementite is the most stable of all the ferrite and cementite aggregates, with graphite being the most stable in the Fe-C system. Graphite rarely appears in steels because the rate of decomposition at normal operating temperatures is extremely slow. The formation of spheroidised cementite is the slowest when the starting structure is pearlite and the coarser the pearlite structure the more difficult it is to spheroidise [2]. It has been reported that spheroidisation will more readily occur above 552˚C and that graphitisation will occur below 552˚C [2]. This transition temperature is variable in practice and sometimes a combination of spheroidisation and graphitisation can be observed.

Foulds and Viswanathan characterise two basic forms of chain/ planar graphitisation: “weld heat affected zone (HAZ) graphitization” and “base metal graphitization” hereafter referred to as parent material (PM) graphitisation [3]. In-service failures have mostly been reported on HAZ related graphitisation with

only recent occurrences of non-weld related graphitisation [3]. Both types of graphitisation have been documented in main steam pipework of old South African power stations [7].

Graphitisation is affected by two factors: the existence of an appropriate nucleation site (which will be discussed first) and the availability of free carbon to produce the required nucleus size. The two types of graphitisation, mentioned above, follows two distinct nucleation processes [3].

Weld HAZ graphitisation occurs primarily in the Over Tempered Heat Affected Zone (OTHAZ) and is associated with carbon supersaturation caused by the formation of austenite [3]. It is theorised that this part of the OTHAZ experiences peak temperatures during the welding cycle, that are slightly above the lower critical A_{c1} temperature (730˚C). Graphite nucleation sites are then produced by the decomposition of cementite to Fe and the carbon rich carbide ($Fe_{2.2}C$) to cementite [3]. The primary driving force for the transformation is the carbon activity gradient between the austenite (which has a high carbon solubility) and the ferrite matrix (which has a low carbon solubility) [3,7]. This results in the aggravation of age-related secondary graphitisation by providing the pre-existing nuclei to facilitate graphite growth. Nucleation sites can take the form of grain boundaries, inclusions and strain induced defect clusters which are in abundance in the OTHAZ within a thin band which is parallel to the welding gap.

It has been suggested that Cottrell atmospheres associated with dislocations may be instrumental in PM related graphitisation. When two dislocations move towards each other on their glide planes, and meet at an intersection they will react and form a new partial dislocation which reduces the strain energy. This results in three partial dislocations called Cottrell-Lomer dislocations that have three different glide planes. These dislocations are called super-sessile because the combination cannot move without disassociating, and this blocks the motion of dislocations on either side of the two intersecting glide planes [5]. A cold worked metal can have 10,000 times more dislocations as its soft annealed counterpart [2]. Strain aging is due to diffusion of carbon atoms in solution, to dislocations that have been generated by plastic deformation. This may produce carbon supersaturation which aids graphitisation [3,6].

In order to establish the rate of graphitisation one needs to understand the growth kinetics of graphite nodules. The rate at which such growth occurs is essentially controlled by the rate at which free carbon can be created and transported to the graphite particle and where the volume changes of graphite nucleation can be accommodated as described by equation 1 and Figure 1 [3]. The large volume difference between cementite and graphite acts as an impeding force for the nucleation of graphite. This is one of the main reasons why graphitisation only occurs after extended exposure to service temperatures, even though cementite is a metastable phase and there is a free energy decrease when it transforms to iron and graphite.

$$y = Ae^{(-Q'/RT)}t_g^{\,m} \qquad (1)$$

where

y: Fraction of transformation (0-1)
Q': The activation energy for the controlling process, is approximately equal to Q, the activation energy for diffusion of carbon in ferrite
A: Constant
T: Exposure temperature in absolute units
R: Universal gas constant
t_g: Exposure time after incubation
m: Time dependence power

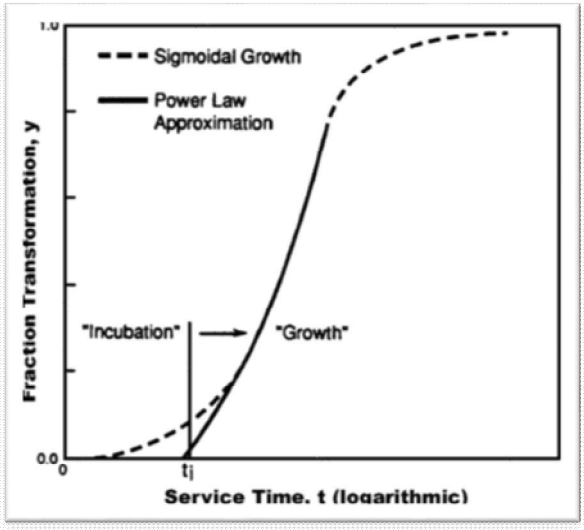

Figure 1. Schematic of graphite growth kinetics. Sigmoidal growth is represented by the dashed line, while the solid line represents a power-law approximation for the major portion of the curve. Note that the definition of an incubation period is as a consequence of the approximation [3].

The time dependence power (m) of the growth rate in carbon steels is not a function of material chemistry, microstructure or original heat treatment. However, the incubation period and actual graphite growth rate is dependent on material chemistry, microstructure and the initial heat-treatment condition [3].

The rate controlling process is established through the measurement of the activation energy. Table 1 summarises the published or, derived from published data for activation energy for selected diffusing species [3].

Table 1. Activation energy, Q as published or derived from published data [3].

Material	Process	Activation Energy Q kcal/mol (kJ/mol)
α-Fe(ferrite)	Diffusion of C in α-Fe	20 (84)
α-Fe(ferrite)	(Self/ vacancy) Grain boundary core diffusion	41 (174)
α-Fe(ferrite)	(Self/ vacancy) lattice diffusion	60 (251)

According to Foulds and Viswanathan it has been proven that chemistry has very little effect on the activation energy of graphite growth for carbon steel [3]. The author would argue that aluminium above a certain value will promote graphite nucleation, thereby sensitizing the material to graphitisation. A similar correlation was found during a failure investigation and outage of a South African power plant more than 20 years ago [7].

Attempts have been made to determine what the rate controlling process would be by measuring the activation energy. Quenching from just above the Ac_1 temperature, as in the case of the HAZ of a weld, the graphite growth activation energy is lowered to 20kcal/mol, that of diffusion of C in α-Fe (ferrite) [3].

As-normalised steel has similar graphite growth characteristics to that of vacancy/ self-diffusion along grain boundaries and dislocation cores with an activation energy of 41kcal/mol. Cold-work induced by the forming process can however reduce the as normalised activation energy by half (20kcal/mol), the activation energy of diffusion of C in α-Fe [3].

From the three points discussed above it has been concluded that the activation energy for weld HAZ graphitisation of diffusion of C in α-Fe can be used (20kcal/mol). For PM graphitisation it has been proposed that the activation energy for grain boundary and core diffusion (41kcal/mol) be used to calculate the growth rate of graphite as there does not exist sufficient data on the effect of cold work and plastic strain on graphitisation [3]. Weld HAZ graphitisation thus requires a lower activation energy than PM graphitisation, which is the general trend seen by the author. However, the presence cold working (from the forming process), lowers the required activation energy to similar values as that of weld HAZ graphitisation.

1.2 Creep Formation and Propagation

Creep is a time dependant and thermally activated deformation process that occurs at stresses below the yield strength [1]. Creep can technically occur at any temperature above absolute zero, however the strain developed in the process is a function of time, temperature and stress. As a result, the higher the temperature and stress the more significant the creep phenomena becomes. It is generally accepted that carbon steel objects that operate at temperatures above 370°C (700°F) are subject to creep [12]. It should be noted that creep has been documented at temperatures between 300-420°C (~570-790°F) and is associated with very high stress [6].

The creep resistance of a material is dependent on the microstructure. A creep resistant steel will contain a very large number of very fine precipitates. The purpose of precipitates is to impede the motion of dislocations. It should however be noted that most precipitates will coarsen with time and during welding, and their distribution will become less dense and subsequently less effective at resisting creep deformation [1].

A fine grained microstructure will impede dislocation movement at low temperatures, but at a creep initiating level they provide the process with sources of atoms and vacancies which allow for dislocation climb. The temperature at which this transition occurs is called the equicohesive temperature [1]. Crystal lattice diffusion occurs which includes vacancy diffusion and dislocation climb and mobility. For this process to occur an atom must possess an energy greater than the activation energy in order for it to break away from its neighbouring atoms. At the creep initiating level, the increased thermal energy allows increased dislocation mobility, allowing them to climb, jog and side-step obstacles in the material which would normally impede their motion. During the movement of these dislocations, vacancies and atoms fill the voids, allowing the dislocation to climb out of its initial slip plane and continue steady state creep. Therefore, a fine grained microstructure will reverse its role at high temperatures from resisting creep deformation to aiding creep deformation [1].

High stresses will drive dislocation movement, resulting in faster creep rates and higher strain levels. High initial stresses, primarily residual stresses from forming, may be sufficient to initiate cracking. Two effects of pre-straining have been noted with regards to creep crack propagation. The first is an increase in immobile dislocation density which will slow the relaxation of crack tip stresses and favour cavitation and micro-cracking. The relaxation of stress concentrations at microstructural features such as carbides, inclusions and grain boundaries will also be inhibited. The second effect is the generation of internal stress fields due to the formation of dislocation pile-ups. These initial stresses will relax with operating time, however service stresses, will continue to drive the cracking and result in failure in later years [6].

Operation at a temperature 10°C above the intended temperature consumes the component twice as fast, while operation at a temperature 10°C below increases the life of the component by double [1,8]. High temperatures will coarsen impediments to dislocation movements and also result in a fast creep rate and high strain [1]. Once plastic deformation starts in a given area, the metal will be softened which in turn leads a relatively large plastic deformation. The material in the adjoining region will then yield because of the stress concentration at the boundary of the deformed and un-deformed areas.

After a sustained period of time under creep conditions, cavities will start to form on the grain boundaries. These cavities will initially be isolated, but given enough time they will start to align and link together to form micro-cracks. These cracks act as stress concentrating features which generate a highly stressed area ahead of the crack tip. This in turn, leads to relatively large strains that develop in small areas, resulting in ductility exhaustion and the growth of the crack by the link up of cavities [1].

The basic equation to describe creep rate is:

$$\dot{\varepsilon} = Ae^{-q/kT}. \quad (2)$$

where

$\dot{\varepsilon}$: Creep strain rates
q: The activation energy per atomic scale
T: Absolute temperature
k: Boltzmann's constant ($13.8X10^{-24}$J/K)[4]

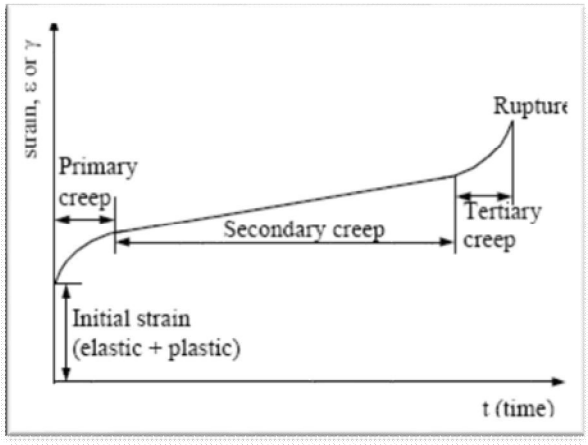

Figure 2. Schematic representation of the three stages of a typical creep curve [2].

2. Microstructural features

The microstructural features of aged steam piping affected by creep and graphitisation fall into the two major categories identified above. Weld HAZ related damage and PM related damage. Ideally carbon steels, in the form of high pressure pipework, have not been designed to operate within the creep regime for extended periods of time.

Table 2 was taken from Dooley and McNaughton shows the maximum oxidation limit for different carbon steels [6]. It has been noted that extended operation above 800˚F (427˚C) may lead to graphitisation and/or spheroidisation.

Table 2. Maximum Metal Temperatures (Oxidation Limit)[6].

Steel Type	ASME Spec. No.	ASME Max.1 °F (°C)	Mfr #1 Max.2 (°C) °F	Mrf #2 Max.3 (°C) °F	Mfr #3 Max.4 °F (°C)
Carbon Steel	SA-178 C	1000 (538)[1,2]	950 (510)	850 (454)	850 (454)
	SA-192	1000 (538) [1,2]	950 (510)	850 (454)	850 (454)
	SA-210 Al	1000 (538) [1,2]	950 (510)	850 (454)	850 (454)

[1]Prolonged exposure to temperatures above 800˚F (427˚C) may convert the carbide phase of carbon to graphite
[2]Only killed steels shall be used above 850˚F (454˚C)

2.1 Microstructural Features of Weld HAZ related Graphitisation

The mechanisms for graphite nucleation and growth is better understood with regards to HAZ related graphitisation and has been the topic of multiple failure investigations over the years. As discussed above, graphite nucleation is bolstered by carbon supersaturation directly as a result of the welding process. The IC/ OTHAZ is particularly rich in nucleation sites with an abundance of grain boundaries (fine grain structure), inclusions and strain induced defect clusters. Graphite growth is further encouraged by a lowered activation energy of the HAZ. Figure 3 is a micrograph depicting the relatively early stages of HAZ graphitisation, with a lot of fine graphite nodules nucleating on the spheroidised pearlite grains of the over tempered zone.

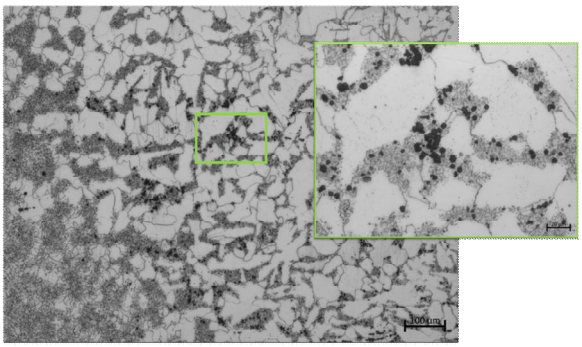

Figure 3. Micrographs of HAZ graphitisation. Taken at a magnification of 100x and 500x respectively.

2.2 Microstructural Features of PM related Graphitisation

Parent material related damage has been observed in two distinct planar forms. For the purpose of this paper they will be referred to has longitudinal planar graphitisation and angled planar graphitisation. Both types of planar graphitisation have been noted in main steam components of South African power plants [7].

The longitudinal graphitisation originates from the HAZ and runs into the PM, more or less perpendicular to the direction of the weld. This phenomenon has to date only been observed in carbon steels that have not been fully normalised. The partial normalisation of the material is believed to be the underlying reason for this kind of graphitisation. Normalising establishes a more uniform carbide size and distribution. Large banded carbides might be responsible for this kind of graphitisation. Partial normalisation also means that the internal stresses created when forming the component i.e. rolling has not been fully relieved. A requirement for graphitisation is a nucleation site or rather the presence of volume-change accommodating defects [3]. These defects can take the form of vacancies and dislocations which are associated with grain boundary inclusions and strain induced defects. Once plastic deformation starts in a given area, the metal will be softened which in turn leads a relatively large plastic deformation. The material in the adjoining region will then yield because of the stress concentration at the boundary of the deformed and un-deformed areas [6]. This explains why the planar longitudinal graphite has a higher concentration and appears to originate at heat affected zones or high strain areas associated with the forming process. Further graphite then nucleates on areas that require less activation energy – like the rolling direction of a pipe that was not properly heat treated or fully normalised or the fact that the carbide size and distribution is not uniform. Residual stresses also lower the activation energy required for graphite growth. The green arrows in Figure 4 highlights an example of longitudinal planar graphite.

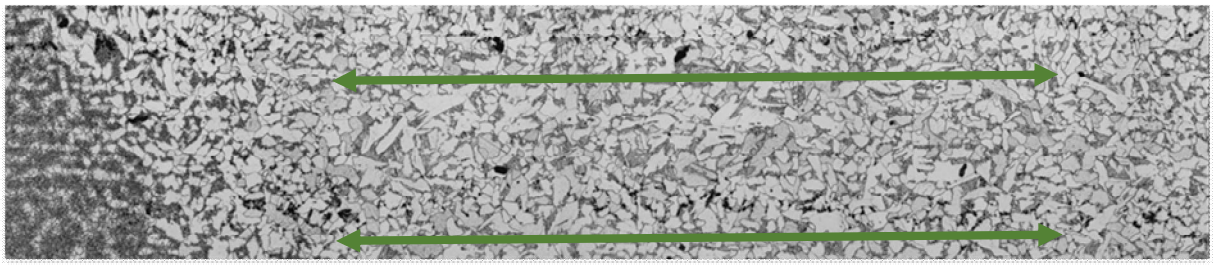

Figure 4. Micrograph showing longitudinal planar graphitisation. Taken at a magnification of 50x.

The second type of graphitisation, angled planar graphite, has only been observed in formed T-pieces and manifolds thus far [7]. The residual stresses induced during the forming process and the complex geometry of the T-piece results in a large number of defects. Bands of angled planar graphite nucleate and grow on in the direction of principle residual stress induced during the forming process – similar to that of longitudinal planar graphite. An example of angled planar graphite can be seen in Figure 5.

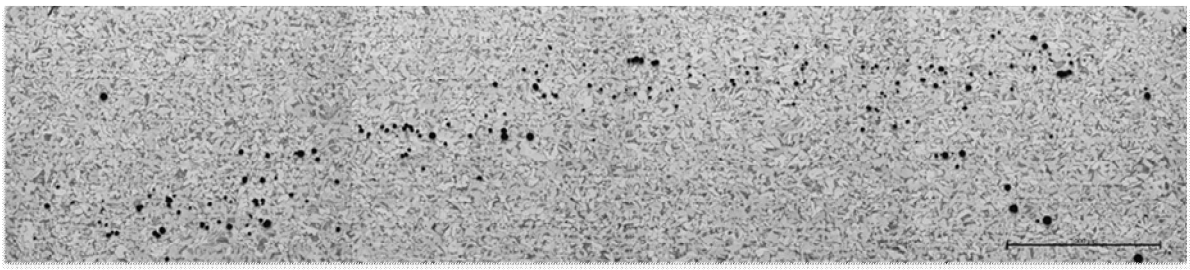

Figure 5. Micrograph showing angled planar graphitisation. Taken at a magnification of 50x

2.3 Microstructural Features of Creep

Creep has been well documented and studied over the years because of the large amount of catastrophic failures associated with this phenomenon. It should be noted, however, that carbon steel was never meant to operate in the creep region for extended periods of time and that the information available is therefore not as extensive as the low alloy and stainless steel counterparts.

Creep void formation and graphitisation are similar in that voids also prefer to form in the HAZ of a weld. This is in a large part due to the stress and strain redistribution that takes place in the weldment envelope which is referred to as “off-loading” [8]. The damage however is more consistently spread through the thickness of the component and can often extend 10mm into the PM (PM10). Only when the damage has progressed to such an extent that void alignment and linking occurs, will the distribution of voids become preferred, usually ahead of a stress front. Carbon steel shows an alarming tendency to only form creep cavitation very late in the service life of a component. It is largely believed that when creep does appear that it is already within the tertiary creep phase, and subsequent cavitation, linking and crack growth is exponential with time. The micrograph in Figure 6 is an example of micro-cracking.

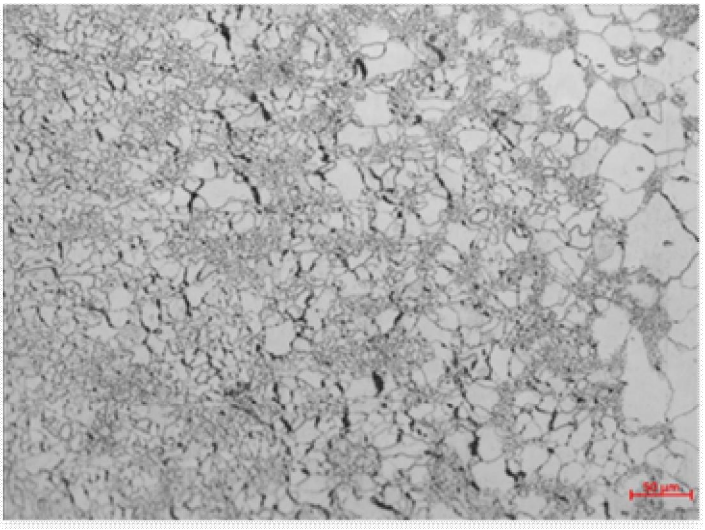

Figure 6. Micrograph of replica taken on the HAZ of a severely creep damaged surface

2.4 Microstructural Features of Creep and Graphitisation as a Combined Mechanism

During the course of multiple investigations, it has been found that graphitisation and creep are not mutually exclusive, and often the one accompanies and augments the other.

Replication of a component seen in Figure 7 revealed not only the presence of graphitisation, but also the presence of aligned and linking creep voids – the early stages of micro-cracking. The intercritical heat affected zone (ICHAZ) and OTHAZ is an area that is prone to void formation because of the coarsening of precipitates. The fine grained microstructure also provides the process with sources of vacancies (by the intersection of dislocations) which allow for dislocation climb. During the movement of these dislocations, vacancies and atoms fill the voids, allowing the dislocation to climb out of its initial slip plane and continue steady state creep [2].

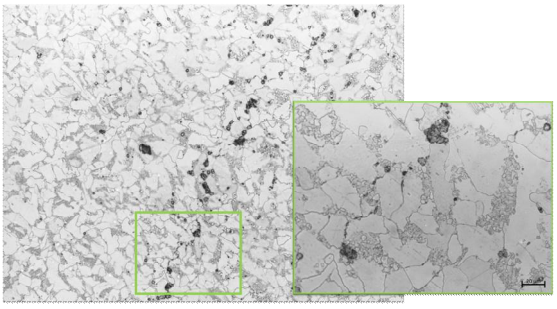

Figure 7. Micrographs of creep and graphitisation taken on the same location as the micrographs of Figure 3. Taken at a magnification of 50x and 500x respectively.

From observation of multiple failed and un-failed samples in various stages of degradation it has been found that creep and graphitisation appear to follow a similar pattern of growth. The micrograph seen in Figure 8 is of a rather large graphite nodule in the PM of a carbon steel sample. The microstructure directly adjacent to the nodule is slightly deformed with multiple aligned creep voids surrounding the nodule. High stresses, caused by the volume change associated with graphitisation, will drive dislocation movement, resulting in faster creep rates and higher strain levels.

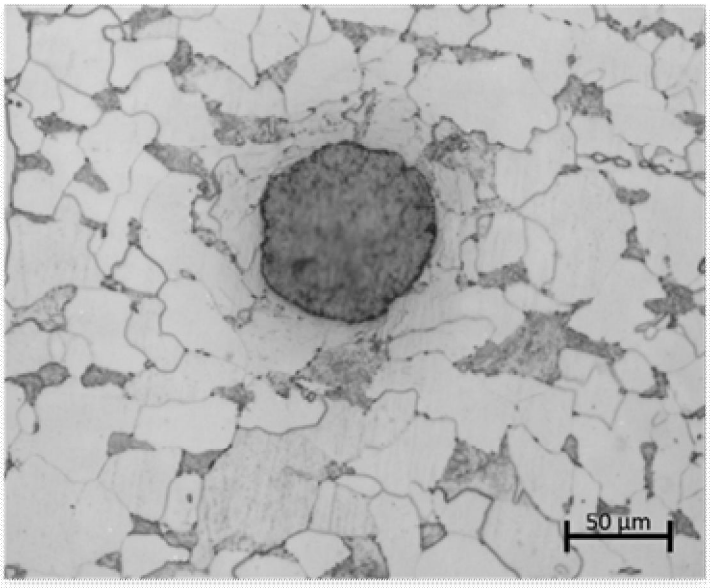

Figure 8. Micrograph of a graphite nodule with surrounding creep cavitation. Taken at a magnification of 200x.

Of the two mechanisms graphitisation takes longer to develop enough aligned nodules to progress into a through-wall crack. In the micrograph of Figure 9 it can be seen that the graphite nodules become linked by voids. Creep cavitation is affected by the size of the precipitate/graphite nodule. The larger the size of the nodule, the more creep strain accumulation takes place at the matrix-particle interface. A large amount of aligned graphite nodules decreases the load bearing area, thereby also increasing the effective stress.

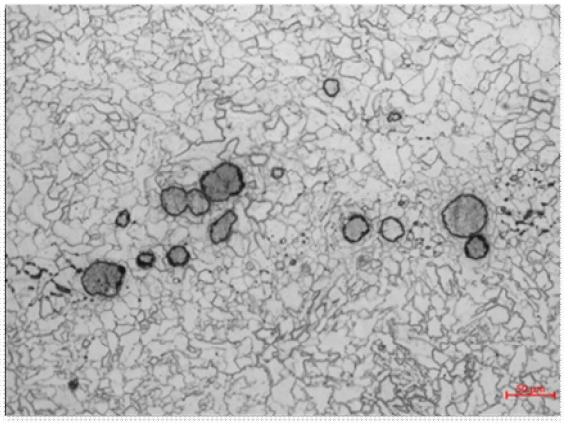

Figure 9. Micrograph of graphite nodules linked by creep cavitation. Taken at a magnification of 200x

Micro- and macro-cracking will soon follow, similar to the crack seen in Figure 10. These cracks act as stress concentrating features which generate a highly stressed area ahead of the crack tip. This in turn, leads to relatively large strains that develop in small areas, resulting in ductility exhaustion and the growth of the crack by the link up of cavities [1]. The final result is a through-wall crack as seen in Figure 11.

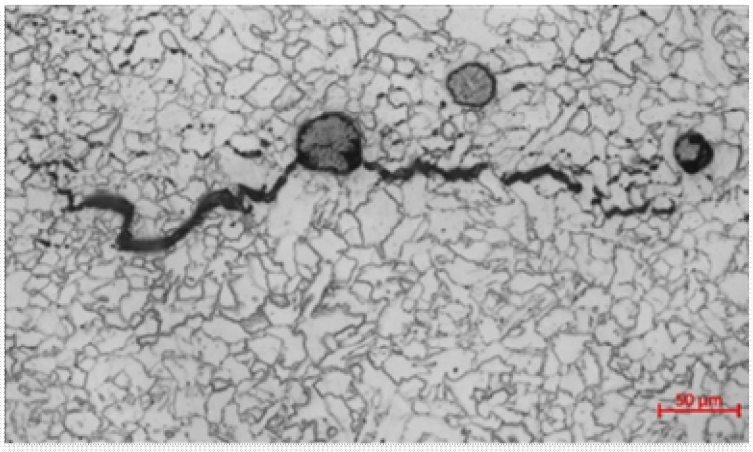

Figure 10. Micro and macro-crack formation through a graphite nodule. Taken at a magnification of 200x.

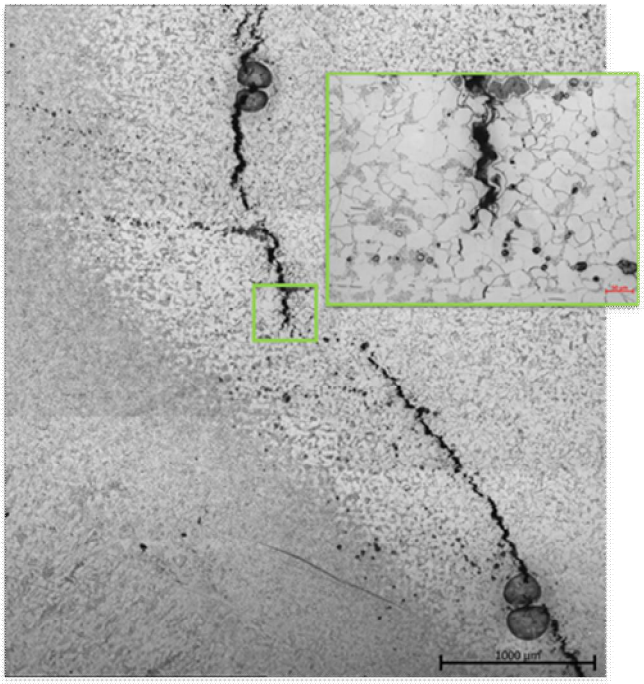

Figure 11. Through-wall crack, showing linked cavities and graphite nodules. Taken at a magnification of 50x and 200x respectively.

3. Detection methods for creep and graphitisation

Non-destructive testing (NDT) techniques for the detection and evaluation of creep damage have been well established in the industry and will be touched upon in the paragraphs below. Graphitisation detection and evaluation is, however not as well established and researched.

3.1 Surface replication

Surface replication is a NDT technique that can be used in the detection of both creep and graphitisation. This technique is limited in that only surface damage is detected.

For the purpose of detecting creep, it has been proven that replication is adequate – sometimes (where possible) deeper grinding is required in order to establish a more accurate picture of the damage profile [8]. Extensive damage models have been developed in order to quantify creep damage both in homogenous materials as well as in butt welds. These models have been refined over the years with post and pre-exposure creep tests [8,9,10].

Graphitisation does not have established damage models and still much uncertainty exists with regards to the nucleation and growth kinetics of PM related graphitisation. However, replication can be used for the detection of graphitisation. HAZ related graphitisation has proven to be the most consistently detectable form of graphitisation with regards to replication. Surface replication might miss angled planar graphitisation, which will appear to be a cluster of random graphite nodules when viewed on the surface plane. It might also be that the angled planar graphite remains undetected by replication because the damage does not extend all the way to the surface of the component. Longitudinal planar graphitisation might also remain undetected, depending on the depth of replication.

A fairly safe and conservative approach would be to assume that wherever creep nodules are detected in carbon steels, graphitisation is sure to be present. Where graphite nodules are detected without the presence of creep, additional NDT techniques must be utilised in order to gauge the extent of the damage. A carbon steel component that is subject to graphitisation is very close the end of its service life and should be replaced wherever possible.

3.2 Magnetic Particle Inspection (MPI)

MPI will not detect graphitisation or creep damage, but will detect surface indications. If creep or graphitisation is detected on a component with a linear surface indication, the life of the component must be reassessed. If the minimum wall thickness is compromised by the removal of the indication, or if it is found that the indication is actively growing by either mechanism, the component should rather be replaced. Failing replacement, the component must be operated under less severe conditions and, where possible, monitored by use of capacitive strain gauges. The interval for replacement and inspection is at the discretion of the relevant engineer.

3.3 Ultrasonic Testing (UT)

UT is not only used in the industry to determine the wall thickness of a component but also to detect if there are any volumetric flaws. UT cannot detect creep damage, but is often used to screen for subsurface defects which may develop into creep cracks in aged materials.

Graphitisation has however been detected more than 20 years ago by use of ultrasonic testing at a South African power plant, by the identification of laminar inclusions next to a butt weld. This butt weld was removed and sectioned due to the size and orientation of the inclusions and it was confirmed to be graphitisation [7].

Recently more advanced techniques like time of flight diffraction (ToFD) and phased array ultrasonic testing (PAUT) have been developed for the detection of volumetric discontinuities.

ToFD utilises a transmitter and receiver probe in order to detect volumetric defects. During recent trials ToFD consistently picked up weld related or manufacturing defects, but showed no conclusive evidence of detecting graphitisation.

The recent increase in computing power has allowed for new ultrasonic processing techniques based on full matrix capture (FMC) acquisition method, such as total focusing method (TFM) and multi-mode total focusing method (MTFM). FMC is based on the theory of firing on a single element in an ultrasonic array transducer and receiving on all elements – this is referred to as “fire on one and receive on all”. This process then repeats itself until all elements in the array have fire once. A TFM algorithm is used to fully focus all points within the insonified area in order to provide an image [11].

PAUT TFM showed promise of detecting severe graphitisation, with particular success in detecting angled planar and weld HAZ related graphitisation. Further research and formal trials are however necessary to validate this method.

3.4 Chemical analysis – aluminium

An extensive sampling program, undertaken more than 20 years ago, established a correlation between aluminium content and graphitisation. It was decided to use the percentage acid-soluble aluminium as a measure of graphitisation potential. A threshold value of 0.005% was chosen and any value above this was classified as being susceptible [7]. In recent sampling, it has been found that butt welds with an aluminium composition of less than 0.009 mass% tended to form only random graphite nodules, while butt welds with more aluminium content tended to be more severely graphitised. More sampling is being undertaken to map the exact amount of aluminium required for graphitisation.

4. Conclusions & Recommendations

The following conclusions and recommendations, based on the review and analysis of published literature and field data on creep and graphitisation of carbon steel high pressure pipework, have been reached:

- Graphitisation and creep are similar in that both mechanisms show a propensity for forming in the IC/OTHAZ of a component. Though the mechanisms by which they form might differ slightly, the root causes are the same. An abundance of grain boundaries (fine grain structure), inclusions and strain induced defect clusters as well as the coarsening of precipitates.
- The longitudinal planar graphitisation originates from the HAZ and runs into the PM, more or less perpendicular to the direction of the weld. This phenomenon has, to date, only been observed in carbon steels that have not been fully normalised. The fact that this kind of planar graphitisation runs perpendicular to the weld, makes it less likely to fail catastrophically, however this kind of graphitisation is invariably associated with weld HAZ graphitisation.
- The second type of graphitisation, angled planar graphite, has only been observed in formed T-pieces and manifolds thus far[7]. Bands of angled planar graphite nucleate and grow in the direction of principle residual stress and like failures seen in high pressure tubing, this might lead to catastrophic failures. Whether creep cavitation is likely to link the graphite nodules have not yet been established, however the possibility exists.
- Creep cavitation for carbon steels show very late in a components life and a large uncertainty exists over how to accurately predict the rate at which creep cracks may appear and grow. A creep model can be established by means of post exposure creep testing and accelerated creep testing.
- The various forms of planar graphitisation are not as easy to detect as creep. However, a fair amount of accuracy has been established for the detection of weld HAZ related graphitisation. For formed components miniature specimen test approaches should be used on areas of highest stress.
- Further testing and qualification of PUAT TFM should be explored as a means of detecting graphitisation.
- Quantification of aluminium content and graphitisation should be undertaken as future work.

5. Acknowledgement

The author wishes to acknowledge the assistance and mentorship of Prof. W. Stumpf, the input from Mr G von dem Bongart, Mr A Bissel, Mr M Yates and Mr P Rubbers. Special thanks to Mr A Carr for his input as well as the opportunity. Special thanks to the mentorship of Mr A Downes.

References

1. Robertson, DG and Simandjuntak, S Masuyama, F; Ford, J and Shibi A. 2010. E-lifing, A Compendium for Lifing Procedures for Steam Power Plants. European Technology Development Ltd, UK, p. 231-232, p. 254.

2. Reed-Hill, RE. and Abbaschian, R. 1994. Physical Metallurgy Principles. PWS Publishing Company, Boston, pp. 282-283.

3. Foulds, JR and Viswanathan, R. 2000. Graphitization of Steels in Elevated-Temperature Service. ASM International.

4. Honeycombe, RWK. and Bhadeshia HKDH. 1995. Steels Microstructure and Properties, Edward Arnold.

5. Verhoeven, JD. 1975. Fundamentals of Physical Metallurgy. John Wiley and Sons, Canada.

6. Dooley, RB and McNaughton, WP 2007. Boiler and Heat Recovery Steam Generator Tube Failures: Theory and Practice. Volume 3: Steam-Touched Tubes, EPRI, 59-1 to 59-5.

7. Havinga, FH. Graphitisation of Carbon Steel, Eskom, South Africa.

8. Van Zyl, FH. 1996. Life assessment of High Temperature and Pressure Components in South Africa – an Overview of the Philosophy, Methodology and Techniques in use. Eskom Technology Group, South Africa.

9. Van Zyl, FH. 2000. An Overview of Material's Engineering and Research Activities in TSI (Eskom) with Respect to Life Assessment and Integrity of High Temperature and Stressed Components, TSI, Johannesburg, South Africa.

10. VGB PowerTech e.V. 2002. Microstructure Rating Charts for Evaluating the Microstructure and Creep Damage of High-Temperature Steels for High-Pressure Piping and Boiler Components. VGB PowerTech Services GmbH, Essen.

11. TWI. 2003. Advanced Ultrasonic Imaging Techniques for Industrial Applications" Publishable Summary, 23218.

12. EPRI. 2007. Carbon Steel Handbook. Electric Power Research Institute Inc., California, p. 67.

Monitoring and in-service experiments on power plants

Satu Tuurna & Pekka Pohjanne

VTT Technical Research Centre of Finland Ltd
Kemistintie 3, Espoo, Finland

Abstract

Corrosion of metals in the presence of high temperature flue gases and deposits has long been a challenge in boilers, furnaces and industrial process plants. The maximum achievable operation temperature and pressure are usually limited by corrosion. The repair actions due to corrosion failures are often highly expensive. Monitoring gives valuable information of the operational parameters (temperature, pressure, fuel etc.) of the plant and thus allows for proactive control of parameters to possibly extend the life of tubes and pipings. In-service experiments can be also utilised for wider scope in the life assessment. Increasing operational parameters promote the growth rate of nearly all damage mechanisms, e.g. corrosion, creep and aging mechanisms are accelerated to shorten the expected lifetime. Systematic monitoring provides a cost-effective way to improve reliability of critical components, reduces unscheduled breakdowns and increases overall business profitability.

1. Introduction

Corrosion of key components is one of the major challenges in many process plants. It is one of the most serious damage mechanisms impacting the equipment and assets. The substitution of fossil fuels through alternative fuels (e.g. waste and biomass) is of great interest not only for the environmental but also for the economic aspect. The properties, e.g. energy density, slagging and corrosion potential, of alternative fuels are usually the reason for increasing operational costs. To limit and assess corrosion risks in advance, it is essential to know the behaviour and effects of fuels on the process equipment and components. At the moment the most challenging in preventing corrosion assessment seems to be the limited knowledge of simultaneous effects of different corrosive components, such as heavy metals, chlorides, sulphates and oxides, on corrosion. Uncontrolled corrosion can cause leaks and component failures, leading to reduction of both the performance and reliability of equipment. In extreme cases, corrosion can lead to unexpected failures that can be costly in terms of repair costs, environmental damage and also potential harm to people working around. And thus different monitoring systems are needed to follow and estimate the progress of corrosion phenomena in the processes. [1-4] The most accurate steps to assess corrosion is done during maintenance shutdowns but that is a rather late stage, and thus different kinds of in-service monitoring systems based on metal loss and/or electrochemical measurements have been developed and are still under further development. [5-7]

At the same time with larger variety of fuels, there is the pressure to improve efficiency by higher steam values. Increasing operation parameters promote the growth rate of nearly all damage mechanisms. The rate of steam side oxidation is promoted by increasing temperature that will also continuously increase with the growth of the insulating oxide layer, when an approximately constant heat flow is extracted through the

heat transfer surfaces. The loss of load bearing wall thickness and the temperature increase resulting from decreased heat transfer due to forming oxides may lead to creep failures. [8-10] Many material options used in conventional power plants have failed in the waste to energy and even in biomass plants; even with the decreased steam temperatures and pressures component failures occur. Alloy modification, the use of higher alloyed materials, is one way to mitigate corrosion and other failure modes, and improve the efficiency of energy generation.

Next chapters describe the ways used to assess corrosion and lifetime of high temperature components, and give some general examples of studies carried out on-site.

2. Inspection and offline monitoring

Typically corrosion inspection and measurements are performed during maintenance breaks with applicable NDE methods (ultrasonic, eddy current etc.), when the damage has already occurred or at least is in progress. The challenge of NDE methods is that they are manpower intense and quite slow. Thus thickness measurements are often taken over a relatively small percentage of the total boiler wall and statistical analysis is used to determine the overall condition of the boiler tubing [8].

The simplest metal loss inspection type is a destructive inspection with the weight loss sample, which is the most commonly used technique in corrosion research. The sample can be either a simple coupon or clamp (Figure 1), which is anchored on the area of interest. Another option is the use of sample tubes/panels (Figure 2.) or sample loops. A sample, with known weight, is installed during the overhaul, exposed to the process for a known period (e.g. to the next overhaul) and the weight loss is measured as a function of time. Although this test is simple, the life prediction according to the obtained results might be challenging. The sample requires a relatively long exposure to the studied process to yield accurate results. In addition, some corrosion modes occur with a small mass change (i.e. pitting) and thus it is difficult to detect from weight loss. The parallel samples and visual inspection of cross sections are needed to verify a prevailing corrosion mode and remnant load carrying thickness. [12,13] To study internal oxidation of tube materials, the tube samples need to be removed from the interest area, no coupons or clamps can be utilised in the case.

In the case of steam loop, the separate sample coil next to the interest area, the advantages compared to a coupon or clamp sample are that the test conditions are real operation conditions for materials and there is possibility for longer exposure times. The loop allows material testing in several temperatures at same time due to temperature gradient along the loop. Test sections can also be longer allowing the identification of possible variations in material quality along a tube, and both steam-side oxidation and fireside corrosion properties can be tested at the same time [14].

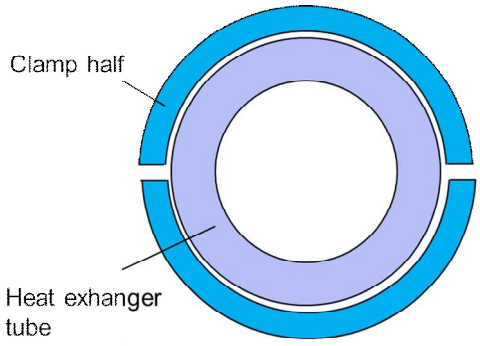

Figure 1. Schematic picture of clamp specimen around a heat exchanger tube

Creep is the primary life limiting mechanism on high temperature and pressure power station components. Creep evaluation is currently achieved by surface inspection of microstructure (replicas) during maintenance breaks; a methodology is quite time consuming and considered inadequate. Creep deformation can be monitored using offline and online measurement techniques. Offline techniques, such as ARMAC [15], allow manual data collection during plant shutdown. Whilst these technologies are generally cheap to

install, technicians and equipment (access to sensors) are needed to take measurements. The frequency of measurements is low and not periodically spaced (will only detect tertiary creep after significant running time in this regime). [16]

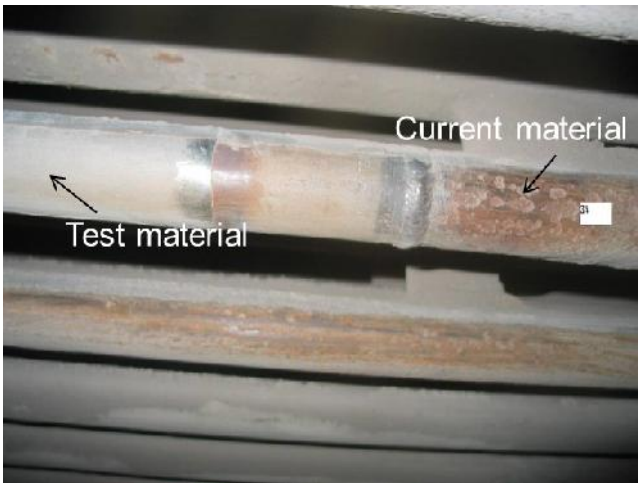

Figure 2. Material testing in heat exchanger tube, new test material in the left hand side of weld, in the right hand side current tube material

The inspection result obtained during maintenance break has limited value for pro-active corrosion management because it provides historical data, and thus monitoring methods obtaining continuous data has been developed.

3. Monitoring during service

Corrosion monitoring with the different types of probes measure process stream conditions. The probes are inserted into the process stream and are continuously exposed to the process environment. There are various corrosion probe systems available in the markets; besides corrosion the probes can be used to monitor various phenomena of combustion processes, such as the gas flow and ash composition. Roughly probes can be divided to mechanical probes (fouling, metal loss), which are analyzed after removal from the process, and those ones continuously collecting data (electrochemical probes). Typically online measurement results are compared to results obtained from calibration rings (weight loss samples), which are installed in the same probe with electrochemical system [12].

Corrosion probes either with an air or water cooling system are used for monitoring corrosion in boilers and chemical process industry. Probe testing enables long term material testing in real boiler conditions. Probes provide valuable information on the nature of the corrosion attack and forming corrosion products, and the behaviour of alloys in real boiler conditions [17-19]. The benefits of corrosion probe compared to coupon samples or clamps are an accurate temperature control of probe and a shorter testing time; the probe can be removed when sufficient exposure time is reached without a maintenance shutdown.

Electrochemical online corrosion measurements are based on determining the corrosion current within a confined system. Corrosion rate can be calculated according to Faraday's law, when the corrosion current is known, stating that the amount of dissolving material in electrochemical reactions is directly proportional to the current between anode and cathode. An electrochemical online corrosion probe system can be used to validate materials for boiler parts e.g. superheater and economiser tubes or to study the effects of boiler operation and fuel quantity on service life. Electrochemical corrosion monitoring can be applied in boiler applications when specimens/tubes are covered with ash deposits as the ash serves as the electrolyte for electrochemical measurements. The probe does not see oxidation or other mechanisms where electrochemical reactions are not involved and for this kind of purposes electrical resistance (ER) probe is one possible to increase the reliability of measurement. [12,20]

Figure 3 shows the principle of an air-cooled probe used in the measurement campaign in a waste to energy boiler [21]. Typical fuel mixture during the campaign was the recycled and waste wood from construction sites, forest residues and recovered fuel mainly from the packing industry. The measurement campaign was carried out with three different materials TP347H, HR3C and Sanicro 28. A temperature controlled, air cooled probe was placed in the superheater area in the second pass where the mean gas temperature was about 850°C. The probe was cooled to a surface temperature of 550°C, and the temperature of the test probe was adjusted by pressurized air. PID-controller, connected to one of the thermocouples, adjusted the cooling air flow with a pneumatic control valve. The temperatures of the other thermocouples were monitored and logged by an online datalogger during testing.

Figure 4 shows an overview of the probe after the testing campaign. A continuous deposit was formed on probe surface during the test. After exposure a section was taken from each specimen and moulded in plastic after which the prepared and polished sample cross-sections and alloy microstructures were characterized. Assessment of material performance was based on the estimation of the depth of the material degradation and oxide thickness measurements.

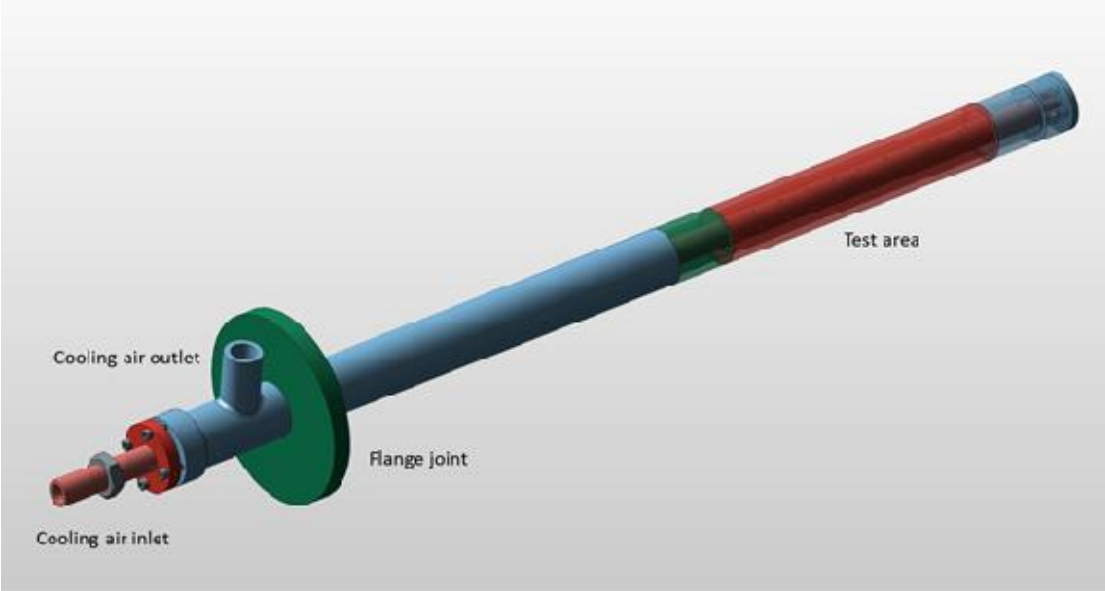

Figure 3. Schematic presentation of the air-cooled corrosion probe

Figure 4. Overview of corrosion probe head after testing campaign

Figure 5 presents the close-up from the online probe head showing sample and calibration (weight loss) rings separated with ceramic insulation rings. The deposit accumulating on the sample rings forms the electrolyte for electrochemical measurements between reference and corrosion rings. The summary of

online measurement data is illustrated in Figure 6 showing the increase of corrosion rate during the campaign, and also temperature variation due to soot blowing.

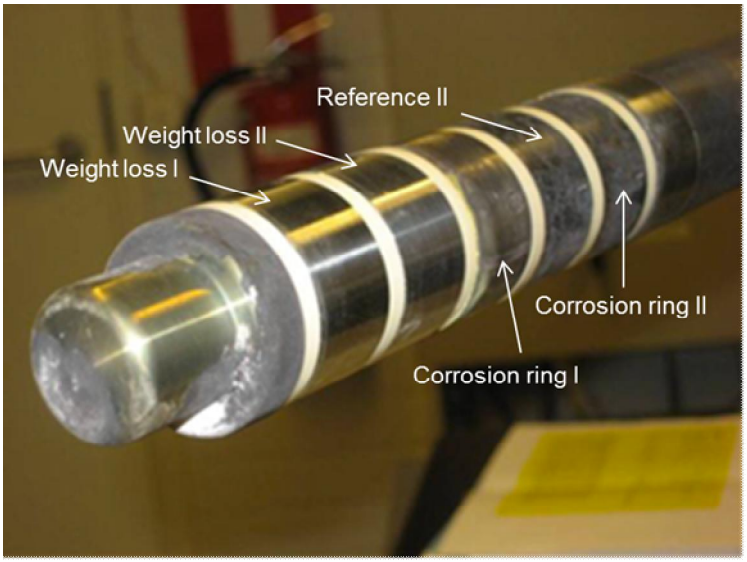

Figure 5. Close-up from the probe head before measurement campaign

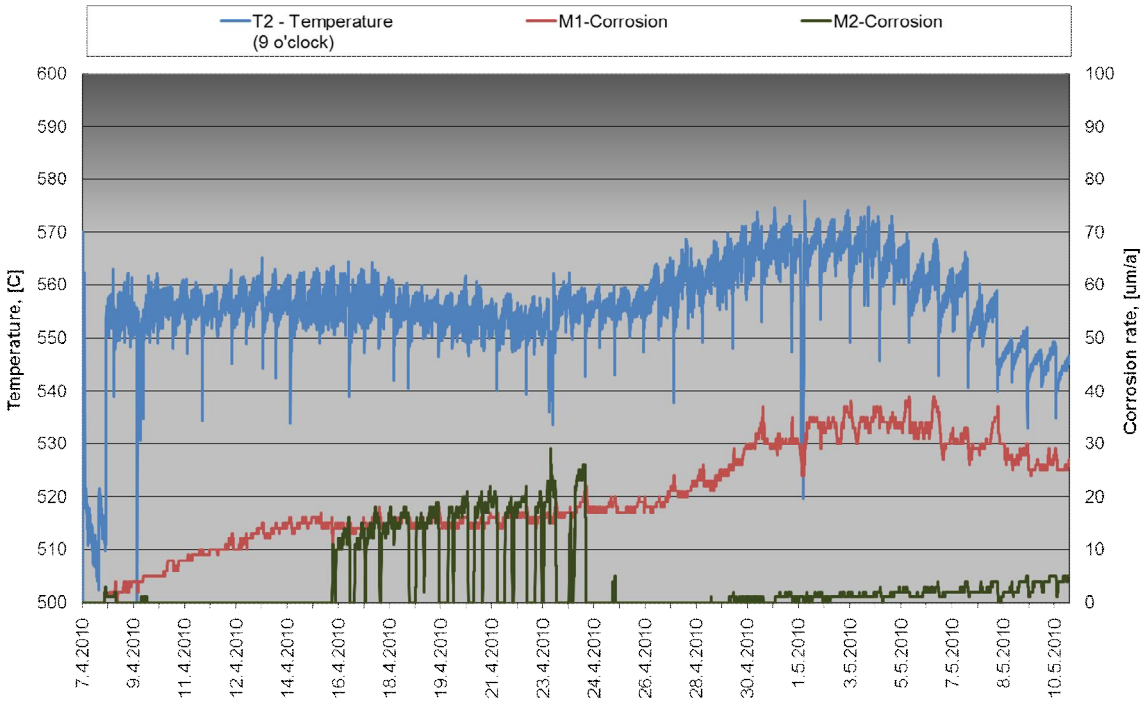

Figure 6. Summary from the probe data, collected during the measurement campaign

Probes can be also used to define the critical temperature ranges of materials for example during the planning of foreseeing changes in operational parameters. In that case, a single material is used in the probe, and the operation-dependent temperature gradient is applied to the probe, Figure 7. According to

the measurement results the optimal conditions and the critical temperature limits can be determined for the tested material. The gradient probe can be utilised e.g. for dew point corrosion measurements. [4]

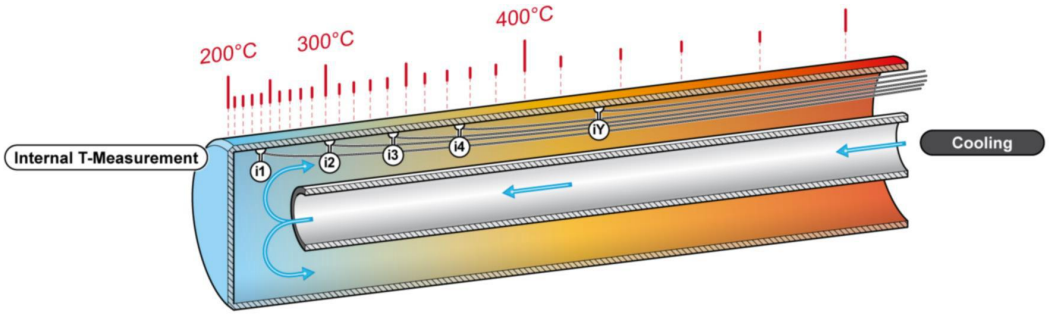

Figure 7. Principal of gradient probe [22]

Utilising a real time measurement with probe it is possible to follow fouling and corrosion tendency of tube surfaces and the influence fuel changes on process parameters and corrosion. The monitoring supports the operability during material and fuel changes, and also gives information for more accurate maintenance planning and optimisation of soot blowing intervals (Figure 8). Systematic corrosion monitoring provides a cost-effective way to improve reliability of critical components (information for remaining life assessment and aging management), plant uptime and increase overall business profitability.

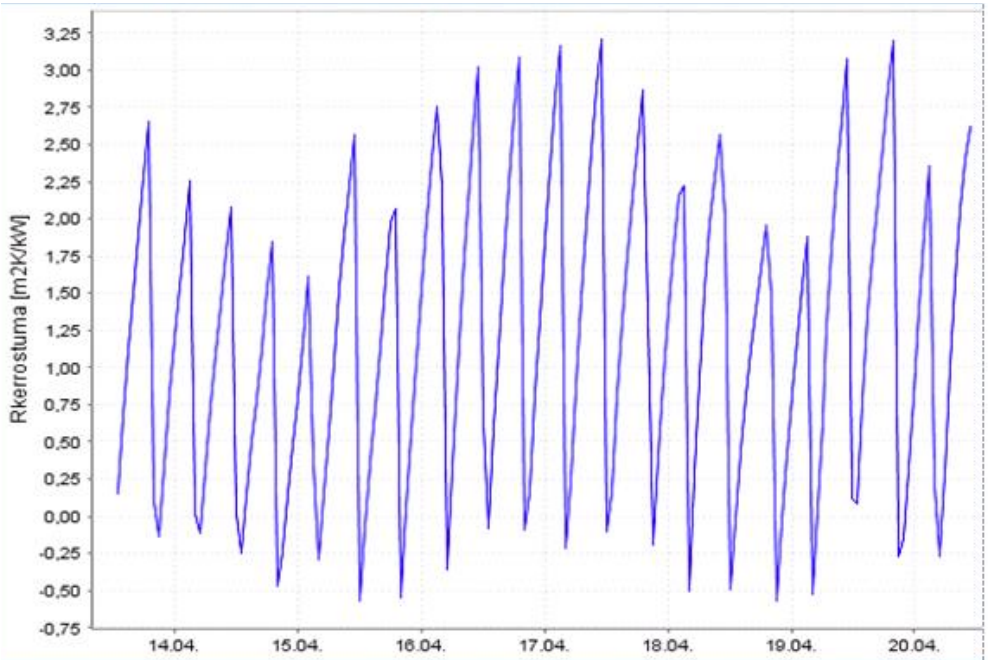

Figure 8. The effect on soot blowing, short term measurement

Online techniques for creep, such as strain gauges or potential drop methods, have been developed, but are not very commonly used. These techniques allow continuous and automated data collection during plant operation. Online measurements allow earlier and robust detection of accelerated creep, although are more expensive to install due to instrumentation and cabling costs [21].

4. Discussion and conclusions

Corrosion monitoring is used to measure material losses and/or corrosion rates in industrial process systems. Both direct and indirect measurement systems are available for the measurements. Indirect systems are usually based on e.g. chemical or process data analyses, and direct systems are mainly based on either coupon samples or clamps anchored on component surfaces (delay of results) or corrosion probes.

The benefits of corrosion probe compared to coupon samples or clamps are an accurate temperature control of probe and a shorter testing time; the probe can be removed when sufficient exposure time is reached without a maintenance shutdown. Table 1**.** compares the benefits and drawbacks of coupon/tube samples and online monitoring.

Table 1. Comparison of usability of corrosion samples (exposure testing) and online probes

	Applicability	Environment	Reaction rate for process changes	Availability of results
Exposure samples	- All corrosion modes - Average corrosion rate - Joints, welds	All conditions	Slow	Long exposure times (accuracy)
On-line measurements	- Indication of corrosion risk - Momentary corrosion rate - Cumulative corrosion rate - Corrosion mode	Resistance – all conditions Electrochemical – conductive solutions & process medias	Fast	Fast

Corrosion monitoring can be used to evaluate material performance in real service conditions, to evaluate and control process conditions (e.g. plant measurements; the corrosion risk with different fuels / fuel mixtures) and to obtain the Information for life assessment and material selection. The on-site experiments can be used e.g. for the demonstration of materials to improve the expected life of boiler tubes under severe corrosive/erosive service conditions.

By combining data from the online monitoring with process data (steam values, fuel and flue gas compositions etc.) more detailed information of the variation of process conditions and process disturbances on material corrosion behaviour can be obtained.

In future new probe systems with better temperature control and more reliable online measurements are needed for more accurate corrosion monitoring. Hybrid probes combine the advantages of fouling and online probes, and thus could be the next development stage.

In-service experiments can be also utilised for a wider scope in the life assessment [23]. The lifetime of the various process plant components will be shortened by corrosive substances at different operation temperatures. Power and process plant pipes, tubes and other components will also experience the mechanical loads affecting e.g. creep and fatigue properties of components. Creep is often one design-limiting mechanism in high temperatures, but also gradual material aging or microstructural changes are shortening the lifespan. Temperature and load fluctuations can also accelerate the formation of creep-fatigue failures. The daily based degradation of plant components can be seen as in-service experiments, and life assessment is based on the inspection of these components utilizing process history (T, p, design & material data). If the temperature history is not monitored at the worst locations with high risk of failures, it can be estimated by microstructural inspection and relatedmeasurements of e.g. hardness and/or the condition of theinternal oxide. Such assessments may be used for predicting the remaining life or the safe time to the next in-service inspection for critical components, e.g. in the case when

- component or plant is approaching design life
- process disturbance has occurred (overheating or -loading), or
- changes in the process parameters or type of service are required (base load to cycled use).

References

1. Viklund, P., Hjörnhede A., Henderson, P., Stålenheim, A., Pettersson, R., Corrosion of superheater materials in a waste-to-energy plant, Fuel Processing Technology, Vol 105, pp. 106–112 (2013).

2. Pettersson, R., Flyg, J., Viklund, P., High temperature corrosion under simulated biomass deposit conditions, Corrosion Engineering Science and Technology, Vol 43, pp. 123-128, (2008).

3. Otsuka, N., Chemistry and melting characteristics of fireside deposits taken from boiler tubes in waste incinerators, Corrosion Science, 53, p 2269-2276 (2011).

4. Magel, G., Spiegel, W., Herzog, T., Müller, W., Schmidl, W. Lifetime prediction achieved by periodic boiler inspections
http://www.chemin.de/Publikationen/PDF/2011/Lifetimeprediction_by_periodic_boiler.pdf (15.3.2016)

5. Pohl, M., Bernhardt, D., Ncube, S., Beckmann, M., Spiegel, W., Müller, W. Diagnostic methods into the corrosion potential of alternative fuels i.e. biomass and refuse derived fuels. Conference on Impacts of Fuel Quality on Power Production and Environment, Saariselkä (2010), 15 p.

6. Cappeln, F, Bjerrum, N.J, Petrushina, I.M. Corrosion monitoring in a straw-fired power plant using an electrochemical noise probe. Materials and Corrosion 58, pp. 588-593, (2007).

7. Ban, H., Zuoping L. A novel capacitance sensor for fireside corrosion measurement. Review of Scientific Instruments 80, 115107 (2009)

8. Ennis, P.J., Quadakkers, W.J., Implications of steam oxidation for the service life of high-strength martensitic steel components in high-temperature plant, Pressure Vessels and Piping, Vol 84, pp. 82-87 (2007).

9. Lukaszewicz, M., Dudziak, T., Nicholls, J.R., Simms, N.J., Steam oxidation of superheater / reheater alloys: Impact of steam flow rates and specimen geometries, EUROCORR 2011–Proceedings, pp. 1788-1815 (2011).

10. Wright, I.G., Dooley, R.B. A review of the oxidation behaviour of structural alloys in steam, International Materials Reviews, Vol 55, pp. 129 – 167, (2010).

11. Cramer, K., Jacobstein, R., Reilly, T. Boiler tube corrosion characterization with a scanning thermal line. Technical Report NASA, National Aeronautics and Space Administration, 12 p., (2001).

12. Ban, H., Zuoping L. A Novel Sensor and Measurement System for Fireside Corrosion Monitoring in Coal-Fired Boilers. DE-FC2601 NT41281, 59 p., (2003).

13. Oksa, M., Auerkari, P., Salonen, J., Varis, T. Nickel-based HVOF coatings promoting high temperature corrosion resistance of biomass-fired power plant boilers. Fuel Processing Technology 125 pp. 236 – 245. (2014).

14. Mahanen, J., Vänskä, K., Coda Zabetta, E. Full-scale testing of corrosion and oxidation resistant materials for high-efficiency future boilers. Alihankintamessut 2015.

15. Morris, A.P., Maharaj, C., Kourmpetis, M., Dear, I., Puri, A., Dear, J:“Optical strain measurement techniques to assist in life monitoring of power plant components, ASME Journal of Pressure Vessel Technology, 131, 024502-1-8.

16. Corcoran, J. Creep monitoring using permanently installed potential drop sensors. Thesis of Doctor of Philosophy, Imperial College London (2015).

17. Kawahara, Y. Applications of high temperature corrosion-resistant materials and coatings under severe corrosive environment in waste-to-energy boilers, Journal of Thermal Spray Technology, Vol 16, p. 202-213 (2007).

18. Farrell, D., On-line monitoring of fireside corrosion in power plant, 12th International Corrosion Congress, Corrosion Control for Low-Cost Reliability, (1993).

19. Linjewile, T., Valentine, J., Davis, K. Harding N, Cox W. “Prediction and real-time monitoring techniques for corrosion characterisation in furnaces” In Life Cycle Issues in Advanced Energy Systems, Science Reviews, pp. 175-184, (2003).

20. Covino, B., Bullard, S., Cramer, S., Holcomb, G., Ziomek-Moroz, M. Electrochemical Corrosion Rate Probes for High Temperature Energy Applications. Advances in Materials Technology for Fossil Power Plants: Proceedings of the Fourth International Conference, 2004.

21. Tuurna, S., Yli-Olli, S., Pohjanne, P., Meskanen, J., Heikkilä, J. Boiler material optimisation with corrosion probe measurements. 10th Liege Conference on Materials for Advanced Power Engineering Liege, 14 - 17 September 2014, Liege, Belgium.

22. Herzog, T. Old method, new application: Innovative ways of temperature measurements. Prewin General Assembly at Harlingen, 12 -13.11.2015.

23. Auerkari, P., Salonen, J., Holmström, S., Laaksonen, L., McNiven, U., Lehtinen, O., Mäkinen, S., Väänänen, V., Nikkarila, R. Life assessment for vintage boilers. Baltica VIII. Life Management and Maintenance for Power Plants. Vol. 2. Auerkari, Pertti & Veivo, Juha (eds.). VTT Symposium 265. VTT. Espoo (2010), pp. 78 - 89.

Improving passivation of carbon steel in steam cycles of power plants with a film forming amine

Essi Jäppinen, Timo Saario & Konsta Sipilä

VTT Technical Research Centre of Finland Ltd
P.O. Box 1000, FI-02044 VTT, Finland

Abstract

Different types of corrosion phenomena present a threat for economical, uninterrupted and safe operation of both conventional and nuclear power plants. Many types of corrosion damage are induced by impurities that tend to accumulate in crevices or beneath corrosion product deposits. Especially important phase for corrosion protection is during different transitions, shut-downs and at two-phase regions.

Several efforts for decreasing general corrosion rate and thereby also corrosion product accumulation on power plant surfaces have been done by changing the plant water chemistry. One very promising protecting method is treating systems with film-forming amines (FFA), such as octadecylamine (ODA). FFAs form a thin, some nanometers in thickness, film on metallic surfaces. Application of ODA decreases the rate of flow assisted corrosion (FAC) in the feed water line and thus reduces the amount of iron oxide that is available for deposition. ODA has also been observed to decrease the amount of crevice corrosion and stress corrosion cracking by hindering the enrichment of chloride ions and changing electrochemical properties of the surface.

Recent studies at VTT show that at high temperatures (T=228-300°C) under ammonia water chemistry, ODA reduces carbon steel corrosion rate by a factor of three and that the once-formed film also remains stable at surfaces at high temperatures.

1. Introduction

The economical and continuous operation of a power plant can be compromised by different corrosion phenomena. Many corrosion processes in the secondary side of a pressurized water reactor and also in conventional power plants are initiated or enhanced by deposition of corrosion products. These corrosion product particles mainly originate in carbon steel feed water lines and other components, from where they are removed by flow accelerated corrosion. Particles are transferred by water and deposited on e.g. steam generator (SG) surfaces. These deposits, consisting mostly of magnetite (Fe_3O_4), tend to deposit on the SG tubes, tube sheets and tube support structures and they can be difficult to remove. Once formed, the deposits accumulate impurities, hinder heat transfer and cause thermal-hydraulic instabilities through blockage of tube supports. The economical usage of a steam generator is compromised both by formation of an insulating scale and through removal of tubes from service and by increase of plant down-time.

One common method for decreasing corrosion is to use alternative water chemistry, e.g. by using oxygen-free water with elevated pH (9.6<pH<10), in which pH-range the dissolution rate of carbon steel is at minimum. Conditioning for high pH can be achieved by using ammonia alone or a combination of different amines. They both decrease flow-accelerated corrosion (FAC) and deposition of magnetite particles on the surfaces. [1] Even better results can be achieved by using film-forming amines (FFA), such as octadecylamine (ODA) in addition with pH-altering amines. ODA forms a thin, some nanometers thick, film on surfaces. This film is capable for both protecting surfaces from FAC and decreasing the deposition rate of iron oxides. [2].

2. Properties and effects of octadecylamine

Aliphatic amines are generally used as filming amines. They belong to oligo-alkyl-amino fatty amine family and their general chemical formula is R1-[NH-(R2)-]$_n$-NH_2, where n is an integer between 0 and 7, R1 is an unbranched alkyl chain with 12 to 18 carbon atoms and R2 is a short chain alkyl group with 1 to 4 carbon atoms. Octadecylamine (ODA) belongs to this group, and is the simplest of them with n=0 and R1=$C_{18}H_{37}$. ODA is commonly used as a filming amine for the protection of industrial condensate and boiler systems. Usually pH controlling amines are used together with filming amines. [3] ODA addition changes pH of the system, because it releases ammonia and also acts itself as an alkaline medium. [4]

The amine nitrogen of ODA has a free electron pair which makes ODA to have a strong affinity to metal surfaces. While amino groups bond with the metal surface, the carbon chains protect the surface (see Fig. 1). [5] Because of its active group, ODA can also be absorbed on surfaces of individual colloidal particles. The adsorption-desorption equilibrium is adjusted by temperature and concentration of ODA. [4] Film formed by ODA molecules protects surface from corrosive substances like oxygen, carbon dioxide and carbonic acid and the hydrophobic alkyl group makes the surface to repel water [6]. ODA can also chemically bound chlorides, decreasing corrosion rates. [4] Once formed film is quite stable and remains intact if the dosage of ODA is interrupted for a short while. [5].

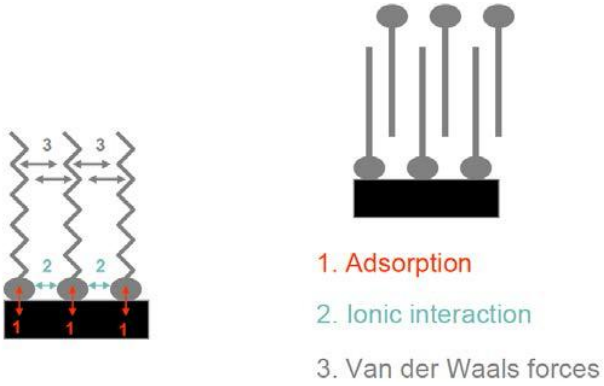

Figure 1. Adsorption of amines on a structural material surface in high-temperature water. [5]

Steam volatility, i.e. distribution coefficient, of the ODA is greater than one, so higher concentration of ODA is always expected to be at steam-condensate line during constant dosage of ODA in the steam-water cycle. Likewise to other long-chained surfactants, the solubility to water of ODA has three characteristic areas: area of real solubility, area of micelle formation and 2-phase area. These areas depend on temperature, ODA concentration and presence of other ions. In general, ODA is not very soluble to water at room temperature, but at least one commercial aqueous lipo-amine emulsion of ODA is available (ODACON® by Reicon GmbH). ODA reduces strongly the surface tension of the water. This causes better wettability of

the component in water phase, smaller droplet diameter in wet steam region and decrease of vapour bubbles in the evaporation. [4]

Several properties of ODA decrease the corrosion rate. Local corrosion is hindered, because ODA decreases enrichment of chloride ions in crevices and under deposits. This however is only achieved with constant availability of ODA. Chloride enrichment is prevented because ODA forms ODA-chloride compounds and also the ODA-film forms a diffusion barrier for impurities. ODA can even remove already enriched chloride. [4]

ODA also reduces erosion corrosion processes. ODA reduces droplet erosion because of its surface tension of water lowering properties, which changes droplet size and distribution in the wet steam region. Erosion corrosion in wet steam is lowered to a quarter of the initial value. In feed water, plain carbon steel is better protected with an ODA addition than Cr-alloyed steel without inhibitor, when complete coverage with ODA-film is achieved. ODA film also protects from cavitation, but only if it is constantly present in the medium. [4]

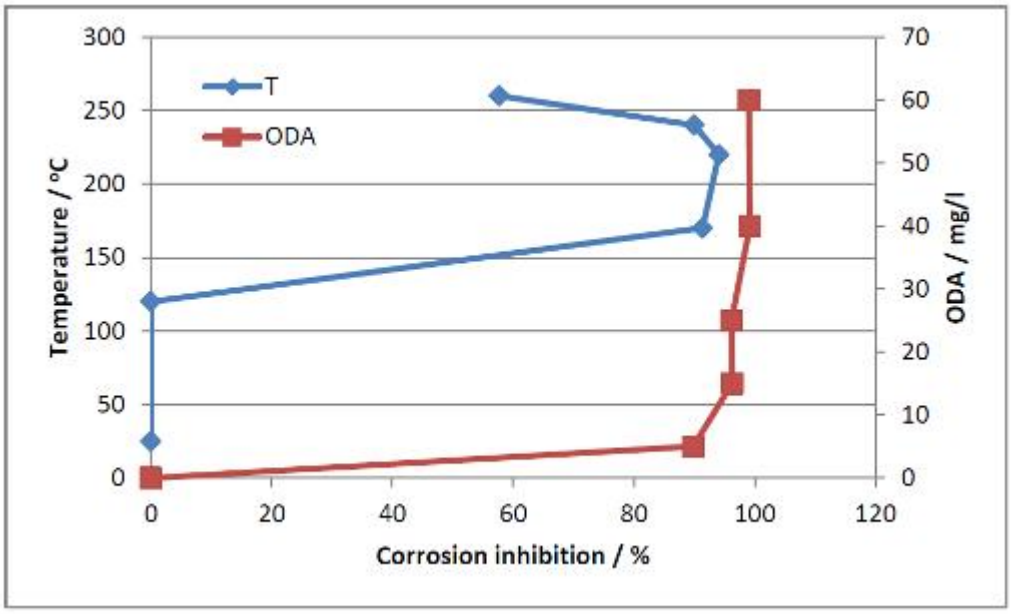

Figure 2. Effect of ODA concentration (exposed for 3 h in steam at T = 220°C) and exposure temperature (exposed for 3 h at 5 mg/l ODA) on corrosion inhibition efficiency of carbon steel. Modified from [7]

The ODA film formation occurs at temperatures above about T = 120°C, Fig. 2. In the example given in Fig. 2, the best protection is achieved if the concentration is higher than about 5 mg/l. The amount of ODA in the system is controlled by colorimetric determination of the free film forming amine concentration in the cooling water and a concentration above 1mg/l is usually recommended. Because the intention is that ODA is absorbed onto the surfaces, there is no simple correlation between added ODA amount and the concentration of free ODA in the water. ODA can have an effect on different sensors used for conductivity, pH or dissolved oxygen monitoring, and this must be taken into account.

3. Experimental studies concerning corrosion preventing properties of octadecylamine

Several studies concerning properties of octadecylamine have been recently performed at VTT. Experiments have been performed in a static autoclave, i.e. no external water chemistry preparation loop was connected to the autoclave. NH_3-additions were used together with ODA to control water chemistry. Octadecylamine was added either in a form of powder manufactured by Merck Schuchardt OHG or in a form of

emulsion of ODACON® by Reicon GmbH. ODA was added either straight to the autoclave at the beginning of the experiment or with a LC-pump. Studied material in carbon steel experiments was carbon steel type 22K with a composition (in weight percent) as follows: 0.19-0.26%C, 0.7-1.0%Mn, 0.17-0.4%Si, <0.04%P, <0.035%S, <0.3%Cr, <0.3%Ni, <0.3%Cu, balance Fe. Experiments were conducted in an oxygen-free environment. Both electrochemical measurements and weight gain/loss measurements were conducted during the experiments and the thickness of the formed oxide was estimated also from the cross-sections of the coupons using scanning electron microscopy (SEM). In some cases also Tafel slopes were measured in order to estimate corrosion rates.

Autolab PGSTAT302F was used to measure electrochemical impedance spectra (EIS) of carbon steel samples using controlled distance electrochemistry (CDE) arrangement (Fig. 3) in the two electrode arrangement. In this arrangement the other specimen is used as a working electrode and the other both as a counter and a reference electrode. In the-CDE arrangement, the distance of the specimens is controlled by a loading rod, moved with a step motor, allowing distance controlling with an accuracy of about 10^{-11} m/step. Used distance was 55μm between the electrodes. The mixed potential of the carbon steel specimens was measured against an Ag/AgCl/0.01M(or in some cases 0.05M) KCl-reference electrode and recalculated to the Standard Hydrogen Scale (SHE).

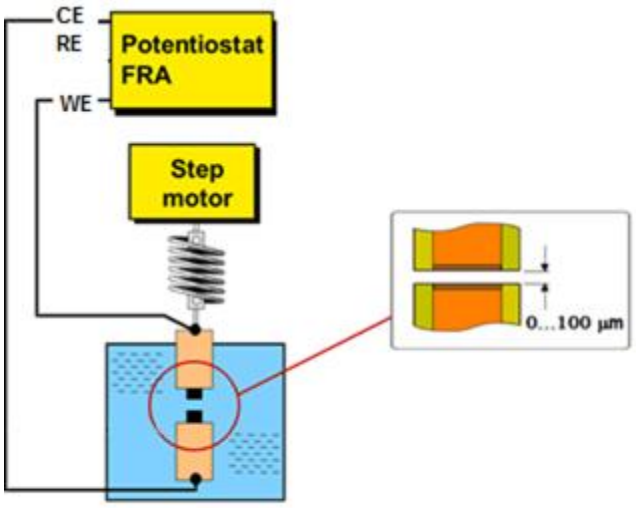

Figure 3. Schematic picture of the Controlled Distance Electrochemistry (CDE) arrangement. FRA = Frequency Response Analyser, WE = Working Electrode, CE = Counter Electrode, RE = Reference Electrode.

Experiments have been performed in a temperature range between 25°C and 300°C, initial ODA concentration varying between 0 and 25 ppm and ammonia controlled pH varying from 9.2 to 9.8. During these measurements, several observations have been made: Addition of ODA to the secondary side water treated with NH_3 decreases corrosion rate of the studied carbon steel (22K) at T = 228°C [9] and at T=300°C [8] by a factor of 3 (0.07-0.28 mm/y without ODA, 0.02-0.09mm/y with ODA). Also, ODA-film once formed at T=228°C remains stable at T=300 °C for a prolonged period of at least a week [8]. Furthermore, ODA addition has the same effect on the corrosion rate whether it has been added at the beginning of the exposure (fresh surface) or after a period of pre-oxidation of the carbon steel surface during which a stable magnetite film was grown. This indicates that ODA would effectively slow down also the corrosion of carbon steel at locations where flow assisted corrosion (FAC) takes place. [9]

One example of a set of experimental results gained at T = 228^{o}C is shown in Fig. 4. The three repetitions without ODA show roughly three times lower magnitude of impedance than the four repetitions with ODA. Magnitude of impedance at the end of each data set (the length of the vector from zero to the the last data point) is a measure of corrosion resistance – the lower the magnitude the higher the corrosion rate. Repeatability of independent experiments is rather good.

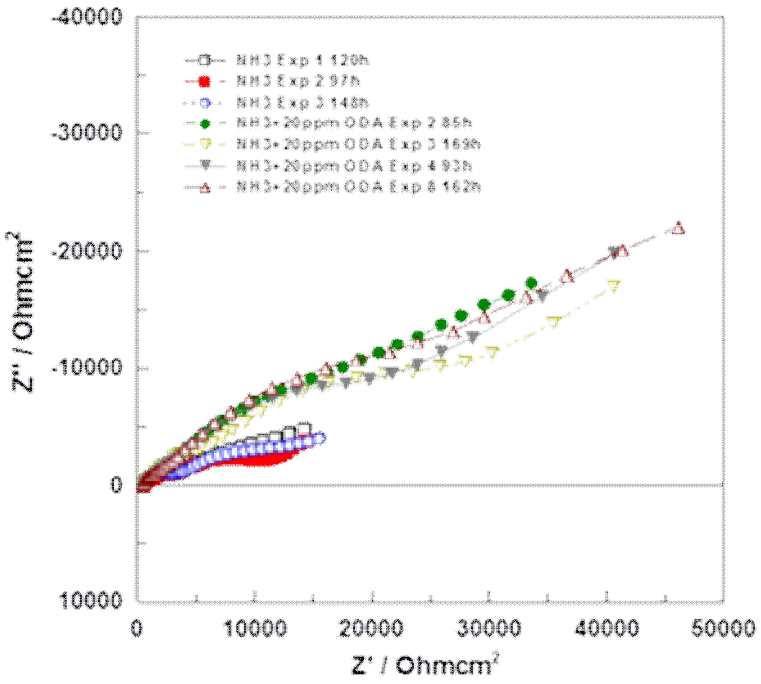

Figure 4. Compilation of electrochemical impedance spectroscopy data. Carbon steel in ammonia water with pH = 9.2, T = 228°C. Three repetitions without ODA show roughly three times lower magnitude of impedance than the four repetitions with ODA.

Figures 5 and 6 are scanning electron microscope pictures taken after experiments. The surface morphology of these samples show a typical double layer structure where the inner layer is presumed to be ingrown whereas the outer layer is formed by crystals deposited back onto the surface from the solution. The average crystal size is clearly higher for the experiment with ODA and longer exposure time than for experiment without ODA and shorter exposure time. [8] However, as the surface morphology is essentially the same with similar double layer structure, it can be said, that the corrosion protective effect of ODA cannot be seen from SEM pictures but electrochemical measurements are needed for corrosion protection evaluation.

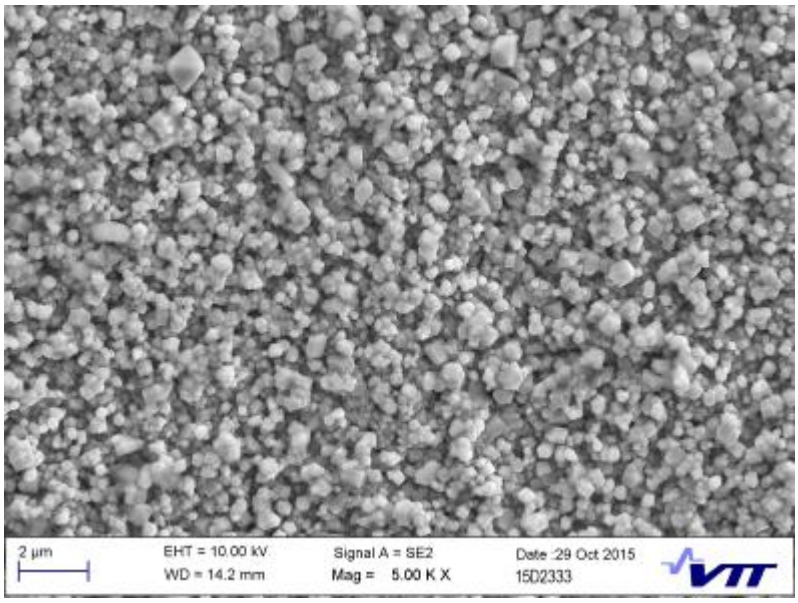

Figure 5. Surface morphology of the carbon steel sample after experiment without ODA (T = 300°C, [ODA] = 0 ppm, t = 147 hrs). [8]

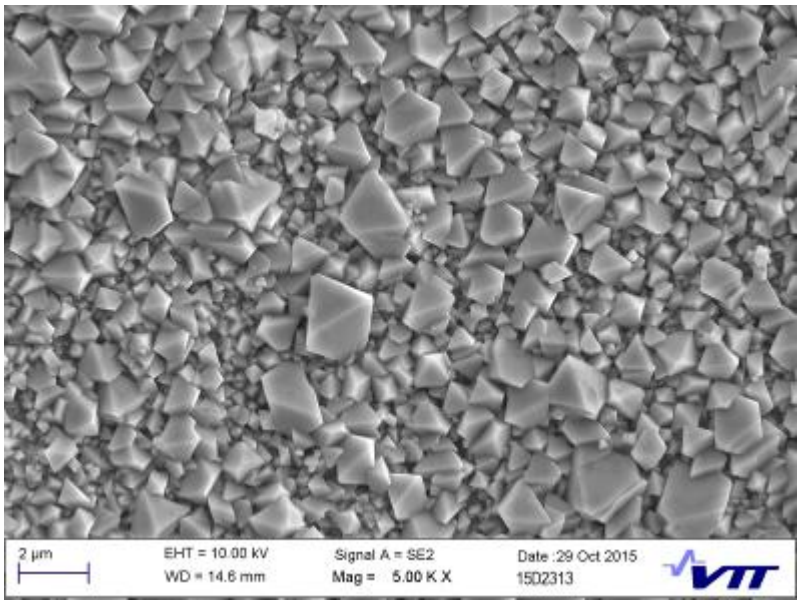

Figure 6. Surface morphology of the carbon steel sample after experiment with ODA (T = 228°C ->300°C, [ODA] = 20 ppm, t = 48 hrs at 228°C+242 hrs at 300 °C). [8]

4. Conclusions

Film forming amines can be used for corrosion protection of surfaces of power plants because they form a thin, protective film on surfaces. These amines are typically aliphatic amines and are used together with pH controlling amines. Most common of these amines is octadecylamine (ODA). Application of ODA decreases the rate of flow assisted corrosion (FAC) in the feed water line and thus reduces the amount of iron oxide that is available for deposition. ODA has also been observed to decrease the amount of crevice corrosion and stress corrosion cracking by hindering the enrichment of chloride ions and changing electrochemical properties of the surface. The protective properties of ODA can be explained by the fact that the amine nitrogen of a film forming amine has a free electron pair which makes amine to have strong affinity

to metal surfaces. This film protects surfaces from corrosive substances like oxygen, carbon dioxide and carbonic acid and the hydrophobic alkyl group makes the surface to repel water.

Several studies concerning properties of octadecylamine have been recently performed at VTT. In these experiments it has been shown that at high temperatures (T=228-300°C) under ammonia water chemistry, ODA reduces carbon steel corrosion rate by a factor of three and that the once-formed film also remains stable at surfaces at high temperatures.

References

1. Vepsäläinen, M., Saario, T. 2010. Magnetite dissolution and deposition in NPP secondary circuit. VTT Technical Research Centre of Finland. Research Report VTT-R-09735-10.

2. Betova, I., Bojinov, M., Saario, T. 2014. Film-Forming Amines in Steam/Water Cycles – structure, properties, and influence on corrosion and deposition processes. VTT Technical Research Centre of Finland. Research Report VTT-R-03234-14.

3. Bäßler, R., Uhlemann, M., Mummert, K. 1999. Inhibiting effect of octadecylamine on pitting corrosion behavior of stainless steel type 1.4571 up to 250 °C. Materials and Corrosion 50(3), 146-153.

4. REICON Wärmetechnik und Wasserchemie Leibzig GmbH. Eigenschaften und Wirkungen des ODACON® - Wirkstoffes" . Technical booklet.

5. Hater, W., Olivet, D. 2009. Organic Boiler Feed water Additives Based upon Film Forming Amines, VGB Powertech, 89(3) 75-79.

6. Voges, N., Hater, W. 2010. Distribution ratio and average surface coverage of film forming amines. VGB PowerTech Volume 90(3), 72-76.

7. Ge, H.-H., Zhou, G.-D., Liao, Q.-Q., Lee, Y.G., Loo, B.H. 2000. A study of anticorrosion behavior of octadecylamine-treated iron samples, Applied Surface Science 156, 39–46.

8. Jäppinen, E., Sipilä, K., Saario, T. 2016. Effect of octadecylamine on copper and carbon steel corrosion under PWR secondary side conditions. VTT Technical Research Centre of Finland. Research Report VTT-R-00275-16.

9. Sipilä, K., Saario, T. 2014. Effect of octadecylamine on carbon steel corrosion under PWR secondary side conditions. VTT Technical Research Centre of Finland. Research Report VTT-R-06077-14.

The structural stability of weld joint of P92 and CB2 steels under creep conditions

Josef Kasl[1], Dagmar Jandová[1] & Eva Chvostová[1]

[1]Research and Testing Institute Plzen
Tylova 1581/46, 301 00 Plzeň, Czech Republic

Abstract

A trial weld joint of CB2 and P92 steels was produced using the GTAW method and a filler metal of Thermanit MTS 616. Creep testing was carried out at temperatures from 575 °C to 650 °C and stresses from 60 MPa to 180 MPa. Creep data were evaluated in relation to the Larson-Miller parameter. Ruptured bars underwent fractographic and microstructural analyses. To date, six creep tests have been completed with the longest time to rupture of 6,661 hours. All fractures occurred in P92 steel: in the base material after tests at higher stresses, and in the heat affected zone after tests at lower stresses. All structures corresponded to tempered martensite with a high density of chromium carbides at grain and subgrain boundaries and fine intragranular vanadium nitrides. Fine grained and critically reheated heat affected zones revealed the highest susceptibility to creep failure. Bands of fine grains/subgrains with coarse carbides were formed along prior austenite grain boundaries and adjacent large grains/subgrains with very low dislocation density and low density of fine nitrides. Plastic deformation under creep conditions was concentrated in the large grains. Fast growing Laves phase particles precipitated during creep, especially in the heat affected zones, serving as nucleation centres for cavities and cracks.

1. Introduction

A significant portion of worldwide energy production will be based on fossil fuels in the coming decades. However, the increase in fuel costs on the one hand and the required limitation of emissions on the other, have led to strong pressures to push the service temperatures and pressure parameters of steam in fossil fuel-fired power plants to their limits. The increase of these parameters needs new advanced materials operating under severe service conditions for several decades. In order to minimize investment costs, which also influence the effective cost of electricity generation, use must be made of ferritic-martensitic steels for all major components in both boilers and turbines. The class of 9-12% Cr steels is currently used for critical components in plants operating at ultra-supercritical conditions of steam. These steels show high mechanical strength, high long-term creep strength and oxidation resistance in steam, along with ease of welding and fabrication of large forgings, castings and pipe sections. Additionally, they still offer some further potential regarding their creep strength, although oxidation resistance must be carefully taken into consideration if higher temperatures are targeted.

Welded joints are the most critical parts of plants operating at high temperatures, and are commonly susceptible to fracture. A rupture usually initiates in a specific region as a result of structural heterogeneity of the weldment formed either during fabrication or during service. Since cyclic thermal and stress loading after each weld pass affects the steel structure, great attention has to be paid to welding technologies and the selection of appropriate filler materials.

Doosan Škoda Power Ltd. has recently established a new station for vertical welding of turbine rotors supplied by Polysude which enables automated welding of rotors for single-casing turbines intended for high-temperature steam input (600 °C) as well as for low-pressure components of the highest output rating turbines with rotors up to 135 tonnes in weight, rotor discs of a maximum diameter of 2.2 m, and a maximum length of 12 m. The maximum permissible weld thickness is 135 mm for diameters ranging from 400 mm to 1,200 mm. Several projects concerning welding of heavy turbine parts have been started. One of the testing programmes deals with the optimization of the welding procedure for forged pipes and cast parts of turbines made of steel P92 and steel CB2 respectively.

Grade P92 (X10CrWMoVNb9-2, ASME SA 335) is ferritic 9Cr - 1.75W - 0.5Mo steel micro-alloyed with vanadium and niobium and with controlled boron and nitrogen contents. Due to its excellent creep properties and high corrosion/oxidation resistance, which are equal to other high chromium ferritic steels, it is used for production of headers, boiler superheater and reheater tubes and main steam pipes for extremely severe steam conditions (temperatures exceeding 600 °C and pressures of over 25 MPa) in advanced power plants [1]. Steel P92 has a creep strength from 110 to 120 MPa at 600 °C for 10^5 hours. This steel contains only a small amount of nitrogen to reduce its bond to boron. The slow speed of coarsening of $M_{23}C_6$ particles positively influences the microstructural stability of this material. During tempering and/or creep exposure an intensive precipitation of Laves phase occurs, which leads to tungsten depletion of the solid solution. However, there does not tend be a more prominent decrease of creep strength. Despite the number of MX particles being rather low, only a moderate recovery as well as slow growth of subgrain occurred.

Cast steel CB2 (GX13CrMoCoVNbNB 10 1 1) developed in the European COST Projects is one of the most promising alloys for the production of steam turbines operating at temperatures up to 620 °C [2]. Its chemical composition is balanced with the aim of improving oxidation and creep properties. It is a variation of P91 steel (GX12CrMoVNbN 9-1). In contrast to P91, which contains up to 9% chromium and 1% molybdenum, CB2 is also alloyed with cobalt and boron. Limitation of nickel content improves creep strength. Addition of cobalt compensates for the low Ni content and restrains the formation of δ-ferrite. Nitrogen, together with vanadium and niobium, can increase precipitation strengthening and boron can restrict the coarsening of chromium carbides that pin grain and sub-grain boundaries and causes an increase in sub-structural strengthening. A balanced content of molybdenum and tungsten increases solid solution strengthening and long-term structural stability. It is currently used for the production of various parts of high efficiency power plants.

This paper deals with the study of creep properties and microstructure evaluation in samples from a trial of a dissimilar weld joint of steel P92 and COST CB2. This weldment was prepared in the same conditions used for welded rotor production.

2. Experiments

2.1 Materials and welding procedure

The dissimilar weld joint was prepared from pipes with an external diameter of 310 mm and thickness of 60 mm. The cast part of CB2 was supplied by SAFAS. Heat treatment was: 1100 °C/5 h/AC + 755 °C/10h + 730 °C/(8.5 h)/FC. Forged steel was produced by FORGITAL Fmdl; heat treatment consists of 1040 °C/5 h/AC + 780 °C/6 h/AC. Böhler Thermanit MTS 616 (W-ZCrMoWVNb 9-0.5-1.5) was used as filler material. Chemical compositions of both the base materials and consumables are shown in table 1.

The experimental weld was carried out using automated welding method 141+111 (TIG HOT WIRE) into a narrow gap with internal protection by argon. The thickness of the welded walls was 60 mm. Inductive heating with thermal insulation ensured a preheating temperature ranging from 200 to 250 °C.

The welding interpass temperature was kept below 300 °C. Pipes were joined in PC position (longitudinal axis of tubes was vertical). A post weld heat treatment (PWHT) was applied. The ultrasonic testing TOFD method as well as standard NDT surface inspection were used for examining the welded zones after PWHT.

The weldment was cut into four segments that were used for fabrication of samples for testing the structural and mechanical creep properties.

Table 1. Chemical composition in weight %.

Part	Element																		
	C	Mn	Si	P	S	Cr	Ni	Mo	V	Co	W	Nb	Ti	N	B	Al	Sn	As	Sb
Base material CB2	0.12	0.82	0.41	0.019	< 0.001	9.00	0.18	1.00	0.18	0.92	< 0.01	0.04	< 0.01	0.007	0.013	0.007	0.005	0.005	< 0.001
Weld metal MTS 616	0.11	0.79	0.23	0.008	0.007	1.00	0.63	0.50	0.20	0.02	1.89	0.04	< 0.01	0.042	0.004	0.001	0.006	0.007	< 0.001
Base material P92	0.11	0.52	0.36	0.017	0.005	1.00	0.38	1.00	0.19	0.02	1.68	0.04	< 0.01	0.033	0.002	0.001	0.007	0.007	< 0.001

2.2 Sample preparation and methods used

Smooth cross-weld specimens with a length of 92 mm and a diameter of 8 mm were fabricated from the weld joint. Creep tests to rupture of these specimens and of specimens machined from both the base materials were carried out. However, only a few samples prepared from the base material have been broken so far. Fracture surfaces of ruptured samples were observed using a scanning electron microscope (SEM).

The specimens were cut along their longitudinal axis. Macrostructure was revealed using Vilella-Bain´s reagent and the position of the fracture in the weldment was located. Hardness measurement along the specimen axis was carried out.

The microstructure of longitudinal sections was observed using light microscopy (LM) and scanning electron microscopy (SEM). The substructure was evaluated using a transmission electron microscope (TEM). The foils were thinned by jet polishing in 6% solution of perchloric acid in methanol at -40 °C. Energy dispersive X-ray microanalysis (EDX) and electron diffraction were used to identify secondary phases.

3. Results

3.1 Mechanical properties

The integrity and mechanical properties of the weld joint were evaluated according to the welding standards EN 288-2,3. All results were satisfactory.

The mechanical properties of the segment which was used for creep test sample preparation are summarised in Tables 2a, 2b, and 2c.

Table 2a. Basic mechanical properties of the weld joint.

Mechanical properties	Temperature [°C]	$Rp_{0.2}$ [MPa]	R_m [MPa]	A [%]	Z [%]	Fracture location
CB2	20	566	725	20.2	54	CB2
	600	329	383	23.6	81	CB2
	600	339	381	22.0	79	CB2
P92	20	524	676	23.0	70	P92
	600	308	326	21.0	88	P92
	600	298	315	21.8	87	P92
Weld joint	20		675			P92
Weld joint	20		686			P92
Weld joint	20		673			P92
Weld joint	20		694			P92
Weld joint	20		685			P92
Weld joint	20		686			P92

Table 2b. Mechanical properties of the weld joint - results of impact tests.

Impact test	Temperature [°C]	KV [J]				FATT [°C]
		1	2	3	Average	
CB2	20	29	31	30	30	**36.6**
HAZ CB2 - face of weld	20	36	25	35	32	
CFB2 - weld root	20	25	27	32	28	
P92	20	51	60	95	69	**14.9**
HAZ P92 - face of weld	20	107	64	83	85	
HAZ P92 - weld root	20	81	62	51	65	
WM- face of weld	20	55	64	62	60	**16.9**
WM- root of weld	20	53	49	38	47	

Table 2c. Mechanical properties of the weld joint – results of hardness measurements.

Hardness HV10	Temperature [°C]	1	2	3	Average
FB2 - face of weld	20	221	215	222	219
HAZ FB2 - face of weld	20	212	227	245	228
WM - face of weld	20	236	249	254	246
HAZ P92 - face of weld	20	218	225	233	225
P92- face of weld	20	222	225	224	224
CB2 - weld root	20	230	227	225	227
HAZ CB2 - weld root	20	225	238	249	237
WM - weld root	20	270	274	268	271
HAZ P92 - weld root	20	224	205	205	211
P92 - weld root	20	219	213	224	219

3.2 Creep tests

Creep rupture testing was carried out in air at temperatures ranging from 575 °C to 650 °C and stresses from 80 MPa to 160 MPa. The longest time to the rupture of samples so far is about 7,000 hours. A list of specimens investigated is given in Table 3.

Table 3. Creep testing conditions, time to rupture in hours (brackets mean testing is in progress) and fracture position.

		Stress [MPa]						
		60	80	100	120	140	160	180
Temperature [°C]	575				(27 117)	(6 338)	7 759, 5 051 P92 near HAZ P92	
	600				(6 338)		471 P92 near HAZ P92, crack in HAZ of P92	115 P92 near HAZ P92, contraction of HAZ CB2
	625	(27 140)	(6 338)	6 661 OH/FG HAZ P92		118 P92 near HAZ P92		
	650	(6338)	2 530 FG/CG HAZ of P92					

The creep data were evaluated using the Larson-Miller parametric equation:

$$LMP = T * [C + \log \tau], \quad (1)$$

where T represents temperature in Kelvin, C is a specific constant for a given material (value of 36 was used) and τ means time to rupture in hours.

Results from creep tests compared with the creep rupture strength data of CB2 and P92 steel are shown in Fig. 1. Creep rupture strengths of COST CB2 as well as P92 steels were used as reference data because only two samples prepared from the base materials P92 used in this experiment have ruptured so far. Open symbols in Fig. 1 indicate creep tests which are still running.

Creep strengths of all ruptured samples tested are in the permitted scatter band ± 20 % of the creep strength of the base material P92. Six samples are still being tested.

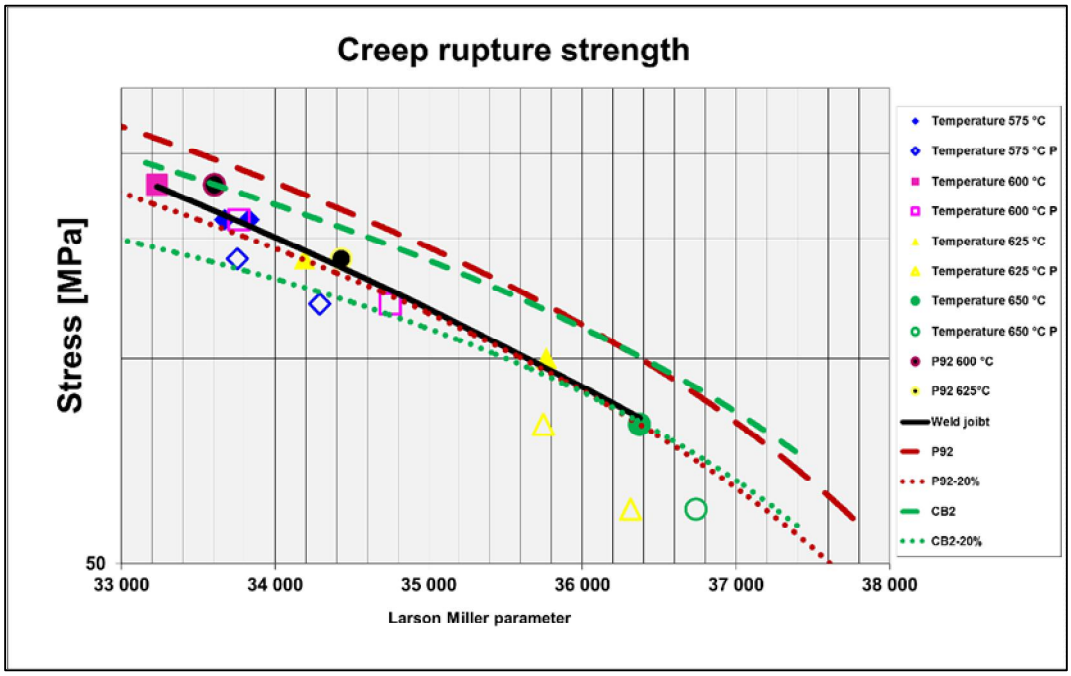

Figure 1. Creep rupture strength vs. LMP.

3.3 Fractographic analysis

Fractographic analysis of broken samples was performed. Firstly, it should eliminate the influence of possible defects formed during the welding process on creep results, and secondly it should find the growth mechanisms of the cracks.

This analysis and observation of longitudinal sections of the ruptured crept samples showed that locations of fractures depended on the creep conditions. These positions are summarised in Table 3. The samples tested at lower temperatures and higher stresses failed in the base material (BM) of steel P92 unaffected by welding, while those tested at higher temperatures and lower stresses ruptured in various regions of the heat-affected zone (HAZ) of the base material of steel P92 - coarse grained part (CG), fine grained part (FG) or in the intercritically reheated part (IC). Ductile fracture in the BM usually occurred after short durations of creep tests, however this type was exceptionally found also after duration of 5,000 hours. The fractures were transcrystalline ductile with considerable macroplastic deformation and with the dimple morphology of the fracture surface (Fig. 2a, 2b). Its appearance is similar to ductile rupture during tensile testing at the same temperature. Other samples ruptured by transgranular creep fracture in the HAZ of the base steel P92. Elongations of these specimens were usually a few percent. Individual small cracks formed of growing cavities joined in cracks and spread step by step across the body of the test bar (Fig. 3a, 3b). The exact positions of the fracture change from the IC part of the HAZ to the boundary between the fine grained and coarse grained part of the HAZ with increasing temperature and decreasing stress (see Table 3).

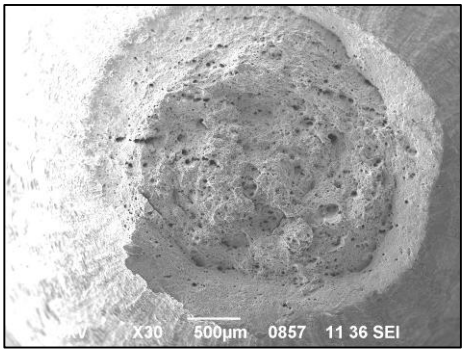

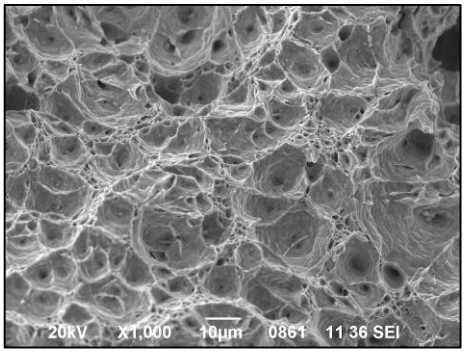

Figure 2a, 2b. Fracture surface of sample tested at 600 °C, 160 MPa, rupture of 471 hours.

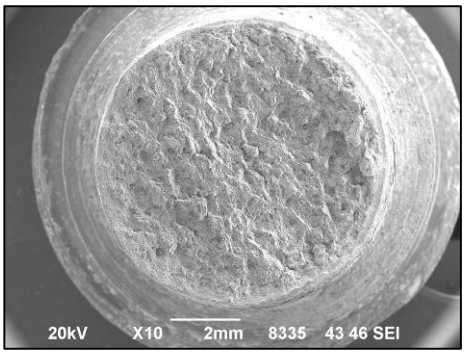

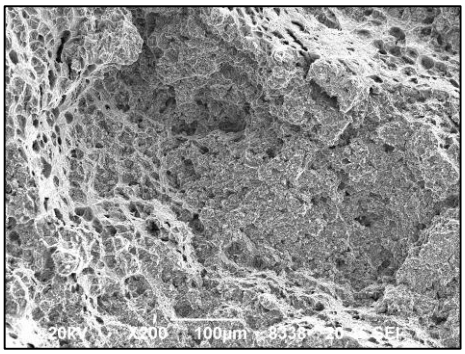

Figure 3a, 3b. Fracture surface of sample tested at 625 °C, 100 MPa, rupture of 6,661 hours.

3.4 Hardness profiles

Hardness HV10 profiles across the weld joints were determined for the weld joint before and after creep testing. Before creep testing, the average hardness of the base material CB2 was about 220, of the base material P92 205 and of the weld metal (WM) about 240. Local minima were found in the fine grained or in the overheated part of the HAZs – 205 in CB2 steel and 190 in P92 steel. Figure 4a shows one of the measured profiles – the base material CB2 is on the left and the base material P92 on the right; the zero position of the x-coordinate is in the middle of the weld metal.

During creep testing (up to about 7,000 hours) the most significant decrease of hardness occurred in the FG part of the HAZ of P92 steel. After the creep test at 625°C and 100 MPa the hardness falls to about 180. A decrease of hardness of both the base materials by about 15 and of the weld metal by about 20 was found. The hardness of the sample tested at 625°C/100 MPa, duration 6,661 hours is shown in Figure 4b.

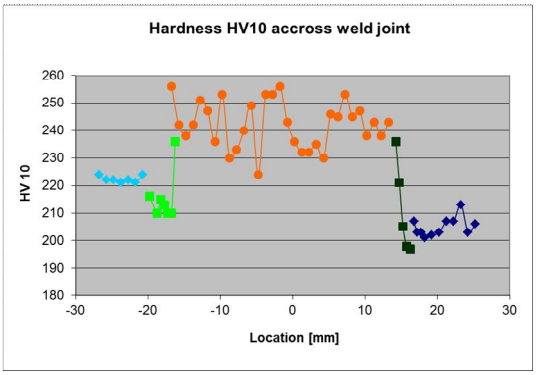

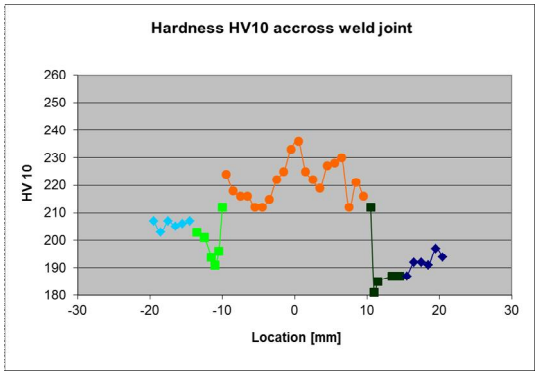

Figure 4a. Hardness profile after PWHT.

Figure 4b. Hardness profile after test 625°C, 100 MPa.

3.5 Investigation of the weldment microstructure

The macrostructure of the cross-section of the weld joint is shown in Fig. 5. The thickness of the heat affected zone (HAZ) on the side of steel CB2 is about 2.5 mm. The widths of the coarse grained region (CG) and the fine grained region (FG) are 0.5 mm and 2.0 mm respectively); the width of the HAZ on the side of steel P92 is about 3.0 mm (the CG region is indistinct – it shows only slight coarsening of the microstructure). The microstructures of the base materials and the weld metal were formed of heavy tempered martensite.

Steel CB2 showed rare larger pores, and common small pores containing clusters of small oxides of an irregular shape and a size of about several micrometres (Fig. 5). Larger non-metallic inclusions, especially aluminates of globular shape and size of several tens of micrometres, occur relatively rarely. Steel was practically without δ-ferrite and without coarse BN nitrides. Laves phase particles were often present together with non-metallic inclusions in interdendritic spaces (Fig. 7).

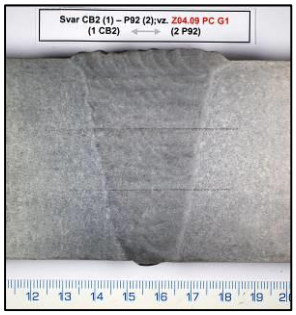

Fig. 5. Macrostructure.

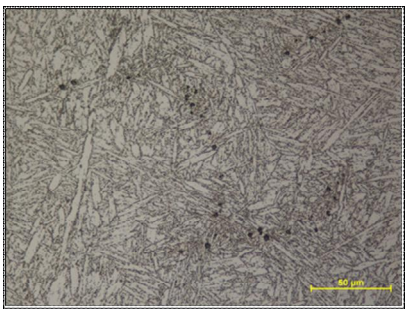

Fig. 6. Microstructure of CB2, LM.

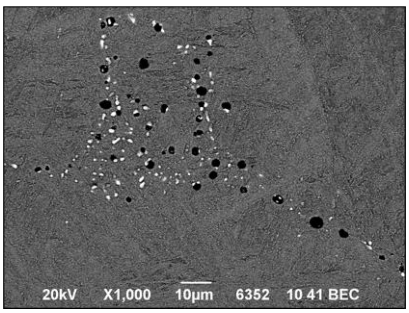

Fig. 7. Microstructure of CB2, SEM.

The density of precipitates was relatively high and particles were homogeneously distributed. The main precipitates are $M_{23}C_6$ carbides rich in chromium. Particles of Laves phase Fe_2Mo and fine precipitates of MX ((V,Nb)N) were also identified using TEM.

The microstructure of the weld metal was similar to the microstructure of the base materials, but was more heterogeneous and coarser (Fig. 8). WM contained fine pores and defects. Small inclusions of silicates of about 1 µm were found (Fig. 9). Particles of $M_{23}C_6$ predominantly precipitated at the boundaries of prior austenitic grains (PAG) and ferritic laths. The density of fine MX precipitates was uneven.

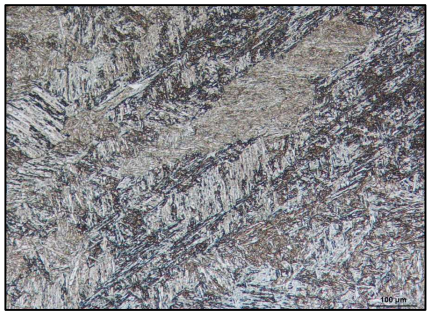

Fig. 8. Microstructure of WM, LM.

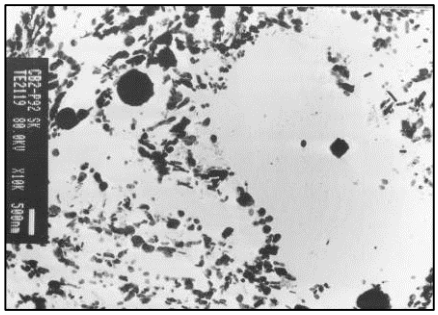

Fig. 9. Microstructure of CB2, TEM-extraction replica.

Lines of small non-metallic inclusions of aluminates and manganese sulphides were found in the base material P92. The microstructure consisted of heavy tempered martensite; it was free of islands of δ-ferrite (Fig. 10). The content of particles of $M_{23}C_6$ was higher and the size is rather smaller than in CB2 steel. Particles of Laves phase were not found. The distribution of fine precipitates of MX was not uniform. They

occupied the boundaries of the PAG in some regions, while they formed fine dispersions inside grains in others.

The microstructure of the HAZ on the side of steel P92 close to the fusion line is similar to that of steel P92 (Fig. 11). Small particles of δ-ferrite, a relatively low density of intragranular precipitates and coarser particles of $M_{23}C_6$ at boundaries were found in this CG region. The content of fine MX precipitates increased as the distance from the fusion line increased. Some martensitic laths are subdivided into well-developed subgrains with low dislocation density (Fig. 12). On the other hand, some subgrains contained many partly arranged dislocations (Fig. 13).

The FG part of the HAZ of steel P92 was formed of polyhedral-like grains and subgrains (Fig. 15). The dislocation density and the carbide distribution were inhomogeneous. $M_{23}C_6$ carbides (diameter from 50 to 600 nm) are coarser than the carbides in steel P92 and in the HAZ close to the fusion line. Relatively small grains/subgrains (several micrometres) with a low dislocation density were found in inside areas with a high density of coarse precipitates. These grains appeared close to the PAG (Fig. 15). The different crystallographic orientation of these grains gives evidence for the occurrence of partial recrystallization. The density of fine MX precipitates is smaller than outside the HAZ.

.

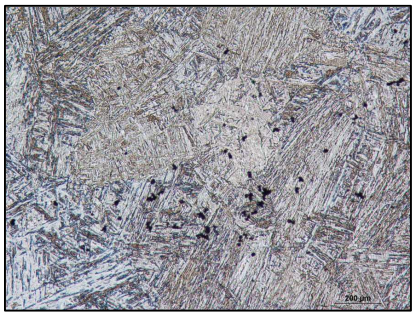

Fig. 10. Microstructure of P92, LM.

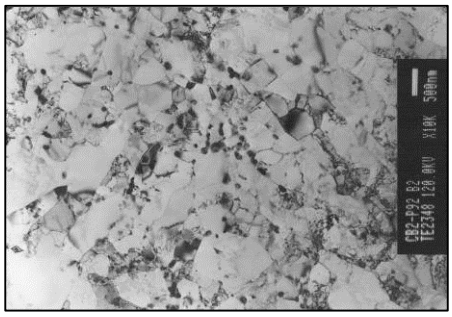

Fig. 11. Substructure of P92, TEM-thin foil.

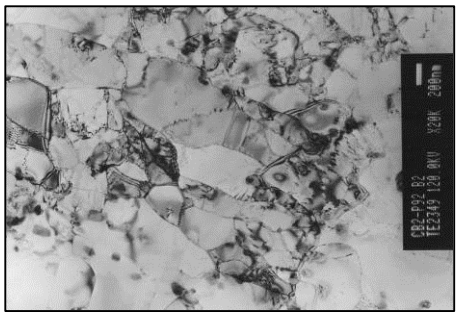

Fig. 12. Substructure of HAZ P92, TEM-thin foil.

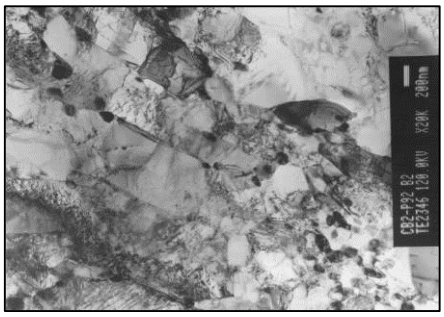

Fig. 13. Substructure of HAZ P92, TEM-thin foil.

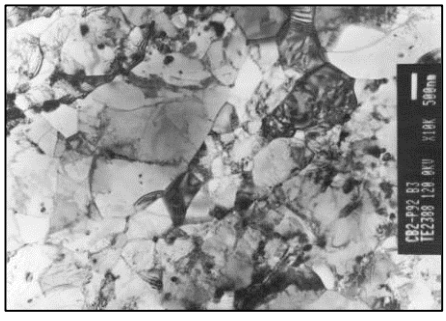

Fig. 14. Substructure of HAZ P92, TEM-thin foil.

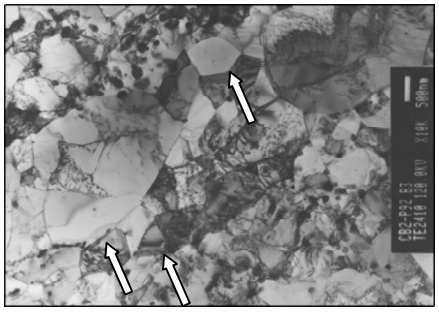

Fig. 15. Substructure of HAZ P92, TEM-thin foil.

After creep tests of samples ruptured in HAZ of steel P92, cavities were concentrated in the FG regions of both the base materials. However, fractures occurred in the HAZ of steel P92, in the FG and/or IC regions. Cracks were formed by cavitation coalescence and they propagated parallel to the fusion line (Fig. 16a, 16b). A significant increase in the number of particles occurred inside the HAZ of P92 in comparison with the conditions after PWHT (Fig. 17). In addition to Cr-carbides, relatively coarse particles of Laves phase $Fe_2(W,Mo)$ were present (Fig 18). They usually nucleated at carbides situated at the boundaries. This increase was not prominent in the base material P92. Precipitation of fine particles of MX and M_2X, only slight coarsening of $M_{23}C_6$, and sporadic precipitation of Laves phase, occurred close to the fusion line. Higher temperatures and stresses promoted nucleation and growth of Laves phase. Dislocation at boundaries, which were occupied with large particles and clusters, formed pile ups and stresses in their surroundings and initiated cavitation. Recovery and recrystallization of the matrix were in progress at the same time. Cavities nucleated at clusters and coarse particles of Laves phase were surrounded by a 'soft' region of recovered/recrystallized subgrains/grains. Thus, space distribution of cavities depended on the number of initiation centres of new particles, the rate of their growth and extent of recovery. These phenomena also control the position of the maximum concentration of cavities in the HAZ.

Fig. 16a. HAZ P92, LM-bright field, sample 625 °C/ 100 MPa/ 6,661 h.

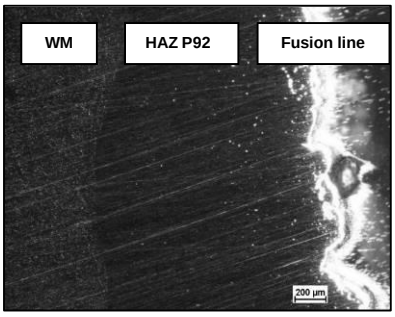

Fig. 16b. HAZ P92, LM-dark field, sample 625 °C/ 100 MPa/ 6,661 h.

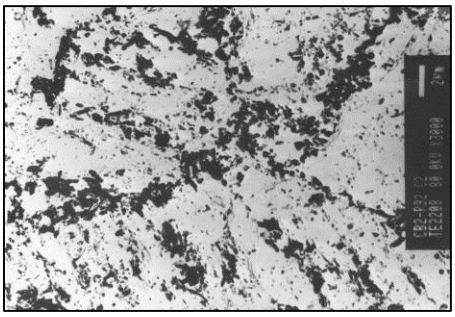

Fig. 17. HAZ P92, TEM-replica, sample 625 °C/ 100 MPa/ 6,661 h.

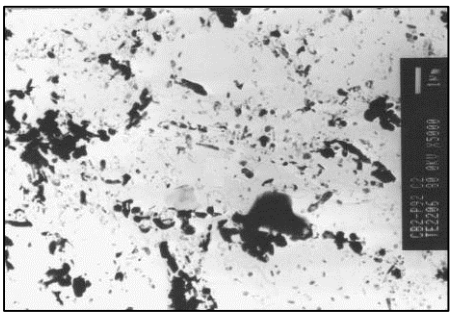

Fig. 18. HAZ P92, TEM-replica, sample 625 °C/ 100 MPa/ 6,661 h.

4. Conclusions

Doosan Škoda Power Ltd has successfully completed structural welding of cast-forged turbine parts made from steel types COST CB2 and P92 to meet the recent demands of customers.

From results gained so far, the following conclusions can be made:

The critical part of the weld joint in terms of creep strength is steel P92. The samples tested at lower temperatures and higher stresses failed in the base material of steel P92 by a ductile mechanism, while those tested at higher temperatures and lower stresses ruptured in the grain refined part or in the intercritically reheated part of the heat-affected zone of the base material of steel P92 by creep rupture.

The creep strength of the examined weld joint falls into ±20% scatter band of the creep strength of the corresponding base material P92.

After post-weld heat treatment, the hardness of the weld metal was 240 HV10; local minima were situated in the fine-grained parts of the heat affected zones in both the base materials. During creep testing the greatest decrease in hardness occurred in the intercritically reheated part of the HAZ of steel P92, where samples failed after testing at higher temperatures and lower stresses.

Crystallographic slip was the main damage mechanism when high stress was applied during creep tests. Stress activated many sources of dislocation and several slip systems were activated in each grain. This resulted in plastic deformation similar to tensile testing at elevated temperatures. Failure was concentrated in steel P92, which showed lower strength. The heat-affected zones were stronger owing to dislocation strengthening in the CG part of the HAZ and grain boundary strengthening in the FG part of the HAZ.

The stress drop caused a decrease in the number of dislocation sources and active sliding systems. The failure was controlled by dislocation creep – recovery and grain boundary sliding. Cavities originated, then grew and formed cracks. Development of cavitation damage was promoted by the occurrence of coarser particles of Laves phase. The critical part of the weldment is the FG region with a large surface of grain boundaries, high density of coarser particles at the boundaries and low density of fine precipitates and dislocations. The majority of cavities originated in the IC part of the HAZ under specific conditions, where bands of fine subgrains/grains with a high density of coarse particles were formed. On the boundaries of these bands there are fine, newly recrystallized grains and large subgrains formed by moving subgrain boundaries during recovery. Deformation was concentrated in these bands, and grain boundary ledges were formed; pile-up of dislocations occurred at obstacles formed by clusters of coarse particles. These barriers inhibited the grain boundary motion. Cavities were formed at these sites. On the other hand, intensive recovery and precipitation of Laves phase occurred at higher temperatures. Dislocation density decreased in the HAZ, and the difference between the dislocation strengthening and the matrix strengthening dropped. The distribution of cavities was more uniform and the cracks were formed at the boundary between the FG and CG regions.

Creep testing of several samples of the weldment as well as the base materials is still ongoing. A more detailed evaluation of the microstructure will be done when samples broken after longer times are available.

Acknowledgement

This work was supported by Grant MSM 4771868401 from the Ministry of Education, Youth and Sports.

References

1. “The T92/P92 Book”. Vallourec & Mannesmann Tubes, edition 2000.

2. Staubli M, Hanus R, Weber T, Mayer K-H and Kern T U 2006 in: Proc. 8th Liege Conf. Materials for Advanced Power Engineering. (Lecomte-Beckers J, Carton M, Schubert F and Ennis P J; Eds.), (Jülich, Germany: Forchungszentrum Jülich GmbH), pp 855-870.

3. ECC data sheets of steels CB2 and P92.

Power & process:
Turbines & turbine materials

Restoring steam turbine dimensions, tolerances and efficiency

Juha Sipilä[1], Juha Rintala[1] & Pertti Auerkari[2]

[1]Telatek Service Oy
Öljytie 8, FI-37150 Nokia, Finland

[2]VTT Technical Research Centre of Finland Ltd
Kemistintie 3, FI-02044 VTT, Finland

Abstract

Steam driven turbogenerator units with size up to nearly 2 GW provide large fraction of the electric power in the world. Steam turbines may show good reliability, but their disturbances tend to be associated with significant cost so that preventive and corrective maintenance is generally easily justified. However, it is often not simple or convenient to implement repairs or replacements when unexpected damage is found at the time of opening the casing. This is because many turbine components are large in size or unique by design, and possibly only available from a limited number of suppliers and even then with a long lead time. Fortunately alternative measures can be often taken, and two types of steam turbine damage are considered here: steam erosion of inner casings and other stationary components subjected to flowing wet steam, and steam leaks of the main flange surfaces.

From the user point of view, it may matter that much of the manufacturers' knowledge on turbines resides far away, partly because unlike some decades ago, the number of manufacturers in the world is now small. Together with low number of comparable machines, this may to some extent limit the local availability of expertise and experience for successful maintenance. It helps however that many features such as materials and operating conditions in steam turbines are not particularly daunting in the required knowledge accumulation, and that today the manufacturers may agree to offer help in the turbine maintenance regardless of the original manufacturer. Challenges may appear when outsourced turnkey maintenance implies shipping of major turbine sections or components to factory, to correspondingly extend the shutdown period because of the geographic distance involved, even if the maintenance project were to stay within schedule. It is demonstrated in the paper that successful on-site repair is often a viable and attractive alternative to conventional full repairs or replacements.

1. Introduction

Steam turbines provide the rotary motion to generators for conversion to electric power, and also bled steam for e.g. preheaters, industrial processes and district heating. Steam turbines are available at a very wide range of power ratings up to nearly 2 GW, and essential for the power systems of nearly all countries of the world. Although steam turbines are among the most reliable subsystems of a power plant, requiring only infrequent full overhauls, perhaps about once in 6-12 years, troubles or shutdowns because of the turbine disturbance tend to be associated with significant cost [1-5]. This cost depends on components involved and may not be accurately counted for all turbines (Figures 1 and 2) but the worldwide total must be annually hundreds of millions if not billions of euro (and USD). Hence successful mitigation of the related trouble is likely to be economically justified (Figure 1). It is also worth noting that even when the observed deviations do not end up in insurance claim statistics, steam leaks are among the most frequent items to monitor in the maintenance role of the operating personnel (Table 1). Turbine flange leaks are major causes of concern in maintaining the health of the machine.

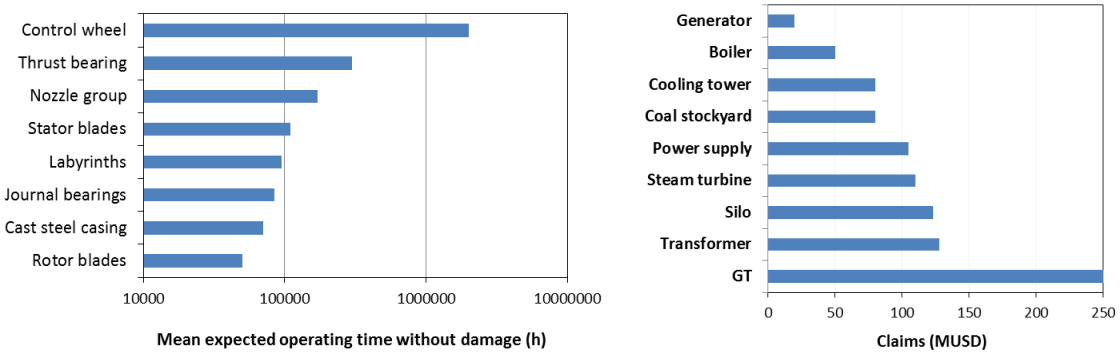

a) b)

Figure 1. a) Average operating hours for components of reaction turbines without damage; data from [1]; b) sources of power related claims in a multinational insurance group in 2012 [2]

Table 1. Principles of scheduling typical maintenance tasks of steam turbines [1,3]

Frequency	Maintenance tasks (typical)
Up to daily	Visual *inspection for leaks*, unusual vibration/noise, plugged flow, abnormal operation
Up to weekly	Trending of vibrations, testing emergency backup, aux lube oil pumps and tank, oil pressure alarms, simulated overspeed trip, cycling of main stop & throttle valves, control & extraction/admission valves (if steady)
Up to monthly	Sampling & analysing lube oil, conducting deferred weekly tests/cycling
Annually	Visual & functional testing of valves for wear, damage or leakage, internal inspection of non-return valve actuators, visual inspection of seals, bearings & lubrication systems, drain systems, and any thermal or mechanical distress; visual/mechanical/electrical inspection of instrumentation, protection & control, including alarms, backup lubrication & cooling systems; overspeed testing, gearbox testing
Minor outages every 2-4 years	Visual inspection or endoscopy of nozzle inlet/exhaust stages for damage, internal inspection of major valves for weak, leakage and damage; checking for alignment of gearbox with turbine/generator; calibration of alarms, trips & protective systems; foundations, slides and anchoring
Major outages up to about every 12 years	Overhaul of the turbine and its main components, with full opening of casings; timing and extent depend on e.g. turbine service and case-by-case requirements

However, it may not be simple or convenient to implement significant repairs or replacements for steam turbines when unexpected damage is found at the time of overhaul. This is because the components tend to be large in size and unique by design, and possibly only available from few suppliers in the world and

even then only with long lead time. Fortunately there are often alternative measures that can be taken faster and at lower cost, and examples of such measures are given in this paper. In these examples we consider two relatively common types of steam turbine damage: steam erosion of inner casings and other stationary components subjected to flowing wet steam, and steam leaks of the main flange surfaces.

In a small country like Finland, from the point of view of user, operation and maintenance (O&M) provider or an individual wishing to learn from the existing experience, it matters that steam turbines have never been made in the country, and unlike about 40 years ago today there are not very many original engine manufacturers (OEM's) left in the world. Together with smallish total number of turbines in the country, this tends to limit the local knowledge base on e.g. design, materials, and other experience relevant to the condition, maintenance and ageing. However, many features such as materials and operating conditions in steam turbines are very conventional in comparison to e.g. those in gas turbines, and as steam turbines are relatively long-living equipment, the required knowledge accumulation rate is also somewhat modest. Even that can become challenge if outsourced turnkey maintenance implies component shipping to the factory and hence extended shutdown periods because of the geographic distance between the plant and the factory, even if the maintenance project were to stay within its schedule.

It is demonstrated below that successful on-site repair is often a well justified alternative to conventional full repairs or replacements. The advantages include the ability to restore local damage with minimally intrusive approach, adding or removing material only where and when necessary to simultaneously limit the time of restoration, cost and lead time of replacement or spare parts, and associated maintenance effort.

In case of certain components of an ageing plant it not unusual that some clear improvements have been introduced to newer plants or equipment, for example by upgrading the controls and instrumentation. Although implementing such changes may not be always justified in an older plant, all modifications are not excluded there either. One common option is seen in internal coatings that can be used to build up missing material where material is lacking or lost, and where the composition of such replacement coating can be made to sustain the service loads better than in the original arrangement. Such "improving maintenance" is in the general case so rare that it is not widely used (in English) in the maintenance vocabulary. The concept of "cheaper, faster, better" is attractive, although it cannot be fully generalized for the simple reason that in any serial process the system performance only improves by removing or streamlining all comparable bottlenecks. Yet by removing a clear weak spot by improved replacement material can result in a clearly better performing component, equipment, and plant.

Turbines of the same size, model and type are not in reality identical, and it can be challenging to find a fitting spare part stored at the OEM or elsewhere. This can extend the replacement part lead times that tend to be long anyway. It is then very attractive to restore – and possibly improve - the dimensions and performance of the original part, as such modification can be initiated more or less immediately. Also, many steam turbine components are large and challenging to dislodge from the machine and transport for external repairs. In contrast, local maintenance operations will only require minimal storage space around the machine. Restoring ad improving original components in new ways is an example of activities that in the generally conservative atmosphere of power plants can encourage the habits to seek and benefit from new opportunities. Positive attitudes towards technical development can be seen particularly useful in a country where no turbine fabrication has ever taken place, and also generally in the current environment where equipment manufacturing business has strongly consolidated and is now dominated by relatively few companies worldwide, unlike the situation few decades ago.

2. Maintenance of steam turbines

Maintenance in general aims to retain an optimal level of availability, productivity and asset value of the turbine plant, but the optimal strategy may depend on the characteristics of the equipment, business environment and available resources. Rather extreme examples of maintenance and operational strategies could be relatively short term operation at high rate of life exhaustion, and on the other hand repeated restoration of the equipment to an as-new condition.

With the delivery of a steam turbine, the owner will receive (and should request for) the user's manual that includes drawings, dimensions, tolerances and materials information of the machine. The details should include a description of the guaranteed and tested machine performance at the time of delivery and acceptance, because this will indicate the originally achieved level of machine condition. Such details are

essential information for planning and implementation of any repairs, but the available data can be incomplete and may require OEM or comparable support. The maintenance actions and outcomes must be carefully documented together with the original data and those on any changes to the machine assembly, to properly support the later cycles of maintenance and its planning [6,7].

When the timing of major overhauls is based on machine condition rather than expired time in service, the guiding causes for maintenance action are often efficiency loss or increasing other deviations from the required condition, such as indicated leakage, defect growth, vibration, or deformation. It is nevertheless common that some fraction of such significant and growing deviations remain undetected until the machine is opened at the time of the overhaul, so that also some unexpected damage need to be addressed by the maintenance action. Such hidden damage often includes corrosion, deposits, wear/erosion, or distortion of the internal surfaces that may lead to efficiency losses through e.g. increasing seal clearances and steam bypass or leakage. Some accumulating damage is eventually to be expected (Figure 2), but the damage can be markedly accelerated by e.g. poor water chemistry and corrosion. Another natural source of common damage in steam turbines is the cyclic loading (vibration) of the rotating machine (less often by flow excitation). Therefore the most common damage modes are loss of surface material by wear, erosion or corrosion, and surface cracking by fatigue. The damage can be also promoted by thermal gradients or high temperature.

Figure 2. Surface damage of a turbine main flange (width ca. 150 mm; photo T. Tenkula, Telatek Service)

Some of the most important in-service indications of the turbine condition, apart from steam leaks, are provided by the sensors for vibration monitoring. Such monitoring is usually able to indicate e.g. shifting in the base plate or foundations under the turbine (and generator), loosening of attachments, blade and seal damage, growth of clearances, and casing and rotor distortion as characteristic changes in the vibration patterns that can be utilized in preventive and predictive maintenance. Even when damage is not indicated in this way, there can be reasons to suspect some damage for example at locations that operate within the creep regime: high temperature bolting, inlet hot components of HP and IP turbines.

Nevertheless, some of the damage may remain hidden until it becomes obvious through leakage or easy visual observations during the maintenance campaigns. For example in the case of wet steam erosion damage of a casing, shown in Figure 3, such damage can be locally repaired in a manner that protects better against erosion than the original material, as demonstrated by the very limited damage at the previous layer of thermal spray coating and extensive erosion damage outside the protected area.

Figure 3. Steam erosion of a turbine casing body below a 35 mm layer of thermal spray restoration that did not suffer erosion and protected the flange surface (photo: J. Rintala, Telatek Service).

When aiming to restore or improve the component condition during a maintenance campaign, it is naturally important to avoid introducing damage from the maintenance operation itself, for example through incomplete drying, corrosion protection, or bending of a stationary rotor.

The foreseen maintenance requirements, timing and methodology are usually described at the planning stage of the original turbine delivery, and possibly already in the preceding specifications. These descriptions and their later adjustments will include recommendations on setting the timing and action in the overhauls, but the details will be tuned according to the results from measurements and other information from maintenance and condition monitoring. Typical targeted components regarding machine health and life are hot end section parts such as inlet steam piping, control and stop valves, blading, rotor and disks, seals, and components operating in the creep regime, and other parts that may need repair, replacement or stocking of spares for trouble-free performance in the next service period.

In the regime of saturated and wet steam the requirements for flanges are relatively tighter that for dry (superheated) steam in the sense that fast moving liquid water droplets of the steam leak can erode the flange joint faster, and especially so when the flange is made of unalloyed (carbon, carbon-manganese or low alloy molybdenum) steel. However, leakage of superheated high pressure steam through a flange can be dangerous to personnel because it is in practice invisible. Any flange leak tends to grow in time, so that the related hazard will also increase if not properly intervened.

Turbine casings are mostly built in two parts so that the larger and more massive outer casing resides at considerably lower temperature than the inner casing that carries the turbine vane elements. Both are normally made as steel castings as two halves connected by bolting at the main flange. The only exceptions are some seamless bottle-type HP turbines made without longitudinal flanges. At the steam inlet side, the stop and control valves and the steam piping are connected to the casings by welds or with flanges.

With wear and tear of ageing turbine, its overall equipment efficiency (OEE) will decrease, but successful maintenance can restore the original or even better condition and performance regarding dimensions, material properties, and life. Wide range of techniques can be applied for this purpose, including e.g. thermal spray and welding methods, and material to be added by threaded/bolted joints [8-10].

3. On-site repair of steam turbines: procedure, benefits & limitations

The experience from turbine overhauls has shown that most of them involve damage that requires unplanned repair [4-6]. Many of these are due to slowly developing damage that could have been prevented or deferred by better condition monitoring and inspections. The improvements in the monitoring and inspection techniques are providing opportunities for preventive means to avoid adverse consequences. Nevertheless, turbine overhauls commonly take longer than expected because of unplanned repairs.

In general, on-site repair can be recommended when the targeted components are inconveniently large, complex or expensive to fully dismantle for off-site maintenance, or when repair is faster and more economical to conduct on-site. Restoring old parts for example by coating (Figures 4 and 5) is often the faster alternative in case of old or otherwise special components, or when it is a challenge to find a relevant spare part, or when the lead time is long for a replacement part. It also easily happens that the "original" replacement part does not fit because a nominally similar turbine is not identical in reality.

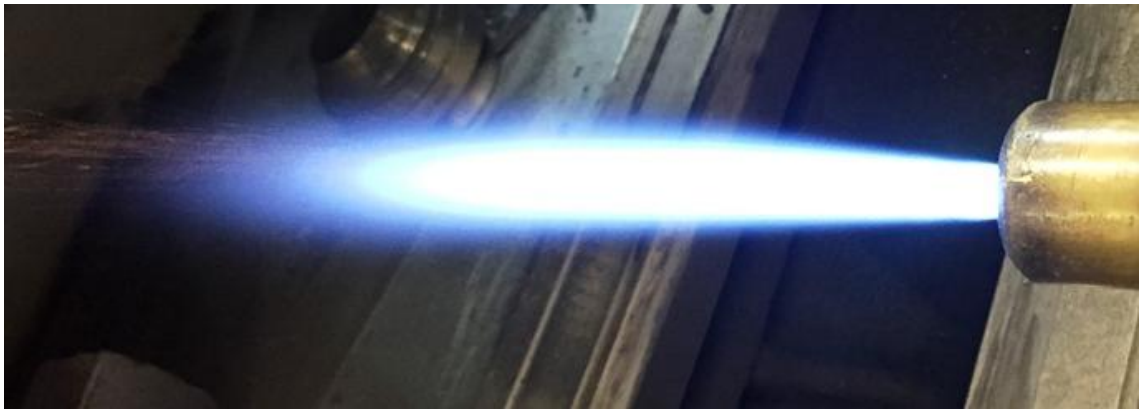

Figure 4. Carrier flame of high velocity oxy-fuel (HVOF) process for on-site restoration coating; the process requires about 500 mm free space in front of the surface to be coated; nozzle diameter about 40 mm (photo: J. Sipilä, Telatek Service).

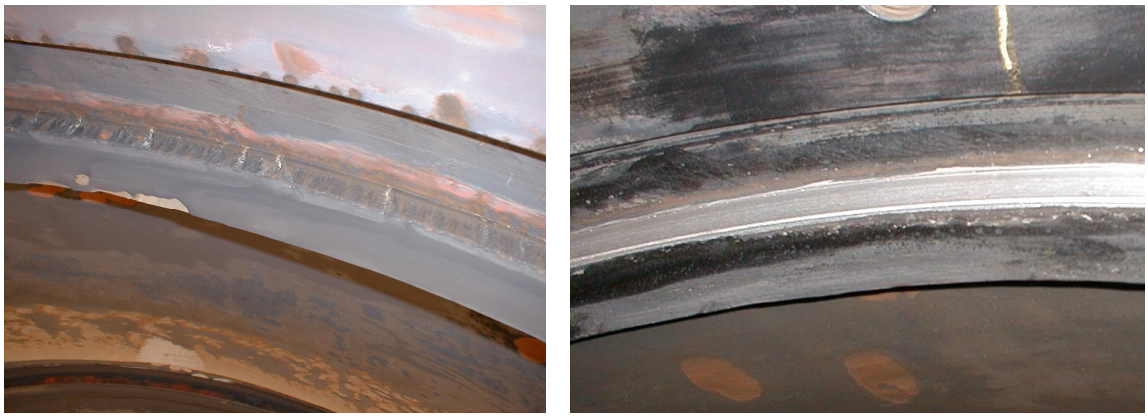

a) b)

Figure 5. Vertical sealing surfaces of turbine top casings: a) after long term service; b) after restoration to improve alignment, tightness, erosion resistance and turbine efficiency (photos: J. Rintala, Telatek Service).

Field machining equipment have been designed to be transported to the site for milling, turning, boring, grinding, honing, etc. Machining on site is the cheapest alternative when the part of interest cannot be separated from the turbine mainframe, and the maintenance work must be conducted in shortest possible downtime. The advantages can be usually easily demonstrated even in urgent cases, when the cost of lost production is known. The advantages also easily compensate for e.g. the somewhat lower rigidity and

machining rates (cutting speeds and forces) than with conventional shopfloor machine tools. A typical restoration on-site process of a major flange then proceeds to weld coating of edges, grit blasting of the surfaces and thermal (e.g. arc) spray coating, coarse machining and grinding to rough dimensions, and finally scraping and fine grinding until achieving satisfactory contact, tested by blue contact colour inspection to minimum of 80% of surface width (Figures 6 to 9).

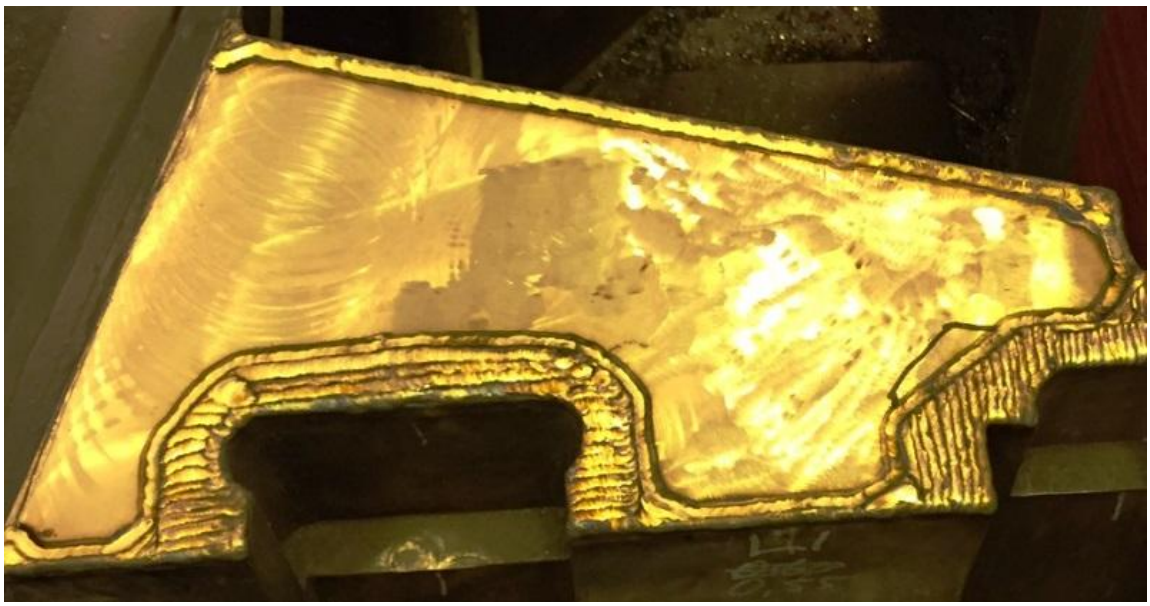

Figure 6. Flange surface after edge welding (photo: J. Sipilä, Telatek Service) .

a) b)

Figure 7. a) Surface restoration by thermal spray; b) machining of the flange surface after coating (photos: J. Sipilä, Telatek Service).

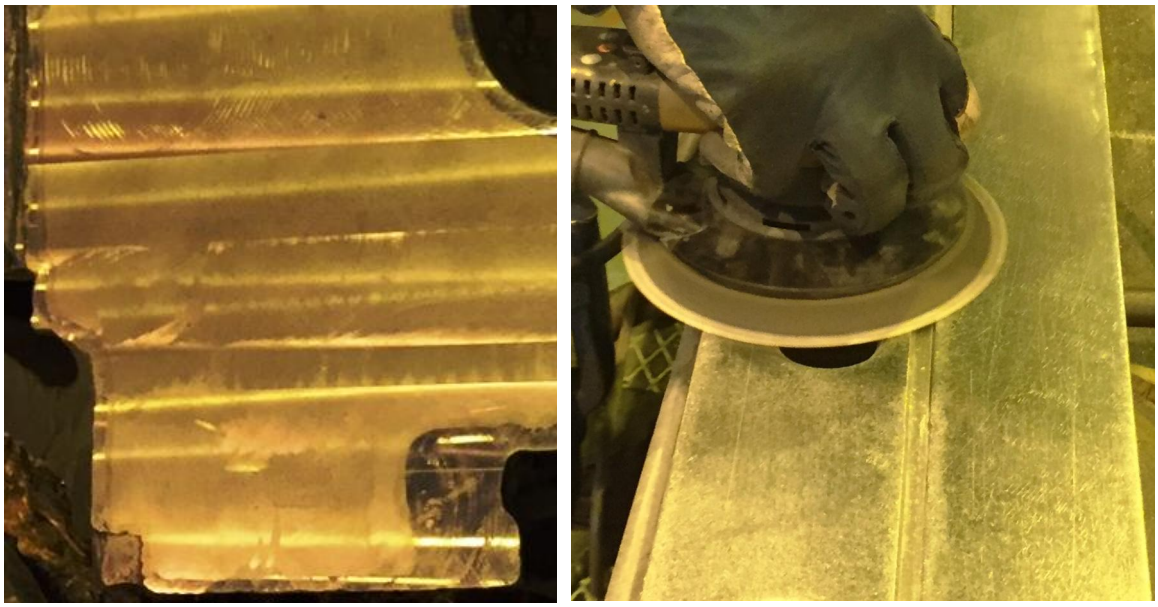

a) b)

Figure 8. a) Restored flange surface after milling; b) grinding after coarse machining (photos: J. Sipilä, Telatek Service).

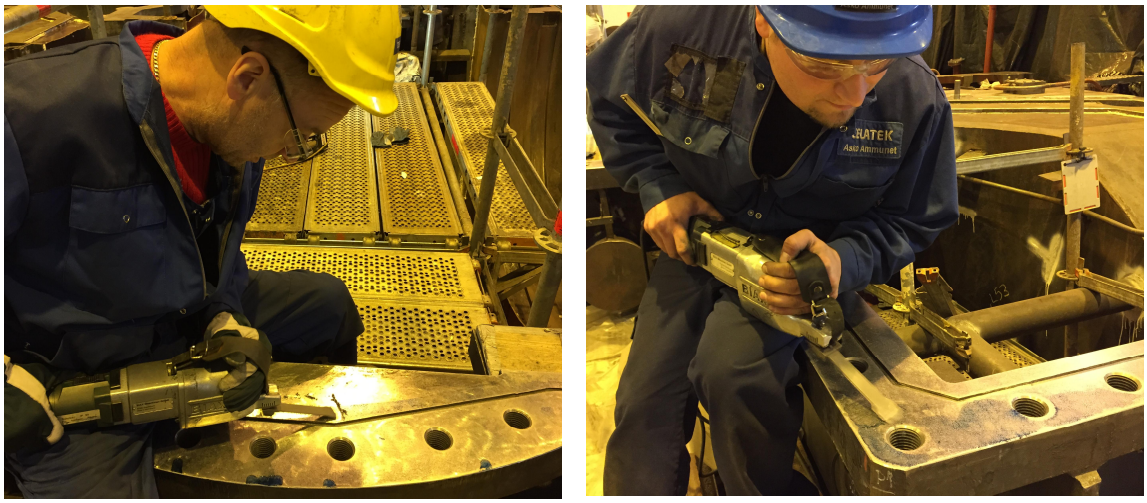

Figure 9. Scraping combined with surface colour inspection for achieving good surface contact (photos: J. Sipilä, Telatek Service) .

When needed, internal repairs can be done by similar methods of machining, thermal spray coating and final dimensional adjustment to achieve leak-tight fitting of e.g. nozzle/vane elements. In all cases the last phase is the assembly of the machine, final inspections and test operation for overhaul acceptance.

One limitation for on-site repair can be access to information on the machine and component dimensions and tolerances.

A number of factors can promote flange distortion in turbine casings, largely related to design but also fabrication and operation. Examples are asymmetric repeated heating and cooling, relaxation of residual stresses, vibration, incomplete support or movement of foundations, and fast cooling and load reduction due to turbine trips. It may be challenging to influence some of the root causes, but for example when technically feasible, residual stresses could be reduced by suitable stress relief heat treatment that can reduce stresses up to the point of the corresponding yield stress. It is also important to make sure that the

condition of the turbine (and generator) foundations (bottom plate and its ground support) work in an appropriate manner, with adjustment to the resonance frequencies and compensation for movement or any misalignment of the machine.

4. Discussion

Steam turbine is using water in its liquid and gaseous phases for mediating energy conversion. Although we do not call it a water turbine or hydropower, much of the potential trouble in a steam turbine is related to the characteristic behaviour and properties of water when it flows and transforms in the machine.

For example, valve seals, fittings and flange surfaces can suffer from erosion by both flowing steam and water, and their mixtures, and increasingly with growing velocity of the medium, growing percentage (and size) of liquid water droplets, and decreasing content of protective oxide forming elements in the affected metal. The hot end of turbine is subjected to steam oxidation and erosion by oxide particles carried by steam flow, and also affected by deposit formation by decreasing pressure and solubility of solids in steam. Some significant fraction of these solids can originate from the boiler or piping, when thermal expansion (or contraction) descales oxide flakes that fly with steam to impact turbine blading and adjacent surfaces. Towards the low temperature end, decreasing pressure results in both solid and liquid particles to precipitate and impact the turbine internals. Such high velocity impacts have potential to cause erosion, but the solids can also build up deposits and liquid layers can facilitate corrosion, stress corrosion and corrosion fatigue. In the LP turbine the environmental (corrosion) effects are exacerbated near the Wilson zone where water droplets start to form and may create conditions where impurities become enriched to corrosive concentrations in a liquid surface film [11-14]. It may be of interest and importance that the insurance terms can often have exclusion clauses for example on stress corrosion and other slowly and predictably developing types of damage.

To repair the resulting damage, there are in principle the options of conducting the required work on-site or to take the affected components off-site, for example to be repaired at the works of OEM. Overall comparison and characteristics of the two options are shown in Table 2.

In general, on-site repair by the above described procedures have the distinct and rather major advantages of requiring less time and cost when the approach is established and applicable, like it is for example in restoring flanges and other sealing surfaces, shafts and bearing surfaces, local defect repairs and local heat treatments. Also, under favourable conditions on-site restoration can improve the material to a better than as-new state, and avoid the need for spares, foreign specialists, and travel for QA abroad, or any associated delays. Further benefits are expected when major outages can be deferred to a more favourable time by quick on-site repairs.

Table 2. Comparison and characteristics of typical on-site and off-site repair or overhaul of steam turbines

On-site repair: facilitates	**Off-site repair: may facilitate better**
• Restoration of flanges and other sealing surfaces (see above)	• Full size machining of the sealing surfaces, possibly with design modification
• Repair of cracks (solution case by case)	• Complex repairs, replacements or design modifications
• Repair or restoration option	• Major component replacement if necessary
• Local heat treatment	• Full heat treatment of main components

Nevertheless, there are also cases where off-site effort can bring benefits, either as such or in combination with on-site work. These include cases where design modification is applied, for example when the blading and the flow paths are improved for better efficiency, and other design modifications or complex repairs or replacements of major components, or full heat treatments of such parts.

Cases where it is most likely that at least some support may be needed from the manufacturer (OEM, licencee or comparable) include detailed materials information, and local distributions and effects of service stresses and temperatures, particularly during in-service transients. Support may also be needed for details in dimensions, tolerances and fabrication drawings, design information on the effects of changes and safe limits, experience on operation and changes made elsewhere in the world.

When the turbine is needed as a part of a process, for example in providing district heating for a city or steam for an industrial process, high dependability is important during the high load production of the main process. The techniques of on-site repairs can help to restore production with minimal delays and to defer more extensive overhaul to a more favorable time if needed, or to apply permanent restoration to keep the machine running.

One of the involved parties with an interest in the performance of a steam turbine may be an insurance company. In general, an insurance company is aiming to the shortest solution to a problem or a challenge, and while some large customers may have preferred relying on the insurance and longer routes with off-site work at the OEM, today the few manufacturers that are left are happy to repair the turbines regardless of the origin. The attitudes can be affected by the increasing responsibilities and decreasing number of the persons in charge. Typically before, during and after overhaul, much attention and effort is needed on one hand to ensure safe service for the next period of operation, and on the other hand to justify the required spending on the maintenance investment. Under the current squeeze on pricing of electricity and other forms of energy like district heat, it helps if maintenance, repairs and restoring or even improving the condition of steam turbines can be done in a cost-effective manner through on-site services.

5. Conclusions and summary

Steam turbines are generally quite reliable, but shutdown due to turbine disturbance is often costly and relatively easily justifies the usual modest regimes of maintenance. However, it can be less convenient to implement full repairs or replacements when unexpected damage is found at the time of opening the casing. This is because the components tend to be large in size and unique by design, and possibly only available from few suppliers in the world and even then only with long lead time. Fortunately there are often alternative measures that can be taken faster and at lower cost, and examples of such measures are given in this paper. In these examples we consider two relatively common types of steam turbine damage: steam erosion of inner casings and other stationary components subjected to flowing wet steam, and steam leaks of the main flange surfaces.

In a small country like Finland, from the point of view of user, O&M operator or even an individual wishing to learn from the existing experience, it matters that steam (or gas) turbines have never been made in the country, and unlike about 40 years ago today there are not very many original engine manufacturers (OEM's) left in the world. Together with smallish total number of turbines in the country, this tends to limit the local knowledge base on e.g. design, materials, and other experience relevant to the condition, maintenance and ageing. However, many features such as materials and operating conditions in steam turbines are very conventional in comparison to e.g. those in gas turbines, and as steam turbines are relatively long-living equipment, the required knowledge accumulation rate is also somewhat modest. Even that can become challenge if outsourced turnkey maintenance implies component shipping to the factory and hence extended shutdown periods because of the geographic distance between the plant and the factory, even if the maintenance project were to stay within its schedule.

The above described on-site repairs of steam turbines are often feasible, and due to cost and scheduling reasons provide attractive alternatives to conventional full repairs or replacements.

References

1. Allianz Versicherungs-AG. Der Maschinenschaden 1970; 43(1): 1-40.

2. Willis Ltd. Power market review. London, Oct 2013. 70 p.

3. IMIA WGP42: Maintenance and overhaul of steam turbines. IAEI 38th Conference, Moscow 2005. 46 p.

4. IMIA Statistics, Large claims 2009-2014.

5. Valta, V. Turbogenerator risk level under assessment. IF's Risk Management Journal 2006; (1): 18-19.

6. Valta, V. Large claims statistics for turbines and generators. IF's Risk Management Journal 2008; (2): 10-11.

7. Etelämäki, M. Power plants in a changing world. IF's Risk Management Journal 2015; (1): 16-19.

8. Tenkula, J. Hitsauspinnoitus (Weldsurfacing, in Finnish). Hitsaustekniikka (Welding Technology) 1981; 31(2): 4-18.

9. Tenkula, J. Paikan päällä tapahtuva pinnoitus ja koneistus (On-site coating and machining, in Finnish). Voima ja Käyttö 1986; 80(11-12): 41-45.

10. Tenkula, J., Hellman, B. & Majava, J. A coating, and a coating method, for a steam turbine and adjoining steel surfaces. WO 1992004480 A1. Patent publication Mar 19, 1992, 4 p.

11. Leyzerovich, A. S. Steam turbines for modern fossil-fuel power plants. The Fairmont Press, Lilburn, GA. 2008, 537 p.

12. Chaplin, R. A. Steam turbine components and systems. Thermal power plants, Vol. III. EOLSS Publishers, Oxford, UK. 2009, p. 89-121.

13. Latcovich, J. A., Jr. Turbine optimization programs to extend outage periods and manage equipment breakdown risk. Power Generation Asset and Portfolio Management Conference, March 27-28, 2002, Atlanta, Georgia. 12 p.

14. Beddick, S. A planned outage spurs a unique approach for turbine maintenance. Maintworld 2015; 6(3): 18-19.

Assessment of metal conditions and ability for further operation of ageing steam turbine rotors

Dedov A, Klevtsov I, Lausmaa T & Hlebnikov A.

Tallinn University of Technology, Department of Thermal Engineering
Ehitajate tee 5, 19086 Tallinn, Estonia

Abstract

One of the most critical components of ageing thermal power plant is a steam turbine. To date the service time of steam turbines at Narva power plants is about 300 thousands hours that exceeds the design life-time three times. In this case, the metal inspection and assessment of durability and reliability of turbines is highly significant. Long-term exposure of steam turbines causes inevitable degradation of the structure and properties of materials due to creep and cyclic fatigue. This paper presents the experience in assessment of metal conditions of steam turbine K-200-130 rotors fabricated from steel 25Ch1M1F. The results of FEM of stress and temperature distribution in high-pressure and intermediate-pressure rotors are presented. Tensile properties of rotors metal have been determined by testing of miniature specimens fabricated from samples extracted from post-exposed rotors. The creep deformation of rotors bore has been analyzed based on diameter measurements. Creep deformation for the next 100 thousands hours of operation are estimated on the basis of cumulated deformation by use of empirical equations.

1. Introduction

More than 90% of electrical power consumed in Estonia is produced in Narva power plants where 200 MW condensing steam turbines K-200-130 are operated. Turbines are manufactured in 1960-70 at LMZ in Russia. Today the service time of turbines is about 300 thousands hours that exceeds the design lifetime three times. Ensuring the reliable and safe operation of such ageing units is impossible without continuous monitoring of metal conditions. It is necessary to increase continuously the amount of inspection and to involve all possible methods.

Steam turbines K-200-130 were designed for a live steam 565 °C/12.75 MPa and reheat steam 565 °C/2.28 MPa. Turbine K-200-130 consists of three parts, high-pressure (HP), intermediate-pressure (IP) and low-pressure (LP). Turbine rotors shafts are connected via coupling. LP rotor is exposed at low temperature that is out of the creep range and therefore is not considered in this paper. Longitudinal cross-section of HP and IP rotors of turbine is presented in Figure 1. HP and IP rotors are integrated bored rotors fabricated from steel 25Ch1M1F. The chemical composition of this steel is presented in Table 1. Rotors are centrally bored out in order to remove poor quality material and impurities that are formed in the centre during forging process. Rotor bore is also needed for metal inspection. Based on measurements of rotor bore diameter cumulated creep deformation can be determined.

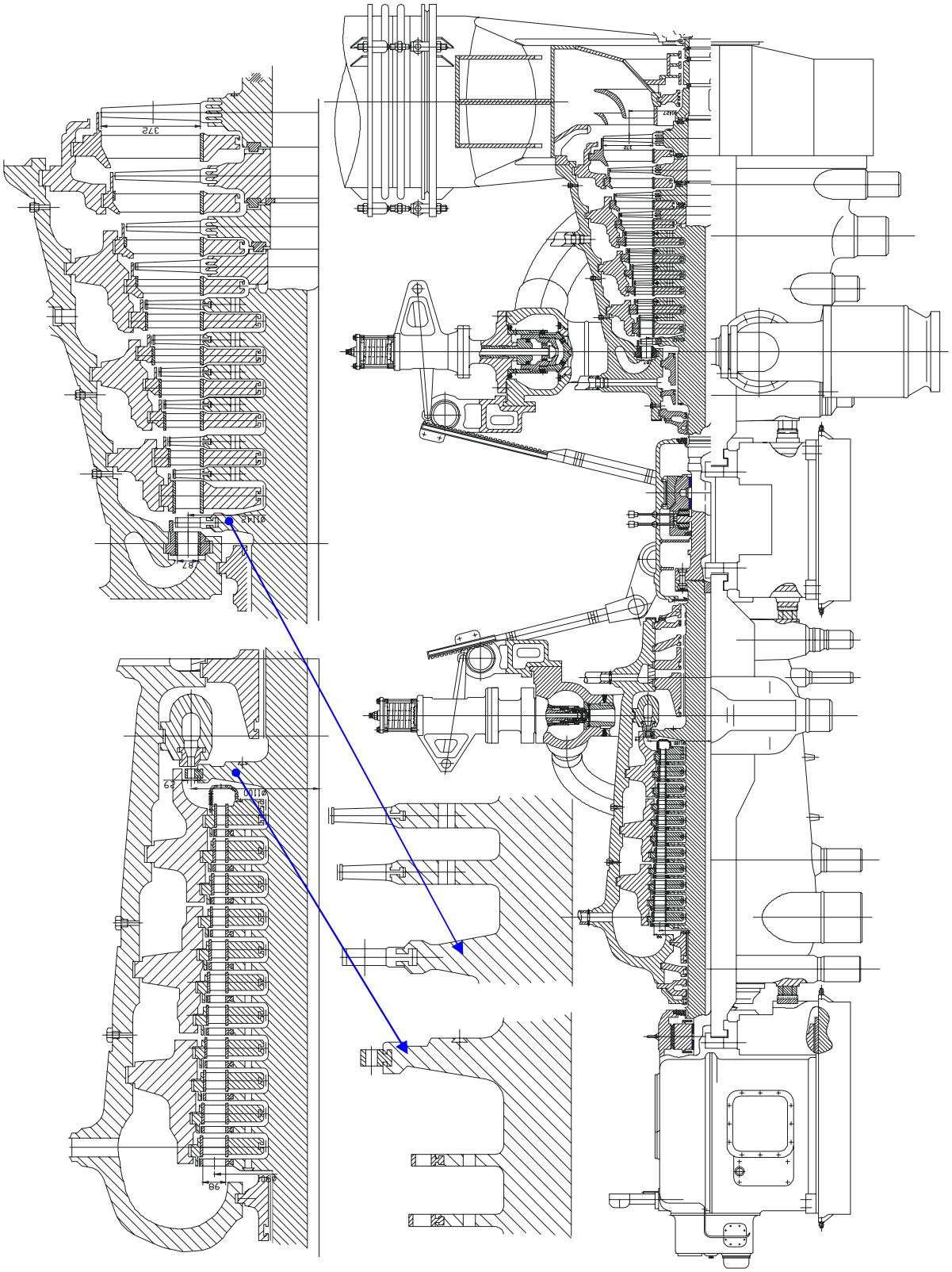

Figure 1. Longitudinal cross-section of HP and IP rotors of steam turbine K-200-130.

Table 1. Chemical composition of steel 25Ch1M1F in wt.%.

C	Si	Mn	Cr	Mo	V	Ni	Cu	S	P
0.21-0.29	0.25-0.5	≤0.7	1.4-1.8	0.9-1.05	0.22-0.32	≤0.3	≤0.2	≤0.025	≤0.03

The nominal design lifetime of turbine K-200-130 is specified in standard [1] as 100 thousands hours. However, at Narva power plants the steam temperature at the turbines inlet is lower and amounts 502–516 °C. Industrial standard [1] defines the park lifetime of turbines operated under such lower temperature as 220 thousands hours and allowable number of startups/shutdowns as 600. According to standard [2], the lifetime of further operation can be repeatedly extended, but not more than for 25 thousands hours each time. The next lifetime extension is allowed only in case if the results of the metal inspection meet all requirements concerning detected defects, metal structure, hardness, mechanical properties, creep deformation etc. These parameters are used for assessment of current condition of metal and set the time till the next mandatory inspection. This approach of steam turbine rotors metal condition assessment is implemented at Narva power plants.

This paper presents the experience in assessment of metal conditions of steam turbine rotors. The results of finite element modeling (FEM) of stress and temperature distribution in HP and IP rotors are presented. Moreover, small samples have been extracted from post-exposed rotors and subjected to tensile testing and structure investigation. The experience in monitoring of rotors creep deformation and the assessment of the ability for further reliable and safe operation of steam turbines rotors based on measured creep deformation is presented in this paper as well.

2. Experiments

2.1 FEM of stress and temperature distribution in rotors

In order to estimate the current state of metal creep degradation the distribution of stresses and temperature in the rotors is required. Stress and temperature distribution has been analysed for HP and IP rotors by means of FEM in COSMOS/M. The problem has been solved as 2-dimensional model using axis-symmetrical elements.

Stresses in the rotor are caused by centrifugal forces, steam pressure and temperature gradient. During the stationary operation mode, the stresses are formed basically due to centrifugal forces. Thermal stresses are quite low because temperature gradient in radial direction is negligible. During turbine startup the radial temperature gradient appears that leads to significant increase of total stresses. Thermal stresses during strartup depend mainly on rate of metal warming-up. Real startup curves obtained from power plants have been used for FE analysis.

2.2 Mechanical properties determination

Small samples have been extracted from post-exposed rotors for mechanical properties determination. Metal has been sampled mechanically from the surface of the rotor bore at the distance of 100 mm from the first stage of HP and IP rotors. Sampling has been performed by sampling machine developed in Thermal Engineering Department of Tallinn University of Technology (Figure 2). The location of the sampling area has been approved by turbines manufacturer LMZ. Samples have been subjected to microstructure investigation and then miniature specimens have been fabricated from samples and tested in tension at room temperature according to ISO 6892-1:2010.

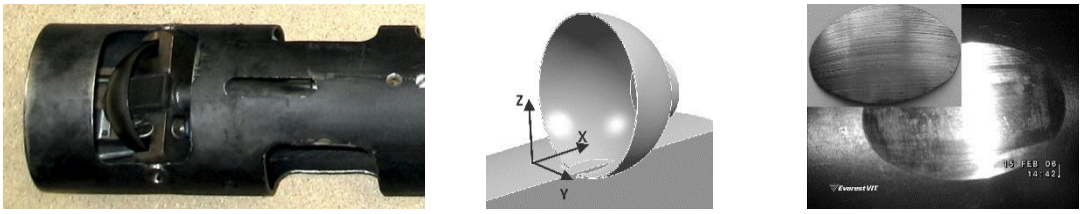

(a) (b) (c)

Figure 2. Sampling machine (a) for sampling from bores, cutting element (b) of the machine and remained cavity with sample (c).

2.3 Creep deformation measurement

Steam turbine rotor is exposed at high temperatures and stresses that causes a plastic deformation of material. Plastic or creep deformation monitoring has been carried out by measurements of diameter of rotors bores. Bore micrometer is presented in Figure 3. The diameter has been measured every 100 mm along the length of rotors.

Figure 3. Bore micrometer for measurement of bore diameter

3. Results and discussion

3.1 Stress and temperature distribution in rotors

The results of FE analysis are shown in Figures 4 and 5 where temperature and von-Mises stress distribution in the two initial stages of HP and IP rotors at the stationary operation mode are presented. Temperatures and stresses in the critical positions during startup are presented in Table 2. It is seen, that the highest stresses are in the areas of fillets between rotor and disks. During startup of HP rotor the maximal stress is on the surface of the bore. In all cases, the highest stresses on the surface of bores are in the area of the first stage where the highest creep deformation of bores occurs.

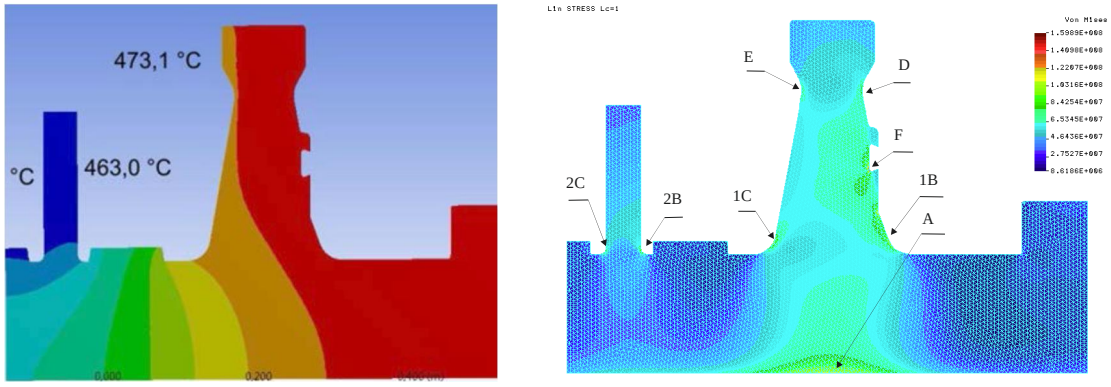

(a) (b)

Figure 4. Temperature (a) and stress (b) distribution in the two initial stages of HP rotor at stationary operation mode

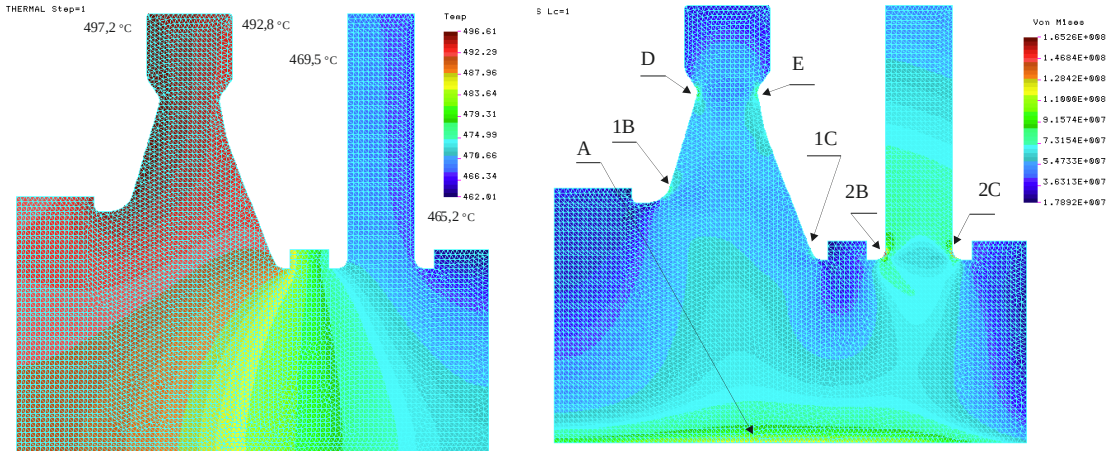

(a) (b)

Figure 5. Temperature (a) and stress (b) distribution in the two initial stages of IP rotor at stationary operation mode

Table 2. Temperatures and stresses in the metal of HP and IP rotors at stationary and startup modes in different critical positions.

Position	HP rotor			IP rotor		
	Stationary mode		Startup	Stationary mode		Startup
	Temperature, °C	Stress, MPa		Temperature, °C	Stress, MPa	
A	470	123.9	212.2	497	137.5	268.3
1B	461	134.1	211.0	497	95.8	428.7
1C	473	122.1	202.6	493	87.6	349.5
2B	463	114.4	180.3	470	190.1	276.8
2C	462	98.2	165.7	465	175.5	258.4
D	461	99.2	86.9	497	111.9	155.4
E	473	87.2	91.2	493	119.4	153.8
F	461	182.9	205.7			

3.2 Metal structure and mechanical properties

The results of metal structure investigation and tensile properties are presented in Table 3. The results have shown that tensile properties at room temperature of two rotors do not satisfy requirements for new material. Allowable decrease of properties for ageing material is not specified in standards. It should be mentioned that the ratio of yield strength to tensile strength $R_{p0.2}/R_m$ is quite high (over 0.8) for rotors of units No.3 and No.5. Although this ratio is not limited for rotor material it is limited for the boiler components manufactured from the same class of materials operated at lower temperatures and it shall not be greater than 0.75 for piping and 0.8 for drums [3]. Increased ratio $R_{p0.2}/R_m$ indicates the tendency of material to embrittlement that increases the risk of brittle fracture during cold startup.

Table 3. Tensile properties and metal structure degradation of steam turbines rotors at Narva power plants.

Unit	Service time kh	Startups/ shutdowns	Rotor	R_m, MPa	$R_{p0.2}$, MPa	$R_{p0.2}/R_m$	Structure damage
No.1	244	420	HP	614	446	0.726	Isolated cavities
			IP	589	390	0.662	Isolated cavities
No.2	243	404	HP	653	487	0.746	No cavities
			IP	670	486	0.725	Isolated cavities
No.3	232	328	HP	659	568	0.852	No cavities
			IP	654	570	0.872	Isolated cavities
No.4	256	336	HP	662	466	0.704	No cavities
			IP	703	517	0.735	No cavities
No.5	222	301	HP	659	543	0.824	No cavities
			IP	659	533	0.809	No cavities
No.6	237	290	HP	732	433	0.592	No cavities
			IP	662	503	0.760	No cavities
No.7	239	280	HP	716	542	0.757	No cavities
			IP	717	570	0.795	No cavities
Required for new material				≥618	409-667		

Summarizing the results of mechanical properties measurements it could be concluded, that further operation of rotors is not restricted in terms of tensile and yield strength. However, since it is not possible to determine the degree of embrittlement by non-destructive methods, the rotor should be inspected regularly (visual inspection by endoscopy in the axial bore, magnetic particle inspection etc.) for cracks and hardness in critical points should be measured as well.

Metal microstructure investigation of samples has shown that 10 of the 14 microstructures are undamaged by creep cavities and four structures are damaged by isolated creep cavities that also does not impose additional restrictions on further operation of the rotors.

3.3 Creep deformation

According to industrial standard [3] the cumulated creep deformation shall not be greater than:

- 0.7 % till 100 thousands hours of operation,
- 0.9 % till 200 thousands hours of operation,
- 1.0 % for operation over 200 thousands hours.

The results of creep deformation measurements of rotors at Narva power plants are presented in Figure 6 and Table 4. As it could be seen, the creep deformation of rotors does not exceed 0.55 % and therefore the requirements [3] are fulfilled.

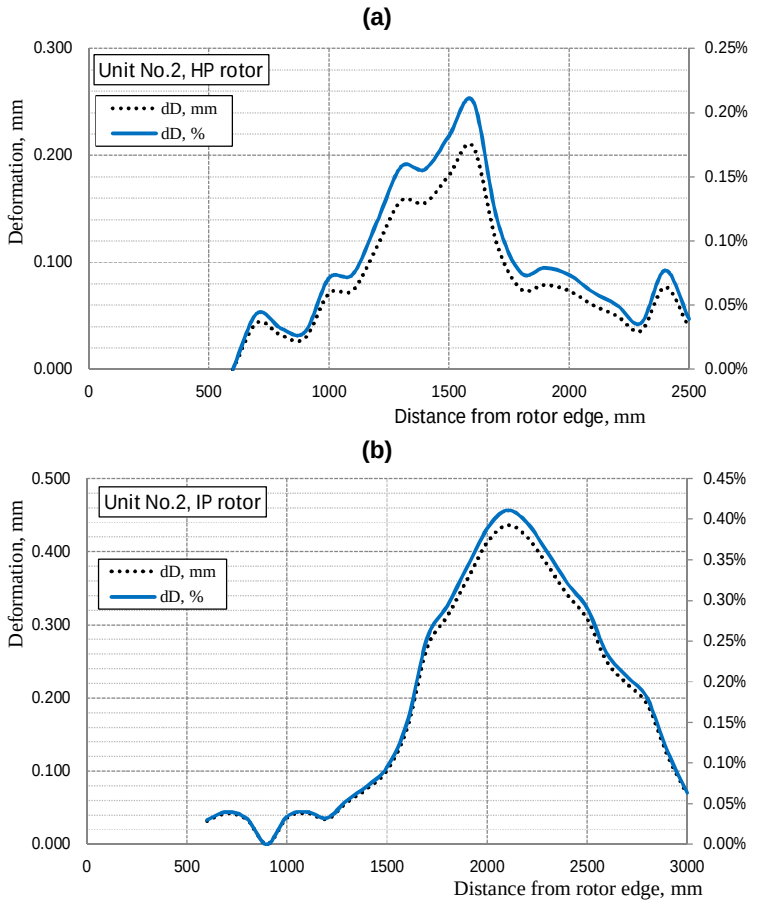

Figure 6. Creep deformation of HP and IP rotor of unit No.2

Table 4. Cumulated creep deformation of steam turbines rotors at Narva power plants.

Unit	Service time kh	Startups/ shutdowns	Rotor	Creep deformation, %
No.1	289	461	HP	0.155
			IP	0.198
No.2	302	471	HP	0.209
			IP	0.411
No.3	294	381	HP	0.144
			IP	0.472
No.4	280		HP	0.331
			IP	0.18
No.5	294	384	HP	0.194
			IP	0.552
No.6	294	367	HP	0.203
			IP	0.371
No.7	284	341	HP	0.436
			IP	0.375
Required				≤1.0

Creep properties of rotor steel 25Ch1M1F have been investigated in details in [4]. Based on great number of laboratory creep tests with duration of 10-40 thousands hours and statistical analysis of initial creep curves the authors have been obtained the equation for creep process characterisation as follows:

$$\dot{\varepsilon}_r = \mathrm{C}_1 \cdot T^{-1} \sigma_0 (1 + \varepsilon_0 + \varepsilon_r)(\varepsilon_0 + \varepsilon_r)^{\cdot -1,08} exp\left[-\frac{C_2 - C_3 \cdot \sigma_0 (1+\varepsilon_0) - (C_3 \cdot \sigma_0 + C_4) \cdot \varepsilon_r}{T}\right] \quad (1)$$

where C_1 = exp(25.84);
C_2 = 40921;
C_3 = 28.46;
C_4 = 75982.

Equation (1) has been used in the given paper for analysis of creep process of steam turbine rotors at Narva power plants taking into account the stresses and temperatures obtained from FEM for real conditions. Figures 7 and 8 represent the results of creep deformation measurements and creep curved obtained on the basis of equation (1) and taking into account the temperatures and stresses in the area of the first stage of HP and IP rotors. It is seen in the Figure 7, that all measurements of cumulated creep deformation are in a good agreement with calculation curves for metal temperatures in the range of 467-477 °C (which correspond to live steam temperatures 516-526 °C) with exception of unit No.4. The prediction of creep deformation of HP rotor till 400 thousand hours of operation could be done by using these curves. As it could be seen from Figure 7, the maximal creep deformation could be estimated as 0.35 %.

The results of creep deformation measurements in the IP rotors bores (Figure 8) are in a satisfactory agreement with calculated curves for metal temperatures in the range of 460-492 °C (which correspond to reheat steam temperatures 484-516 °C). The maximal creep deformation of IP rotors for 400 thousands of operation can be predicted as 0.7 % (Figure 7b) that is steel below the allowable deformation.

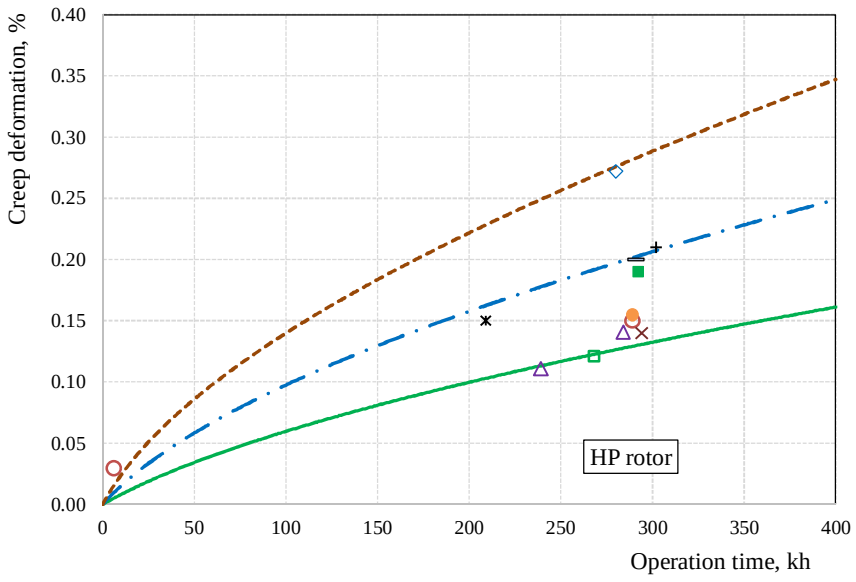

Figure 7. Measured creep deformation of HP rotors of Narva power plants and prediction for 400 kh.

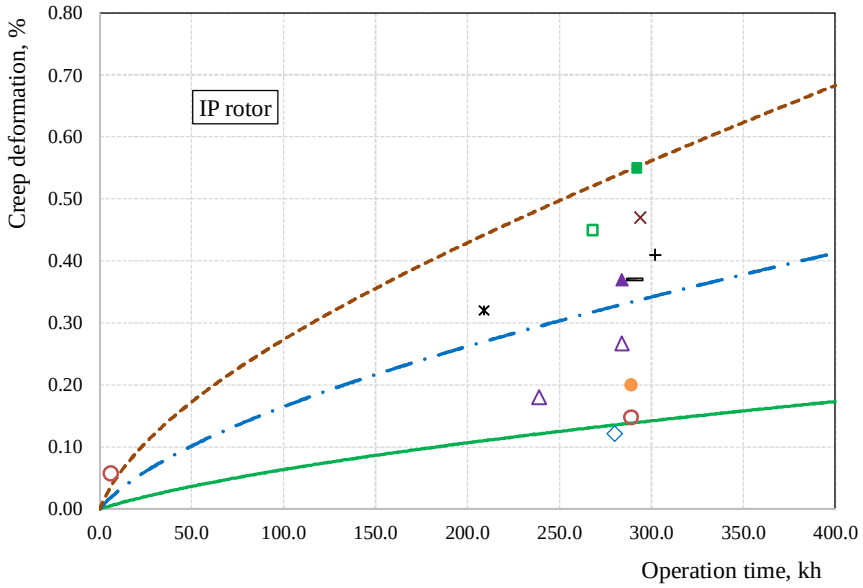

Figure 8. Measured creep deformation of IP rotors of Narva power plants and prediction for 400 kh.

4. Conclusions

Finite element modeling of stress and temperature distribution in HP and IP rotors has been carried out on the basis of real operating parameters of steam turbines K-200-120 at Narva power plants. The results have shown that the highest stresses are located in the area of fillets and on the surface of the axial bore under the first stage.

Metal microstructure have been investigated by testing the small samples taken from post-exposed rotors. Tensile properties of rotor have been measured by testing of miniature specimens fabricated from taken samples. The results have shown, that tensile and yield strength of two rotors are below the minimum required for new material. Tensile properties of the rest of the rotors satisfy requirements for new material. It was found, that the ratio of yield to tensile strength is quite high for some rotors and exceeds 0.8. It might indicate that the material becomes brittle and the risk of brittle fracture increases. The analysis of microstructure has shown that four rotors of fourteen are damaged by isolated cavities and the rest of them are undamaged. According to valid standards, such changes in structure and mechanical properties of metal do not restrict rotors further operation.

Creep deformation of the rotors has been determined based on rotors bore diameter measurements. The results have shown that the maximal creep deformation occurs under the first stage. Taking into account the measurement results and empirical equations creep deformation of rotors has been predicted for 100 thousand hours of further operation. According to the results the maximal measured creep deformation was 0.55 % and after 100 thousand hours of operation it will not exceed 0.7 % that is steel below the maximal allowable deformation of 1 % specified in industrial standard for this material. Thus it could be concluded that further 100 thousand hours of operation is safe in terms of creep deformation.

References

1. CO 153-34.17.421-2003. Regulations for metal inspection and remaining life assessment of thermal power plant boilers, steam turbines and piping, Industrial standard (in Russian).

2. CO 153-34.17.440-2003. Regulations for steam turbines lifetime extension beyond base lifetime, Industrial standard (in Russian).

3. СТО 17230282.27.100.005-2008. Basic components of boilers, turbines and piping of thermal power plants. Metal inspection. Standards and requirements, Industrial standard (in Russian).

4. N. V. Bugai, T. G. Berezina, I. I. Trunin, The efficiency and durability of metal of power equipment, Energoatomizdat, Moscow, 1994, (in Russian).

Fatigue performance of steam turbine blading

Juha Viuhko[1], Jarmo Ivaska[1], Pertti Auerkari[2] & Jarkko Metsäjoki[2]

[1]Helen Oy
Helsinki, Finland

[2]VTT Technical Research Centre of Finland Ltd
Espoo, Finland

Abstract

Steam turbine is a rotating machine and therefore fatigue is an important damage mechanism to consider already in turbine design, and it is remains necessary to consider the risk of initiation and growth of fatigue cracks in the later in-service inspection and maintenance activities. With successful design and fabrication, and operation within the intended limits, the expected fatigue life is relatively long but nevertheless finite and variable. The design features and materials of steam turbine blades are generally well established, and conventional methods of inspection and maintenance are widely applied to monitor and limit the evolution of in-service damage. As the fatigue performance of a blade is simultaneously sensitive to material characteristics, structural/loading geometry and surface condition, the combined potential range of these factors explains in principle the observed wide scatter in turbine blade life. In this paper, examples on reduced blade life are discussed based on recent experience with a case example.

1. Introduction

Fatigue is a damage mechanism that initiates and grows cracks by fluctuating stress. It commonly sets the design criteria for rotating parts of machinery such as steam turbines, for example for the rotor blading, but also means that the risk of initiation and growth of fatigue cracks must be considered in the in-service inspections and maintenance. Fatigue strength decreases with increasing number of comparable cycles and with increasing temperature. Although fatigue strength is characteristic for a material, fatigue life is strongly reduced by stress raising local features of component geometry or defects, to such an extent that particularly high cycle fatigue (HFC) performance is relatively less influenced by material or temperature when compared to creep [1]. The progression of fatigue damage can be broadly classified into the following stages:

- Initiation to nucleate permanent damage from structural features such as surface defects, corrosion pits, manufacturing or other defects (possibly microstructural), or high stress concentrations like sharp corners
- Growth of microscopic cracks and coalescence to macroscopic size (several mm or more)
- Stable propagation of dominant macroscopic crack(s)
- Structural instability or complete fracture.

The initiation stage is often important in turbine blades as it tends to make a large contribution to the total fatigue life. Even when the design is appropriate, early fatigue cracking and failure can occur due to a

defects related to manufacturing, operational or other damage to create or enhance stress concentrations. As a result, fatigue alone or in combination with other mechanisms such as corrosion is the most common failure mechanism of steam turbine blades [2]. A case example is considered below with observed blade cracking after 45000 h of service.

2. Case example

Crack indications were observed in the surface and UT inspected rotor disk rims and blades during an outage (Figure 1). At this IP6 stage of the turbine the steam temperature is approximately 380°C and pressure about 17 bar. The blades have been in operation for 45000 h, and the blade material is X12Cr13, i.e. tempered martensitic steel nominally with 13% chromium.

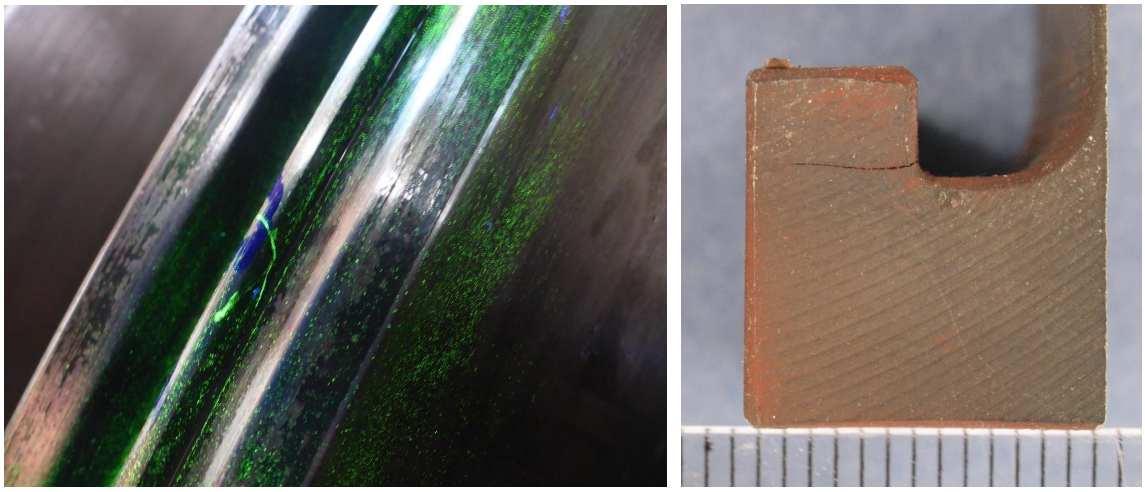

a) b)

Figure 1. Cracks in a) the rim of a rotor disk and b) root groove of blade (108)

In one of the blade root grooves (blade 45) a corner piece was already missing (Figure 2). The fracture surface was oxidised and visually relatively smooth. In another blade (blade 108) a crack was observed at the root groove (Figure 1b and 3).

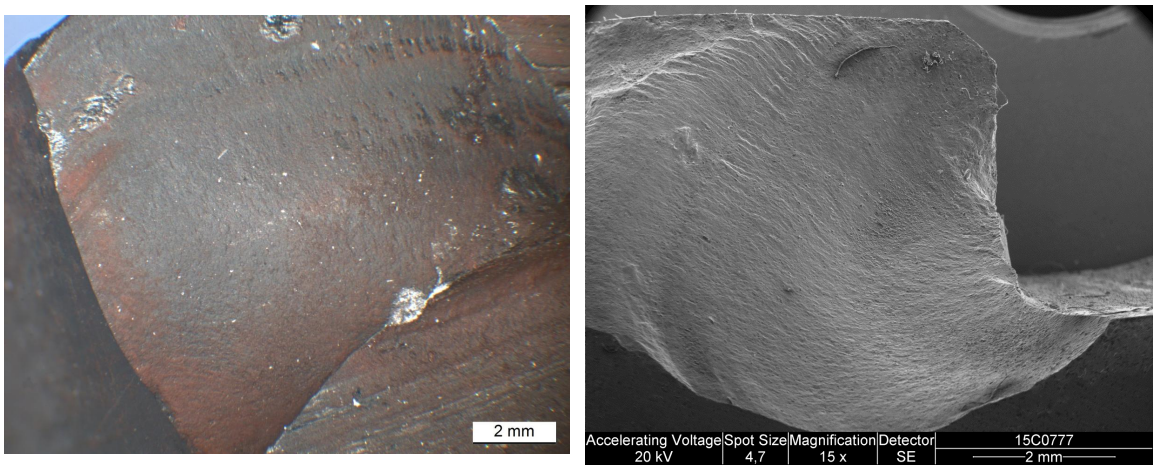

a) b)

Figure 2. Fracture surface at the blade root of the blade with the detached piece (blade 45).

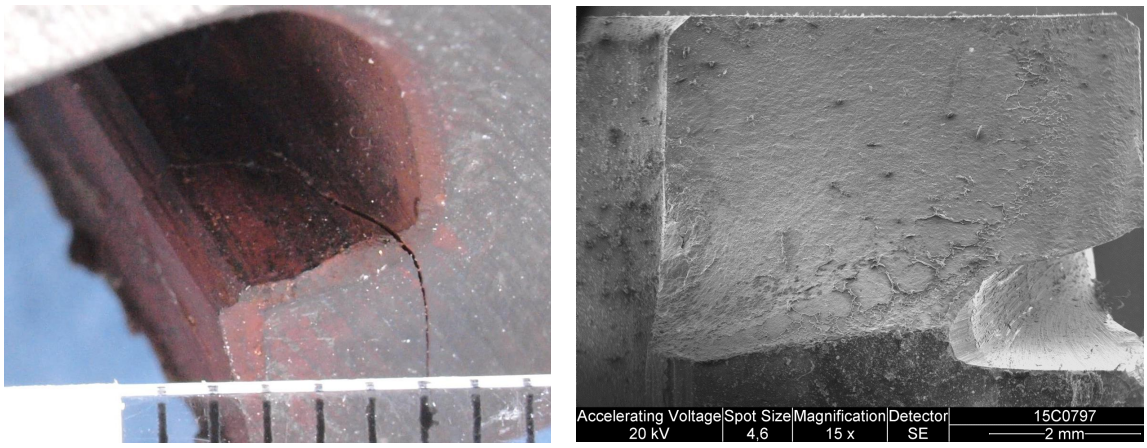

a) b)

Figure 3. a) Crack in blade 108 and b) opened fracture surface (grinding on the right for opening)

The fracture surface was oxidised most extensively in the vicinity of the initiation site (Figure 4-7). The microstructure of the blade was tempered martensite consistent with the chromium steel X12Cr13 (Figure 6 and 8). The measured blade hardness was in accordance with the certificate provided by the blade manufacturer (Table 1). Also the chemical composition was similar to that in the certificate for the blade material (Table 2). There was hence no indication of the mechanical properties of the bulk blade material deviating from those stated in the material certificate of the manufacturer.

The fatigue crack of both cracked blades has initiated from the root groove, and the fracture surfaces (Figures 2 and 3) indicate growth by relatively steady high-cycle fatigue (HCF). The cracks grew in an oblique manner across the groove corner and not along the groove bottom. In addition, the crack centre at the initiation (groove side) front showed in blade 108 some surface anomaly that turned out to be a relatively thick oxide at the crack mouth (Figures 5 and 6).

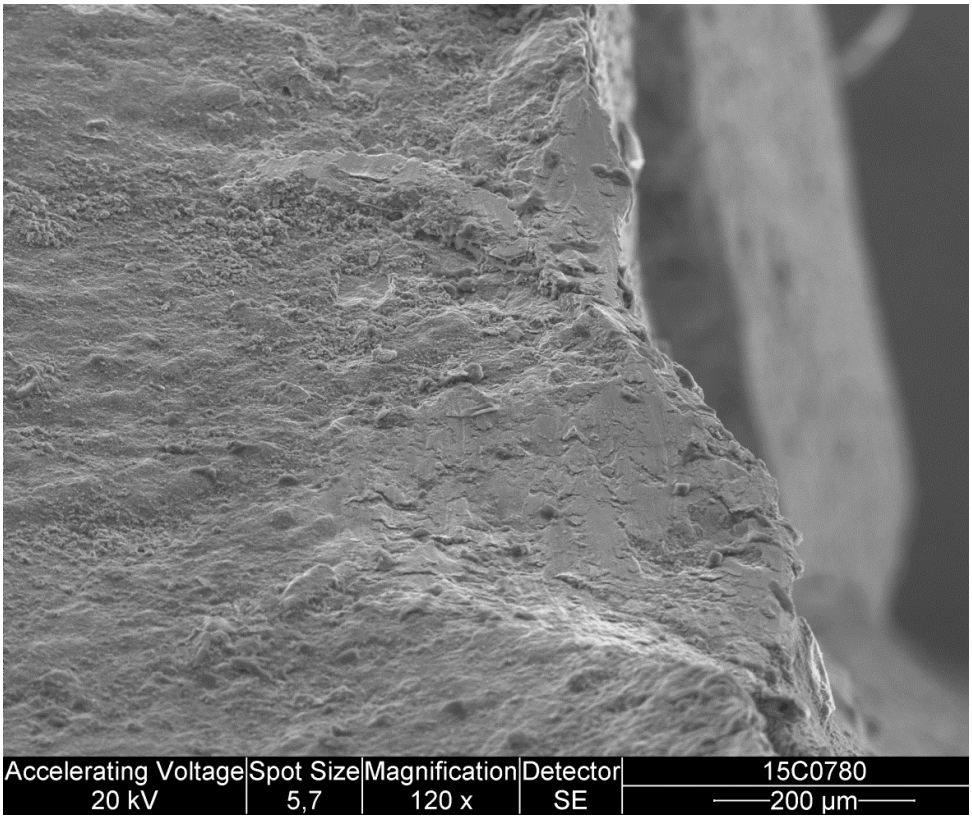

Figure 4. Detail from Figure 2b, near the fracture initiation (blade 45).

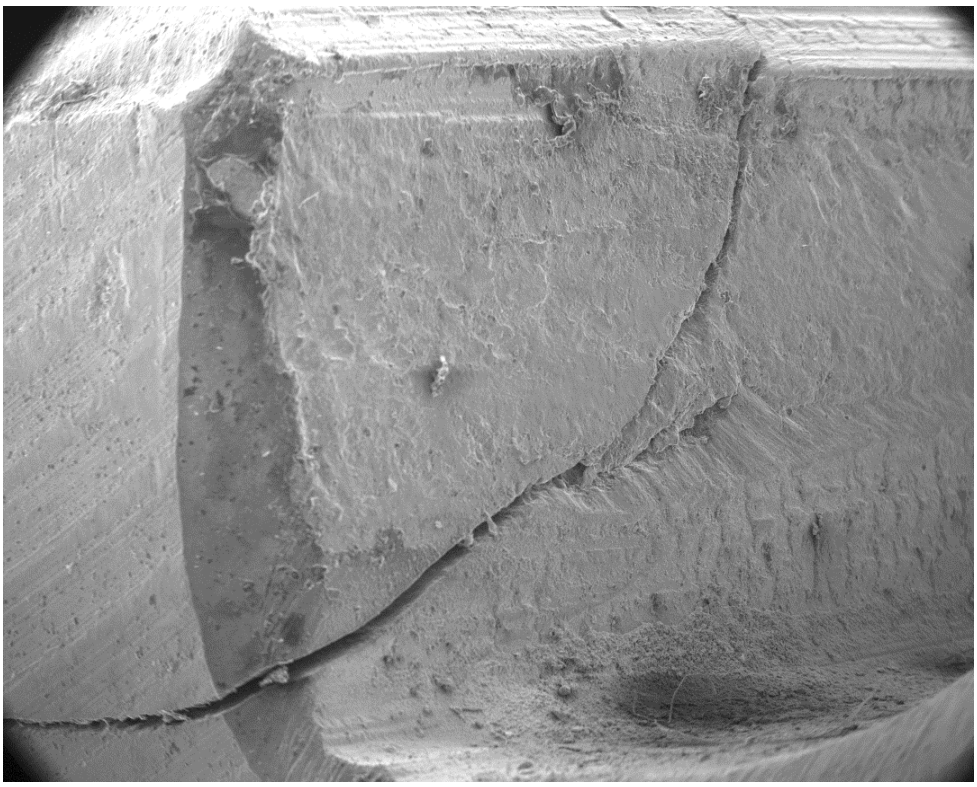

Figure 5. Crack of blade 108 as seen from the top side of Figure 3a.

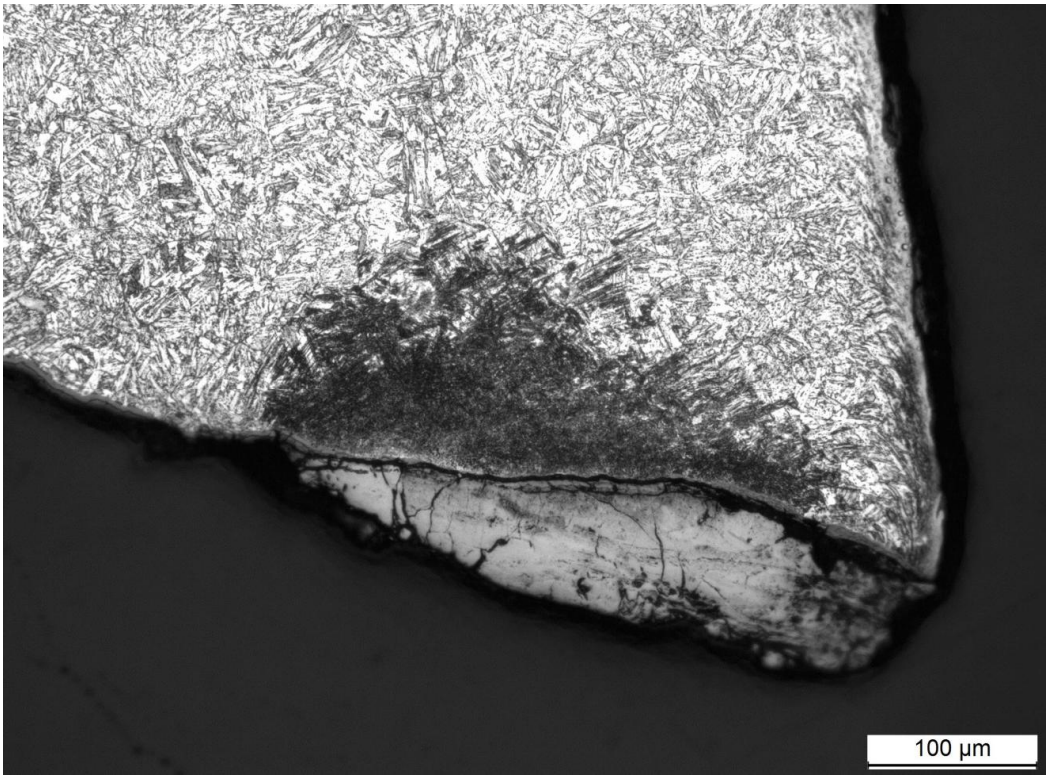

Figure 6. Cross-section with surface oxide at the fracture initiation site of blade 108.

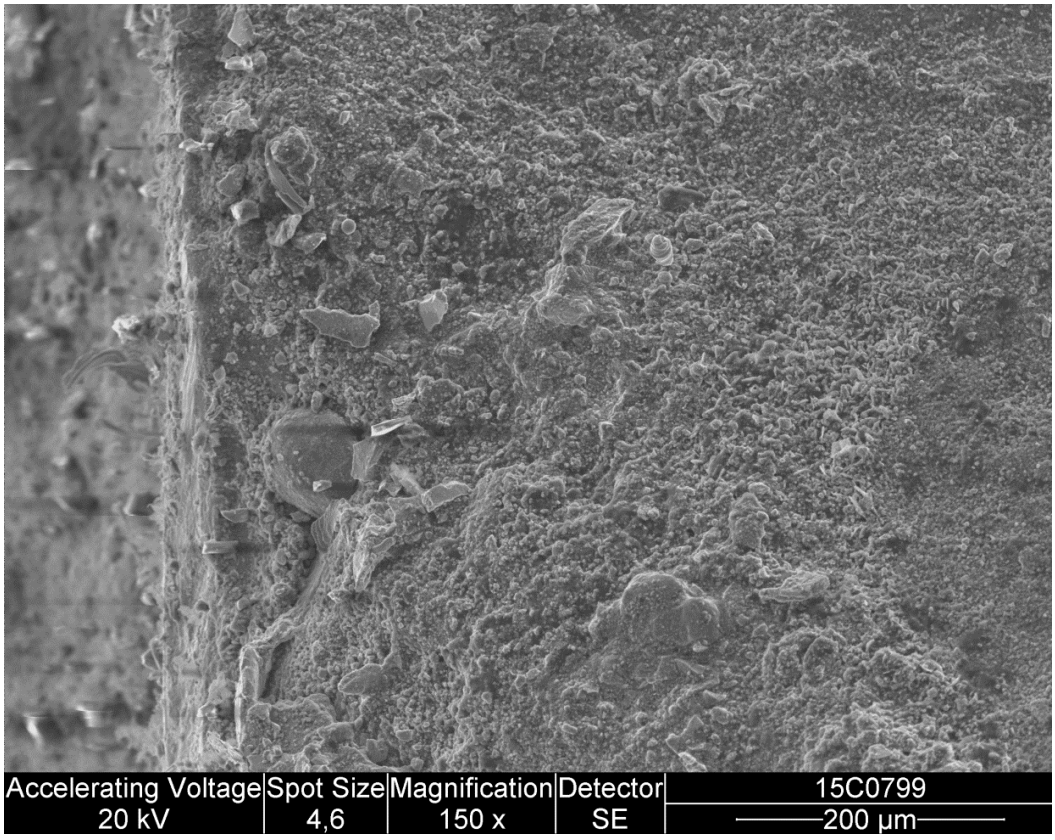

Figure 7. Surface of the fracture initiation site of blade 108.

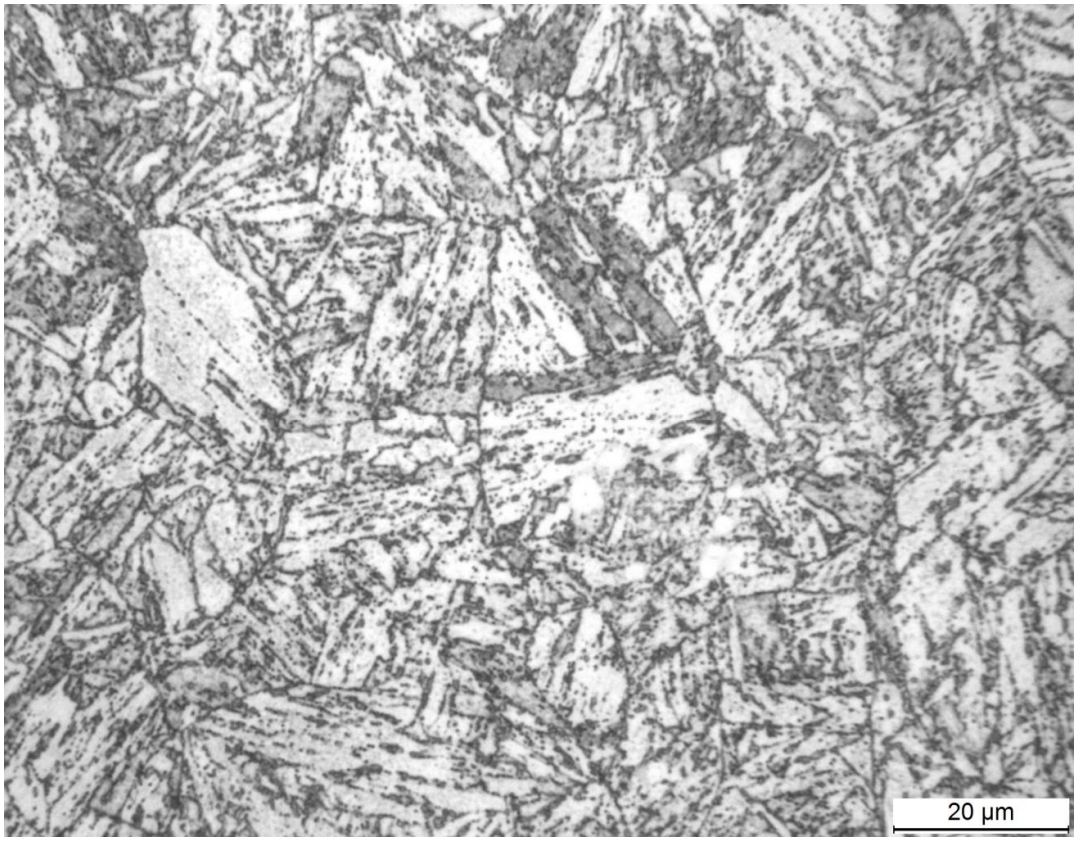

Figure 8. A detail of the tempered martensitic microstructure of blade 108.

Table 1. Hardness of the blade samples

Blade	Hardness
No. 45	244 ± 5 HV5
No. 108	241 ± 2 HV5
Certificate	239 - 245 HB

Table 2. Chemical composition (wt-%) of the sample blades

Ni	Blade	C	Si	Mn	S	P	Cr	Cu	Al
0,45	45	0,12	0,27	0,71	-	0,018	12,3	0,22	0,009
0,45	108	0,12	0,27	0,71	-	0,016	12,2	0,22	0,011
0,45	100b	0,12	0,27	0,71	-	0,016	12,3	0,22	0,009
0,44	Cert.[1)]	0,120	0,26	0,75	0,009	0,020	12,41	-	-

[1)] According to the manufacturer's certificate

It was not possible to check the dimensional tolerances between the blade root and the attachment of the disk rim for the sample blades. Loose attachment and subsequent vibration is one possible source of additional HCF loading.

The blade 45 appears to have initiated cracking close to the bottom groove corner but the initiation site has suffered some local indentation or impact at this location after failure (Figures 2 and 4). After initiation much of the crack front has proceeded to grow in an oblique manner with respect to the groove bottom, and therefore stress concentration at the groove corner was significant only close to the initiating side of the root.

The groove corner geometry had even less influence in the initiation of the crack of blade 108, since the crack does not pass through this corner (Figures 3a and 5). Instead, an oxide slab 85 µm in thickness at the crack mouth, well away from the groove corner (Figure 6), is the likely first major initiation point. Such an oxide cannot have arisen in the service conditions on X12Cr13 steel and may rather indicate a fabrication defect.

In blades operating in dry steam, i.e. outside the low pressure section where mechanisms such as corrosion, stress corrosion and corrosion fatigue can be active, about 40% of blade failures can be related to fatigue and another 40% to unknown mechanisms [2]. The observed fatigue cracking is therefore not overly unusual, considering the expired time in service of 45000 h and the conventional experience that some blade failures could be expected by about 40000 to 50000 operational hours [5]. Nevertheless, the fact that this only applied to some of the blades, possibly with fabrication defect, indicates potential for improvement.

3. Conclusions and summary

The chemical composition, hardness and microstructure of the investigated turbine blade samples were generally in accordance to the information provided by the blade manufacturer. The fractures in the investigated blades have initiated from a region close to the mounting groove and the fracture surfaces indicate a slow long term high frequency fatigue fracture. In one blade (108) a thick oxide was observed near the initiation site of the fracture. This oxide cannot have arisen from the operation hours (45000 h) at about 380°C in X12Cr13 steel. Therefore, a manufacturing defect of some sort can be considered at least in blade 108.

References

1. Leyzerovich AS. Steam turbines for modern fossil-fuel power plants. The Fairmont Press, Lilburn, GA. 2008, 537 p.

2. C. De Michelis, C. Rinaldi, C. Sampietri & R. Vario. Condition monitoring and assessment of power plant components. In: Power plant life management and performance improvement. J.E. Oakey (ed.), Woodhead Publishing 2011, p. 38-109.

3. B. M. Schönbauer, S. E. Tchegg, A. Perlega, R. N. Salzman, N. F. Rieger, S. Zhou, A. Turnbull, D. Gandy. Fatigue life estimation of pitted 12% Cr steam turbine blade steel in different environments and at different stress ratios, Fatigue of Metallic Materials – Mechanisms and Life Estimation, Vol 65, August 2014, pp. 33-43.

4. E. Plesiutschnig, P. Fritzl, N. Enzinger & C. Sommitsch, Fracture analysis of a low pressure steam turbine blade, Case Studies in Engineering Failure Analysis, Vol. 5-6, April 2016, pp. 39-50.

5. Allianz Versicherungs-AG. Der Maschinenschaden 1970; 43(1): 1-40.

Fatigue performance of blade steel T671 for different kinds of loading

Janoušek J[1,2], Hřeben S[3], Špirit Z[1,2], Strejcius J[1] & Kasl J[4]

[1]Research Centre Rez
Hlavní 130, 250 68 Husinec-Řež, Czech Republic

[2]University of West Bohemia, Faculty of Mechanical Engineering,
Department of Material Science and Technology
Univerzitní 22, 306 14 Plzeň, Czech Republic

[3]Doosan Škoda Power
Tylova 1/57, 301 28 Plzeň, Czech Republic

[4]Research and Testing Institute Plzen
Tylova 1581/46, 301 00 Plzeň, Czech Republic

Abstract

This contribution is based on the experiments and assumptions which have been described in the previous authors' works. The experimental programme, which deals with the issue of blade steel T671 fatigue damage, has been extended for another comparison. The specimens were taken from a reference material delivered for blade production and from the low pressure blade body of L-0 stage of a turbine generator set. Since this is the area of the steam condensation (phase transition zone), the specimens were also tested in the corrosion cell under pre-stress of 300 MPa. The chloride solution of 35 ppm was chosen as the environment at the temperature of 80°C. Such an environment can be considered as the limit state that should not occur during the operating regime. The results were compared with previous experiments and the conclusions were summarized.

1. Introduction

This study is strictly concerned with fatigue behaviour of blade steel Böhler T671 in the air and in an aggressive environment. Nevertheless, this material is used especially for last stage blades manufacturing such as it corresponds with [1]. The meaning of these tests is an effort of life extension. According to [2] the cost varies from 20 to 30% of cost of constructing a new plant and thus the benefit-to-cost ratios are very high. In [3] the results of specimens taken from the fir tree root of low pressure steam turbine blade were published. They were tested in the air and with pre-stress 450 MPa. Fatigue limit came to value of 360 MPa for this case. Afterwards the tests in a corrosion cell were released in [4]. These experiments were carried out for the same pre-stress 450 MPa in solution of 22 % NaCl at the temperature of 80°C. The results revealed that in such an aggressive environment no fatigue limit occurs since lifetime values

according to [5] in range of $5x10^7$ up to 10^8 cycles were not achieved for any specimen. The tests were performed for frequency 80 Hz and the testing machine Electropuls E10000 by a company Instron was used.

2. Experiments

2.1 Test materials

The experimental programme was extended in order to specimens taken from the body of low pressure steam turbine blade. Furthermore tests were performed on a material heat treated as a last stage blade (reference material). And also extension included the tests in aggressive environments such as NaCl solution at different concentrations. Pre-stress was chosen for all subsequent tests to 300 MPa. This value should reflect the real operating loads more accurately.

Table 1. Chemical composition of the steel T671. [6]

Cr	Ni	Cu	Mo	Mn	Nb	Si	C
14.23	6.33	1.29	0.64	0.47	0.41	0.40	0.04

The steel Böhler T671 was used as a reference material. The chemical composition of the specimens is mentioned in Table 1. It is a high strength martensitic precipitation-hardened steel which exhibits a ferromagnetic behaviour.

Table 2. Heat treatment of the steel T671. [6]

	Target temperature [°C]	Heat-up rate [°C/h]	Soaking time @ target temperature [min]	Cooling time [min]	Cooling rate [°C/min]	Coolant
Quenching	1040	103±5	60	360	14±2	Air
Tempering	510	95±5	240	>240	2,5±0,5	Air
Stress relieving	500	95±5	120	>240	1,5±0,5	Air
Heat treatment n°:	**5396**					

The material was quenched at the temperature of 1040°C, tempered at 510°C and then stress relief annealed at 500°C. Heat treatment is described in Table 2. The mechanical properties (see Table 3) should correspond with the hardness higher than 341 HB, the yield strength higher than 1103 MPa and the ultimate strength higher than 1172 MPa. All these properties were verified on the given material.

Table 3. Mechanical properties of the steel T671. [6]

Orient.	**HB** ≥ 341	**Re** [MPa] ≥ 1103	**Rm** [MPa] ≥ 1172	**As** [%] ≥ 10	**Z** [%] ≥ 40	**KV** [J] ≥ 75		
Long.	401	1171.9	1199.1	15.5	64	89	155	175
Trans.	401					174	162	161
Long.	388	1134.2	1172.7	18.5	65	165	154	153
Trans.	388					166	151	149

2.2 Fatigue test equipment

The resonant testing machine TESTRONIC 250 made by a Switzerland firm RUMUL was used for all following experiments (see Fig. 1). It is a dynamic testing machine which works in full resonance for loads up to 250 kN. The maximal oscillating stroke extension is available up to 4 mm. The resonant operating frequency is given in ranging from 40 up to 250 Hz by the oscillating masses and among others by the stiffness of the specimen. The load of specimen is a combination of a static and a dynamic force. Both parts are controlled separately. Measuring accuracy is better than 0.5 %. The dynamic drive with springs, masses and driving magnet is located in the upper part of the machine. The dynamic drive operates as a mechanical resonator and is excited by an electromagnet. Maximal dynamic load is ± 125 kN. The main inertia on the upper part and the lower part of the machine oscillate against each other. The resulting elasticity, which mainly determines the operating frequency, is being built out of the specimen and the spring rods. The main inertia can be varied in 8 steps. The static drive to apply the mean load is placed in the lower part of the machine and consists of a ball screw spindle with preloaded nuts, which are mounted in a cross bar. The cross bar, the columns and the upper part build the load frame. The ball screw spindle is being driven by a gear from the servo-motor controlled in closed loop. Maximal static load in tension or compression is 150 kN. Speed of the static drive is from 0 to 150 mm per minute. The power units for both static and dynamic drive are also located in the lower part of the machine. The main board of the control unit with amplifiers and processor is placed outside the machine below a cover. The load frame and the whole lower part of the machine are built to be the counter mass. The machine is designed to consume electrical power below 1 kW. This is a more economical advantage compared to servo-hydraulic systems (likewise maintenance for pumps, valves and cooling is not necessary).

Figure 1. The resonant testing machine TESTRONIC 250 with corrosion cell set-up.

2.3 Experiments in the air

The specimens for the next experimental programme were taken from body of low pressure steam turbine blade. In the Fig. 2 these specimens are marked by red colour. The roughness of the samples was chosen as 0.2 which is better value than in standard ČSN 42 0363 dealing with fine turning. The blade was made as a forging which was subsequently machined on CNC machine.

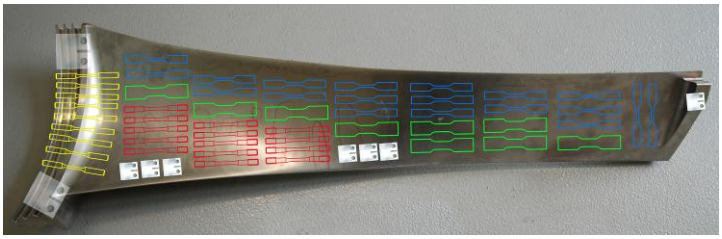

Figure 2. Cut the blade up to individual specimens.

Dimensions and shape of the sample are shown in Fig. 3. The shape of the specimen was chosen because of the possible application of corrosion cell on a straight work area. Since it is a high-strength material, it was found that when such dimensioned specimen leads to cracking in the clamping threads and subsequent damage to the clamp insert.

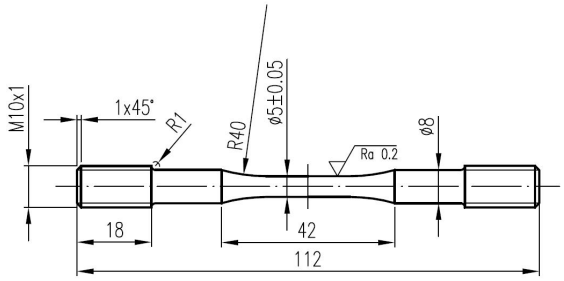

Figure 3. Specimen shape and dimensions. Specimens (red colour) taken from blade body.

For other tests, specimens were taken from the material provided for the manufacture of blades (reference material). Dimensions and shape of specimen are shown in Fig. 4. The test section was machined in the form of hour-glass. The tests again showed that due to a large diameter of the working part a substantial part of the specimens cracked again in the place of a threaded clamping, especially at levels close to the fatigue limit.

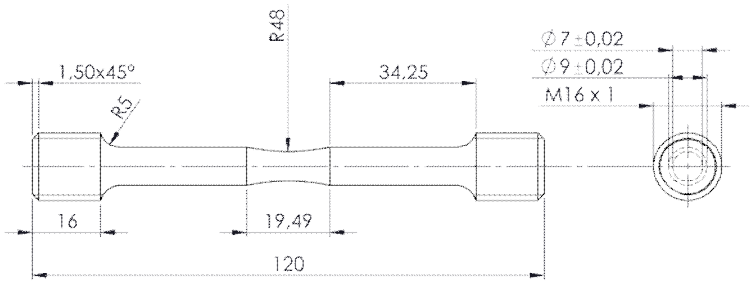

Figure 4. Specimen dimensions for another tests in the air.

2.4 Experiments in corrosion cell

The corrosion measuring cell was designed, engineered and manufactured for tests in a corrosive environment. The cell is made of an inert material, Teflon, glass and silicone rubber. Its appearance is shown in Fig. 5. The cell has a flow volume of 1 litre, the entire electrolyte solution is about 1000 litres per hour and electrolyte is tempered to a required temperature with an accuracy of 1 °C. The bubbling an inert gas enables to control the content of dissolved oxygen in the electrolyte. It is also possible to adjust the pH. The control of electric conductivity is performed continuously. During the test of corrosion fatigue the electrode potential of specimen is also recorded.

Figure 5. Corrosion cell.

The specimens of 240 mm length with a straight working part and a diameter of 8 mm were tested in the flow cell. (See dimensions in Figure 6).

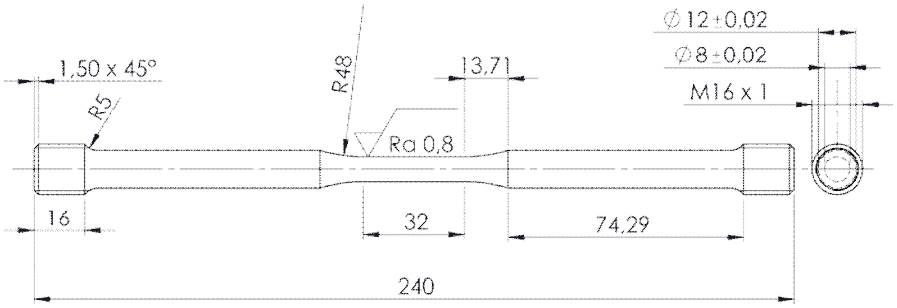

Figure 6. Specimen dimensions.

3. Results

The specimens taken from the body of the blade were tested in the air at 300 MPa pre-stress. Ten specimens have been tested and 2 tests were invalid due to a fracture in the threaded attachment. The results are shown in Table 4. The frequency was chosen intentionally low to prevent heating of the specimen.

Table 4. Results of fatigue tests for specimens taken from blade body (pre-load 300 MPa).

Specimen	Ø [mm]	σ_a **[MPa]**	f [Hz]	N_a	comment
A_1	5	**460**	63.8	3 369 905	**fracture in thread**
A_2	5	**455**	63.8	8 989 651	
A_3	5	**465**	63.9	484 650	
A_4	5	**470**	63.8	16 041 210	
A_5	5	**475**	63.7	604 034	
A_6	5	**480**	77.6	10 726 097	
A_7	5	**440**	69.6	15 502 731	
A_8	5	**470**	69.5	10 409 059	**fracture in thread**
A_9	5	**460**	69.7	20 018 803	
A_10	5	**490**	69.7	673 283	

The slanted branch of the S-N curve was fitted by a Fletcher's version of the Levenberg-Maquardt algorithm for the minimization of a sum of squares of equation residuals. The program was created in numeri-

cal computing environment and programming language MATLAB. This regression line curve is defined by an equation that was found by a probabilistic approach as

$$\log N_a = 74 - 25 \log \sigma_a. \quad (1)$$

The S-N curve is depicted in Fig. 7. The red points are valid, green arrows indicate invalid points which were not taken into the linear regression.

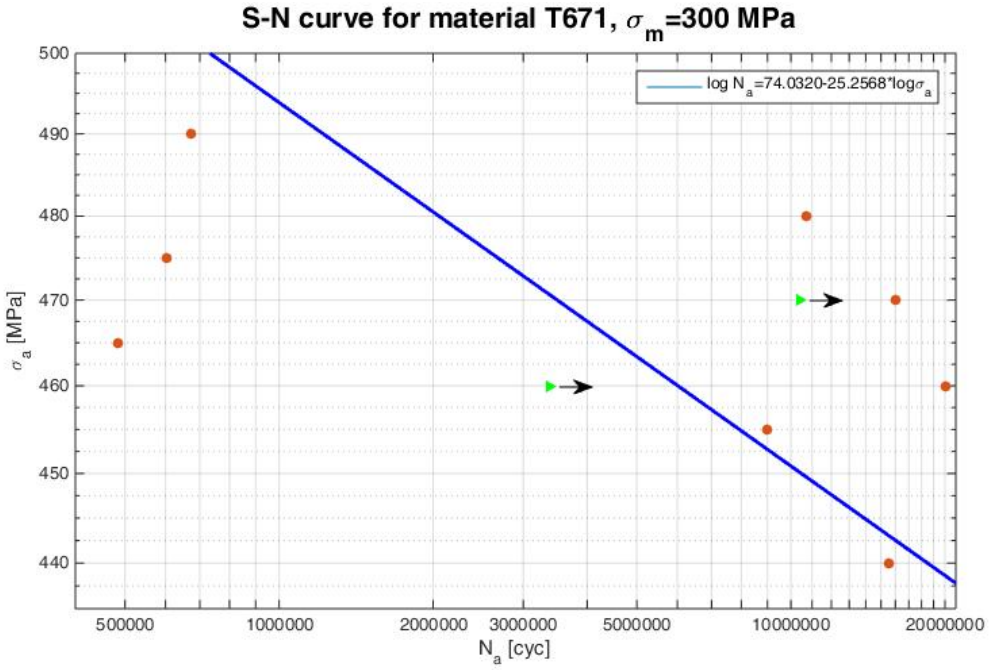

Figure 7. S-N curve for steel T671 for specimens taken from the blade body with pre-stress in a normal component σ_m = 300 MPa tested in the air.

The reference material was inspected in the following tests. The specimens' diameter was 7 mm. Cracking occurred frequently inside the insert threads as Table 5 shows. The frequency ranged from 70 to 80 Hz.

Table 5. Results of fatigue tests in the air for specimens made of steel T671 (pre-load 300 MPa).

Specimen	Ø [mm]	**σ_a [MPa]**	f [Hz]	**N_a**	comment
2	7,04	**450**	74.25	541 421	
3	7,05	**430**	74.04	12 697 695	without fracture
4	7	**470**	73.89	10 000 006	without fracture
5	7,07	**490**	74.23	11 842 493	
6	7,07	**510**	71.94	520 610	
7	7,06	**540**	74.08	196 262	
8	7,05	**530**	74.13	257 138	
9	7,07	**520**	74.05	7 513 730	**fracture in thread**
10	7,07	**515**	73.9	822 640	
11	7,08	**505**	74.2	1 333 318	**fracture in thread**
12	7,04	**500**	74.2	170 255	
13	7,07	**495**	74.2	195 594	
14	7,07	**485**	74.1	466 660	
15	7,08	**475**	74.1	346 784	
16	7,02	**465**	73.8	858 854	**fracture in thread**

Specimen	Ø [mm]	**σ_a [MPa]**	f [Hz]	**N_a**	comment
17	7,05	**460**	74.2	389 704	
18	7,05	**445**	74.1	10 239 646	**fracture in thread**
20	7,06	**440**	80.5	3 149 942	**fracture in thread**
21	7,04	**440**	80.3	13 857 227	

The formula for slanted branch of S-N curve was determined by the linear regression in the form:

$$\log N_a = 13 - 3 \log \sigma_a. \quad (2)$$

The S-N curve is depicted in Fig. 8.

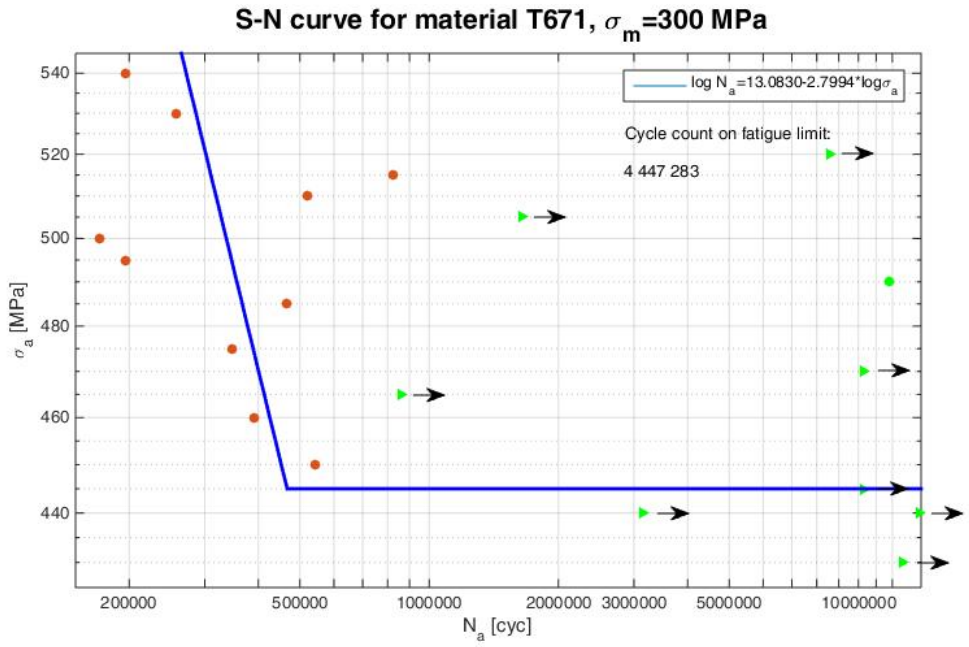

Figure 8. S-N curve for steel T671 with pre-stress in normal component σ_m = 300 MPa tested in the air.

A subsurface fatigue crack initiation called "Fish-eye" occurred within the tested sample on level of 490 MPa. This phenomenon is predominantly observed at high-strength steels. It appears when surface defects are significantly removed. The initiators of fatigue cracks are usually precipitates, inclusions, and other microstructural heterogeneity. In this case, the active crack initiator was a globular inclusion of Al_2O_3 of diameter 20 micron, which was located 1.2 mm under the surface of the sample. The crack spread in the radial direction to the sample surface and created flat and circular surface. The appearance of the fracture surface, including the dominant inclusions, is shown in Fig. 9.

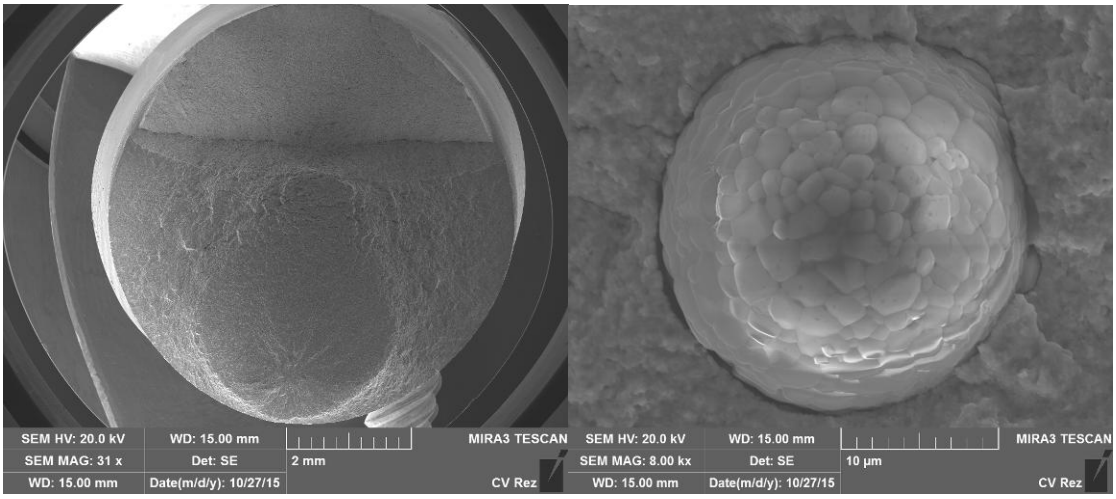

Figure 9. The fracture surface of the sample 5 with subsurface initiation (on the left) and focus of fracture surface with Al_2O_3 inclusion (on the right).

The NaCl solution with concentration of 35 ppm chlorides was chosen for testing in a corrosive environment at the temperature of 80°C. The content of oxygen was not controlled.

Table 6. Results of fatigue tests for steel T671 (reference material) with pre-stress in normal component σ_m = 300 MPa tested in a corrosion cell for an aggressive environment (solution of 35 ppm chlorides) at the temperature of 80°C.

Specimen	Ø [mm]	**σ_a [MPa]**	f [Hz]	**N_a**	comment
B1a	8.06	**400**	66.6	87 349	
B1b	8.06	**300**	66.7	165 867	
B2a	8.04	**200**	115.2	85 766 253	fracture in reducing part
B2b	8.07	**150**	113.9	200 000 000	without fracture
B3a	8.06	**250**	115.2	38 017 532	
B3b	8.09	**150**	113.7	104 512 004	without fracture
B4a	8.05	**250**	115.2	960 726	
B4b	8.03	**200**	114.0	45 296 313	
B5a	8.05	**250**	115.2	2 266 746	**fracture in thread**
B5b	8.06	**270**	114.5	3 689 014	
B6a	8.08	**240**	114.6	48 843 537	
B6b	7.77	**220**	114.7	23 096 113	
B7a	8.06	**290**	114.4	265 808	
B7b	7.79	**200**	114.6	100 000 000	without fracture
B8b	8.01	**150**	114.6	120 000 000	without fracture

The formula for slanted branch of S-N curve for a corrosive environment was determined by the linear regression in the form:

$$\log N_a = 33 - 11 \log \sigma_a. \quad (3)$$

The S-N curve is depicted in Figure 10.

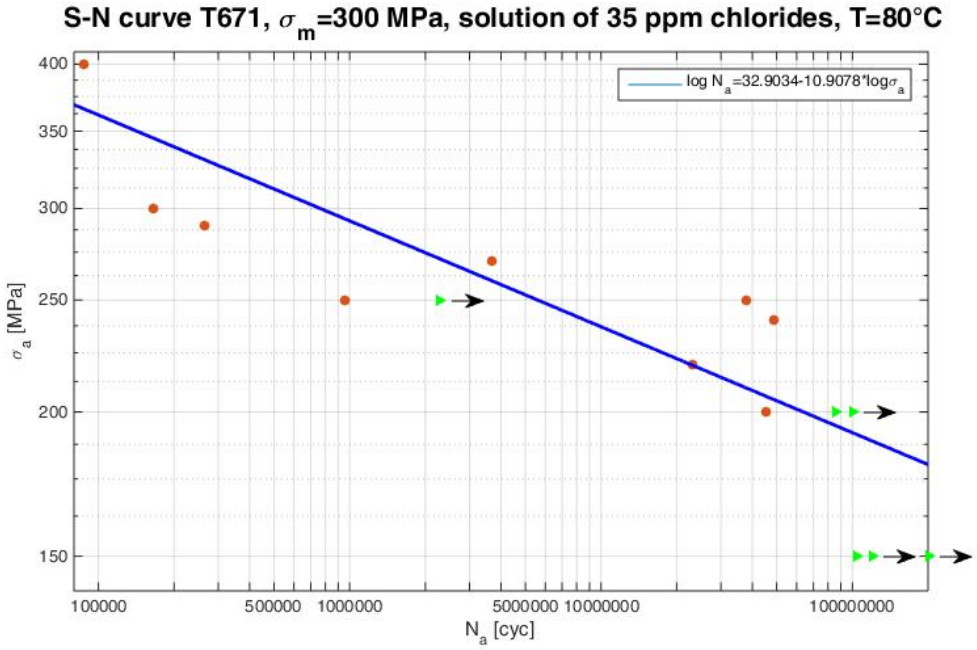

Figure 10. S-N curve for steel T671 with pre-stress in normal component σ_m = 300 MPa tested in a corrosion cell for an aggressive environment (solution of 35 ppm chlorides) at the temperature of 80°C.

The value of 10^8 cycles was established for fatigue limit in accordance with standards. If this value is substituted for the slanted branch equation (3) it refers the stress amplitude value of 191,9 MPa. That means that under this value the steel could endure more than 100 millions of cycles. Since it is obvious from the graph that no fatigue limit exists the stress stage around 188.7 MPa should be investigated further. The reason is that this is a relatively appropriate cycle amount for a testing machine. The test at stress amplitudes 150 MPa were finished after 200 millions of cycles without a damage. If this value is substituted for the slanted branch equation (3) a specimen should endure almost 1.5 billion cycles. If the test should be completed under 200 millions of cycles the stress amplitude is limited by 180 MPa.

4. Discussion

It is possible to compare the results with regard to performed tests with several points of view. Initially, the first from this aspects could be the strength characteristics for specimens taken from the fir tree root (the results presented in [3]) and from the body of low pressure steam turbine blade. These results can be compared with experiments performed on a reference material which is used for blade manufacturing. In case of corrosive tests performed on specimens taken from the fir tree root (published in [4]), the results could be compared with new experiments performed on a reference material for different pre-stress and concentration of chlorides. Finally these results can be compared with tests in the air.

4.1 Tests in the air

The specimens taken from the fir tree root were tested for pre-stress 450 MPa and correspond with the red line (1) in the Fig. 11. New experiments for pre-stress 300 MPa and for specimens taken from the body of low pressure steam blade are identical with the blue line (2) in the Fig. 11. Although the difference between pre-stress is 150 MPa in the graph, it is evident that the results are moved from each other of 100 MPa. The directions of both lines are very similar, as it is the same material. Nevertheless, if the blue line (2) is compared to the reference material (in the Fig. 11 it corresponds with the green line (3)), which is used for blade manufacturing and which was tested for the same pre-stress, it is possible to realize that under the dynamical level of 520 MPa the material from real blade indicates much longer lifetime.

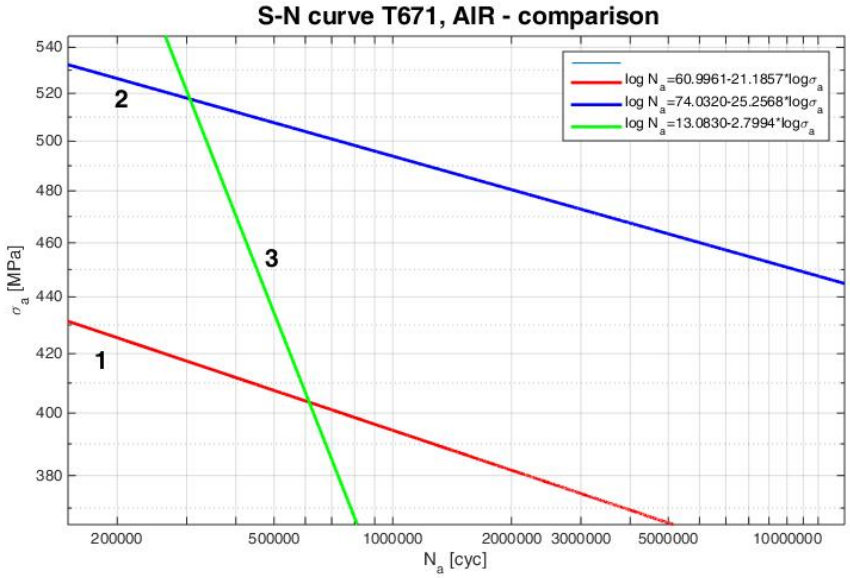

Figure 11. Comparison of S-N curves for steel T671 for specimens prepared from the fir tree root with pre-stress in normal component σ_m =450 MPa – red line (1), from blade body with σ_m =300 MPa – blue line (2) and reference material with σ_m =300 MPa – green line (3) tested in the air.

Since the tests were performed on specimens taken from blade for two different values of pre-stress, it is possible to construct Haigh diagram using the formula

$$\sigma_{cm} = \sigma_c \left[1 - \frac{\sigma_m}{\sigma_F} \right]^{k_H}, \tag{4}$$

where σ_F is so called fictive stress and coefficient k_H is used for experimental determination. For k_H = 1 the previous function becomes a straight line that goes through the points (0, σ_c) and (σ_F, 0), where σ_F is often defined as strength limit R_m. [7, 8] If the safe area of tenseness could be obtained, it is necessary to accomplish intersection of this line with line $\sigma_m + \sigma_a = R_e$, where the amplitude is given as $\sigma_a = (\sigma_{max} - \sigma_{min})/2$. [9] Tenseness given by point under both lines is safe from the point of view of fatigue life and no fatigue cracks should occur within thus designed constructions. [10]

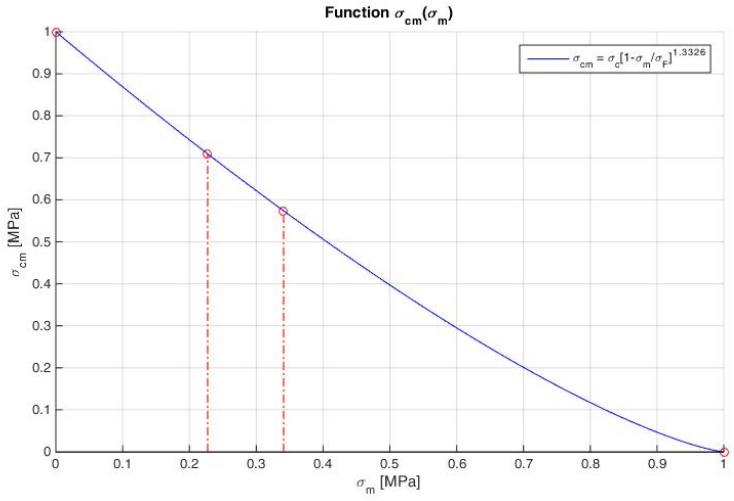

Figure 12. Haigh diagram for tensile mean stresses is plotted in normalized coordinates.

It was necessary to determine the ultimate strength for construction of Haigh diagram. The value was determined to 1320 MPa based on Brinell hardness measuring (HB 2.5/187.5) according to ISO 18265 (A1). The average hardness on specimens taken from the blade refers to approximately 390 HB. The fatigue limit for zero pre-stress was determined to a value 627 MPa. The vector of residuals was defined as an anonymous function in the program. The estimated value p_0 of a number 0.5 was selected as an initial solution. The final result was obtained in five iterations as a parameter p multiplied by initial solution p_0. The final value for coefficient k_H of curve in the Haigh diagram for points of normal pre-stress components was computed as 1.3326 as shown in Fig. 12.

4.2 Tests in a corrosion cell

The corrosive test was performed on reference material. As it is shown in Fig. 11, the next comparison for the corrosive environment is not suitable between reference material and specimens taken from completed low pressure steam blade due to different directions. However, if the results mentioned in [4] are compared, the life curve will be the closest to the initial of coordinates. Extremely low lifetime is caused by a significantly aggressive environment (solution of 22 % NaCl) and as well as higher pre-stress 450 MPa. This state is depicted in Fig. 13 via blue line (1). The curves of a reference material are compared in the same graph. These curves are obtained for the same pre-stress of 300 MPa. The green line (3) is identical with Fig. 11 and is valid for the air and room temperature. The red line (2) then corresponds with the 35 ppm chloride environment at the temperature of 80°C. This comparison is strictly hypothetical because the slanted branch of S-N curve for testing in the air ends in the surroundings of a point of 440 MPa.

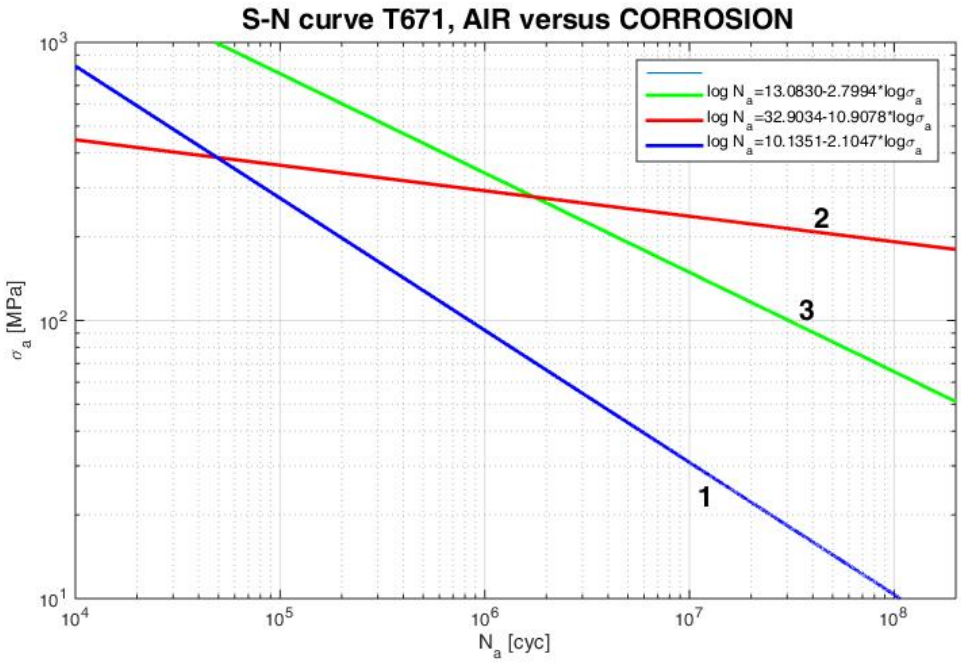

Figure 13. Comparison of S-N curves for specimens taken from the fir tree root of a low pressure steam turbine blade, tested inside the corrosive 22% solution of NaCl at the temperature of 80°C - blue line (1). Specimens from reference material T671, σ_m =300 MPa tested in a corrosion cell with the NaCl solution of 35 ppm chlorides at the temperature of 80°C – red line (2) and tested in the air – green line (3).

5. Conclusions

The results of high cycle fatigue tests are summarized in the article. These tests were performed on blade steel Böhler T671 in the air and in a corrosive environment in a flow cell. The cell was designed, engineered and manufactured for these purposes. The chloride solution of 35 ppm was chosen as the environment at the temperature of 80°C. Such an environment can be considered as the limit state that

should not occur during the operating regime. The specimens were taken from the low pressure blade body of L-0 stage of a turbine generator set and from a reference material delivered for blade production as well. The results were compared with previous experiments published in [3, 4]. Haigh diagram for tensile mean stresses was constructed in normalized coordinates with the value for coefficient k_H computed as 1.3326.

Another experimental programme for this steel includes corrosion fatigue tests on specimens with improved surface corrosion resistance. There are several techniques available for such kind of surface treatment like shot peening or laser peening.

Acknowledgement

This work has been supported by the SUSEN Project CZ.1.05/2.1.00/03.0108 realized in the framework of the European Regional Development Fund (ERDF) and by the Technology Agency of the Czech Republic (TA CR) under project TA04020685.

References

1. Development of a Corrosion-Fatigue Prediction Methodology for Steam Turbine Blades: AISI 403/410 (12% Cr) and 17-4PH Blade Steels, EPRI, Palo Alto, CA: 2015.

2. P. Konopík, J. Džugan, R. Procházka, Evaluation of local mechanical properties of steel weld by miniature testing technique. Materials Science and Technology 2013, Montreal, Quebec, Canada.

3. J. Janoušek, J. Strejcius, S. Hřeben, The Environment Influence On Bladed Steel During Operational Conditions, Applied Mechanics and Materials Vol. 827 (2016) pp 185-188.

4. J. Strejcius, E. Folková, J. Kasl, J. Řehořek, Z. Špirit, CORROSION-FATIGUE STRENGTH OF PRECIPITATION HARDENED MARTENSITIC STEELS MLX17 & T671 IN A CHLORIDE IONTS - CONTAMINATED STEAM CONDENSATE, Increase of Lifetime for Components of Energy Equipment in Power Plants, Srní, Czech Republic, 2015, (in Czech).

5. ČSN 42 0363 – Methods of fatigue testing of metals.

6. Atest.

7. J. Janoušek, M. Balda, M. Chocholoušek, Influence of Combined Mean Stresses on Lifetime under High-Cycle Fatigue, Applied Mechanics and Materials Vol. 732 (2015) pp 107-110.

8. J. Janoušek, M. Balda, J. Svoboda, The mean stress influence on lifetime under high-cycle fatigue combined loading, Applied and Computational Mechanics 7 (2013) 31-38.

9. J.P. Strizak, L.K. Mansur, The effect of mean stress on the fatigue behavior of 316 LN stainless steel in air and mercury, Journal of Nuclear Materials 318 (2003) 151-156.

10. M. Balda, Introduction of statistical mechanics, UWB Pilsen, 2001, (in Czech).

Power & process:
(small scale) testing & analysis

Determination of Current Mechanical Properties of Components in Service Using Sub-Sized Specimens

Pavel Konopik [1], Jan Dzugan[1], Martin Rund[1] & Radek Prochazka[1]

[1]COMTES FHT a.s., Dobrany, Czech Republic

Abstract

Degradation of the properties of metal materials can lead to loss of reliability and safety of machines and metal structures in power plants during their operation. However, a number of these machines or metal structures (e.g. turbines, boilers and steam lines) could be used for longer time than has been predicted by their designed lifetime. A component's residual life can be evaluated with standard mechanical test techniques, such as the tensile test, the fatigue test, the Charpy or the fracture toughness test. However, for these tests there is usually insufficient material to sample non-invasively from the component. Therefore, non-destructive techniques are being developed as well as testing methods using mini-samples.

One of the widely used methods of mini-samples testing is the Small Punch Test (SPT). The SPT is usually based on conversion of the obtained results into conventional mechanical characteristics. However, it requires known correlation parameters determined for the specific material and must be verified for each new material. On the other hand, there exist small specimen testing techniques (e.g. the micro-tensile test, the miniature fatigue test and the mini-Charpy test) respecting the same loading mode as in the case of standard samples and maintaining minimal material requirements without requiring previously established correlations.

This paper focuses on the applicability and reliability of these testing techniques for determining current mechanical properties of components in service. Therefore, material degradation can be correctly and non-destructively determined.

1. Introduction

The current paper presents the potential of small size samples application to mechanical materials properties determination. The aim of the application of these methods is the residual service life evaluation, evaluation of local material properties, and material properties assessment in cases when limited volume of the experimental material is available (e.g. development of nanostructures materials by sever plastic deformation methods, development of special thermo-mechanical treatment with the use of a physical simulator, etc.). Several non-destructive or semi-destructive methods such as the Small Punch Test (SPT) [1], [2] or the Automated Ball Indentation (ABI) [3] used for considered purposes have been developed. The disadvantage of these methods is the fact that, for the material of interest, they require a previously established correlation relation between the considered property and these non-standard testing techniques. Moreover, these correlations have limited validity and higher tolerance bounds stemming from the measurement and evaluation uncertainties due to different loading modes between

these methods and standard testing methods (e.g. SPT x Charpy impact notch toughness, ABI x fracture toughness, etc.).

Therefore, the development of small size specimen techniques using miniaturized standard size samples is important because these tests maintain a very important advantage – the same loading mode as standard test samples [4]. The main problem with samples miniaturization is the availability of appropriate measuring devices suitable for testing samples of the volume of a few cubic millimetres. Load transducers are not so critical, but for example direct strain measurement on mini-tensile sample requires special optical methods, such as the Digital Image Correlation (DIC), that have become widely available only recently. Using the newest measurement equipment and techniques using miniature samples derived from standard samples provides much more reliable data than presently used methods using the correlation approach.

This paper will present several methods using mini-samples for mechanical properties evaluation: the micro-tensile test, the miniature fatigue test and the mini-Charpy test for evaluation FATT and fracture toughness.

2. Methods

Though various types of tests are presented here, all tested specimens are possible to produce from small sampled pieces taken by electric discharge sampling equipment. Further, these tests will be compared each other and their reliability will be discussed:

- Standard tensile test vs. Micro-tensile test
- Fracture toughness determination using standard 3PB samples vs. mini-Charpy specimens
- FATT determination by standard Charpy samples vs. mini-Charpy test
- Standard high cycle fatigue test vs. miniature fatigue test

2.1 EDSE

A portable electric discharge sampling equipment (EDSE) features easy handling, low-pressure coolant circuit (minimize spatter), quick electrode release and replace and a possibility to design own geometry and last but not least high sampling efficiency. Due to this facts, the device is suitable for an in situ sampling out of in-service components. **Figure 1** presents sampling on roller (for rolling mills) and part from steam turbine generator as an example.

The device enables to adjust a wide range of work-piece thicknesses whereas the work-piece (boat sample) width of 20 mm is given by the electrode geometry. The thickness of the extracted material can be from 1 mm to 5 mm. In most cases, the depth was set to 3 mm using the adjustment screw. Used electrodes were customized in order to reduce a stress concentration on edges and were made of W-Co alloy. Extraction takes approximately from 1 to 3 hours depending on the material and surface curvature.

The influence of electro-erosive machining on the work piece is demonstrated in the **Figure 2**. The depth of the affected layer is about 10μm in thickness.

Figure 1. The set-up of EDSE left: sampling from roller, right: sampling from a part of steam turbine generator

Figure 2. Influence of EDS machining on microstructure – affected depth is less than 10µm the

2.2 Micro-tensile test (M-TT)

There has been paid lot of attention to development of SPT within last two decades. Sampling devices were developed as well as testing procedures. Recently thanks to proposed code of practice (CWA 15627 [5]) sample size was also standardized and recommended disc geometry is diameter 8 mm and thickness 0.5 mm. There are already many applications using this sample size for example for surveillance program, thus this geometry was used as a base for newly developed testing procedure. The target was to run real tensile test, free of any necessary correlations, on specimens using the same material volume as SPT. Some FEM calculations were performed and sample geometry shown on **Figure 3** was proposed. Subsequently, the comparison of triaxiality development during tests between SPT, standard and micro-tensile test were done using FEM calculations, see **Figure 4**. Therefore, SPT loading mode is completely different and the reliability is limited for narrow selection of material as was shown in many works (for example in [6]).

There were carried out tests of several various materials with wide range of tensile properties. Namely, Al-alloy, Ni-alloy, Titanium Gr. 5, and several steels were compared while tested on standard size specimens and with the use of M-TT. Standard size samples were round with diameter ranging from 5 to 10mm and in one case steel segment of pipe was tested.

Deformation of the specimens was measured by ARAMIS. The grips for M-TT and an example of measurement of the deformation during the M TT by ARAMIS can be seen in **Figure 5**. The ARAMIS system tracks the grey value patterns in images recorded during the test. Images are compared to each other to detect the displacement of a selected point. As a single point is too difficult to find, an area of several points, in ARAMIS called facets, is tracked instead. Each facet has a unique distribution of grey levels (i.e. light and dark pixels of varied light intensity). Based on assumption that grey level of each facet does not change during the test, individual facets are located in reference images and all following images. Strains and other quantities can be calculated from changed position of tracked facet displacements.

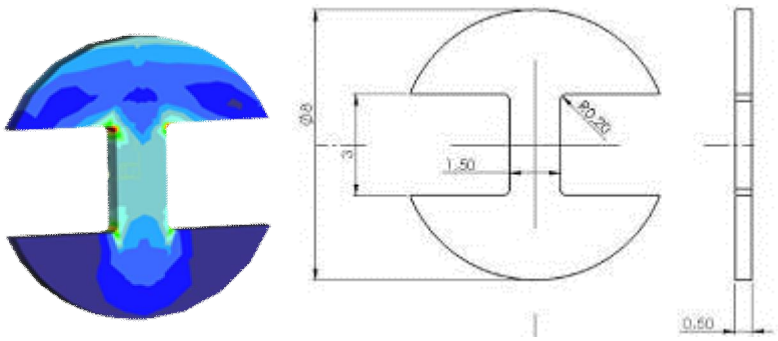

Figure 3. M-TT specimen

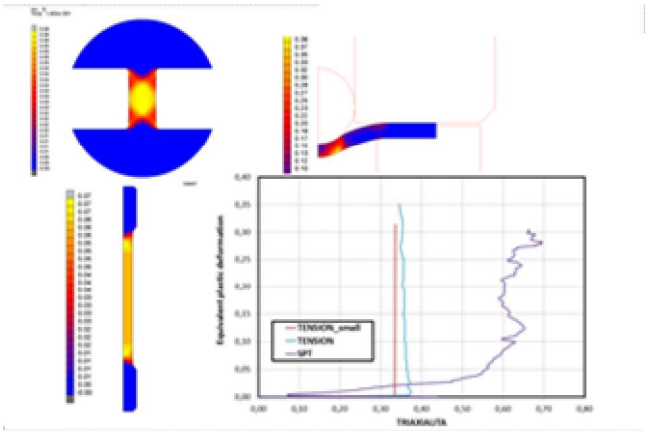

Figure 4. Comparison of triaxiality between SPT, standard and micro-tensile test

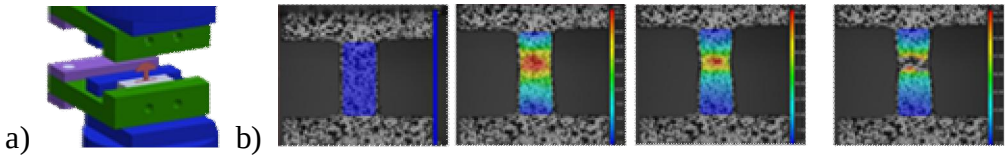

Figure 5. a) Grips for M-TT, b) Measurement of deformation during M TT

The resulting curves of these tests are graphically summarized in **Figure 6** and the results is summarized in

Table 1. There can be found excellent agreement for all materials investigated between standard size specimens and M-TTs for whole range of strength levels from about 250MPa up to 1250 MPa.

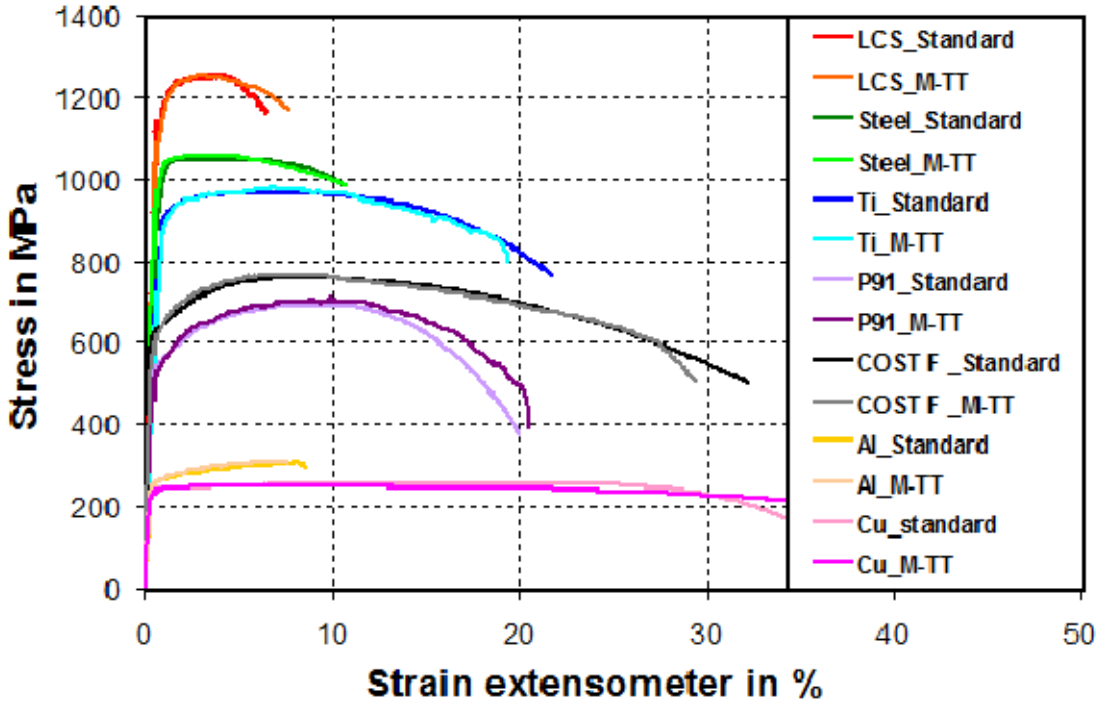

Figure 6. Comparison of tensile records obtained with DIC for M-TT measurement of various metallic materials

Table 1 Standard and micro-tensile test results

Material	Specimen	Tensile tests results				
		$R_{p0,2}$	R_m	A_g	A	Z
		[MPa]	[MPa]	[%]	[%]	[%]
Experimental Low Carbon Steel	LCS_Standard	1143.4	1258.0	3.6	15.6	71.1
	LCS_M-TT	1133.0	1255.3	2.4	13.9	74.4
Low Carbon Steel (segments)	Steel_Standard	964.1	1051.6	4.0	15.9	62.7
	Steel_M-TT	990.1	1061.9	2.7	20.3	64.2
Titanium Gr.5	Ti_Standard	913.5	965.1	5.2	16.3	42.0
	Ti_M-TT	892.3	981.2	5.9	18.6	35.8
X14CrMoVNbN10-1	COST F _Standard	622.1	762.3	8.0	20.7	63.9
	COST F _M-TT	592.3	769.2	7.0	21.7	62.8
P91	P91_Standard	540.7	696.2	9.3	20.0	74.3
	P91_M-TT	520.9	710.4	9.5	22.8	74.4
Aluminium Alloy EN AW 6005 T6	Al_Standard	264.4	309.3	7.6	11.3	13.5
	Al_M-TT	264.1	311.0	5.6	8.2	11.4
Copper 99.99%	Cu_standard	234.6	260.0	16.3	34.2	73.7
	Cu_M-TT	235.7	254.5	4.4	35.4	70.5

M-TT is powerful methods also for other applications:

- investigation of local properties in heterogeneous weldment [7]
- strain rate sensitivity [8]
- anisotropy on thin components [9]
- calibration of fracture locus [10]

2.3 Fracture toughness determination by mini-Charpy samples

Fracture mechanics in particular has attained high significance in establishing ultimate load limitations and assessing the integrity of a large number of engineering structures of multifarious types. Standard mechanical tests used to determine the fracture toughness involve extraction of large blocks of material and therefore are not applicable to in-service components.

There is a chance to produce mini-Charpy specimen from boat sample, see sampling plan in **Figure 7** as an example.

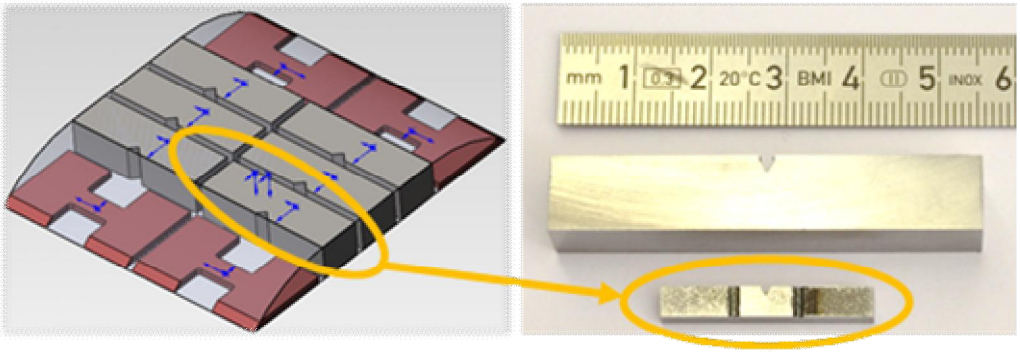

Figure 7. Sampling plan from boat sample with dimension of 20 x 20 x 3 mm

Verification of applicability was done on widely used 34CrNiMo6 steel. Both standard geometry of 3PB samples and mini-Charpy samples were used for fracture toughness determination. The evaluation was done according to ASTM E 1820. Samples were machined then fatigue pre-cracked with the final stress intensity factor of about 20 MPa.m$^{1/2}$. Test pieces were side-grooved after pre-cracking and subsequently tested. Tests were performed according to the multiple specimen method. Crack lengths after tests were measured by digital image processing and the fracture toughness value was determined for the material investigated. The J-R curve was determined and the fracture toughness value, defined as the intersection of the 0.2 mm offset construction line with the J-R curve, was calculated. Due to small size of mini-Charpy samples, the dimension criteria for size independent fracture toughness given by ASTM E1820 standards were not fulfilled. Therefore, this test is denoted as J_Q in the results table. Test results obtained from mini-Charpy specimens and compared with standard test results are shown in **Table 2**. J-R curves of both geometries are depicted in **Figure 8**. The deviation between both fracture toughness values is only 1.7 %.

Table 2 Fracture toughness results

Material	Sample size mm	J_{IC},J_Q kN/m	Error %
34CrNiMo6 state-as delivered	**15x30**	**189,9**	
	3x4	**193,2**	**1.7**

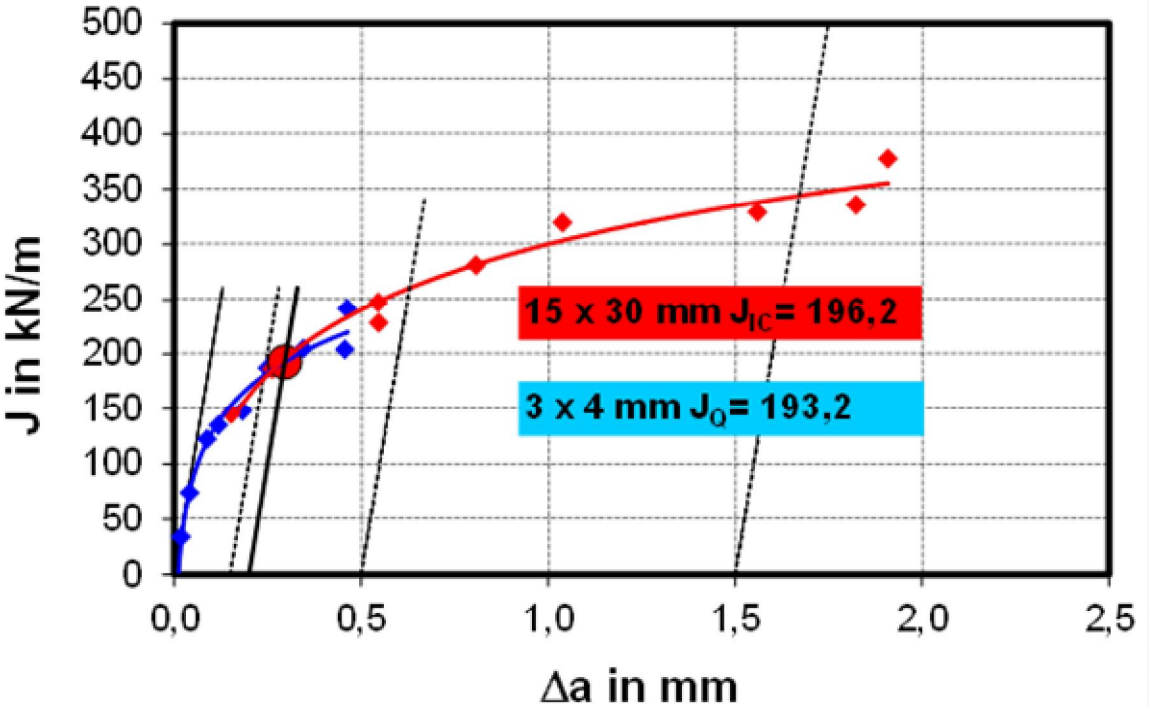

Figure 8. J-R curves of 34CrNiMo6, state as delivered

2.4 FATT determination by mini-Charpy test

The Charpy impact test is performed to determine the ductile–brittle transition temperature (DBTT) of the material. As the specimen size is reduced, the value of the DBTT is also reduced compared to the full size specimen. The relationship (3) is used in the test to estimate the DBTT [11].

$$DBTT_{full\ size} = DBTT_{subsize} + C \quad (3)$$

Where C is a material constant (a shift of DBTT due to specimen size) in °C

Hence, in order to estimate the absolute value of DBTT, it was necessary to establish the value of the constant C by testing full sized and sub sized specimens. Chosen material was experimental weldment consisting of two chromium-molybdenum heat-resistant steels and weld metal. This type of weldment is widely used in the oil and gas industries and in fossil fuel and nuclear power plants. Macroetching of the weld is shown in **Figure 9**.

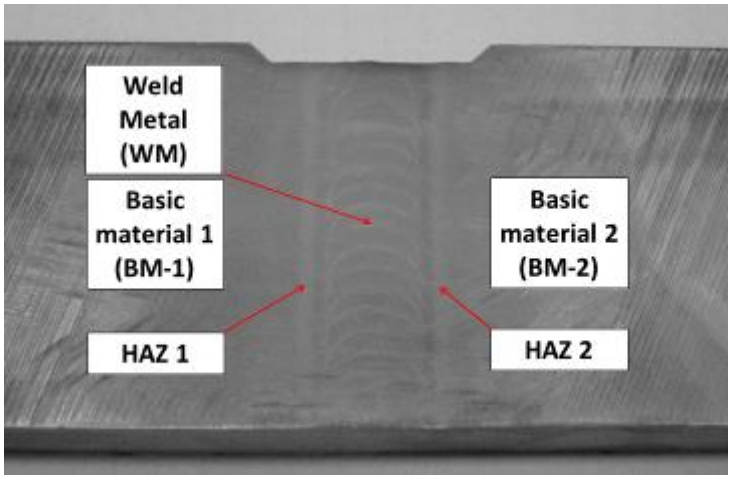

Figure 9. Macroetching of the weld investigated

Instrumented Charpy standard and mini-Charpy impact tests (according to ISO 14556:2000) were performed for all five investigated zones. Tests were carried out at the instrumented Charpy pendulum with the impact energy of 300J and at the instrumented Charpy pendulum with the impact energy of 15J. For samples geometry see **Figure 10**. Testing was performed at various temperatures in order to determine transition temperatures FATT. Transition curve for BM2 is depicted in **Figure 11** as an example, transition temperatures FATT and the value C are summarized in **Table 3**.

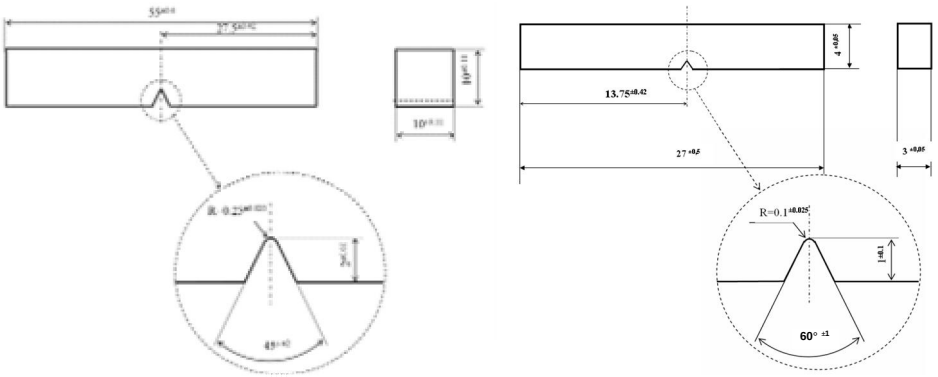

Figure 10. Geometry of standard (left) and Mini-Charpy (right) test specimens

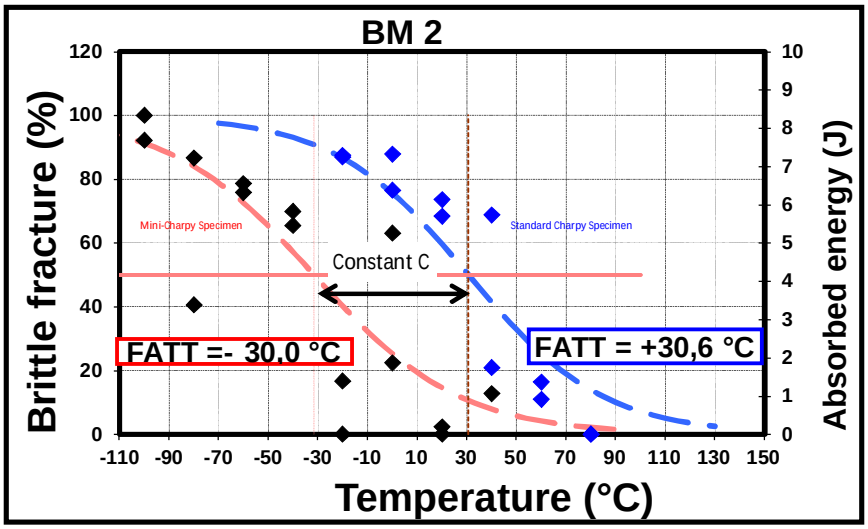

Figure 11. Transition curves of BM2

Table 3 Results of Charpy and mini-Charpy impact test

Material	FATT [°C]		Constant C
	Specimen size [mm]		
	10x10	3x4	°C
BM 1	13.1	-48.38	61.5
HAZ 1	-11.7	-69.90	58.2
WM	52.1	-8.70	60.8
HAZ 2	21.1	-39.37	60.5
BM 2	30.6	-30.03	60.6

2.5 Miniature fatigue test

Applicability of miniature fatigue samples will be shown on 11CrMo9-10 steel alloy that is widely use in energetics (water boilers or super-heater tubes). The microstructure consists of tempered martensite, see **Figure 12**. Average grain size evaluated according to ASTM E112 was 41.1 µm.

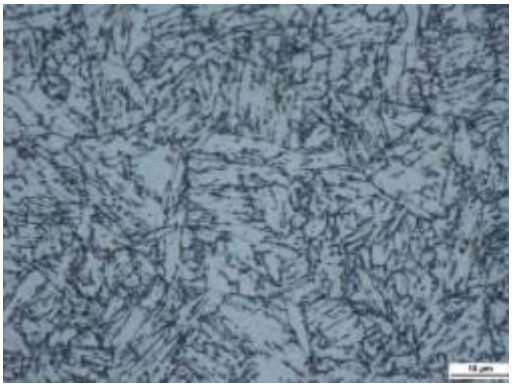

Figure 12. Microstructure of 11CrMo9-10 steel at 500x magnification

Both standard geometry of fatigue samples and mini-fatigue samples were used for fatigue limit evaluation. Standard samples were tested according to the standard ASTM E466 with load ratio of R= -1 at RT and evaluated according to ASTM E739.

For mini-fatigue samples dimensions and geometries were developed on the basis of extracted piece of the experimental material. Cutting scheme within the extracted piece of material can be seen in **Figure 13**.

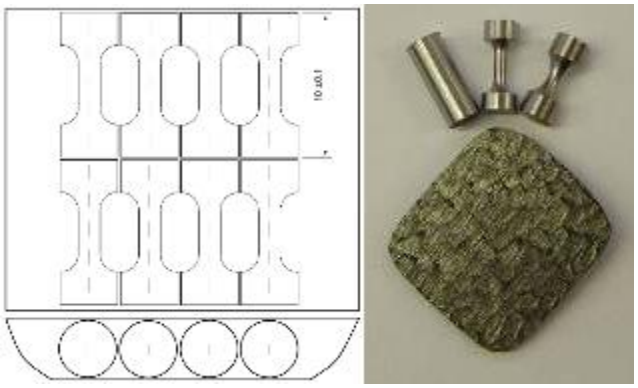

Figure 13. Specimens cutting scheme within EDSE extracted material

The following specimen geometries was proposed for a HCF test (**Figure 14**). Specimens were produced by wire-cut electric discharge machine. A surface roughness of the specimens after ED machining

didn't exceed 1.1 µm. After machining, a fine grinding was applied to reach the average roughness of 0.3 µm by means of wet sanding with 600 and 1200 grit silicon carbide sandpapers.

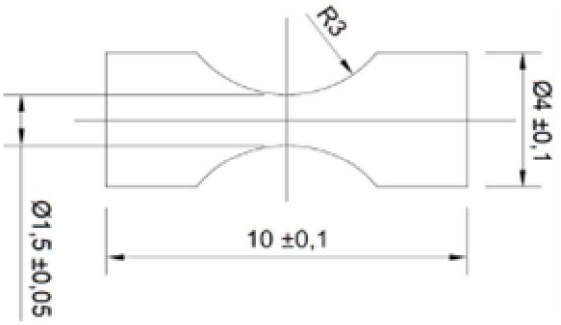

Figure 14. The geometry and dimensions of fatigue specimens

HCF tests on miniaturized specimens were conducted on servo-hydraulic testing machine MTS Bionix with load-carrying capacity of 25kN in tension-compression mode. Tests were carried out in load control with load ratio of R= -1 at frequency of about 50 Hz. Dimension of samples were measured using an optical measuring system to avoid scratching. If a scratch occurred the surface was additionally regrinded and measured. Wedge grips are attached to the testing machine in appropriate way to avoid bending stresses that was done with the use of alignment fixtures. After this, a fatigue specimen was put in jaws of the testing machine and the pre-load was set at zero. Size comparison with a standard HFC specimen can be seen in **Figure 15**.

Figure 15. Comparison of HCF specimens

This test results are presented as the number of cycles to failure which are plotted against the stress amplitude in the semi-logarithmic scale and two separate linear regressions were used. Dots represent non-standard HCF tests and the continuous horizontal line denotes its fatigue limit. Those of specimens which survived 10^7 cycles are denoted by arrows. Both fatigue test results are widely scattered, this corresponds to R squared of 0.582 and 0.638, respectively. Therefore, the fatigue limit $\sigma_{C\ mini\text{-}fatigue}$ and $\sigma_{C\ standard}$ were evaluated as the maximum stress amplitude at which the sample didn't crack even after 10^7 cycles. At this stress level, at least two valid tests had to be conducted. The summary of fatigue limits is shown in **Table 4**. Results of non-standard and standard fatigue tests are shown in **Figure 16**.

Table 4 Results of standard and sub-size HCF tests

Type of test	Fatigue limit [MPa]
Mini-fatigue HCF	385
Standard HCF	395

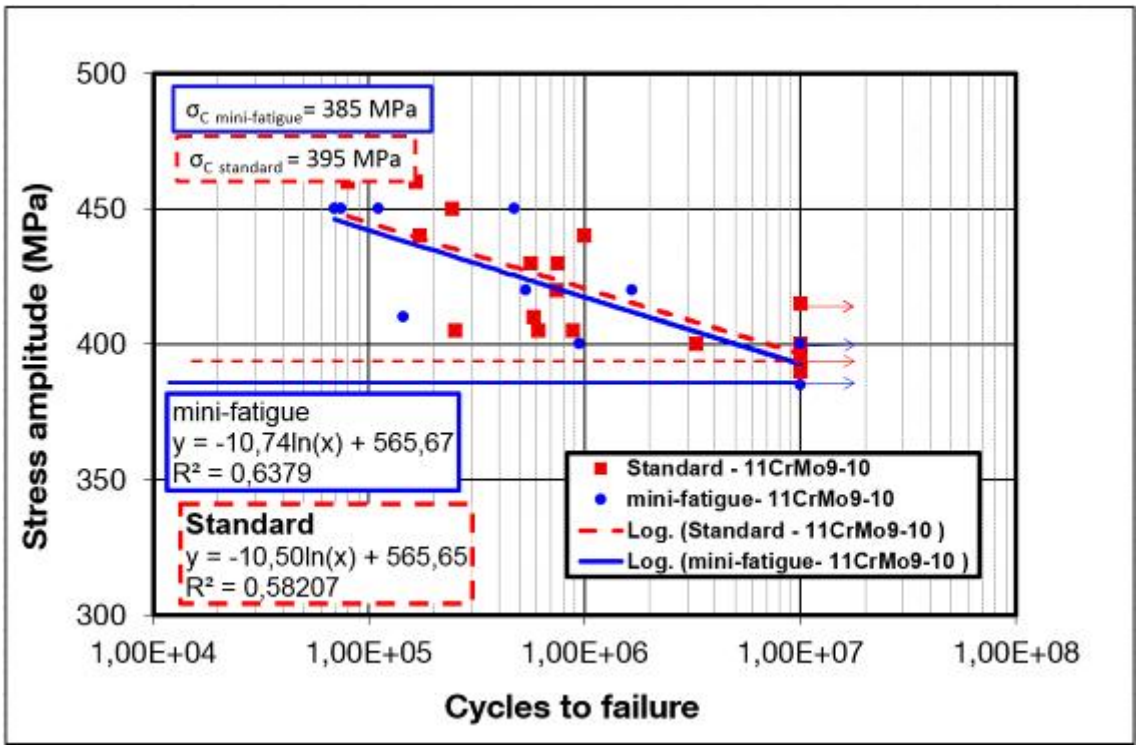

Figure 16. Comparison of HCF specimens

3. Conclusions

The study presented here documents potential of small size specimens testing, comparability to results obtained on standard size specimens and its wide application potential.

For type of tests have been presented in this paper:

1. Standard tensile test vs. Micro-tensile test
2. Fracture toughness determination using standard 3PB samples vs. mini-Charpy specimens
3. FATT determination by standard Charpy samples vs. mini-Charpy test
4. Standard high cycle fatigue test vs. miniature fatigue test

Tests 1, 2 and 4 does not need further correlation and the results can be directly used for application.

The obtained stress – strain curves (test 1) and results of M-TT are fully comparable with the results of the standard ones. The crucial factor for determining of yield strength is the elastic modulus. Its determination was carried out using DIC system which employs the ARAMIS system and very good agreement with typical values for this kind of the material is found, even for this kind of very sensitive measurement.

Multiple-specimen method (test 2) using mini-Charpy specimens (3x4x27 mm) was used for fracture toughness determination. Though the J-R curve could not exceed 0.5 mm, the evaluated fracture toughness J_Q was in a good agreement to the standard one J_{IC}.

Results of fatigue tests (test 4) provided also very promising results. As it could be expected, a higher data scatter is obtained with small size samples. However, fitted trend curves closely follow each other and good agreement is found between small and standard test pieces for both material investigated.

Test 3 (FATT determination) needs to determine coefficient C, which can lead to slight uncertainty. However, in our case, the transition temperatures were shifted to 60 ±2 °C in all cases.

All these applications show possibility to obtain reliable and repeatable results with the mini specimens. Moreover, some applications are rather difficult or impossible on large samples that make techniques using min-specimens even more attractive and further development of these techniques is essential for deeper insight into material behaviour.

Acknowledgements

This paper was created by project Development of West-Bohemian Centre of Materials and Metallurgy No.: LO1412, financed by the MEYES of the Czech Republic.

References

1. Prochazka, R.: Determination of Mechanical Properties of Structural Materials by using Miniature Specimen Test Techniques. Diploma work. Department. of Materials Science and Metallurgy. West Bohemian University. Pilsen. Czech Republic 2013.

2. Konopík, P., Dzugan, J., Prochazka, R.: Determination of fracture toughness and tensile properties of structural steels by small punch test and micro-tensile test, Metal 2013, 15-17.5. 2013, Brno, Czech Republic.

3. Haggag, F.M.: In Situ Measurement of Mechanical Properties Using Novel Automated Ball Indentation System, Small specimen Test Technique Applied to Nuclear Reactor Pressure Vessel Thermal Annealing and Plant Life Extension. 1993. In: Corwin, W.R., Haggag, F.M., Server, W.L. (Eds.), ASTM STP 1204, ASTM, Philadelphia, PA, pp. 27–39.

4. Brynk, T., Molak, R.M., Pakiela, Z., Kurzydlowski, K.J.: Mini-samples technique in tensile and fracture toughness tests of nano-structured materials, Materials Challenges and Testing for Supply of Energy and Resources, 2012, pp 221-234.

5. Small punch test method for metallic materials, Part B: A code of practice for small punch testing for tensile and fracture behaviour, CWA 15627.

6. Konopík P., Džugan J.: Determination of Tensile Properties of Low Carbon Steel and Alloyed Steel 34CrNiMo6 by Small Punch Test and Micro-Tensile Test, 2st International Conference SSTT, 2.10.-4.10.2012, Ostrava, Czech Republic, ISBN 978-80-260-0079-2, pp. 319-328.

7. Konopík, K., Džugan, J, Procházka R: Evaluation of Local Mechanical Properties of Steel Weld by Miniature Testing Techniques, Materials Science & Technology 2013, Montreal, Canada, October 27–31 2013, ISBN 978-0-87339-762-9

8. Konopik, P., Dzugan, J., Rund, M.: Dynamic Tensile And Micro-Tensile Testing Using DIC Method, Metal 2014, May 21st – 23rd 2014, Brno, Czech Republic, ISBN 978-80-87294-52-9.

9. Džugan, J., Konopík, P., Procházka, R.: Local Dynamic Properties Determination Of Titanium Turbine Blade, Asian Conference on Mechanics of Functional Materials and Structures, 10-13 October 2014, Nara, Japan. ISBN 978-4-9904352-1-9

10. M. Španiel, A. Prantl, J. Džugan, J. Růžička, M. Moravec, J. Kuželka: Calibration of fracture locus in scope of uncoupled elastic–plastic-ductile fracture material models, Advances in Engineering Software, Volume 72, June 2014, Pages 95-108

11. CORWIN W.R. and HOUGHLAND A.M., "Effect of Specimen Size and Material Condition on the Charpy Impact Properties of 9Cr1MoVNb Steel", ASTM, STP 888, (1986), pp. 325-338.

Tensile and creep property determination of 15-15Ti fuel cladding steel by small punch testing

Stefan Holmström[1], Igor Simonovski[1], Stefan Ripplinger[1], Eberhard Altstadt[2], Remi Delville[3], Marta Serrano[4] & Vasile Radu[5]

[1] European Commission, Joint Research Centre (JRC), Petten, the Netherlands

[2] Helmholtz-Zentrum Dresden-Rossendorf (HZDR), Dresden, Germany

[3] SCK•CEN, Belgian Nuclear research Centre, Mol, Belgium

[4] CIEMAT - Structural Materials Division, Madrid, Spain

[5] Institute for Nuclear Research (INR), Pitesti, Romania

Abstract

The integrity of the fuel cladding in present and future nuclear fuel concepts is critical for the safe performance of the power plants. The material performance of 15-15Ti (1.4970) thin walled fuel cladding tubes are presently being evaluated in the EERA JPNM pilot project TASTE. The TASTE objectives are to compare existing testing methodologies for claddings and to determine the tensile and creep properties of the 15-15Ti (1.4970) steel in the final product form. In this paper the small punch (SP) test technique is assessed in more detail for testing the 24% cold worked cladding provided by SCK·CEN. The SP test results are compared with results from tensile (axial) tube tests and ring tension (hoop) tests. It is shown that the SP tensile test can produce robust estimates on the tensile strength in the temperature range from room temperature to 800°C. The presented equation for transfering maximum force to engineering stress is shown to work for all the three test set-ups of the participating laboratories. For creep it is shown that the SP tests do not provide comparable results to internal pressure of classical creep test due to low creep ductility and premature creep cracking already at low deflections imposed at by the testing technique.

1. Introduction

The integrity of the fuel cladding in present and future nuclear fuel concepts is critical for the safe performance of the power plants. Presently the material performance and mechanical properties of thin walled fuel cladding tubes are evaluated through a number of testing techniques and evaluation methodologies. To improve the understanding of the limitations and usefulness of these methodologies a round-robin was launched in the EERA JPNM pilot project TASTE. The main project material is the 15-15Ti (1.4970) cladding steel in its final product form, i.e. 24% cold worked (24% cw) thin-walled tube provided by the Belgian Nuclear research Centre (SCK•CEN).

The testing in TASTE incorporates old, classical and new promising methods for material property determination such as sub-sized and micro specimen axial testing, Ring Tension and Ring Compression, internal pressure, small punch and cone mandrel testing.In this paper the test results from the Small Punch (SP) tensile tests and SP-creep tests are mainly assessed.

SP-tensile test have been performed in a temperature range from room temperature to 800°C. The SP tests were performed at three laboratories, the Structural Materials Division in Spain (CIEMAT), the Helmholtz-Zentrum Dresden-Rossendorf in Germany (HZDR) and at The Joint Research Centre (JRC-IET) in The Netherlands. Creep SP-tests were conducted at JRC-IET in the temperature range 550-700°C.

For comparison, Ring Tension tests (RT) were conducted in Romania by the Institute for Nuclear Research (INR) and axial tensile tube tests were performed by CIEMAT, HZDR and SCK·CEN.

2. Materials and Methods

For TASTE the nuclear grade Titanium stabilized DIN 1.4970 '15-15Ti' stainless steel cladding was chosen as reference material to be tested by all partners and test methologies. The 15-15Ti is the primary choice for fuel cladding of several current fast spectrum research reactor projects [1-3]. The bulk of the tests were performed on 15-15Ti cladding tubes manufactured by Sandvik on behalf of SCK•CEN [4]. The specifications for the fabrication of the cladding tubes are based on past production of similar tubes for sodium-cooled fast reactor projects in Europe [5]. The tight quality specifications include stringent composition, grain sizes and mechanical properties (yield strength, tensile strength and elongation at rupture), product tolerances (diameters, straightness and ovality), roughness and defects control. 10t of steel were melted at Sandvik (Sandviken, Sweden), cast into billets and transformed into 'hollows' ('thick'-walled tubes) by extrusion of billets followed by cold-pilgering. Thin-walled tubes were obtained at Sandvik-Précitube (Charost, France) by several passes of cold-drawing following by short annealing (1100°C). The last cold-drawing determines the degree of cold-work of the cladding tubes. The "standard" cladding tubes were 24% cold-drawn (24 wt.%). A smaller batch with a cold-work level of 46% cw was also produced. At this deformation level, one approaches a work-hardening saturation as demonstrated by the small difference between YS and UTS and the reduction in total elongation. This mimics irradiation hardening that presents similar stress-strain curves [6]. The cladding tubes produced have an external diameter of 6.55 mm and a wall thickness of 0.45 mm. The material properties (axial) at room temperature performed on full tubes (no waist) are given in Table 1 and the manufacturer chemical composition determined by XRF (X-ray fluorescence), ICP-MS (Inductively Coupled Plasma Mass Spectrometry) and OES (Optical Emission Spectroscopy) depending on the element is given in Table 2.

Table 1. Room temperature (manufacturer) tensile properties of the 15-15Ti test materials for two levels of cold work (cw) obtained by tensile testing for full tube section.

CW level	R_{p02} (MPa)	R_m (MPa)	Total elongation (%)
24% cw	690	810	25%
46% cw	950	925	10%

Table 2. Chemical composition in wt. % of the fuel cladding tubes

C	**Si**	**Mn**	**P**	**S**	**Cr**	**Ni**	**Co**	**Mo**
0.10	0.56	1.83	0.013	<0.001	15.08	15.04	0.02	1.21
B	**N**	**Ti**	**V**	**Ta**	**Cu**	**Ca**	**Fe**	
0.0028	0.011	0.49	0.034	<0.005	0.026	<0.010	Bal.	

The importance of minor alloying elements for the precipitation behaviour of this steel at high temperature, under stress and under irradiation has been shown in several studies [7-9]. The resistance of the DIN 1.4970 steel to thermal creep and irradiation-induced phenomena (swelling, irradiation induced creep, embrittlement) compared to other austenitic steels [10,11] lies in the fine-tuning of its minor alloying element that will allow the nucleation of specific phases during operating conditions.

2.1 SP test set-ups

The specimen grips for the SP test sampels used by HZDR and JRC are presented in Figure 1 A and B. CIEMAT used a smaller specimen extracted from the tube by wire erosion (see Figure 1C). The specimen sample holders were designed to comply with the different specimen sizes, receiving hole and ball diameters (see Table 3). The tensile tests to be used for comparison were conducted on sub-sized tensile specimen as shown in Figure 2. The Ring Tension tests (RT) that give estimates on the hoop direction properties were performed with special grips for the specified cladding tube inner diameter (Figure 3). The estimated tensile properties from the RT tests do not take bending into account.

A B C

Figure 1. A) HZDR sample holder, Receiving hole radius R=1 mm, B) JRC-IET sample holder, R=2 mm, C): CIEMAT; left over tube after EDM specimen extraction.

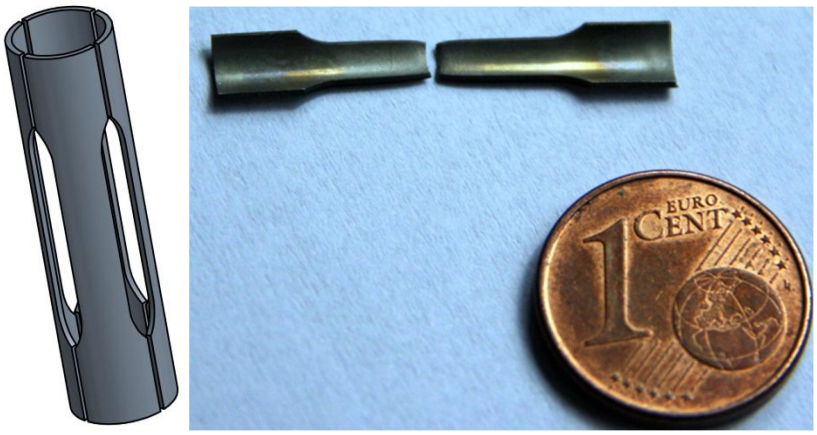

Figure 2: A) HZDR sub-sized test specimen for determining axial material properties.

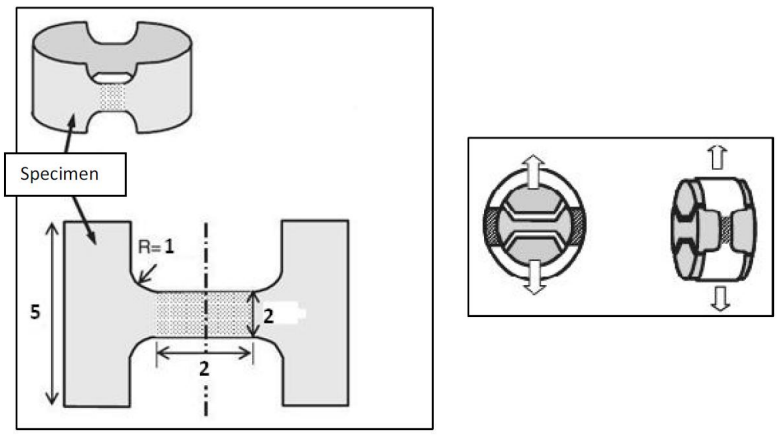

Figure 3: A) INR test specimen for determining hoop properties by Ring tension test.

Table 3. Test-setup specifics and test programme for the participating small punch testers.

Testing lab / set-up	Spec. thickness h_0 (mm)	Ball radius. r (mm)	Receiving hole radius. *R* (mm)	Test temperatures
CIEMAT	0.2	1	1.5	22, 300, 500 °C
HZDR	0.4	1	2	Cryogenic to 22 °C
JRC-IET / A	0.45	2	*4*	22-800 °C
JRC-IET / B	0.45	2.5	*4*	22-800 °C

2.2 Load to stress conversion for SP test set-ups

As a testing technique the Small Punch (SP) test is a relatively simple test well suited for material ranking and material property estimation in situations where standard testing is not possible or considered too material consuming. An interesting question is however how well the method suits for testing thin walled tube material such as fuel claddings.

It has been shown that for SP-tensile tests [12-14] that the (true) uniaxial tensile strength R_m is directly proportional to the maximum force F_m of the SP load-deflection curve.

$$R'_m(F_m, D_m) = \alpha \cdot \frac{F_m}{u_m \cdot h} \Rightarrow \frac{F_m}{R_m} = \frac{u_m \cdot h_0}{\alpha}, \quad (1)$$

Where α is a correlation factor, h_0 is the specimen thickness, u_m the deflection at maximum force. Note that in this work the u_m is not measured but the theoretical value calculated by Chakrabarty membrane stretching equations are used [12].

$$\frac{u}{r} = (1 - \cos\theta_0) + \sin^2(\theta_0) \cdot \ln\left(\frac{\tan(\theta_0/2)}{\tan(\theta/2)}\right) \quad (2)$$

$$\sin(\theta) = \frac{r}{R}\sin^2(\theta_0) \quad (3)$$

The theoretical value is being used since different test set-ups, specimen thicknesses and the curvature of the specimen in relation to the SP puncher ball influence the measured u_m.

To determine the correlation factors α of Eq. 1, the optimized ratio for F/σ from the SP Code of Practice [15] intended for calculating the nominal creep stress, is used, Eq. 2. This equation accounts for all the test-setup parameters; specimen thickness (h_0), puncher ball (r) and receiving hole radious (R).

$$\frac{F}{\sigma} = 3.33 \cdot k_{SP} \cdot \frac{r^{1.2}}{R^{0.2}} \cdot h_0 \qquad (4)$$

By analysing both SP-tensile and SP-creep tests JRC-IET has shown [15] that the ductility parameter k_{SP} (Eq. 2) is force (and temperature) dependent. The k_{SP} reaches a maximum value of $(1+h_0/r)$ at the very short duration creep tests, i.e. tests that are comparable to SP-tensile tests. Using this value for k_{SP} the F_m/R_m ratio can be determined by combining equations 1 and 4;

$$\frac{\alpha}{u_m} = \frac{0.3 \cdot R^{0.2}}{r^{0.2} \cdot (h_0 + r)} \qquad (5)$$

The above equation enables comparing the SP tensile test results of HZDR, CIEMAT and JRC-IET. The calculated F_{max}/R_m ratios for the laboratory specific test-setups are given in Table 4.

It is to be noted that Eq. 5 can be applied when the material response in the SP-tensile tests is ductile, i.e. the measured u_m is close to the Chakrabarty theoretical value. In the case of the 46% cw test material this is not necessarily the case. For the 46% cw tensile strength estimates the ultimate tensile strength has to be "true-stress" corrected. How this correction is performed will be covered in future papers.

Table 4. Calculated nominal "free space" ($2R-2r-2h_0$) for deformation, k_{SP}, F_{max}/R_m ratios and the theoretical deflection at maximum force u_m for the different SP test setups.

Testing lab - set up	2R-2d-2h (mm)	$1+h_0/r$ k_{SP} (mm)	Theor. Max defl. u_m (mm)	Theor. F_m/R_m
CIEMAT	0.1	1.5	0.609	0.434
HZDR	0.2	1.8	0.703	1.04
JRC-A	*1.1*	*1.45*	1.406	1.89
JRC-B	0.6	1.36	1.574	2.32

The calculated R_m estimates from the SP testing can now be compared to the hoop strength estimates acquired from the ring tension tests performed at IRN and the axial strength values acquired from sub-size wasted tube test specimen test performed by HZDR and CIEMAT.

For creep, Eq. 4 has been used, with an initial value of 1 for the ductility parameter k_{SP}.

3. Results

3.1 SP-tensile test for ultimate tensile strength

All the laboratories performed room temperature tests. The measured tensile strength from the axial tests and the estimates from both ring tensile and SP tests are presented in Figure 4.

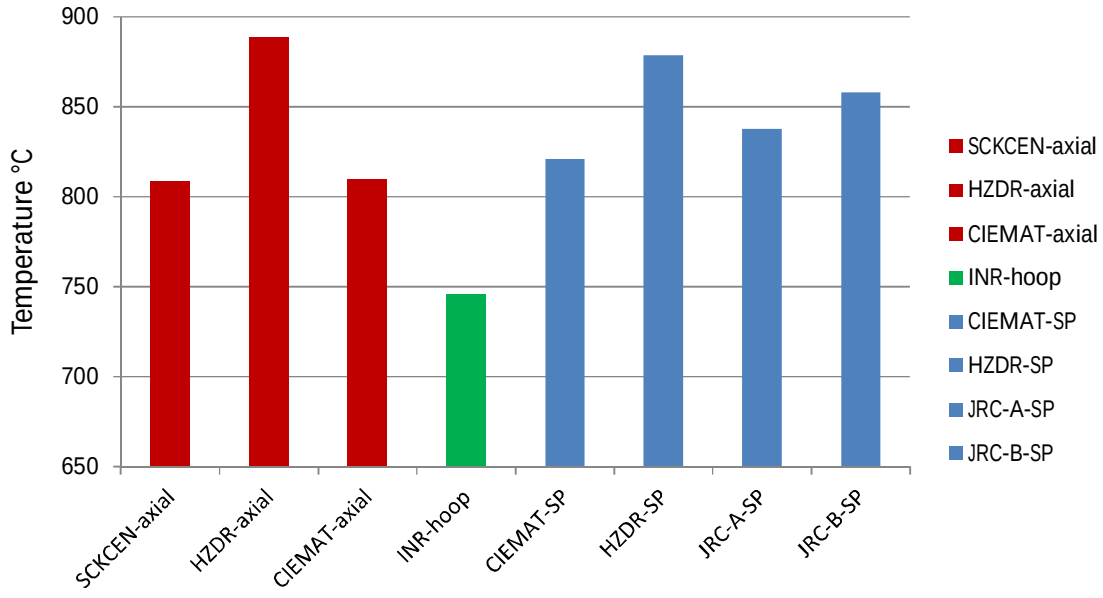

Figure 4 Comparison of room temperature tensile strength estimates from sub-sized axial specimen, Ring-Tension and SP tests.

The high temperature results from the tensile tests by HZDR, INR, CIEMAT and JRC-IET are presented in Figure 5. It can be seen that the SP-tests results and the Ring Tension test estimates are similar at the test temperatures 300 and 500°C.

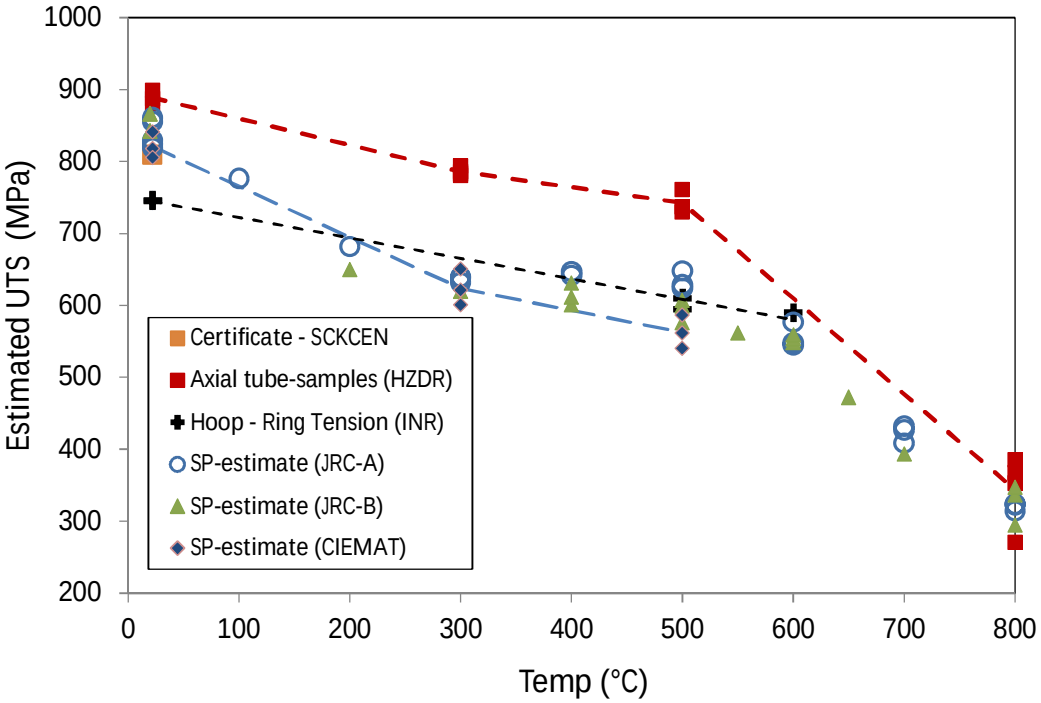

Figure 5 Comparison of RT-800°C tensile strength estimates from sub-sized axial specimen, Ring-Tension and SP tests.

3.2 SP-creep test

SP creep tests were conducted at temperatures between 500 and 650°C. The loads were estimated using Eq. 2 and stress to rupture estimates from 15-15Ti creep-rupture tests (pressurized tubes) by SCK•CEN. Six SP tests were performed with a 2 mm ball (JRC-A) and four using the larger diameter ball of 2.5 mm (JRC-B) as shown in

Table 5.

For SP creep test results the high load test with the test-setup JRC-A comply with the behaviour predicted by the multiaxial burst test by SCK•CEN. However the at lower forces and with the larger ball diameter (JRC-B set-up) the measured rupture times (t_r) were alarmingly low. The Wilshire [17] plot in Figure 6 shows deviation from the predicted creep behaviour. The explanation of the poor behaviour was found in the post-test assessment of the failed samples. It is evident that there is a change in failure mode (see Figure 7) for the JRC-B tests at lower load ratios (F/F_m) in relation to the fracture type found in SP-tensile tests or at higher load load ratios (JRC-A set-up).

Table 5. 15-15Ti creep test results at 500, 600 and 650°C with two different puncher ball diameters.

Test set-up	Temperature (°C)	Load F (N)	F/F_m	Time to rupture (h)
JRC-A	500	1000	0.83	68
JRC-A	600	900	0.85	0.13
JRC-A	600	850	0.81	0.43
JRC-A	600	800	0.76	0.7
JRC-A	600	750	0.71	2.33
JRC-A	600	700	0.66	2.77
JRC-B	600	700	0.55	2.35
JRC-B	600	550	0.43	4.61
JRC-B	600	400	0.31	22.33
JRC-B	650	550	0.43	3.12

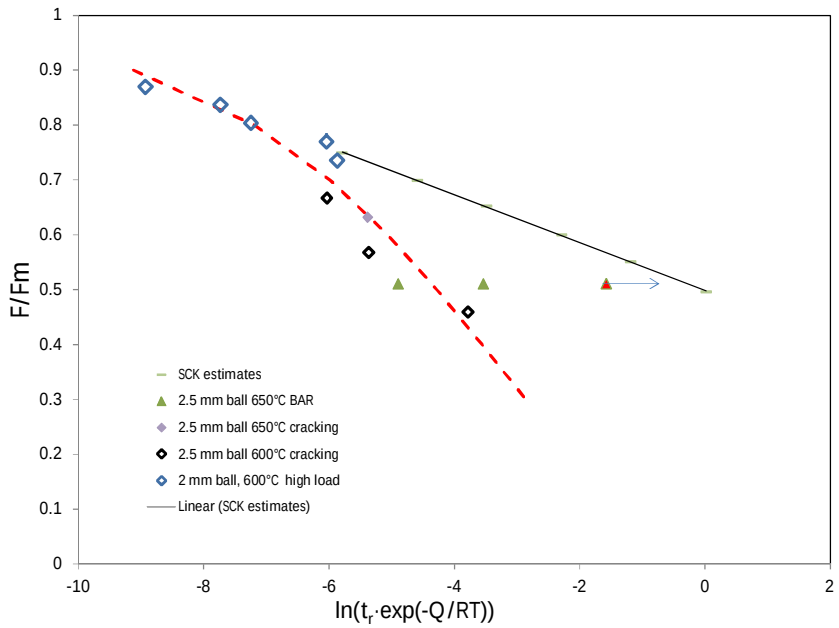

Figure 6. SP-creep tests results plotted as normalized force against temperature compensated time. The reference flat specimen on cold worked bar material (green triangles) behaves as the curved cladding samples. An annealed flat sample (red triangle) that was interrupted (140 h) showed promise of reaching the predicted rupture life.

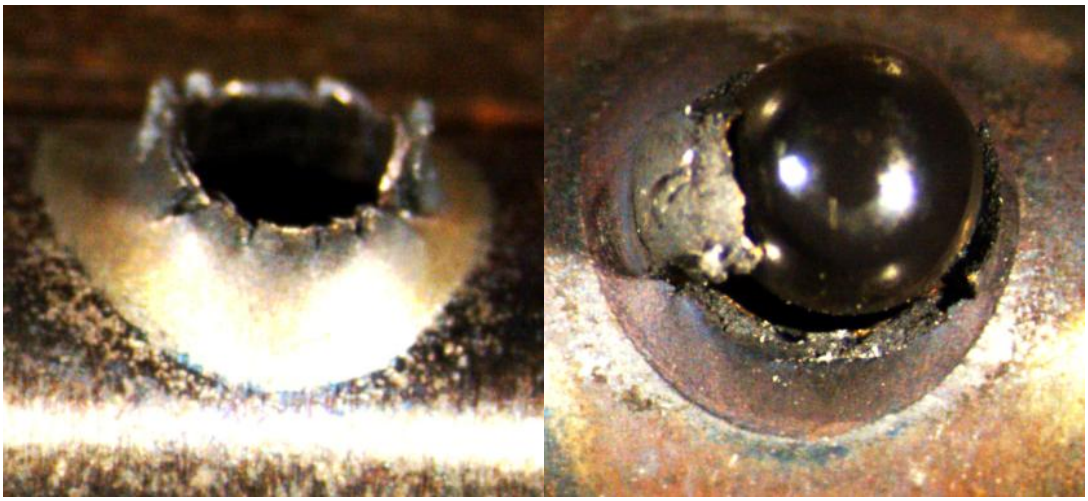

Figure 7. Fractured creep specimen A) ∅2 mm ball 600°C / 700N, t_r=2.8, B) ∅2.5 mm ball, 600°C / 700N. t_r=2.35

4. Discussion

The SP tests seem to give good estimates for tensile strength. The estimated high temperature SP tensile strength of the 24% cw 15-15Ti tube is close to the ones estimated from ring tension tests. The shape of the temperature – tensile strength plots correspond with the uniaxial results for the whole high temperature range.

To further strengthen the claim to use the same correlation factors for transferring maximum force to ultimate tensile strength FEA simulation [18] of flat and curved test samples were performed using the HZDR room temperature true stress-strain tensile curve as material property input. The simulation has been done for the JRC-B test setup configuration as shown in Figure 8. The FEA simulated Force-Deflection curves are presented in Figure 10.

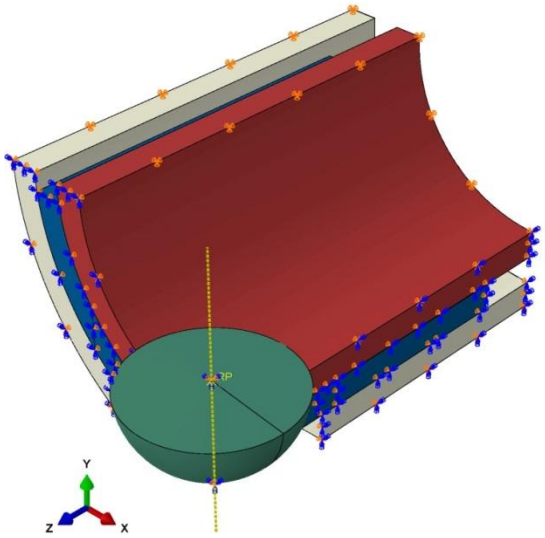

Figure 8: Quarter symmetry FEA model of the SP test on curved (cladding tube) specimen.

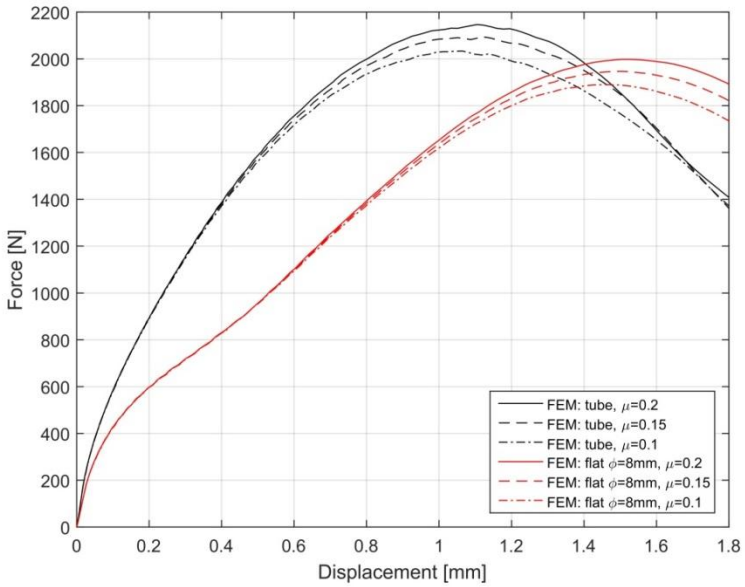

Figure 9: FEA computed force-displacement responses for 15-15Ti curved (cladding tube) specimen and standard flat specimen. Simulations with Friction coefficients μ=0.1, 0.15 and 0.2, specimen thickness 0.45 mm.

The simulated F_m values for the curved tube specimen are 4-6% higher than that from the corresponding flat specimen. Also the u_m at maximum force is decreased by a factor of about 1.5.

To established the limits of use for the SP creep tests of low ductility or "creep brittle" materials it is of significant importance to define the limit loads / deflections / test setups that are likely to initiate creep cracking at an early stage of the test. X-Ray Computer tomography (XCT) images of a tensile specimen and a creep brittle specimen are shown in Figure 10, both performed with the 2.5 mm puncher ball (JRC-B). The XCT measurements performed on an interrupted creep tests (650°C / 400N) is shown in Figure 11. The image clearly shows extensive cracking at a low deflection (0.18 mm) and a "nominal" calculated strain (according to the Code of Practice).

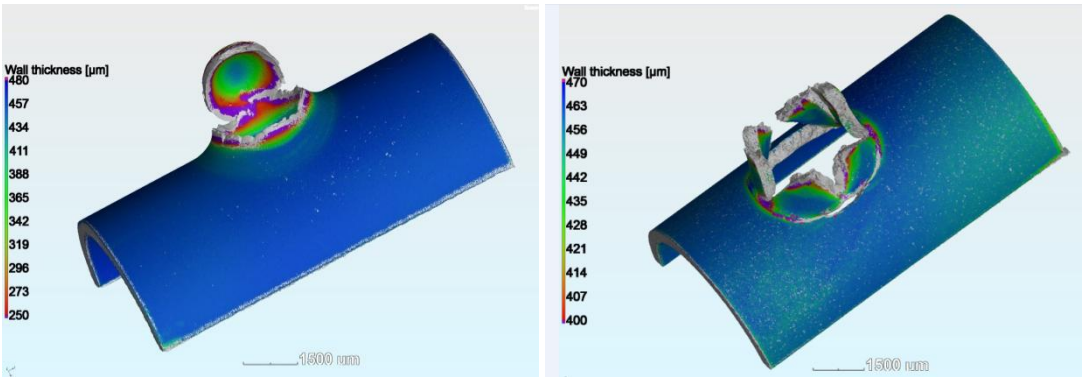

A B

Figure 10: Difference in fracture mode of A) SP tensile specimen after test at 600°C and B) SP creep specimen ruptured after 22 h at 600°C/400N.

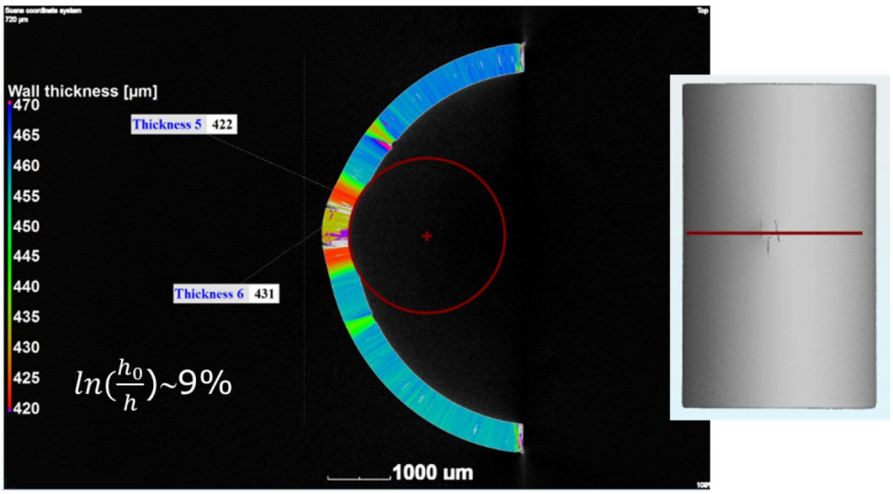

Figure 11: X-ray tomography scan of interrupted creep test (after 382 h at 650°C / 250N). The calculated "nominal" local strain when cracking has occured is below 9%.

5. Conclusions

A round robin has been performed for determining the tensile and creep material properties for 15-15Ti fuel cladding material with different testing techniques. The interlaboratory small punch tests shows that good estimates on the tensile strength can be acquired by the SP technique with curved test specimen. The estimated high temperature SP tensile strength of the 24% cw 15-15Ti tube are close to strength values acquired by ring tension tests. The creep low ductility of the test material causes cracking and premature failure for the JRC-B test setup configuration and reliable creep rupture results can not be acquired.

References

1 Jayakumar, T., Mathew, M.D., Laha, K., and Sandhya, R., Materials development for fast reactor applications. Nuclear Engineering and Design, 265 (2013) 1175-1180.

2 Aït Abderrahim, H., Baeten, P., De Bruyn, D., and Fernandez, R., MYRRHA – A multi-purpose fast spectrum research reactor. Energy Conversion and Management, 63 (2012) 4-10.

3 Delville, R., et al., R&D programme for the fuel qualification of the research fast reactor MYRRHA in DESIGN, MANUFACTURING AND IRRADIATION BEHAVIOUR OF FAST REACTOR FUEL Obninsk, Russian Federation, 30 May - 03 June, 2011. IAEA.

4 Delville, R., Stergar, E., and Verwerft, M., Results of a new production of nuclear-grade 1.4970 15-15Ti stainless steel fuel cladding tubes for GEN IV reactors in 22nd International Conference on Nuclear Engineering ICONE22. Prague, Czech Republic July 7-11, 2014. ASME.

5 Specification Tube de gainage - Experiences d'irradiation SAPHIR et SNR-Phénix I Belgonucléaire-Interatom, Report Nr.: 322.52/100/s/103, (1982).

6 C. Pokor,C, Brechet Y, Dubuisson P, Massoud, J-P. Averty, X. Irradiation damage in 304 and 316 stainless steels: experimental investigation and modeling. Part II: Irradiation induced hardening, Journal of Nuclear Materials 326 (2004) 30–37.

7 Kesternich, W., Microstructural evolution and mechanical properties of an advanced high-temperature steel. Journal of Nuclear Materials, 155-157 (1988) 1025-1031.

8 Ehrlich, K., The role of precipitates for the development of irradiation-induced swelling and high-temperature embrittlement in an austenitic stainless steel of type X10 CrNiMoTiB 15 15. Z. Metallk., 94 (2003) 485-491.

9 Padilha, A.F., Schanz, G., and Anderko, K., Precipitation Behavior of Titanium Stabilized 15-Percent Cr, 15-Percent Ni, 1-Percent Mo-Ti-B Austenite Steel (Din-Material Number 1.4970). Journal of Nuclear Materials, 105 (1982) 77-92.

10 Hubner, R. and Ehrlich, K., Influence of minor alloying elements and stress on microstructural evolution and void swelling of austenitic steels under neutron irradiation, in Effects of Radiation on Materials: 19th International Symposium, M.L. Hamilton, et al., Editors. 2000. 778-791.

11 Herschbach, K., Schneider, W., and Ehrlich, K., Effects of minor alloying elements upon swelling and in-pile creep in model plain Fe-15Cr-15Ni stainless steels and in commercial DIN 1.4970 alloys. J. Nucl. Mat., (1993) 233-248.

12 E. Altstadt, H. Ge, V. Kuksenko, M. Serrano, M. Houska, M. Lasan, M. Bruchhausen, J.-M. Lapetite, Y. Dai, Critical evaluation of the small punch test as a screening procedure for mechanical properties, Journal of Nuclear Materials 472 (2016) 186-195, doi:10.1016/j.jnucmat.2015.07.029

13 T.E. García, C. Rodríguez, F.J. Belzunce, and C. Suárez, Estimation of the mechanical properties of metallic materials by means of the small punch test. Journal of Alloys and Compounds 582:708–717, 2014.

14 J. Chakrabarty, A theory of stretch forming over hemispherical punch heads, International Journal of Mechanical Sciences 12(4), pp.315-325, 1970

15 Holmstrom, S, et Al. Small punch creep testing for material characterization and life time prediction, 10th Liege Conference : Proc. Materials for Advanced Power Engineering 2014, ISSN 1866-1793. (2014). 627-635

16 CEN Workshop Agreement CWA 15627: Small Punch Test Method for Metallic Materials: European Committee for Standardization, CWA 15627: 2007

17 B. Wilshire, P.J. Scharning, Extrapolation of creep life data for 1Cr– 0.5Mo steel, International Journal of Pressure Vessels and Piping 85 (2008) 739– 743

18 ABAQUS 6.14-2, Dassault Systemes, 2015.

Development of testing machines and equipment for testing miniaturized samples, proposals for improvement of CWA 15627

Daniel Omacht, Zdenek Kubanek & Roman Dolezal
Material and Metallurgical Research Ltd.
Pohranicni 31, Ostrava, Czech Republic

Abstract

The need to determine the mechanical properties of materials of machine parts working in operating conditions without shutdown of the entire unit and disintegration machine parts in the past led to the development of miniaturized specimens associated with the generation of special test procedures and methods. During many years the developed methods have been refining, the results are compared with conventional testing methods, the shape and dimensions of specimens are modified. The enormous development of information technologies in the last decades enabled the emergence of a new field of science - mechatronics - a multidisciplinary field of engineering that includes a combination of systems engineering, mechanical engineering, electrical engineering, telecommunications engineering, control engineering and computer engineering. Progress in the field of mechatronic together with development of new materials, new CNC machining methods for metallic and non-metallic materials, miniaturization of sensors of physical quantities, fast, accurate data sampling and recording significantly influenced the development of the testing devices and allowed to construct machines which was not possible in the past.

Content of this paper presents the latest design, features of a test device for determining the residual life of machine components working at elevated temperatures (SPUTT500®), equipment for tensile and fracture testing small samples under the normal and low temperatures (CRYOSET®) and the scoop sampling machine (ESTIM®) used not only for further research but also for development and evaluation of small samples testing technology. The final part of this article comprises the proposal for improvement the Code of practise for small punch testing (CEN Workshop Agreement 15627).

1. Introduction

Estimates of the remaining service life of mechanical structures and devices are unthinkable without the knowledge of the state, respectively the degree of degradation of the structural materials due to the effects of long term exposure in operating conditions. For nearly half a century material engineers have been trying to develop a method for testing materials, which would use the minimum amount of removed material preferably without damaging the machine components and at the same time without stopping the operation of a working unit and could determine the current mechanical properties.

Over the years several test methods with different sizes and shapes of specimens have been examined The method of penetration tests became one of the most promising methods suitable for determining the mechanical properties, in which the test sample is a disc with the diameter of 8 mm and the thickness of 0.5 mm (Fig.1). The method was originally designed to determine the residual life of structural components

operating at elevated temperatures [17], later it was extended for determining the tensile and fracture behaviour of the material.

Figure 1. Dimension of the sample intended for penetration tests.

2. Development of testing machines and equipment

2.1 The history of the penetration test development at MATERIAL AND METALLURGICAL RESEARCH Ltd. (MMV)

Today's MMV (up to 2001 Vitkovice - Research and Development Ltd.) began working with penetration tests in the 90s of the 20th century thanks to close cooperation with the University College of Swansea [1]. Based on the first experiences the first simple mechanical test equipment were built in the MMV company. Correlations between classical methods and penetration tests were made on the basis of obtained results [2]. During many years the method was used in MMV and obtained correlations were refined. Results of research and development in this field have been published continuously at various conferences or in professional journals [2-15].

The test methodology of penetration tests was formulated in the document – CEN WORKSHOP AGREEMENT "Small Punch Test method for Metallic Materials" (CWA 15627) by standards body CEN and an international group of material specialists in 2004. It serves as Code of Practice for penetration tests performing. The document was issued in December 2007 [16].

2.2 SPUTT 500

SPUTT 500 is a testing machine for residual life determining of structural components operating at elevated temperatures using a miniaturized test samples and the penetration test. The first version (V1.3 – Fig.2) based on Code of practice (CWA 15627) started to develop in 2010. At the end of the year the machine was built and its testing started. The device was semiautomatic, the temperature measurement wasn´t carried out directly on its surface, but in the possible closest point (about 10 mm from the sample). The temperature of the sample was recalculated based on the mathematical dependence created by an automatic calibration process. Using the arm and LVDT sensor (Fig. 3) dependence of the punch displacement in time was measured and recorded. The punch and the lower die were made of a creep resistant nickel alloy and the sample penetration was made using the ceramic ball. Protection of the sample was ensured by argon, which was controllably (10 ml/min.) injected into the cartridge with specimen (Fig. 4).

Figure 2. SPUTT 500 V1.3.

Figure 3. Meas. of punch displacement.

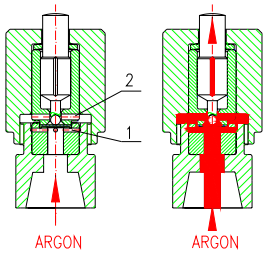

Figure 4. Sample protection.

During testing of the machine it has been found that although the resultant curve had the correct shape (Fig. 5), the punch was occasionally “jammed” in upper die guiding (mostly at long-term tests). This fact was accompanied by an extension of the test duration and difficulties associated with the cartridge opening at the end of the test.

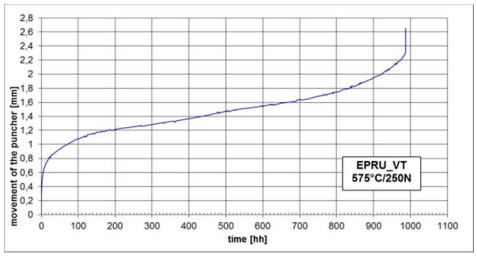

Figure 5. Dependence of the punch movement vs. time (SPUTT500 V1.3).

In 2011 we replaced the original version V1.3 with version V1.4 (Fig. 6), where we changed the load measurements, including sensors, further we replaced the existing temperature measurements for more accurate and changed the design of cartridge together with its imposition to the test thorn (easier removal after test).

During 2012 we built three test machines in which were control SW redesigned (V1.7). Since the end of 2012, extensive testing was carried out wherein it was found that each device has its own characteristic. This fact led to deeper reflection. The main causes were seen in the punch deformation (Fig. 7) during the test, respectively the ball indentation into the punch and the possibility of inaccurate measurement of the sample temperature.

The idea of a new design solution has been brought due to the 3rd International Conference SSTT in Graz, Austria. Originally we considered the idea of Mr. Juhani H. Rantala (VTT) to measure the sample temperature and simultaneously its deflexion of its bottom side to be technically impossible. Finally, after several attempts, we managed to find a design solution for the existing version V1.7 - changing indirect measurement of sample temperature for the direct one and add measuring deflection. As a result we obtained a smoother curve deflection sample vs. time. Unfortunately the curve of the creep rate vs. time (Fig. 8) remained still unacceptably shaky.

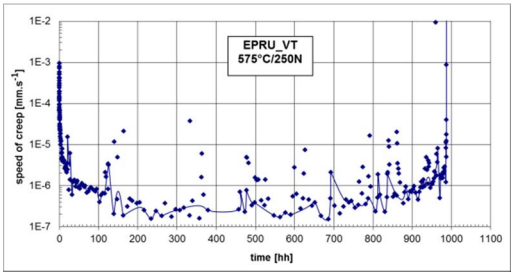

Figure 6. SPUTT 500 V1.4. **Figure 7.** Punch deformation. **Figure 8.** Creep rate (SPUTT500 V1.4).

A deeper analysis of the problem resulted in the following possible reasons:

1) Friction of guiding parts (during beginning of loading the arm is pushed by a spring of LVDT sensor and causes a misalignment of the drawing fork)
2) Imperfect protection of the sample (argon flow around the sample and it ensures only partial protection)
3) Deformation of the lower die chamfer (0,2x45°) under load (nickel alloys are not sufficiently resistant against deformation at certain load)
4) The use of the testing ball (possibly punch deformation (Fig. 7) causes misalignment of the load axis with respect the center of the sample)

Next further negative effect which should be also necessary to consider is the sample preload that is given by dead weight of the testing fork, cartridge and arm.

The removal of all causes could not have been done by modifying the existing machine, it was necessary to create a completely new design. Development was conducted during 2015. An entirely new version V3.1 SPUTT500 (Fig. 9) was the result of development conducted during 2015.

Figure 9. SPUTT 500 V3.1.

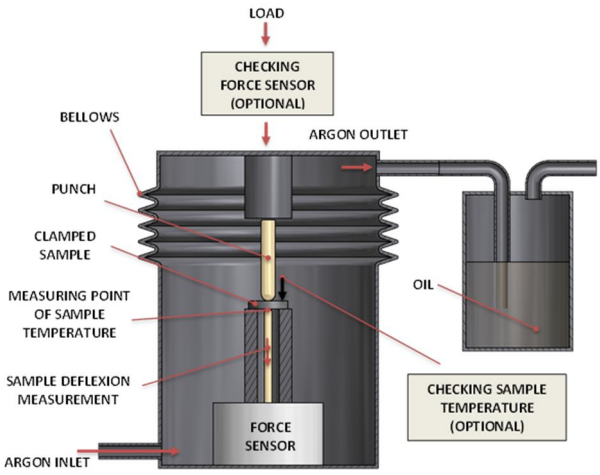

Figure 10. Gas-tight chamber of SPUTT500 V3.1.

The new version (V3.1) differs from the previous in all directions - complete new design (Fig.10) guarantees 100% full argon protection of the sample via gas-tight chamber with bellows (tested by helium test with allowable leakage rate $1x10^{-9}Pa.m^3s^{-1}$), accurate temperature measurement directly on the sample surface (thermocouple type S, class 1), entirely smooth line load (ball bearings), direct load measurement under the sample (measurement accuracy 0.1% of MR), a new construction of the cartridge with the ceramic punch and the lower die and the new control software (Fig.11,12,13) for fully automatic system with nine user-programmable cycles (Fig. 12). The preload of the sample has been eliminated completely. Minimum torque of the cartridge was set to preserve the initial diameter of the sample throughout the test. The resulting dependence of sample deflection vs. time is entirely smooth (Fig.14,15). Three stages of creep can be clearly identified from the curve of the creep rate (Fig.16,17).

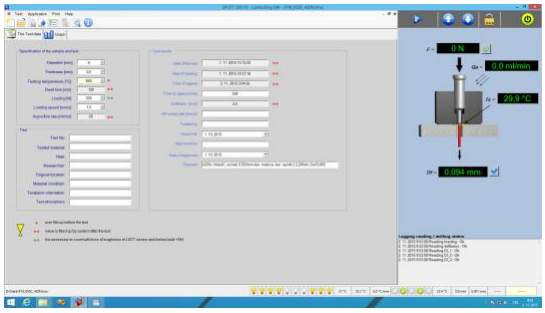

Figure 11. Setting the main parameters of the test.

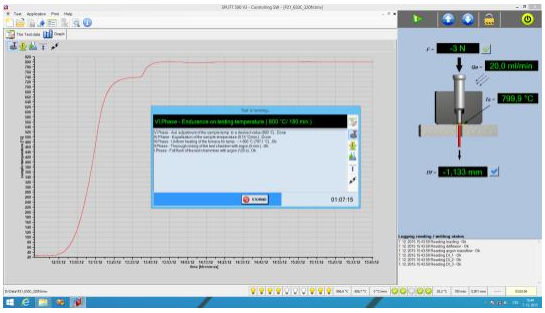

Figure12. Nine automatic stages of the test.

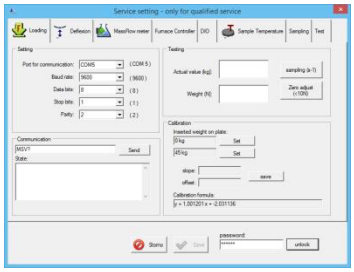

Figure 13. Calibration of main measured values.

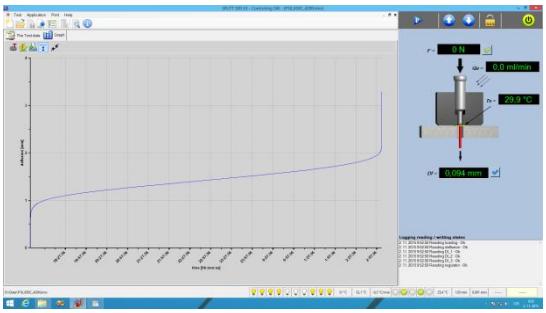

Figure 14. The resulting curve.

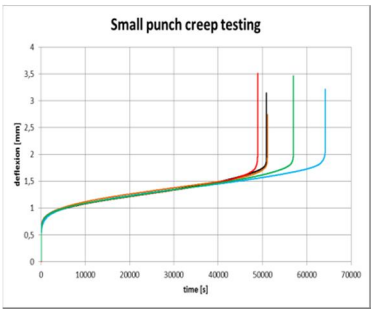

Figure 15. Results comparison.

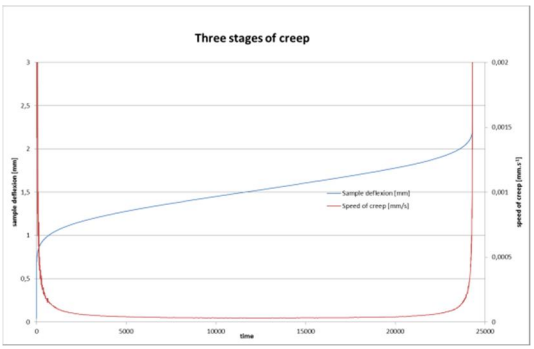

Figure 16. Three stages of creep.

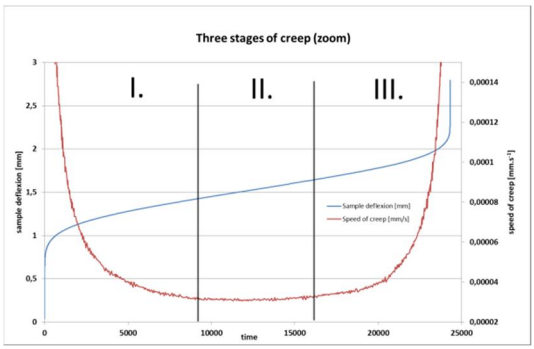

Figure 17. Three stages of creep (zoom).

The machine evolution still continues. Team of designers strives to increase the maximum testing temperature from current 800°C to 1000°C by selecting appropriate materials and construction. Even more accurate load measurement, reducing the resistance of the bellows and new linear guidance of deflection stick will provide the most accurate test results. The new version SPUTT 500, due to its original design, recently represents the most sophisticated device for creep testing of small samples by penetration method in the world.

2.3 CRYOSET

CRYOSET is equipment for tensile and fracture material properties determining using a miniaturized test samples and the penetration test.

In 2011 MMV started with innovation of the old system for performing penetration tests in normal and low temperatures. The developed equipment was built according to CWA 15627 Part B (tensile and fracture behaviour) and was called “CRYOSET”. The principle of sample cooling is in the automatic dispensing system - a special probe inserted into a Dewar container with liquid nitrogen (Fig. 18). Nitrogen is extruded from container by the help of regulating the pressure and conducted into the chamber with the test sample (Fig. 19), which is connected to the loading frame. The sample temperature is measured directly on its surface and maintained by a control unit (Fig. 20, 21). As soon as the required temperature is reached, it is possible to perform a test. Excellent geometry of the punch and the lower die together with excellent material toughness and abrasion resistance provides very good measurements repeatability. The device contains elements for safe operation and rapid exchange of the sample. The control system (Fig. 22) enables to heat the critical parts of the system (top side of the chamber and test housing). The innovation took more than two years and during that time two versions have been developed. The equipment was delivered to several testing laboratories.

Figure 18. Special probe in Devar container.

Figure 19. Test chamber.

Figure 20. Control unit.

Figure 21. Control unit (back side).

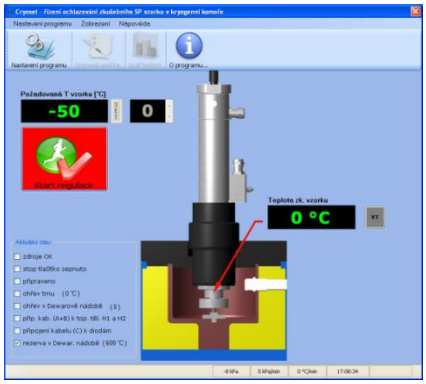

Figure 22. Control Software.

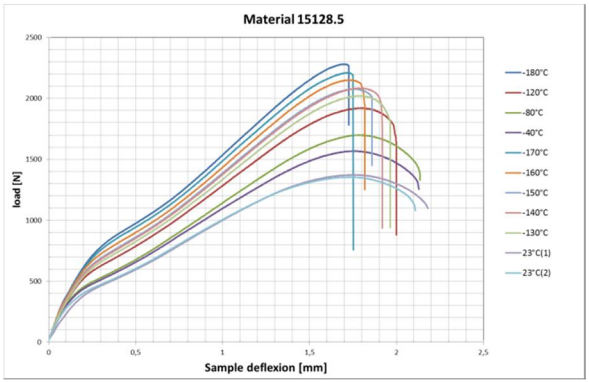

Figure 23. Measured values.

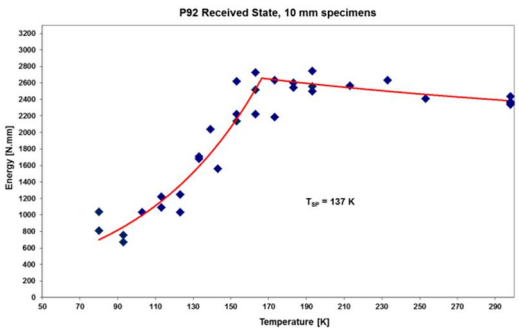

Figure 24. Tsp determination.

2.4 ESTIM

Traditional sampling method by in-service equipment represents besides necessary shutdowns also inappropriate interference into the integrity of the tested part. Referred destructive methods require the repair of sampled place, mostly by welding with heat treatment and many of non-destructive inspections. The sampled place, which has undergone a series of temperature cycles during welding, very often becomes a source of other problems, including the possibility of cracking during subsequent operation.

These apparent disadvantages are eliminated by using of scoop sampling system, which removes material to a depth from 0,5 to 4 mm without affecting the structural component, virtually without notch [23]. The principle of sampling, which is schematically shown in Fig. 25, comprises a grinding of the interlayer between the sample and a part using a rotating tool of a spoon shape, thickness about 0,3 mm and diameter about 50 mm (Fig. 26). The cutter is coated with diamond or CBN grit. The tool is moved to cut very slowly by the help of simple lever mechanism.

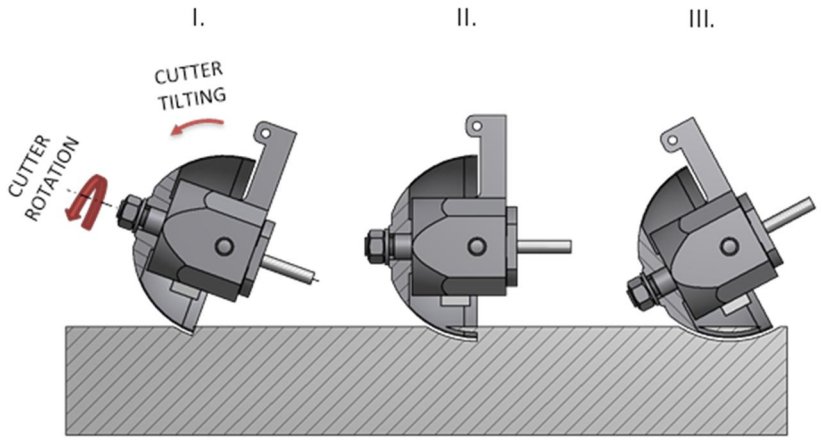

Figure 25. Scoop sampling system.

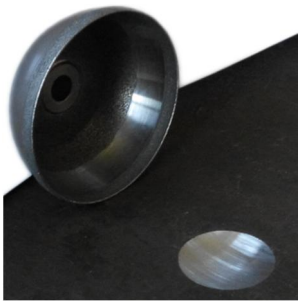

Figure 26. Tool and sampled place.

The entire process of collection lasts approximately 1-3 hours. It allows getting the sample in the shape of a spherical cap with radius about 25 mm, flat surface of about 3 cm^2. High peripheral speed with low movement of the grinding tool to cut and intensive cooling ensures absence thermal and deformation effect.

Collected sample allows to provide besides ordinary chemical, metallurgical, or electron microscopic analysis also determination of mechanical properties, creep resistance, fracture toughness etc.

MMV company has been using the sampling machine Rolls-Royce SSAM-2 since 1996. Over the years the equipment was repaired by our staff, reviewed and improved. Based on gained experience MMV has developed own sampling machine called ESTIM (Fig. 27, 28, 29). Its design is built on the principle spoon

sampling. The unique method of swivel head attachment ensures an accurate and efficient cut. The result is the minimization of the cutting time and smoother surface of the cut on sample parts - smaller notch. The control system (Fig. 30) allows rotation of the tool up to 16,000 rpm, selection of cutting direction and programming of the cutting angle. For easy and quick clamping the machine to sampled components we have developed a fixture called “SPIDER”. Cooling of the sample provides two-headed peristaltic pump, one head leads the coolant to the cutting area, the second one transports the coolant from the cut to the reservoir. A new version is being developed for use at higher temperatures. Examples of realized samplings in operating conditions are shown in Fig. 23.

Figure 27. Estim.

Figure 28. Estim transport package.

Figure 29. Suitcase with accessories.

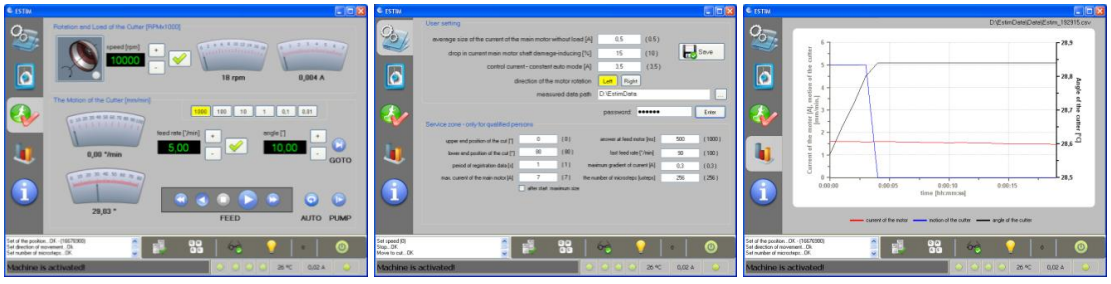

Figure 30. Estim control system.

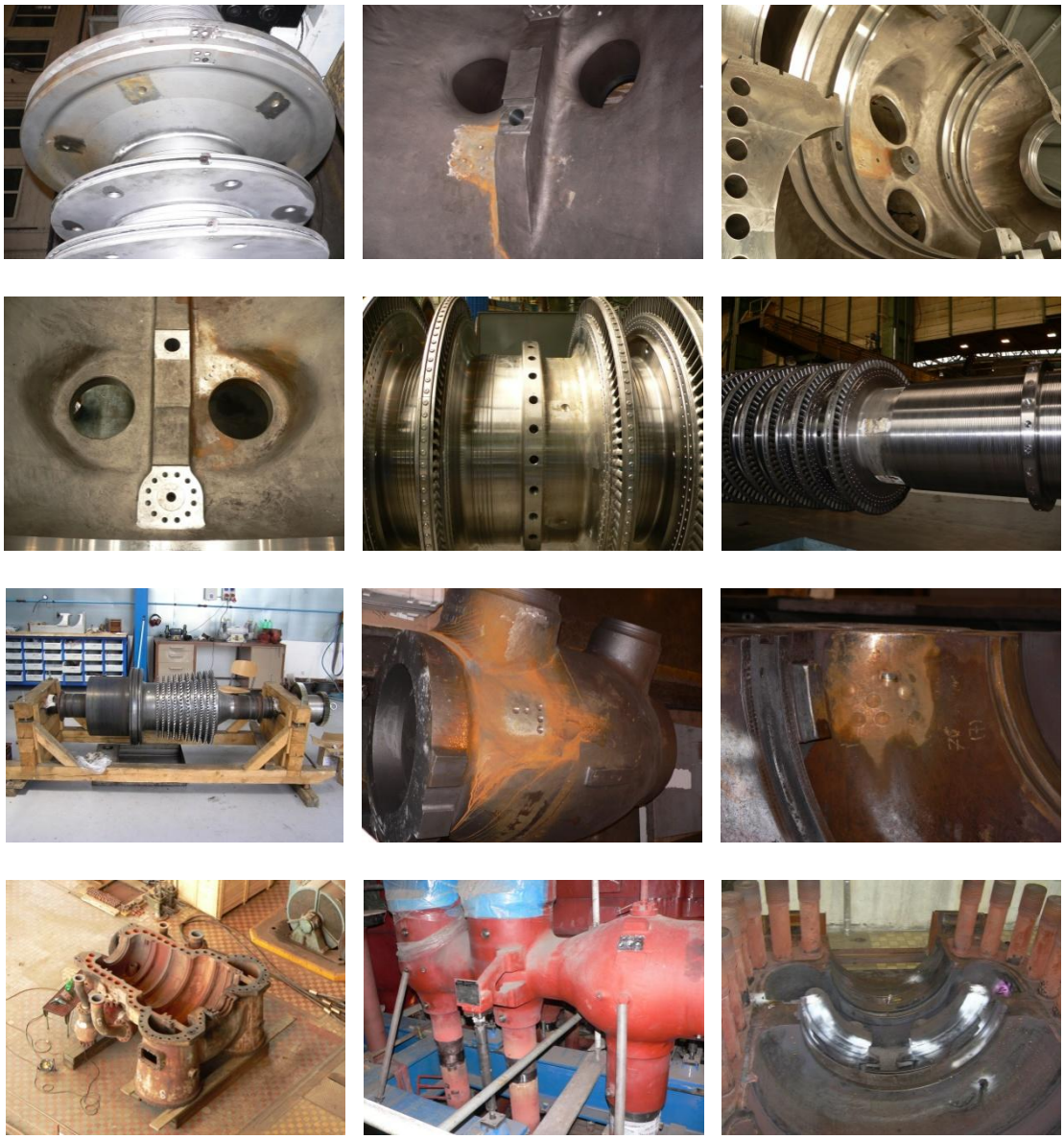

Figure 31. Examples of realizations.

3. Proposals for improvement of CWA 15627

The method for detecting the mechanical properties of material by penetration tests of miniaturized samples is not only indispensable in the industry, but also economically very advantageous. Unfortunately, the small amount of test material is an extremely rigorous for compliance and testing methodology.

Critical points of the method rely primarily on:

- Compliance with precise geometry of the sample (tolerance of the sample thickness, parallelism and surface roughness)
- Compliance with precise geometry of punch and lower die
- Ensuring the least possible friction emerging by load application
- Ensuring complete protection against the oxidation of the sample
- Setting an accurate sample temperature and maintaining it throughout the testing process
- Setting the load sample (elimination of forces acting against load as the resistance of the bellows, necessary pressure sensors)

- Ensuring the correct and accurate measurement of the sample deflection (mounting, coaxiality of the punch and the lower die).

Although the test method is used in laboratories around the world, testing standard has been adopted only in Japan [1] (only for SPC). In Europe (eventually in the USA) was accepted only implementing legislation CEN Workshop Agreement CWA 15627. There is more than desirable to create from this document test standard, then the method would become sufficiently credible for wider utilization in the industry. The results of previous comparative tests have shown that the existing legislation (CWA 15627) is insufficient and it is necessary to revise.

Based on knowledge acquired by machine and equipment construction intended for penetration tests and many years of testing, we propose to specify CWA 15627 as follows:

Part A (creep testing):

1) utilize punch (Ø2 or Ø2.5mm) with tolerance ± 0.005mm, made of ceramic Al_2O_3, respectively ZrO_2 - material with coefficient of Thermal Expansion (7÷9 10–6/°C), testing ball is not recommended because of possible misalignment of center axis between punch and lower die, punch should be marked for further inspection
2) utilize lower die with hole Ø4H6 ($^{+0.008}_{-0.000}$) radius R0.2± 0.05mm instead of chamfer, made of ceramic Al2O3, respectively ZrO2 - material with coefficient of Thermal Expansion (7÷9 10–6/°C). The edge of chamfer at nickel alloys is deformed at ceramics during the test, the edge is sometimes chipped. Lower die should be marked for further inspection
3) The measurement of temperature is necessary to have directly on the sample and the device must allow an occasional checking by the second independent thermocouple - preferably on the opposite side of the sample (Fig. 32)
4) the load should be measured directly below the specimen (opposite the loading force) to eliminate friction between the punch and the guidance, pressing force of deflection rod and stiffness of the bellows in the gastight chamber. It is recommended to have occasional possibility of checking the applied load by second independent strain gauge during all the test.
5) measure the sample deflexion instead of punch movement - because of different toughness of each testing system, possibility of creep of punch or load thorn
6) in the testing protocol is recommended to register exact thickness of the sample, the hole diameter of the lower die and the diameter of the punch for correct determination of the resulting strain.

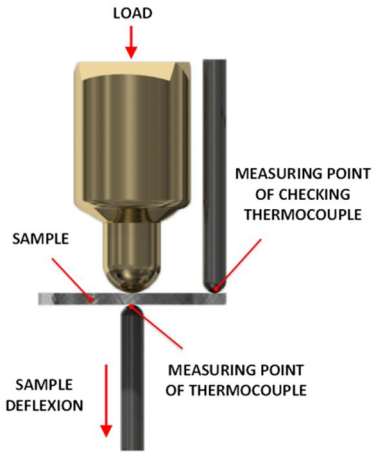

Figure 32. Checking the sample temp. measurement.

Part B (tensile and fracture behaviour):

1) measure the sample deflexion instead of punch movement - different stiffness of each testing machine (Fig. 26)
2) utilize one size punch - Ø2 with tolerance ± 0.005mm, hardness > 55HRC, made of material with coefficient of Thermal Expansion (7÷9 10–6/°C)
3) use lower die with hole Ø4H6 ($^{+0,008}_{-0.000'}$) hardness >55HRC, radius R0.2± 0.05mm instead of chamfer, made of material with coefficient of Thermal Expansion (7÷9 10–6/°C)
4) temperature measuring directly at the surface sample, pressing force <2N

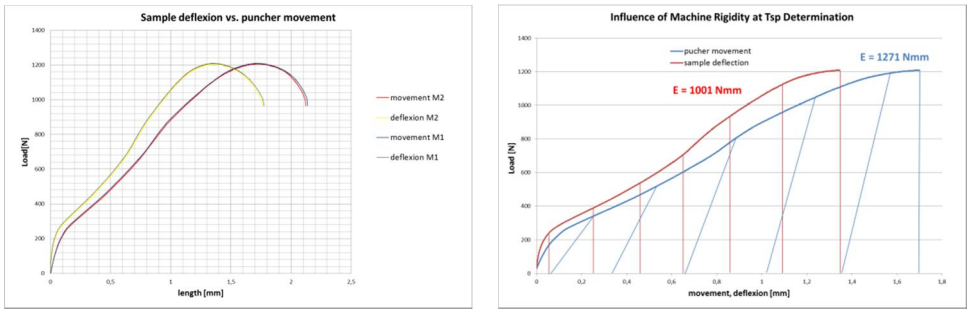

Obr. 26. Influence of load frame rigidity.

4. Conclusions

Even slight inaccuracies in the above various critical points due to their potentially large number may result in quite different results of testing. This fact leads us to the idea of having several classes of etalons. With these etalons the entire metering system of the testing machine could be validated very easily a reliably.

Acknowledgement

This work was created due to the implementation of project no. LO1203 “Regional Materials Technology Centre-sustainability program” funded by the Ministry of Education, Youth and Sports of the Czech Republic and Technology Agency of the Czech Republic under identification number TA01020427.

References

[1] PURMENSKÝ, J.: Rewiew of small punch techniques (bend test, bulge test and shear punch test). Materials Dept. of University College, Swansea, May 1991.

[2] PURMENSKY J., MATOCHA K.: Zkoušeni malych vzorků ve fyzikalni metalurgii. In: Metal 2001 10th International Metallurgical and Materials Conference, 15-17 May 2001, Ostrava, Czech Republic.

[3] PARKER, J.D., PURMENSKÝ, J.: Assessement of performance by monitoring in service changes in material properties. Proc. Reliability and Structural Integrity of Advanced Materials - Ninth European Conference on Fracture, Varna, September 1992.

[4] PURMENSKÝ, J., KUPKA, V.: Hutnické listy 7-8, 1993, s. 65.

[5] PURMENSKÝ, J., WOZNIAK, J.: Small samples method application for the evaluation of mechanical properties at elevated temperatures. Proc. IX. Int. Symposium „CREEP 1996", Belaria, Czech Republic, September 1996, s. 142.

[6] PURMENSKÝ, J., FOLDYNA,V., SOJKA, J., KARÁSEK, J.: Small sample testing methods for conditional assessment of high energy equipments. Int. Conf. Compass 1999. Ed. W.J. Evans, A.W. Evans, M.R. Bache. Swansea, UK, March - April, 1999, s. 227.

[7] MATOCHA, K., PURMENSKY, J., MIŠCICKI, M., MARSZALEK, P.: Determination of actual tensile and fracture properties of steam turbine rotor by small punch tests. Advances In Materials Science, Vol. 7, No. 2(12) June 2007, ISSN 1730-2439, p. 32.

[8] PURMENSKY J., MATOCHA K.: Determination of long term material properties degradation using small specimen testing. Pressure Vessels and Piping. Volume IV, Inspection and Life Management. Editors: B. Raj, B. K. Choudhary, A. Kumar. Published by N. K. Mehra for Narosa Publishing House Pvt. Ltd., 2009, New Delhi, India. Pp. 213 – 220. ISBN 978-81-8487-003-9.

[9] MATOCHA K., KUBOŇ Z., PURMENSKY J.: Ductile-brittle transition behaviour of circumferential weld of reheater header determined by small punch tests. Proc. 1st Int. Conf. SSTT (Small Sample Test Techniques), Vol. 63, pp. 103-107; 2010, Metallurgical Journal.

[10] MATOCHA K., KUBOŇ Z., PURMENSKY J.: Ductile-brittle transition behaviour of circumferential weld of reheater header determined by small punch tests. Proc. 1st Int. Conf. SSTT (Small Sample Test Techniques), Vol. 63, p. 103–107; 2010, Metallurgical Journal.

[11] HURST R.C., MATOCHA K.: Where are we now with the European Code of Practice for small punch testing? Proc. 2nd Int. Conf. SSTT.

[12] LI Y., HURST R., MATOCHA K., ČIŽEK P., BLAGOEVA D.: New approach to determine fracture toughness from the small punch test. Proc. 2nd Int. Conf. SSTT, Determination of Mechanical Properties by Small Punch and other Miniature Testing Techniques, Ostrava 2012, p. 94-102.

[13] MATOCHA K.: Determination of actual tensile and fracture characteristics of critical components of industrial plants under long term operation by SPT. Proc. of the ASME 2012 Pressure Vessels & Piping Division Conference PVP 2012, July 15-19, 2012, Toronto, Ontario, Canada (CD-ROM).

[14] MATOCHA K., FILIP M., KARTHIK V., KUMAR V., LACALLER R., TONTI A.: Results of the round robin test for determination 26 of TSP of P22 steel small punch tests. Proc. 2nd Int. Conf. SSTT, Determination of Mechanical Properties by Small Punch and other Miniature Testing Techniques, Ostrava. 2012, p.227-232.

[15] MATOCHA K.: Small punch testing for tensile and fracture behaviour – Experiences and way forward. Application of Miniature Small Punch Test Specimen in Determination of Tensile Properties, Small Specimen Test Techniques. 6th International Symposium, ASTM STP1576, ASTM International, West Conshohocken, PA 19428-2959, 2014.

[16] CEN WORKSHOP AGREEMENT, Small punch test method for metallic materials, CWA 15627:2007 D/E/F, December 2007.

[17] Hurst, R. Experiences with the European Code of Practice for small punch testing for creep, tensile and fracture behaviour. 3rd Conference SSTT, Graz, Austria, 2014.

[18] Standard for Small Punch Creep Test. Ed. by The Committee on High Temperature Strength of Materials. The Society of Materials Science, Japan, September (2012).

[19] BISBEE, L.H., MERCALDI, D.W. and PARKER, J.D.: SSam - a system for nondestructive materials sampling. Proc. COMADEM 91, Ed. Raj B.K.N. Rao & A.D. Hope, IOP Publishing, UK,1991.

Impression creep testing for the HAZ of a P22 weld

Juhani Rantala[1] & Jan Storesund[2]

[1]VTT Technical Research Centre of Finland Ltd.
Kemistintie 3, Espoo, Finland

[2]Inspecta Technology
P.O Box 30100, Stockholm, Sweden

Abstract

Impression creep testing was applied in a research project funded by Värmeforsk, Sweden, in order to study the creep rate in a HAZ of a girth weld in a P22 (10CrMo910) power plant piping. In the project a special routine was developed to transfer the results of a global piping stress analysis into a detailed 3D FE model of an individual piping component. In the 3D analysis the real HAZ creep rates were modelled on the basis of the impression creep tests.

1. Introduction

Elastic pipe stress analyses are performed on new pipe systems by routine within the design review to check that the stresses due to thermal expansion and dead weight in addition to the internal pressure do not exceed allowed values. After long term operation it is crucial to update the input data to such analyses since hanger and support adjustments change. It is also common that refurbishments of the pipe system are carried out during its lifetime.

Elastic stress analyses are normally used to pinpoint areas with enhanced stresses at the start of the operation but the effect of creep relaxation is normally not considered. Stress redistribution due to creep relaxation changes the stress levels and may also change or introduce new positions that are critical with respect to creep damage development [1-3]. Thus, it is possible that the elastic analysis cannot fully determine critical positions for replica testing. The elastic analysis will over-estimate the stress levels at some positions and under-estimate them at others and can therefore not be used for estimations of creep life.

By introduction of creep deformation in the analysis it would not only be possible to identify critical position. It would also be possible to calculate the creep strain as a function of time at such positions. This would give a straight forward measure of the consumed life time. The remaining life can be estimated with a high precision and the analysis can be verified by replica testing. Creep analyses of complex pipe systems require powerful hardware and software. Therefore, it is not until recently such analyses can be expected to be performed in a reliable manner.

The purpose of the Värmeforsk project was to develop i) analyses that can pinpoint critical positions for testing correctly and in detail, ii) analysis methods that can be used for creep life assessment of live steam

pipe system components, iii) use creep data of weld constituents from results of miniature creep testing iv) make comparisons between analyses by use of tabulated data and those where creep test data for the analysed component are used.

2. Impression creep experiments

For impression creep (IC) testing a non-standard test procedure was chosen. Because the purpose of the IC testing was to provide material parameters - strain rates particularly - for the HAZ of the T-piece for the FE analysis by Inspecta, it was decided to deviate from the practice in terms of the specimen thickness. While the standard specimen is 10*10*2.5 mm in size, an “oversize” specimen was made with thickness of 10 mm in such a way that the HAZ was parallel with the surface to be indented. After each 500 h test cycle a 0.5 mm layer was ground off from the indented surface, rotated by 90° in order to reduce the effect of the deformation from the previous test, and then the testing was continued with the same specimen until all layers of the sample were tested, starting from the base material (BM), across the HAZ, and finally ending up in the weld metal (WM). The corresponding uniaxial stress in these tests is 110 MPa.

After each 500 h test cycle the minimum displacement rate was calculated and this was converted to a corresponding uniaxial strain rate by using a simple analytical equation established by Nottingham University for impression creep to uniaxial conversion. Also the displacement curves (indentation depth) were converted to uniaxial strain curves as shown in Fig. 1 where the curves of the nine first tests are shown. The continuous strain rate curves were calculated by moving a 100 h “calculation window” from the beginning of the test to the end as shown in Fig. 2. It is seen that towards the end of each test the scatter increases when the strain rates become very small. In another project it was defined that below a strain rate of about $3*10^{-6}$ the accuracy will reduce. This is also partly due to the fact that towards the end of the test the number of data points in the 100 h calculation window reduces and in fact the last rate is calculated by a window of only 50 h. A linear trend line was fitted through the data of the last 100h of each test in order to calculate the corresponding uniaxial minimum creep rate of each test. These creep rates are shown in Table 1.

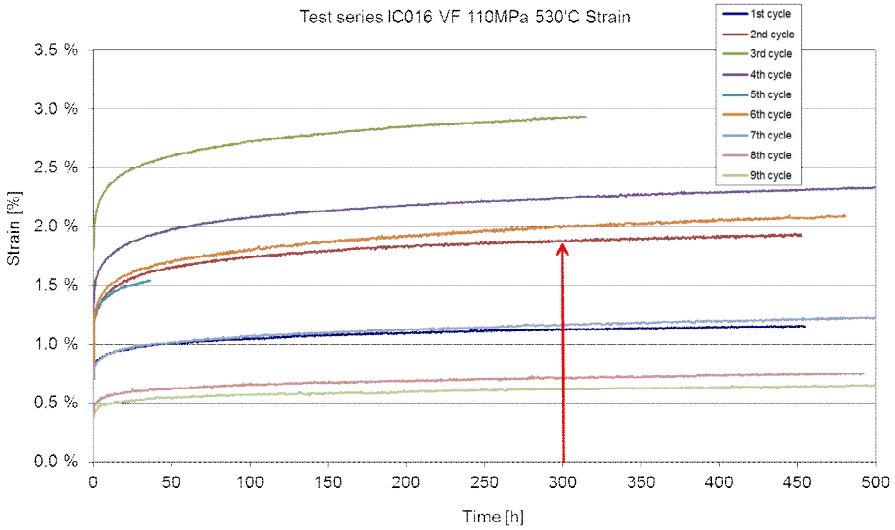

Figure 1. Corresponding uniaxial strain curves calculated from the impression creep test series for P22 at 110 MPa and 530°C.

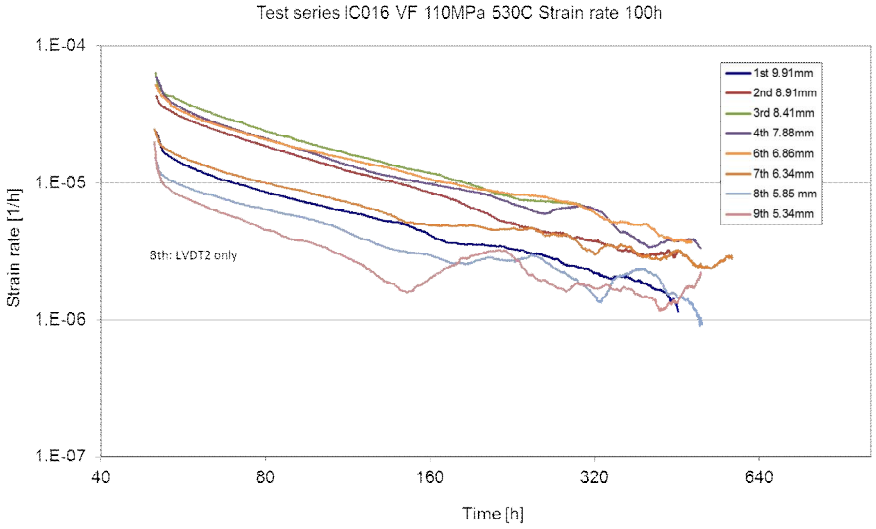

Figure 2. Continuous strain rate curves from the impression creep test series for P22 at 110 MPa and 530°C.

Table 1. Minimum linear strain rates at each specimen thickness.

Specimen thickness [mm]	min. strain rate (corrected) [1/h]
9.91	1.75E-06
8.91	3.26E-06
8.41	3.90E-06
7.88	3.70E-06
6.86	4.58E-06
6.34	2.74E-06
5.85	1.65E-06
5.34	1.44E-06
4.85	1.79E-06
3.88	1.22E-06
3.09	9.47E-07
2.5	5.29E-07

The creep rate varied when moving from BM across the HAZ to the WM. The useful illustration of this behaviour is shown in Fig. 3 where the brown curve shows the corresponding uniaxial strain at a constant time value of 300 h, being a rough relative measure of the amount of primary creep at each material layer. However, the quality of the initial contact between the specimen and the indenter is not necessarily perfect in each test, so there is some uncertainly associated with this strain parameter. However, the strain value (brown curve) and the calculated minimum creep rate (blue curve) for each test seem to go roughly hand in hand. Standard deviation values were added on the strain rate curve as calculated at the same time period as the minimum strain rate.

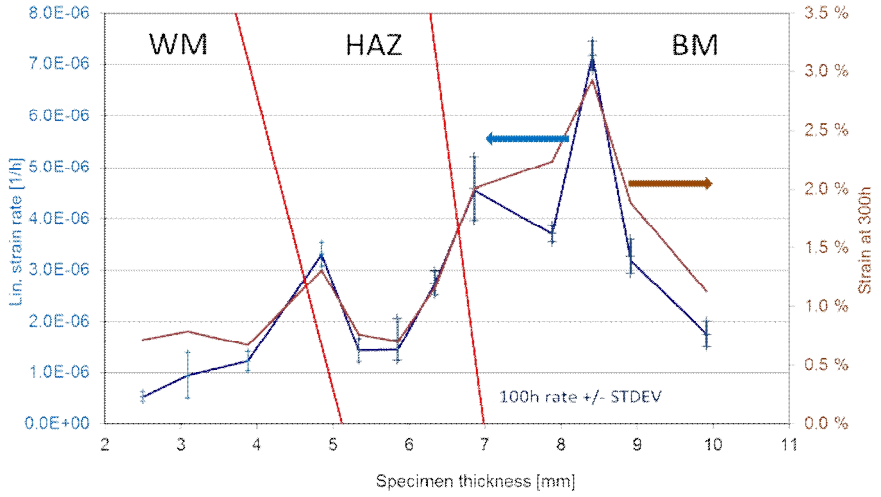

Figure 3. Calculated minimum linear strain rate and the corresponding uniaxial strain at 300 h for each impression creep test at 110 MPa and 530°C.

The test series was started with the specimen thickness of 10 mm and at that thickness the tested surface was in base material. After the first test 1 mm was ground off and in the second test the measured minimum strain rate increased. After the following tests only 0.5 mm was ground off. In the third test the highest minimum strain rate achieved as shown in Fig. 3, which initially indicated that this layer would be the inter-critical zone, which has the weakest creep strength and the highest creep rate. However, this particular test with the highest creep rate and another test (at thicknesses 8.41mm and 4.85mm) were run to only about 300h instead of intended 500h test duration. Based on the general trend in Fig. 2 it was estimated that the creep rate at 500h would be 0.544 times the rate at 300h. When these two test results are corrected the figure changes especially at the location which was thought to be the inter-critical zone, see Fig. 4. The brown curve does not change as all the strain values have been measured at 300h.

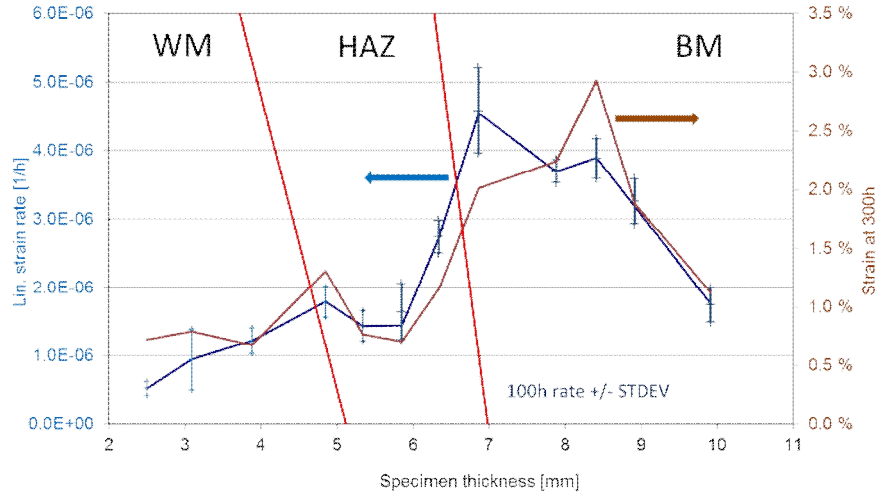

Figure 4. The minimum strains corrected as compared to Figure 3.

Hardness was measured from the new weld and the results are shown in Fig. 5. The locations of the hardness measurements are indicated in Fig. 6. The hardness measurements in Fig. 5 suggest that the width of the HAZ is about 4 mm, which does completely coincide with the measurements taken from Fig. 6. The WM has a much higher hardness (250 HV1) than the BM (160 HV1), which means that the WM is overmatching. The high hardness of the WM is in line with the finding that the creep rate of the WM in Fig. 4 is lower than the creep rate of the BM although the correlation between hardness and creep strength is not universal. It is well known, however, that a good correlation exists between hardness and tensile strength of steels.

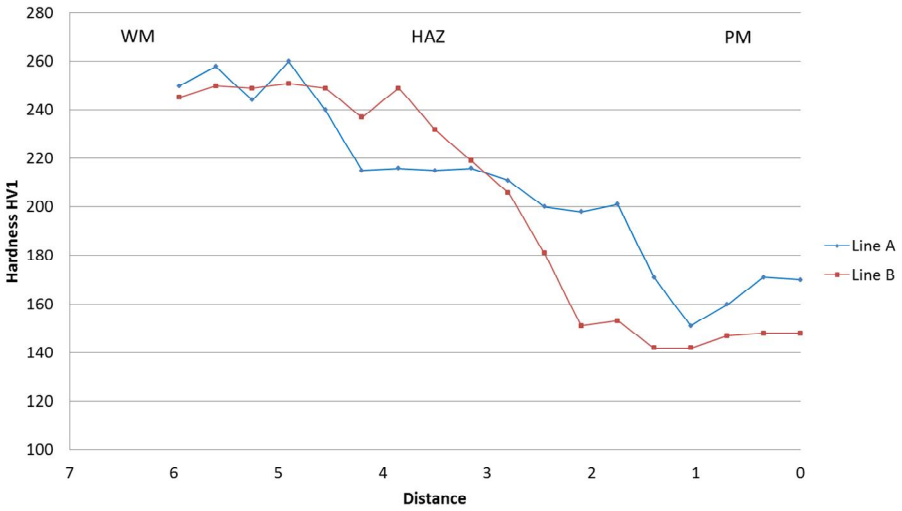

Figure 5. Hardness measurements across the HAZ of the new weld.

Based on the measurements from the cross-section of the new weld in Fig. 6 it can be estimated that on top of the 10*10mm hole the location of the fusion line is at 3.7 mm and at the bottom at 5.1 mm. The location of the IC-HAZ/BM transition is more difficult to define but is located roughly at 6.3 mm on top of the hole and at 7.0 mm at the bottom. From these measurements it can be estimated that the width of the HAZ is 2.6 mm on top of the hole and 1.9 mm at the bottom, which seem like rather small values. The HAZ location has been sketched into Figs. 3 and 4. The CG-HAZ is the strongest zone and has the lowest creep rate. The minimum creep rate results in Table 1 and in Fig. 4 show that the highest strain rate of $4.58*10^{-6}$ is only about 2.6 times higher than in the base material ($1.75*10^{-6}$). However, it was expected that the strain rate in the coarse grained zone would have been considerably lower than in the base material, but this is not the case. The low creep rates measured from the WM as shown in Fig. 4 indicate that the creep strength of the WM is slightly higher than of the BM. The weld is therefore overmatching.

The reported minimum strain rate values did not necessarily hit the lowest and the highest values in the test specimen as the selected grinding thickness of 0.5 mm was a compromise between two factors. First, the smaller the grinding thickness, the smoother the curve in Figs. 3 - 4 would have been (but would have increased the number of test cycles needed to scan through the specimen). Secondly, the smaller the grinding thickness, the more the deformation from the previous cycle would have influenced the following test. The FE analysis of the IC test specimen had shown that the deformation below the indenter does not progress deeper than 0.5 mm. However, this is of course dependent on the stress level.

When testing a HAZ specimen as described above one has to recognise also the fact that the sample is a sandwich structure in terms of material properties. At this point it is not known how the underlying different microstructures will affect the testing of the microstructure on the surface. This would require FE analysis which was not foreseen in the current project.

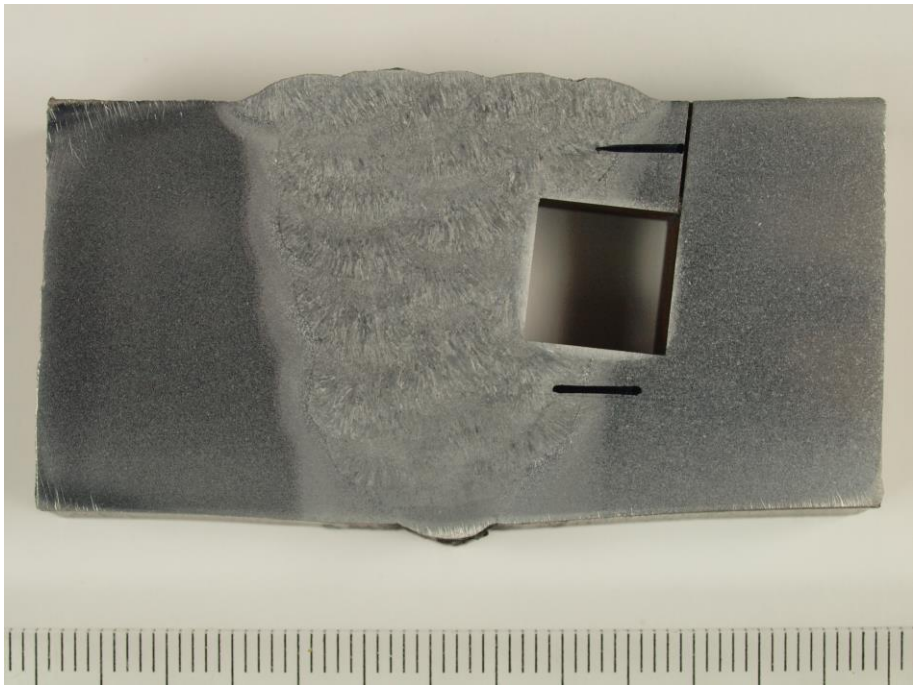

Figure 6. Cross-section and the locations of the impression creep specimens and the hardness measurements across the HAZ, mm-scale at the bottom.

Uniaxial creep tests were carried out for the P22 base material at 530°C at stresses 140, 160 and 180 MPa. The results are shown in Table 2 and are compared with the impression creep data in Fig. 7. It can be seen that strain rate correlation between the uniaxial creep testing and impression creep test results is good. The impression creep rates measured from a service-exposed P22 T-piece indicate higher creep rates than for the P22 base material.

Table 2. Uniaxial creep test results for P22 base material.

Specimen	Stress [MPa]	Temp [°C]	elongation ef [%]	RA [%]	tr [h]	min. rate [abs]
VF-A y433M9	180	530	62.4	87.7	500.2	3.32E-04
VF-B y439M9	160	530	59.7	82.6	1371.5	1.07E-04
VF-C y432M8	140	530	47.8	96.3	4386.6	2.95E-05

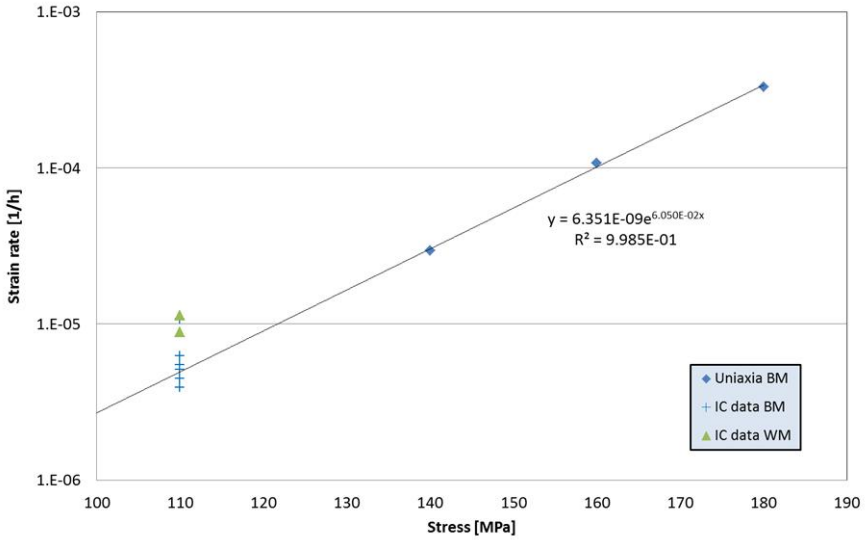

Figure 7. P22 minimum creep rates measured from the new weld at 530°C and the corresponding strain rates of the impression creep tests for the WM and BM taken from a P22 weld.

3. Conclusions

An innovative way of applying impression creep testing was used by manufacturing a “sandwich” type of specimen of a welded joint which allowed the creep rates to be scanned from the base material across the HAZ to the weld metal. The highest creep rate in the inter-critical zone of the welded joint was, however, not as high as was expected: only 2.6 times higher than in the base material. The weld metal is slightly overmatching as compared to the base material. The measured creep rates from the impression creep tests correlate very well with the minimum creep rates measured in the uniaxial creep tests of the base material of the welded joint.

The creep rates measured from the service-exposed T-piece indicate elevated creep rates which are most likely due to the creep damage.

References

1. Vilhelmsen, T. et. al. Utveckling av krypskador hos svetsade komponenter av P91 och X20. Värmeforskrapport 1197. Stockholm, March 2011.

2. Yee, R. K. & Cohn, M. Creep relaxation behavior of high energy Piping. Journal of Pressure Vessel Technology, Vol. 122, November 2000.

3. Segle, P., Algotsson, P. & Samuelsson, Å. Inverkan på ingrepp i ångledningssystem på dess återstående livslängd. Värmeforskrapport 672, August 1999.

Power & process:
Surface & corrosion control

Controlling corrosion with advanced NDT-techniques

Johanna Tuiremo[1], Kari Latvala[1], Jan Storesund[2] & Jouni Koivumäki[1]

[1]Inspecta Oy
Sörnäistenkatu 2, 00580 Helsinki, Finland

[2]Inspecta Technology Ab
Lindhagensterassen 1, Stockholm, Sweden

Abstract

Advanced NDT-techniques create new ways to efficiently map and visualize the critical locations of corrosion in boilers. As traditional NDT-techniques are restricted to a limited number of measuring points and lines, there is risk of missing the area of most severe wall thinning “by half a meter”. Advanced NDT-techniques are not restricted to pre-set locations but produce data from all over the boiler furnace and revealing unsuspected critical locations. When carried out repeatedly and combined with examination of corrosion mechanisms it is possible to predict the corrosion rate and in some cases even to prevent or slow down the corrosion by paying attention to fuel and boiler operation.

1. Introduction

Boilers are pressure equipment and safety is a key issue regarding boiler operation. Legislation is thus governing the manufacture and the use of boilers. In the viewpoint of boiler owner also availability and economical use of boiler is important – unpleasant surprises and unexpected investments are not wanted. Regular inspections are in key position when maintaining safe and economical operation and also planning the future investments and major repairs in a controlled way. Naturally inspections reveal the needs of urgent repairs that have to be carried out right away. The components and surfaces in boilers are numerous. The access might be restricted and it can be challenging how and where to inspect possible “failures”.

Non-Destructive Testing, NDT, is vastly used during boiler shutdowns. Traditional NDT techniques are in major role in inspection and are the good basis. The time of the shutdown can be, however, very limited and sometimes there is no time to carry out all the inspections needed and thus advanced techniques may be applied to get efficiently the information needed. In addition, it is important to know where to look so understanding the corrosion mechanisms is essential when planning the boiler inspections.

This paper reviews corrosion mechanisms in boilers, NDT-methods and techniques and finally how to apply them in the boiler components in order to get information for controlling the corrosion.

2. Corrosion in Boilers

Corrosion and related mechanisms are one of the critical issues regarding the boiler availability. This paper is concentrating on corrosion of black liquor recovery boiler and fluidizing boilers in furnace and superheaters - as they are the most critical parts of boilers.

Before getting into corrosion high temperature oxidation needs to be discussed. High temperature oxidation occurs in all boiler components at the temperatures above 300°C if oxygen is present in the atmosphere. When formed under favourable conditions, the oxide layer protects metal from further corrosion. The rate of oxidation increases with increasing temperature. In boilers also the flue gases and moisture increase the oxidation rate. When material selection has been done correctly oxidation is not normally considered to be a problem, even though it does cause some wall thinning in the long run. Typically 0,1 mm per year wall thinning is allowed. [1, 2]

2.1 Corrosion in Furnace

In boiler furnace material temperature is typically around 350°C. The corrosion mechanisms are highly dependent on the fuel and the type of boiler.

In power boilers the furnace atmosphere is in most cases oxidizing. Traditional fuels like coal based fuels and biomass are not very corrosive in the furnace area as the temperature is rather low. However, erosion-corrosion is a mechanism where corrosion (oxidation) and erosion mutually enhances the wall wastage of the component even though corrosion on its own would not cause problems. Erosion-corrosion is encountered especially in fluidized bed boilers e.g. wall tubes and primary air nozzles. After erosion-corrosion the tube surface can be smooth or rough or bare or covered under deposits, so it may be challenging to identify visually.

In cases where recycled fuels (e.g. industrial or household waste, demolition wood, recycled wood etc.) are co-combusted with traditional fuels, the heavy metals combined with chlorine may cause severe corrosion in furnace tubes. Corrosion can either be caused by solid phase particles like $PbCl_2$ and $ZnCl_2$ or molten phase as heavy metals, chlorine and alkalis decrease the melting point of the deposit. Some examples of melting points: The melting point for $PbCl_2$ is 501°C but when combined with KCl the melting point decreases to 406°C. With $ZnCl_2$ the melting point is as low as 318°C but combined with $FeCl_2$ the temperature lowers even down to 300°C. Molten salts can be very aggressive and lead to high corrosion rates. [3, 4] The heavy metal induced corrosion can be general and leaving uneven heavily corroded surfaces. But with highly alloyed steels and nickel base alloys the corrosion can be pitting which can be difficult to detect.

Sometimes wall wastage had been observed related to low-NOx burner change. The corrosion is concluded to be caused by reducing atmosphere and progressing by sulfidation mechanism. Typically the corrosion is associated with thick and porous scales. If moderate fatigue loading is present it can lead together with sulfidation to corrosion fatigue cracking. [5]

Black liquor recovery boiler acts both as a chemical reactor and a power generator. Thus the furnace environment and also the structure are somewhat different to power boilers. In the lower part of the furnace sodium sulphate is to be reduced to sodium sulphide. The atmosphere is reducing which enables corrosion process to take place via sulfidation mechanism [6]. Also the black liquor can burn on the tube surface and aggressive smelt may cause severe corrosion when getting in contact with tube material. To resist the sulfidation corrosion composite tubes with two-layer structure have been used in recovery boiler floors and lower furnace. In composite tube the outer layer is corrosion resistant material, typically AISI 304 type stainless steel or nickel base alloy. However, the AISI 304 type composite tubes had a tendency to crack as floor tubes. The mechanism is not fully understood but main mechanism is considered to be stress corrosion cracking. During the operation of a boiler the tensile stresses may develop in the cladding of composite tubes and sulfur-bearing compounds can form a corrosive environment, especially during operation as a result of thermal cycling or during shut-down in the water wash. High-levels of polysulfides

may contribute to lowering the melting point of the bed material, disturbing the protective frozen smelt layer on the floor tubes [7, 8]. In some cases thermal fatigue has also had a role in floor tube cracking. [7, 8]

In the composite tube to non-alloy steel change line a special form of corrosion occurs. The wall thinning is concentrating on the non-alloy steel side for very short distance. The mechanism is not fully understood, but as it is located within only few centimeters from the change line, some galvanic corrosion mechanism is likely to take part.

2.2 Corrosion in Superheaters

Superheater is the most critical part of the boiler. The hottest superheater defines the temperature of the steam and thus the efficiency of the boiler. As the superheater is the hottest component in the boiler it is also vulnerable to corrosion. Typical locations of the corrosion are the hottest parts of the superhater, lower bends that are under radiation, tubes near the sootblowers etc.

Several corrosion mechanisms act in superheater area:

Gas phase corrosion is not very common in superheaters. Chlorine gases like hydrogen chlorine can cause corrosion of superheaters at high temperature when the concentration of corrosive gas is high. However, in black liquor recovery boilers gaseous hydrogen sulphide (H_2S) may cause gas phase corrosion causing sulfidation. [9]

Solid phase corrosion can take place when solid deposits react with a tube material. Some typical corrosive particles are KCl, NaCl, $PbCl_2$, $ZnCl_2$. [3, 4, 10]

“Active oxidation” is a commonly used theory related to chlorine-induced corrosion. The chlorides in the deposits accelerate oxidation via formation of $FeCl_2(g)$ which further oxidizes to hematite $Fe_2O_3(s)$. This process leads to the formation of a porous non-protective oxide layer while chlorine still partially remains in the oxide layer continuing the corrosion cycle. In recent years, the role of potassium in corrosion process has also been investigated. In high chromium steels potassium chromate has been detected and the corrosion process has been suggested to progress via formation of chromates [10]. With low alloy steels the corrosion causes wall thinning and rough surface visual to eye. However, with stainless steels the corrosion may progress via grain boundaries and is not causing wall thinning in the first stage.

Traditionally 450°C has been considered a threshold temperature for superheater corrosion if corrosive species exists in the boiler. [2] With material selection and controlling fuel (additives) the superheater temperature can be increased.

However, during last few years there has been lot of research activity regarding heavy metal chloride induced corrosion which may also occur in solid phase [3, 4] In waste application the corrosion can start at the lower temperatures range, 350…450°C, when induced by heavy metal chlorides. [3, 4] This may happen at the low temperature superheaters (primary superheaters).

In **molten phase corrosion** the molten deposit reacts with the tube material typically leading to high corrosion rates. This corrosion rate is dependent on the amount and aggressiveness of the melt. The main components causing this kind of corrosion in recovery and biomass boilers are alkali chlorides (KCl and NaCl), which initiate corrosion by lowering the first melting temperature of the deposits. In black liquor recovery boilers sulphides also decrease the T_0. The first melting temperature T_0, is defined as a temperature when the first melt appears in the deposit. One of the design criteria has been to keep the tube metal temperature below the temperature where the first melt appears in the deposit [10]. Heavy metal chlorides also decrease the first melting temperature of the deposits to even lower level than alkali chlorides. [3]

In recovery boiler **carry over corrosion** may occur at the first superheaters in the direction of flue gases. Carry over particles, which are mostly unburnt black, hit the superheater tube and may cause severe material wastage if molten. [2] The carry over corrosion creates typically deep craters on the tube surface. It is fairly easy to visually detect but the depth may be difficult to measure with NDT-methods.

2.3 Water-steam circulation

There is another life of the boiler components when looking from the water-steam side. The water quality and treatments are essential when a protective magnetite layer needs to be formed inside the tubes. Thick films and deposits may increase the metal surface temperature and expose the component to corrosion.
Also the deposits itself may cause corrosion. Hydrogen attack is a mechanism where due to a corrosion process inside the tubes atomic hydrogen penetrates into the steel and forms CH_4 gas. The gas expands and cause micro cracks and may lead to thick walled ruptures. Typically the corrosion is very local and often concentrating on locations where the heat load is high and the water circulation is disturbed, like opening tubes. [11]

Other water-side corrosion mechanisms are oxygen corrosion where oxygen dissolved in water corrodes deep hemisphere holes. Oxygen corrosion is most typical in idle boilers. Caustic corrosion results from NaOH in water and is causing local gouging and deposits. [11]
Also stress corrosion cracking of austenitic stainless steel has been encountered.

The internal deposits and corrosion on water-steam side are not visible to the eye and their detection can be challenging.

3. Non Destructive Testing

The inspection of the boiler is done mainly by NDT, Non Destructive Testing methods. There are many different methods so it is important to understand the capability of different methods for each component and probable failure mechanisms. In recent years there has been a lot of development with NDT- techniques. Even brand new testing techniques have been developed but also a lot of development has been carried out by combining different methods. There had been also development with the measurement probes, increasing their number and combining the probes with crawlers. One important development area has been the user interface, measurement data can be processed with computer enabling better visualization of the test results.

3.1 Traditional NDT-methods and advanced techniques

In this chapter the traditional NDT-methods and the advanced techniques developed based on them are discussed.

Visual Inspection, VT
Visual inspection is the corner stone of NDT-methods and it is based on the eye of an experienced inspector. Visual inspection is used to get the overall picture of the condition of the boiler or for just a single component and to determine other inspection methods for the components. Typical targets for visual inspections can be color changes, welding defects, dimensional changes/bulging, internal and external deposits, geometrical discontinuity and of course corrosion damage. Typical accessory equipment includes lights, endoscope and piping camera.

Magnetic Particle Testing, MT
Magnetic particle testing is used to detect cracks in ferritic materials. It is based on flux leakage of magnetic field. A magnetic field is typically created with a magnetic yoke. There are two techniques to reveal the discontinuities – color and fluorescent techniques. In color technique a contrast color (white) is applied to a metal surface before spraying iron particles to the surface. In fluorescent technique no contrast color is needed. The iron particles are applied in fluorescent form and ultra violet lamp is used to see the discontinuities. In both techniques the surface needs to be cleaned proper way e.g. by grinding before inspection. Typical locations for magnetic particle testing are welds, especially fittings, ends etc.

Liquid penetrant test, PT

Liquid penetrant test is alternative for magnetic particle testing and is typically applied to non-magnetic materials like e.g. austenitic stainless steels. In this method a colored liquid is applied to the inspected surface. The liquid penetrates capillary in to discontinuities. Excess liquid is removed from the surface and a developer is applied to reveal the cracks, defects or other discontinuities. It can be applied only to the defects that open into the surface. It is applied to welds, tanks and e.g. recovery boiler floor tubes and openings.

Ultrasonic testing, UT

Ultrasonic testing, UT, is nowadays a well-established inspection method: an ultrasonic pulse is transmitted to the component via couplant and by detecting the returning echo information is gained from the component. The information in question could be wall thickness, internal defects or other discontinuities. The basis of method lies in the velocity and reflection of the sound. The signal received depends on material, temperature, geometry of the components and the orientation of the defect. Thus reference samples, multiple measurements and experienced personnel are needed to receive reliable results.

Phased array UT

An advanced UT technique is phased array UT. The main differences to traditional UT are the use of multiple measurement probes, possibility to modify the sound beam and save the encoded data. Also the display of the reflecting sound is more informative and thus the discontinuities of different orientation are easier to detect, see figure 1. Commonly data evaluation is done on computer with dedicated software.

Detection of internal oxide films

The detection of internal oxide films e.g. from superheaters, is possible with UT. The technique is based on traditional UT-method but there are special requirements for the ultra sound, probe and the couplant.

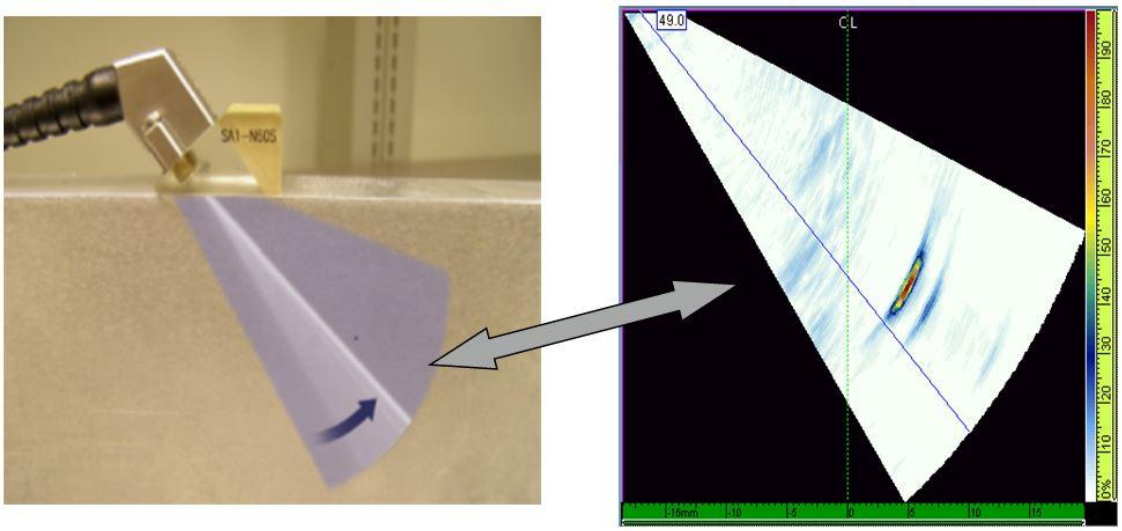

Figure 1. Example of the use and display of a defect by phased array UT.

Radiography

In radiography an image is formed on the film using a radiation source. Different wall thicknesses pass the radiation differently and show as intensity differences on the film. Radiography is a good at detecting wall thickness wastage, volumetric discontinuities, weld defects and deposits.

DDA – Digital Detector Array

Advanced technique of radiography is Digital Detector Array, shortly digital x-ray. It is a fast and real-time inspection technique for corrosion mapping and welding defects. No removal of insulation is needed for corrosion detection. In digital x-ray technique the x-ray image is produced in a digital form. The image can be modified to bring out the details of interest and also the storing of images is easier. No time consuming development is needed.

Eddy current testing, ET
Eddy currents are loops of electrical current created by changing the magnetic field in a conductive material. The currents are concentrated on the surface of the material. Discontinuities change the loops and are detected by receiver. The technique is used to find discontinuities without thoroughly cleaning the surface. The verification of defects is usually done by other methods like liquid penetrant testing.
Array ET
An advanced technique of eddy current method is array ET. It consists of multiple probes that are arranged in the measurement head modified specially to the inspected component. It enables relatively fast and extensive inspection of challenging components, e.g. recovery boiler floor tubes, see figure 2.

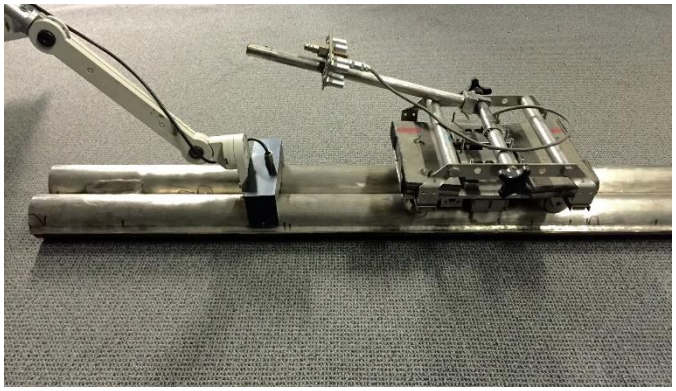

Figure 2. The special measurement heads for recovery boiler floor tubes and fins, array ET.

3.2 Other Advanced NDT Techniques

In recent years new NDT techniques have been developed by creating new ones or combining old traditional methods.

Crawlers
Different crawlers are developed to extent the NDT examination to location of difficult access. The crawlers have typically magnetic attachment to the surface so their use is restricted to ferro-magnetic materials. The crawlers can be used combined to several different techniques.

EMAT – Electromagnetic Acoustic Transducer
One of the most interesting innovations from recent years is EMAT. It is an ultrasonic testing method with a special feature that no contact or couplant is needed between the probe and the inspected body since the sound is directly generated within the material by using changing electromagnetic fields. The surface of the inspected body can be slightly dirty and grinding is not needed as is the case with traditional UT. EMAT can be used to detect wall thickness, especially gradual thinning. The advantage is that it can be easily applied for larger areas than traditional UT.

T-Scan
T-Scan is a brand name for tube scanning method that combines EMAT, crawler and a client view, C-scan. Basically in T-Scan the crawler with three probes measures the tube wall thickness from fin-to-fin and the crawler moves the probes through the whole furnace from bottom to top of the boiler, see figure 3. The special C-Scan client view displays the results in 3-D form and the customer gets the software for adjusting the color scheme appropriate to the purpose, e.g. red color for locations where the wall thickness is below the minimum allowed value. T-Scan is developed specially for inspecting of straight furnace tubes with membrane structure, but it can also be applied for superheaters in the areas were accessibility is possible. No grinding is needed for the surface. For opening tubes and lower bends manual EMAT can be applied.

Figure 3. T-Scan crawler scanning the boiler membrane wall.

SLOFEC

SLOFEC (Saturation Low Frequency Eddy Current) is a technique where flaws are detected with eddy currents and magnetic fields. Important feature of the technique is the software for analyzing the signals and 3D imaging of the data. SLOFEC is very good detecting e.g. pitting corrosion and the location (depth) of defect can also be determined, see figure 4. No thorough cleaning is needed.

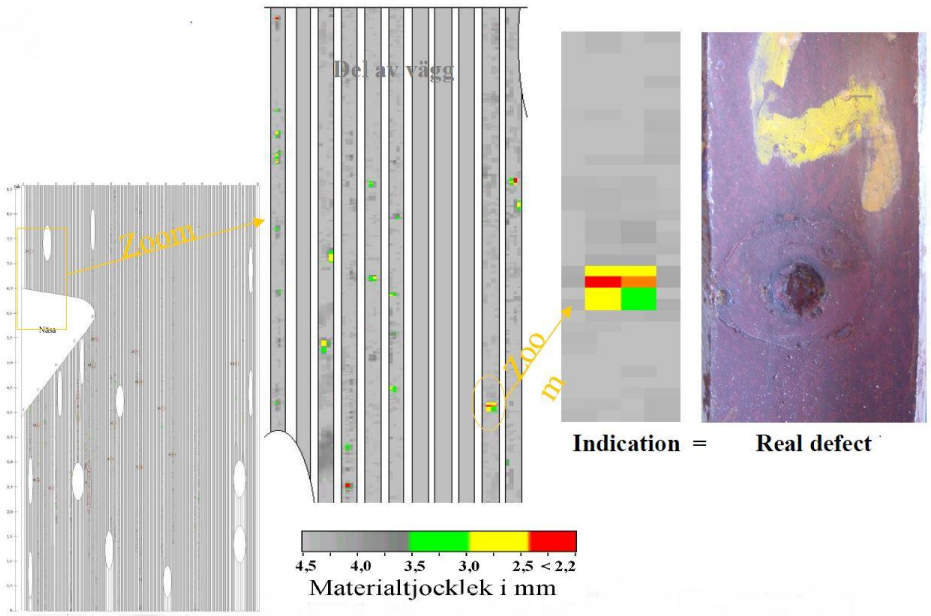

Figure 4. Example of detecting pitting corrosion on boiler membrane wall.

4. Destructive testing

NDT-methods are in essential role when inspecting and finding the possible corrosion or other damages in the boiler. However, sometimes it is needed to take a sample tube and carry out destructive testing to find out the real extent and mechanism of the damage in question. Destructive testing includes mechanical testing (e.g. strength, hardness, impact toughness), cross-sectional metallographic sample that is examined with optical microscopy for microstructure, depth and characterization of corrosion and/or cracks, eg. grain boundary corrosion is detected from cross-sectional samples, see figure 6. The cause of corrosion can be examined with a help of scanning electron microscopy (SEM) EDS-analyzer. It can be used to analyze the chemical composition of corrosion products and deposits as well as corrosion front, see figure 5. Erosion-corrosion damage can also be identified with SEM. Combining the results with the knowledge of location in a boiler, fuel and temperature data this gives information of the reasons that have led to corrosion/material wastage.

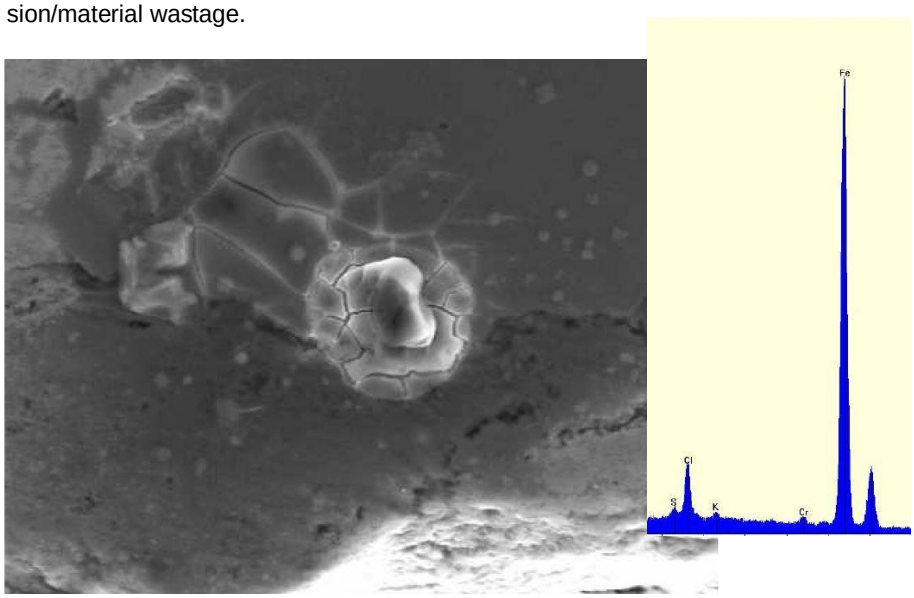

Figure 5. SEM image (magnification X1700) and EDS-analysis of corroded superheater tube. Based on the analysis of corrosion product (Fe, Cl and small amounts of S and K) active oxidation is the most probable corrosion mechanism.

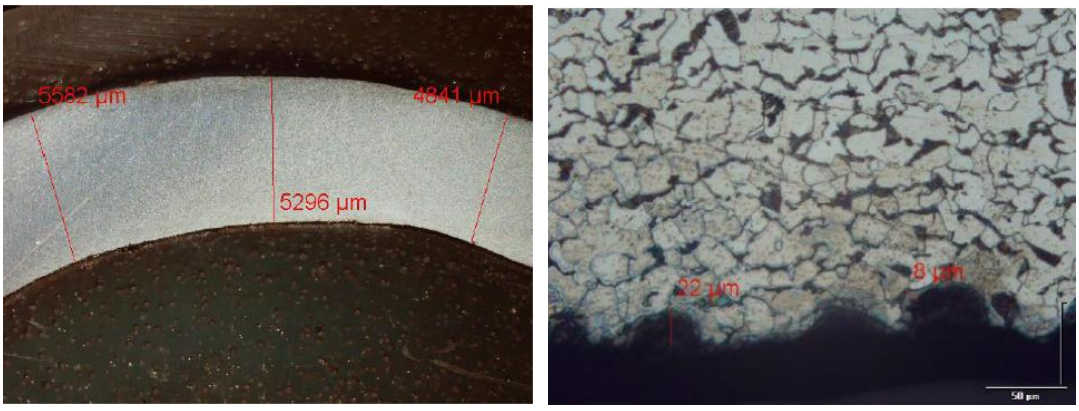

Figure 6. From the cross section a minimum wall thickness and oxide layer thickness can be measured.

5. Inspection of boilers

In previous chapter the corrosion mechanism and their locations in the boiler as well as different NDT methods and advanced techniques are discussed. The purpose of this chapter is to summarize which methods are suitable for examining different boiler components and areas.

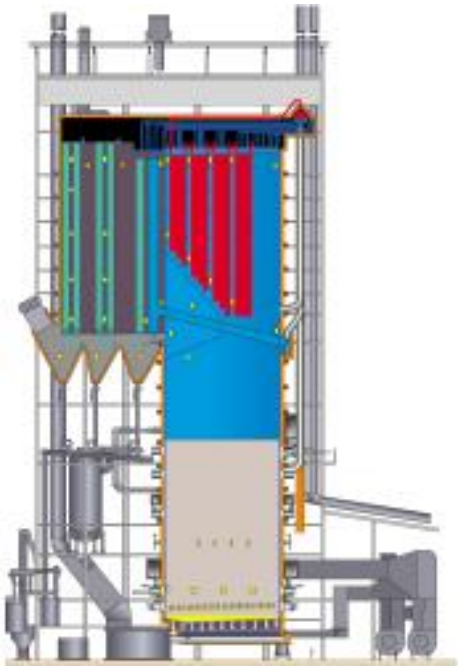

Figure 7. Sideview of a recovery boiler manufactured by Valmet.

5.1 Furnace Wall Tubes

Visual inspection is the most important method to start the inspection due to corrosion damage. Uneven surface, craters and non-typical deposits can be signs of corrosion. To verify the wall thinning the most common method is **traditional UT**. Typically measurement lines are defined and they are measured year after year thus following the development. This gives a good knowledge and understanding of possible corrosion and even possibilities to predict the future, provided that the boiler operation and fuel remains the same. The restriction of the method is that the inspected area is narrow and surface preparation is needed (grinding). There had been cases where the corrosion has been outside the anticipated area. To get the information of the whole furnace **T-Scan** technique can be applied since it enables scanning the whole furnace without thoroughly cleaning the boiler. The opening tubes and discontinuities should be inspected with **manual EMAT** or traditional UT. T-Scan has been applied to many boilers all around the world for both recovery and power boilers, see figure 8.

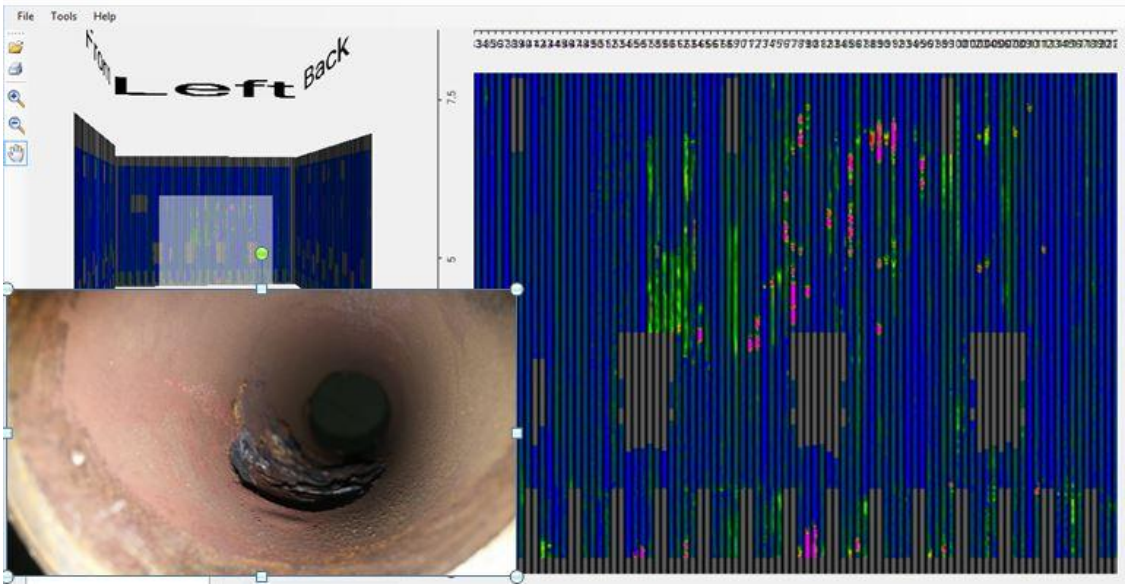

Figure 8. C-Scan 3D image of T-Scan results from a boiler with local wall thinning (red areas) from the water side and a picture of a sample tube.

Other techniques for furnace wall tubes are **SLOFEC** which is good scanning method for detecting pitting corrosion, see figure 4**. Liquid penetrant** or **magnetic particle** testing is often carried out for opening tubes for detecting cracking phenomena. **Digital X-ray** may be used to detect hydrogen attack by finding internal deposits and local wall thinning associated with it. The final verification of hydrogen attack, however, needs to be done by **metallographic analysis**. Also for detecting the cause and real depth of corrosion damage, grain boundary corrosion, internal deposits or other mechanisms **destructive testing** is needed.

Opening tubes cannot be inspected with T-Scan and they are usually inspected by traditional UT for wall thickness. Also magnetic particle or liquid penetrant tests are used if cracking are suspected at the area. An alternative to UT is manual EMAT, since larger areas could be easily detected as grinding is not needed before testing.

One special location in recovery boilers is the **Non-alloy steel and composite tube change line.** The best way to inspect this is visually. Since the occurrence is very local on the non-alloy steel side and the weld disturbs different techniques, the depth is very challenging to measure accurately. Traditional UT or slide gauge may be applied.

5.2 Floor tubes in recovery boiler

Recovery boiler floor tubes are usually inspected with traditional **UT** for wall thinning. The special feature of recovery boiler environment and materials creates a need for inspection also for cracking. This is usually carried out by **liquid penetrant testing.** However, the method needs careful cleaning of the surfaces before inspection. Advanced techniques may be applied here as well. With **array eddy current** recovery boiler floors can be scanned with less cleaning. A special measurement probe has been developed for separately floor tubes and fins, see figure 2. The indications produced by this technique are verified with liquid penetrant testing. A lay out picture of findings with hyperlink to crack photograph can be produce to help quickly visualize the extent of damage, see figure 9. The technique is fast compared to only PT testing and thorough cleaning was only done for the locations where array ET gave a signal.

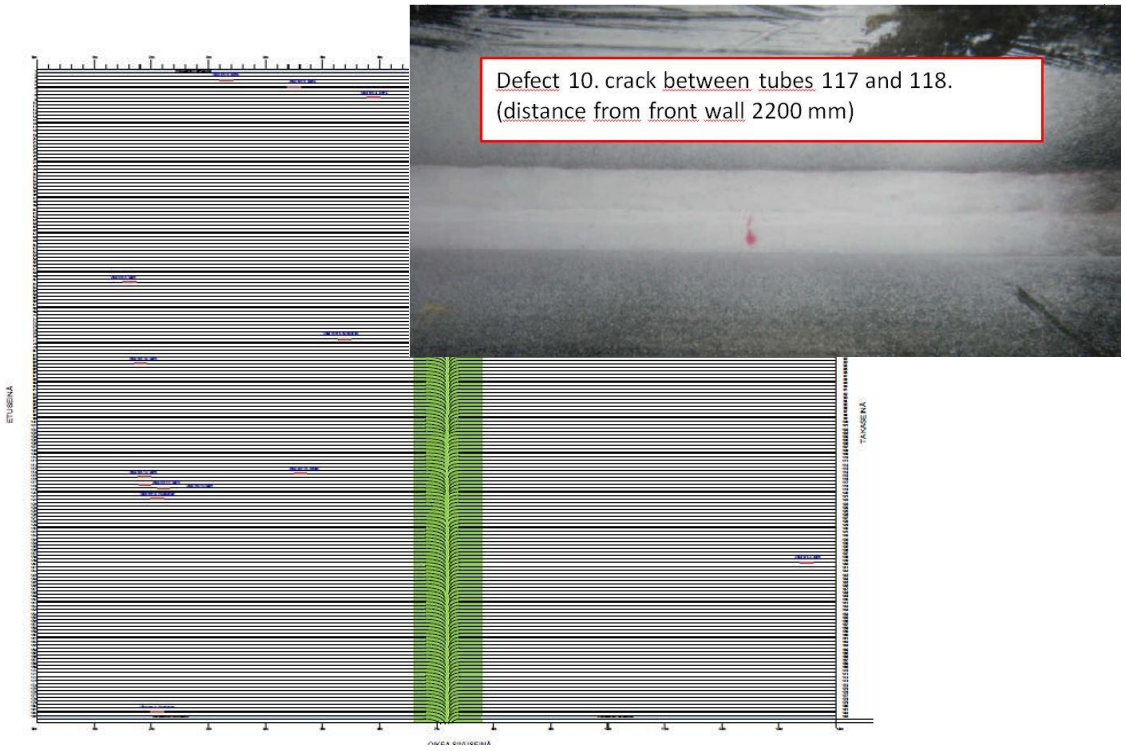

Figure 9. Map of detected defects with array ET and example of a crack verified by PT.

5.3 Superheaters

In superheater area **visual inspection** and **traditional UT** are widely used for pre-set locations – typically lower bends and areas near the sootblowers. **Manual EMAT** could be applied here to increase the inspected area. **T-Scan** has also been modified to inspect the whole length of horizontal superheaters. However, this has been only applied to the top and bottom row of superheater due to restriction of space. Internal oxide layers can be detected with special UT if the oxide scales are thick enough.

Every now and then a **metallographic examination** for sample tubes may be needed to examine the cause and real depth of corrosion damage, grain boundary corrosion, internal deposits or other mechanisms. As superheater is the hottest component in boiler also the aging of tube material is recommended to be checked at the same time.

6. Conclusions

Controlling the corrosion in boilers means in an ideal case prevention of corrosion or keeping the corrosion rate in acceptable level. Usually this is taken into account when designing the boiler for certain fuel and capacity; selecting materials, setting temperatures, possibly using additives in fuels etc. However, in real world this is not always the case since there might be changes in process and fuels that had not been anticipated. In any case, it is important that at least the corrosion rate of critical components can be predicted in order to plan the maintenance and major repairs.

With the help of traditional and advanced NDT-techniques the corrosion rate can be followed and ensure that unpleasant surprises are not developing without noticing. As the time for shutdowns is limited advanced techniques can be applied to efficiently get the inspection data needed. Then combining the information from NDT-inspections, knowledge of different corrosion mechanisms and examined tube sam-

ples the reason for excess wall thinning can be found – fuel, air-distribution, increased temperatures, water chemistry etc. This information is needed to find a solution how to control the lifetime of the boiler.

References

1. Salmenoja, K. Field and Laboratory Studies on Chlorine-induced Superheater Corrosion in Boilers Fired with Biofuels, Academic Dissertation, Åbo Akademi, Turku, Finland, 2000.

2. Mäkipää, M., Pohjanne, P. Review of recovery Boiler Superheater Material Studies, International Recovery Boiler Conference, Tampere, Finland June 11th, 2014.

3. Enestam, S. Corrosivity of hot flue gases in the fluidized bed combustion of recovered waste wood, Academic Dissertation, Åbo Akademi, Turku, Finland, 2011.

4. Bankiewicz, D. Corrosion behaviour of boiler tube materials during combustion of fuels containing Zn and Pb, Academic Dissertation, Åbo Akademi, Turku, Finland, 2013.

5. Huijbregts, W. M. M., Janssen, J. B., Rens, O. C. J. Corrosion in Low NOx Firing Conditions, Power-Gen –'98, Milan, Italy, June 9-11, 1998.

6. Hupa, M., Recovery Boiler Research Highlights – 10 Step Forward, International Recovery Boiler Conference, Tampere, Finland, June 11th, 2014.

7. Saarinen, P., Hänninen, H., Tuiremo, J., Salmi, K. The Inner and Outer Surface Cracking of the Recovery Boiler Floor Tubes, Tappi Engineering Conference, Atlanta, USA, September 17-21, 2000

8. Haaga, K. XXL Recovery Boilers – How We Developed Them, International Recovery Boiler Conference, Tampere, Finland June 11th, 2014.

9. Tuiremo, J., Salmenoja, K., Control of Superheater Corrosion in Black Liquor Recovery Boilers, 10th International Symposium on Corrosion in the Pulp and Paper Industry, (10th ISCPPI), Helsinki, Finland, 21-24 August, 2001.

10. Tuiremo, J., Enestam, S., Hupa, M., Superheater Corrosion at Temperatures Below Deposit First Melting Temperature, Tappi Engineering Conference, Memphis, USA, October 11-14, 2009.

11. Port, R. D., Herro, H. M. The Nalco Guide to Boiler Failure Analysis, McGraw-Hill, Inc., USA, 1991.

Comparison of Laser Clad Coatings Under Simulated 100%Biomass Firing Conditions

A T Fry[1],D G Gorman[1]

[1]National Physical Laboratory

Hampton Road, Teddington, Middlesex, TW11 0LW, UK

Abstract

Pulverised fuel (PF) firing of biomass is becoming increasingly important to meet legislative targets to reduce net carbon emissions within the power generation sector. Although co-firing of biomass with coal in PF combustion systems has become relatively common, particularly at low levels, it is rare for PF combustion systems to be fired on 100% biomass, with just a handful of plants worldwide in operation and in all known cases there has been little information published regarding the success of these conversions or the extent of any negative impacts on the boilers. As part of a recent Innovate UK project (ASPIRE), a number of laser clad and HVOF coatings have been subjected to laboratory and plant exposures with the aim of developing understanding and data on the relative performance of candidate coatings under 100% biomass firing conditions. This paper provides a qualitative account ofthe relative performance of FeCrAl, NiCr and NiCrAlY coatings during exposures designed to simulate the combustion of eucalyptus and wood.

1. Introduction

There exist many projections on future global energy demand based on a wide range of assumptions. However, recent predictions made by the International Energy Authority (IEA),published in 2015, suggest that the global energy demand will continue to grow by nearly one-third between 2013 and 2040[1]. The decarbonisation of the energy industry continues in the UK in an attempt to reduce emissions of CO_2 and other greenhouse gases (GHGs). For power generation systems, there are several potential routes to reduce CO_2 emissions (all of which have both advantages and disadvantages) that are being developed, these include increasing the efficiency of plant by increasing steam temperatures and pressures, increasing the use of biomass firing and co-firing, carbon capture and storage and through increased use of renewables[2].Over recent years, the rise in renewables has been unprecedented in the UK, but with government subsidies and incentives coming to an end, the rate of installation is likely to slow. Whilst there has been an increase in renewable sources, there remains a role in the UK energy portfolio for more traditional forms of power generation to provide grid balancing and energy security to underpin the increased use of renewables. There is a growing appreciation that biomass combustion has an important role to play in the future energy market and consequently 100% fired boilers or lowlevel co-firing boilers are of interest to the industry. A report by the Environment Agency compares the greenhouse gas

emissions from a range of biomass fuels and discusses the implications of land use, transport cost and production routes on the net carbon emissions[3]. When considering the reduction in emissions it is important to consider the whole lifecycle of the fuel, this subject is beyond the scope of this paper, suffice to say that by choosing the best biomass fuel with the lowest carbon overhead, in terms of production and transport, significant reductions in emissions can be made, as shown in Figure 1.

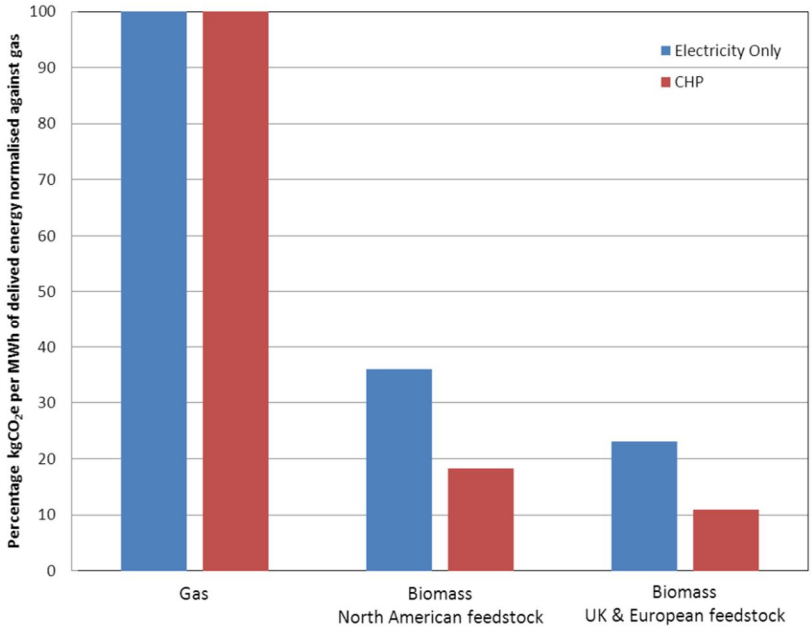

Figure1. Comparison of emission from biomass normalised against a gas turbine [3].

Whilst the co-firing and firing with biomass clearly has the potential to lower emissions, there are implications to the materials used within the boiler due to the potential for increased levels of fireside corrosion due to changes in the flue gas composition and chemistry. Fireside corrosion occurs as the name implies at the interface between the furnace/tube walls and the gaseous and molten and/or solid combustion products. This form of high temperature corrosion is a major threat to the integrity of boiler materials. This form of corrosion has been fairly well characterised in the past, with the principle impurities responsible for the accelerated corrosion being identified as chlorine, sulphur, sodium and potassium.

There are two main regimes within the boiler where fireside corrosion occurs, namely at the furnace wall, where the gas temperature in the furnace can be above 1500 °C and the tube metal temperature in normally maintained below 450 °C; and in the Superheater and Reheater zone, where the metal temperature maybe 650 °C [4].

Fireside corrosion of Superheaters and Reheaters in coal-fired boilers occurs as a result of the deposition of alkali metal sulfates on to the tubing surfaces. With surface metal temperatures in excess of 550ºC, the alkali metal sulfates such as sodium and potassium sulfate can lead to the formation of molten alkali iron trisulfates [$(Na,K)_3Fe(SO_4)_3$], shown schematically in Figure 2. These are generally stable over a fairly limited temperature range determined by the ratio of sodium to potassium. Once formed, the molten trisulfate dissolves the normally protective oxide scale formed on the tubing. The scale dissolved in the melt diffuses away from the metal surface into the hotter region of the ash where the melt becomes thermodynamically unstable, releasing the iron to form porous, un-protective iron oxides[5,6]. The mechanism sets up a continual transport of iron and sulphur leading to rapid metal loss and the recycling of the active corrodent species.

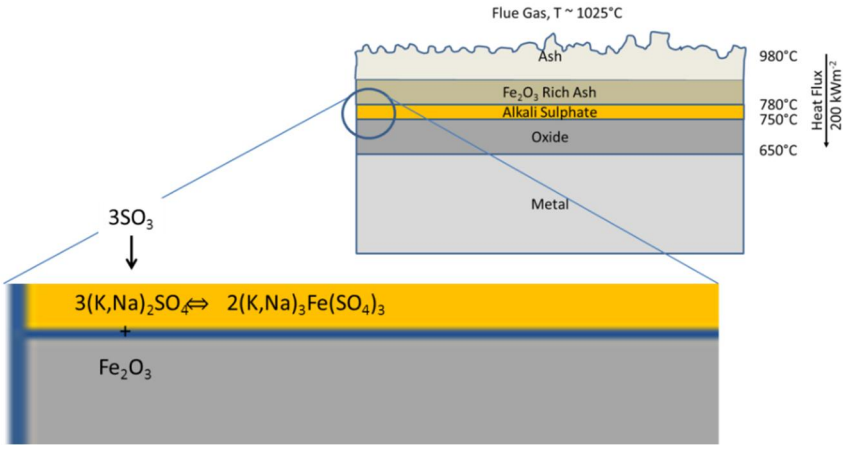

Figure 2. Schematic showing the corrosion mechanism associated with superheaters and reheaters.

There exists a wide range of fuels that are being considered for use in biomass co-firing energy generation, consisting of specifically cultivated biomass crops such as coppiced willow and miscanthus, waste biomass like straw, wood waste and forest residues, and world traded biomass products such as palm nut residue, olive residues and cereal co-product. Such a range of biomass will inevitably have a wide range of combustion properties, emission characteristics and implications for fireside corrosion. In general biomass contains less sulphur than coal, but often has increased levels of chlorine. Figure 3 shows the range of sulphur and chlorine generally found in world traded coal and biomass[7].

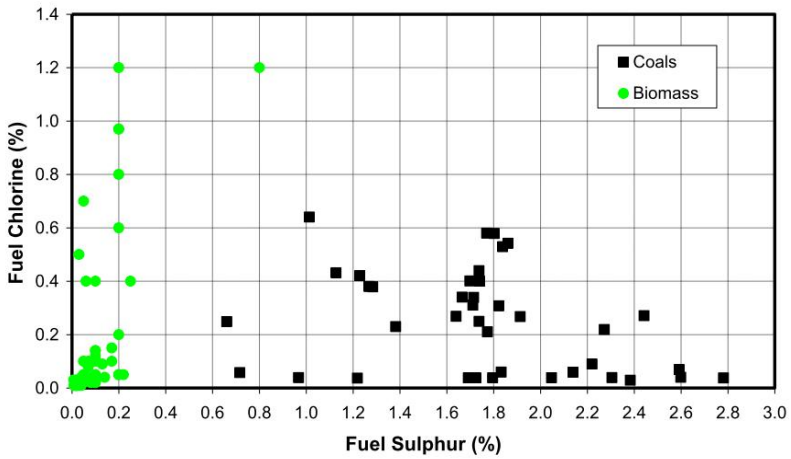

Figure 3. Variation of fuel chlorine and sulphur contents for a range of biomass and coals[7].

Although co-firing of biomass with coal in Pulverised Fuel (PF) combustion systems has become relatively common, particularly at low levels, it is rare for PF combustion systems to be fired on 100% biomass, with just a handful of plants worldwide in operation and in all known cases there has been little information published regarding the success of these conversions or the extent of any negative impacts on the boilers. PF firing of biomass may raise several technical challenges such as flame stability and burnout, ash deposition and corrosion. A number of these issues are linked to the inorganic constituents of biomass. Compared to coal, biomass is characterised by a relatively large content of inorganic elements that are easily vaporised during combustion, these released elements – particularly the alkali metals and chlorine, may form compounds that lead to boiler tubing fireside corrosion. With higher metal temperatures it becomes possible for the sulfatic deposits to become molten and begin to dissolve or flux the normally protective corrosion scales.

Chloride-containing ash phases can be deposited with the ash on to boiler tubing. These usually take the form of alkali or heavy metal chlorides. At relatively low temperatures these may be in solid form and serve to moderately increase the corrosion rate through increasing the concentration of chlorine in the environment local to the tube surface. In this case, the chlorides inhibit the growth of the desired dense and protective oxide corrosion scale that would otherwise form on the tube surface. The scale formed in these circumstances is less dense, more defective, mechanically weak and does not provide an effective diffusion barrier to limit further corrosion damage. Coupled with high gas velocities this leads to the phenomenon of corrosion-erosion in which the mechanically worn scales are easily removed and carried away by the gas stream revealing fresh, un-protected metal to be corroded by the aggressive combustion environment.

At higher tube metal temperatures, the alkali or heavy metal chloride ash deposits can be molten. In this instance, the corrosion rates can be dramatically increased as the molten ash deposits actively dissolve the protective corrosion scales that would ordinarily have formed on the tube surface. This effectively removes any diffusion barrier that might have existed between the tube metal and the combustion environment, allowing free access for the corrosive environment to interact with the bare tube metal. Such molten chloride attack can result in catastrophic wastage rates (>200nm/h) causing tube failures in less than one year of operation.

The purpose of this work and the results reported herewith was to determine the effectiveness of different coatings to the protection from corrosion caused by biomass combustion. Within the work programme ASPIRE, HVOF and laser clad coatings were evaluated for two different fuels at two different temperatures. The work reported here focuses on the laser clad coatings at 650°C.

2. Method

2.1 Experiment Setup

Two biomass fuel compositions were chosen to simulate the firing of both eucalyptus, a relatively clean fuel with low HCl, and waste wood, a potentially dirty fuel with high HCl. The fuel analysis is shown in Table 1 and the ash analysis in

Table **2**.

Table 1. Fuel analysis, dry, ash free (weight %)

	C	H	N	S	Cl	O
Wood (yard waste)	51.93	5.61	1.06	0.30	0.38	32.21
Eucalyptus	50.28	6.17	0.29	0.01	0.03	43.20

Table 2. Ash matrix (weight %)

	Al_2O_3	BaO	$CaCO_3$	Fe_2O_3	K_2O	MgO	Na_2O	P_2O_5	SiO_2	TiO_2	MnO	CaO	SO_3
Wood (yard waste)	3.1	-	-	2.0	3.0	2.2	1.0	2.0	56.7	0.3	-	23.8	2.5
Eucalyptus	8.9	0.2	25.6	6.0	12.0	6.9	3.0	2.9	21.1	0.4	2.0	-	-

An isothermal test campaign was initiated using a fixed chemistry deposit of KCl and K_2SO_4 (2:1 by weight) and a flowing simulated combustion gas consisting of 15ppm SO_2, 13.6% O_2, 16.7% CO_2, Bal N_2 + Low HCl (3wt %). The HCl was added to the gas mixture by bubbling the dry N_2through acid/water saturators maintained in a thermostatic water bath at 63°C, this is shown schematically inFigure 4. The

concentration of HCl could be adjusted so as to produce the required vapour pressure at 63 °C given a gas flow rate of N_2 at 23 ml/min.

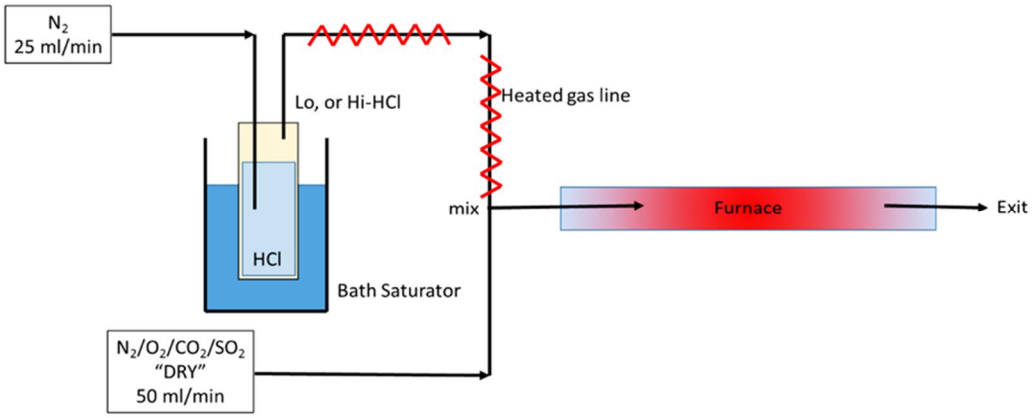

Figure 4. Schematic of the HCl/water vapour delivery system for the isothermal furnace exposures.

Samples were manufactured by applying the laser clad coatings to lengths of Super 304H tubing. Exposure coupons were then cut from the coated tubes by spark machining the coupons as schematically shown in Figure **5**.

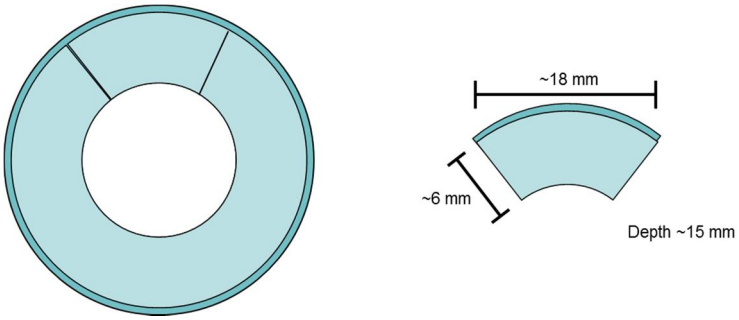

Figure 5. Schematic showing the dimensions of the coated samples used in the isothermal exposures.

The isothermal tests were conducted at 450 and 650 °C using simulated conditions as described previously. Tests were conducted for 1000, 2000 and 3000 hours with the deposit being replacedevery 250 hours. For the purposes of this paper only the tests at 650 °C will be considered. The deposit was prepared and mixed with propanol and pipetted onto the coupons surface. If necessary, further drops of propanol wereused to disperse the deposit. The propanol was then allowed to evaporate. Any excess salt was brushed from the edges of the coupons to reduce the substrate attack and to avoid undercutting of the coating. Figure 6 shows a selection of samples with the salt deposit applied. Once prepared, the alumina boat was positioned in the hot zone of the preheated tube furnace at 150 °C. The furnace was then subsequently sealed and the exposure cycle initiated.

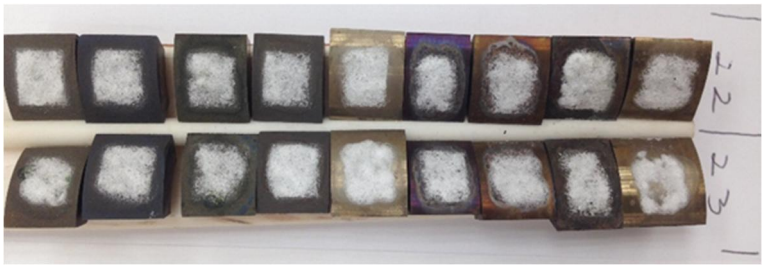

Figure 6. Example of samples with deposit applied.

After each250 hour interval,the furnace was cooled to 150 °C and the samples removed and allowed to cool to room temperature in air. Once cool the samples were weighed, lose deposit brushed off and reweighed before having new deposit applied and the final mass recorded prior to the next exposure cycle. On exposure of the samples to elevated temperatures, it was often observed that regions of the loose KCl and K_2SO_4 deposit became fused to the sample surface making removal difficult during the weighing phase. If it was not possible to remove a region of fused deposit by brushing alone they were left on the sample.

After a number of predetermined exposure cycles, the samples were cut and mounted in a conductive polymer before being polished using diamond suspensions up to a 0.25 micron finish. To avoid leaching of any water soluble chlorides during sample preparation both cutting and polishing phases were performed using nonaqueous diamond suspensions and lubricants and cleaned using ethanol. After the samples had been polished they were carbon coated and stored in desiccator cabinets. Uncoated samples left for longer than a couple of days in humid atmospheres required their final polishing phases to be repeated as corrosive products were observed to be evolved from the salts within the oxidation region, which, subsequently wetted and etched the polished surface. The carbon coating also provided a conductive layer to prevent charging of the samples during the analysis phase. The analysis was performed on cross-section micrographs using a scanning electron microscope (SEM)fitted with an energy dispersive x-ray spectrometer (EDS)to allow for imaging and relative chemical distribution mapping respectively.

2.2 Materials

The purpose of these exposures were to generate understanding of the corrosion mechanism and rates for potential coatings to mitigate against fireside corrosion in biomass combustion. Within the ASPIRE project,a number of different coating chemistries were investigated using two different coating methodologies, laser cladding and high velocity oxy-fuel (HVOF) coating, however,for the purposes of this paper only laser clad FeCrAl, NiCr and NiCrAlY coatings are discussed. The compositions of the three coatings under investigation and that of the substrate are presented in Table 3.

Table 3. Coating name and composition.

Material Name	Composition, Wt% (from EDS analysis)									
	Fe	Ni	Cr	Al	Si	Mn	Nb	Cu	Y	Trace*
FeCrAl	70.5	2.3	20.5	3.5	1.2	0.8	-	0.7	-	-
NiCr	10.5	42.7	42.9	-	3.6	-	-	-	-	-
NiCrAlY	18.34	44.6	20.6	13.1	-	-	-	-	0.5	-
Substrate S304H	68	10.5	19	0.003	0.3	1	0.6	3.5	-	P, S, B, W

* Nominal composition form literature, values below EDS detection limit

Laser cladding makes use of the high energy densities achievable using modern laser technology to melt metallic powders with a portion of the substrate thus creating a region of bonded coating material. Figure 7

shows a simple schematic of the laser cladding process detailing the formation of a clad layer, bonding zone and a heat affected zone.

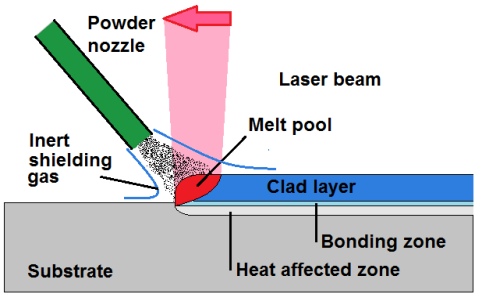

Figure 7. Schematic representation of the laser cladding process.

The samples featured in this paper were cut from sections of laser clad tube. Laser cladding of the external surface of the tubes prior to sectioning was performed with a stationary coating assembly by rotating the tube. To ensure continuity of the coating, successive passes of the beam are overlapped, consequently, slight variations in coating thickness are observed undulating along the length of the tube. To homogenise the surface finish across all samples the tubes, once clad, were ground on a lathe. Although grinding of the tubes after laser cladding resulted in a consistent OD the undulating boundary of the clad layer and bonding zone still resulted in a varied coating thickness making metal loss measurements problematic.

3. Results& Discussion

3.1 Deposit

Figure 8showsa cross-section through a region of deposit that formed on NiCr exposed for 3000 hours at 650°C in a high chlorine environment. Potassium is common throughout the deposit but a distinction can be made between the KCl and K_2SO_4 from the chlorine and sulfur concentration. The chromium EDS map also shows the presence of chromium within the sulfur-rich regions of the deposit suggesting presence of a chromium potassium sulfate compound.

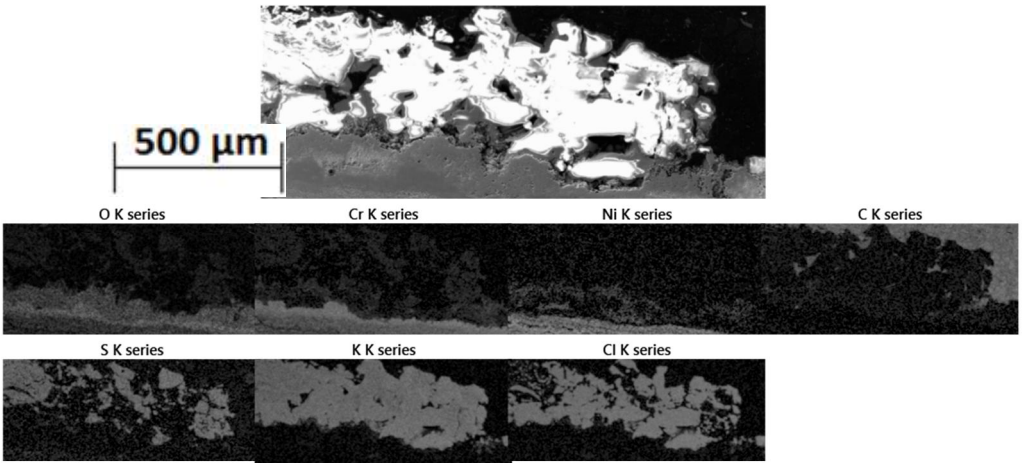

Figure 8. Low mag images of laser coated NiCr exposed to a) simulated eucalyptus (low HCl) and, b) simulated wood (high HCl) combustion atmospheres for 3000 hours at 650 °C.

Upon completion of the test the exposure furnace and acid delivery system was disassembled and visually inspected revealing significant attack of the heated316 tubing that supplied acid/water vapour to the

furnace. 316 resists chemical attack by forming chromium(III) oxide, it is conceivable that some chromium was introduced into the gas stream from this source. It is, therefore, uncertain whether or not the chromium present within the deposit was supplied solely by the underlying alloy.

3.2 FeCrAl

Heavy spallation of both the substrate and coating made deconvolution of the mass change data pertaining to coating performance difficult. Consequentially a qualitative approach has been adopted making use of SEM and EDSanalysis. The OD of the tubing was ground prior to sectioning into coupons and subsequent exposure which resulted in a smooth curved face. Figure 9 shows a cross-section of the FeCrAl coating after exposure to both high and low HCl concentrations.The observable departure from the original smooth face is indicative of material loss, corroborating the observation of scale spallation during the test.

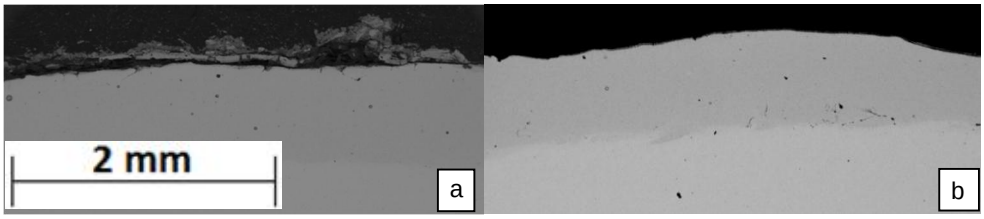

Figure 9. SEM micrographs of cross-sectioned laser clade FeCrAl exposed to a) simulated eucalyptus (low HCl) and, b) simulated wood (high HCl) combustion atmospheres for 3000 hours at 650 °C.

Figure 10 shows the oxide scale which formed on FeCrAl coating after exposure to eucalyptus simulated atmospheres for up to 3000 hours. At 1000 hours a thick layer of K_2SO_4 can be observed to have fused to a thin layer of chromia. The chromia exhibits a laminated structure with successive layers being lifted off of the alloy and incorporated into the K_2SO_4. The mechanical interlocking between the chromia layer and the potassium sulphate explains the tendency for the salt to become fussed to the alloy surface. The fused layer of potassium sulfate may have acted as a barrier for the direct access of potassium chloride to the oxide surface. After 2000 hours of exposure the outer layer of oxide has been further incorporated into the potassium sulfate with a thicker more dense oxide has formed underneath. The dense oxide exhibited numerous laminar voids. Some internal attack is also observed within the alloy. The 3000 hour exposed coupon featured a thick oxide scale with a large cavity separating it from the alloy. The lack of any observable oxide layer on alloy surface within the cavity suggests that the scale was pulled from the surface during the mounting of the sample. Alternatively volatile chlorides could set up a gas phase bridge across the cavity. The oxide scales of the coupons exposed in the high HCl environment for both 2000 and 3000 hours detached whilst being prepared for analysis suggesting that the scale is poorly adhered and increasing the HCl increases the likelihood of spallation. Furthermore, portions of thick oxide scale can be observed within the fused potassium sulfate in Figure 10c suggesting that the coupon had undergone prior spallation events.

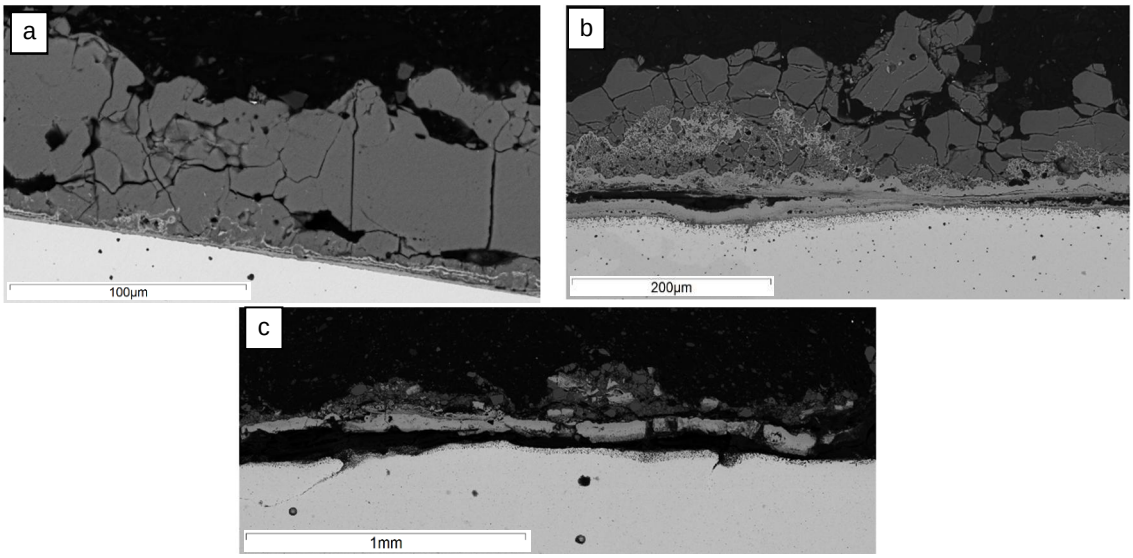

Figure 10. SEM micrographs of laser clad FeCrAl exposed to simulated eucalyptus combustion atmosphere at 650 °C for a)1000, b) 2000 and c) 3000 hours.

Figure 11 shows an EDS map of the cross-sectioned oxide scale of the low-HCl exposed sample. The majority of the external scale was comprised of iron oxide with a thin discontinuous band of chromium and aluminium on its outer surface and a slightly thicker but similarly discontinuous chromium rich band on its inner surface. Some nickel oxide was also observed on the inner surface of the oxide scale. The alloy surface features a region of nickel enrichment which is severely denuded of chromium and aluminium and exhibits an iron-rich internal oxide up to a depth of ~30 µm.

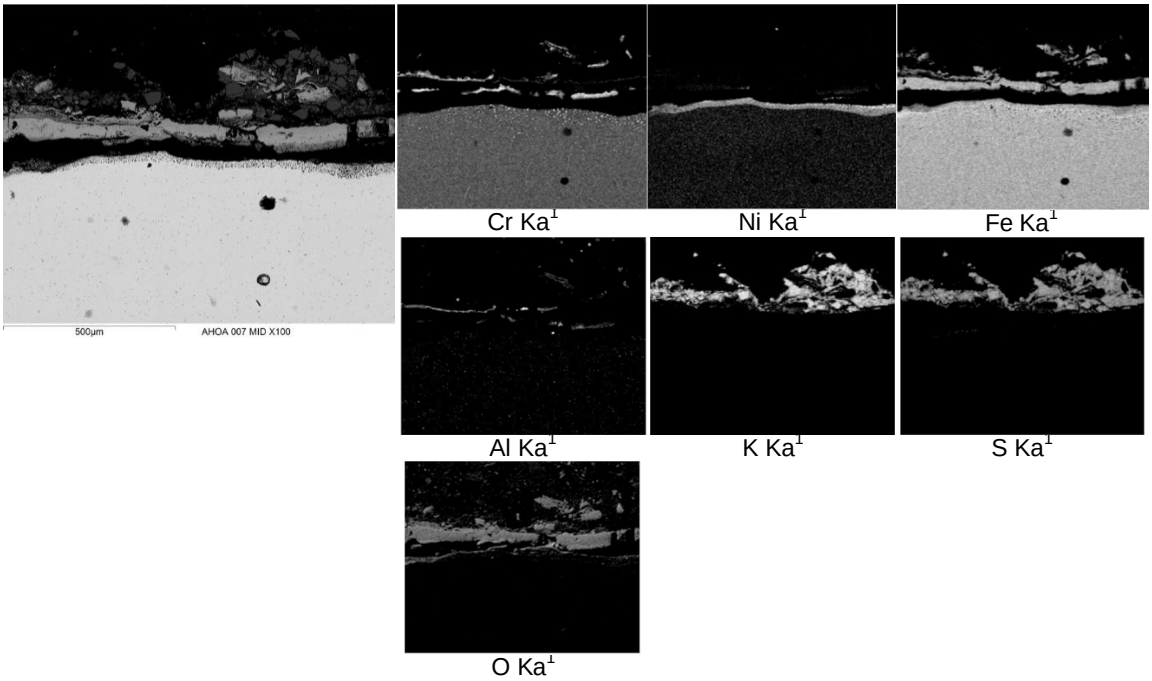

Figure 11. EDS analysis of the laser clad FeCrAl coating exposed to simulated eucalyptus combustion atmosphere for 3000h at 650 °C.

Figure 12provides EDS spot analysis showing that small amounts of chlorine were observed to have penetrated the scale and were associated with the regions of internal attack.

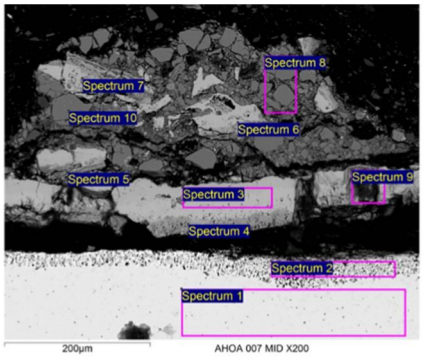

Spectrum	In stats.	O	Mg	Al	Si	S	Cl	K	Ca	Cr	Fe	Ni	Cu	Mo	Total
Spectrum 1	Yes	0.84		4.32	0.66					21.52	69.00	2.87	0.80		100.00
Spectrum 2	Yes	6.82	0.27	1.27	2.03	0.33	0.07		0.11	3.60	67.53	16.21	1.76		100.00
Spectrum 3	Yes	25.25		0.13	0.10			0.14		1.63	71.92	0.82			100.00
Spectrum 4	Yes	29.04		8.11	1.37		0.24	0.13		54.43	6.30	0.13		0.25	100.00
Spectrum 5	Yes	36.99		14.58	0.94	5.68		21.45		13.16	5.84	0.43	0.93		100.00
Spectrum 6	Yes	24.87		0.13				0.13		3.72	71.15				100.00
Spectrum 7	Yes	28.94		0.36	0.15	2.77	0.08	6.60		36.81	24.17	0.12			100.00
Spectrum 8	Yes	31.47	0.11		0.16	19.60		47.02		0.87	0.78				100.00
Spectrum 9	Yes	20.30	0.74	1.54	3.49			0.21	0.19	2.73	69.30	1.51			100.00
Spectrum 10	Yes	30.13			0.06	20.07		49.09		0.38	0.27				100.00

Figure 12. EDS analysis of the laser clad FeCrAl coating exposed to simulated eucalyptus combustion atmosphere for 3000h at 650 °C.

3.3 50:50 NiCr

The NiCr coating did not spall, developing instead a thin external oxide with regions of deep internal attack. Figure 13 shows low magnification SEM micrographs of the high and low HCl exposed coupons after 3000 hours at 650 °C. The smooth outer surface, when compared to the FeCrAl coating, is indicative of less material loss. The large fissures observable in Figure 13bwere pre-existing defects introduced during the cladding process. A layer of fused potassium sulfate can be observed to cover both coupons. Figure 13b also exhibits lightly contrasted regions above the potassium sulphate which were confirmed using EDS to be potassium chloride. The potassium chloride is prevented form coming in physical contact with the oxide by the potassium sulfate layer.

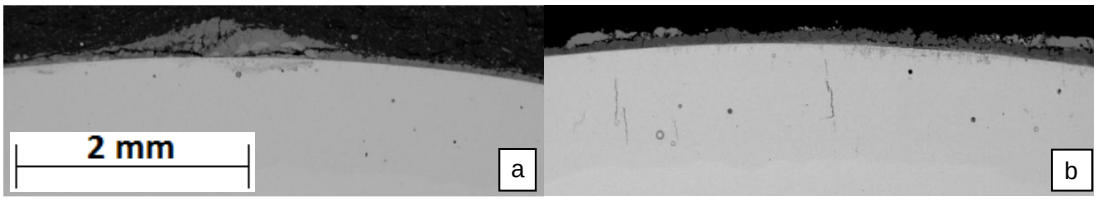

Figure 13. Low mag images of laser coated NiCr exposed to a) simulated eucalyptus (low HCl) and, b) simulated wood (high HCl) combustion atmospheres for 3000 hours at 650 °C.

Figure 14 shows the oxide scale which formed on the NiCr coating after exposure to eucalyptus simulated atmospheres for up to 3000 hours. The scale morphology after 1000 hours is similar to that observed on the FeCrAl coating with the addition of minor internal attack. After 2000 hours the oxide scale exhibits two distinct regions consisting of an outer porous region that has been incorporated into the potassium sulfate and an inner dense layer featuring some laminar voids observable both at the alloy/scale boundary and within the oxide scale. Internal attack is observed which tended to intrude into the coating along preferred

paths. The extent of the internal attack was not homogenous across the surface instead exhibiting regions of enhanced ingress. The laser cladding process is knows to produce regions of dissimilar grain structure, some of which can form large columnar grains. It is conceivable that the preferred paths exhibited by the internal attack were grain boundaries and the inhomogeneous rate of ingress was a consequence of dissimilar grain structures. The 3000 hour exposed coupons were similar to the 2000 hour exposed coupons with the addition of thick oxide scale associated with regions of extensive internal attack. The thick oxide scale had a tendency to become detached though it is unclear whether this occurred during the exposure cycles or during post exposure sample preparation.

Figure 15 provides EDS maps of the scale and underlying alloy and confirms that the external oxide scale comprises of chromia and the regions of internal attack are associated with chlorine. The EDS maps also show that the internal chloridation is associated with a chromium depletion region which is accompanied by the relative enrichment of iron and nickel. The enhanced chromium depletion within regions of chloridation is necessary to form the thick oxide observed on the 3000 hour exposed coupons, however, it is unclear whether it is the grain structure that facilitates greater mobility of the chromium or a consequence of the chloridation. The chromium concentration within the depletion zone is independent of depth correlating instead with the presence of chlorides. The average chromium concentration is ~45% of its original value within the alloy.

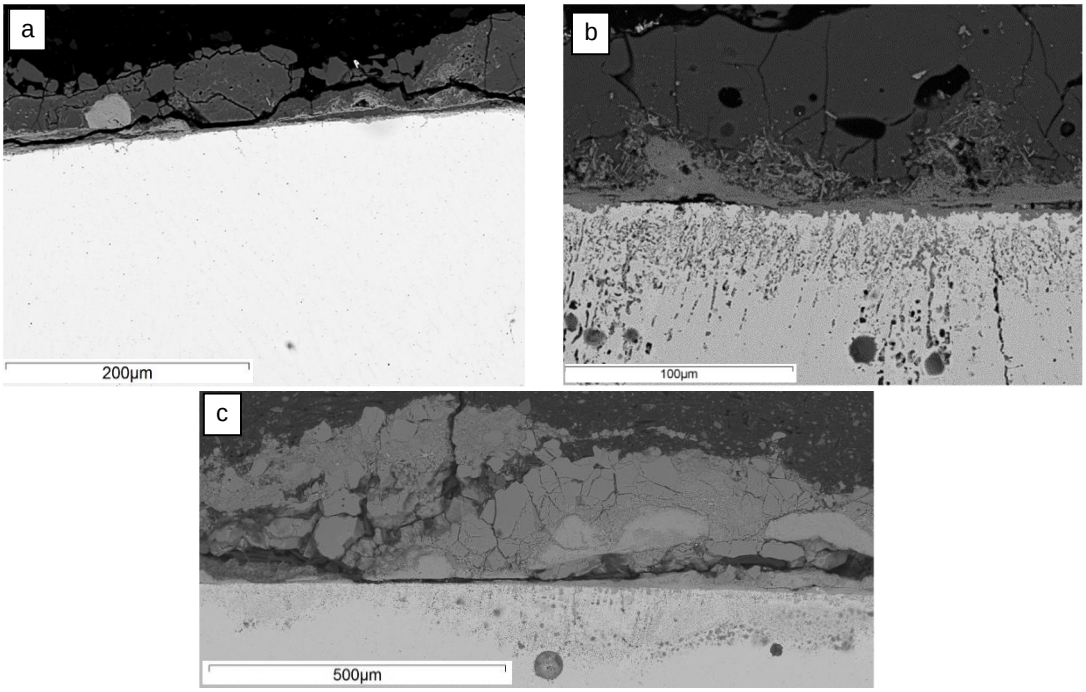

Figure 14 SEM micrographs of laser clad NiCr exposed to simulated eucalyptus combustion atmosphere at 650 °C for a)1000, b) 2000 and c) 3000 hours.

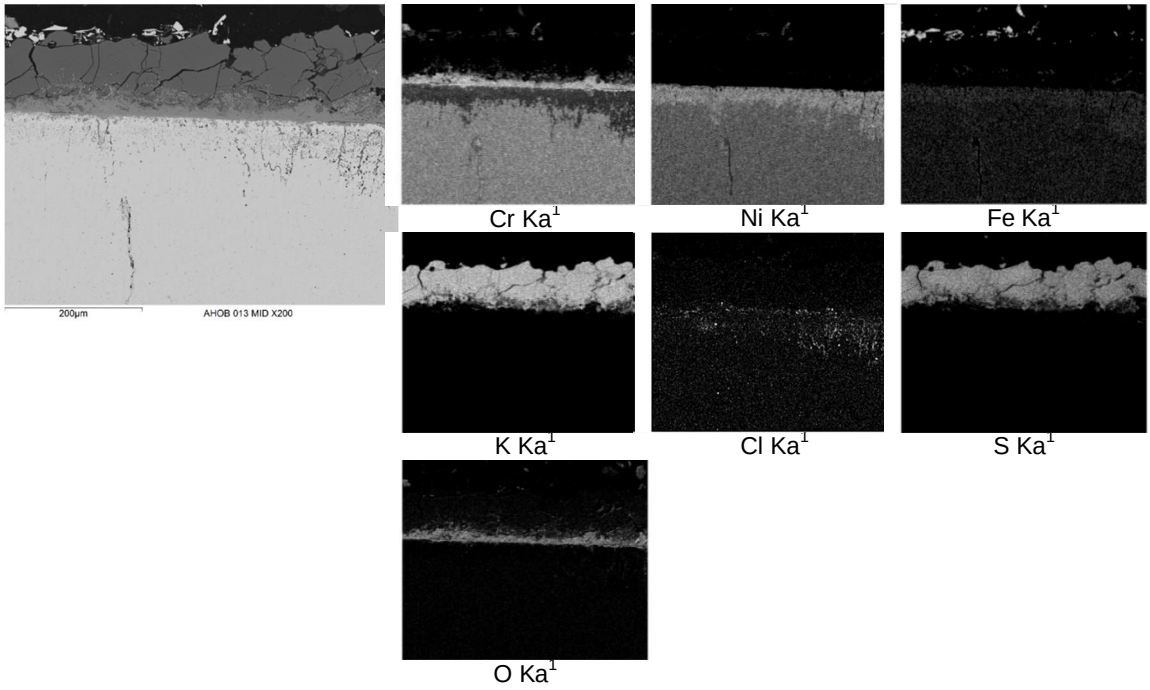

Figure 15.EDS relative chemical distribution maps of laser clad NiCr exposed to simulated wood (high HCl) combustion atmospheres for 3000 hours at 650 °C.

3.4 NiCrAlY

The NiCrAlY coating differed from both the FeCrAl and NiCr coating by the absence of fused potassium sulfate on its outer surface. The absence of potassium sulfate allowed physical contact of potassium chloride with the surface, as observed in Figure 16b, and may have facilitated greater chlorine attack. The coatings exhibited a relatively smooth surface when compared to the FeCrAl coating indicative of less spallation, however, close inspection revealed regions of thick oxide extending inhomogeneously into the coating; most notably for the high HCl exposed coupons.

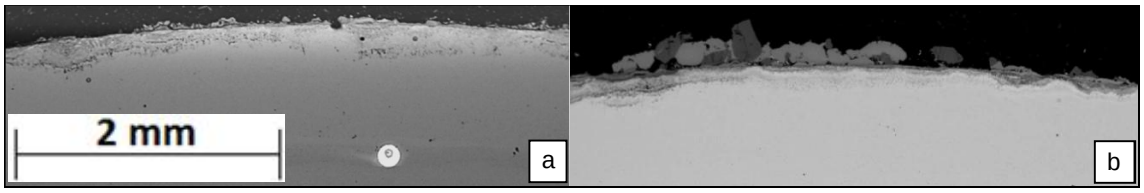

Figure 16. Low mag SEM micrographs of laser clad NiCrAlY exposed to a) simulated eucalyptus(low HCl) and, b) simulated wood (high HCl) combustion atmospheresfor 3000 hours at 650 °C.

Figure 17shows the absence of an outer potassium sulfate layer. The observable oxide scale displays numerous defects and an irregular outer surface, which, in conjunction with the absence of an external scale in regions that do not exhibit enhanced attack suggests that some of the scale has spalled during the post exposure sample preparation.

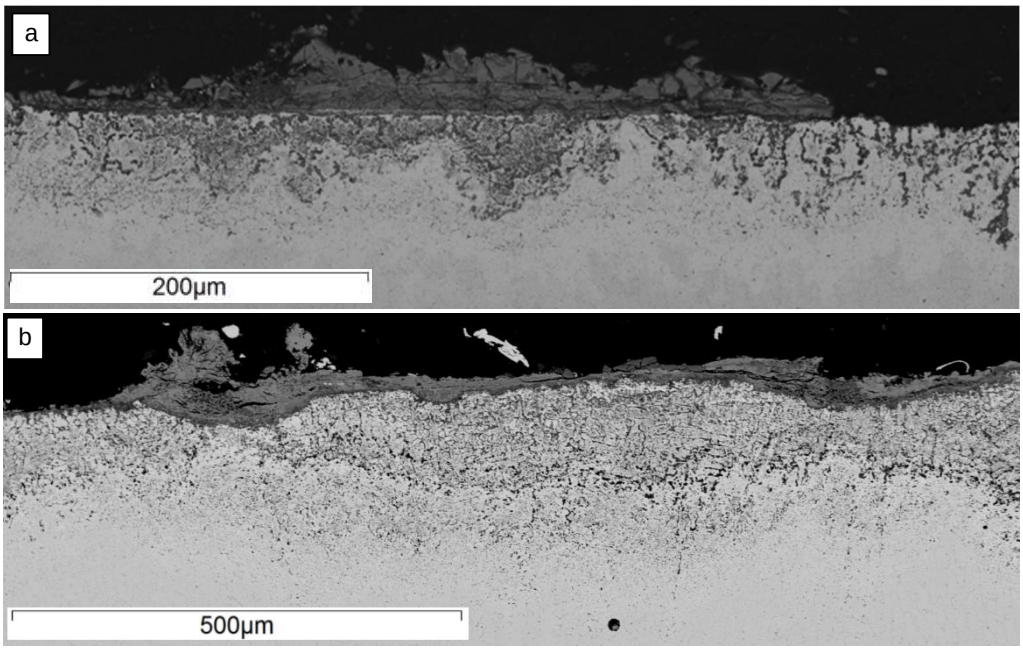

Figure 17. SEM micrographs of laser clad NiCr exposed to simulated eucalyptus combustion atmosphere at 650 °C for a) 2000 and b) 3000 hours.

EDS analysis of the oxidation affected zone for the low-HCl environment shows the outer scale to consist of chromium and aluminium. Yttrium was not observed to play an obvious role in the oxidation process, however, yttrium is known to segregate to the coating surface during the cladding process which was removed during the sample preparationby grinding of the tube exteriors. The internal oxide adjacent to the alloy/scale boundary is comprised of alumina which formed preferentially down grain boundaries. The region underneath the alumina is not associated with oxygen but instead with chlorine featuring a band of chromium chloride over a region or aluminium chloride.

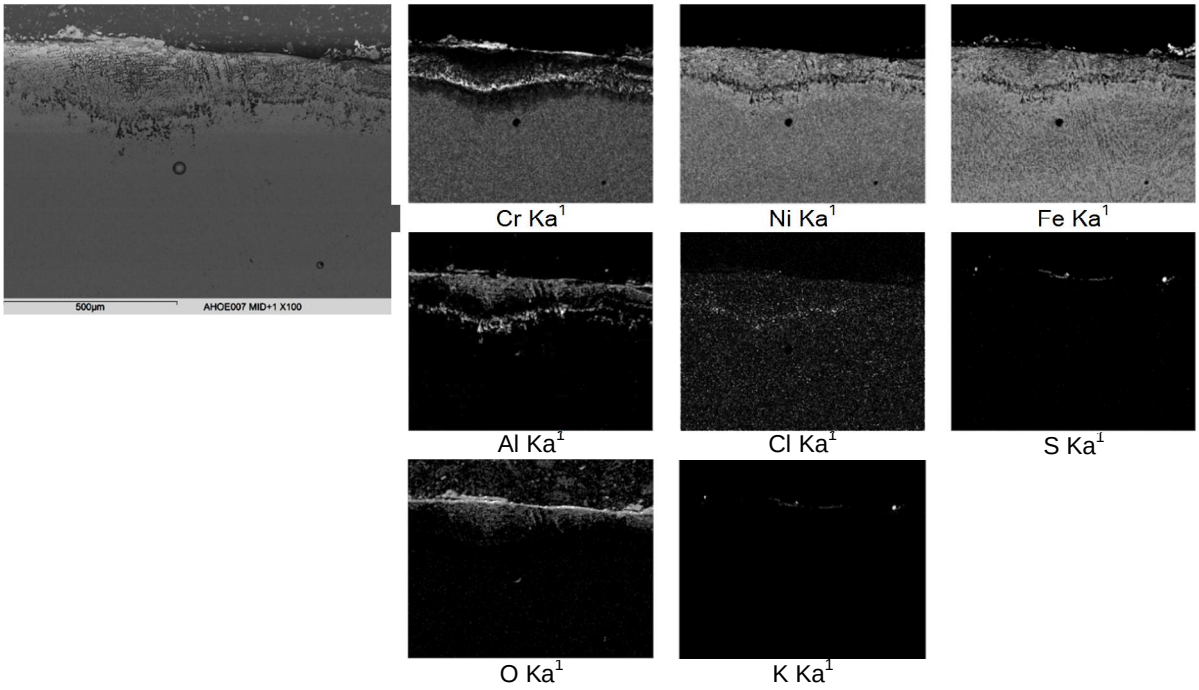

Figure 18. EDS relative chemical distribution maps of laser clad NiCr exposed to simulated eucalyptus (high HCl) combustion atmospheres for 3000 hours at 650 °C.

4. Discussion

Simultaneous oxidation and chloridation has been the subject of work relating to fuel gasification and has shown that upon exposure to HCl in atmospheres with high p(O) both oxides and chlorides form at the alloy surface, these oxides quickly overgrow the chlorides resulting in a continuous oxides scale with chlorides at the alloy/scale boundary [8,9]. Oxides which form under these condition are greatly affected by chloride volatilisation resulting in porous morphologies. The transition from porous morphologies to the more dense protective scales presented in this paper could be attributed to a reduction in chloride concentration at the alloy/scale boundary partially due to internal ingress of chlorine and partially as a consequence of continued scale growth i.e. chlorine could become trapped within the laminar bands of the growing oxide observable after 1000 hours and is thus removed from the alloy/scale boundary. Chlorides may also volatilise and be transported to regions way from the alloy/scale boundary before being oxidised. The formation of internal alumina within the NiCrAlY sample could explain the absence of the laminar chromia bands and resultant fused potassium sulfate layer by facilitating enhanced chlorine migration into the alloy thus reducing chlorides at the alloy/scale boundary. This also has the deleterious effect of enhancing internal attack.

In nickel based alloys chromium diffusion is known to be enhanced down the interphase boundary between the alloy matrix and internal alumina which would result in the observed chromium denuded region beneath the external scale in the NiCrAlY sample. The internal alumina may also potentially facilitate the inward transport of oxygen and chlorine. Chlorine within the alloy reacts with chromium to form a band of chlorides under the internal alumina. As oxidation progresses and the alumina extends further into the alloy the chlorides are destabilised by the rising oxygen potential. The chlorine is then free to migrate further into the alloy. This effectively sets up a reaction front analogues to the external scale consisting of a band of chromium chloride with associated chromium depletion region and sub-band aluminium chlorides. The undulating alloy/scale boundary observed for the high HCl coupon can be attributed to the rapid oxidation of the denuded region associated with the internal aluminium oxide.

5. Summary and Conclusions

All coatings provided a level of protection delaying the onset of spallation and reducing the rate of chemical attack. Differences were observed in coating performance which manifested as both extensive scale formation and subsequent spallation and extensive internal chloridation.

The iron based, FeCrAl, coating initially formed a thin layer of chromia and exhibited minimal internal chloridation, however, after 3000 hours significant spallation had occurred associated with the formation of iron based oxides. The tendency for spallation to occur appeared to increase with increasing HCl concentration.

The NiCr coating arguably provided the greatest protection when comparing the observable scale thickness and internal attack although chlorine was still observed to have penetrated the scale and enhanced chromium diffusion and some mitigating factors must be considered for the NiCrAlY coating.

The NiCrAlY coating formed internal alumina which may have facilitated the transport of chlorine into the alloy resulting in extensive internal attack. Potassium sulfate was observed to fuse to the surface of both the FeCrAl and NiCr coatings but not on the NiCrAlY coating. The absence of the fused potassium sulfate may have allowed for greater access of both the potassium chloride and hydrochloric acid to the oxide surface thus increasing attack. Furthermore, the performance of this coating system may have been influenced by the pre-exposure sample preparation in which the outer surface of the coated tube was ground down potentially removingyttrium that is known tosegregate to thecoatings surface during the cladding procedure.

References

1. IEA. World Energy Outlook Special Report: Energy and Climate Change. **2015**.
2. Simms, N. J.; Kilgallon, P. J.; Oakey, J. E. Fireside issues in advanced power generation systems. *Energy Materials***2007**, *2*, 154–160.
3. *Environment Agency Summary Report; "Biomass: Carbon sink or carbon sinner?"*; 2009.
4. Lant, T.; Keefe, C.; Davies, C.; Fry, A. T. *Modeling Fireside Corrosion of Heat Exchanger Materials in Advanced Energy Systems*; 2011.
5. Makkonen, P. Neural network for prediction of superheater fireside corrosion in CFB boilers. In *Proceedings of the 6th International Conference on Fluidized Beds*; 1999.
6. Reid, W. T. *External corrosion and deposits: boilers and gas turbines*; American Elsevier Publishing Co., Inc., New York, NY, 1971.
7. Simms, N.; Fry, A. Modelling fireside corrosion of heat exchangers in co-fired pulverised fuel power systems. *Materials for advanced power engineering***2010**.
8. Spiegel, M.; Zahs, A.; Grabke, H. Fundamental aspects of chlorine induced corrosion in power plants. *Materials at high temperatures***2003**, *20*, 153–159.
9. Grabke, H. Fundamental aspects of oxidation, sulfidation, chloridation and carburization in the gasifier environment. *Materials at high temperatures***1993**, *11*, 23–29.

Coatings for high temperature corrosion protection in advanced power plants

Maria Oksa & Jarkko Metsäjoki

VTT Technical Research Centre of Finland Ltd
P. O. Box 1000, FI-02044 VTT, Finland

Abstract

When aiming to decrease of greenhouse gas emissions and higher cost-efficiency, power plants would benefit from increased efficiency. Advanced power plants are aiming for up to 750°C steam temperatures. Higher steam temperatures will set higher requirements to tube materials, as especially difficult fuels can cause severe corrosion conditions. Biomass and waste include chlorides, sulfates and heavy metals, such as NaCl, KCl, K_2SO_4, Pb and Zn, that can substantially accelerate the corrosion even at lower temperatures.

Corrosion protection properties of thermal spray coatings were validated in a co-fired boiler using biomass, coal and solid recovered fuel. Material testing was performed with a temperature controlled probe at 550 and 750°C for 3000 hours. Corrosion performance of six high velocity oxy-fuel (HVOF) coatings, FeCr, Ni46Cr, Ni26Cr, NiCrAlY and Al_2O_3, were evaluated, and a ferritic steel T92 and a nickel based alloy 740H were applied as reference materials. Maximum corrosion rates varied from 0.01 mm/y of Ni-based coatings to 0.4 mm/y of T92 at 550°C and from 0.1 mm/y of A740H to 0.5 mm/y of Fe-based coating at 750°C. The nickel-based coatings and the ceramic Al_2O_3 coating gave excellent protection to the ferritic steel at 550°C and sufficient protection at 750°C.

1. Introduction

Energy consumption and supply has been growing globally and the trend is upwards, Figure 1. Despite of emerging renewable energy sources, large amount of world's energy is still produced with fossil fuels. Towards meeting EU2030 targets [1] and low carbon economy, and further by 2050, when the EU should achieve an overall 80% reduction in domestic emissions, energy production should be efficient and clean. In accordance with the EU's goals regarding the grand challenges ("20-20-20" targets) [2], the share of renewable energy sources continues to grow. Therefore, future power plants should be designed for higher steam parameters and higher share of renewable fuels (biomass and waste). Carbon capture and storage (CCS) should also be contributing to the goal of decreasing emissions.

Several materials and structures designed for operating in very severe environments are required to display thermal stability and enhanced oxidation/corrosion resistance at high temperature. Fireside corrosion occurs in the high temperature gas phase, high temperature gas and liquid phase or low temperature liquid phase, mainly by sulfur and chlorine species or low melting point salts forming in the deposits [3-5]. In order to overcome future challenges in more efficient energy production with utilisation of biomass,

novel material solutions must be developed and validated. In this study, corrosion performance of thermal spray coatings was tested and analysed in co-fired biomass boiler conditions.

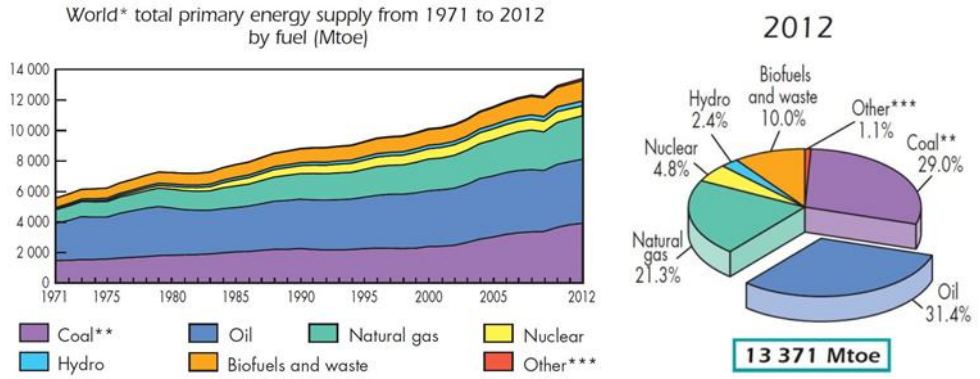

Figure 1. World total primary energy supply from 1971 to 2012 by fuel (Mtoe) [6].

2. Experiments

High temperature corrosion resistance of several thermal spray coatings in biomass firing conditions was tested in a circulating fluidized bed (CFB) boiler. The test exposure was performed with a controlled probe measurement with duration of 3000 hours. Two material test temperatures were set to 550 °C and 750 °C. The probe was in the boiler during two shutdowns, hence the total duration inside the boiler was 3540 h.

2.1 Materials

The tested coating materials were high velocity oxy-fuel (HVOF) sprayed Ni- and Fe-based high chromium alloys and an aluminium oxide coating with a bond coat. The coatings were sprayed on ferritic steel T92 (550 °C) and nickel super alloy A740H (750 °C) substrates, which were applied as reference materials in the exposure. Chemical composition of the coating materials are presented in Table 1 and reference materials in Table 2.

Table 1. Chemical composition of the Ni- and Fe-based coating materials and reference materials.

Material	Ni	Fe	Cr	Mo	Nb	W	C	B	Mn	Si	Cu	Ti	Y
NiCr	Bal.	1.1	46	...	...	...	0.1	...	...	2.1	...	...	...
Ni21Cr	Bal.	0.9	21.2	9.0	...	9.3	0.8	0.7	...	...	4.2	...	...
NiCrAlY	Bal.	...	22	...	...	...	...	...	...	...	...	...	1.0
FeCr	...	Bal.	18.6	3.6	7.1	8.6	2.1	< 5.0	1.1	1.6	...	...	...

Table 2. Chemical composition of the substrate / reference materials.

	Ni	Fe	Cr	Mo	Co	Nb	W	Ti	V	Mn	Si	Al
T92	0.3	Bal.	9	0.3	...	...	2	...	0.2	0.5	0.2	0.2
A263	Bal.	0.5	20	5.7	20	...	...	2.1	...	0.4	0.2	0.7
A740H	Bal.	0.7	25	0.5	20	2.0	...	1.8	...	0.3	0.5	0.9

The thermal spray coating was performed with HVOF torches DJ Hybrid (DJ), carbide jet spray (CJS) and HV2000 (HV). The used coating powders were Ni-980-1/1260F from Praxair for **NiCr**, Diamalloy 4006 from Sulzer Metco for **Ni21Cr**, Amperit 413 from H.C.Starck for **NiCrAlY**, SHS9172HV1 from Nanosteel for **FeCr** and A1-1110-HP from Praxair; purity min. 99.3 % for **Al_2O_3**. Process parameters for the coatings are shown in Table 3.

Table 3. Process parameters of the HVOF coating [l/min]. Spraying distance was 250 mm for DJ and CJS, and 150 mm for HV2000.

Material	Method/Nozzle	Feed rate [g]	H_2	Kerosene	Propane	O_2	N_2	Air
FeCr	CJS 140 mm	50	100	20		1000	12	
FeCr	DJ 2701	40			62	290	12.5	400
NiCr	DJ 2701	40			62	290	12.5	400
Ni21Cr	DJ 2701	40			62	290	12.5	400
NiCrAlY	DJ 2701	40			62	290	12.5	400
NiCrAlY+ Al_2O_3	HV2000 22 mm	10	750			300	20	

2.2 Material testing probe

VTT has developed an advanced water- and air-cooled probe, which can be used for controlled material testing in boiler conditions. The probe is approximately two meters long and has two sections with six test rings in each. One section is water- and air-cooled and was exposed to metal temperatures of approximately 550 ºC and the second is air-cooled with metal temperatures around 750 ºC. The probe with the two separate sample regions is presented in Figure 2. The temperatures were measured on windward side (the control temperature) and leeward side and they were recorded once a minute throughout the exposure. The flue gas temperature was measured in the tip of the probe with one covered thermo-couple. Process data was collected from the plant's reporting systems after the exposure together with monthly fuel data. The amounts of sulfur dioxide SO_2 and hydrogen chloride HCl were monitored during the exposure.

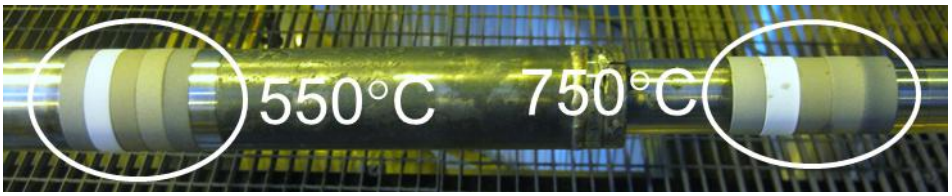

Figure 2. The test probe with two temperature regions: lower temperature (550 °C) with water- and air-cooling, and higher temperature (750 °C) with air-cooling.

2.3 Plant exposure

The material testing was conducted at Alholmens Kraft power, in a 550 MWth circulating fluidised bed boiler which has live steam parameters of 194 kg/s, 165 bar, 545 °C. The probe was inserted into super-heater area after the cyclones, as presented in Figure 3. The facility is in one of the largest biomass fuelled power plants in the world producing electricity, district heating and process steam and heat for the UPM-Kymmene pulp and paper mill. The plant is combined condensing and combined heat and power (CHP) plant. The plant capacities are: power 240 MWe, process steam 100 MWth and district heating 60 MWth. The boiler efficiency is about 92%. Combustion of different fuel mixtures or single design fuel is possible. Fuel mixture has strong influence on the deposit formation and hence corrosion of the boiler tubes [7]. Optimal fuel for this boiler design is biomass. Valmet Power was in charge of the design and manufacturing of the boiler. In the design minimum slagging, fouling and corrosion risk is expected with optimal fuel mixtures and material selection. During the material testing period, the boiler was fired with varying shares of peat, coal, biomass (forest residues, industrial wood and bark etc.) and solid recovered fuel (SRF). The minimum and maximum shares were 16-36% for peat, 32-39% for coal, 21-40% for biomass and 5-8% for SRF. Average values of fuel ratios are shown in Figure 3. Daily fluctuations in the fuel shares can be wide as well as the fluctuations in the whole process parameters due to changes in production rates.

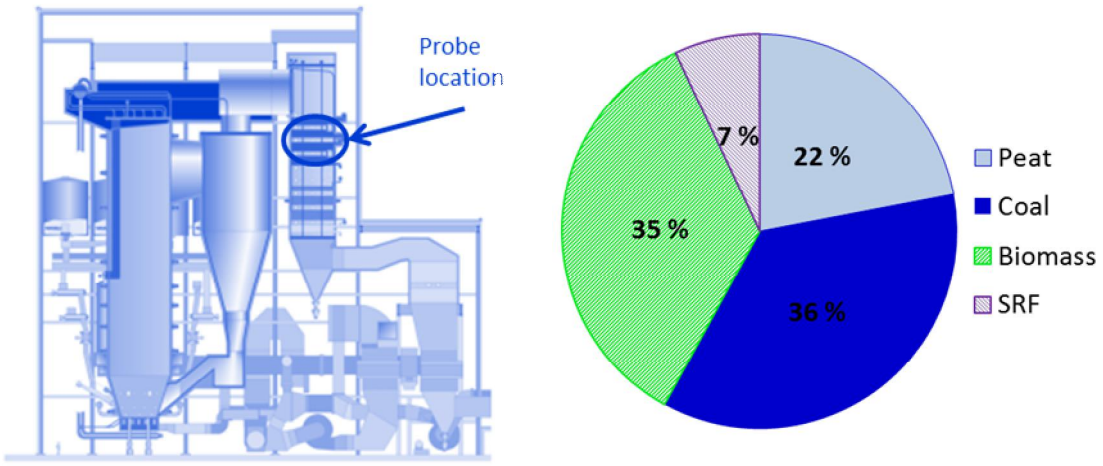

Figure 3. Schematic of the Alholmens Kraft power plant and average fuel ratios during the materials testing period (peat, coal, biomass and solid recovered fuel).

2.4 Characterisation

Microstructure of the as-sprayed coatings was characterised from cross-sections of reference specimens that were sprayed alongside the probe specimens. The cross-sectioning was performed using standard metallography methods. After the exposure in boiler, the specimens were removed from the probe and embedded in resin on-site. The specimens were cross-sectioned by grinding and polishing. Ethanol was used in grinding instead of water to preserve water soluble compounds. The cross-sections were first studied with an optical microscope and subsequently with a scanning electron microscope (SEM) equipped with an energy-dispersive X-ray spectroscope (EDS). For the SEM studies, the cross-sections were washed in ethanol in an ultrasonic bath and carbon coated for electric conductivity. A separate deposit sample was detached from the probe near the sample material rings and it was analysed with X-ray fluorescence analysis (XRF).

3. Results and discussion

3.1 As-sprayed coatings

The coatings showed a typical lamellar structure for thermal spray, Figure 4. Ni-based coatings were thick and dense, with some oxidation of lamellar boundaries, Fig.3 a) and b). The aluminium oxide coating layer was thin in order to reduce thermal expansion differences and prevent strong thermal isolation effect. CJS sprayed FeCr coating was thinner than targeted (about 250 µm) and uneven, with some porosity. Quality of FeCr coating sprayed with DJ was not sufficient; it was very thin and showed loose lamellas. Reason for poor quality of FeCr coatings, DJ sprayed in particular, was studied, and based on chemical and powder size distribution analysis together with previous studies [8-9] it was concluded that the particle size of the coating powder was too large. That prevented sufficient heating of the powder particles during spraying and caused poor bonding of the particles and low accumulation of the coating.

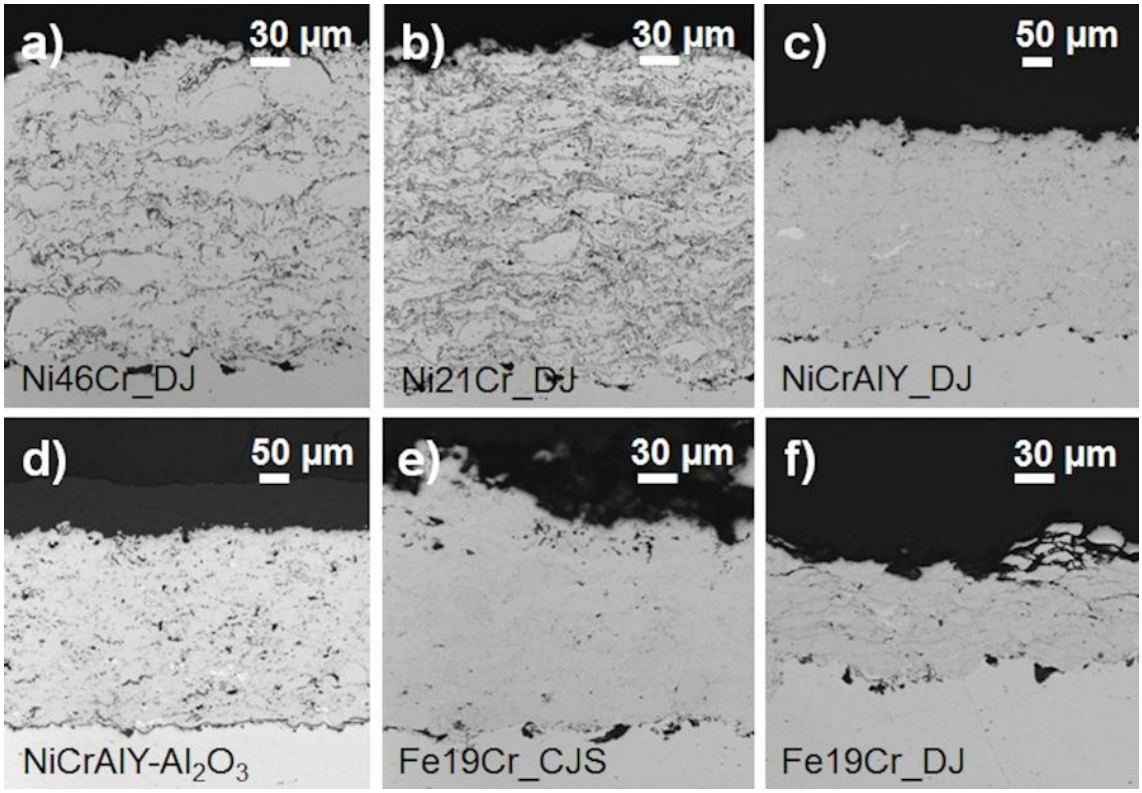

Figure 4. Optical micrographs of the cross-sections of the as-sprayed coatings before the boiler exposure. a) NiCr, b) Ni21Cr, c) NiCrAlY, d) NiCrAlY-Al_2O_3 (Al_2O_3 layer darker grey), e) FeCr (CJS) and f) FeCr (DJ).

3.2 Boiler conditions

The probe had a thick, light brown deposit in the windward side of the lower temperature (550 °C) region, Figure 5. In the higher temperature region (750 °C), the deposit was thin throughout the probe rings, and the deposit had mainly pealed-off on one sample ring.

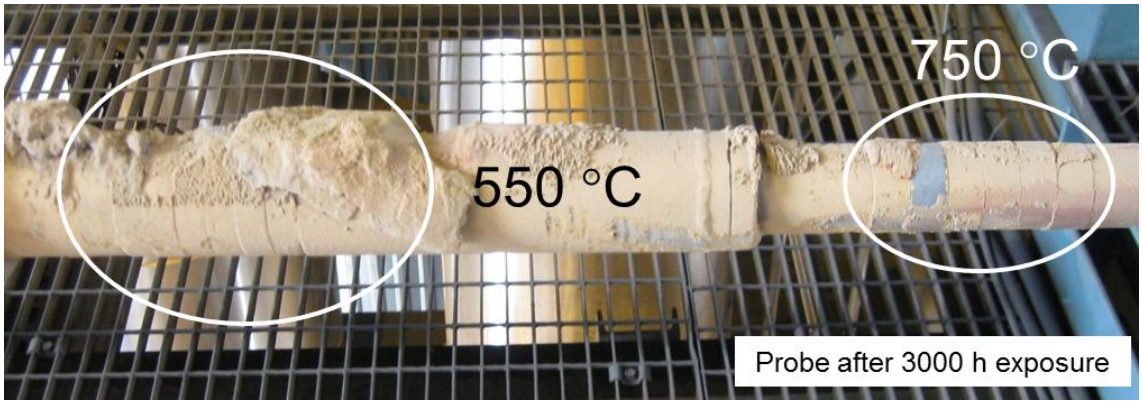

Figure 5. The corrosion testing probe after the boiler exposure.

The mean/max temperatures of flue gas side were 549/551 °C at the lower temperature region, and 700/749 °C at the higher temperature region. The measured temperatures are shown as stability curves in Figure 6. The temperature measurements reveal that the boiler was not operated with full load the whole time, as the targeted control temperatures were reached only 1600 h (550 °C) and 1100 h (750 °C) out of the 3000 h the exposure. This reflects well with the plant electricity output that varied a lot in short intervals depending on the electricity markets, Figure 7.

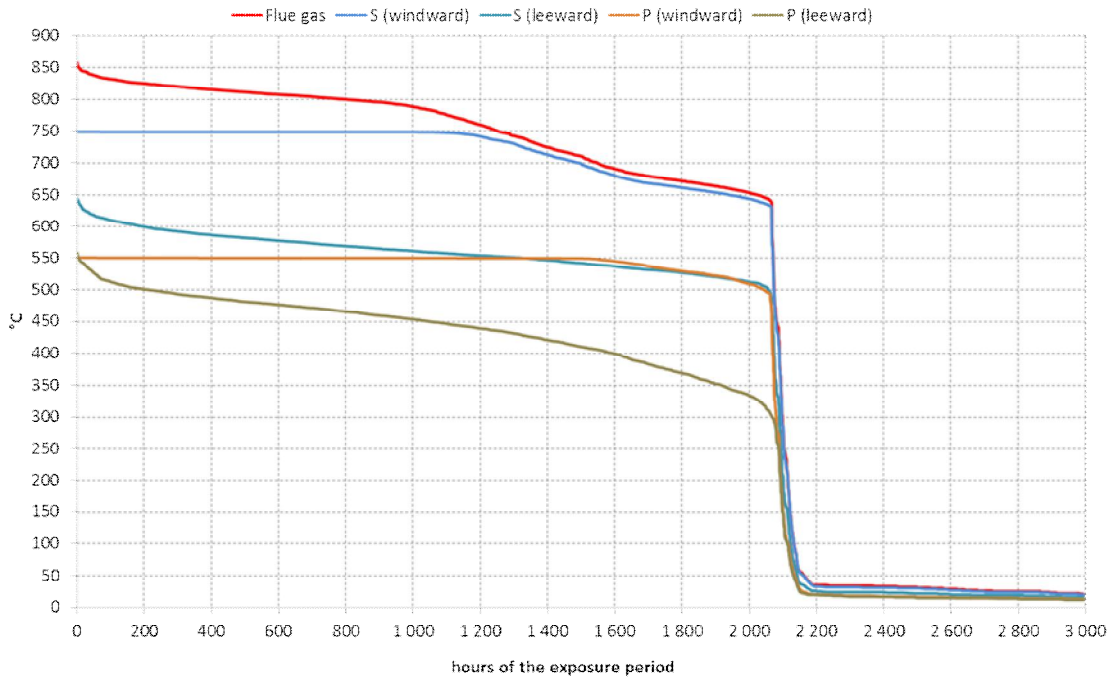

Figure 6. The measured temperatures during the 3000 (3400) h exposure presented as stability curves. Red line presents flue gas temperature, upper blue line windward side temperature and lower blue leeward side temperature at higher temperature region; yellow line presents windward side and green leeward side temperature at lower temperature region.

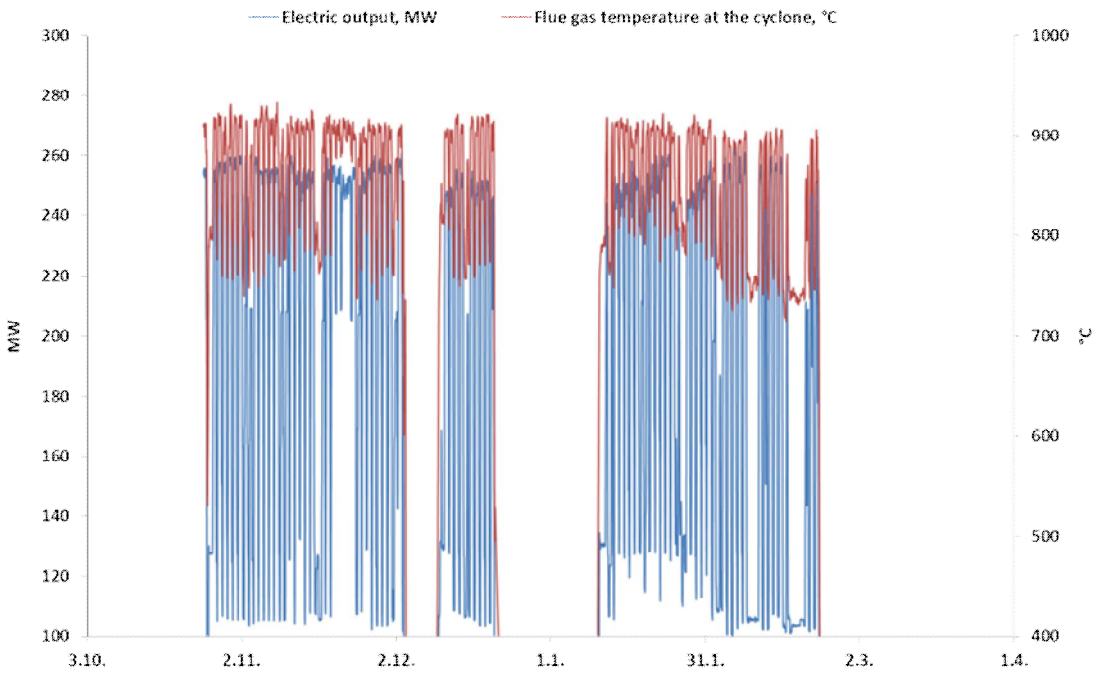

Figure 7. Electric output [MW] and flue gas temperature [°C] measured in the cyclone area during the exposure, x-axis presenting the test dates.

Maximum measured values for SO_2 and HCl in the flue gas were 210 and 338 mg/Nm^3, respectively, Figure 8. The average values were 76 mg/Nm^3 for SO_2 and 144 mg/Nm^3 for HCl, including also values during the shutting down and starting of the boiler.

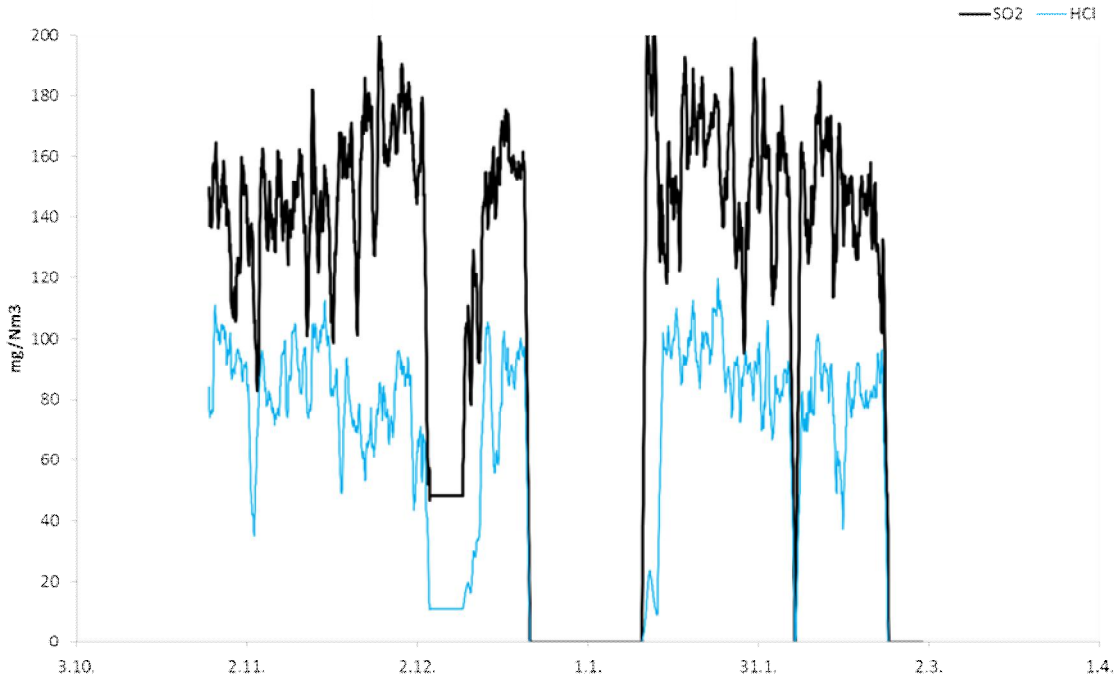

Figure 8. SO2 and HCl content in the flue gas during the measurement period. Black line represents SO2 and blue line HCl contents.

3.3 Deposit composition on the probe specimens

The probe had a thick deposit layer on the flue gas side, on the lower temperature area in particular. According to the XR Fanalysis, the deposit contained high amounts of sulphur, calcium, potassium, silicon, sodium, aluminium and iron, Table 4. Small amounts of e.g. copper, lead and chlorine were detected in the deposit. SEM images and EDX analyses of the deposit on A740H alloy at 750°C are presented in Figure 9. In the flue gas side, the deposit was more uniform compared to the side of the probe, with solidified deposit between porous areas.

Table 4. Chemical composition of the deposit samples from the lower and higher temperature region of the probe [w.%; oxygen excluded].

Element	550°C	750°C	Element	550°C	750°C
Sulphur, S	12	14	Manganese, Mn	0.28	0.31
Calcium, Ca	11	11	Barium, Ba	0.28	0.33
Potassium, K	7.6	8.2	Copper, Cu	0.14	0.14
Silicon, Si	9.0	7.0	Lead, Pb	0.12	0.08
Sodium, Na	3.9	4.2	Strontium, Sr	0.10	0.1
Iron, Fe	4.6	4.1	Chromium, Cr	0.07	0.07
Aluminium, Al	4.5	4.0	Rubidium, Rb	0.04	0.04
Magnesium, Mg	1.2	1.3	Chlorine, Cl	0.03	0.02
Phosphorus, P	0.80	0.83	Nickel, Ni	0.03	0.03
Titanium, Ti	0.68	0.74	Zirconium, Zr	0.02	0.05
Zinc, Zn	0.30	0.33			

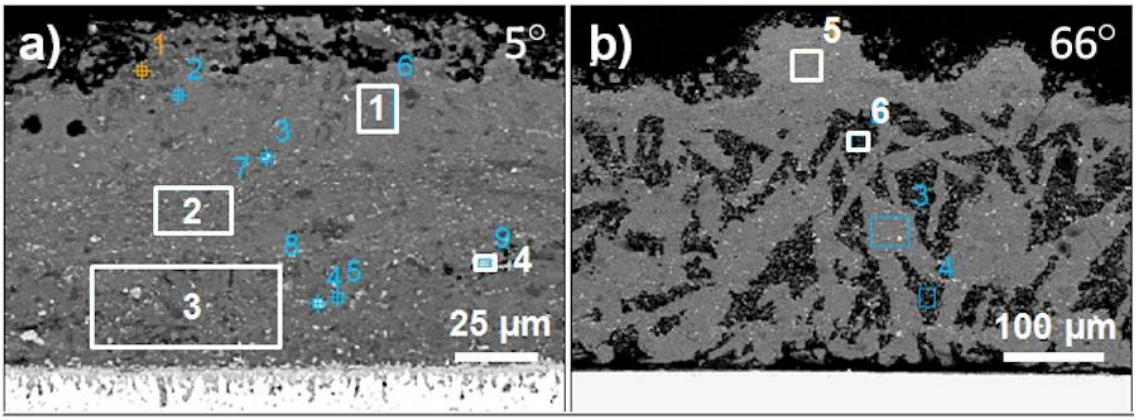

#	O	S	Ca	K	Al	Si	Fe	Na	Mg	P	Ti	Cr	Ni	Zn	Mn	Cu	Cl
1	41.4	16.7	14.9	13.6	2.2	3.5	2.1	1.0	1.5	1.1	1.0	0.1	...	0.1	0.5	0.2	0.1
2	40.6	9.6	9.5	11.8	7.3	9.8	5.2	1.5	1.2	1.2	1.0	0.2	0.3	0.5	0.1	...	0.1
3	42.8	15.1	16.8	4.9	4.3	6.0	2.5	2.4	0.5	0.7	0.7	1.9	0.5	0.5	...	0.1	0.1
4	31.3	2.4	1.9	1.6	2.0	0.2	32.6	1.7	3.1	0.1	1.4	13.7	3.6	2.6	1.0	0.9	...
5	44.4	13.6	11.6	11.0	4.9	6.7	2.8	1.7	1.2	0.8	0.4	0.1	0.2	0.1	0.1	0.3	0.1
6	43.1	0.6	0.3	11.5	11.4	17.6	7.2	0.9	1.2	2.8	1.5	0.3	...	0.6	0.1	...	0.8

Figure 9. SEM images (back scattered electrons - BSE) and EDX analyses of the deposit on A740 material in the flue gas side (5°) and in the side of the probe ring (66°).

3.4 Corrosion performance of the materials

During the exposure at 550°C, the reference material T92 ferritic steel had formed a uniform, multi-layer oxide on the surface. Thermal spray coatings NiCr, Ni21Cr and Al_2O_3 showed high corrosion performance and had a very thin corrosion layer on their surface. The aluminium oxide coating had endured the exposure in principle intact. Both FeCr coatings protected the substrate material in the exposure. However, FeCr coating sprayed with DJ contained horizontal cracks, which probably had led to spalling of some of the coating making it very thin in some regions. FeCr coating sprayed with CJS was thicker, but showed porosity. Corrosion of the materials was strongest in the flue gas side (0-45°). Images of the materials tested at 550°C are presented in Figure 10.

After the 750°C exposure, the nickel alloy 740H had a uniform, thin oxide layer and internal grain boundary attack up to 35 µm. The oxide layer in the surface contained aluminium in the outer layer and chromium and titanium in the inner layer, Figure 11. Sulfur was present in the upper oxide layer.

NiCr coating showed excellent corrosion resistance all other areas of the probe ring except at the side area at 36°. A thin chromium oxide layer had formed on the surface of the coating, Figure 12. Small amounts of zinc and copper were detected in the oxide layer. In the corroded area, nickel had diffused from the coating and reacted with e.g. oxygen and sulfur.

NiCrAlY coating showed adequate corrosion resistance in the flue gas side (0°) and the opposite side (180°), where corrosion layers of about 40 µm 10 µm were detected. In the side areas, however, it had corroded strongly during the exposure. The corrosion started as a localised pitting and extended to a uniform, about 160 µm thick corrosion layer, Figure 13. Aluminium, and nickel had diffused from the coating and chromium had formed a thick oxide layer.

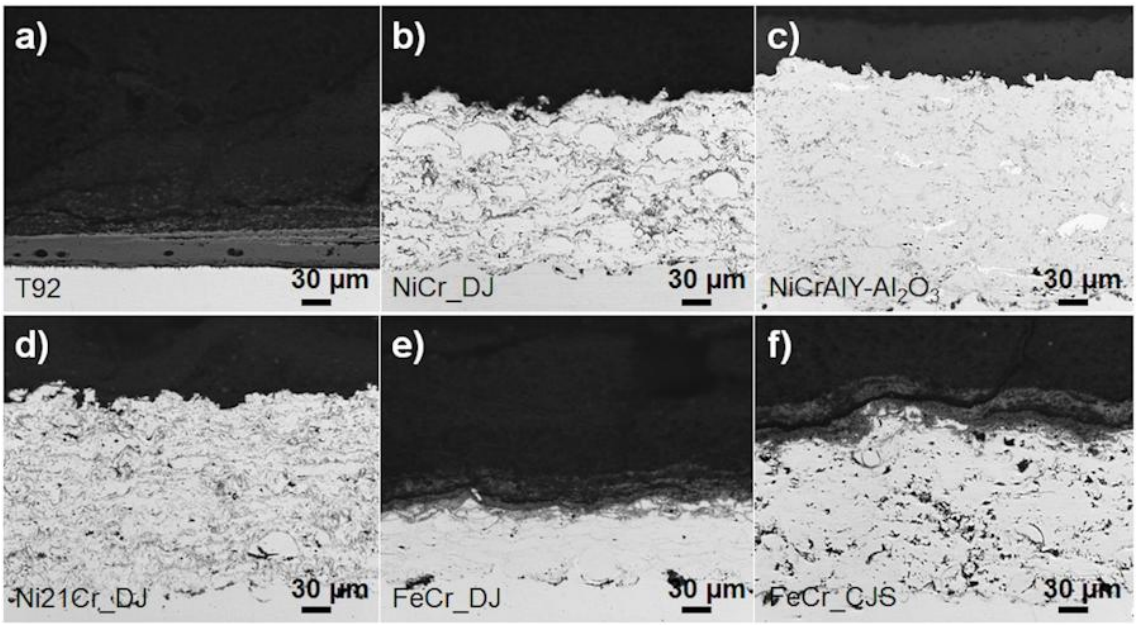

Figure 10. Optical micrographs of the materials after the 3000 h exposure in co-fired boiler at 550°C. a) T92 steel, b) NiCr, c) NiCrAlY-Al2O3 (Al2O3 layer darker grey), d) Ni21Cr, e) FeCr (CJS) and f) FeCr (DJ).

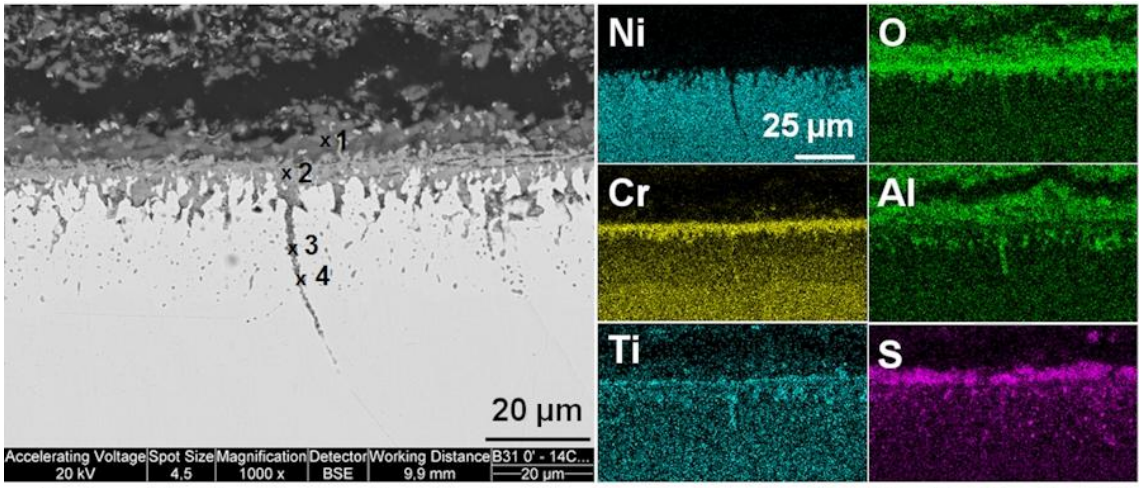

#	O	Na	Mg	Al	Si	P	S	K	Ca	Ti	Cr	Mn	Fe	Co	Ni	Cu	Zn	Nb	Mo
1	42.3	3.6	1.3	11.0	11.3	0.4	5.1	9.5	2.1	0.3	4.9	0.3	1.3	1.0	1.7	0.2	3.0	0.1	0.6
2	32.1	0.2	...	4.0	0.2	0.1	2.7	0.5	0.1	1.7	51.4	...	3.4	0.4	1.3	...	...	1.3	0.5
3	14.0	...	...	12.0	...	...	5.6	...	...	13.9	31.1	0.1	0.1	6.6	13.9	...	...	1.7	0.7
4	...	...	...	3.1	0.1	...	0.2	...	0.1	1.2	56.5	...	...	8.3	19.5	...	...	10.4	0.4

Figure 11. SEM image (BSE) and EDX analyses of A740H after the boiler exposure in the flue gas side.

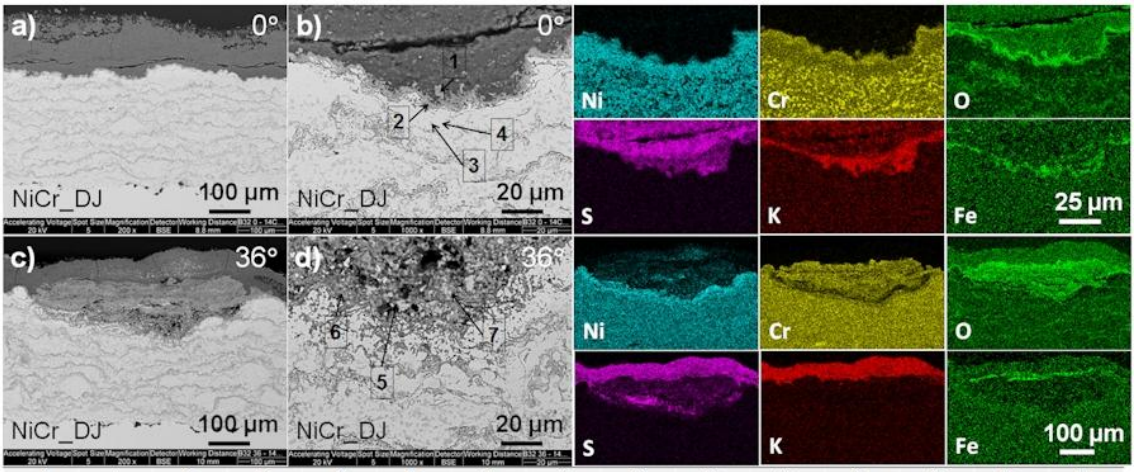

#	O	Cr	Ni	Al	Fe	Ti	K	S	Zn	Cu	Ca	Si	Mg	Na
1	31.5	41.0	1.2	2.2	20.9	0.9	0.3	0.3	0.8	0.1	0.4	0.2	0.2	…
2	30.2	60.9	4.4	0.6	1.7	0.3	0.1	0.3	…	…	0.2	0.7	0.1	0.1
3	1.3	32.1	63.0	0.7	1.5	…	…	…	…	0.2	0.1	1.0	…	…
4	…	87.0	11.6	0.5	0.4	…	0.1	…	…	…	0.1	…	…	…
#	O	S	Cr	Ni	#	O	S	Cr	Ni	#	O	S	Cr	Ni
5	3.0	22.7	5.8	68.0	6	26.5	0.6	69.7	2.7	7	5.0	17.6	17.3	59.9

Figure 12. SEM image (BSE) and EDX analyses of NiCr coating after the boiler exposure in the flue gas side (0°) showing excellent corrosion resistance and local severe corrosion at 36°.

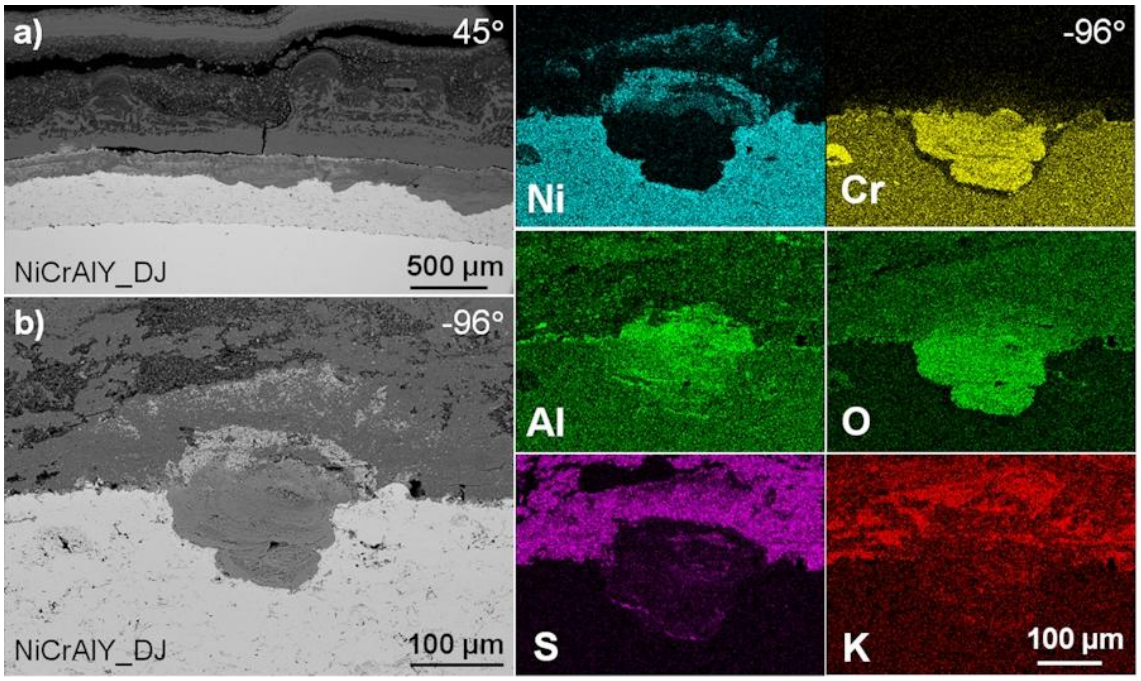

Figure 13. SEM image (BSE) and EDX maps of NiCrAlY coating after the boiler exposure in the side areas of the probe ring (45° and -96°).

Al_2O_3 coating showed very good corrosion resistance in the exposure, Figure 14 a). However, the coating had cracked from the bond coating in some areas. Because corrosion products were not detected below the detached coating, it was assumed that the coating had broken in the removal of the probe ring. The positive remark of the aluminium oxide coating was that the deposit was not attached to the coating and hence could perform well as a non-sticking coating in the boiler conditions.

FeCr coatings showed adequate performance in the exposure, because they had protected the substrate material, Figure 14 b) and c). Both coatings had thick corrosion layers: DJ sprayed 23…66 µm and CJS sprayed 57…171 µm. The coating quality should be improved by proper powder size and careful spray process selection, in order to ensure their long term corrosion resistance.

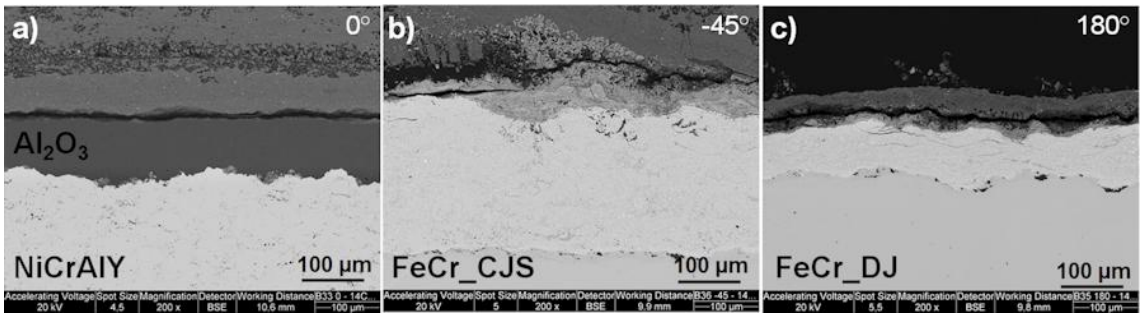

Figure 14. SEM images (BSE) of a) Al_2O_3, b) FeCr (CJS) and c) FeCr (DJ) coatings after the test at 750°.

Maximum corrosion rates of the materials varied from 1.3 µm/1000h of the Ni-based coatings, to 46 µm/1000h for T92 steel at 550°C. In the higher temperature exposure of 750C, corrosion was considerably harsher for the materials; corrosion rates were 12 µm/1000h for A740H and Al_2O_3, and 57 µm/1000h for FeCr coating. The maximum corrosion rates are presented in Table 5.

Table 5. Maximum corrosion rates of the tested materials in the boiler exposure at 550°C and 750°C.

	T92	A740H	NiCr	Al_2O_3	Ni21Cr	NiCrAlY	Fe19Cr (CJS)	Fe19Cr (DJ)	
550°	46.1	-	1.3	0.7	0.7	-	21.3	21.3	µm/1000h
550°	0.40	-	0.01	0.01	0.01	-	0.19	0.19	mm/y
750°	-	11.7	50.0	11.3	-	53.7	22.0	57.0	µm/1000h
750°	-	0.10	0.44	0.10	-	0.47	0.19	0.50	mm/y

4. Conclusions

Corrosion performance of six thermal spray coatings and two reference metal alloys were evaluated in co-fired biomass boiler conditions for 3000 hours in superheater area at two test temperatures, 550°C and 750°C. Following conclusions can be drawn from the results.

- The conditions were not very severe, as corrosion rates stayed moderate. Maximum corrosion rate was 0.40 mm/y for T92 ferritic steel at 550°C and 0.50 mm/y for FeCr coating at 750°C.
- All the tested coatings, NiCr, Ni21Cr, Al2O3 and FeCr, showed high or sufficient corrosion resistance at 550°C in the exposure conditions, corrosion rates being 0.01-0.19 mm/y.
- Best performing corrosion resistant materials at 750°C were nickel alloy A740H and Al_2O_3, though the ceramic coating had cracked, probably during removal of the probe. The corrosion rate was 0.10 mm/y.
- NiCr and NiCrAlY had high overall corrosion resistance, but suffered from localised corrosion, which caused corrosion rates of 0.44 mm/y and 0.47 mm/y, respectively.
- FeCr coatings protected the substrate material despite their insufficient quality, with corrosion rate of 0.19 mm/y for CJS sprayed coating and of 0.50 mm/y for DJ sprayed coating.

Acknowledgements

This study was performed in the FP7 EU project NextGenPower - Efficiency increases in existing and new build pulverised coal power plants with a view to CCS. The authors would like to thank Alholmens Kraft Ab

for the opportunity to use the power plant for the experiments, and Research Team Leader Janne Kärki and his team, VTT, for taking care of the probe testing.

References

1. http://ec.europa.eu/energy/en/topics/energy-strategy/2030-energy-strategy

2. http://ec.europa.eu/clima/policies/package/index_en.htm

3. Montgomery, M., Jensen, S.A., Borg, U., Biede, O. and Vilhelmsen, T. Experiences with high temperature corrosion at straw-firing power plants in Denmark. Materials and Corrosion 61 (2010) 1-14. DOI: 10.1002/maco.201005856.

4. Theis, M., Skrifvars, B.-J., Zevenhove, M. and Hupa, M. Fouling tendency of ash resulting from burning mixtures of biofuels. Part 2: Deposit chemistry. Fuel 85 (2006) 1992–2001.

5. Enestam, S., Mäkelä, K., Backman, R. and Hupa, M. Occurrence of zinc and lead in aerosols and deposits in the fluidized-bed combustion of recovered waste wood. Part 2: Thermodynamic considerations. Energy Fuels 25 (2011) 1970-1977.

6. Key World Energy Statistics, IEA 2014.

7. Barisic, V. and Hupa, M. On changes in bed-material particles from a 550 MWth CFB boiler burning coal, bark and peat. Fuel 86 (2007) 464–468. Doi:10.1016/j.fuel.2006.07.016.

8. Oksa, M., Metsäjoki, J. and Kärki, J. Thermal spray coatings for high-temperature corrosion protection in biomass co-fired boilers. Journal of Thermal Spray Technology 24 (2015) No: 1, 194-205. Doi: 10.1007/s11666-014-0155-5.

9. Oksa, M. and Metsäjoki J. Optimizing NiCr and FeCr HVOF coating structures for high temperature corrosion protection applications. Journal of Thermal Spray Technology February 2015, Volume 24, Issue 3, pp 436-453. Doi: 10.1007/s11666-014-0192-0.

Possible solutions to reduce the furnace wall corrosion in used wood power stations

Yousef Alipour[1] & Pamela Henderson[2]

[1]Inspecta Technology AB
Lindhagensterrassen 1, 10425, Stockholm, SWEDEN

[2]Vattenfall AB, Stockholm, SWEDEN

Abstract

Corrosion problems have arisen in the furnace walls area due to an increasing use of recycled wood in power plants. Used wood often contains high amounts of chlorine, alkali and heavy metals which causes more corrosion than fossil and forest fuels. One method suggested to reduce the attack is coating the furnace walls. Nickel-based alloys are shown to reduce the corrosion but these alloys are expensive and still corrode. FeCrAl alloys have successfully been tested and shown to reduce the corrosion rate of superheaters. However, no tests have been done in the furnace walls area where the oxygen level is very low.

In this work two specimens of FeCrAl alloy, one Ni-base alloy together with a 16Mo3 alloy were exposed in a recycled wood-firing commercial boiler at the furnace walls for 6 weeks. Corrosion rates of the samples were measured. The corrosion behaviours were evaluated by SEM and EDS. The corrosive environment was thermodynamically modelled.

1. Introduction

The use of used wood (also called waste wood and recycled wood) as a fuel in power plants is becoming more widespread in northern Europe, since it is a renewable energy source and also a CO_2 neutral energy source [1].

However it is more corrosive than coal and forest fuel [2]. It contains chlorine, alkali and heavy metals [3] which can lead to severe corrosion problems [4-5].

A part of boiler which is subjected to a high corrosion risk is the furnace wall or water walls, made of low alloyed carbon steel [6]. The area usually has low oxygen amounts, as low as 0.2%. This leads to corrosion problems, because no or less protective oxide can be formed.

One strategy to reduce high temperature corrosion attack in waterwalls, is to coat the waterwall tubes with more corrosion-resistant alloys. Nickel-based alloys are commonly used as a coating [7]. However nickel-based alloys are expensive and still corrode in used-wood firing boilers. FeCrAl alloys have successfully been tested to reduce the corrosion rate of superheaters [8]. But few tests have been done in the furnace walls and corrosion mechanisms are usually studied in laboratories. Research results on commercial power boilers are less frequently reported.

To fill in the gap, in this work Kanthal® APMT© FeCrAl alloy specimens along with a nickel-based alloy are exposed to a real boiler environment. The samples are analysed metallographic and chemically.

2. Experimental protocols and methods

In order to achieve the aforementioned objectives, two specimens of Kanthal APMT FeCrAl alloy, one Ni-based Alloy 625 and one 16Mo3 steel (as a reference material) were exposed in a real boiler environment. A specially designed air-cooled probe was used to perform the exposure.

2.1 Field exposure

The Idbäcken plant consists of a bubbling fluidised boiler (BFB) for CHP operation and is located in Nyköping, Sweden. The boiler, since 2008, is operated on 100% used wood. The final steam data is around 535 ºC and 140 bar, which gives the water temperature of 343 ºC and walls material temperature of 393 ºC.

A specially designed air-cooled probe was used for long-term corrosion testing, Figure 1. It contains four coupons with the dimensions of 48 mm length, 7 mm width and 6 mm thickness. Air can flow in the probe to control the temperature. Temperature was measured by a thermocouple inserted centrally at the back of each specimen.

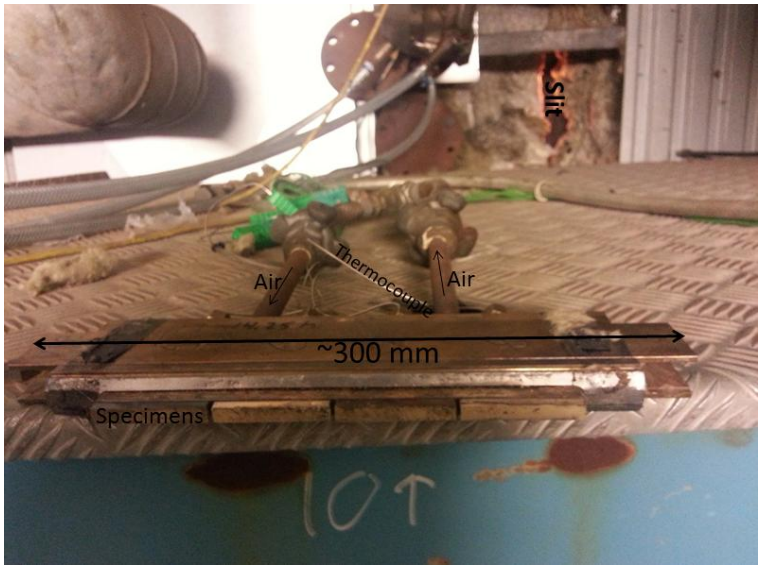

Figure 1. A fin wall probe after exposure, Specimens are shown in the figure. A slit is made between two tubes where the probe is exposed.

The probe is vertically inserted into a slit made in the fins between two tubes at the furnace walls area. The insulation was removed. The total exposure time was six weeks and the probe temperature was set at 400°C.

The samples tested are listed below in Table 1. The samples were a16Mo3 steel as reference material, an Alloy 625 as a popular coating material and two Kanthal APMT specimens as a potential coating material. Kanthal APMT is delivered preoxidised by the material supplier to form a 1 µm protective alumina layer on the sample. The heat treatment process is to heat up the sample for 8 hours in circulating heated air at 1050 ºC.

Table 1 Nominal chemical compositions of probe test samples (wt%) [9]

Alloy	C	Mn	Si	Ni	Cr	Mo	Other
16Mo3	0.16	0.55	0.22	-	-	0.3	Cu 0.3%
APMT	0.08	0.4	0.7	-	21.0	3.0	Al 5%
A 625	0.008	0.35	0.2	63	21.0	9.0	Na+Ta 3%

2.2 Corrosion rate

The thickness of each coupon was measured by a micrometer at four equally spaced distances along the centre line, see Figure 2. After exposure in the boiler, the specimens were cut at the measuring point. The top part was cut without water. Four parts of each specimen were mounted in the bakelite. Each part was measured at 5 points. The thickness loss results are shown in Figure 4.

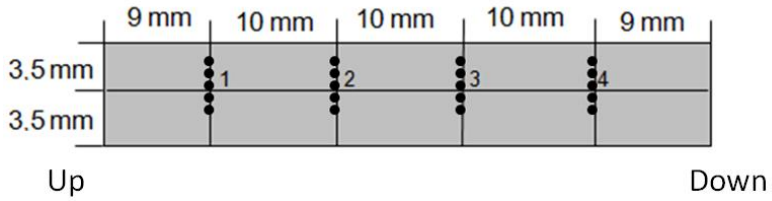

Figure 2. A sketch of the sample after exposure. The vertical lines are the cuts and the numbers 1-4 are showing the measuring points before exposure, the black dots are the measuring points after exposure. They are at ± 0.5 and ± 1 mm positions.

The top part of each sample was left unmounted for EDS analyses, section 2.3.

2.3 Chemical analyses

The deposit on the top of the un-mounted part of each sample was analysed with help of energy dispersive spectroscopy (EDS). Three different areas with the size of 2 mm x 2.5 mm were analysed under SEM/EDS. The average results are shown in Table 2.

The edge of each sample was polished without water to avoid washing away the corrosion products, see Figure 3. The interface between deposits and substrate was analysed under SEM with an EDS.

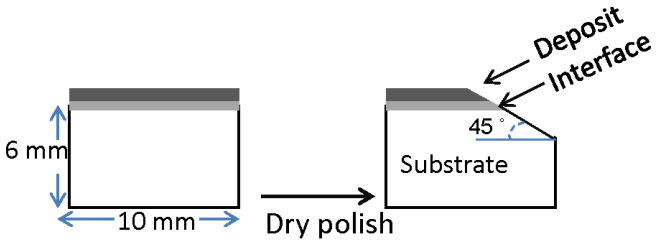

Figure 3. Schematic figure of un-mounted part of the sample, the polishing method. Polishing in this way facilitates the analyses of the substrate, oxide and interface.

3. Results and discussion

Figure 4 shows the thickness loss from the tests from 20 measurement points. The results show that 16Mo3, as expected, has the highest corrosion rate.

Kanthal APMT samples showed very low corrosion rates and were comparable with Alloy 625. This indicates that APMT alloy could potentially be an alternative to Alloy 625 to reduce the corrosion rate. The material supplier now has overlay welded APMT to a waterwall tube planned for installation in a boiler [10].

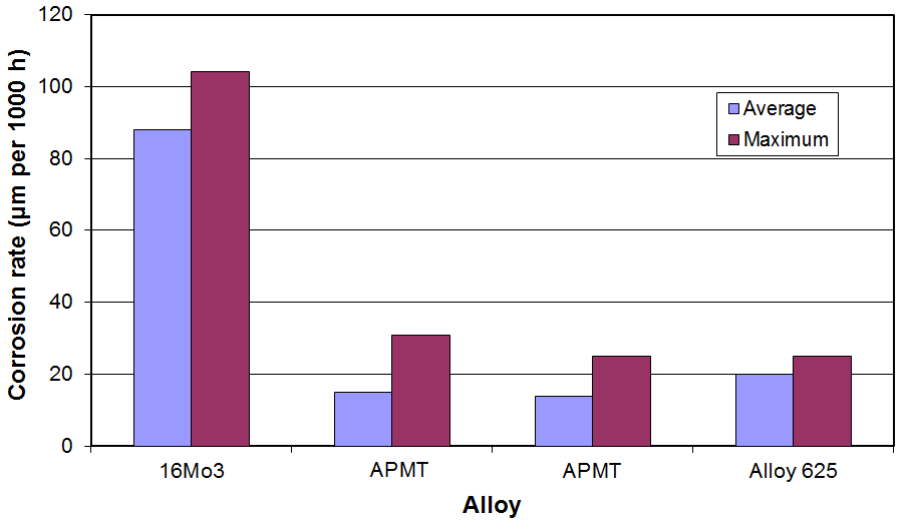

Figure 4. Thickness loss for tested alloys, the results are normalised to 1000 h.

Table 2 presents the average chemical composition of the deposits on the samples. Chlorine, potassium and calcium are found in all the deposits but lead was not present in the deposits of Kanthal APMT .
One possible reason could be the thickness of the deposit. The deposit thickness on the APMT is lower than one the Alloy 625, due to different formation mechanisms [11]. Lead is a heavy element and needs a thicker deposit to be detected under EDS. It can also be seen that Pb was found together with K in the elemental mapping of the corrosion front in Alloy 625 shown in Fig. 6.

Table 2. Average chemical composition in wt% of the deposits on the all the samples, the results are normalised to 100%. The carbon amount is excluded from the results; however the amount was 5-10 wt%.

Alloy	O	Na	Mg	Al	Si	S	Cl	K	Ca	Cr	Fe	Ni	Mo	Pb
16Mo3	22	1.7	-	2.8	0.4	-	7.5	1.9	0.4	11.4	50	-	-	0.4
APMT	23	2.3	-	2.6	-	1.9	6.5	2.5	0.5	14.8	41.4	-	2.2	-
APMT	23.8	1.4	-	2.4	-	1.1	6.3	1.4	0.4	14.9	44.3	-	3.4	-
A 625	38.1	5.6	0.7	3.1	2.6	11	2.3	9.5	10.4	0.4	1.7	0.7	-	13.5

In a used wood firing boiler alkali metals, chlorine and heavy metals are present in both the flue gas and deposits (Table 2) and can take part in the corrosion process. To have more information about the corrosion product the deposit/ substrate interface is mapped with SEM equipped with Inca EDS detector. The results are shown in Figure 5-7.

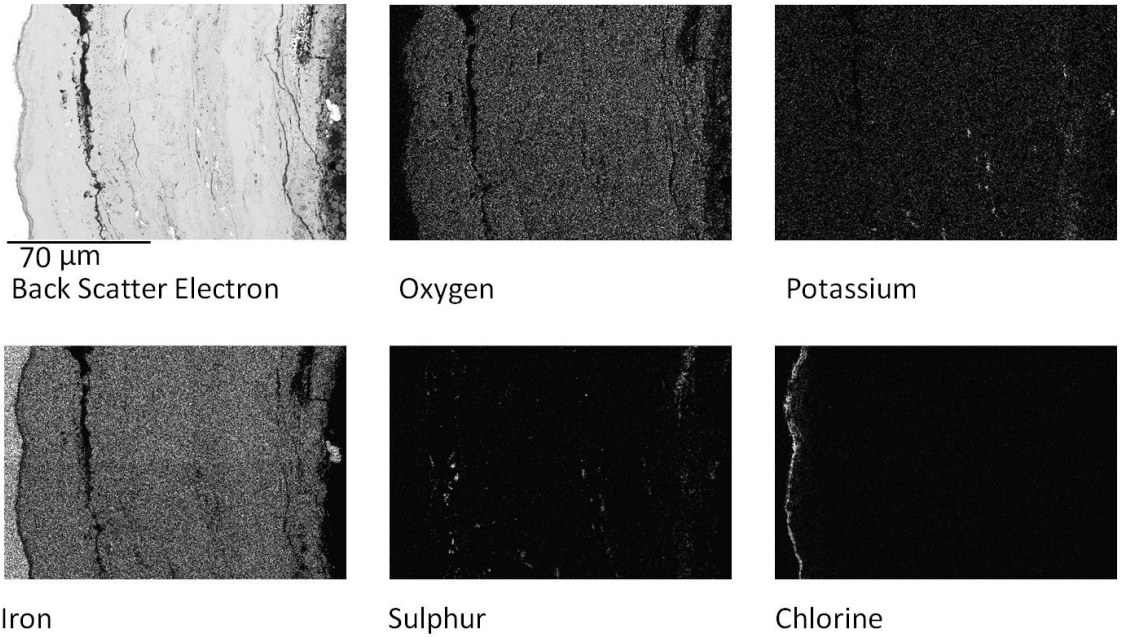

Figure 5. Elemental mapping of 16Mo3 sample, the left side of the figure is substrate. Chlorine is found in the corrosion front and is penetrated to the iron.

Figure 5 shows that corrosion product in the 16Mo3 sample is mainly iron, chlorine and oxygen. One mechanism suggested is chlorine cycle [12] which occurs by the diffusion of the gaseous chlorine through a defect oxide and attack of the metal iron to form iron chloride. The Iron chloride formed is volatilised and diffuses outward and reacts with the oxygen and releases chlorine. The chlorine can again participate in the process. However the vapour pressure of the iron chloride is insignificantly small under a thick deposit at lower temperatures [13]. It also has been shown than [14] gaseous chlorine is not thermodynamically stable at 400 ºC and HCl (g) is more thermodynamically favoured. Other mechanisms proposed for chlorination include diffusion of chloride ions through the oxide scale or oxide grain boundaries [15].

Results from this work (Figure 5) shows that the main causes of corrosion are associated with chlorine attack. As shown in the Figure 5, the corrosion front underneath a thicker iron oxide later is governed by iron chloride formation. It is a thin chloride layer and seems not to grow continuously in thickness with time.

On the other hand Alloy 625 result (Figure 6) does not show the presence of chlorine. Corrosion mechanism is dominantly governed by potassium and lead, see Figure 6.

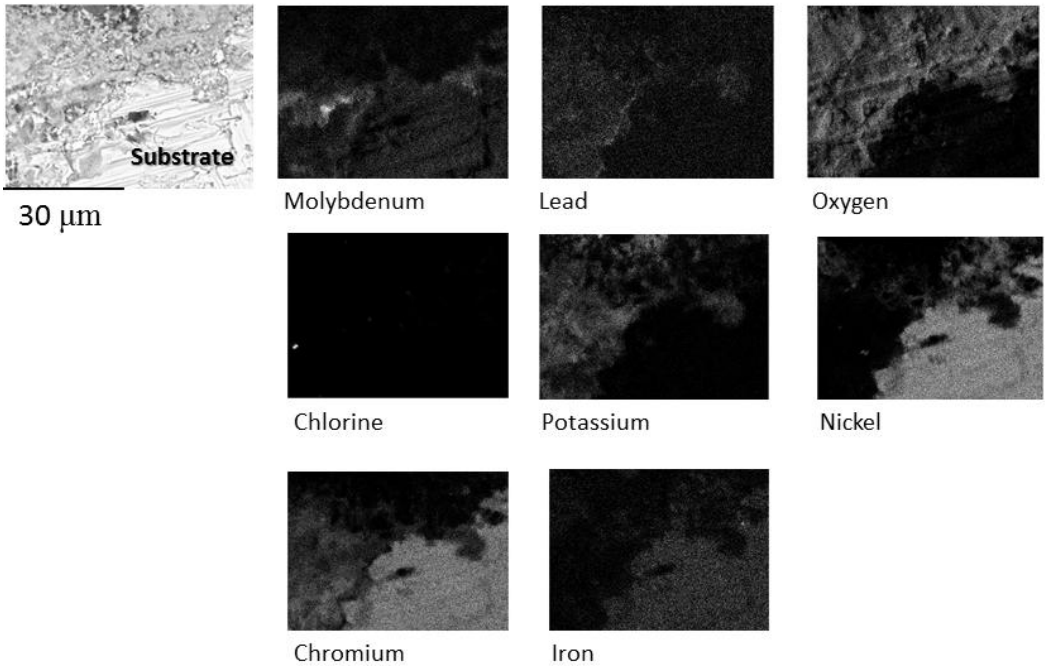

Figure 6. Elemental mapping of Alloy 625 sample, the right side of the figure is substrate. Chlorine is not found in the corrosion front, however lead and potassium are found. Chromium is enriched in the corrosion product.

Nickel-based alloys are expected to be less prone to chlorine/chloride induced corrosion. But it has been shown that [16] lead can attack nickel based alloys and form lead chromate. Potassium [17] and sodium [18] have also shown to attack the protective chromia scale and form non-protective chromates. Results from this work shows that lead together with potassium can attack the chromia layer. X-ray diffraction in other work [19] has shown the form of potassium lead chromate [$K_2Pb(CrO_4)_2$].

Figure 7 shows the elemental distribution of Kanthal APMT. It can be noted that the alumina layer formed by pre-oxidation is not maintained. Previous laboratory studies, simulating a biomass/waste fired atmosphere at 600 ºC lasting for 860 hours showed that pre-oxidising did not have any positive effect on the corrosion rate [20]. Results from our own research showed that the alumina layer appeared to be destroyed after only 14 hours exposure in a used wood fired boiler [21]. Lead was not found in the corrosion product (in contrast with Alloy 625), but Cl and K are present.

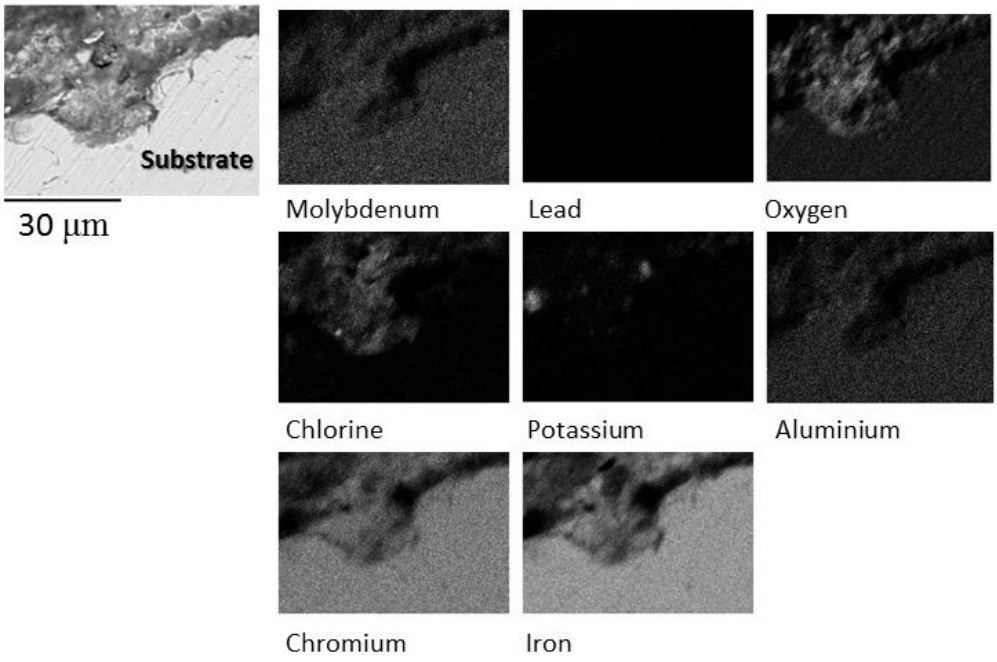

Figure 7. The Elemental mapping of an APMT sample, the right side of the figure is substrate. Chlorine together with potassium is found in the corrosion front, however lead is not found. Chromium is enriched in the corrosion product. The other FeCrAl sample showed a similar elemental distribution.

Figure 7 shows that the dominant corrosion mechanism is chloride attack. Potassium is also present (see Figure 7). It seems likely that potassium attacked part of the protective oxide layer and that chloride corrosion also occurred, albeit at a very low rate.

Used wood is a heterogeneous fuel and contains lead. Thermodynamics calculation by Thermo-Calc ® show that the solution attack of lead is much higher in Nickel-based alloys compared to iron-based alloys, see Figure 8.

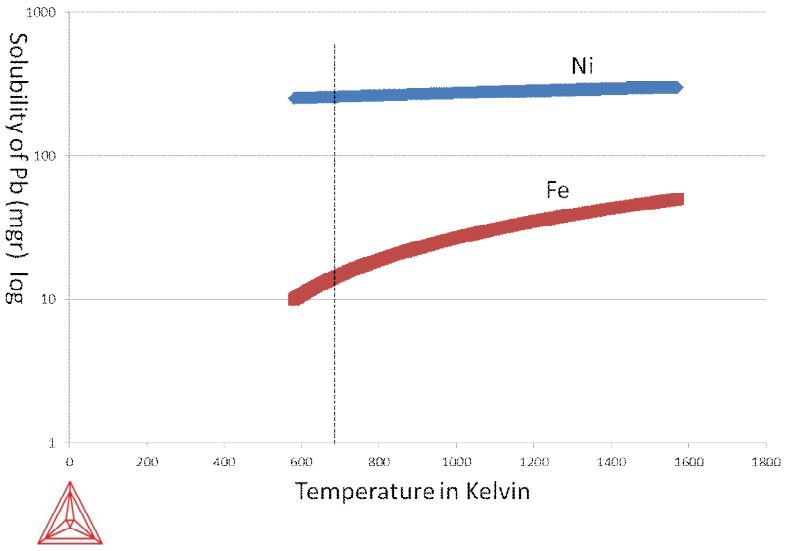

Figure 8. Solution attack of lead in iron and nickel. Both Kanthal APMT and Alloy 625 have 21%Cr amount. So the Cr amount is excluded. The actual temperature of wall material is shown by a vertical line.

This means that Kanthal APMT can be an alternative to Nickel based alloys, especially when burning a high lead-containing used wood.

4. Conclusions

The results from this work showed that 16Mo3 exhibited the highest corrosion rate. Alloy 625 and Kanthal APMT had the lowest corrosion rates. Kanthal APMT is produced by a powder metallurgical route and cladding procedures have been developed by the material supplier for full scale furnace tube tests.

Although the deposits on the four probe specimens had similar chemical compositions, they are attacked with different mechanisms. The dominant corrosion in 16Mo3 was found to be chloride attack leading to the formation of a continuous layer of iron chloride. Attack by a potassium-lead combination seemed to be the main mechanism in the Alloy 625. Kanthal APMT alloy was attacked by potassium and chloride.

5. Acknowledgment

We greatly appreciate Mattias Mattson, Vattenfall AB, for the valuable help in this project. This work was financed by Vattenfall AB and by the KME Materials Technology Consortium, which consists of power plant manufacturers, energy and materials companies and the Swedish Energy Authority. Sandvik Heating Technology is thanked for the supply of APMT material. When the work was performed the authors were doctoral student and associate professor at the Royal Institute of Technology KTH, Stockholm.

References

1. Stevens J. D., *Biomass conversation: an overview of the IEA bioenergy agreement Task VIII,* Biomass and Bioenergy, 1992 (2), 213-217.

2. Enestam S., *Corrosivity of hot flue gases in the fluidized bed combustion of recovered waste wood,* Dissertation, Åbo Akademi, Finland, 2011.

3. Krook J., Mårtensson A., Eklund M., *Metal contamination in recovered waste wood used as energy source in Sweden,* resources Conservation and Recycling, 2004 (41), 1-14.

4. Hohman U., Mohr G., *High temperature corrosion in biomass-fired boilers,* VGB PowerTech, 2005 (85), 47-52.

5. Henderson P., Kjörk A., Ljung P., Nyström O., *Superheater corrosion in combustion of biofuels, Värmeforsk report 700,* Sweden, 2000.

6. Högberg J., Henderson P., Mattsson M., Engel E., *Measurement of waterwall corrosion in a boiler, Värmeforsk report 777,* Sweden, 2002.

7. Kawahara Y., *High temperature corrosion mechanisms and effect of alloying element for materials used in waste incineration environment,* Corrosion Science, 2002 (44), 223-245.

8. Israelsson N., *High temperature oxidation and chlorination of FeCrAl alloys,* Dissertation, Chalmers University of Technology, Sweden, 2014.

9. Sandvik material database, www.sandvik.com, accessed 2016-03-24.

10. Henderson P. Private communication from KME 508/518, 2016.

11. Kaufmann H., Nussbaumer T., Baxter L., Yang N., *Deposit formation on a single cylinder during combustion of herbaceous biomass*, Fuel, 2000 (79), 141-151.

12. Zahs A., Spiegel M., grabke H.J., *Chloridation and oxidation of iron, chromium, nickel and their alloys in chloridizing and oxidizing atmospheres at 400 - 700ºC,* Corrosion Science, 2000 (42), 1093-1122.

13. Spiegel M., Zahs A., Grabke H.J, *Fundamental aspects of chlorine induced corrosion in power plants,* Materials at high temperature, 2003 (20), 153-159.

14. Alipour Y., Henderson P., Szakalos P., *Effect of temperature on corrosion of furnace walls in a waste wood fired boiler,* Materials at high temperature, 2015 (32), 188-195.

15. Folkesson N., Johansson L.G., Svensson J.E., *Initial stages of the HCl-induced high-temperature corrosion of alloy 310,* Journal of Electrochemical Society, 2007 (154), 515-521.

16. Chatterji D., McKee D.W., Romeo G., Spacil H.S., *The effect of lead on hot corrosion of nickel-base alloys,* Journal of Electrochemical Society, 1975 (122), 941-952.

17. Pettersson J., Asteman H., Svensson J.E., Johansson, L.G., *KCl induced corrosion of a 304-type austenitic stainless steel at 600 ºC, the role of potassium,* Oxidation of Metals, 2005 (64), 23-41.

18. Karlsson S., Pettersson J., Johansson, L.G., Svensson J.E., *Alkali induced high temperature corrosion of stainless steel: the influence of NaCl, KCl and $CaCl_2$,* Oxidation of metals, 2012 (78), 83-102.

19. Alipour Y., Henderson P., Szakalos P., *The effect of a nickel alloy coating on the corrosion of furnace wall tubes in a waste wood fired power plant,* Materials and Corrosion, 2014 (65), 217-225.

20. Svensson J.E., Johansson L.G., Hellström K., Pettersson J., Israelsson N., Jönsson B., Chandrasekaran D., Norling R., *FeCrAl alloys for superheaters in biomass and waste fired boilers a feasibility study*, Elforsk, Sweden, 2009.

21. Alipour Y., Talus A., Henderson P., Norling R., *The effect of co-firing sewage sludge with used wood on the corrosion of an FeCrAl alloy and a nickel-based alloy in the furnace region,* Fuel Processing Technology, 2015 (138), 805–813.

Lifetime assessment: modelling of steamside oxidation

Sanni Yli-Olli[1], Pertti Auerkari[1], Satu Tuurna[1], Rami Pohja[1] & Stefan Holmström[2]

[1]VTT Technical Research Centre of Finland Ltd
Espoo/Tampere, Finland

[2] European Commission, Joint Research Centre IET
Petten, The Netherlands

Abstract

The performance of materials in critical high temperature components of power and process plants is one of the major technical reasons limiting both the component life and process efficiency. New structural materials can be attractive in principle, but it has been challenging to simultaneously achieve good mechanical strength, oxidation resistance and cost-effective composition in the candidate alloys. The optimal material solutions for a given component depend on multiple factors, but one typical limiting factor is the waterside oxidation resistance at highest operating temperatures and pressures that extend to the supercritical (SC) or even ultra-supercritical (USC) range. To facilitate development of improved alloys for the new demanding applications, the methods of materials modelling can be useful to explore the effects of new ranges of chemical composition and fabrication routes. In the current paper oxidation modelling based on the concept of Cr and Ni equivalents is presented and applied to long term operation of superheaters made of nominally similar 11%Cr steel. The model quantifies the impact of the alloying elements on steam side oxidation to facilitate prediction of the oxide growth according to the alloy composition. The model can be used to predict the effect of variation of particular alloying elements, to explore the effects of alloying modification on performance for alloy development, and for life prediction when life is limited by water/steam side oxidation. The model prediction shows generally good agreement with the observed oxide layer thickness and also with prediction from conventional parabolic expressions when available for the alloy.

1. Introduction

Elevated temperature and pressure levels to improve steam plant efficiency can be justified if it is more than compensated by return on investment and other benefits like reduced emissions. The development of production in thermal power plants has shown the systematic improvement by elevating the maximum temperature and pressure of the process, Figure 1.

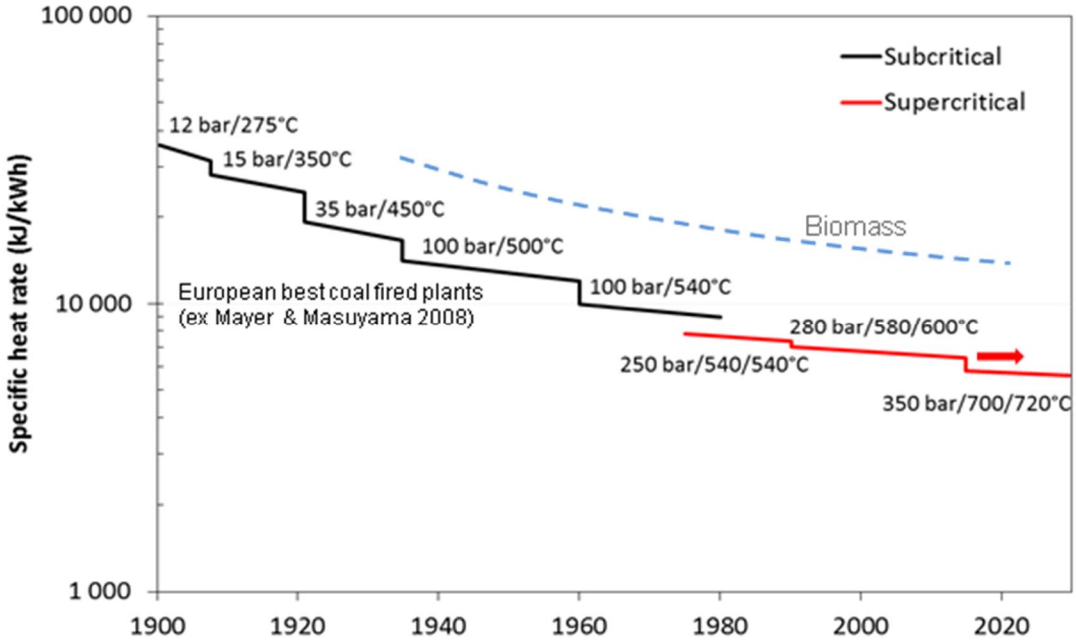

Figure 1. Heat rate development in (European) thermal power plants; data from [1,2].

New structural materials can be attractive in principle, but it has been challenging to simultaneously achieve good mechanical strength, oxidation resistance and cost-effective composition in the candidate alloys. The optimal material solutions for a given component depend on multiple factors [3]-[6], but one typical limiting factor is the waterside oxidation resistance at highest operating temperatures and pressures that extend to the supercritical (SC) or even ultra-supercritical (USC) range. The formation of internal oxide scales can impair the material and component performance through lost load-bearing wall thickness, matrix depletion of protective elements when these are oxidising, and increasing material temperature due to the thermal insulation by the growing oxides, leading to faster rates of creep and other temperature-dependent damage mechanisms to significantly shorten the component life [7]-[8].

Further challenges arise from future production tendencies; the increasing share of renewables, wind and solar, will enhance the fluctuation of supply, with the consequence that the balancing thermal power plants that were designed and used as base load plants will have to operate in a more demanding cyclic and ramping mode to maintain grid stability [9]-[10]. Cyclic use will increase the wear and tear of components, also leading to higher oxidation rates among other consequences. The spallation of internal oxides of tubes might increase due to increasing frequency of start-ups and shutdowns.

The critical high temperature components for steam plants, apart from turbines, are pressurized steam piping and headers, and superheaters and reheaters. Currently highest rated standard ferritic steels (like P92, X10CrWMoVNb9-2) for piping and headers can be used to metal temperatures of up to about 620°C from purely creep point of view, and corrosion/oxidation may limit their use to below 600°C [11]-[12]. There are currently no obvious new ferritic candidate steels for future service in thick-wall components, with simultaneously improved creep strength, also in welds, and steam oxidation resistance. Austenitic steels are less suitable for the purpose, and nickel alloys are expensive. However, at service temperatures of about 600-650°C austenitic steels such as 347 or 310 are widely used in superheaters. At these temperatures chromium no more dominates but Ni (or a Ni equivalent together with a Cr equivalent) is important for corrosion and oxidation resistance. What unfortunately will partly compensate for the higher protective capability of the composition is the high coefficient of thermal expansion of austenitic steels, resulting in spalling of thinner oxide layers than in ferritic steels. Unlike in the case of ferritic materials, the spallation of austenitic steels usually concerns the outer layer of internal oxide.

In this paper, a parametric oxidation model is presented and applied for components where waterside oxidation can limit the service life.

2. Methods

For modelling purposes, steam oxidation resistance of selected ferritic, martensitic and austenitic alloys was tested in a supercritical water autoclave up to 675°C/250 bar with 150 ppb dissolved oxygen in the inlet flow and a pH of 7 (measured at room temperature in the low pressure part of the recirculation loop). The test duration was up to 3000 h. The autoclave is connected to a recirculation water loop, Figure 2. The high pressure loop consisted of a high pressure pump, a heat exchanger and a preheater. The flow rate during the exposure was around ~5 ml/min resulting in refresh time of the autoclave roughly every 2 hours. Specimens were hung up on the specimen holder rack using electrically insulating ZrO_2 rings.

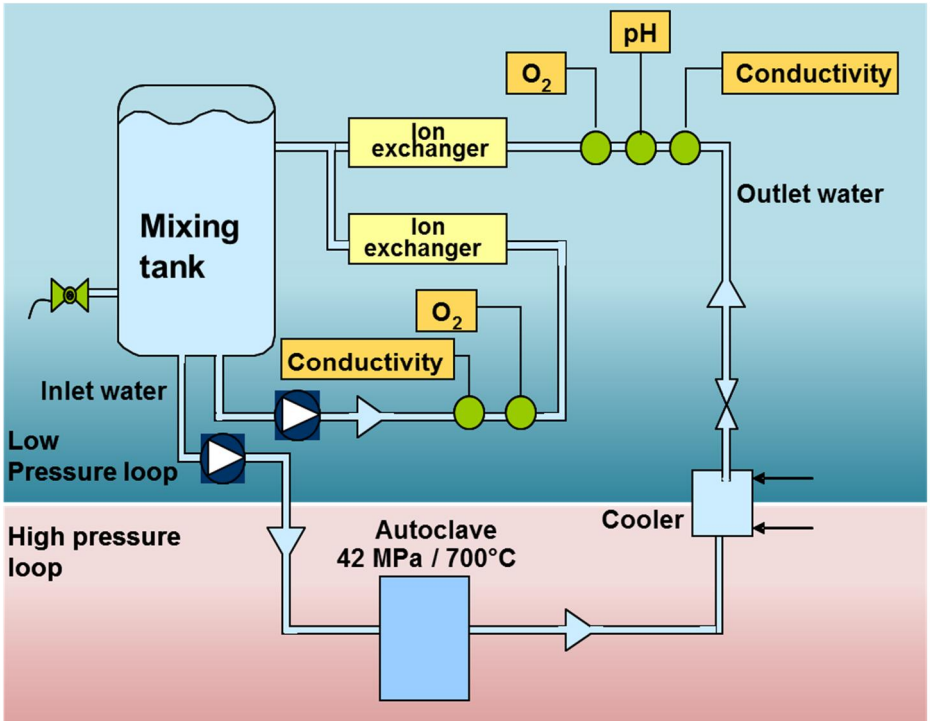

Figure 2. A schematic presentation of the supercritical water autoclave system with water recirculation loops [13].

Some of the typical alloying elements of steel, like Si, Mo, Al, Ti, can be more or less beneficial for providing protective oxide at the surface and/or microstructural defects to help such elements to diffuse to the surface. In the parametric oxidation model (P_{OX}) they are combined as a Cr equivalent. On the other hand, another set of alloying elements (such as Co, Mn, Cu, combined as a nickel equivalent) can be beneficial in retarding diffusion of unwanted elements from the environment into the metal.

In the Schaeffler diagram (Figure 3) the positions of some common boiler steels are shown with the values of chromium and nickel equivalent [14]. Such diagrams have been used for e.g. welds and castings to estimate ferrite content and austenite stability. In the parametric oxidation (P_{OX}) model these equivalents have been adapted and modified to correspond to the influence in steam oxidation resistance.

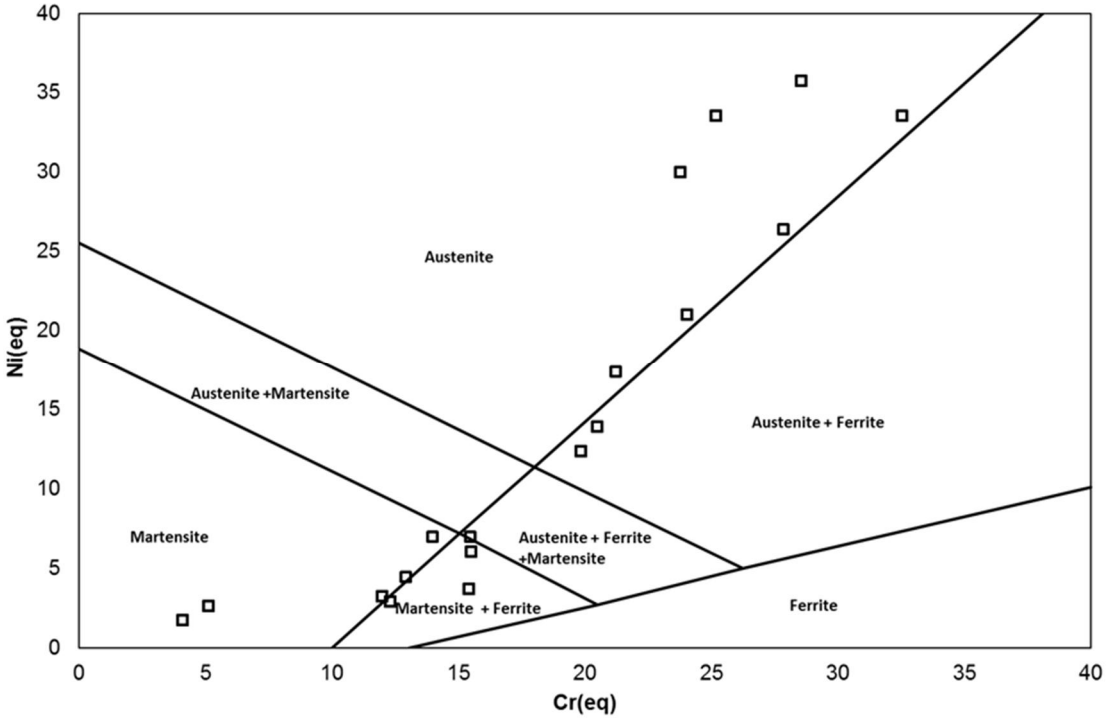

Figure 3. Test materials plotted in the Schaeffler diagram according to the P_{OX} model.

The simplified modelling approach (P_{OX}) is used to explicitly account for the alloy performance according to its chemical composition, so that for the oxide layer thickness (Δx) in time t and temperature T

$$\log \Delta x = \alpha + \beta T\left(\log t + C\right) + \delta P_{OX} \tag{1}$$

where

$$P_{OX} = a_1 Cr_{eq} + a_2 Ni_{eq} + a_3 Cr_{eq} Ni_{eq} \tag{2}$$

with

$$Cr_{eq} = Cr + b_1 Si + b_2 Mo + b_3 V + b_4 Al + b_5 Nb + b_6 Ti + b_7 W \tag{3}$$

and

$$Ni_{eq} = Ni + c_1 Co + c_2 C + c_3 N + c_4 Mn + c_5 Cu \tag{4}$$

where α, β, δ, C, $a_1 \ldots a_3$, $b_1 \ldots b_7$ and $c_1 \ldots c_5$ are fitting constants, and the element names correspond to their concentrations in the alloy. The fitting constants may also depend on the alloy class, due to their specific ranges of oxidation kinetics.

The current model is based on empirical data on material composition, time and temperature. In the case of austenitic steels the model basically includes the inward growing oxide, and in the case of ferritic and martensitic steels the total grown oxide.

3. Comparison to conventional parabolic estimates for X20 superheaters

The principal uncertainty in the observed alloy performance arises from the high temperature sensitivity of the process of oxidation. Also, considerable sensitivity can occasionally arise to the composition of the alloy. A good example is 11%Cr steel X20CrMoV11-1 that shows a transition in the oxidation resistance within its standard range of chromium content (Table 1). Therefore in superheater service it may matter whether the steel is selected with a lower bound Cr content of about 10% that would perform clearly worse than an upper bound batch with about 12% Cr.

Table 1. Chemical composition of X20CrMoV11-1 (EN 10216-2, wt-%).

C	Si	Mn (max)	P (max)	S (max)	Cr	Ni	Mo	V	Cu (max)	Al (max)
0.17-0.23	0.15-0.50	1.00	0.025	0.02	10.0-12.5	0.3-0.8	0.80-1.20	0.25-0.35	0.3	0.04

To compare the P_{OX} model predictions with those from conventional parabolic ones, the effective temperatures of four superheater tubes made of X20CrMoV11-1 were evaluated from the internal oxide using both oxidation models. The first example superheater (SH1) has been in service for 117000 h, the second superheater (SH2) for 177800 h and the third and fourth (SH3, SH4) for 220000 at the time of sampling.

The microstructure of the SH1 tube is of expected type, i.e. tempered martensite with limited features from long term use at high temperature, showing only slight coarsening of the substructure (Figure 4a). In service an approximately 145 µm thick somewhat uneven oxide had grown on the internal surface (Figure 4b) due to the location/use of the component.

The microstructure of the SH2 tube is also tempered martensite but with clearer features of significant thermal coarsening of the substructure and precipitates (Figure 5a). The internal oxide was up to 288 µm in thickness and shows clear porosity in both inner and outer layers (Figure 5b).

The microstructures of the SH3 and SH4 tube samples were also tempered martensite but with some features of thermal coarsening of the substructure and precipitates (Figures 6a and 7a). The internal oxide was up to 375 µm in thickness in SH3 (Figure 6b) and 295 µm in SH4 (Figure 7b), and especially SH3 shows significant porosity in both inner and outer oxide layers (Figure 6b).

Because of the thermal insulation provided by the oxide, with constant heat transfer the growing oxide will increase the wall temperature of the superheater. The general experience across several superheater materials suggests that as long the inside oxide is relatively even and dense, the effective temperature estimated from assumed isothermal growth is surprisingly similar to the corresponding estimate that takes into account the accelerating oxide growth. However, this apparent equivalence may not hold for thick and porous oxides with worse thermal conductivity.

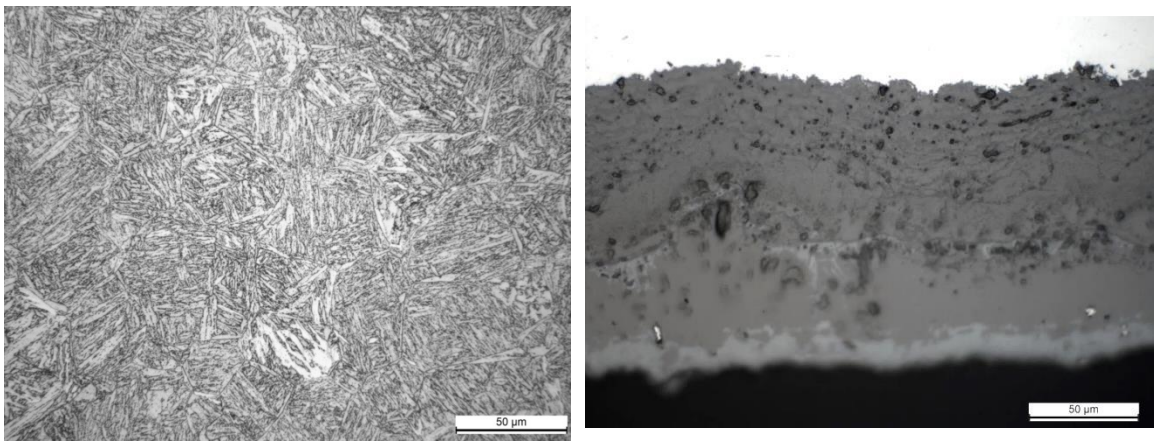

a) b)

Figure 4. The observed a) microstructure and b) internal oxide of SH1 tube.

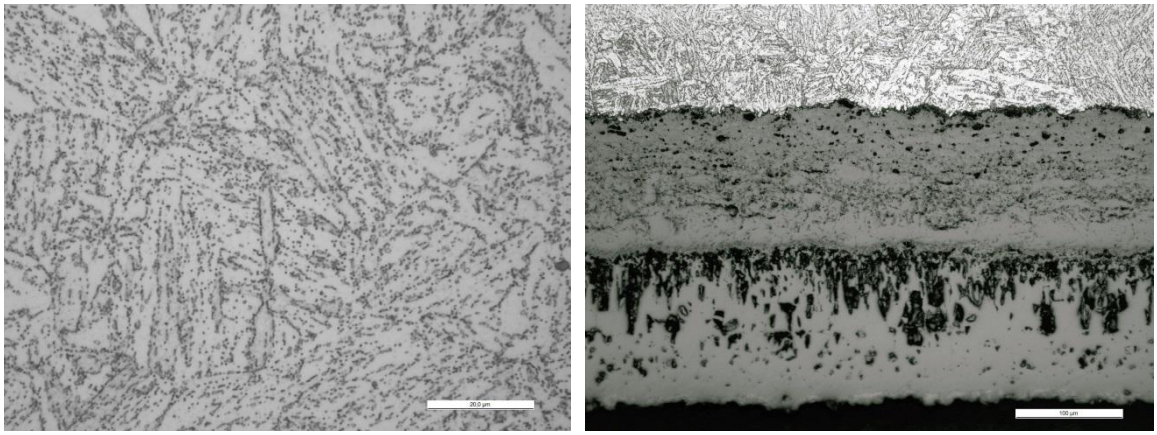

a) b)

Figure 5. a) Microstructure and b) internal oxide of SH2 tube.

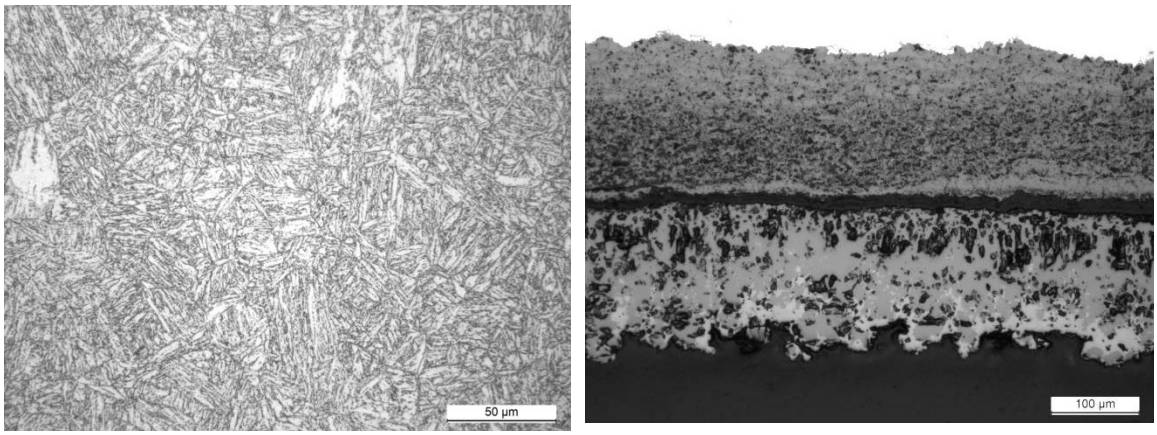

a) b)

Figure 6. a) Microstructure and b) internal oxide of SH3 tube.

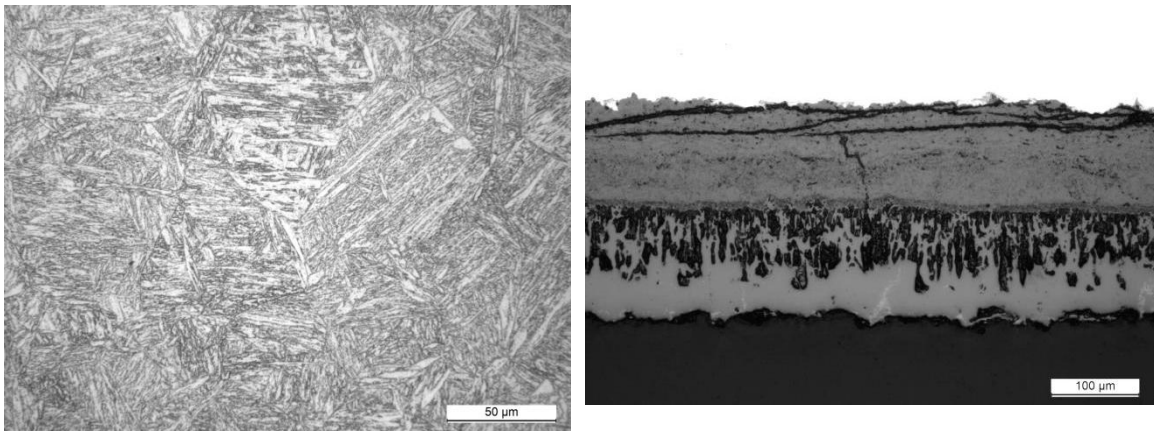

a) b)

Figure 7. a) Microstructure and b) internal oxide of SH4 tube.

In the efficient temperature evaluation with the P_{OX} model, mean standard composition (Cr 11.25%) was used. The estimates form the two oxidation models and microstructural model were made with the actual time in service assuming steady operation, because the respective plants were operated effectively in base load mode. In addition, a design-type estimate was added by taking the recorded mean steam temperature at superheater outlet and adding 35ºC to it, i.e. assuming convective heat transfer. The estimated effective metal temperatures are shown in Table 2.

Table 2. Estimated effective material temperatures from conventional parabolic and P_{OX} models.

Method	**SH1**	**SH2**	**SH3**	**SH4**
Oxide scale (conventional parabolic)	(615ºC)	(649ºC)	(662°C)	(644°C)
Oxide scale (P_{OX} model)	570°C	598°C	607°C	594°C
Oxide scale (P_{OX}, full Cr range)	559-583°C	586-610°C	595-619°C	582-606°C
Microstructural degradation	-	590°C	570°C	560°C
Steam temperature + 35ºC	570ºC	586ºC	570ºC	575ºC

The two different oxide scale based estimates of the effective metal temperatures for all superheaters show a consistent difference of about 45-50ºC, so that the conventional parabolic estimate is higher. The ranges of temperature estimates from the P_{OX} model corresponding to the full range of the standard Cr content are symmetric around the mean content.

The temperature estimates based on microstructures are in turn lower than from the P_{OX} model, and probably affected by the initial microstructure and showing no clear effect of service in case of SH1.

The coarse design-based estimates from the measured high-end steam temperatures plus 35ºC for a convective superheater are the same for SH1 as from P_{OX} model but 12-37ºC lower than from the P_{OX} model for the other superheaters.

The predicted effect of uncertainty in the chromium content of the standard range of X20CrMoV11-1 on the resulting oxide thickness is seen from Figures 8 and 9 for all four superheaters when using the P_{OX} model.

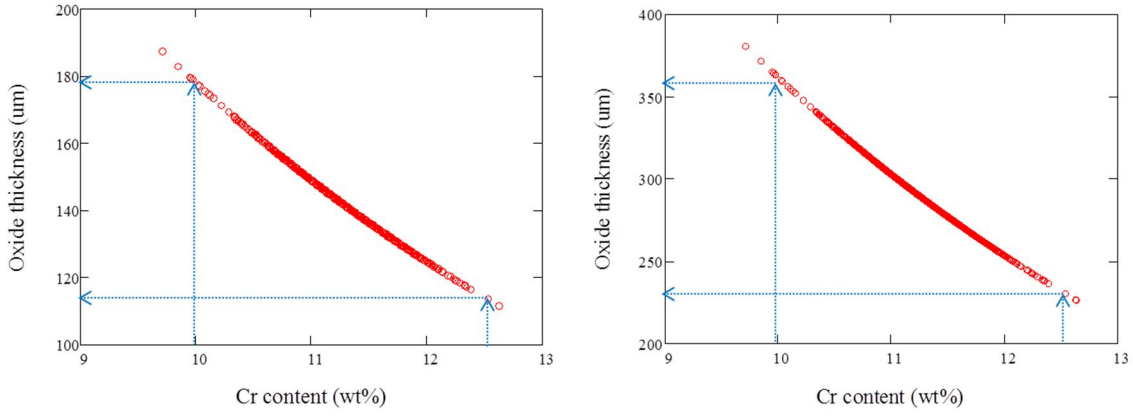

Figure 8. Effect of Cr content on oxide thickness in the example cases of a) SH1 and b) SH2.

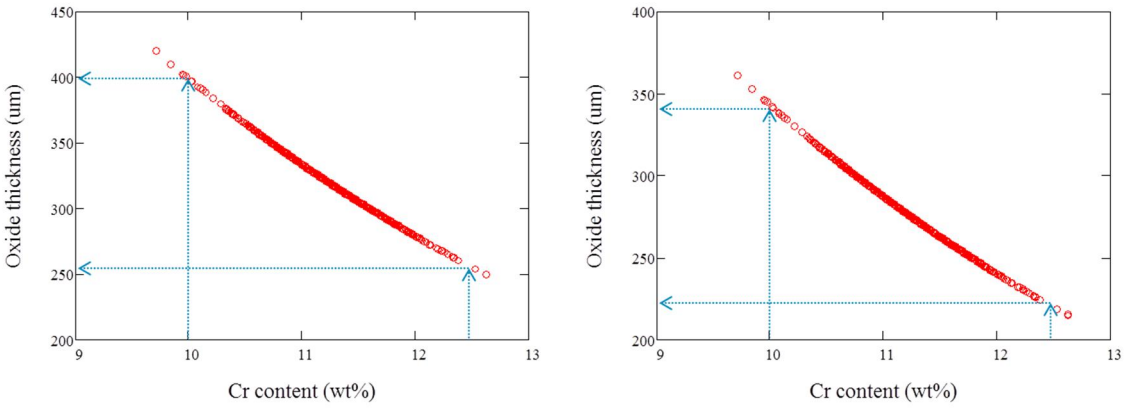

Figure 9. Effect of Cr content on oxide thickness in the example cases of a) SH3 and b) SH4.

4. Conclusions

The presented parametric oxidation (P_{OX}) model describes the steam/water side oxidation of boiler alloys for the high temperature end of the plant according to alloy content. The model applies equivalence expressions by collapsing the multi-variable problem of chemical composition, time of exposure and oxide growth to a set of equations where the required fitting constants have been experimentally determined. For comparison, the measured in-service steam oxide data has been compared with the model predicted oxide growth using various model assumptions in case of four superheaters after long term boiler service. The results from the case examples showed considerable variation in the estimated effective material temperatures, but comparison to e.g. design type of bounding and measurements from steam and surface temperatures suggest that the P_{OX} model is likely to provide reasonably conservative temperature estimates. Considering the simplicity of the model, it appears to provide good potential for further optimisation for predictions beyond the conventional range of alloy compositions that limit the application of the conventional models.

Acknowledgements

The authors wish to gratefully acknowledge the support of the Finnish energy companies providing the background data for the present study.

References

1. F. Abe, T.-U. Kern & R. Viswanathan, Creep resistant steels. Woodhead Publishing, Cambridge, UK, 2008.

2. P. Auerkari & S. Holmström, presented in International VDI Conference Alloys in Power Plant Technology, Berlin, Germany, 12-13 June, 2012.

3. R. Viswanathan, J. R. Foulds & D. I. Roberts, presented at Conference on Boiler Tube Failures in Fossil Plants. EPRI CS-5500-SR, EPRI, Palo Alto, CA 198, pp. 3-35 - 3-53.

4. J. E. Oakey, Power plant life management and performance improvement., Woodhead Publishing, Cambridge, UK, 2011, pp. 453-489.

5. A. Fry, S. Osgerby & M. Wright, NPL Report MATC(A)90, Teddington, UK.

6. I. G. Wright & R. B. Dooley, Inter. Mater. Rev., 2010, 55, 129.

7. P. J. Ennis & W. J. Quadakkers, Int. J. Pressure Vessels Piping, 2007, 4, 82.

8. P. Bullinger, presented at Power-Gen Asia, Bangkok, 3-5 October, 2012.

9. M. Fübi, F. F. Krull & M. Ladwig, VGB Powertech, 2012, 92, 30.

10. R. Jeschke, B. Henning & W. Schreier, VGB Powertech, 2012, 92, 64.

11. P. M. Barnard, L. W. Buchanan & M. Barrie, presented at 9th Liege Conference Materials for Advanced Power Engineering, Liege, Belgium, 27-29 September, 2010, pp. 39-54.

12. J. Zurek, L. Nieto Hierro, J. Piron, L. Niewolak, L. Singheiser & W. J. Quadakkers, Mater. Sci. Forum, 2004, 461-464, 791.

13. A. Toivonen & S. Penttilä, Baltica IX, International Conference on Life Management and Maintenance for Power Plants, Espoo, Finland, June 2013, pp. 174 – 193

14. A. J. Sedriks, Corrosion of Stainless Steels, ISBN 0-471-05011-3, John Wiley & Sons, Inc. 1979.

Nuclear plant:
Management of life & integrity

Hydrogen-assisted Cracking in Nuclear Power Plants? – The Doel 3 and Tihange 2 Case

Walter F. Bogaerts[1], Digby D. Macdonald[2] & Aleksandar S. Jovanovic[3]

[1] University of Leuven (KU Leuven), Dept. MTM & Center for Nuclear Engineering
Belgium

[2] University of California, Berkeley, Nuclear Engineering & Materials Science and Engineering
USA

[3] Eu-VRi, European Virtual Institute for Integrated Risk Management
Germany

Abstract

Some three years after the first detection of (thousands of) "hydrogen flaws" in its Reactor Pressure Vessel (RPV), the Belgian nuclear power reactors Doel 3 and Tihange 2 were restarted at the end of 2015. However, the potential problem of (hydrogen-related) cracks in the RPV and the related longer-term aging problems of the reactor are still imminent, probably more than ever. This paper briefly elaborates on some reported findings and identifies possible mechanisms and risks for further growth of these defects in the reactor pressure vessel wall.

The current study shows that – despite a number of counter-arguments – there are, for instance, significant potential risks or uncertainties about process-generated hydrogen problems. These are sufficiently grave to raise concerns about the fitness-for-service of the affected reactors, and also about similar reactors world-wide. Just one example of the latter is the finding of similar "UST-indications" in the Swiss nuclear power plants Beznau 1 (and 2).

From a life-management and safety point of view, it has to be recommended that meticulous inspection and continuous monitoring or surveillance programs be set up and implemented when keeping these aging reactors into operation.

1. Introduction

The inner surface of most western PWR reactor pressure vessels (RPV) is cladded with austenitic stainless steel in order to reduce corrosion rates and CRUD formation. Some of instances have been reported of this lining developing cracks, which will create direct contact of the base RPV metal (a ferritic low-alloy steel) with the high-temperature water of the primary circuit and possible progress of the cracks into the base material.

In June 2012 ultrasonic in-service inspections (UST), using a new technique/instrumentation, were performed at the Belgian Doel 3 nuclear power plant, in order to check for such under-clad cracking in the reactor pressure vessel, as had e.g. been found at Tricastin 1 in France.

Figure 1 shows a schematic illustration of the Doel 3 RPV. The total height of the vessel is approx. 13 meters (incl. the spherical top lid), with a diameter of 4.4 meters and a wall thickness of the cylindrical part of 205 mm. The primary water side of the RPV is cladded with a stainless steel Type 308/309 lining of approx. 7 mm thickness. The RPV base material is a SA 508 Cl. 3 low-alloy Mn-Mo-Ni steel (i.e. 1.2-1.5% Mn, 0.45-0.60% Mo, 0.40-1.00% Ni, max. 0.25% Cr, max. 0.25% C).

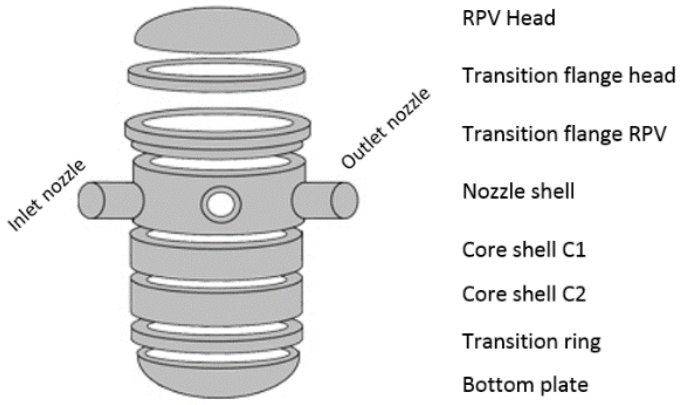

Figure 1. Illustration translated from FANC, showing the original forged steel ring sections of the RPV separated for clarity. These rings are welded together and cladded internally with a stainless steel lining to form the reactor pressure vessel.

2. Experimental findings

No under-clad cracking defects were detected. However, unexpected a-typical UST-"indications" in the RPV shells were found in the first 30 mm of the material depth of the irradiated part of the Doel 3 RPV core shells. Hence, the operator ordered a full thickness RPV shell inspection in July 2012, which confirmed high numbers (thousands) of similar "indications" [1, 2, 3] down to a depth of 120 mm into the material, measuring from the reactor's primary water side. It appeared that flaws were particularly dominant in the bottommost and upper core shells. The bulk of them are located in the base metal, outside the weld regions. Flaw densities as high as 40 indications per dm^3 had been found, with an initially reported total of 7776 indications in the core lower shell (core upper shell showed 931 indications).

The flaws appeared "almost circular in shape" with a reported average diameter of 10-14 mm, "although some had diameters as large as more than 20-25 mm" (some available data, however, showed significantly higher values, cf. infra – See Figures 2 and 3) [4, 5]. It was also observed that the detected defects are oriented laminar or quasi-laminar [2, 6, 7] and that their position and orientation showed a pattern similar to the pattern of a zone of assumed macro-segregations [8]. Bridging was found to occur only between flakes that are very close to each other.

At that time, FANC (national Federal Agency for Nuclear Control) apparently also declared that similar UST inspections of the RPV head and upper rings in the 1990s found only a few indications [1]. Old UST-inspection records, dating from the time of fabrication of the forgings, also did not mention the significant presence of "indications".

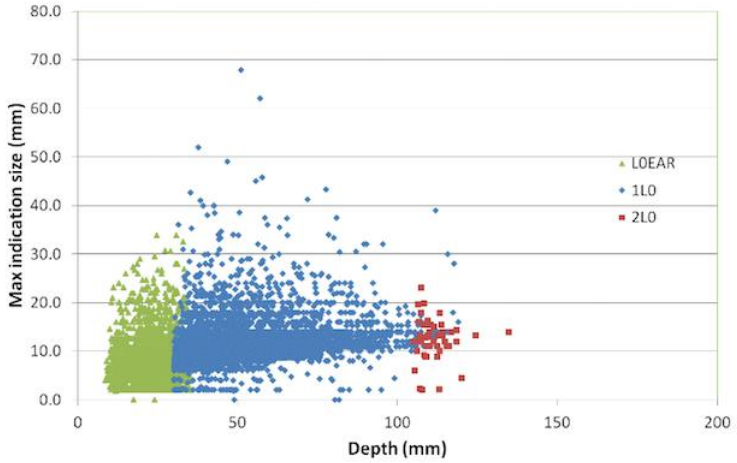

Figure 2. Doel 3 – Size of indications [max (x,y)] versus depth into the RPV steel wall (data 2012) [4].

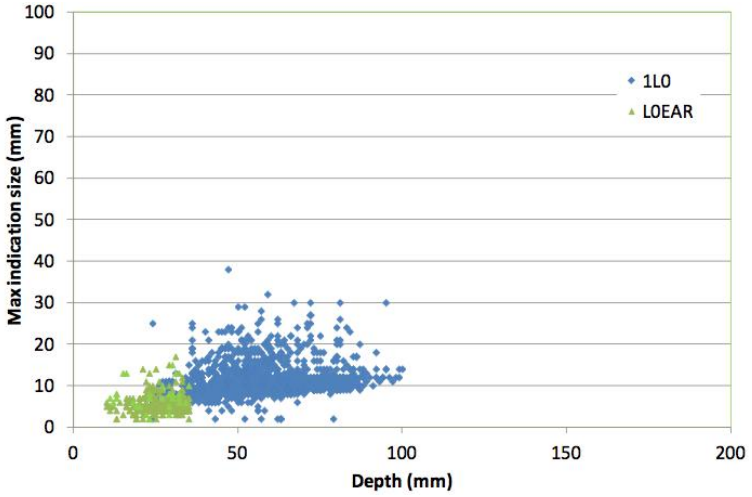

Figure 3. Tihange 2 – Size of indications [max (x,y)] versus depth into the RPV steel wall (data 2012) [5].

In September 2012 the same type of “indications”, but to a lesser extent, was also found in the Tihange 2 RPV shells during a similar inspection [5] (Figure 3). Both RPV forgings were produced by the same fabricator with steel from the same supplier.

3. Discussion

3.1 Causes of the cracks

Different investigations have been carried out since the flaws were first discovered [e.g. 2, 6, 8, 9]. They have highlighted so-called *'hydrogen flakes'* as being the root cause of the problem. These hydrogen flakes might arise during the fabrication of large steel ingots [10]. Solidification of a large mass of steel is characterized by significant development of micro- and macro-defects in the ingot structure and a changing solubility of different elements during cooling. For example the solubility of hydrogen (e.g. originating from thermal dissociation of water molecules from damp scrap, fluxes, atmospheric humidity, etc.) decreases during solidification and cooling down of the steel ingot. The solubility of hydrogen in steel at room temperature is approx. 0.1 ppm, compared with 30 ppm in the steel melt.

Hydrogen atoms possess a high mobility in the steel matrix, but are collected at internal voids, such as non-metallic inclusions (sulfides, oxides), shrinkage pores, cracks caused by internal stresses, etc. Hydrogen atoms collected at such internal micro-voids combine and form gaseous hydrogen molecules H_2, which may cause formation of cracks ("flakes", in the traditional steel jargon) when the gas pressure exceeds the steel strength. In fact, the "hydrogen flakes" are internal cracks extending radially in all directions from a center (e.g. inclusion), with the typical characteristics of a hydrogen-induced (transcrystalline) brittle fracture.

Hydrogen flakes (sometimes also called '*shatter cracks*': internal fissures seen in large forgings due to segregated hydrogen) were well-known from the past and their possible formation is particular dangerous for parts fabricated from large ingots. A potential remedy is to use vacuum ladle degassing methods to decrease the content of hydrogen to 2 ppm, which should avoid or mitigate flake formation.

Not all forged components of the Doel 3 and Tihange 2 RPVs contain the same amount of flaws. Based on an analysis of the ingot size and the combined sulfur and hydrogen content, there appears to be a good correlation with the intrinsic susceptibility to hydrogen flaking and the amount of flakes found in each forged component.

The key question remaining is about the possible evolution over time of these so-called "hydrogen flakes". The position of the regulatory authorities and the operator, so far, has been that the defects found in the Doel and Tihange RPV "are usually associated with manufacturing and are not due to aging" and that it is "improbable" that the flaws have evolved since their formation. The only theoretical propagation mechanism still considered is 'low cycle fatigue' [6]. Also the limited experience about the influence of irradiation on flaw propagation in zones with hydrogen flakes is, however, recognized.

One of the main reasons for concluding that it is unlikely there has been a significant evolution of the voids over time is the claim that "there is currently no source of hydrogen anymore" which could cause propagation of the cracks. Recognizing that the inner surface of the RPV is in contact with an aqueous solution (primary coolant), this is clearly an erroneous conclusion.

3.2 Water chemistry, corrosion effects and hydrogen sources

3.2.1 Hydrogen from cathodic partial corrosion reaction

The flaking phenomenon described above is very reminiscent of the well-known 'hydrogen blistering', 'water blistering' or hydrogen-induced fracture phenomena from corrosion in the chemical and petrochemical industries. Hydrogen blistering can occur when hydrogen enters steels as a result of the reduction reaction (hydrogen evolution via water and/or proton reduction) on a corroding metal surface. In this process, single-atoms of "nascent" hydrogen diffuse through the metal until they react with another atom, usually at inclusions or defects in the metal. The resultant diatomic hydrogen molecules are then too large to migrate through the metal lattice and become trapped. Eventually, a gas blister or internal crack builds up and may split the metal as schematically illustrated in Figure 2. Practical examples are shown in Figure 3.

In the presence of already existing cracks (cf. the "hydrogen flakes") the newly generated hydrogen may be responsible for further crack growth in two ways: either through the pressure build-up by molecular hydrogen, or through the concentration of hydrogen atoms and embrittlement phenomena at the crack tips. Both processes will have the same deleterious effect on the metal structural properties.

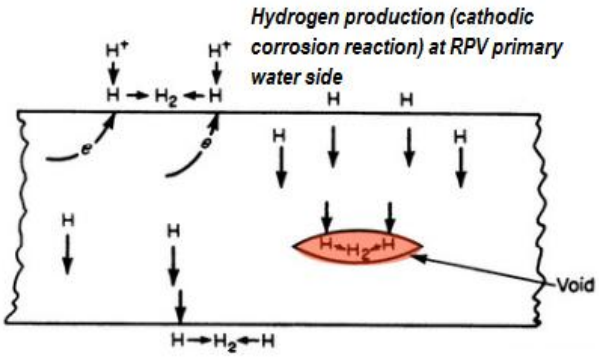

Figure 2. Schematic diagram of hydrogen diffusion and blister formation.

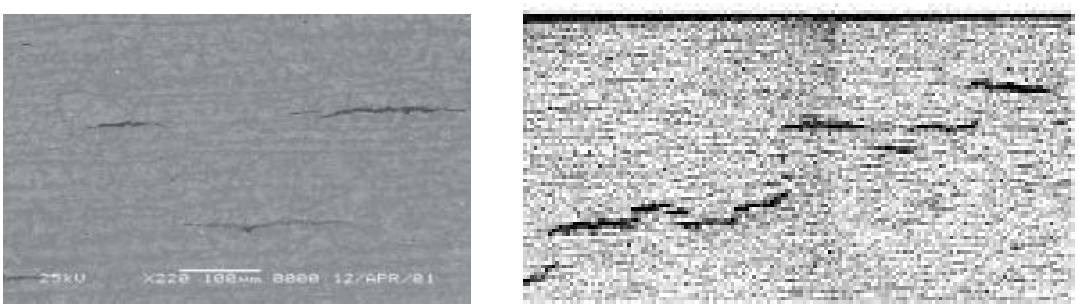

Figure 3. Typical hydrogen induced cracks (source: MTI Atlas of Corrosion and Related Materials Failures – electronic ed.)

Hydrogen blistering or cracking is controlled by minimizing corrosion and is normally not a problem in neutral or alkaline environments and with high-quality steels that have low impurity and inclusion levels. Nevertheless also under the primary water chemistry conditions of the reactor coolant system (RCS) of PWRs, with a typical pH_T of approx. 6.9 to 7.4 (corresponding to a room temperature pH around 10), the primary cathodic corrosion reaction will be:

$$H_2O + e^- \rightarrow H + OH^-$$

Even for very low corrosion rates of the stainless steel cladding (e.g. 0.1 to 1 micron/yr) this will result in significant quantities of corrosion-generated hydrogen atoms that will evolve and may enter into the base metal of the RPV (> 10^{24} - 10^{25} atoms/yr). In this respect, Tomlinson [11] has shown that in oxygen-free high-temperature water more than 90% of the hydrogen generated in the cathodic corrosion reaction is indeed absorbed by the steel.
The austenitic stainless steel cladding is sometimes considered to prevent hydrogen diffusion and potential hydrogen-induced cracking problems in the pressure vessels. This, to our knowledge, has never been proven experimentally in an adequate way [12] and, at most, the cladding probably has only a “delaying” effect in transferring the nascent hydrogen to the cladding/base metal boundary, and further into the RPV steel matrix. The presence of flaws in this matrix (cf. “hydrogen flakes”) represents ideal sinks (traps) for the hydrogen injected into the metal from the cathodic corrosion reaction.

3.2.2 Hydrogen from coolant radiolysis

In addition to the corrosion-generated hydrogen, there is also the issue of hydrogen radicals being formed as a result of the radiolysis of water and the reactions of H_2 with the radiolysis products [13] (e.g. OH· +

$H_2 \rightarrow H\cdot + H_2O$); hydrogen is used in the RCS to suppress radiolytic oxygen and hydrogen peroxide formation. More details of all these effects are discussed elsewhere [14].

3.3 Earlier international observations

Finally, there are earlier observations of hydrogen-induced blister cracking which have been reported in nuclear structural materials [15], and in the past there has been considerable debate about the issue. A very old, specific, example of failures attributed to hydrogen occurred in retaining rings used to connect inlet assemblies to the reactor process tubes in a Hanford water-cooled production reactor. Failures occurred in carbon steels and Type 420 stainless steel. The reported hydrogen sources were the fabrication process, hydrogen generated during corrosion of the ring by the process water, and from galvanic coupling [16].

3.4 Aging risks and crack growth

In view of all of the above, the “trapping” of cathodically-generated hydrogen (due to primary water corrosion reactions), or from radiolytic hydrogen, inside existing “hydrogen flakes” is not improbable. Moreover, the (original) flakes may act as a stress raiser, which will enhance the diffusion of the hydrogen to the stressed areas in the metal.

Also, the additional effect of irradiation is still largely unknown. Traditionally it has been assumed that hydrogen significantly affects the fracture properties of pressure vessel steel in both the unirradiated and irraditated states at hydrogen contents above 2 ppm. Some studies have measured the hydrogen content of the cladding and found it to be 3 - 4 ppm after prolonged irradiation in PWR water [17]. This can also be assumed to be the equilibrium content at the cladding/base material interface. Although hydrogen diffuses quickly in the RPV steel at high temperatures the presence of efficient hydrogen traps, such as the “hydrogen flakes” poses a severe threat. The effect of irradiation and the importance of hydrogen in some observed low fracture toughness values clearly requires further research. More details will be discussed during the presentation.

4. Conclusions

At this point in time, it remains unclear if the cracks found in the Belgian NPPs Doel 3 and Tihange 2 are "only" manufacturing artefacts, or if there is also an "operational component" contributing to the current problems and operational risks; i.e. whether the cracks are still progressing and whether there are other phenomena, e.g. similar to 'hydrogen blistering' processes, contributing to the problem. Additional hydrogen might indeed come from the cathodic corrosion reactions occurring on the primary water side of the reactor pressure vessel, or from radiolytic hydrogen of primary water decomposition. During operation, there is a permanent flux of (corrosion-originating or radiolytic) atomic hydrogen – although the flux might be small – and this hydrogen could easily get trapped into the voids that are present in the wall of the RPV. An eventual pressure build-up in the flakes will result in growing cracks and other materials degradation phenomena.

It is also not just Doel 3 and Tihange 2 in Belgium that could be affected [18]. The RPVs were fabricated by the now bankrupt RDM (Rotterdamsche Droogdok Maatschappij, Netherlands), which also manufactured RPVs for at least 20 other reactors that are operating in seven countries around the world, including some 10 in the United States. Also, more recently similar phenomena as in the Belgian reactors have been detected in the Swiss reactor Beznau 1 and, to a lesser extent, Beznau 2. These RPVs have a different manufacturer, which demonstrates that other factors, like steel supplier, cladding process and final assembling, may also have played an important role in the development of the observed damage.

This being said, it should be recognized that a pressure vessel with a density of fault “indications” as they were found in 2012 in both Belgian RPVs would not have been accepted at the time of construction.

If some of the hypotheses discussed above were to be proved to be true, there might be a huge impact on currently operating PWRs.

References

1. C. Peachey. Cracks found at Doel 3. Nuclear Engineering International, October 2012, p. 10.

2. N.N. (Bel-V). Flaw indications in the RPVs of Doel 3 and Tihange 2 – Safety Evaluation Report R-SER-13-001-0-e-0 (Internal report), January 2013, 34 pp.

3. N.N. (AIB-Vinçotte). Synthesis Report Doel 165 (Internal report), January 2013. 10 pp.

4. N.N. (Electrabel). Safety Case Report: Doel 3 – Reactor Pressure Vessel Assessment. December 2012.

5. N.N. (Electrabel). Safety Case Report: Tihange 2 – Reactor Pressure Vessel Assessment, December 2012.

6. N.N. Doel 3 and Tihange 2 reactor pressure vessels – Final Evaluation Report. FANC (Federal Agency Nuclear Control, Belgium). May 2013. 33 pp.

7. N.N. Defects in the reactor pressure vessels of Doel 3 and Tihange 2. The Greens / European Free Alliance (European Parliament), March 2014. 41 pp.

8. E. van Walle. The detection of hydrogen flakes in the Belgian Doel3/Tihange2 reactor pressure vessels – Overview of technical developments to support restart justification. NENE 2013, Bled, Slovenia, September 2013.

9. N.N. Flaw indications in the reactor pressure vessels of Doel 3 and Tihange 2 – Progress Report 2014. FANC (Federal Agency Nuclear Control, Belgium). December 2014. 10 pp.

10. R.J. Fruehan. A review of hydrogen flaking and its prevention. Iron & Steelmaker, 1997, Vol. 24, No. 8, p. 61.

11. L. Tomlinson. Mechanism of corrosion of carbon and low alloy ferritic steels by high temperature water. Corrosion, 1981, Vol. 37, No. 10, p. 591.

12. R.E. Mazel, V.G. Grinenko & T.P. Kuznetsova. 1980. Influence of cladding on the resistance to hydrogen embrittlement of the metal of a nuclear reactor vessel. Teploenergetika, 1980, Vol. 27, No. 10, p. 29.

13. D.D. Macdonald & M. Urquidi-Macdonald. The Electrochemistry of Nuclear Reactor Coolant Circuits. Encyclopedia of Electrochemistry, Vol. 5, Electrochemical Engineering, Eds. D.D. Macdonald and P. Schmuki, Wiley-VCH Verlag, 2007. Pp. 665-720.

14. W.F. Bogaerts. J.H. Zheng. A.S. Jovanovic & D.D. Macdonald. Hydrogen-induced Damage in PWR Reactor Pressure Vessels. Corrosion 2015, Research in Progress Symposium, NACE, 2015.

15. T.K.G. Namboodhiri. Trans. Indian Inst. Metals, 1984, Vol. 37, p. 764.

16. R.E. Westerman. An analysis of the Truarc Ring Failure Problem, HW-71631, November 8, 1961; cited in: S.H. Bush & R.L. Dillon, 'Stress Corrosion in Nuclear Systems', Proc. Int. Conf. on Stress Corrosion Cracking and Hydrogen Embrittlement of Iron Base Alloys (NACE-5), June 1973, p. 61.

17. J. Koutsky & K. Splichal. Hydrogen and radiation embrittlement of CrMoV and CrNiMoV ferritic RPV steels. Int. J. of Pressure Vessel and Piping, 1986, Vol. 24, p. 13.

18. N.N. Activities in WENRA countries following the Recommendations regarding Flaw Indications found in Belgian Reactors. WENRA (Western European Nuclear Regulators Association). December 2014. 27 pp.

Demonstration of fatigue for LTO license of NPP Borssele

F.J. Blom[1], M.H.C. Hannink[1], C.G.M. de Bont[1], P.W.B. Quist[2] A.E. de Jong[2] & W. Besuijen[2]

[1]NRG
Westerduinweg 3, 1755 ZG, Petten, The Netherlands

[2]EPZ
Zeedijk 32, 4454 PM, Borssele, The Netherlands

Abstract

Long Term Operation (LTO) of nuclear power plants (NPPs) requires an ageing management review and a revalidation of Time Limited Ageing Analyses (TLAAs) of structures and components important for nuclear safety. An important ageing effect to manage is fatigue. In this paper, the methodology for the revalidation of fatigue TLAAs is demonstrated for LTO of NPP Borssele in the Netherlands.

The LTO demonstration starts with a scope, which was defined by assessment against international practice and guidelines and engineering judgment. Next, a methodical review was performed of all existing fatigue TLAAs. This also includes the latest international developments regarding environmental effects. In order to reduce conservatism, a comparison was made between the number of cycles in the analyses and the number of cycles projected to the end of the intended LTO period. As a result of the review, further fatigue assessment or assessment of environmental effects was necessary for certain locations. New analyses were performed using state-of-the-art calculation and assessment methods. Fatigue management of the NPP is ensured by means of the fatigue concept where load monitoring, transient counting and fatigue assessment are coupled through an integrated approach during the entire period of LTO.

1. Introduction

NPP Borssele is one of the first NPPs in Europe whose originally planned operation time of 40 years has been extended to 60 years. In the original Safety Report of the plant, which is in commercial operation since 1973, ageing stressors for 40 years of operation were assumed. Over the last few years, NPP Borssele has carried out an LTO demonstration programme to demonstrate safe operation until 2034. The programme was set up according to IAEA guidelines of Safety Report No. 57 [0] and Safety Guide No. NS-G-2.12 [0]. A schematic overview of the adopted approach is depicted in Figure 1.

One of the steps in the demonstration of safe LTO is the revalidation of fatigue TLAAs (marked red in Figure 1). It has to be demonstrated that the fatigue TLAAs have enough safety margin until the end of the intended period of LTO and that fatigue ageing effects are adequately managed. In this paper, the methodology is presented that was jointly developed for this by NRG and utility EPZ. Based on the LTO

assessment, the license of NPP Borssele was revised comprising operation until 2034 (60 years of operation).

A schematic overview of the LTO fatigue programme of NPP Borssele is shown in Figure 2. In the schedule the following items can be identified:

1. Scope
2. Methodical review of fatigue TLAAs
3. International developments
4. Further assessment measures
5. Load monitoring
6. Fatigue management

In this paper, these items will be addressed in the same order. A picture of NPP Borssele is shown in Figure 3.

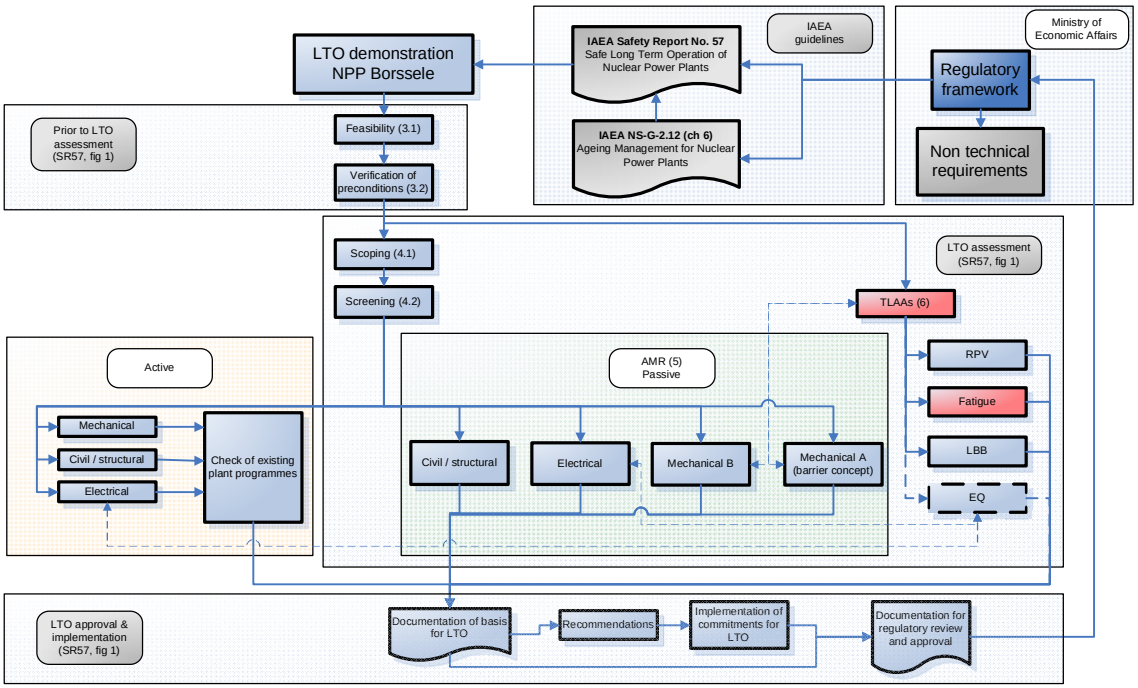

Figure 1. Schematic overview of LTO fatigue programme within LTO demonstration programme.

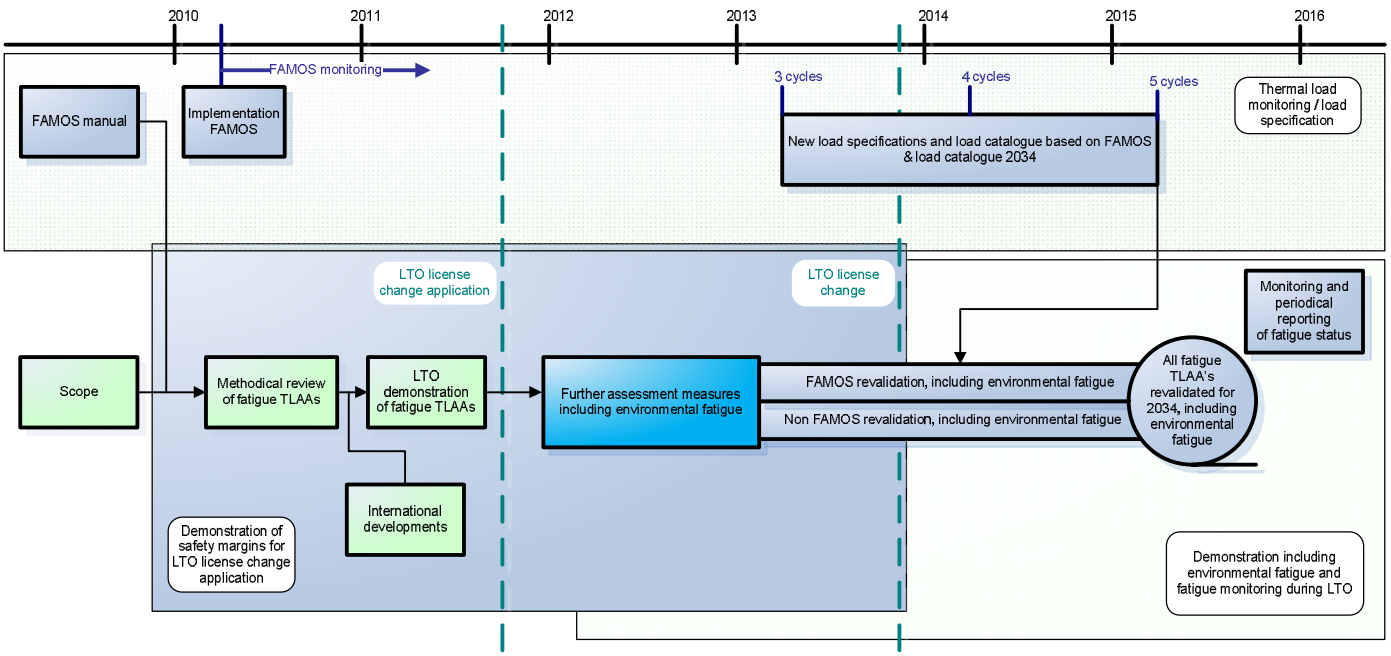

Figure 2. Schematic overview of LTO fatigue programme of NPP Borssele.

Figure 3. NPP Borssele, The Netherlands.

2. Scope

The first step in the revalidation of fatigue TLAAs is to determine the components and locations for which fatigue assessments are relevant. For completeness, this was done independently of the available existing fatigue analyses which are part of the current design base. A first definition of the scope was made by assessment against international practice and guidelines and engineering judgment. Then, the scope was verified by comparing it to the scope of a similar NPP in Germany and the set of fatigue analyses available at NPP Borssele. The four steps that were taken are summarized as follows:

1. Identify components
2. Identify component locations
3. Additional existing fatigue analysis locations
4. Comparison to scope of similar NPP

In the first step, the scope of fatigue relevant components was defined. This was done based on the safety functions of Systems, Structures and Components (SSCs) as defined in IAEA Safety Reports Series No. 57 [0]. As a result, the following set of components was selected:

- Reactor pressure vessel
- Steam generator
- Pressurizer
- Main coolant pumps
- Main coolant piping
- Surge line
- Spray lines and auxiliary spray lines
- Feedwater piping
- Main steam piping

Then, the locations of the selected components were determined that require a fatigue assessment. This selection was made based on assessment against international practice and guidelines and engineering judgment. Examples of international guidelines that were used are IAEA-TECDOCs on ageing of different components, NUREG 1801 [0], NUREG/CR-6260 [0], ASME Boiler and Pressure Vessel Code, and KTA standards. Also, design and manufacturing specifications of the components and the results of the 10-yearly periodic safety review were included in the survey.

In the third step, locations with existing fatigue TLAAs were added to the scope, in line with US nuclear guidance on license renewal NEI 95-10 [0]. Finally, the scope consisted of 50 component locations that had to be assessed for fatigue.

As a last step, a verification was made by comparing the scope of NPP Borssele with the scope of a similar NPP in Germany. Herewith it was demonstrated that the scope of NPP Borssele is in line with international practice.

3. Methodical review

For all component locations in the scope, a methodical review of the fatigue analyses was performed. With these reviews, the safety margins for LTO were identified. The reviews were performed in a systematic way by applying a list of evaluation criteria on a wide range of topics to each analysis. The topics include: geometry, material properties, boundary conditions, analysis method, loads, fatigue analysis method, conservatism/margins, relevant operating experience, fatigue monitoring, and environment.

To assess the fatigue status of the different locations for LTO, the loads applied in the fatigue analyses were revalidated until 2034. First, a thorough survey was made of the applied load cases. Next, the numbers of cycles associated with these load cases were projected until 2034.

In most cases, the projected numbers of cycles until 2034 are based on numbers of cycles that actually occurred in the plant so far. Figure 4 shows an example of such an extrapolation. The slope of the projected line was determined by averaging the counted number of cycles, without the higher frequency of occurrences during the start-up phase of the reactor (i.e. the first two years). In the case no counts were available, e.g. for emergency cases, a projected number of cycles of at least 1 was taken into account.

Most of the components of NPP Borssele are in operation since the commissioning of the plant. During a modification project that has taken place at the plant in 1997, various components have been (re)placed or changed. This means that fatigue analyses were performed for different operation times and that also the numbers of load cycles experienced by the components differ.

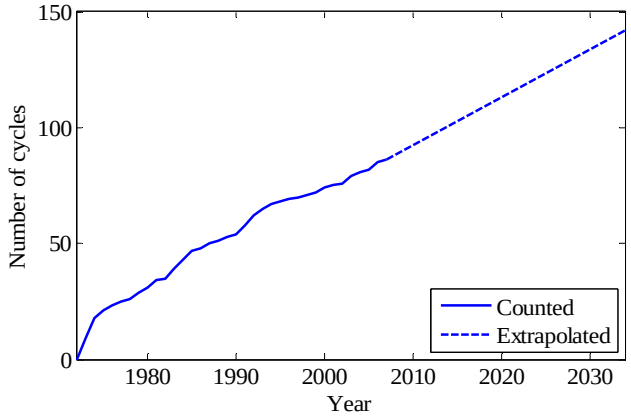

Figure 4. Extrapolation to determine projected number of cycles.

Depending on the specifications of the components, the fatigue assessments were performed using different codes. Over the years, different versions of the German safety standards KTA and the ASME Boiler and Pressure Vessel Code were used. For the revalidation of the fatigue analyses, a comparison was made between the most recent versions of these codes and the versions used in the analyses. Since no major differences were found in the assessment methods for fatigue, guidelines used in the original analyses were found to be adequate for LTO.

As a result of the methodical review, all existing fatigue analyses were assessed and, if possible, usage factors were revalidated until 2034. For 44 of the 50 component locations it was demonstrated that the cumulative usage factors until 2034 are within the regulatory limits. For 6 component locations further fatigue assessment was necessary. In the section "Further Assessment Measures", the approach followed for the new analyses of these components is presented.

4. International developments

In addition to the items addressed in the methodical review, there is a number of topics that is still under international discussion. The two most important are high-cycle thermal fatigue and environmentally assisted fatigue. Both are discussed in this section.

4.1 High-Cycle Thermal Fatigue

Worldwide, cracking events due to (high-cycle) thermal fatigue phenomena, which were not included in the initial design, have occurred at several NPPs. At NPP Borssele, structural integrity regarding most of the thermal fatigue phenomena (low-cycle fatigue) is covered by the design analyses and the fatigue monitoring system FAMOS. High-cycle temperature fluctuations (for example in a mixing tee, see Figure 5), however, are too fast to be detected by common plant instrumentation systems and are generally not included in the design analyses.

To assess the possibility of high-cycle fatigue damage at NPP Borssele, an overview was created of international high-cycle thermal fatigue events. In literature various overviews of such events are given (IAEA-TECDOC-1361 [0]; Gosselin et al. [0]; Hirschberg [0]; Paffumi and Radu, [0]). At NPP Borssele, feedback on external events related to ageing issues is recorded in an ageing management database.

Most literature cases were therefore already documented. Events requiring a more extensive analysis are subsequently discussed in separate reports, where the influence on NPP Borssele components is assessed. Based on the available information, none of the reported events appeared to be applicable to NPP Borssele. International developments in this field will be followed until the end of the intended period of LTO.

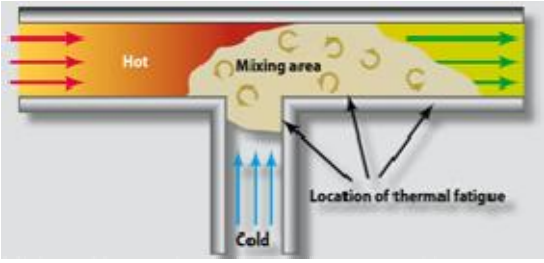

Figure 5. Example of high-cycle thermal fatigue event.

4.2 Environmental fatigue

Another topic that is addressed world-wide is the effect of the reactor coolant environment on fatigue life. To define an adequate procedure for incorporating environmental effects in the fatigue assessment for LTO, first a survey was conducted on the latest international developments in this field. At the time of the survey, most developments were taking place in the US and Germany. Since NPP Borssele was designed by Siemens/KWU (Germany), it was decided to follow the environmental fatigue guidelines of the German safety standards KTA 3201.2 [0]. The first step in these guidelines is to perform a screening with awareness thresholds of 0.2 for austenitic materials and 0.4 for ferritic materials. If the cumulative usage factor is smaller than these thresholds, no additional measures have to be taken regarding environmental effects. If the cumulative usage factor exceeds the awareness thresholds, one of the following measures has to be taken (KTA 3201.2 [0]):

- Including the component into a fatigue monitoring programme according to KTA 3201.4 [0]
- Performing appropriate experiments
- Detailed fatigue analyses taking into account environmental fatigue correction factors

At NPP Borssele, the last option was applied. A new detailed fatigue analysis was performed including environmental fatigue correction factors (Fen factors). The Fen factors were calculated according to NUREG-CR/5704 [0] for austenitic steels and NUREG-CR/6583 [0] for ferritic steels. To calculate the Fen factors under conditions where temperature and strain rate are changing over time, the so-called modified rate approach (Chopra and Shack [0]) was used.

By screening the component locations, it was shown that for a few of these locations environmental fatigue correction factors had to be applied.

5. Further assessment measures

As discussed in the previous sections, for certain component locations further fatigue assessment was required to demonstrate safe operation for the period of LTO. For these locations, new fatigue analyses were performed including the assessment of environmental fatigue.

The first step in the further assessment measures was a reassessment of the load specifications. In the load specifications, the temperature transients are defined that have to be taken into account in the fatigue analyses. In some cases, the design transients as used in the original fatigue analyses are very conservative with respect to the actual transients. To reduce this conservatism, a set of new temperature transients

was defined based on FAMOS measurements. Before incorporating them into the updated load specifications, the effects of the measured transients were assessed by the NRG fatigue model.

After updating the load specifications, new fatigue analyses were performed using state-of-the-art calculation techniques and assessment methods. Depending on the level of detail needed, different fatigue assessment methods were applied. Figure 6 summarizes these methods in order of increasing complexity. The level of detail needed depends on the necessity to reduce conservatism in the assessment. The more conservatism is allowed, the less time consuming the calculations. All fatigue analyses were performed according to ASME Boiler and Pressure Vessel Code, Section III, Division 1 or equivalent methods described in the KTA safety standards. In method 1 and 2, plastic effects are taken into account by multiplying the alternating stress intensities resulting from an elastic analysis by so-called Ke or Kv factors. In method 3, usage factors are determined by performing elastic-plastic analyses. Fatigue assessment method 1 is available in the finite element (FE) software ANSYS that was used. For the other two assessment methods, NRG developed a fatigue analysis module that can be used in combination with any FE program. If the resulting cumulative usage factors were larger than the awareness thresholds for environmentally assisted fatigue, environmental fatigue correction factors were applied as presented in the previous section. Also for this, the NRG fatigue analysis module was used.

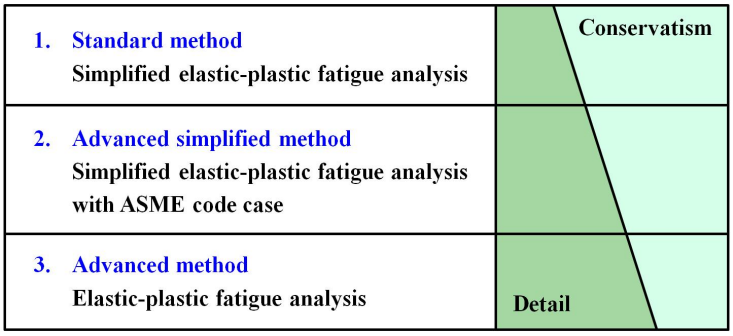

Figure 6. Fatigue assessment methods.

With the results of the new fatigue analyses, it has been demonstrated that for the pressure boundaries of all locations, the cumulative usage factors until the end of the intended LTO period are within the regulatory limits. The results of the measures taken for the locations that needed further assessment were presented before entering LTO.

6. Load monitoring

Temperature fluctuations at the fatigue sensitive locations of NPP Borssele are monitored by the Fatigue Monitoring System FAMOS (installed by Areva). The monitoring system was implemented during the annual refuelling outage in April 2010. A total of 25 measurement sections were installed at different locations. At locations where stratification was expected (14 out of 25), the measurements sections contain 7 thermocouples. An example of this are the 3 measurement sections on the surge line, as shown in Figure 7. At the other locations, 2 thermocouples are present.

The temperature measurements registered by FAMOS are used for two different purposes (see also Figure 2). First of all, they were used for verification and update of the load specifications and load catalogue. The updated versions of these documents form the basis of the fatigue analyses until 2034. Five cycles of measurements were used for verification of the load specifications and load catalogue to have a statistical representation of the thermal transients associated with the different load cases.

Secondly, FAMOS will be used for fatigue monitoring. During the entire period of LTO, temperature measurements will be made to register thermal transients at the different locations. Based on these transients and the underlying fatigue analyses, the fatigue status will be reported annually.

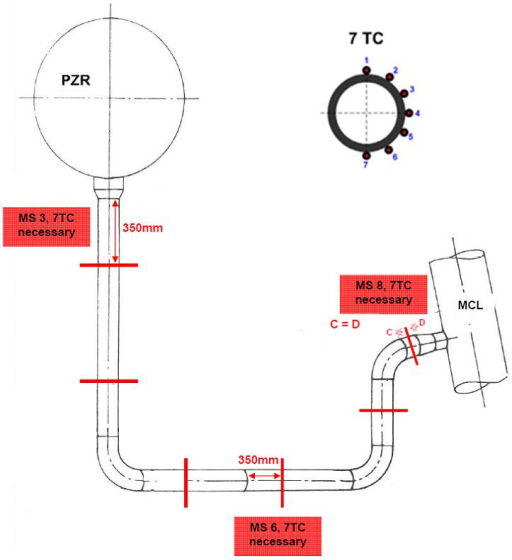

Figure 7. FAMOS measurement sections on surge line.

7. Fatigue management

The basis of the fatigue analyses until 2034 is formed by the load catalog and the load specifications of the different components. In the load catalogue a description is given of the possible load cases and the projected numbers of cycles until the intended end of the LTO period. The load specifications defined for each component are the temperature and pressure transients that are associated with the different load cases.

To ensure that the assumptions that were made in the fatigue analyses remain valid during the entire period of LTO, fatigue management is an important aspect. The implemented fatigue management approach couples load monitoring, transient counting and fatigue assessment in a sophisticated way.

The fatigue management approach follows the Plan, Do, Check, Act cycle, as shown in figure 8. The fatigue basis (central part), consisting of the scope, load catalog, load specifications and fatigue analyses is described in the previous chapters. Fatigue management is subsequently carefully planned and data is collected during operation (Plan and Do). The projected numbers of cycles are verified by load case counting, and the thermal transients are verified by evaluating temperature measurements with the load evaluation application LEAF, a software tool developed for fatigue (Check). If necessary measures can be taken to manage the fatigue effects (Act). In addition, international developments are followed and fed into the PDCA cycle. Based on the results of the approach, the actual fatigue status of the various components can be monitored and reported, to demonstrate management of fatigue during LTO.

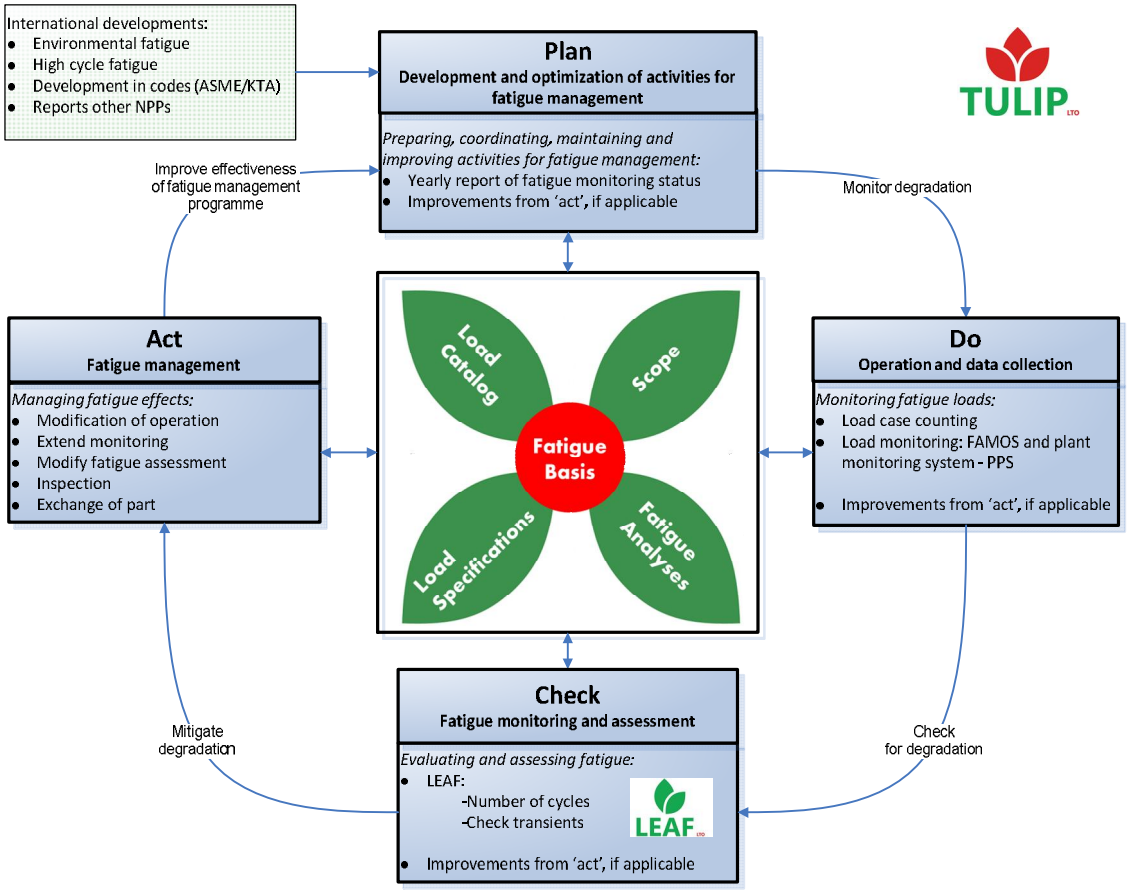

Figure 8. Fatigue management by PDCA cycle.

8. Conclusion

In this paper, the methodology is presented for the revalidation of fatigue TLAAs for LTO of NPP Borssele in the Netherlands. The different steps of the developed programme are in line with the international standards and guidelines. Based on the LTO assessment, the license of NPP Borssele was revised comprising operation until 2034 (60 years of operation). Fatigue management of NPP Borssele is ensured by means of the fatigue concept where load monitoring, transient counting and fatigue assessment are coupled through an integrated approach during the entire period of LTO. A sound basis was developed for the prevention of crack initiation by fatigue.

References

1. Ageing Management for Nuclear Power Plants (2009). Safety Guide No. NS-G-2.12, International Atomic Energy Agency, Vienna.

2. Assessment and management of ageing of major nuclear power plant components important to safety: Primary piping in PWRs (2003). IAEA-TECDOC-1361, International Atomic Energy Agency.

3. Paffumi, E. and Radu, V. (2009). Status on the knowledge on crack network evolution under spectrum loading; Crack propagation and possible arrest/penetration, Report NULIFE (09) 10.

4. Chopra, O.K. and Shack, W.J. (1998). Effects of LWR Coolant Environments on Fatigue Design Curves of Carbon and Low-Alloy Steels, Technical Report NUREG/CR-6583, ANL-97/18, U.S. Nuclear Regulatory Commission.

5. Chopra, O.K. (1999). Effects of LWR Coolant Environments on Fatigue Design Curves of Austenitic Stainless Steels, Technical Report NUREG/CR-5704, ANL-98/31, U.S. Nuclear Regulatory Commission.

6. Chopra, O.K. and Shack, W.J. (2006). Effect of LWR Coolant Environments on the Fatigue Life of Reactor Materials, NUREG/CR-6909.

7. Gosselin, S.R., Simonen, F.A., Heasler, P.G. and Doctor, S.R. (2007). Fatigue Crack Flaw Tolerance in Nuclear Power Plant Piping; A basis for Improvements to ASME Code Section XI Appendix L, NUREG/CR-6934, PNNL-16192.

8. Hirschberg, P. (2000). Operating experience regarding thermal fatigue of unisolable piping connected to PWR reactor coolant systems (MRP-25), Report 1001006, EPRI, Palo Alto (CA), US.

9. Industry Guidelines For Implementing The Requirements of 10 CFR Part 54 - The License Renewal Rule (2005). NEI 95-10 Revision 6, Nuclear Energy Institute.

10. KTA 3201.2 (2011). Komponenten des Primärkreises von Leichtwasserreaktoren, Teil 2: Auslegung, Konstruktion und Berechnung, Änderungsentwurf, Safety Standards of the Nuclear Safety Standards Commission (KTA).

11. KTA 3201.4 (1999). Components of the Reactor Coolant Pressure Boundary of Light Water Reactors, Part 4: In-service Inspections and Operational Monitoring, Safety Standards of the Nuclear Safety Standards Commission (KTA).

12. NUREG 1801 (2005). Generic Ageing Lessons Learned (GALL) Report, Vol.1, Rev.1 and Vol.2, Rev.1.

13. Safe Long Term Operation of Nuclear Power Plants (2008). Safety Report Series No. 57, International Atomic Energy Agency, Vienna.

14. Ware, A. G., Morton, D. K. and Nitzel, M. E. (1995). Application of NUREG/CR-5999 Interim Fatigue Curves to Selected Nuclear Power Plant Components, NUREG/CR-6260.

Study on safety margins assessment practices

Otso Cronvall

VTT Technical Research Centre of Finland Ltd
Espoo, Finland

Abstract

This study concerns Finnish safety factor definitions applied to structural integrity analyses of nuclear power plant (NPP) piping components. On global level, International Atomic Energy Agency (IAEA) provides information and definitions on safety margins and safety factors of NPP components. In Finland, the significant documents concerning the safety factors of NPP components are YVL Guides. However, they do not give the actual safety factor data, but instead refer to certain applicable standards. These are mainly ASME code Sections III and XI. Both deterministic and probabilistic crack growth analyses were performed for two representative BWR piping components. For comparison purposes, the analyses were carried out both with and without safety factors. Due to various kinds of safety factors and conservative assumptions, it is difficult/ impossible to define what is the total safety margin of a structure or component. Structural integrity analyses of structures and components would benefit from such more specific definitions of safety factors that would give a more accurate assessment of the total safety.

1. Introduction

This study concerns collection and review of Finnish safety factor definitions applied to structural integrity analyses of NPP piping components as well as representative analysis examples showing the effect and underlying uncertainties concerning the safety factors.

IAEA publishes internationally important documents concerning safety of application of nuclear energy. The top level IAEA documents are the safety standards, which are or will be adopted by all European regulators as the basis for their assessments of NPPs. The INSAG reports are complementary reports but are not adopted by the national regulators and, therefore, are not fully followed in the national safety assessments. IAEA publishes also other important documents, such as TECDOC series reports. These documents are presently not adopted by national regulators.

The following IAEA safety standards have connections with safety assessment and safety margin assessments:

- NS-R-1 Safety of Nuclear Power Plants: Design [2],
- SSR-2/2 Safety of Nuclear Power Plants: Commissioning and Operation [3],
- SSG-2 Deterministic Safety Analysis for Nuclear Power Plants - Specific Safety Guide [4],
- NS-G-2.14 - Conduct of operations at nuclear power plants [5],
- NS-G-2.2 - Operational limits and conditions and operating procedures for nuclear power plants [6],
- NS-G-2-12 - Ageing management for nuclear power plants [7].

Instead of specifying what safety margins actually mean, the covered IAEA documents use terms limits and levels. In addition, there exist several kinds of margins. Some of these represent demanded margins to be used in safety assessment, others represent uncertainties concerning knowledge of methods/data that are included in the assessment. There exist almost always margins that are remaining margins for which there exist no demands in the safety guides or by the regulators. Only in IAEA report NS-R-2 - Safety of Nuclear Power Plants: Operation [8] are safety factors mentioned. Therein it is mentioned in connection to safety assessment that the strategy for the review and the safety factors to be evaluated shall be approved or agreed by the regulatory body. However, presently the report SSR-2/2 [3] supersedes report NS-R-2 [8], and in the former report nothing is mentioned concerning safety factors.

The demands on never passing safety limits have to be fulfilled by the NPPs independent of the age of the plant. Guides and standards specify methods to be used in performing safety assessments and in ways to determine safety limits. These guides and standards specify that conservative approach is to be used in such assessments. The conservative approach represents different kinds of margins. Used data and calculation methods include certain degree of uncertainty. The uncertainty part of the margins will be decreased when knowledge concerning the issue in question is increased.

There exist no specified values for safety margins in safety guides or regulatory demands. Safety margins consist of margins from several different structures, systems and components. It is not possible to calculate an overall value for safety margins with the commonly used deterministic methodology [9].

In every safety assessment, there exists a remaining margin between the output from the safety assessment and the safety limit. This remaining margin, which can only be quantified with best estimate analyses, is not part of the safety margin and there are no quantitative requirements for it [9].

Establishment of a value that could represent the total safety status (safety margin) of a NPP has to be done by probabilistic terms with risk analysis approach. Distances to different risk limits can give insight in the total safety margins of the plant. This also allows ranking different safety issues against each other.

2. Safety margins and limits associated with safety factors

To provide technical background for safety factors, a short summary of safety margins and limits concerning NPP components and their relation to safety factors is described in the following. This is carried out in international level, as based on documents published by IAEA. The detailed definitions of the safety factors are a country specific issue, mainly as presented by the local regulators.

In performing deterministic safety assessment, several kinds of margins can be used with high confidence to support that specified limits are not violated. In each assessment, the following margins exists:

- **Margins between safety limit and incorrect function or failed barrier, M1**; This margin is specified in international standards or regulatory demands, by specifying the safety limits. Deterministic safety assessments have to prove that this margin exists for all initiating events and barriers by never exceeding the specified safety limits.
- **Margins between conservative and non-conservative safety assessment, M2**; Performing safety assessment includes that certain methodology is used, as steered by guidance or regulatory demands. The methodology specifies certain conservatism to be used. This includes the application of safety factors. The desired degree of conservatism affects the choice of analysis codes, procedures and data to be used in the assessment. This margin is represented by the difference in outputs between realistic assessment and conservative assessment. The degree of conservatism depends on the knowledge of the phenomena in question and on the ability of the analysis procedure to represent a certain phenomenon. By research and other developments, the demands on used conservatism can be changed. When more knowledge and analysis procedures are available, it is in most cases accepted to reduce the conservatism. Some types of conservatism are specified in different guidance or regulations and cannot be reduced without change in regulations.
- **Margins on operating position or effects of ageing on material, M3**; In performing safety assessment, the current condition of systems, structures and components needs to be specified. For this purpose, ageing effects to material properties shall be specified in a conservative way, so as to represent a broad group of initiating positions of the events and material conditions. With operating experiences and with modern knowledge on material ageing, the conservatism used for the initiating parameters represent the M3 margin in the safety assessment. Deterministic safety assessments have no

specific demands on the M3 margin itself for any initiating events and barriers. It is important that a positive margin exists for all operational modes.

- **Remaining margin, R**; The output value of safety assessments shall be shown not to override the specified safety limits for the specific event/case. The differences between the output value of the assessment and the value of the safety limit represent the remaining margin. There exist no specific demands on the value of this margin. It can be zero or very large. In some cases, the methodology defines how to assure that this margin is large enough to cover the uncertainty in the assessment. In most cases, the uncertainty is included in the output value from the assessment. The change in remaining margin can be evaluated when modifications are performed at the plant. In most cases, a change in remaining margin does not affect the other margins.
- **Uncertainties, U**; The margins M1 to M3 include effects of chosen conservatism and uncertainties. The basic demand in the safety assessment is to assure that the specified limit is not exceeded. Uncertainties exist in all parts of a deterministic safety assessment. Especially the analytical margins of type M2 include a certain degree of uncertainty, e.g. based on how well the used thermo-hydraulic code can represent a certain scenario. This uncertainty is part of the margins but has to be included only as long as the uncertainty exists based on lack of knowledge, code validations or data. It is important that the degree of uncertainties is quantified or at least positioned towards used conservatism in the assessment. The uncertainties shall be part of the value for the margin and may never exceed the value of a specific margin.

Each NPP component has to fulfil demands specified in the final safety analysis report (FSAR) and in some cases specified in national or international norms/standards. On the component level, these demands can vary in different event classes. Safety cases are evaluated with different load combinations. Concerning piping components, different load combinations will, as based on the frequencies of occurrence, be evaluated against different acceptance criteria, i.e. safety limits. To have different acceptance criteria in different event classes is also valid for other components. For instance, US NPP code ASME prescribes different stress limits for different event classes.

The safety limits are developed in such a way that demands on system level and plant level will be fulfilled. Concerning NPP piping, the criteria are set to certify that the loss-of-coolant-accident (LOCA) frequencies support the event frequencies on these different events specified in the FSAR. For certain assessments of components, specific demands are specified for data conservatism (M3 safety margins) and on methodologies (M2 safety margins) to be used for the evaluations. For instance, the ASME code identifies specific data and methodologies to be used in the assessment of stresses on piping or maximum pressure in structural systems.

In these assessments for each component, there are safety margins in:

- The conservatism in specifying the acceptance criteria for the different components in each event class (M1 safety margins).
- The conservatism in data and methodologies used in the assessment (M2 and M3 safety margins).
- The conservatism of the selection of material (including specified material properties), which is part of the M3 safety margin value.

The existing margins in categories M1, M2 and M3 can be changed by changing the method for specifying the acceptance criteria or by altering the definition of the conservatism in used assessment methodologies.

Uncertainties U exist in all margins. The M2 margins include uncertainties in the used methodologies and their validation levels. The safety factors belong mainly to the M2 safety margins. As for the M3 margins, they include uncertainties in the initial material properties. The remaining margins R can be changed by ageing, plant modifications and changes in operating procedures. The overall integrity margin or component margin is therefore the following sum: M1+ M2+ M3.

An overall presentation of the various types of NPP safety margins is shown in Figure 1. An illustration of the NPP design margins is shown in Figure 2. An illustration of the NPP safety margins associated with the acceptance criteria is shown in Figure 3.

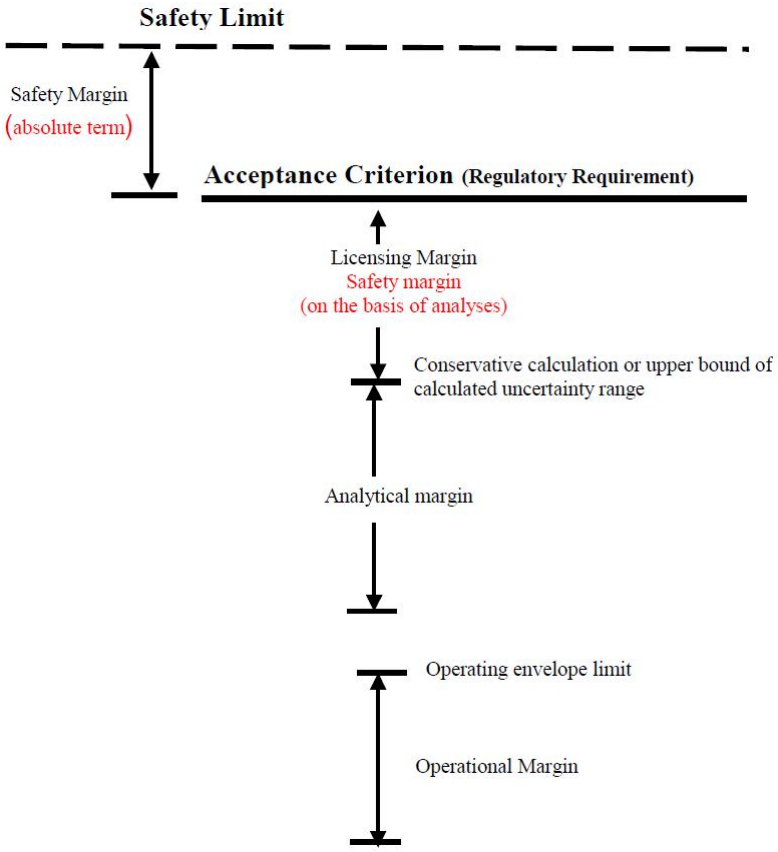

Figure 1. The various types of NPP safety margins [10].

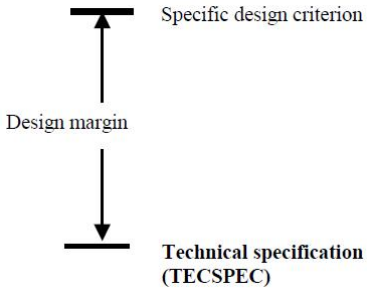

Figure 2. Illustration of NPP design margins [10].

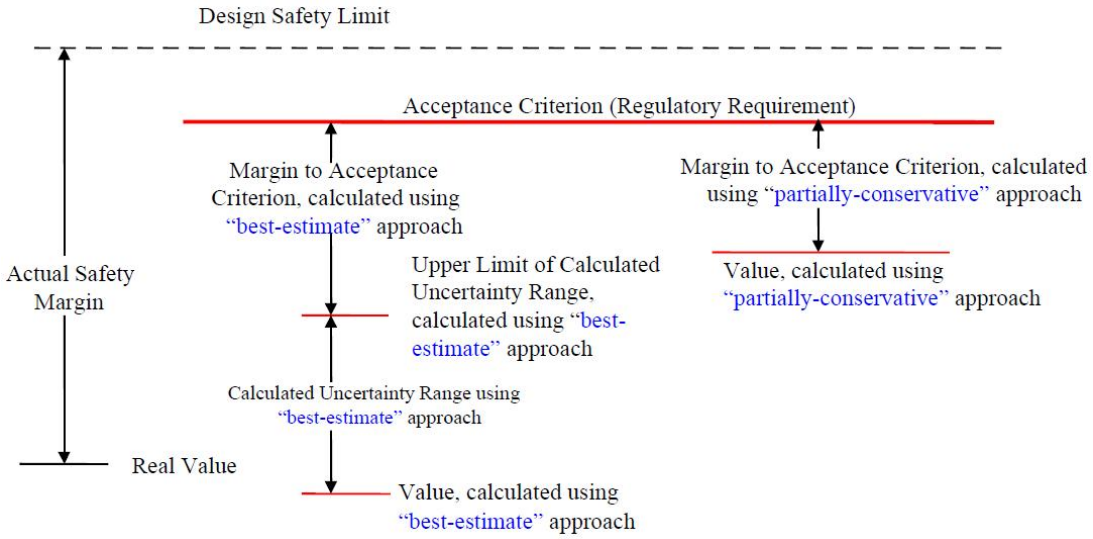

Figure 3. Illustration of the NPP safety margins associated with the acceptance criteria [10].

3. Review of safety factors concerning degradation analyses of NPP components

A review of safety factors concerning degradation analyses of NPP piping components is presented in the following. The scope is limited to domestic safety factor definitions, mainly given by STUK in the YVL Guides. The acronym YVL corresponds to Finnish words that as translated to English stand for: regulatory guides on nuclear safety. However, in a number of cases the YVL Guides refer to international standards, so those are mentioned too with presenting the relevant definitions therein. The issues considered in this chapter are:

- YVL guides on safety factors and safety margins,
- YVL guides on analyses requiring application of safety factors,
- relevant international standards on analyses applying safety factors.

The YVL Guides and most relevant international standards covered in this study are:

- GUIDE YVL A.8, Ageing management of a nuclear facility [11],
- GUIDE YVL B.3, Deterministic safety analyses for a nuclear power plant [12],
- GUIDE YVL E.3, Pressure vessels and piping of a nuclear facility [13],
- GUIDE YVL E.4, Strength analyses of nuclear power plant pressure equipment [14],
- GUIDE YVL E.5, In-service inspection of nuclear facility pressure equipment with non-destructive testing methods [15],
- ASME Section III, Rules for Construction of Nuclear Facility Components [16],
- ASME Section XI, Rules for In-service Inspection of Nuclear Power Plant Components [17],
- IAEA Safety Standard NS-G-2.6, Maintenance, Surveillance and In-Service Inspection in Nuclear Power Plants [18],
- WENRA Reactor Safety Reference Levels, Issue K [19],
- Standard ASTM E 1921-11 [20],
- Standard ASTM E 1820-11 [21],
- Standard Review Plan 3.6.3, Rev.1, Leak-Before-Break Evaluation Procedures [22].

YVL Guides that contain no information on the safety factors and safety margins, but do contain classifications and other important data are:

- GUIDE YVL A.6, Conduct of operations at a nuclear power plant [23],
- GUIDE YVL A.7, Probabilistic risk assessment and risk management of a nuclear power plant [24],
- GUIDE YVL B.2, Classification of systems, structures and components of a nuclear facility [25],
- GUIDE YVL B.5, Reactor coolant circuit of a nuclear power plant [26].

3.1 YVL guides on safety factors and margins

To summarise for safety factors, YVL guides refer to applicable standards and nuclear codes, e.g. it is stated in GUIDE YVL E.5 [15]: “A calculation method that complies with ASME Code, Section XI [17] Subarticle IWB-3600 shall be used to calculate pressure equipment crack growth during the inspection interval or during its remaining service life. The standards list the service loading safety factors in question.”

To summarise for safety margins, YVL guides present the following definition. According to chapter “1 Introduction” of GUIDE YVL A.8 [11], chapter “1 Introduction” of GUIDE YVL E.3 [13] and chapter “1 Introduction” of GUIDE YVL E.4 [14]: “The design, construction, operation, condition monitoring and maintenance of a nuclear power plant shall provide for the ageing of systems, structures and components (SSCs) important to safety in order to ensure that they meet the design-basis requirements with the necessary safety margins throughout the service life of the facility.”

3.2 YVL guides on analyses requiring application of safety factors

For NPP piping components, the main YVL Guide on design and other analyses requiring application of safety factors is YVL E.4 [14]. Other YVL Guides do not contain anything significant on that issue.

In general, it is stated in chapter “5 Stress analysis” of GUIDE YVL E.4 [14] that: “A stress analysis in accordance with the present Guide shall be conducted on pressure equipment or their parts which are to be constructed in accordance with the highest safety and quality requirements applicable to a nuclear power plant. Items of special importance include Safety Class 1 primary circuit components including main circulating pumps”.

According to chapter “5.4 Acceptance limits” of GUIDE YVL E.4 [14]: “Stress analysis shall demonstrate the fulfilment of the service limits set by the applicable standard for the item of pressure equipment in question or its part in accordance with its classification, service load grouping, number of pressure tests and the analysis methods used. The states of stress calculated by stress analysis shall, therefore, be classified into stress types which are significant for the maintenance of integrity and operability and relative to which each service limit is set. This procedure shall be repeated for all analysed structural parts and loads of the item of pressure equipment.”

According to chapter “6.3 Qualification input information” of GUIDE YVL E.5 [15]: “A calculation method that complies with ASME Code, Section XI [17] Subarticle IWB-3600 shall be used to calculate pressure equipment crack growth during the inspection interval or during its remaining service life. The standards list the service loading safety factors in question.”

According to chapter “2 Scope of application” of GUIDE YVL E.4 [14]: “Loadings comprise the mechanical and thermal stress factors arising in the nuclear power plant’s normal operation, and design basis and design extension operational conditions, against which the pressure equipment design shall present adequate safety margins, demonstrated by strength analyses. The strength analyses include stress analysis, brittle fracture analysis and analyses demonstrating the implementation of the leak before break principle (LBB). To be analysed are also loadings when their values are to be derived by calculations from the operation of systems, behaviour of buildings or loading conditions exerted on pressure equipment by local phenomena. The LBB principle is presented as a procedure for excluding pipe break induced impact loads from the design bases.”

According to chapter “6.6 Operational occurrences and accidents” of GUIDE YVL E.4 [14]: “The acceptance criterion shall be in accordance with the safety margin required in the applicable standard as regards the growth of a postulated crack. An analysis of the safety margin provided by crack arrest may be considered as an additional justification on a case-by-case basis.”

According to chapter “7.7 Analysis methods” of GUIDE YVL E.4 [14]: “LBB analysis shall demonstrate by analysis of fracture and fluid mechanics the safety margins required in reference [22] as regards leak detection and critical defect size.”

According to chapter “7.7 Analysis methods” of GUIDE YVL E.4 [14]: “Determination of critical defect size shall be based on crack growth resistance values representing the materials and welding procedures used in manufacturing, which are determined by testing in accordance with an applicable standard [21] at a temperature corresponding to normal operation. The crack growth resistance values must be valid for the stable crack extension, based on which critical defect size and the safety margin for it are determined. In using extrapolation, the method applied and its qualification data shall be presented.”

3.3 Relevant standards on analyses applying safety factors

The relevant standards containing safety factors applicable to NPP piping components are considered in the following. The YVL Guides do not give the actual safety factor data, but instead refer to these standards. These are ASME code Sections III [16] and XI [17].

In chapter "5.2 Applicable standards" of GUIDE YVL E.4 [14] it is stated that: "In conducting a stress analysis of pressure equipment and pumps in accordance with the present Guide, the standard ASME Boiler and Pressure Vessel Code Section III, Division 1 [1616] shall apply as a general rule. The mandatory regulations stated in its Articles NB 3200 and NB 3650 as well as in its Subsections NF and NG apply in these cases in so far as STUK has not presented more detailed requirements."

After that the YVL E.4 [14] moves on to state that another design and strength analysis standard for Safety Class 1 pressure equipment can be applied too, on the condition that it has been applied previously in the construction of NPPs of the same type.

To provide technical background associated with the application of the safety factors, the definitions of the safety classes of the NPP components, service level loads and necessary stress components are summarised first. This description is limited to metallic components.

According to YVL B.2 [25] the NPP components divide into safety classes, corresponding to criteria ensuring structural resistance, integrity and leak-tightness, as follows:

- **Safety Class 1** shall include nuclear fuel as well as structures and components whose failure could result in an accident compromising reactor integrity and requiring immediate actuation of safety functions. Safety Class 1 includes the reactor pressure vessel (RPV) and those components of the primary circuit whose failure results in a primary circuit leak that cannot be compensated for by systems relating to normal plant operation.
- **Safety Class 2** components include main components and piping of the emergency core cooling system, structures of the core support and reactor shutdown system, primary circuit piping supports and brackets, fuel storage racks, certain less risk significant small-diameter piping and components, as well as components which can be isolated from the reactor coolant system.
- **Safety Class 3** includes mainly structures and components relating to barriers to the dispersion of radioactive substances or structures relating to the handling of radioactive materials not assigned to higher safety classes.

The four service level loads A, B, C and D are defined in Appendix H of ASME Section XI [17] as follows:

- **Level A service loadings** are any loadings arising from system start-up, operation in the design power range, hot stand-by, and system shutdown, and excepting only those loadings covered by other service level loads.
- **Level B service loadings** correspond to incidents of moderate frequency. These loadings are deviations from Level A service loadings that are anticipated to occur often enough that design capability should withstand them without operational impairment. The events causing Level B service loadings include transients resulting from any single operator error or control malfunction, transients caused by a fault in a system component requiring its isolation from the system, and transients due to loss of load or power. These events include any abnormal incidents not resulting in a forced outage and also forced outages for which the corrective action does not include any repair of mechanical damage.
- **Level C service loadings** correspond to infrequent incidents. These are deviations from Level A service loadings and require shutdown for correction of the loadings or repair of damage in the system. The conditions have a low probability of occurrence, but are included to provide assurance that no gross loss of structural integrity will result as a concomitant effect of any damage developed in the system. The total number of postulated occurrences for such events may not exceed 25.
- **Level D service loadings** correspond to limiting faults. These are combinations of loadings associated with extremely low probability, postulated events whose consequences are such that the integrity and operability of the nuclear energy system may be impaired to the extent that only considerations of public health and safety are involved.

For NPP piping components, the necessary stress components are defined in Article NB-3000 of ASME Section III [16] as follows:

- **General primary membrane stress, P_m,** is any normal stress or a shear stress developed by an imposed loading which is necessary to satisfy the laws of equilibrium of external and internal forces and moments. The basic characteristic of a primary stress is that it is not self-limiting. A thermal stress is not classified as a primary stress. A general primary membrane stress is distributed so in the structure that no redistribution of load occurs as a result of yielding. An example of primary stress is general membrane stress due to internal pressure or to distributed live loads.
- **Local primary membrane stress, P_L,** corresponds to membrane stress produced by pressure or other mechanical loading and associated with a discontinuity that would cause excessive distortion in the transfer of load to other portions of the structure. When the size of the more severely stressed region remains within certain limits, it can be considered local, with the limiting stress value being membrane stress intensity of 1.1 times the design stress, S_m.
- **Primary bending stress, P_b,** is the variable component of normal stress, which in turn is the stress component normal to the plane of reference. The variation may or may not be linear across the thickness. The loads causing the primary bending stress are the same as those causing the general primary membrane stress.
- **Expansion stress, P_e,** results from restraint of free end displacement of the piping system.
- **Secondary stress, Q,** is a normal stress or a shear stress developed by the constraint of adjacent material or by self-constraint of the structure. The basic characteristic of a secondary stress is that it is self-limiting. Local yielding and minor distortions can satisfy the conditions which cause the stress to occur and failure from one application of the stress is not to be expected. Examples of secondary stresses are general thermal stress, and bending stress at a gross structural discontinuity.
- **Peak stress, F,** is that increment of stress which is additive to the primary plus secondary stresses by reason of local discontinuities or local thermal stress, including the effects of stress concentrations. The basic characteristic of a peak stress is that it does not cause any noticeable distortion and is objectionable only as a possible source of a fatigue crack or a brittle fracture. Examples of peak stresses are thermal stress in the austenitic steel cladding of a carbon steel component, the stress at a local structural discontinuity, and surface stresses produced by a thermal shock.

The use of safety factors applicable to NPP piping components are often associated with local crack like flaws and their allowable sizes. The maximum sizes of such NPP piping flaws that need not be analysed further are defined in Subarticle IWB-3514 of ASME Section XI [17], in Subarticle IWB-3514.2 for ferritic piping and in Subarticle IWB-3514.3 for austenitic piping. For surface flaws detected by in-service inspection (ISI), the maximum depth of these flaws varies between 5.5 and 14.8 % of wall thickness. Thus, NPP piping flaws deeper than that need to be analysed.

According to Subarticle IWB-3640 of ASME Section XI [17], NPP piping containing flaws exceeding the acceptance standards of IWB-3514.1 may be evaluated by analytical procedures to determine acceptability for continued service to the next inspection or to the end of the evaluation period. A pipe containing flaws is acceptable for continued service for a specified evaluation time period if the criteria of Subarticles IWB-3642, IWB-3643, or IWA-3644 are satisfied.

This corresponds to the statement given in GUIDE YVL E.5 [15], that “A calculation method that complies with ASME Code Section XI [17] Subarticle IWB-3600 shall be used to calculate pressure equipment crack growth during the inspection interval or during its remaining service life.”

The above mentioned Subarticles IWB-3642, IWB-3643 and IWA-3644, in turn, refer to Appendix C or H of ASME Section XI [17] on determining the maximum allowable flaw sizes.

According to Appendix C of ASME Section XI [17], the flaws in a NPP piping component are evaluated by comparing the maximum flaw dimensions at the end of the evaluation period with the maximum allowable flaw size, or by comparing the applied pipe stress with the maximum allowable stress for the flaw size at the end of the evaluation period. The following maximum allowable flaw size and stress component definitions are used:

- a_{allow} is maximum allowable flaw depth,
- l_{allow} is maximum allowable flaw length,
- S_c is maximum allowable bending stress for circumferentially flawed pipe,
- S_a is maximum allowable hoop membrane stress for an axially flawed pipe,
- S_t is maximum allowable membrane stress for a circumferentially flawed pipe.

The evaluation for maximum allowable flaw size or maximum allowable stress requires the application of the safety factors. According to Appendix C of ASME Section XI [17], the safety factors are applied individually to membrane and bending stresses as SF_m and SF_b, respectively. The safety factors depend on the service level and flaw orientation. The considered loading conditions are those associated with Service Levels A, B, C, and D, for the piping system design. Test conditions are evaluated as Service Level B.

According to Appendix C of ASME Section XI [17], the maximum allowable stress for the flawed pipe is a function of pipe stresses, the required safety factors, pipe material properties, end-of-evaluation-period flaw length and depth, flaw orientation, and pipe failure mode.

The safety factor values for primary membrane and primary bending stresses when calculating the maximum allowable depths for circumferential and axial flaws for piping components are as presented in Tables 1 and 2, as according to Appendix C of ASME Section XI [17].

Table 1. For circumferential flaws in Class 1, 2, and 3 piping, the safety factors to be applied on primary membrane and primary bending stresses in calculating maximum allowable flaw depth [17].

Service Level	**Membrane Stress, SF_m**	**Bending Stress, SF_b**
A	2.7	2.3
B	2.4	2.0
C	1.8	1.6
D	1.3	1.4

Table 2. For axial flaws in Class 1, 2, and 3 piping, the safety factors to be applied on primary membrane stress in calculating maximum allowable flaw depth [17].

Service Level	**Membrane Stress, SF_m**
A	2.7
B	2.4
C	1.8
D	1.3

To start a structural integrity analysis of NPP piping components with safety factors on maximum allowable flaw size or/and maximum allowable stress, the sequence used to determine the failure mode and analysis method for NPP piping components are needed first. These are determined in Article C-4000 of ref. [17]. Therein it is stated that for flaws in wrought base metal, non-flux welds, weld metal, or cast product in which ferrite content is less than 20 %, plastic collapse is the controlling failure mode. For flaws in flux welds of wrought pipe, elastic-plastic analysis methods shall be applied.

The next step is to use the procedures described in Articles C-5000, C-6000 or C-7000 of ref. [17], as applicable to the failure mode, to determine the maximum allowable flaw depth, a_{allow}, or the maximum allowable applied stress, S_c or S_a, and the maximum allowable flaw length limit, l_{allow}:

- Article C-5000 gives a limit load criteria based procedure,
- Article C-6000 gives an elastic-plastic fracture mechanics (EPFM) criteria based procedure, and
- Article C-7000 gives a linear-elastic fracture mechanics (LEFM) criteria based procedure.

Article C-5000 of ref. [17] contains:

- for circumferential flaws tabulated solutions with safety factors for maximum allowable flaw depth, and analytical solutions for maximum allowable applied stress,
- for axial flaws both tabulated and analytical solutions with safety factors for maximum allowable flaw depth.

Article C-6000 of ref. [17] contains:

- for circumferential flaws tabulated solutions with safety factors for maximum allowable flaw depth, and analytical solutions for maximum allowable applied stress,
- for axial flaws both tabulated and analytical solutions with safety factors for maximum allowable flaw depth.

Article C-7000 of ref. [17] contains for both circumferential and axial flaws analytical solutions with safety factors for maximum allowable mode I stress intensity factor, K_I, which is to be compared to corresponding fracture toughness, K_{Ic}. Actually, the fracture toughness of the material is determined by two properties K_{Ia} and K_{Ic}, which represent critical values of the stress intensity factor K_I. Whereas K_{Ia} is based on the lower bound of crack arrest critical K_I values measured as a function of temperature. K_{Ic} is based on the lower bound of static initiation critical K_I values measured as a function of temperature.

Concerning conducting a stress analysis of pressure equipment and pumps, GUIDE YVL E.4 [1414] refers to ASME Section III, Division 1 [16], and therein in particular to Subarticles NB-3200 and NB-3650. These both are parts of Article NB-3000, which concerns Class 1 components. Actually, Article NB-3000 refers to safety margins or safety factors only in one subarticle. This is in NB-3222.4 Analysis for Cyclic Operation, where it is stated that: "The fatigue curves are obtained from uniaxial strain cycling data in which the imposed strains have been multiplied by the elastic modulus and a design margin has been provided so as to make the calculated stress intensity amplitude and the allowable stress intensity amplitude directly comparable. Where necessary, the curves have been adjusted to include the maximum effects of mean stress, which is the condition where the stress fluctuates about a mean value that is different from zero." Thus, ASME Section III [16] does not refer to safety margins but design margins. This corresponds to the purpose of ASME Section III [16], which concerns the design of NPP components. Whereas it is ASME Section XI [17] that concerns the operation of the NPP components. According to NUREG/CR-6909 report [27], the safety factor values of 2 on stress and 20 on load cycles have been used in defining the fatigue curves. These safety factors intend to cover the effects of variables that can influence fatigue life in air and light water reactor (LWR) environments, and they are broadly classified into the following three groups:

- material variability and data scatter,
- loading sequence,
- environment.

4. Description of NPP piping integrity analysis examples

As for the performed NPP piping integrity analyses in the associated VTT study [1], two representative boiling water reactor (BWR) piping cross-sections were considered, denoted as BWR-1 and BWR-2. The outer diameter and wall thickness of BWR-1 are 168 mm and 14 mm, and those of BWR-2 are 273 mm and 22 mm, respectively. Their material is austenitic stainless steel SA-376 TP304. The applied pressure and temperature are 7.0 MPa and 286 °C, corresponding to normal operational conditions in Finnish BWR units [28]. For comparison purposes, the process load induced stresses were applied in the analyses both with and without safety factors. The weld residual stresses (WRSs) used in the analyses are the recommendations in the R6 Method, Revision 4 [29] and the SSM handbook [30]. The WRSs are the governing stress component, varying in axial direction for BWR-1 and BWR-2 at inner surface approximately from 250 to 300 MPa, while the axial stresses induced by pressure and temperature vary from approximately 40 to 65 MPa, respectively. The considered degradation mechanism is stress corrosion cracking (SCC), and the considered flaw postulate is a circumferentially oriented crack opening to inner surface. The fracture mechanics based model to describe the propagation of SCC is the rate equation, see refs. [31, 32]. Both deterministic and probabilistic crack growth analyses were performed, using VTTBESIT code [33, 34, 35, 36, 37] developed by VTT and Fraunhofer-Institut für Werkstoffmechanik (IWM) as well as using the Markov application [38] developed by VTT. For detailed description of the used input data and applied analysis procedures, see the associated VTT study [1]. The results for the deterministic analysis cases are presented in Figure 4 and Figure 5, where in the legends R6 and SSM mean the respective WRS recommendations, whereas SFs means safety factors.

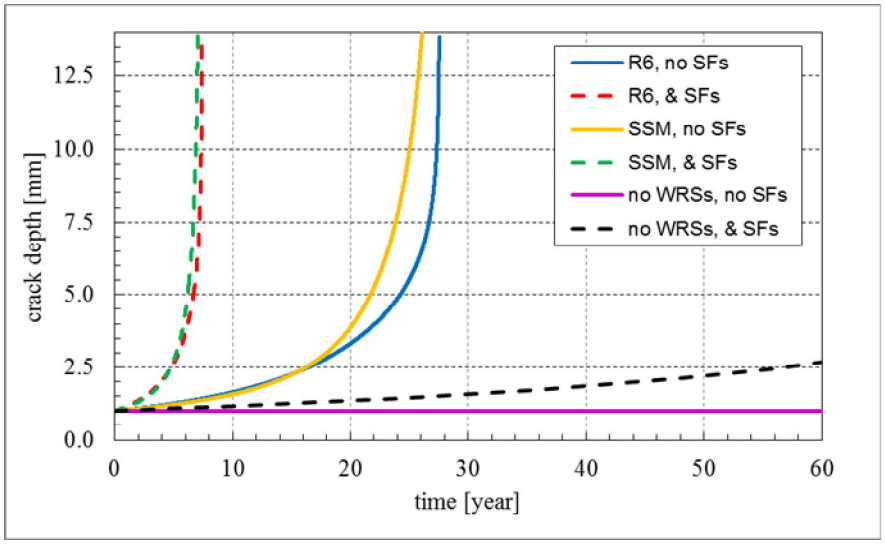

Figure 4. Deterministic VTTBESIT crack growth analysis results for BWR-1 cases [1].

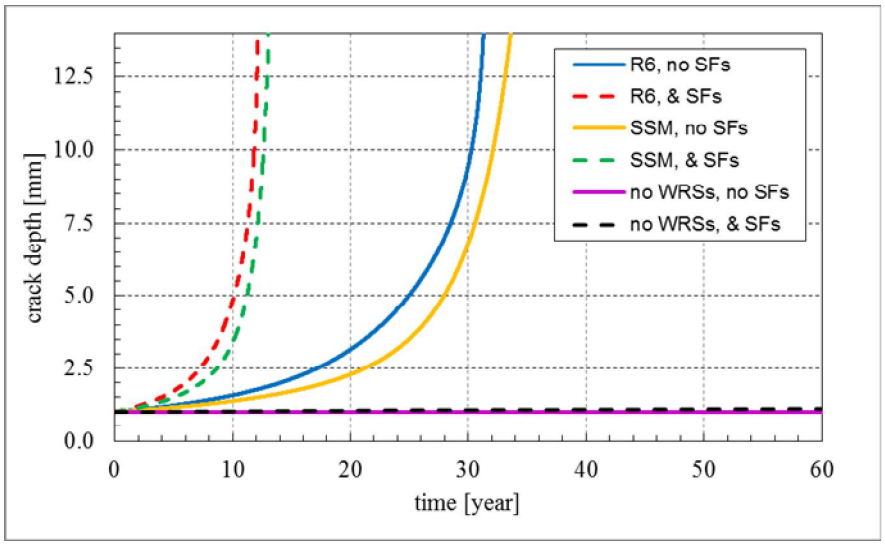

Figure 5. Deterministic VTTBESIT crack growth analysis results for BWR-2 cases [1].

According to the deterministic crack growth analysis results, the use of safety factors clearly has an effect to the crack growth analysis results. For the analysed cases the increase in tensile stress due to using safety factors varies approximately between 60 to 100 MPa. For the analysis cases with WRSs, the cracks grow through wall approximately 20 years sooner for cases with safety factors as compared to those without. On the other hand, for the analysis cases without WRSs, the cracks grow very slowly, and during 60 years the maximum growth is less than 3 mm. These latter results reveal the significant role of WRSs in SCC growth analyses. This corresponds to the experienced SCC behaviour, as the tensile stresses must be relatively high before SCC becomes significant. The effect of wall thickness to the analysis results is such for the cases with WRSs, that for cases D7 to D10 with 8 mm thicker wall than that of cases D1 to D4, the time for cracks to grow through wall is approximately 10 years longer.

5. Summary and conclusions

This study concerns collection and review of Finnish safety factor definitions applied to structural integrity analyses of NPP piping components as well as representative analysis examples showing the effect and underlying uncertainties concerning the safety factors.

On international level, IAEA provides information and definitions on safety margins and safety factors of NPP components. The detailed definitions of the safety factors are a country specific issue, mainly as presented by the local regulators. The top level IAEA documents are the safety standards, which are or will be adopted by all European regulators as the basis for their assessments of NPPs. The INSAG reports are complementary reports but are not adopted by the national regulators and, therefore, are not fully followed in the national safety assessments. IAEA publishes also other important documents, such as TECDOC series reports. These documents are presently not adopted by national regulators.

Instead of specifying what safety margins actually mean, the IAEA documents use terms limits and levels. In addition, there exist several kinds of margins. Some of these represent demanded margins to be used in safety assessment, others represent uncertainties concerning knowledge of methods/data that are included in the assessment. There exist almost always margins that are remaining margins for which there exist no demands from the safety guides or the regulators.

The demands on never passing safety limits have to be fulfilled by the NPPs independent of the age of the plant. Guides and standards specify methods to be used in performing safety assessments and in ways to determine safety limits. These guides and standards specify conservatism to be used in such assessments. The conservatism represents different kinds of margins. Used data and calculation methods include certain degree of uncertainty.

There exist no specified values for safety margins in safety guides or regulatory demands. Safety margins consist of margins from several different structures, systems and components. It is not possible to calculate an overall value for safety margins with the commonly used deterministic methodology [9]. Establishment of a value that could represent the total safety status (safety margin) of a NPP has to be done with probabilistic terms by risk analysis approach.

In performing deterministic safety assessment, the following margins exist:

- Margins between safety limit and incorrect function or failed barrier, M1,
- Margins between conservative and non-conservative safety assessment, M2,
- Margins on operating position or effects of ageing on material, M3,
- Remaining margin, R,
- Uncertainties, U.

In component level or structural integrity level assessments there are safety margins in:

- The conservatism in specifying the acceptance criteria for the different components in each event class (M1 safety margins).
- The conservatism in data and methodologies used in the assessment (M2 and M3 safety margins).
- The conservatism of the selection of material (incl. specified material properties), which is part of the M3 safety margin value.
- The overall integrity margin or component margin is therefore the following sum: M1+ M2+ M3.

In Finland, the significant documents concerning the safety factors of NPP components are:

- Finnish YVL guides by the authority STUK (Radiation and Nuclear Safety Authority of Finland, Säteilyturvakeskus in Finnish),
- relevant international standards.

The YVL Guides that contain information on safety factors and safety margins are:

- GUIDE YVL A.8, Ageing management of a nuclear facility [11],
- GUIDE YVL B.3, Deterministic safety analyses for a nuclear power plant [12],
- GUIDE YVL E.3, Pressure vessels and piping of a nuclear facility [13],
- GUIDE YVL E.4, Strength analyses of nuclear power plant pressure equipment [14],
- GUIDE YVL E.5, In-service inspection of nuclear facility pressure equipment with non-destructive testing methods [15].

However, the YVL Guides do not give the actual safety factor data, but instead refer to certain applicable standards. These are ASME code Sections III [16] and XI [17]. Some main definitions for safety factors given in these refs. are summarised in the following.

According to Appendix C of ref. [17], the evaluation for maximum allowable flaw size or maximum allowable stress requires the application of the safety factors. These are to be applied individually to membrane and bending stresses as SF_m and SF_b, respectively. The safety factors depend on service level and flaw orientation. The considered loading conditions are those associated with Service Levels A, B, C, and D, for the piping system design. Test conditions are evaluated as Service Level B.

According to Appendix C of ref. [17], the maximum allowable stress for the flawed pipe is a function of pipe stresses, the required safety factors, pipe material properties, end-of-evaluation-period flaw length and depth, flaw orientation, and pipe failure mode.

The safety factor values for primary membrane and primary bending stresses when calculating the maximum allowable depths for circumferential and axial flaws for piping components are as presented in Tables 1 and 2, as taken from Appendix C of ref. [17].

Article C-7000 of ref. [17] contains for both circumferential and axial flaws analytical solutions with safety factors for maximum allowable mode I stress intensity factor, K_I, which is to be compared to corresponding fracture toughness, K_{Ic}. Actually, the fracture toughness of the material is determined by two properties K_{Ia} and K_{Ic}, which represent critical values of the stress intensity factor K_I. Whereas K_{Ia} is based on the lower bound of crack arrest critical KI values measured as a function of temperature. K_{Ic} is based on the lower bound of static initiation critical KI values measured as a function of temperature.

Fatigue end-of-life curves are applied for design of NPP components against cyclic loading. According to Article NB-3000 of ref. [16] the fatigue curves are obtained from uniaxial strain cycling data in which the imposed strains have been multiplied by the elastic modulus and a design margin has been provided so as to make the calculated stress intensity amplitude and the allowable stress intensity amplitude directly comparable. The safety factor values of 2 on stress and 20 on load cycles have been used in defining the fatigue curves. These safety factors intend to cover the effects of variables that can influence fatigue life in air and LWR environments.

According to the pipe break probability results, the use of safety factors has an effect to the break probability analysis results, though it is much less visible than for the deterministic analysis results. For the analysis cases with WRSs, the pipe break probabilities are less than half a decade higher than for cases with safety factors as compared to those without. As for the effect of WRSs, the pipe break probabilities are approximately 10 decades higher with them than for those without. Again these latter results reveal the significant role of WRSs in SCC growth analyses. The effect of wall thickness to the analysis results is much less visible than for deterministic crack growth analysis results. For the covered analysis cases the effect of inspections is hardly visible. This is outcome is not according to expectations, but is explained by the used applied loading. Namely, the used as-welded state WRS recommendations are quite high, often of the scale of material yield stress or higher. Thus, it is recommendable to use more accurate WRS data in the analyses, obtained with finite element (FE) simulations and/or from experiments.

Based on the results of this study, in the structural integrity or fitness-for-service (FFS) analyses, safety margins are maintained by introducing various kinds of safety factors and conservative assumptions. This makes it difficult, or even impossible, to define what is the total safety margin of a structure or component, e.g. how much more loading it could bear beyond that caused by plant operation, including experienced and anticipated transient loading events. Further, possible new degradation mechanisms and unexpected local loading conditions challenge the structural safety margins in ways that are difficult to predict. Structural integrity analyses of structures and components would benefit from such more specific definitions of safety factors that would give a more accurate assessment of the total safety. This is suggested as a future research and development issue. For the time being, establishment of a value that could represent the total safety status (safety margin) of a structure or component has to be done with probabilistic terms by risk analysis approach.

References

1. Cronvall, O. Study on Status of Safety Margins Assessment Practices. Research Report VTT-R-06265-15, Technical Research Centre of Finland (VTT), Espoo, Finland, January 2016. 40 p.

2. Safety of Nuclear Power Plants: Design. IAEA Safety Standards Series report NS-R-1, International Atomic Energy Agency (IAEA), Vienna, Austria, September 2000. 73 p.

3. Safety of Nuclear Power Plants: Commissioning and Operation. IAEA Safety Standards report SSR-2/2, International Atomic Energy Agency (IAEA), Vienna, Austria, July 2011. 71 p.

4. Deterministic Safety Analysis for Nuclear Power Plants - Specific Safety Guide. IAEA Safety Standards report SSG-2, International Atomic Energy Agency (IAEA), Vienna, Austria, December 2009. 84 p.

5. Conduct of operations at nuclear power plants. IAEA Safety Standards report NS-G-2.14, International Atomic Energy Agency (IAEA), Vienna, Austria, August 2008. 66 p.

6. Operational limits and conditions and operating procedures for nuclear power plants. IAEA Safety Standards Series report NS-G-2.2, International Atomic Energy Agency (IAEA), Vienna, Austria, November 2000. 47 p.

7. Ageing management for nuclear power plants. IAEA Safety Standards report NS-G-2.12, International Atomic Energy Agency (IAEA), Vienna, Austria, January 2009. 65 p.

8. Safety of Nuclear Power Plants: Operation. IAEA Safety Standards report NS-R-2, International Atomic Energy Agency (IAEA), Vienna, Austria, September 2000. 40 p.

9. Hultqvist, G. Safety margins in safety assessment of nuclear power plants. NULIFE Report (11) 11, EU's Network of Excellence NULIFE (Nuclear Plant Life Prediction) under EURATOM FP6 Program, September 2011. 34 p.

10. Implications of power uprates on safety margins of nuclear power plants. IAEA-TECDOC-1418, International Atomic Energy Agency (IAEA), Vienna, Austria, September 2004. 172 p.

11. AGEING MANAGEMENT OF A NUCLEAR FACILITY. GUIDE YVL A.8, Radiation and Nuclear Safety Authority of Finland (STUK), 20 May 2014. 20 p.

12. DETERMINISTIC SAFETY ANALYSES FOR A NUCLEAR POWER PLANT. GUIDE YVL B.3, Radiation and Nuclear Safety Authority of Finland (STUK), 15 November 2013. 14 p.

13. PRESSURE VESSELS AND PIPING OF A NUCLEAR FACILITY. GUIDE YVL E.3, Radiation and Nuclear Safety Authority of Finland (STUK), 15 November 2013. 62 p.

14. STRENGTH ANALYSES OF NUCLEAR POWER PLANT PRESSURE EQUIPMENT. GUIDE YVL E.4, Radiation and Nuclear Safety Authority of Finland (STUK), 15 November 2013. 24 p.

15. IN-SERVICE INSPECTION OF NUCLEAR FACILITY PRESSURE EQUIPMENT WITH NON-DESTRUCTIVE TESTING METHODS. GUIDE YVL E.5, Radiation and Nuclear Safety Authority of Finland (STUK), 20 May 2014. 50 p.

16. ASME Boiler and Pressure Vessel Code, Section III, Rules for Construction of Nuclear Facility Components, Division 1, American Society of Mechanical Engineers (ASME), New York, US, 2010.

17. ASME Boiler and Pressure Vessel Code, Section XI, Rules for In-service Inspection of Nuclear Power Plant Components, Division 1. American Society of Mechanical Engineers (ASME), New York, US, 2010.

18. IAEA Safety Standards Series No. NS-G-2.6, Safety Guide, Maintenance, Surveillance and In-Service Inspection in Nuclear Power Plants, Vienna, 2002.

19. WENRA Reactor Safety Reference Levels, January 2008, Issue K: Maintenance, In-service inspection and Functional Testing.

20. Standard Test Method for Determination of Reference Temperature, To, for Ferritic Steels in the Transition Range, ASTM E 1921-11. American Society for Testing and Materials (ASTM).

21. Standard Test Method for Measurement of Fracture Toughness, ASTM E 1820–11. American Society for Testing and Materials (ASTM).

22. Leak-Before-Break Evaluation Procedures, Standard Review Plan 3.6.3, Rev.1, United States Nuclear Regulatory Commission (U.S. NRC), March 2007.

23. CONDUCT OF OPERATIONS AT A NUCLEAR POWER PLANT. GUIDE YVL A.6, Radiation and Nuclear Safety Authority of Finland (STUK), 15 November 2013. 14 p.

24. PROBABILISTIC RISK ASSESSMENT AND RISK MANAGEMENT OF A NUCLEAR POWER PLANT. GUIDE YVL A.7, Radiation and Nuclear Safety Authority of Finland (STUK), 15 November 2013. 13 p.

25. CLASSIFICATION OF SYSTEMS, STRUCTURES AND COMPONENTS OF A NUCLEAR FACILITY. GUIDE YVL B.2, Radiation and Nuclear Safety Authority of Finland (STUK), 15 November 2013. 9 p.

26. REACTOR COOLANT CIRCUIT OF A NUCLEAR POWER PLANT GUIDE YVL B.5, Radiation and Nuclear Safety Authority of Finland (STUK), 15 November 2013. 12 p.

27. Chopra, O., K., Shack, W., J. Effect of LWR Coolant Environments on the Fatigue Life of Reactor Materials. Report NUREG/CR-6909, U.S. Nuclear Regulatory Commission (US NRC), Washington, DC, U.S.A., 2007. 115 p.

28. Nuclear power plant units Olkiluoto 1 and Olkiluoto 2. Teollisuuden Voima Oyj (TVO), 24 November 2011. 51 p, PDF Publication in English, from http://www.tvo.fi.

29. R6 Method; Assessment of the Integrity of Structures containing Defects, Revision 4. 2004 update of 2001 edition. British Energy (BE).

30. Dillström, P. et al. 2008. A Combined Deterministic and Probabilistic Procedure for Safety Assessment of Components with Cracks – Handbook. SSM Research Report 2008:01, Swedish Radiation Safety Authority (Strålsäkerhetsmyndigheten, SSM). Stockholm, Sweden, 2008. 27+196 p.

31. Hazelton, W.S., Koo, W.H. Technical Report on Material Selection and Processing Guidelines for BWR Coolant Pressure Boundary Piping. Springfield. U.S. Nuclear Regulatory Commission (NRC), Office of Nuclear Reactor Regulation, NUREG-0313-Rev2-F, Final Report. U.S., Jan 1988. 25 p.

32. Congleton, J., Craig, I., H. "Corrosion Fatigue" in Corrosion Processes, Parkins, R., N., Ed., Applied Science Publishers, 1982.

33. Vepsä, A. Verification of the stress intensity factors calculated with the VTTBESIT software. Technical Research Centre of Finland (VTT), Research Group Structural Integrity, Research Report TUO72-044578. 40+2 p.

34. Cronvall, O., Vepsä, A. Further development and validation of probabilistic analysis application VTTBESIT. VTT Report VTT-R-01837-12, Technical Research Centre of Finland (VTT), March 2012, Espoo, Finland. 49 + 7 p.

35. Varfolomeyev, I. et al. BESIF 1.0: Stress Intensity Factors for Surface Cracks under 2D Stress Gradients. IWM-Report T 14/96, Fraunhofer-Institut für Werkstoffmechanik (IWM), 1996. 42 p.

36. Busch, M. et al. KI-Factors and Polynomial Influence Functions for Axial and Circumferential Surface Cracks in Cylinders. IWM-Report T 18/94, Fraunhofer-Institut für Werkstoffmechanik (IWM), October 1994. 41 p.

37. Busch, M. et al. Polynomial Influence Functions for Surface Cracks in Pressure Vessel Components. IWM-Report Z 11/95, Fraunhofer-Institut für Werkstoffmechanik (IWM), January 1995. 88 p.

38. Cronvall, O., Männistö, I., Simola, K., Development and testing of VTT approach to risk-informed in-service inspection methodology, Research Notes 2382, Technical Research Centre of Finland (VTT), Espoo, 2007, 43 p.

Damage relaxation in cyclic strained stainless steel

Jussi Solin

VTT Technical Research Centre of Finland Ltd
Espoo, Finland

Abstract

Improved endurance in fatigue tests with intermediate holds and annealing to roughly simulate steady state normal operation between fatigue transients in nuclear power plant (NPP) components has been reported [1]. Similar effect is expected in plant components – e.g. in a pressurized water reactor (PWR) surge line or in pressurizer spray lines. Quantification of this effect is a topic of continued research on fatigue performance of niobium stabilized austenitic stainless steel.

Holds affect cyclic stress strain response. Stress amplitude, tensile mean stress and apparent elastic modulus are increased immediately after a hold, while decreased by cycles in between. A decrease of volume is measured during hot holds at zero external stress and a stress is generated, when applying a constant temperature hold in strain control. This all suggest cyclic accumulation of lattice defects and recovery during holds. Recovery may occur through thermally activated dislocation migration together with diffusion, grouping and annihilation of lattice defects.

A mechanism informed explanation and thermodynamic model is sought for to improve transferability of laboratory data to real plant components and accuracy of fatigue usage assessment. Anticipated mechanisms behind gradual changes in material responses are discussed in relation to quantitative effects of holds.

1. Introduction

Fatigue assessment of nuclear components – and also other pressure equipment – is based on a local strain approach, codified stress analysis and design curves. The design curves to be used for fatigue assessment according to ASME Code Sections III and VIII division 2 shall be derived based on strain controlled low cycle fatigue (LCF) data in room temperature. [2]

1.1 Test method for fatigue design relevant data

The ASME Code design by analysis philosophy assumes that the designer has relevant material data available. The designer needs to know how the material data has been generated and the limits of its applicability. When providing data to support codified fatigue assessment, the test laboratory shall follow the standard test methods. Strain controlled axial fatigue testing of solid specimens is performed according to ASTM E-606 or similar procedure. This gives the basis for follow-up of cumulative fatigue usage and design of risk informed inspection programs for the primary circuit components in NPP's.

Different types of experimental data are also needed for case specific analyses assessing growth rates of found or postulated cracks and to exclude alternative failure modes such as embrittlement of reactor pressure vessel (RPV), brittle fracture or stress corrosion cracking. Non-standard material tests and component testing are also used for research and verification, e.g. to demonstrate leak before break (LBB), but the design and monitoring of applicable service life of critical pressure piping in new reactors such as the European Pressurized Water Reactor (EPR) for Olkiluoto 3 and Flamanville 3 is based on fatigue design rules based on material performance in standard LCF tests. Therefore, the ASTM E-606 procedure is the basis of all work reported in this paper.

1.2 Transferability of laboratory data

Transferability of laboratory data to the operational conditions is of high concern in nuclear industry. This was carefully considered already, when the ASME Code Sections III and VIII division 2 were developed. Even "environmental effects" affecting the material performance were included in the transferability margin[1] of the design. [2]

But new data on environmental effects have been reported and applicability of design curves has been questioned for components subjected to primary coolant water [3]. However, the most severe reductions in fatigue endurance have been measured at highest operational temperatures combined with very slow strain rates, which do not occur during the fatigue relevant cycles. In addition, this alarming data was determined using non-standard test methods, stroke controlled or using thin walled tubular specimens. Adopting standard test methods also for tests in hot water, VTT has not been able to measure similar environmental effects [4]. It seems fair to assume that the concern on environmental effects is partially due to overly conservative test data, and partially because the original principles and assumptions included in the design by analysis philosophy and assessment rules have been forgotten or ignored by many researchers. [5]

In addition to environmental effects, another concern on transferability of laboratory fatigue data to the operational conditions has been thoroughly discussed in recent conferences, in particular in the Fourth International Conference on Fatigue of Nuclear Reactor Components in 2015 [5]. This concern arises from the long periods of normal operation in elevated temperature between the fatigue transients in NPP primary circuit. The standard fatigue tests are continuously conducted until failure, but normal operation without fatigue relevant cycles often continues for months. It has been shown that already short hold periods in normal operation temperatures may extend fatigue life of laboratory specimens and this effect is assumed even more effective in long term operation of NPP components [1].

This paper aims to discuss the hot hold effects and in particular, what happens during the holds. It is assumed that part of the "damage" and energy accumulated in metal lattice by cyclic strain can relax at rates controlled by thermal activation, i.e. depending on temperature and time.

2. Normal operation between fatigue transients

Periodically used spray lines introducing cold water in the pressurizer and the surge line connecting the pressurizer with the primary loop are typical locations for time-dependent temperature changes and fatigue accumulation in a PWR primary circuit, Fig. 1. Fatigue transients at the surge nozzle in bottom of the pressurizer are schematically shown in Fig. 2.

A thermal gradient within the nozzle wall is abruptly created, when a surge event begins. The gradient slowly decreases during a continued surge. This creates a half cycle strain transient on the inner surface of the nozzle. A reversed direction surge completes the full cycle. The strain amplitude of the fatigue cycle depends on the temperature difference between the water flows during the transients. Thermal transients occur always when the water temperature inside a piping component changes. However, the thermal gradients and plastic strains within the component remain small, when the temperature changes are small or slow.

[1] The margins applied between the mean curve of laboratory data and the design curve are often called safety margins, but this is misleading. To respect the code basis and avoid misunderstanding, the current author proposes consistent use of term "transferability margin".

Major thermal transients occur during start-up or shut-down phases. Temperature gradients across the piping walls are also created, when the steady state operation is disturbed by relevant power adjustment, valve operation or other action causing a change of local water temperatures. But the NPP's are designed for base load power generation and in such use the normal operation between transients may continue for months, in maximum occupying most of the interval between outages. This keeps the number of fatigue cycles low and allows the strained metal good time to relax in between[2]. Until recently, the damage relaxation during normal operation periods has been ignored. The mechanisms and consequences of relaxation are not yet properly studied. The following will not provide a conclusive explanation, but selected experimental observations and discussion on possible mechanisms involved.

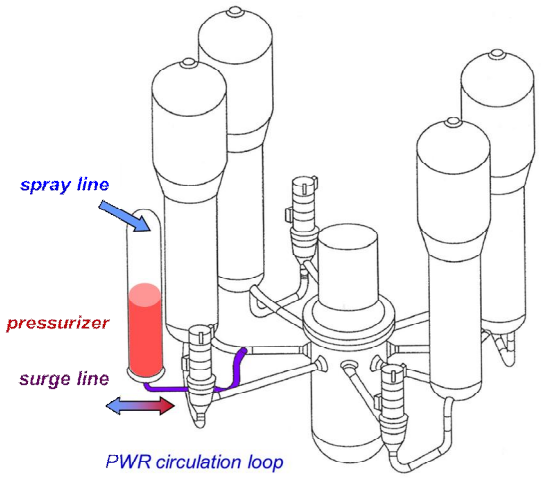

Figure 1. Fatigue critical components, spray and surge lines in a PWR primary circuit pressure boundary.

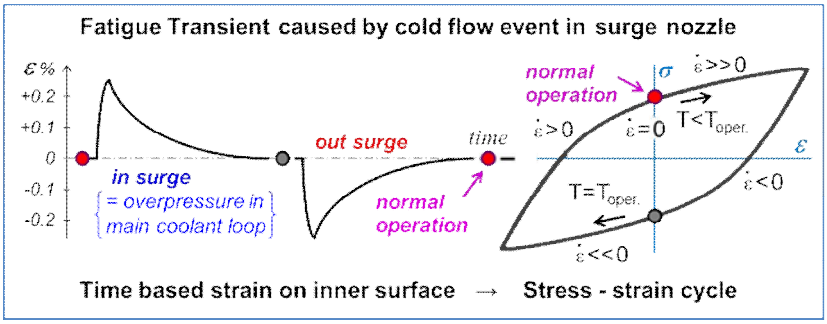

Figure 2. Fatigue transient at the surge nozzle in bottom of the pressurizer.

3. Experimental

3.1 Test material and specimens

Solution annealed niobium stabilized austenitic stainless steel (X6CrNiNb1810 mod) was received as a ϕ360x32 mm pipe, which fulfils all German KTA material requirements for primary components in LWR. The chemical composition and strength properties are given in Tables 1-2. The material report classified 50 % of grain sizes in this pipe to ASTM 0-1 and 50 % to ASTM 2-3.

[2] In Finland the NPP's are still used for base load only, but this is not the case everywhere. For example in Germany the share of unpredictable wind power and temporary overproduction has grown high enough to force part of the NPP's to operate in load follow mode. In addition to increased risk of problems in reactor core, also fatigue usage of critical primary circuit components is increased. But adjusting the blades of windmills is still considered more harmful. Confidence in safe and economic operability of NPP's is so high.

Table 1. Chemical composition of the test material (wt %).

C	N	Si	Mn	Cr	Ni	Mo	Nb	P	S
0.031	0.021	0.235	1.885	17.30	10.29	0.405	0.357	0.030	0.004

Table 2. Monotonic strength properties of the test material.

data source	E	$R_{p0,2}$	UTS
minimum of 5 tests	195 GPa	224 MPa	535 MPa
maximum of 5 tests	201 GPa	249 MPa	559 MPa
average of 5 tests	197 GPa	238 MPa	544 MPa
material report / pipe	-	239 MPa	548 MPa
material report / melt	-	251 MPa	544 MPa

Smooth round bar specimens were turned from longitudinal samples of the pipe. All fatigue specimens had a polished gauge section with diameter of 8 mm. See Fig. 3 for two alternative geometries. The geometry shown on the right hand side was used only for tests, where the specimens were repeatedly disconnected from the test rig for annealing in a separate oven during the holds.

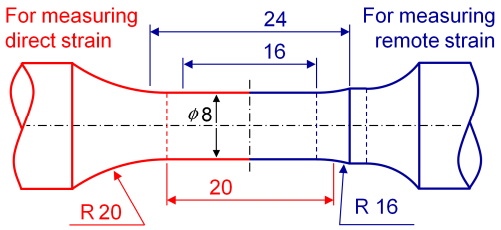

Figure 3. Specimen geometries. On left for standard LCF tests and tests with holds in fatigue rig. On right for hold tests with annealing in a separate oven and remote strain control using a 25 mm extensometer.

3.2 Experimental methods

LCF Tests in air were performed in MTS 100 kN and 250 kN rigs with precision alignment grips and MTS 653 furnace. Alignment of load train was adjusted with strain gauged specimens according to the ASTM E 1012-05 procedure. Strain controlled low cycle fatigue tests were performed according to the ASTM E 606 procedure. Triangular waveform (R = -1) with constant strain rate of 0.005 $^{1}/_{s}$ was used for tests in elevated temperatures and with holds. Lower rates 0.000 1 $^{1}/_{s}$ or 0.000 01 $^{1}/_{s}$ were used to study combined effects of temperature and strain rate.

A simplified and conservative definition of fatigue life (N_{25}) was adopted to avoid practical problems with variable cyclic softening and hardening behaviour typical for stainless steels. A 25 % drop of peak stress is measured from its absolute maximum. This selected failure criterion was not decisive to the obtained lives.

3.3 Procedures for tests with holds

In this paper “hold” refers to a pause between fatigue cycles. The tests with holds aim to simulate typical fatigue transients in NPP components subjected to temporary cold flow between periods of normal operation at a higher temperature. In such cases, the holds occur in higher temperatures than cyclic straining.

In laboratory tests the two basic options are to perform holds load-free at a greater temperature than used for cyclic loading, or fixed-strain holds at a constant temperature. Fixed strain holds at a higher temperature than used for cycling are not recommended because thermal expansion during heating and cooling would cause significant fatigue loading cycles. Different positions for holds according to Fig. 4a were used for comparison. In situ holds in the test rig make removal of the specimen and detachment of the extensometer unnecessary, allowing also monitoring of the strain during the hold.

Load-free holds according to Fig. 4b are very convenient because each set of fatigue cycles can finish at zero strain, as assumed in standard LCF procedures. After the cyclic straining is paused at (ε=0; σ>0) the load is removed to (ε<0; σ=0) and the hold sequence is started. The hold can be performed at elevated temperatures either in an oven installed in the fatigue rig or in a separate oven after disconnecting the specimen from the test rig. Annealing in a separate oven is more effective, when long duration holds are applied for a large number of specimens.

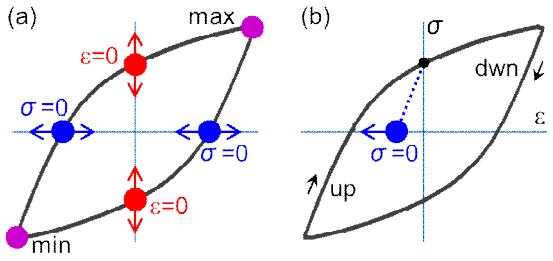

Figure 4. Alternative hold positions within a hysteresis loop (a). Practical sequence for performing a load free hold (b).

Holds at peaks of the hysteresis loop (min/max) are often applied in creep-fatigue testing, but they are not recommended in this case, because the relevant fatigue transients in NPP's are different. However, our experiments with 347 and 304 L stainless steels have shown similar hold-hardening occurring irrespective of the hold position, even when holds are applied at the peaks.

4. Results

4.1 Stress response and life extension

We have measured changes in cyclic stress response and fatigue life when simulating normal operation between fatigue transients by simplified laboratory tests composed of cyclic straining blocks and holds in elevated temperatures [6,1]. The effects in stress response and life are notable, when low strain amplitudes are applied, Figs. 5-6. Based on thermodynamics, in these tests applied 16 hours in 420 ºC corresponds to a few months at about 300 ºC.

Annealed austenitic stainless steels normally experience cyclic softening after a short cyclic hardening phase. At low amplitudes – and long enough fatigue lives – a secondary hardening phase follows the softening, Fig. 5. Part of the energy stored in metal lattice during cyclic straining relaxes during the holds, but this also causes hardening. In this case the stress amplitude is increased by about 40 MPa, almost 20 %. Part of this hardening is removed by subsequent cyclic softening, but in various similar tests it shown to be repeatable for more than 80 times and depending on strain amplitude, the hardening can remain effective for tens of thousands cycles. In other words, the hardening cannot be explained by a simple edge dislocation pinning mechanism, like strain ageing.

Extension of fatigue life has been demonstrated using different fatigue test and hold parameters. The effect is pronounced for low strain amplitudes, Fig. 6. Hold hardening reduces plastic strain amplitude and it can be assumed that this reduces fatigue damage accumulation after the hold. Hardening and life extension coexist consistently, but hardening is still not necessarily the only and direct reason for life extension.

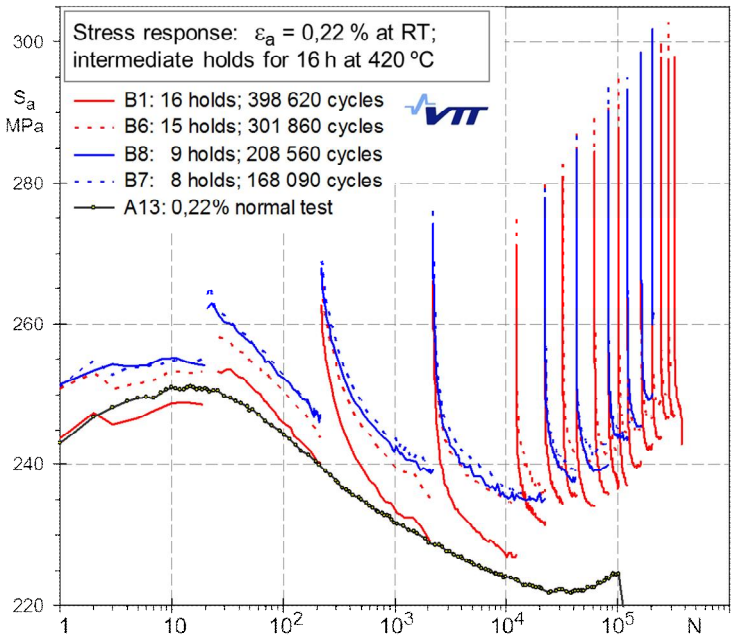

Figure 5. Change in stress response caused by holds in elevated temperature. [6]

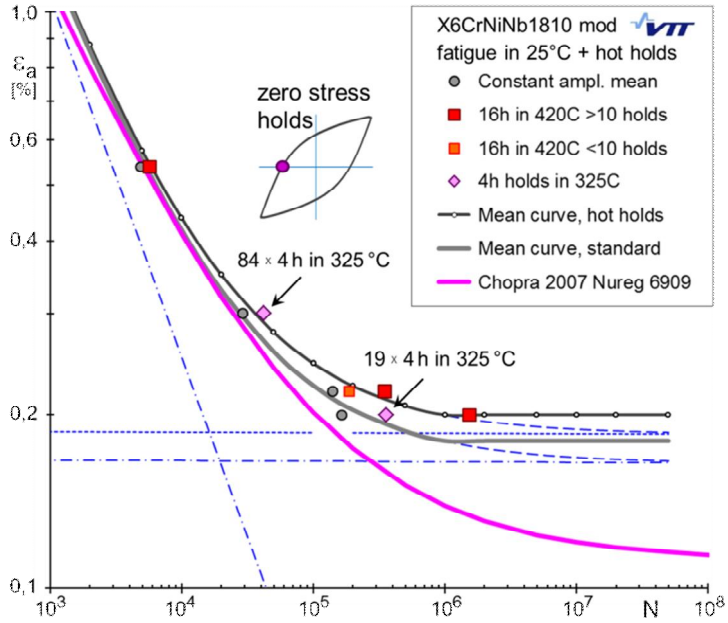

Figure 6. Extension of life and increase of endurance limit caused by holds in elevated temperature. [1]

4.2 Relaxation during a load free hold

A load free hold is performed free of external stress in the hold position shown in Fig. 4b. This allows non-constrained thermal elongation during increase of temperature to accelerate relaxation processes. Heating for the hold was done in the fatigue rig without removing the specimen or extensometer. This allowed monitoring of thermal expansion and relaxation during the temperature cycle. Time dependent changes during a hold are shown in Figs. 7-9.

The first hold preceded 25 000 cycles, which accumulated a notable amount of driving force for the relaxation processes. The hold applied for 72 hours in 420ºC is estimated to correspond about one year of normal operation in a PWR surge nozzle [1]. Quantitative changes depend on test parameters, but they are well repeatable. Figs. 7-9 can be considered more or less typical for cases, where good amount of driving force is provided by the preceding cyclic deformation and the combination of hold temperature and time provide sufficient thermal activation. Less driving force or thermal activation would result to slower relaxation processes.

The oven was programmed to reach the desired hold temperature in ten minutes, but stabilization of the specimen temperature takes couple more minutes. After having reached the peak thermal elongation, the specimen begins to contract, Fig. 7. In linear time scale the rate of contraction reduces but continues for the three days and results to about 0.1 % change in length.

The same data in terms of change of strain since the peak elongation is shown in logarithmic time scale in Fig. 8. The relaxation begins before the temperature through the specimen is fully stabilized. This mixed phase is excluded from regression of relaxation rate and the hold period is divided into two phases. We have measured similar data for many specimens annealed in temperatures ranging from 200ºC to 420ºC. A double rate response is consistently observed with a transition in 1 to 3 hours of hold.

As the specimen is cooled down after completion of the hold, the reversed thermal elongation leads the strain to a compressed value in comparison of the value before the hold. This is shown in form of hysteresis loops before and after the hold in Fig. 9. Also the result of hardening can be seen in Fig. 9.

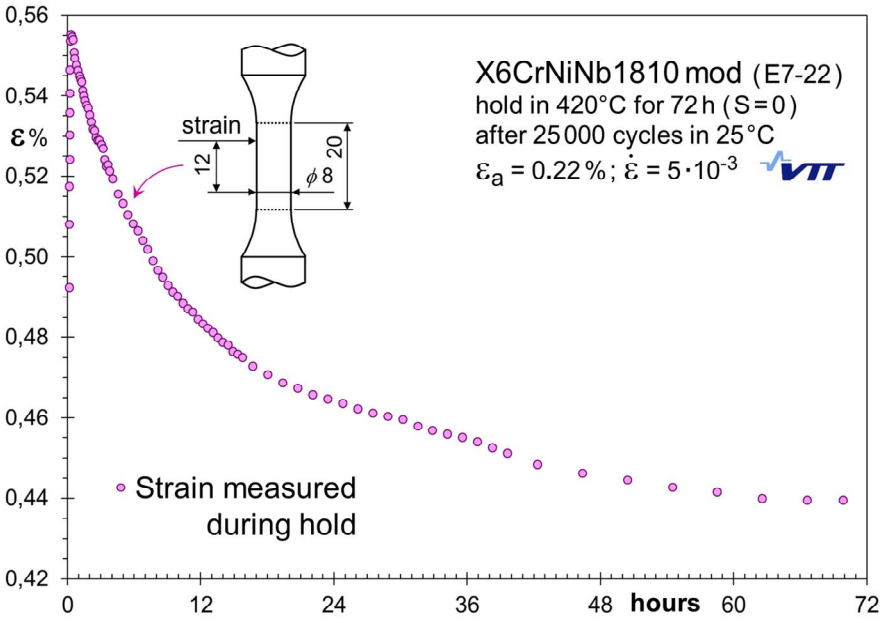

Figure 7. Contraction of the specimen during a hold in elevated temperature. [1]

4.3 Relaxation during a strain controlled hold

The previous example showed the strain response, when external stress is controlled and kept as zero. Next we will see what happens, if the strain controlled and kept constant during a hold. For this purpose we select an elevated temperature also for the phase of cyclic straining, because the temperature shall be kept constant during the whole test.

Increase of stress during the hold for three days with hysteresis loops before and after the strain controlled holds are shown in Figs. 10-11. Straining was stopped during the rising or decreasing strain ramps near zero load position to monitor the stress response during the holds. In both cases, external stress ranging over 100 MPa was created. Qualitatively, this reaction is identical to the contraction measured during the load-free holds.

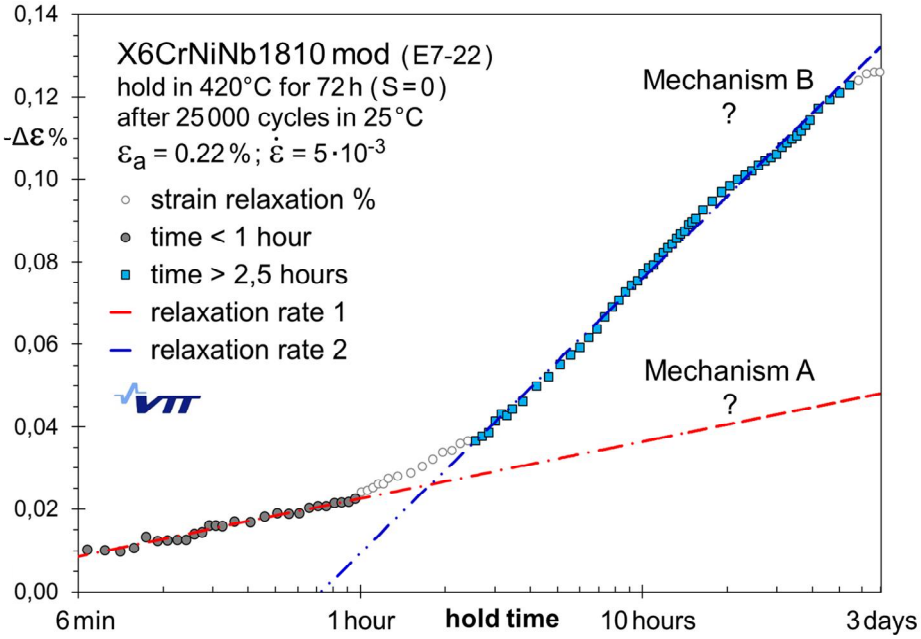

Figure 8. The same data as in Fig. 7, but in reversed strain and logarithmic time scale. [1]

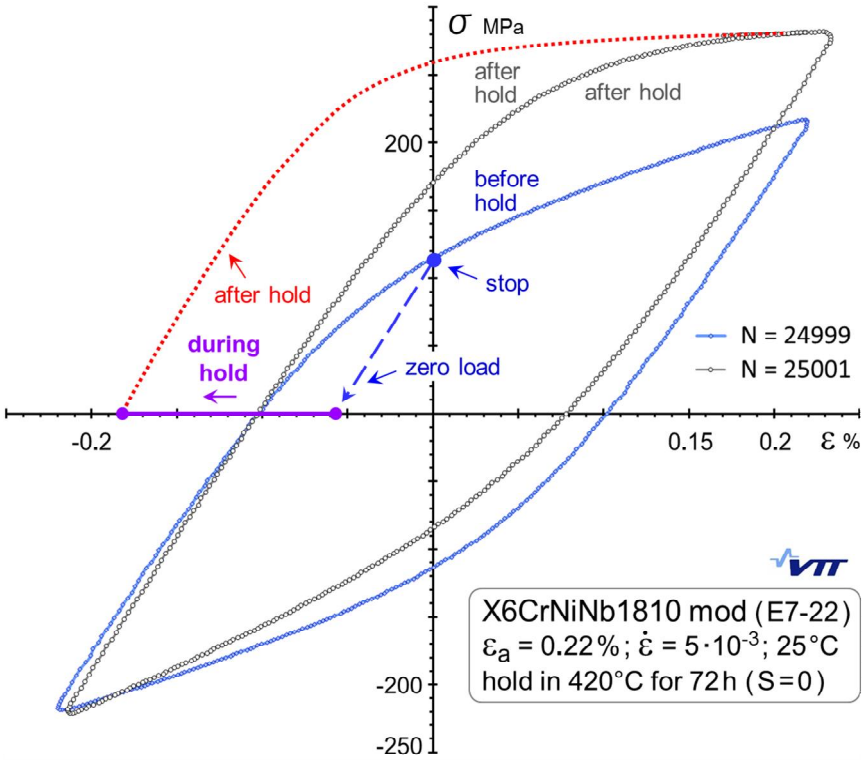

Figure 9. Hysteresis loops before and after the hold shown in Fig. 7. [1]

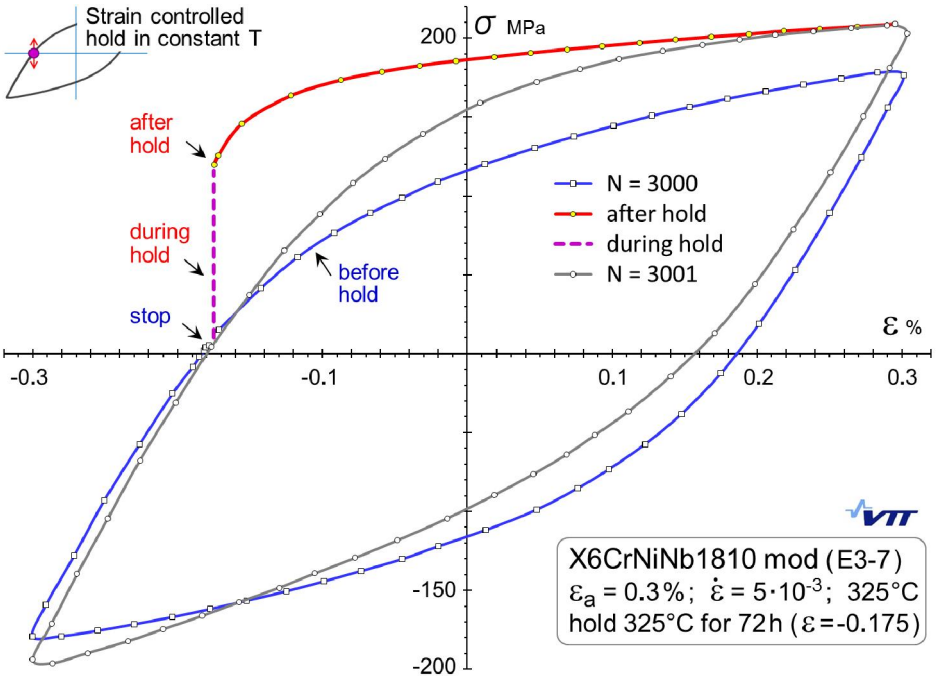

Figure 10. Hysteresis loops before and after a strain controlled hold. Straining is stopped for three days during the rising strain ramp.

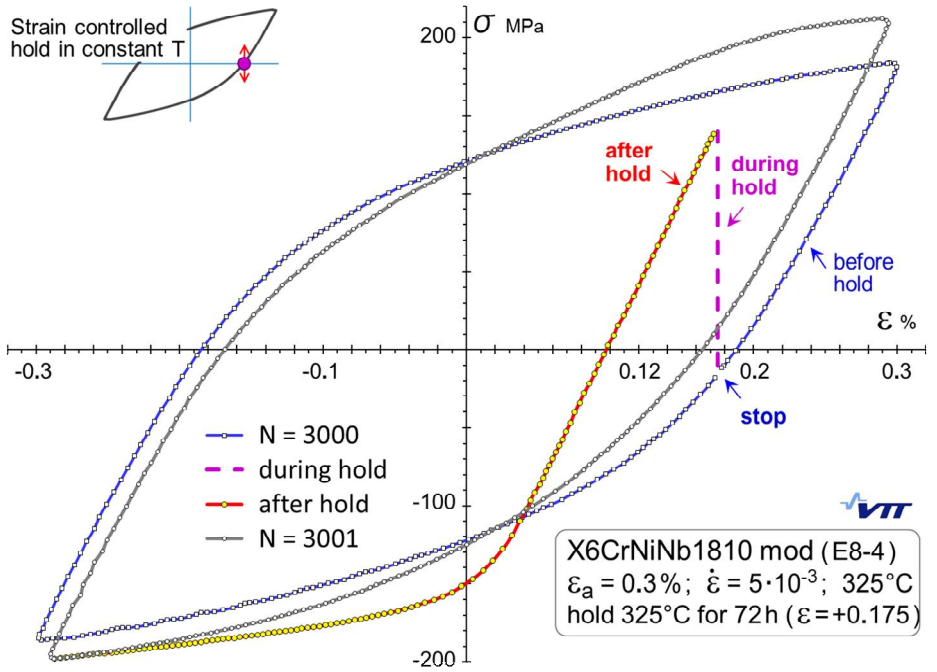

Figure 11. Hysteresis loops before and after a strain controlled hold. Straining is stopped for three days during the decreasing strain ramp.

4.4 Changes of elastic modulus

As previously reported [7], the apparent elastic modulus (E*) gradually drops during cyclic straining, Fig. 12. Recently it was also shown that the modulus can be restored during a hold, Fig. 13.

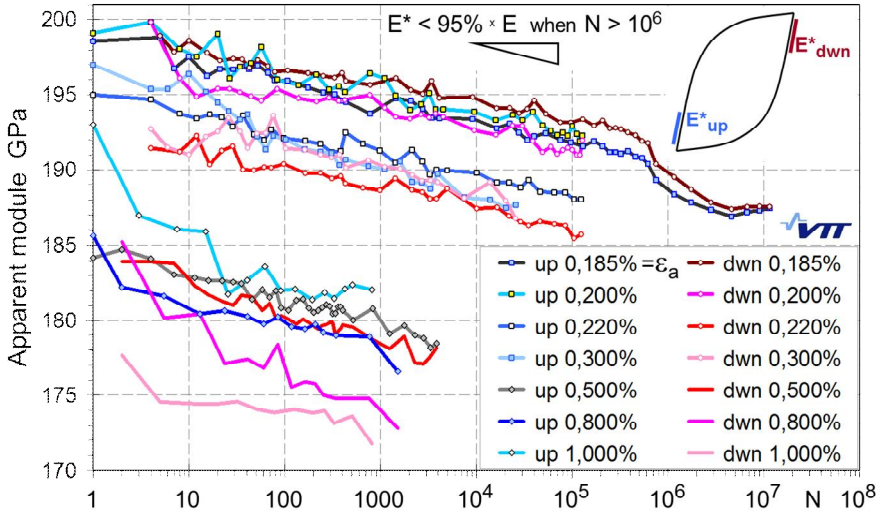

Figure 12. Modulus drift during fatigue tests at several strain amplitudes. [7]

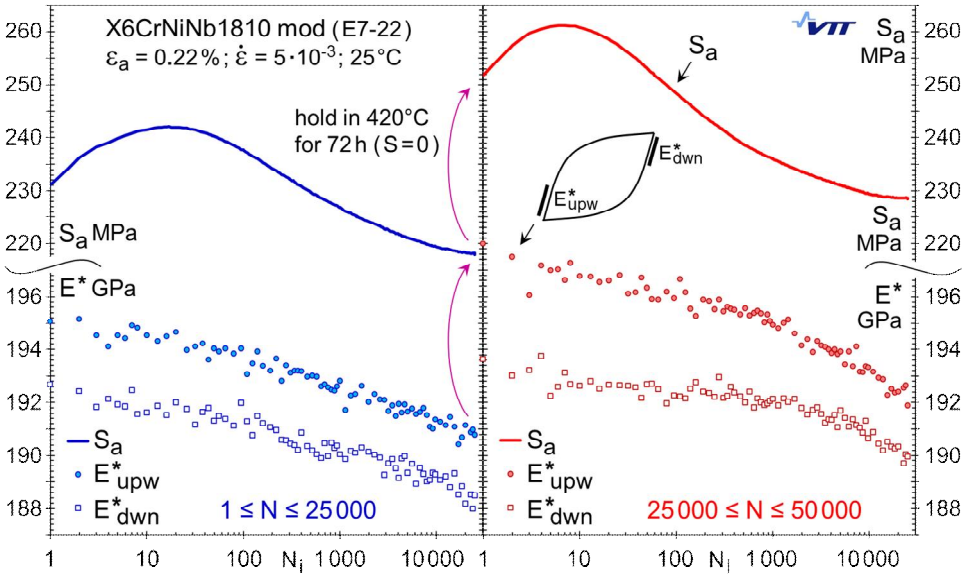

Figure 13. Modulus drift during cyclic straining and a shift during the hold shown also in Figs. 7-9. [1]

5. Discussion

So far, we have no proof on the detailed mechanisms responsible for damage relaxation. Figures 7-11 strongly point in direction of removal of lattice defects. Probably not physically correct, but for modelling purposes good assumption might be accumulation of point defects (vacancies, voids) during cyclic straining followed by their migration, agglomeration and/or annihilation during holds. Also, changes in modulus (Fig. 13) are explainable with such simplification. In simplest form, both dimensional and modulus changes could be explained through density changes by accumulation and removal of vacancies.

Diffusion of vacancies (and interstitial solute atoms) towards grain boundaries, dislocations and other disarrays in the lattice would be controlled by thermally activated processes and result to trends similar to that shown Fig. 8. Amount of vacancies accumulated during cyclic straining has been estimated high e.g. in the German team of Max Plank Institute [8]. However, explanation of the generation of external stresses and changes in material density and modulus solely in terms of vacancy migration and annihilation would require very high densities of vacancies. Vacancies may play an important role, but we must assume that other thermally activated processes can also contribute to the measured changes.

Further research is needed to explain the mechanisms involved. But from engineering point of view, we already have experimental evidence on relaxation of stored energy and lattice damage accumulated during cyclic straining. This has introduced a new concern on transferability of laboratory fatigue data to fatigue assessment of NPP primary circuit components, which experience periods of normal operation between fatigue relevant transients. Such transferability factor was first introduced in 2013 into the German KTA Standard No. 3201.2 for design and analysis of reactor coolant pressure boundary components [9].

6. Conclusions

Fatigue of Niobium stabilized austenitic stainless steel (X6CrNiNb1810 mod) has been comprehensively studied using specimens extracted from a relevant NPP primary piping material batch. The following conclusions and recommendations are derived from results related to relaxation of damage during normal operation:

1. Accelerated tests simulating the effect of normal operation between fatigue relevant transients reveal consistent hardening behaviour. This can be linked to extension of fatigue life.
2. Detail mechanisms responsible for extension of life have not been identified, but for engineering purposes they can be modelled as thermally activated processes similar to diffusion.
3. Careful evaluation of the existing data and prediction models, together with development for refined fatigue analysis methodology is recommended to determine both the life reducing and extending factors needed for transferring the laboratory data to the components in NPP operational conditions.
4. Effects of environment, temperature and loading patterns including hold times at operational temperatures shall be considered together with the design procedure. This approach has been adopted into the German KTA Standard No. 3201.2 and similar improvements are recommended also to the other international codes.

Acknowledgements

This paper is based on research funded by E.ON Kernkraft GmbH. Experiments were carried out at VTT, mainly by Mr. Jouni Alhainen and Mr. Esko Arilahti.

References

1. Solin, J., Reese, S., Karabaki, H.E. & Mayinger, W. Research on hold time effects in fatigue of stainless steel - Simulation of normal operation between fatigue transients (PVP2015-45098). Proceedings of ASME Pressure Vessel and Piping Division Conference, Boston, USA, July 19-23, 2015. 9 p.

2. Criteria of the ASME Boiler and Pressure Vessel Code for design by analysis in sections III and VIII division 2. Pressure Vessels and Piping: Design and Analysis, A Decade of Progress, Vol. One, ASME 1972, p. 61 - 83.

3. Chopra, O. & Shack, W. Effect of LWR Coolant Environments on the Fatigue Life of Reactor Materials, Final Report. NUREG/CR-6909, ANL-06/08, Argonne National Laboratory, 2007. 118 p.

4. Solin, J., Reese, S., Karabaki, H.E. & Mayinger, W. Fatigue of stainless steel in simulated operational conditions: effects of PWR water, temperature and holds (PVP2014-28465). Proceedings of ASME Pressure Vessel and Piping Division Conference, Anaheim, CA, July 20-24, 2014. 11 p.

5. Solin, J., Roth, A. & Mayinger, W. The Consideration of the Mismatch between Environmental Fatigue Behaviour of Laboratory Specimens and Plant Components in Real Environment. Fourth International Conference on Fatigue of Nuclear Reactor Components, OECD/NEA, September 28 – October 1, 2015, Seville, Spain. 22 p.

6. Solin, J., Reese, S. & Mayinger, W. Long life fatigue performance of stainless steel (PVP2011-57942). Proc. of ASME Pressure Vessel and Piping Division Conference, Baltimore, Maryland, USA, July 17-21, 2011. 9 p.

7. Solin, J., Nagel, G. & Mayinger, W. Cyclic behavior and fatigue of stainless surge line material (PVP2009-78138). Proc. of ASME Pressure Vessel and Piping Division Conference, Prague, Czech Republic, July 26-30, 2009. 9 p.

8. Essman, U., Gösele, U. & Mughrabi, H. A model of Extrusions and Intrusions in fatigued Metals I: point-defect production and the growth of extrusions. Philosophical Magazine A 44 (1981), pp. 405 - 426.

9. KTA Program of Standards, Standard No. 3201.2, Components of the Reactor Coolant Pressure Boundary of Light Water Reactors, Part 2: Design and Analysis, issue 11-2013.

Past, present and future of long term operation in Spanish NPPs

Ignacio Marcelles, Eva Frutos, Pablo Martínez & Xavi Jardí

Tecnatom,s.a.
Avda. Montes de Oca, 1; San Sebastián de los Reyes
28703 Madrid, Spain

Abstract

Spanish nuclear industry is preparing LTO of the complete fleet. For this reason, an important number of activities are being currently developed in order to achieve the safe and economical life extension of the operational life of the plants.
In the paper main activities and work performed to meet the licensing requirements in order to be granted with an operating license for LTO will be described, as follows:

Engineering work to develop AMPs and TLAAs
Development of databases and software tools to support LTO
Execution of AMPs: NDT, NDE, etc.
Research projects to increase knowledge, supplementing international R&D programs

Examples of the R&D Spanish programmes (e.g. cables, concrete, etc.) will be also defined.

1. Introduction

Since 80s year, Spain Nuclear Industry has been working on Ageing Management, preparing Long Term Operation of the plants. In July, 2009, the regulator published the Safety Instruction 22 (IS-22) for the development of Lifetime Management in the Nuclear Power Plants within Spain. This new regulations applies during the period of normal operation based on equipment design life, and also for the Long Term Operation period as well as for the application to justify this LTO. The mentioned IS-22 is mainly based on the USA regulations 10CFR54, NUREG-1800, NUREG-1801 and the technical guide NEI 95-10.

As results of this issue, the plants have performed a convergence process, adjusting their previously existing Lifetime management plants to the new requirements, taking into account specificities of each plant. The documents generated and the work performed has been re-adapted following the publication of revision 2 of GALL, NUREG-1801 and IAEA iGALL report and attachments.

This paper tries to present a perspective of such processes status, the work performed to achieve the goal of guarantying the safety Long Term Operation of the plants and the future activities to complete the implemented effort.

2. Framework

2.1 NPPs in Spain

Currently, there are seven plant in operation.

Spanish NPPs are near 30 years old and there are not any plans for building new plants. These aged plants generate more than 20 % of the electricity consumed in Spain.

It is evident the interest of the nuclear industry to accomplish all requirements for safe Long Term Operation of existing plants.

Figure 1. Spanish NPPs: age and model.

Nowadays, all the Spanish NPPs are preparing the life extension, including Sta Mª de Garoña, which has operated more than 40 years and is performing work to fix post-Fukushima requirements.

2.2 Previous activities

Spanish NPPs begin ageing management programmes since the beginning of the operation. The plants formally develop and adopt a methodology in years 90's. This methodology was well considered by Spanish regulator and applied in all Spanish plants at the first 2000's. This former methodology included economical and availability aspects jointly with safety requirements.

This methodology has never converted in a legal framework. After publication of the 10CFR54 and the Spanish IS-22 based mainly on it, the plant programmes were adapted to the new rules. Subsequent modifications in the methodology applied by the plants were following publication of new revisions of NUREG-1801 and IAEA documents, particularly iGALL Specially, Spanish Nuclear industry have an active involvement in the development of iGALL.

2.3 Legal framework

The Spanish Nuclear Safety Council (CSN - Consejo de Seguridad Nuclear) regulates the operation of nuclear and radioactive facilities in Spain to ensure that they uphold safety criteria. The CSN proposes rules and regulations to the government and adjusts domestic legislation to comply with international one. Legislation usually comes from the technology origin country.

At present, in Spain there does not exist any legal limitation in the operational live of the plants. However, in the case of NPP of a western design, like the Spanish ones, 40 years is usually considered the plant design lifetime due to the analyses supporting the plant safety assessment were carried out using that hypothesis.

Spanish NPPs are obliged to undertake a PSR, at least once every 10 years according to the Safety Guide 1.10 "Revisiones periódicas de la seguridad de las centrales nucleares" in order to renew its license.

The scope of the PSR includes the assessment of programmes under way to improve safety in the facility or the establishment of new programmes. After assessing the results of the PSR carried out by the facilities, the CSN sets additional safety requirements for the licensees if it considers needed.

CSN Instruction number IS-22, of July 1st 2009, summarizes the process to be followed by the licensees of Spanish NPPs to implement a process for management of ageing of the components including LTO beyond the design lifetime defined for each plant. This instruction includes the reference contained in

standard 10CFR54 and its enacting documents and other from the nuclear industry, such as NUREG-1800, NUREG-1801 and NEI 95-10 of the American Nuclear Industry Association. The requirements laid down in the Instruction are applicable to all plant operating conditions.

3. Implementation of AM programmes

The following paragraphs are based on IS-22 rule:

3.1 Development of AM programmes

The licensee shall perform AM activities to cover the facility design lifetime and beyond it:

- Within the design lifetime: The licensee shall carry out the necessary plant SSC AM activities, such that these include measures for the surveillance, control and mitigation of the ageing mechanisms to identify the proposals for improvements incorporated to detect these mechanisms and control their effects. The conclusions of this periodic review shall be included in the Lifetime Management Plan;
- LTO period;
- Within the LTO period.

The licensees of the NPPs shall draw up periodic reports based on the activities mentioned above.

The scope and content of the Lifetime Management Plan shall be based on the methodology of the standard 10 CFR 54 “Requirements for renewal of the operating permit”, articles 54.3, 54.4 and 54.21, until the end of its design lifetime, with the exception of the requirements of articles 54.3a and 54.21c on specific time limited analysis (TLAA) of components.

The scope of the Life Management Plan is provided in Tab.1

Table 1. Scope of Lifetime Management Plan.

Period	Reports	Timeframe
Design lifetime	Lifetime Management Plan	First six months of each calendar year.
LTO	a) Integrated Ageing Assessment b) TLAA c) Final Safety Analysis report supplement d) Technical Specification revision	Three years prior to the date for renewal. Updating shall be submitted a year before the date of renewal.
During LTO	Long term AM Plan	First six months of each calendar year.

3.2 Scope setting and screening

Safety-related SSC’s that are required to continue operating during and after any design basis event that might occur, in order to guarantee the following functions:

- The integrity of the reactor coolant pressure boundary;
- The capacity to shut down the reactor and maintain it in safe shutdown conditions; or
- The capacity to prevent or mitigate the consequences of accidents, such that off-site radioactive exposures are kept below the established limits.

SSC’s within the scope shall be:

- Passive components since the application of the Maintenance Rule (regulated in CSN Instruction IS-15 [32]) to active components guarantees that the critical functions of components are within the acceptance levels.
- Not included in any replacement programme based on qualified lifetime maintenance or any other replacement programme.

As a reference, check-list type documents for each SSCs are developed in order to support and compile this process.

The SSC scope Check list is presented in Fig. 2.

Figure 2. SCC scope Check list.

TABLA 1.1:

	SI		NO
1. Función relacionada con la seguridad (RS):			
1.1 Integridad de la barrera de presión del refrigerante del reactor.	☑	1_1	☐
1.2 Parada y mantenimiento de condición segura	☑	1_2	☐
1.3 Prevenir o mitigar accidentes con fugas al exterior	☐	1_3	☑
2. Función esencial No Relacionada con la Seguridad y/o función implicada en el cumplimiento de otros sucesos regulados			
2.1 El fallo impide una de las funciones de seguridad anteriores (No contestar si es función RS).	☐	2_1	☐
2.2 Protección contra incendios (10 CFR 50.48)	☐	2_2	☑
2.3 Calificación ambiental (10 CFR 50.49)	☑	2_3	☐
2.4 Choque térmico a presión (PTS) (10 CFR 50.61)	☑	2_4	☐
2.5 Transitorio anticipado con fallo de disparo (ATWS) (10 CFR 50.62). (No se produce el disparo auto.)	☐	2_5	☑
2.6 Station blackout (SBO) (10 CFR 50.63). Pérdida completa de suministro de corriente alterna.	☐	2_6	☑
2.7 Sistema sujeto a requisitos de operabilidad en las especificaciones técnicas, limitando condiciones de operación	☑	2_7	☐
2.8 Análisis Probabilístico de Seguridad (APS)	☑	2_8	☐
2.9 Contemplado en los procedimientos de emergencia (No contestar si es función RS).	☐	2_9	☐
2.10 El fallo puede provocar el disparo del reactor o la actuación de un sistema relacionado con la seguridad (No contestar si es función RS)	☐	2_10	☐
2.11 El fallo puede causar un transitorio de la planta o requerir una actuación operacional inesperada (contingencia)	☑	2_11	☐
2.12 Necesario para solventar un transitorio operacional o accidente (No contestar si es función RS).	☐	2_12	☐
2.13 Aplica Calificación Sísmica.	☑	2_13	☐
3. Generación Eléctrica y Fiabilidad			
3.1 Transporta energía térmica del núcleo del reactor a la turbina	☐	3_1	☑
3.2 Conversión de energía térmica a eléctrica	☐	3_2	☑
3.3 Transporte de energía eléctrica del generador a la red	☐	3_3	☑
3.4 El fallo podría provocar el fallo de una de las 3 funciones anteriores	☐	3_4	☑
3.5 Afecta al camino crítico durante recargas	☑	3_5	☐
3.6 Puede parar la planta	☑	3_6	☐

3.3 Identification of relevant ageing mechanisms

For each component included within the scope defined, the potential ageing mechanisms and their possible causes and consequences should be analysed. Then, they may be analysed individually or as families, considering their design and/or functional similarity.

As a result, the ageing effects and mechanisms considered to be significant and requiring surveillance, control or mitigation activities to ensure that the functionality of the structure is not limited during its service lifetime, will be determined.

3.4 Mitigation and prevention of ageing effects

The causes and consequences of significant ageing effects and mechanisms shall be duly overseen, controlled and mitigated by the maintenance practices, bearing in mind that these do not include only predictive and preventive maintenance practices themselves but also inspection, testing, control of operating parameters, surveillance, etc..
Maintenance, inspection and testing activities required by the current licensing basis will be valid for the AM of the affected SSC, with respect to the ageing effects and mechanisms dealt with therein.
Evaluation of the maintenance practices will consist of a comparison between the sur-veillance and mitigation activities suitable for each ageing effect and mechanism (significant for each structure or component) and the actual content of the maintenance practices performed on that structure or component. The result of the evaluation will include the improvements to the maintenance processes necessary to establish an adequate AM and, where required, the implementation of new maintenance practices.

3.5 Review of AM process

Within the scope, content and period for submittal of the documentation relating to the PSR of the facilities, a revision of the Lifetime Management Plan shall be included:

- The ageing and degradation mechanisms of safety-related and safety relevant elements;
- Unexpected ageing mechanisms and effects;
- New relevant information;
- The most adequate methods and tools available for AM;
- The effectiveness of maintenance management, in accordance with the results of the practices implemented.

4. LTO applications in Spain

In the case of LTO, all the analyses and calculations performed by the licensee shall fulfil the following conditions to classify as a TLAA:

1. SSCs considered within the scope of AM;
2. Take into account the effects of time and LTO;
3. Adhere to hypotheses of limited design lifetime;
4. Conclude with the capacity or not of the stress corrosion cracking (SCC) to continue to operate, in accordance with their defined functions, after having exceeded the limited design lifetime hypotheses;
5. The calculation or analysis was considered relevant in a safety assessment;
6. The calculation or analysis is part of the current licensing basis of the facility.

4.1 Plant programmes status

All the Soanish NPPs are developing the Long Term Operation programmes according to IS-22 requirements and all of them has ageing management programmes running based on PRS GS.1.0 requirements. Table 2 show the relevant dates for each plant,

Table 1. Spanish NPPs, RPS.

NPP	Type	Electric Power (MWe)	Commissioning year	Next RPS	40 years	60 years
Garoña	BWR	466	1971	--	2011	2031
Almaraz I	PWR	1049,5	1983	2017	2021	2041

NPP	Type	Electric Power (MWe)	Commissioning year	Next RPS	40 years	60 years
Almaraz II	PWR	1044,5	1984	2017	2023	2043
Ascó I	PWR	1032,5	1984	2018	2023	2043
Ascó II	PWR	1027,21	1985	2018	2025	2045
Cofrentes	BWR	1092	1984	2018	2024	2044
Vandellós II	PWR	1087,14	1988	2017	2027	2047
Trillo	PWR	1066	1988	2021	2028	2048

4.2 Approach

As previously described Spanish NPP LTO processes are performed mainly in agreement with USA 10CFR54 (see Fig. 3).

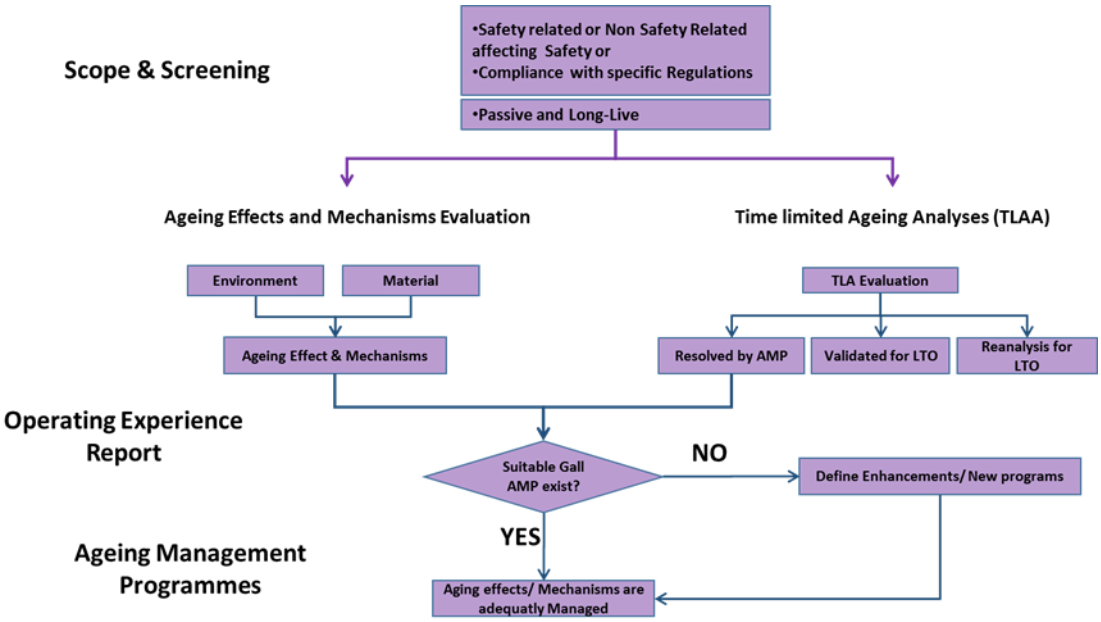

Figure 3. LTO process.

A typical PWR plant has an average of 50 to 60 AMPs most of them identical to GALL AMPs and more than 120 possible TLAAs are analysed of which around 40 need to be solved. Only one or two are usually plant specific.

4.3 Review of LTO processes

The Spanish NPPs, to verify the effectiveness of AMPs, for each programme, perform every 3 years the following activities:

- Analysis of results;
- Compliance with the requirements of the programme;

- Identification of activities performed and their results;
- Acceptance criteria compliance;
- Corrective actions performed, if needed;
- Monitoring and trending analysis;
- Verification of qualification of inspectors.

The results of these activities contribute to the identification of gaps, including: activities not performed as scheduled and real frequency compliance, incomplete, no adequate or inexistent inspection records and AMP results not evaluated or treated properly. Remedial actions are proposed to avoid these gaps.

Continuous improvement of programmes is implemented based on Operating Experience review and analyse as well as international organizations recommendations:

- Cause evaluations and extent of condition are performed;
- Inspection frequencies are adjusted when needed;
- Sample size is expanded when required;
- Review of operating experience related with the programme, internal and external (EPRI, INPO/WANO, NEI (Nuclear Energy Institute), US NRC…). Changes to activities if applied. Detailed analysis and identification of recurring failures (example: leakage in containment penetration valves testing).

The aim is the identification of proposals for improvement, if needed, included in the corrective action programme of the plant. The correct resolution of previous improvements is studied as part of this continuous improvement process.

4.4 Other work performed

In addition to the required analysis and studies, an important support work has been performed. This work includes the development of databases and other software tools linked with plant existing applications The new tools are providing support in the different process described but also for future revision of the components:.

Moreover this specific tools, upgrade of some existing applications to support inspection has been performed, i.e fig 4.

Figure 4. Inspection support tool: WebISI.

The Spanish Fleet is still in the process of refining the scope of the Aging Management Programs. Some of the inspections related to the implementation of the AMPs have already been performed to address specific operating experiences of the Plants (e.g. a plant performed Guide Card Wear measurements and inspections, most plants have performed extended cables testing programmes) or to accomplish with regulator requirements.

Other inspections are expected from 2017 on, starting with the first Reactor Vessel Internals Inspections based on EPRI MRP-227/228 guidance for Long Term Operation.

5. Research activities

Spanish Nuclear sector is developing some specific research project but also contributing in a wide number of international research projects in order to acquire and disseminate the Nuclear Knowledge from Long Term Operation. The most relevant are:

- National project: Cable ageing management: on going set of projects to determine main degradations, monitoring and surveillance techniques and influence of different stresses on cable long term performance.
- National project: Irradiation concrete characterization, taking advantage of Zorita NPP, a decommissioned PWR plant with high irradiated concrete.
- International project examination: Cut and remove part of the Zorita NPP Internal Reactor Vessel, for laboratory testing, and evaluating the extracted materials degradation and aging properties.
- Euratom/H2020 projects: **Soteria**, Safe Long Term operation of light water reactors based on improved understanding of radiation effects in nuclear structural materials; **Adfam**. ADvanced FAtigue Methodologies to optimize fatigue assessment of critical components, etc.

6. Conclusions

In summary, in the process for Long Term Operation is well established with regulations fully developed. The requirements are in agreement with the international (IAEA) recommendations and the process follows the state-of-art and international best practices.

All the Spanish NPPs are developing the Long Term Operation programmes according the regulator requirements and all of them has ageing management programmes running.

Acronyms

AMP - Ageing Management Programme
CSN – Nuclear Safety Council (Spanish Regulatory Body)
LTO - Long Term Operation
NDE - Non Destructive Examination
NDT - Non Destructive Test
NEI - Nuclear Energy Institute
PSR – Periodic Safety Review
R&D - Research and Development
SCC – Stress Corrosion Cracking
SSC – Systems, Structures and Components
TLAA - Time Limited Ageing Assessment
ZIRP – Zorita Internals Research Project

References

1. CSN IS-22 Safety Requirements for the Management of Ageing and Long Term Operation of Nuclear Power Plants, 2009.

2. CSN GS 1.10 Periodic Safety Reviews at NPP's Rev. 1. 2008.

3. CEIDEN: R&D Spanish Nuclear Platform Rev 6. 2015.

4. Safety regulation in a contradictory industrial and socio-political environment. Dr. Antoni Gurguí, Commissioner, CSN, RIC 2015.

5. Current Status and Plans for NPP Long Term Operation in Spain. Lorenzo Francia, Nuclear Directorate, UNESA - Spanish Utilities Association, TWG-LMNPP 2015.

Collaborative tools for improved maintenance and inspection of power generation plants

Ignacio Marcelles[1], Pablo Martínez Levy[1], César Martínez[1], Juan Azcue[1], Carlos Casado[2]

[1]Tecnatom, Avda Montes de Oca 1, 28703, Spain

[2]Endesa, Avda Ribera del Loira 60, 28042, Spain

Abstract

Managing "In Service Inspections" includes an important number of activities. For this reason, it is necessary to implement in power plants, applications and tools to improve these activities in order to help the engineers to know their status. In addition, these systems allow the power plant staff to develop inspection and maintenance plans and provide inspections data of the facility in an user friendly way. Moreover, it is necessary to have a specific module to schedule and to survey all the activities performed at power plants in order to reduce the inspection time requirements.

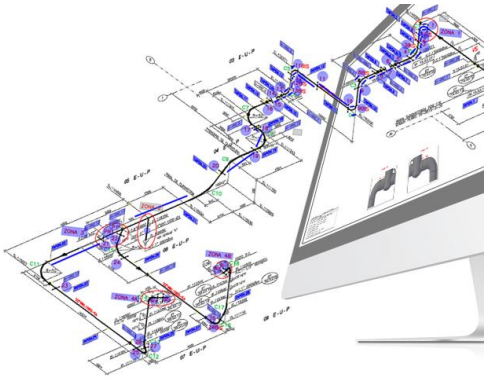

1. Introduction

All systems, components and structures, depending on their design, construction and environmental and operating conditions, are affected in different degrees, by some form of degradation and ageing. This makes the life operating equipment, very different from each other. Deterioration due to ageing suffered by main components should be controlled and mitigated by implementing non-destructive testing and life management plans.

Moreover, the inspection outages are being determined by two important factors:

- Minimization of outages time
- Reduced budgets for inspection and maintenance

In order to improve the in service inspection processes, Tecnatom has developed different tools to support the power plant engineers to perform and survey their activities saving time and costs. In this paper two

systems, extensively used by most Spanish utilities will be described. These applications are used to improve the inspection and maintenance process:

- Web ISI, system developed to plan and store, inspections performed at nuclear power plants.
- GIWE, system developed to plan, manage, store and analyze inspections performed at fossil power plants.

2. Inspection process optimization

Previously to the outage, it is necessary to plan the scope of the inspection taking into account all the related activities. It is necessary to know what to inspect, the scope, when to inspect, and how to perform the inspection. Using these tools, maintenance staff selects the areas to be inspected. This process includes the following activities:

- Inspection Manual: the areas are selected based on the plan described on the manual. This manual is included in the system in order to know the scope of each inspection and moreover to have an updated of the results of each inspection.
- Available inspection results: All the previous results are consulted in order to identify which areas have experienced previous defects and have to be inspected. In addition, these systems allow to check which areas were inspected in the previous inspections and to change them for others that never have been inspected.
- Automatic preprogramming inspection: based on the Inspection Manual recommendations, previous results and additional information, the system generates a preliminary inspection which has to be approved by the maintenance staff. This plan can be modified.

Figure 1. Inspection process.

- Once the inspection plan is approved a Gantt diagram based on the inspection management module is generated, in order to plan each task related to the inspection. This Gantt diagram is used to survey the inspection progress. Each task will be updated by the respective responsible and by the system after storing once the data worksheet is stored. The information related to the inspection can be analyzed after the inspection in order to improve the inspection management.
- Data storage. These systems generate the worksheet in order to store directly the information generated during the inspection.
- Data Analysis. Once the information is stored, it is possible to check the following:

    - Status of each equipment
    - Flaws
    - Areas inspected
    - Remnant life
    - Repairs
- Inspection reports. These systems generate different reports about inspections such as, inspection progress, results, etc.
- Post-Inspection manual update. Using the information obtained during the inspection, the manual has to be updated after having including the necessary recommendations and subsequent calculations.

Using these systems, it is possible to optimize time and budget for the in service inspections.

The features and benefits of each system are described below.

2. WEB ISI

Tecnatom performs inspections at nuclear power plants. Moreover, our engineering department provides the required support to plan and manage these inspections. In order to plan, store, analyze and manage all the activities and information generated during the inspection process, Tecnatom has developed the "Web ISI".

The main system capabilities are:

- Management of the refueling outage Inspections Plans (10 years intervals plan), including in service inspections (ISI) and in service testing (IST) scope.
- Storage of historical data of all performed inspections and tests, (based on the information of every inspected component or area).
- Data Worksheets storage.
- Survey the inspections plan and requirements for every refueling outage program.
- Generation of Inspections Reports, for refueling outages, periods or intervals

Figure 2. Web ISI main page.

The system includes several modules in order to survey the inspection process performed at power plants. The main modules are:

- Non Destructive Testing techniques.
- Valves.
- Snubbers & Supports.
- Erosion / Corrosion (FAC).

- Containment Dome, Visual Inspection.
- Components leakages.
- Wire testing.

In addition, the Web ISI includes all the information related to each component of the plant and the required information to perform the inspections:

- Inspection areas.
- Materials.
- PID's.
- Codes & Standards.
- Prcedures.
- Results.

Each module has a dashboard in which it the main information related to the module is displayed. This dashboard allows consulting the information related to previous inspections, the status of the plant, detected flaws, etc.

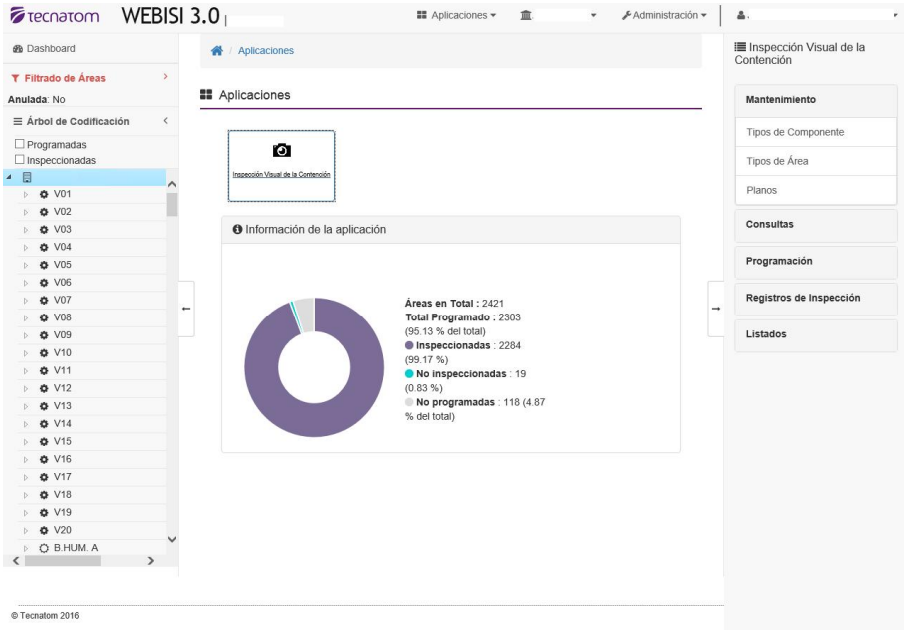

Figure 3. BI page.

This system allows optimizing the inspection process management surveying the required areas in orde to meet the nuclear regulatory body requirements.

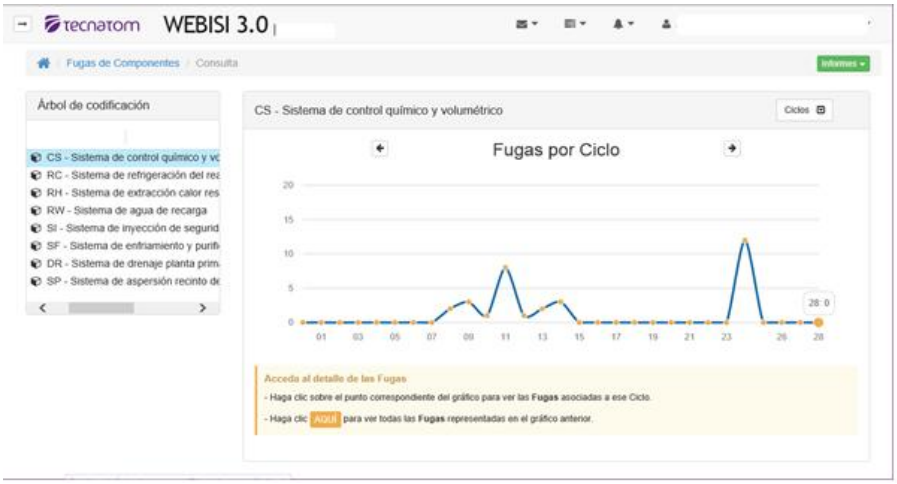

Figure 4. Module Dashboard.

All Spanish and Argentinian NPPs are using this software to manage the outages.

3. Inspection Management Integrated System (GIWE)

As inspection requirements are different for nuclear and fossil power plants, Tecnatom has developed a specific tool to manage the inspection process at fossil power plants. This system has the following capabilities:

- Inspection data of the facility available in an easy way.
- Access to all the information that is arises during inspections.
- Schedule inspections considering all degradation processes and failures that are affecting the facility.
- Set the scope of the plan inspection.

This system includes the following features:

- Inspection plan programme.
- Inspection Manual in electronic format.
- Drawings, including inspection areas.
- Double navigation:
    - Drawings.
    - Power plant codes.
- Data worksheets generation.
- Data worksheets storage.

Main modules included:

- Programming module.
- Reports generation.
- Eddy Current.
- Thickness surveillance.
- Inspection plan management. Gantt diagram.
- Longitudinal welding surveillance.
- Remnant life calculation.

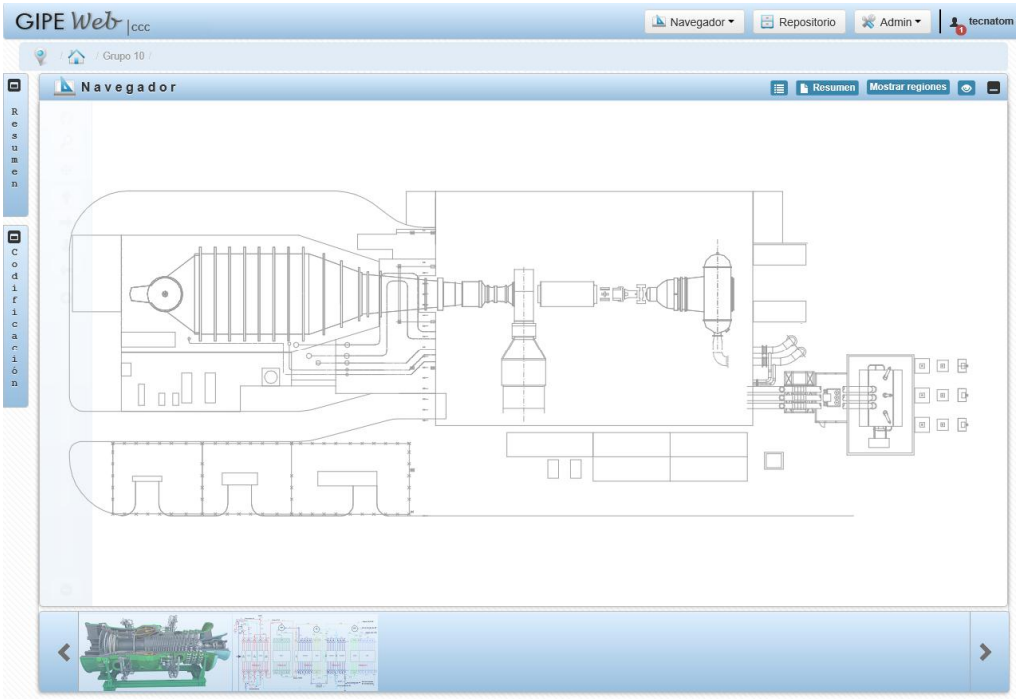

Figure 5. GIWE Main screen.

The system includes the inspection manual in electronic format, so that the inspection can be programmed directly by means of manual. There exists a specific module to programme each area.

The drawings include all the represented areas which can be programmed directly inside the drawings. Clicking on a component all the related information is displayed

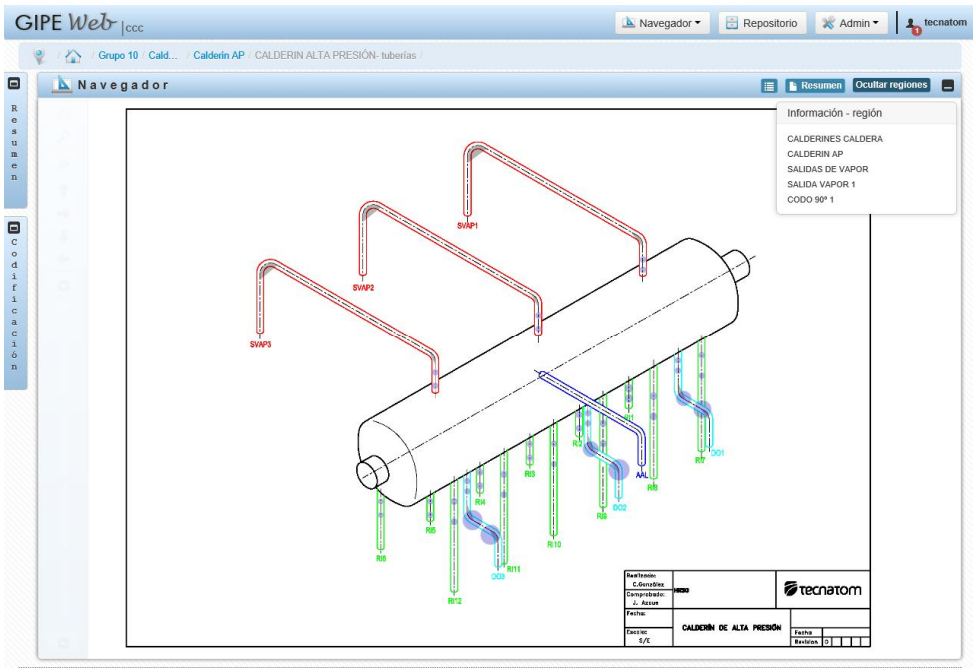

Figure 6. Drawings including represented areas.

This tool includes an advanced feature in order to manage the inspection process. The generated Gantt diagram is based on the inspection scope. After that the user includes the information related to the timing for each task. The responsible for each task uploads the information related to the task progress and the

system automatically updates the information related to the inspections and tests performed, based on the stored results.

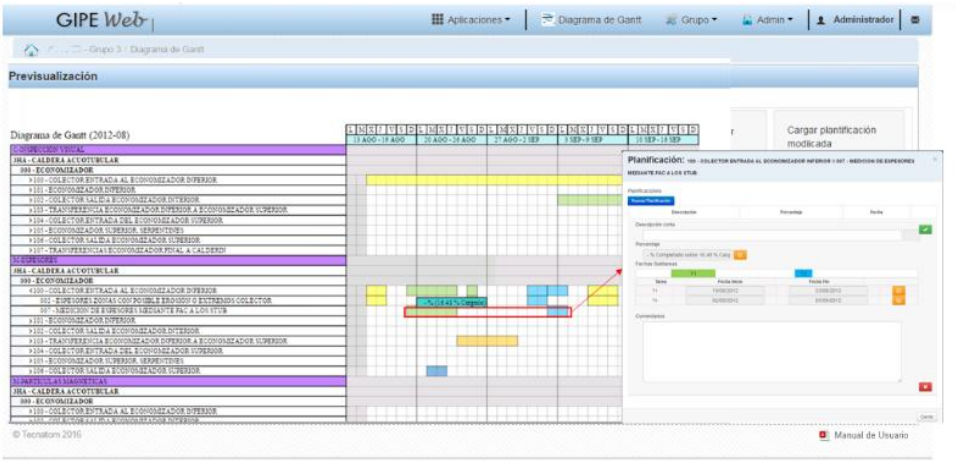

Figure 7. Gantt diagram.

This system has been developed with the collaboration of Endesa (Technical Service Department).

Conclusions

The optimization process of the maintenance activities during power plant outages begins with a suitable inspection plan in order to guarantee that the inspection plan is according to the updated information of the power plant component status, in service inspection manual and the results obtained from previous inspections.

Due to the present tendency to extend the power plants lifetime it is necessary to implement management tools which allow us to manage an important amount of inspection data in order to analyze the component status. Based on that information it is possible to focus on critical components. At present, maintenance budgets are being reducing in order to maintain profit margins. This situation forces the power plants to optimize their inspection and maintenance strategy.

Nuclear plant:
Spent fuel management & ageing

Relaxation behaviour of copper in disposal canisters

Juhani Rantala, Rami Pohja, Pertti Auerkari, Anssi Laukkanen & Tom Andersson

VTT Technical Research Centre of Finland Ltd
Kemistintie 3, Espoo, Finland

Abstract

A full 3D creep FE analysis has been performed for the nuclear waste disposal canister with a cast iron insert and a copper overpack under external pressure. The FE mesh of the canister contains a model of the joint line hooking and the oxide particle zone, where the strength of the material is assumed to be zero. The material model includes elastic, plastic, creep and relaxation models. The total strain distribution after predicted 1000 years of exposure are presented.

1. Introduction

In the repository for spent fuel, the temperature of the canister surface is expected to peak at about 75-90°C before the first hundred years [1], with gradual cooling to the level of the bedrock environment. The top temperature will depend on the rate of wetting in individual disposal holes, which might vary a lot, depending on the flow of water in the bedrock. The development of the bentonite swelling pressure will also depend on the rate of wetting.

For the protective copper (Cu-OFP) overpack of the canister, creep and corrosion are included as potential damage mechanisms under the repository conditions [1]. Although relatively mild in usual engineering terms, the repository conditions imply a technical challenge to life estimation for ensuring the integrity of the overpack. This is because of the discrepancy between the longest achievable laboratory tests (decades) compared to the design life that is of the order of glaciation cycles (about 10^5 years) to reduce the radioactivity of the contents close to the background level. The time difference by a factor of almost 10^4 also exceeds the usual range of extrapolation from laboratory experiments to real service conditions in most (or any) comparable engineering applications.

2. Experimental work

At areas of stress concentration in the canister, especially at the area around the natural notch high stresses will develop, but these will relax quickly [2] increasing the stresses elsewhere slightly. In the previous report [2] the relaxation behaviour predicted by the LCSP creep model [3] and a relaxation model was compared, showing a clear difference. Experimental data had been generated by using two testing facilities: a servo-hydraulic material testing machine and a pneumatic bellows system. More detailed description of the test facilities are given in [2].

The available experimental data set has been re-fitted by using the Kohlrausch relaxation model [4]:

$$\sigma = \frac{\sigma_0}{e^{\alpha \cdot t^b}} \qquad (1)$$

where $\alpha = \left(\frac{\ln(T)}{a}\right) \cdot e^{\frac{-Q}{RT}}$ $\beta = \left(\frac{\log(\sigma_0)}{\sigma_{UTS}}\right) \cdot b$

The experimental data and the fitted model are shown in Figs. 1 - 2.

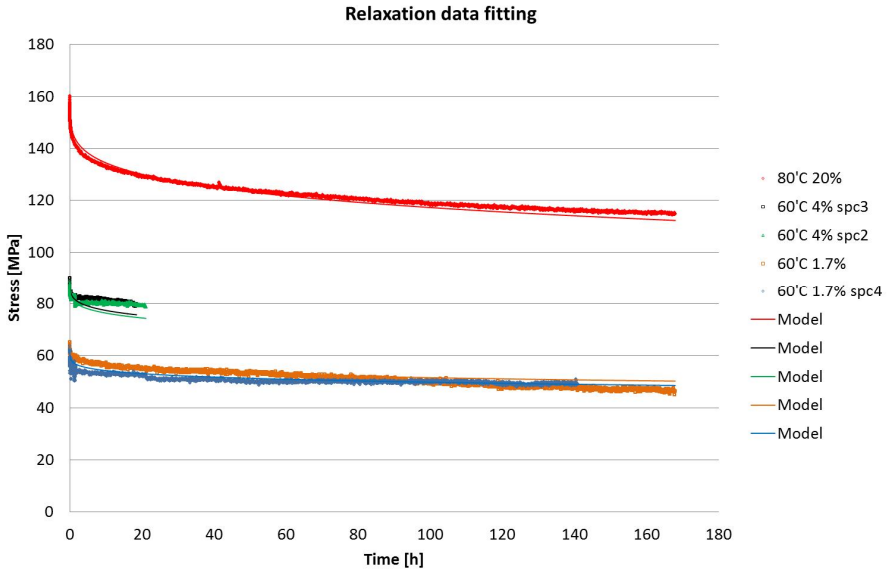

Figure 1. Experiment and fitted relaxation data of Cu-OFP at 60°C and 80°C on linear time scale.

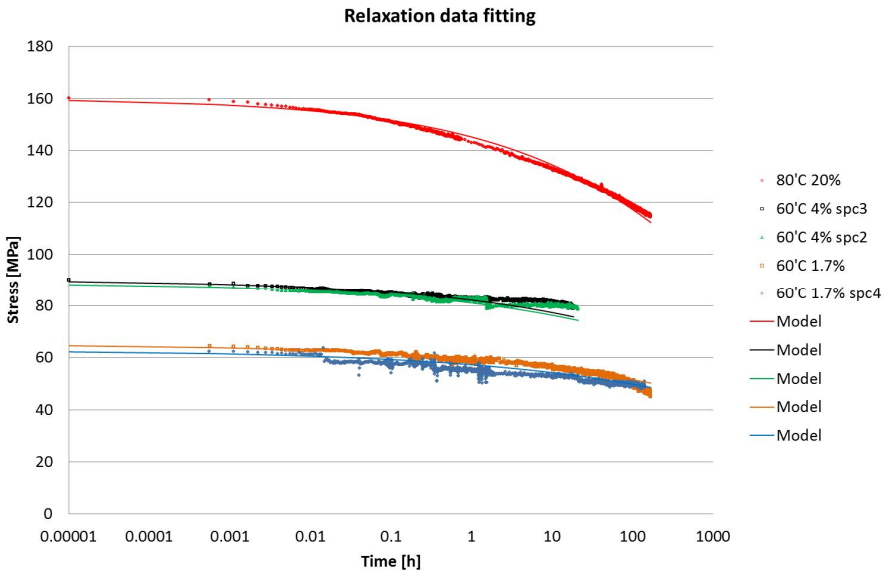

Figure 2. Experiment and fitted relaxation data of Cu-OFP at 60°C and 80°C on logarithmic scale.

3. FE analysis of the canister

The stresses and strains in the canister were analysed by approximating the FSW geometry as shown in Fig. 4. The oxide particle zone (Fig. 3) and the joint line hooking were both modelled as 0.5 mm height and 1 mm wide ”box”. Distance between them is 8.3 mm. The FS weld metal was modelled with a weld strength reduction factor of 0.95 and the joint line hooking and oxide particle zone with strength of 80 % of the strength of the weld.

In order to simplify the analysis constant temperature of 80°C and instant pressure of 14 MPa were used. The material model was LCSP primary + secondary and a relaxation model. The additional notches at the joint line hooking and oxide particle zone caused some time-consuming numerical problems during the analysis, so in the future the material model needs to be developed further to be more robust around regions with large stress gradients. One possibility would be to use elements that can be damaged (i.e. elements are deleted when certain damage criterion is achieved) to avoid too high stress (and thus strain rate) levels.

In Figs. 5-6 the total strain distributions after 100 and 1000 years have been plotted (on top of the un-deformed mesh). It can be seen that the maximum strains of 25% (after 100 years) and 30% (after 1000 years) are much bigger than what has been reported before. In [2] the maximum principal strain predicted was about 3 % located near the FSW joint tip after 56 100 years. It is likely that the omission of tertiary creep model in the present analysis plays a role here. If tertiary creep is included then there will be high strains at the tip of a crack, but they are contained in a rather limited area around the crack tip.

This rather simplified analysis seems to suggest that stress levels around the oxide particle zone are low enough that this zone could be disregarded in the future. It seems that the oxide particle zone doesn’t play a significant role especially if the joint line hooking is included in the component model. The current practice in the FSW process is to use a protective atmosphere, so in the future it is probably not necessary to include the oxide particle zone at all in the analysis.

However, most likely the joint line hooking will still be present, and more realistic assumptions have to be made about its shape, size and strength. The stress concentration at the tip of joint-line hooking governs the weld’s (failure) behaviour.

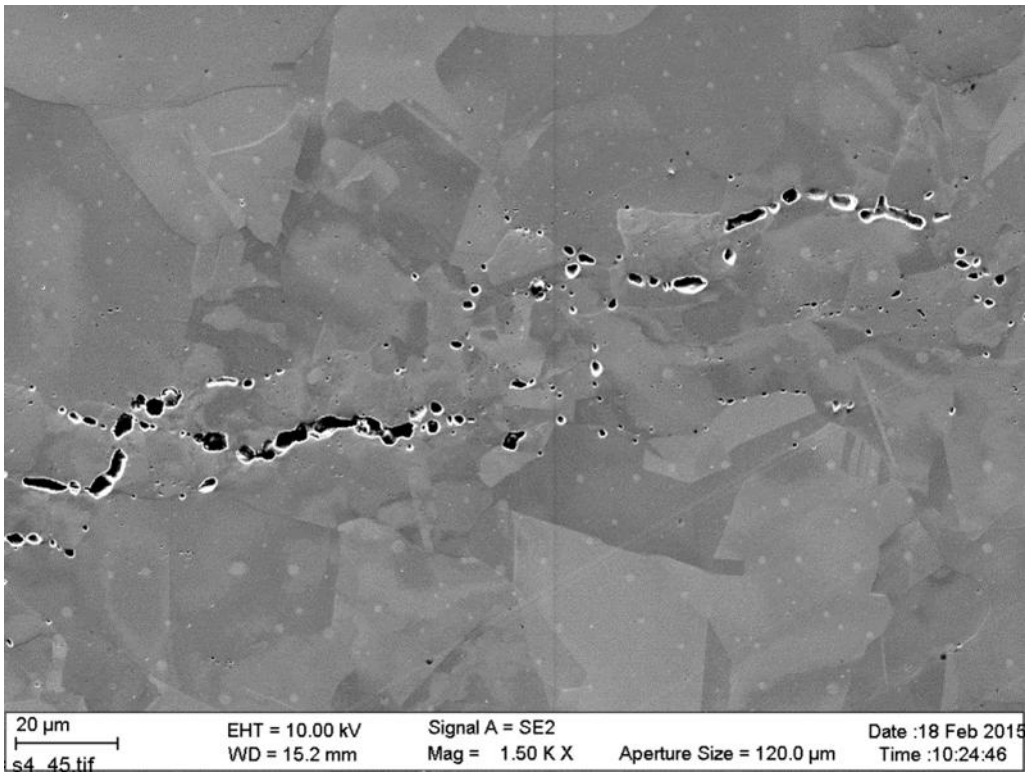

Figure 3. Oxide particle zone in a CT specimen after 50.000 h of testing at 175°C at 35MPa√m.

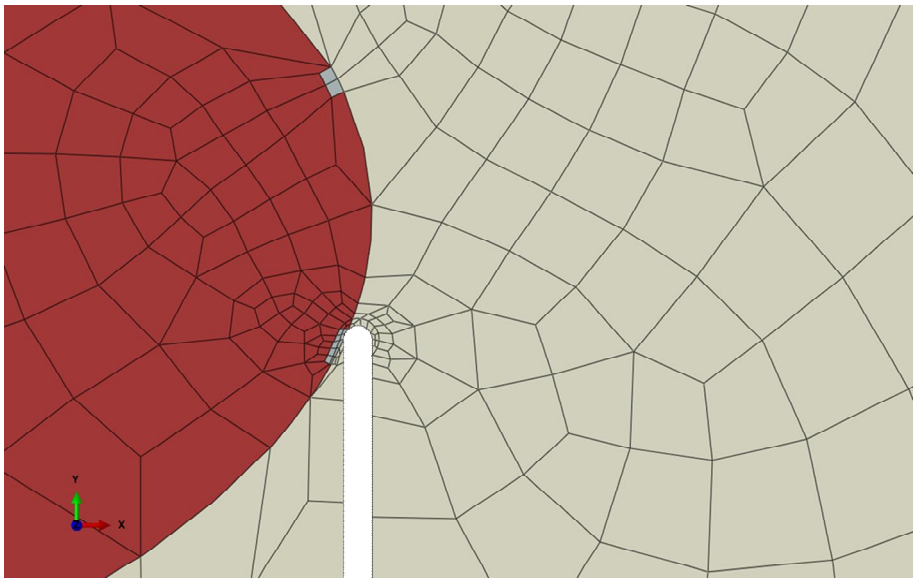

Figure 4. Detail of the FE mesh at the FSW root with cracks at the locations of the joint line hooking and oxide particle zone.

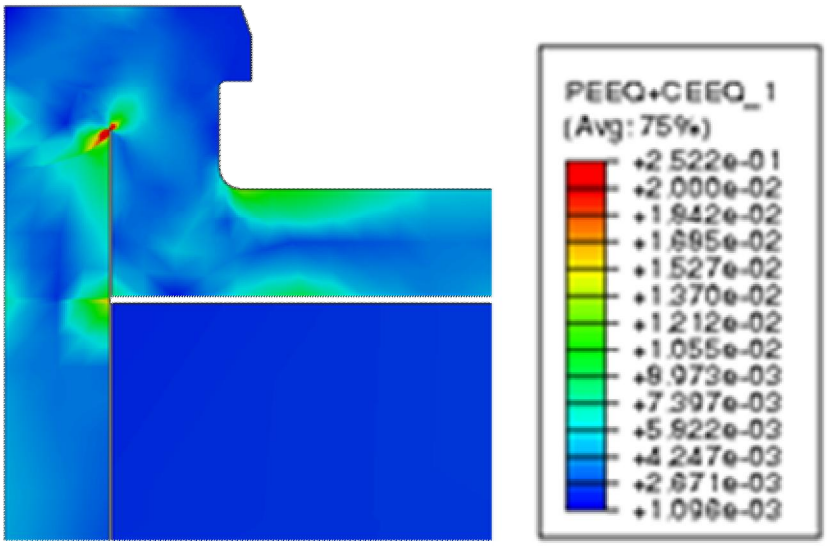

Figure 5. The total strain distribution after 100 years, plotted on top of the un-deformed mesh.

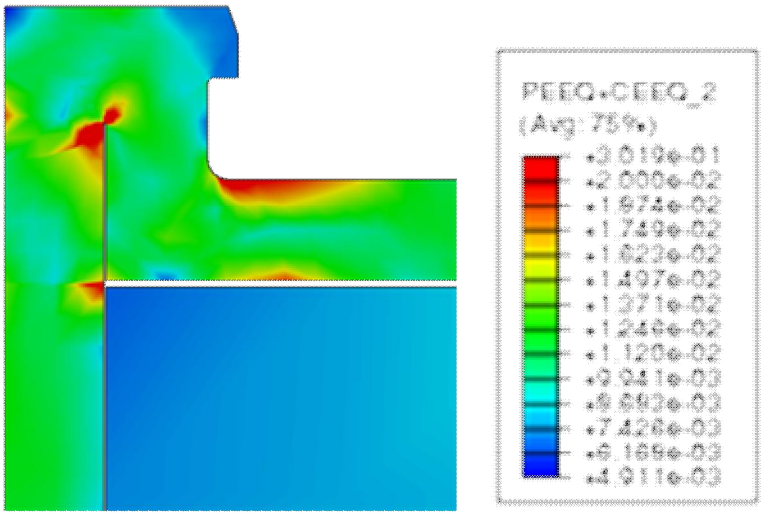

Figure 6. The total strain distribution after 1000 years, plotted on top of the un-deformed mesh.

As this analysis was performed with a material model which takes plasticity, creep and relaxation into account it would be essential to compare the results against a similar analysis where relaxation is not considered. However, because of the different weld geometry and the modelling of the joint line hooking and the oxide particle zone, there is no analysis of this particular geometry with plasticity and creep models omitting relaxation. Therefore a simple comparison was made by using a single element with two different material models:

1) Plasticity and creep with LCSP model
2) Plasticity, creep with LCSP model and relaxation

The results of this comparison are shown in Fig. 7. The results show that with the relaxation model the stresses relax much faster in the beginning than with the LCSP creep model.

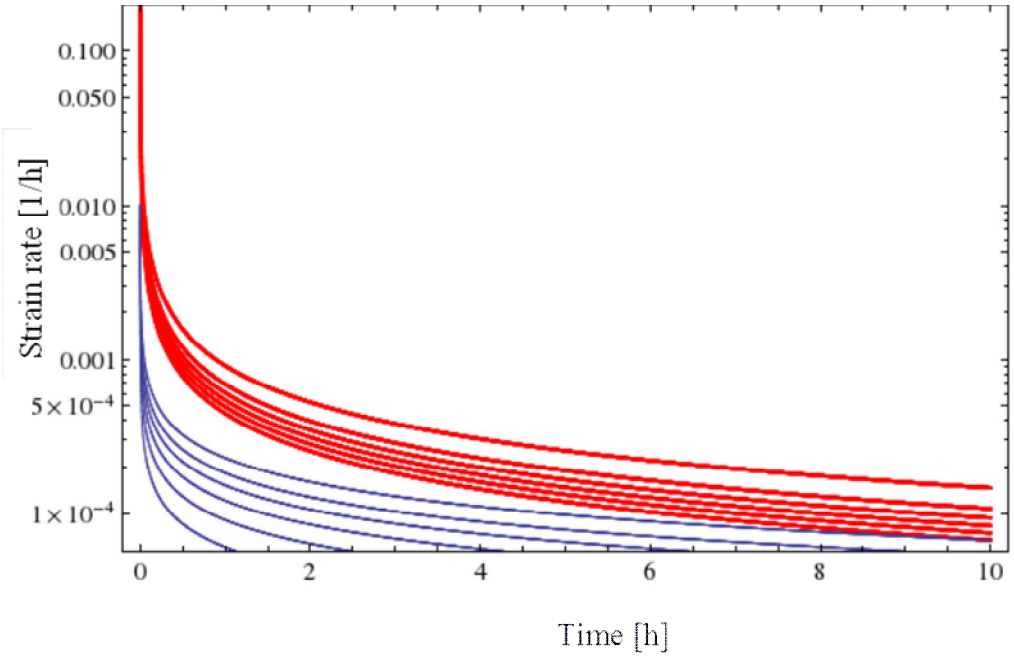

Figure 7. Comparison of strain rates predicted by FE by using the LCSP creep model (red curves) and the Kohlrausch relaxation model (blue curves).

4. Conclusions

The initial results indicate that in the analysis of the copper canister it is essential to use an appropriate relaxation model. The amount and quality of relaxation data is still rather limited, but the stress analysis with the current relaxation model has shown that the stresses relax much faster when a relaxation model is included in the analysis.

It has also been proposed by VTT that a simple model component test should be performed in order to test the capability of various material models (or combination of models including or omitting a relaxation model) to predict the load history when a model component is subjected to a forced displacement and the load is measured. A suitable model component could be for example a ring which is compressed in the radial direction to a fixed displacement. In a ring shape component there are stresses from compressive to tensile and this would provide an appropriate test for the capability of different material models to predict relaxation. One particular material model could produce very accurate predictions at a limited stress range, but the situation could be different when the range of stresses in the test component is very wide.

References

1. Raiko, H. Canister Design 2012. Report POSIVA 2012-13, Posiva Oy.

2. Rantala, J., Auerkari, P., Laukkanen, A., Andersson, T. & Saukkonen, T. Material integrity of welded copper overpack – Annual report 2014. Espoo, VTT, 2015. Research Report VTT-R-00773-15.

3. Holmström, S. Engineering tools for robust creep modeling. Dissertation. Espoo, VTT, 2010. Publication 728. 94 + 53 p.

4. Kohlrausch, R. Nachtrag über die elastische Nachwirkung beim Cocon- und Glasfaden, und die hygroskopische Eigenschaft des Ersteren. Pogg. Ann. Phys. (Leipzig), 12 (1847), pp. 393-425.

High temperature mechanical properties of a 17wt%Cr High Performance Ferritic (HiperFer) steel strengthened by intermetallic laves phase particles

Michal Talík & Bernd Kuhn
Forschungszentrum Jülich, Germany

Abstract

Application of Advanced Ferritic-Martensitic (AFM) steels, like P91, P92 or Save 12, allowed an increase of working parameters of Ultra Super Critical (USC) power plants. Utilization of AFM class materials at temperatures above 620 °C seems to be doubtful because of limited steam oxidation resistance of 9 wt % Cr steels [1] and decreasing long-term creep strength of 12 wt% Cr steels [2]. Presented HiperFer steel exhibits superior steam oxidation resistance and creep strength at 600 °C beyond P91 steel [3]. Creep properties of HiperFer steel are significantly influenced by its initial thermomechanical treatment state. The influence of different rolling procedures of HiperFer steel on creep properties in the temperature range from 625 up to 675 °C will be presented.

Keywords: creep, Laves phase, thermomechanical treatment, modeling

1. Introduction

State of art 9 wt% Cr ferritic martensitic steels with tempered martensite structure, e.g. E911 or P92, are commonly used materials for construction of thin- and thick wall components of modern Ultra Super Critical power plants [1, 2]. Creep strength of these steels is governed by fine precipitation of MX particles in subgrain interiors, $M_{23}C_6$ particles on subgrain boundaries, solid solution strengthening, and, in the initial stages of creep, by high dislocation density [4, 5]. The application temperature of these 9 wt% Cr steels is restricted to 620 °C, because of their limited steam oxidation resistance [1]. 12 wt% Cr ferritic martensitic steels like VM12 have higher corrosion resistance [3, 6], but these materials do not have sufficient long term creep strength because of the formation of coarse Z-phase particles at the expense of fine MX precipitates [1, 7].

Newly developed ferritic stainless (18 – 23 wt% Cr) steels strengthened by intermetallic Laves phase particles exhibit creep strength at 600 °C comparable with modern ferritic martensitic steels [Kuhn1], and have substantially better oxidation resistance in steam compared to 9-12 wt% Cr steels [Kuhn1]. Creep strength of this type of steel is ensured by fine precipitation of $(Fe, Cr, Si)_2(Nb, W)$ Laves precipitates; oxidation resistance by sufficiently high chromium content at levels of 17 – 18 wt%.

HiperFer steel is an age hardenable creep resistant steel like most of austenitic steels and nickel-base alloys for high temperature application. The beneficial influence of enhanced dislocation density, resulting from increased rolling deformation will be discussed.

2. Experimental

2.1 Materials and Preparation

The experimental material was vacuum melted by the Institute of Ferrous Metallurgy, RWTH Aachen. The nominal chemical composition is given in Table 1. The ingots 17Cr1_1, 17Cr1_2, 17Cr1_3 and 17Cr2_4 were hot rolled down to 16 mm thickness at with systematic variations in rolling temperature and deformation per rolling step to yield variations in grain size and dislocation density after rolling.

Table 1. Nominal chemical composition of the experimental steel (wt%).

C	S	N	Cr	Mn	Si	Nb	W	Fe
<0.003	<0.001	<0.003	17-18	0.2-0.5	0.2-0.3	0.5-0.6	2.4-2.6	R

2.2 Annealing experiments

Cube specimens of 4 – 5mm in lateral length were precipitation annealed in a tube furnace at 650 °C. The samples were kept in alumina crucibles. Temperature was controlled by K-type (Ni/CrNi) thermocouples placed in vicinity of specimens.

2.3 Mechanical testing

Standard cylindrical specimens with a gauge diameter of 6.4 mm and a gauge length of 32 mm were used for creep testing. Dead weight loaded lever arm type, single specimen creep machines were used for testing. 3 type S (Pt/PtRh) thermocouples were placed along the gauge section of each specimen. Temperature varied less than ± 3 °C during testing. Creep deformation was recorded continuously by a pair of electronic extensometers, which were attached to the specimens gauge lengths.

2.4 Microstructural evolution and investigation

Metallographic specimens were prepared by standard metallographic methods. Samples for SEM observations were electrolytically etched at 1.5 V for 3 – 5 sec in 5% H_2SO_4 to increase the particle/matrix contrast. Micrographs were captured utilizing a Zeiss Supra 50 VP SEM and the commercial software package AnalysisPro® was applied for quantitative microstructure evaluation.

2.5 Thermodynamic modelling

MatCalc version 6.00 using database mc_fe_v2.057.tdb was employed for thermodynamic modelling of experimental steel.

3. Results and discussion

3.1 Thermodynamic modelling

Experimental HiperFer steel is based on the development of Crofer® 22H steel – an intermetallic particle strengthened, high chromium Solid Oxide Fuel Cell material [3, 8]. The HiperFer steel development is an ongoing effort focused on the increase of creep resistance in the temperature range from 550 to 650 °C for the application in steam power plants and chemical plants.

A phase diagram of trial HiperFer steel (nominal composition in wt%: 17.5Cr, 2.5W, 0.55Nb, 0.475Mn, 0.25Si) modelled in MatCalc is given in Figure 1. The modelling result predicts formation of a strengthening

Laves phase from 900 °C and its content to be at around 2.2 – 3 vol% in the application temperature range from 550 to 650 °C. Formation of the undesirable (Fe,Cr)–σ phase is suppressed down to temperatures less than 600 °C.

3.2 Initial microstructure

The rolling structure of the experimental steel batches is presented in Figure 2. Large, equiaxial grains were observed in the 17Cr1_1 material (Figure 2a), finer grains were observed in the 17Cr1_2 batch (Figure 2b). Significantly deformed and coarsened grains were encountered in the 17Cr1_3 material (Figure 2c). Fine grains elongated along the rolling direction were observed in the 17Cr2_4 batch (Figure 2d).

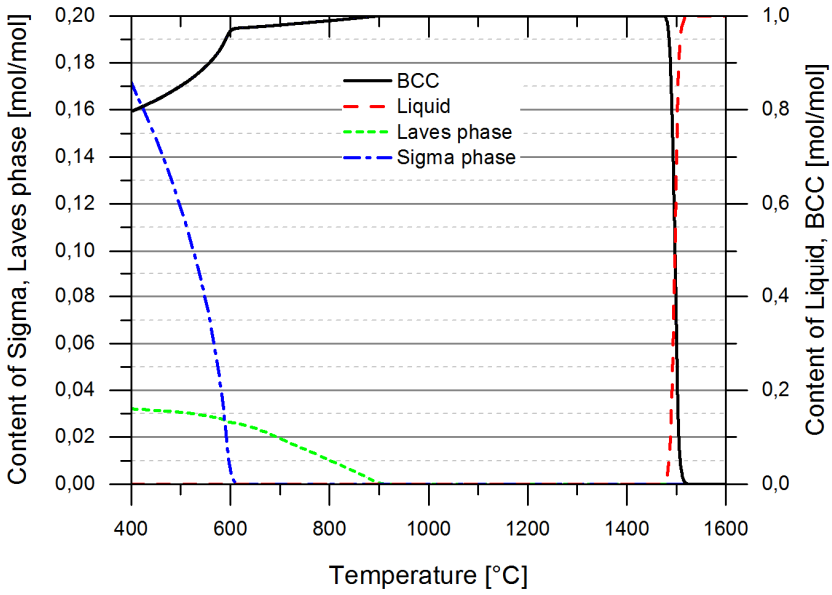

Figure 1. Phase diagram of trial HiperFer steel modelled by MatCalc.

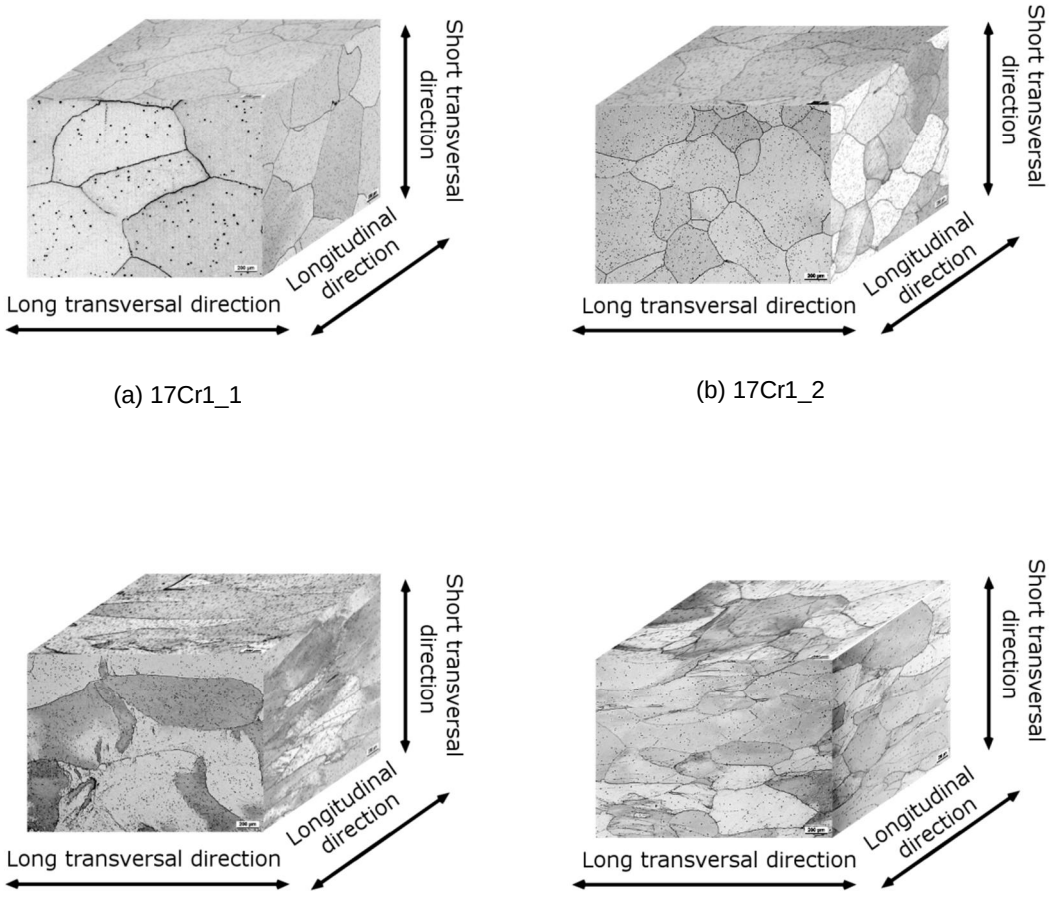

(a) 17Cr1_1

(b) 17Cr1_2

(c) 17Cr1_3

(d) 17Cr2_4

Figure 2. Macrostructure of differently rolled HiperFer batches.

3.3 Microstructural development

Limited applicability of advanced ferritic – martensitic steels is caused by a lack of corrosion resistance [3], rapid coarsening of MX and $M_{23}X$ particles [4], and coarsening of the martensitic lath structure [9, 10] at temperatures above 600 °C.

Microstructural of HiperFer steel (batch 17Cr1_1) during stress free isothermal annealing is presented in Figure 3. In the initial state, fine Laves phase particles were observed at grain boundaries (Figure 3a). A fine distribution of Laves phase particles in the subgrain interiors and densely decorated subgrain boundaries were observed after 3 h of annealing at 650 °C (Figure 3b). Coarse particles at grain boundaries without distinct particle free zones were observed after 1,000 h annealing at 650 °C (Figure 3d). The average subgrain diameter increased from 1.5 μm in the as received state (Figure 3a) up to 2.2 μm after 1,000h of annealing (Figure 3d). The mean Equivalent Circular Diameter of the Laves phase particles in the grain interiors was below 70 nm after annealing at 650 °C for 1,000 h (Figure 3d).

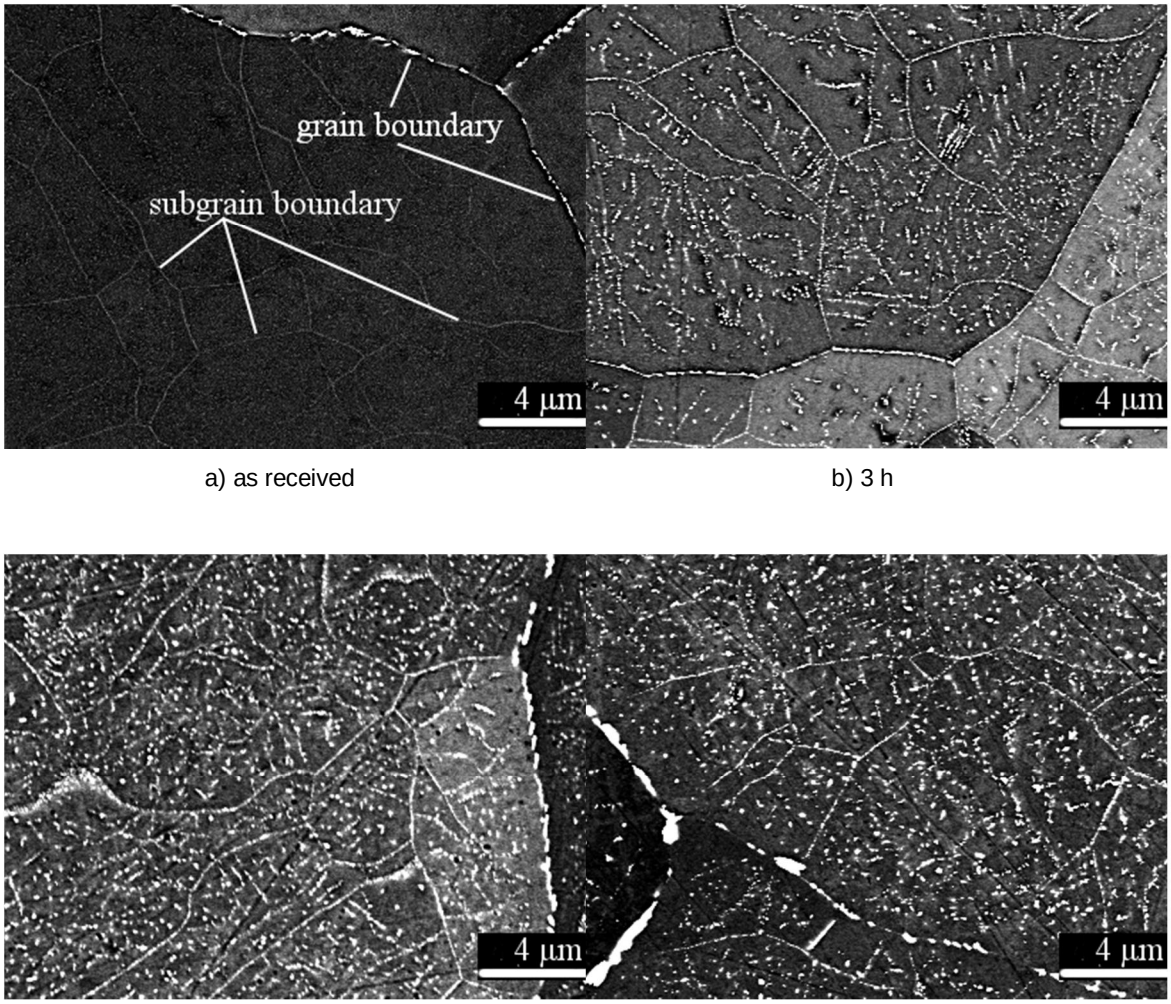

a) as received b) 3 h

c) 10 h d) 1,000 h

Figure 3. SEM micrographs of 17Cr1_1 steel during isothermal annealing at 650 °C; a) as received, b) 3 h, c) 10 h, d) 1,000 h.

3.4 Creep properties

HiperFer steel is age hardenable, and for this reason its creep properties are significantly dependent on processing. Creep strength of hot rolled HiperFer steel is ensured by a) fine distribution of thermodynamically stable Laves phase particles, and b) stable subgrain structure.

650 °C creep strength of the four material batches is presented in Figure 4. There was observed no significant difference of creep strength of the 17Cr1_1 and 17Cr1_2 batches. Times to rupture of the both batches were shorter than of P91 steel [11] at stress levels of 120, and 110 MPa; but at 100 MPa, lifetime of the both batches was longer than in case of P91 and close to VM12 [6], nevertheless still shorter than the lifetime of P92 [12] steel. Creep life of the 17Cr1_3 batch is comparable to the properties of P92 at 120 and 100 MPa. The 17Cr2_4 batch exhibited slightly longer creep life than P92 at stresses of 120 and 100 MPa. Experiments of all the four batches are still in progress at lower stress (70 MPa). None of these samples has reached the minimum creep rate yet. The 125 MPa specimen of the 17Cr2_4 batch entered the tertiary stage of creep (in March, 2016).

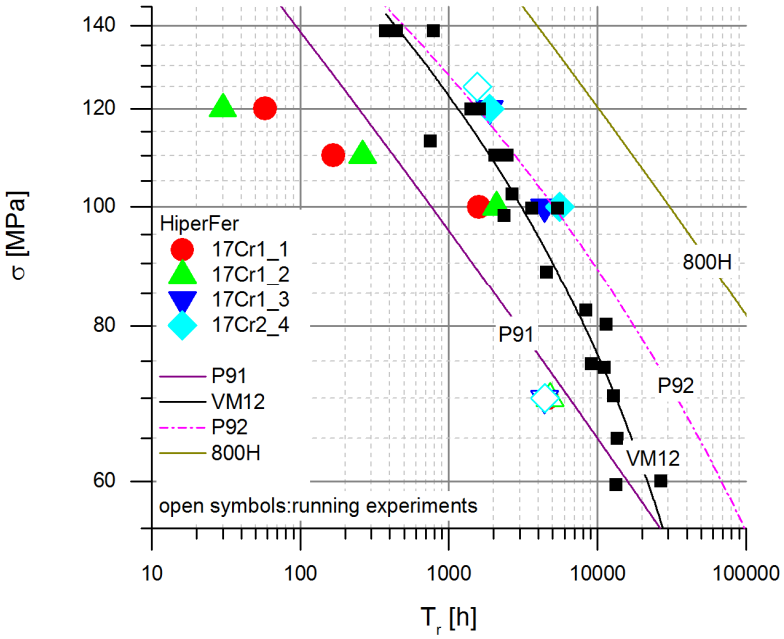

Figure 4. Creep strength of different batches of HiperFer Steel compared to state of the art ferritic-martensitic steels at 650 °C [6, 11, 12, 13].

Because of the positive interim results the 17Cr2_4 batch was chosen for a broader testing program and the results compared to P92 steel are given in Figure 5. The rupture times of the finished experiments at 650 and 675 °C are comparable to the rupture times of P92 steel. Currently, tests are still in progress at 625 °C / 150 MPa, and at 650 °C / 125 MPa with expected rupture times between one and two thousand hours. Both the experiments already entered the tertiary stage. Another experiments running at 650 °C / 70 MPa is still in the primary stage of creep after more than 4,000 h.

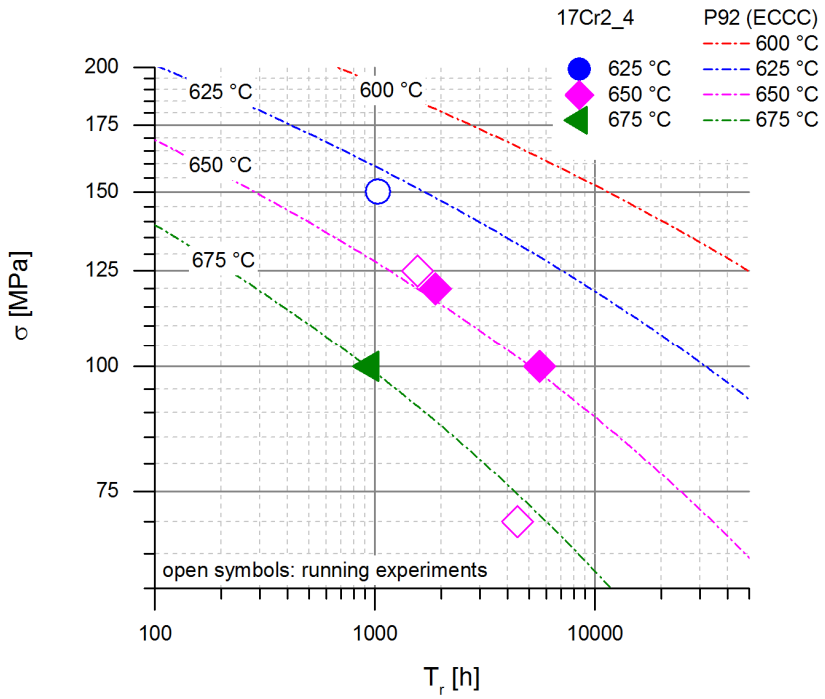

Figure 5. Creep strength of the 17Cr2_4 batch at various temperatures in comparison to P92 steel [P91].

4. Conclusion

The creep properties of novel, fully ferritic, high chromium, Laves phase strengthened HiperFer steel were presented. The creep strength of the recent HiperFer 17Cr2_4 batch is comparable to the creep strength of P92 steel at temperatures from 625 to 675 °C and rupture times up to 6,000 h (Figure 5).

Creep strength of hot rolled HiperFer steel is ensured by dense precipitation of thermodynamically stable Laves phase particles in subgrain interiors. After 1,000 h of annealing at 650 °C their size was below 70 nm (Figure 3). The subgrain structure, which results from rolling, is stabilized by dense decoration of subgrain boundaries by the Laves phase particles. The average subgrain diameter increased from 1.5 µm in the initial state up to 2.2 µm after isothermal annealing at 650 °C for 1,000 h (Figure 3).

Creep strength of HiperFer steel is dependable on thermomechanical treatment history (Figure 4). Optimized initial microstructure and in consequence increased creep strength was achieved by an improved optimized rolling procedure, which not only influences grain structure, but has an impact on dislocation strengthening and accelerated heterogeneous precipitation of the $(Fe,Cr,Si)_2(Nb,W)$ Laves phase particles.

HiperFer steel does not just offer superior creep performance, it furthermore exhibits superb corrosion resistance [3]. This is guaranteed by comparatively high Cr content (17 – 18 wt%). The chemical composition of HiperFer trial steel was based on thermodynamic modelling (Figure 1). Formation of the undesirable, potentially embrittling (Fe.Cr)–σ phase was successfully restricted to temperatures below 600 °C. The expected content of strengthening Laves phase particles was modelled to be 2.2 – 3 vol% in the application temperature range from 550 to 650 C.

References

1. F. Abe, T.-U. Kern, R. Viswanathan: Creep–resistant steels; Woodhead Publishing Limited 2008, ISBN: 978 1 84569-401-2, pp. 546-570.

2. R. Viswanathan, W. Bakker; J. Mater. Eng. Perform. 10 (2001), pp. 81-95.

3. B. Kuhn et al, “Development of high chromium ferritic steels strengthened by intermetallic phases”, *Materials Science and Engineering A*, 594 (2014), pp. 372-380.

4. V. Sklenicka, K. Kucharova, M. Svoboda, L. Kloc, J. Bursik, and A. Kroupa. Long-term creep behavior of 9–12%Cr power plant steels. Materials Characterization, 51(1):35–48, 2003.

5. Kouichi Maruyama, Kota Sawada, Jun-ichi Koike: Strengthening Mechanism of Creep Resistant Tempered Martensitic Steel; ISIJ International, Vol. 41 (2001), No. 6, pp. 641-653.

6. B. Vandenberge, B. Lefebre, J. Gabrel, J.-C. Vaillant: Development of a new 12%Cr steel for tubes and pipes in power plants with steam temperatures up to 650 °C. Conference Journées d’Etudes Européennes sur les Equipements sous Pression. Paris, 28, 29 and 30 Septembre.

7. H.K. Danielsen, J. Hald, VGB Power Tech., 5 (2009), pp. 68-73.

8. J. Froitzheim, G.H. Meier, L. Niewolak, P.J. Ennis, H. Hattendorf, L. Singheiser, W.J. Quadakkers, Development of high strength ferritic steel for interconnect application in SOFCs. Journal of Power Sources, Volume 178, Issue 1, 15 March 2008, Pages 163-173, ISSN 0378-7753.

9. R.P. Chen, H. Ghassemi Armaki, K. Maruyama, and M. Igarashi. Long-term microstructural degradation and creep strength in gr. 91 steel. Materials Science and Engineering: *A*, 528(13–14):4390 – 4394, 2011.

10. H. Ghassemi-Armaki, R.P. Chen, K. Maruyama, and M. Igarashi. Contribution of recovery mechanisms of microstructure during long-term creep of gr.91 steels. Journal of Nuclear Materials, 433(1–3):23 – 29, 2013.

11. Steel grade 91 (X10CrMoVNb9-1), ECCC Dataheets 2014.

12. Steel ASTM Grade 92, ECCC Dataheets 2014.

13. Incoloy® alloy 800H & 800HT, Publication Number SMC – 047, Special Metals Corporation, 2004.

The Materials Ageing Institute: R&D programme and scientific network to understand and anticipate the ageing phenomena of the main NPP components

By A. Al Mazouzi and R. Nhili

EDF Lab. Les Renardières, Materials Ageing Institute, Avenue des Renardières-Ecuelles, 77818 Moret sur Loing, France

By 2020, one third of the world's nuclear fleet will be 40 years old or more. In 2030, this figure will increase to 80%. Since short term replacement of current generation capacity without a massive increase in CO2 emission is not technically feasible, ensuring the safety of nuclear plant operations beyond 40 years is currently considered to be the best option. In 2008 EDF proposed to other plant operators to found the Materials Ageing Institute (MAI), on the belief that sharing research, experimental results, feedback and scientific information on materials degradation can contribute significantly to the long term operability and life extension of power plants and, more specifically, nuclear plants. Management of nuclear power plant ageing is increasingly considered to be a key energy challenge worldwide.

The MAI addresses this crucial issue from an applied research and development (R&D) perspective. By teaming up with utilities and related industries as well as academic partners, the MAI is able to combine operational expertise and theoretical knowledge, and to apply experiments and computer modelling to the understanding of the ageing process in materials and components. Since establishment of the MAI in 2008 by the world's largest nuclear power plant operator, EDF, other nuclear plant operators and organizations have joined the Institute. In 2013, eleven members include the Tokyo Electric Power Company (TEPCO, Japan), Kansai Electric Power Company (KEPCO, Japan), the US Electric Power Research Institute (EPRI), EDF Energy (United Kingdom), CGN (China), Rosenergoatom (REA, Russia), Mitsubishi Heavy Industries (MHI, Japan), Central Research Institute of Electric Power Industry (CRIEPI, Japan), Areva (France) and the French Atomic Energy Commission (CEA, France).

In addition scientific partners are brought together through the MAI Scientific Network, MAI-SN. This network consists of 25 partners, including prominent universities from the USA, Japan, UK and France as well as several research institutes. Its purpose is to create a strong and permanent link between academic researchers and the MAI. This link fosters the development of a shared knowledge base with a focus on methods and approaches required to address the scientific questions on ageing involving metallurgy, mechanical properties, chemistry, applied mathematics and numerical modelling, to name a few. Scientific seminars and workshops are organized on a regular basis allowing partners to share perspectives, information on new developments and innovations in the field of materials behavior.

This presentation will highlight the main research topics under investigation within the MAI and the link established with the academia via the MAI-SN.

Contact :

Abderrahim.al-mazouzi@edf.fr

Introduction

Materials issues have the largest impact on Nuclear Plant safety and plant performance and can lead to significant costs. Several utilities around the world have the objective to extend the lifetime of their nuclear fleet (up to 60 years or even 80 years). Long Term Operation of NPPs requires a deep understanding of the key ageing processes to be able to predict and anticipate any types of degradation. It is more than ever necessary for Utilities to share required effort at international level and to develop large collaborative research programme.

The Materials Ageing Institute (MAI) is an international research institute founded in 2008. Sharing research, experimental results, operating experience and scientific information on materials degradation significantly contribute to the safe long term operation of nuclear power plants all over the world. By teaming up with utilities and related industries as well as academic partners, the MAI is able to combine operational expertise and theoretical knowledge, and to apply experiments and computer modelling to the understanding of the ageing processes in materials and components. Since its establishment in 2008 by EDF, EPRI and TEPCO, 8 other nuclear plant operators and organizations have joined the MAI. Current members are EDF (France), EDF Energy (UK), Kansai (Japan), EPRI (USA), CGN (China) and REA (Russia). As such, the MAI represents over two-third of the World's installed nuclear power and benefits from close to 5000 combined years of reactor operating experience. In addition, industrial organizations involved in nuclear engineering and specifically in the maintenance of components or materials research also participate in MAI activities as associate members. Current associate members are Mitsubishi Heavy Industries (MHI), TEPCO and Central Research Institute of Electric Power Industry (CRIEPI) from Japan, and CEA and AREVA from France.

Members are actively engaged in the development of the MAI (strategy, research priorities, education and training...). In particular, all members contribute technically to the MAI research programme according to their key areas of expertise.

The major objectives of the MAI are to understand, model, predict and anticipate the ageing of materials used in the electricity generating plants, to develop knowledge about the behavior of materials to be used in future plants, and to capitalize on shared resources, maintain and share knowledge and skills to help plant operators incorporate the highest standards of safety.

Working scheme

The MAI is established and owned by EDF as a division of EDF and not as a separate legal entity. Each Member participates and acts based on its own interest and retains its full autonomy as a separate organization. A member's participation in the institute does not constitute the formation of a corporation, company, consortium, partnership or joint venture.

The MAI has financial support of Full Members and Associate Members, collectively referred to as the MAI "Members". Furthermore, The MAI has partnerships with academic organizations (Scientific Partners).

Full Members are companies owning and/or operating energy generation facilities or scientific research organizations whose membership includes such companies and wish to participate in and benefit from the MAI Program. Full Members provide human, technical and/or financial resources.

Full Members have a seat on the Governing Board, are represented on the Program Committee and have voting rights proportional to their overall financial and technical contribution to the MAI.

New Members may be admitted to the MAI at any time. Expressions of interest for joining the MAI are received by the MAI Director who shall negotiate the conditions and fee and keep the Governing Board informed of the progress on discussions.

R&D programme

Research areas of the MAI cover a wide range of materials: stainless steels and alloys (reactor vessel internal structures, primary and secondary circuits), polymer materials (electric cables, coatings and insulator materials) and concrete structures such as reactor containment and spent fuel pools. Key processes studied are stress-corrosion cracking, thermal and irradiation induced embrittlement, fatigue, chemical corrosion, flow assisted corrosion, fouling and wear. Experiments, modelling and operational feedback are the 3 pillars of the MAI.

The MAI R&D programme is developed and carried out in a truly collaborative approach with the active contribution of all members. Members bring their own knowledge and technical expertise: they provide technical (in-kind) contributions to the MAI programme. They send also dispatched researchers to the MAI to work as one team with MAI staff for several months up to several years. Currently, around 100 researchers and technicians are working on MAI projects for a total budget of 11 M€ in 2016. This long-term collaborative effort is vital in actively supporting long term operation of NNPs. In the following, the objectives and the scope of the on-going projects are briefly described:

Lifetime of the Reactor Pressure Vessel (RPV)

Objective

- To provide tools and data for the demonstration of the safe operation of the RPV significantly beyond 40 years of operation

Scope

- Benchmark of the atom probe analysis procedure
- Development of an annealing procedure to assess the contribution of each irradiation mechanism (hardening and non-hardening)
- Assessment of long term ageing effects on vessel material
- Crack arrest phenomenon modeling
- Crack front length effect (size effect) characterization
- Evaluation procedure considering constraint effect
- Sensitivity of 3D mechanical calculation to mechanical properties
- Nozzle integrity justification

Stress Corrosion Cracking in primary water

Objective

- Improve models to predict stress corrosion cracking (SCC) of austenitic Ni alloys (Alloys 600/182/82) and cold worked or aged stainless steels (AISI 304L/316L) exposed to the primary water

Scope

- Characterization and testing of a wide variety of materials, manufacturing processes and environmental parameters, with focus on SCC initiation, effect of cold-work, dissolved H_2 and Zn concentration;
- Validation of underlying mechanisms of degradation, including oxidation, deformation, resistance to failure of oxidized grain boundary using simulation.
- Coupling calibrated behaviors (oxidation, deformation, cracking) to deliver a new engineering SCC model (Ni alloys and stainless steels).

Lifetime of the Reactor internal structures

Objectives

- Loadings: determine the neutronic and thermal gradients on the internal structures.
- Material properties: advance in our understanding of material degradation mechanisms to better predict ageing kinetics and justify safe long term operation.

Scope

- Uncertainty and sensitivity analysis of loadings calculated for internal structures.
- Benchmark: dose and Temperature profiles in heavy reflector geometries
- Determine PWR conditions leading to void swelling through simulations and observations
- Understand swelling mechanisms due to neutron irradiation through microstructure investigations
- Improve understanding of IASCC through both experiments and microstructure analysis of decommissioned components.

Thermal & environmental fatigue

Objectives

- Give a scientific support to Industry for a new codification in fatigue issue for austenitic stainless steels
    - Fatigue life curves
    - Parameters (Environment) effects on fatigue life
- Improve the advanced method to assess the fatigue damage
    - Cyclic behavior modeling
    - Crack initiation criteria assessment
    - Effects of parameter on fatigue-life at in-service conditions
    - Transfer of results from specimens to structures (upscaling)

Scope

- Experimental tests on standard specimens and mock-ups
- Thermal-mechanical numerical simulations and modeling

Behavior of materials and chemical species in the primary circuit of NPP

Objectives

- Optimization of the chemistry of the primary system
- Reduction of the personal exposure of the primary circuit through a better control of the contamination
- A better knowledge of the phenomena which reduce the plant's availability

Scope

- Experimental studies with MAI experimental Loops
- Numerical development

Improvement of the secondary circuit chemistry

Objectives

- Predict fouling kinetics evolution which allows to determine the periodicity of soft chemical cleanings
- Determine the origin of the hard sludge formation which is necessary to set convenient cleaning procedures
- Limit fouling and hard sludge formation

Scope

- Understand corrosion products and impurities behavior in feedwater system to limit their accumulation in Steam Generators
- Understand fouling and hard sludge formation mechanisms
- Test new chemical conditionings

Concrete degradation

Objective

- To better understand and characterize concrete ageing to support long term operation of civil infrastructures. The general and long-term aim is to replace “consultant expert advice” and purely empirical based decisions

Scope

- Spent Fuel Pool (SFP) leakage effects on structural integrity of the reinforced concrete substructure.
- 3-D Materials Modeling to predict carbonation and Corrosion in reinforced concrete using electrochemical approaches
- Non Destructive Testing of Chloride Migration in Concrete

Vibrational wear

Objective

- Have a better estimation of wear kinetics of 690 alloy Steam Generator (SG) tubes and better understand wear mechanisms

Scope:

- wear experiments with 690 tubes
- Design and construction of a wear test bench
- Benchmark of wear test benches
- Parametric study of wear kinetics
- Metallurgical analyses to assess wear mechanisms

Cable ageing

Objectives

- Provide scientific insight in the degradation process of polymer materials
- Identify a suitable non destructive methodology for on-site inspection of cables
- Validate lifetime expectancy of nuclear cables

Scope

- Refinement, application and extension of the kinetics model of polymer ageing
- Identification of relations between the polymer evolution at the molecular or macromolecular scales and its macroscopic properties
- Comparison of experimental results obtained on cables removed from sites with simulated results

Non Destructive Examination

Objectives

- To obtain validated, operational tools and methods to justify the performances and limitations of NDE techniques in support of plants needs.
- To solve physical problems exhibiting complex requirements (anisotropic and heterogeneous structures, irregular component geometry, damaged surface condition, complex flaw detection,…).

Scope

- Development and validation of NDE codes and innovative methods: MODERATO code for Radiography Techniques, ATHENA code for Ultrasonic Testing, Code_Carmel3D for Eddy Current Testing
- Training sessions for all three codes offered periodically to the MAI members
- Evaluation of NDE codes by comparisons with physical experiments and third party NDE simulation software.

Experimental facilities

Experimental research is based on observation and tests on specimens specifically developed by and for the MAI. The MAI cannot handle in-house irradiated or contaminated materials. Irradiation is one of the most significant processes that contribute to the ageing of metals and alloys, and hence a major factor in limiting overall reactor lifespan. **Members** extend MAI's capabilities with access to hot facilities for studying irradiation-induced ageing of materials.

The **Microstructural Laboratory** allows for metallographic analysis and observation down to the atomic scale which are necessary to study ageing mechanisms. The MAI holds the latest generation of scanning electron microscopes (SEM, ESEM) and a dual-beam nanolab, providing two or three dimensional images of damaged areas down to the nanoscopic scale. The ultrahigh resolution TITAN microscope is the flagship technology of the microstructural laboratory with a resolution of 70 pm, below the atomic scale. The MAI also holds APT capabilities via some members.

Figure 1: FEI TITAN 80-300 kV FEG STEM electron microscope of MAI

The **Chemistry and Corrosion Laboratories** provide equipments which contribute to the fundamental understanding of chemically induced ageing mechanisms and therefore to safety, availability, radioprotection, and environmental impacts. There are several experimental loops to study corrosion under primary and secondary circuit conditions as well as many commonly used chemical analysis apparatus (e.g. ICP-AES, ICP-MS, CPL, etc.) and around 60 autoclaves. Examples of the newly installed corrosion loops are illustrated in figure:

Figure 2: CAMELIA loop for corrosion under primary water conditions and ENERGIE loop for diphasic water circulation to simulate steam generator conditions.

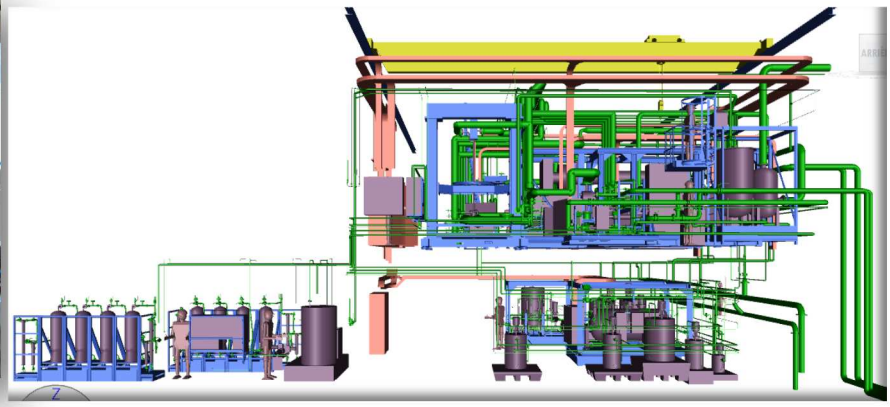

The **Mechanical Laboratories** provide experimental tools and analysis to study components and material integrity, mechanical degradation, fatigue and creep. Specific constitutive laws of materials are established to feed numerical models to simulate micro-mechanical behaviour at the crystalline scale. The laboratory contributes significantly to component lifetime assessments.

Modelling is one of the central activities of the MAI. Mathematical models do not only allow to test the understanding of fundamental processes such as stress corrosion cracking, corrosion fatigue and creep, they also enable to capitalize knowledge on databases through parametric studies. Furthermore, they are of key importance in assessing the durability of components and materials for periods beyond reasonable duration and under conditions beyond experimental reach. The MAI performs complex numerical simulations, including dislocation dynamics, molecular dynamics, *ab initio* modelling, Monte Carlo simulations, as well as simulation of complex 3D structures of materials.

As an example of the newly installed facility: VERCORS A real containment at 1/3 scale drying effects are about 9 times faster on the mock up because of scale effects A 10+ year research program to federate an international network of scientist and experts

Figure 3: VERCORS facility constructed in 2015

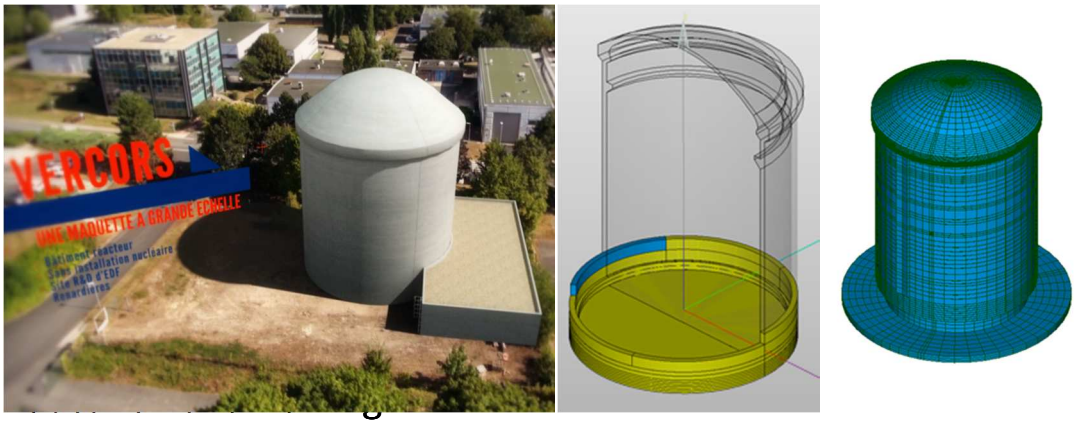

A core mission of the MAI is education and training. Courses on materials ageing are developed and offered to graduate and postgraduate students as well as to working engineers in the nuclear industry. In addition, seminars and workshops are organized by the MAI to promote discussions and knowledge sharing on technical subjects.
The MAI organizes events, courses, seminars, workshops and conferences for students and engineers seeking basic or advanced training in materials ageing in nuclear plant components. Some MAI courses are given by members in their countries. The Institute has conference facilities which allow to host events.
The MAI collaborates in an international educational programme with universities in France based on the needs expressed by utilities. This programme provides students with a deeper understanding of materials engineering science and the fundamentals of the mechanics of solids to improve their knowledge of recent developments in these fields. The programme is organized into specific modules given by MAI members.

Scientific network

Scientific and academic partners allow the MAI to benefit also from fundamental scientific studies and provide expertise and support to improve the quality and credibility of its research results. Scientific partners are brought together through the MAI Scientific Network (MAI-SN). This network consists of approximately 25 partners including prominent universities from the USA, Japan, UK and France as well as several research institutes.

The purpose of the MAI-SN is to create a strong and permanent link between academic researchers and the MAI. This link fosters the development of a shared knowledge base to address scientific questions on ageing. This involves metallurgy, mechanical properties, chemistry, applied mathematics and numerical modelling, to name a few. Scientific seminars and workshops are organized on a regular basis to share perspectives, information on new developments and innovations in the field of materials degradation.

In addition to the needed in-depth knowledge of the materials under consideration, many ageing phenomena are still not well understood and necessitate a substantial effort both experimentally and theoretically. In the following, some of the main ageing issues that have been identified:

- Under irradiation (RPV, Internal, Zr-alloys, polymers), the main challenge is to identify the role of the nano-features produced by irradiation on the micro/macroscopic behaviour of the material. These very localised "defects" have not only to be thoroughly characterised and simulated/predicted using the right tools but most importantly their direct or indirect effects on the integrity of the material under consideration. This issue has been and being the subject of many investigations (at EDF and worldwide) using appropriate materials (model alloys when needed) that have been subjected to irradiation under controlled conditions followed by in-depth characterisation in terms of microstructure and mechanical behaviour. Remain to be investigated are the effect of the initial material state (in terms of microstructure, chemistry ...) on the evolution of radiation damage. Within 2013-2014 work programme of MAI-SN, few projects have been initiated to figure out how to deal with this issue but many questions are still open, such as, the role of P/bainitic laths/... in RPV steels, precipitation versus swelling in stainless, hydridation versus growth in Zr-alloys and degradation of polymers. The effects of these local microstructural changes on the meso/microscopic mechanical behaviour will have to be investigated as well
- Thermal ageing at representative temperatures and durations affect the thermodynamical stability of the materials as some deleterious phases/precipitates may appear. Their prediction needs a relevant thermodynamic database.
- The understanding of the corrosion/erosion of the materials in contact with water necessitates among other fundamental knowledge of the diffusion processes as well as the interaction between the various ionic elements (elemental or molecules) with the formed oxide layers
- Preferential oxidation/corrosion depends on many external and internal parameters and in fact most of the investigations within MAI-SN are dealing with this issue. Remaining still to be understood the interaction between the internal/external loads and the oxidation kinetics in different representative media. Importantly as well, the quantification of the local stress and strains introduced by the formation of the oxides along specific paths.
- Ageing does not affect only the materials in contact with water but also the composition of the latter. One of the challenges identified is how to deal with the corrosion products in terms of formation, distribution as function of the local gradients and their interaction with the neighbouring materials.
- As for environmentally assisted cracking prediction (SCC), efforts are being ongoing to build models combining elementary behaviors (crystal plasticity, oxidation and cracking) and rely on quite basic principles (incubation, crack initiation, slow crack growth then fast growth). The robustness of these models will need further development of physically based criteria and local laws, and also on the relevance of the assumed ageing scenarios (coupling between deformation, oxidation and failure). In addition to the on-going actions regarding the intergranular oxidation, the failure of oxidized grain boundaries, the effects of H and the mechanical gradients it deemed necessary to investigate the electrochemical conditions in cracks and occluded areas more precisely.

- In concrete, given the important role played by water, it is necessary to take into account the coupling between hydraulics and mechanics to develop relevant behavior laws. As for Creep, which physical source within the CSH gel, progress is needed on the morphological, physical, mechanical characterization at this scale (magnitude of heterogeneity: some nm). Characterization today remains partial and difficult, due to the small scale and the presence of water. At the level of the cement paste, no reference model describing the evolution of the morphology is available as the area is occupied by the different phases: anhydrous, hydrates, liquid, and gas. The behaviour of the concrete -steel bonding, corrosion in particular, remains poorly modelled today.
- The influence of irradiation on the behaviour of the storage-materials (retaining galleries or cells MAVL) is another open issue similar to the RAG (swelling of the aggregate). An estimation model of the evolution of this swelling remains to be developed.
- As for the aging of concrete due to water / heat / corrosion / erosion, models are lacking that could give precise estimates (now results a few tens of percent). This requires both a transport model of chemical species in the concrete, a prediction of time to corrosion initiation and precise description of the chemical reactions leading to corrosion.
- As for Polymers, the main topics that have been identified are:
    - Multiscale study of thermal aging of PE / PEO using various experimental methods.
    - Permeability measurements during aging of polymers, to determine the evolution of these properties with time.
    - Improvement of the homogenization of mechanical properties of polymers.
    - Characterization of support / polymer interfaces: assessment of existing experimental techniques.

Conclusion

The MAI is a very original and unique collaborative institute that gathers 11 members worldwide with an annual 11M€ joint R&D programme. The 40 years of operating experience and plant life management expertise represented by the MAI members constitute a unique and valuable resource for the study of materials ageing mechanisms. Operational feedback data are obtained using samples of material that are made available by utilities after replacement of specific components.

MAI members greatly benefit from:

- A worldwide collaborative R&D programme driven by utility needs and supporting long term operation and plant performance
- An access to world class expertise and state-of-the-art experimental capabilities
- The development of common methods and approach with key nuclear industry players, reinforcing the credibility of their own research results
- A significant leverage of technical and financial resources
- An excellent way to promote skills, knowledge and know-how at international level
- An access to a renowned education and training programme supporting technical skills development

References

www.themai.org

Nuclear plant: Microstructure & ageing

Influence of repair welding on microstructure of VVER 1000 pressure vessel

Dagmar Jandová[1], Miroslava Matějová[1] & Josef Kasl[1]

[1]Research and Testing Institute Plzen
Tylova 1581/46, 301 00 Plzeň, Czech Republic

Abstract

A method for repair welding a VVER 1000 pressure vessel was developed using the tempered bead welding technique. Trial welds were produced and their structures were investigated using light, scanning and transmission electron microscopy. Two filler metals (Inconel 52 and Inconel 52M) were deposited on the materials used for production of the pressure vessel: the base material of 15CHMNFA steel, the weld metal of the circumferential weld joint and the austenitic cladding of the inner surface of the pressure vessel. This paper concentrates on the microstructural study of the heat affected zones (HAZ) beneath the repair weld of Inconel 52. Microhardness was measured along the fusion line and in selected areas up to 2 mm from the fusion line. Special attention was paid to triple points, where three different materials were joined. Microhardness was correlated with the microstructures. All the structures observed in the HAZ corresponded to tempered bainite and martensite. Carbon depleted zones along the fusion line with the Inconel alloy were narrow and fine separated ferritic grains occurred only in specific areas. Various bainitic structures were observed – upper and lower bainite, acicular ferrite with cementite and chromium carbides at grain boundaries and fine precipitates inside grains. No fresh martensite or M-A constituent were found. All areas beneath the fusion line with the repair filler metal were tempered.

1. Introduction

Reactor pressure vessels (RPVs) are the most critical component for the safe, long term operation of a nuclear power plant. The reliability and operability of an RPV are the limiting factors for the safe operation of the whole plant.

An RPV is the only pressure boundary component that operates in the field of strong reactor radiation, mostly of fast neutrons, which induce defects in the material of the vessel and could cause its gradual embrittlement. Degradation continues over the course of further irradiation as a consequence of lattice defects, crack nucleation and propagation. As the RPV deteriorates over time, there is an ever-increasing chance that the vessel would fail in an emergency or extreme operation situation.

The proper inspections of each RPV are carried out during regular shut-downs. Inner as well as outer surfaces of the vessel are scanned using ultrasonic, eddy current and visual tests. Detected defects have to be removed and repaired by welding. An appropriate welding method has to be developed, which does

not deteriorate the base material and includes filler metals resistant to radiation damage in operation conditions.

Light water VVER type reactors are used in all nuclear power plants in the Czech and the Slovak Republics. VVER 440 have been in operation for between 15 and 30 years, VVER 1000 for 15 years. The method for repair welding of VVER 440 was qualified more than 10 years ago as a result of the EU "Smart Weld" research project [1]. Up until now, no defects have been detected which have needed repairing. Nevertheless, it is necessary to modify this method for repair welding, as VVER 1000 is being produced from other materials and operates under more severe radiation.

Repair welding has been successfully applied in the USA for repairs of RPVs [2,3,4] using filler metals based on Inconel alloys, which provide sufficient corrosion and irradiation resistance in service conditions.

Trial repair welds were deposited on materials which were not irradiated, as well as materials after irradiation, which simulate current conditions in real service. The tempered bead welding technique (TBW) was applied, which is defined as follows: 'A weld bead places at a specific location in or at the surface of a weld for the purpose of affecting the metallurgical properties of the heat affected zone or previously deposited weld metal' [5]. This results in stress release and transformation of undesirable hard structural components of high carbon or low alloyed steel in heat affected zones (HAZ), which can initiate cracking, into more tough structures. It also causes refinement of the coarse grained heat affected zone (CG HAZ) adjacent to the fusion line. TBW is normally used in lieu of performing post weld heat treatment after repair welding carbon and alloy steels. It is not done to austenitic stainless steels, aluminium, copper, nickel or titanium alloys [6].

The microstructures of repair weldments were investigated; i.e. the microstructures of the welding overlays of Inconel alloys as well as changes in the base materials and the heat affected zones. This paper deals with the study of the weldments of unirradiated materials and concentrates on the base materials beneath the repair welds. The microstructures of the weld metals, Inconel 52 and 52M have been described in the proceedings of another conference [7].

2. Experimental procedures

2.1 Experimental materials

Repair welding was carried out using GTAW without preheating and post-weld heat treatment. Repair weld overlays (RW) of Inconel alloy 52 were deposited on flat specimens made of different materials, which were used for production of VVER 1000 pressure vessels: 1) low alloyed 15Ch2MNFA steel used for production of the rings and cover (BM); 2) weld metal of a circumferential weld joint used for joining individual rings (WM) and 3) austenitic cladding used for the protection of the inner surface of the vessel (AC). Test coupons were machined out from different parts, which also included the heat affected zones of a circumferential weld joint and austenitic cladding. The chemical compositions of all the above mentioned materials are given in Table 1.

The welding overlay consisted of several layers, from 1 up to 5 (Fig. 1a). Step-by step investigations of specimens with different weld layers were carried out including mechanical testing, hardness measurement and metallographic analyses [8]. Numerical simulations were used for the optimization of the welding process. Different combinations of heat inputs of different weld layers were used in order to obtain suitable microstructures in the heat affected zones. The bead side shift depth and the shape of root penetration were taken into account. Tempering occurs in the first layer when successive weld beads overlap previous weld beads by 30 to 70%. The energy from each bead of the second layer affects not only the neighbouring beads just like in the first layer, but that energy penetrates into the weld layer below the second layer, where it further tempers that weld metal and some of the HAZ beneath the layer. It is desirable that the second layer HAZ overlaps the coarse-grained regions of the first layer completely as well as a large portion of the fine-grained regions. A criterion for maximum permissible hardness of 350 HV along the interface between the weld metal and repair filler metal at a distance of 0.5 mm beneath the fusion line was defined in compliance with welding standards and results from the research project [1,9].

This paper deals with the investigation of specimens containing the base material, the weld metal and austenitic cladding, which were covered by 5 layers of Inconel alloy 52 using the same optimized welding method (Fig. 1b).

Table 1. Chemical composition of materials [wt-%].

Material	C	Mn	Si	P	S	Cr	Ni	Co
Inconel 52	0.026	0.24	0.14	0.0004	0.001	29.19	61.00	0.007
BM-15Ch2MNFA	0.16	0.46	0.30	0.009	0.010	2.18	1.29	0.012
WM - Sv12Ch2N2MAA + FC-16A, requirements	0.05 0.12	0.50 0.90	0.15 0.45	max 0.010	max 0.015	1.40 2.10	1.20 1.90	max 0.025
Aust. Cladding - 1st layer requirements	max 0.09	0.80 2.00	0.30 1.20	max 0.030	max 0.020	22.00 26.00	11.00 14.00	max 0.05
Aust. Cladding – 2nd layer requirements	max 0.04	1.30 2.20	max 0.80	max 0.030	max 0.020	17.50 20.50	8.50 11.00	max 0.05

Material	Mo	V	Cu	AL	Fe	Ti	Nb	Ta
Inconel 52	0.01	-	0.01	0.38	8.59	0.38	0.01	
BM - 15Ch2MNFA	0.58	0.11	0.05	-	bal.	-	-	-
WM - Sv12Ch2N2MAA + FC-16A, requirements	0.45 0.75		Max 0.08					
Aust. Cladding - 1st layer requirements	-	-	-	-	-	-	-	-
Aust. Cladding – 2nd layer requirements	-	-	-	-	-	-	0.45 0.70	-

a b

Figure 1. Inconel alloy 52 deposited on 15Ch2MNFA steel: a) specimen covered by 1(A), 2 (B), 3(C) and 5(D) layers, b) macrograph of cross section in part D.

2.2 Experimental methods

Metallographic examination was carried out using specimens of repair weld deposited on the following materials: the base material (specimen 7A26), the base material and austenitic cladding (specimen 1/4 with a triple point TP1 of RW/BM/AC), the base material with circumferential weld joint and austenitic cladding (specimen TP 23/4 with triple points TP2 of RW/WM/AC and TP3 of RW/BM/WM) shown in Fig. 2. Metallographic samples were prepared using etching in 3% nital solution and observed using light optical (LM) and scanning electron microscopy (SEM) and energy-dispersive X-ray microanalysis (EDS).

Vickers microhardness measurement was performed along the fusion line between Inconel 52 and the base material or the weld metal and along the normal lines to the fusion line in selected areas beneath welded overlayers. The step of measurement was usually 0.1 mm.

Thin foils used for transmission electron microscopy (TEM) were produced using jet electropolishing in 6% solution of perchloric acid in methanol at a temperature range from -60°C to -50°C and a voltage of

21 V and 30 V for low alloy and austenitic steel respectively. Phases were identified using EDS microanalysis and selected area electron diffraction (SED). Dislocation density was evaluated using the Keh-Weismann intersection analysis [10]. Thin foils were prepared from the following areas: the base material of 15Ch2MNFA steel, austenitic cladding, the weld metal on the basis of low alloyed steel, the repair weld metal of Inconel 52, HAZ of BM and HAZ of WM in 0.5 mm from the fusion line with Inconel 52, HAZ of WM close to the triple point TP 2 of RW/WM/AC materials.

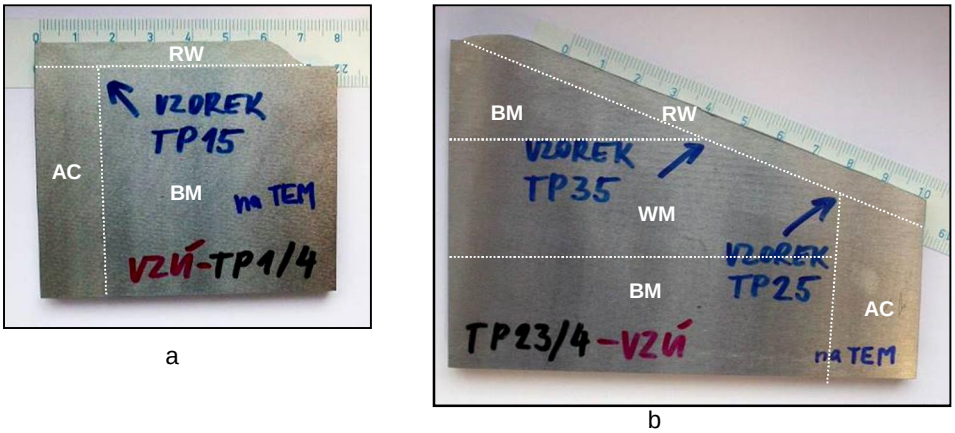

a b

Figure 2. Specimens for metallographic study: a) TP1/4 with TP1 triple point of RW/BM/AC and b) TP 23/4 with TP2 triple point of RW/WM/AC and TP3 triple point of RW/BM/WM.

3. Results

3.1 Microhardness measurement

The areas in the heat affected zones selected for microhardness measurement are shown in the following figures. They included the interface between the repair weld and other materials. Vickers microhardness HV 0.1 is plotted in relation to the distance from the fusion line. Individual curves are numbered in compliance with the lines in the micrographs. A gradual decrease of micro hardness with increasing distance from the fusion line can be observed in all localities. In the HAZ of BM close to the fusion line up to a distance of 0.7 mm hardness values exceeded the permitted limit 350 HV (Fig. 3). The highest value of 370 was determined in regions adjacent to the fusion line.

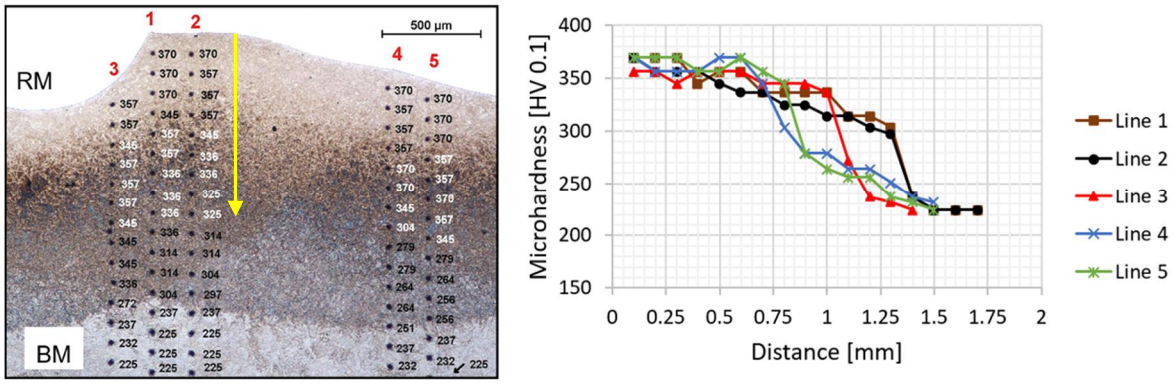

a b

Figure 3. Specimens 7A26: a) SM micrograph with indentations, b) microhardness profiles across the heat affected zone.

Almost the same curve profiles were obtained in another locality of the HAZ BM along lines 6 and 7 (Fig. 4). The hardness along Line 7 in the heat affected zone beneath the austenitic cladding, which was again reheated during repair welding, was rather lower and satisfied the requirements. The hardness in the austenitic cladding was not influenced by the repair welding (line 8).

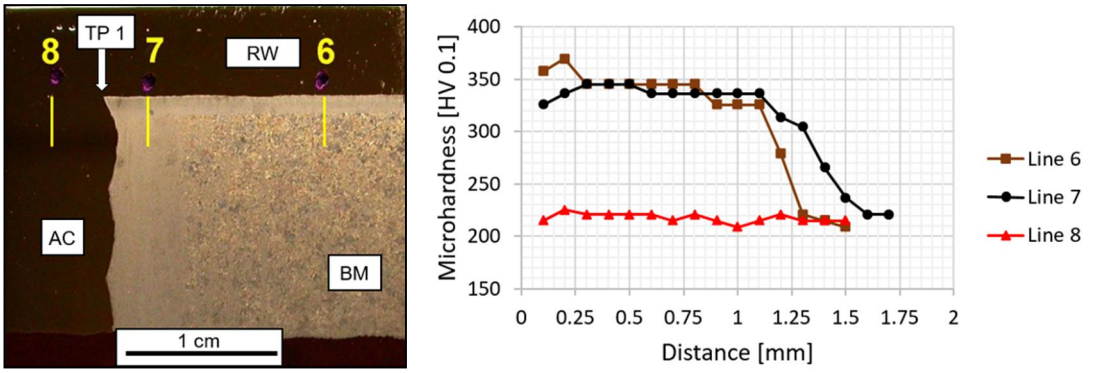

a b

Figure 4. Specimens 1/4: a) SM micrograph with indentations, b) microhardness profiles across the heat affected zones along lines indicated from 6 to 8.

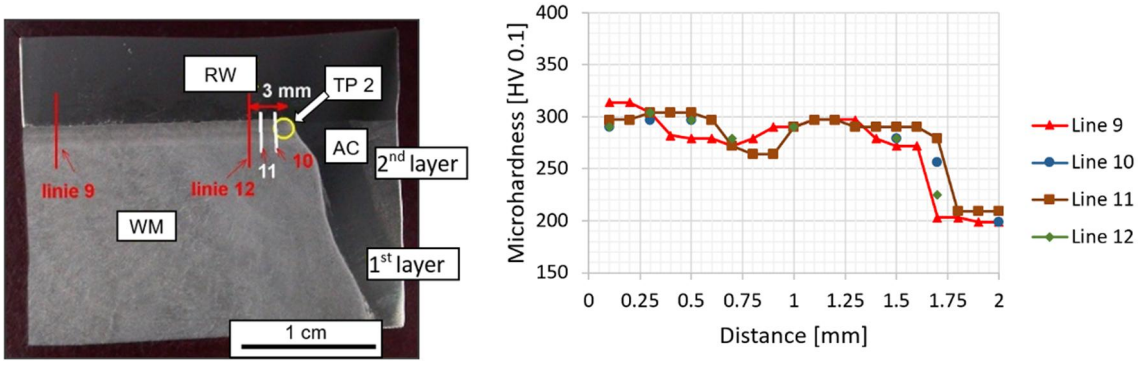

a b

Figure 5. Specimens 23/4: a) SM micrograph with indentations, b) microhardness profiles across the heat affected zones along lines indicated from 9 to 12.

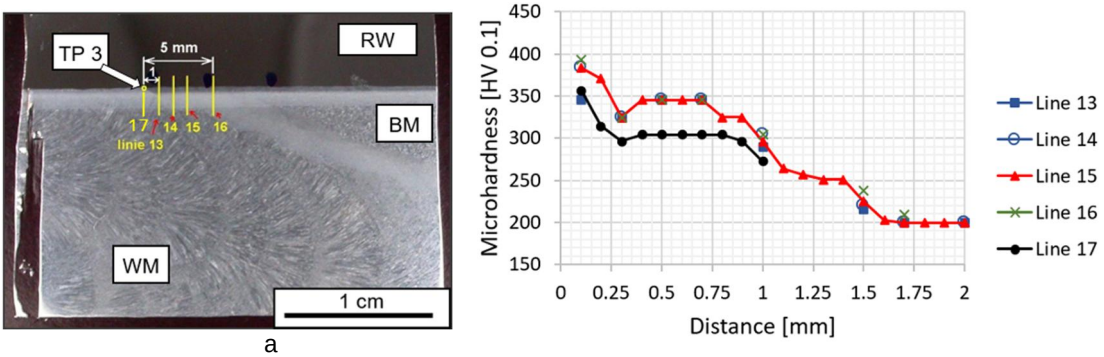

a

b

Figure 6. Specimens 23/4: a) SM micrograph with indentations, b) microhardness profiles across the heat affected zones along lines indicated from 13 to 17.

Microhardness of the weld metal heat affected by the repair welding shown in Fig. 5 satisfies the requirements – it is below 350 HV across the whole measured interval. The heat affected zone of the base material which was again reheated during repair welding revealed too high hardness close to the fusion line and satisfactory hardness at more than 0.25 mm from the fusion line.

3.2 Microstructure of the base material of 15Ch2MNFA steel (BM)

The microstructure of the base material corresponds to tempered bainite (Fig. 7a). Particles of precipitates decorate the boundaries of previous austenitic grains, packets of laths and desks and boundaries between individual ferritic laths and/or desks (Fig. 7b). The mixture structure consists of lower bainite of ferritic desks with intragranular lath-like particles of cementite and sparsely spread globular particles of chromium rich $M_{23}C_6$ and upper bainite of ferritic laths with cementite at the lath boundaries. Fine precipitates – lath-like Cr_7C_3 carbides and equiaxed VC carbides were identified inside the grains.

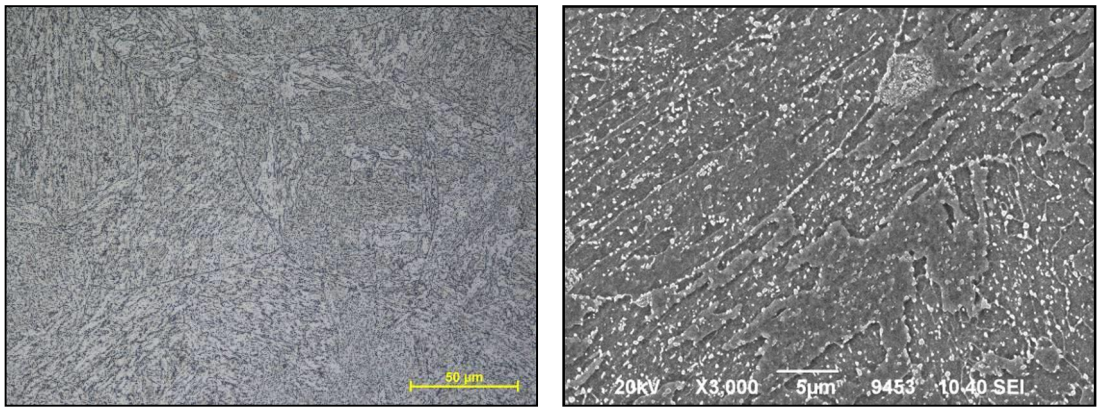

a b

Figure 7. Microstructure of BM: a) LM micrograph and b) SEM micrograph. Microhardness 230 HV 0.1.

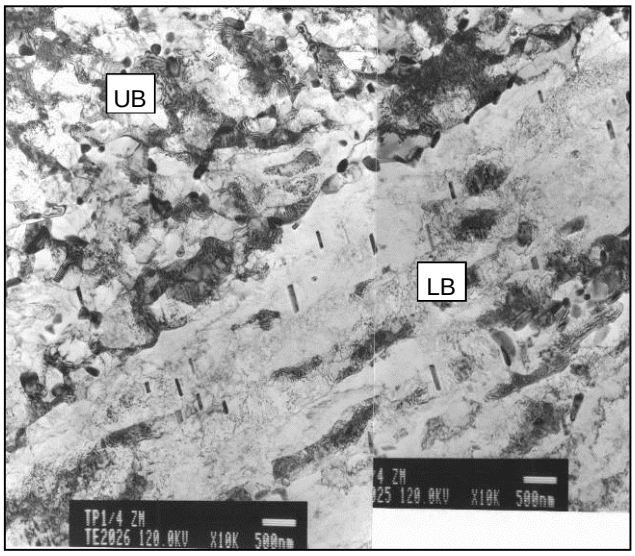

Figure 8. Substructure of BM - a mixture of lower (LB) and upper bainite (UB). TEM micrographs.

3.3 Microstructure of heat affected zone of the base material (HAZ BM)

All structures in HAZ BM correspond to highly tempered bainite. Different structures were observed in the coarse grained (CG HAZ) and the fine grained zones (FG HAZ). A ferritic matrix with fine precipitates was observed in CG HAZ close to the fusion line, while conspicuous coarse particles 1 μm in size, together with fine precipitates were spread all over the band of FG HAZ from 0.5 mm to 1.5 mm from the fusion line. The fine particles were new particles which precipitated during the welding process, while the coarse particles were present in the base material before welding and they grew as a result of heating during the welding process (Fig. 9).

Thin foils were prepared from two localities of HAZ BM at distances of 0.5 and 0.7 mm from the fusion line. There is an unclear substructure of acicular ferrite with high dislocation density, relatively coarse $M_{23}C_6$ carbides and cementite at the grain boundaries and fine Cr_7C_6 and VC carbides within grains (Fig. 10)

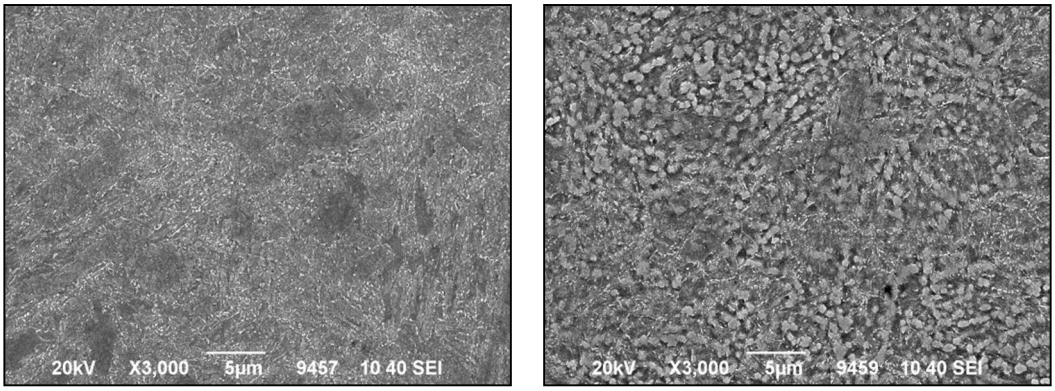

a b

Figure 9. Microstructure of HAZ BM along line 4: a) at a distance of 0.1 mm and b) at a distance of 0.5 mm from the fusion line. SEM micrographs. Microhardness of 370 HV 0.1 in both localities.

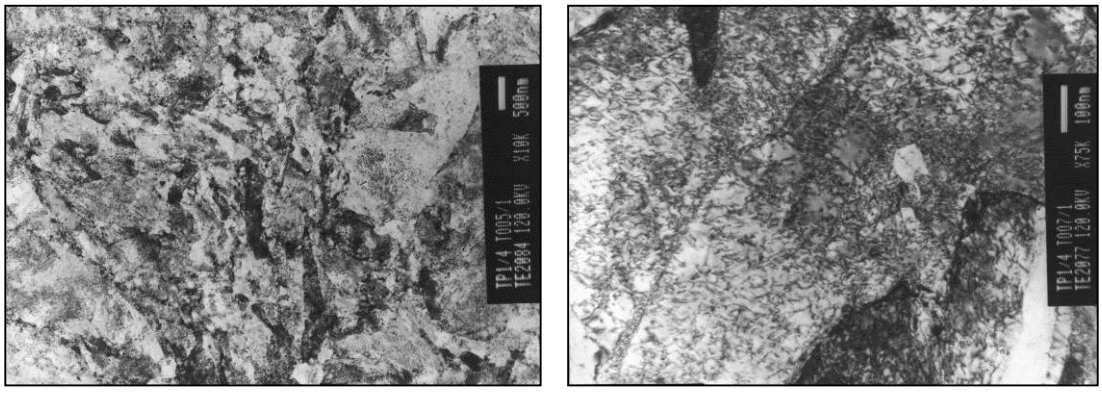

a b

Figure 10. Substructure of HAZ BM at a distance of 0.5 mm from the fusion line: a) overview and b) dislocation net. TEM micrographs.

3.4 Microstructure of the weld metal of the circumferential weld joint (WM)

The microstructure of the weld metal is heterogeneous; bands of columnar grains alternate with fine grained grains. The structure is again tempered bainite with a relatively low density of precipitates and globular silicon oxides (Fig. 11). The dislocation density in the lath-like ferritic matrix is relatively low; some

of the laths are subdivided into subgrains (Fig. 12). Cementite and $M_{23}C_6$ carbides occupy the grain and subgrain boundaries. Fine particles within the grains were detected and identified as Cr_7C_3 and M_2C carbides using electron diffraction.

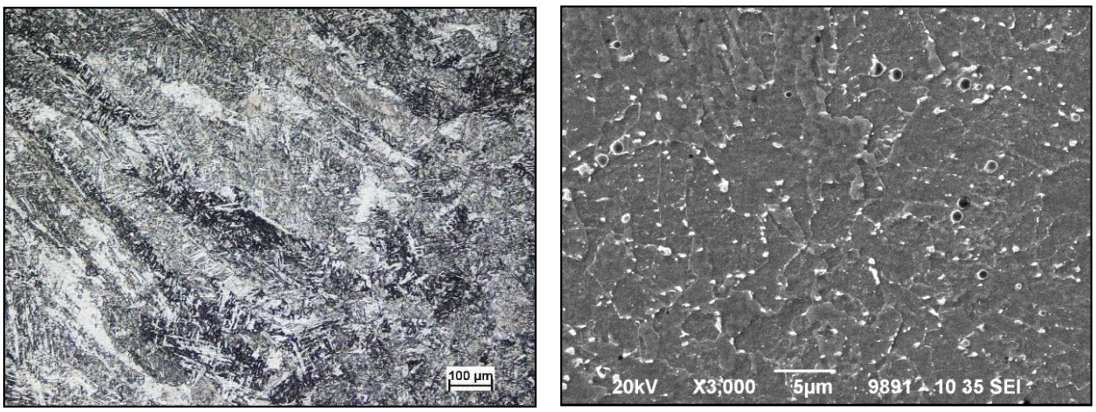

a b

Figure 11. Microstructure of WM: a) LM micrograph and b) SEM micrograph. Microhardness 200 HV 0.1.

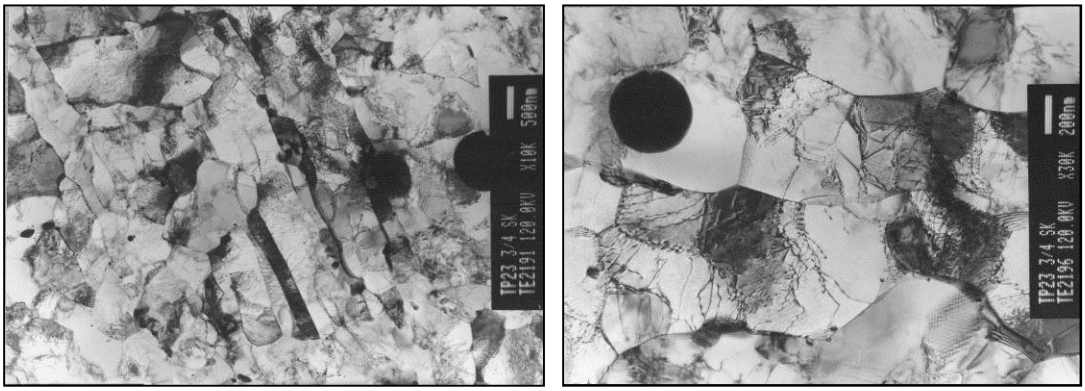

a b

Figure 12. Substructure of WM: a) overview and b) subgrains. TEM micrographs.

3.5 Microstructure of the heat affected zone of the weld metal (HAZ WM)

The heat affected zone of the weld metal close to the fusion zone was decarburized. A narrow discontinuous band of ferritic grains adjacent to the fusion line (Fig. 13a) is followed by tempered bainite with acicular ferritic matrix and fine carbides (Fig. 13b). The fine grain HAZ at a distance of 0.5 mm from the fusion line revealed a similar structure to that shown in Fig. 9b. The dislocation density increased in comparison with the weld metal non-affected by repair welding (Fig. 14). Different substructures were observed in HAZ, which contained or coarse columnar or fine equiaxed grains before deposition of repair weld overlayers.
The coarse grains contained higher dislocation density and a lower density of precipitates; in contrast, the finer grains had a lower dislocation density and more relatively coarse $M_{23}C_6$ and Mo_6C carbides. Globular silicon oxides were spread over the whole weld metal.

A heavily tempered structure occurred in HAZ WM close to the triple point TP2 (Fig. 15). The tempered bainite consisted of a ferritic matrix (acicular ferrite or packets of laths) with coarse particles of cementite and Mo_6C carbides (up 200 nm in size) at grain boundaries, chromium carbides ≈ 50 nm inside grains and fine intragranular precipitate that was not identified. A disordered dislocation net with high dislocation density and warped grain boundaries were observed.

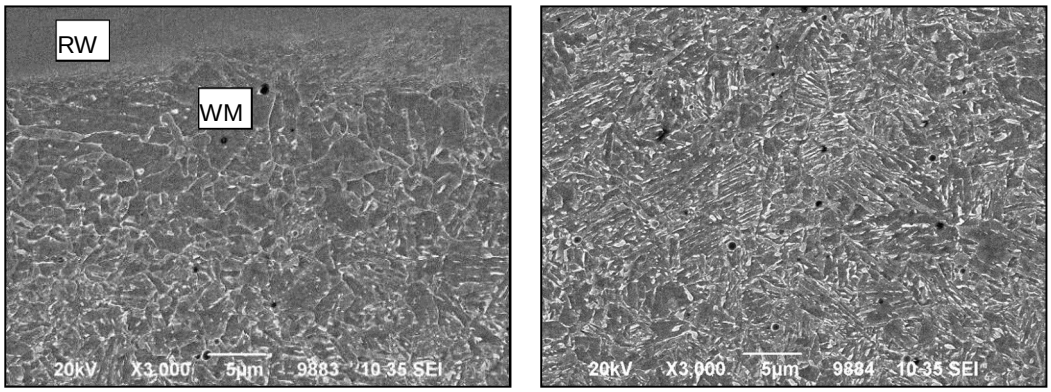

a b

Figure 13. Microstructure of HAZ WM along line 9: a) area adjacent to the fusion line, microhardness 256 HV 0.1, and b) at a distance 0.1 mm, microhardness 314 HV 0.1. SEM micrographs.

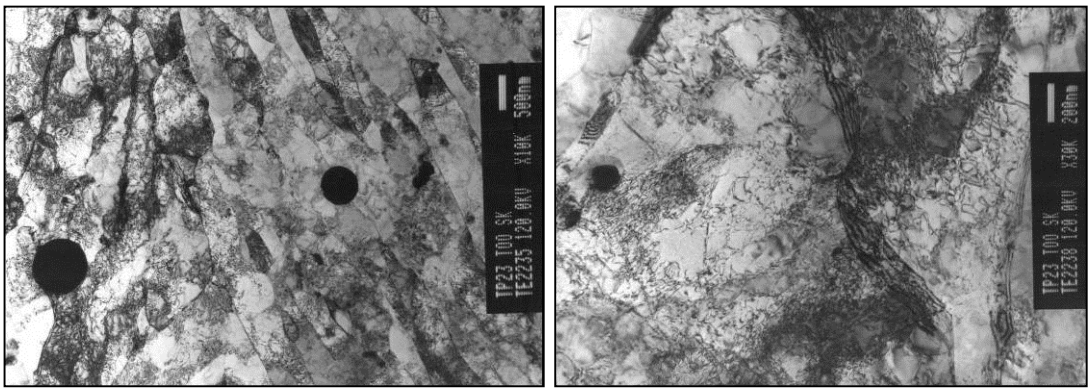

a b

Figure 14. Substructure of HAZ WM at a distance of 0.5 mm from the fusion line: a) overview and b) dislocation net. TEM micrographs.

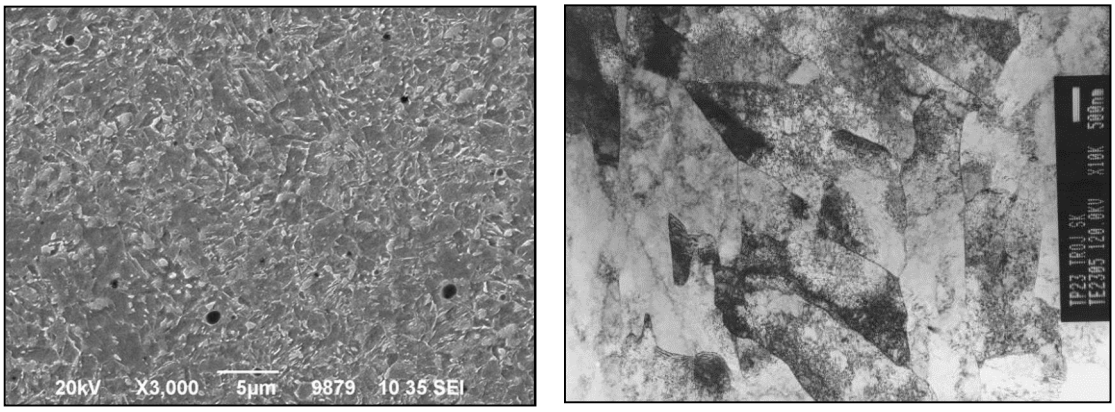

a b

Figure 15. Microstructure of HAZ WM near triple point TP2, line 10, at a distance of 0.5 mm from the fusion line: a) SEM micrograph and b) TEM micrograph. Microhardness 297 HV 0.1.

4. Discussion

Microstructural investigation was carried out in selected areas beneath the weld deposit together with microhardness measurement. The main results are summarized in Table 2. Not all areas satisfied the criterion for maximum Vickers hardness in HAZ, which should be 350 HV 0.1 at a distance of 0.5 mm from the fusion line. From this point of view, the areas of the base material of 15Ch2MNFA seem to be critical. Some differences were found between localities beneath the overlaps of adjacent beads of the 1st overlay and the central parts of individual beads. These conditions are shown schematically in Fig. 16, which corresponds to the micrograph in Fig. 3 and was drawn from the observed microstructures.

Three zones are distinguished in HAZ: CG HAZ, FG HAZ and IC HAZ (intercritically reheated zone). In this scheme only two layers were taken into account. Structures below the fusion line were tempered by heat input from adjacent beads from the same layer or from the beads of the subsequent layer. Coarse grain twice highly reheated structures below the bead overlaps were reaustenitized and structures was refined. In addition, structures beneath the fusion line underwent tempering in consequence of heat input from the 3rd overlayer. All observed structures were tempered. The microstructures corresponded to tempered bainite and/or martensite. No hard structures such as fresh martensite or M-A constituent were detected, which serve as stress raisers and can initiate cracking below the weld deposit. Nevertheless, microhardness in this area slightly exceeded the stated hardness limit of 350 HV beneath the overlapping beads at distances of 0.1 mm and 0.5 mm from the fusion line as a result of the high density of fine carbides and high dislocation density in the tempered martensite.

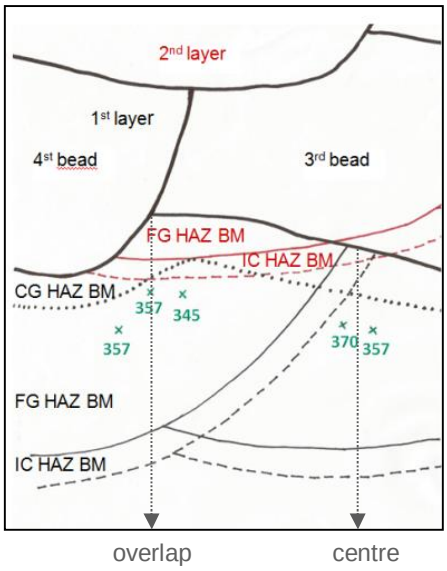

Figure 16. Scheme of HAZ BM. Zones from the 1st overlay and the 2nd overlay indicated by black and red lines respectively. Green marks with numbers correspond to microhardness HV 0.1 at a distance of 0.5 mm from the fusion line.

Unexpected increase in hardness was measured beneath the central parts of the beads in the 1st overlayer at distances from 0.5 to 0.7 mm from the fusion line. A high density of carbides with bimodal distribution of their size and high dislocation density were typical features in these areas. Coarse carbides were those which occurred in the bainitic structure before the weld deposit. They were not dissolved during repair welding as the heat input from welding was not sufficient; it caused growth of the particles. The fine carbides Cr_7C_3 and VC precipitated as new particles during heat input from the deposition of subsequent beads. The same processes occurred in HAZ WM, however the density of the fine precipitates was significantly lower. VC carbides were not present.

The highest hardness values were found in the narrow band of HAZ BM close to the triple point TP3. However, at 0.5 mm from the fusion line hardness dropped below the required limit. Depletion of carbon close to the fusion line was low and therefore tempered martensite with a high density of fine carbides and high dislocation density occurred there, resulting in relatively high hardness. The region at a distance of 0.5 mm from the fusion line with Inconel alloy belonged also to the HAZ of the circumferential weld joint of the RPV that could cause a reduction of hardness.

Table 2. Summary of the microstructural study.

Zone	Microhardness [HV 0.1] ...distance from FL [mm]	Dislocation density [10^{14}. m^{-2}]	Microstructure
BM	225 - 237	4.2 ± 0.9	Mixture of HB and UB. Carbides at boundaries. TEM: Coarse cementite and $M_{23}C_6$ particles < 200 nm and fine particles ≈10 nm of VC in laths and Cr_7C_3 at lath boundaries. Lath-like or plate-like cementite in length 500 nm.
HAZ BM beneath RW	300 ... close FL 370 ...0.1mm 350 **...0.5 mm 357 – 370*...0.5 mm 357 – 370*...0.5 – 0.7 mm 225 –345...0,75 – 1.7 mm	14 ± 6 0.5 mm from FL	Close FL: Depletion of C up to 0.03 mm from FL – mixture of F and tempered M. 0.1 mm from FL: mixture of tempered M and B, fine carbides from 10 to 100 nm in size. 0.5 mm from FL: tempered B with coarse globular carbides ≈ 1μm and fine carbides from 10 to 100 nm in size. 0.5 – 0.7 mm from FL (TEM): Acicular ferritic matrix with high dislocation density, coarse cementite particles up 250 nm at boundaries, fine Cr_7C_3 at lath boundaries, and VC in laths. 1.3 mm from FL: Bainite with fine precipitates and still some coarse globular carbides ≈ 1 μm.
WM	199 - 203	1.7± 0.6	Tempered B. TEM: Acicular ferrite with coarse cementite and $M_{23}C_6$ particles up 200 nm at grain boundaries, fine M_2C and M_7C_3 particles ≈10 nm in size inside grains. Lower density of precipitates than in BM. Globular silicon oxides ≈1 μm. Disordered dislocation net or subgrains.
HAZ WM beneath RW	314...close FL 275 - 345...0.5 mm 270 - 345...0.5 – 0.7 mm 200 – 297...1,0 – 2.0 mm	5 ± 2 0.5 mm from FL	Close FL: Depletion of C up to 0.03 mm from FL – mixture of F and tempered M with low density of fine carbides. 0.5 mm from FL (TEM): ferritic laths with high uneven dislocation density, coarse particles of cementite, M_5C and $M_{23}C_6$ ≈ 200nm in size, unidentified fine precipitate inside grains. 1.0 mm from FL: Bainite with fine precipitates and still some coarse globular carbides ≈1 μm.
AC	215 – 221...1th layer	3.7 ± 1	1th layer: austenite with Cr, Ti and V carbides at grain boundaries and inside grains. 2nd layer (TEM): austenite grains with δ-ferrite at grain boundarie,s fine intragranular Nb(C.N) precipitate 10 nm in size. Disordered dislocation net.
HAZ AC beneath RW	209 - 225	-	Increased occurrence of carbides in the 1th layer.
HAZ BM close TP1	325 ...0.1 mm 345...0.5 mm	-	Close FL: Depletion of C, mixture of F and tempered B. Prevailing F up to 0.02 mm from FL, sporadic occurrence of fine ferrite grains a few 1 μm in size up up to 0.09 mm. Fine carbides in ferritic matrix.
HAZ WM close TP2	260...0.1 mm 280...0.5 mm	4.4 ± 1 0.5 mm from FL	Close FL: Depletion of C, mixture of F and tempered B. 0.1 mm from FL: Tempered fully bainitic structure, globular silicon oxides ≈ 1μmin size 0.5 mm from FL (TEM): Acicular ferrite or packets of laths with cementite and Mo_5C carbides up 200 nm in size at boundaries, chromium carbides ≈ 50 nm in size inside grains. Fine unidentified intragranular precipitate. Disordered dislocation net.
HAZ WM close TP3	270...close FL 350 ...0.1mm 305...0.5 mm	-	Close FL: Tempered B with low density of carbides and islands of tempered M. 0.1 mm from FL: Tempered B and M with fine carbides. 0.5 mm from FL: Tempered B with coarse globular carbides ≈ 1 μm and fine carbides from 10 to 100 nm in size.
HAZ BM close TP3	264 – 279...close FL 383...0.1 mm 345...0.5 mm	-	Close FL: Tempered B with low density of carbides. 0.1 mm from FL: Tempered B and M with high density of fine carbides. 0.5 mm from FL: Tempered B with coarse globular carbides ≈1 μm and fine carbides from 10 to 100 nm in size.

F...ferrite, M...martensite, B...bainite, UB...upper bainite, LB...lower bainite, FL...fusion line with repair welding overlay,
*... beneath the centre of the bead in the first overlayer, **...beneath the overlap of adjacent beads in the first overlayer.

The microstructure of HAZ AC was also investigated. As welding deposits of Inconel alloy did not influence the structure of austenitic steel, the results were not included in this study.

5. Conclusions

The method of repair welding for reactor pressure vessels developed for VVER 440 was modified for VVER 1000. GTAW and tempered weld bead technique was applied to trial weld deposits on all the materials which are used for pressure vessel production. Results from hardness testing and microstructural analyses demonstrated adequate tempering of the heat affected zones in all the materials, including the heat affected zones from the circumferential weld joint and austenitic cladding of the inner vessel surface. The stated criterion of maximum hardness of 350 HV 0.1 in areas below Inconel 52 deposit was exceeded by approximately 20 units of HV 0.1 in the fine grained heat affected zones beneath the central parts of individual weld beads of the 1st overlayer. High dislocation density and high density of fine precipitates, namely vanadium carbides, are reasons for the increased hardness in these areas.

It can be concluded, on the basis of previous experiments which used various welding methods under different conditions and the results from microstructural studies, that it is hard to satisfy the above mentioned criterion. Slightly higher hardness seems not to be a decisive factor in the deterioration of the mechanical properties of the repair welds. A direct relation cannot be established between the hardness and the toughness of the materials being investigated. In addition, microstructural analyses did not reveal any occurrence of brittle phases in the heat affected zones, which could initiate cracking.

Acknowledgement

We are very grateful to the Technology Agency of the Czech Republic for the financial support of our research from the project TE 01020118.

References

1. Brumovský, M., Ellinger, J., Wilam, M.: Qualification for new materials for replacement/repair of original materials in WWER components, Simplified Qualification Programme for Replaced Welding Materials, Project Phare 2.03/97, Deliverable 6, report No. DITI 300/122/R1, NRI Řež plc, 2001.

2. Conference Proceedings: EPRI-RRAC Fifth International Conference on Welding and Repair Technology for Power Plants, EPRI, Palo Alto, CA: 2002. 1007013.

3. RRAC Code Justification for the Removal of the 100 Square Inch Temper Bead Weld Repair Limitation. EPRI, Palo Alto, CA: 2005. 1011898.

4. Welding Irradiated Material. EPRI, Palo Alto, CA: 2010. 1021174.

5. Sperko W.J.: Exploring Tempered Bead Welding, Welding Journal, Vol. 84, No. 7 (2005) pp. 37-40.

6. ASME Boiler and Pressure vessel Code, Section IX, 2013, go.asme.org/bpvc13.

7. Matejova M., Jandova D., Kasl J.: Summary of structure analyses in experimental welds for repair welding VVER 1000. Key Engineering materials, Vol. 647 (2015) pp.131 – 140.

8. Jandová D., Kasl. J., Matejova M.: The microstructure of Inconel Alloys Used for Repair Welding of VVER 1000, Material Science Forum, Vol. Metallography XVI. In print.

9. Czech welding standard: ČSN EN ISO 15614-1.

10. Keh A.S., Weismann S.: Electron Microscopy and Strength of Crystals. New York: Wiley, 1963, p. 231.

Short-range ordering of Alloy 690 aged for 10 000 h at 420, 475 and 550 °C

Roman Mouginot[1], Teemu Sarikka[1], Ulla Ehrnstén[2], Young Suk Kim[3], Sung Soo Kim[3] & Hannu Hänninen[1]

[1]Aalto University School of Engineering, Engineering Materials
Otakaari 4, 02150 Espoo, Finland

[2]VTT Technical Research Centre of Finland LTD
Kemistintie 3, 02150 Espoo, Finland

[3]Korea Atomic Energy Research Institute
Daedeok-daero, 989-111, Yuseong, Daejeon, 34057, Republic of Korea

Abstract

Alloy 690 is used in critical components of nuclear power systems. It has a high intergranular stress corrosion cracking (IGSCC) resistance, but questions remain concerning its long-term primary water stress corrosion cracking (PWSCC) resistance during the service life of pressurized water reactor (PWR) components. To study the effect of thermal ageing, four conditions of Alloy 690 (solution annealed, cold-rolled and/or heat-treated) were aged at 420, 475 and 550 °C for 10 000 h and characterized by SEM, EBSD and nanoindentation. Thermal ageing of Alloy 690 triggered intergranular (IG) carbide precipitation and all conditions showed evidence of short-range ordering (SRO), with the start of a disordering reaction at 475 °C. Prior heat treatment induced ordering prior to thermal ageing, as compared to water-quenched specimens. IG carbide precipitation increased with increasing ageing temperature, as well as diffusion-induced grain boundary migration (DIGM).

Keywords: Alloy 690, thermal ageing, short-range ordering, Ni_2Cr, carbide precipitation, heat treatment, cold work.

1. Introduction

Alloy 690TT (Ni-30Cr-10Fe) is replacing Alloy 600 for critical components in nuclear power systems, mostly to improve the primary water stress corrosion cracking (PWSCC) resistance of components in pressurized water reactors (PWR) 0. The alloy has an austenitic matrix, with annealing twins, large TiN particles and mostly intergranular Cr-rich $M_{23}C_6$ carbides 0-0. Due to the long service life of PWR components, the evolution of the PWSCC resistance of Alloy 690 after long-term thermal ageing is a concern. Especially, high levels of cold work (CW) significantly increase the PWSCC susceptibility and result in IG cracking [0]-0 and thermal ageing of Alloy 690 can increase the PWSCC susceptibility to

similar levels 0. The reason why thermal ageing of Alloy 690 affects its PWSCC resistance is still unclear. The main microstructural changes noticed after thermal ageing of Alloy 690 are IG carbide precipitation and atomic ordering 0. IG carbides can produce inhomogeneous strain localization at GB 0]-0, 0, 0-0, while lattice contraction due to ordering increases the hardness and reduces the mechanical properties 0, 0. It is a concern for the long-term operation of PWRs, especially when considering higher operating temperatures and longer service times 0. The ordering reaction in Alloy 690 during thermal ageing is based on the formation of the Ni_2Cr phase under a critical temperature, above which a disordering reaction occurs 0, 0. The critical temperature is composition dependent. Notably, increasing the Fe content to more than 9 wt.% decreases the critical temperature from 550 °C to less than 420 °C 0, 0. Under 350 °C, the nucleation of the ordered phase is more difficult and requires long ageing times. As such, the occurrence of long-range ordering (LRO) in a commercial Alloy 690 component is unlikely, but the formation of short-range ordering (SRO) during the service life of PWRs is expected and may affect the PWSCC resistance 0 as even small lattice contractions due to SRO are reported to cause IG cracking under applied tensile stress 0. Concerning the occurrence of SRO, the prior condition of the material has a great influence. Water quenching after solution annealing retains a disordered structure, unlike furnace cooling which allows the ordering reaction to occur prior to ageing. CW destroys the ordered structure and leads to initiation times similar to that of a water-quenched condition 0. CW, however, promotes the formation of SRO by generating vacancies in the lattice, while carbon in solution can trap excess vacancies, therefore suppressing the formation of SRO nuclei 0. The presence of SRO is, however, more difficult to assess than that of LRO and has to be studied with indirect methods. In addition, most studies have been conducted on model Ni-Fe-Cr alloys, and there is a need of data on the effects of thermal aging on commercial Ni-based alloys, notably on the combined effects of ordering, CW and IG carbides. The aim of this study is therefore to observe the influence of cold work and previous heat treatment on the ordering levels in Alloy 690 aged for 10 000 h at 420, 475 and 550 °C.

2. Experimental methods

Alloy 690 samples were prepared from a commercial melt from INCO to produce different levels of SRO. The composition of the alloy used in this study is given in Table 1, with notably 9.18 wt.% Fe. All samples were solution annealed and water quenched. The first batch of samples was kept as-received solution annealed (SA). The second batch was 20% cold-rolled (SACW). The third batch was heat treated at 700 °C for 17 h (TT). The fourth batch was heat treated at 700 °C for 17 h and 20 % cold rolled (TTCW). Samples were then kept in the original conditions or aged at 420, 475 and 550 °C for 10 000 h, corresponding to the temperatures highlighted in the introduction: 550 °C is considered the upper critical temperature for any melt of Alloy 690, while 420 °C is expected to be the critical temperature for Alloy 690 with 9 wt.% Fe. All 16 samples shown in Table 2 were ground with Struers SiC grinding papers up to 4000 grit and then polished with 3 µm and 1 µm Struers DiaPro diamond solutions. The last deformation layers were removed in a colloidal silica alkaline suspension for 16 h. The microstructures were observed by scanning electron microscopy (SEM) and electron backscatter diffraction (EBSD). The ordering levels were assessed by nanohardness measurement. The assumption was that the changes in the lattice parameter or hardness are related to the changes in the fraction of the ordered phase. For that reason, matrices of 20x20 nanoindentations were done with 1.5 mN load and 5 µm steps, omitting measurements close to the grain boundaries to avoid the influence of IG carbide precipitation, as illustrated in Figure 1. The hardness levels were calculated with the Oliver and Pharr method 0 from the nanoindentation measurements and were found to have a standard deviation of 6 % in average.

Table 1. Chemical composition of Alloy 690 used in this study.

Element	Ni	Cr	Fe	Mn	Si	P	Cu	C	S
wt. %	62.6	28.7	9.18	0.21	0.12	0.08	0.0048	0.037	<0.001

Table 2. Summary of the 20 conditions of Alloy 690.

As-received conditions		Ageing temperature (°C)		
	Code	420	475	550
SA + WQ	SA	SA420C10H	SA475C10H	SA550C10H
SA + WQ + 20 % CW	SACW	SACW420C10H	SACW475C10H	SACW550C10H
SA+ WQ + TT	TT	TT420C10H	TT475C10H	TT550C10H
SA + WQ + TT+ 20 % CW	TTCW	TTCW420C10H	TTCW475C10H	TTCW550

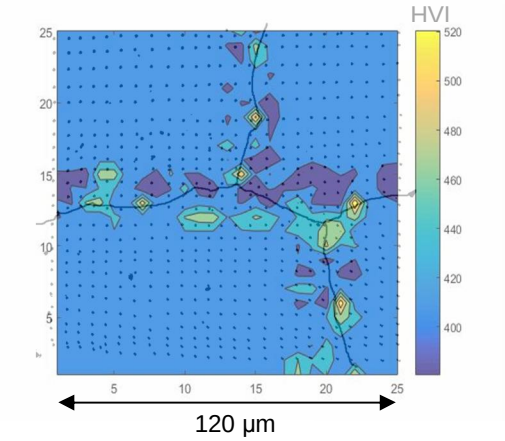

Figure 1. Hardness mapping of the TT condition after 10 000 h at 475 °C (TT550C10H), generated from the nanoindentation matrix. Hardness variations are clearly visible in the GB regions, in contrast to the more homogeneous grain interiors.

3. Results

3.1 Microstructures

Figure 2 shows the differences in microstructure between the original conditions of the alloy. The SA Alloy 690 showed annealing twin boundaries, no visible deformation and very few IG carbides. In the TT condition, the heat treatment promoted extensive IG carbide precipitation, increased the density of twin boundaries, while the strain level remained the same. Cold work after water quenching (SACW) promoted strain localization mostly around GBs, which was also observed in the TTCW condition which included IG carbides as in the TT condition. TiN particles were observed in all conditions. Figure 3 shows the evolution of GB in the SA condition during thermal ageing depending on the ageing temperature. Carbide precipitation was observed at all ageing temperatures, with an especially significant increase between 420 and 475 °C. Wavy GB regions were observed, especially at 475 and 550 °C, typical for diffusion-induced grain boundary migration (DIGM). The growth of one grain into another is illustrated by an EBSD mapping of grain orientation (Figure 3 for the ageing at 550 °C). Carbides were observed to precipitate within the zone between the original position of the GB and the new migrated GB, resulting in cellular-like carbide structure (Figure 3). The TT, SACW and TTCW microstructures showed similar results, although the extent of carbide precipitation and DIGM were much higher. Especially, extensive carbide precipitation and

growth was observed within recrystallized area around GBs at 550 °C in both SACW and TTCW conditions.

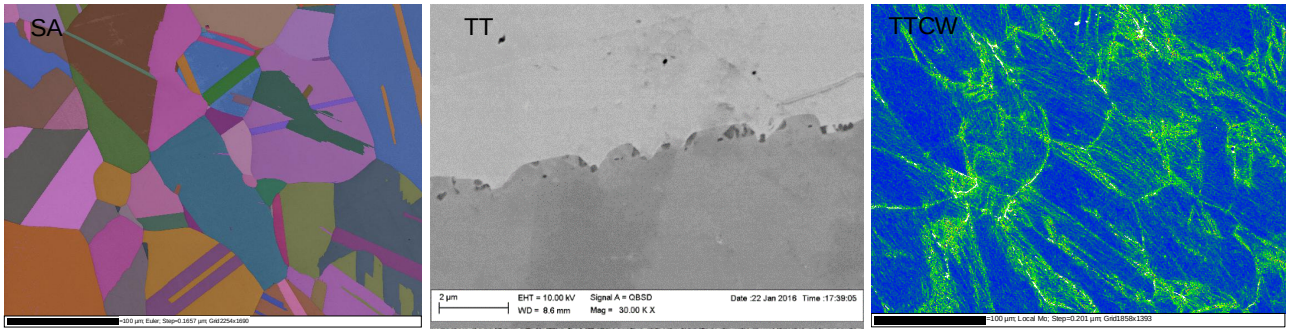

Figure 2. EBSD mapping of the as-received SA condition showing the austenitic matrix with twin boundaries (SA), SEM imaging of the as-received TT condition showing IG carbides (TT), and kernel average misorientation map (KAM) of the as-received TTCW condition showing high strain levels and strain localization at GBs (TTCW).

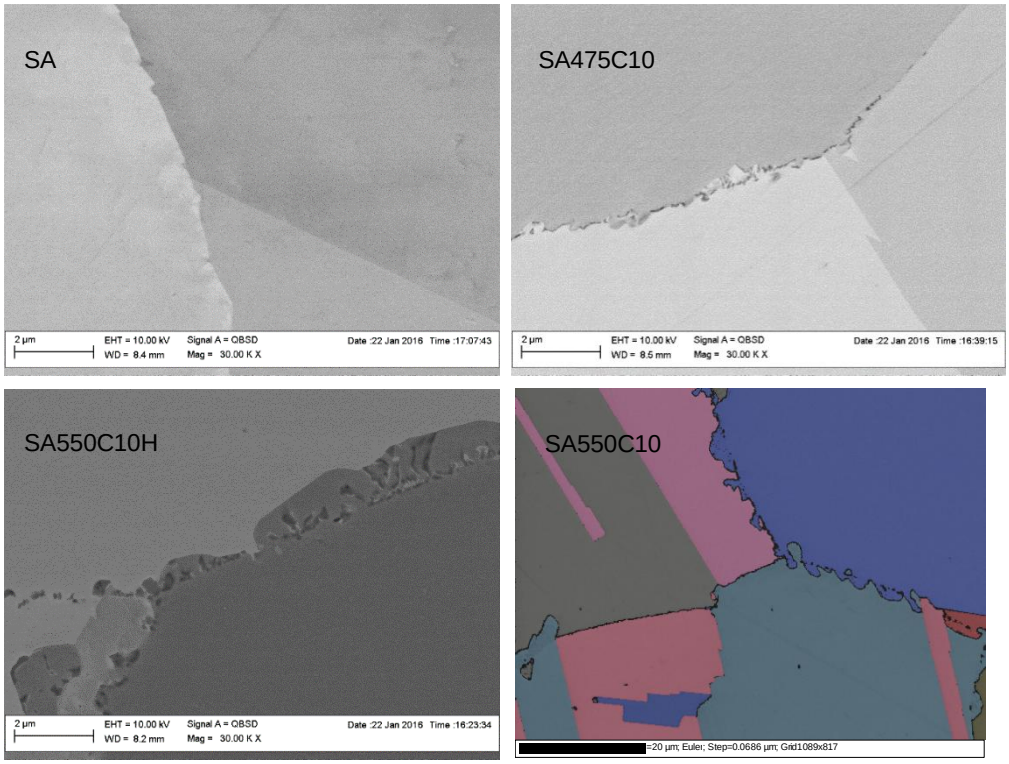

Figure 3. Evolution of GBs in the SA condition from the as-received state (SA) and after 10 000 h at 475 °C (SA475C10H) and 550 °C (SA550C10H). An EBSD mapping for the SA550C10H sample (bottom right) confirms the occurrence of GB migration.

3.2 Hardness measurements

Figure 4 shows the hardness levels of the SA, TT, SACW and TTCW conditions before and after ageing at 420, 475 and 550 °C for 10 000 h. In the original conditions, cold work increased the hardness of the alloy (from 371 to 465 HV_{IT} for SA to SACW and from 413 to 507 HV_{IT} for TT to TTCW, respectively), while heat-treated conditions were harder than the water-quenched conditions (371 and 413 HV_{IT} for SA to TT, respectively). In all conditions, thermal ageing at 420 °C for 10 000 h increased notably the hardness of Alloy 690, especially for the TT condition (from 413 HV_{IT} before ageing to 544 HV_{IT} after 10 000 h at 420°C). At 475 and 550 °C, the hardness increase was more limited in the TT condition and a hardness decrease was observed in the SACW and TTCW conditions. In the SA condition, a hardness increase was still noticeable at 475 °C, and hardness decreased at 550 °C.

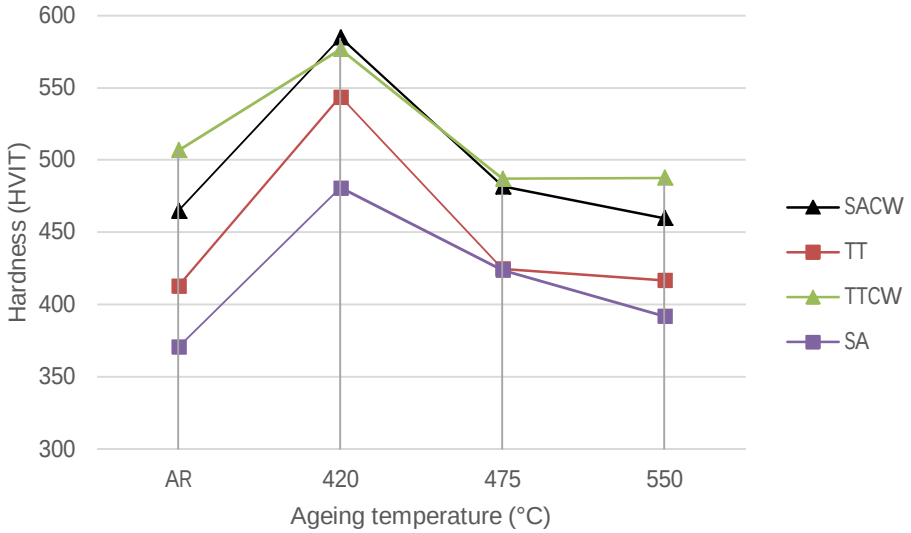

Figure 4. Nanohardness of as-received samples (AR) and after ageing at 420, 475 and 550 °C for 10 000 h.

Table 3. Hardness variations of aged SA, SACW, TT and TTCW conditions with ageing temperature relative to the respective as-received condition.

T (°C)	SA	SACW	TT	TTCW
420	+ 30 %	+ 26 %	+ 32 %	+ 14 %
475	+ 14 %	+ 4 %	+ 3 %	– 4 %
550	+6 %	– 1 %	+ 1 %	– 4 %

4. Discussion

Figure 4 shows changes of the hardness with ageing temperature for the different conditions. For more clarity, however, the results will be discussed based on the relative variations (%) of the hardness, as shown in Table 3. Prior to thermal ageing, heat treatment increased the hardness of the TT condition as compared to water quenching in the SA condition (Figure 4). The main visible change in the TT condition as compared to the SA condition is IG carbide precipitation due to heat treatment (Figure 2). The expected consequence is usually a drop in hardness resulting from a decrease in solid solution hardening by carbon after carbide precipitation. Therefore, a higher hardness in TT conditions than in SA ones suggests the occurrence of SRO upon cooling from the heat treatment. Indeed, as mentioned in the literature, SRO can

nucleate more easily as carbon atoms are not trapping vacancies anymore. Cold work increased the hardness of the as-received SACW and TTCW conditions as compared to the SA and TT conditions (Figure 4), related to higher strain levels seen in Figure 2. A high hardness increase was seen for all conditions aged at 420 °C, expected to be close to the critical temperature for the ordering of Alloy 690 with a 9 wt.% Fe content. The hardness increase is especially strong for the TT condition, which comes close to the hardness of the cold-worked conditions (Figure 4). Upon ageing at 475 °C, the hardness decreased in all conditions as compared to the hardness observed upon ageing at 420 °C (Figure 4), indicating the start of a disordering reaction as this temperature is above the expected critical temperature for the ordering of Alloy 690 with 9 wt.% Fe content. Some SRO remained, as the hardness was higher in the SA, SACW and TT conditions than in their as-received state (Table 3). Upon ageing at 550 °C, the hardness decreased further from the levels observed upon ageing at 420 °C, indicating a stronger influence of the disordering reaction. In the case of the heat-treated samples, the hardness decrease was reduced, indicating that the ordering reaction may become saturated (Figure 4). Stress relaxation at higher temperatures occurred in parallel with the disordering reaction as the hardness decrease was more pronounced in the CW conditions at 475 and 550 °C. Ageing at 550 °C generated hardness levels similar to those of the as-received conditions.

5. Conclusions

The effects of thermal ageing on Alloy 690 were studied, with a special focus on SRO, including the influence of ageing temperature, cold work and heat treatment. The presence of SRO was assessed via hardness measurements and the results fitted well with previous research. The uncertainty of the nanoindentation technique was decreased by the high number of measurements. The following were the main findings of this study:

- IG carbide precipitation increased with ageing temperature, while DIGM was promoted at 475 and 550 °C resulting in a typical wavy appearance of GB and bulged zones. Carbides were observed to grow within the migrated zones forming cellular structures.
- SRO was observed in all conditions at 420 °C, while a disordering reaction was noted at 475 and further at 550 °C, confirming the critical temperature for ordering at around 420 °C for 9.18 wt.% Fe.
- Heat treatment promoted SRO prior to ageing. A lower carbon content after IG carbide precipitation favors the nucleation of SRO.
- Cold work increased the hardness of Alloy 690 prior to ageing due to high strain levels, and stress relaxation was observed during ageing at higher temperatures, accentuating the hardness decrease related to the disordering reaction.

Acknowledgements

Samples were aged and provided by the Korea Atomic Energy Research Institute (KAERI). The study was carried out at Aalto University and VTT within the “Thermal ageing and EAC research for plant life management” (THELMA) project of the Finnish Research Programme on Nuclear Power Plant Safety 2015 – 2018 (SAFIR 2018).

References

Harrod D.L., Gold R.E., Jacko R.J. (2001) Alloy optimization for PWR steam generator heat-transfer tubing. JOM. Vol. 53. 7. P. 14-17.

Webb G. L., Burke M. G. (1995) Stress corrosion cracking behavior of Alloy 600 in high–temperature water. Proceedings of the 7th International Symposium on Environmental Degradation of Materials in Nuclear Power Systems-Water Reactors, NACE International, Houston, TX. P. 41–55.

Kuo T., Lee H. (2002) Effects of filler metal composition on joining properties of alloy 690 weldments. Materials Science and Engineering. Vol. 338. P. 202-212.

Wang M., Zha X., Gao M., Ma Y., Liu K., Li Y. (2015) Structure, microsegregation and precipitates of an Alloy 690 ESR ingot in industrial scale. Metallurgical and Materials Transactions A. Vol. 46. P. 5217-5231.

Andresen P.L., Morra M.M., Ahluwalia A., Wilson J. (2011) SCC of Alloy 690 and its weld metals. Proceedings of the 15th International Symposium on Environmental Degradation of Materials in Nuclear Power Systems-Water Reactors. Colorado Springs, CO. P. 161-176.

Hou J., Peng Q.J., Lu Z.P., Shoji T., Wang J.Q., Han E.-H., Ke W. (2011) Effects of deformation degrees on grain boundary characters and strain concentration on grain boundaries in nickel-base Alloy 600. Corrosion Science. Vol. 53. P. 1137–1142.

Arioka K., Yamada T., Miyamoto T., Terachi T. (2011) Dependence of stress corrosion cracking of Alloy 690 on temperature, cold work, and carbide precipitation - Role of diffusion of vacancies at crack tips. Corrosion. Vol. 67. 3. P. 1-18.

Young G.A. (2014) Long range ordering in model Ni-Cr-X alloys, Proceedings of the International Symposium Fontevraud 8 on the Contribution of Materials Investigations and Operating Experience to LWRs' Safety, Performance and Reliability, September 14-18, 2014, Avignon, France.

Mouginot R., Sarikka T., Heikkilä M., Ehrnstén U., Kim Y.S., Kim S.S., Hänninen H. (2015) Effect of heat treatment and cold work on the ordering of Alloy 690 at 475°C. Proceedings of the 17th International Conference on Environmental Degradation of Materials in Nuclear Power Systems - Water Reactors. Ottawa, Ontario, Canada. August. 9-12, 2015. 17 P.

Toloczko M.B., Olszta M.J., Bruemmer S.M. (2011) One-dimensional cold rolling effects on stress corrosion crack growth in Alloy 690 tubing and plate materials. Proceedings of the 15th International Symposium on Environmental Degradation of Materials in Nuclear Power Systems-Water Reactors. Colorado Springs, CO. P. 91-106.

Casales M., Salinas-Bravo V.M., Martinez-Villafan A., Gonzalez-Rodriguez J.G. (2002) Effect of heat treatment on the stress corrosion cracking of alloy 690. Materials Science and Engineering A. Vol. 332. P. 223–230.

Dutta R.S., Tewari R., De P.K. (2007) Effects of heat-treatment on the extent of chromium depletion and caustic corrosion resistance of Alloy 690. Corrosion Science. Vol. 49. P. 303–318.

Vaillant F., Buisine D., Prieux B. (1995) Comparative behaviour of Alloys 600, 690 and 800. Proceedings of the 7th International Symposium on Environmental Degradation of Materials in Nuclear Power Systems - Water Reactors. Breckenridge (CO), August 1995. Vol. 1. P. 219-231.

Yu G.P., Yao H.C. (1990) The relation between the resistance of IGA and IGSCC and the chromium depletion of Alloy 690. Corrosion. Vol. 46. 5. P. 391-402.

Bruemmer S. M., Charlot L. A., Henager C. H. (1988) Microstructure and micro-deformation effects on IGSCC of Alloy 600 steam generator tubing. Corrosion. Vol. 44. 11. P. 782-788.

Norring K., Stiller K., Nilsson J.O. (1991) Grain boundary microstructure, chemistry and IGSCC in Alloy 600 and Alloy 690. Proceedings of the 5th International Symposium on Environmental

Degradation of Materials in Nuclear Power Systems – Water Reactors. Monterey, CA, August 25-29, 1991. P. 482-487.

Kim S., Kim Y.S. (2013) Effects of ordering reaction on mechanical behavior in Alloy 690. Nuclear Materials Development, Korea Atomic Energy Research Inst.

Young G.A., Tucker J.D., Eno D.R. (2013) The kinetics of long range ordering in Ni-Cr and Ni-Cr-Fe alloys. Proceedings of the 16th International Conference on Environmental Degradation of Materials in Nuclear Power Systems - Water Reactors. Asheville, NC, August 11-15, 2013. 21 P.

Marucco A. (1995) Phase transformations during long-term ageing of Ni-Fe-Cr alloys in the temperature range 450–600 °C. Materials Science and Engineering A. Vol. 194. P. 225-233.

Kim S., Kuk I.H., Kim J.S. (2000) Order-disorder reaction in Alloy 600. Materials Science and Engineering A. Vol. 279. P. 142-148.

Delabrouille F., Renaud D., Vaillant F., Massoud J. (2009) Long range ordering of Alloy 690. In Proceedings of the 14th International Conference on Environmental Degradation of Materials in Nuclear Power Systems, Virginia Beach, VA. August 23-27, 2009. P. 888-894.

Young G.A. (2015) Personal communication. EPRI meeting, December 2015.

Barnard L., Young G.A., Swoboba B., Choudhury S., Van der Ven A., Morgan D., Tucker J.D. (2014) Atomistic modeling of the order–disorder phase transformation in the Ni2Cr model alloy. Acta Materialia, Vol. 81, 2014, P. 258–271.

Kim Y.S., Maeng W.Y., Kim S.S. (2015) Effect of short-range ordering on stress corrosion cracking susceptibility of Alloy 600 studied by electron and neutron diffraction. Acta Materialia. Vol. 83. P. 507–515.

Oliver W.C., Pharr G.M. (1992) An improved technique for determining hardness and elastic modulus using load and displacement sensing indentation experiments. Journal of Materials Research, Vol. 7. 6. P. 1565-1583.

Fracture mechanical and microstructural characterization of narrow-gap safe-end dissimilar metal weld

Matias Ahonen[1], Roman Mouginot[2], Sebastian Lindqvist[1], Teemu Sarikka[2], Pekka Nevasmaa[1], Ulla Ehrnstén[1] and Hannu Hänninen[2]

[1]VTT Technical Research Centre of Finland Ltd
Vuorimiehentie 3, Espoo, Finland

[2]Aalto University, Department of Mechanical Engineering
Otakaari 4, Espoo, Finland

Abstract

Dissimilar metal welds (DMWs) have several different microstructural zones in the vicinity of the low-alloy steel – Ni-based weld metal fusion boundary that have an effect on the mechanical and fracture mechanical behaviour of the weld joint. These microstructural zones are especially small when modern narrow-gap (NG) gas tungsten arc welding (GTAW) technique is utilized. Determination of the fracture toughness properties of the microstructural zones of a DMW joint is of utmost importance for successful structural integrity and lifetime analyses. This paper presents the results from fracture resistance (J-R) tests, microhardness measurements and microstructural characterization performed for a DMW mock-up manufactured by Mitsubishi Heavy Industries (MHI). The studied material is fully representative to that of OL3 EPR pressurized water reactor safe-end weld. The results show that the DMW joint is tough at the SA 508 low-alloy steel – Alloy 52 weld metal interface, which typically is the weakest area of a DMW. Fracture surfaces of the J-R test specimens tested in T-L orientation show a wavy appearance that follows the weld bead boundaries. Crack propagation path was studied also using optical 3D profilometry. Microhardness results show that there is a steep hardness gradient at the fusion boundary where the carbon-depleted zone (CDZ) of the SA 508 exhibits the lowest hardness and the narrow zone exhibiting the highest hardness is located right next to the fusion boundary at the Alloy 52 side.

1. Introduction

Nickel-based alloy weld metals are often used when welding dissimilar metal combinations, such as bainitic pressure vessel steels (low-alloy carbon steels) to stainless steels. In these applications, several inherent properties of nickel-based alloys make them an ideal choice of material. When austenitic stainless steels are welded directly to carbon steels, the difference in coefficient of thermal expansion (CTE) can lead to fatigue and creep failures in the heat-affected zone (HAZ) of the carbon steel [1]. The CTE of Ni lies between those of austenitic stainless steels and carbon steels and thus it provides a smooth transition of CTE across the weld joint and better distributes to thermal stresses that originate from the different

CTEs of the joined materials. Nickel-based weld metals also have good corrosion resistance in as-welded condition [2] and good impact toughness at low temperatures [3]. Previously widely used Alloy 600 and its weld metal alloys 182 and 82 have recently been substituted with higher Cr containing Alloy 690 and its weld metal alloys 152 and 52 due to their better resistance to stress corrosion cracking (SCC) in light water reactor (LWR) environments [4,5].

Dilution of the two different base metals causes a heterogeneous composition distribution within the fusion zones, which may degrade the properties of the weldment in some cases [6]. Large compositional gradients exist in the fusion boundary region when welding carbon steels with Ni-based alloys. C diffuses from the HAZ to the fusion zone during welding due to this gradient [7] which can result in formation of martensite according to the Schaeffler diagram [8]. The tendency for C to migrate from HAZ into the weld metal during post-weld heat treatment (PWHT) is especially strong in high-Cr alloys, such as Alloy 52 [9,10].

The previous work [10,11] have shown that among the different weld zones, the fusion boundary/near interface zone exhibits the lowest fracture resistance. The fracture mechanical testing has demonstrated that dissimilar metal welds are prone to abrupt crack path deviations from the original cracking plane (i.e., the location of the pre-fatigue crack tip) into the neighbouring microstructures. This deflection tendency is shown to be affected by the strength mis-match state. Topographic characterisation of J-R test specimen fracture surfaces using optical 3D profilometry has been shown capable of revealing sudden crack path deviations and it illustratively describes the details of the fracture surface. Scanning electron microscopy (SEM) examinations have shown that the crack path deflection is in most cases caused by small weld defects detected in post-test fractography on the fracture surfaces [10].

This paper presents results from material characterization studies performed for as-received DMW mock-up manufactured by Mitsubishi Heavy Industries (MHI). Within the same project the effect of thermal aging on fracture behaviour of the mock-up will also be studied. Thermal aging is performed at 400 °C for 5000 and 10000 h in order to evaluate thermal aging of the actual plant components during 60 years of operation. The dominating aging phenomenon of the studied DMW joint is believed to be phosphorous segregation, which has been shown to increase the ductile-to-brittle transition temperature of low-alloy steels [12]. Other possible metallurgical aging mechanisms include dissolution of cementite (Fe_3C), carbon diffusion into Alloy 52 weld metal and extension of the carbon-depleted zone (CDZ), as well as strain aging [13].

2. Experiments

The studied material was a 1:1 scale DMW safe-end mock-up manufactured by MHI. The received piece of the mock-up is presented in Figure 1. A cross-section of the mock-up showing the SA 508 low-alloy steel, AISI 308 cladding, Alloy 52 weld metal and AISI 316L stainless steel is presented in Figure 2. The MHI mock-up is fully representative to the joint that is used in OL3 EPR between the reactor pressure vessel feedwater nozzles and safe-ends. The weld is manufactured by applying the narrow-gap (NG) gas tungsten arc welding (GTAW) method without buttering and using Alloy 52 as welding consumable. After welding the NGW mock-up weld was post-weld heat treated at 550°C for 20 h and at 610°C for 16 h.

This paper concentrates on microstructural and fracture mechanical characterization of the MHI mock-up. The applied experimental methods include optical microscopy of the cross-section samples, scanning electron microscopy (SEM), microhardness measurements, fracture resistance (J-R) testing, and optical 3D profilometric measurements of the J-R test fracture surfaces. J-R testing was performed according to ASTM E 1820-13 standard using 1” C(T) specimens. The nominal fatigue pre-crack location was at the fusion boundary and the specimen orientation was T-L. A schematic image showing the cutting of the C(T) specimens from the mock-up is presented in Figure 3. J-R tests were conducted in air at 300 °C.

Cross-section samples were extracted from the mock-up and prepared using standard metallographic sample preparation techniques. Samples for the optical examination of SA 508 were etched using 2 % Nital solution and samples for studying Alloy 52 weld metal were etched using Aqua Regia (20% HNO_3 + 60% HCl). Unetched cross-section samples were used for microhardness measurements. Microhardness measurements were performed using a CMS micro-combi tester equipped with a Vickers tip using an indentation load of 350 mN and a 50 µm step size.

Figure 1. Received piece of the MHI narrow-gap weld mock-up.

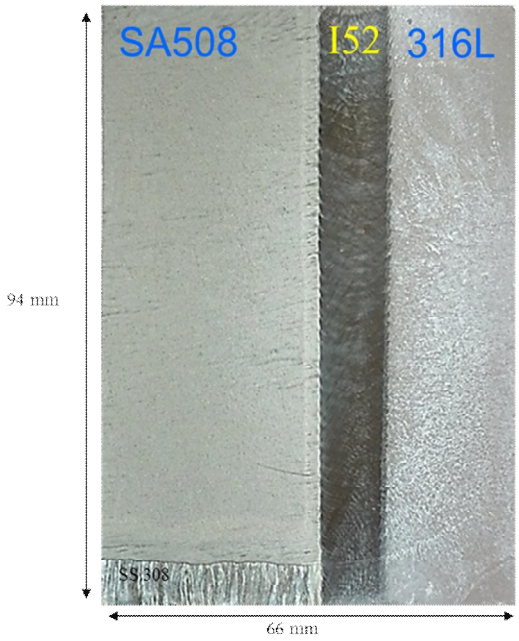

Figure 2. Cross-section of the MHI narrow-gap weld mock-up.

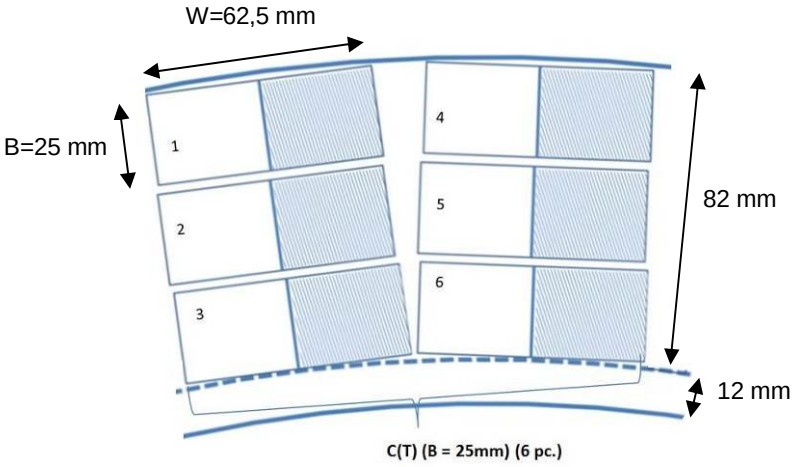

Figure 3. Cutting of the C(T) specimens from the MHI narrow-gap weld mock-up. Pre-crack plane is the dashed area in the image.

3. Results

3.1 Optical microscopy

The general microstructural appearance of the SA 508 side of the DMW joint is illustrated in Figure 4. Width of the HAZ is about 2 mm. The bainitic microstructure of the base metal shows lighter appearing areas and darker bands in the optical microscopy after etching. The appearance is typical of low-alloy steel with segregation bands (so called ghost lines). The banded appearance is similar also in the HAZ, with the difference that the general appearance is darker. The microstructure near the fusion boundary is presented in Figure 5. Some carbon depletion is observed close to the fusion boundary in SA 508. The carbon-depleted zone (CDZ) is not clearly defined and the extent of carbon depletion varies along the fusion boundary. The average width of the CDZ is small, about 50 µm. Some grain coarsening is observed close to the fusion boundary but only to a limited extent, which is mainly due to the low heat input of the NG-GTAW technique.

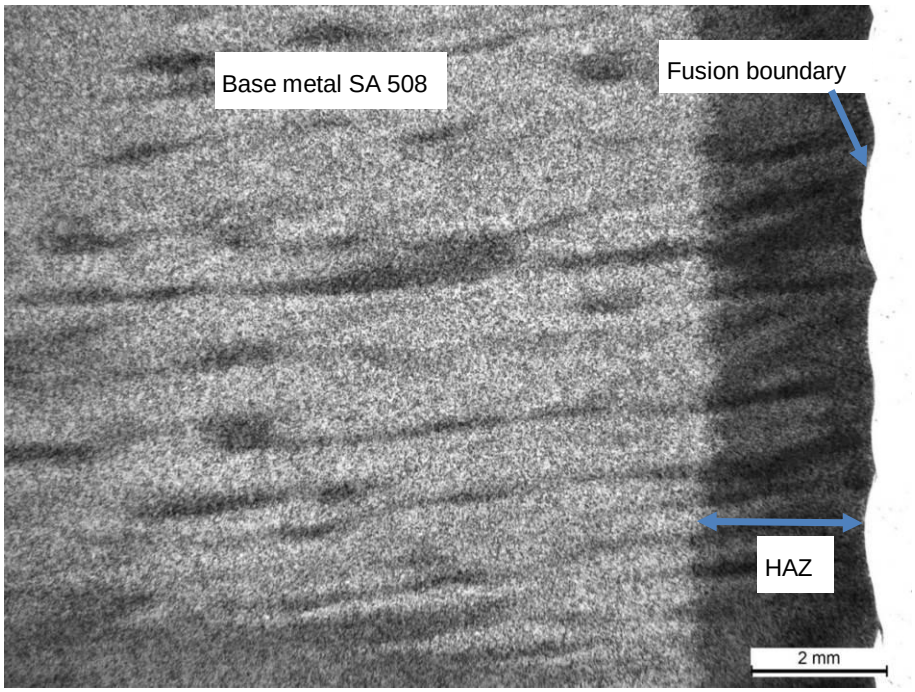

Figure 4. Optical microscope image showing the base metal SA 508, HAZ, fusion boundary and a part of the Alloy 52 weld (appearing light on the right).

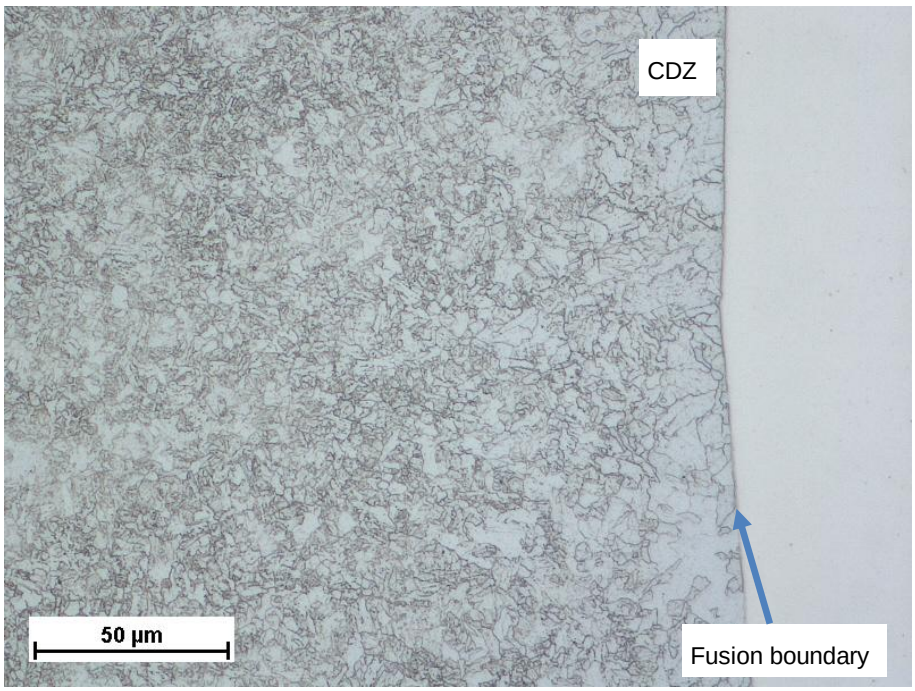

Figure 5. Optical microscope image showing the SA 508 microstructure near the fusion boundary.

Microstructure of the Alloy 52 weld metal is presented in Figure 6. Weld metal exhibits columnar dendritic microstructure typical of Alloy 52. Some of the grains are very large and elongated having lengths of several millimetres and the largest ones extend through multiple weld beads. Weld bead (size) thickness at the location of Figure 6 is about 1,5 mm. Based on the optical microscopy examinations (Figure 4), some weld beads are slightly larger having a size of about 2 mm. Some swirls of unmelted SA 508 steel have penetrated into the weld metal at the locations of weld bead boundaries, appearing dark in Figure 6. More detailed views of the fusion boundary area are presented in Figure 7. Close to the bead boundaries some Type II boundaries [14] are observed (Figure 7 a). In the middle of the bead such boundaries are not present (Figure 7 b).

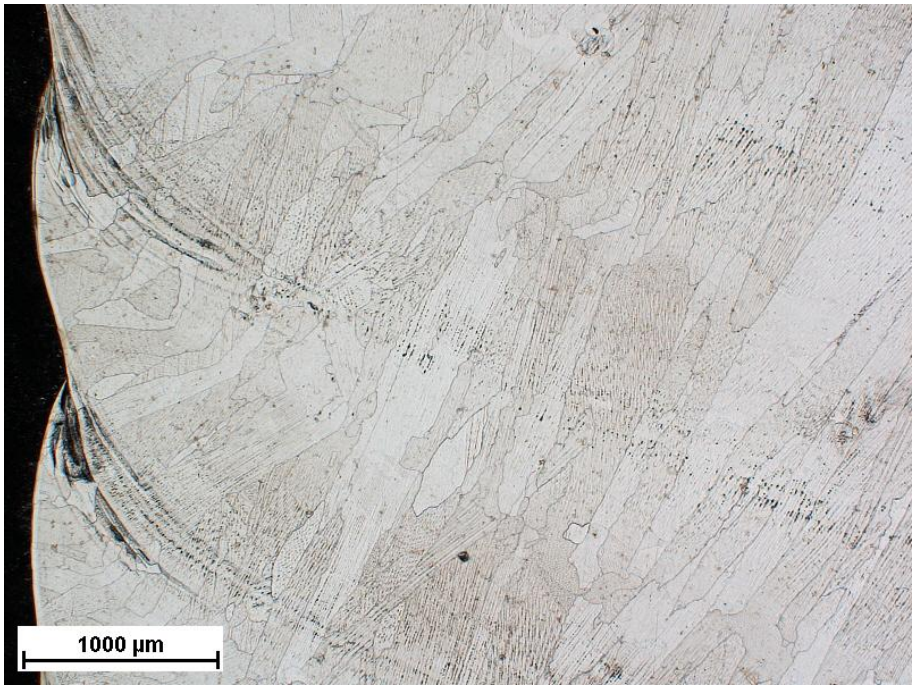

Figure 6. Optical microscope image showing the weld metal microstructure close to the SA 508 fusion boundary.

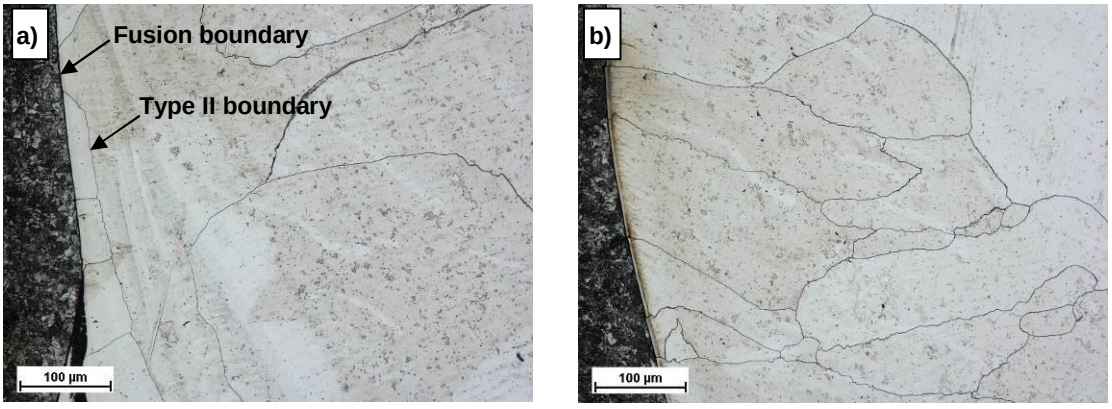

Figure 7. Optical micrographs from two different locations of the SA 508 – Alloy 52 fusion boundary area. a) a location of a bead boundary where Type II boundary is observed. Further away from the bead boundaries, b), there are no Type II boundaries present.

3.2 Microhardness measurements

Results from the microhardness measurements are presented as a calculated Matlab map and a hardness profile across the fusion boundary in Figure 8. The map shows the microhardness profile measured from the base metal SA 508 (on the left) over the fusion boundary to Alloy 52 weld metal (on the right). The matrix of the measurement points relative to the cross-section is presented in Figure 8. Both the microhardness map and the profile show that the hardness decreases when moving from grain refining (GR) zone towards the fusion boundary and the CDZ. The highest microhardness, however, is right at the other

side of the fusion boundary at Alloy 52 weld metal side. The lowest measured microhardness values in the CDZ are 200-250 HVIT, whereas the highest values at the narrow hard layer in the weld metal side are 600-650 HVIT. Thus there is a great gradient in hardness within a distance of a few micrometres. It was observed that the base metal (SA 508) exhibits bands of higher hardness. This observation fits well with the banded appearance observed in optical microscopy presented in Figure 4, and explains the scatter observed in the LAS HAZ in the hardness profile.

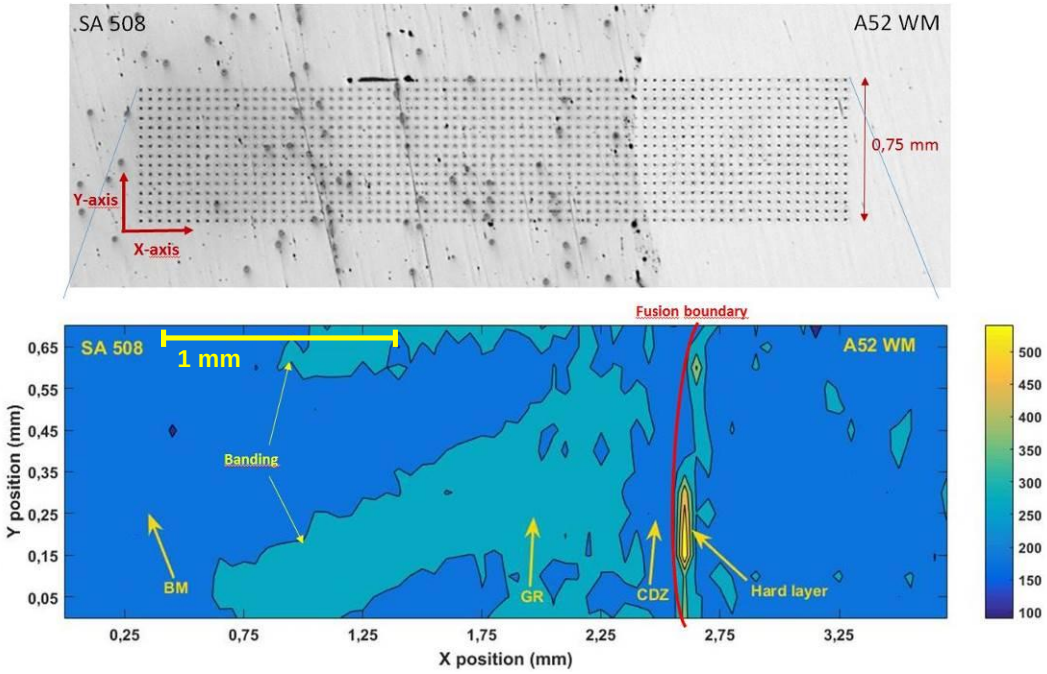

Figure 8. Microhardness measurements performed for the fusion boundary region, starting from the base metal (SA 508) on the left to the HAZ, CDZ, fusion boundary and finally Alloy 52 weld metal. From top to bottom a visualization of the matrix of indentations, the corresponding hardness map and the corresponding hardness-profile, respectively.

3.3 J-R tests

The J-R test results presented in Figure 9 show that the MHI DMW is tough at the interface. The J_Q and J_{1mm} values presented in the graph (374 and 558 kJ/m^2, respectively) are calculated for the test data between exclusion lines of 0,15 and 1,5 mm acquired for all six specimens. The obtained J_Q values for single specimens range between 331-474 kJ/m^2. The J-R curves have similar shape, although different amounts of RPV steel and weld metal are visible on the fracture surface.

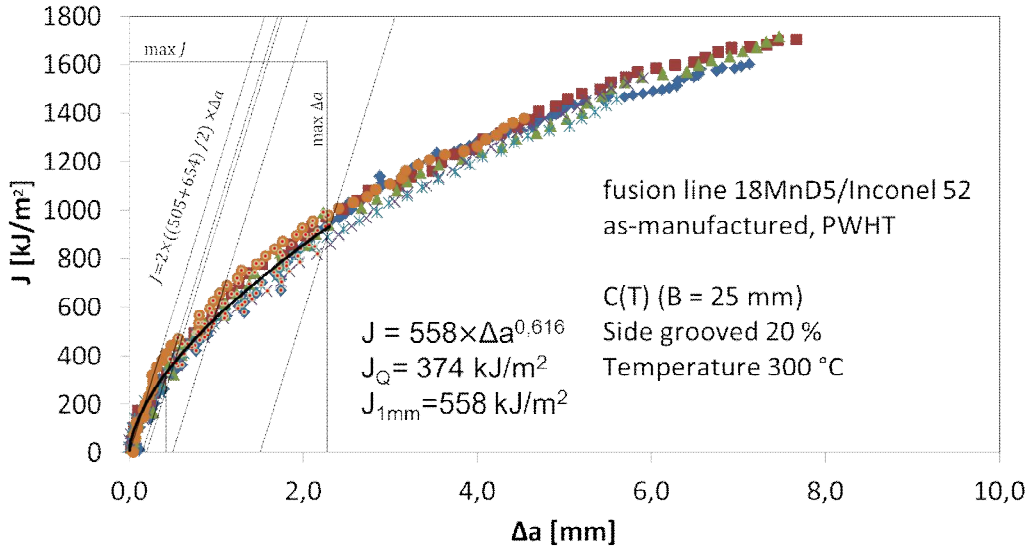

Figure 9. J-R curves for as-received MHI narrow-gap weld mock-up DMW. Nominal fatigue pre-crack location was at the SA 508 – Alloy 52 fusion boundary

The photographs of the fracture surfaces are presented in Figure 10. The fracture morphology follows the wavy shape of the fusion boundary illustrated in the cross-section image (Figure 4). The bead size corresponds well with the frequency of the wavy fracture surface morphology, and the fracture surface appearance is similar in all the studied samples. Based on the photographs it was observed that the location of the fatigue pre-crack was very close to the fusion boundary because in all cases both materials of the joint, i.e. Alloy 52 weld metal (lighter in photographs) and SA 508 low-alloy steel (darker in photographs), are present on the fatigue pre-crack fracture surface. The wavy appearance of the onset of the J-R test part of the specimen fracture surface is different from the fatigue pre-crack fracture surface where the morphology is smoother typical of a fatigue pre-crack. The wavy topography is illustrated in optical 3D topography image shown in Figure 11. It was observed from the sides of the specimen halves that the Alloy 52 weld metal side of the specimens, shown on the left in images (a) – (f) in Figure 10, were more deformed during the J-R test than the SA 508 low-alloy steel side.

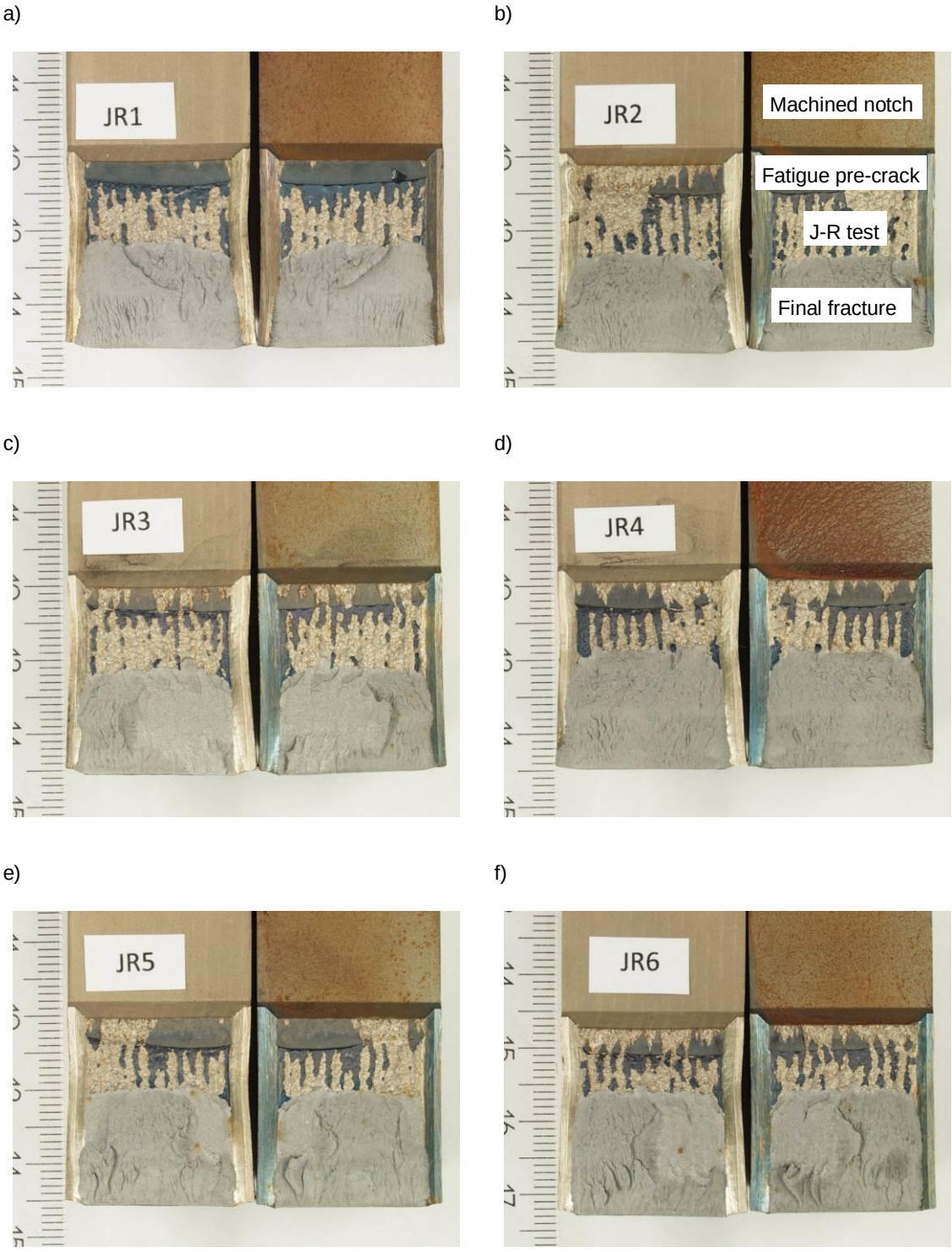

Figure 10. Photographs of fracture surfaces of the J-R test specimens JR1-JR6 from a) to f), respectively. The different regions of the fracture surface are marked in b), illustrating the specimen JR2, and they exhibit the same pattern for each specimen.

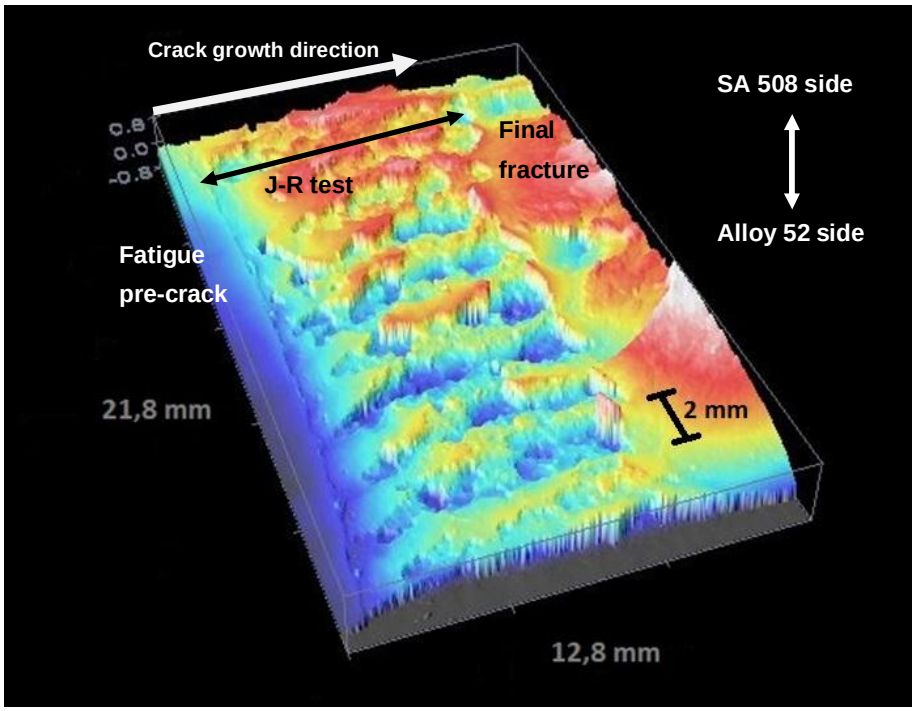

Figure 11. 3D topography image of fracture surface of specimen JR1. The wavy fracture surface topography exhibits a period of roughly 2 mm.

The fracture surface features were studied in more detail using SEM. Both sides of JR1 specimen were studied in order to study the morphology of fracture. Figure 12 shows that the mating specimen sides match with each other. A significant amount of plastic deformation and some secondary cracking have effected on the fracture process and thus the mating fracture surfaces do not match exactly.

The end of the fatigue pre-crack and the start of the J-R test at one representative location are presented in Figure 13. This image, as well as Figure 11, illustrates the Alloy 52 weld metal side of the fractured specimen, which essentially means that the material at the lower level of the fracture surface is Alloy 52 weld metal and at the higher level SA 508 low-alloy steel. This was confirmed by performing EDS (Energy dispersive X-ray spectroscopy) analyses from various locations of the fracture surface. As can be seen in Figures 12-13, cracking occurs after pre-crack tip blunting entirely in the SA 508 side. However, after some ductile crack propagation the crack deflects to the Alloy 52 weld metal side at various locations that are about 2 mm apart in specimen width direction (Figure 11).

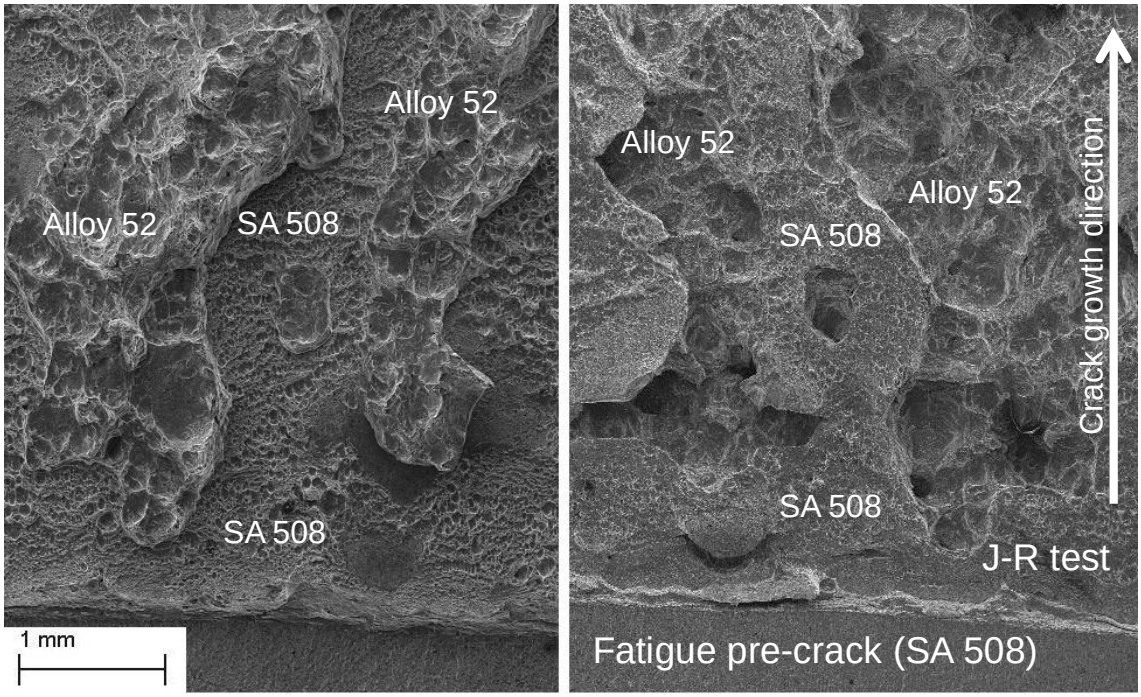

Figure 12. SEM images from the both sides of the fractured specimen at the same location showing alternating areas of Alloy 52 weld metal and SA 508 low-alloy steel.

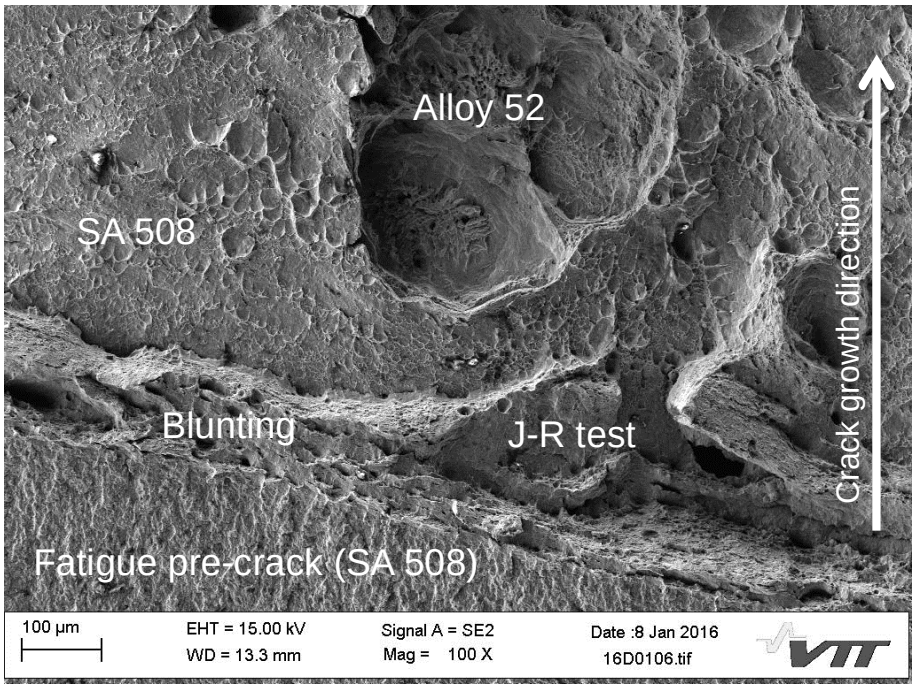

Figure 13. A SEM (secondary electron) image showing the fracture surface of the J-R test specimen JR1 at the early part of the test. Fatigue pre-crack tip blunting occurs almost entirely in the SA 508 side of the joint. After blunting crack propagation onsets in the SA 508 side of the joint and occasionally crack deflects to Alloy 52 weld metal side (larger dimples).

At some locations there were small weld defects observed on the bottom of the large dimples at the Alloy 52 weld metal side. Two examples of those are presented in Figures 14-15 including detailed views of weld defects. Some parts of the fracture surface have undergone significant plastic deformation before fracture and show rough appearance whereas some other areas have a smooth appearance indicating that the surface represents the solidification structure. The fracture surface is deformed also at the smooth areas as evident from many slip lines, manifested especially in Figure 14 b), and some cracking of small particles was observed in these areas. There are also numerous small pores (1-10 µm in diameter) in the weld defect areas. The total amount of weld defects is, however, small.

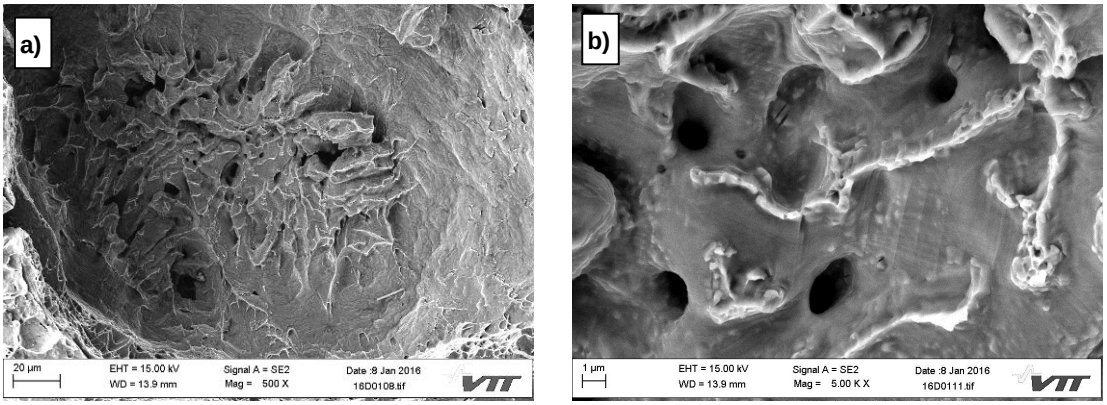

Figure 14. In a), a SEM (secondary electron) image of the fracture surface of the J-R test specimen JR1 showing an area where the crack has propagated in the weld metal side of the joint. At the bottom of the large dimple there is a small weld defect and some pores. Detailed view of the weld defect is shown in b).

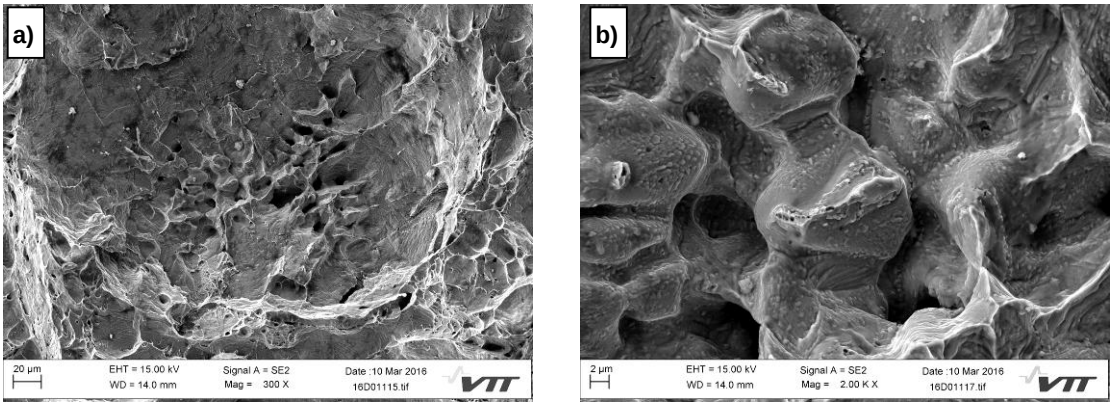

Figure 15. In a), a SEM (secondary electron) image of the fracture surface of the J-R test specimen JR1 showing another example of an area where the crack has propagated in the weld metal side of the joint. At the bottom of the large dimple there is a small weld defect and some pores. Detailed view of the weld defect is shown in b).

4. Discussion

The fracture mechanical and microstructural examinations were carried out in order to evaluate the as-received (PWHT) condition of the studied MHI narrow-gap weld mock-up that will be studied later in thermally aged condition. The results presented in this paper have some similarities and some differences with

the results presented in the earlier study [10] where an Alloy 52 NG DMW mock-up manufactured by Aalto University was studied.

It was observed in the optical microscopy study that the SA 508 steel exhibits a banded microstructure (Figure 4) where the darker appearing bands show higher values in microhardness measurements (Figure 8). This indicates that the bainitic microstructure is inhomogeneous regarding the carbon distribution. The appearance is typical for macrosegregation from the manufacturing. The microstructure of Alloy 52 is dendritic including some smooth and some more tortuous grain boundaries. In addition, non-continuous Type II boundaries were observed close to the fusion boundary in the vicinity of weld bead boundaries.

It should be noted that the hardness values were measured directly from the indentation load and displacement data with a load of 350 mN (corresponding to a load of about 36 g, i.e. HV0,03). Therefore the hardness values are not directly comparable to the traditional Vickers hardness values determined optically from the cross-sections of the indentations. It must also be pointed out that the microhardness map is an approximation that is based on the limited amount of data points. The map is not showing exactly the actual hardness at an arbitrary location because its accuracy is limited to the measured points and the map calculation cannot take into account possible changes in hardness that may occur between the measurement points. This is manifested especially at the area of the narrow hard zone (located right next to the fusion boundary in weld metal side) that seems discontinuous in the map. However, the apparent discontinuity can be explained by the positions of the hardness measurement points with respect to the hard zone. In the case of some rows of the measurement matrix the measurement has hit quite exactly the location where the hard zone is, resulting in high microhardness values. In some other rows the measurement points are located at both sides of the hard zone but not exactly at the hard zone, which misleadingly indicates that the hard layer is non-existent at some locations. In spite of that, the hardness map illustrates the overall microhardness distribution quite well. In addition to the hardness map, the hardness profile gives a good representation of the hardness levels across the fusion boundary. The combination of both hardness map and hardness profile can well characterize the interface, by giving both the localization and the hardness levels of the hard and soft zones: the softest zone is found in the CDZ of the LAS with 200 HVIT, while the hardest zone is situated at the fusion boundary in the weld metal side with up to 650 HVIT. As such, the hardest and softest zones are located next to each other, increasing the strength mis-match of the weld interface. The influence of banding in the LAS HAZ is well seen in the hardness map.

It was reported by Hänninen et al. [10] that the crack occasionally deflected over the fusion boundary from SA 508 to Alloy 52 in J-R tests, and the cracking in Alloy 52 side was usually nucleated at small weld defects observed on the bottom of the large dimples. The same phenomenon was observed in the present study. However, the different orientation of the J-R test specimens (T-L in the present study, T-S in the previous study) apparently is a factor resulting in the different morphology of the fracture surface. In the earlier studied T-S orientation specimens, made from Aalto University's mock-up, crack deflected first to the Alloy 52 weld metal side and typically returned to the SA 508 side during the test continuing to grow in the CDZ close to the fusion boundary. In this study, a wavy pattern showing a period of about 2 mm in specimen thickness (B) direction was observed on the fracture surfaces of the J-R test specimens. This pattern is consistent with the bead size. Thus it appears that cracking follows the pattern of the wavy fusion boundary shown in Figure 4 and deflections towards the Alloy 52 weld metal occur at locations where the distance from the original cracking plane to the weld metal side is shortest. As can be seen in Figure 10, once the crack deflects to the Alloy 52 side it typically never returns to the SA 508 side.

The fracture resistance J_Q values for the six specimens range between 331-474 kJ/m^2 which is similar to the results obtained for as-welded (AW) specimens in the previous study, and somewhat higher than the results obtained for PWHT specimens, which probably was the condition similar to the condition of the now studied MHI mock-up. There are several possible reasons contributing to the observed difference. The specimen type was different, C(T) vs. SE(B), and additionally the specimen size was larger in the present study. Specimen type and size affects the shape of the J-R curves, but initiation toughness (J_Q) values are comparable. As mentioned earlier, the specimen orientation was also different (T-L vs. T-S). Test temperature in the present study was 300 °C, whereas the J-R tests of the previous study [10] were conducted at room temperature. Also, one has to anticipate the possibility that the local strength mismatch state between two neighbouring microstructures is different at 300 °C and at room temperature, which may affect the crack propagation behaviour. However, instead of increasing, the higher temperature may decrease

the J_Q value, which indicates that the MHI narrow-gap weld mock-up is very tough at the weld interface compared to the Aalto University mock-up, which showed some J_Q values as low as 100 kJ/m^2 in PWHT condition when tested at room temperature. In the case of ductile crack growth the fracture toughness is largely governed by the amount of particles that act as nuclei for the dimples, and for the part where the fracture propagates in the CDZ the difference in fracture resistance for the two mock-ups may be partly explained by the amount and size of secondary phase particles. However, the particle distribution has not been studied in detail thus far for the SA 508 steel of the present study. Probably more important factor affecting the J-R behaviour is the fact that in the case of the studied C(T) specimens (MHI mock-up) the fracture occurred for the large part (59-73 %) in the weld metal side of the joint. Although there were some small weld defects observed in the weld metal, it is assumed based on the previous studies that the fracture resistance of Alloy 52 weld metal is superior to that of the low-alloy steel. In order to study the possible effects of specimen orientation and temperature, additional tests will be performed for the MHI narrow-gap weld mock-up material in T-S orientation and at room temperature.

5. Conclusions

Based on the results from J-R tests and microstructural characterization it was concluded that the carbon migration from the LAS to the weld metal promotes the formation of hard and soft zones on both sides of the weld interface. A soft zone (200 HVIT) was identified in the LAS side close to the fusion boundary and related to the CDZ of the LAS. A hard zone (650 HVIT) was identified in the weld metal within 0.1 mm of the fusion boundary. Banding was observed in the LAS side which resulted in harder areas in the HAZ.

The fracture resistance of the interface varied between J_Q = 331-474 kJ/m^2 and the fracture surfaces of all the studied specimens consisted of ductile fracture. The crack propagation formed wavy patterns on the fracture surfaces of the J-R tested specimens. The pattern consisted of alternating fracture surface areas of SA 508 and Alloy 52 and the alternation is consistent with the weld bead size. Thus, it appears that the cracking morphology follows the wavy fusion boundary and deflections towards the Alloy 52 weld metal occur at the locations in which the distance from the original cracking plane to the weld metal is the shortest. Unlike in some previous studies, once the crack deflects to the Alloy 52 weld metal side, it does not return to the SA 508 side of the fusion boundary.

Acknowledgement

This work has been performed within NIWEL (Nickel-Base Alloy Welding Forum) project, which is financed by TEKES (the Finnish Funding Agency for Technology and Innovation), Teollisuuden Voima Oyj, Fortum Power and Heat Oy, Ringhals AB and OKG AB. Their support is highly appreciated.

References

1. Lippold, J. C., & Kotecki, D. J. 2005. Welding Metallurgy and Weldability of Stainless Steels. USA: John Wiley and Sons, Inc., Hobocken, N.J., ISBN 0-47147379-0.

2. Kiser, S. 1990. Nickel-Alloy Consumable Selection for Severe Service Conditions. Welding Journal, 69(1), pp. 30-35.

3. Hilkes, J., Neesen, F. & Caballero, S. 2004. Electrodes for Welding 9% Nickel Steel. Welding Journal, 83 (1), pp. 30-37.

4. Andresen, P. L., Morra, M. M., Hickling, J., Ahluwalia, A. & Wilson, J. 2007. PWSCC of Alloys 690, 52 and 152. In: Proceedings of the 13th International Symposium on Environmental Degrada-

tion of Materials in Nuclear Power Systems - Water Reactors, Whistler, Canada, April 19-23, 2007. Canada: CNS-SNC (CD-ROM).

5. Buisine, D., de Bouvier, O., Rupa, N., Thebault, Y., Barbe, V. & Pitner, P. 2010. French Steam Generator Tubes: An Overview of Degradations. In: Proceedings of the 7th Fontevraud Conference, Avignon, France, September 26-30, 2010. France: SFEN (CD-ROM).

6. Jeng, S. L., Lee, H. T., Rehbach, W. P., Kuo, T. Y., Weirich, T. E. & Mayer, J. P. 2005. Effects of Nb on the Microstructure and Corrosive Property in the Alloy 690–SUS 304L Weldments. Materials Science and Engineering A, 397 (1-2), pp. 229-238.

7. Lundin, C. D. 1982. Dissimilar Metal Welds – Transition Joints Literature Review. Welding Journal, 61 (2), pp. 58-63.

8. DuPont, J. N., Robino, C. V., Mader, A. R., Notis, M. R., and Michael, J. R. 1988. Solidification of Nb-Bearing Superalloys: Part I. Reaction Sequences. Metallurgical and Material Transactions A, 29A, pp. 2785-2796.

9. Mouginot, R & Hänninen, H. 2013. Microstructures of nickel-base alloy dissimilar metal welds. Aalto University publication series Science + Technology. Helsinki: Unigrafia Oy. 178 p. ISBN 978-952-60-5065-2.

10. Hänninen, H., Brederholm, A., Sarikka, T., Mouginot, R., Holmström, P., Saukkonen, T., Toivonen, A., Karjalainen-Roikonen, P., Nevasmaa, P., Keinänen, H., Leskelä, E., Ahonen, M., Ehrnstén, U. & Aaltonen, P. 2014. Structural Integrity of Ni-base Alloy Welds. VTT Technology 175. Espoo: VTT Technical Research Centre of Finland, 257 p. ISBN 978-951-38-8259-4.

11. Nevasmaa, P., Holmström, P., Karjalainen-Roikonen, P., Sarikka, T., Ahonen, M., Mouginot, R., Ehrnstén, U., Brederholm, A., Aaltonen, P. & Hänninen, H. Fracture mechanical characterisation of ferrite-austenite dissimilar metal welds (DMWs) for elevated temperature service in view of metallurgical mis-match. In: Baltica IX – International Conference on Fast Tools for Condition and Life Assessment of Power Plants, Helsinki and Stockholm, June 11-13, 2013. Finland: VTT Technical Research Centre of Finland.

12. McMahon, C. J. & Marchut, L. J. 1978. Solute Segregation in Iron-Based Alloys. Vac. Sci. Technol., 15, (2), pp. 450-466.

13. Corwin, W. R., Nanstad, R. K., Alexander, D. J., Odette, G. R., Stoller, R. E. & Wang, J. A. 1995. Thermal Embrittlement of Reactor Pressure Vessel Steels. United States, UNT Digital Library. http://digital.library.unt.edu/ark:/67531/metadc706620/. Accessed September 25, 2015.

14. Nelson, T. W., Lippold, J. C. & Mills, M. J. 2000. Nature and Evolution of the Fusion Boundary in Ferritic-Austenitic Dissimilar Metal Welds—Part 2: On-Cooling Transformations. Welding Journal, 79 (10), pp. 267-277.

Linearization of supports with gaps in dynamic piping analyses

Aapo Ristaniemi

VTT Technical Research Centre of Finland Ltd
Kemistintie 3, 02150 Espoo, Finland

Abstract

Nuclear power plant piping systems exhibit dynamic behaviour, and piping supports keep the displacements of the pipes within acceptable limits. The aim of the research is the development of a simplified way to take into account the nonlinear displacement behaviour of the supports in linear dynamic piping analyses. The research was started as a Master's thesis with focus on supports with gaps and friction and was further continued regarding supports with gaps.

The linearization procedure and methods are found in literature and they were further developed in this study. The goal is to represent the nonlinear system as accurately as possible by an equivalent linear system. The linearization procedure was investigated in time-domain and frequency-domain analyses using simplified piping systems. Frequency-domain is of particular interest as nonlinearities cannot be incorporated into classical mode-based methods.

Equivalent linear systems were determined for the selected load cases and comparison was made between the equivalent linear and original nonlinear systems, time-domain and frequency-domain linearization results and three different linearization methods. Correspondence between equivalent linear and original nonlinear systems was not found accurate, time- and frequency-domain linearization gave similar results and different linearization methods resulted in equivalent linear systems very close to each other.

1. Introduction

Nuclear power plant piping systems exhibit dynamic behaviour as a result of various sources of excitation in the system. There are various types of piping supports aimed at keeping the pipe movements within acceptable limits. Often the support forces do not behave linearly with system displacement or velocity, thereby introducing nonlinearities to the system. Nonlinear dynamic problems are commonly solved by means of time history analysis. However, solving linear dynamic problems, for example, with response spectrum method, usually requires less computing effort compared with nonlinear analyses.

The aim of the research is the development of a simplified way to take into account the nonlinear displacement behaviour of the supports in linear dynamic piping analyses. The research was started as a Master's thesis [1] with focus on supports with gaps and friction and was further continued regarding supports with gaps. The linearization procedure and methods are found in literature and they were further developed in this study. The goal is to represent the original nonlinear system as accurately as possible by

an equivalent linear system. The linearization procedure was investigated in time-domain and frequency-domain analyses using simplified piping systems. Frequency-domain is of particular interest as nonlinearities cannot be incorporated into classical mode-based methods.

This conference paper presents the results of the current study that focused on supports with gaps in time history and response spectrum analyses. It is highlighted that the scope of this conference paper is limited to supports with gaps. In Section 2 the methods are presented by introducing an iterative procedure together with linearization and analysis methods. In Section 3 the piping system and load case are presented. In Section 4 the results are shown and in Section 5 the relevant discussion is given and conclusions are drawn.

In the previous study [1], the linearization procedure was applied to an actual piping system with four gap supports using a sinusoidal point force as the excitation. The equivalent linear system obtained was compared to the original nonlinear system. Displacements at support locations were of the same order of magnitude but large differences were observed at single locations. The support forces were generally found to be smaller in the equivalent linear system. Pipe bending moments at support locations were observed to be significantly different, being both higher and smaller in the linear system.

2. Methods

2.1 Iterative procedure to determine equivalent linear system

The iterative procedure to determine the equivalent linear system presented here is identical to procedures portrayed in references [2], [3], [4] and [5]. The nonlinear gap supports are replaced by linear springs to obtain a linear system and an iterative procedure is used to determine the equivalent spring constants. To illustrate a nonlinear gap support and a corresponding linearized system, single degree-of-freedom systems are shown in Figure 1 with corresponding force-displacement relationships. The iterative procedure is presented in the flow chart of Figure 2 for a single support. Damping of the supports is neglected for simplicity in this study.

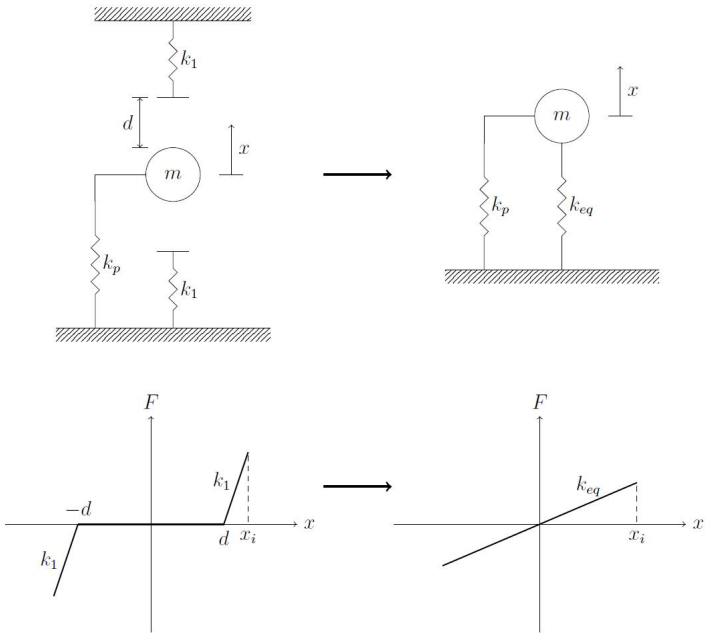

Figure 1. Illustration of a nonlinear system and a corresponding equivalent linear system for a single degree-of freedom gap support with corresponding force-displacement relationships. In the figure d is the gap size, m the mass of the system, k_p the system stiffness, k_1 the nonlinear support stiffness, k_{eq} the equivalent stiffness, F the support force, x the displacement of the system and x_i the maximum displacement of the system. [1]

The spring constant of the linear system is determined based on the maximum displacement obtained from dynamic analysis. The dynamic analysis is performed over the full time period of the loading using the linear system. In other words, the maximum displacement is a function of linearized system stiffness, which in turn is a function of the maximum displacement. Therefore, an iterative procedure is needed to find such maximum displacement, that gives an equivalent stiffness, that gives the same maximum displacement in the analysis.

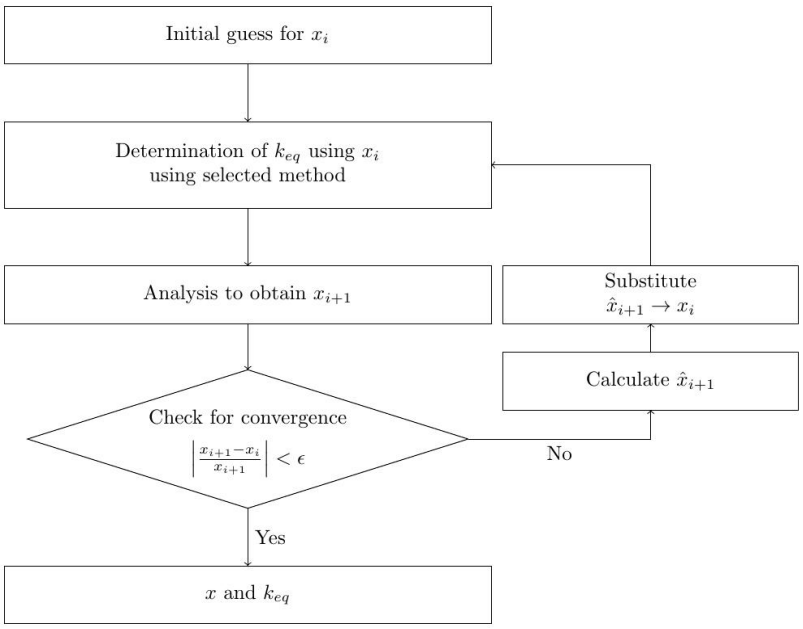

Figure 2. Flow chart of the iterative procedure for a single support.

Figure 2 shows the iterative procedure to create the equivalent linear system. An initial guess is given for the maximum displacement of the system x_i. Determination of the equivalent stiffness k_{eq} using x_i is performed with Caughey's method, secant stiffness method or equivalent energy approach presented in Section 2.2. The analysis is performed to obtain the maximum displacement x_{i+1}. In this study the analysis was conducted by applying both time history analysis and response spectrum method. If the starting point x_i and the resulting displacement x_{i+1} are relatively close enough to each other, the iteration is considered converged and the equivalent linear system is obtained.

The starting point (initial value) for the next iteration step $\hat{x}_{i+1}$ is calculated using under-relaxation method [6]

$$\hat{x}_{i+1} = x_i + (x_{i+1} - x_i)\,\alpha \tag{1}$$

where x_i is the initial value of maximum displacement for the iteration step i (i.e. starting point of iteration i), x_{i+1} the resulting maximum displacement of iteration i and α is the relaxation parameter. The parameter α can be held constant or modified between iterations and the value is in the interval $0<\alpha<1$. Under-relaxation method was used to improve convergence of the iteration since the iteration was found to be unstable (divergent).

2.2 Linearization methods

2.2.1 Equivalent stiffness by Caughey's method

Caughey's method is based on minimization of mean squared error between the nonlinear and equivalent linear support force-displacement response at the maximum displacement x_i. The method has been used in piping analyses in [2], [7], [8], [9], and in structural analyses in [3]. The derivation was performed in [10] and the equivalent stiffness according to Caughey's method is [2]

$$k_{eq} = k_1/\pi*(\pi - 2\theta - \sin 2\theta) \tag{2}$$

where

$$\theta = \arcsin(d/x_i) \tag{3}$$

and k_1 is the support stiffness, d the gap size and x_i the maximum displacement.

2.2.2 Equivalent stiffness by secant method

The equivalent stiffness by secant method is the slope of the line from the origin to the nonlinear force-displacement curve at displacement x_i. Secant stiffness has been used in analyses of hysteretic systems and in seismic analyses of buildings in [3], [11], [12], [13], [14], [15], [16] and [17] and in piping analyses in [2]. The equivalent stiffness according to secant stiffness is

$$k_{eq} = k_1 * (1 - d/x_i) \tag{4}$$

where k_1 is the support stiffness, d the gap size and x_i the maximum displacement.

2.2.3 Equivalent stiffness by equivalent energy approach

Based on the ideas of references [4], [5] and [18] an energy approach can be applied to calculate the equivalent stiffness. The idea is that the potential energy stored in the spring at the maximum displacement x_i is equal in the nonlinear and equivalent linear systems. The equivalent stiffness by equivalent energy approach is calculated as

$$k_{eq} = k_1 * (1 - d/x_i)^2 \tag{5}$$

2.3 Analysis methods

Time history analysis and response spectrum method were used as the analysis methods to obtain the maximum displacements of the piping system at the support locations. With time history analysis, the loading (acceleration time history) is applied to both pipe ends and the displacement solution is found by integrating the equations of motion using forward Euler explicit time stepping scheme.

The response spectrum method to determine maximum displacement amplitudes is based on calculating the response of each mode of vibration to the excitation and combining the responses of the modes to get the overall system response. In this study, the square root of the sum of squares method (SRSS) was used to combine the modal responses.

3. Description of system and loading studied

3.1 System

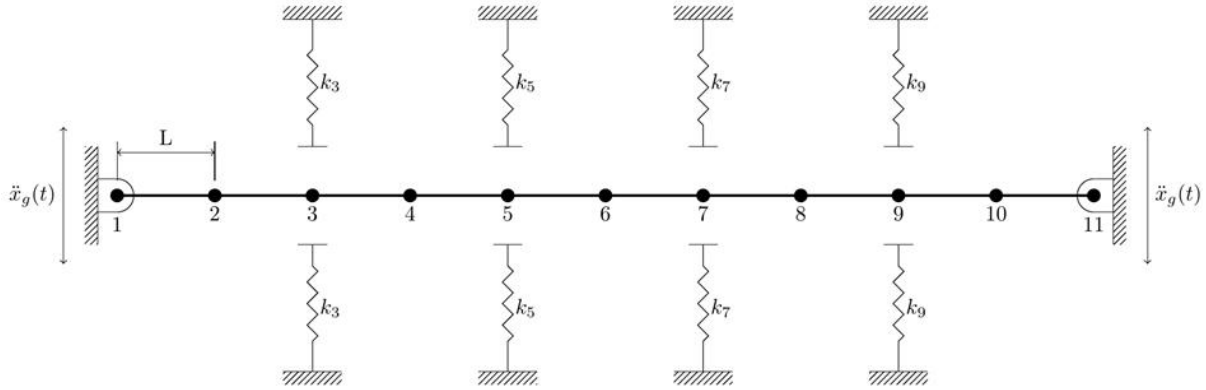

Figure 3. The example piping system studied. It consists of a 10-element Bernoulli beam with four gap supports. Nodes and node numbering is shown. The beam is simply supported at its ends and mass of the beam is lumped to the nodes

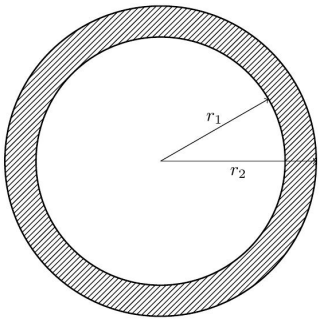

Figure 4. Cross-section of the beam where r_1 is the inner radius and r_2 is the outer radius.

The simplified piping system investigated in this study is shown in Figure 3 and the cross-section is shown in Figure 4. The system consists of a 10-element Bernoulli beam with four gap supports. Nodes and node numbering are indicated in the figure. Each node has two degrees-of-freedom, translation in the direction of the excitation and rotation about an axis perpendicular to the figure. The beam is simply supported at its ends and masses and inertias are lumped to the nodes. The translation of the end nodes is controlled by the loading which is applied directly to them. Properties of the beam are shown in Table 1.

The pipe is supported with four gap supports at the locations indicated in the figure. The supports produce reaction forces if the displacements of the pipe are large enough so that the gap closes. After gap closure, the supporting force is proportional to the penetration and the supports are modelled as springs. The supports are symmetrical so that gap sizes d_i and support stiffnesses k_i are equal on both sides of the pipe. However, the values of support stiffnesses k_i vary between the supports. Gap sizes and support stiffnesses are shown in Table 2. The stiffnesses of the supports are of the same order of magnitude as in piping whip supports of a nuclear power plant.

Table 1. Properties of the beam.

Parameter	Symbol	Unit	Value
Inner radius	r_1	m	0,145
Outer radius	r_2	m	0,16
Beam element length	L	m	3
Density	ρ	kg/m^3	7850
Young's modulus	E	GPa	204

Table 2. Gap sizes and support stiffnesses.

Parameter	Symbol	Unit	Value
Gap size	d_3	m	0,1
Gap size	d_5	m	0,1
Gap size	d_7	m	0,1
Gap size	d_9	m	0,1
Support stiffness	k_3	N/m	$1,6*10^9$
Support stiffness	k_5	N/m	$3,3*10^9$
Support stiffness	k_7	N/m	$2,5*10^9$
Support stiffness	k_9	N/m	$2,9*10^9$

3.2 Loading

The pipe is loaded by the 1940 El Centro earthquake. For the frequency-domain analyses response spectra are available and for the time-domain analyses the acceleration time history is known [19]. The loading was applied at both ends of the pipe and in the time history solution also the supports were moving according to the acceleration time history. The acceleration time history of the earthquake is shown in Figure 5 and the displacement response spectrum for 0 % damping is shown in Figure 6.

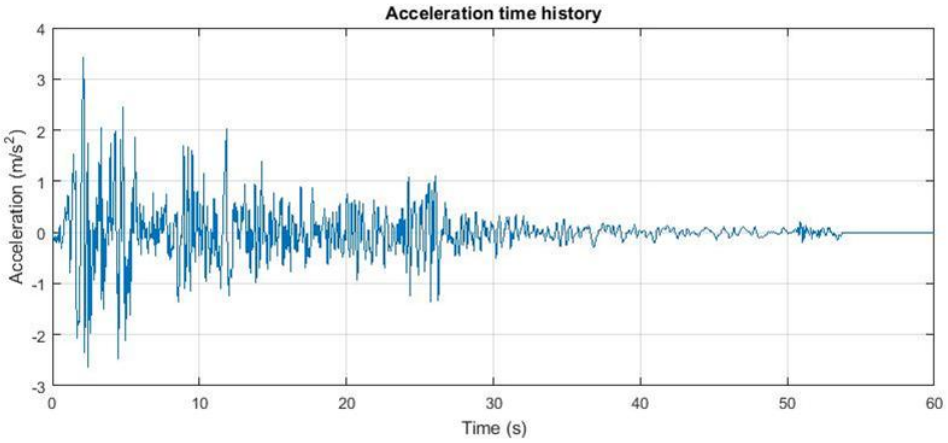

Figure 5. The acceleration time history of 1940 El Centro earthquake [19].

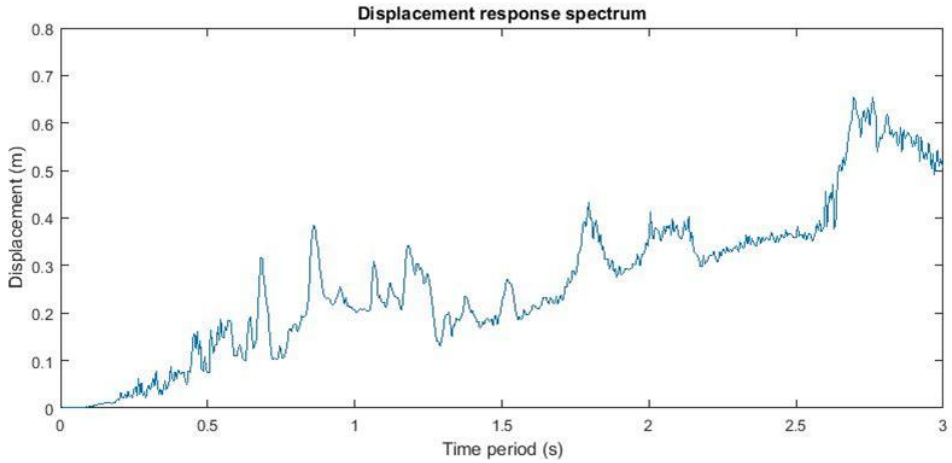

Figure 6. Displacement response spectrum for 0 % damping for the 1940 El Centro earthquake. Produced with the code provided in [19].

In this study, the following load cases were studied:

- Free pipe with no supports
  - Time history analysis
  - Response spectrum analysis
- Pipe with supports
  - "Exact" nonlinear analysis using time history analysis
  - Equivalent linear analysis using time history analysis
  - Equivalent linear analysis using response spectrum method
  - Equivalent linear analysis using response spectrum method: comparison of different linearization methods

4. Results

4.1 Original nonlinear system and equivalent linear systems

The displacement results of the free pipe loaded by El Centro earthquake are shown in Table 3 and the displacement results of the pipe with supports are shown in Table 4. The equivalent stiffnesses for the equivalent linear systems are presented in Table 5 and maximum support forces in Table 6. The 10 lowest eigenfrequencies are shown in Table 7. Caughey's method was used to calculate the equivalent stiffnesses. The convergence criterion used was ϵ=0,0005 and the relaxation parameter was assigned the value of α=0,00005 for the time history analysis and α=0,00001 for the response spectrum analyses to find the solutions.

Table 3. Maximum displacements at support locations of the free pipe loaded by El Centro earthquake loading.

Displacement	Time history analysis (m)	Response spectrum (SRSS) (m)
x_3	0,1509	0,1503
x_5	0,2433	0,2432
x_7	0,2433	0,2432
x_9	0,1509	0,1503

Table 4. Maximum displacements at support locations of the pipe with supports loaded by El Centro earthquake loading.

Displacement	Nonlinear, time history analysis (m)	Equivalent linear, time history analysis (m)	Equivalent linear, response spectrum (SRSS) (m)
x_3	0,1007	0,06658	0,06568
x_5	0,1007	0,10014	0,10005
x_7	0,1008	0,10006	0,10016
x_9	0,0926	0,06652	0,06583

Table 5. Equivalent stiffnesses of the supports for the equivalent linear systems.

Equivalent stiffness	Equivalent linear, time history analysis (kN/m)	Equivalent linear, response spectrum (SRSS) (kN/m)
$k_{3,eq}$	0	0
$k_{5,eq}$	113,33	114,17
$k_{7,eq}$	114,07	113,06
$k_{9,eq}$	0	0

Table 6. Maximum support forces for the nonlinear and equivalent linear systems.

Force	Nonlinear, time history analysis (kN)	Equivalent linear, time history analysis (kN)	Equivalent linear, response spectrum (SRSS) (kN)
F_3	1171,7	0	0
F_5	2204,3	11,348	11,423
F_7	1987,1	11,414	11,324
F_9	0	0	0

Table 7. Lowest natural frequencies of the free pipe and the equivalent linear systems.

Frequency	Free pipe (Hz)	Equivalent linear, time history analysis (Hz)	Equivalent linear, response spectrum (SRSS) (Hz)
1	0,96	1,98	1,98
2	3,78	3,93	3,93
3	8,34	8,41	8,41
4	14,42	14,52	14,52
5	21,78	21,78	21,78
6	30,13	30,17	30,17
7	39,16	39,17	39,17
8	48,58	48,58	48,58
9	58,09	58,10	58,10
10	67,43	67,43	67,43

4.2 Comparison of different linearization methods

The different linearization methods, Caughey's method, secant stiffness method and equivalent energy approach, were compared against each other. The response spectrum method was used as the analysis method. Table 8 shows the displacement results of converged equivalent linear systems and Table 9 presents the equivalent stiffnesses of the systems. To obtain precise equivalent linear systems, the convergence criterion was assigned the value of ϵ=0,000001 and relaxation parameter had to be assigned the value α=0,000005 (α=0,000001 for secant stiffness) to find the solutions.

Table 8. Maximum displacements at support locations of the pipe with supports loaded by El Centro earthquake loading. Comparison of Caughey's method, secant stiffness method and equivalent energy approach.

Displacement	Equivalent linear, Cauhey's method (m)	Equivalent linear, secant sitffness method (m)	Equivalent linear, equivalent energy approach (m)
x_3	0,06574	0,06568	0,06604
x_5	0,10009	0,100003	0,10059
x_7	0,10011	0,100005	0,10068
x_9	0,06576	0,06568	0,06615

Table 9. Equivalent stiffnesses of the supports for the equivalent linear systems. Comparison of Caughey's method, secant stiffness method and equivalent energy approach.

Equivalent stiffness	Equivalent linear, Cauhey's method (kN/m)	Equivalent linear, secant sitffness method (kN/m)	Equivalent linear, equivalent energy approach (kN/m)
$k_{3,eq}$	0	0	0
$k_{5,eq}$	113,71	113,62	114,03
$k_{7,eq}$	113,52	113,61	113,16
$k_{9,eq}$	0	0	0

During the analyses for comparing the different linearization methods it was found that there was more than one solution of the iterative procedure, i.e. there were multiple equivalent linear systems for the load case studied. In Table 10, the equivalent stiffnesses are presented for the other equivalent linear systems found for the three linearization methods using response spectrum method. The solution where the equivalent stiffnesses are ~160 kN/m was found also using time history analysis.

Table 10. Equivalent stiffnesses of the supports for the equivalent linear systems. Comparison of Caughey's method, secant stiffness method and equivalent energy approach.

Equivalent stiffness	Equivalent linear, Cauhey's method (kN/m)	Equivalent linear, secant stiffness method (kN/m)	Equivalent linear, equivalent energy approach (kN/m)
$k_{3,eq}$	0	0	0
$k_{5,eq}$	126,00/160,31/240,30	125,91/160,22/240,21	126,30/160,58/240,56
$k_{7,eq}$	125,79/160,08/240,02	125,90/160,21/240,19	125,39/159,59/239,43
$k_{9,eq}$	0	0	0

5. Discussion and conclusion

As seen in Table 3, time history analysis and response spectrum method gave well corresponding displacement results for the free pipe. Displacements of the free pipe were large enough so that when the supports were introduced in the system the gaps were closing and they produced reaction forces. In Table 4 it can be seen that in the nonlinear system the gaps at supports 3, 5 and 7 are closing and at support 9 the gap is left open. The supports restrict efficiently the displacements. In the equivalent linear systems the displacements at supports 5 and 7 were slightly higher than the gap magnitudes, while at supports 3 and 9 the displacements were below the gap magnitude. In the nonlinear model the gap at support 3 is closing while in the equivalent linear systems the displacement at support 3 is below the gap magnitude. Time history analysis and response spectrum method results were close to each other. The equivalent stiffnesses of the equivalent linear systems shown in Table 5 were also close to each other.

The support forces shown in Table 6 were considerably higher in the nonlinear system compared with the equivalent linear systems. In the equivalent linear systems, the support forces were however close to

each other. Comparison of the lowest natural frequencies in Table 7 shows that the lowest natural frequencies were different between the free pipe and the equivalent linear systems. From the fourth natural frequency onwards the frequencies were very close to each other. The results for the equivalent linear systems obtained with time history analysis and response spectrum method were identical within the accuracy of the shown results.

Different linearization methods, Caughey's method, secant stiffness method and equivalent energy approach, resulted in equivalent linear systems very close to each other. The displacements at supports 3 and 9 were around 0,066 m and at supports 5 and 7 only slightly higher than the gap magnitude as shown in Table 8. The equivalent energy approach resulted in higher displacements than the other methods, though the differences were practically negligible. At support locations 5 and 7, where the equivalent stiffnesses have non-zero values, the displacements were very close to the gap magnitude. The resulting equivalent stiffnesses for all the methods had the values ~114kN/m but showed no clear pattern.

During the analyses, it was found that there were multiple solutions to the iterative procedure, i.e. multiple equivalent linear systems for the load case studied. These different solutions were found by changing the iteration starting point. The solutions for the equivalent stiffnesses $k_{5,eq}$ and $k_{7,eq}$ were found to be ~126 kN/m, ~160kN/m and ~240kN/m in addition to the ~114 kN/m solution. When examining the same solution, the different methods gave very similar results and showed no clear pattern. The solution ~160 kN/m was found also using time history analysis. The multiple solution phenomenon is thought to originate from the loading used in this study. For example, when looking at the response spectrum in Figure 6, there are points where different natural periods result in same displacement response.

The results found using time-domain and frequency-domain analyses corresponded well and there was no significant difference. Upon this load case and system studied, equivalent linear systems obtained by time-domain and frequency-domain analyses are well corresponding, on condition that the same solution is found. Regarding multiple solutions, some criterion is needed to decide which equivalent linear system is the most relevant.

The conclusions of this study are summarized as follows:

- Equivalent linear system does not accurately correspond to the original nonlinear system
- The nonlinear system support forces are considerably different from the equivalent linear system support forces
- For this problem, the higher natural frequencies of equivalent linear systems remain the same with the free pipe, but the lowest natural frequencies are different
- For this system and loading, different linearization methods result in similar equivalent linear systems
- Multiple solutions exist for the load case studied, a phenomenon thought to originate from the nature of the loading
- Different solutions can be found by altering the iteration initial values
- Equivalent linear systems obtained by time-domain and frequency-domain analyses are well corresponding, on condition that the same solution is found

6. References

1. A. Ristaniemi, Linearization of piping supports in dynamic analyses. Master's thesis, Espoo, Finland: Aalto University, 2015.

2. H. Murakami, T. Hirai, M. Nakata, T. Kobori, K. Mizukoshi, Y. Takenaka and N. Miyagawa, "Seismic analysis of equipment system with non-linearities such as gap and friction using equivalent linearization method," in *Transactions of the 10th International Conference on Structural Mechanics in Reactor Technology (SMiRT 10), Anaheim, California, USA, August 22-27, 1989*.

3. Y. M. Parulekar, G. R. Reddy, K. K. Vaze, a. K. Ghosh, H. S. Kushwaha and R. Ramesh Babu, "Seismic response analysis of RCC structure with yielding dampers using linearization techniques," *Nuclear Engineering and Design,* vol. 239, pp. 3054-3061, 2009.

4. J. Pop Jr., S. Singh and M. A. Pressburger, "Response spectrum analysis of piping systems with elastic-plastic gap supports," *Nuclear Engineering and Desing,* vol. 181, pp. 131-144, 1998.

5. Robert L. Cloud Associates Inc., "A Simplifed Piping Support System With Seismic Limit Stops," EPRI NP-6442 Project 2349-1 Interim Report, 1989.

6. J. H. Ferziger and M. Peric, Computational Methods for Fluid Dynamics, Springer, 2002.

7. Y. J. Park, C. H. Hofmayer and N. C. Chokshi, "Applications of equivalent linearization approaches to nonlinear piping systems," in *Transactions of the 14th International Conference on Structural Mechanics in Reactor Technology (SMiRT 14), Lyon, France, August 17-22, 1997.*

8. Y. J. Park and C. H. Hofmayer, "Practical application of equivalent linearization approaches to nonlinear piping systems," in *Joint ASME/JSME pressure vessels and piping conference; Honolulu, HI (United States); 23-27 July 1995; BNL-NUREG-61620; CONF-950740-27, 1995.*

9. Y. M. Parulekar, G. R. Reddy, K. K. Vaze and K. Muthumani, "Passive Control of Seismic Response of Piping Systems," *ASME Journal of Pressure Vessel Technology,* vol. 128, pp. 364-369, 2006.

10. T. K. Caughey, "Equivalent Linearization Techniques," *The Journal of the Acoustical Society of America,* 35(11), 1963.

11. H. Dwairi and M. Kowalsky, “Investigation of Jacobsen's equivalent viscous damping approach as applied to displacement-based seismic design,” in *13th World Conference on Earthquake Engineering, Vancouver, B.C., Canada, August 1-6, 2004, number 228, 2004.*

12. H. Dwairi, M. J. Kowalsky and J. M. Nau, “Equivalent Damping in Support of Direct Displacement-Based Design,” *Journal of Earthquake Engineering,* vol. 11, pp. 512-530, 2007.

13. A. C. Guyader, “A Statistical Approach to Equivalent Linearization with Applications to Performance-Based Engineering,” PhD thesis, California Institute of Technology, 2003.

14. T. Liu, “Equivalent linearization analysis method for base-isolated buildings,” PhD thesis, University of Trento, 2014.

15. A. Occhiuzzi, “Seismic ductility of base isolated structures,” Master's thesis, Massachusetts Institute of Technology, 1994.

16. A. Yavas and S. Saylan, “Effect of equivalent linearization in direct displacement based seismic design of bridge columns,” in *13th World Conference on Earthquake Engineering, Vancouver, B.C., Canada, August 1-6, 2004, number 2687, 2004*.

17. R. Zaharia and F. Taucer, “Equivalent period and damping for EC8 spectral response of SDOF ring-spring hysteretic models,” European Commission, Joint Research Centre, Scientific and Technical Reports, JRC 45403, 2008.

18. W. D. Iwan, “Predicting the earthquake response of resiliently mounted equipment with motion limiting constraints,” in *Proceeding of the 6th World Conference on Earthquake Engineering, New Delhi, India, pages 3292-3297, 1977*.

19. S. S. Kolukula, “Response Spectra file package,” 16.09.2011. [Online]. Available: http://www.mathworks.com/matlabcentral/fileexchange/32913-response-spectra.[Accessed 22.10.2015].

GenIV challenge

Creep-fatigue lifetime assessment for cyclic softening steels

Jarir Aktaa & Mario Walter

Karlsruhe Institute of Technology, Institute for Applied Materials
Eggenstein-Leopoldshafen, Germany

Abstract

For more efficient energy systems ferritic martensitic steels are developed with high tensile and creep strengths which however are remarkably reduced under cyclic loading due to non-saturating cyclic softening. This phenomenon is more pronounced and complex under creep-fatigue loading as introducing hold-time to the loading cycle not only yields additional softening but also induces asymmetric deformation behavior. The resulting creep-fatigue lifetime is consequently just as complex and its reliable prediction requires deep understanding of the softening mechanisms and their consideration in predictive tool for deformation and damage.

Based on existing lifetime and damage models a new approach is proposed for the assessment of creep-fatigue lifetime of components made out of cyclic softening steels. For the application of the new approach among others lifetime data from special tests, in particular creep tests on pre-fatigued specimens are required. To reduce the number of tests needed and hence the efforts for generating these data a deformation model for cyclic visco-plasticity with softening is utilized beside well established procedures for accelerated creep testing.

1. Introduction

For future fusion and GEN-IV fission power plants ferritic-martensitic (F/M) steels are selected as primary structural material candidates [1,2] mainly due to their high resistance to irradiation induced swelling [3]. In addition the F/M steels have in comparison to the austenitic steels lower thermal expansion coefficient which make them good option for constrained high-temperature components, e. g. the pipes of heat exchanger. During planned operation the F/M steels are subjected to cyclic thermo-mechanical loadings yielding cyclic softening dependent on the loading level and lifetime limiting creep, fatigue and thus creep-fatigue interaction.

Developing creep-fatigue lifetime assessment rules for the reduced activation F/M steel EUROFER, a structural material candidate for in-vessel components of future fusion power plants, two approaches are pursued. Within the first approach creep-fatigue rules already established in design codes are considered, evaluated and modified for reliable sufficiently conservative assessment [4, 5]. The second approach consists of the formulation and verification of new creep-fatigue design rules based on advanced recently developed damage model [6, 7]. However, both approaches require for the development and qualification of the rules proper material data to be generated in suitable tests, among others low cycle fatigue (LCF)

tests with long hold-times in which the influence of dwell time on cyclic softening and lifetime is characterized [8].

The assessment performed within the first approach for the applicability of the creep-fatigue accumulation rule of the ASME-BVP and RCC-MR codes to 9-Cr steels has shown that due to cyclic softening creep damage is underestimated by the rules what yields quite small allowable creep-fatigue values and hence too conservative creep-fatigue interaction diagram (envelope), as it is incorporated in the ASME-BVP code for Grade-91, 9-Cr steel similar to EUROFER [9, 10].

Improving their applicability to cycling softening F/M steels the creep-fatigue accumulation rule of well-established design codes is modified based on the knowledge collected so far.

2. Creep-fatigue accumulation rule for F/M steels

Taking into account the facts that cycling softening reduces creep strength and that it, as observed in LCF tests, mostly appear in the first 10% of the cyclic lifetime the following modification of the creep-fatigue accumulation rules is proposed:

- Calculation of creep damage portion in the creep fatigue accumulation rule in
  - first 10% of the lifetime using S_i from monotonic stress strain curves and design creep curves of as received material assuming no effect of cyclic softening on stress-to-rupture curves
  - remaining 90% of the lifetime using S_i from cyclic stress strain curves and design creep curves of cyclic softened material
- Using allowable total creep fatigue damage values of RCC-MR for SS 316 and Grade 91 - envelope with (0.3,0.3) tip point.

The application of this modification requires material data usually not available for F/M steels, in particular creep lifetime data for cyclic softened material. Due to cyclic softening accelerated creep and consequently shorter life time are expected. Quantitatively these effects will depend on the amount of cyclic softening which increases with increasing loading (strain) amplitude applied during cycling [6]. Therefore at least two strain amplitudes shall be selected in the test matrix for this type of experiments with which at least two levels of pre-softening shall be investigated (Figure 1). In the subsequent creep tests the stress is chosen based on the creep data available for the considered F/M steel. Thereby two types of tests can be aimed, creep to failure and creep to minimum creep rate (s. Figure 1). The evaluation of both types is then carried out based on the Monkman-Grant relation [11] between minimum creep rate and creep rupture time which was found in similar investigations on other steels showing cyclic softening to be independent on pre-cycling and cyclic softening, respectively [12]. The creep tests to failure (1^{st} type) will be used to verify for the considered F/M steel the independence of the Monkman-Grant relationship on cyclic softening. With the verified Monkman-Grant relationship and the minimum creep rates of the 2^{nd} type of creep tests the data base of creep lifetime on cyclic softened steel can be than extended to longer lifetimes.

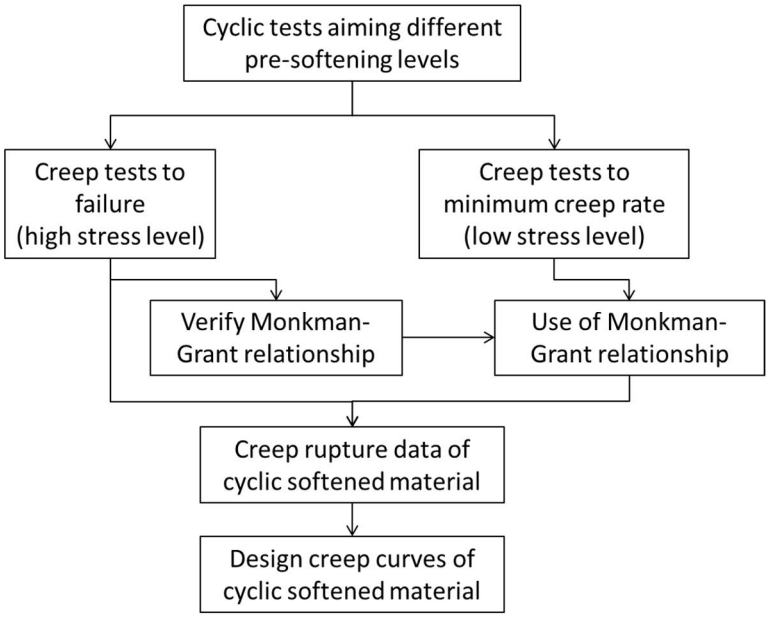

Figure 1. Flow chart of the experimental approach proposed for generating design creep curves of cyclic softened steel.

Having the creep lifetimes determined for the considered F/M steel pre-softened to different levels, ψ a cyclic softening stress factors, $K_\psi = f(\psi)$ will be then identified with which the stresses of design creep curves of as received material are reduced to obtain the design creep curves of cyclic softened material. With this simplification the modified creep-fatigue rules can be easily implemented by only introducing two calculation steps to the existing rules:

Step 1. Determination of the cyclic softening level ψ as function of total strain range and temperature by using monotonic and cyclic stress-strain curves.

Step 2. Determination of the cyclic softening stress factor K_ψ given as function of ψ and applying it to the stress considered for calculating creep damage.

3. Conclusions

Cyclic softening of ferritic martensitic steel and its impact on creep strength are identified as the main reason for the strong non-linear creep-fatigue interaction evaluated using conventional creep-fatigue rules. Based on these findings modification of the creep-fatigue accumulation rules of ASME-BPV and RCC-MR codes as well as an experimental approach for generating data required for its use and verification have been proposed. Beside the modification proposed for the creep-fatigue accumulation rule alternative rules derived from advanced creep-fatigue damage modelling are under development.

Acknowledgement

This work has been carried out within the framework of the EUROfusion Consortium and has received funding from the Euratom research and training programme 2014-2018 under grant agreement No 633053. The views and opinions expressed herein do not necessarily reflect those of the European Commission.

References

[1] A. Hishinuma, A. Kohyama, R. L. Klueh, D. S. Gelles, W. Dietz and K. Ehrlich, Current status and future R&D for reduced-activation ferritic/martensitic steels. Journal of Nuclear Materials, 258-263 (1998) 193-204.

[2] A Technology Roadmap for Generation IV Nuclear Energy Systems, Issued by the U.S. DOE Nuclear Energy Research Advisory Committee and the Generation IV International Forum 2002.

[3] R.L. Klueh and D.R. Harries. High-chromium ferritic and martensitic steels for nuclear applications. American Society for Testing and Materials, 2001.

[4] J. Aktaa, High temperature creep-fatigue structural design criteria for EUROFER 97 and ist weld joints. Wissenschaftliche Berichte des Forschungszentrums Karlsruhe, FZKA-7449, Forschungszentrum Karlsruhe, October 2009.

[5] J. Aktaa, M. Weick and M. Walter, High temperature creep-fatigue structural design criteria for fusion components built from EUROFER 97. Wissenschaftliche Berichte des Forschungszentrums Karlsruhe, FZKA-7309, Forschungszentrum Karlsruhe, August 2007.

[6] J. Aktaa and R. Schmitt. High temperature deformation and damage behavior of RAFM steels under low cycle fatigue loading: Experiments and modeling. Fusion Engineering and Design, 81:2221-2231, 2006.

[7] J. Aktaa and C. Petersen, Modeling the constitutive behavior of RAFM steels under irradiation conditions. Journal of Nuclear Material, Vol. 417, pp. 1123-1126, 2011.

[8] U. Führer, J. Aktaa, Creep-fatigue interaction and cyclic softening of ferritic-martensitic steels. Baltica X - Life Management and Maintenance for Power Plants, Helsinki - Stockholm, June, 2016.

[9] "'Boiler Pressure Vessel Code (BPVC) Section III: Rules for Construction of Nuclear Facility Components, Division 1: Metallic Components," American Society of Mechanical Engineers, 2013.

[10] M. Porton, J. Aktaa, C. Bachmann, P. Fernandez, M. Kalsey, T. Lebarbe, C. Petesch and W. Timmis, Structural Design Criteria Development Needs for a European DEMO. Fusion Science and Technology, Vol. 66, pp. 18-27, 2014.

[11] F. C. Monkman and N. J. Grant, Am empirical relationship between rupture life and minimum creep rate in creep-rupture tests. Proc. ASTM, pp. 593-620, Vol. 56, 1956.

[12] L. Binda, Advanced creep damage and deformation assessment of materials subject to steady and cyclic loading conditions at high temperatures. ETH Zürich, PhD Thesis, 2010.

Creep-fatigue interaction and cyclic softening of ferritic-martensitic steels

Ulrich Führer & Jarir Aktaa

Karlsruhe Institute of Technology, Institute for Applied Materials
Eggenstein-Leopoldshafen, Germany

Abstract

In this study, creep-fatigue behavior of modified 9Cr1Mo ferritic-martensitic steel P91 is investigated by uniaxial low cycle fatigue tests with hold time at 550°C. The influence of hold time duration and position on softening behavior is of major interest. Further, the impact of hold time on lifetime is characterized.

Additionally to isotropic cyclic softening characteristic of ferritic-martensitic steels, hold time periods added to the loading path yield further softening only in the direction of loading during hold times – hold time under tension results in lower stresses under tension in the following cycles, and hold time under compression results in lower compressive stresses, respectively.

A clear reduction in lifetime was observed for compressive hold times, whereas the influence of tensile hold time is ambiguous: Short hold times improve lifetime, but longer hold times will lead to shorter lifetimes than in tests without hold time.

Generally, the influence of hold time on cyclic softening as well as lifetime increases with decreasing total strain amplitude.

1. Introduction

The increasing share of renewable energy in power supply demands higher flexibility of conventional power plants. As renewable energy supply is fluctuating and large-scale energy storage systems able to balance power supply are not ready yet, conventional power plants have to compensate changing power outputs. Additionally to varying steam pressures, the required load changes lead to thermal gradients on structural components of power plants. This results in additional fatigue loads interacting with creep loading already present in high temperature, high pressure environments. Plants originally designed for base load thus see higher damage rates and premature failures of structural components. Furthermore, required improvements in plant efficiency necessitate even higher steam temperatures and pressures.

The ferritic-martensitic steel P91 is a frequent choice for high temperature/pressure piping and heat exchangers in steam-based power plants [1]. Major advantages are good creep strength, low thermal expansion and, in nuclear applications, low irradiation swelling [2,3]. A crucial limitation of ferritic-martensitic steels under fatigue loading is cyclic softening without stabilization [4], which is based on microstructural degradation [5,6]. This softening behavior is even more pronounced under combined creep-fatigue loading [4,7].

Strain-controlled low-cycle fatigue (LCF) tests with hold times under tension and/or compression are used to represent creep-fatigue loadings in laboratory tests. Although many studies on low cycle fatigue behavior of ferritic-martensitic steels include tests with hold time only limited data is available on the influence of hold times on cyclic softening, especially for compressive hold times [8].

2. Experimental observations

This work was divided into two phases. Due to tolerances in composition of Grade 91 steels, different heats show different stresses and lifetimes in LCF tests. The chemical composition of the material used in this study is listed in Table 1. Aluminum content is also within tighter limits of T91. The plate was first austenitized at 1050°C for 30min and then tempered at 780°C for 1h [9]. To compare this material to other heats, LCF tests without hold time were carried out first. The softening behavior shown in these tests is subsequently used as a reference for hold-time tests.

Table 1. Chemical composition of studied P91 heat, from [9]

C	Cr	Mo	V	Nb	Mn	Si	N	Al	Ni	P	S
0.086	8.91	0.917	0.198	0.08	0.363	0.324	0.041	0.018	0.149	0.017	0.001

Figure 1 shows observed softening behavior typical for ferritic-martensitic steels [3,5]. Symmetrical stresses under tension and compression were found. Stresses in all diagrams are true stresses calculated as $\sigma_{true}=\sigma(1+\varepsilon)$. Lifetime is normalized to the number of cycles to failure of the respective tests. Detailed information on lifetime of each test can be found in Figure 7. Generally, the LCF lifetimes observed in this study lie on the lower end of the range reported in [8].

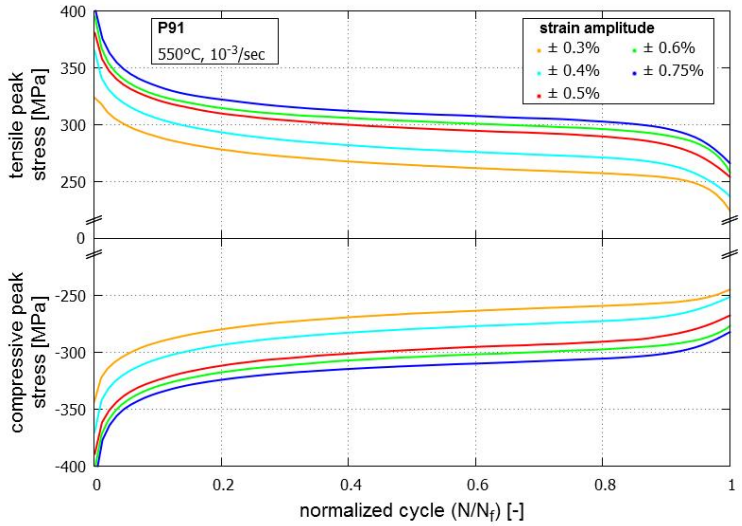

Figure 1. Cyclic softening of P91 in LCF reference tests without hold time.

In phase 2, tests with hold time under tension, compression and combined tension and compression in every cycle were carried out. Beside hold time position, varied parameters are its duration and total strain amplitude of the test. Hold times of up to 3 hours were considered.

Figure 2 gives an example for the influence of hold time position on cyclic softening. Two tests without hold time are included to examine the scatter of peak stresses and lifetime between different tests. Varia-

tion of peak stresses between tests with identical parameters is almost non-existent. Additionally to the softening in LCF tests without hold time, further softening occurs after hold time. Interestingly, tensile hold time only reduces tensile peak stresses whereas compressive stresses are similar to tests without hold time. Accordingly, compressive hold time yields lower compressive stresses only, tensile peak stresses are not reduced by compressive hold time. Lastly, combined hold time under tension and compression results in further softening under tension and compression of the same magnitude as in tests with hold time on one side of the loading cycle only. This behavior was found for all considered strain amplitudes and hold time durations.

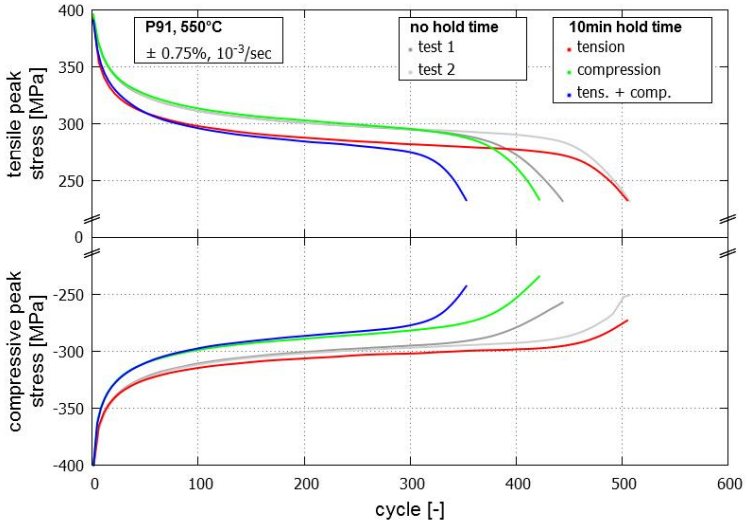

Figure 2. Influence of hold time position on cyclic softening.

The amount of additional softening depends on duration of hold time period. Comparing the peak stresses for tests with tensile hold time of different length (see Figure 3), longer tensile hold times result in lower tensile peak stresses. Equal behavior was observed for compressive hold times. This effect saturates after 1h of hold time (for this set of parameters), a further increase up to 3h yields no additional softening.

Even though softening behavior is not affected by increase of hold time duration from 1h to 3h, the impact on lifetime is significant. Tensile hold times up to 1h show an ambiguous influence on lifetime – the 1min hold test reached more cycles than the 10min hold test, but less than the 1h hold test. Overall, a slight increase in lifetime was observed for tests with short tensile hold times. On the other hand, increasing hold time from 1h to 3h reduced lifetime by almost 50%.

In Figure 4, the influence on cyclic softening of 1min hold time under tension is compared for different total strain amplitudes. It can be noticed that the additional softening due to hold time becomes more pronounced with decreasing strain amplitude. In particular, reduction of strain amplitude from 0.5% to 0.3% results in a significant increase of hold time induced softening.

This dependence on strain amplitude was also found for cycles to failure (being defined as a 10% load drop compared to the linear region). For 0.3% strain amplitude, the number of cycles to failure increased by more than 1500 cycles, which equals to about 30%. In contrast, for larger strain amplitudes and comparatively short tensile hold times, either a modest increase or decrease in lifetime was observed.

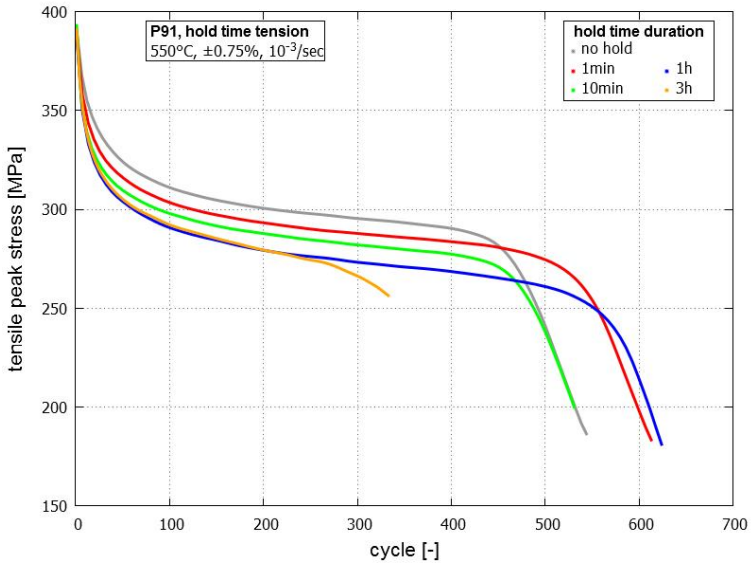

Figure 3. Influence of hold time duration on cyclic softening.

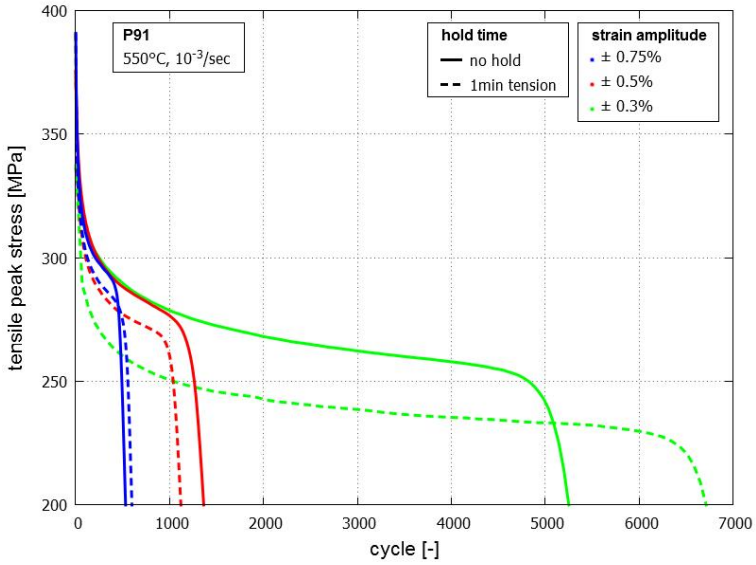

Figure 4. Influence of 1min tensile hold time on cyclic softening for different strain amplitudes.

Figure 5 compares the softening behavior and lifetime of tests with 10min compressive hold time. Similarly to tests with tensile hold time, the influence of hold time on cyclic softening increases with decreasing strain amplitude. Due to longer hold time, this effect is more pronounced than in Figure 4. E.g. for strain amplitude of 0.3%, compressive peak stress at half-life is reduced by almost 50MPa due to 10min compressive hold time.

This holds especially true for the detrimental effect of compressive hold time on lifetime of ferritic-martensitic steels. Table 2 summarizes cycles to failure of tests presented in Figure 5. Remarkably, the lifetime for strain amplitude of 0.3% was reduced to one third of the reference test by addition of compressive hold time. This reduction is much more severe than the drop in lifetime measured for higher strain amplitudes. Tests with both hold time under tension and compression showed similar lifetime behavior.

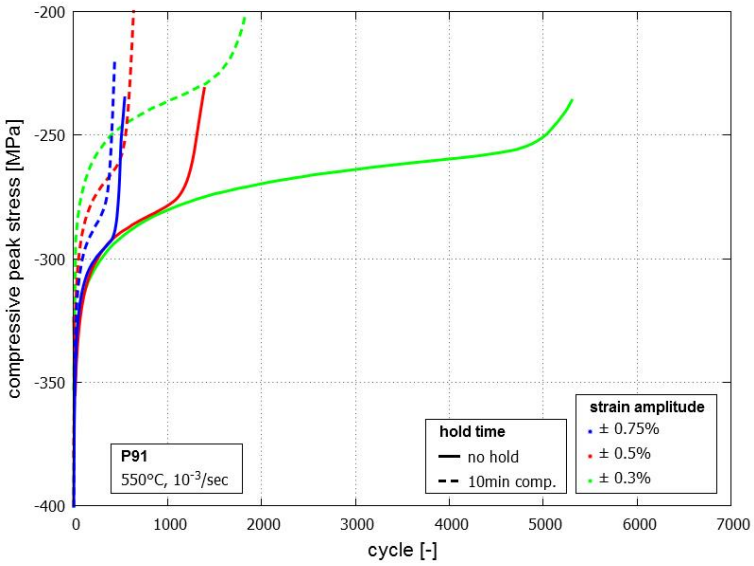

Figure 5. Influence of 10min compressive hold time for different strain amplitudes.

Table 2. Influence of compressive hold time on lifetime

Strain amplitude	Lifetime – no hold	Lifetime – 10min comp.	Reduction in lifetime
±0.3%	5151 cycles	1831 cycles	64%
±0.5%	1290 cycles	599 cycles	53%
±0.75%	488 cycles	406 cycles	17%

3. Discussion

Cyclic softening is based on microstructural degradation. Reduction of dislocation density and coarsening of grains and carbides due to inelastic deformation leads to a continuous decline of material strength, which is assumed to be of isotropic nature [6,10]. At first glance, additional softening under tension (or compression, respectively) only cannot be explained by this phenomenon solely.

To get a better understanding of the deformation behavior, additional tests with segments of different hold time were carried out. Figure 6 shows peak stresses of one such test consisting of 1000 cycles with 1min compressive hold time, 1000 cycles with no hold time (pure cyclic loading), 1000 cycles with 1min tensile hold time and continuous cycling without hold time till failure.

After compressive hold time is removed from the loading path, a transient stage (lasting for about 10 cycles) is followed by symmetrical peak stresses. Stresses in this second stage are lower than in a test without hold time from the beginning, with stress range similar to the last cycles with compressive hold time. This indicates additional isotropic softening due to hold time. This additional softening is overlaid by a kinematical shift of hysteresis loops during hold time under tension or compression only. This shift happens again after tensile hold time is introduced, with strain range again being equal than in the last cycles without hold time. After 3000 cycles, hold time is excluded again and difference in peak stresses between test without hold time from the beginning and test with intermittent hold time increased again, indicating further additional isotropic softening due to tensile hold period.

Concluding, additional softening under tension only for tensile hold times (or compression for compressive hold times, respectively) is a result of additional isotropic softening (due to increased inelastic deformation), which is still present during subsequent continuous cycling, and an overlaid kinematic shift of stresses during hold-time phases.

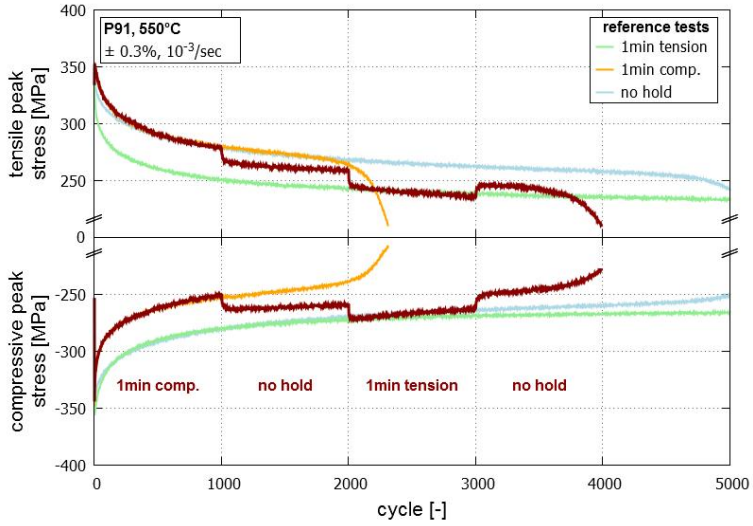

Figure 6. Test with changing hold time position compared to tests with same loading in every cycle.

To estimate lifetime in LCF tests, Coffin-Manson-model is commonly used [11]. This model links inelastic deformation per cycle to the number of cycles to failure. Repeated inelastic deformation leads to formation of persistent slip bands and to subsequent crack initiation [12]. Concerning influence of hold time on cycles to failure, Figure 7 summarizes the different tests of this study in a Coffin-Manson-plot. Parameters of Coffin-Manson relation are given in this figure; only tests without hold time were used to calculate these parameters. Note that the choice of half-life cycle for calculation of parameters is arbitrary and only based on convention, this cycle is not representative for ferritic-martensitic steels like it would be for a material with stable cyclic behavior after a given number of cycles. Again, the increasing influence of hold time on lifetime with decreasing strain amplitude as well as the detrimental effect of compressive hold time can be noted.

Accumulated inelastic deformation alone cannot explain the difference in lifetime between tensile and compressive hold time as inelastic strain range is equal in both cases. But, for crack formation tensile stresses as well as rate during inelastic deformation are also of importance [13,4]. To understand the damaging influence of compressive hold time (compared to tensile hold time) Figure 8 shows inelastic strain range and tensile peak stresses for different tests with 0.75% total strain amplitude after 250 cycles.

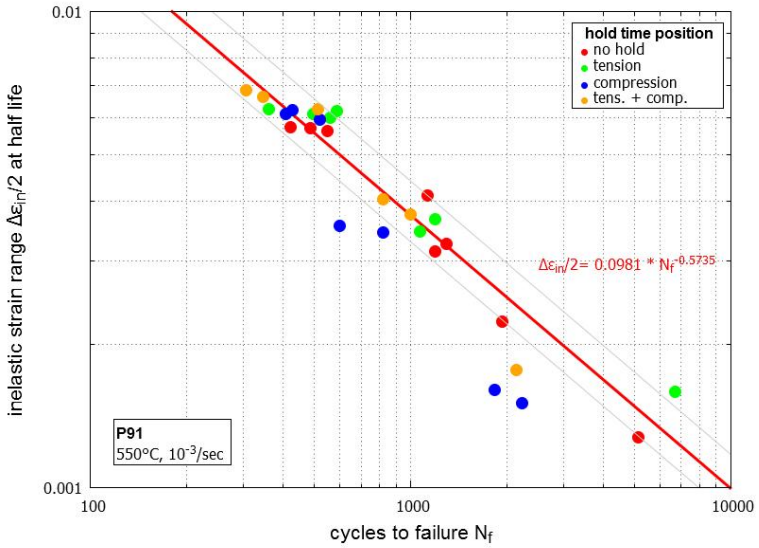

Figure 7. Coffin-Manson-plot for tests with and without hold time.

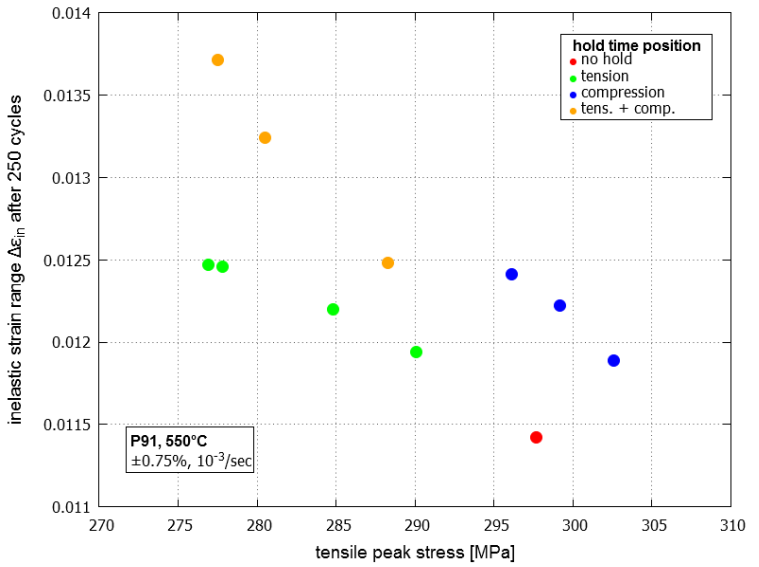

Figure 8. Tensile peak stress and inelastic strain range for different hold time positions and durations.

Here, different influence on lifetime of different hold time positions can be understand: Compared to tests without hold time, adding compressive hold period increases inelastic deformation per cycle while tensile peak stresses are similar to tests without hold time [4]. Furthermore, added inelastic deformation with high rate takes place under tensile loading entirely, as can be seen in Figure 9. The material deforms inelastically with low rate under compression during hold time, followed by high-rate inelastic deformation under tension during load change. On the other hand, adding tensile hold time increases inelastic deformation per cycle by similar amount, but peak tensile stresses are reduced and added high-rate inelastic deformation takes place under compression where crack formation is unlikely. This difference in loading during high-rate inelastic deformation explains faster crack formation in tests with compressive hold time.

For tests with combined tensile and compressive hold time, further increase in inelastic deformation goes along with a decrease in tensile stresses. Notably, the increased inelastic deformation at high rate

under tension is also present, albeit at a lower stress than for compressive hold time only. Therefore, the same reasons for reduced lifetime as in tests with only compressive hold time apply, with similar detrimental effects.

The influence of oxidation has been suggested [14] as a reason for shorter lifetimes with compressive hold time. Here, formation of oxide layer during compressive hold time and subsequent cracking of brittle oxide layer during tensile loading is assumed as basic cause for earlier crack initiation. On the other hand, an oxide layer formed during tensile hold time does not crack during compressive loading; therefore faster crack formation is not happening for tensile hold times. Although different cracking behavior for tensile (almost no secondary cracks) and compressive (lots of small coalescing cracks) hold time was noted in this study, oxidation is not assumed as main cause for shorter lifetime. Local cracking of oxide layer would be more pronounced for larger strain amplitudes than for small strain amplitudes, accordingly the impact of local failures in the oxide layer as a starting point for cracks should be larger for larger strains. But, as shown in Figure 5 and Table 2, the detrimental effect of compressive hold time is more pronounced for smaller strain amplitudes.

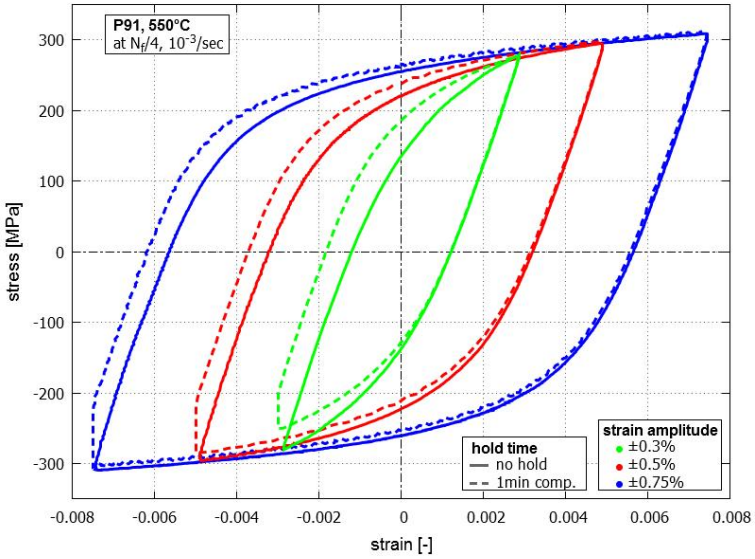

Figure 9. Hysteresis loops for tests with and without compressive hold time at one quarter lifetime.

Figure 9 shows hysteresis loops of LCF tests without hold time at one quarter lifetime and corresponding loops of tests with 1min compressive hold time of the same cycle number. Here, the bigger influence of compressive hold time on lifetime for smaller strain amplitudes can be explained: Increase of inelastic deformation per cycle (around 0.05%) is of similar amount for all strain amplitudes shown. But, the relative increase compared to each test without hold time (+25% for amplitude of ±0.3%, +4% for ±0.75%) is considerably larger for smaller strain amplitudes, which could justify the larger impact on lifetime.

4. Conclusions

Ferritic-Martensitic steels show desirable mechanical properties in high-temperature applications for power plants. But, cyclic softening without stabilization leads to continuous degradation of these materials. For safe and reliable design of plants and components, influences on cyclic softening have to be characterized and understood.

In this study, the influence of hold time periods on softening behavior was investigated. Additional softening due to hold times was found. The magnitude of additional softening increased with decreasing total

strain amplitude. Further, the detrimental influence of compressive hold time on lifetime was analyzed. Like for the amount of additional softening, the largest decrease in lifetime due to added hold time was also found for the smallest total strain amplitude.

This relationship between strain amplitude on one hand and hold time influence on cyclic softening and lifetime on the other hand is of particular importance. Most test results reported are at comparatively high strain amplitudes and low number of cycles to failure due to long test duration. But, tests with hold time at low total strain amplitudes are needed as the influence of hold time at in-service conditions is underestimated otherwise.

Acknowledgement

The research leading to these results is partly funded by the European Atomic Energy Community's (Euratom) Seventh Framework Programme FP7/2007-2013 under grant agreement No. 604862 (MatISSE project) and in the framework of the EERA (European Energy Research Alliance) Joint Programme on Nuclear Materials.

References

[1] R.W. Swindeman, M.L. Santella, P.J. Maziasz, B.W. Roberts and K. Coleman. *Issues in replacing Cr-Mo steels and stainless steels with 9Cr-1Mo-V steel*. International Journal of Pressure Vessels and Piping, 81:507-512, 2004.

[2] R.L. Klueh and D.R. Harries. *High-chromium ferritic and martensitic steels for nuclear applications*. American Society for Testing and Materials, 2001.

[3] J.R. DiStefano, V.K. Sikka, J.J. Bass, C.R. Brinkman, J.M. Corum, J.A. Horak, R.L. Huddleston, J.F. King R.W. McClung and W.K. Sartory. *Summary of Modified 9Cr-1Mo Steel Development Program: 1975-1985*. Oak Ridge National Laboratory, ORNL-6303,1986.

[4] J. Aktaa and R. Schmitt. *High temperature deformation and damage behavior of RAFM steels under low cycle fatigue loading: Experiments and modeling*. Fusion Engineering and Design, 81:2221-2231, 2006.

[5] P.J. Ennis and A. Czyrska-Filemonowicz. *Recent advances in creep-resistant steels for power plant applications*. Sādhandā 28:709-730, 2003.

[6] B. Fournier, M. Sauzay, A. Renault, F. Barcelo and A. Pineau. *Microstructural evolutions and cyclic softening of 9%cr martensitic steels*. Journal of Nuclear Materials, 386-388:71-74, 2009.

[7] B. Fournier, M. Sauzay, C. Caës, M. Noblecourt, M. Mottot, A. Bougault, V. Rabeau and A. Pineau. *Creep-fatigue-oxidation interactions in a 9Cr-1Mo martensitic steel. Part I: Effect of tensile holding period on fatigue lifetime*. International Journal of Fatigue, 30:649-662, 2008.

[8] T. Asayama and Y. Tachibana. *Collect Available Creep-Fatigue Data and Study Existing Creep-Fatigue Evaluation Procedures for Grade 91 and Hastelloy XR*. Japan Atomic Energy Agency, 2007

[9] K. Zhang and J. Aktaa. *Characterization and modelling of the ratcheting behaviour of the ferritic-martensitic steel P91*. Journal of Nuclear Materials, 472:227-239, 2016.

[10] V. Shankar, M. Valsan, K. Bhanu Sankara Rao, R. Kannan, S.L. Mannan, S.D. Pathak. *Low Cycle fatigue behaviour and microstructural evolution of modified 9Cr-1Mo ferritic steel*. Materials Science and Engineering A, 437:413-422, 2006.

[11] L.F. Coffin. *A study of the effects of cyclic thermal stresses on a ductile metal*. Transactions of ASME, 76:931-950, 1954.

[12] D. Munz, K. Schwalbe and P. Mayr. *Dauerschwingverhalten metallischer Werkstoffe*, Vieweg, 1971.

[13] Y.N. Rabotnov. *Creep Rupture*, 12th International Congress of Applied Mechanics, Stanford, 1968.

[14] B. Fournier, M. Sauzay, C. Caës, M. Noblecourt, M. Mottot, A. Bougault, V. Rabeau and A. Pineau. *Creep-fatigue-oxidation interactions in a 9Cr-1Mo martensitic steel. Part II: Effect of compressive holding period on fatigue lifetime*. International Journal of Fatigue, 30:663-676, 2008.

Creep performance of fuel cladding

Rami Pohja, Ville Tulkki, Timo Ikonen, Pekka Moilanen, Juhani Rantala, Santtu Huotilainen & Ulla Ehrnstén

VTT Technical Research Centre of Finland Ltd
P. O. Box 1000, FI-02044 VTT, Finland

Abstract

The understanding of the creep behavior of nuclear fuel claddings is essential to predict safely and reliably the thermal performance and mechanical integrity of fuel rods. Fuel cladding tubes experience a range of changing conditions during their reactor life, further complicating the analysis. Today's nuclear reactors widely use zirconium alloys as fuel cladding material. Zirconium alloys exhibit anisotropic creep properties and their creep behavior depends significantly on the material condition. As for envisaged Gen-IV reactors, modified austenitic stainless steels and ODS alloys are candidate materials for claddings because of higher temperatures expected in operating conditions. This paper describes the research activities related to the creep behavior of cladding materials carried out at VTT. These activities include experimental research using the newly developed Pneumatic Loading Apparatus (PLA), which is capable of testing the steady state and transient creep properties of fuel cladding specimens with internal pressure of up to 700 bar and an additional axial force of up to 4 kN in tensile or compressive direction. Furthermore, creep models for cladding materials are being developed using viscoelastic modelling approach and Logistic Creep Strain Prediction (LCSP) method.

1. Introduction

The fuel cladding tubes act as the first barriers to the spread of radionuclides in nuclear reactors. The fuel claddings are subjected to radiation, oxidizing environments as well as to inward and outward stresses during their service life. Many factors, such as microstructural stability, swelling and creep properties as well as the oxidation resistance, define the performance of fuel claddings from material point of view. Today, the two most common types of nuclear reactors in electricity generation are pressurized water reactors (PWR) and boiling water reactors (BWR), collectively known as light water reactors. In light water reactors the nuclear fuel is in the form of near-cylindrical UO_2 pellets with a length and diameter of the order of 1 cm. The pellets are stacked inside a thin-walled tube made from zirconium alloy that is several metres in height and internally pressurized with helium. The fuel rods are organized into fuel assemblies that together with the cooling water form a critical configuration capable of sustaining the nuclear chain reaction.

The Fukushima accident has increased the interest in advanced materials for accident-tolerant fuel claddings that could withstand accident scenario environments, such as very high temperature exposure in steam, for several hours. Austenitic stainless steels and Oxide Dispersion Strengthened (ODS) alloys are candidate materials for accident-tolerant fuel claddings. For the envisaged Gen-IV reactors, where the fuel cladding materials will be subjected to considerably higher temperatures than in currently running reactors,

austenitic stainless steels, high-cromium ferritic/martensitic (F/M) steels and ODS alloys are also relevant candidates because of their better creep resistance compared to zirconium-based alloys. [1-3]

Zirconium exhibits a low neutron cross-section, and thus is especially suited to be a structural material in a nuclear reactor. As zirconium is too soft and prone to corrosion to be used as a cladding in itself, various zirconium-based alloys have been developed for nuclear fuel applications. Zirconium alloys exhibit a pseudo-compact hexagonal structure (HPC) with α-phase stable until about 800°C. The zirconium alloys used in fuel claddings are either in cold-worked and stress-relieved or in (partially or fully) recrystallized material condition. The recrystallized material is usually more equiaxed than stress-relieved material, which exhibits elongated grains in the laminating direction. Typical grain size in the cladding tubes made of zirconium alloys is in the range 2–10μm. [1-3]

Specific austenitic stainless steels, such as 15-15Ti, also known as grade 1.4970 austenitic stainless steel, are candidate materials for fuel claddings for the Gen-IV prototype lead-cooled fast nuclear reactors. The main advantages of these materials are their good thermal creep behaviour and their excellent mechanical properties. However, the swelling properties of austenitic stainless steels may not be sufficient for long term exposure in expected demanding conditions. High-cromium ferritic/martensitic (F/M) steels exhibit superior swelling resistance which should allow for higher burnup and increased safety margins. The mechanical strength of (F/M) steels is normally limited for higher temperatures (typically above 650ºC). ODS alloy versions of ferritic steels, reinforced by a distribution of nano-oxides (or nano-clusters, NC), show higher creep strength and maintain the swelling resistance, making them good candidates for the cladding of advanced fast reactors. Therefore, ODS ferritic and F/M steels are envisioned as reference claddings for high burn up fuel in fast reactors. However, manufacturing and especially welding/joining of ODS steels pose a significant challenge, because fusion welding process causes agglomeration of fine oxide particles resulting in loss of strength and creep properties of ODS joints. [4]

It is important to understand the creep behavior of nuclear fuel claddings to be able to predict safely and reliably the thermal performance and mechanical integrity of fuel rods. This paper gives an overview of the research activities carried out at VTT, which are intended to deepen the knowledge of the creep behavior of cladding materials. These activities include demanding multiaxial creep tests for specimens made of fuel cladding materials and creep modelling using viscoelastic modelling approach and Logistic Creep Strain Prediction (LCSP) method.

2. Experimental

Biaxial creep properties of the fuel cladding materials are usually studied by carrying out creep tests for internally pressurized tubes and measuring the axial and hoop strain. In the majority of experimental equipment intended for biaxial creep testing of tubes the axial and hoop stress are produced to the test specimen by the internal pressure only. In such applications the hoop:axial stress ratio (α) is constant (2:1) and cannot be manipulated by the testing facility. The VTT biaxial creep testing concept utilizes also the internal pressure for producing the axial and hoop stress to the test specimen, but the pneumatic loading units can additionally produce axial load for the tubular test specimen either in push or pull direction, which enables testing with variable hoop:axial stress ratios. The device is capable of testing the steady state and transient creep properties of tubular specimens with internal pressure of up to 700 bar and an additional axial force of up to 4 kN in tensile or compressive direction. The functionality of additional axial load system by bellows technology has also been demonstrated in several other applications [5-7].

The VTT bi-axial creep testing device has been utilized in EU FP7 projects MATTER and MatISSE. In these projects, the creep to rupture properties of grade 1.4970 austenitic stainless steel, 9% Cr ODS steel and 14% Cr ODS steel have been tested with $\alpha = 2$ at the temperature range of 550-700°C. Figure 1 shows the VTT test results (stress vs. Larson-Miller parameter) for grade 1.4970 austenitic stainless steel at 24% cold-worked condition and literature data from [8] at the temperature range of 550-750°C.

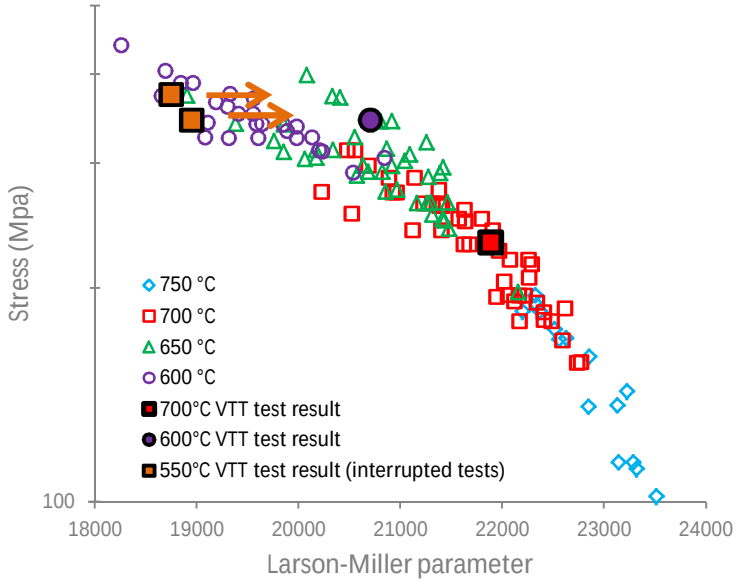

Figure 1. Larson-Miller parameter as a function of stress for cold-worked pressurized tubes made of grade 1.4970 austenitic stainless steel at 550-750°C. The Larson-Miller parameter is plotted as a function of the hoop stress at the clad mid-wall [8].

A future objective for the VTT bi-axial creep testing device is to launch a test programme for zirconium-based fuel cladding alloys to support the modelling activities described in later in this paper. The intended test matrix includes tests with variable α values and transients in temperature and stress. The capability of the device to perform tests which include transients was demonstrated by carrying out a test with stress ratio of α = 1 and with a temperature transient (from 360°C to 400°C) after 500 hours. Based on the test results, the testing concept and equipment proved its capability to perform reliably and accurately demanding biaxial creep tests of fuel cladding materials.

3. Creep models for fuel claddings

Two modelling approaches have been applied at VTT to characterize the creep behaviour of Zircaloy-4 cladding material. The modelling approach based on the LCSP creep strain model and the viscoelastic modelling methodology are described in this paper.

3.1 LCSP modelling approach

A modelling approach utilizing The LCSP creep strain model and the Wilshire creep to rupture model has been applied to describe the creep strain behavior of Zircaloy-4 material [9]. The LCSP model describes the creep curve of material with end limits from the time to rupture. The LCSP function is a non-linear asymmetric transition function with a steepness regulated by two variables p and x_0 and coefficient C. The transition equation is simple to invert, also giving an algebraic solution for strain as a function of time. Derivation can the give the strain rate at a specified time and further derivation and finding the root of the expression gives the minimum creep rate. The LCSP model creep curve is given by [10]:

$$\log[t(\varepsilon)] = \frac{\log(t_r)+C}{1+(\frac{\log(\varepsilon)}{x_0})^p} - C \quad \log[t(\varepsilon)] = \frac{\log(t_r)+C}{1+(\frac{\log(\varepsilon)}{x_0})^p} - C \tag{1}$$

where x_0 and p are stress and temperature dependent variables and C is coefficient. The applicable limits of stress and temperature for reliable strain prediction by this approach are set by the available creep rupture and strain data.

The time to rupture values for the LCSP creep strain model were modelled using the Wilshire modelling approach. The Wilshire model uses tensile strength normalized creep stress and the model curve is fitted to temperature compensated time. The Wilshire model avoids the varying stress exponent n, which is utilized in the Norton law related creep models, and the apparent creep activation energy is definable in a straightforward way. The Wilshire equation for normalized stress (σ/σ_{UTS}) as a function of time to rupture (t_r) is defined as [11]:

$$t_r = [{}^{-1}/_{k} \cdot ln({}^{\sigma}/_{\sigma_{UTS}})]^{\frac{1}{u}} \cdot exp({}^{-Q_c^*}/_{RT}) \quad \log[t(\varepsilon)] = \frac{\log(t_r)+C}{1+(\frac{\log(\varepsilon)}{x_0})^p} - C \qquad (2)$$

where k and u are fitting constants, Q_c^* is the apparent activation energy, R is the gas constant, σ is the applied stress and σ_{UTS} is the tensile strength at test temperature (T).

The effect of irradiation on the creep behaviour with this modelling approach can also be taken into account. The irradiation has been found to cause considerable material hardening, i.e. increase in both yield stress and ultimate tensile strength and significant decrease of ductility. Irradiated zirconium-based materials usually exhibit longer creep to rupture times and decreased creep ductility, at least for the short duration tests. Thus, a correlation between stress parameter (as a function of fluence) and Arrhenius-dependent time-temperature parameter can be created to incorporate the effect of irradiation as shown in Figure 2 [11-13].

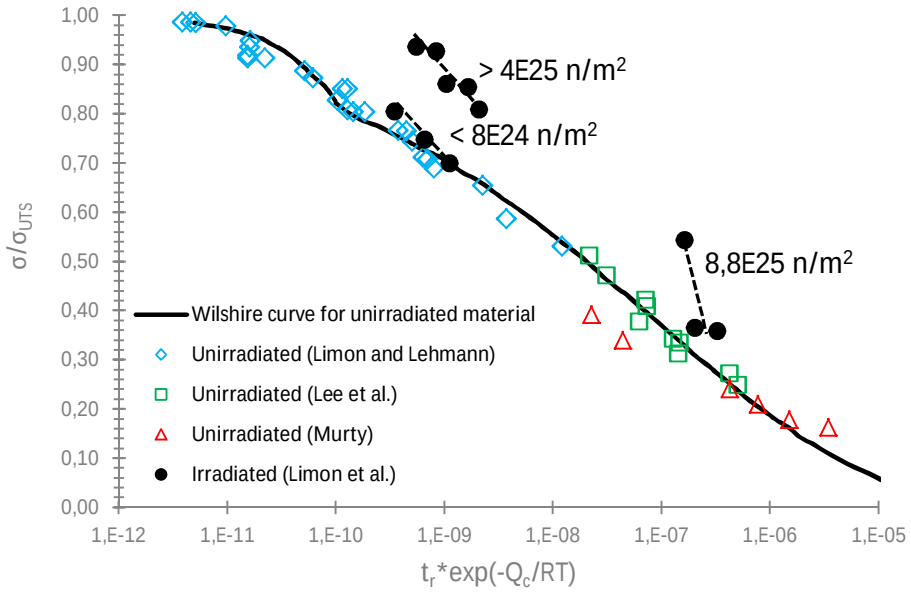

Figure 2. Wilshire model master curve for unirradiated creep data and creep test results for irradiated and unirradiated samples [12-14]. The level of irradiation (fluence) is given next to the irradiated data. Using the irradiated test data the corresponding Wilshire model parameters can be calculated for irradiated data.

In an earlier study, a preliminary FEA simulation utilizing the LCSP creep model was carried out for a zirconium alloy cladding tube at 500°C with an initial maximum principal stress of around 91 MPa to simulate a system disturbance in reactor leading to elevated temperature. The calibration for the LCSP model for the case was carried out using two creep datasets; a cold-pilgered material with two intermediate heat treatments and with a final stress relieving (460°C for 7 h) and a commercial fuel cladding with 74% reduction in cross section at last rolling (CW = 74%), which was stress-relieved at 500°C for 2.5 h [12, 15]. The stress range was from 68 MPa to 150 MPa and the temperature range was between 450°C and 502°C in the datasets used for the model calibration. The temperature range, which is above the normal operating conditions in reactors, was justified by a postulated system disturbance scenario leading to

elevated temperature, for which the creep model was calibrated. The scenario parameters lie in the range where thermal creep dominates, creep strain propagates rapidly and the effect of irradiation on the creep strain is considered negligible. Thus, the effect irradiation creep was not included in the preliminary case. In the preliminary FEA simulation the strain accumulated rapidly at the free end of the postulated 500 mm tube length, leading to nearly 2% strain in 3 hours. The other end of the tube was rigidly constrained in the FEA simulation.

The LCSP model exhibited a satisfactory correlation between observed and predicted time to strain for the assessed datasets ([12] and [15]) at higher temperatures (450-500°C).However, when assessing the LCSP creep strain model performance at lower temperatures (300-400°C), it was observed that the model overpredicted the creep strains at lower temperatures. Under normal operating conditions, the fuel rods in commercial reactors are stressed by the coolant overpressure at the beginning of irradiation (compressive hoop stress of 40-80 MPa) and eventually by fuel swelling at the end of life (tensile hoop stress up to >50 MPa for pressurized water reactor (PWR) fuel rods and up to >100 MPa for boiling water reactor (BWR) fuel rods). The cladding outer-surface temperature is in case of BWR claddings about 290°C and significantly higher in case of PWR claddings, 320-360°C. Maximum exposure times are up to 10 years for BWR fuel and up to 6 years for PWR fuel [2]. Figure 3 shows the LSCP model predictions and creep test results at 360°C for cold-worked and stress-relieved Zircaloy-4 material [16, 17].

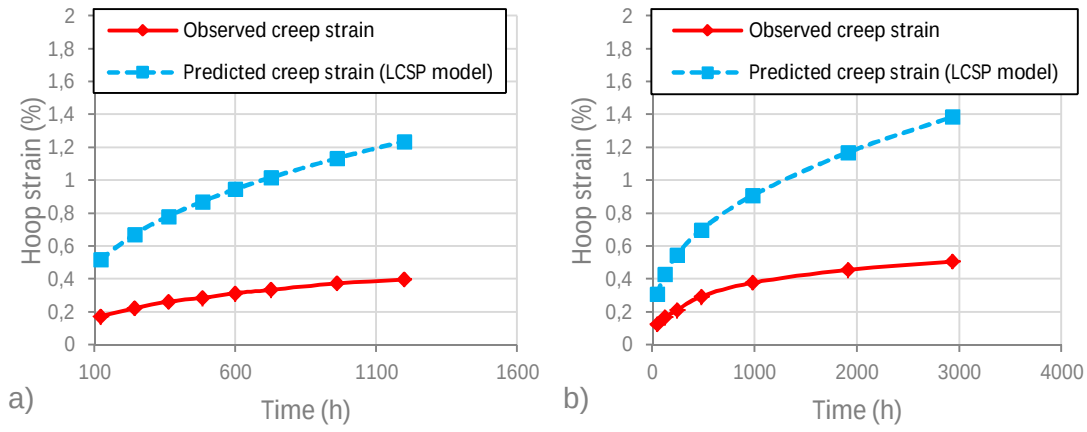

Figure 3. The creep test results a) 360°C / 78MPa [11], b) 360°C / 90MPa [12] and LCSP model predictions for cold-worked and stress-relieved Zircaloy-4 samples with parameters calibrated using datasets from [12] and [15].

The LCSP model clearly overpredicted the hoop strains throughout the test times with 109.2% error for the 360°C / 78 MPa test and 215.8% error for the 360°C / 90 MPa test. The error (E_{tot}) for the model performance is given by:

$$E_{tot} = \left|\frac{\sum(\varepsilon_{pred})}{\sum(\varepsilon_{meas})} - 1\right| \cdot 100\% \quad \log[t(\varepsilon)] = \frac{\log(t_r)+C}{1+(\frac{\log(\varepsilon)}{x_0})^p} - C \tag{3}$$

where ε_{pred} is predicted strain at given time and ε_{meas} is measured strain at given time. It should be noted that for the 360°C / 90MPa test creep strain results were only given from time range of 100 - 1200h.

In order to improve the performance of the LCSP model at lower temperatures a new calibration was carried out for the model using the datasets from [14, 16-18]. With optimized parameters the performance of the LCSP model was improved for temperatures and stresses relevant to normal operating conditions as shown in Figure 4. The model predictions were compared to the creep tests carried out at 360°C / 78 MPa and 360°C / 90 MPa for cold-worked and stress-relieved Zircaloy-4 material from [16, 17]. The LCSP model predicted satisfactorily the hoop strains with optimized parameters throughout the test times with 4.3% error for the 360°C / 78 MPa test and 11.8% error for the 360°C / 90 MPa test.

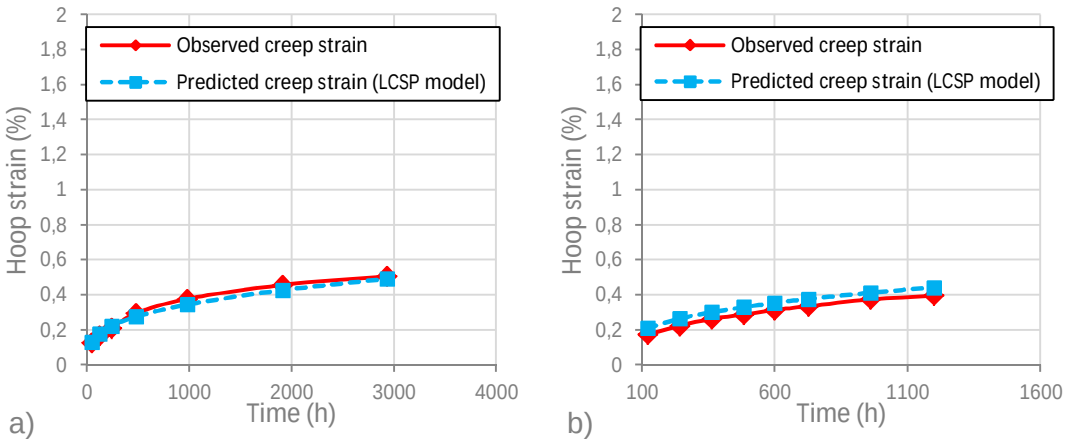

Figure 4. The creep test results a) 360°C / 78MPa [16], b) 360°C / 90MPa [17] and LCSP model predictions for cold-worked and stress-relieved Zircoloy-4 samples with optimized model parameters.

The performance of the LSCP model was also assessed in transient creep conditions. Originally the modelling approach utilizing the LCSP creep strain model and the Wilshire creep to rupture model is intended to describe the creep strain behavior of Zircaloy-4 under steady-state conditions. Thus, the application of this modelling approach requires an additional method to address the effects of changes in stress and/or temperature. A common method to account for the changes in temperature or stress for a steady-state creep model has traditionally been the utilization of time-hardening or strain-hardening rules. With the time-hardening rule the cumulative time at the point of stress or temperature change determines the creep strain rate, which is still calculated using the original model equation. For the strain-hardening rule, the cumulative creep strain is also determined by means of the original creep model equation, but the creep rate for changed stress or temperature level now depends on the cumulative strain so that strain must be tracked in the solution process as a path-dependent history variable.

To evaluate the model performance for load increase the LCSP model predictions were calculated using three different approaches; LCSP (primary) creep curve without hardening, LCSP time hardening and LCSP strain hardening. The predictions were compared to hoop creep strain data points from a test for a cold-worked and stress-relieved Zircaloy-4 specimen with 78 MPa stress at 390°C for 950 hours followed by stress increase to 148 MPa for 500 hours, as shown in Figure 5 [19].

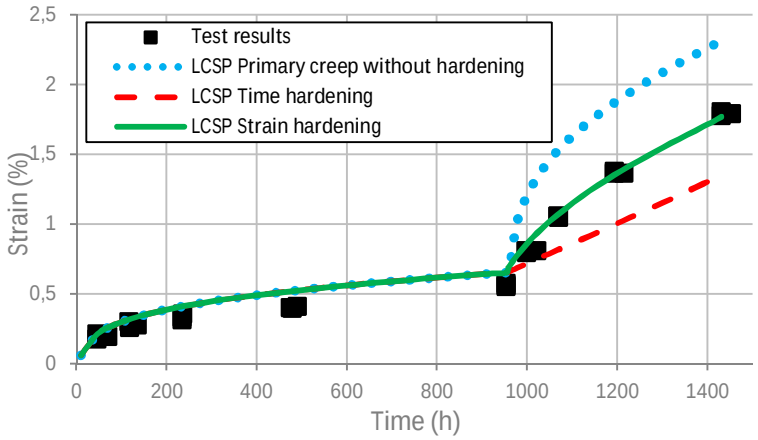

Figure 5. Experimental results for Zircaloy-4 hoop creep strain with load increase and LCSP model predictions [19].

The LSCP model predicted accurately the first part of the test (78MPa / 390°C / 950h). After the load increase the best performance was obtained by strain hardening method with 4.7% error. The error for LCSP (primary) creep curve without hardening method was 32.9% and 15.5% for LCSP time hardening method.

To evaluate the model performance for load reversals the LCSP model predictions were calculated using three different approaches; LCSP (primary) creep curve without hardening, LCSP time hardening and LCSP strain hardening. The predictions were compared to hoop creep strain data points from a test for a cold-worked and stress-relieved Zircaloy-4 specimen with load reversal from tensile stress of 148 MPa to compressive stress of 78 MPa and vice versa at 391°C with 250 hour intervals [19]. As expected, the LCSP model predicted accurately the first part (up to 250 hours) of the test, but none of the three approaches (LCSP (primary) creep curve without hardening, LCSP time hardening or LCSP strain hardening) was able to produce satisfactory predictions thereafter. Especially the hardening rule approaches underpredicted significantly the strain changes during load reversals.

3.2 Viscoelastic model

Several experiments investigating cladding creep response to stress transients have been performed at the Halden Boiling Water Reactor, the most successful to date being IFA-585 [24] and IFA-699 [25]. Halden reactor features the ability for on-line measurements of in-pile experiments, and these provide a valuable asset for model development and validation. It was observed in both IFA-585 and IFA-699 experiments that the total saturated transient creep is proportional to the change in the applied stress. This observation challenges the use of the strain hardening rule as there is no evidence of a hardening behaviour during subsequent stress steps.

The anelastic contribution to cladding mechanical behaviour has been investigated and accounted for in some models in the 1970s and 1980s [27, 28]. However, later on it has been neglected [23, 26, 29-34], either implicitly or explicitly, and several experimentally observed cladding transient responses have remained unexplained. A modelling approach taking the anelastic deformation into account [20-22] is here described via so-called mechanical analogues. These combine springs representing the elastic component of the material to dashpots representing the viscous components. The springs' displacement ϵ_i is linearly proportional to stress σ ($\epsilon_i = \sigma/\kappa_i$) and the dashpots' displacement rate is linearly proportional to stress ($\dot{\epsilon}_i = \eta_i \sigma$).

A model is constructed with a spring for elastic response, *n* number of parallel spring-dashpot ("Kelvin") units and a dashpot for creep deformation, all in series. While conventionally the creep deformation includes the primary creep, in this model the primary creep is as a whole given by the Kelvin units. This is in line with observed in-reactor creep behaviour [24, 25]. The system for *n* = 2 is displayed in Figure 6.

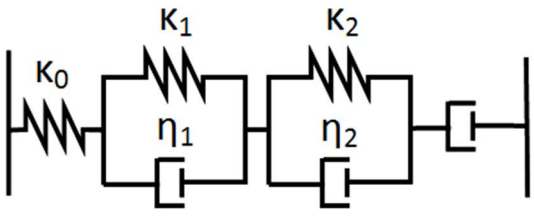

Figure 6. A mechanical analogue for the viscoelastic model.

The number of the components in a system as depicted in the Figure 6 as well as the non-linearity of most creep deformation correlations makes finding an analytical solution to the system challenging. A common engineering solution is to use the internal variable approach, where the strain of each individual component is calculated.

For stress relaxation an explicit numerical solution is used, calculating the stress arising from the elastic deformation of the lone spring based on the difference between the imposed strain and the strain of Kelvin units and the lone dashpot as per Equation (4). This stress determines the system stress as a whole. Then

the strains of the Kelvin units and the lone dashpot are calculated assuming the stress stays constant for the duration of the time step. The strains of the Kelvin units are calculated based on Equation (5) and the steady state creep strain from Equation (6):

$$\sigma(t) = (\epsilon_{tot}(t) - \epsilon_s(t) - \sum_{i=1}^{n} \epsilon_i(t))\kappa_0 \log[\mathrm{t}(\varepsilon)] = \frac{\log(\mathrm{t_r})+\mathrm{C}}{1+(\frac{\log(\varepsilon)}{\mathrm{x_0}})^{\mathrm{p}}} \text{-C} \quad (4)$$

$$\epsilon_i(t + \Delta t) = \epsilon_i(t) + (\sigma(t) - \epsilon_i(t)\kappa_i)\left(1 - e^{-\frac{\Delta t}{\tau_i}}\right)\kappa_i^{-1} \log[\mathrm{t}(\varepsilon)] = \frac{\log(\mathrm{t_r})+\mathrm{C}}{1+(\frac{\log(\varepsilon)}{\mathrm{x_0}})^{\mathrm{p}}} \text{-C} \quad (5)$$

$$\epsilon_s(t + \Delta t) = \epsilon_s(t) + f(\sigma(t))\Delta t \log[\mathrm{t}(\varepsilon)] = \frac{\log(\mathrm{t_r})+\mathrm{C}}{1+(\frac{\log(\varepsilon)}{\mathrm{x_0}})^{\mathrm{p}}} \text{-C} \quad (6)$$

where ϵ_{tot} is the total (imposed) strain, κ_0 the elastic spring constant, ϵ_i, κ_i and τ_i are the strain, spring constant and characteristic time of the *i*th Kelvin unit, ϵ_s is the steady state creep strain, Δt the time step used and $\sigma(t)$ the stress. The function $f(\sigma(t))$ denotes the steady state creep rate, which may be a simple function of stress or a more complex function such as the ones used by Matsuo [18]. This solution scheme requires using very short time steps.

For solving the system during imposed stress (creep experiment), Equations (5) and (6) can be directly used as the stress $\sigma(t)$ is known and each Kelvin unit as well as the lone spring and the lone dashpot experiences the same stress. In order to find out the strain of the whole system ϵ_{tot} the individual strain components are combined:

$$\epsilon_{tot}(t) = \frac{\sigma}{\kappa_0} + \epsilon_s(t) + \sum_{i=1}^{n} \epsilon_i(t) \log[\mathrm{t}(\varepsilon)] = \frac{\log(\mathrm{t_r})+\mathrm{C}}{1+(\frac{\log(\varepsilon)}{\mathrm{x_0}})^{\mathrm{p}}} \text{-C} \quad (7)$$

For the simulations initial values for the internal strains ϵ_i are needed. In this work an assumed value of $\epsilon_i(0) = 0$ has been used unless otherwise specified.

The cases investigated with the developed model were the in-pile experiments IFA-585 (BWR segment) [20, 24] and IFA-699 (Zircaloy-4 segment) [21, 25]. For the analysis the FRAPCON-3.4's steady state correlation was used [34] along with the anelastic model with coefficients as listed in Table 1. Model with *n*=1 was considered sufficient for creep experiments. There were uncertainties in the IFA-585 test results [24], especially related to the effect of the different rates of oxide layer growth between the sample and the end plugs and experimentally measured secondary creep rate [24]. For the steady state creep it has been noted that the IFA-585 experiment features very high secondary creep rates [24] compared to other creep experiments. This was also seen in the initial analysis. For IFA-585 analysis the FRAPCON-3.4 correlation used for secondary creep rate was multiplied by a factor of 2 in order to better match the experimental results.

The comparison between the simulated and measured strain, along with the applied effective stress for IFA-585 experiment, is shown in Figure 7. The mid-wall effective stress with positive values signifying tension and negative values compression is also shown in Figure 7. The match between the experiment and the simulation is good, especially at the beginning of the experiment. However, errors compound during the simulation. These can be mostly attributed to the uncertainties in the secondary creep rate. It can thus be argued that as the error seen in Figure 7 is mostly due to the uncertainty in the secondary creep rate, the creep response to stress reversal can be modelled using the viscoelastic model.

Table 1. Coefficients for the anelastic model used in this work.

Cladding	κ_0 (MPa)	κ_1 (MPa)	τ_1 (h)
IFA-585	N/A	$5.2*10^5$	100
IFA-699	N/A	$2.0*10^5$	40

For IFA-699 Zircaloy-4 experiment the measured values are shown as dots and the base simulation as the solid line in Figure 8. The measured values in Figure 8 consistently trend toward the positive (or tensile, outward) direction. An oxide growth contribution was included to the simulations according to Equation (8): [35]

$$w = Ke^{-Q_0/RT}t^{1.02474}\ \log[t(\varepsilon)] = \frac{\log(t_r)+C}{1+(\frac{\log(\varepsilon)}{x_0})^p} - C \quad (8)$$

where w is the oxide layer thickness in micrometres assuming a constant temperature, K = 23663.76 $\mu m \cdot h^{-1}$, Q_o/R = 8645.4 K is the activation energy term for the oxide formation, T = 625 K is the interaction layer temperature and t is time in hours. As the oxidation replaces metal with less dense oxide, the net effect is the increase of the apparent diameter by a fraction of one third of the oxide layer thickness. The creep with oxide layer contribution is shown with dashed line in Figure 8. This case would represent a situation where the Zircaloy-4 segment is heated by the fuel inside and thus oxidises faster than the measurement calibration piece which was assumed to be at coolant temperature (approximately 50 K lower than the test sample). The used oxide layer equation is a simple formula fitted to publicly available post-irradiation data for PWR fuels with Zircaloy-4 cladding, and as such caution should be used when utilizing it for samples in the Halden flask conditions.

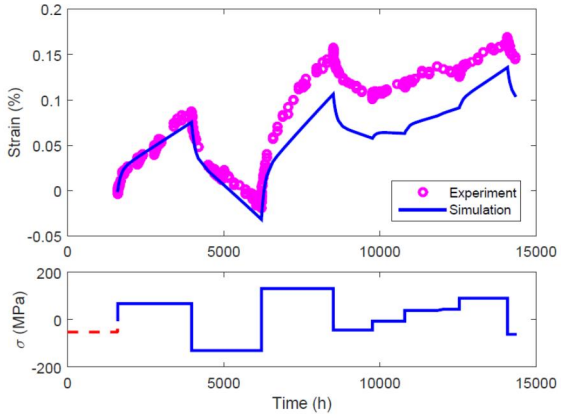

Figure 7. Comparison between IFA-585 measurements (circles) and the simulation (line) [24].

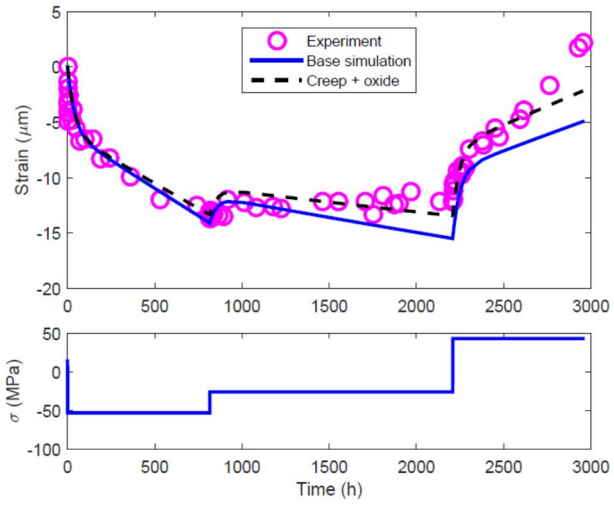

Figure 8. Comparison between IFA-699 Zircaloy-4 measurements (circles) and the simulated values (lines). Blue line corresponds to base simulation, the dashed black line includes an addition of an oxide layer contribution [25].

4. Discussion

The LSCP modelling approach has been satisfactorily implemented to predict the creep behavior of cold-worked and stress-relieved Zircaloy-4 fuel cladding materials in steady state creep conditions and in cases of simple load increase. However, a more advanced creep modelling approach than a one utilizing conventional strain hardening rule is desired when the loading history includes load drops and/or reversals, which are the situations where the strain-hardening rule is experimentally known to fail. Shifting the stress state between tension and compression leads to the resumption of primary creep and to relatively large changes in creep rate. Neither of these conditions are addressed by either standard time- or strain-hardening rules. It is an objective of further research to explore whether a methodology, which introduces internal state variables to a LCSP creep model to represent directional hardening and recovery, or some other methodology can be implemented into LSCP modelling approach to characterize the transient creep behaviour of zirconium based nuclear fuel cladding materials. It may also turn out that the LCSP modelling approach cannot be reasonably implemented to characterize the transient creep behaviour, which would mean that the development activities should be targeted towards the prediction of creep behaviour in storage conditions and/or “straightforward” system disturbance conditions, such as the one described in [9].

The viscoelastic model described in this paper is able to provide a qualitative interpretation of the observations on the cladding response to transient stresses such as load drops, creep reversal and stress relaxation. In scenarios where a commonly used strain hardening rule is known to work, such as stress increases, the viscoelastic model behaves similarly to strain hardening models. The observed time evolution of the primary creep can be explained by various concurrent processes operating at different time scales and approximated by a series of relaxation processes. The model can be used to simulate various creep experiments performed both in laboratory conditions and in-pile.

A future objective is to study whether the creep modelling approaches described above can be straightforwardly implemented to characterize the creep behaviour of Gen-IV candidate fuel cladding materials. It should be noted here that the zirconium-based alloys and candidate materials for Gen-IV fuel cladding exhibit significantly different material properties and the temperatures for the Gen-IV conditions are considerably higher.

5. Conclusions

Based on the research activities related to the creep behavior of fuel cladding materials, the following conclusions were drawn:

(1) The newly developed Pneumatic Loading Apparatus (PLA) for bi-axial creep testing is capable of performing demanding creep tests for fuel cladding materials with variable hoop:axial stress ratios and with temperature and/or stress transients.
(2) The LCSP modelling approach is capable of describing satisfactorily the steady-state creep behavior of Zircaloy-4 in cold-worked and stress-relieved condition with existing data.
(3) The viscoelastic modelling approach is able to provide a qualitative interpretation of the observations on the cladding response to transient stresses such as load drops, creep reversal and stress relaxation.

6. Acknowledgements

The authors wish to acknowledge the support from the Finnish SAFIR2018 project PANCHO, Academy of Finland project IDEA and TASTE project under the umbrella of EERA Joint Program Nuclear Materials.

References

1. Tulkki, V. Modelling nuclear fuel behaviour and cladding viscoelastic response. A doctoral dissertation. VTT Science: 109. 2015. ISBN 978-951-38-8346-1.

2. Adamson, R. et al. In Reactor Creep of Zirconium Alloys, A.N.T International 2009.

3. Dryepondt, S. et al. Advanced ODS FeCrAl alloys for accident-tolerant fuel cladding. Oak Ridge National Laboratory Report ORNL/TM-2014/380, Oak Ridge, Tennessee. 2014.

4. Fazio, C. et al. European cross-cutting research on structural materials for Generation IV and transmutation systems. J. Nucl. Mater. 392 (2009) 316-323.

5. Pohja, R. et al. Multifunctional high precision pneumatic loading system (HIPS) for creep-fatigue testing. Procedia Engineering. 55 (2013) 573-577.

6. Guimbal, P. et al. MELODIE, an advanced device for study of the irradiation creep of LWR cladding with online biaxial control of stress and strain. In: 12th Conference - IGORR International Group on Research Reactors. Beijing, China 2009.

7. Moilanen, P et al. New applications of pneumatically powered testing equipment for extreme environments. In: Baltica IX - International Conference on Life Management and Maintenance for Power Plants. Espoo, Finland 2013.

8. Delville, R. Guidelines for thermal creep and creep-rupture testing of material DIN 1.4970 cold worked for use as fuel cladding tube in MYRRHA. WP3 report for EU FP7 project MATTER. Belgium 2012.

9. Holmström, S. et al. Creep properties of Zircaloy-4 for nuclear fuel cladding FEA simulation. In: Baltica IX - International Conference on Life Management and Maintenance for Power Plants. Espoo, Finland 2013.

10. Holmström, S. and Auerkari, P. Robust prediction of full creep curves from minimal data and time to rupture model. Energy Materials, Materials Science & Engineering for Energy Systems. 1 (2006) 249–255.

11. Wilshire, B. et al. A new approach to creep data assessment. Mater. Sci. Eng. A 510-511 (2009) 3-6.

12. Lee, S. et al. Circumferential creep properties of stress-relieved Zircaloy-4 and Zr-Nb-Sn-Fe cladding tubes. J. Nucl. Mater. 392 (2009) 53-60.

13. Murty, K. The internal pressurization creep of Zr alloys for spent-fuel dry storage feasibility. Journal of Minerals, Metals and Materials (JOM). 52 (9) (2000) 34–38.

14. Limon R. and Lehmann, S. A creep rupture criterion for Zircaloy-4 fuel cladding under pressure. J. Nucl. Mater. 335 (2004) 322–334.

15. Mayuzumi, M. and Onchi, T. Creep deformation and rupture properties of unirradiated Zircaloy-4 nuclear fuel cladding tube at temperatures of 727 to 857 K. J. Nucl. Mater. 175 (1990) 135-142.

16. Matsuo, Y. Thermal creep of zircaloy–4 cladding under internal pressure. J. Nucl. Sci. Technol. 24 (1987) 111–119.

17. Nam, C. et al. Creep strength of Zircaloy-4 cladding depending on applied stress and annealing temperature. J. Nucl. Mater. 305 (2002) 70–76.

18. Kim, Y.-S. Generalized creep model of Zircaloy-4 cladding tubes. J. Nucl. Mater. 250 (1997) 164–170.

19. Matsuo, Y. Creep Behavior of Zircaloy Cladding Under Variable Conditions. ASTM STP-1023, (1989) 678-691.

20. Tulkki, V. and Ikonen, T. Modeling of Zircaloy cladding primary creep during load drop and reversal. J. Nucl. Mater. 445 (2014) 98–103.

21. Tulkki, V. and Ikonen, T. Viscoelastic modeling of Zircaloy cladding in-pile transient creep. J. Nucl. Mater. 457 (2015) 324–329.

22. Tulkki, V. and Ikonen, T. Modelling anelastic contribution to nuclear fuel cladding creep and stress relaxation. J. Nucl. Mater. 465 (2015) 34–41.

23. Lucas, G. and Pelloux, R. Some observations on time-hardening and strain-hardening rules for creep in Zircaloy-2. Nucl. Technol. 53 (1981) 46–57.

24. Foster, J. and McGrath, M. In-reactor creep behavior of zircaloy-2. In: Proceedings of the 2007 LWR Fuel Performance Meeting, 2007.

25. Hanawa, S. In-reactor creep behaviour of LWR fuel claddings: Initial results from IFA-699, HWR-882, 2008.

26. Rossiter, G. Development of the ENIGMA fuel performance code for whole core analysis and dry storage assessments. Nucl. Eng. Technol. 43 (2011) 489-498.

27. Murty, K. and Yoon, K. Prediction of creep transients in Zircaloy fuel cladding using anelastic strain model. In: Transactions of the 5th International Conference on Structural Mechanics in Reactor Technology (SMiRT-5), vol. C3/6, 1979.

28. Causey, A. et al. Measurement of irradiation creep of zirconium alloys using stress relaxation. J. Nucl. Mater. 159 (1988) 101–113.

29. Long, Y. et al. ZIRLO high performance fuel cladding material high stress creep model. In: Proceedings of 2010 LWR Fuel Performance Meeting. Paper 054, 2010.

30. Zhou, G. et al. Evaluation and modeling of in-reactor creep and stress-relaxation tests of ZIRLO fuel cladding under wide stress conditions. In: Proceedings of 2011 Water Reactor Fuel Performance Meeting. Paper T2–038, 2011.

31. Delobelle, P. et al. A model to describe the anisotropic viscoplastic behaviour of Zircaloy-4 tubes. J. Nucl. Mater. 238 (1996) 135–162.

32. Limbäck, M. and Andersson, T. A model for analysis of the effect of final annealing on the in- and out-of-reactor creep behavior of zircaloy cladding. ASTM STP-1295, (1996) 448–468.

33. Kozar, R. et al. In situ monitored in-pile creep testing of zirconium alloys. J. Nucl. Mater. 444 (2014) 14–22.

34. Geelhood, K. et al. FRAPCON-3.4: A computer code for the calculation of steady-state thermal-mechanical behavior of oxide fuel rods for high burnup. NUREG/CR-7022, Vol.1, 2011.

35. Kättö, J. Corrosion and its modeling in nuclear reactor fuel cladding. M.Sc thesis, Aalto University. 2013.

Overview of SCWR candidate materials stress corrosion tests

Aki Toivonen & Sami Penttilä

VTT Technical Research Centre of Finland Ltd
P. O. Box 1000, FI-02044 VTT, Finland

Abstract

Slow strain rate tests on several SCWR candidate materials were done over the last 10 years at VTT. The test materials were austenitic stainless steels with 15-23% Cr and 10-15% Ni and oxide dispersion strengthened ferritic/martensitic steels with 12-20% Cr. The tests were performed in supercritical water at 250 bar in the temperature range of 500-650^{o}C with 100-150 ppb dissolved oxygen. With regards to the stress corrosion susceptibility and ductility, the best performer in the tests was AISI 316L steel. On the other hand, large heat to heat variation can be expected: another heat of 316L was very susceptible to intergranular stress corrosion cracking. DL-EPR test revealed that at least some heats of low carbon 316 are subject to fast thermal sensitisation at 550^{o}C in supercritical water.

1. Introduction

Supercritical water reactors (SCWR) require materials that are resistant to high temperature supercritical water, have adequate strength, and, in some locations, are as transparent to fission neutrons as possible. No single cladding alloy has been identified for the thin-walled fuel pins of SCWRs that can well meet these operational requirements. General corrosion and stress corrosion cracking (SCC) resistances are two important requirements. The fuel cladding is thin, in the range of 0.5 mm, and has to have low content of neutron absorbing alloying elements as possible. Zr-alloys are used as a cladding material in present day LWRs because of their good neutron transparency. Tests have shown that some Zr-alloys form a stable and protective oxide film in the SCWR conditions at temperatures up to 500^{o}C [1]. However, the peak cladding temperature of European High Performance Light Water Reactor (HPLWR) is ~630^{o}C which is too high for Zr-alloys. The coolant outlet temperature of the HPLWR is 500^{o}C.

Ferritic–martensitic (F/M) steels have superior SCC resistance in supercritical water. On the other hand, they suffer from high oxidation rates in SCW. Austenitic stainless steels and Ni-base alloys have better oxidation resistance but both are more susceptible to SCC than F/M steels. Ni-base alloys are not wanted for internal core components of SCWR due to high Ni concentration. Nickel has a high neutron absorption cross section compared to Fe or Zr. A higher enrichment is needed for UO_2 fuel if high Ni alloys are used. Ferritic/martensitic oxide dispersion strengthened (ODS) steels are one of the long term candidate material groups for in-reactor applications. They have, typically, Cr content in the range of 9 to 20 % (w) and the rest is mainly Fe. High temperature strength and creep resistance follow from nano-scale yttrium oxide particles. Higher Cr range ODS steels are also as resistant against general corrosion as austenitic stainless steels. Unfortunately, they are expensive due to the difficult manufacturing processes and they

are typically rather brittle. The SCC resistance of the ODS steels in SCW is not a clear issue. As F/M steels, they can be assumed to be resistant to SCC in SCW. However, there has previously not been much SCC test data publicly available on the ODS steels.

Tests have been done at VTT on F/M ODS and austenitic stainless steels within EU FP 6 and 7 programs in projects GETMAT, HPLWR Phase 2, and SCWR-FQT. The results are summarized in this report.

2. Experimental procedures

2.1 Test procedures

The tests were slow strain rate tensile (SSRT) test in supercritical water and air. The strain rate during the tests was either 3e-7 1/s or 1e-7 1/s. After the tests, the fracture surfaces and the side surfaces of the gauge sections of the specimens were studied and photographed with a scanning electron microscope (SEM). For two heats grain boundary sensitivity tests were performed.

2.2 Test materials and matrices

Different materials or different heats of the same nominal materials were tested in the above mentioned three EU projects at VTT.

GETMAT:
Two actual GETMAT materials, 12 and 14% Cr containing ODS steels, and additionally PM2000, were tested at 550^{o}C in SCW. The 12Cr and 14Cr ODS steels were tested also at 650^{o}C in SCW. PM2000 was tested additionally at 550^{o}C in air. The compositions are given in Table 1.

Table 1. Chemical compositions of the GETMAT ODS steel (w%), Fe = balance.

Material	Cr	Ni	W	Mn	Ti	Al	Si	Other
12Cr ODS	12		2		0.25			0.2Y
14Cr ODS	14	0.15	1	0.3			0.3	0.3Y
PM2000	20	0.03		0.0.08	0.43	5.5	0.02	0.5Y

HPLWR Phase 2:
Five materials were tested at 500^{o}C in SCW: PM2000, 316NG, 1.4970, BGA4 and 347H. Three of those materials, 316NG, 1.4970 and 347H, were tested also at 650^{o}C in SCW. The compositions of the austenitic stainless steels are given in Table 2. The PM2000 was not of the same heat as was tested in the GETMAT project but the composition is assumed to be close to that presented in Table 1. Of the tested steels, BGA4 is an experimental creep resistant steel with high Cr and Mn contents.

Table 2. Chemical compositions of the HPLWR Phase 2 steels (w%), Fe = balance.

Material	C	Si	Mn	P	S	Ni	Cr	Mo
316NG	0.014	0.42	0.8	0.032	0.001	11.3	16.6	2.11
1.4970	0.095	0.53	1.68	0.007	0.001	15.3	15	1.18
BGA4	0.11	0.49	6.1	0.024	0.0024	15.4	22.9	0.14
347H	0.048	0.29	1.84	0.013	0.013	10.7	17.58	-

SCWR-FQT:
Initially, three materials were selected for SSRT tests in the beginning of the SCWR-FQT project, 316L, 347H and 08Cr18Ni10Ti which is analogous to grade 321 stainless steel. Later on one additional material was selected in order to have a look at the heat-to-heat or product form influence on the SCC susceptibility. The initially tested 316L, 347H and 08Cr18Ni10Ti were in the form of (cross-) rolled and annealed plates and the tube was cold drawn, annealed and pickled. The chemical compositions are shown in tables 3 and 4.

Table 3. Chemical composition of the initially tested stainless steels (w%), Fe = balance.

Material	C	Si	Mn	S	P	Cr	Ni	Others
316L	0.22	0.65	1.86	0.001	0.03	16.6	10.12	Mo = 2.06
347H	0.048	0.29	1.84	0.013	0.026	17.6	10.7	Nb = 10xCmin to 1.0 max
O8Cr18Ni10Ti	0.085	0.45	1.07	0.009		18.0	10.0	Ti = 0.64

Table 4. Chemical composition of the additional 316L tube (w%), Fe = balance.

C	Si	Mn	P	S	Ni	Cr	Mo
0.024	0.45	1.26	0.033	0.001	12.06	16.3	2.06

2.3 Specimens

The specimens were mostly plate type tensile specimens. The additional tests on the 316L tube material in the SCWR-FQT project were sectors cut from a tube with mainly the same dimensions as those of the plate specimens. The plate specimens were polished with #600 emery paper after cutting. The surfaces of the specimens cut from the tube remained in the as-received condition except that the side surfaces (cutting surfaces) were polished with the #600 emery paper. In addition to specimens cut from the as-received tube, two specimens were cut from a tube that had a circumferential TIG weld in it. 316L filler metal was used for the TIG weld. Two of the four specimens cut from the tube without the weld remained in the mill-annealed/pickled/polished condition and two specimens were shot peened prior to the tests (the cutting surfaces of the weld and shot peening specimens were also polished). The reasons of the tests on welded and shot peened specimens were that welds have not much been studied in SCW and surface cold work has been shown to increase general corrosion resistance in SCW in some cases but at the same time is detrimental to SCC resistance at least in subcritical LWR water. The specimen geometries and cutting plans are shown in Figure 1.

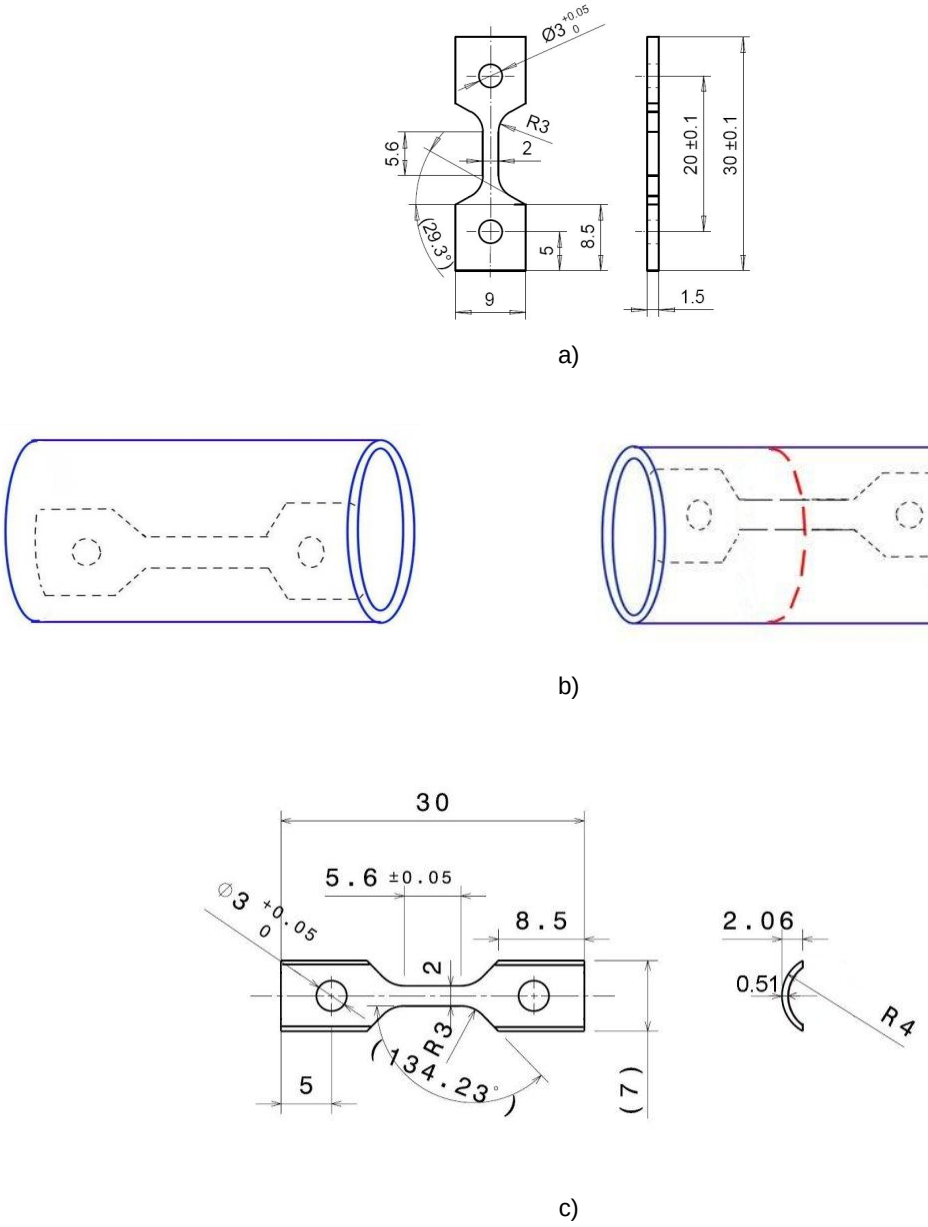

Figure 1. Geometry of the plate type specimen cut from larger samples used in most of the tests a) cutting schematic of specimens from as-received or shot peened ~8x0.5 mm tube (left hand side) and from a tube that had a circumferential TIG weld in it (right hand side) b) and geometry of the specimens cut from the ~8x0.5 mm tube.

2.4 Test equipment and environment

The specimens were exposed to high temperature water in a supercritical autoclave which was connected to a recirculation water loop, Figure 2. The maximum working temperature and pressure of the system at VTT is 700°C and 42 MPa, respectively. The high pressure loop is pressurised using a diaphragm pump and a back pressure regulator. The maximum flow rate of the high pressure loop is 5 dm^3/h. The SSRT tests were performed using a stepper motor controlled loading device. The tests were performed in SCW with inlet oxygen content between 100 and 150 ppb. During the tests the inlet water conductivity was

below 0.1µS/cm and outlet conductivity between 0.2 and 0.5 µS/cm. Outlet oxygen content could not be measured because of slow flow rate used in the tests, 2-10 ml/min (flow rate was limited due to stability reasons). The reference tests in air were performed in the same autoclave using the same loading equipment as in the tests in SCW.

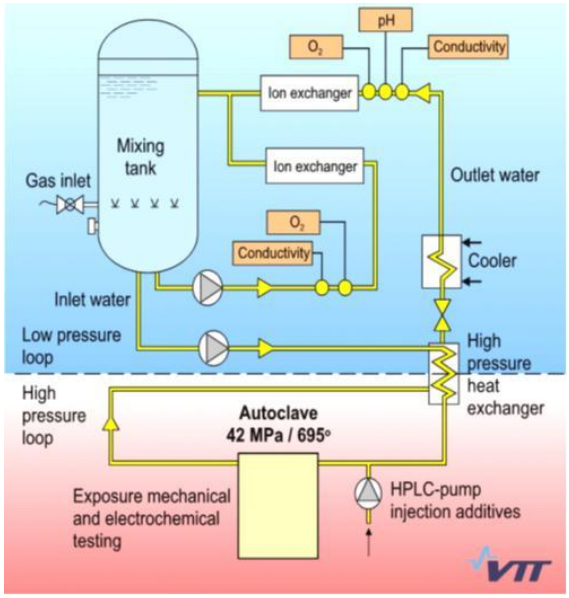

Figure 2. A schematic presentation of the SCW testing system at VTT.

3. Results and discussion

GETMAT:

The SSRT stress-strain curves of all tests are shown in Figure 3 and the main results are collected in Table 5. All steels exhibited minimal strain hardening both at 650°C and 550°C. The 12Cr and 14Cr ODS steels showed clearly higher ductility and strength at 550ºC than at 650°C. At 550°C the strains to failure were ~12 - 18% and the ultimate tensile strengths ~470 - 510 MPa. At 650°C, the failure strains were only ~3 - 4% and the ultimate tensile strengths 320 - 380 MPa. Due to negligible strain hardening, the yield and ultimate tensile strengths were in the same range. The yield strengths were determined at 1.0% permanent strain instead of the typically used 0.2% due to distinguishing problems related to the low stiffness of the testing machine. The measured strengths and ductilities of the specimens were considerably lower than reported in GETMAT deliverables [2, 3]. The most apparent reason for the differences is the applied strain rate. The previously reported values [2, 3] were obtained by standard tensile tests while the results of this work were obtained by slow strain rate tests.

The appearances of the gauge sections and fracture surfaces of the 12 and 14Cr specimens after tests at 550°C are shown in Figures 4 and 5. The fracture surfaces were covered by thick oxide layers and the microscopic morphology (brittle/ductile, intergranular/transgranular) could not be determined. Overall the appearance of the 12Cr ODS steel fracture surface is very planar without any clear features whereas the appearance of the fracture surface of 14Cr ODS steel reveals the under-laying microstructure of the steel. The fracture surface of the 14Cr ODS steel specimen resembles intergranular stress corrosion cracking, but that may also result from the microstructure of the material instead of any environmental effect. The appearances of the fracture surfaces were similar after tests at higher test temperature (650°C), Figure 6.

In the case of the 12Cr ODS steel, the sides of the gauge section were filled with numerous secondary cracks. Similar side cracking has been observed on ferritic-martensitic forged steels after SSRT tests in SCW [4]. In ref [4] the cracking is attributed to the oxide film: brittle failure of the film results in oxidation of the revealed metal and subsequent re-cracking due to stress concentration. On the 14% Cr ODS steel, either the mechanical properties and/or smaller thickness of the film prevent this process.

Both 12 and 14Cr ODS steels show higher strength compared to the high Cr ODS steel PM2000. The yield and ultimate tensile strengths of PM2000 were in the range of 110 - 120 MPa at 550°C in SCW and also in air. The strength values are below those given by the original materials supplier [5]. However, the history of the tested heat is not known and the low strengths may be a result of recrystallization. No side cracking was observed and the tests, when they were continued till the specimens failed, resulted in ~100% necking without any clear fracture surface.

In general, SCC tests in supercritical water have shown that SCC is a significant problem throughout the SCWR temperature range, i.e. from 290°C (feed water) to 650°C (~outlet water or cladding temp.) with austenitic stainless steels and nickel base alloys (< 20% Cr) and, in a lesser degree, with F/M steels [6-11]. However, very little data is available in open literature for the SCC susceptibility of ODS steels in SCW environment. No clear evidence of SCC was observed in this work, either.

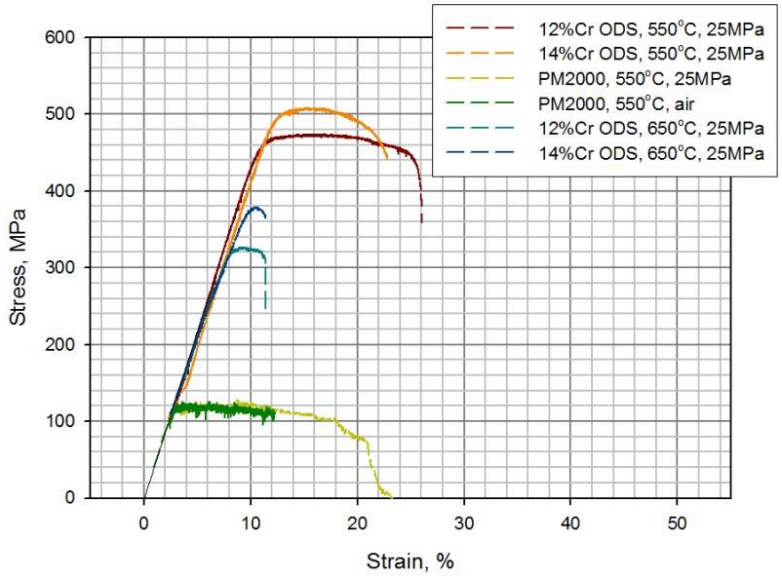

Figure 3. Stress-strain curves of the studied ODS steel in SCW and/or air conditions at 550°C and 650°C. Strain rate was 3e-7 1/s.

Table 5. Summary of GETMAT SSRT tests on three ODS steels at 550 and 650°C in SCW / air.

Specimen / temperature	$Rp_{1.0\%}$	Rm, MPa	Ap, % at max stress	Ap, % at failure	Fracture mode	Side cracks
12Cr ODS @ 550°C	465	473	4.3	17.8	Brittle*	Oxide cracking**
12Cr ODS @ 650°C	325	327	1.4	6.0	Brittle*	Oxide cracking**
14Cr ODS @ 550°C	502	507	3.9	12.1	Brittle* (macroscopically resembles IGSCC)	No
14Cr ODS @ 650°C	378	379	1.4	2.7	Brittle* (macroscopically resembles IGSCC)	No
PM2000 @ 550°C	118	120	6.1	23.3	Ductile	No
PM2000 @ 550°C in air	119	119	1.3	interrupted at 9.9	-	No

*Brittle based on negligible reduction in area. Microscopically could not be determined due to oxidation.
**Side cracks caused by brittle repeatedly cracking oxide film.

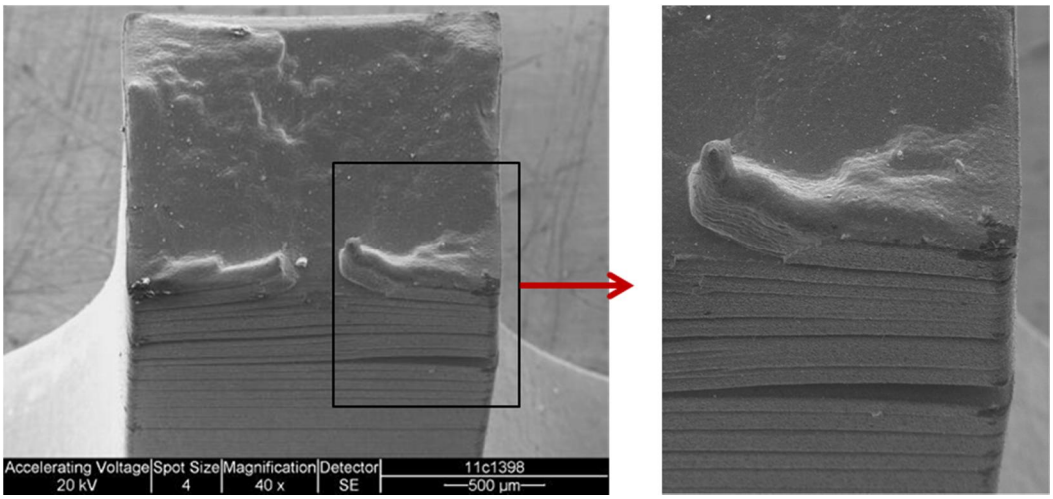

Figure 4. Post-test SEM photograph of the fracture surface of 12Cr ODS steel specimen after test in SCW at 550°C.

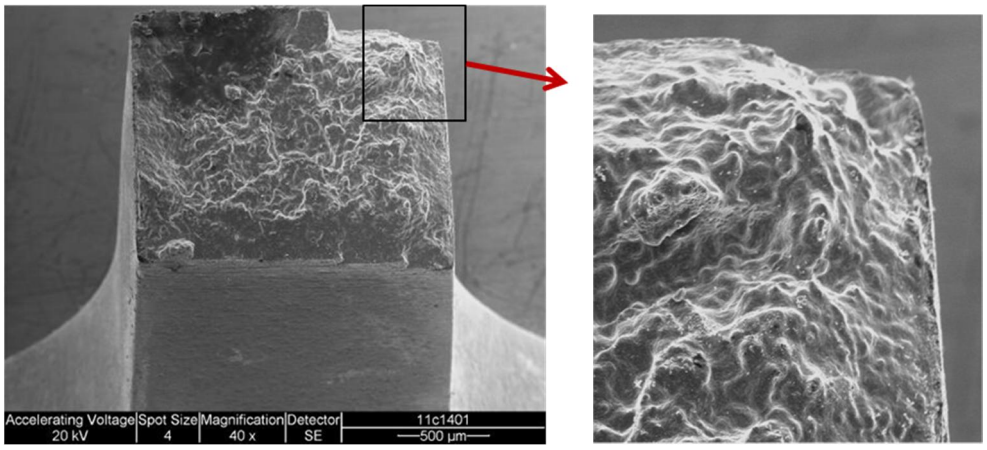

Figure 5. Post-test SEM photograph of the fracture surface of 14% Cr ODS steel specimen after test in SCW at 550°C.

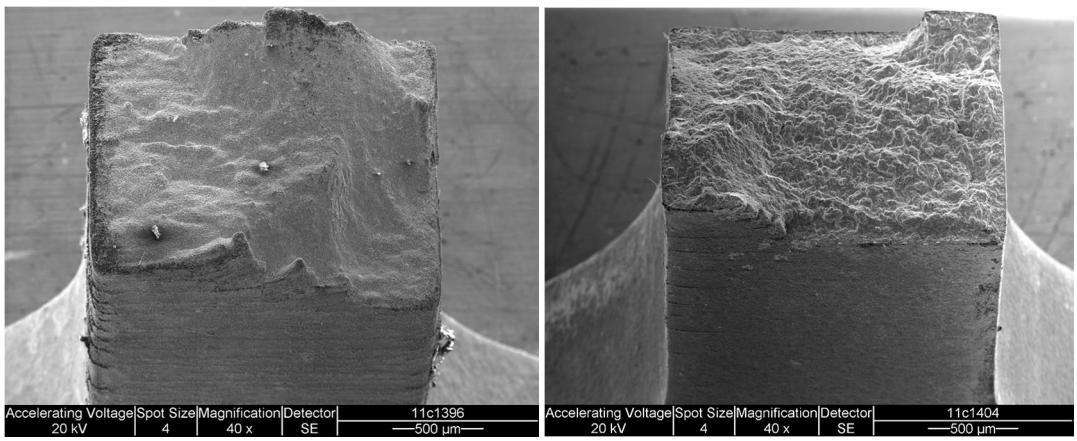

Figure 6. Post-test SEM photograph of the fracture surface of 12Cr ODS (left) and 14Cr ODS steel specimens after test in SCW at 650°C.

HPLWR Phase 2:

Stress-strain curves of the tested specimens at 500°C and 650^{o}C are shown in Figures 7 a) and b), respectively. All austenitic stainless steels exhibited strain hardening at 500°C although the degree of strain hardening of 1.4970 was rather low. The low degree of strain hardening resulted from cold work done when the component from which the specimen was cut was prepared. Typically all austenitic stainless steels behave in the same way as 1.4970 after cold work. Cold work also decreases the strain to failure, which can be seen in Figure 7 a when 1.4970 steel is compared to the other austenitic stainless steels which were in solution annealed condition.

The oxide dispersion strengthened steel PM2000 shows two different yielding values because the specimen was loaded using a strain rate of 3e-8 1/s in the beginning after which the strain rate was changed to 3e-7 1/s (at about 10% strain). The sudden increase in the stress level when the strain rate was changed indicates that there is a time dependent component present in the stress-strain behavior, i.e., creep. The PM2000 specimen did not show any considerable strain hardening.

When Figures 7 a) and b) are compared, it is evident that the test temperature has a considerable influence into the stress-strain behavior of all of alloys tested at both temperatures. All strength values have decreased considerably as the test temperature has been increased from 500 to 650^{o}C (strain rate was the same, 3x10^{-7} 1/s, in both cases). Especially remarkable decrease has taken place in the yield stress of PM2000, which has decreased to ~1/3. The reason for this decrease is probably again related to re-crystallisation as in the GETMAT tests. The decrease in the yield stress was confirmed by performing a second test (interrupted at 17% strain) using the same test parameters, Figure 7 b).

Post-test SEM studies of the SSRT specimens showed that 347H, 316NG and 1.4970 are possibly slightly susceptible to SCC at 500°C. No clear SCC was observed on the fracture surfaces, but on side surfaces there were small cracks of which morphology, however, could not be identified except in the case of 316NG (which had both inter and transgranular cracks. On the other hand, the experimental creep resistant steel BGA4 specimen contained a considerable amount of IGSCC both on the fracture surface and the side surfaces. At 500^{o}C, PM2000 did not show any susceptibility to SCC at all. Examples of the fracture surfaces are shown in Figures 8 and 9 (1.4970 and BGA4 tested at 500^{o}C, respectively).

Post-test SEM examination of 316NG specimen after the test at 650^{o}C revealed both IGSCC and TGSCC on the fracture surface, but no cracks were observed on the side surfaces. The fracture surface of the 1.4970 specimen was badly oxidized and the fracture morphology could not be identified. This specimen had also cracks on the side surfaces, but as after the test at 500^{o}C, the morphology did not have clear transgranular or intergranular features. PM2000 did not show any stress corrosion or other types of cracking, but necking continued until the specimen failed (i.e., the fracture location was almost “knife edge” sharp). The main observation made from the SSRT tests are collected into Table 6.

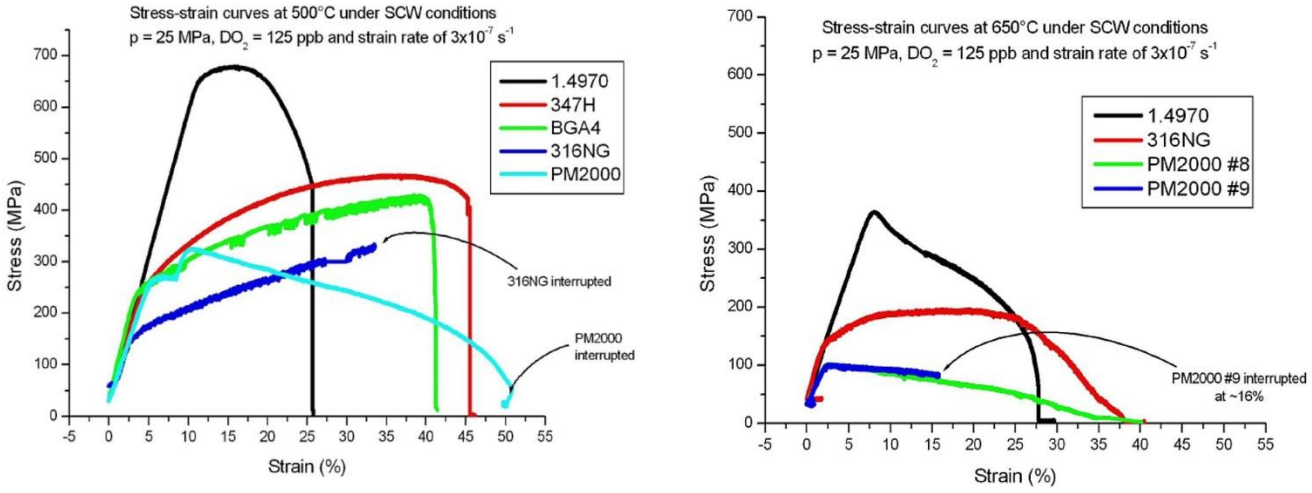

Figure 7. Stress-strain curves of the studied alloys in SCW conditions at a) 500°C and b) 650°C. Strain rate was 3e-7 1/s (except in the beginning of the test of PM2000 at 500°C the strain rate was 3e-8 1/s).

Table 6. Summary of HPLWR Phase 2 SSRT tests at 500°C and 650°C in SCW.

Alloy	Rm, MPa	Ap, %	TGSCC (y/n)	IGSCC (y/n)
347H@ 500°C	455	39	No	No
316NG@ 500°C	Interrupted at 325	Interrupted at 28	No	No
316NG@ 650 °C	190	38	Yes	Yes
1.4970 500°C	640	18	No	No
1.4970@ 650°C	360	28	Badly oxidized	Badly oxidized
BGA4 500°C	240	35	Yes	Yes
BGA4 650°C	NA	NA	NA	NA
PM2000@ 500°C	320	Interrupted at 50	No	No
PM2000@ 650°C	100	40	No	No

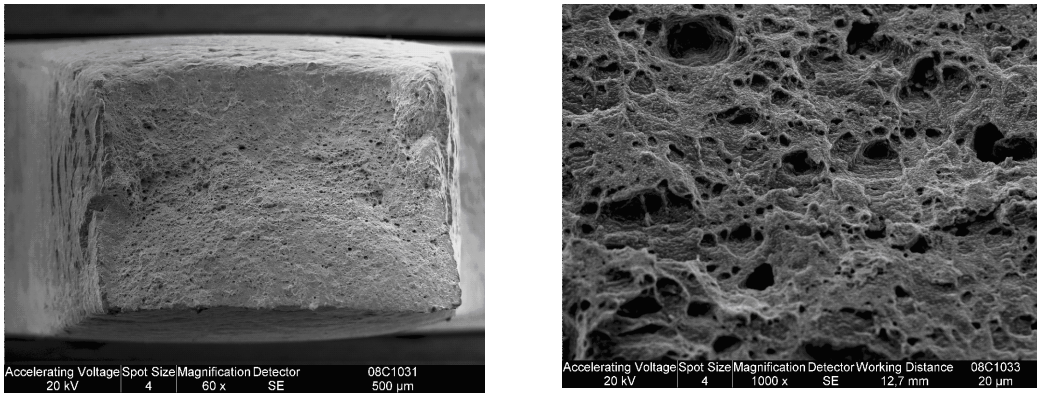

a) b)

Figure 8. SEM images of the fracture surface of stainless steel 1.4970 after SSRT at 500°C. The SEM photograph shows ductile dimple cracking on the main fracture surface.

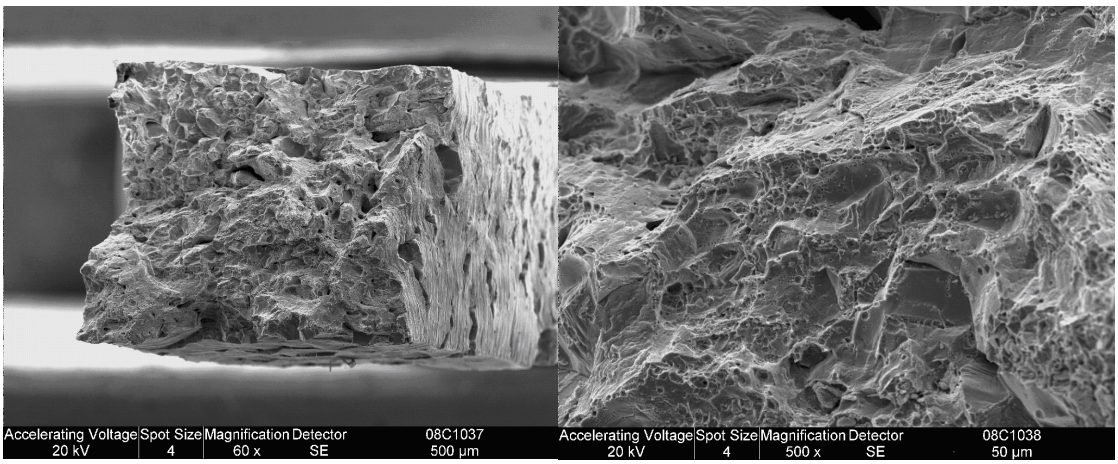

a) b)

Figure 9. SEM images of the fracture surface of alloy BGA4 after SSRT at 500°C showing ductile dimple cracking, TGSCC and IGSCC on the main fracture surface.

SCWR-FQT:

The SSRT test results of all initially selected materials are shown in Figure 10. All austenitic stainless steels except 08Cr18Ni10Ti exhibited considerable strain hardening at 550°C in SCW. 316L showed the highest ductility. 347H and 08Cr18Ni10Ti had only half of the strain to failure of that of 316L. Grade 08Cr18Ni10Ti showed the lowest strength of all three steels. Indications of transgranular stress corrosion cracking were seen on the fracture surfaces and side surfaces of other austenitic stainless steels except 316L which showed only ductile dimple cracking and no side cracks. An example SEM photograph of the fracture surface of the 08Cr18Ni10Ti specimen is shown in Figure 11.

The main observation made from the initial SSRT tests are collected into Table 7. In the tests performed within HPLWR Phase 2, the SSRT tests indicated that 316L might be susceptible to SCC at 500^{o}C although that was not seen in the initial SSRT tests performed in SCWR-FQT project. The HPLWR Phase 2 tests were performed with “316NG”, which actually is 316L with some nitrogen alloying (typically also 316L has some nitrogen in order to increase yield strength). Therefore additional tests were performed on the 316L tube material within the SCWR-FQT project.

The SSRT curves of the additional 316L tests are shown in Figures 12 a) and b). The curves in Figure 12 a) were measured in air at 550^{o}C and the curves in Figure 12 b) in SCW at the same temperature. For

comparison purpose the curves measured on the initial 316L heat are shown in the same figures. In the tests performed in air the yield strengths of the as-received and the welded tube material were in the same range as that of the initially tested plate material. However, the elongations to failure were larger and also the tensile strengths. No notable differences can be seen between the as-received and the welded tube specimens.

Yield and tensile strengths of the shot-peened tube specimen were much higher than those of the other specimens. Also, the elongation to failure decreased to less than half of those of the other specimens. These changes follow from the strain hardening caused by the shot-peening process. The fracture surfaces of all specimens tested in air were fully ductile with related dimpled structure.

A very notable decrease in mechanical performance caused by the SCW environment can be seen in the maximum stresses and elongations to failure in all of the specimens cut from the ~8*0.5 mm tube. However, no notable change can be seen in the yield stress, maximum stress or elongation to failure in the case of the initially tested 316L specimen cut from the plate. The decrease in the values of the tube specimens is related to the change in the failure mechanism: a considerable amount of intergranular cracking was seen on the fracture surfaces of the tube specimens, Figure 13. Yield strengths (Rp1.0%), ultimate tensile strengths and strains to failure are shown in Table 8 and examples of the fracture surfaces in Figure 14.

It was expected that the two heats of mill-annealed 316L steel would behave in a similar manner in SSRT tests in SCW. Both heats have rather similar mechanical properties in air (except the specimen hardened by shot-peening), similar chemical compositions (slightly more Ni in the tube), similar grain sizes and both were annealed after cold drawing or cross rolling.

The Double Loop EPR test results give an indication of the underlying reasons for the different behaviour of the two heats (Table 9): the specimens exposed to SCW have Ir/Ip (catodic/anodic current peaks during the polarisation loop) ratios of 0.04 (plate) and 0.049 (tube). According to the standard EN ISO 12732, the ratios below 0.01 indicate that the material is not sensitised, 0.01-0.05 indicates it is slightly sensitised and >0.05 indicates that it is sensitised [12]. The Ir/Ip ratio of the fresh tube is below 0.01. Cathodic current peak could not be distinguished from the polarisation curve. No fresh samples were available from the initial SCWR-FQT 316L plate.

Although it seems that the critical degree of sensitization for intergranular cracking in the specific SSRT test/test environment combination is between the Ir/Ip ratios of 0.04 and 0.049, the reason for the different degree of sensitisation is not very clear. Although low carbon austenitic stainless steels are generally considered resistant to sensitisation, long exposures to high temperature can result in carbide growth/sensitisation in the grain boundaries in them. The sensitisation typically takes place faster the higher the carbon content. However, the carbon contents of the tested two heats are close to each other and the less sensitised heat was exposed to SCW at 550^{o}C for considerably longer time (i.e. ~1500 h vs. ~500 h).

Several issues have been recognised to affect the sensitivity to intergranular stress corrosion cracking or degree of sensitisation (DOS). All of them are not linked to grain boundary carbide growth.

- Parvathavarthini et al. [13] propose that Grain boundary engineering in order to produce lower effective grain boundary energy (EGBE) lowers the tendency to sensitisation. EGBE is a combined factor of several aspects of the nature of the grain boundary.

- According to Parvathavarthini et al. [14], the limit of carbon content with which a steel is not susceptible to sensitization is closely connected to the presence of other alloying elements like chromium, molybdenum, nickel, nitrogen, manganese, boron, silicon as well as titanium and niobium in stabilized steels. Chromium has a pronounced effect on the passivation characteristics of stainless steel. With higher chromium contents, time to reach the resistance limit of chromium depletion at the grain boundaries is shifted to longer time. Alloys with higher chromium contents will be more resistant to sensitization.

- Oh et al. [15] report that their DL-EPR test results indicate that cold work (CW) levels up to 20% enhance sensitization while 40% CW suppresses sensitization at all aging times. Also, the increase in the nitrogen content at the similar carbon content accelerated the sensitization at CW levels below 20%.

- Deformation type during production (e.g. cross rolling of a plate vs. cold drawing of a tube) results in different microstructures. Nezakat et al. [16] report that rolling mode in their tests had a direct effect on the deformation texture of the remaining austenite. Unidirectional rolling resulted in Brass, Goss and γ-fibre textures, whereas cross-rolling formed mainly Brass texture in deformed austenite after 90% reduction in thickness.

- The effect of grain size on the intergranular corrosion susceptibility of 316L stainless steel was investigated by Li et al. [17]. Both DL-EPR tests and microstructure inspections of 316L with different grain sizes showed that the susceptibiltity to intergranular corrosion decreased with increasing grain size. Li et al. [17] suggest that increasing grain size to an optimum level could be an effective way to increase the intergranular corrosion resistance, but on the other hand, it is a big challenge to improve corrosion resistance without losing good mechanical properties resulting from small grain size.

- Terada et al. [18] reported DL-EPR test results of 316L(N) steel creep tested at the temperature of 600^{o}C for 7500 h and for 85000 h. The DL-EPR tests showed clear sensitisation to intergranular corrosion. However, they did not observe $M_{23}C_6$ carbides at grain boundaries. Instead, they attribute the sensitisation to intergranular corrosion to intermetallic phases (mainly sigma phase).

At the present stage, the underlying reason for the different behaviour of the two heats tested here is not clear. The microstructures of the steels in as-received (mill-annealed) conditions as well as after the exposure to SCW should be studied more closely before any comparisons to the results of the above mentioned authors can be done.

Based on the fact that the mill-annealed tube was sensitised during the exposure, it is not surprising that the shot-peened specimen also failed by intergranular fracture. Shot-peening was performed in order to simultaneously increase the yield strength of the steel and also to decrease its oxidation rate which both would be beneficial to SCWR fuel cladding. The oxidation rate of austenitic stainless steels has been observed to decrease by surface cold work [19]. Cold work also increases the yield strength but at the same time increases the risk of SCC. In this case, the increased risk could not be distinguished due to the susceptibility already present in the mill-annealed (+exposure to SCW) condition.

The weld specimen failed in the middle of the weld. The fracture mechanism was intergranular/inter-dendritic. The strain to failure and also the yield and tensile strengths were very similar to those of the mill-annealed specimen, i.e. apparently the degree of sensitisation was similar as or higher than the degree of sensitisation in the base metal. Typically, in sensitised stainless steels, stress corrosion initiates and propagates in the heat affected zone (HAZ) of the weld due to thermal sensitisation resulting from the heat input of the welding process. Apparently the welding process did not result in excess sensitisation of the HAZ in this case.

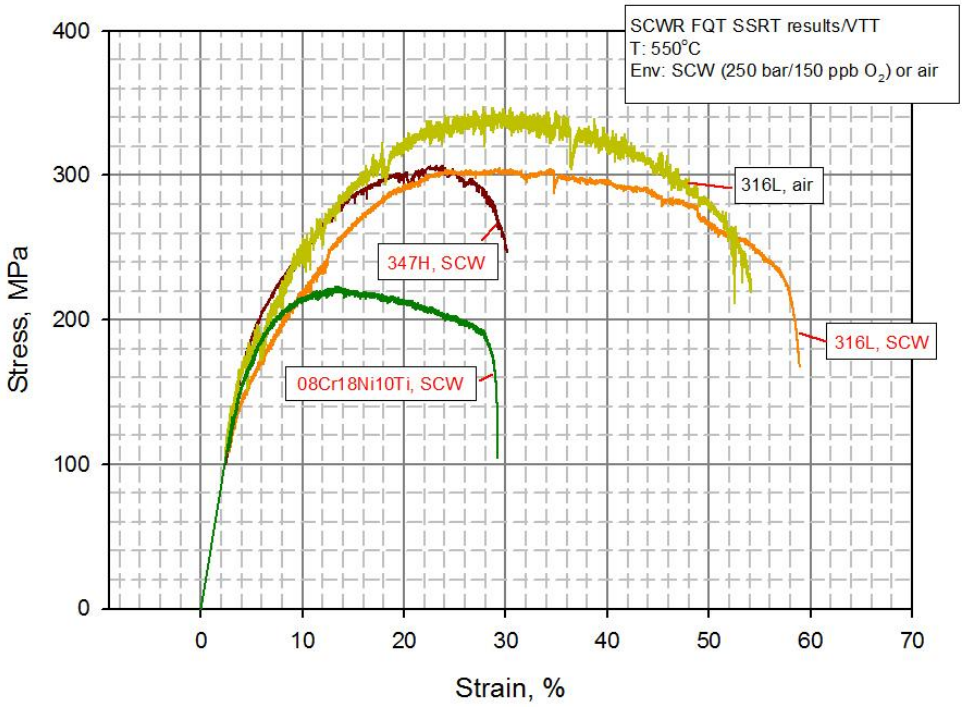

Figure 10. Stress-strain curves of the initially selected SCWR-FQT steels in SCW and air at 550°C. Strain rate was 1e-7 1/s.

Table 7. Summary of the initial SCWR-FQT SSRT tests performed at 550°C in SCW.

SCWR-FQT ($1x10^{-7}$ 1/s)	$Rp_{0.2\%}$, MPa	Rm, MPa	Ap, %	TGSCC (y/n)	IGSCC (y/n)	Side cracks (y/n)
316L @ 550°C	138	305	55.2	n	n	n
347H @ 550°C	181	307	24.1	y	n	y
08Cr18Ni10Ti @ 550°C	155	223	26.8	y	n	y

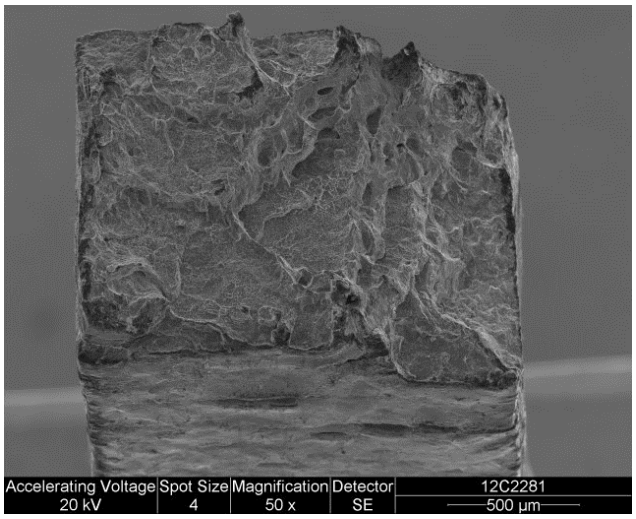

Figure 11. Fracture surface of 08Cr18Ni10Ti steel specimen after a test in SCW at 550°C.

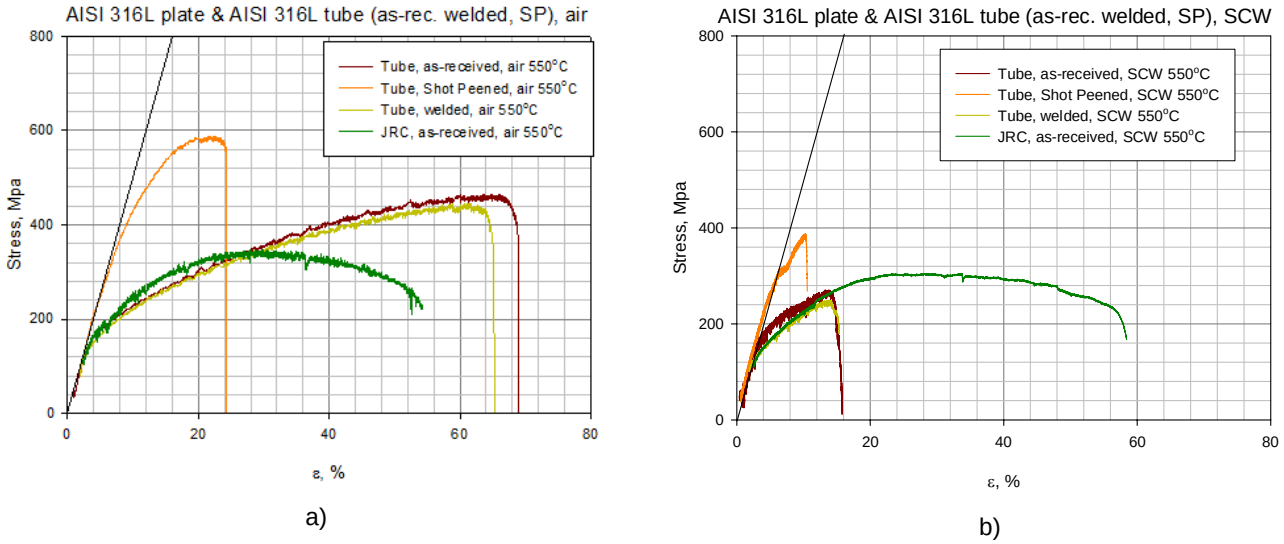

Figure 12. Stress-strain curves of the additional 316L SCWR-FQT steel in air a) and SCW b) at 550°C. Strain rate was 1e-7 1/s in each test. The initial 316L results are also shown for comparison.

Table 8. Yield strengths ($Rp_{1.0\%}$), ultimate tensile strengths (Rm) and plastic strains to failure (Ap) of the two 316L heats tested within SCWR-FQT project.

Material	Environment	$Rp_{1.0\%}$, MPa	Rm, MPa	Ap, %	Fracture mode
Plate	Air	170	340	49	Ductile
Plate	SCW	155	300	55	Ductile
Tube, mill-annealed	Air	170	460	61	Ductile
Tube, mill-annealed	SCW	180	265	16	Intergranular
Tube, welded	Air	160	440	58	Ductile
Tube, welded	SCW	145	245	12	Intergranular/ interdendritic
Tube, shot-peened	Air	310	580	12	Ductile
Tube, shot-peened	SCW	305	380	5	Intergranular

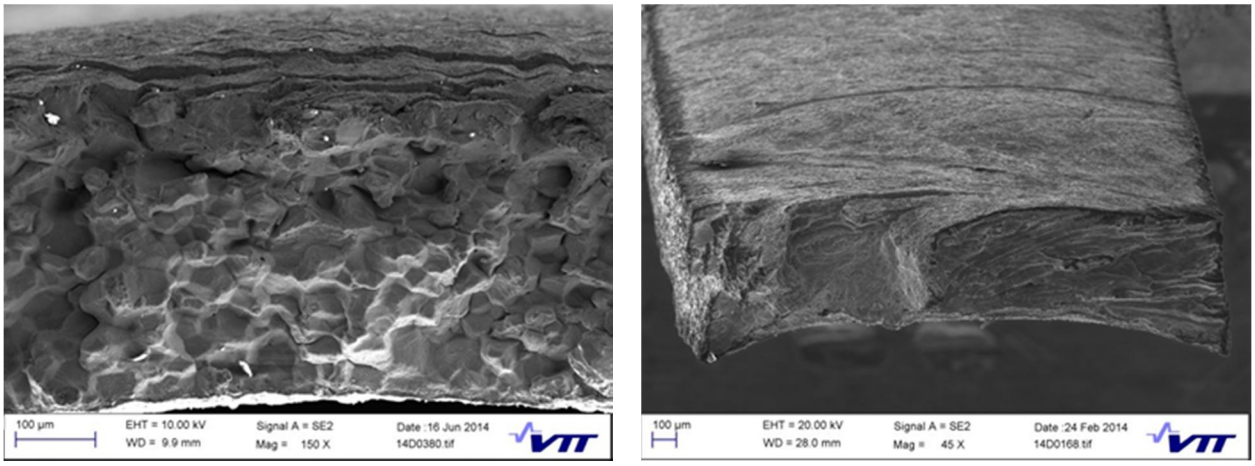

a) b)

Figure 13. Fracture surfaces of specimens cut from the ~8*0.5 mm 316L tube after the SSRT test in SCW at 550°C. As-received specimen a) has almost fully intergranular failure, and welded specimen (fracture in the middle of the weld) b) has mostly intergranular/interdendritic failure.

Table 9. Double loop EPR test results of the two heats in mill-annealed condition before and/or after the exposure to SCW at 550°C.

Material	Ir, µ A	Ip, µ A	Ir/Ip
Plate, exposed	330	8200	0.040
Plate, ref	NA	NA	NA
Tube, exposed	490	10 000	0.049
Tube, ref	<100 *	10 300	<0.01

*No clear reactivation peak

4. Conclusions

The results indicate that the ODS steels are possibly less susceptible to SCC than austenitic stainless in SCW at 550-650°C. However, ODS steels have been tested very little in SCW and more data is required in order to make any final conclusions.

The austenitic stainless steels with 15-18% Cr showed a range of behaviours with respect to their SCC resistances. According to literature there are many possible mechanisms affecting the sensitisation process in the temperature range relevant to supercritical water reactors. The best performers of austenitic stainless steels in this study were 1.4970 and 316L. On the other hand, another heat of 316L was unarguably the worst performer.

If austenitic stainless steels with 15-18% Cr are used in this temperature range in SCW, the sensitisation behaviour of the specific heat should be studied before the heat is used.

Acknowledgements

This paper was written with the funding of EU FP 6 and 7 projects GETMAT, HPLWR Phase 2 and SCWR-FQT, and Finnish national SAFIR 2018 program's project GenXFin, which are gratefully acknowledged.

References

1. A. T. Motta, A. Yilmazbayhan, M. J. Gomes da Silva, R. J. Comstock, G. S. Was, J. T. Busby, E. Gartner, Q. Peng, Y. H. Jeong, J. Y. Park, Zirconium alloys for supercritical water reactor applications: Challenges and possibilities, Journal of Nuclear Materials 371 (2007) 61–75..
2. A. Heinzel, M. Rieth, G. Muller, A. Weisenburger, Basic characterisation of 12CrODS, GETMAT deliverable D1.13b.
3. Y. de Carlan, Basic characterisation of 14Cr1WYTi ferritic ODS, GETMAT deliverable D1.2b.
4. S. Hwang, B. Lee, J. Kim, J. Jang, SCC and corrosion evaluations of the F/M steels for a supercritical reactor. Journal of Nuclear Materials 372 (2008) 177-182.
5. http://www.matweb.com/
6. G. S. Was, T. R. Allen, “Time, temperature, and dissolved oxygen dependence of oxidation in austenitic and ferritic-martensitic alloys in supercritical water”, Proceedings of ICAPP’05, Seoul, Korea, paper 5690 (2005).
7. S. Teysseyre, G. Was, Stress corrosion cracking of austenitic alloys in supercritical water. Corrosion, 62, No. 12. (2006).
8. G. S. Was, P. AmpornratT, G. Gupta, S. Teysseyre, E. A. West, T. R. Allen, K. Sridharan, L. Tan, Y. Chen, X. Ren, and C. Pister, Corrosion and stress corrosion cracking in supercritical water. Journal of Nuclear Materials, 371 (2007) 176 – 201.
9. S. Penttilä, A. Toivonen, L. Rissanen and L. Heikinheimo, Generation IV material issues – Case SCWR. Journal of Disaster Research, 5, No.4, (2010) 469 – 477.
10. R. Novotny, P. Hähner, J. Siegl, P. Hausild, S. Ripplinger, S. Penttilä, A. Toivonen, Stress corrosion cracking susceptibility of austenitic stainless steels in supercritical water conditions. Journal of Nuclear Materials, 409, Issue 2 (2011) 117-123.
11. W. Zheng, J. Luo, M. Li, D. Guzonas, W. Cook, Stress corrosion cracking of SCWR candidate alloys: A review of published results. The 5th Int. Symp. SCWR (ISSCWR-5) P095, Vancouver, BC, Canada, March 13-16, (2011).
12. Electrochemical potentiokinetic reactivation measurement using double loop method, EN ISO 12732, 2008.
13. N. Parvathavarthini, S. Mulki, R. K. Dayal, I. Samajdar, K. V. Mani, B. Raj, Sensitization control in AISI 316L(N) austenitic stainless steel: Defining the role of the nature of grain boundary. Corrosion Science 51 (2009) 2144–2150.
14. N. Parvathavarthini, R.K. Dayal, Influence of chemical composition, prior deformation and prolonged thermal ageing on the sensitization characteristics of austenitic stainless steels. Journal of Nuclear Materials 305 (2002) 209–219.
15. Y.J. Oh, J.H. Hong, Nitrogen effect on precipitation and sensitization in cold-worked Type 316L(N) stainless steels, Journal of Nuclear Materials 278 (2000) 242-250.
16. M. Nezakat, H. Akhiani, M. Hoseini, J. Szpunar, Effect of thermo-mechanical processing on texture evolution in austenitic stainless steel 316L, Materials Characterization 98 (2014) 10–17.
17. S-X. Li, Y-N. He, S-R. Yu, P-Y. Zhang, Evaluation of the effect of grain size on chromium carbide precipitation and intergranular corrosion of 316L stainless steel, Corrosion Science 66 (2013) 211–216.
18. M. Terada, D.M. Escriba, I. Costa, E. Materna-Morris, A.F. Padilha, Investigation on the intergranular corrosion resistance of the AISI 316L(N) steel after long time creep testing at 600^{o}C. Materials Characterization 59 (2008) 663–668.
19. S. Penttilä, A. Toivonen, J. Li, W. Zheng, R. Novotny, Effect of surface modification on the corrosion resistance of austenitic stainless steel 316L in supercritical water conditions. Journal of Supercritical Fluids 81 (2013) 157–163.

Inspection performance

Towards a guideline for a smart in-service inspection concept using the damage tolerance methodology

Detlef Rieck[1], Axel Schulz[2] & Gerhard Dreier[3]

[1]ENCOS GmbH & Co. KG, TÜV NORD GROUP
An den Wurthen 28, 17489 Greifswald, Germany

[2]TÜV NORD SysTec GmbH & Co. KG
Große Bahnstraße 31, 22525 Hamburg, Germany

[3]TÜV NORD Systems GmbH & Co. KG
Große Bahnstraße 31, 22525 Hamburg, Germany

Abstract

The operation regime of thermal power plants turns out to be more and more flexible. Low cycle fatigue due to cyclic thermal transients and internal pressure ranges therefore becomes a limiting factor for operation lifetime, especially for thick-walled components.

The Damage Tolerance concept, based on Fracture Mechanics evaluations, can help to prolong components' operation lifetime and can be basis for a smart in-service inspection standard.

The paper gives an overview of objectives, partners and methodical approaches of the running research project THERRI, started to establish the foundations of Damage Tolerance applications to operating thermal power unit components.

Currently the experimental and numerical studies are in their final state. The research results, like measured fatigue crack growth rates of martensitic power plant steels, are exemplarily applied on thick-walled components in the reference power plant.

Based on the results of THERRI, a draft directive for a smart in-service inspection concept for power plant components on Fracture Mechanics-based Damage Tolerance methodology has been formulated.

The conceptual structure of the draft directive is presented in the paper. The directive consists of two parts: The first one is a handbook for the methodological application of the Damage Tolerance concept. This handbook places special emphasis on the application for thermal power plants. Furthermore the methodology is extendible for applications in other power industries or even other industrial branches like process and petrochemical industry.

The second part of the draft directive consists of compilations of standard values and approaches for all the input that is necessary for assessing maximum allowable in-service inspection intervals according to part one of the directive. These compilations are supplemented by the computational and experimental results of the THERRI project.

1. Introduction

Three years ago, at the BALTICA IX conference 2013, the authors presented a concept that allows, on the one hand, a reduction of conservative assumptions in material fatigue assessments, and on the other hand the development of new safety standards in the evaluation of the remaining operation lifetime of thermal power plants in flexible operation regimes /1/.

The conceptual prognosis tools of this concept should allow a timely optimization of plant operating modes, a smart non-destructive inspection (NDT) concept and finally reduce the lifetime consumption and the maintenance efforts /1/.

As mentioned in our 2013 presentation /1/, an adequate measure to handle high fatigue utilization factors of components due to flexible plant operation is given by the Damage Tolerance concept on the basis of fatigue crack propagation analyses in the scope of linear-elastic Fracture Mechanics. Within this concept, the maximum acceptable in-service inspection intervals can be quantified and the inspection instructions can be optimized.

To establish the foundations of Damage Tolerance applications to components of thermal power units, the German joint research project THERRI was started in autumn 2013 by TÜV NORD together with scientific and industrial partners /2/.

2. Flexible plant operation and damage tolerance concept

The stipulated flexible operation regimes cause a paradigm shift in the in-service material degradation mechanisms for the thermal power unit components (coal and gas power plants as well as solar power plants and methane production). Low-cycle fatigue due to more and faster start-up and shut-down pressure and thermal transients gains in relevance versus creep degradation at constantly high operation temperature.

Following the causes and preconditions of the degradation mechanisms creep and fatigue, therefore no longer the components with large strain amplitudes during constant full load at high temperature operation, such as pipelines, in particular bends, but the thick-walled components with large local thermal stress amplitudes during start-up and shut down get higher lifetime consumption increments.

The lifetime of a component that is dominantly exposed to cyclic loads can be seen as successive periods of fatigue degradation and fatigue crack growth. The stable phase of fatigue crack growth is a credible degradation mechanism that can be controlled by means of in-service non-destructive inspections. This opens - under conditions of plant operation with dominant cyclic loads - significant reserves for the lifetime assessment as well as for design optimization at least of thick-walled components, as is shown in Figure 1.

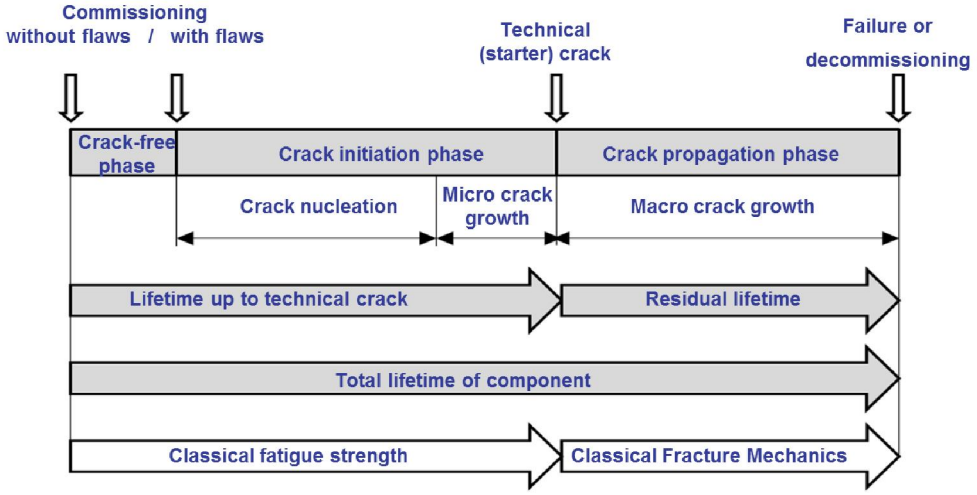

Figure 1. Component lifetime under dominant cyclic loads

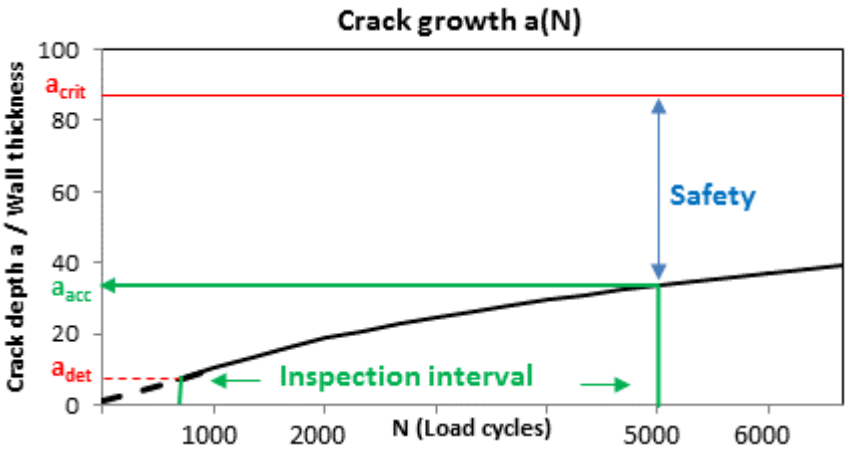

Figure 2. Schematic crack growth diagram (Damage Tolerance diagram)

Figure 2 gives an image of the Damage Tolerance methodology in principle and its results. The methodology includes the following basic work steps:

- Postulate of an initial crack assumption
  (crack postulate depth = NDT detection limit a_{det})
- Calculation of critical crack depth a_{crit}
- Calculation of fatigue crack growth for predicted cyclic loads
- Comparison of calculated and acceptable crack depth a_{acc}
  (a_{acc} = a_{crit} / safety factor)
- Necessary in-service NDT before reaching acceptable crack depth a_{acc}
  → max. acceptable inspection interval

This step list shows the interaction between the in-service inspection and the Fracture Mechanics evaluation within the Damage Tolerance concept.

Moreover, the Damage Tolerance analysis is the only calculation method to quantify maximum acceptable in-service inspection intervals and thereby to optimize the in-service inspection concept.

The Damage Tolerance[1] concept is well-regulated and proven in several industries (see e.g. /3/ to /5/) but not in thermal power plant industry.

3. Intention and objectives of research project THERRI

3.1 Intention and partners

In fact, there is no clear and normative methodology for handling the new requirements and challenges for thermal power plants in flexible operation regimes. The existing thermal power plants were originally built to continuously produce power. Consequently, focusing more on creep and corrosion than on fatigue cracking degradation, within the rules commonly used for German as well for other European thermal power plants no Fracture Mechanics methods are described for application. All current regulation assessments (e.g. in EN 12952 as well as in EN 13445) of plant components' fatigue lifetime are restricted in regarding only the period of component fatigue degradation but not the subsequently following period of stable fatigue crack growth acc. to Figure 1.

On the other hand, Fracture Mechanics applications are not in contradiction to the existing rules. There is a small note in EN 12952-4, that if necessary, more detailed methods of assessment may be used, e.g.

[1] The authors have already proposed in previous publications to use the clearer term "*Degradation Tolerance analysis*" instead of the usual but misleading term "*Damage Tolerance analysis*" since only a potential local component degradation (crack) can be tolerated while the damage (failure) of the component must be excluded.

using British Standard PD 7910 "*Guide to methods for assessing the acceptability of flaws in metallic structures*" which has been the 1st interbranch but national standard for Fracture Mechanics component assessment.

Another obstacle of a wide and common application of the Damage Tolerance concept is the very small data base of Fracture Mechanics parameters (static fracture toughness and fatigue crack propagation rates) for steels applied in power plants, in particular ferritic-martensitic steels at elevated temperatures.

Knowing this background, essential basics for the application of the Damage Tolerance concept for thermal power plant components are developed within the research project THERRI.

The research project THERRI, which complete project title is "*Determination of characteristic values to evaluate thermal fatigue crack growth in power plants*", has been conceived and launched by TÜV NORD together with the scientific partners University of Rostock and Forschungszentrum Jülich as well as with the hard coal-fired power plant KNG Kraftwerk Rostock as our industrial project partner.

The project under the supervision of TÜV NORD has a 3 years run-time and will be finished according to plan at the end of 2016. The acronym THERRI is derived from the German term "*Thermisches Ermüdungsrisswachstum*", which means Thermal Fatigue Crack Growth. The project is funded by the German Federal Ministry for Economic Affairs and Energy (Bundesministerium für Wirtschaft und Energie (BMWi)).

3.2 Main objectives

One key aspect of the THERRI research project is the experimental determination of the fatigue crack propagation parameters of martensitic and ferritic-martensitic power plant steels in the temperature range of 300 - 600°C.

The research project has been oriented already by the choice of material to the residual lifetime determination and extension of existing power plants - not in competition but in addition to other research projects for development and improvement of austenitic and nickel-based materials for new power plants with higher operation temperatures,.

For all measurements within the THERRI project we got martensitic X 20 CrMoV 12 1 sample material of two dismantled and replaced turbine bypass valves (HDU) from our industrial project partner Rostock power plant.

The Fracture Mechanics experiments run in Rostock (*University of Rostock, Professorship in Structural Mechanics StM*) and Jülich (*Forschungszentrum Jülich, Institute of Energy and Climate Research, Microstructure and Properties of Materials IEK-2*). In Jülich take place crack propagation measures in air and in water steam environment as well as with and without holding times during the load cycles. The fatigue crack growth experiments with holding times are carried out for the demarcation to the influence and dominance of creep crack growth at higher temperatures. In Rostock, fatigue crack propagation tests with temperature transients are scheduled in addition to the tests at constant temperatures.

The experimental crack growth tests are accompanied by numerical studies to develop and improve assessment tools for thermodynamic and stress as well as Fracture Mechanics analyses of thick-walled plant components for their industrial applicability.

These themes are supplemented by the further development and qualification of ultrasonic measurement techniques (particularly phased array technique) for thick-walled, multi-curved power plant components. The results of these investigations will be summed up in a process specification.

The overall result of the research project THERRI will be a complete methodology using the Fracture Mechanics and in-service inspection tools of a Damage Tolerance analysis to disclose and apply the residual lifetime reserves of thick-walled power plant components beyond the classical fatigue analysis.

Going beyond the scope of scientific technical publications, the methodology is manageable described in a draft directive prepared for general use in thermal power plant industry and to give in the validation process by the proper industrial boards. This draft directive is currently arising with the actual working title "*Determination of Inspection Intervals of Power Plant Components by Damage Tolerance Analysis"*.

Furthermore, to show the practicality of the methodology as well as of the draft directive, the method is exemplified applied to several thick-walled components of the project reference object, the industrial project partner Rostock power plant. A part of these demonstrator components are the above mentioned turbine bypass valves (HDU) where the new ones have the same design as the replaced ones. The other demonstrator object is a boiler circulation pump, see below.

4. Intention and content of the draft directive

4.1 Directive main part

The topic of the currently arising draft directive is to be a guideline to establish the basics for a smart in-service inspection concept for power plant components on Fracture Mechanics-based Damage Tolerance methodology.

Because we did not want to invent the wheel again, the conceptual structure of the draft directive is similar to other international authorized Fracture Mechanics codes and standards as e.g.:

- R6 procedure of British Energy, BNFL Magnox Generation and AEA Technology
- British Standard BS 7910
- API 579-1/ASME FFS-1 Fitness-for-Service
- European FITNET/SINTAP procedure
- Swedish proSACC Handbook (SSM report 2008: 01)
- German FKM Directive for Fracture Mechanics
- German Merkblatt DVS 2401
- Appendices of ASME Boiler & Pressure Vessel Code, Section XI
- German KTA 3206

(The sequence of the listed codes is without any judgement, and there is no guarantee for the completeness of the list.)

Like these basic rules our draft directive consists of two parts: The directive's main part is a handbook describing the methodological application of the Damage Tolerance concept. Although it places special emphasis towards the assessment of thick-walled, high temperature transient loaded components in flexible operating thermal power plants, the methodology is extendible for applications in other power industries or even other industrial branches like process and petrochemical industry.

And – although in contradiction to some of the above mentioned international codes and standards we do not establish a general Fracture Mechanics application guideline – our draft directive offers guidance for two Fracture Mechanics applications beyond and besides the pure Damage Tolerance concept to prolong component residual lifetime and to quantify the maximum in-service inspection intervals in existing plants on the basis of non-existing, postulated cracks:

- Evaluation of detected real crack-like indications (Damage analysis)
- Component lifetime forecast during the project planning and design phase of new plant projects

Keeping this in mind the table of contents of the draft directive is self-explanatory as follows:

- Scope and limitations
- Methodology of Damage Tolerance analysis
- Transient and stress analysis - component and load ranking
- Requirements for non-destructive in-service inspections – derivation of initial crack postulates
- Calculation procedure:
  Crack growth and frequency of in-service inspections – maximum acceptable inspection intervals
- Damage analysis of crack-like indications
- Damage Tolerance analysis as a design criterion

The limitations of the concept are set by the dominance of the herewith considered degradation mechanism fatigue crack growth in comparison to other degradation mechanisms (particularly creep and corrosion).

One limiting factor is the component operation temperature range. Creep crack growth is relevant above about 550°C while corrosion fatigue / strain induced corrosion cracking is relevant below about 300°C.

Another influencing factor is the character of the operation loads, i.e. the load frequency and the occurrence of holding times at high or lower temperatures. Fatigue crack growth dominates in a real cyclic load regime. Holding times at high temperatures forward creep degradation mechanisms while corrosion mechanisms can act at any temperatures under high stresses or strains.

The Fracture Mechanics experiments carried out by the THERRI project partners in Rostock and Jülich among others attend to define the limitations of the dominance of the fatigue crack growth and therefore the applicability of the concept and methodology as described in the draft directive.

The transient and stress analysis for typical operating regimes in coal-fired power plants is another work package within THERRI and is worked out by University of Rostock, *Professorship of Technical Thermodynamics LTT*, and TÜV NORD with the immediate support by the industrial project partner Rostock power plant. The Finite Element stress analyses, partly combined with Computational Fluid Dynamics (CFD) analyses and eXtended Finite Element analyses (XFEM), are carried out by TÜV NORD in collaboration with Uninversity of Rostock, StM. These analyses serve to determine the component and load case-matrix (ranking) which should be the basis of the application of the Damage Tolerance concept in power plants. The main features of our data evaluation of Rostock power plant and other power stations are written into the draft directive.

An indispensable prerequisite for application of the Damage Tolerance concept including optimization of the in-service inspection intervals is the verified "crack-free" status in the considered component to determine the crack size postulate on basis of the detection limits of the applied non-destructive testing methods. To meet this, dedicated general requirements are formulated for the NDT in-service inspection methods in the draft directive. More specific requirements are listed in the related appendix, see below.

The calculation procedure for determining the critical crack depths, the predicted crack growth for the initial crack postulates and the derived maximum inspection intervals is illustrated for the user in the draft directive in a detailed and understandable manner, as is sketched in Figure 2.

4.2 Directive appendices

The annex part of the draft directive consists of compilations of standard values (case catalogues and data collection) and approaches for the input for the assessment of maximum allowable in-service inspection intervals according to the main part of the directive. To carry out a practical Damage Tolerance analysis and to unify and simplify the handling of the draft directive the following appendices are attached - analogous to the modular structure of the above-mentioned Fracture Mechanics codes and standards:

- Typical component geometries and initial crack configurations
- Load determination (transient and stress analyses) for thermal power plant analyses – Catalogue of standard load cases and stress profile approaches
- NDT process specification for thick-walled power plant components
- Stress intensity factor and plastic collapse solutions
- Fracture Mechanics parameters of ferritic/martensitic power plant steels (fracture toughness and crack propagation rates)
- Safety factors for the acceptable inspection intervals
- Examples of use

As can be seen these appendix titles are similar to the working areas of the research project THERRI. In these appendices the detailed results of each THERRI work package are directly incorporated, together with data from open literature and available data bases. The structure of these appendices is designed such that the database can be extended at any time.

4.3 Further application and verification process

During and after completion work within the research project THERRI we will demonstrate the industrial applicability of the Damage Tolerance concept using the draft directive. On the other hand, in parallel with its industrial application, the resulting draft directive is to be routed through a validation process by the relevant industrial boards. We aspire the acceptance of the methodology by the plant licensees and the notified bodies / approved inspection agencies as well as the licensing and regulatory authorities – not only in Germany.

The draft directive offers guidance for two extended Fracture Mechanics applications beyond and besides the pure Damage Tolerance concept, as already mentioned above. For these applications the methodology as described in the draft directive's main part is completely usable with the special features and variations explained in the specific chapters "*Damage analysis of crack-like indications*" and "*Damage*

Tolerance analysis as a design criterion", respectively. All the data collected and the approaches described in the directive's appendices are completely usable for the Damage analysis of detected crack-like indications too and usable in parts for the design phase of new plants (where perhaps newer materials with better Fracture Mechanics properties will be inserted).

As our working experiences have shown, the assessment of crack indications detected within the in-service inspections is a good gateway to introduce and establish Fracture Mechanics evaluations in industrial practice /6/. Moreover, in these cases the eXtended Finite Element Method (XFEM) is often helpful in search of cause and origin as well as of possible further development of the detected cracks in power plant collectors, coolers, pumps or fittings.

An essential expandability for the industrial applicability of the Damage Tolerance concept can be gained when the results of THERRI will be brought together with the available approaches and data for creep and creep-fatigue crack growth in power plant steels at higher temperatures. For this purpose, presently common considerations and discussions occur with amongst others MPA Stuttgart, which have a leading role in this field, see e.g. /7/.

5. Example: analysis of a boiler circulation pump

We were ask by our industrial project partner to test the Damage Tolerance analysis for its practicability as evaluation methodology for the remaining lifetime and the necessary inspection intervals of the repaired circulation boiler pump in Rostock power plant.

Due to a damage event (component failure) of the boiler circulating pump in a German coal-fired power plant in 2014, the identical designed component in Rostock power plant was inspected immediately. In the ultrasonic testing (mechanized phased array technique) extensive circumferential cracks of variable depth were detected in the pump housing, starting from the relief groove in the pump bottom end plate. The damaged bottom end plate was removed and the housing was completed again by a new forged end plate of similar design. The power plant was put into further operation with the overhauled circulation pump.

The results of the ultrasonic inspection of the impaired and therefore replaced pump end plate emphasized the evidence of a qualified non-destructive inspection method for thick-walled, multi-curved power plant components: Only the mechanized phased array ultrasonic testing has identified the circumferential cracks in the relief groove of the pump end plate.The further material and destructive testing investigations of the pre-cracked and replaced bottom end plate took place at MPA Stuttgart. These investigations have confirmed the circumferential cracks of varying depth in the relief groove, see Figure 5 further below.

Fatigue crack growth was find out as main cause of the total pump failure in 2014 as well as of the detected cracks in the circulation pumps in Rostock and some other German power plants.

For our Damage Tolerance analysis of the repaired and furthermore operating pump in Rostock power plant according to the guidance of our draft directive we have compiled and evaluated the thermodynamic loads, done the FEA stress analyses and the Fracture Mechanics calculations (including XFEM analysis).

An extra component ranking was not necessary in this case – the choice of the circulation pump was made by the experience of the damage of the identically designed pump.

To determine the real loads which have led to the crack growing in the replaced end plate and which could lead to possible crack nucleating and growing in the repaired pump, extensive transient measurements and analyses were done. An extra temperature measurement equipment with 7 vertical positions was installed at the external pump housing surface additionally to the since 1994 existing online monitoring system, see Figure 3.

On the basis of the temperature and internal pressure measurement results, the load case list shown in Figure 4 was derived including the model transient "*Cold start-up*" as typical cyclic load in the pump housing. Furthermore the transient-depending heat transfer coefficient between medium and pump inner wall was calibrated within the FEA wall temperature analyses in comparison with the measured temperature transients.

Figure 3. Boiler circulation pump housing with extra temperature measurement positions

Load case overview

- Preset load (1.45 mm preset elongation) ①
- Full load (p = 266 bar + preset load, T = 260°C) ⑤
- Light load (p = 160 bar + preset load, T = 160°C) ⑥
- Model transient Cold start-up (+ preset load)

Time in min	T in °C	p in bar	
0	30	0	①
30	100	0	②
240	150	0	
270	20	120	
420	350	120	③
600	280	266	④

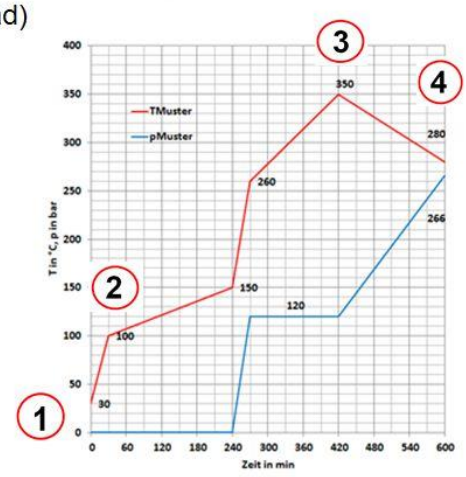

Figure 4. Load cases and model transient "*Cold start-up*"

The performed XFEM calculations confirmed the crack nucleation position as well as the crack propagation direction and shape in good concordance which the investigation results of MPA Stuttgart, as can be seen in Figure 5.

Figure 6 shows the FEA-calculated normal stresses in the pump wall perpendicular to the crack plane for the determining load cases according to Figure 4. The arrows refer to the maximum stress ranges within the model transient "*Cold start-up*" and between the stationary load conditions "*Full load*" and "*Light load*", respectively.

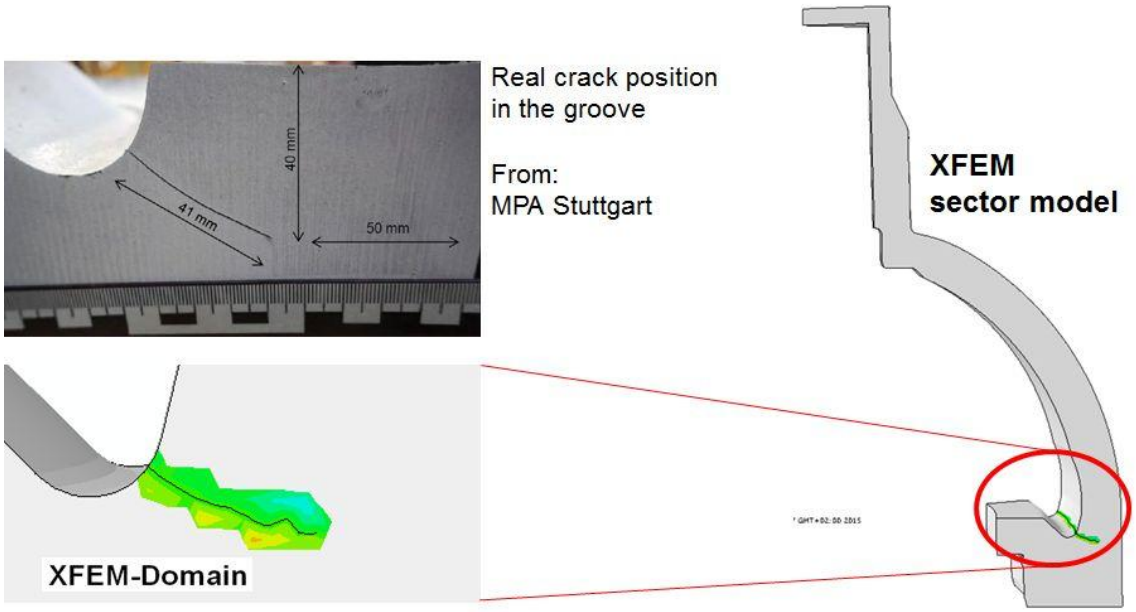

Figure 5. XFEM analysis and comparison with destructive testing results

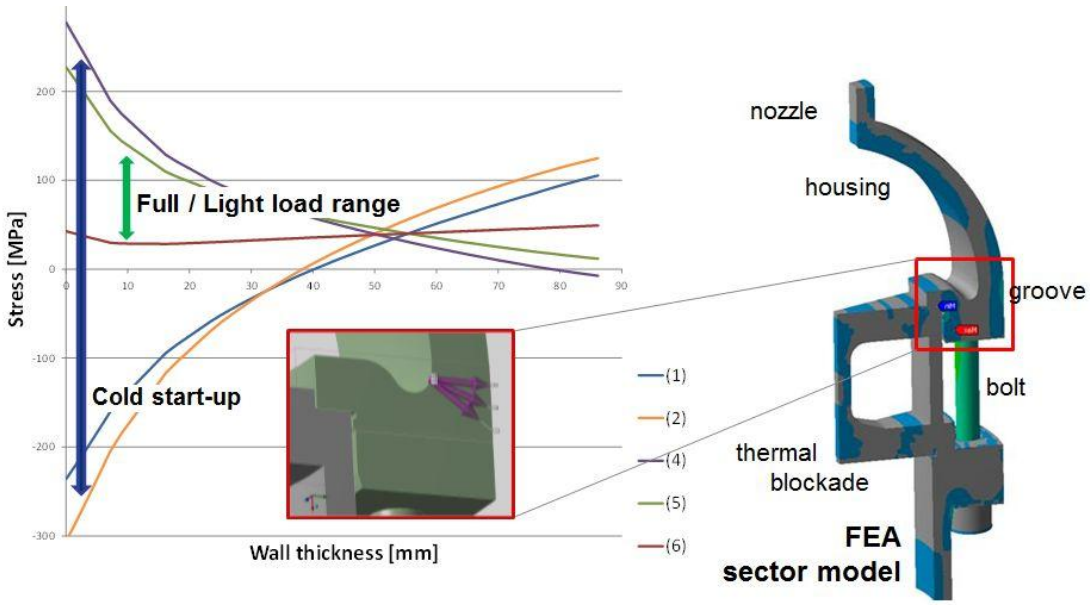

Figure 6. FEA-calculated stresses normal to the crack plane

For the Fracture Mechanics analyses we could use the current THERRI standard input data set for ferritic / martensitic steels because the pump housing is made of the ferritic high-temperature steel 15 NiCuMoNb 5 (WB 36, 1.6368). For the static fracture toughness we used a value of 100 MPa $m^{1/2}$ in good accordance with all measured values, see e.g. /9/.

For the crack propagation rate we used the covering bilinear curve of Clark /10/ and ASME Code, Section XI /11/ as shown in Figure 7. This conservative curve has not yet taken into account the actual measuring values of the THERRI experiments but common and accepted open literature values as you can find in our draft directive.

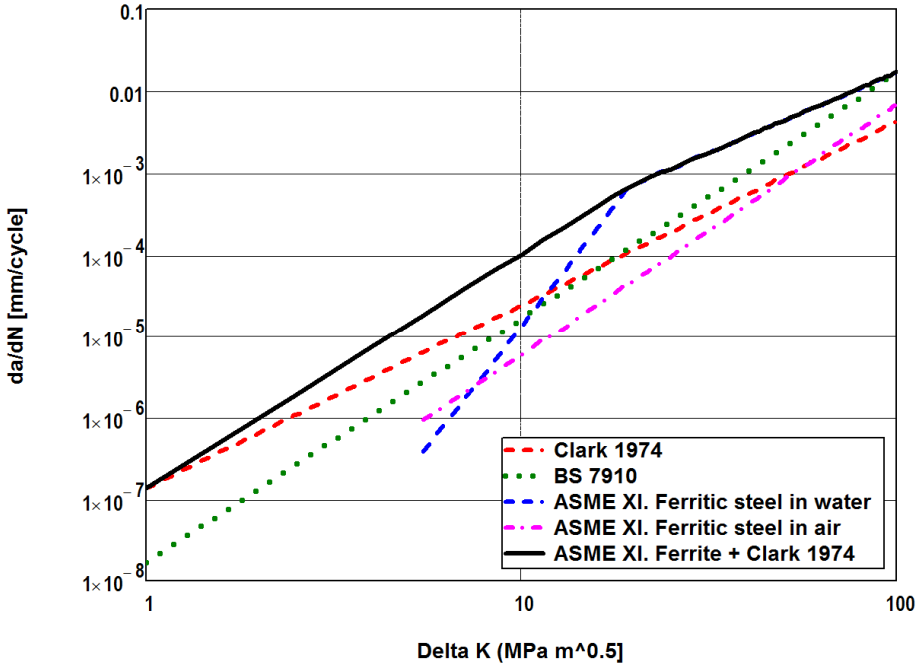

Figure 7. Fatigue crack propagation rates in steel (at stress ratio R = 0)

Using these Fracture Mechanics property values and the loads shown in Figure 4 and Figure 6 we could establish the Damage Tolerance diagram as shown in Figure 8. The calculated crack growth started at a postulated crack depth of 2 mm because this crack depth is excluded in the new bottom end plate of the circulation pump by the manufacturing inspection. Also included in Figure 8 (as in Figure 2) are the calculated critical crack depths a_crit for the load cases "*Full load*" and for the moment of maximum load within the model transient "*Cold start-up*" (36,000 s after transient begins).

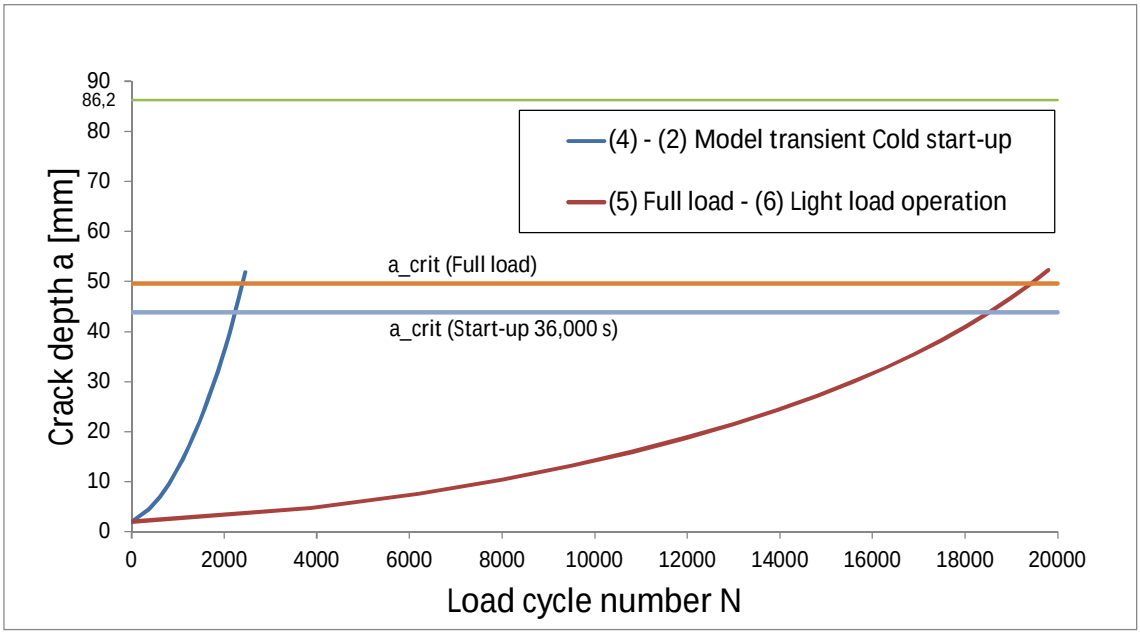

Figure 8. Crack growth diagram on basis of different load ranges

Comparing with the schematic crack growth diagram (Damage Tolerance diagram) of Figure 2 one can see the basically feasibility of the methodology but a qualitatively different tendency of crack growth. In the case of the considered circulation pump under the certain loads the calculated fatigue crack growth of the postulated (not real) crack increases with increasing crack depth. This underlines the importance of the appropriate choice of safety factors against the critical crack depth to get acceptable crack depth and acceptable inspection intervals.

In a first evaluation of the driven load cycle numbers of cold and warm start-ups as well as of a simple forecast of the future operation of Rostock power plant we got the average numbers of 56.1 start-ups per year and of 34.0 load ranges “Full load” – “Light load” per start-up. In this first evaluation we did not differ between cold and warm start-ups, we did not differentiate the “Light load” cases and the forecast only involved the extrapolation of the driven load cycle numbers per year into future operation but no change of operation regime.

With these assumptions we got the crack growth diagram / Damage Tolerance diagram of Figure 9.

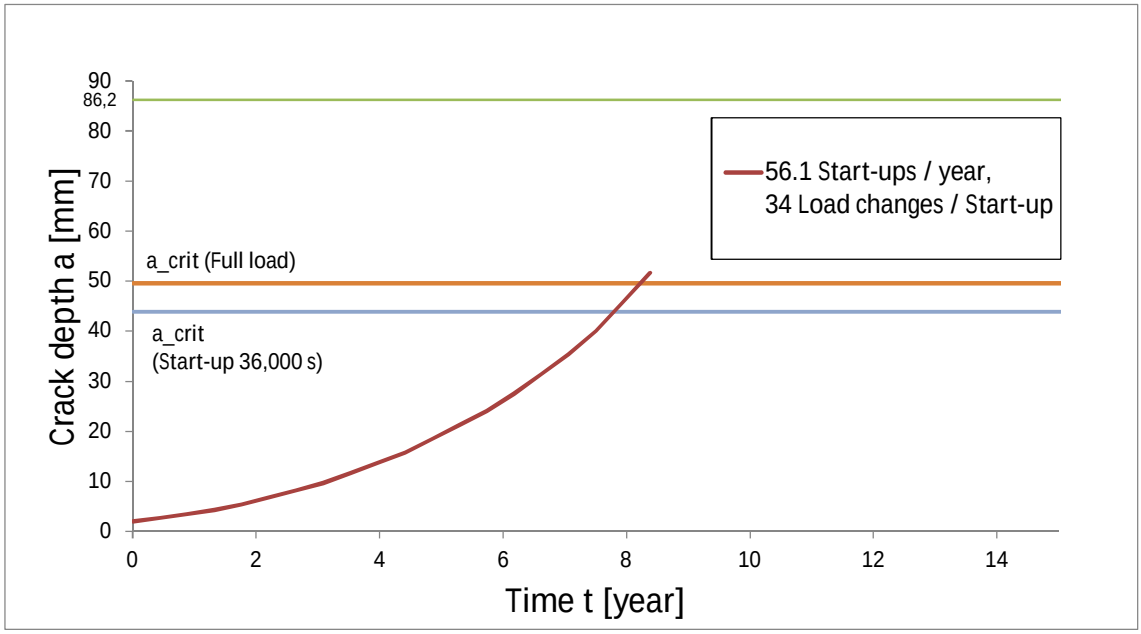

Figure 9. Crack growth diagram (Damage Tolerance diagram)

As can be seen in Figure 9, the degradation mechanism fatigue crack growth is not excluded for the new bottom end plate of the circulation pump with only slightly changed design. Moreover, the results indicate this degradation mechanism as main cause for the detected extended cracks in the replaced end plate as shown in Figure 5. Although together with our project partners we will enhance the forecast assumptions of the future power plant operation regime, already the rather simple analysis according to Figure 9 gives the licensee good advice to plan the further in-service inspections of the repaired circulation pump.

6. Conclusions

The draft directive - established as a main result of the joint research project THERRI - is not in contradiction to the common rules. The rules, in particular EN 12952 parts 3 and 4, shall not be changed but supplemented. The draft directive takes up the fatigue assessment where EN 12952-4 offers no appropriate approach for thick-walled components under the conditions of flexible plant operation. Moreover, the draft directive provides a practicable tool to plan and optimize in-service inspection intervals. The shown example demonstrates the applicability of the described Damage Tolerance methodology as well as of the draft directive.

Both methodology and directive are extendible for other applications in power industries, like evaluation of detected real crack-like indications or optimizing of component design, or even applicable for other industrial branches.

Acknowledgements

The authors wish to thank the German Federal Ministry for Economic Affairs and Energy (Bundesministerium für Wirtschaft und Energie (BMWi)) for financially supporting the joint research project THERRI, contract number 03ET7024A-D. Furthermore, all THERRI project partners are gratefully acknowledged for their intensive and valuable cooperation to date.

References

1. Goers, S, Rieck, D., Schulz, A., Wernicke, R. TÜV NORD concept COOP - A Powerful Tool to Meet the Challenges of Power Plant Flexibilization. BALTICA IX, Int. Conf. on Life Management and Maintenance for Power Plants, Helsinki - Stockholm - Helsinki, June 2013.

2. Rieck, D, Schulz, A. THERRI – A Joint Research Project to Meet the Challenges of Power Plant Flexibilization by a Smart In-Service Inspection Concept, Power-Gen Europe, Amsterdam, June 2015.

3. U.S. Code of Federal Regulations - Title 14: Aeronautics and Space - 14 CFR 23.573 Damage tolerance and fatigue evaluation of structure.

4. ASME Boiler & Pressure Vessel Code, Section XI: Rules For Inservice Inspection Of Nuclear Power Plant Components, Nonmandatory Appendix L, L-3000: Flaw Tolerance Evaluation.

5. Zerbst, U., Mädler, K., Vormwald, M. Entwicklung eines Schadenstoleranzkonzeptes für Komponenten des Rad/Schiene Systems am Beispiel von Radsatzwellen, DVM-Tag: Werkstoffe für die Systemtechnik Bahn, Berlin, 2003.

6. Rieck, D., Fellmann, A., Schulz, A. Bruchmechanische Befundbewertung – veränderte Belastungen erfordern moderne Bewertungsmethoden (Poster), 47. Kraftwerkstechnisches Kolloquium, Dresden, October 2015.

7. Speicher, M., Klenk, A., Coleman, K. Creep-Fatigue Interactions in P91 Steel, 13th Int. Conf. on Fracture, Beijing, June 2013.

8. MPA Stuttgart, Untersuchungsbericht Umwälzpumpe, Auftrags-Nr. 902 8904 000, December 2014.

9. Altpeter, I., Dobmann, G., Katerbau, K.-H., Schick, M., Binkele, P., Kizler, P., Schmauder, S. Copper Precipitates in the Steel 15 NiCuMoNb 5 (WB 36): Material Properties and Microstructure, Atomistic Simulation, NDE by Micromagnetic Techniques, 25. MPA-Seminar, Stuttgart, October 1999.

10. Clark, W. G. How fatigue crack initiation and growth properties affect material selection and design criteria, Metals Engng. Quarterly 16, 1974.

11. ASME Boiler and Pressure Vessel Code, Section XI. Rules for Inservice Inspection of Nuclear Power Plant Components, Nonmandatory Appendix A, A-4300: Fatigue Crack Growth Rate.

POD as a function of flaw location in component

Jonne Haapalainen

VTT Technical Research Centre of Finland Ltd
Espoo, Finland

Abstract

The probability of detection (POD) curves are often used to estimate the capability of a non-destructive testing (NDT) method to find flaws. However, the POD information typically requires very many expensive measurements, so much effort can be spared by obtaining comparable data from computer simulations.

In this study CIVA ultrasound simulation software was used to generate 150 simulations from ultrasonic inspection of a nozzle. The results were used for training of neural networks that were then used to generate POD-curves. The results of POD-calculation where presented as a function of flaw characteristics and location in the component.

The results show that the smallest detectable flaw size can be very different in different parts of the component. The smallest and largest detectable flaws differ by more than an order of magnitude depending of the flaw location.

The benefits and limitations are discussed with respect to the used methodology that combines ultrasound simulations with metamodeling and POD-calculations.

1. Introduction

The flaw finding capability of the selected method is essential information to everyone who needs to do any kind of NDT. If the method can find small flaws with very high reliability, the period between inspections can be extended compared to a method which can find only large flaws. The capability of NDT-method can be measured in multiple ways. Most typical reliability assessments are conducted by a qualification process, where inspectors aim to detect known artificial flaws in test piece(s) (open trial qualification). If the flaws are found, the method has passed the qualification and the reliability of the method is considered sufficient.

For detailed experimental evaluation of NDT performance, typically tens, hundreds or even thousands of measurements are needed. As this is very expensive and laborious, simulation results are often used to support and complement the evaluation. In this study, ultrasound simulations are combined with metamodeling to obtain a large number of results which are then used to evaluate smallest detectable flaws of ultrasound simulation as a function of flaw position.

1.1 POD

A good measure to quantify the reliability of non-destructive testing is probability of detection (POD). In typical POD-curve the probability to find flaw with certain size (length, height, area etc.) is presented as a

function of flaw sizes. POD-curves are typically generated by measuring ca. 40 to 60 flaws and then recording their response to NDT method and their real size [1]. An example POD-curve is presented in Figure 1.

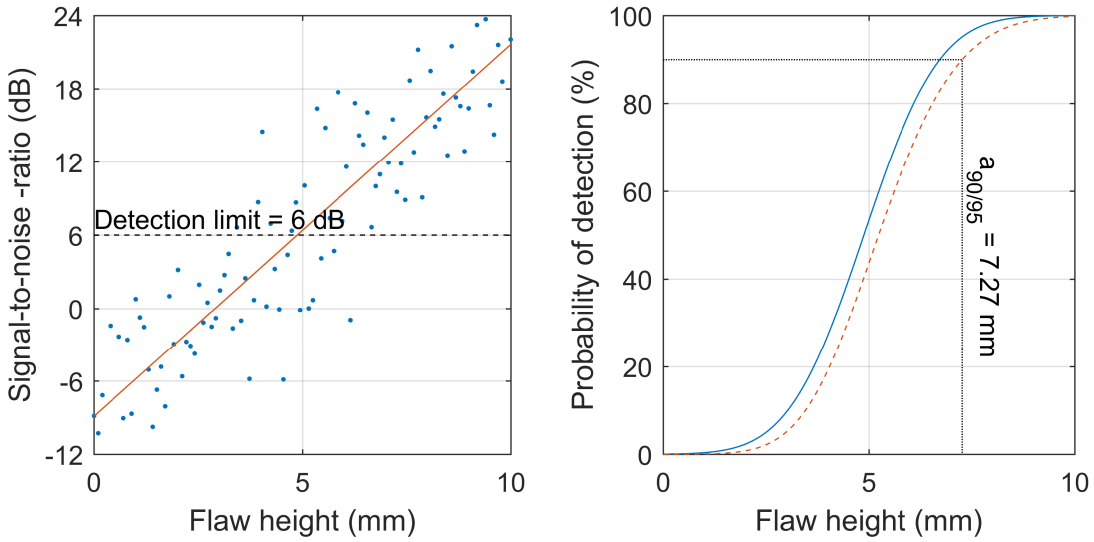

Figure 1. On left, a vs â –plot shows data points of signal amplitude vs. flaw height, linear fit to the data points and detection limit. On right, a calculated POD-curve from the data and its lower 95% confidence limit [2]. Typically the 90% probability of detection from the 95% confidence limit curve ($a_{90/95}$) is used as a single number that represents the capability of the NDT method.

1.2 Ultrasound simulation

The set of 40 to 60 different flaws, which are required to make an experimental POD-curve, is typically expensive to manufacture and inspect. Therefore, recently simulation of NDE has given new ways to estimate NDT responses on different types of reflectors and to determine of probability of detection curves [3]. With computational models, detection probabilities can be rapidly estimated before any measurement is done. In this study CIVA simulation software with ultrasound module was used. The challenge with the simulations is that although they are faster than measurements, a complex simulation can require hours of computation time. If the hours of computation time is multiplied by the high number of simulations required for one POD-curve, many days or even weeks of computational effort has to be spent.

1.3 Metamodeling

In order to speed up the simulation process, metamodeling can be used to estimate the results of the ultrasonic inspection [4]. In metamodeling, interpolation, artificial neural networks or similar mathematical models are used to make fast approximations of a more complex model to reduce the computation time. In this study, the neural network toolbox of MATLAB was used to approximate the complex ultrasound simulations.

The idea of metamodeling is that, first a set of real input parameters are taken and a real simulation tool is used to simulate the output of the input parameters. Then the combination of input and output parameters are used to train the metamodel so that it can be then used to estimate output parameters for a new set of input parameters. After the training of the metamodel, it can be easily used to create data for POD calculations (also called meta-POD [5]).

2. Materials and methods

To demonstrate the used method, an ultrasound inspection of a nozzle was simulated. The simulation was done with following parameters:

- Sample geometry:
  - Primary cylinder: outer diameter 1000 mm, wall thickness 50 mm
  - Secondary cylinder: outer diameter 100 mm, wall thickness 20 mm,
  - Fillet: inner radius 15 mm, outer radius 15 mm
  - Material: Steel with c_L = 5900 m/s and c_S = 3230 m/s
- Probe: 8×8 elements, 3×3 mm² element size, 2 MHz (bandwidth 80%)
- Wedge: Angle 1 45°, Angle 2 10°
- Array settings: Incidence angle 0-80° (step 10°), skew angle 0-70° (step 10°), wavemode longitudinal (Figure 2)
- Flaw: Semi elliptical crack with aspect ratio of 3:1, orientation parallel to secondary pipe. Flaw positions are calculated from the end of the 100 mm long secondary cylinder (Figure 3).
- Inspection was done from the nozzle fillet by scanning the probe 45° over the flaw. The flaws were always at 0° position.

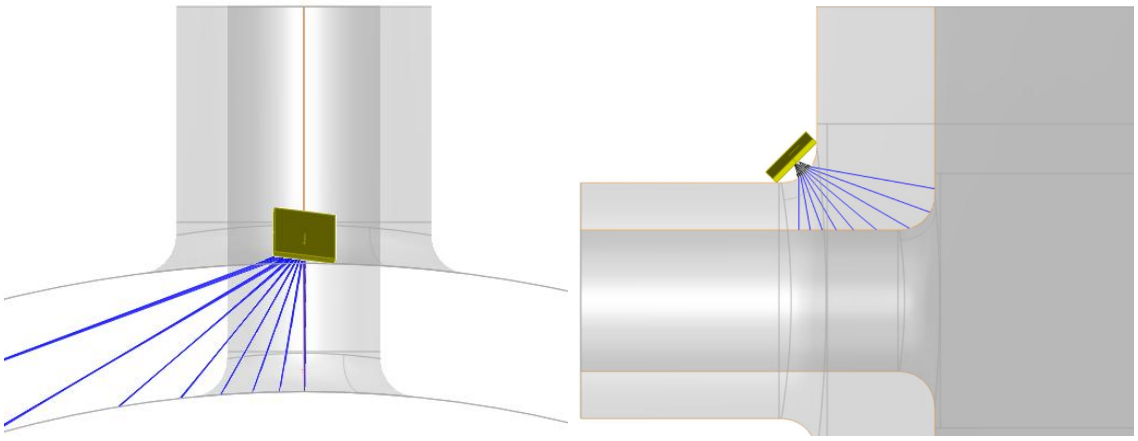

Figure 2. Top (left) and side (right) view of the nozzle showing scan and skew angles of the probe. The flaws were situated in the secondary cylinder parallel to its axis.

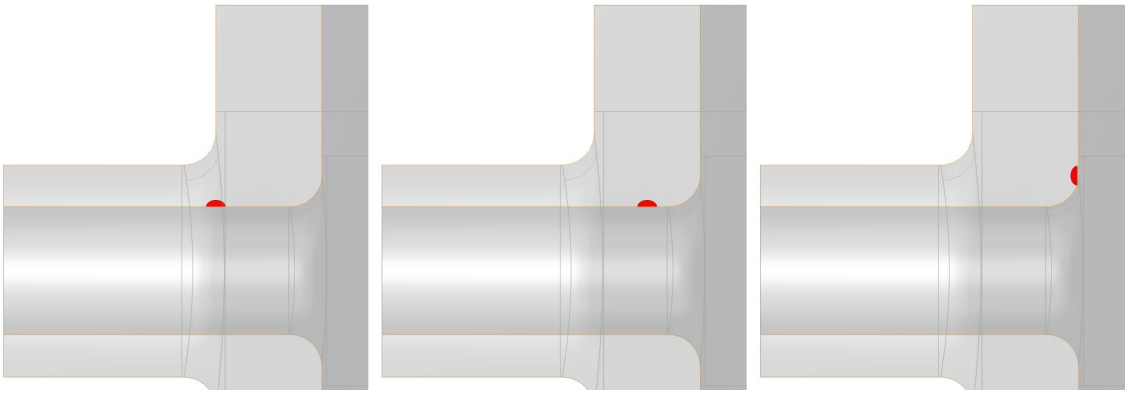

Figure 3. The flaw positions are calculated from the end of the secondary cylinder and position 100 mm equals the outside wall level of the primary cylinder (left image), 125 mm is in the middle of the wall (center picture) and 150 mm equals the inside wall level of primary cylinder (right).

In total 150 simulations were generated with 4 random parameters: flaw height (from 0 to 5 mm), flaw position (from 100 to 150 mm), tilt and skew angle (±10°). Each simulation took ca. 20 minutes of normal laptop computers calculation time to finish.

After the simulations were done, the maximum amplitude from each simulation was stored, and a neural network with three hidden and one output layers was trained. Four parameters (size, position, skew and tilt) were taken as an input parameters and the maximum amplitude as an output parameter. Data was divided so that 100 randomly selected data points were used to train the neural network, 25 data points were used to validate the fitting process and 25 data points were used to measure the goodness of the fit. Neural network was trained until its RMSE was below 3 dB after which it was stored and the process was repeated again so that 100 different neural networks were stored. Because the neural network training is typically started with random parameters, all 100 neural networks were different.

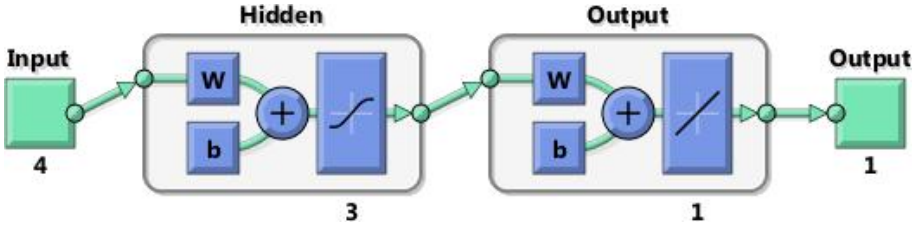

Figure 4. Schematic representation of the artificial neural network showing 4 input parameters, 3 hidden layers and 1 output layers that are trained to calculate 1 output parameter from the input parameters.

The final POD curves were created in the following way:

1. Certain flaw position between 100 and 150 mm was chosen and 10 000 flaws with increasing size and random tilt and skew angle (standard deviation of 5°) were created
2. The artificial neural network was used to estimate the flaw amplitudes from the input parameters.
3. a vs â –technique was used to calculate the flaw size which is found with 90% probability. Amplitude level of 12 dB below ø3 mm flat bottom hole was used as a detection limit.

This procedure was repeated for 50 positions between 100 mm and 150 mm as well as for each stored neural network. Computation time for 500 000 simulations with neural networks was less than one minute.

3. Results

The results of neural network training are presented in Figure 5. The average error between CIVA simulation and neural network estimate was 2.11 dB. The training of one neural network took ca. 15 seconds of computing time and when it was used to estimate output parameters, the computation time for one estimate was few milliseconds.

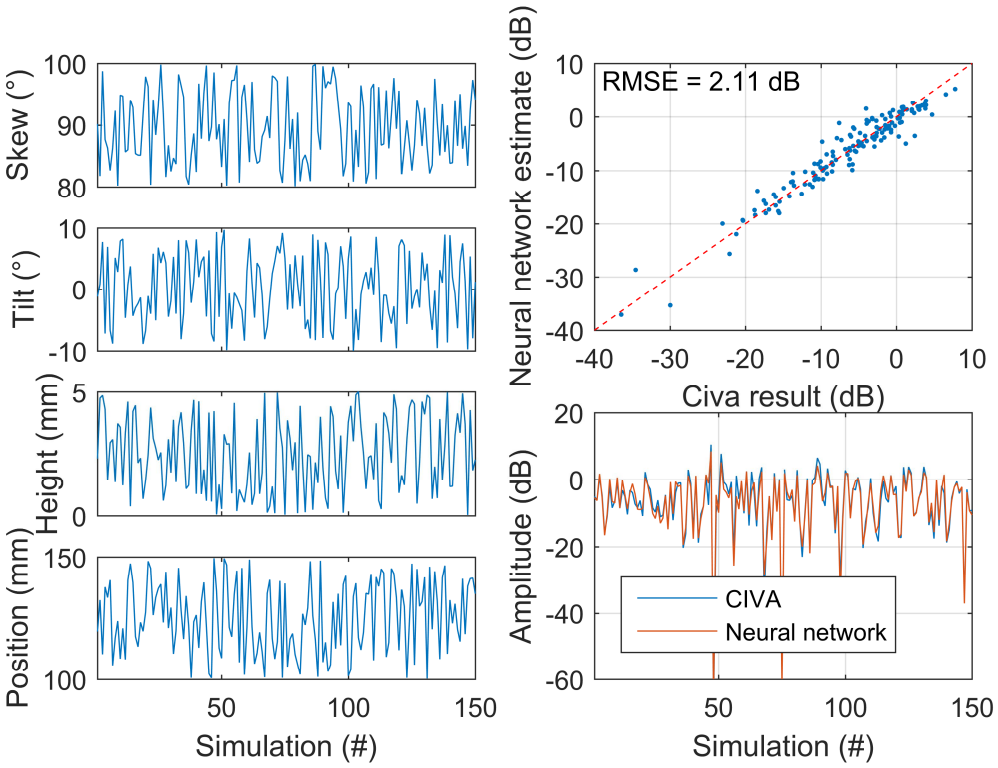

Figure 5. Input parameters of the training set (left) and comparison of CIVA results to ANN results (right). Average error between CIVA simulation and its neural network estimate was 2.11 dB.

Neural network estimations between amplitude as function of position are presented in Figure 6. The calculation was done with and without random tilt and skew variation (standard deviation of 5°) to see the effect of flaw orientation to the calculation.

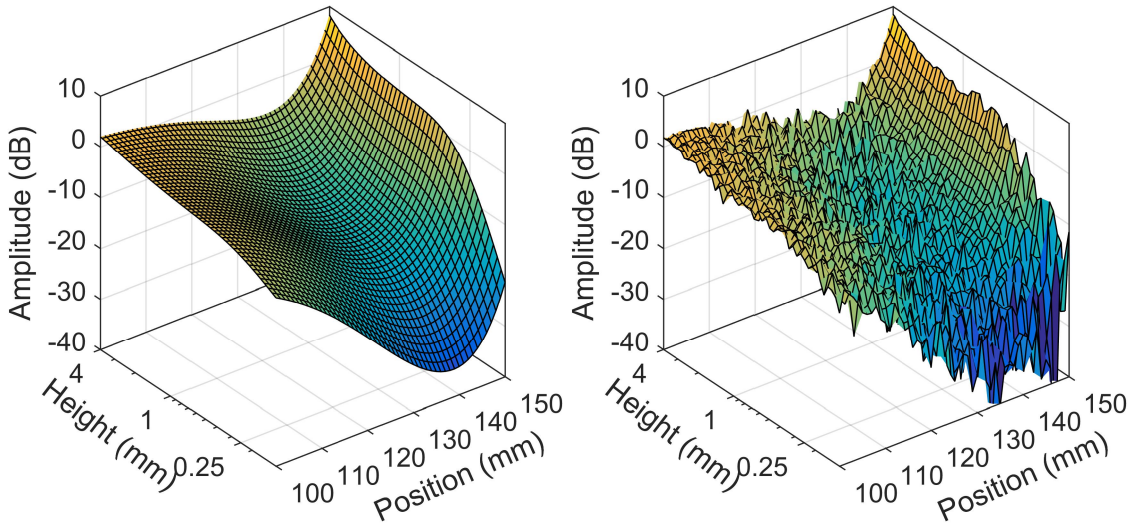

Figure 6. The neural network predicted ultrasound amplitude for different height flaws in different positions. On left, no skew nor tilt angle is applied. On right, random ±5° SD in tilt and skew angles are added to the input parameters.

After POD was calculated for each position between 100 and 150 mm, the calculation was repeated for each stored neural network and average of the $a_{90/95}$-sizes was calculated (Figure 7). The smallest detectable flaw is (0.05±0.09) mm at position 100 mm and the largest (3.2±0.6) mm at position 136 mm. The POD was also calculated so that the position was random parameter between 100 mm and 150 mm and the a90/95-value was (2.9±0.6) mm.

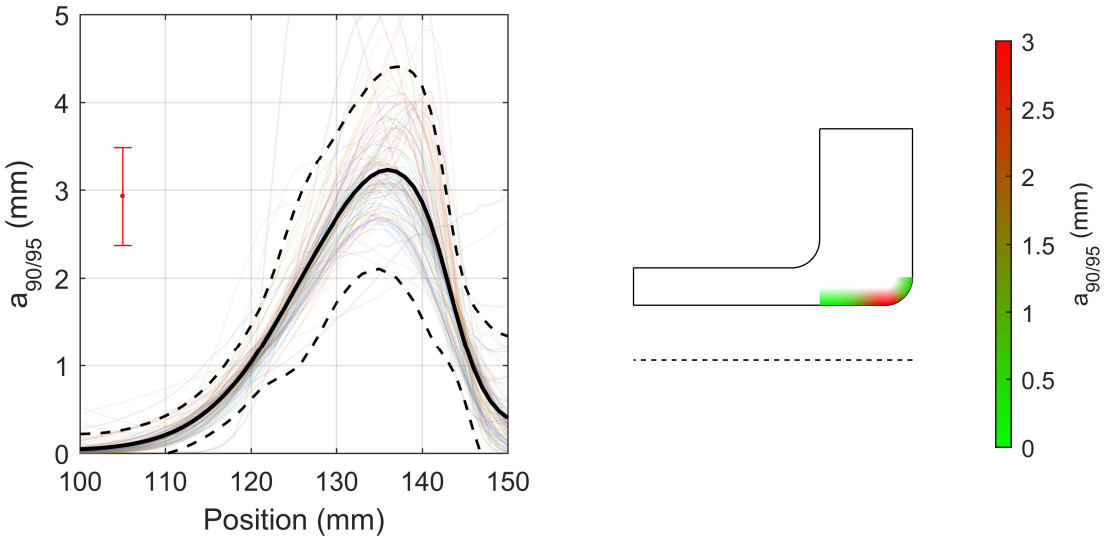

Figure 7. The smallest detectable flaw size as a function of position. On left, an average $a_{90/95}$ flaw size as a function of flaw position for 100 different neural networks (light lines), average (solid black line) and 95% confidence limits (dashed black line). If the POD is calculated with random position instead of point-by-point calculation, $a_{90/95}$ will be (2.9±0.6) mm which is shown as red point in the left. On right image the $a_{90/95}$ flaw size is presented over the nozzle image to show the areas with high and small detectable flaw size.

4. Discussion

According to Figure 7, more than one order of magnitude differences are seen in smallest detectable flaw size as a function of flaw location. The smallest flaws are found near the probe scanning location due to small distance as well as due to beneficial angle between sound beam and the flaw. When the distance between flaw and probe increases, the smallest detectable flaw size also increases. However, when the flaw starts to reach the primary cylinder surface, the distance between the probe and flaw again decreases and the angle between sound beam and flaw turns again beneficial which then rapidly reduces the smallest detectable flaw size.

If the POD would have been calculated in a traditional way, the flaw position should have been also a random parameter. This would have meant that $a_{90/95}$ –value would have been 2.9 mm which is very much larger than the position dependent POD in most of the parts of the component. In other words, the traditional POD would have given very conservative POD values.

The problem with the position dependent POD comes from the neural network. Because the training of a neural network starts with random values, each neural network is different and the reliability of the methods can be estimated by comparing the results from each individual neural network to each other. If 95% confidence limits are calculated from the 100 repetitions, a typical error is ca. 20% of the average value. With small average values, the relative error however rises to >100%. The optimal input/output –parameters for the training of the metamodel, and its effect to the errors, should be studied in next stage of the study.

As is typical for model assisted POD calculations, the results are very hard to verify. As the number of simulations done in this project was 500 000, there is no possibility ever to compare the results to measured ones in similar scale.

References

[1] C. Annis and L. Gandossi, *ENIQ TGR Technical Document - Influence of Sample Size and Other Factors on Hit/Miss Probability of Detection Curves (ENIQ report N. 47)*, no. 47. 2012.

[2] C. Annis, “Nondestructive Evaluation System Reliability Assessment,” MIL-HDBK-1823A, 2009.

[3] M. Wall, S. F. Burch, and J. Lilley, “Review of models and simulators for NDT reliability (POD),” *Insight - Non-Destructive Test. Cond. Monit.*, vol. 51, no. 11, pp. 612–619, 2009.

[4] G. Ribay, X. Artusi, F. Jenson, C. Reece, and P. Lhuillier, “Model-Based POD Study of Manual Ultrasound Inspection and Sensitivity Analysis Using Metamodel,” *AIP Conf. Proc. 1706*, vol. 200006, no. May, pp. 1–7, 2016.

[5] P. Hammersberg, G. Persson, and H. Wirdelius, “The Potential in Simulations and Meta-Modelling for Understanding and Development of NDE,” in *European-American Workshop on Reliability of NDE*, 2013.

Artificial flaw detection with ultrasound in austenitic stainless steels

Tuomas Koskinen[1], Esa Leskelä[1] & Minnamari Vippola[2]

[1]VTT Technical Research Centre of Finland Ltd.
Espoo, Finland

[2]Tampere University of Technology
Tampere, Finland

Abstract

Ultrasonic testing is the main tool to inspect the structural integrity of primary circuit components in nuclear power plants (NPPs) during in-service inspection (ISI). In order to validate an inspection method and to train inspectors, reference flaws are needed. However, there are not enough real flaws available to be used for these purposes so artificial flaws must be used. Ultrasonic response from an artificial flaw must be representative enough so that it can be used as a reference flaw. Otherwise this could lead to a false result during an ISI. Unfortunately ultrasonic testing is highly dependent on the geometry of the component, the flaw type and the material in which ultrasound propagates. Therefore numerous flaws are needed to cover the probable flaw types, sizes and locations.

The aim is to study artificial flaws and acquire wider knowledge on ultrasonic indications from artificial flaws in austenitic stainless steel weld and to compare them to the results from CIVA simulation. The study focuses on notches made by electrical discharge machining (EDM). EDM notches were chosen, since they represent a rough estimate of a crack type flaw and they are fairly quick and easy to manufacture.

1. Introduction

Austenitic stainless steel welds are transversely isotropic. This means that the elastic properties are independent on direction on one plane as in Figure 1 the XY-plane. The elastic properties are dependent on the plane perpendicular to it. In austenitic welds the isotropic XY-plane is along the welding direction. Because of this inhomogeneous anisotropic columnar grain structure, it is difficult to detect flaws in or in the vicinity of the weld, since this structure affects the propagation of the ultrasound. For example, shear wave may be reflected from the fusion line. Also it can be reflected due to grain structure of austenite, causing a false flaw indication and excess attenuation. Longitudinal wave is more favourable in these situations even though it also suffers from attenuation. Mode conversions on the fusion line and columnar grains from longitudinal to shear waves cause problems in evaluating the weld's integrity. [1,2]

It is also possible to use mode conversion as an advantage in inspection. When shear wave probe is set to the first critical angle, longitudinal wave is also produced into the material. This refracted longitudinal wave can be used to inspect the weld. This procedure requires experienced operator, since it is important to distinguish the shear wave and the lateral wave from each other. Rayleigh waves and creeping waves

are also special wave types from mode conversion, which can be used as an advantage in ultrasonic inspection. Especially creeping waves are considered advantageous when testing anisotropic materials. [3,4]

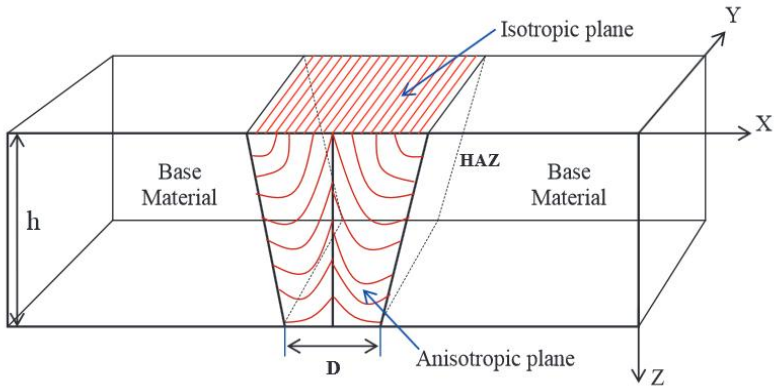

Figure 1. Transverse isotropic symmetry of austenitic weld [2].

Ultrasonic testing can be used to find following flaws: Cracks, lack of fusion, lack of penetration, cavities, inclusions, pores, excess penetration, undercut, concavity, burn-trough, mismatch and lamination. Artificial flaws are required to resemble the postulated types of defects in order to validate a procedure. In this study the focus is on crack types which are found in ISI. These types of cracks can be artificially produced by mechanical or thermal fatigue and electric discharge machining (EDM). Although these cracks can be identified with surface inspection methods such as liquid penetrant testing, cracks usually form in places where only one surface is accessible. Such an example is the ISI of piping welds in NPPs where a crack usually forms on the inside surface of the pipe. [5,6]

EDM notches are usually produced in a reference mock-up. Manufacturing process is nonconventional machining process, in which the material is removed very accurately in a controlled environment. Cutting is done with an electrode, which is shaped to resemble the desired flaw, only a bit shorter than the flaw desired. The electrode can either cut or burn the material in order to achieve the desired flaw shape and size. The parameters of a resulted flaw can be easily inspected with cast replica method to ensure that the desired flaw has been achieved. A typical cross-section of an EDM notch can be seen in Figure 2. [7]

Figure 2. an EDM notch [8]

Unlike thermal fatigue crack tip, EDM notch tip does not have any stresses, which affects the detection by ultrasound. Due to lack of versatility, EDM notches are normally used as robust artificial flaws, which are used when mechanical or thermal fatigue crack would be hard to produce on a certain place or the cost of producing other types of flaws is an issue. [8]

2. Experiments

The agenda of the work was to scan the specimen which had the same kinds of artificial flaws with different locations around the weld. Experiments were conducted with phased array and conventional ultrasonic methods. Second phase was to compare these results with each other and also with the result from CIVA simulation.

2.1 Parameters for the test piece

The test piece was 200 mm wide and 299 mm long. Two plates were welded together so that the weld was placed in the middle of the specimen. The base material was rolled AISI 316L. The weld crown and the root were completely ground off and the whole surface of the test plate was ground evenly to a thickness of 22,1 mm. The weld itself was a 60° V-groove butt weld done with MAG welding. The width on top of the weld was measured with a ruler as 26 mm. The schematics of the specimen can be seen in Figure 3. The dashed line in the figure represents a surface flaw on top of the surface of the specimen. The unintended flaw is also marked as an 's' on the figure. This visible flaw could not be detected with ultrasound when the specimen was inspected for unintended flaws before the machining of the EDM notches, thus it is not presumed to affect the testing result either.

The idea was to scan the specimen from both sides of the weld, on top side of the plate and approximately on the same distance from the weld. In this thesis these sides are referred as a- and b-side, of which the a-side is the one closer to the origin. EDM notches were placed on the back side of the plate in four different locations near or in the weld. The flaw number 2 was placed in the vicinity of the weld in a way it would not be in direct contact with the weld metal. The fifth EDM notch was placed on the base material as a reference. The depths and the locations of the EDM notches were measured during the machining of the flaws approximately 5 mm, with exception of flaw number 1 with depth of 5,3 mm. The length of the flaws was 15 mm.

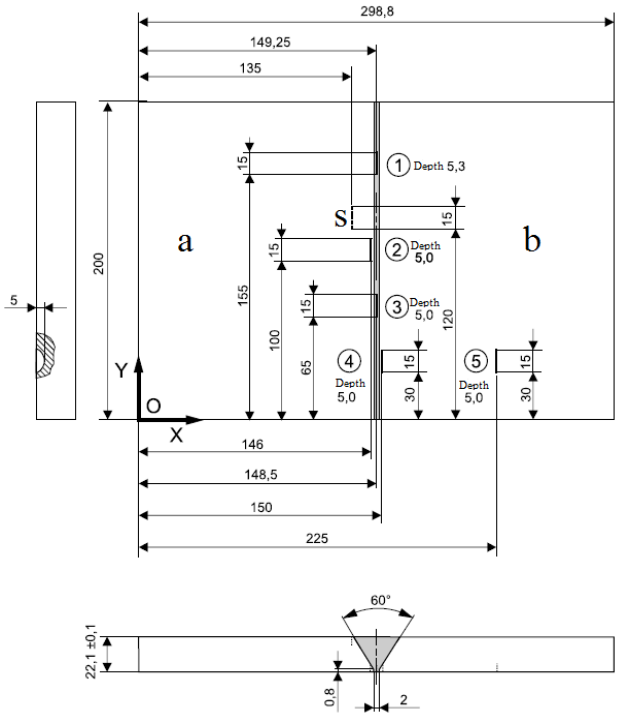

Figure 3. The test specimen described from the bottom. Letters a and b represent the side from the scan was made and s the position of the unintended surface flaw. Numbers 1-4 are the EDM notches inside the weld and number 5 in the base material.

For phased array ultrasonic inspection Zetec Omniscan MX 16/128PR flaw detector was used, which was linked to a laptop PC for data acquisition and evaluation. Manually used Zetec Manual Pipe Scanner was used to measure the probe position during scanning of the specimen. Since the scanner was operated manually, larger variations may have been caused by this factor.

2.2 Ultrasonic testing and simulation procedures

The summary of the used probes, their frequencies and wavelengths can be seen in Table 1. Longitudinal and transverse wave velocity was set to 5770 m/s and 3150 m/s [9] respectively.

Table 1. Summary of the probes, their frequencies and wavelengths.

	2,25 MHz PA 40-75°	**5 MHz PA 40-75°**	**2 MHz MWB 45° N2**	**2 MHz MWB 60° N2**	**1,5 MHz TRL 40-70°**
***f* (MHz)**	2,25	5	2	2	1,5
***λ* (mm)**	1,4	0,63	1,58	1,58	3,84

For linear phased array inspection, a 16 element 5 MHz 5L16A10 and a 16 element 2,25 MHz 2.25L16A10 probes with SA10-N55 Rexolite wedge and shear wave were used. The focal laws were set according to an azimuthal scan between angles 40° and 75° with a step of 1° and to a true depth focus to 22 mm. Water was used as couplant and it was applied to the surface of the specimen via spraying from a spray bottle with constant intervals. The calibration of the probes was done with calibration block for range setting according to SFS-EN ISO 22825 [3] (V2) before conducting the inspection with the probe.

For dual matrix phased array inspection, two 1,5 MHz probes with TRL Rexolite wedge and scan angles between 40° - 70° with step of 1° were used with focus to true depth of 22 mm. In addition, skew angles of -15° and 15° were applied. The calibration procedure and the couplant were the same as for linear phased array probes.

For comparison, two conventional 2 MHz MWB 45° N2 and MWB 60° N2 shear wave probes were used. The calibration was made also with the V2 block. These angles were chosen, since they are in the range of the angles of the phased array inspection and the ultrasonic beam from 60° probe would scan the weld groove perpendicularly with full skip inspection.

Maximum amplitudes were extracted from the acquired data in the positions of the flaws. The noise of the weld was measured between the flaws 1 and 2 for both a- and b-side. The noise was determined from the maximum amplitude between these two flaws, with an average of three measurements. The maximum amplitude was determined by inspecting the echo dynamics of the peak to assure it is not a random amplitude peak. When the noise for a specific technique had been determined, SNR was calculated for each individual flaw and technique.

CIVA version 11.1 was used in the simulation experiment. Simulation was made for 2,25 MHz linear phased array probe similar to the one in the conducted test. The specimen was modelled into the simulation software and the anisotropic matrix for the weld was set from an average of two 316L welds from the literature [10]. The inspection area was narrowed for y direction to the highest points of the elliptical flaws. The X-coordinates were the same as in the test specimen, with 5 mm steps. Structural noise and mode conversion were not taken into account in the computation of the model. For flaw response calculation Kirchoff & GTD model was used.

3. Results

Maximum amplitude is the maximum signal response from a flaw. The lower the amplitude response is the more the ultrasonic wave has attenuated between the flaw and the ultrasonic transducer. In these tests flaw number 5 in the base material was chosen as a reference so that the maximum signal response from this flaw was set to approximately 80% of the full screen height. The scanning was repeated three times,

so the represented values are the average maximum amplitudes of these results. Letter labelling after the flaw number means the side the flaw was scanned e.g. flaw number 1a represents the average result for flaw number 1 scanned from the a side.

3.1 Maximum Amplitude

The results for all the techniques for flaw numbers 1-4 can be seen in Figure 4. In this figure, the amplitude response was changed to decibels, where the acquired maximum amplitude in % was compared to a 100 % amplitude response.

Weld center was chosen as a point of origin. The figure represents the distance from the weld center along the X-axis. The results are also combined to represent the scanning from the near side and the far side more clearly. This means that if the flaw location was on the other side than the probe of the weld center, the flaw would be on the far side, represented as a positive value in the figure. If the flaw was located on the same side as the probe, the flaw would be on the near side, represented as a negative value in the figure. The figure shows how the austenitic weld attenuates the propagating ultrasonic wave, thus lowering the amplitude response.

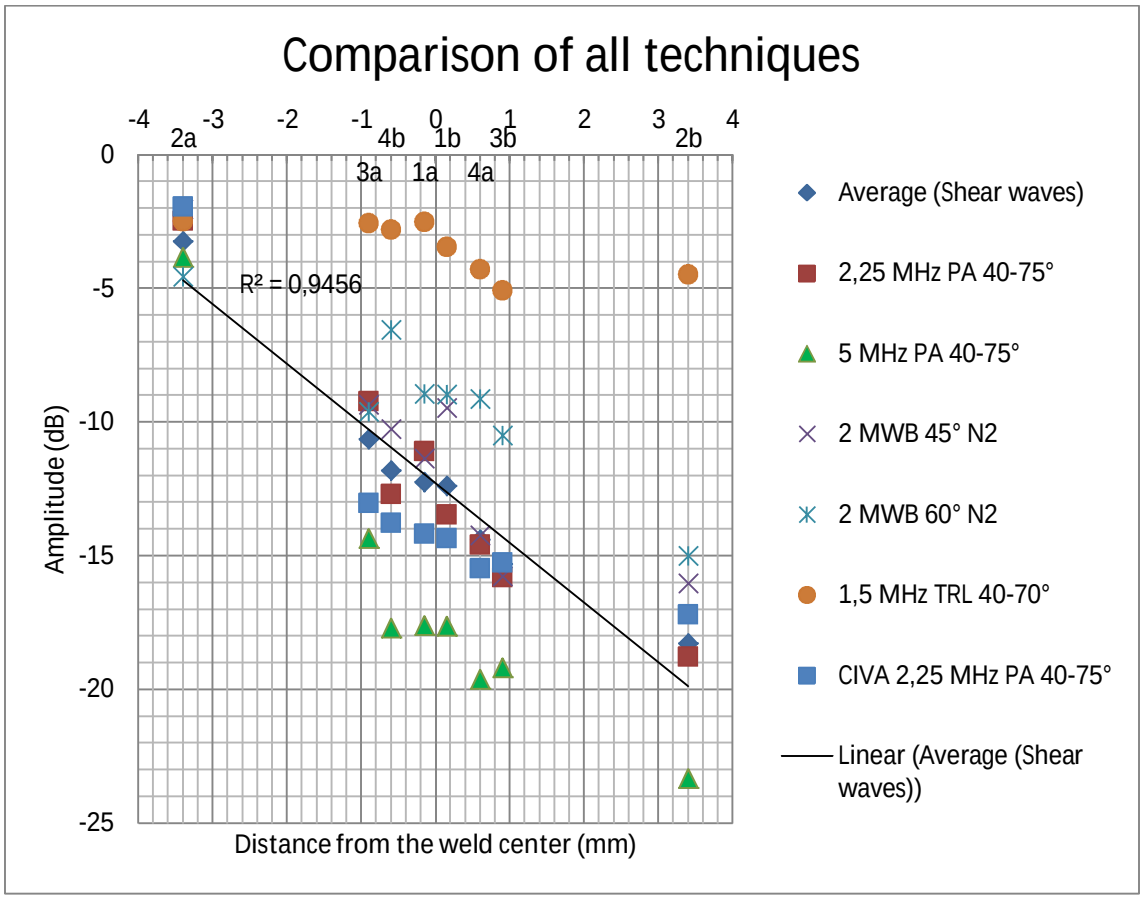

Figure 4. Comparison of all used techniques. 0 represents the weld center and the flaws are plotted along the X-axis according to their distance from the weld center. – represents the near side and + the far side.

For the flaws within and in the vicinity of the weld, the flaw number 2 gave the highest amplitude response from the a-side for all probes and the lowest for the b-side, with exception of TRL probe where the flaw number 3 gave the lowest amplitude response from the b-side. This might be a consequence of a better deviation of sound beam to the flaw number 2 than flaw number 3 from the b-side. The probe had a skew angle of 15° so the deviation of the probe does not seem plausible.

When comparing all the techniques together, excluding these previous observations, the results seem consistent. TRL probe suffers the least from attenuation and the 5 MHz phased array probe the most, as expected. The reason for TRL probe to attenuate less than the other probes is due to the fact that TRL probe uses longitudinal waves whereas the other probes use shear waves. Also the frequency is lower than that of the other probes, however this lowers the resolution and accuracy of the probe compared to other probes. The highest amplitude response for TRL probe was achieved from creeping waves, indicating lesser attenuation compared to other wave types in the anisotropic austenitic weld.

The conventional 60° probe gave better amplitude response than the conventional 45° probe. The 60° probe excelled against the phased array probes while the 45° probe got roughly the same or slightly higher amplitude response as the 2,25 MHz linear phased array probe. Conventional probes had slightly lower nominal frequency than the linear phased array probes, however the difference between the results was higher than expected.

3.2 Signal-to-noise ratio (SNR)

A good SNR was determined as 3 to 1 according to the report [11]. It has been described as a line in the following figures. Since good SNR is usually determined 2 to 1 or 3 to 1, ratio of 3 to 1 was chosen for the most secure result. SNR is used to determine how well the flaw is distinguished from the noise, the higher the SNR the better the flaw stands out from the noise. SNR was calculated using equation 1 with the acquired maximum amplitude response and maximum noise from the weld.

$$SNR = \frac{A_{flaw}}{A_{noise}} \quad (1)$$

Where A_{flaw} is the average maximum amplitude response for a flaw and A_{noise} is the average maximum noise level measured for the technique. The results can be seen in Figure 5.

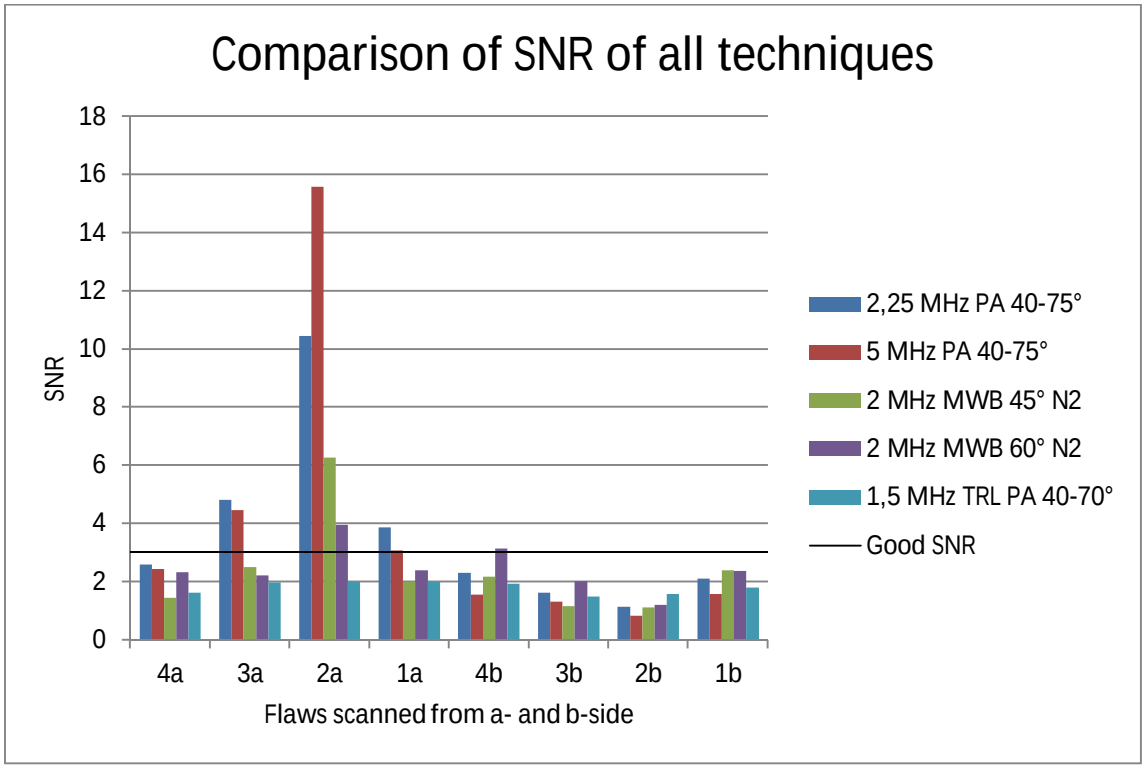

Figure 5. Comparison of signal-to-noise ratio of all techniques for a- and b-side.

For linear phased array probes, flaw numbers 1-3 gave a good SNR from the a-side. However, when scanning through the weld, shear wave probes were unable to reach good SNR in any of the artificial flaws with only exception of 60° conventional probe, which was the only probe achieving a good SNR from flaw number 4.

Table 2. SNR comparison matrix.

	2,25 MHz PA 40-75°	**5 MHz PA 40-75°**	**2 MHz MWB 45° N2**	**2 MHz MWB 60° N2**	**1,5 MHz TRL PA 40-70°**
4a	**4**	3	0	2	1
3a	**4**	3	2	1	0
2a	3	**4**	2	1	0
1a	**4**	3	1	2	0
4b	3	0	2	**4**	1
3b	3	1	0	**4**	2
2b	2	0	1	3	**4**
1b	2	0	**4**	3	1
tot.	**25**	14	12	20	9

Despite having the worst overall results for SNR, the SNR of TRL does not improve or reduce much depending on the location of the flaw. TRL actually gave the best SNR for the flaw number 2 from the b-side.

The probes are compared to each other in Table 2. The best SNR for each flaw was given 4 points and 0 to the worst SNR. The points were summed together and 2,25 MHz linear phased array probe achieved the best overall score. 5 MHz linear phased array probe had the best SNR when scanning the flaw number 2 from the a-side. This is expected, since there is not much noise for 5 MHz noise and the ultrasonic wave has not yet attenuated by the anisotropic weld at all since the flaw was located outside the weld.

4. Discussion

The test piece was an austenitic stainless steel plate with butt weld and it was scanned with linear phased array probes, conventional probes and TRL 2D matrix phased array probe. The test piece was also modelled with CIVA software and tested with linear phased array. Maximum amplitudes from the flaws were recorded and SNR was calculated from the achieved results.

Linear phased array probes had an excellent signal-to-noise ratio compared to the other probes. Furthermore, attenuation was so strong that the flaws scanned through the weld were not recognizable.

Conventional probes fared surprisingly well in the conducted experiments. However, when compared to other techniques scanning with conventional probes was significantly slower than for the phased array probes. This was due to that the beam angle stayed the same, covering a narrower area compared to the phased array sectorial scan of 40-75°. So in order to get the best possible result, the step size along the X-axis had to be changed to 2 mm. Also the conventional probes were more susceptible to amplitude loss from misalignment or loss of couplant.

TRL probe gave the strongest amplitude responses from the flaws. Its advantages were the utilization of longitudinal waves and by mode conversion creeping waves, lower frequency and separate elements transmitting and receiving. The 15° skew angle did not give much of an advantage. However it may have reduced possible amplitude loss if the probe was not completely perpendicular to the flaw. The downside of the TRL probe is also the longitudinal waves. Since longitudinal waves also mode convert to shear waves and creeping wave during the inspection at the interfaces, analysis is not as straight forward as for only shear wave probes. It was important to set the data cursors to right depth in order to prevent excess noise from mode converted signals. Still the noise level was a limiting factor for this technique.

When evaluating all the SNR results, it can be noted that no single probe achieved the best SNR for every flaw. Thus, it would be advisable to use different kind of probes during the inspection of the weld allowing the best possible scope to find flaws in wide range of locations.

It must be noted that the gain in the experiment was set according to the maximum amplitude response from flaw number 5. It is possible to detect the flaws 4, 3 and 1 through the weld as well with linear phased array probes and conventional probes by increasing the software gain during the data analysis or hardware gain during the data acquisition. However, comparing the maximum amplitude responses with each other would be impossible since most of the flaws would have 100% amplitude response with high gain setting. One plausible way would be to record the gain for each flaw with a constant amplitude response and compare the difference. However, this experiment method would take a lot of time to conduct.

CIVA simulation software proved to be a useful tool in simulating ultrasonic probes and welds. However, setting the parameters of the weld, probe and the specimen geometry is not a straightforward process. In order to achieve the best possible result, there is a requirement for accurate information on the microstructure of the weld. Also the HAZ needs to be taken into account separately for more accurate results. Without these values CIVA can only give indicative results.

Testing setup was not an ideal one, since the scanner was moved manually, causing some possible deviation of the results. Also the attachment point for the probes seemed to move a bit during the scanning, causing the slight misalignment of the probe during scanning. Water acted as a good couplant between the probe and the specimen. However it was applied also manually, which may have caused loss of couplant during some parts of the scan.

EDM notches performed well as artificial flaws. The flaws were hard to detect through the weld and gave strong amplitude response in front of the weld as expected. Even though they are just rough estimates of a real flaw they give an excellent and cheap option to study ultrasonic attenuation in different locations of the weld.

5. Conclusions

Ultrasonic inspection of austenitic stainless steel welds is difficult due to the anisotropic and dendritic structure of the weld. This causes scattering, distortion, deviation and attenuation of the ultrasonic wave, complicating the conducted inspection.

Artificial flaws are used to study the capability of an ultrasonic method to detect flaws of different sizes and locations. The electric discharge machining (EDM) notches used in this thesis proved to be a reasonable way to produce rough estimates of a crack. The artificial flaws gave expected amplitude responses from different locations of the weld metal. The responses varied also with different ultrasonic techniques used in the experiments.

Maximum amplitudes were the strongest for the 1,5 MHz separate transmit-receive longitudinal wave (TRL) 40-70° matrix probe and the lowest for 5 MHz linear phased array probe. However, signal-to-noise ratio (SNR) was the best for 2,25 MHz linear phased array probe and the worst for the TRL probe. CIVA simulation represented the ultrasonic propagation of 2,25 MHz phased array probe fairly well, so it can be assumed that with more accurate modelled structure of the weld there can be reliable results from the simulation as well. When scanning through the weld, only TRL probe could detect the furthest flaw with creeping waves. This indicates that it would be advisable to use this technique when inspection from both sides of the weld is not possible. Also it is advisable to use multiple different probes to inspect a weld to achieve best possible SNR from a flaw regardless the flaw location.

The results were congruent with the theory. When frequency of the probe was lowered, the amplitude response was stronger. Also the creeping wave proved to give an excellent amplitude response for TRL probe and it did not suffer from attenuation as much as the shear waves.

The aim of this thesis was to study artificial flaws in austenitic stainless steel. It can be concluded that it is feasible to study the propagation of ultrasound in austenitic stainless steel with artificial flaws and also to use simulation tools to support the achieved results from experimental tests.

References

1. T. Mansour, W. McGaughey, Ultrasonic Testing Applications in Welding, in: Nondestructive Testing Handbook Volume Seven Ultrasonic Testing, 2nd ed., American Society for Nondestructive Testing, Inc., 1996, pp. 551–568.

2. S. Kolkoori, Quantitative Evaluation of Ultrasonic Wave Propagation in Inhomogeneous Anisotropic Austenitic Welds using 3D Ray Tracing Method: Numerical and Experimental Validation, 2014.

3. Sfs-En Iso 22825 Non-Destructive Testing of Welds . Ultrasonic Testing . Testing of Welds in Austenitic Steels and Nickel-Based Alloys (Iso 22825 : 2012), 2016.

4. L. Cartz, Ultrasonic Testing, in: Nondestructive Testing, ASM International, Materials Park, OH, USA, 1995, pp. 81–126.

5. International Atomic Energy Agency, Guidebook for the Fabrication of Non-Destructive Testing (NDT) Test Specimens, Iaea-Tecdoc-Tcs-13. 2001.

6. A. Koskinen, E. Leskelä, Comparison of Artificial flaws in Austenitic Steel Welds with NDE Methods, Espoo, VTT Technical Research Centre of Finland, 2014.

7. P.J. Herman, Manufacturing NDT Reference Standards, The NDT Technician. 2005 , pp. 1–4.

8. M. Kemppainen, I. Virkkunen, J. Pitkänen, R. Paussu, H. Hänninen, Advanced flaw production method for in-service inspection qualification mock-ups, Nuclear Engineering and Design. Vol. 224 2003 , pp. 105–117.

9. J. Berlanger, F. Laprise, Procedure for Encoded, Manually Driven, Phased Array Ultrasonic Flaw Detection and Length Sizing in Ferritic and Wrought Austenitic Piping Welds, 2006.

10. S. Bannouf, D. Elbaz, B. Chassignole, N. Leymarie, P. Recolin, Validation of simulation tools for ultrasonic inspection of austenitic welds in the framework of the MOSAICS project, 2014.

11. Anderson, Crawford, Diaz, Prowant, Cinson, Doctor, Final Assessment of Manual Ultrasonic Examinations Applied to Detect Flaws in Primary System Dissimilar Metal Welds at North Anna Power Station, 2014.

Non-destructive evaluation of the spent nuclear fuel disposal canisters

Ari Koskinen & Tarja Jäppinen

VTT Technical Research Centre of Finland Ltd
Kemistintie 3, 02150 Espoo, Finland

Abstract

The Finnish concept of high activity nuclear waste disposal is based on deep geological storage in copper canisters with cast iron inserts. The development of disposal concept and final disposal in Finland is managed and organised by Posiva Oy. Disposal canisters will be embedded in Olkiluoto bedrock at a depth of approximately 400 metres. Therefore it is essential to inspect the canisters with non-destructive testing (NDT) methods as well as possible before the final disposal.

The lid of the copper disposal canister for high activity nuclear waste is sealed with a weld. Before accepting the canister to the final disposal the weld is planned to be inspected by four non-destructive testing methods. These methods are ultrasonic testing (UT), radiographic testing (RT), eddy current testing (ET) and remote visual testing (VT) using cameras. The copper overpack and the lid are also inspected with multiple NDT methods; UT, ET and VT. The nodular cast iron insert is inspected with UT and VT.

In this paper the four NDT inspection methods (UT, RT, ET, VT) for inspection of different parts of the disposal canister are presented in brief. All information in this paper is collected and summarised from public reports and from the procedures of each method and inspection records. All of the four NDT methods detect defects in slightly different directions and based on different physical principles. The four methods are therefore supplements to each other in inspection of different parts of the disposal canister.

1. Introduction

The Finnish concept of nuclear waste disposal is based on deep geological storage in copper canisters with a cast iron insert. The development of disposal concept and final disposal in Finland is managed and organised by Posiva Oy. Canisters will be embedded in Olkiluoto bedrock at a depth of approximately 400 metres. Therefore it is essential to inspect the canisters with non-destructive inspection methods as well as possible before the final disposal.

The final disposal canister for high activity nuclear waste consists of a copper overpack, a copper lid and a nodular cast iron insert. The nodular cast iron insert gives strength to the structure of the canister to withstand the mechanical stress originating from the bedrock in the underground repository. Oxygen-free copper overpack forms a corrosion resistant shell to the canister. The copper lid of the canister will be sealed with friction stir welding (FSW) to the copper overpack.

During manufacturing defects may be generated in the components. The welding process may produce different types of welding defects, for instance voids, internal root defects, porosity and cavities [4]. Lifting of the canister at the encapsulation plant is one factor which could cause defects or make small existing defects grow. Thus, there is a limited number of lifts allowed. Possible handling incidents could cause defects on the outer surface of the copper overpack.

The disposal canister material quality as well as quality of the weld has to be verified according to acceptance criteria before the final disposal of the canister. Acceptance criteria for the canister are created to control and ensure the adequate strength and corrosion resistance levels for the canister. Non-destructive testing (NDT) methods give possibility to reveal defects in the base material and the weld. The four NDT methods used at the moment in the research are: ultrasonic testing (UT), radiographic testing (RT), eddy current testing (ET) and remote visual testing (VT) using cameras.

Several different inspection methods are used to gain the best possible information on different types of discontinuities. Ultrasonic and radiographic methods are used for volumetric inspections. Visual and eddy current methods are used for surface and near surface inspections.

Non-destructive testing of the canister weld is carried out in the encapsulation plant before the decision to move the canister to final disposal. The encapsulation plant (Figure 1) is located at the ground level above the actual repository. All NDT methods will be remotely controlled. Non-destructive testing in encapsulation plant is operated automatically in an isolated area because of the radiation from the high active spent nuclear fuel in disposal canister. The objective of the NDT testing is to acquire and analyse the data to detect possible manufacturing defects in the closure weld of the disposal canister.

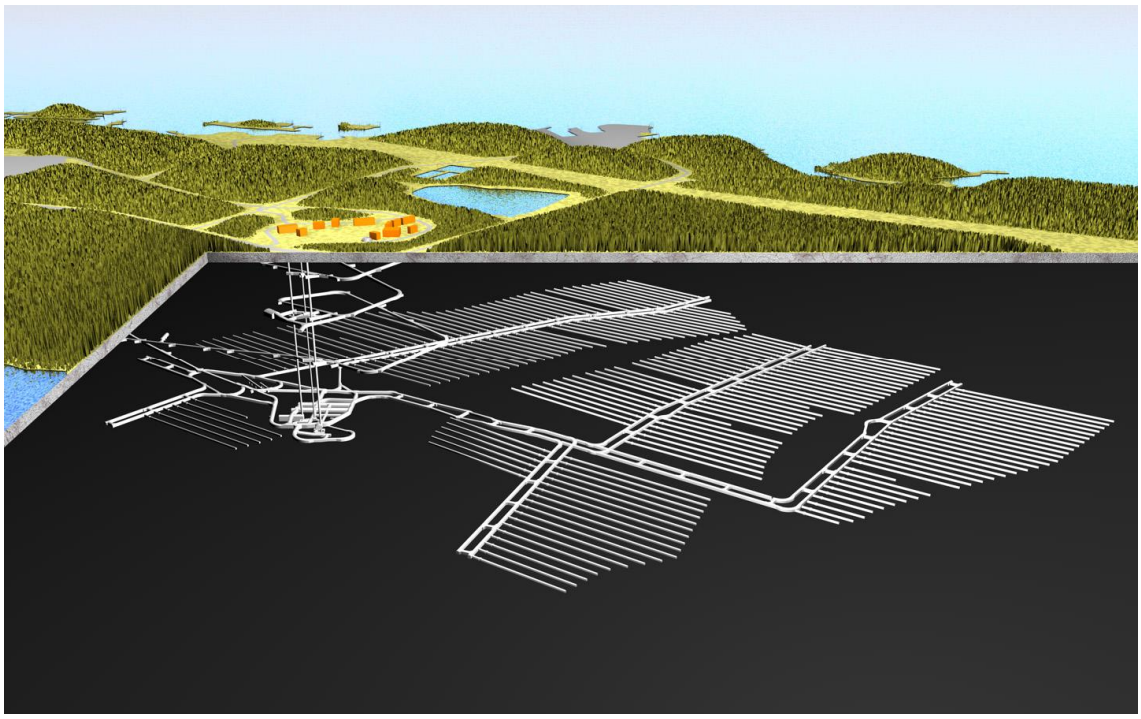

Figure 1. The encapsulation plant is located above the actual repository (Posiva Oy).

2. Disposal canister

The disposal canister consists of nodular cast iron insert, copper overpack and copper lid (Figure 2).

Figure 2. The disposal canister (Posiva Oy).

2.1 Nodular cast iron insert

The main task for the nodular cast iron insert is to give adequate strength to the structure of the canister to withstand the mechanical stress originating from the bedrock in the underground repository. There are three different types of cast iron inserts (Figure 3), one for Loviisa 1 and Loviisa 2 (VVER 440 type), second one for Olkiluoto 1 and Olkiluoto 2 (BWR type) and third one for Olkiluoto 3 (EPR type).

Figure 3. Different types of nodular cast iron inserts for VVER 440, BWR and EPR (from left to right) (Posiva Oy).

2.2 Oxygen-free copper overpack and lid

Overpack including the bottom and the lid of the canister are made of oxygen-free copper which forms a corrosion resistant shell to the canister. Thickness of the overpack is 50 mm. In the first stage the geometry of the lid depended on the chosen welding method due to different weld orientation between electron beam welding and friction stir welding. In 2014 friction stir welding was chosen to be the welding method for the lid closure weld.

3. Non-destructive evaluation

At the moment four different methods are used for non-destructive evaluation of disposal canister. For surface and near surface inspections remote visual testing and eddy current testing are used. For volumetric inspections ultrasonic testing and radiographic testing are used. In all inspections inspectors shall be qualified according to SFS-EN 473/SFS-EN ISO 9712 level 2 suitable for used method. Only in radiographic inspections the operator shall have at least a level 1 certification according SFS-EN 473/SFS-EN ISO 9712. Nevertheless the person evaluating the radiographic images shall have a level 2 certification according SFS-EN 473/SFS-EN ISO 9712.

3.1 Visual testing

Visual testing is conducted for all the disposal canister components including welds. The visual inspection in the encapsulation plant will be done remotely with cameras.

After the welding the surface of the upper part of the lid is to be inspected. Especially 100 % of the weld area and the entire upper end of the lid are inspected. Also the vertical upper outer surface of the lid shell and the vertical inner surface of the lid are inspected. The illuminance degree is required to be high enough (minimum 500 lx). Additional lightning is needed from multiple lightning directions due to the variable reflection of the copper surface because of the characteristics of copper and its oxides. The surface to be examined is required to be clean.

The purpose of the visual testing is to verify, document and evaluate the surface area. During this inspection both manufacturing originated surface defects and handling defects can be detected. This information is critical for the integrity of the canister but also for verifying the indications primarily detected in eddy current testing and secondly by ultrasonic and radiographic testing. Especially outer surface defects which can be seen in radiographic images. Indications that exceed reporting limits will be reported by location, dimensions and defect type. Indication sizes correspondingly locations are tabled and compared to the relevant acceptance criteria. There are also stamped identification marks in the weld, lid and shell that need to be documented and checked.

3.2 Eddy current testing

Eddy current testing is a well-known and widely used surface inspection technique. In disposal canister inspection studies eddy current testing is a combination of low frequency and high frequency probe measurements. With high frequency technique surface breaking defects and surface extensions can be accurately measured. With low frequency eddy current technique deeper surface breaking defects and defects having small ligament can be evaluated. Overpack, lid and weld are inspected with eddy current technique. At moment the inspection is performed with specially designed equipment and analysis and visualisation software. The scan is visualised with in a form of colour coded C-scan (Figure 4).

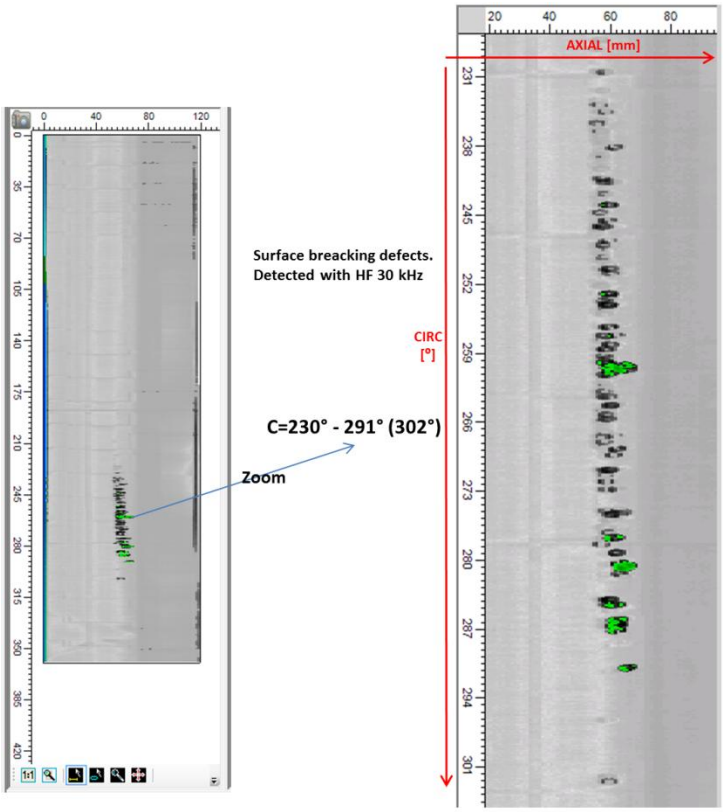

Figure 4. Example of scan visualisation from high frequency coil FSW weld inspection.

A probe array consisting of pancake coils is held on the surface of the copper lid with a probe holder. The array and the holder are moved by a manipulator (Figure 5).

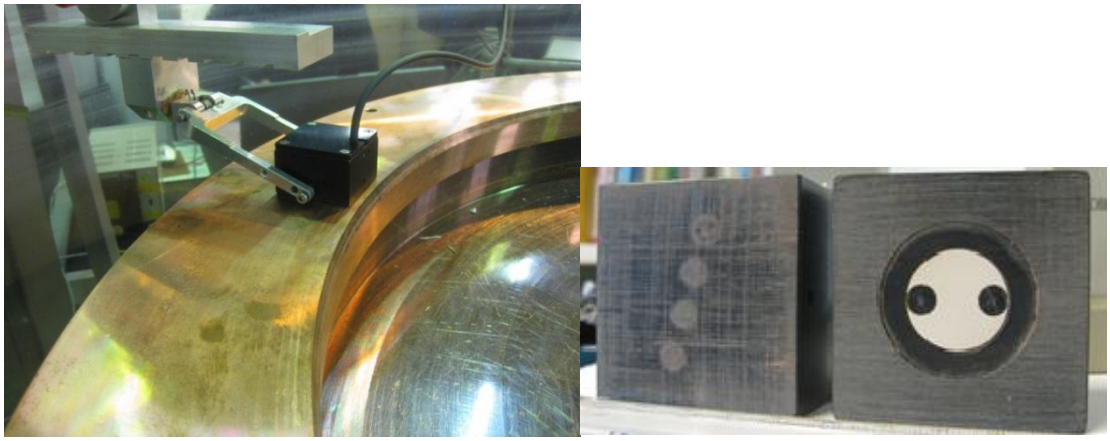

Figure 5. Eddy current probe holder on the left, HF and LF coils on the right.

The lid is inspected using a coil probe array in order to detect defects. In inspection surface breaking defects will be detected, sized and classified. The inspection speed depends on the effective width of the probe array and on the frequency of the probe.

3.3 Ultrasonic testing

Ultrasonic testing is a volumetric testing method and in disposal canister inspections it is used for all the components of the canister. Phased array ultrasonic inspection is used for all inspections due to possibility to modify electrically the sound field during the inspection. This enables the sound field adjustment dynamically for different situations and for detection of different types of flaws. In cast iron insert inspections also other ultrasonic methods are used. Frequency of phased array effects on detectability and sizing and therefore a good compromise 3.5 MHz for both is chosen for copper part inspections. At the moment ultrasonic inspections are performed using the Multi 2000 phased array ultrasonic system of M2M with 128 channels. During the examination of the FSW weld an ultrasonic transducer is scanning the top of the lid and the outer surface of the lid in circumferential direction. Simultaneously the phased array probe also carries out electronic scanning in axial direction. A-scan data in RF-form each measurement is stored. There are about 1500 measurement positions only in circumference.

As can be seen in Figure 6 the ultrasonic phase array probe is positioned on the outer horizontal surface of the canister at the distance of 0.1 mm from the scan surface.

An electronic scan is performed in the direction of the weld penetration. The longitudinal wave velocity in copper is v = 4760 m/s. The attenuation of the sound is dependent on the grain size in copper, bigger grains more attenuation. Large grains extending over 2 mm occur in the weld in circumferential direction. In radial direction the grain size is smaller but large enough to produce higher attenuation compared to base material of the tube and lid. In some cases also in the tube and the lid large variations in grain size can be detected. The grain size is controlled in the manufacturing process of the base material in order to minimise the grain size and its distribution. The ultrasonic testing will be carried out in local immersion at the encapsulation plant.

Before and after the examination the performance and the stability of the system is verified with a reference block containing different kind of reflectors. The block has the same geometry and material properties as the canister.

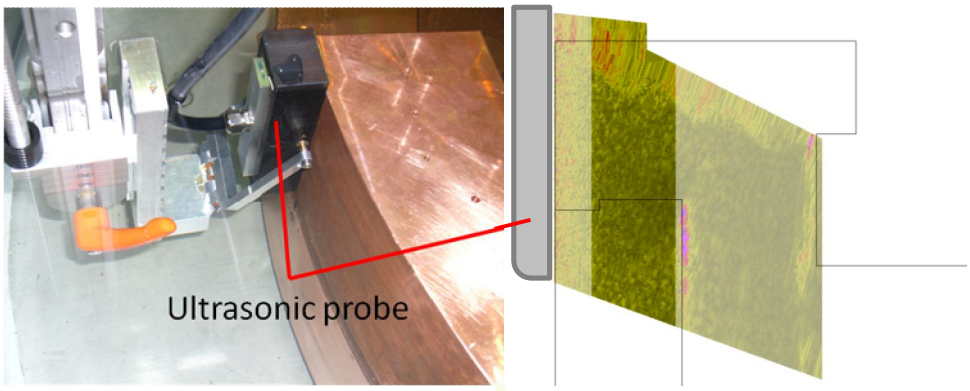

Figure 6. Linear phased array ultrasonic testing of FSW weld.

Nodular cast iron insert is also inspected with ultrasonic methods. The longitudinal wave velocity in nodular cast iron is v = 5600 m/s. Inspection is performed from the outer surface of the insert. First inspection is performed with 5 MHz phased array probe to verify the steel channel edge location and the channel distortion in casting (Figures 7 and 8).

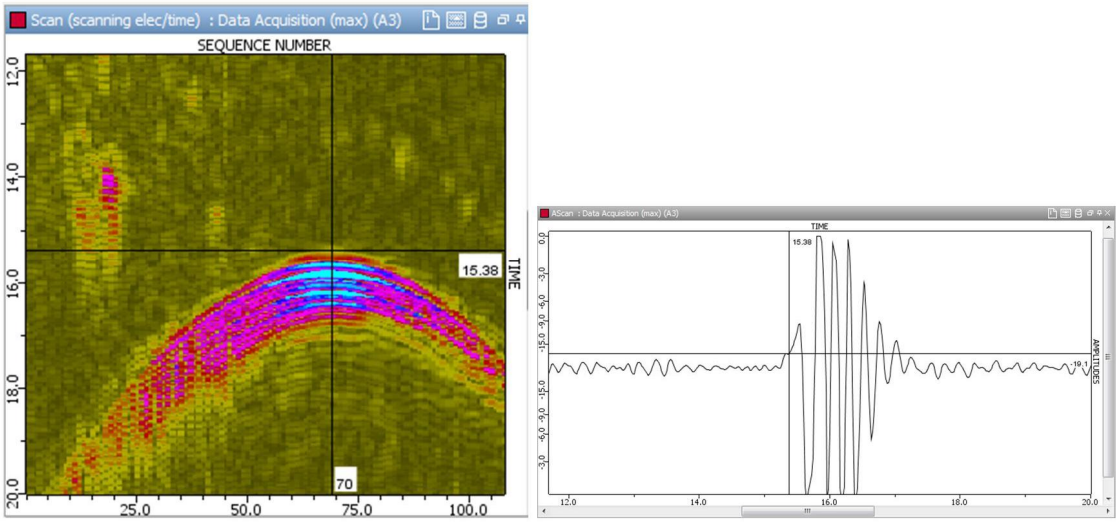

Figure 7. Nearest edge distance point in A-scan is the cross point of the back wall signal and noise where the signal rises up clearly from the noise.

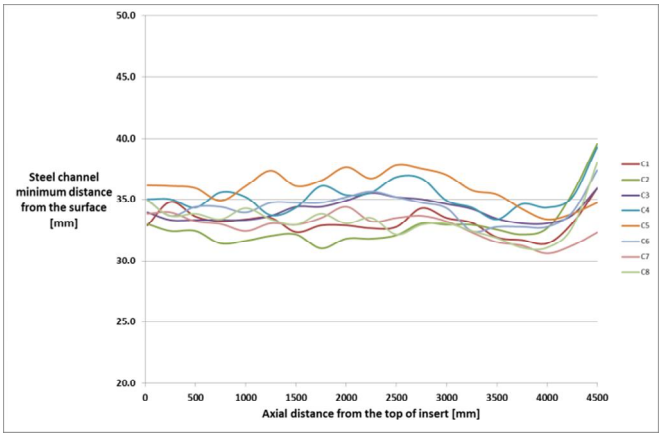

Figure 8. The minimum distance variation of each steel channel from the surface in axial direction measured from the top of the insert in millimetres.

After steel channel inspections 0^0 longitudinal wave curved 5 MHz phased array probe using different focus depths is used for certain areas of insert. Near surface area is inspected with TRL-70^0 longitudinal wave (conventional) probes using four inspection directions (0^0, 90^0, 180^0, 270^0). Technique TRL A means that the scanning occurs in axial direction and TRL C corresponding the scanning direction in circumferential direction. The fourth ultrasonic inspection for insert is performed using transmission technique with 2 MHz phased array probes to detect defects between the steel channels. At the same time with the same probes also transmit-receive inspection is performed for the same area. Due to three different types of inserts (BWR, VVER 440 and EPR) inspection is also highly dependent on the insert type.

3.4 Radiographic testing

Another used volumetric method is radiographic inspection. Radiographic inspection is used for the disposal canister welds and due to thickness of the component it is carried out at the moment with a 9 MeV linear accelerator. The centreline of accelerator beam is directed at 8° angle to the weld [8]. For radio-

graphic inspection a digital x-ray detector is used. As can be seen in Figure 9 the detector is placed behind the outer surface of the canister.

The high energy X-ray equipment used by SKB in Oskarshamn for pilot examination of the lid to canister weld consists of a 9 MeV linear accelerator (Varian Linatron 3000), a collimated line detector and a manipulator system.

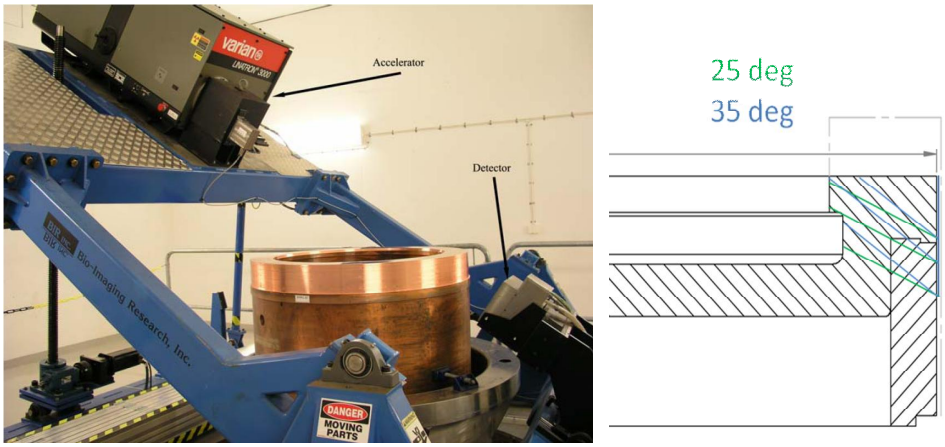

Figure 9. The radiographic setup with accelerator and the detector in SKB Oskarshamn site [8].

The canister will be rotated in a carrier. Rotation speed is controlled by the RT-software that controls the radiation source and the detector. Before placing the canister on the carrier it is important to center it, the distance tolerance is maximum 1.5 mm. 100 % of the weld and the surrounding base material; is inspected. There is a marked zero-point on the canister surface. In the circumferential direction scanning exceeds the total circumference with suitable overlap. The 0 -point and the rotation direction are marked also to the examination plan.

Before the actual measurement of the canister, calibration test for intensity setting shall be carried out to check the proper intensity of the detector. A separate calibration block made of the same material as the canister with known wall thickness is used for calibration. The calibration of the measurement is carried out simultaneously with the weld inspection.

An image quality indicator (IQI) is placed on the detector side surface of the canister so that the calibration hole in IQI is visible on the x-ray image. Because the quality of the image cannot be controlled during scanning, the quality of the picture is monitored afterwards with IQI sensitivity and intensity value.

For examination the exposure voltage is nominal voltage of the 9 MeV x-ray accelerator. The minimum distance from source to object is defined as a factor of maximum allowed geometric unsharpness (Ug).
A minimum contrast ratio is defined for the display in order to evaluate data properly. The images are analysed partly already during the scan in the encapsulation plant.

4. Welding

Lid of the canister is welded with friction stir welding. Friction stir welding and electron beam welding methods have been studied and the final choice was made in 2014 by Posiva Oy.

4.1 Friction stir welding

Friction stir welding (FSW) is a solid state joining method originally developed by TWI. Basic principle is that the rotating tool is plunged between the pieces to be welded when the friction between the tool and the piece generates heat and plasticizes the welded material (Figure 10). Then the tool is moved to the

wanted welding direction. There are many advantages in FSW. For example mechanical properties are good in as-welded state, automation is fairly easy and it can be operated in all welding positions [2].

In spite of advantages in FSW there are several possible defect types in FSW. These include [3,4]:

- pores and porosity
- worm hole
- voids
- oxide inclusions and entrapped oxide
- tool trace material
- incomplete penetration
- joint line hooking
- faying surface flaw

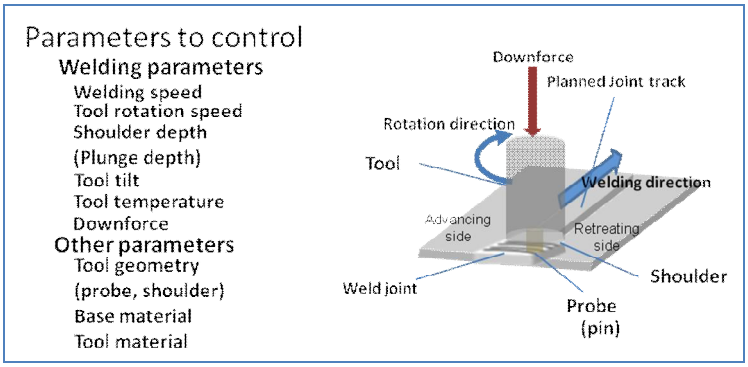

Figure 10. Basic principle of FSW and parameters to control [5].

5. Discussion and comparison to design criteria

Cast iron insert is giving the main mechanical strength to entire disposal canister. Therefore it is essential to identify the criteria to be met. In the shear loading case a semi-elliptical flaw has been identified as the most dangerous flaw. Acceptable dimension of the flaw are 4.5 mm in depth and 27 mm in length [6,7]. As mentioned before for the insert surface area TRL ultrasonic inspection is used. In damage tolerance design $a_{90/95}$ is commonly used as a measure of the minimum size of the reliably detected flaw. With TRL ultrasonic inspection it is shown that in insert inspection this reliably detected flaw is 15.9 mm2. Compared to acceptable dimensions the reliably detected flaw could be almost six times larger. Therefore it can be concluded that this system is adequate for this inspection task. [6]

Above mentioned criteria is of course not the only criteria for the cast iron insert. There are many other criteria for example related to location of steel channels and geometry etc. which also partly applies to copper parts of the canister. These issues are not in the scope of this paper and are not presented in detail.

Copper overpack and the lid are the corrosion resistant and gas tight barrier of the disposal canister. One critical part of the copper canister is the weld. It is known that welding can cause different types of flaws in material as mentioned already earlier. FSW weld is inspected with all four NDT methods in the encapsulation plant. Studies made for SKB [7] have shown that for the copper part of the canister, no kind of postulated crack, defect or cavity of reasonable size has proven to be critical. The copper shell withstands the design loads with a good margin even with large postulated defects. The large variety of material testing that has been conducted during the studies has shown that the cracks in copper blunt under tension load and no crack growth is detected at applicable temperatures. With copper shell the main design criteria is the corrosion barrier and therefore all the found indications with different NDT methods are added together to verify the needed corrosion barrier thickness all over the disposal canister. In final disposal environment creep of the copper shell has been an issue of interest and there are several studies regarding creep behaviour of copper shell.

6. Conclusions

The disposal canister is designed to resist corrosion and to have adequate mechanical strength for final disposal environment. To be able to predict and ensure the integrity of the disposal canister certain design criteria has to be set. To ensure that the criteria are met non-destructive methods for inspections are needed. In this paper the four NDT inspection methods (UT, RT, ET, VT) for inspection of different parts of the disposal canister are presented in brief. All of the four NDT methods detect defects in slightly different directions and are based on different physical principles. The four methods are therefore supplements to each other in inspection of different parts of the disposal canister.

It is shown in different studies [6,7] that applicable criteria for cast iron insert is found and criteria can be verified with used NDT methods. For the copper parts of the canister as well as weld the most important criteria is the adequate corrosion barrier for the final disposal timeline. Studies have shown that the welds can be categorized according the quality and defects have been found [6]. Nevertheless there is still some techniques that need to be improved. At the moment there are lot of studies going on to improve the inspections in the area of non-destructive testing of disposal canisters. These studies include for example probability of detection, simulation, human factors, combination of inspection results etc..

References

1. Raiko, H. Disposal Canister for Spent Nuclear Fuel. Posiva Oy, 2005. Design Report 2005-02.

2. Nicholas, E. D. Developments in the friction-stir welding of metals. ICAA-6: 6th International Conference on Aluminium Alloys, 1998. Toyohashi, Japan.

3. Bird, C. R. and Kleiner, D. The phased array inspection of friction stir welded aluminium plant, Proceedings of OMAE 2004: 23rd International Conference on Offshore Mechanics and Arctic Engineering, Vancouver, Canada, 20 - 25 June 2004.

4. Pitkänen, J. Inspection of Bottom and Lid Welds for Disposal Canisters, Report POSIVA 2010-04, Posiva Oy, 2010.

5. Pitkänen, J. & Lipponen, A. Surface and near surface defect detection in thick copper EB-welds using eddy current testing, Baltica VIII Life Management and Maintenance for Power Plants, Vol. 1, 18-20 May 2010, Helsinki-Stockholm-Helsinki, Finland-Sweden, pp. 240-255.

6. Pavlovic, M., Mueller, C., Ewert, U. & Pitkänen, J. Safe product design – the role of the NDT reliability analysis. MP Materials Testing 04/2013, pp. 270-275.

7. Raiko, H., Sandström, R., Rydén, H. & Johansson, M. Design analysis report for the canister. SKB Technical Report SKB TR-10-28. ISSN 1404-0344, 2010.

8. Pitkänen, J., Haapalainen, J., Lipponen, A. & Sarkimo, M. NDT of Friction Stir Welds PLFW 1 to PLFW 5 (FSWL 98, FSWL 100, FSWL 101, FSWL 102, FSWL 103), NDT Data Report, Working Report 2014-53, Posiva Oy, 2014.

Corrosion and biofouling on stainless steels in Baltic sea water environment: a cooling water pilot study

Maija Raunio, Pauliina Rajala, Outi Priha, Elina Huttunen-Saarivirta & Leena Carpén

VTT Technical Research Centre of Finland Ltd
P. O. Box 1000, FI-02044 VTT, Finland

Abstract

In power plants, a reliable operation of the cooling water circuit is of primary importance. Where natural water is used for cooling, corrosion and biofouling may pose challenges to materials integrity. The brackish water in Baltic sea is characterized by a relatively low salt content and unique microbial communities, thus the material challenges may be different from those occurring in sea water.

In this study, biofouling on and corrosion behaviour of stainless steels AISI 304L (EN 1.4307), AISI 316L (EN 1.4404) and 254 SMO (EN 1.4547) were investigated in a pilot scale cooling water circuit using brackish water of Baltic sea, obtained from Tvärminne zoological station. The pilot was in operation for 8 weeks, during which open circuit potential recording (OCP) was performed. Other electrochemical methods, cyclic anodic and cathodic polarization measurements and electrochemical impedance spectroscopy (EIS) were applied before and at the end of the pilot experiment. The biofilm coverage was calculated on surfaces. In this paper the obtained results are presented and discussed.

1. Introduction

Cooling systems are used to remove heat from components and industrial equipment. Cooling of large industrial facilities, such as chemical factories, petroleum refineries and power plants, is typically carried out using water. Due to the operation temperature range of the cooling water circuit, and the temperature changes that occur due to absorption of heat, it is susceptible to biofouling and scaling. Biological growth on heat exchanger surfaces decreases the water flow and the cooling capacity of the system and enhances corrosion [1-2]. Brackish sea water in the Baltic sea differs from average sea waters in being lower in salinity, higher with respect to oxygen content and lower in temperature [3], and containing a unique fauna of micro- and macro-organisms accommodated to these conditions. Because of the special characteristics of the environment, it is interesting to see how various stainless steels behave in cooling water circulations using brackish sea water. Although the conventional austenitic stainless steels, such as types 304L and 316L, are reasonably corrosion resistant, they are prone to local attack, such as pitting and crevice corrosion in aggressive environments, mainly affected by chlorides, dissolved oxygen and temperature [4]. The pitting corrosion resistance of stainless steels can be achieved by bulk alloying with nitrogen (N), chromium (Cr) and molybdenum (Mo) [4], and described by a so-called pitting resistance equivalent number (PREN). Typically, the higher the PREN value, the greater is materials resistance to

corrosion. For example, for AISI 304L (EN 1.4307), AISI 316L (EN 1.4404) and 254 SMO (EN 1.4547), the PREN values of about 19, 26 and 46, respectively, have been reported [5]. Generally, PREN of about 40 is considered the minimum for sea water pitting resistance [5].

Micro-organisms, i.e., bacteria, archaea, algae and fungi, which exist practically in all natural aqueous environments, have a tendency to attach to and grow on the surfaces of structural materials [1-2,6]. Attachment of micro-organisms and the development of biofilm have been suggested to have an influence on the localized corrosion of passive metals, including stainless steel [1,7-9]. The attack on metal occurs as a result of microbial activity, which creates localized chemical gradients at the metal surface [10-11]. Ennoblement is a phenomenon in which open circuit potential of the metal is elevated easily triggering localized corrosion. Biologically catalysed ennoblement of stainless steels has been detected in natural sea water environments [12] as well as in brackish water [13] and natural fresh waters [14-15]. However, indications also exist that certain types of biofilm may inhibit rather than catalyse the localized corrosion [16].

In this study, corrosion of and biofouling on stainless steels AISI 304L (EN 1.4307), AISI 316L (EN 1.4404) and 254 SMO (EN 1.4547) were investigated in a pilot scale cooling water circuit using brackish sea water from Tvärminne zoological station and being operated for 8 weeks at ambient temperature. Electrochemical results from OCP, anodic and cathodic polarization measurements and EIS are presented and discussed to distinguish the possible differences in the behaviour of the three stainless steels in the cooling water circuit. Microbiological analyses of the biofilms formed on the stainless steels surfaces were performed to define the complex effect of microbes on the corrosion.

2. Materials and methods

2.1 Materials

The materials studied were AISI 304L (EN 1.4307), AISI 316L (EN 1.4404) and 254 SMO (EN 1.4547), from which chemical compositions were analysed with an optical emission spectrometer (Table 1). Surfaces of the samples were as received with a surface finish 2B for AISI 304L and 316L and 2E for 254 SMO. Before the experiment the sample surfaces were cleaned with 100 % ethanol.

Table 1. The measured chemical compositions of the three stainless steels and the calculated PREN values (PREN = % Cr + 3.3 x % Mo)

Material	C	Si	Mn	P	S	Cr	Ni	Mo	Cu	Al	W	V	Ti	Co	Nb	PREN
AISI 304L (EN 1.4307)	0.03	0.48	1.52	0.02	0.001	18.0	9.3	0.23	0.17	0.004	0.04	0.07	<0.01	0.1	0.01	19
AISI 316L (EN 1.4404)	0.02	0.46	1.73	0.03	0.002	17.0	10.0	2.03	0.42	0.006	0.06	0.06	<0.01	0.2	0.03	24
254 SMO (EN 1.4547)	0.01	0.34	0.54	0.02	0.001	20.1	17.7	6.26	0.8	0.017	0.04	0.05	0.01	0.2	0.01	41

The sea water in the water circuit was obtained from 34 m depth, 780 m offshore in front of Tvärminne zoological station (Hanko, Finland, 59°51’32’’N, 23°15’79’’E). Chemical composition of the brackish sea water used in the experiment was analysed before and after the experiment (presented in Results section,

Table 2). Furthermore, water in the circulation was renewed every two weeks; also here, as-received water was analysed.

2.2 Methods

The pilot cooling water circuit (Fig. 1) is a closed water cycle. Water tank, from which the water flowed through the whole circulation, was filled in the beginning of the experiment and changed every two weeks. The samples were attached to Robbins type polyacetal flow-through sample holders: one for samples for electrochemical measurements and one for microbiological specimens. Flow rate of the water was maintained at 6 l/min. The circuit was operated at room temperature for 8 weeks, starting on 17 June 2015.

Electrochemical methods: open circuit potential recording (OCP), cyclic anodic and cathodic polarization measurements and electrochemical impedance spectroscopy (EIS) were used for determining the corrosion behaviour of the materials in the water circuit. Four parallel samples of each material were used. Samples were inserted in a resin with an exposure surface of 3.6 cm^2. An Ag nail in the brackish sea water was used as an Ag/AgCl reference electrode in the potential measurements. The used counter electrode was platinum. Potential values from all electrochemical measurements were converted and shown in saturated calomel electrode (SCE) scale for consistency. Redox potential of the platinum was also monitored regularly during the experiment.

OCP records were initially collected by an Agilent multi-channel recorder every minute, and after 5 days of measurements, the sampling frequency was decreased to 5 minutes, which was retained until the end of the measurement period. OCP measurements were carried out for all parallel samples.

Cyclic polarization curves and EIS measurements were performed before starting the experiment, using new plate specimens, a separate capillary cell, an exposed working electrode area of 3.1 cm^2, and an Ag/AgCl reference electrode filled with saturated KCl, and at the end of the experiment for the exposed specimens using the included Ag nail reference electrodes. Cyclic anodic polarization was conducted (for one of the parallel samples) from OCP to 800 mV vs. Ag/AgCl and back, while cathodic polarization was conducted from OCP to -600mV vs. ref. Scan rate was 0.3 mV/s in both polarization measurements. EIS measurements were conducted for the same sample, for which cathodic polarization was performed by applying alternating current of the potential amplitude of 10 mV (rms) in the frequency range from 100 kHZ to 1 mHz. Polarization and EIS measurements were carried out using a Gamry Instruments potentiostat model Reference 600TM and DC105 and EIS300 software and the data was analysed by using a Gamry Instruments Echem Analyst software. EIS data was then analysed using the software by fitting appropriate electrical equivalent circuits and quantifying the numerical values for the circuit components. After experiment the electrochemical samples were washed with ethanol and air-dried.

Figure 1. Photograph of the pilot cooling water circle.

2.3 Biofilm detection

Six parallel samples for microbiological analysis of each material were included into the cooling water circuit in a Robbins type sample holder, as described above. Two specimens of each material were removed from the system after 4 weeks of experiment and replaced with new specimens. From each time point (4 weeks from the beginning, 4 remaining weeks and whole 8 weeks period) one specimen of each material was analysed with epifluorescence microscopy and one specimen was subjected to molecular biological analyses except for the 8 weeks specimens, both of which went to molecular biological analyses. At 8-weeks sampling epifluorescence microscopy was performed to specimens which had been in OCP measurements.

Coupons for microbiological analyses were subjected to biofilm extraction immediately after they were removed from the cooling water cycle. The biomass from the coupon surfaces was removed by sonicating the coupons for 10 min (Bransonic 2210-DTH, 47 kHz, 70W) in sterile Ringer-solution and thereafter vortexing for 1 min. The biomass suspensions were filtered into Sterivex-GP 0.22 µm filter units (Millipore, Billerica, MA, USA) and stored frozen (-80°C) until DNA was extracted. Subsequently the Sterivex filter units were aseptically broken with a hammer, and the Sterivex filters were cut into pieces with a sterile scalpel and placed into the lysing tube of the DNA extraction kit with sterile forceps. DNA was extracted using Fast DNA Spin Kit for Soil (MP Biomedicals, USA) according to manufacturer's instructions, with the modification that the cells were homogenized in a FastPrep-24 instrument (MP Biomedicals, USA) at 6 m s^{-1} for 3 min.

The bacterial and archaeal biomass on the surfaces of the samples was evaluated with quantitative PCR (qPCR) with SYBR Green based detection of double stranded DNA, using the LightCycler 480 instrument (Roche Diagnostics, Basel, Switzerland). The DNA concentration of all samples was adjusted to $\leq$ 10 ng μl^{-1} prior to qPCR in order to avoid PCR inhibition. For bacteria an approximately 200 bp fragment of the 16S rRNA gene was amplified with primers 358F (5'-CCT ACG GGA GGC AGC AG-3´) and 534R

(5´-ATT ACC GCG GCT GCT GG-3) [17]. The amplification was done in 10 µL reaction volume with KAPA Sybr Fast qPCR Master mix optimized for Roche LightCycler 480 (KAPA Biosystems, USA), 150 nM of each primer and 1 µL of sample DNA. The amplification reaction consisted of initial denaturation at 95°C for 15 min, 45 cycles with 10 s at 95°C, 35 s at 57°C and 30 s at 72°C, a final elongation of 3 min at 72°C, and a melting curve analysis. As an external standard, a dilution series (100 – 10^8 cfu / µL) of *Escherichia coli* VTT E-90418 genomic DNA was used. For archaea an approximately 400 bp fragment of the 16S rRNA gene was amplified with primers A344F (5′-ACG GGG TGC AGC AGG CGC GA-3′) [18] and A744R (5'-CCC GGG TAT CTA ATC C-3') (modified from 744RA of [19]). The amplification was done in 10 µL reaction volume with KAPA Sybr Fast qPCR Master mix optimized for Roche LightCycler 480 (KAPA Biosystems, USA), 300 nM of each primer and 1 µL of template DNA. The amplification reaction consisted of initial denaturation at 95°C for 15 min, 45 cycles with 10 s at 95°C, 35 s at 56°C and 30 s at 72°C, final elongation of 3 min at 72°C, and a melting curve analysis. As an external standard, a dilution series of *Halobacterium salinarum* VTT E-103154^T genomic DNA was used (100 – 10^7 cells / µL).

For epifluorescence microscopy analyses the specimens were stained using Acridine orange (BD 212536) for 2 minutes, rinsed with MQ-water and air dried. Biofilm was detected using Zeiss Axio Imager.M2 epifluorescence microscope using 63×/1.4 Oil Plan-Apochromat objective (Carl Zeiss, Germany). Imaging was performed using AxioCam MRm camera and Zen Pro software.

3. Results

3.1 Electrochemical measurements

Examples of OCP records for the three stainless steels are shown in Fig. 2. OCP for all the specimens started at about 0 mV vs. SCE. A clear increase in OCP (ennoblement) was detected for all the three materials during the experiment. OCP of AISI 304L rose close to 400 mV vs. SCE after 27 days of experiment, and experienced significant scatter, possibly indicating pitting corrosion initiation. OCP of AISI 316L rose to 330 mV vs. SCE after 28 days of experiment and showed only minor scatter compared to that of AISI 304L. Scatters, which are seen at the same time points as water renewals (Fig. 2, arrows), are most likely the consequence of changes in the water oxygen level; in each case, the oxygen content of the water that was circulated in the system decreased towards the end of the two-week period, whereas the fresh water contained relatively more oxygen. OCP of 254 SMO increased close to 400 mV vs. SCE after 27 days of experiment and did not show significant scatter. OCP measurements showed a gap in the data for AISI 304L and 316L between 42 and 53 days due to interference of the measurement, but it can be seen that the potential levels before and after the gap were roughly the same. According to thermodynamics [20] stainless steels are expected to be in the passive zone at these potential ranges, and therefore no general corrosion would be expected, but pitting corrosion, however, is possible.

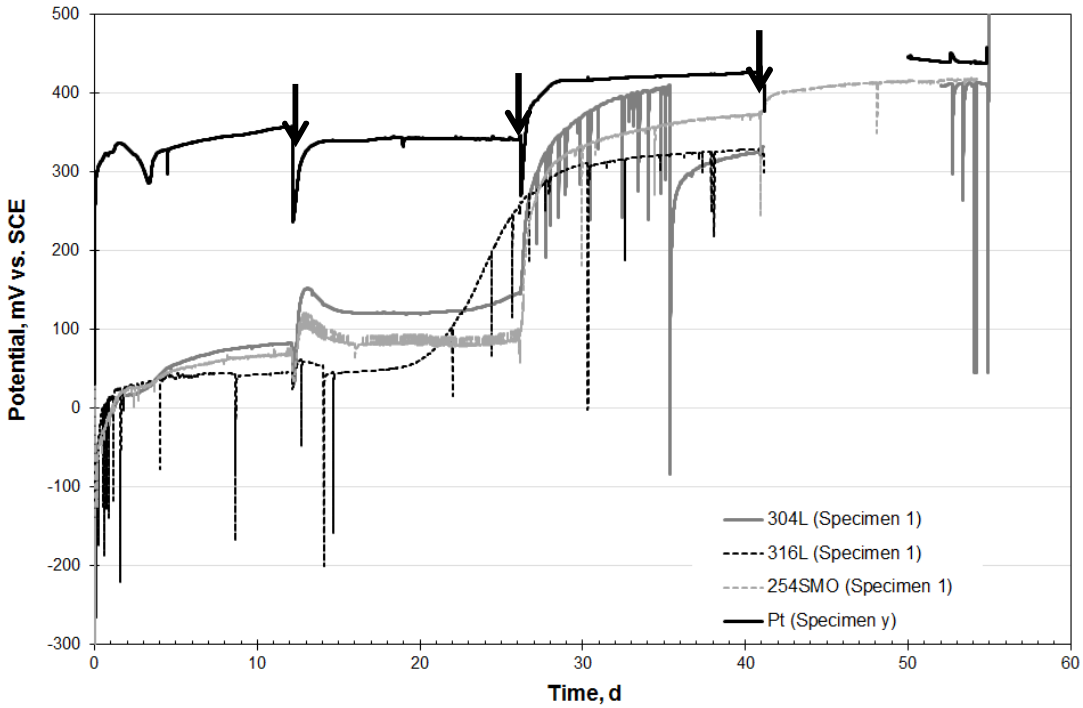

Figure 2. OCP recording of one of the specimen for each material and platinum, time points for renewal of the test water are showed with arrows.

Cyclic anodic polarization curves before (initial state) and at the end (final state) of the experiment are shown in Fig. 3. Final polarization curves indicated that ennoblement had taken place in all three materials, and that the final anodic polarization curves were located at higher potentials compared to the initial curves. For AISI 304L, OCP changed from the initial value of 0 mV vs. SCE to the final potential level of 150 mV vs. SCE for this sample, whereas the OCP measurements in the previous section showed that the OCP of parallel samples increased close to 400 mV vs. SCE. For AISI 316L and 254 SMO, the OCP changed from 50 mV to 400 mV vs. SCE, showing similar or even larger potential changes as described above for OCP measurements. The curves for AISI 304L and 316L indicated the possibility for pitting corrosion, as charged based on the hysteresis loops that were observed in the curves. AISI 304L experienced increase in the pitting potential (P_p) from 400 mV vs. SCE to close to 600 mV vs. SCE. Pitting potential of 316L increased from 500-600 mV vs. SCE to 700 mV vs. SCE), which was similar or slightly smaller change than for 304L. Polarization curve for 254 SMO did not reflect pitting corrosion, as no indication of hysteresis loop formation was obtained. Repassivation potential (P_{rp}) for AISI 304L was 100 mV vs. SCE and for 316L 100-200 mV vs. SCE at the initial state (at the final state, repassivation was not achieved, but according to the Fig. 3 a, P_{rp} is much lower than the initial value at least in the case of AISI 304L). According to [21], P_{rp} for AISI 316L was close to 200 mV vs. SHE (-44 mV vs. SCE) at temperature of 23 °C in chloride content of 0.2 M. Thus, to summarise, hysteresis loops in anodic curves for AISI 304L and 316L indicated the possibility for pitting corrosion, and with progress of the exposure to brackish sea water, the potential difference between OCP and pitting potential became narrower in the case of AISI 316L, implying an easier initiation of pitting corrosion. However, in both cases, the pitting potentials exist at such noble values that they require extremely high oxidation capacity from the environment which may be brought up by e.g. the presence of an oxidizer stronger than oxygen.

Examples of cathodic polarization curves for sample AISI 304L (Fig. 4) confirmed the assumption of a more noble behaviour of the material after the experiment; cathodic polarization curves for AISI 316L and 254 SMO showed a similar behaviour. Furthermore, for AISI 304L and 254 SMO, cathodic reaction was

inhibited in the final state as compared to initial one, as the curves were shifted towards lower current densities. For AISI 316L the final curve showed possible acceleration of the cathodic reaction.

Surface of the electrochemical samples after experiment are shown in Fig. 5 (original samples, no polarization applied). According to stereomicroscopic inspections the surfaces of AISI 304L and 316L were similar and typical of surface finish 2B. Their appearance did not differ remarkably from the initial sample surfaces. The surfaces of specimens of 254 SMO were clearly rougher than those of the other two steel grades, typical of finish 2E. No clear evidence of localized corrosion was detected on any of the test materials. It may also be seen in Fig. 5 that some fouling had occurred on the specimens of AISI 304L and 316L.

a)

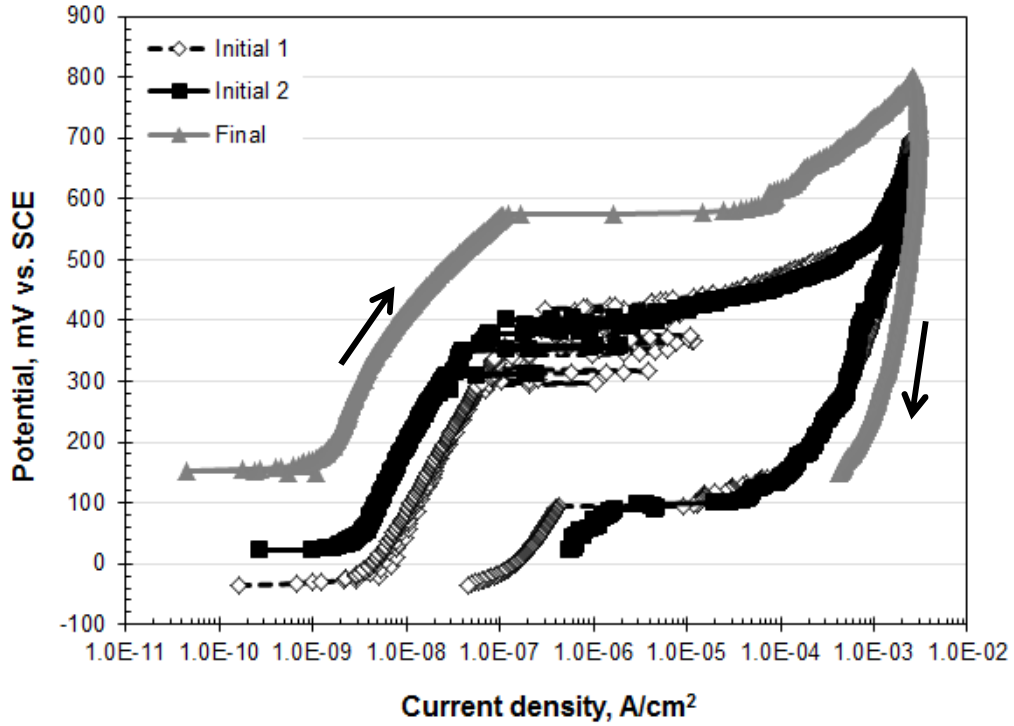
Initial 1
Initial 2
Final
900
800
700
600
500
400
300
200
100
0
-100
Potential, mV vs. SCE
1.0E-11 1.0E-10 1.0E-09 1.0E-08 1.0E-07 1.0E-06 1.0E-05 1.0E-04 1.0E-03 1.0E-02
Current density, A/cm²

b)

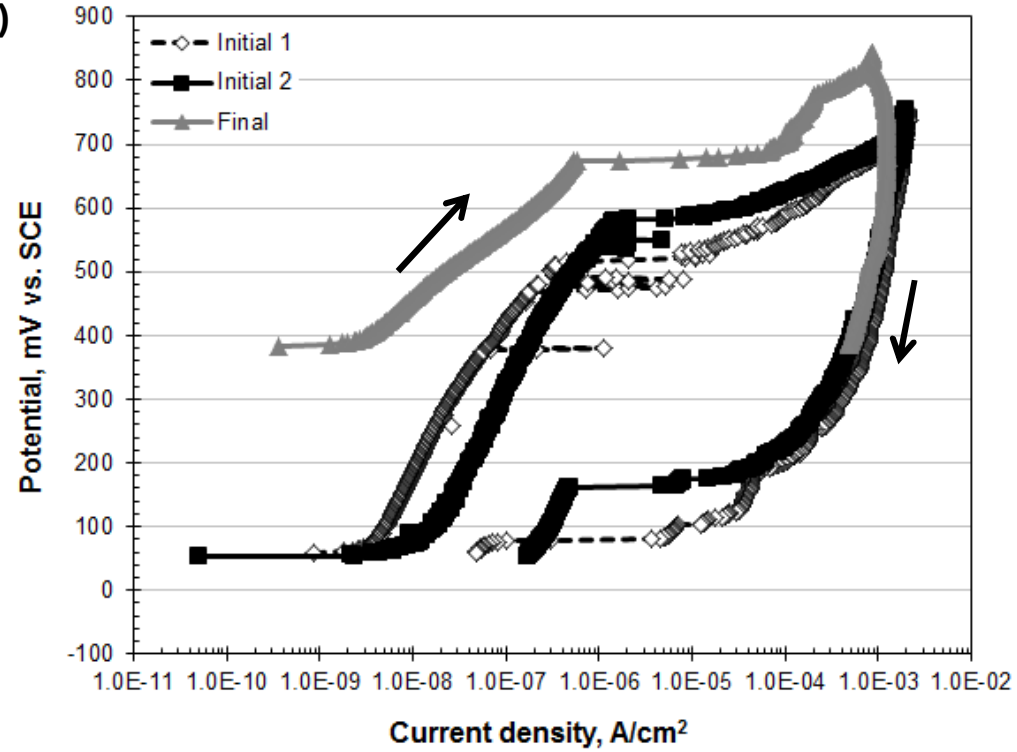
Initial 1
Initial 2
Final
900
800
700
600
500
400
300
200
100
0
-100
Potential, mV vs. SCE
1.0E-11 1.0E-10 1.0E-09 1.0E-08 1.0E-07 1.0E-06 1.0E-05 1.0E-04 1.0E-03 1.0E-02
Current density, A/cm²

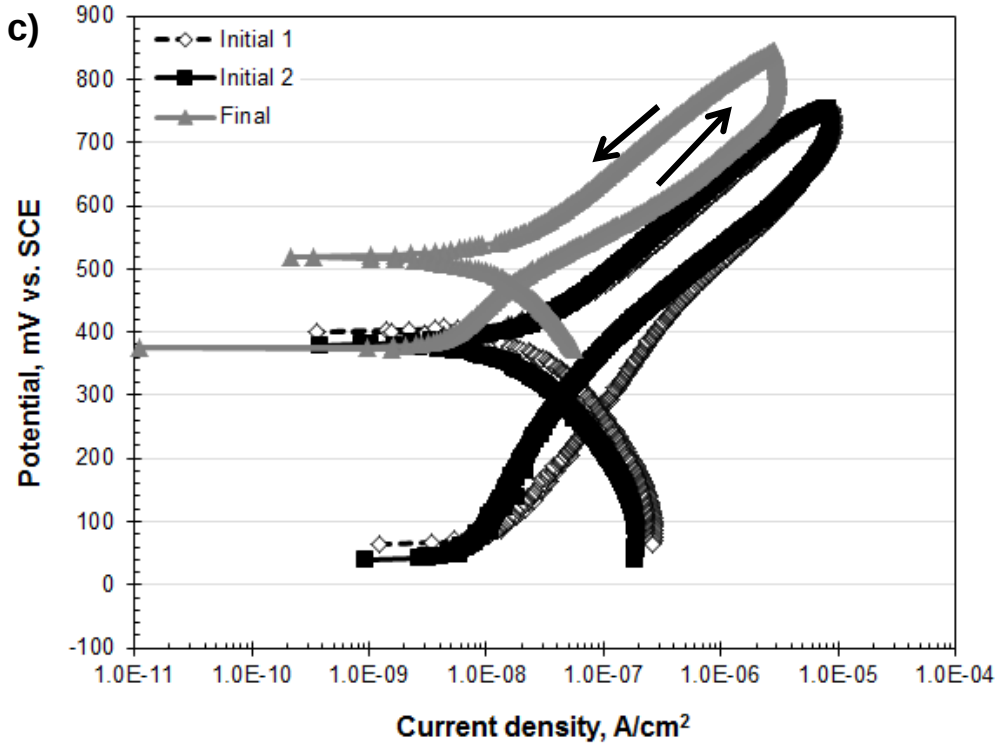

Figure 3. Cyclic anodic polarization curves before and after the experiment for a) AISI 304L, b) AISI 316L and c) 254 SMO.

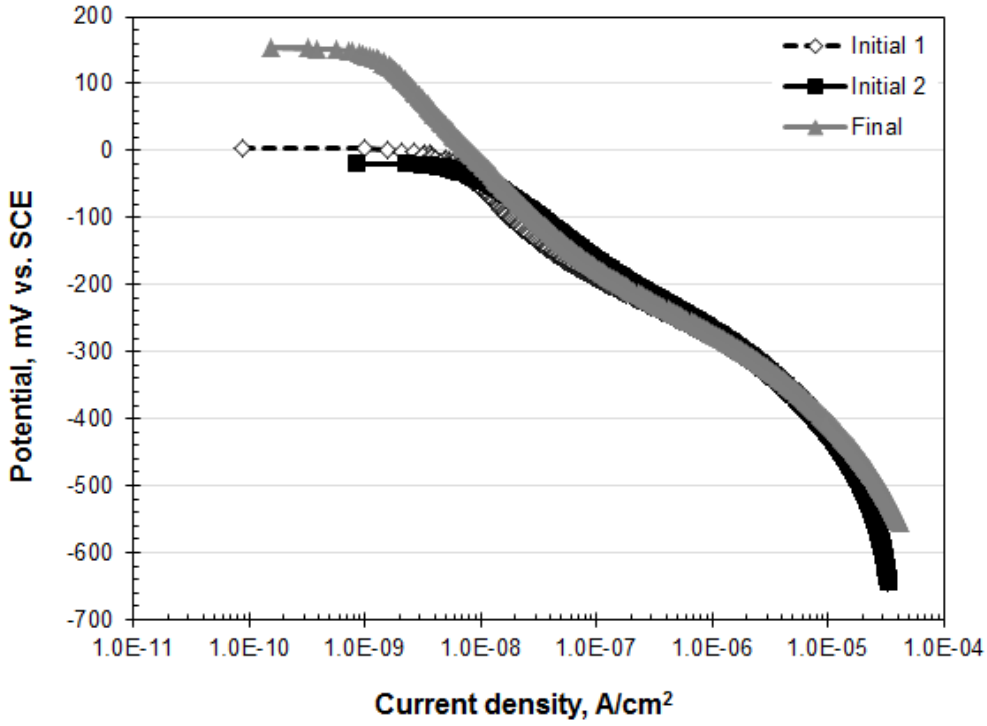

Figure 4. Cathodic polarization for AISI 304L before and after the experiment.

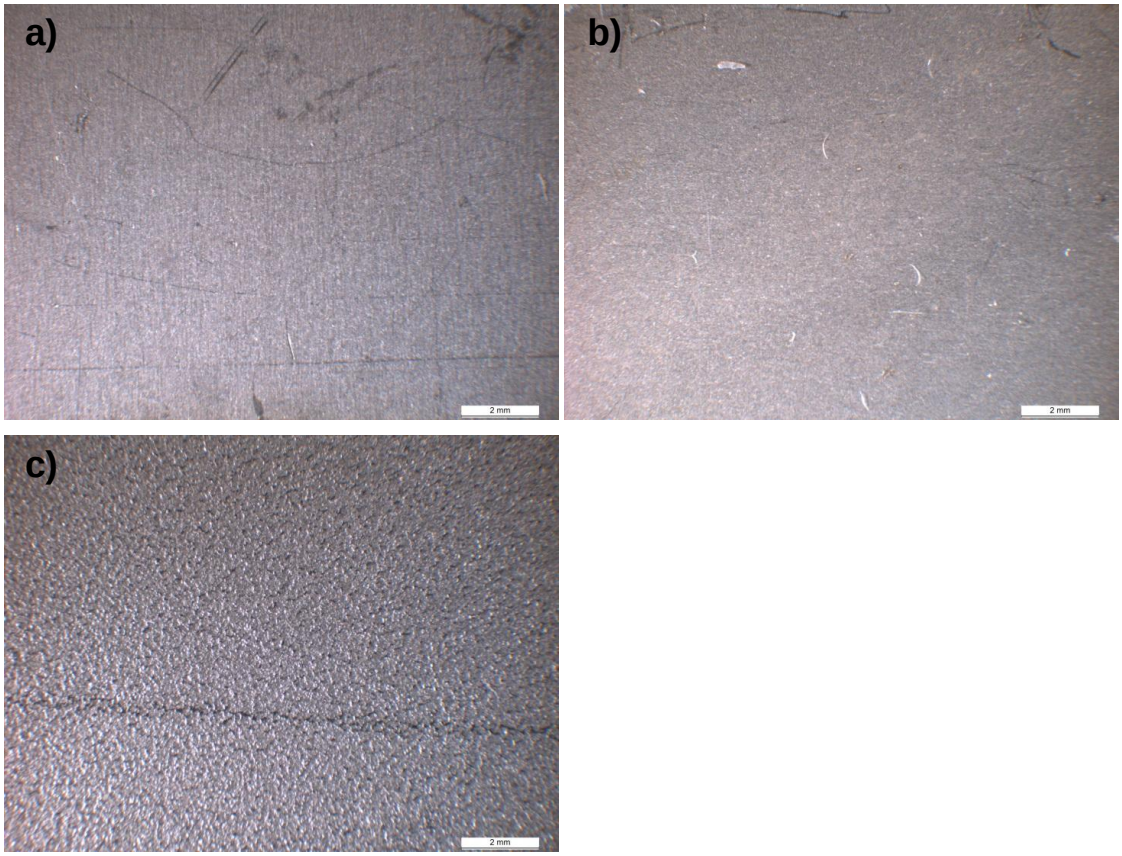

Figure 5. Surfaces of the electrochemical samples after experiment, stereomicroscopic inspection (original samples, no measurements applied): a) AISI 304L, b) AISI 316L and c) 254 SMO. Surfaces appeared similar compared to the initial sample surfaces.

Example of collected EIS spectra is shown in Fig. 6, and the numerical values, describing for the two-time constant system behaviour, for all the materials before and after the experiments are shown in Table 2. For most of the cases, resistance values of R_1 and R_2 increased during the experiments, indicating improved resistance to corrosion. This may be a result of thickening of the passive film or development of the (protective) biofilm, with the latter explanation being more probable. In the case of 254 SMO, the values for n_1 were slightly lower than for the other two materials, indicating slightly more irregular electrolyte-metal interface. This observation is consistent with findings from specimen photographs (Fig. 5).

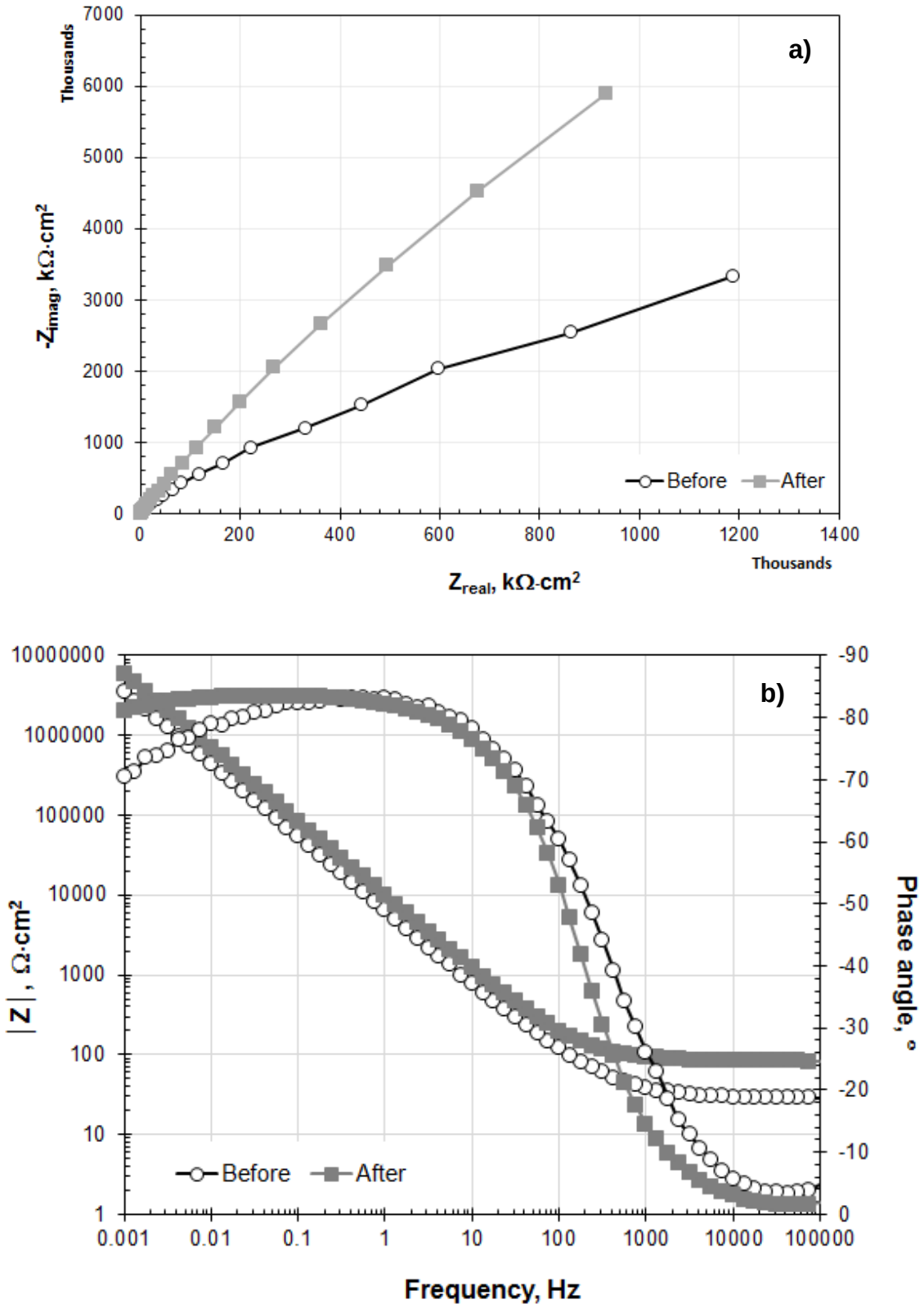

Figure 6. EIS spectra for 304L: a) Nyquist plot, b) Bode plots.

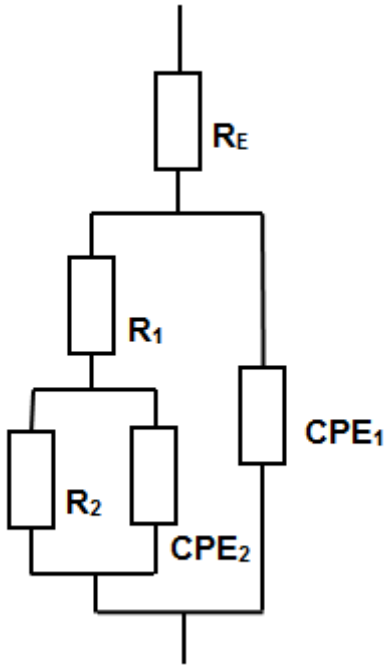

Figure 7. Electrical equivalent circuit used for data modelling.

Table 2. Numerical values extracted from EIS data modelling using electrical equivalent circuit shown in Fig. 7. R is the resistance, C is the capacitance and n the constant phase element parameter obtaining values from 0 to 1 (n=1 represents real capacitance).

Alloy	Timing	R_1, Ω·cm^2	C_1, µF/cm^2	n_1	R_2, MΩ·cm^2	C_2, µF/cm^2	n_2
AISI304L/ EN1.4307	Initial	164	11	0.91	13	14	0.93
AISI304L/ EN1.4307	Final	310	8	0.93	220	11	0.91
AISI316L/ EN1.4404	Initial	186	7	0.91	27	25	0.93
AISI316L/ EN1.4404	Final	3035	9	0.90	231	7	0.92
254SMO/ EN1.4547	Initial	302	7	0.86	41	5	0.96
254SMO/ EN1.4547	Final	33	2	0.89	209	24	0.92

3.2 Water analysis

Water analysis of the initial and renewed brackish sea water as well as from the water at the end of the experiment is shown in Table 3. The initial and renewed values include the lowest and highest values from all the sea water inputs. The amount of manganese (Mn) was lower at the end of the experiment than in the initial and renewed waters; the decreased level of manganese might indicate microbial activity. However, the level of sulphate (SO_4^{2-}) was higher at the end of the experiment than in the initial and renewed

waters, indicating that no remarkable sulphate reduction had taken place. The pH level and alkalinity of the sea water had slightly decreased during the experiment.

Table 3. Water analysis of the initial and renewed water as well as from the water at the end of the experiment. Initial and renewed water includes minimum and maximum values from all the water inputs.

Element	Initial and renewed waters	Water at the end
Al (mg/l)	<0.010	<0.010
Ca (mg/l)	70.6- 84.4	72.2
Fe (mg/l)	0.0026- 0.0313	0.0034
Mg (mg/l)	187- 219	178
Mn (mg/l)	0.00155- 0.00713	<0.00050
Na (mg/l)	1560- 1910	1800
pH	7.81- 7.86	7.71
Alkalinity (mmol/l)	1.65- 1.78	1.63
SO_4^{2-} (mg/l)	277-477	491
Cl^- (mg/l)	3400-3820	3430
NO_3^- (mg/l)	<2.0- 2.5	<2.00
NO_2 (mg/l)	<0.6-3.0	<0.800
NH_4^+ (mg/l)	<0.05- 0.303	0.255
TOC (mg/l)	<2.50- 8.74	4.81
PO_4^{3-} (mg/l)	<0.04- 0.4	0.056

3.3 Biofilms

According to microscopy analyses, heterogeneous biofilm, containing structures resembling bacteria, fungi, algae, and protozoa were found on the stainless steel surfaces (Figs. 8-9). Quantitative PCR was used to determine the number of bacterial and archaeal 16S rRNA genes and thus estimate the amount of bacteria and archaea on the surfaces. No significant differences in biofouling on different materials were detected. During the first 4 week period the number of bacteria was in the range of 10^5/cm^2 and that of archaea 10^2-10^3/cm^2. During the second 4 week period biofouling was slightly more intensive, the number of bacteria being 10^5-10^6/cm^2, and number of archaea 10^4-10^5/cm^2. Biofilm formation continued during the whole experiment period and the number of bacteria was in the range of 10^6/cm^2 and that of archaea 10^5/cm^2 after 8 weeks of exposure.

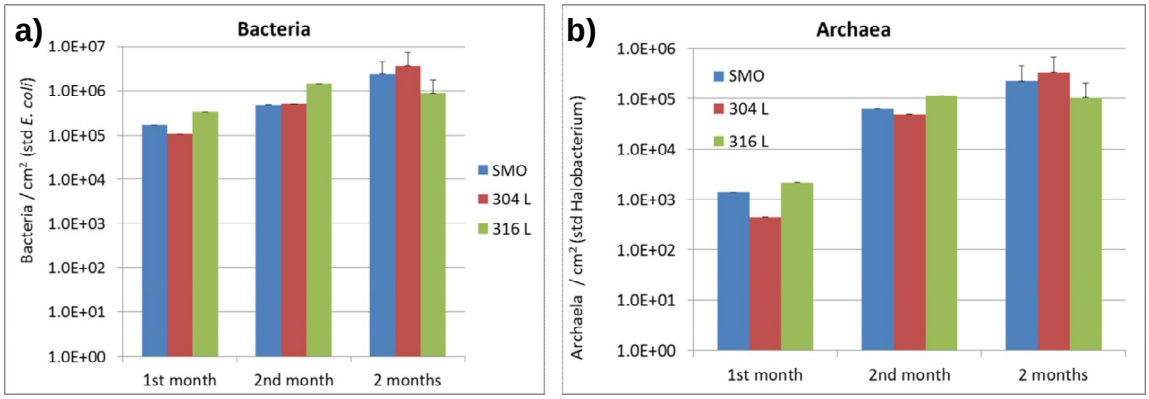

Figure 8. Quantity of bacteria (a) and archaea (b) on the coupon surfaces, determined using quantitative PCR.

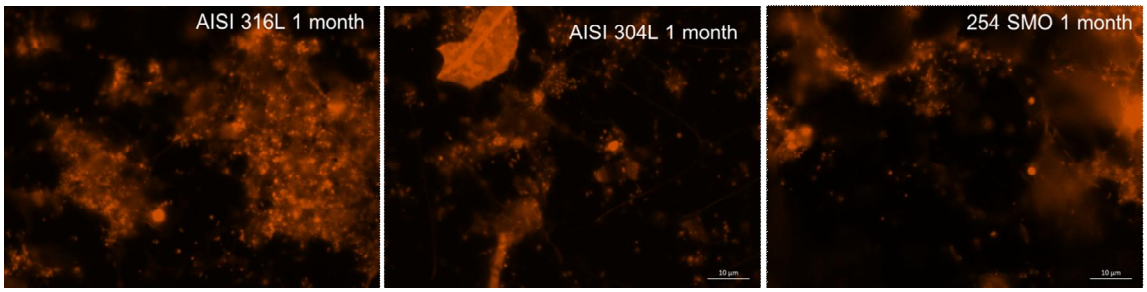

Figure 9. Epifluorescence microscopy images of coupons after 1 month exposure.

4. Discussion

Differences in the behaviour of stainless steels AISI 304L, AISI 316L and 254 SMO were detected in pilot cooling water circuit using the brackish sea water. As mentioned above, the corrosion resistance of 254 SMO was predicted to be highest of the studied stainless steels based on the amounts of chromium, nitrogen, and molybdenum in the alloy. The results show that 254 SMO did not experience or show any type of indication of the possibility for localized corrosion, whereas the findings for AISI 304L and AISI 316L revealed the possibility for pitting corrosion and/or metastable pitting. Ennoblement took place in all the three stainless steels, probably as a result of the accumulation of the biofilm. EIS results demonstrated the greatest increase in resistance values for AISI 316L, suggesting the most efficient protective scale formation. However, the anodic polarization results suggested the possibility for pitting corrosion for AISI 304L and 316L, yet only under conditions of extremely high oxidation capacity. Under OCP conditions, such high potential values were not reached and no clear evidence of pitting corrosion was obtained. However, for example, the disinfection of the water by the use of, e.g., ozone or hypochlorite, is not recommended in the systems involving 304L and 316L, because these oxidisers may increase the potential of the material to the level where pitting is possible. Also longer exposure in a pilot circuit could have induced pitting corrosion in 304L and 316L as has been shown in earlier studies either in the laboratory conditions [13,22] or in the actual Baltic sea [23].

Pitting corrosion of materials in chloride containing environments, like sea water, is one of the most widely encountered problems in corrosion studies [4]. As mentioned before, brackish sea water differs from average sea water. Ions know to inhibit pitting corrosion of stainless steels in Cl^- -containing solutions are, to mention few, OH^-, NO_3^-, CH_3COO^-, ClO_4^-, ReO_4^-, CrO_4^-, MoO_4^{2-}, and SO_4^{2-} [24]. According to the water analysis (Table 2) at least NO_3^- and SO_4^{2-} (and also OH^-) were detected in the brackish sea water. However, it should be noticed that the amount of NO_3^- and SO_4^{2-} was low in the brackish sea water compared to the amount of chloride ions, indicating that these ions might have played a negligible role in inhibiting the pitting corrosion of stainless steel.

Biofilm was formed on the stainless steel surfaces in this pilot scale system. The intensity of biofilm formation was linked to the temporal changes, and was more intensive in the second half of the experiment, late summer. Especially archaeal part of biofilm was increased during the second half of the experiment. The effect of the biofilm formed on the stainless steel surfaces was protective, since the biofilm/scale formation increased the surface resistance of the alloys. The potential role of some biofilms in corrosion protection has been suggested before [25-26].

In this study the effect of temperature changes was not considered, though temperature variation will remarkably affect the corrosion and scaling behaviour in the cooling water systems [4]. Due to the short experiment period, differences between the initial and final state are not as pronounced as would be for longer exposure periods. Another longer experiment in the cooling water circle was started at the end on year 2015, the results of which will be presented later on.

The results showed that during as short a period as 8 weeks, biofouling occurs on stainless steels in cooling water system using brackish sea water of Baltic sea. On all three materials, biofouling occurred equally, i.e., there were no significant differences in biofouling on different materials. However, there were differences in the corrosion behaviour between the materials, with common austenitic grades AISI 304L

and 316L, showing the possibility of pitting corrosion under extremely highly oxidizing conditions even during short exposure periods, while 254 SMO was shown to be intact to pitting corrosion in the used brackish sea water.

5. Conclusions

In this study, the corrosion and biofouling on stainless steels AISI 304L (EN 1.4307), AISI 316L (EN 1.4404) and 254 SMO (EN 1.4547) was investigated in a pilot scale cooling water circuit using brackish water of Baltic sea, obtained from Tvärminne zoological station. Conclusions made based on the results are:

- Cyclic anodic polarisation curves for AISI 304L and AISI 316L disclosed the possibility for pitting corrosion during relatively short exposure periods under highly oxidising conditions, whereas 254 SMO was not revealed to be susceptible to pitting corrosion in the used brackish sea water. These findings are consistent with the PREN values calculated (Table 1) and the recommendation of PREN 40 for sea water environment.
- Ennoblement was detected for all the three materials. The pitting potential of AISI 304L was the lowest among the studied alloys. Pitting potential shifted upwards during the experiment for AISI 304L and 316L.
- The effect of the biofilm formed on the stainless steel surfaces was protective: increase in surface resistance of the alloys was detected, as well as slight changes in pitting tendency.

Acknowledgement

The work was carried out within the Finnish Metals and Engineering Competence Cluster (FIMECC) and its Breakthrough Steels and Applications (BSA) program. We gratefully acknowledge the financial support from the participating companies and the Finnish Funding Agency for Technology and Innovation (Tekes). Tvärminne zoological station is thanked for enabling the water acquisitions. VTT Technical Research Centre of Finland Ltd is also acknowledged for funding and supporting the experiments. The laboratory personnel at VTT, Seppo Peltonen and Tiina Ikäläinen, are thanked for conducting the experiments. Tarja Nordenstedt and Helena Hakuli are thanked for their skilful technical assistance.

References

1. E. Huttunen-Saarivirta, M. Honkanen, T. Lepistö, V.-T. Kuokkala, L. Koivisto, and C.-G. Berg, “Microbiologically influenced corrosion (MIC) in stainless steel heat exchanger,” Applied Surface Science, vol. 258, no. 17, pp. 6512–6526, 2012.

2. R. Lane, “Under the microscope: Understanding, detecting, and preventing microbiologically influenced corrosion,” *Journal of Failure Analysis and Prevention*, 2005.

3. L. Carpén and T. Hakkarainen, “Ruostumattomien terästen mikrobikorroosio Itämeren vedessä,” 1997.

4. G. Latha and S. Rajeswari, “PITTING AND CREVICE CORROSION BEHAVIOUR OF SUPERAUSTENITIC STAINLESS STEELS IN SEA WATER COOLING SYSTEMS,” pp. 429–456.

5. M. Davies and P. J. B. Scott, *Guide to the use of materials in waters*. Houston, USA: NACE international, 2003.

6. C. H. Liang, H. Wang, and N. B. Huang, “Effects of sulphate-reducing bacteria on corrosion behaviour of 2205 duplex stainless steel,” *Journal of Iron and Steel Research International*, vol. 21, no. 4, pp. 444–450, 2014.

7. L. Carpen, L. Raaska, K. Kujanpää, and T. Hakkarainen, “Microbially induced corrosion of stainless steels in technical applications involving natural water,” in *COST 520 Biofouling and Materials, Final Workshop*, 2002.

8. X. Shi, R. Avci, M. Geiser, and Z. Lewandowski, “Comparative study in chemistry of microbially and electrochemically induced pitting of 316L stainless steel,” *Corrosion Science*, vol. 45, no. 11, pp. 2577–2595, 2003.

9. M. Geiser, R. Avci, and Z. Lewandowski, “Microbially initiated pitting on 316L stainless steel,” *International Biodeterioration and Biodegradation*, vol. 49, no. 4, pp. 235–243, 2002.

10. I. B. Beech, “Corrosion of technical materials in the presence of biofilms—current understanding and state-of-the art methods of study,” *International Biodeterioration & Biodegradation*, vol. 53, no. 3, pp. 177–183, 2004.

11. I. B. Beech and J. Sunner, “Biocorrosion: towards understanding interactions between biofilms and metals,” *Current Opinion in Biotechnology*, vol. 15, no. 3, pp. 181–186, 2004.

12. P. W. Baker, K. Ito, and K. Watanabe, “Marine prosthecate bacteria involved in the ennoblement of stainless steel,” *Environmental Microbiology*, vol. 5, no. 10, pp. 925–932, 2003.

13. K. Mattila, L. Carpen, L. Raaska, H.-L. L. Alakomi, T. Hakkarainen, and M. S. Salkinoja-Salonen, “Impact of biological factors on the ennoblement of stainless steel in Baltic seawater,” *Journal of Industrial Microbiology and Biotechnology*, vol. 24, no. 6, pp. 410–420, 2000.

14. P. Linhardt, “Twenty years of experience with corrosion failures caused by manganese oxidizing microorganisms,” *Materials and Corrosion*, vol. 61, no. 12, pp. 1034–1039, 2010.

15. L. Carpén, L. Raaska, K. Kujanpää, and T. Hakkarainen, “Effects of Leptothrix discophora on the potential behavior of stainless steel,” *Materials and Corrosion*, vol. 54, no. 7, pp. 515–519, 2003.

16. T. J. Hakkarainen, “Microbiologically influenced corrosion of stainless steels – What is required for pitting?,” vol. 509, pp. 503–509, 2003.

17. G. Muyzer, E. de Waal, and A. Uitierlinden, “Profiling of complex microbial populations by denaturing gradient gel electrophoresis analysis of polymerase chain reaction-amplified genes coding for 16S rRNA,” *Applied and Environmental Microbiology*, vol. 59, pp. 695–700, 1993.

18. N. Bano and J. Musarrat, “Characterization of a novel carbofuran degrading Pseudomonas sp. with collateral biocontrol and plant growth promoting potential,” *FEMS Microbiology Letters*, vol. 231, no. 1, pp. 13–17, 2004.

19. S. M. Barns, R. E. Fundyga, M. W. Jeffries, and N. R. Pace, “Remarkable archaeal diversity detected in a Yellowstone National Park hot spring environment.,” *Proceedings of the National Academy of Sciences of the United States of America*, vol. 91, no. 5, pp. 1609–1613, 1994.

20. D. A. Jones, *Principles and Prevention of Corrosion*. New York: Macmillan Publishing Company, 1992.

21. A. Anderko, N. Sridhar, and D. S. Dunn, “A general model for the repassivation potential as a function of multiple aqueous solution species,” *Corrosion Science*, vol. 46, no. 7, pp. 1583–1612, 2004.

22. L. Carpen, L. Raaska, K. Mattila, M. Salkinoja-Salonen, and T. Hakkarainen, “Laboratory simulation with natural bacteria populations,” in *Aspects of Microbially Induced Corrosion papers from EUROCORR ’96 and The EFC Working Party on Microbial Corrosion*, Institute of Materials, European Federation of Corrosion, 1997, Number 22, pp. 113–122.

23. L. Carpen, L. Raaska, M. Salkinoja-Salonen, and T. Hakkarainen, “Microbially induced corrosion of stainless steels in the Baltic seawater,” in *Proceedings of International Conference on Microbially Influenced Corrosion*, 1995, pp. 11/1–11/13.

24. C. J. Donohoe and G. O. H. Whillock, “Localized Corrosion of Stainless Steel in a Nuclear Waste Cooling Water System-Part 1: Crevice Corrosion Studies,” *Corrosion*, vol. 69, no. 2, pp. 107–121, 2013.

25. R. Zuo, E. Kus, F. Mansfeld, and T. K. Wood, “The importance of live biofilms in corrosion protection,” *Corrosion Science*, vol. 47, no. 2, pp. 279–287, 2005.

26. M. Grooters, K. Harneit, M. Wöllbrink, W. Sand, R. Stadler, and W. Fürbeth, “Novel steel corrosion protection by microbial extracellular polymeric substances (EPS) - Biofilm-induced corrosion inhibition,” *Advanced Materials Research*, vol. 20–21, pp. 375–378, 2007.

Series title and number

VTT Technology 261

Title	Baltica X International Conference on Life Management and Maintenance for Power Plants
Author(s)	Pertti Auerkari (ed.)
Abstract	The Conference aims to provide an updated review on current experience and emerging technology, tools and solutions for managing the condition and life of materials, components and facilities in power and process plants, including the nuclear side. At a time of a clear impact from public energy policies, turbulent fuel market, and disruptive technology, Baltica X is addressing the technical options to support the operational economy of both new and ageing plants. Venues: 7.–8.6.16 M/S Silja Symphony, 9.6.16 Radisson Blu Royal Hotel, Helsinki
ISBN, ISSN, URN	ISBN 978-951-38-8435-2 (USB) ISBN 978-951-38-8436-9 (URL: http://www.vttresearch.com/impact/publications) ISSN-L 2242-1211 ISSN 2242-122X (Online) http://urn.fi/URN:ISBN:978-951-38-8436-9
Date	June 2016
Language	English
Pages	618 p.
Name of the project	BALTICA X
Commissioned by	VTT, Helen, Fortum, TVO
Keywords	power plant, process plant, nuclear plant, boiler, turbine, condition, life, fuel, maintenance, inspection, monitoring, risk, reliability, material, damage, degradation
Publisher	VTT Technical Research Centre of Finland Ltd P.O. Box 1000, FI-02044 VTT, Finland, Tel. 020 722 111

VTT TECHNOLOGY 261

Baltica X

Baltica X

International Conference on Life Management and Maintenance for Power Plants

ISBN 978-951-38-8435-2 (USB)
ISBN 978-951-38-8436-9 (URL: http://www.vttresearch.com/impact/publications)
ISSN-L 2242-1211
ISSN 2242-122X (Online)
http://urn.fi/URN:ISBN:978-951-38-8436-9